

Displacement stability revisited – A new criterion for the onset of viscous fingering

Jos G. Maas^{1,*}, Niels Springer², Albert Hebing¹, and Steffen Berg³

¹PanTerra Geoconsultants BV, Leiderdorp, The Netherlands

²GEUS, København, Denmark

³Shell Global Solutions International B.V., Amsterdam, The Netherlands

Abstract. Any process in which a high mobility fluid is displacing a lower mobility fluid is prone to instability. Pertinent present-day examples are CO₂ injection for carbon capture and sequestration (CCS), gas injection for underground storage or for pressure maintenance. Over the years, several criteria have been developed to predict the onset of viscous fingering. However, there is no consensus on what criterion is truly valid and more recently several studies have been reported to empirically decide on what criterion is the most reliable. In this work, we present a new approach derived from first principles. The results are shown to unify all earlier derived criteria whether for porous rock, or for Hele-Shaw cells, with and without gravity, immiscible and miscible, through proving that these are special cases, of limited validity, of a more general formulation. The new criterion is more restrictive in terms of viscosity ratio than the Hagoort shock-front mobility ratio, but less restrictive than the straightforward viscosity ratio. 2-Phase flow simulations have been conducted to demonstrate the validity over a wide parameter range. In addition, we have studied the impact of fingering in SCAL laboratory tests employing the unsteady-state (“Welge”) technique. The results were analysed through interpretation-by-simulation using the automatic history matching tool AutoSCORES.

1 Introduction

The study of displacement stability has a very long history and goes back to at least 1857 when Jevons [1] reported on the cirrus form of cloud. Lord Rayleigh [2] was prompted by the observations of Jevons to analyse displacement stability using linear perturbation theory and presented a criterion for the onset of instability based on density gradients in 1883. It appears that the first sequel to this work only came about in the late 1940’s. de Korver and Douwes Dekker [3] (1949) derived a criterion for stable displacement of viscous oil by brine for the Schoonebeek field in the Netherlands. Their analysis is based on the behaviour of a macroscopic “gravity tongue” rather than on the analysis of the fate of a small wave-like perturbation that Lord Rayleigh conducted. As we will demonstrate in section 2, both approaches produce the same result. The criterion derived by de Korver and Douwes Dekker includes a critical displacement velocity that depends on both density and viscosity differences between the brine and the oil.

Also in 1949, Taylor [4] presented a linear perturbation analysis of wave-like perturbations of an accelerating interface between two immiscible liquids moving in open space, i.e. not within a porous medium, so viscosities do not enter. He showed that perturbations will grow initially exponentially or rather shrink exponentially dependent on the density difference. In a companion paper, Lewis [5] presented experimental results on finger growth in a

“vertical channel” that were in line with the theoretical predictions.

Hill [6] (1952) published the derivation for the onset of instability in a sugar solution displaced by water in a vertical column filled with charcoal, as used in industrial sugar refining operations. Through an analysis of pressure gradients at both sides of the interface between the two liquids, he showed that both density and viscosity differences control a critical displacement velocity for instabilities to develop. He tested the theory successfully with experiments conducted in rectangular perspex cells, filled with glass beads.

Dietz’s [7] (1953) well-known (see e.g. [8, 9]) stability criterion is a direct extension of the work published by de Kramer and Douwes Dekker [3].

Saffman and Taylor [10] published their land-mark paper in 1958. They introduced the effect of interfacial tension (IFT) as counter-acting mechanism against the viscous-unstable growth into the linear perturbation analysis and show that a continuum of wavelengths λ would exist for fingers to develop, with the stability index (initial exponential growth factor) dependent on λ . A critical wavelength and a critical displacement velocity were identified. On a general note, they claim the experimental conditions in so-called Hele-Shaw [11] cells (two parallel glass plates with an open channel in between) to be representative for the study of displacement stability in porous media. It is of interest that Saffman and Taylor make

* Corresponding author: jgmaas@gmail.com

a remark on Dietz's work: "did not explicitly consider stability of the interface". In section 2, as for the case with the analysis by Lord Rayleigh, we will demonstrate that as far as determining the onset of instability, both approaches give the same result. Another point of interest is that the introduction of IFT created an important problem: the solution for the stability index becomes unbound for IFT moving to zero. This problem has been studied by a number of authors [e.g. 12, 13, and 14]

As also observed by Homsy [15] in his overview paper, Chuoke¹ et al. [16] (1959) published an approach into developing a stability criterion closely related to the work by Saffman and Taylor [10] (who actually referenced Chuoke). Chuoke et al. show that a wavelength of maximum instability growth rate can be identified (by subsequent authors referred to as "most dangerous" wavelength or wave number, see e.g. [17, 18, and 19]). Note that Chuoke et al. [16] use a loosely defined "effective" IFT that needs to be determined experimentally and may depend on rock and fluids (and on IFT between the two fluids for that matter).

Dumoré [20], building on Hill's work [6], derived a stability criterion in 1964 including a critical displacement velocity for a miscible drive under reservoir conditions.

In 1974 Hagoort [21] derived a new stability criterion by assuming that saturations upstream of the displacement front in porous rock are close to the shock front saturation. Hagoort derived his criterion first with the assumption that the capillary pressure between brine and oil equals zero. He then proposed an "energetic" approach to include the effect of capillary pressure.

Finally, the work by Chuoke et al. [16] was extended by Peters and Flock [22] (1979) with the introduction of spatial boundary conditions for displacements with circular and rectangular cross-sections. Due to these boundary conditions, the continuum spectrum of wavelengths of the perturbations was replaced by a discrete spectrum. As a result, two new stability criteria (one for the circular and one for the rectangular case) appeared that honour the exclusion of the continuum spectrum of wavelengths.

To the best of our knowledge, Peters and Flock are the last authors who proposed a criterion for the onset of instability that can be calculated analytically.

Numerous authors [see e.g. 23, 24, 25, 26, 27, and 28] have studied the growth of fingers once that these become into existence. Often, a criterion for the onset of instability is not mentioned explicitly. If it is, various choices seem to have been made: just the viscosity ratio M_μ (see nomenclature at the end of this paper) being larger than unity, or the end-point mobility ratio M_{end} larger than unity, without prove of validity.

Others have conducted experiments and/or simulations [29] to establish which criterion is closest to reality. The experiments fall into three classes: a) experiments in Hele-Shaw cells or micro models, using optical means to detect or monitor fingering [e.g. 30, 31, and 32]; b) experiments on porous media using X-ray CT [e.g. 33, 34]; c) experiments that infer instability from the value of a chosen criterion [e.g. 35, 36].

Some 10 years ago, Tang and Kovscek [37] showed experimental results demonstrating an example of unstable displacement with $M_{s_hag} < 1$, putting the approach of Hagoort [21] in doubt. Ott et al. [38] defined instabilities observed for $M_{s_hag} < 1$ as "channelling" features as opposed to fingering observed for $M_{s_hag} > 1$. More recently, the uncertainty around the validity of M_{s_hag} as a stability criterion was further demonstrated by Bouquet et al. [39], who investigated four different mobility criteria, testing these against numerical results. The results favoured Hagoort's M_{s_hag} criterion. However, the overall impression remained that the M_{s_hag} criterion for stability is basically an empirical criterion that like the other criteria works best for specific situations. Today, still no consensus exists as to what the correct criterion is to predict the onset of fingering in the general case.

With increasing interest in injection processes (as opposed to simple depletion) and increased focus on gas-injection such as CO₂ and H₂, a solid criterion that predicts the onset of unstable displacement will prove its value in the design of carbon sequestration projects, underground gas storage, but also for water drives, polymer or other chemical injection projects, low salinity flooding and CO₂ EOR projects.

1.1 Considerations developing a stability criterion

To predict fingering, it is not sufficient to focus only on the stability of the shock front. The classical Saffman-Taylor criterion is strictly speaking only valid for very small finger amplitudes and does not cover the growth of large amplitudes. Therefore, the question whether perturbations of a shock front can really grow further involves – because of the displacement-related fractional flow physics – a wider range of saturations (and relative permeability and capillary pressure) outside the shock front. The other extreme is the endpoint mobility ratio criterion that basically says that in the end fingers can only grow if they are unstable over the full mobile saturation range. That is too restrictive, because an actual displacement may not cover the saturation range all the way to the endpoints. In Hele-Shaw cells this issue does not occur, because there, due to the simple geometry, relative permeability and capillary pressure are constant and independent of saturation.

In this paper, we present a holistic criterion to predict the onset of instability of a drive against fingering. The new criterion is built up from first principles and is based on a new concept that generalises the conditions necessary for unstable displacement. In essence, we start out by following Hill [6], who realised that for a perturbation to grow, the pressure gradients near the interface needs to promote that. Hill then assumed constant saturations and effective permeabilities to analyse the pressure profile upstream and downstream of the interface. In contrast, our approach recognises the fact that a so-called Buckley-Leverett [8, 40] profile will appear, due to fractional flow physics, which impacts the pressure gradients around the displacement front. Additional considerations are explained in the next section.

The new criterion still has the form of a test on mobility ratio. It differs from the existing tests in that it accounts not

¹ Mistakenly spelled by Homsy as Chouke

only for viscosities and relative permeability values at some chosen saturation, but rather depends on viscosities and on the shape of the relative permeability curves. The new criterion is found generally to be less restrictive than the end-point mobility criterion but more restrictive than Hagoort's M_{s_hag} [21].

We present in the next section the derivation of the new criterion and show how the earlier derived criteria are special cases of a more general formulation. In section 3, we discuss simulation results studying the new criterion and demonstrate why the results in the literature can appear contradictory. Section 4 deals with the possible impact of fingering on SCAL measurement results. Section 5 discusses the experimental work that has been carried out. Conclusions are presented in section 6.

2 The onset of unstable displacement

To be clear, we define “onset” here as the mathematical condition *necessary* for a small frontal perturbation not to die out immediately after that it comes about, irrespective of how the perturbation occurred. We emphasize that this mathematical condition may well be *not sufficient*: other parameters may still impede a perturbation to grow. An example of that is capillary pressure, which will be addressed in section 2.8.

With this definition in mind, consider an unsteady-state (“Welge”) experiment at constant injection rate of a fluid 1, displacing a fluid 2, with a displacement front moving through a homogeneous porous medium in the x-direction. Injection of fluid 1 occurs over the whole y-z plane at $x=0$, production exits the porous medium through the y-z plane at $x=L$, far away. The displacement front is flat and extends in the y- and z-direction. The porous rock is initially saturated with fluid 2 (only). Fractional-flow physics [40] prescribes the build-up of a shock front.

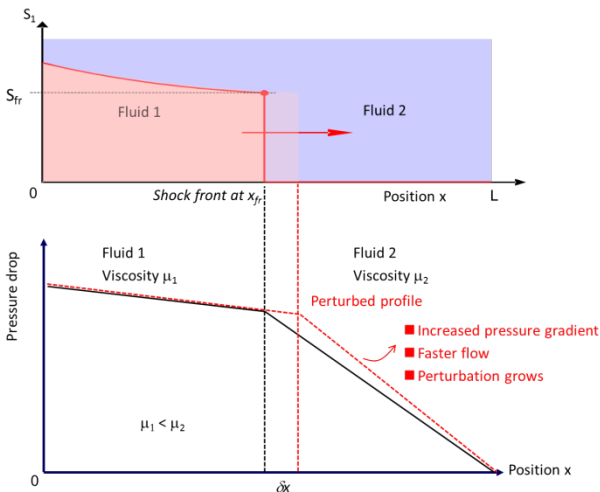


Fig. 1. Saturation and pressure profile through an unperturbed stream tube, combined with the profiles in the stream tube with a single, sudden and infinitesimally small perturbation.

Fig. 1 shows a typical saturation profile and pressure profile through a stream tube along the x-direction at some time t . Let's further assume that at this time t , a sudden and infinitesimally small perturbation appears only at one point

(y_p, z_p) in the otherwise flat y-z front and reaches into position $x_{fr} + \delta x$.

The early fate of the perturbation, i.e. whether it can grow and outrun the flat front, or rather be taken over by the flat front is the anchoring point for our stability analysis. To study the early fate of this perturbation over time one needs to solve the flow equations. As a first step, following the reasoning of Lord Rayleigh [2], Taylor [4] and many others [e.g. 22, 26, and 41] we can approximate the pressure function and saturation distribution far upstream and downstream of the front by the unperturbed values. This is equivalent to solving the flow equations of the perturbed system under the boundary condition of a constant pressure drop ΔP across the sample. The unperturbed pressure drop follows from the parameters controlling the unsteady-state experiment just before the perturbation occurred.

The second step we took is to use the fact that according to fractional flow theory each saturation travels at its own speed [40]. When we consider the perturbation in Fig. 1 from that perspective, we note that the position of the front at the perturbation deviates from the flat front, but the shock front saturation itself is unchanged. For the shock front saturation we have² according to [40]:

$$v_{fr} = \frac{q}{\phi} \left(\frac{\partial f_w}{\partial s} \right)_{s_{fr}} \quad (1)$$

From inspection of the flow equations it follows that we can interpret the perturbation as this part of the front been shifted in time by an infinitesimally small amount. Therefore, the early fate of the perturbation is determined by how the velocity of the front at the perturbation, or equivalently (see Eq. 1) the flow rate q through a stream tube through the perturbation would change at an infinitesimally-small time shift, with the pressure drop across the stream tube kept constant. In line with our definition of “onset”, see above, the necessary condition for a perturbation not to die immediately translates into the requirement that the velocity of the interface should increase with t at constant ΔP . Using (1), the new concept to determine the onset of instability therefore is expressed mathematically by the condition

$$\left(\frac{\partial q}{\partial t} \right)_{\Delta P} > 0 \quad (2)$$

This concept reduces the dimensions of the frontal perturbation of a 2D or 3D interface/displacement front to effectively one dimension, studying acceleration of flow in a stream tube at constant ΔP .

It is important to note that our concept makes use of the same equations and same assumptions implicitly used by previous authors. The criterion comes about naturally when the assumptions are made explicit, in particular the notion that equations are solved under the boundary condition of a constant ΔP . The important difference between this approach and the work by previous authors is that these all chose to approximate saturations upstream and downstream of the interface to be at some constant value, while we apply

² For an explanation of symbols, see the Nomenclature at the end of the paper.

fractional flow theory that predicts a Buckley-Leverett profile. The constant saturations certainly are a good approximation in Hele-Shaw cells, but much less so in porous media.

Starting with condition 2 we can derive a relation to use in the laboratory or the field in practical terms to predict the onset of instability. From Darcy's equation (neglecting gravity for the moment) we have for 2-phase flow

$$q_{tot} = -K \left[\frac{k_{rw}(S)}{\mu_w} + \frac{k_{ro}(S)}{\mu_o} \right] \frac{dp}{dx} \quad (3)$$

In order to simplify the notation, define

$$R = R(x, t) = \left[\frac{k_{rw}(S)}{\mu_w} + \frac{k_{ro}(S)}{\mu_o} \right]^{-1} \quad (4)$$

and

$$G = G(t) = \int_0^{x_{fr}} R dx + \int_{x_{fr}}^L R dx \quad (5)$$

We get

$$\Delta P = K^{-1} q G \quad (6)$$

So

$$\left(\frac{dq}{dt} \right)_{\Delta P} = \frac{-q}{G} \frac{dG}{dt} \quad (7)$$

Combining Eq. 7 with condition 2, we find that unstable displacement will occur for

$$\frac{dG}{dt} < 0 \quad (8)$$

Condition 8 allows us to work out a number of examples for comparison with historic criteria for stability.

2.1 Onset of instability in Hele-Shaw cells

The conditions in Hele-Shaw cells are $S_{upstream}=1$ and $S_{downstream} = 0$, with S the saturation of the injected phase. When injecting water to displace oil, we find for G (see Eqs. 5 and 4)

$$G = x_{fr} \mu_w + (L - x_{fr}) \mu_o \quad (9)$$

Therefore

$$\frac{dG}{dt} = \frac{dx_{fr}}{dt} (\mu_w - \mu_o) \quad (10)$$

Combining Eq. 10 with condition 8, we find that the displacement will be unstable for $\mu_o > \mu_w$, as expected.

2.2 Onset of instability in the cases of Saffman and Taylor and Chuoke

Both Saffman and Taylor [4] and Chuoke [16] assume that the upstream saturation is constant and equal to $1-S_{or}$, while the downstream saturation equals S_{wc} when water is displacing oil. Similar to the derivation for the Hele-Shaw cells, we now find

$$\frac{dG}{dt} = \frac{dx_{fr}}{dt} \left\{ \left[\frac{k_{rwor}}{\mu_w} \right]^{-1} - \left[\frac{k_{rowc}}{\mu_o} \right]^{-1} \right\} \quad (11)$$

Combining Eq. 11 with condition 8, we find that the displacement will be unstable for

$$\frac{k_{rwor}}{\mu_w} > \frac{k_{rowc}}{\mu_o} \quad (12)$$

i.e. for $M_{end} > 1$, identical to the results obtained by these authors.

2.3 Onset of instability according to Hagoort

Hagoort [21] argued that the upstream saturation could be approximated by the shock front saturation. Similar to the cases treated above, we find now

$$\frac{dG}{dt} = \frac{dx_{fr}}{dt} \left\{ \left[\frac{k_{rw}(S_{fr})}{\mu_w} + \frac{k_{ro}(S_{fr})}{\mu_o} \right]^{-1} - \left[\frac{k_{rowc}}{\mu_o} \right]^{-1} \right\} \quad (13)$$

Combining Eq. 13 with condition 8 results immediately into the criterion as derived by Hagoort: the drive is unstable for

$$\frac{k_{rw}(S_{fr})}{\mu_w} + \frac{k_{ro}(S_{fr})}{\mu_o} > \frac{k_{rowc}}{\mu_o} \quad (14)$$

2.4 Onset of instability in Steady-State experiments

Lenormand et al. [42] show in their Fig. 4 a pressure drop profile as it typically occurs in steady-state experiments: the pressure drop first increases at each step in fractional flow and then decreases. From the examples discussed above, it becomes clear that the criterion of instability as presented in condition 8 will play its role in Steady-State experiments. We consider here two consecutive steps: a step with fractional flow f_1 followed by a step at f_2 . We define $S_{upstream} = S_2(f_2)$ and $S_{downstream} = S_1(f_1)$. Similar again to previous cases, we find

$$\frac{dG}{dt} = \frac{dx_{fr}}{dt} \left\{ \left[\frac{k_{rw}(S_2)}{\mu_w} + \frac{k_{ro}(S_2)}{\mu_o} \right]^{-1} - \left[\frac{k_{rw}(S_1)}{\mu_w} + \frac{k_{ro}(S_1)}{\mu_o} \right]^{-1} \right\} \quad (15)$$

Combining Eq. 15 with condition 8 predicts the displacement to be unstable for

$$\frac{k_{rw}(S_2)}{\mu_w} + \frac{k_{ro}(S_2)}{\mu_o} > \frac{k_{rw}(S_1)}{\mu_w} + \frac{k_{ro}(S_1)}{\mu_o} \quad (16)$$

Berg et al. [43] show in their Fig. 3 that oscillations become apparent at or near the top of the differential pressure plot vs time. The criterion in condition 16 may well be the trigger for the oscillations. Note that our present results are limited to understanding the onset for instability and cannot be used to analyse the oscillations themselves.

2.5 Onset of instability with impact of gravity for miscible displacement according to Dumoré

Dumoré [20] studied the onset for instability in a vertically downward displacement of oil by solvent injection, under the assumptions of constant saturations upstream and downstream of the displacement front. Notably, he assumed $k_{rw}=k_{rowc}=1$, with no oil flowing upstream and no solvent flowing downstream. Moreover, he assumed constant viscosities upstream and downstream. Inserting this data

into condition A9 (see Appendix), it follows immediately that the displacement is stable for

$$q < gK \frac{(\rho_o - \rho_s)}{(\mu_o - \mu_s)} \quad (17)$$

This is identical to the result obtained by Dumoré, who identified the right-hand side of condition 17 as a critical displacement rate for stable miscible, vertical, displacement.

2.6 Onset of instability with impact of gravity for immiscible displacement according to Dietz

Dietz [7] (or in fact de Korver and Douwes Dekker [3]) studied the onset of instability of water-oil displacement in a reservoir dipping at an angle θ with respect to the horizontal. Similar to Dumoré [20], he assumed the saturations upstream and downstream to be constant. However, he used for the relative permeabilities the values at the saturation end-points k_{rwor} and k_{rowc} respectively. As in section 2.5, inserting this data into condition A9, calculation of the onset of instability is straightforward. We find the displacement to be stable for

$$1 - M_{end} > -\frac{K}{q} g \sin\theta \Delta\rho \frac{k_{rwor}}{\mu_w} \quad (18)$$

We have three cases:

a) $M_{end} = 1$

The displacement will be stable for $\Delta\rho > 0$ and unstable for $\Delta\rho < 0$

b) $M_{end} < 1$

The displacement will be stable for

$$q > -\frac{K}{(1 - M_{end})} g \sin\theta \Delta\rho \frac{k_{rwor}}{\mu_w} \quad (19)$$

c) $M_{end} > 1$

The displacement will be stable for

$$q < \frac{K}{(M_{end} - 1)} g \sin\theta \Delta\rho \frac{k_{rwor}}{\mu_w} \quad (20)$$

The results for cases a, b, and c are identical to what is shown in Dake [8] as a summary for ‘‘Dietz’’ tonguing.

It is noteworthy that our concept that considers infinitesimally small perturbations, leads to results identical as was found by Dietz or de Korver and Douwes Dekker, while these authors studied the stability of displacement at a macroscopic scale in the field.

2.7 Onset of instability in a more general case

For the case of water displacing oil, we find (for details see Appendix A) as a necessary condition for stable displacement in the absence of gravity two cases: a) $M_{end} \leq \alpha$: stable displacement, independent of the value of M_{s_hag} ; b) $M_{end} > \alpha$: stable displacement only if

$$M_{s_hag} < M_\alpha < 1 \quad (21)$$

with

$$M_\alpha = \frac{1 - \alpha}{1 - \frac{\alpha}{M_{end}}} \quad (22)$$

α given in Eq. A16, $0 < \alpha < 1$. So we have $0 < M_\alpha < 1$.

From the condition 21, we find that our new criterion is more restrictive than Hagoort’s [21] criterion, when seen as a function of the viscosity ratio: the original Hagoort criterion requires M_{s_hag} only to be less than unity, while now it needs to be less than M_α .

Note that the expression for α (Eq. A16) is amenable to numerical integration. As a result, for given viscosity ratio and fractional flow function, one can easily test for stability of the displacement. In our experience, α is in the order of 0.3 to 0.7, which allows for a quick check.

2.7.1 Impact of gravity

In Appendix A, we show the complete formulation accounting for the impact of gravity, injecting fluid 1 to displace fluid 2. Three situations come about: a) $M_{end} \leq \alpha$: stable displacement, independent of the value of M_{s_hag} and of flow rate; b) $M_{end} > \alpha$, $M_{s_hag} \leq M_\alpha$: stable displacement independent of the rate; c) $M_{end} > \alpha$, $M_{s_hag} > M_\alpha$: stable displacement only if the flow rate is less than a critical rate q_{crit} :

$$q_{crit} = \left\{ K \Delta\rho g \sin(\theta) \left[\frac{k_{r2_end}}{\mu_2} \right] \frac{1}{(1 - \alpha)} \frac{(M_{sh} + \beta)}{(M_{sh} + 1)} \left[\frac{1}{M_\alpha} - \frac{1}{M_{s_hag}} \right]^{-1} \right\} \quad (23)$$

with β given in Eq. A26, $0 < \beta < 1$ and M_{sh} defined in Eq. A29. It is of interest to note that the first term, between the accolades, equals Hagoort’s ‘‘free fall filter velocity’’ [44]. So, the remainder of condition 23 can be seen as an adjustment to the free fall velocity. Note also that the new critical rate is not dependent on (k_{r1_end}/μ_1) as is the case in the original Dietz criterion, see condition 20.

In summary, we see that gravity brings about a stabilising effect, up to a critical rate. This is in line with the classical stability criteria for viscous fingering derived by linear stability analysis [3, 7, and 20].

Although the formulas get much more complicated when accounting for gravity, these (including Eq. A26 for β) are still easily tractable by numerical integration and therefore allow for a screening of parameters for stable displacement.

2.8 Impact of capillary pressure on the onset of instability

The concept discussed above does allow for accounting for capillary pressure, but implementing capillary pressure into the flow equations would not result in a transparent criterion for the onset of instability. Too many parameters would appear. Instead, we have chosen to assess generically the impact of capillary pressure on the criterion as derived above. In addition, we have tested our assessment with simulations discussed in section 3.

2.8.1 Generic impact of capillary pressure on the onset of instability

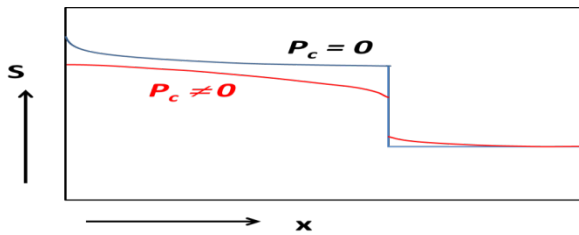


Fig. 2. Typical Buckley-Leverett saturation profile with zero capillary pressure (blue) and saturation profile accounting for capillary pressure (red).

Fig. 2 shows the impact of capillary pressure on the saturation distribution of a water-oil displacement. Upstream of the shock front, the water saturation is reduced with respect to Buckley-Leverett profile observed in the absence of capillary pressure. This is due to the positive branch of the imbibition capillary pressure. On the other hand, downstream, the water saturation is increased, due to the negative branch of the capillary pressure. As a result, the mobility contrast between upstream and downstream moving fluids is reduced with respect to the situation with a zero capillary pressure.

Our criterion for the onset of instability is reflecting that contrast, so we conclude that the onset of instability in the presence of capillary pressure will be shifted to higher values for the viscosity ratio.

For oil-water or gas-water drainage, the capillary pressure has only a positive branch. Therefore, the impact of capillary pressure will only be upstream of the displacement front. Still, the contrast in mobility upstream and downstream will be reduced, be it less. This is demonstrated in section 3.

3 The onset of fingering tested with simulations

As discussed in section 2, the criterion for the onset of instability in displacement processes is determined by the condition $(\partial q/\partial t)_{\Delta P} > 0$. The criterion analyses the early fate of an infinitesimal perturbation over an infinitesimally small time span. The analysis is independent of the actual boundary conditions, whether the injection rate is constant or whether the pressure drop is maintained constant.

We can now take this one step further: for a displacement at constant pressure drop, the condition $(\partial q/\partial t)_{\Delta P} > 0$ will bring about an accelerating flow rate throughout. This means the integrated total mobility is increasing. Therefore, for a displacement at constant injection rate, rather than at constant pressure drop, with the same input parameters for viscosity, relative permeability, etc., when the onset of instability is met, the pressure drop will have to decline, in line with the increasing integrated total mobility. This can easily be proven mathematically by inspecting $(\partial \Delta P/\partial t)_q$. Moreover, we have verified this “rule” with simulations, as discussed below.

3.1 One-dimensional simulations

First we have run a number of unsteady-state simulations with SCORES [42, 45] in 1-D. We ran simulations in drainage mode, incompressible flow, with a viscosity for the injected phase of 0.02cP to mimic CO₂ injection. Corey parameters, porosity and permeability were set to the same values as used in our earlier work on OBKN outcrop [46], that also shows what definition was used for Corey parameters.

To fully screen the displacement behaviour for stability, we ran 10 different cases, varying the viscosity of the displaced phase from 0.01cP (which corresponded to $M_\mu = 0.5$, $M_{\text{end}} = 0.28$, $M_{s_hag} = 0.11$, $M_\alpha = 17.5$, so judged by all criteria as stable) to 10cP (which corresponded to $M_\mu = 500$, $M_{\text{end}} = 281$, $M_{s_hag} = 1.84$, $M_\alpha = 0.59$, so unstable by all criteria).

With P_c set to zero, we found perfect correspondence between the behaviour of the pressure drop and the integrated total mobility concept: $\Delta P(t)$ was increasing before breakthrough when our new criterion would predict a stable displacement and it remained constant exactly at the calculated point of onset. The pressure drop was declining before breakthrough for cases where the point of onset was surpassed. There was no dependence on flow rate, as expected.

We then applied the capillary pressure curve used in earlier work by Maas et al. [46]. The behaviour of $\Delta P(t)$ changed in line with expectations. At low flow rate, the tipping point for an increasing $\Delta P(t)$ before breakthrough into a decreasing of $\Delta P(t)$ moved to a higher viscosity ratio. At high flow rate, the tipping point did not move noticeably compared to the zero P_c cases. This is due to the viscous forces being strong enough to reduce the effect of P_c .

3.2 Simulations in 2-D

Of course, in one-dimensional simulations one can only observe the character of $\Delta P(t)$, but fingering itself cannot occur. Therefore, we moved subsequently to simulations in 2-D. It is well known that fingering in simulations can only be observed if the right triggering [e.g. 47, 48, and 49] is incorporated. We used a Gaussian distribution for porosity, with a standard deviation of 0.02. Permeability in each individual grid block was then set through an exponential correlation, as used by Maas et al. [46]. Therefore, the permeability distribution is log-normal. The permeability variation factor V [50] (similar to the Dykstra Parsons [51] coefficient) equalled 0.42, which is still quite homogeneous in view of the V cut-off of 0.9 [46] and therefore acceptable for SCAL experiments. Gridding was as used by Berg and Ott [29]: 400 (perpendicular to flow) x 200 grid blocks in the flow direction. The behaviour of $\Delta P(t)$ before breakthrough was very similar to the 1-D cases discussed above, both for P_c set to zero and for P_c set as in Maas et al. [46]. Note that P_c was different for each individual grid block: we used one dimensionless Leverett-J function, scaled per grid block with the square root of the individual porosity divided by the individual permeability.

3.2.1 Fingering observed in the saturation maps

Fingering is clearly visible in the saturation map at high viscosity ratio, both with P_c set to zero and with the P_c inputted as mentioned above, with only a nominal difference in appearance. At the lowest viscosity ratio where all criteria predict stable displacement, the difference was more visible. At zero P_c , the saturation map showed a well-defined sharp and flat front, while the rock is definitely heterogeneous with its Gaussian porosity and log-normal permeability distribution. However, with the P_c switched on, and at low flow rate, the front became slightly irregular at the lowest viscosity ratio, see Fig. 3. In addition, these irregularities did not grow with the advancing front. At high flow rate, the irregularities disappeared. Apparently, high viscous forces reduce the impact of a non-zero capillary pressure, similar as discussed above.

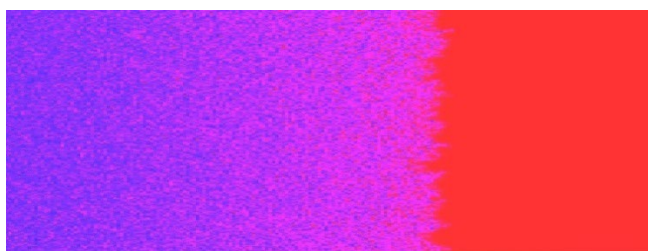


Fig. 3. Displacement front for CO₂ injection at extreme favourable viscosity ratio ($\mu_{CO_2} = 0.02\text{cP}$, $\mu_w = 0.01\text{cP}$). The frontal irregularities do not grow over time: “capillary fingering”.

Note that these simulations are in primary drainage mode, so the capillary pressure function has no negative branch and therefore no injected fluid will be “sucked” in ahead of the front proper. We conclude that the irregularities are caused by the strongly varying local capillary pressure functions. One could call these irregularities therefore “capillary fingering” [see e.g. 31].

Varying the water viscosity, we have also reviewed cases close to the switch-over point from stable to unstable displacement as predicted by the new criterion (around $\mu_w = 0.27\text{cP}$ for our data set). The saturation maps were not really different just below or just over the switch point. We interpret this as the initial growth rate of the fingers being too small to become visible on the time scale of the experiments. The initial growth rate will be proportional to $(\partial q/\partial t)_{\Delta P}$, which is just above zero when above, but close to, the switching point.

Finally, we have revisited the stability screening work as was published by Berg and Ott [29]. We focused on their “Case a” that was deemed stable at the time. We calculate for that case $M_{s_hag} = 1.0$ and $M_\alpha = 0.7$, so unstable according to the new criterion. First, we duplicated their results, using a flat permeability distribution with a width of $\pm 2\text{mD}$ around a mean of 100mD and homogeneous $P_c(S_w)$ as specified in [29]. We observed no fingering in the saturation map, in line with what was reported in [29]. Subsequently, we simulated *Case a* using the same approach as discussed above: we implemented a Gaussian porosity distribution with standard deviation of 0.02 and a log-normal permeability distribution. The local capillary pressure function in each grid block was made dependent on

the local porosity and permeability as discussed above. This time, the saturation map shows clear fingering (Fig. 4).

This demonstrates the impact of the triggering mechanism in simulations to study fingering: a flat permeability distribution together with a homogeneous $P_c(S_w)$ apparently was less successful in promoting fingering than our present approach.



Fig. 4. “Case a” of Berg and Ott [29] revisited, Gaussian porosity and log-normal permeability distribution applied, all other parameters set to values published in [29]. Fingering is observed, in line with the new criterion.

One may argue that one approach is more realistic than another, but in fact the choice remains very subjective. For instance, we may as well have chosen a standard deviation of 0.01 or 0.04 rather than 0.02 for the Gaussian porosity distribution. Detailed measurements of the actual porosity and permeability distributions of the rock would be required to resolve this.

We have also used the new criterion to re-evaluate the stability map shown in Fig. 4 of Berg and Ott [29]. The picture has changed significantly. Displacement is unstable for nearly all points in that figure, except for some points in the top right-hand corner. Stability is calculated for n_{CO_2} between 4.0 and 5.0, if n_{brine} equals 4.5 or 5.0; and for the single point with $n_{CO_2} = 4.0$, $n_{brine} = 5.0$. The contour lines as shown in Fig. 4 of Berg and Ott [29] do not exist anymore: one needs to set-up contour lines for M_{s_hag} in one plot and for M_α in another and then select the points for which holds $M_{s_hag} < M_\alpha$.

Another issue that has come to light now is that also the identification of fingering with a saturation map is highly subjective. Just comparing the fingering in Fig. 4 with the “fingering” in Fig. 3 illustrates this. It is physically impossible that the parameter choice used for Fig. 3 would generate viscous fingers (viscosity of the injected phase is twice as large as that of the displaced phase), but clearly the front is not flat because of the capillary heterogeneity. Fig. 18 in of Berg and Ott [29] provides another reason why saturation maps may not be a reliable way of determining fingering because they are the consequence of numerical simulations with a specific choice of scale, but for $P_c \neq 0$ the visco-capillary balance causes the fingers to appear potentially at a larger scale than simulated.

All-in-all we conclude that saturation maps are not a good tool to establish objectively whether fingering occurs.

4 Impact of fingering on SCAL measurements

The impact of fingering on production behaviour has been studied by various authors, both on the scale of the field [e.g. 52, 53, and 54] and on the scale of the core plug in the

laboratory [e.g. 55, 56, and 57]. A general problem, both in the field as well as in the laboratory is that heterogeneity may have a strong and often unknown impact that may enhance the effect of fingering.

As discussed above, the base of our simulation study is a well-defined characterisation of the permeability variability through the parameter V . As shown in [46], the chosen value of $V = 0.42$ gives rise to porosity and permeability distributions that will not affect the relative permeabilities determined in a SCAL experiment, when state-of-the-art history matching is applied of the production data obtained from stable displacements. We have now extended the work to unstable displacements.

Our approach was to compare the relative permeabilities characterisations generated by the automatic history matching tool AutoSCORES [46] on a stable drive with the results obtained on an unstable drive. To that end, we took the production data of the synthetic drainage experiments discussed in section 3.1, for the case with $\mu_w = 0.01\text{cP}$ (so stable by all criteria) and for the case with $\mu_w = 10\text{cP}$ (so unstable by all criteria). We ran AutoSCORES to extract the Corey description for the relative permeabilities and compared that with the “truth”, i.e. the input data for the relative permeability and capillary pressure data used in the 2-D simulations. Since AutoSCORES is based on the Levenberg-Marquardt method, also estimates on the standard deviation of each parameter are reported [46, 58]. It appeared that the difference between the two sets of Corey parameters was statistically insignificant, and that the difference of each with the “truth” data also was statistically insignificant, in both cases at the 5% as well as at the 1% level of significance. However, running AutoSCORES to history match flooding experiments in isolation is risky: the reported standard deviations generally are large even when matches themselves may appear to look “well”. This has an immediate impact on the outcome of the statistical analysis. At this stage, one would need to run a synthetic multi-speed centrifuge experiment and set-up an analysis of the synthetic USS and centrifuge data combined. In view of the already large run times for the USS simulations, we decided not to go that route. Instead, we chose to investigate the situation through laboratory experiments.

5 Experimental program

To test our conclusions in section 4, we have conducted an experimental program consisting of unsteady-state experiments in drainage mode at two extreme viscosity ratios. As explained and demonstrated in [46], it is possible to assess the significance of seemingly different experimental outcomes, even using a small set of three or so experiments, by applying the appropriate statistics frame work. With this in mind, we ran one experiment at a very unfavourable viscosity ratio to compare with a set of three experiments at a favourable viscosity ratio.

5.1 Experimental design

As before [46], we used Obernkirchener (OBKN) sandstone outcrop samples and the simulator SCORES [45] for the detailed design. The drainage experiments were augmented

with one bump (increased flow rate) flood. The base case runs were conducted on samples B2 (twice) and G2, with a Klinkenberg corrected permeability of about 5 mD and 10 mD respectively. As injection fluid we used a mineral oil with a viscosity of about 3 cP, to displace brine with a viscosity of about 1 cP. The samples are saturated initially at 100% brine. The initial injection rate was at 0.2 cm³/min, bumped to 1 cm³/min after some 4 hours.

For the experiment at unfavourable viscosity ratio we used Isopar L with a viscosity of 1.4 cP to displace a glycerol-water mixture with a viscosity of 87 cP. Also in this experiment, the sample initially is saturated at 100% glycerol mixture. Initial flow rate was set at 0.2 cm³/min, bumped to 2 cm³/min after about 19 hrs.

At the end of each experiment Dean-Stark was executed to verify material balance. For the glycerol experiment we checked material balance through NMR.

In the design phase, estimating $k_{r\text{wor}}$ at 0.5, we calculated M_{end} at 0.67 for the mineral oil displacing brine, possibly not quite a safe value for stable displacement with the new criterion requiring $M_{\text{end}} < \alpha$ (section 2.7), and generally $0.3 < \alpha < 0.7$. However, with P_c estimated for OBKN as before [46], SCORES simulations showed $d\Delta P(t)/dt > 0$ before breakthrough, indicative of stable displacement (section 3.1). This was subsequently borne out in each of the three base case experiments.

For the glycerol experiment, we estimated M_{end} at 130 and $M_{s_{\text{hag}}}$ at 1.4. These numbers are clearly indicating unstable displacement, which was also borne out both by the SCORES design run and by the experiment: we observed $d\Delta P(t)/dt < 0$ before breakthrough.

At the end of the experiments, AutoSCORES was used to interpret the production data in terms of the Corey parameters for the relative permeabilities, just as we did for the synthetic cases in section 4. To constrain the solutions, we fed AutoSCORES the data of the multi-speed centrifuge experiment that measured P_c , similar to our approach in [46]. The results are listed in Table 1.

Table 1. Corey parameters from AutoSCORES, determined through history matching the three base case experiments and one experiment with glycerol, each combined with the data of a multi-speed centrifuge experiment.

Exp/Param	S_{wc}	$k_{r\text{wor}}$	n_w	n_o
B1.1 base	0.06±0.03	0.61±0.11	4.16±0.16	3.18±0.20
G2 base	0.04±0.02	0.47±0.02	4.35±0.23	2.11±0.16
B1.2 base	0.04±0.01	0.56±0.05	4.80±0.18	2.72±0.17
G2 glycerol	0.01±0.01	0.23±0.01	4.87±0.21	2.95±0.08

The two missing Corey parameters S_{or} and $k_{r\text{orc}}$ were kept constant at 0.01 and 0.98 respectively. Note that in these drainage experiments S_{or} should be taken as the percolation threshold saturation. The outcome of the history matching is not sensitive to its exact small value, for which we just used an estimate based on experience. The standard deviations reported in Table 1 are estimated by AutoSCORES, as discussed in [46].

5.2 Statistical analysis of the AutoSCORES results

At first glance, it may appear that the data in Table 1 show quite some overlap, given the reported standard deviations, and that therefore the Corey parameters of the unstable glycerol experiment, or at least most of these, cannot be distinguished from the Corey parameters of the base case stable experiments.

Similar to our earlier work, a statistical analysis was conducted by testing for the formal “H₀” hypothesis that says: “there is no significant difference between the Corey parameters of the base case experiments and of the glycerol experiment”, using a t-test [46]. As mentioned in [46], a t-test considers the difference between two averages, using the respective standard deviations and the number of simulations in the SCAL experiments. The calculated t-value is then compared against a critical test value at a 5% (or 95% confidence) or 1% (or 99% confidence) test level found from a standard table of the t-probability density distribution [59]. For the data in Table 1 we found that the hypothesis is to be rejected on both levels of statistical significance. In other words: the -unstable- glycerol experiment shows Corey parameters that do deviate from the -stable- base case.

It is important to note that this conclusion could only be reached after interpreting the USS data with the centrifuge data combined with AutoSCORES. The results from an history match of USS “solo” are just not reliable enough for such assessment.

6 Conclusions

- We have presented a new concept to build a criterion for the onset of instability in 2-phase displacement. The new criterion encompasses all historic criteria for the onset of instability: these are special cases of our more general formulation.
- Also the Dietz criterion [7] for macroscopic displacement stability in the field is shown to be a special case of the new more general formulation.
- Displacement will be stable if $M_{end} \leq \alpha < 1$, with $0 < \alpha < 1$, different from the common assumption of stability for $M_{end} < 1$.
- For $M_{end} > \alpha$, the new criterion is more restrictive than Hagoort’s [21] criterion, because we have now $M_{s_hag} < M_{\alpha} < 1$ as a requirement for stable displacement, if gravity is assumed zero.
- For $M_{end} > \alpha$ and non-zero gravity, there exists a critical flow rate for stability that is shown to be related to Hagoort’s “free fall filter velocity” [44]. As a result, Dietz’s critical rate needs to be modified.
- Saturation maps are not a good tool for an objective assessment whether fingering occurred.
- The new criterion provides a necessary but not a sufficient condition for the onset of fingering. Fingering may not develop due to capillary forces, or due to the effect of gravity, or due to spatial or other boundary conditions, or due to e.g. perfect homogeneity of the rock (i.e. $V = 0$).
- It is important to present results in the context of statistical significance.

- It is recommended to conduct history matching of flooding experiments and multi-speed centrifuge experiments combined to constrain the results and improve the statistical significance.
- Laboratory experiments were successfully used to demonstrate the impact of fingering onto SCAL measurements in unsteady-state experiments.
- A quantitative assessment of heterogeneity is an important part of the study into the impact of fingering, both for SCAL as well as for the field.

Nomenclature

f	[-]	fractional flow
G	[m.Pa.s]	defined in Eq. A5
g	[m/s ²]	gravity constant
H	[kg/m ²]	defined in Eq. A6
K	[m ²]	permeability
k _r	[-]	relative permeability
L	[m]	distance between injection and production
M _{end}	[-]	mobility ratio at end-point saturations (defined in Eq. A19)
M _{sh}	[-]	mobility ratio at shock front (defined in Eq. A29)
M _{s_hag}	[-]	Hagoort shock front mobility ratio (defined in Eq. A18)
M _α	[-]	limit used in new criterion for onset instability (defined in Eq. A21)
M _μ	[-]	viscosity ratio, equal to μ ₂ /μ ₁
n	[-]	Corey exponent, as defined in [46]
P	[Pa]	pressure
q	[m/s]	flow rate m/s
R	[Pa.s]	defined in Eq. A2a
R _p	[kg/m ³]	defined in Eq. A2b
S	[-]	saturation
t	[s]	time
V	[-]	homogeneity number (defined in [50])
v	[m/s]	velocity
x	[m]	distance

Greek

α	[-]	given in Eq. A16
β	[-]	given in Eq. A26
Δ		difference operator
θ	[degrees]	angle
φ	[-]	porosity
μ	[Pa.s]	viscosity
ρ	[kg/m ³]	density

subscripts

I	invading phase
2	displaced phase
c	capillary
fr	shock front
s	solvent
o	oil
or	residual oil
w	water
wc	connate water

superscripts

‘ first derivative

The CT-scans of the OBKN material were made available courtesy of Prof. Pacelli Zitha, TUDelft, and conducted expertly by Mrs. Ellen Meijvogel-de Koning. The glycerol/oil interfacial tension was measured by DataPhysics Instruments GmbH, using an OCA25 pendant drop system. We thank Dario Santonico for his energetic and professional managing and overall support of the flow experiments.

References

1. W.S. Jevons, On the cirrus form of cloud, *Phil. Mag. J. Sc.* 4th Series, **14**, 90, 22-35 (1857)
2. Lord Rayleigh, Investigation of the character of equilibrium of an incompressible heavy fluid of variable density, *Proc. Lond. Math. Soc.* **14**, 170–177 (1883)
3. J.W. de Korver and H.L. Douwes Dekker, Enkele beschouwingen over het aardolieveld Schoonebeek, 1948-1949 Jaarboek der Mijnbouwkundige Vereeniging te Delft, Delft. Uitg. Mij. Delft (1949)
4. G. Taylor, The instability of liquid surfaces when accelerated in a direction perpendicular to their planes. I, *Proc. R. Soc. Lond. A* **201**, 192–196 (1949)
5. D.J. Lewis, The instability of liquid surfaces when accelerated in a direction perpendicular to their planes. II, *Proc. R. Soc. Lond. A* **202**, 81–96 (1949)
6. S. Hill, Channeling in packed columns, *Chem. Eng. Sc.* **1** (6) 247-253 (1952)
7. D. Dietz, A theoretical approach to the problem of encroaching and by-passing edge water, *Proc. Kon. Ned. Akad. Wetenschap.* **B56**, 83-92 (1953)
8. L.P. Dake, *Fundamentals of reservoir engineering*, Elsevier 1978
9. F.J. Fayers and A. Muggeridge, Extensions to Dietz theory and behavior of gravity tongues in slightly tilted reservoirs, SPE-18438 (1990)
10. P.G. Saffman and G. Taylor, The penetration of a fluid into a porous medium or Hele-Shaw cell containing a more viscous liquid, *Proc. R. Soc. Lond. A* **245**, 312–329 (1958)
11. H.S. Hele-Shaw, Experiments on the nature of the surface resistance in pipes and on ships, *Trans. Inst. Naval Archit.* **39**, 145-156 (1897)
12. D. Bensimon, Stability of viscous fingering, *Phys. Rev. A* **33**, 1302-1308 (1986)
13. M. Mineev-Weinstein, Selection of the Saffman Taylor finger width in the absence of surface tension: an exact result, *Phys. Rev. Lett.* **80** (10), 2113-2116 (1998)
14. S. Tanveer, Surprises in viscous fingering, *J. Fluid Mech.* **409**, 273-308 (2000)
15. G.M. Homsy, Viscous fingering in porous media, *Ann. Rev. Fluid Mech.* **19**, 271-311 (1987)
16. R.L. Chuoke, P. van Meurs, and C. van der Poel, The instability of slow, immiscible, viscous liquid-liquid displacements in permeable media, SPE-1141-G (1959)
17. E.D. Chikhliwala, A.B. Huang, and Y.C. Yortsos, Numerical study of the linear stability of immiscible displacement in porous media, *Transp. Porous Med.* **3**, 257-276 (1987)
18. A. Riaz and E. Meiburg, Three-dimensional miscible displacement simulations in homogeneous porous media with gravity override, *J. Fluid Mech.* **494**, 95-117 (2003)
19. A.E. Kampitsis, W.J. Kostorz, A.H. Muggeridge, and M.D. Jackson, The life span and dynamics of immiscible viscous fingering in rectilinear displacements, *Phys. Fluids* **33**, 096608 (2021); doi: 10.1063/5.0064955
20. J.M. Dumoré, Stability considerations in downward miscible displacements, SPE-961-PA (1964)
21. J. Hagoort, Displacement stability of water drives in water-wet connate-water-bearing reservoirs, SPE-4268-PA (1974)
22. E.J. Peters and D.L. Flock, The onset of instability during two-phase immiscible displacement in porous media, SPE-8371 (1979)
23. J.W. Sheldon, On the fingering of slow, immiscible, viscous liquid-liquid displacements, SPE-1552-G (1960)
24. S. Bachu and G. Dagan, Stability of displacement of a cold fluid by a hot fluid in a porous medium, *Phys. Fluids* **22** (1), 54-59 (1979)
25. J.W. McLean, I The fingering problem in flow through porous media; II The kinetic equation for hamiltonian systems, Thesis, Cal. Inst. Techn. (1980)
26. A.B. Huang, E.D. Chikhliwala, and Y.C. Yortsos, Linear stability analysis of immiscible displacement including continuously changing mobility and capillary effects: Part II - General basic flow profiles, SPE-13163-MS (1984)
27. J.N.M. van Wunnik and K. Wit, A simple analytical model of the growth of viscous fingers in heterogeneous porous media, Conf. Proc. 1st ECMOR, Cambridge UK, July 1989
28. A.P. Aldushin and B.J. Matkowsky, Selection in the Saffman Taylor finger problem and the Taylor Saffman bubble problem without surface tension, *Appl. Math. Lett.* **11** (6) pp 57-62 (1998)
29. S. Berg and H. Ott, Stability of CO₂-brine immiscible displacement, *Int. J. Greenhouse Gas Control* **11**, 188-203 (2012)
30. G. Coskuner and R.G. Bentsen, A new approach to the onset of instability for miscible fluid - fluid displacements in porous media, SPE-16475 (1987)
31. R. Lenormand, E. Touboul, and C. Zarcone, Numerical Models and Experiments on Immiscible Displacements in Porous Media, *J. Fluid Mech.* **189**, 165-187 (1988)
32. E. Lajeunesse, J. Matin, N. Rakotomalala, D. Salin, and Y.C. Yortsos, Miscible displacement in a Hele-Shaw cell at high rates, *J. Fluid Mech.* **398**, 299-319 (1999)

33. F.F. Craig Jr, T.M. Geffen, and R.A. Morse, Oil recovery performance of pattern gas and water injection operations from model tests, SPE-413-G (1954)
34. A. Skauge, K. Sorbie, P.A. Ormehaug, and T. Skauge, Experimental and numerical modeling studies of viscous unstable displacement, 15th Eur. Symp. Impr. Oil Rec., Paris, France, April 27-29, paper A28 (2009)
35. J. Peters and S. Khataniar, The effect of instability on relative permeability curves obtained by the dynamic-displacement method, SPE-14713-PA (1987)
36. H.K. Sarma and R.G. Bentsen, An experimental verification of a modified instability theory for immiscible displacements in porous media, J. Can. Petr. Tech. **26** (4), 88-99 (1987)
37. G.-Q. Tang and A.R. Kovscek, High resolution imaging of unstable, forced imbibition in Berea sandstone, Transp. Porous Med. **86** 617-634 (2011)
38. H. Ott, S. Berg and S. Oedai, Displacement and mass transfer of CO₂-brine in sandstone, En. Proc. **23**, 512-520 (2012)
39. S. Bouquet, S. Leray, F. Douarche, and F. Roggero, Characterisation of viscous unstable flow in porous media at pilot scale - Application to heavy oil polymer flooding, IOR 2017-19th Eur. Symp. Impr. Oil Rec. 1, 1-30 (2017)
40. S.E. Buckley and M.C. Leverett, Mechanism of fluid displacement in sands, Trans. AIME **146**, 107-116 (1942)
41. R.A. Wooding, The stability of a viscous liquid in a vertical tube containing porous material, Proc. R. Soc. Lond. A **252** 120–134 (1959)
42. R. Lenormand, K. Lorentzen, J.G. Maas, and D. Ruth, Comparison of four numerical simulators for SCAL experiments, SCA2016-006 (2016)
43. S. Berg, H. van der Linde, N. Brussee, M. Rücker, H. Dijk, E. Unsal, T.G. Sorop, and M. Appel, Physical origin of pressure- and saturation fluctuations in steady-state core floods, SCA2021-020 (2021)
44. J. Hagoort, Oil recovery by gravity drainage, SPE- 7424 (1980)
45. J.G. Maas, B. Flemisch, and A. Hebing, “Open source simulator DuMux available for SCAL data interpretation”, SCA2011-08 (2011)
46. J.G. Maas, N. Springer, and A. Hebing, Defining a sample heterogeneity cut-off value to obtain representative Special Core Analysis (SCAL) measurements, SCA2019-024 (2019)
47. D.W. Peaceman and H.H. Rachford Jr., Numerical calculation of multidimensional miscible displacement, SPE-1524-G (1960)
48. P. Sigmund, H. Sharma, D. Sheldon, and K. Aziz, SPE-14368 (1988)
49. A. Riaz and E. Meiburg, Vorticity interaction mechanisms in variable-viscosity heterogeneous miscible displacements with and without density contrast, J. Fluid Mech. **517**, 1-25, 2004
50. J.G. Maas and A. Hebing, “Quantitative X-ray CT for SCAL plug homogeneity assessment”, SCA2013- 004 (2013)
51. H. Dykstra and R.L. Parsons, The prediction of oil recovery by water flood, Secondary recovery of oil in the United States, 2nd edition, API, 160-174 (1950)
52. E.J. Koval, A method for predicting the performance of unstable miscible displacement in heterogeneous media, SPE-450 (1963)
53. M.R.Todd and W.J. Longstaff, The development, testing, and application of a numerical simulator for predicting miscible flood performance, SPE-3484 (1972)
54. F.J. Fayers, M.J. Blunt, and M.A. Christie, Comparisons of empirical viscous-fingering models and their calibration for heterogeneous problems, SPE-22184 (1992)
55. H.S. Al-Shuraiqi, C.A. Grattoni, and A.H. Muggeridge, Numerical and experimental investigation into the effects of viscosity and injection rate on relative permeability and oil recovery, SCA2005-40 (2005)
56. H. Luo, K.K. Mohanty, M. Delshad, and G.A. Pope, Modeling and upscaling unstable water and polymer floods: dynamic characterization of the effective finger zone, SPE-179648-MS (2016)
57. B.M. Ferreira Pereira, Accounting for viscous fingering in relative permeability estimation of special core analysis measurements, Thesis, Herriot-Watt (2017)
58. S. Berg, E. Unsal, and H. Dijk, Non-uniqueness and uncertainty quantification of relative permeability measurements by inverse modelling, Comp. Geotech. **132** (2021) 103964 (2021)
59. R.A. Fisher, F. Yates, “Statistical tables for biological, agricultural and medical research”, London, Oliver & Boyd (1963)

Appendix A. Derivation of a general criterion for the onset of instability

The onset of instability occurs at $(\partial q/\partial t)_{\Delta P} > 0$ (see main text), so we analyse $(\partial q/\partial t)_{\Delta P}$. Consider liquid 1 to be injected, to displace liquid 2. Define $q = q_1 + q_2$, assume incompressible flow, assume $P_c=0$, use angle θ with respect to the horizontal, apply Darcy’s equation to each phase and add, we find for 1-D flow [8]

$$q = -K \left\{ \left[\frac{k_{r1}(S)}{\mu_1} + \frac{k_{r2}(S)}{\mu_2} \right] \frac{dp}{dx} + g \sin(\theta) \left[\rho_1 \frac{k_{r1}(S)}{\mu_1} + \rho_2 \frac{k_{r2}(S)}{\mu_2} \right] \right\} \quad (A1)$$

Noting that $S = S(x, t)$ and in order to simplify the notation, define

$$R = R(x, t) = \left[\frac{k_{r1}(S)}{\mu_1} + \frac{k_{r2}(S)}{\mu_2} \right]^{-1} \quad (A2a)$$

and

$$R_\rho = R_\rho(x, t) = \frac{[\rho_1 \frac{k_{r1}(S)}{\mu_1} + \rho_2 \frac{k_{r2}(S)}{\mu_2}]}{[\frac{k_{r1}(S)}{\mu_1} + \frac{k_{r2}(S)}{\mu_2}]} \quad (\text{A2b})$$

and define pressure drop ΔP from inlet to outlet

$$\Delta P = - \int_{p(x=0)}^{p(x=L)} dp \quad (\text{A3})$$

we get

$$\Delta P = \frac{q}{K} \int_0^L R dx + g \sin(\theta) \int_0^L R_\rho dx \quad (\text{A4})$$

Define

$$G = G(t) = \int_0^L R dx \quad (\text{A5})$$

and

$$H = H(t) = \int_0^L R_\rho dx \quad (\text{A6})$$

Combining Eqs. A4, A5 and A6, gives

$$\Delta P(t) = K^{-1} q(t) G(t) + g \sin(\theta) H(t) \quad (\text{A7})$$

Take the total derivative with respect to t at constant pressure drop and solve for $(\partial q / \partial t)_{\Delta P}$:

$$\left(\frac{\partial q}{\partial t} \right)_{\Delta P} = - \frac{q}{G} \left(\frac{\partial G}{\partial t} \right)_{\Delta P} - K \frac{g \sin(\theta)}{G} \left(\frac{\partial H}{\partial t} \right)_{\Delta P} \quad (\text{A8})$$

As mentioned before, a drive will experience the onset for instability if $\frac{\partial q}{\partial t} > 0$. So with q and G positive, the onset occurs for

$$\frac{\partial G}{\partial t} < \frac{-K g \sin(\theta) \partial H}{q \partial t} \quad (\text{A9})$$

Note that for a horizontal 1D case ($\theta = 0$), condition A9 simplifies into

$$\frac{\partial G}{\partial t} < 0 \quad (\text{A10})$$

as condition for the onset of instability while the flow rate q does not play a role for the onset.

A.1 Calculation and interpretation of $\partial G / \partial t$

Consider a drive, liquid 1 displacing liquid 2 in 1-D, with $S_1 = S_{1r}$ downstream of the displacement front. Breaking up the integral in Eq. A8 into two parts; before and after the shock front $x_{fr}(t)$ we obtain

$$G(t) = \int_0^{x_{fr}(t)} R dx + (L - x_{fr}(t)) \left[\frac{k_{r2_end}}{\mu_2} \right]^{-1} \quad (\text{A11})$$

Take first derivative (employing chain rule including boundary of integral):

$$\frac{\partial G}{\partial t} = R(S_{fr}) \frac{\partial x_{fr}}{\partial t} + \int_0^{x_{fr}(t)} \left(\frac{\partial R}{\partial t} \right)_x dx - \frac{\partial x_{fr}}{\partial t} \left[\frac{k_{r2_end}}{\mu_2} \right]^{-1} \quad (\text{A12})$$

We have

$$\int_0^{x_{fr}(t)} \left(\frac{\partial R}{\partial t} \right)_x dx = \int_{R(1-S_{2r})}^{R(S_{fr})} - \left(\frac{\partial x}{\partial t} \right)_{S(R)} dR \quad (\text{A13})$$

Applying the mean value theorem, we obtain

$$\int_{R(1-S_{2r})}^{R(S_{fr})} - \left(\frac{\partial x}{\partial t} \right)_{S(R)} dR = - \left(\frac{\partial x}{\partial t} \right)_{S_{1m}} \{ R(S_{fr}) - R(1 - S_{2r}) \} = - \left(\frac{\partial x}{\partial t} \right)_{S_{1m}} \left\{ R(S_{fr}) - \left[\frac{k_{r1_end}}{\mu_1} \right]^{-1} \right\} \quad (\text{A14})$$

with value for S_{1m} unknown at this point with $S_{fr} < S_{1m} < 1 - S_{2r}$. Transforming the velocity at S_{1m} into a scaling factor in relation to shock front velocity

$$\left(\frac{\partial x}{\partial t} \right)_{S_{1m}} = \alpha \left(\frac{\partial x}{\partial t} \right)_{S_{fr}} \quad (\text{A15})$$

i.e. transforming S_{1m} into α , with $0 < \alpha < 1$. It can be proven that

$$\alpha = \frac{\int_{(1-S_{2r})}^{S_{fr}} f_1'(S) R'(S) dS}{f_1'(S_{fr}) \left\{ R(S_{fr}) - \left[\frac{k_{r1_end}}{\mu_1} \right]^{-1} \right\}} \quad (\text{A16})$$

Note this expression is amenable to numerical integration to calculate α .

Combining Eqs. A12, A13, A14, and A15 we have

$$\frac{\partial G}{\partial t} = \left(\frac{\partial x}{\partial t} \right)_{S_{fr}} \left\{ R(S_{fr})(1 - \alpha) + \alpha \left[\frac{k_{r1_end}}{\mu_1} \right]^{-1} - \left[\frac{k_{r2_end}}{\mu_2} \right]^{-1} \right\} \quad (\text{A17})$$

Note from the definition of the Hagoort shock-front ratio [21] and Eq. A2, we have

$$M_{s_hag} = \frac{k_{r1}(S_{fr})/\mu_1 + k_{r2}(S_{fr})/\mu_2}{k_{r2_end}/\mu_2} = R^{-1}(S_{fr}) \left[\frac{k_{r2_end}}{\mu_2} \right]^{-1} \quad (\text{A18})$$

Define the end-point mobility ratio as the ratio of the saturation end-point mobility of the injected liquid 1 over the saturation end-point mobility of the displaced liquid 2:

$$M_{end} = \frac{\frac{k_{r1_end}}{\mu_1}}{\frac{k_{r2_end}}{\mu_2}} \quad (\text{A19})$$

For $\theta = 0$ (so in the absence of gravity), apply Eq. A17 to condition A10, and using $\partial x_{fr} / \partial t > 0$, we find as stability criterion for the onset of instability

$$\left[\frac{k_{r2_end}}{\mu_2} \right]^{-1} (1 - \alpha) \left\{ \frac{1}{M_{s_hag}} - \frac{(1 - \frac{\alpha}{M_{end}})}{(1 - \alpha)} \right\} < 0 \quad (\text{A20})$$

For $M_{end} = \alpha$, we have stable displacement because condition A20 cannot be fulfilled, irrespective of the value of M_{s_hag} , since we have $0 < \alpha < 1$ (and $M_{s_hag} > 0$).

For $M_{end} \neq \alpha$, we can define

$$M_\alpha = \frac{1 - \alpha}{1 - \frac{\alpha}{M_{end}}} \quad (\text{A21})$$

Combining Eqs. A21 and A20, we find as criterion for the onset of instability

$$\left\{ \frac{1}{M_{s_hag}} - \frac{1}{M_\alpha} \right\} < 0 \quad (A22)$$

We have two cases

$M_{end} < \alpha$: therefore $M_\alpha < 0$ (see Eq. A21), so condition A22 is never fulfilled, i.e. displacement will be stable for any value of M_{s_hag} .

$M_{end} > \alpha$: From the condition A22, we find for the onset of instability for $M_{s_hag} > M_\alpha$, or vice versa stable displacement for

$$M_{s_hag} < M_\alpha < 1 \quad (A23)$$

Note that this condition is more restrictive than the original Hagoort criterion that predicts stability for $M_{s_hag} < 1$.

A.1 Calculation and interpretation of $\partial H / \partial t$

Consider a drive liquid 1 displacing liquid 2 in 1-D, with $S_1 = S_{1r}$ downstream of the displacement front. Similar to Eq. A11 we have

$$H(t) = \int_0^{x_{fr}(t)} R_\rho dx + (L - x_{fr}(t))\rho_o \quad (A24)$$

Analogous to Eq. A17 we find for the first derivative

$$\frac{\partial H}{\partial t} = \left(\frac{\partial x}{\partial t} \right)_{S_{fr}} \{ R_\rho(S_{fr})(1 - \beta) + \beta\rho_1 - \rho_2 \} \quad (A25)$$

with β defined analogous to α (see Eqs. A14 and A15) and can be numerically calculated (analogous to Eq. A16) through

$$\beta = \frac{\int_{(1-S_{2r})}^{S_{fr}} f_1'(s) R_\rho'(s) ds}{f_1'(S_{fr}) \{ R_\rho(S_{fr}) - \rho_1 \}} \quad (A26)$$

Combining Eqs. A9, A17 and 25 into an expression for the criterion for the onset of instability gives

$$\left\{ R(S_{fr})(1 - \alpha) + \alpha \left[\frac{k_{r1_end}}{\mu_1} \right]^{-1} - \left[\frac{k_{r2_end}}{\mu_2} \right]^{-1} \right\} < \frac{-Kgsin(\theta)}{q} \{ R_\rho(S_{fr})(1 - \beta) + \beta\rho_1 - \rho_2 \} \quad (A27)$$

Use definition of M_{s_hag} (Eq. A18) and of M_{end} (Eq. A19) we have for the onset of instability

$$\left\{ \frac{(1-\alpha)}{M_{s_hag}} + \frac{\alpha}{M_{end}} - 1 \right\} < \frac{-Kgsin(\theta)}{q} \left[\frac{k_{r2_end}}{\mu_2} \right] \{ R_\rho(S_{fr})(1 - \beta) + \beta\rho_1 - \rho_2 \} \quad (A28)$$

We have two cases:

1) $M_{end} \neq \alpha$

Define mobility ratio at the front M_{sh} , analogous to the end point mobility ratio M_{end}

$$M_{sh} = \left(\frac{k_{r1}}{\mu_2} \right)_{S=S_{fr}} \quad (A29)$$

and define

$$\Delta\rho = \rho_1 - \rho_2 \quad (A30)$$

Define characteristic drainage rate q_{char} (see Hagoort's "free fall filter velocity" in [44])

$$q_{char} = K\Delta\rho gsin(\theta) \left[\frac{k_{r2_end}}{\mu_2} \right] \quad (A31)$$

Using the definition of M_α (Eq. A21), R_ρ (Eq. A2b), M_{sh} , $\Delta\rho$, and q_{char} , the condition for the onset of instability A28 is rewritten as

$$\left\{ \frac{1}{M_{s_hag}} - \frac{1}{M_\alpha} \right\} < \frac{-q_{char} (M_{sh} + \beta)}{q(1-\alpha) (M_{sh} + 1)} \quad (A32)$$

With $0 < \alpha < 1$, $0 < \beta < 1$ and $0 < \theta < \pi/2$, we have that the right hand side of condition A32 is always negative.

We have two situations, Case 1 and Case 2 as follows:

Case 1a: $M_{end} < \alpha$

In this case $M_\alpha < 0$, so A32 is never fulfilled and we have stable displacement for any value of M_{s_hag} and at any flow rate.

Case 1b: $M_{end} > \alpha$

In this case we have $0 < M_\alpha < 1$.

For $M_{s_hag} \leq M_\alpha$, we have no onset for stability irrespective whether gravity is active because condition A32 is never fulfilled.

In the event that $M_{s_hag} > M_\alpha$ we have stability for

$$q \leq \frac{q_{char} (M_{sh} + \beta)}{(1-\alpha) (M_{sh} + 1)} \left[\frac{1}{M_\alpha} - \frac{1}{M_{s_hag}} \right]^{-1} \quad (A33)$$

Summarising: relation A33 imposes a critical rate for stability in the presence of gravity, but only for $M_{s_hag} > M_\alpha$. So, despite $M_{s_hag} \leq M_\alpha$ would not be honoured, gravity brings about a stabilising effect, up to a critical rate (as in the classical stability criteria for viscous fingering derived by linear stability analysis). Above this rate, viscous forces counter balance gravity and the onset of fingering is surpassed. There is no rate dependency for the onset of fingering if $M_{s_hag} \leq M_\alpha$.

Case 2: $M_{end} = \alpha$

From the form of A32, we see that the right hand side of condition A28 is always negative, so for $M_{end} = \alpha$ we have condition A28 is never fulfilled, i.e. we have always stable displacement irrespective of flow rate, and for any value of M_{s_hag} .

Advanced Digital-SCAL measurements of gas trapped in sandstone

Ying Gao^{1,3,*}, Tibi Sorop¹, Niels Brussee¹, Hilbert van der Linde¹, Ab Coorn¹, Matthias Appel² and Steffen Berg^{1,3,4}

¹Shell Global Solutions International B.V., Grasweg 31, 1031 HW Amsterdam, Netherlands

²Shell International Exploration and Production Inc., 3333 Highway 6 S, Houston, TX 77082, USA

³Imperial College London, Department of Earth Science & Engineering, Exhibition Rd, South Kensington, London SW7 2BX, United Kingdom

⁴Imperial College London, Department of Chemical Engineering, Exhibition Rd, South Kensington, London SW7 2BX, United Kingdom

Abstract. Trapped gas saturation (S_{gr}) plays an important role in subsurface engineering such as carbon capture and storage, H_2 storage efficiency as well as the production of natural gas. Unfortunately, S_{gr} is notoriously difficult to measure in the laboratory or field. The conventional method of measurement- low-rate unsteady-state core flooding - is often impacted by gas dissolution effects, resulting in large uncertainties of the measured S_{gr} . Moreover, it is not understood why this effect occurs even for brines carefully pre-equilibrated with gas. In order to address this question, we used high resolution X-ray CT imaging techniques to directly visualize the pore-scale processes during gas trapping. Consistent with previous studies we find that for pre-equilibrated brine, the remaining gas saturation continually decreased with more (pre-equilibrated) brine injected and even after the brine injection was stopped, resulting in very low S_{gr} values (possibly even zero) at the pore scale level. Furthermore, we were able to clearly observe the initial trapping of gas by snap-off effect followed by a further shrinkage of the gas clusters that had no connected pathway to the outside. Our experimental insights suggest that the effect is related to the effective phase behaviour of gas inside the porous medium which due to the geometric confinement could be different than the phase behaviour of bulk fluids. The underlying mechanism is likely linked to ripening dynamics which involves a coupling between phase equilibrium and dissolution/partitioning of components, diffusive transport and capillarity in the geometric confinement of the pore space.

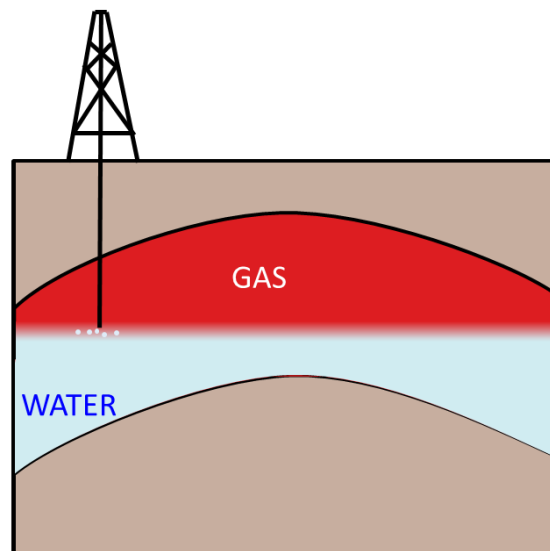
1 Introduction

In the space of multiphase flow in porous media which is encountered in many industrial surface and sub-surface applications such as groundwater management, contaminant hydrology and hydrocarbon recovery the recent focus on climate change and energy transition is also putting a higher priority on subsurface process that involve gasses such as carbon dioxide sequestration (CCS) and underground hydrogen storage [1-4]. For the gas-related processes ranging from natural gas production to CCS and H_2 storage, the trapped gas saturation (S_{gr}) is a key parameter [5-7].

Natural gas is mainly produced from gas reservoirs by pressure depletion. During production the reservoir pore pressure decreases. If a strong aquifer is present, the free water level could then rise during production because of the pressure depletion, causing the water from aquifer to imbibe into the pore space previously filled by gas (as rock in gas reservoirs is predominantly water-wet due to the absence of longer-chain hydrocarbon components), as sketched in Fig. 1. Water imbibition will then lead to capillary trapping of gas and limit the fraction of gas that can be produced, and hence negatively impact the economics of the projects. Similar considerations apply to hydrogen storage and CO_2

sequestration for which the amount of trapping can lead to different storage volumes than otherwise expected.

The trapped gas saturation depends on several parameters ranging from the phase behaviour/pressure-temperature conditions, depletion rate, rock type, wettability and interfacial tensions, and other petrophysical properties (porosity, permeability) to initial gas saturation [5-10].



* Corresponding author: Y.Gao3@shell.com

Fig. 1. Schematics of a gas reservoir with one producing well by pressure depletion, for the case of an active aquifer.

In practice, trapped gas saturations need to be measured experimentally. The importance of core analysis measurements for determination of residual gas saturation has long been recognised and a large amount of experimental work has been conducted in industry. Residual gas saturations reported in the literature range from 5% to 60% for the same porosity and for similar initial water saturations (there are reports suggesting even more than 70%, for tight samples) [11-22]. While it is known that residual saturation does not only depend on average porosity but also the pore structure, this large variation still raises the question whether this very large variation is not caused by other effects. This question was addressed in the study by Cense et al. [6] using one-dimensional in-situ X-ray saturation monitoring (ISSM) in USS core flooding experiments. It was observed that gas starts to dissolve within the core near the inlet while still gas is still displaced at outlet i.e. before trapping was reached [6] even though the injected brine was carefully pre-saturated with gas. That basically means that before reaching a true residual saturation (without any further gas displacement) the dissolution at the inlet may prevent or hide establishing a clear residual gas saturation over the whole sample [5-7] which would negatively impact the reliability of such measurements.

The advancement of pore scale imaging capability by X-ray computed micro tomography [26-27] provides an opportunity to investigate this problem in more detail. The micro-CT technology can provide not only the measurements of porosity, permeability, saturation of different phases, relative permeability, but also characterize the dynamics of gas/oil/water systems inside complex pore geometries at the scale of individual trapped gas bubbles [26,28]. This means that the trapping dynamics can now be visualised at the pore scale [35-40]. Iglauer et al. [41] started to image the trapped gas at the pore scale in a sandstone. Then Chaudhary et al. [42] extended the trapped CO₂ in various bead packs with wettability. Andrew et al. [43,44] imaged the trapped CO₂ in sandstone and carbonate under in-situ reservoir conditions. Furthermore, in addition to the long static images, dynamic imaging capability brings more advantage on study unsteady-state flow [28-34]. However, there has been no dynamic study on trapped gas saturation to learn why the uncertainty of the measured S_{gr} at core scale is so large.

The aim of this study is to address this question and quantify trapped gas saturation in sandstone rock by performing core flooding experiments with *dynamic* imaging by micro-CT which has been successfully applied in the past for studying the dynamic behaviour of the non-wetting phase [28,29,33] and gas [45,46]. In order to understand the reason why trapped gas dissolves despite the brine being saturated, which is one of the causes for the large range of observe S_{gr} , we conducted core flooding experiments with both gas saturated brine and unsaturated brine with dynamic imaging and establish the differences in flow regimes and compare the difference in dissolution characteristics.

2 Materials and methods

2.1. Rock samples and fluid properties

A cylindrical sample of a Bentheimer sandstone with the diameter of 4 mm and length of 20 mm was used in this study, see Fig. 2. The porosity estimated from the micro-CT image was 20.4 %, more details could be found in Section 2.3.2. The permeability measured on the bulk plug, where this mini-plug was drilled, is $2.48 \times 10^{-12} \text{ m}^2$.

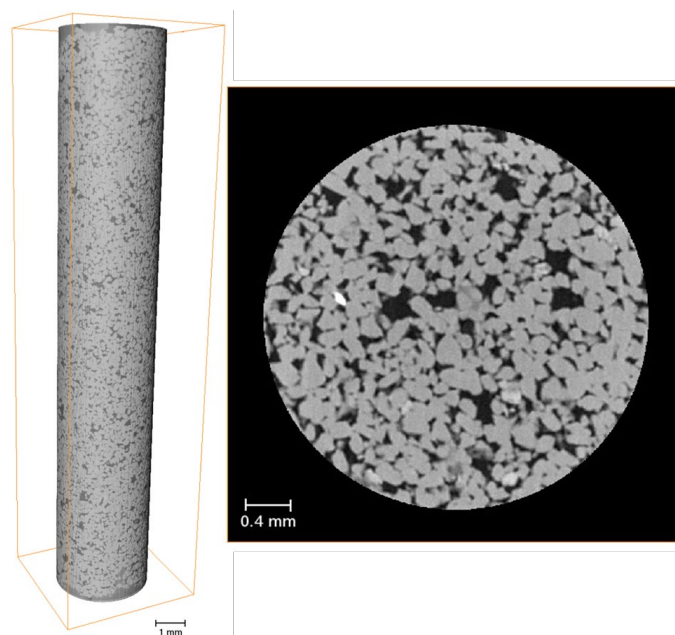


Fig. 2. On the left, three-dimensional X-ray image of the whole sample used in the experiment, with voxel size of 5 μm . On the right, two-dimensional cross sections of three-dimensional micro-CT images of a dry scan. The dark is pore space and the grey is grain.

The brine used in this study is water doped with 5 wt% NaI to increase the contrast and to distinguish the interface between gas and brine. The gas used in this work is compressed air.

2.2 Experimental methods

Unsteady state (USS) brine displacing gas experiments at laboratory temperature were conducted. This study consisted of two main experiments: a) an USS flow experiment performed using the gas saturated brine at 0.5 $\mu\text{L}/\text{min}$; and b) an USS flow experiment performed using unsaturated brine at 0.5 $\mu\text{L}/\text{min}$. From these two experiments, we could compare how gas dissolution impact the trapped gas saturation.

The flow apparatus of these experiments is shown in Fig. 3. The experimental flow apparatus showing the three main components: core holder, differential pressure transducer, and four syringe pumps to apply a constant flow rate as well as confining and back pressure. The sample was placed in a fluoropolymer elastomer (Viton) sleeve in the carbon fibre

Hassler type flow cell. Fluid flow lines were used to connect the core holder with the pumps. The core holder used in this work is shown in Fig. 4.

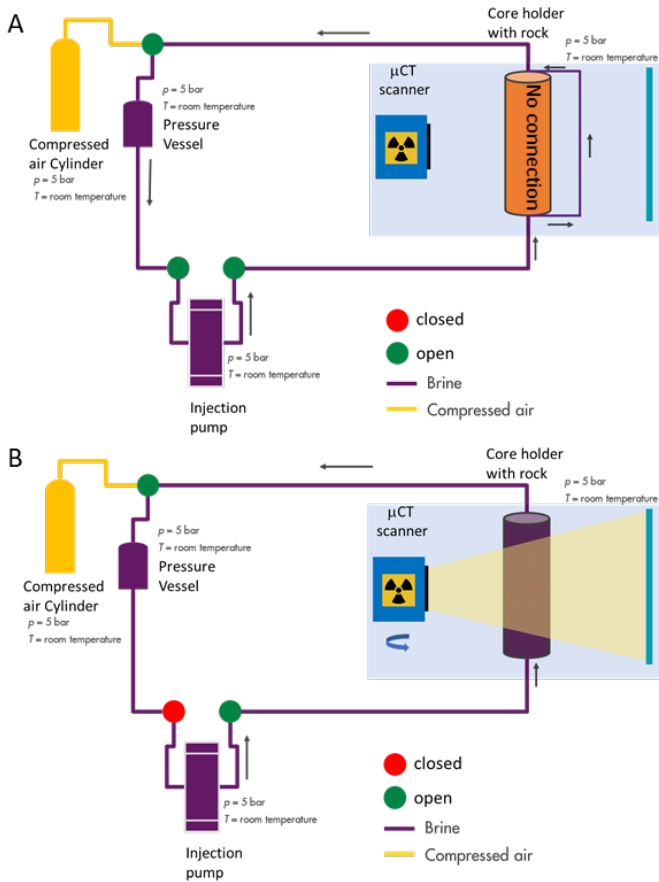


Fig. 3. The experimental flow apparatus used in this work: (A) for mixing brine and compressed air; (B) for displacement experiments.

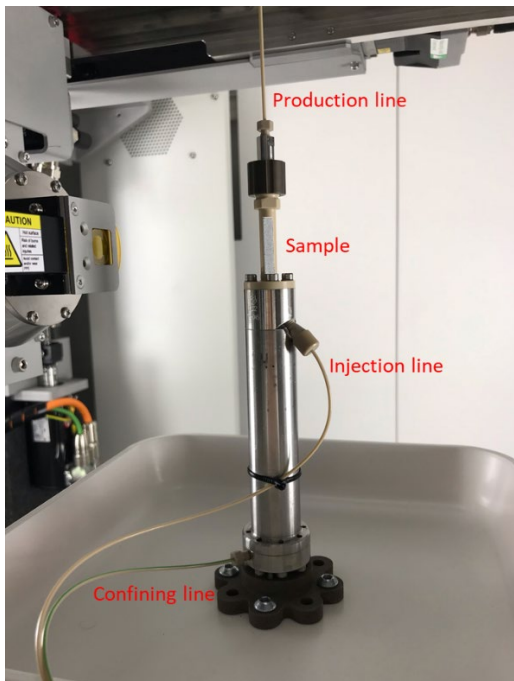


Fig. 4. The core holder used in this study. Brine was injected from the bottom of the sample and the production line is at the top of the core holder.

The experiments were performed by following the steps:

1. The brine was prepared in the Quizix pump at 5 bar.
2. The Bentheimer rock sample was put in the Viton sleeve in the core holder. Fluid flow lines were used to connect the pumps and core holder that was mounted inside the micro-CT scanner.
3. Confining pressure was applied by injecting deionized water into the empty annulus space between the carbon fibre sleeve and the Viton sleeve. To avoid any bypass flow between the sample and the sleeve, the confining pressure was set as 30 bar.
4. A dry scan of the whole sample was taken with the voxel size of 5 μm .
5. The back pressure was set at 5 bar using water saturated compressed air.
6. Brine and compressed air were mixed by recirculating through the flow lines bypassing the sample at 5 bar for more than 48 hours, as Fig. 3(A) shows. The compressed air cylinder was open and the sample was disconnected from the flow line.
7. Only air was inside of the rock sample at the start of the experiment, meaning that the initial gas saturation is 1. Brine was injected at a very low flow rate of 0.5 $\mu\text{L}/\text{min}$ to ensure that the pressure drop across the sample is less than 2% of the pore pressure (as recommended in [6]) to make sure that the pressure gradient along the sample would not be too high to dissolve more compressed air. The pressure drop along the sample would be from 0.6 mbar when it was fully saturated with brine, which is far more less than 5 bar – the back pressure. Fig. 3(B) shows the flow loop for the displacement experiments.
8. Images with voxel size of 5 μm were taken at the same time continually during the coreflooding. It usually takes around 30 minutes for a high-resolution 3D image.

For the first experiment – (USS coreflood performed using the gas saturated brine) we found that after breakthrough the gas saturation changes slowly if we keep injecting beyond 1 PV. At this stage of the experiment, the images were taken once every hour. After injecting 32 PV, the flow rate was increased to 1 $\mu\text{L}/\text{min}$ and then to 2 $\mu\text{L}/\text{min}$ after injecting 46 PV. The experiment was stopped when no gas was found in the sample, after around 60 hours.

For the second experiment – (USS flow experiment performed using the unsaturated brine) we follow a similar protocol, however since we found that all the gas in the sample disappeared after injecting 4 PV, we stopped the tests after around 5 hours.

2.3 Imaging methods and processing

2.3.1 Imaging Method

The 3D images were taken by a TESCAN DynaTOM X-ray microscope (which is a vertical gantry based micro-CT) using a flat panel detector, see Fig. 5. The X-ray energy was 130

keV and the power was 16 W. The number of projections for the dry scan was 2200 and the average of the frame was 10 to enhance image quality and the projections of the dynamic scans was 1500 with 1 frame averaging. There are two key advantages of this scanner when flow experiments were conducted: (1) the gantry rotates 360 degrees with sample fixed on the sample stage without moving the flow lines - keeping the stability of the core flooding experiment, (2) the time resolution for imaging is very quick, so it only takes 30 minutes to take the image of the whole sample length (which was scanned in 4 segments) compared to several hours for a conventional desktop micro-CT scanner for only one segment.

All tomograms were reconstructed into three-dimensional images using the Panteha reconstruction software (TESCAN). The voxel size of all the images is 5 μm and the size of the images was $800 \times 800 \times 3780$.

All images were registered to the dry scan to have the same orientation. The Lanczos algorithm was used to resample the images [46]. A non-local means filter was used to remove noise and smooth the images while preserving edges [48-50].

The images are processed in Avizo using the watershed method for segmentation.

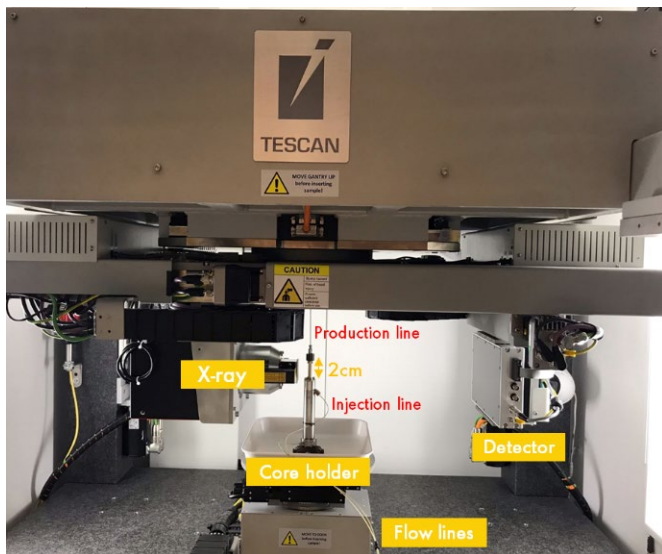


Fig. 5. Flow apparatus placed inside the gantry of the DynaTOM micro-CT scanner.

2.3.2 Characterization of the fluid in the pore space

The cross-section images of the sample are shown in Fig. 6. The top image shows the segmented image of the dry scan, pore space in blue and grains in grey. The bottom image shows the segmented image when 25.6 PV brine was injected, with brine in blue, gas in red and grains in grey.

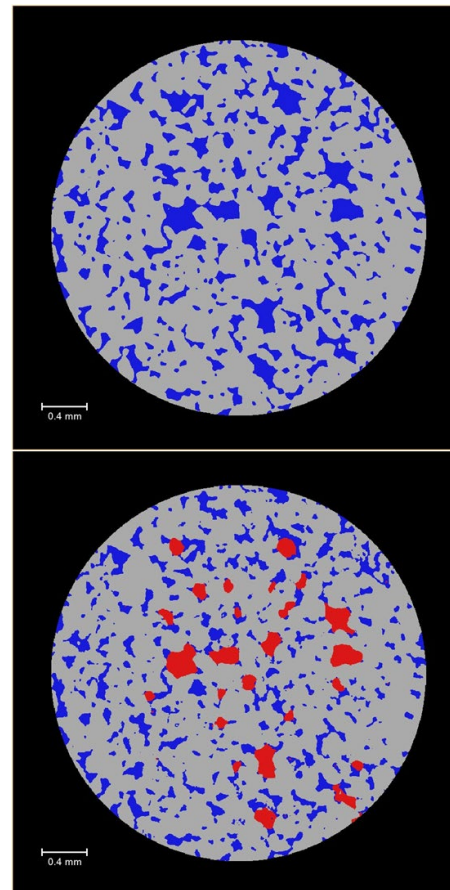


Fig. 6. Two-dimensional cross sections (same slice as in Fig. 2) of three-dimensional segmented images of a dry scan (top). At the bottom we show the same slice for a flow experiment with the gas phase in red and brine in blue.

3 Results and discussion

In the Section 3.1 and Section 3.2 respectively, we present the trapped gas distribution and the quantification of the gas saturation across the sample for the two USS experiments described in the previous section. This is followed by the comparison and discussion of these two experiments: in Section 3.3 on saturation profiles and in Section 3.4 on how trapped gas distributes through the inner pore space.

3.1. USS flow experiment with gas saturated brine

The USS flow experiment using gas saturated brine was performed in 60.1 hours during which 30 whole-sample 3D images were collected. Fig. 7 shows a time sequence with 10 representative examples taken at different stages, displaying the water/gas displacement process. As expected, we found that the brine has invaded the whole sample relatively quickly, aided by the spontaneous imbibition process. As a result, quickly after breakthrough, the gas in the pore throats was displaced leaving ultimately trapped gas in the large pore bodies. If we continue injection, we find however that after about 8 PV injected, the gas completely disappeared first near the inlet of the sample then gradually more gas disappeared from the inlet to the outlet. At the end of the process, if we continue injecting even more brine all of the gas from the sample disappeared.

To quantify the gas saturation at each pore volume injected, images were all segmented using interactive thresholding module in the Avizo software. Fig. 8 shows the average gas saturation in the sample as a function of pore volume injected, as a red curve. Three stages can be identified. For the first stage (from 0 to 1-2 PV) the water/gas displacement process plays a dominant role. We infer this from the gradient of saturation vs. injected volume curve ~ 0.96 , which is very close to 1. Gas saturation decreased from 1 to around 0.38 during the injection of the first PV of brine. For the next two stages we hypothesize that even though we carefully prepared and saturated the brine with gas, the gas-brine dissolution plays an important role. In the second stage (2 to 18 PV injected) a decrease in S_g from 0.38 to 0.1 is observed. We label this as the first stage of dissolution (i.e. Dissolution 1). Next, the dissolution rate decreased to a lower rate (which we label as Dissolution 2) until there is no gas in the pores and throats. Thus, even though the brine was fully saturated with gas before the start of the experiment, gas could still dissolve slowly in the brine. As less and less gas-brine interfaces are available when more PV brine was injected, the dissolution rate decreased leading to two dissolution regimes each with constant dissolution rate (linear decrease of gas saturation with time). At this point it is not entirely clear what these two different regimes represent but it is possible that the Dissolution 1 regime might still contain some displacement (and hence saturation decreases faster) while the Dissolution 2 regime contains only dissolution.

3.2. USS flow experiment with unsaturated brine

At the moment of performing the first tests it was not clear what really causes the dissolution of the gas, even though the injection brine is gas saturated. In order to get a clear reference point to what conventional dissolution would look-like, we performed a second experiment in which we injected unsaturated brine.

This experiment lasted 5.3 hours and 10 images were collected. Fig. 9 shows how gas distributes when more unsaturated brine was injected. Grey-scale images show how gas was displaced.

Fig. 10 shows the gas saturation as a function of pore volume injected. Compared with the USS flow experiments with fully saturated brine (in Section 3.1), we only see two stages in this experiment. Consistent with the first experiment, S_{gr} decreased from 1 to 0.17 when 1.5 PV brine was injected, in which displacement dominated the change on S_{gr} . It is not always possible to completely distinguish the proportion of displacement and dissolution. But when looking at Fig. 11 and 12 it is clear that saturation increase beyond $1-S_{gr}$ has to be dissolution, where S_{gr} is typically in the range of 10% or more, depending on a number of parameters. So saturations close to 100% brine would mean that some dissolution has to have happened. On the other hand, while gas is still connected as visible from the connectivity in Fig. 13 and 14, displacement is the faster process. The discrimination is perhaps best done when looking at the average gas saturation vs. injected PV in Figs. 8 and 10, where we can relate regions

if similar slope with the intervals in Fig. 11 - 14 where we can identify the dominant mechanism. As the absolute value of the gradient of this curve is 0.75, not only displacement, but also the dissolution plays a role on saturation change. Then the S_{gr} decreased to 0 in 3 hours in a very low dissolution rate. However, the dissolution stage starts at earlier stage than the experiment with saturated brine and the displacement and dissolution happened at the same time, as indicated in Fig. 10.

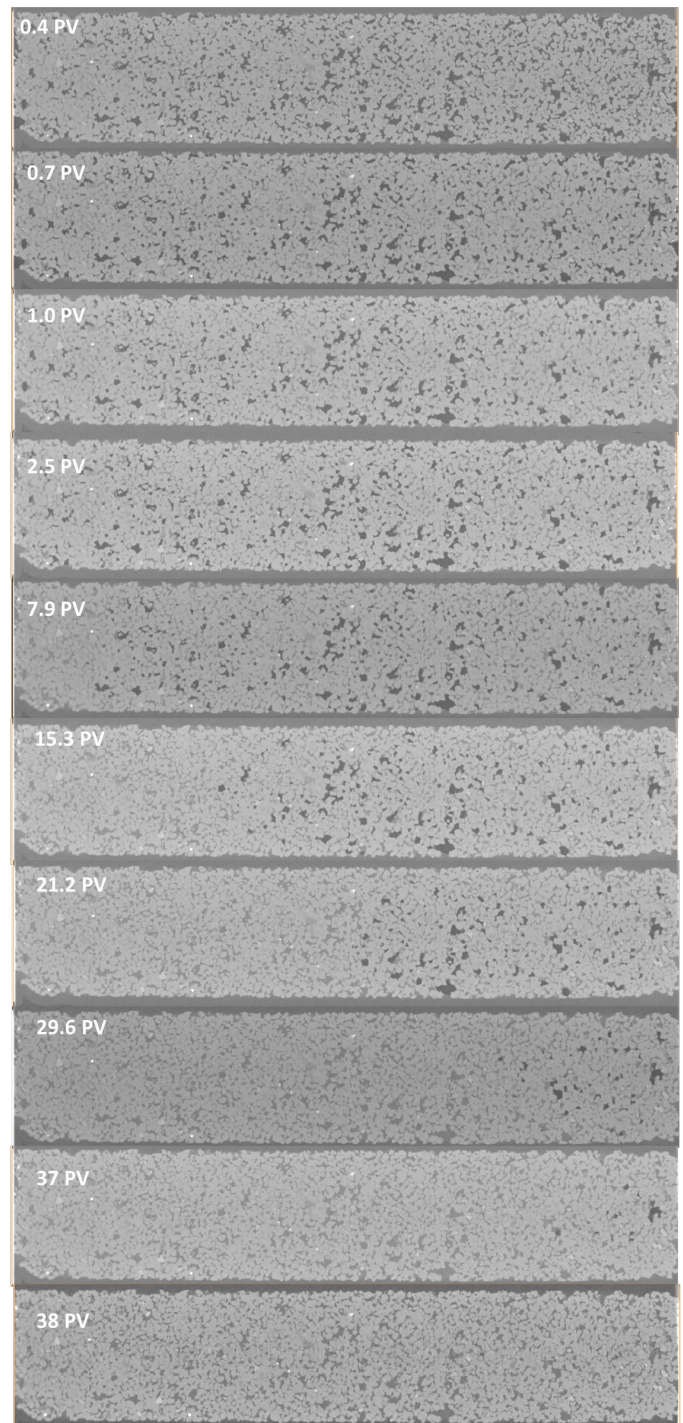


Fig. 7. 2D grey-scale images perpendicular to the flow direction when the sample was flooded by the gas saturated brine. The

injection direction is from left to right. Light grey is grain, dark grey is brine, and the black is gas.

by a combination of interfacial area but also solute dispersion in combination with local thermodynamics and dissolution kinetics which should also scale somehow with factors such as local capillary pressure in the gas bubble and local (super) saturation in the brine.

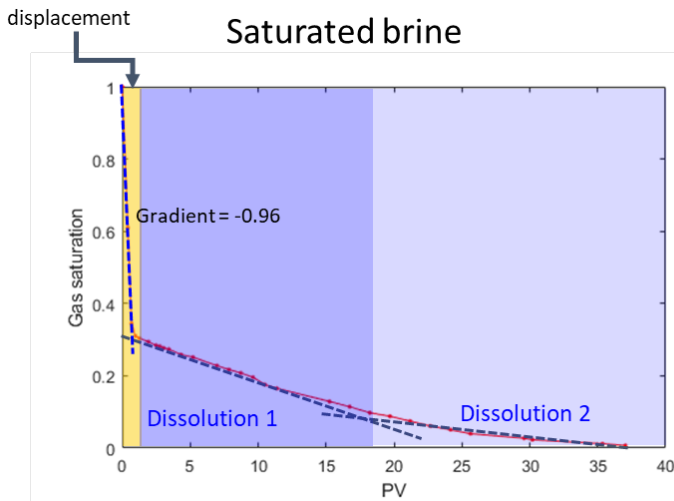


Fig. 8. For the USS flow experiment with gas saturated brine, the red curve shows the trapped saturations as a function of pore volumes injected. The yellow shadow is displacement stage, dark purple represents the “Dissolution 1” stage and light purple represents the “Dissolution 2” stage.

3.3. Saturation profiles

In order to get further insights, the saturation profiles along the cores were computed for the two experiments from Fig. 7 and Fig. 9. From the segmented 3D images the saturation in each slice perpendicular to the long sample axis was averaged and plotted vs. distance from the inlet. The respective saturation profiles shown in Fig. 11 and Fig. 12 illustrate the trend how the gas distributes in the whole sample when injecting saturated and un-saturated brine, respectively.

In Fig. 11, we can see the brine has imbibed into a lot of small pores and throats during the injection of 1-2 PV leading to significant trapping, which is related to the Displacement stage. Then the brine saturation increases throughout the sample in a homogeneous manner, which is a signature for displacement processes. At some point the gas phase starts to disappear from the inlet above the trapping limit at the stage of Dissolution 1 i.e. as a frontal dissolution process. However, we still see some homogeneous increase of saturation during that stage in a similar manner as during the displacement stage which could indicate that during this stage still displacement occurs. Then the Dissolution 2 starts until S_{gr} locally decreases to 0.

Because of the involvement of many parameters in particular the solute dispersion behaviour, and the proportionality to the interfacial area, the dissolution rate limit is not so easy to estimate. At equilibrium, the gas dissolution limit in unsaturated brine at 5 bar is about 2 vol%. But the actual dissolution rate, which could be calculated from the saturation change from Fig. 8 and 10, exceeds the equilibrium assumption, which means that such simple estimates do not work. We think that at the end the dissolution rate is governed

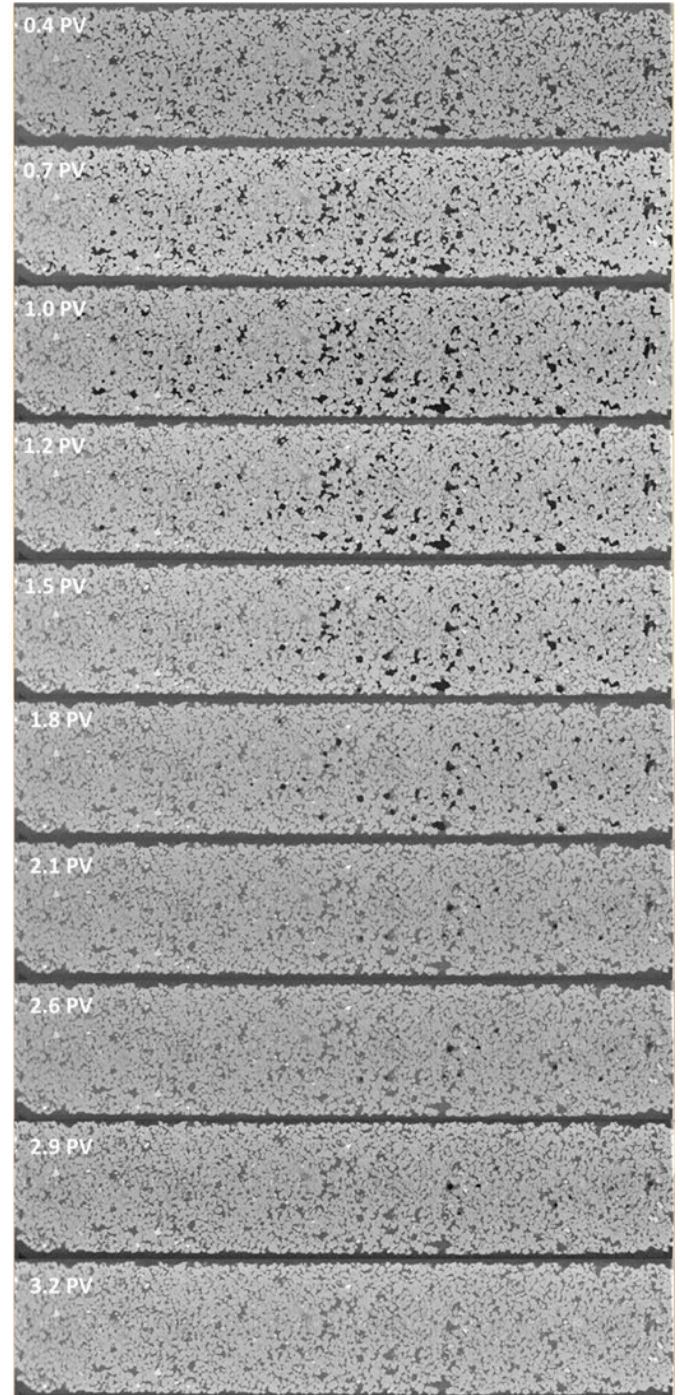
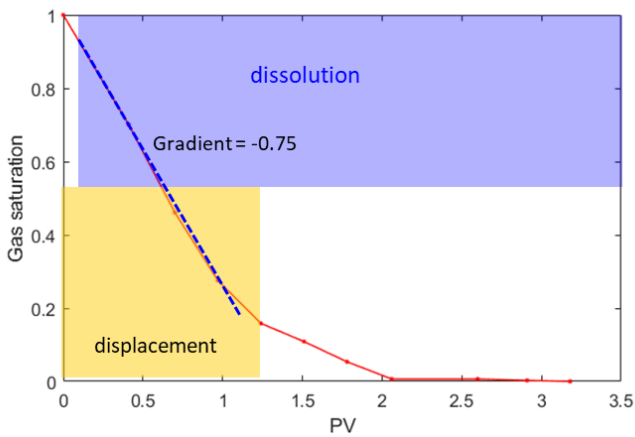


Fig. 9. 2D Grey-scale images perpendicular to the flow direction when the sample was flooded by unsaturated brine. The injection direction is from left to right. Light grey is grain, dark grey is brine, and the black is gas.

Unsaturated Brine



However, for the unsaturated brine case shown in Fig. 12 there are distinct differences compared with the saturated case. At the early stage there is always a superposition of dissolution and displacement. And at the late stage where brine saturation increases above the limit by trapping, i.e. can only increase by dissolution, the dissolution occurs homogeneously over the whole sample, while in the saturated case it was always a frontal dissolution process.

Fig. 10. For the USS flow experiment with unsaturated brine, the red curve shows the trapped gas saturations as a function of pore volumes injected. The yellow shadow represents displacement stage, the purple represents the stage of Dissolution. For unsaturated brine there is a large overlap between displacement and dissolution where dissolution already begins right away in a significant fraction in parallel to displacement processes.

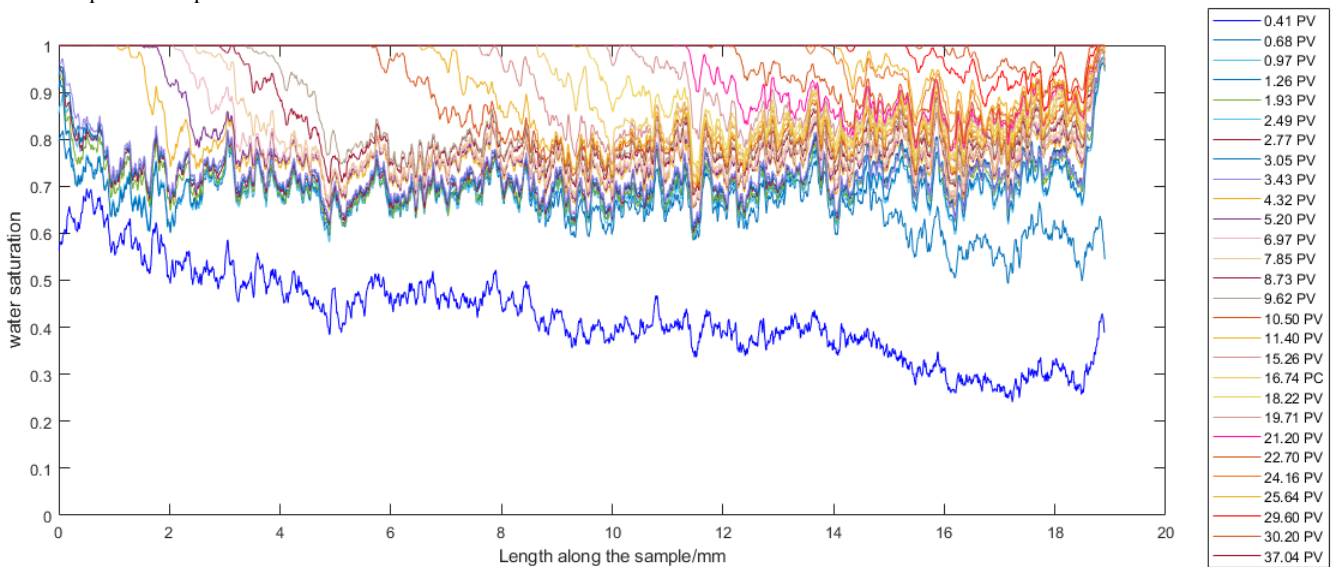


Fig. 11. For the USS flow experiment with gas saturated brine, brine saturation profiles averaged in slices perpendicular to the flow direction at each PV with gas saturated brine injected.

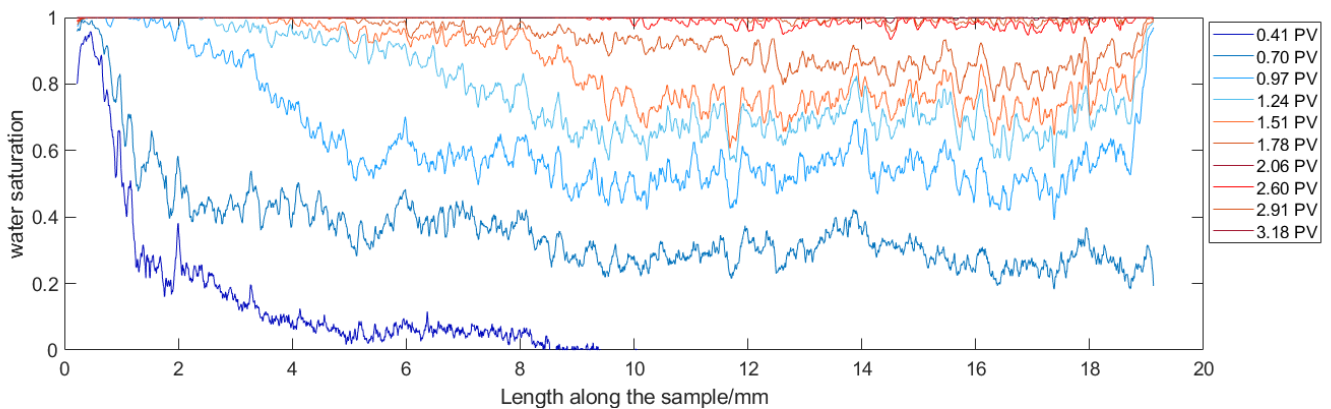


Fig. 12. For the USS flow experiment with unsaturated brine, brine saturation profiles averaged in slices perpendicular to the flow direction at each PV with unsaturated brine injected.

3.4. Trapped gas distribution visualized in 3D

The displacement and dissolution characteristics from the saturation profiles in Section 3.3 are also visible in 3D which allows to visualize also the gas connectivity. Comparing the gas-saturated brine case in Fig. 13 with the unsaturated case in Fig. 14 we found that the gas distribution is very different.

Fig. 13 shows three-dimensional images of the (trapped) gas distribution when it was displaced by *gas-saturated* brine. Each colour represents disconnected gas clusters/ganglia. When 0.4 PV brine was injected, we could see in the gas-saturated brine case the displacement dominated the flow regime and some gas clusters at the inlet start to be isolated while gas volume decreased. When more brine was injected to 0.7 PV, the gas saturated brine has already separated the gas clusters while majority of the gas phase still connected when the similar volume unsaturated brine was flooded. Continually, gas volume decreased with more gas saturated brine injected but gas did not disappear from the inlet of the sample before 7 PV brine was injected.

In other words, the brine passed through the sample first and gas clusters became disconnected first. The dissolution started to play a role after 2 PV brine injected mainly as a frontal dissolution process. During that process, beginning from the inlet side, the volume of each cluster is decreasing gradually until it disappears.

Fig. 14 shows three-dimensional images of the (trapped) gas distribution in the sample when it was displaced by *unsaturated* brine. In general, the volume of disconnected gas cluster/ganglion in Fig. 14 is much smaller and more separated than in the saturated case. The gas decreased much faster and all gas disappeared after injecting around 3 PV brine. However, initially, the gas clusters remain a much higher connectivity in particular towards the outlet indicating that they were not or only very little affected by displacement processes. At the same time, we see already dissolution occurring at the inlet.

Fig. 15 shows an example for the steps how the gas was first trapped and then dissolved in the brine. After 1 PV of gas saturated brine was injected, the gas was trapped in the pore. With more brine was injected, the gas volume is shrinking and gradually becoming a sphere and then eventually disappears completely.

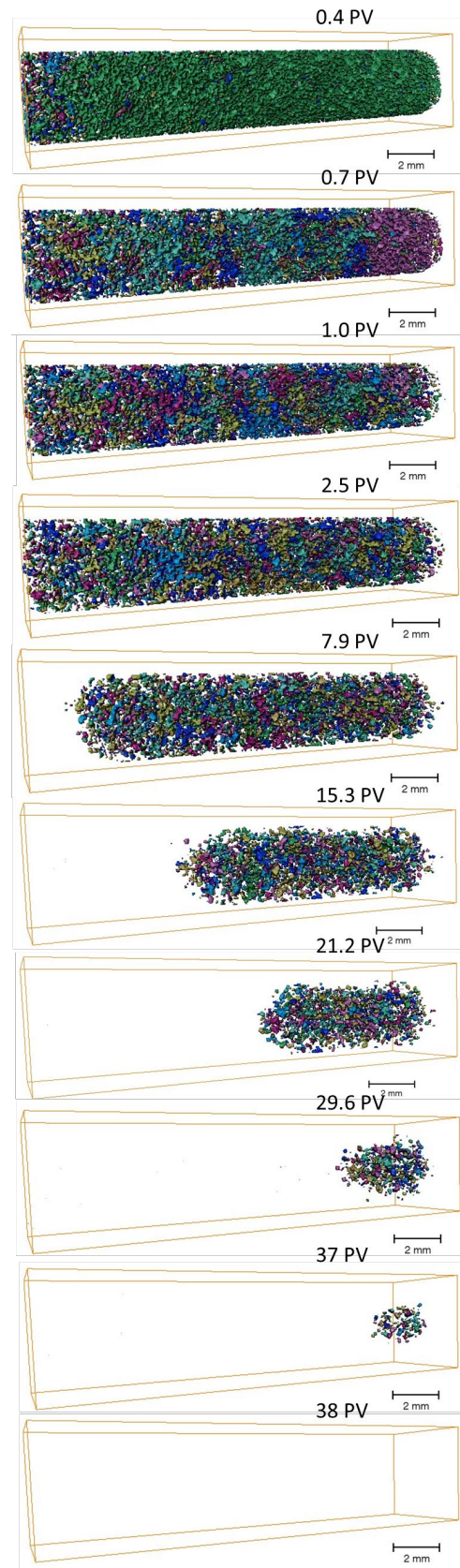


Fig. 13. Three-dimensional images of the configuration of gas along the sample during the USS flow experiment with **gas saturated** brine. Each colour represents separated gas clusters/ganglia.

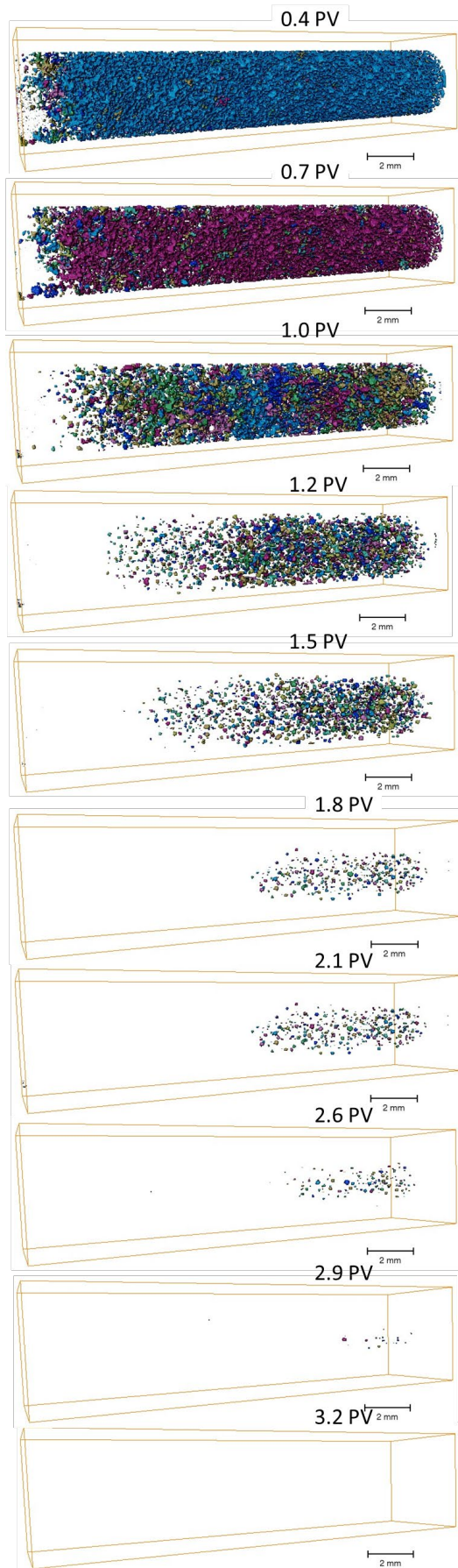


Fig. 14. Three-dimensional images of the configuration of gas along the sample during the USS flow experiment with **unsaturated brine**. Each colour represents separated gas clusters/ganglia.

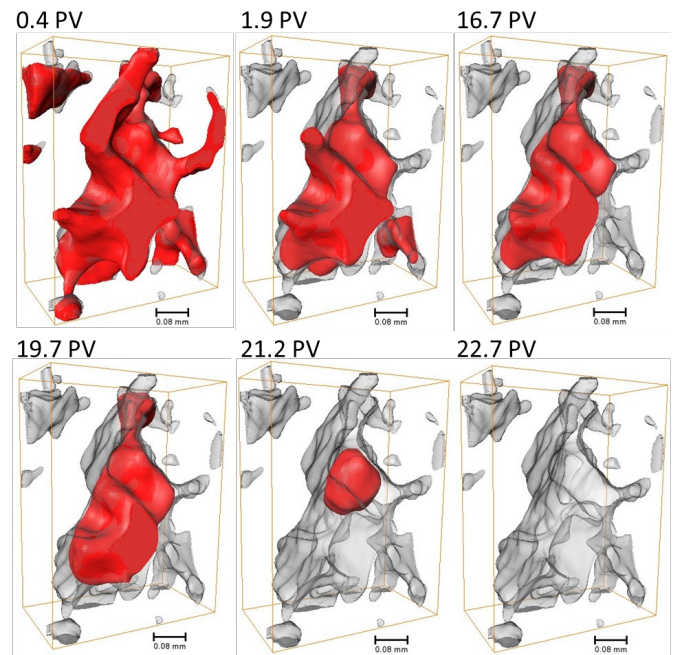


Fig. 15. Gas configuration during injecting at the pore scale. Gas was trapped first and then the volume decreased until disappeared.

That supports the view that the gas-saturated brine must really be at bulk saturation level, i.e. saturation at injection pressure (and temperature). However, in the pore space, that brine is slightly under-saturated with respect to the pore pressure of the gas, which is the injection pressure plus the capillary pressure of the gas. The situation is similar as in ripening dynamics, where local capillary pressure leads to an increase in partitioning of gas into the liquid phase followed by diffusive transport to larger gas bubbles with lower capillary pressure. In absence of external flow, this diffusive exchange leads to the ripening dynamics. As the size of the gas bubble decrease because of the dissolution, the capillary pressure increases which is increasing the dissolution rate.

In previous studies there were already indications for ripening/anti-ripening process occurring in similar situation [45,46,51,52]. This provides a credible setting for the effect observed here as well, only that the situation is slightly different because there is external flow. That means that there is less chance of the traditional ripening to occur where smaller gas bubbles are “eaten” up by larger gas bubbles because that require local super-saturation and diffusive exchange. However, in the presence of an external flow field the advection rate might be locally much higher than diffusion which is then maintaining the concentration at a constant level (saturated to injection pressure at the inlet and due to gas dissolution saturated to a maximum possible saturation throughout the rest of the sample). That prevents the type of mass exchange between smaller and larger bubbles normally seen in Ostwald ripening which is in addition also constrained by pore sizes in porous media.

4 Conclusions

This paper provides fundamentally novel insights into the trapping of gas in sandstone rock, using state-of-the-art imaging techniques during core flooding. An experimental workflow is presented where at the pore scale gas and brine distributions within samples are imaged by 3D X-ray computed micro-tomography, while continuously injecting brine. In contrast to the conventional in-situ saturation monitoring approach, used currently by many SCAL laboratories, this approach has the advantage that the dynamic behaviour of the gas and the changes in saturation are visualized at the pore scale level. This does not only allow us to obtain in situ evidence and to quantification of trapped gas saturation but other impact factors such as capillary effects that may influence the trapping behaviour.

Our experiments reproduce the behaviour reported in the literature [6] that even though gas-saturated brine is injected the trapped gas still dissolves. Without detailed pore scale resolution that allows to discriminate dissolution from displacement at least to some extent, the gas/brine dissolution effect significantly impacts the ability of accurately determining the trapped gas saturation.

By conducting gas trapping flow experiments with both gas-saturated brine and also brine that was not saturated with gas, we could establish a clear difference in pore scale flow regimes between the two situations which differ in dissolution and displacement behaviour. For the non-saturated brine, we observe gas displacement and gas dissolution in parallel, where the gas dissolution follows a predominantly frontal dissolution from the inlet. For the gas-saturated brine, we see a clearer separation of displacement and dissolution processes. Initially the gas saturation decrease is dominated by displacement which leads to disconnected and presumably trapped gas. After almost all gas has been trapped, dissolution occurs more homogeneously throughout the whole sample shrinking first all gas bubbles, followed by a somewhat less pronounced frontal dissolution.

Based on the differences in the displacement/dissolution regime and the observation of the pore scale dissolution dynamics and impact on connectivity, we find supporting evidence that the underlying reason of the dissolution of gas might be linked to ripening dynamics which involves a coupling between phase equilibrium and dissolution/partitioning of components on the one hand and capillarity in the geometric confinement of the pore space on the other hand.

The solution to decrease the impact of dissolution on quantifying trapped gas saturation might be to inject slightly super-saturated brine i.e. brine equilibrated at injection pressure plus a representative capillary pressure, which requires further studies in the future, which are already in the planning.

These insights clearly demonstrate the value of combining multiphase flow experiments with pore-scale imaging because that can provide key insights and lead to solutions to some of the challenges often faced from conventional SCAL experiments. These insights can be used to develop more rigorously validated, physically based pore-scale models of pore scale processes that are more robust than empirical correlations to predict trapped gas saturation under various conditions. For instance, with high quality 3D images of the rock samples with two or three phases flowing through the pore space, how rock structure, flow rate and wettability could impact on the phase behaviours and transport inside of the reservoir subsurface could be clearly captured. The techniques could be adapted for several applications, including EOR, CCS and H₂ storage.

Acknowledgements

The authors would like to thank Rouhi Farajzadeh for very insightful discussions.

References

1. Bachu, S., 2003. Screening and ranking of sedimentary basins for sequestration of CO₂ in geological media in response to climate change. *Environmental Geology*, 44(3), pp.277-289.
2. Benson, S.M. and Cole, D.R., 2008. CO₂ sequestration in deep sedimentary formations. *Elements*, 4(5), pp.325-331.
3. Juanes, R., MacMinn, C.W. and Szulczewski, M.L., 2010. The footprint of the CO₂ plume during carbon dioxide storage in saline aquifers: storage efficiency for capillary trapping at the basin scale. *Transport in porous media*, 82(1), pp.19-30.
4. Blunt, M.J., 2017. *Multiphase flow in permeable media: A pore-scale perspective*. Cambridge university press.
5. Bull, Ø., Bratteli, F., Ringen, J.K., Melhuus, K., Bye, A.L. and Iversen, J.E., 2011, September. The Quest for the True Residual Gas Saturation – an Experimental Approach. In *International Symposium of the Society of Core Analysts*, Texas, USA (pp. 1-12).
6. Cense, A., Reed, J. and Egermann, P., 2016, August. SCAL for gas reservoirs: a contribution for better experiments. In *International Symposium of the Society of Core Analysts held in Snowmass, Colorado, USA* (pp. 21-26).
7. Cense, A.W., Van der Linde, H.A., Brussee, N., Beljaars, J. and Schwing, A., 2014, September. How reliable is in situ saturation monitoring (ISSM) using X-ray?. In *International Symposium of the SCA*.
8. Geistlinger, H., Mohammadian, S., Schlueter, S. and Vogel, H.J., 2014. Quantification of capillary trapping of gas clusters using X-ray microtomography. *Water Resources Research*, 50(5), pp.4514-4529.
9. Herring, A.L., Andersson, L., Schlüter, S., Sheppard, A. and Wildenschild, D., 2015. Efficiently engineering pore-scale processes: The role of force dominance and

- topology during nonwetting phase trapping in porous media. *Advances in Water Resources*, 79, pp.91-102.
10. Gershenzon, N.I., Ritzi Jr, R.W., Dominic, D.F., Mehnert, E., Okwen, R.T. and Patterson, C., 2017. CO₂ trapping in reservoirs with fluvial architecture: Sensitivity to heterogeneity in permeability and constitutive relationship parameters for different rock types. *Journal of Petroleum Science and Engineering*, 155, pp.89-99.
 11. Geffen, T. M., D. R. Parrish, G. W. Haynes, and R. A. Morse. "Efficiency of gas displacement from porous media by liquid flooding." *Journal of Petroleum Technology* 4, no. 02 (1952): 29-38.
 12. Keelan, D.K. and Pugh, V.J., 1975. Trapped-gas saturations in carbonate formations. *Society of Petroleum Engineers Journal*, 15(02), pp.149-160.
 13. Crowell, D.C., Dean, G.W. and Loomis, A.G., 1966. Efficiency of gas displacement from a water-drive reservoir (Vol. 6735). US Department of the Interior, Bureau of Mines.
 14. Pickell, J.J., Swanson, B.F. and Hickman, W.B., 1966. Application of air-mercury and oil-air capillary pressure data in the study of pore structure and fluid distribution. *Society of Petroleum Engineers Journal*, 6(01), pp.55-61.
 15. Land, C.S., 1971. Comparison of calculated with experimental imbibition relative permeability. *Society of Petroleum Engineers Journal*, 11(04), pp.419-425.
 16. Kleppe, J., Delaplace, P., Lenormand, R., Hamon, G. and Chaput, E., 1997, October. Representation of capillary pressure hysteresis in reservoir simulation. In SPE annual technical conference and exhibition. OnePetro.
 17. Suzanne, K., Hamon, G., Billiotte, J. and Trocme, V., 2003, October. Experimental relationships between residual gas saturation and initial gas saturation in heterogeneous sandstone reservoirs. In SPE Annual Technical Conference and Exhibition. OnePetro.
 18. Long, L.C., 1963, June. Experimental research on gas saturation behind the water front in gas reservoirs subjected to water drive. In 6th World Petroleum Congress. OnePetro.
 19. Land, C.S., 1968. Calculation of imbibition relative permeability for two-and three-phase flow from rock properties. *Society of Petroleum Engineers Journal*, 8(02), pp.149-156.
 20. Firoozabadi, A., Olsen, G. and van Golf-Racht, T., 1987, April. Residual gas saturation in water-drive gas reservoirs. In SPE California Regional Meeting. OnePetro.
 21. Holtz, M.H., 2002, April. Residual gas saturation to aquifer influx: A calculation method for 3-D computer reservoir model construction. In SPE Gas Technology Symposium. OnePetro.
 22. Mulyadi, H., Amin, R., Kennaird, T., Bakker, G., Palmer, I., Fletcher, C. and Van Nispen, D., 2000, November. Measurement of residual gas saturation in water-driven gas reservoirs: comparison of various core analysis techniques. In International Oil and Gas Conference and Exhibition in China. OnePetro.
 23. Perrin, J.C. and Benson, S., 2010. An experimental study on the influence of sub-core scale heterogeneities on CO₂ distribution in reservoir rocks. *Transport in porous media*, 82(1), pp.93-109.
 24. Krevor, S.C., Pini, R., Li, B. and Benson, S.M., 2011. Capillary heterogeneity trapping of CO₂ in a sandstone rock at reservoir conditions. *Geophysical Research Letters*, 38(15).
 25. Ni, H., Boon, M., Garing, C. and Benson, S.M., 2019. Predicting CO₂ residual trapping ability based on experimental petrophysical properties for different sandstone types. *International Journal of Greenhouse Gas Control*, 86, pp.158-176.
 26. Blunt, M.J., Bijeljic, B., Dong, H., Gharbi, O., Iglauer, S., Mostaghimi, P., Paluszny, A. and Pentland, C., 2013. Pore-scale imaging and modelling. *Advances in Water resources*, 51, pp.197-216.
 27. Wildenschild, D. and Sheppard, A.P., 2013. X-ray imaging and analysis techniques for quantifying pore-scale structure and processes in subsurface porous medium systems. *Advances in Water resources*, 51, pp.217-246.
 28. Berg, S., Ott, H., Klapp, S.A., Schwing, A., Neiteler, R., Brussee, N., Makurat, A., Leu, L., Enzmann, F., Schwarz, J.O. and Kersten, M., 2013. Real-time 3D imaging of Haines jumps in porous media flow. *Proceedings of the National Academy of Sciences*, 110(10), pp.3755-3759.
 29. Rücker, M., Berg, S., Armstrong, R.T., Georgiadis, A., Ott, H., Schwing, A., Neiteler, R., Brussee, N., Makurat, A., Leu, L. and Wolf, M., 2015. From connected pathway flow to ganglion dynamics. *Geophysical Research Letters*, 42(10), pp.3888-3894.
 30. Berg, S., Armstrong, R., Ott, H., Georgiadis, A., Klapp, S.A., Schwing, A., Neiteler, R., Brussee, N., Makurat, A., Leu, L. and Enzmann, F., 2014. Multiphase flow in porous rock imaged under dynamic flow conditions with fast X-ray computed microtomography. *Petrophysics-The SPWLA Journal of Formation Evaluation and Reservoir Description*, 55(04), pp.304-312.
 31. Spurin, C., Bultreys, T., Bijeljic, B., Blunt, M.J. and Krevor, S., 2019. Mechanisms controlling fluid breakup and reconnection during two-phase flow in porous media. *Physical Review E*, 100(4), p.043115.
 32. Spurin, C., Bultreys, T., Bijeljic, B., Blunt, M.J. and Krevor, S., 2019. Intermittent fluid connectivity during two-phase flow in a heterogeneous carbonate rock. *Physical Review E*, 100(4), p.043103.
 33. Gao, Y., Lin, Q., Bijeljic, B. and Blunt, M.J., 2020. Pore-scale dynamics and the multiphase Darcy law. *Physical Review Fluids*, 5(1), p.013801.
 34. Gao, Y., Raeni, A.Q., Blunt, M.J. and Bijeljic, B., 2021. Dynamic fluid configurations in steady-state two-phase flow in Bentheimer sandstone. *Physical Review E*, 103(1), p.013110.
 35. Al Mansoori, S., Iglauer, S., Pentland, C.H., Bijeljic, B. and Blunt, M.J., 2009. Measurements of non-wetting

- phase trapping applied to carbon dioxide storage. *Energy Procedia*, 1(1), pp.3173-3180.
36. Pentland, C.H., Itsekiri, E., Al Mansoori, S.K., Iglauer, S., Bijeljic, B. and Blunt, M.J., 2010. Measurement of nonwetting-phase trapping in sandpacks. *Spe Journal*, 15(02), pp.274-281.
 37. Bennion, D.B. and Bachu, S., 2010, September. Drainage and imbibition CO₂/brine relative permeability curves at reservoir conditions for carbonate formations. In *SPE Annual Technical Conference and Exhibition*. OnePetro.
 38. Iglauer, S., Wüiling, W., Pentland, C.H., Al-Mansoori, S.K. and Blunt, M.J., 2011. Capillary-trapping capacity of sandstones and sandpacks. *SPE Journal*, 16(04), pp.778-783.
 39. El-Maghraby, R.M. and Blunt, M.J., 2013. Residual CO₂ trapping in Indiana limestone. *Environmental science & technology*, 47(1), pp.227-233.
 40. Khishvand, M., Akbarabadi, M. and Piri, M., 2013. Trapped non-wetting phase clusters: An experimental investigation of dynamic effects at the pore scale using a micro-CT scanner. *SCA*.
 41. Iglauer, S., Paluszny, A., Pentland, C.H. and Blunt, M.J., 2011. Residual CO₂ imaged with X - ray micro - tomography. *Geophysical Research Letters*, 38(21).
 42. Chaudhary, K., Bayani Cardenas, M., Wolfe, W.W., Maisano, J.A., Ketcham, R.A. and Bennett, P.C., 2013. Pore - scale trapping of supercritical CO₂ and the role of grain wettability and shape. *Geophysical Research Letters*, 40(15), pp.3878-3882.
 43. Andrew, M., Bijeljic, B. and Blunt, M., 2014. Reservoir condition pore scale imaging of the capillary trapping of CO₂. *Energy Procedia*, 63, pp.5427-5434.
 44. Andrew, M., Bijeljic, B. and Blunt, M.J., 2014. Pore - by - pore capillary pressure measurements using X - ray microtomography at reservoir conditions: Curvature, snap - off, and remobilization of residual CO₂. *Water Resources Research*, 50(11), pp.8760-8774.
 45. Berg, S., Gao, Y., Georgiadis, A., Brussee, N., Coorn, A., van der Linde, H., Dietderich, J., Alpak, F.O., Eriksen, D., Mooijer-van den Heuvel, M. and Southwick, J., 2020. Determination of critical gas saturation by micro-CT. *Petrophysics-The SPWLA Journal of Formation Evaluation and Reservoir Description*, 61(02), pp.133-150.
 46. Gao, Y., Georgiadis, A., Brussee, N., Coorn, A., van Der Linde, H., Dietderich, J., Alpak, F.O., Eriksen, D., Mooijer-van Den Heuvel, M., Appel, M. and Sorop, T., 2021. Capillarity and phase-mobility of a hydrocarbon gas - liquid system. *Oil & Gas Science and Technology - Revue d' IFP Energies nouvelles*, 76, p.43.
 47. Burger, W. and Burge, M.J., 2016. *Digital image processing: an algorithmic introduction using Java*. Springer.
 48. Benesty, J., Chen, J., Huang, Y. and Cohen, I., 2009. Pearson correlation coefficient. In *Noise reduction in speech processing* (pp. 1-4). Springer, Berlin, Heidelberg.
 49. Buades, A., Coll, B. and Morel, J.M., 2005, June. A non-local algorithm for image denoising. In *2005 IEEE Computer Society Conference on Computer Vision and Pattern Recognition (CVPR'05) (Vol. 2, pp. 60-65)*. IEEE.
 50. Buades, A., Coll, B. and Morel, J.M., 2008. Nonlocal image and movie denoising. *International journal of computer vision*, 76(2), pp.123-139.
 51. Xu, K., Bonnecaze, R. and Balhoff, M., 2017. Egalitarianism among bubbles in porous media: an ostwald ripening derived anticoarsening phenomenon. *Physical review letters*, 119(26), p.264502.
 52. Xu, K., Mehmani, Y., Shang, L. and Xiong, Q., 2019. Gravity - induced bubble ripening in porous media and its impact on capillary trapping stability. *Geophysical Research Letters*, 46(23), pp.13804-13813.

Integrated thermo-poro-mechanical characterization for CO₂ Sequestration at deep aquifer conditions

Sudarshan Govindarajan^{1,*}, Munir Aldin¹, Akshay Thombare¹, Omar Abdulkaki¹, Deepak Gokaraju¹, Abhijit Mitra¹ and Robert Patterson¹.

¹MetaRock Laboratories, 2703 Highway 6 S, Houston, Texas, U.S.A.

Abstract. Modelling and forecasting of injected CO₂ plume behaviour is an essential step in the baseline, monitoring, and verification [BMV] process in the CO₂ sequestration lifecycle. The goal of reduction of uncertainty through forecasting models, can be better realized by accounting for the thermo-poro-mechanical nature of the deep subsurface reservoir systems. The current study focusses on developing and refining a laboratory workflow which will help in generating representative static and dynamic datasets at ambient and deep aquifer conditions. The workflow involves characterizing the poroelastic Biot coefficient and mechanical properties at ambient, high temperatures and at reservoir representative stress conditions. This information will be combined with the dataset from a CO₂ flood experiment which replicates the displacement of brine by super critical CO₂ at ambient and high temperatures and at reservoir representative stresses. Resistivity and acoustic signals will be monitored throughout the flood experiment. Existing analytical models for fluid substitution such as the Biot-Gassman-Brie populated with representative data will be evaluated for finding the best description of the experimental observations. The integrated results of the workflow are meant to help develop better informed static and dynamic models improving the confidence in the BMV process of CCUS.

1 Introduction

The SR15 report [1] released by IPCC in 2018 states the assumption of large-scale deployment of CO₂ removal measures to limit warming to 1.5°C by year 2100. Carbon capture, utilization, and storage (CCUS), as a CO₂ removal measure, has to be implemented on a massive scale to meet the necessitated ambitious net zero emission goals. Geological storage or sequestration has the highest uncertainty through the CCUS lifecycle. Baseline, monitoring and verification programmes have been acknowledged as a fundamental and critical requirement for reducing the uncertainty in long term containment of CO₂ in the subsurface [2]. Rules promulgated by both the EPA in the US and the equivalent CO2CARE program in the EU require post injection site care satisfying strict qualification criteria, to be part of the project scope [3]. Monitorability of the storage complex is dependent on both the subsurface and the surface environment [4]. The method chosen for monitoring whether geophysical (seismic, resistivity), borehole/well based, geochemical tracing, satellite or micro-seismic based geomechanical monitoring is entirely dependent on the purpose (leak detection vs. volumetrics) as well as the geography [4, 5]. Lateral (areal) coverage for plume monitoring is enabled by surface measurements while higher resolution data can be acquired through borehole-based measurements. [4]. An integrated monitoring approach is the ideal recommendation but requires heavy investment [3, 4]. The critical reasoning and potential benefits behind investing in long term post injection monitoring as compared to higher investment in the initial characterization and preventative predictions have been

compared in [3]. The inefficiency of long-term monitoring in lower certainty storage complexes due to lack of established remedial measures was pointed out in [3]. This was contrasted against the advantages of increasing certainty in the storage complexes by investing in accelerated laboratory studies, utilization of natural analogues, scaled field experiments and enhanced understanding of reservoir heterogeneity. Core analysis being the guiding standard has been the norm in the oil and gas industry. The importance of actual core-based laboratory investigations, to be used in an integrated approach with log analysis, field scale geophysical characterization and associated static-dynamic reservoir modelling is well recognized in the historical subsurface industries. This integrated approach is now being applied with greater emphasis, for increasing the certainty in the CCUS lifecycle, from the initial confidence building predictive exercises (site characterization and initial models) to establishing predictive post injection monitoring targets [3, 4, 6, 7, 8, 9, 10]. Core analysis performed at representative conditions on representative rock directly contributes to decreasing uncertainties in subsurface engineering. The comprehensive picture of the subsurface required for the numerical modelling [11] can be obtained with higher certainty when rock properties are measured at representative in-situ conditions. Deep saline aquifers are the most promising storage complexes for CCUS [8]. Characterising the displacement behaviour of the CO₂-brine systems is essential for pore space management as well as risk assessment [8, 11]. The ideal integrated site characterization exercise would incorporate the high stress, pressure and temperature conditions encountered in the deep saline aquifers in the core analysis exercise. This study is a laboratory investigation of

* Corresponding author: sudarshan@metarocklab.com

the influence of in-situ conditions on CO₂ induced brine displacement and the applicable petrophysical models which help estimate the observed phenomenon.

2 Experimental Approach

The uncertainty associated with lack of understanding of rock heterogeneity at the sub seismic resolution scale leads to surprises at the field scale [12]. Geophysical monitoring data and reservoir characterization data, together, help obtain quantitative estimates necessary for verification of field behaviour against modelling estimates within uncertainty bounds [13]. Geophysical parameter behaviour is dependent on the rock mineralogy, porosity, pore fluid content, fluid saturations, in-situ temperatures, and pressures [14, 15]. The ability of seismic (acoustic) methods to monitor trapped CO₂ has been successfully demonstrated in the field however detecting the migrating plume front requires further investigation [16]. Prior uncertainty in petrophysical parameter estimations have a significant effect on geophysical monitorability and there is a need for accurate benchmark measurements and reservoir characterization [14]. Injecting CO₂ under supercritical conditions which can be sustained in the deep aquifers has inherent injectivity benefits [17]. The major challenge for laboratory experimental characterization for CCUS is performing the test at in-situ representative pressure and temperatures while accounting for the solubility between the supercritical CO₂ (SC-CO₂) and water and the properties of the SC-CO₂ [12]. There have been multiple studies aimed at characterizing the fluid substitution phenomenon in the lab space [12, 14, 15, 16, 17, 18, 19, 20, 21]. To replicate CO₂ injection into the deep aquifers, most approaches involved injecting dry CO₂ gas or CO₂-brine solutions into brine saturated rock samples at varied conditions of temperature, pressure, and usually low effective stresses. Experimental observations were obtained through either isolated or combined acoustics, CT scanning and resistivity-based monitoring methods. The current investigation employs the porous plate technique and incorporates injection of dry SC-CO₂ into a brine saturated rock at reservoir representative stress, temperature, and pressure conditions while measuring the resistivity during the entire duration of the experiment. The porous plate technique is a reliable method for replication of the typical distribution of fluids in reservoir rocks [22,23]. Electrical/electromagnetic based surveys have been found to be a good complement to seismic measurements in the field as resistivity is more sensitive to saturation changes than compressional velocities [13]. Resistivity measurements in the lab have been found to be more reliable using the porous plate technique when performed at very slow injection rates following steady state equilibration protocols and a coherent brine saturation – resistivity index measurement is critical for validating logs by developing higher accuracy in fluid saturation definitions [22]. The current study adopts a modification of the established I-S_w protocol by injecting at slow flow rates and using the porous plate for preferential effluent expulsion. The current study also incorporates typical reservoir representative high effective stress conditions for greater reduction in uncertainty.

3 Theoretical Background

Supercritical fluids have the advantage of having low viscosity and relatively low compressibility (Appendix A) [24]. Injecting a material in the supercritical state enables maximising the pore space available in the subsurface. The study of the displacement of brine by non-wetting fluid using the single sample-water wet membrane, porous plate technique following Archie's equations is well established in the industry [22]. The porous plate acts as a barrier to the non-wetting fluid and allows for gradual development towards irreducible water saturations. The resistivity being monitored during this gradual displacement can be plotted in a log-log plot against the water saturation (I-S_w plot) for obtaining the saturation exponent, "n". The saturation exponent has been historically estimated for typical lithologies and reliable ranges for associated saturation exponents have been made. The I-S_w plot is a reliable indicator of the saturation state of the sample. In the present study the brine in the samples is displaced by SC-CO₂ while monitoring the resistivity and the deviation from linearity in the I-S_w plot is used as an indicator of breakthrough or end of experiment. Fig. 1 shows an example of a typical I-S_w plot.

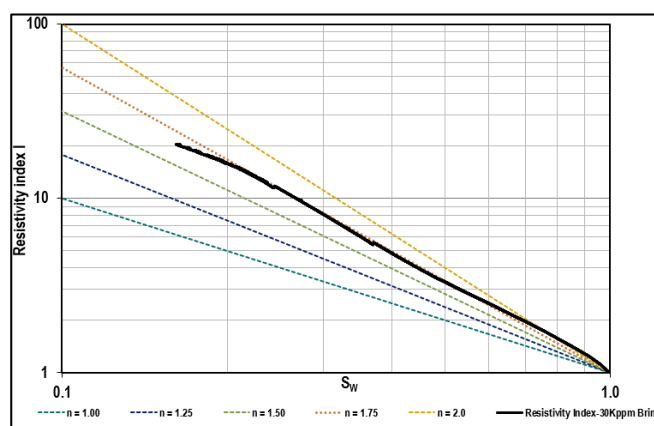


Fig. 1. Resistivity Index Vs. water saturation on log-log plot.

Fluid substitution as a phenomenon occurring during subsurface engineering has been well addressed by the hydrocarbon industry [25]. The general formula for the saturated porous system bulk modulus can be represented as under:

$$K_{SAT} = K_{dry} + \frac{(1 - (K_{dry}/K_0))^2}{(\phi/K_F) + ((1 - \phi)/K_0) - (K_{dry}/K_0^2)} \quad (1)$$

where,

K_{SAT} : Bulk modulus of saturated porous medium

K_{dry} : Drained Bulk modulus

K_0 : Grain modulus = Skeletal modulus = Mineral bulk modulus

K_F : Fluid Bulk modulus

Φ : Porosity as a fraction

The velocity can then be calculated as:

$$V_{PSAT} = \sqrt{\frac{1}{\rho_{sat}} * (K_P + K_{dry} + \mu \frac{4}{3})} \quad (2)$$

where,

$$K_P = \frac{(1-(K_{dry}/K_0))^2}{(\varphi/K_F)+((1-\varphi)/K_0)-(K_{dry}/K_0^2)} \quad (3)$$

V_{PSAT} : Saturated compressional velocity

ρ_{SAT} : Density of saturated rock

μ : G = Shear modulus of rock

Theoretically, the shear modulus for a rock is the same irrespective of saturated or dry condition as the fluids have zero shear velocity. The above equations have been utilised previously such as in reference [18] for interpreting laboratory measurements. However, the critical points mentioned in reference [25] are, that the above formulation was defined for seismic frequencies and may not work as well at the laboratory ultrasonic (1MHz) scale and that the K_{dry} has to be the drained bulk modulus i.e., either at constant pore pressure with free flow of fluid or with pore pressure drained to atmospheric condition in the absence of pore fluid. Reference [17] illustrated another expression for the undrained bulk modulus for a fluid saturated rock as:

$$K_U = K_{dry} + \frac{\alpha^2}{(\varphi/K_F)+((\alpha-\varphi)/K_0)} \quad (4)$$

where,

K_U : undrained bulk modulus of saturated porous medium

α : Biot poroelastic coefficient which is given by:

$$\alpha = 1 - (K_{dry}/K_0) \quad (5)$$

The fluid bulk modulus may be defined for a finely mixed fluid system by the Reuss average (parallel formulation):

$$\frac{1}{K_F} = \sum \frac{S_i}{K_i} \quad (6)$$

The fluid bulk modulus for a patchy saturation can be expressed by the Voigt average (series formulation) as:

$$K_F = \sum S_i * K_i \quad (7)$$

It was also shown in [17] that the Biot-Gassmann-Brie formulation was able to best describe the experimental observations.

$$K_F = S_B^N * K_B + (1 - S_B^N) * K_{CO_2} \quad (8)$$

where:

S_i : saturation of i^{th} component

K_i : Bulk modulus of i^{th} component

K_B : Brine modulus

S_B : Brine saturation

K_{CO_2} : Bulk modulus of CO_2

The combined saturated density of the porous solid filled with the mix of fluids can be estimated as

$$\rho_{SAT} = \rho_{dry} + (\varphi) * \rho_F \quad (9)$$

where:

ρ_{dry} : Dry Bulk density of sample

$$\rho_F = S_B * \rho_B + (1 - S_B) * \rho_{CO_2} \quad (10)$$

where:

ρ_B : Density of brine at temperature, pressure

ρ_{CO_2} : Density of CO_2 at temperature, pressure

4 Experimental System Overview

Prolonged experiments with $SC-CO_2$ at high temperatures and pressure require specialised equipment. The rock mechanics testing system, shown in Fig. 2 has been modified to contain the $SC-CO_2$ without any leaks. The system consists of a servomechanical frame press capable of reaching up to 300,000 psi within an isothermal enclosure. The confining

pressure pump has multivariable control capability and can apply up to 30000 psi (2068 MPa) with μ -inch resolution. The pore pressure pumps are 30 cc pumps capable of reaching 15000 psi (103 MPa) with nano-inch resolution. The pore pressure pumps can handle $SC-CO_2$ and have the necessary higher resolution to address the volume monitoring for saturation estimations. The system has also been modified with requisite channels for making the resistivity measurements. The system has also been modified with a high-resolution acoustics monitoring system, shown in Fig. 3 for live acquisition and display of the compressional velocity data as noted in [26].



Fig. 2. Rock Mechanics Test Equipment.

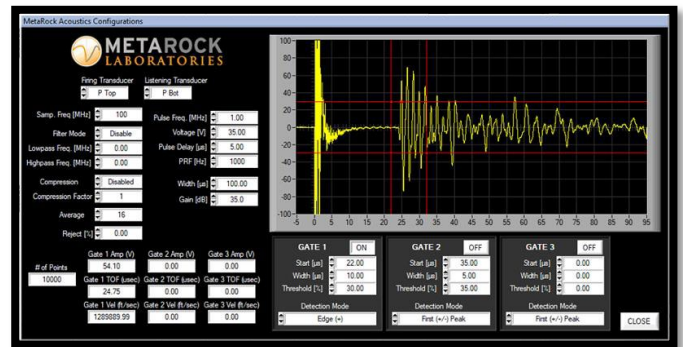


Fig. 3. Data acquisition and monitoring system for live high resolution compressional wave acoustics data.

Ultrasonic (1MHz) acoustic transducers are isolated from pressure and housed within the endcaps. The system is also rated for achieving high temperatures up to 450°C (842F) with acoustic measurement achievable up to 200°C (392F).

5 Experimental Suite, Results and Discussion

5.1. Testing Suite Design and Sample Statistics

The testing suite was defined to address the input requirements for the equations that govern the fluid substitution challenge. The poroelastic coefficient, the dry bulk modulus and the grain modulus are all required inputs. Additional triaxial testing at saturated condition was performed to be able to establish the range of expected velocity variation. The SC-CO₂ flow testing was performed on Buff Berea sandstone at ambient 35°C (95F) and higher temperature of 65°C (149F). Samples belonged to the same outcrop block and were prepared to be approximately 1” in diameter and 2” in length meeting all recommended ASTM/ISRM standards. The permeability range of the sample as obtained from the outcrop database was between 150-350 mD brine (KCl) permeability and 400-500 mD Klinkenberg permeability with N₂ gas. Grain volume and bulk volume of the samples were also measured to ensure uniformity. Table 1 shows the detailed statistics for the sample set.

Table 1. Sample Statistics

Sample Detail	Mean	Std Dev	Coefficient Of Variation
Length (in)	1.997	0.004	0.182
Diameter (in)	0.994	0.001	0.088
Weight (g)	51.074	0.177	0.347
Bulk Volume (cc)	25.507	0.048	0.186
Grain Volume (cc)	19.261	0.066	0.341
Pore Volume (cc)	6.246	0.085	1.361
Grain Density (g/cc)	2.651	0.001	0.056
Bulk Density (g/cc)	2.002	0.008	0.385
Porosity (%)	24.489	0.307	1.253

5.2. Triaxial testing with static and dynamic characterization:

All testing was performed at a high effective stress of 2000 psi (13.78 MPa). Triaxial tests were carried out for the characterization of the dry bulk modulus at both temperature conditions, at confining pressure of 2000 psi (13.78 MPa), under drained conditions, at slow loading rates. The differential stress cycles were unloaded at approximately 7000 psi (48.26 MPa) without taking the sample to failure. Compressional and shear velocities were acquired throughout the duration of the test. Results from the base triaxial testing are displayed from Fig. 4 to Fig. 7. The comparison between the axial and radial strain responses at 35°C (95F) and 65°C (149F) indicate that Buff Berea (being a quartz-rich rock) does not display a marked change in deformation behaviour within that temperature range. However, the compressional and shear velocities are both slightly lowered with the increase in temperature. The choice of 65°C (149F) was done

as sandstones do not exhibit significant changes in elastic properties between 25°C (77F) to 45°C (113F) [27], however even at 65°C (149F) we did not observe significant change in the mechanical and acoustic properties.

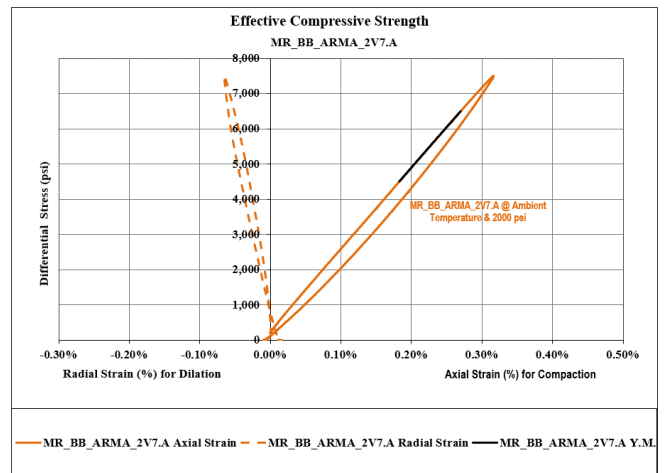


Fig. 4. Stress-strain plot for the ambient (35°C) temperature triaxial test and confining pressure of 2000 psi.

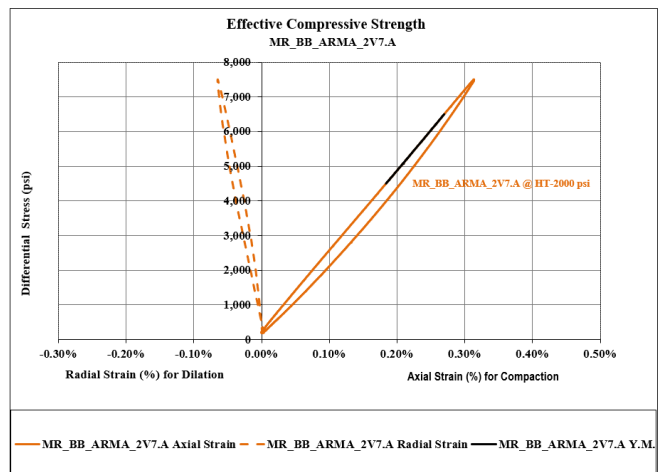


Fig. 5. Stress-strain plot for the high (65°C) temperature triaxial test and confining pressure of 2000 psi.

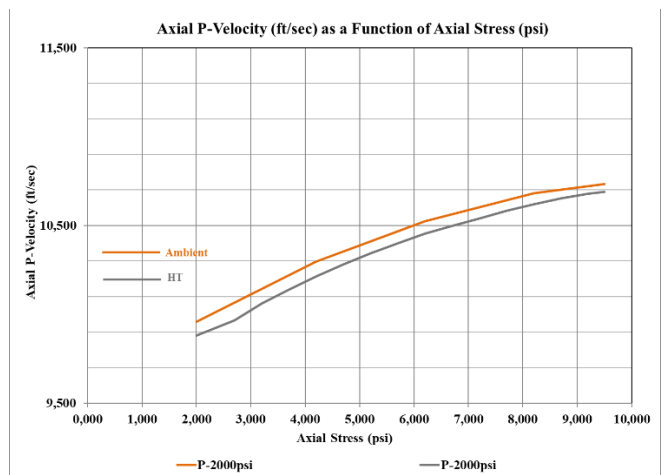


Fig. 6. Compressional velocity comparison at ambient and high temperature.

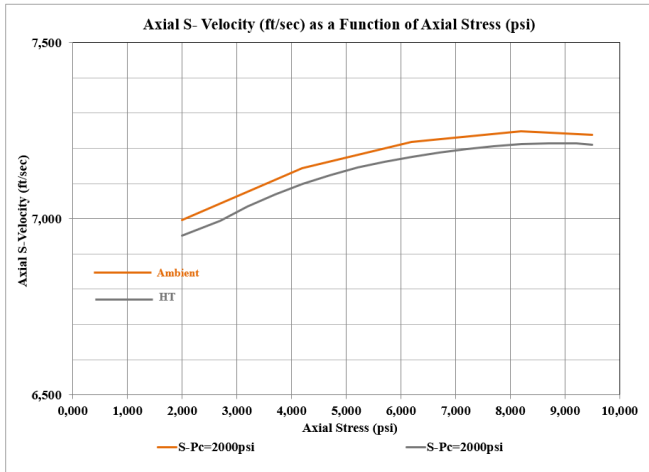


Fig. 7. Shear velocity comparison at ambient and high temperature.

5.3. Poroelastic characterization:

Poroelastic coefficient characterization as per reference [28], was carried out by cycling confining and pore pressures while maintaining the effective stress of 2000 psi (13.78 MPa). Fig. 8, Fig. 9 display the summary and results of the poroelastic coefficient characterization.

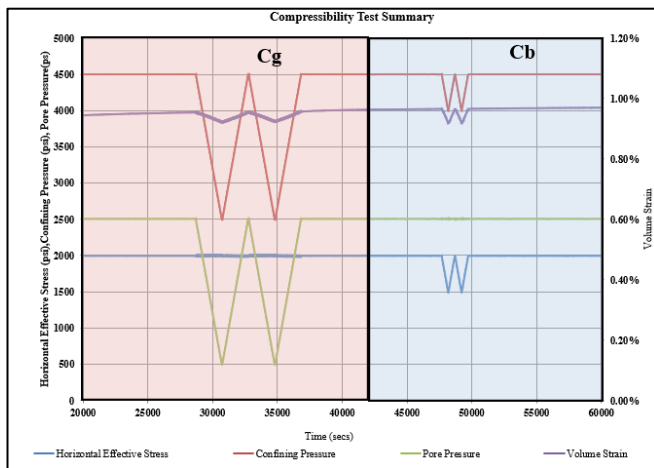


Fig. 8. Poroelastic coefficient measurement experimental summary.

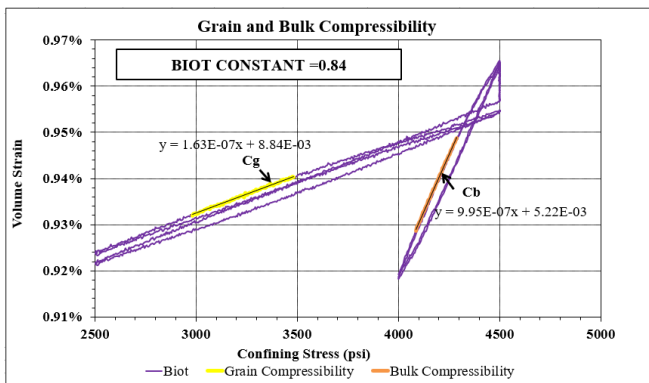


Fig. 9. Experimental results for poroelastic coefficient measurement.

5.4. SC-CO₂ flow study:

5.4.1 Set-up and experimental conditions

The fluid substitution experiment was carried out on two different plugs at ambient and high temperature. The protocol for both involved saturating the sample with brine at stress and flowing SC-CO₂ from the top to the bottom with the porous plate positioned at the bottom end. Fig. 10 shows the simplified flow schematic for the fluid substitution experiment.

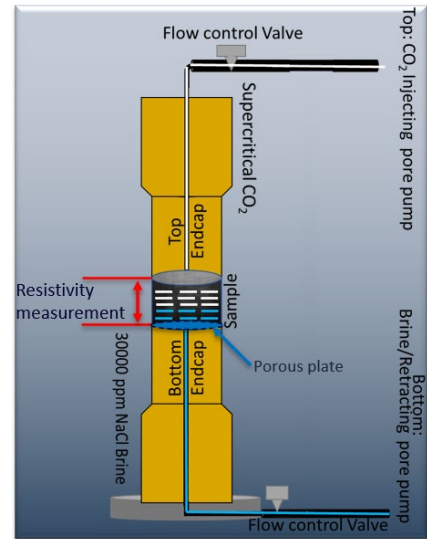


Fig. 10. Simplified flow schematic for the fluid substitution experiment.

Resistance and compressional velocity were monitored throughout the duration of the experiment. Experiments were performed maintaining an effective stress of 2000 psi (13.78 MPa) with confining pressure at 4500 psi (31.02 MPa) and pore pressure at 2500 psi (17.236 MPa). Samples were initially saturated with 30000 ppm NaCl brine at 100 psi pore pressure and confining of 2000 psi (13.78 MPa). The conditions were then progressed to desired experimental conditions of 4500 psi (31.02 MPa) confining and 2500 psi (17.236 MPa) pore pressure at stabilized temperature. Once stabilization was achieved (strain and pore pressure), injection of SC-CO₂ was begun from the top. The total experiment ran for 150 hours approximately. The ideal porous plate I-SW experiment is meant to be performed at very low flow rates of one pore volume over 10-30 days. The injection of the SC-CO₂ results in the creation of differential pressure across the sample. It is recommended to displace the fluid/brine saturating the sample at a constant injection rate with super critical fluids.

The injection is to be done while monitoring resistivity change across the sample along with ultrasonic velocity and the differential pressure across the sample. This investigation studied the use of the differential pressure as a feedback channel for driving the injection in the interest of expediency.

As the injection was begun, initial differential pressure created was around 50 psi (2550 at upstream and 2500 psi at downstream). Once flow stabilized at this differential pressure the system was programmed to respond with flow

rates necessary to maintain a differential pressure of 150 psi. The limiting differential pressure for the experiment, is the differential pressure sustainable across the porous plate which was approximately 200 psi. When injection is started, some time is consumed in establishing an interface between the SC-CO₂ and the brine and there is a delay in the downstream pump response to the upstream pump. The dead volumes within the system must be thoroughly defined to enable higher accuracy in the pump volume-based saturation definitions.

5.4.2 Saturation based on volume and resistivity monitoring:

The volume of effluent brine on the downstream side was deemed as indicative of saturation conditions within the sample. The results of the ambient temperature fluid substitution experiment are shown in Fig. 11 to Fig. 13. The injection was carried out by gradually increasing the desired differential pressure setpoint across the sample. The resistivity was measured across the whole sample in the axial plane. Brine is a conductive fluid. The replacement of the brine in the sample by SC-CO₂ results in the increase in the resistivity of the sample. The time at which the resistivity starts increasing is indicative of sample penetration by the SC-CO₂. The resistivity changed from an initial 5.357 (Ω-m) to 24.787 (Ω-m) which is an increase of 362.7%. The I-Sw plot Fig. 13 indicates that the saturation exponent for the Buff Berea sandstone is 2. This is a value typically expected for sandstones. The measured resistivity across the sample increases exponentially when no more brine is expelled from the bottom of the sample while SC-CO₂ injection is being continued. This could indicate either breakthrough by the SC-CO₂ or achieving residual saturations for that rock type. The ideal I-SW experiment implemented at very low injection rates would entail piston-like uniform displacement of the wetting fluid by the non-wetting fluid. However, since SC-CO₂-brine interactions could entail mixing of the two fluids to some degree, ideal piston like uniform displacement is not expected. The utilization of the differential pressure as a driving mechanism also resulted in relatively higher instantaneous flow rates. The I-SW for the ambient temperature experiment displays deviation from linearity at 48% brine saturation indicating rapid increase in resistivity. The phenomenon was also reflected in the reduced brine effluent volumes and the cessation of the retraction of the downstream pump. Based on the resistivity behaviour, the pump movement and effluent volumes, the residual saturation of water at the end of the experiment is deemed to be approximately 48%.

The current study utilized 30000ppm NaCl brine. The possibility of salt precipitates being left behind as the brine is displaced or due to interaction between brine and dry SC-CO₂ exists, however it was not observed in the current experiment based on visual inspection. Further investigation in the form of thin section analysis or XRD is needed to be performed for increasing confidence in the observation. The phenomenon of salt precipitation is of greater importance in high salinity brines and should be taken into consideration after formation water evaluation.

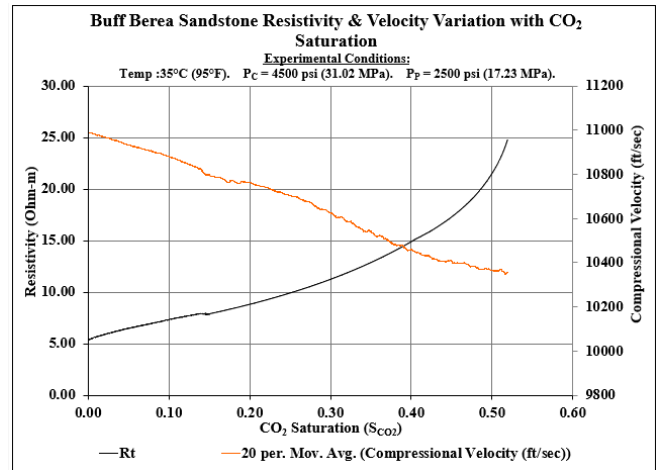


Fig. 11. Resistivity and velocity variation due to fluid displacement at ambient temperature.

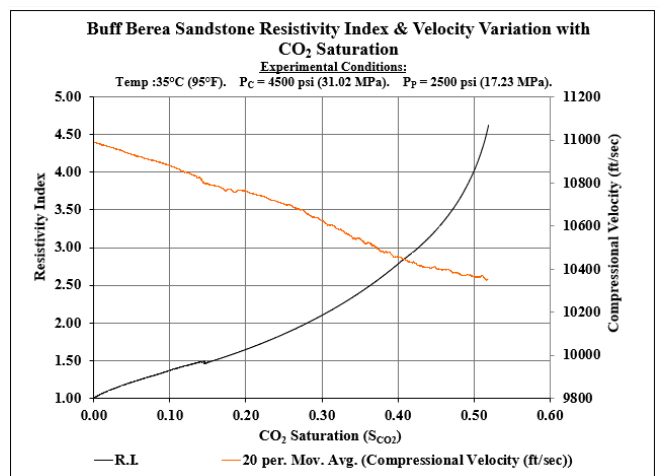


Fig. 12. Resistivity Index and velocity variation due to fluid displacement at ambient temperature.

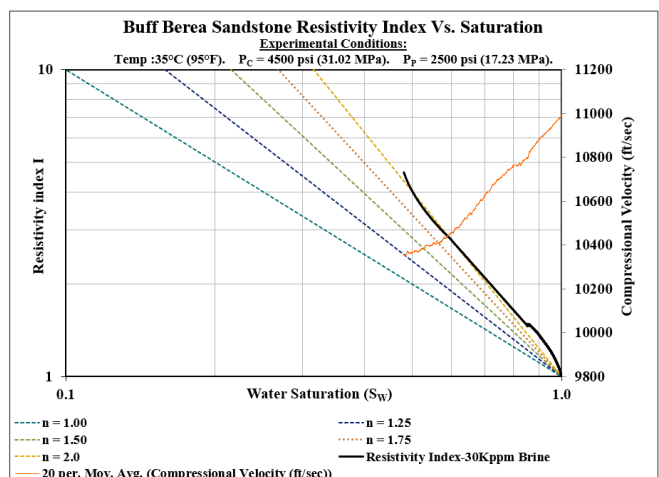


Fig. 13. I-Sw plot for brine displacement by SC-CO₂ at ambient temperature.

5.4.3 Acoustic monitoring:

Brine has greater density than SC-CO₂ under the established experimental conditions. As the brine gets displaced and volume of SC-CO₂ within the sample increases there is a

decrease in the bulk density and modulus of the porous rock system. This decrease causes a decrease in the measured compressional velocity across the sample. The compressional velocity changed from an initial 10991 ft/sec to 10325 ft/sec which is a 6.44% change. This is similar to results obtained by [17], [18] and [27]. Greater decreases in velocities have been observed in carbonates but at lower effective stresses [16]. The sensitivity of acoustic measurements to change in fluid in the samples, were observed, at low effective stresses of 453 psi (3 MPa) and 290 psi (2 MPa) in [18] and [17] respectively. The acoustic data was found to be sensitive to change in water saturation for up to 10-20% S_w by [18] and up to 25% S_w by [17]. In the present study the effective stress utilised was 2000 psi (13.78 MPa). The high-resolution equipment enabled capture of acoustic data at the rate of a measurement every second. The sensitivity of the velocity seemed to be damped only at around 40 % saturation of SC-CO₂ i.e., after displacement of 40% of original brine volume. The different models for fluid substitution were compared against the measured experimental data. Fig. 14. shows the comparison of the different estimates with an averaged curve representing the high resolution, high volume acoustic dataset. The Reuss and Voigt based velocity predictions form the lower and upper bounds respectively for the experimental measurement. The velocity calculated using the modified Voigt i.e., the Biot-Gassmann-Brie expression matches very closely with the measured velocities. The absolute error when comparing the velocity calculated using the Reuss based parallel formulation for finely mixed fluids and the experimental measurements comes to a minimum of 0.01% and a maximum of 5.16%. The absolute error when comparing the velocity calculated using the Voigt based series formulation for patchy saturation and the experimental measurements comes to a minimum of 0.16% and a maximum of 1.7%. The absolute error when comparing the velocity calculated using the modified Voigt i.e., the Biot-Gassmann-Brie based series formulation for patchy saturation and the experimental measurements comes to a minimum of 0.49% and a maximum of 0.82%. The meandering nature of the experimental velocity curve indicates that the fluid distribution is more complicated than can be estimated by the Reuss and Voigt bounds, similar to [17]. The exponent value utilised for the Biot-Gassmann-Brie was 1.25. Even though the Biot-Gassmann-Brie curve matches well, it can still be seen that the experimental curve oscillates between indicating a mixed or patchy saturation. The overall trend in this case is more towards a series displacement which may be the result of the utilization of the porous plate technique. Since the maximum error was found to be between the Reuss or parallel formulation and the experimental measurement, a modification similar to the Biot-Gassmann-Brie is proposed as below:

$$K_F = \frac{K_B * K_{CO_2}}{K_B * (1 - S_B^m) + K_{CO_2} * S_B^m} \quad (11)$$

where:

K_B : Brine modulus

S_B : Brine saturation

K_{CO_2} : Bulk modulus of CO₂

m: modified Reuss exponent

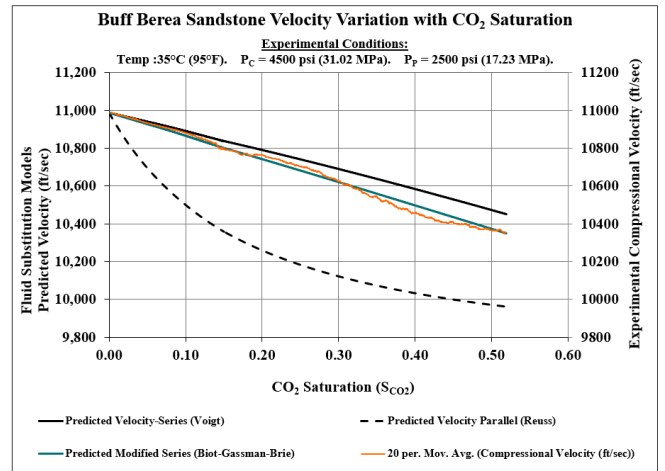


Fig. 14. Comparison of experimental measurement and velocity estimates using different models.

Fig. 15 shows the comparison of the velocity estimate based on the modified Reuss formulation with an “m” value of 0.3. The absolute error when comparing the velocity calculated using the modified Reuss based formulation and the experimental measurements comes to a minimum of 0.05% and a maximum of 1.48%. This enables a reduced uncertainty in the velocity estimate window.

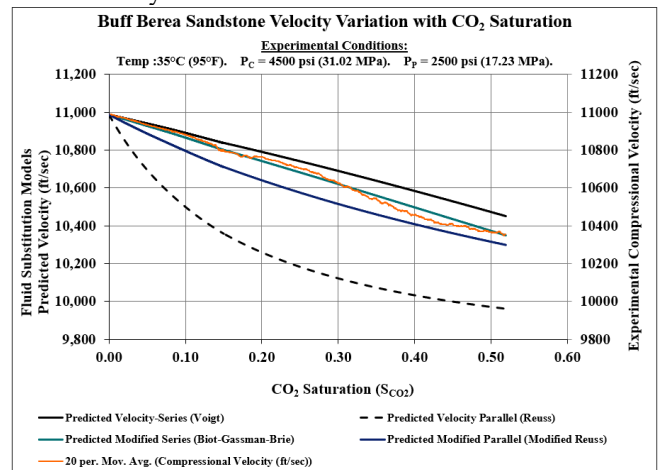


Fig. 15. Modified Reuss based velocity estimate comparison with experimental data.

5.4.4 Failure Envelope Characterization:

After completion of the fluid substitution testing, the same sample was utilised to conduct a multistage triaxial test as per [29]. The samples used for the current study were companion samples used for [29]. [29] had generated a Mohr Coulomb failure envelope based on multiple single stage triaxial testing. Fig. 16 shows the failure envelope and strength data for the fluid substitution sample and Fig. 17 displays the finalized failure envelope and strength data for the virgin Buff Berea sandstone samples. The unconfined compressive strength (U.C.S.) estimate for room temperature testing on virgin samples was 5929.7 psi and that on SC-CO₂ exposed sample was 4518 psi. This indicates a reduction of U.C.S. by 24%. The cohesion for the virgin samples was 1288.3 psi and the SC-CO₂ exposed sample exhibited 1058.4 psi. The reduction in cohesion was 18%. The friction angle changed

from 42.33° for the virgin sample to 39.7°, a change of 6%. The fluid substitution samples did undergo a lot of processes such as saturation and desaturation along with exposure to CO₂ at high effective stress and pore pressure. However, most of those process steps are meant to reproduce the processes seen in the field. As such the difference in strength properties can be taken to be reasonably representative.

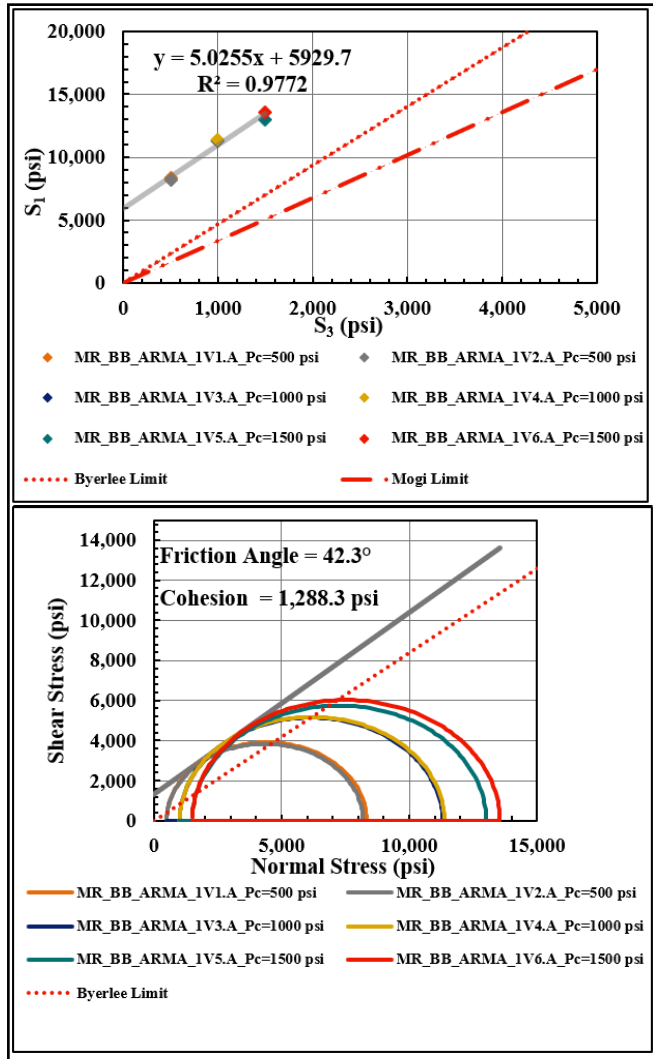


Fig. 16. Mohr Coulomb failure envelope and U.C.S. estimate for Buff Berea Sandstone.

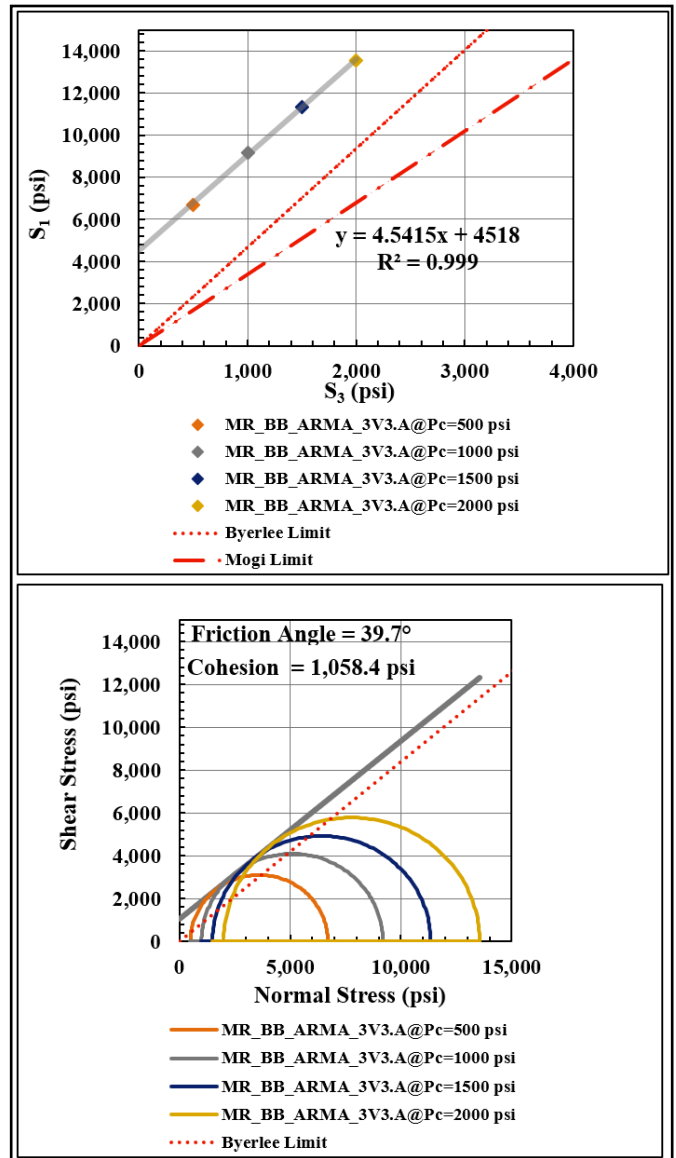


Fig. 17. Multistage triaxial test results on the fluid substitution sample tested at ambient temperature.

The high temperature fluid substitution experiment for the companion Buff Berea sample is summarised in Fig. 18.

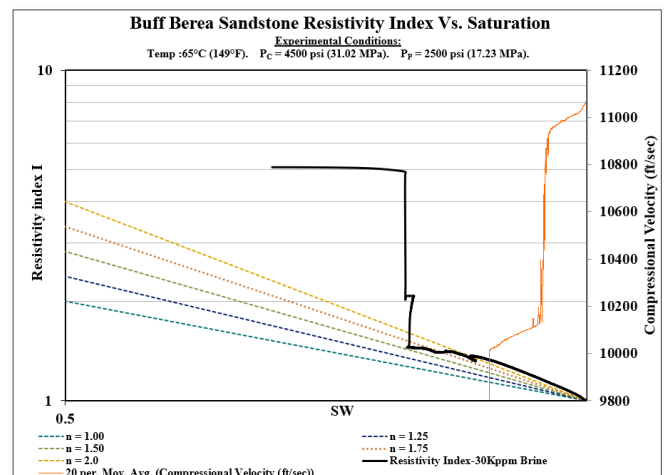


Fig. 18. 65°C (149F) fluid substitution -high injection rate induced breakthrough of SC-CO₂

The injection of the SC-CO₂ in the experiment was driven by the differential pressure across the sample. However, the selected setpoint for the differential pressure initiated a very high flow rate which caused a breakthrough of the SC-CO₂ through the sample. Fig. 19. illustrates an example of gradual sustained injection in a carbonate rock at high temperature of 120°C (248F) and high effective stress of 2500 psi (17.23 MPa). Resistivity index trend in the I-SW plot seems to indicate that the water saturation at the end of the experiment is 0.4 or 40%. The saturation exponent for the SC-CO₂ induced brine displacement through the rock is 1.75. The carbonate sample didn't have any companion samples for performing the triaxial and poroelastic coefficient characterizations required for the velocity predictions which were consequently not evaluated.

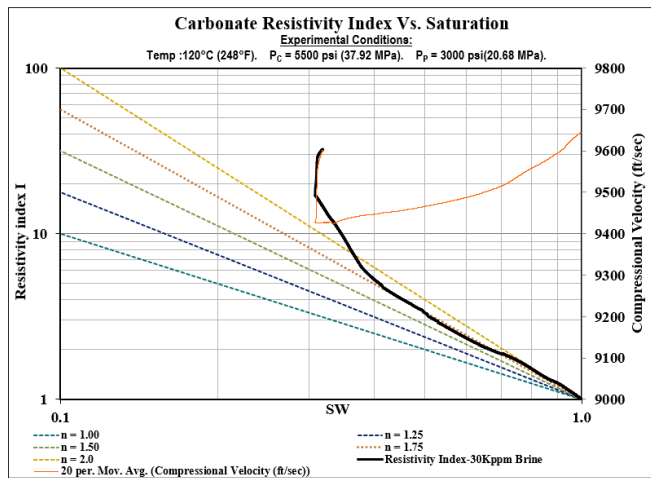


Fig. 19. High temperature, high pressure fluid substitution in carbonate sample.

6 Conclusions

Implementing an integrated, robust, laboratory program for addressing CCUS challenges helps reduce modelling and field scale uncertainty. The Biot-Gassmann-Brie formulation helps predict the acoustic behaviour during laboratory fluid substitution experiment reasonably well. The proposed modified Reuss formulation helps narrow the window for the model-experimental data match.

Appendix A: CO₂ Reference Data

All reference data has been sourced or calculated based on information from [32]. The critical temperature for CO₂ is 30.97°C, the critical pressure is 1070 psia and critical density is 0.467 g/cc. Fig. 20 to Fig. 22 show the variation of density, viscosity and compressibility of CO₂ with increase in pressure under different isothermal conditions of 30°C, 35°C and 65°C. At any temperature, with increase in pressure, phase change is observed. The critical point marks the transition to supercritical phase. Fig. 20 illustrates that in the gaseous phase, at lower pressures, the maximum magnitude of the density only reaches around 0.35 g/cc. In the supercritical phase, at all three temperatures, the densities are much higher. At 35°C, the density of the supercritical phase, is very close to the density of liquid CO₂ at 30°C. The region

of interest (2500 psi) for the current study is marked in a red rectangle. The densities displayed by CO₂ in the supercritical phase are closer to liquid densities than gaseous densities especially with increase in pressure. The viscosity in the supercritical phase decreases with increase in temperature and remains lower than liquid phase viscosities at all pressures and temperatures. The compressibility shown in Fig. 22 has been calculated from density and velocity data as below:

$$C_b = \frac{1}{c \cdot \rho \cdot V_p^2} \quad (12)$$

Where: ρ : Density in kg/m³

V_p : Compressional velocity in m/s

c : 1.4504E-04 (conversion to psi)

Fig. 22 illustrates that the compressibility of CO₂ at higher pressures in the supercritical phase is closer to liquid compressibility than gaseous compressibility.

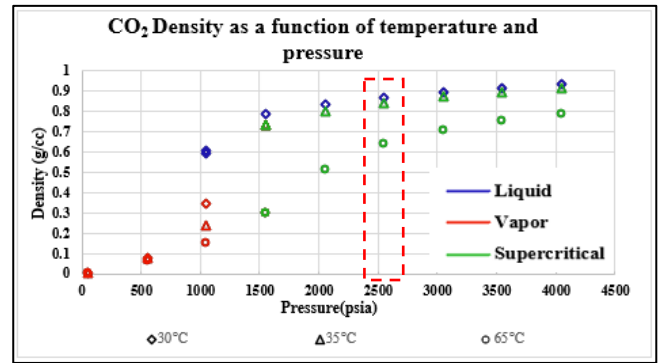


Fig. 20. Change in density of CO₂ as a function of pressure increase at three isothermal conditions of 30°C, 35°C and 65°C. Phase change is mapped by colour coding.

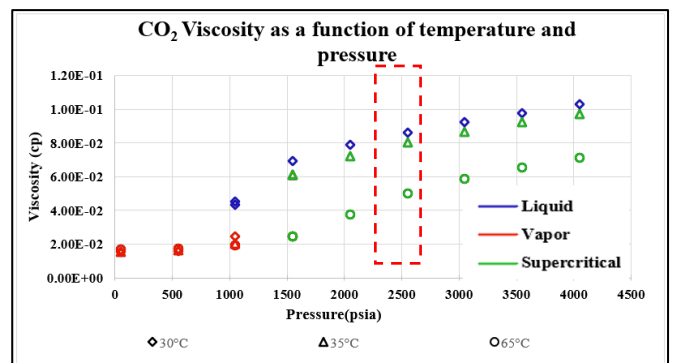


Fig. 21. Change in viscosity of CO₂ as a function of pressure increase at three isothermal conditions of 30°C, 35°C and 65°C. Phase change is mapped by colour coding.

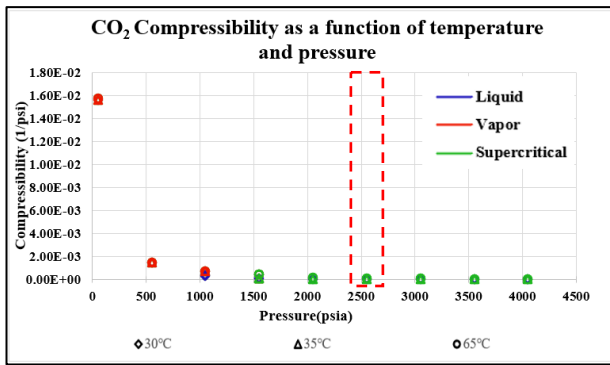


Fig. 22. Change in compressibility of CO₂ as a function of pressure increase at three isothermal conditions of 30°C, 35°C and 65°C. Phase change is mapped by colour coding.

Authors would like to acknowledge the guidance of the late William Mickelson and the kind help of Hamad Aldin, Malik Al Salman, Hatim Aldin and Sneha Kalidindi in the execution of the experimental program.

References

1. Masson-Delmotte, V., P. Zhai, H.-O. Pörtner, D. Roberts, J. Skea, P.R. Shukla, A. Pirani, W. Moufouma-Okia, C. Péan, R. Pidcock, S. Connors, J.B.R. Matthews, Y. Chen, X. Zhou, M.I. Gomis, E. Lonnoy, T. Maycock, M. Tignor, and T. Waterfield. *IPCC, 2018: Global Warming of 1.5°C. An IPCC Special Report on the impacts of global warming of 1.5°C above pre-industrial levels and related global greenhouse gas emission pathways, in the context of strengthening the global response to the threat of climate change, sustainable development, and efforts to eradicate poverty*. In press.
2. A. Simone, E. Mackie and N. Jenvey, En. Proced. **1**, *GHGT-9*, 2219-2226, (2009).
3. S. D. Hovorka, En. Proced. **114**, *GHGT-13*, 3754-3756, (2017).
4. M. Smith, D. Campbell, E. Mckay, and D. Polson, *CO₂ aquifer storage site evaluation and monitoring*. Herriot-Watt University, Edinburgh (2011).
5. S. Carrol, K. Mansoor, X. Yang, T. A. Buscheck and Y. Sun. En. Proced. **114**, *GHGT-13*, 3628-3635, (2017).
6. K. Yamamoto. *CO₂SC Symposium*.26-28, (2006).
7. J. Desroches, L. Jammes, and T. Berard. *CO₂SC Symposium*.238-241, (2006).
8. S. Bachu and B. Bennion. *CO₂SC Symposium*.193-195, (2006).
9. DOE-NETL, *BEST PRACTICES: Site Screening, Site Selection, and Site Characterization for Geologic Storage Projects* (2017). DOE/NETL-2017/1844.
10. J. Rutqvist, J. Birkholzer, and C.F. Tsang. *CO₂SC Symposium*.230-232, (2006).
11. DOE-NETL, *BEST PRACTICES: Risk Management and Simulation for Geologic Storage Projects* (2017). DOE/NETL-2017/1846
12. R. Pini, S. Krevor. Chapter 7-Laboratory studies to understand controls on Flow and Transport for CO₂ storage. Editors, P. Newell, A. G. Ilgen. *Science of Carbon Storage in Deep Saline Formations*. Elsevier, pp 145-180, (2019).
13. B. Dupuy, A. Romdhane, P. Eliasson, H. Yan. Combined geophysical and rock physics workflow for quantitative CO₂ monitoring. *International Journal of Greenhouse Gas Control*,106, 103217, (2021).
14. Z. Xue, T. Ohsumi, H. Koide. An experimental study on seismic monitoring of a CO₂ flooding in two sandstones. *Energy*,30, 2352-2359, (2005).
15. A. JafarGandomi, A. Curtis. Assessing the monitorability of CO₂ saturation in subsurface saline aquifers. *International Journal of Greenhouse Gas Control*.7. pp 244-260.(2012)
16. V. Vilarrasa, R.Y. Makhnenko, J. Rutqvist, Chapter 9 - Field and Laboratory Studies of Geomechanical Response to the Injection of CO₂, Editor(s): P. Newell, A. G. Ilgen, *Science of Carbon Storage in Deep Saline Formations*, pp 209-236, Elsevier,(2019).
17. M. Gutierrez, D. Katsuki, A. Almarabat. Seismic velocity change in sandstone during CO₂ injection. *E3S Web of Conferences*, 205, ICEGT (2020).
18. J. Kim, T. Matsuoka, Z. Xue. Monitoring and detecting CO₂ injected into water-saturated sandstone with joint seismic and resistivity measurements. *Exploration Geophysics*, 42, 58–68, (2011).
19. I. Falcon-Suarez, H. Marin-Moreno, F. Browning, A. Lichtschlag, K. Robert, L. J. North, A.I. Best. Experimental assesment of pore fluid distribution and geomechanical changes in saline sandstone reservoirs during and after CO₂ injection.
20. T. Tsuji, T. Ikeda, F. Jiang. Hydrologic and elastic properties of CO₂ injected rock at various reservoir conditions: Insight into quantitative monitoring of injected CO₂. En. Proced. **114**, *GHGT-13*, 4047-4055, (2017).
21. H. Ott, S. Berg, S. Oedai. Displacement and mass transfer of CO₂/Brine in sandstone. *International Symposium of Society of Core Analysts*. SCA2011-05. (2011).
22. M.Z. Kalam, K.Al. Hammadi, O.B. Wilson, M. Dernaika and H. Samosir. Importance of porous plate measurements on carbonates at pseudo reservoir conditions. *International Symposium of Society of Core Analysts*. SCA2006-28, (2006).
23. D.G. Longeron, M.J. Argaud and L. Bouvier. Resistivity Index and capillary pressure measurements under reservoir conditions using crude oil. 64th Annual Technical Conference and Exhibition of the Society of Petroleum Engineers. (1989).
24. Richard Rosen, William Mickelson, Munir Sharf-Aldin, Basak Kurtoglu, Tobi Kosanke Meghana PaiAngle, Robert Patterson, Faraz Mir, Santhosh Narasimhan, and Amir Amini. Impact of Exp Studies on Unconventional Mechanisms.SPE-168965. SPE Unconventional Resources Conference – USA held in The Woodlands, Texas, USA, 1-3 April, (2014).
25. G. Mavko, T. Mukerji, J. Dvorkin. *The Rock Physics Handbook*. pp 266-339. (2009).

26. D. Gokaraju, M. Aldin, A. Thombare, A. Mitra, S. Govindarajan, R. Patterson. A novel method for experimental characterization of the Poroelastic Constants in Unconventional formations. *URTeC* :2902907, (2018).
27. V. Mikhaltsevitch, M. Lebedev, and Boris Gurevich. Measurements of the elastic and anelastic properties of sandstone flooded with supercritical CO₂. *Geophysical Prospecting*, **62**, pp 1266–1277, (2014).
28. J. W. Dudley, M. Brignoli, B. R. Crawford, R. T. Ewy, D. K. Love, J. D. McLennan, G. G. Ramos, J. L. Shafer, M. H. Sharf-Aldin, E. Siebrits, J. Boyer, M. A. Chertov. ISRM Suggested Method for Uniaxial-Strain Compressibility Testing for Reservoir Geomechanics. *Rock Mech Rock Eng* **49**, pp 4153-4178, (2016).
29. S. Govindarajan, M. Aldin, A. Guedez, A. Thombare, D. Gokaraju, A. Mitra, R. Patterson. Experimental Investigation for Selection of Unloading Criterion in Multistage Triaxial Testing. *ARMA 21–1217, 55th US Rock Mechanics/Geomechanics Symposium* held in Houston, Texas, USA, 20-23 June 2021. (2021).
30. R. Span and W. Wagner. A new equation of state for CO₂ covering the fluid region from the triple point temperature to 1100K at pressures upto 800MPa. *J. Phys. Chem. Ref. Data* Vol. **25**, No 6 (1996).
31. M. Batzle and Z. Wang. Seismic properties of pore fluids. *GEOPHYSICS*, VOL. **57**, NO. 11 P. 1396-1408 (1992).
32. P.J. Linstrom and W.G. Mallard, Eds., NIST Chemistry WebBook, *NIST Standard Reference Database Number 69*, National Institute of Standards and Technology, Gaithersburg MD, 20899, <https://doi.org/10.18434/T4D303>, (retrieved July 4, 2022)

Wireless acquisition for Resistivity Index in Centrifuge – WiRI: A comparative study of three Pc-RI methods

Quentin Danielczick¹ Ata Nepesov² Laurent Rochereau² Sandrine Lescoulié² Victor De Oliveira Fernandes² and Benjamin Nicot²

¹SeaOwl Energy Service, on behalf of TOTAL S.A Editorial Department, 64000 Pau, France

²TOTAL S.A, CSTJF – Experimentation Interpretation Synthesis Department, 64000 Pau, France

Abstract. Technological improvements and innovations are made to offer solutions with superior efficiency in terms of cost, quality, speed or all of them. In the SCAL field, the conventional resistivity index measurement (the porous plate technique) is a cost-effective method that provides good quality results but is very time consuming. For this purpose, several methods were developed to reduce the time taken to acquire resistivity measurements. In 2017, we proposed the Ultra-Fast Capillary pressure and resistivity index measurements (UFPCRI) combining centrifugation, NMR imaging and resistivity profiling. Since 2021 the Wireless Resistivity Index (WiRI) method allows the acquisition of capillary pressure and resistivity index in a matter of days. This method is based on a new in-house system to acquire wirelessly resistivity indexes along a rock sample during a centrifugation. The determination of resistivity versus saturation curve and the n exponent of Archie's Law is done thanks to an optimization algorithm. In this paper we present the results obtained from multiple simulations and experiments for: WiRI, UFPCRI and Porous Plate to discuss the advantages and drawbacks of each method in terms of reliability and experimental duration. Six rock samples are studied. A comparison of the three methods regarding the Archie's n exponent, resistivity indexes and capillary pressure curves is performed.

1 Introduction

Choosing or advising the right measurement solution for the right objective is one of the most important tasks for the petrophysicist in charge of a formation evaluation study. For this purpose, many books [1], [2] are suited to learn and understand the advantages and drawbacks of multiple methods for each laboratory core analysis experiment. These works are solid foundations for conventional methods. The aim of this paper is to bring a focus, and an update regarding the recent developments in determining Capillary pressure (Pc) and Resistivity Indexes (RI) in laboratory.

Since 1942 and the publication of Archie's Law [3] many methods have been proposed to estimate its parameters, particularly the n exponent. Historically, the experimental duration of the reference technique, the Porous Plate (PP) was substantial and multiple experiments were built to tackle this specific problem. Some known methods are the Continuous injection [4], FRIM [5][6] or more recently methods based on Nuclear Magnetic Resonance (NMR) for ultrafast m & n Archie's exponent determination [7]. Since 2017, we proposed two new methods to participate in the improvement of Archie's exponents determination while keeping the determination of the Pc curve with UltraFast Capillary Pressure and Resistivity Index (UFPCRI) [8] and Wireless Resistivity Index (WiRI) [9].

Whether for the reference PP or for the UFPCRI and WiRI experiment, determining Archie's n exponent and Pc

requires measurements of resistivity, water saturation (Sw), and a knowledge of the capillary pressure. However, the way to measure these properties and the way to process these measurements, are different for each method.

The PP technique consists in applying multiple pressure steps and homogeneous saturation profiles. For each step a triplet "Resistivity index – Saturation – Pressure" is acquired. With multiple steps, RI/Sw and Pc/Sw curves are populated, and n exponent determined with linear regression of the log-log RI/Sw curve.

The UFPCRI method is based on inducing a non-uniform saturation profile with a centrifuge (as proposed by Green *et al.* [10][11]), measuring local Sw profile with NMR, measuring multiple resistivities along the sample (1 resistivity each 5 mm of sample) and repeating the sequence with multiple centrifuge steps. For each step multiple points of Pc/Sw and RI/Sw are available, allowing to perform faster than PP the determination of n exponent and Pc curve.

The WiRI experiment follows the same principle as the UFPCRI method. It uses the non-uniformity of the saturation induced by centrifuge, but no NMR is used to measure local saturation along the sample. A mean saturation is recorded using the production volume at the outlet of the sample. A wireless Resistivity measurement system is embedded in the centrifuge and a resistivity profile (1 measurement every 5 mm) is acquired during

the rotation. Then, assuming the validity of Archie's law, resistivity profiles are inverted using an optimization process between Archie's law and measured mean saturation.

To investigate the impact of the differences between these three methods and allowing readers to choose the method that best fits their needs, this work is a comparative study of each experiment in 2 steps:

- 1) Investigation through simulation with Monte Carlo approach [12]. The three experiments are numerically compared in the same conditions, with 3 different synthetic datasets (representing 3 different rocks) in order to assess whether a method is more suitable for one type of sample or another. The impact of measurement uncertainties is also investigated to provide a clear view on which parameter has the most influence on our results.
- 2) Comparison of results on real cases to show the advantages and limits of each method.

2 Materials and methods

2.1 Procedure for simulations

The advantage of simulations is to be able to carry out a large number of synthetic experiments in a short time. In addition, it allows to evaluate different treatments in the same configuration and therefore to compare the differences inherent in the processes without experimental bias. Many simulators (as SCORES [13], DuMu^x [14] or CYDAR [15]) are available to design, interpret and simulate Special Core Analysis (SCAL) experiments. In this study Cydar© is used to generate synthetic data but Lenormand *et al.* [16] have shown that all simulators have given same results (for average saturation simulation) considering PP and centrifuge experiment simulations.

In order to compare PP, UFPCRI and WiRI processing, 3 synthetic samples (S1 – S2 – S3) were created with the same properties:

- Length (L) 50 mm, Diameter (d) 38 mm
- Porosity (Phi) 20 %, Pore Volume (Vp) 11.341 cc

The only variations are made on permeability, capillary pressure curves and irreducible saturations (Swi). Pc curves presented in Fig. 1 are generated from the "log(S-beta)" function with threshold Smax option. Parameters are listed in Table 1. Parameters "P0 (magnitude)", "Pt (Threshold)" and the "Log(S-beta)" function are defined in the Cydar-SCAL User Manual [17].

Table 1. Pc parameters used in Cydar

	Perm (mD)	Swi (frac)	Sw-max (frac)	P0 (mb)	Pt (mb)
S1	10	0.1	1.0	0.05	0.005
S2	100	0.2	1.0	0.5	0.05
S3	1000	0.3	1.0	1	0.5

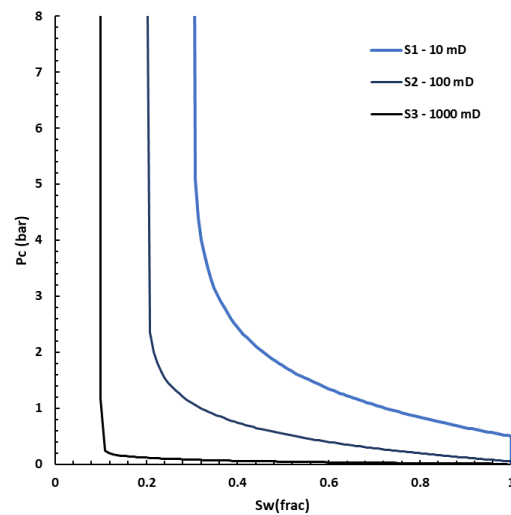


Fig. 1. Capillary pressure curves of synthetic samples S1, S2 and S3, generated with Cydar© and the set of parameters in Table 1

For each synthetic sample, Cydar is then used to generate datasets in Oil / Water drainage mode. Oil density and viscosity are 0.83 g/cc and 12 cP respectively. Water density and viscosity are set to 1 g/cc and 1cP.

- A Porous Plate experiment is simulated for each sample. It provides a production curve versus time. Production endpoints for each pressure steps are converted into resistivity using Archie's law with $n = 2$
- A centrifuge experiment is simulated for each sample. It provides multiple saturation profiles (with a 0.833 mm spacing between each saturation point) among time. They are converted into resistivity profiles using Archie's law with $n = 2$ and then "stacked" according to the UFPCRI and WiRI resistivity profiling resolution (with 5 mm spacing for each method)

Ultimately, 9 datasets are generated (3 experiments for each of the 3 samples).

In order to study the impact of uncertainties and differences between each process with a Monte Carlo approach, Matlab© is used to introduce different random normally distributed errors (through the "randn" function) [18] on each dataset. Each result presented was performed with a minimum of 100 000 simulation.

2.2 Rock samples and fluids for real cases experiments

For consistency between the simulated dataset and the experiments, we used samples with the same range of representative permeabilities, varying from 2100 mD (a Bentheimer outcrop sample), [80 – 400] mD (four reservoir sandstone rocks), and 11 mD (a Richemont outcrop sample).

For the UFPCRI and PCRI method the dimensions of the samples are $d=38$ mm and $L=50$ mm. For the WiRI experiment, due to the constraints of the system, plugs are $d = 30$ mm $L = 45$ mm. Fig. 2 shows the Klinkenberg corrected gas permeability (KgKI) versus Porosity (Phi) plot for samples used for WiRI (triangles), UFPCRI (rounds) and PCRI (squares). Twin samples have been used for every experiment except for the Richemont sample where PCRI and WiRI have been performed on the same sample $d=30$ mm $L=45$ mm (with a cleaning and drying sequence between each experiment).

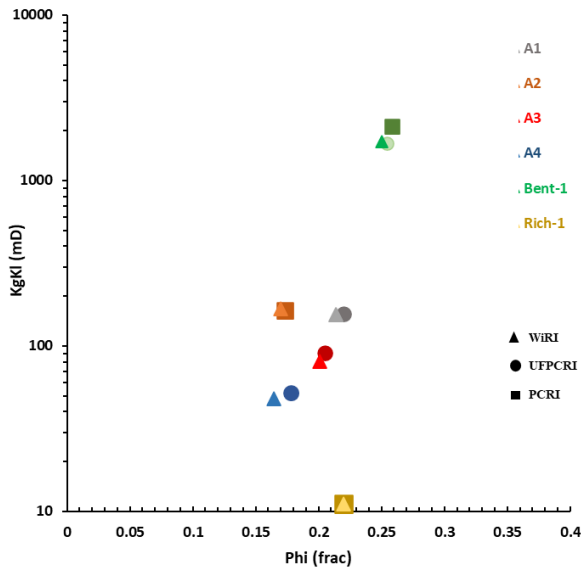


Fig. 2. Klinkenberg corrected gas permeability (logscale) versus porosity (Phi) of the studied samples

The fluids used for both experiments are summarised in Table. 2.

Table 2 : Fluid properties measured at 20°C

Samples	Heavy Fluid	Light Fluid
A1 – A4	Brine $\rho = 1.01\text{g/cc}$ Viscosity = 1.075cP	Air $\rho = 0.0012\text{ g/cc}$ Viscosity = 0.018 cP
Bent-1	Brine $\rho = 1.052\text{g/cc}$ Viscosity = 1.45cP	Marcol52© $\rho = 0.83\text{g/cc}$ Viscosity = 12.3 cP
Rich-1	Brine $\rho = 1.052\text{g/cc}$ Viscosity = 1.45cP	Marcol52© $\rho = 0.83\text{g/cc}$ Viscosity = 12.3 cP

2.3 Procedure for experiments

Both for the reservoir samples and for the outcrop samples the following routine core analysis (RCA) was performed before each experiment.

- Cleaning sequence of toluene and iso-propanol injections; nitrogen flushing; drying in the oven at 80°C
- Measuring dry mass and total volume
- Measuring helium porosity and gas permeability
- Saturating sample with synthetic brine ($S_w=100\%$)
- Determining pore volume (V_p) from helium porosity and/or from weight difference between saturated and dry mass
- Determining fluid properties at 20 °C: brine density and resistivity (R_w), oil density

After the RCA, for the PP experiments:

- Mounting the core in an individual core holder with a porous plate saturated with the same brine
- Applying a confining stress of 50 bars
- Measuring initial resistivity R_o at $S_w = 100\%$
- Applying a first pressure step and wait for production volume stabilization
- Applying multiple pressure steps with stabilization between each one
- Determine P_c/S_w , $\log R_I/\log S_w$ curves, and n exponent with the end points of each pressure step

Tips to maximize PP data quality proposed by [19] have been followed. PP data is acquired when cessation of brine production and stabilization of resistivity is reached at each pressure step for 24 hours minimum. Interpretation is then performed on raw data.

For the UFPCRI and WiRI experiments the exact same sequences and equipment described in [8] and [9] are followed. For both methods, no confining pressure is needed.

3 Simulation Results

The aim of this study is to investigate the sensitivity of the 3 methods (PP, UFPCRI and WiRI) to various parameters. Sections 3.1 and 3.2 respectively show how a random error applied on produced volumes and on resistivities affects each method.

Section 3.3 presents the effect of classical errors (on volume and resistivity) on the results for different samples (Capillary pressure shape, permeability, saturation profiles) in this case the 9 datasets are analysed in parallel.

3.1 Effect of uncertainty on the produced volume V_{prod}

In this part, the results are shown for synthetic sample S2 but observations and interpretations are the same for each sample.

Here, a random absolute error is introduced on the “saturation part” of each method. For the PP and the WiRI

experiment, this error is introduced on the production volumes (representing an experimental error on the reading of volumes). The error is chosen “absolute” because whether in PP or in WiRI it is not dependent on the volume but only on the precision of the system. For UFPCRI the same error is applied directly on the “NMR” volumes generated. 100 000 simulations are performed for 8 normally distributed ranges of random error varying from 0 error to ± 11 saturation units (s.u.). For each error range, we then obtain 100 000 results forming a distribution. The mean exponent n of the distribution is then plotted (Fig. 3) and the 5th and 95th percentiles are used as error bars. (A small shift on the x-axis between each method is applied for better reading. On the y-axis the shift is an observation of the simulation, not an artefact)

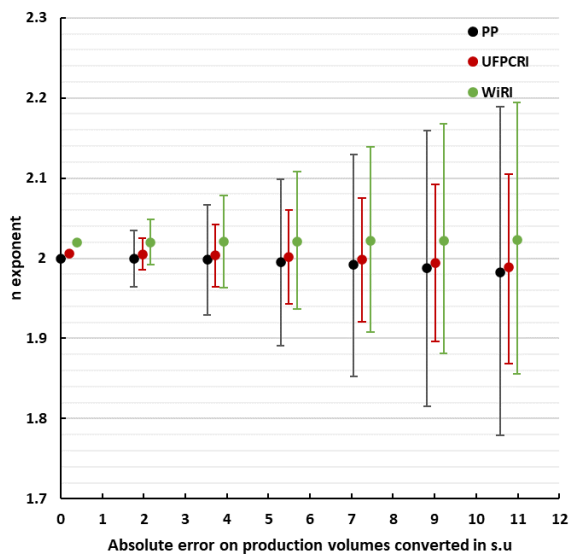


Fig. 3. Impact on each method of an increasing absolute error on production volumes

Observations:

For the PP, increasing the error on production volume leads to an obvious increase in range of error bars, but also to a far less obvious decrease of the mean n value. This is discussed in the interpretation section.

For UFPCRI: 3 observations could be done. First, even with 0 error a small systematic bias on the n exponent exists ($n = 2.006$ instead of 2). Second, increasing error leads to a drift towards lower mean n exponent. This second effect dominates the systematic bias. Third, the range of error bars increases with the error but is always lower than for PP and for WiRI

For WiRI: As for UFPCRI a systematic bias exists on the n exponent (even at 0 error $n=2.019$ instead of $n=2$). Error bars are also increasing with error but no further deviation on the mean is observed.

Interpretation:

First, the drift of the mean n with increasing error on produced volumes in PP and UFPCRI experiments is linked to the interpretation method. The two methods are based on a linear fit of RI versus S_w in log-log scale. Introducing an error on production volume will induce an “error bar” on the saturation. In linear scale the center of the error bar is given by the mean of the measurement, but as shown in Fig. 4 for illustration, an asymmetry appears on logscale. This asymmetry is even higher at lower saturation. In consequence, applying a linear fit on such a dataset leads, on average, to a lower n value than the searched value. Increasing the error on production volumes leads to increase the asymmetry and so, the probability to find an underestimated n value.

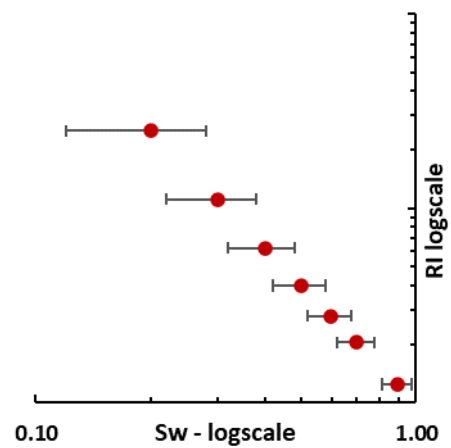


Fig. 4. Illustration of the asymmetry of the error bar on S_w in logscale

The process used in WiRI experiment to calculate the n exponent is based on the determination of the least squares between an estimator (containing the n exponent) and the measured produced volume. It explains why the same drift isn’t observed.

Second, the systematic excess bias observed in UFPCRI and in WiRI arises because of non-uniformity of profiles and the resolution. For WiRI we showed in [9] that a 5 mm spacing induces a small systematic error (less than 1%) on the n exponent. Given that the saturation profiles induced in a centrifuge are known to generally have a convex shape (or flat at the very least), an insufficient resolution (for resistivity measurement) will average the profile upward and therefore increase the n exponent. These two methods are based on imaging (resistivity and saturation imaging for UFPCRI, and resistivity imaging only for WiRI). The steeper the profile, the less accurate the image. This effect is even stronger in WiRI than in UFPCRI. Indeed, while the UFPCRI interpretation is performed with a set of independent RI- S_w points, the WiRI inversion is performed on all the RI data at the same time. Therefore, one «bad average » point will impact all data.

3.2 Effect of uncertainty on Resistivity

Here, a random relative error varying from 0 to $\pm 12\%$ is introduced on the resistivity part of each method. The error is normally distributed and considered relative because of the nature of the equipment's usually used (a precision that decreases with increasing measured values).

The results are also shown for synthetic sample S2 but the observations and interpretations are the same for S1 and S3.

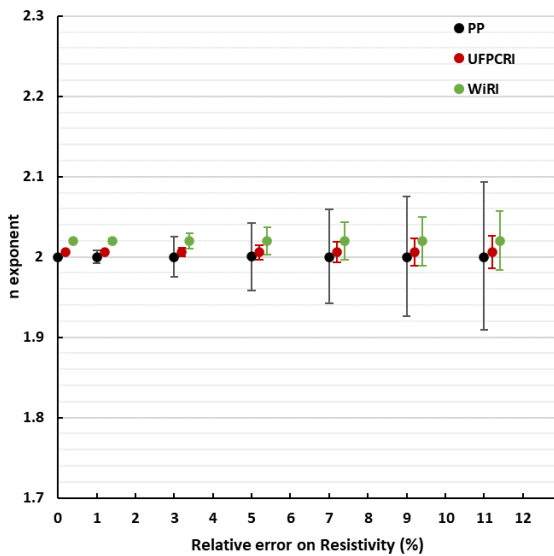


Fig. 5. Impact on each method of an increasing absolute error on resistivity

In Fig. 5, the error bar is the lowest for UFPCRI and the highest for PP method. The main explanation lies in the fact that the error applied in the resistivity is relative. In PP, one resistivity is measured for whole plug while for UFPCRI and WiRI resistivity is measured by sections of 5 mm. Consequently, for the same sample, measurement data in UFPCRI and WiRI are relatively small compared to PP, and therefore the errors too.

Comparing Fig. 4 and Fig. 5, the error on resistivity has a lower impact on the n exponent determination than the error on produced volume. The decrease in mean for UFPCRI and PP is not observed in this case. The following illustration (Fig. 6) allows to understand why an error in resistivity impact less the mean n value than an error in saturation. Even if asymmetry appears again, at low saturation the error bar is quasi-null in logscale and the method for determining n exponent forces the fit in 0, reducing the impact of error at high saturations.

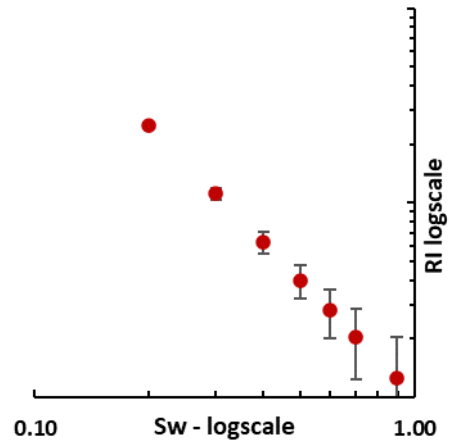


Fig. 6. Illustration of the impact of error in resistivity on the n exponent

3.3 Effect of the plug type (K,Pc) on the combined errors

In this part the investigation is presented for the 3 synthetic samples (S1 with $K = 10$ mD - S2 $K = 100$ mD - S3 $K = 1000$ mD and the associated P_c curves and Sw_i values presented in section 2.1) for the 3 methods. The 3 methods have been simulated (100 000 simulations) with a relative error in resistivity of $\pm 5\%$ and according to [1] an absolute error on produced volumes of ± 3 s.u. Results are the effect of the combined errors on the 3 methods for each sample "type". In Fig. 7, the lines represent the mean for each simulation and dotted lines the 5th percentile (P5) and 95th percentile (P95) confidence interval.

For the PP, the mean n of the 100 000 simulation is not dependent on the sample (the same mean n exponent). In contrast, the error bars (represented by the P5 and P95) decrease with increasing permeability. Indeed, applying the same pressure steps on a "higher permeability" sample (and lower Sw_i) would lead to higher produced volumes. Since the error on volumes, we introduced is absolute, this reduces the impact of error on saturations.

For UFPCRI the combination of errors approximatively has the same impact as the error on saturations only. The same small little bias due to resolution is observed and seems to grow for the higher permeability. The P5- P95 range on the n exponent shows to be the most reliable interval of confidence of all 3 methods.

For the WiRI: on the S1 and S2 ($K = 10$ mD and 100 mD), the combined errors on resistivity and on produced volumes lead to the same observation done in 3.1 (systematic excess bias on n exponent). The WiRI experiment shows a deviation of the average n calculated when error introduced, and the impact is more important for S3 with the higher permeability/lower Sw_i . It forces the mean n exponent away from the target. The confidence interval is tightening with permeability and the probability of finding a biased n is almost certain. The range P5-P95 is [2.08 - 2.13] instead of $n = 2$.

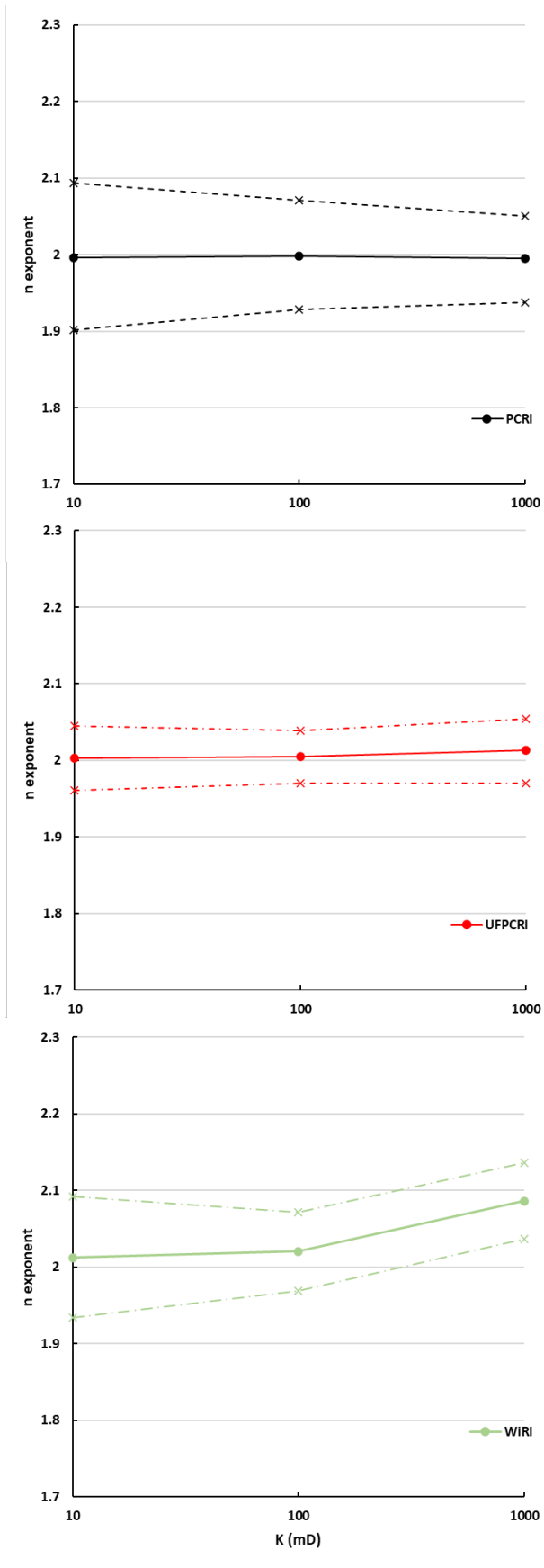


Fig. 7. Effect of the combined errors for each method and each sample

In 3.1 we saw that the WiRI inversion is performed on all the RI at the same time. Therefore, one «bad average» point will impact every single point in the optimization process. The resolution of WiRI measurements is limited by electrode spacing. When the permeability grows, it is more likely to find saturation profiles with stronger convexity. Therefore, the impact on WiRI inversion is higher at higher permeabilities.

4 Experimental results

Here we compare the experimental results obtained on real samples with various experimental methods (PP, UFPCRI and WiRI). For consistency with previous sections, we present the results obtained for high, middle and low permeability samples (Fig. 8 and Fig. 9).

Table 3: n exponent and Swi for Benth-1 – A1 – A4 – Rich-1 and the methods investigated for each sample

Samples	n exponent	Swi (frac)
Benth-1	PP: 1.83	PP: 0.10
	UFPCRI: 1.74	UFPCRI: 0.12
	WiRI: 1.78	WiRI: 0.08 (MICP): 0.09
Rich-1	PP: 1.80 WiRI: 1.72	PP: 0.35 WiRI: 0.36
A1	UFPCRI: 1.33 WiRI: 1.30	UFPCRI: 0.09 WiRI: 0.08 (MICP): 0.10
A4	UFPCRI: 1.45 WiRI: 1.29	UFPCRI: 0.11 WiRI: 0.9 (MICP): 0.15

For the sample Benthimer-1 (top of Fig. 8): The Pc of PP and UFPCRI coincide, and MICP and WiRI also almost superimpose. The n exponents (Table. 3) are close, and the highest n is found for the PP method. This is in contradiction with the high permeability simulations (Fig. 7) predicting a higher n for the WiRI than for the two other methods. Other sources of uncertainty as handling, plug conditioning, measurement techniques and technologies have hidden, in that case, the bias on the n exponent. However, local saturation points and n exponent are both determined at the same time in the WiRI inversion. In 3.1 we observed that WiRI resolution present a systematic upward bias on the n exponent when determining least squares with a 5 mm resolution. In this specific case, measurements of local resistivities and produced volumes have led to determine an n exponent in the interval of PP and UFPCRI. Consequently, it seems logical to find WiRI saturations impacted downwards. Saturations determined by WiRI method are lower (-3 s.u. in average) than saturations determined by PP and UFPCRI at the same Pc.

For sample Richemont-1 (bottom of Fig. 8): Swi has not been reached for both experiments due to leaks, and handling issues. Difference between n (WiRI) and n (PP) is less than 0.1. For the part of the Pc curve investigated, Porous Plate and WiRI curves almost superimpose.

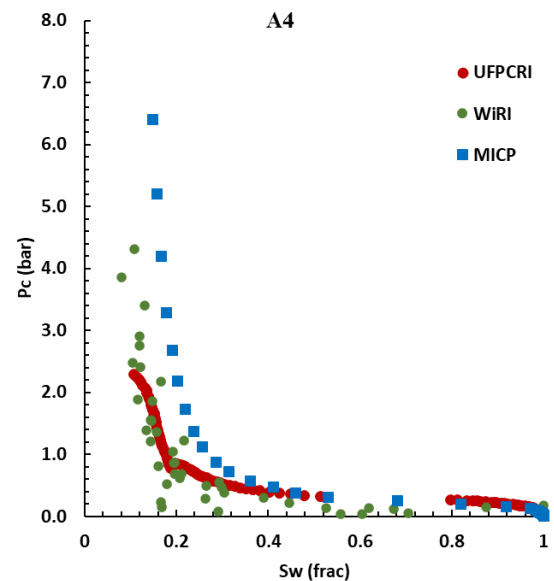
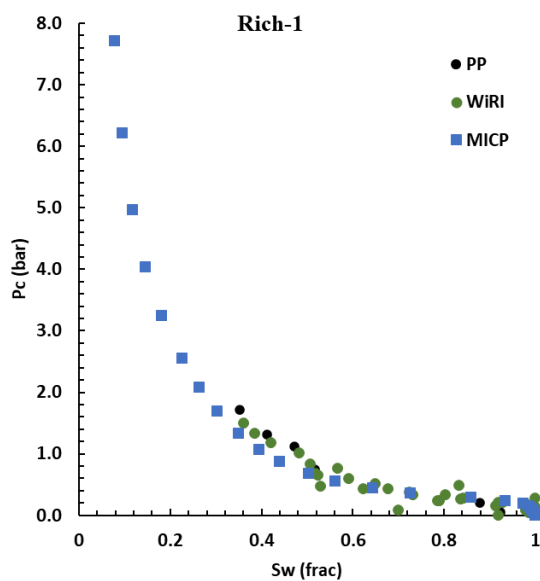
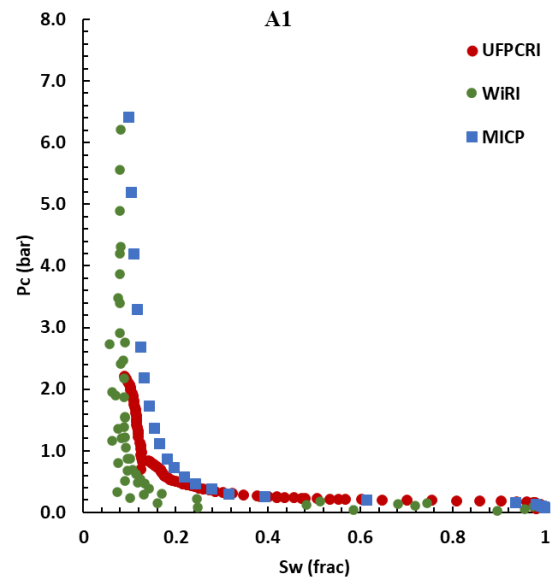
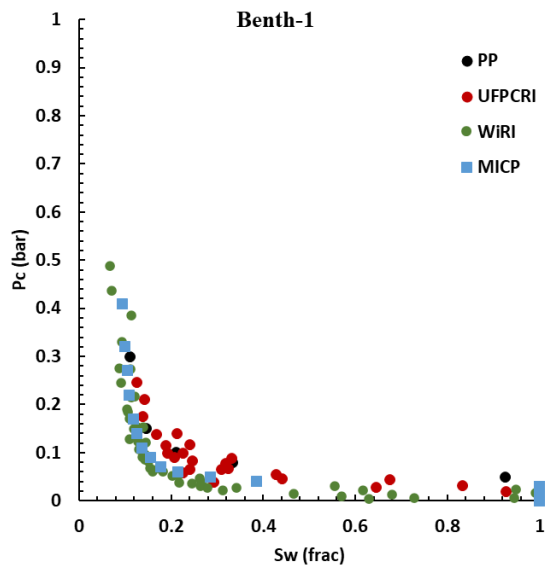


Fig. 8. Pc/Sw (Oil/Water Drainage) for: Benth-1 – K = 1700 mD and Rich-1 – K = 10 mD

Fig. 9. Pc/Sw (Gas/Water Drainage) for: A1 - K = 150 mD and A4 - K = 50 mD

For samples A1 and A4 (Fig. 9): Pc curves obtained with each method show the same behaviour but deviations of saturation at the same pressure is shown (± 4 s.u in average between WiRI and UFPCRI). Swi agrees with better accuracy (± 2 s.u maximum). No “overestimation” of the n exponent is provided by WiRI and last, MICP has a slightly higher Swi for both samples.

These 4 experiments also prove that uncertainty on measurements, noise, equipment, and operators are the major factors influencing the results of PP, UFPCRI and WiRI. Quality of the results is also affected by the homogeneity of the samples and heterogeneity may well dominate all measurement errors. Effect of heterogeneity is discussed in section 5. However, each experiment showed consistency in terms of n exponents and deviations on saturations at same pressure steps are less than 5 s.u in average despite the sources of measurement uncertainties.

5 Discussion: limitations of WiRI

This part tackles the limitations of the WiRI experiments through 2 main examples on real cases:

- The first limitation is the heterogeneity of a sample. As stated in [9] WiRI is based on the inversion of Archie’s law along a sample and implies the homogeneity. An example of WiRI results on non-homogenous sample is shown Table. 4 and Fig. 10
- The second limitation is linked to a “non-Archie behaviour” of the resistivity-saturation data. Because Archie is an assumption of WiRI, a non-Archie behaviour cannot be spotted. This is shown in Fig. 12

Effect of heterogeneity:

Table 4. n exponent and Swi for sample A3 obtained with UFPCRI and WiRI

Sample	n exponent	Swi (frac)
A3	UFPCRI: 1.08 WiRI: 1.74	UFPCRI: 0.12 WiRI: 0.17 (MICP): 0.1

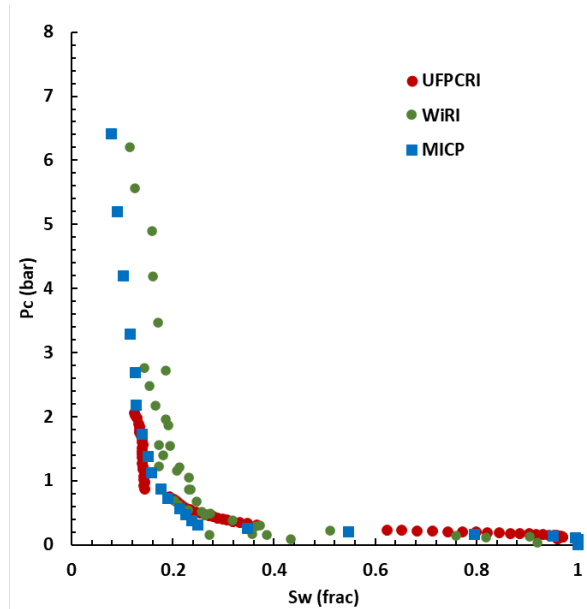


Fig. 10. Pc/Sw curves for sample A3- KgKl = 160 mD: Gas/Water drainage

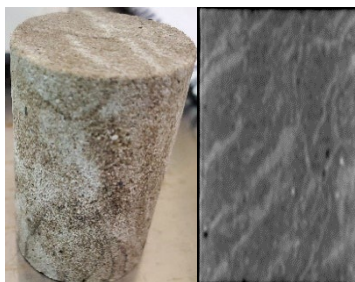


Fig. 11. Photography of the A2 sample at Swi = 17 s.u. on the left – A2 plug CT-scan on the right

Fig. 10 shows a strong disagreement for the n exponent. The Pc/Sw curves from UFPCRI and MICP are superposed while WiRI overestimate Swi.

Fig. 11 left shows the A2 sample in its Swi state. Homogeneity of this sample is clearly questionable and further investigation about its homogeneity could be done from CT scan and an estimation of the coefficient of permeability variation as proposed by Maas *et.al.* in [20] and [21]. Here the lightest parts in the photography are the driest (the most desaturated) while the darkest contains more water. Using a centrifuge, a longitudinal distribution of saturation is expected, whereas here, a radial distribution is (even visually) detected. Since resistivity measurements are acquired with radial electrodes, WiRI process is highly impacted by this effect.

The UFPCRI method is very robust concerning the Pc/Sw curve because Pc is calculated [10] and saturation is measured with NMR (1 measurement each mm). Concerning resistivity and saturation, even with radial electrodes, the UFPCRI resistivity is directly linked to a measured saturation.

Effect of non-Archie behaviour:

Table 5. n exponent and Swi for sample A2 obtained with PP and WiRI

Sample	n exponent	Swi (frac)
A2	PP: 1.60 WiRI: 1.90	PP: 0.09 WiRI: 0.10 (MICP): 0.13

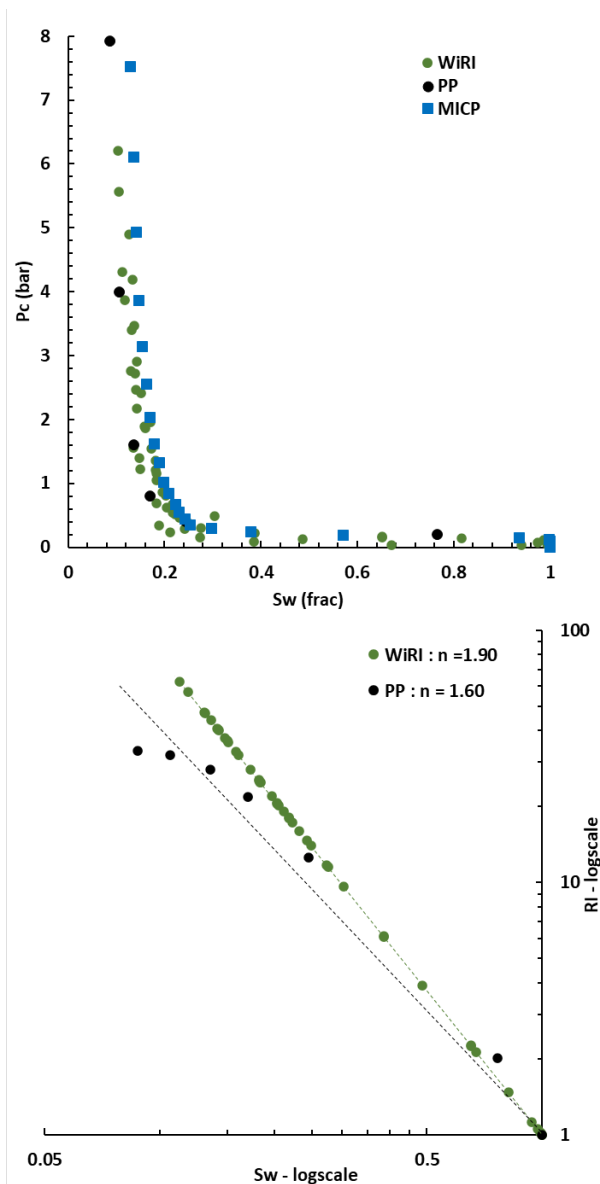


Fig. 12. Pc/Sw curves and log RI/log Sw curves obtained on PP and WiRI for sample A2 – KgKl = 90 mD

In Fig. 12, for sample A3 the n exponent clearly disagrees (n = 1.9 for WiRI and n = 1.6 for PP) while the pc curves do not show different behaviour.

The curvature of $\log RI/\log Sw$ shown in PP is completely missed by WiRI. It is the consequence of Archie's inversion, leading to a straight line in the $\log RI/\log Sw$ plot. Han *et.al.*[22] have shown that a negative deviation at low saturation range could appear due to a water film conduction. With the assumption of validity of Archie's law, WiRI is not able to reconstruct a curvature neither due to a water film nor to any other factor. For the PP experiment, the choice is given to the engineer to choose the model that best describes the observed results. In that case, a Waxman-Smits model (1968) [23], [24], could be a good choice due to the presence of 6% of clays (mainly composed by illite and glauconite) in this sample.

CONCLUSION

In conclusion, simulations have been done with two purposes:

- Investigate and determine which parameter (RI Sw) influences the most the determination of Archie's n exponent. The PP technique is the most impacted, then WIRI and last UFPCR. The 3 methods are more sensitive to an error on produced volume than to an error on resistivity.
- Investigate the "robustness" of 3 methods to different samples (in terms of K , P_c) when measurements suffer from an error. In the PP technique, investigation of "high" permeabilities would generally lead to a tighter P5-P95 confidence interval due to higher produced volume. UFPCR is robust to changes in sample characteristics. WiRI shows a small deviation due to its resolution combined with optimization process. When permeability increases, the convexity of the saturation profiles increases. The more convex, the more n is impacted.

While results of simulations only could lead to prefer the use UFPCR for its major advantages (robustness over different samples, narrower error bars around the n exponent and the possibility to detect heterogeneity during the experiment [8]), the two other methods have shown to be also very robust during experiments. Introduction of handling errors, operators experience and other factors than only measurement errors have, nevertheless, led to determine n exponent with a maximum difference of 0.1 with the 3 methods on homogenous samples. P_c curves shows the same behaviour and at the same pressures, saturations are in a confidence interval of ± 5 s.u.

Simulations have shown that, among the 3 methods, the PP is the most impacted by errors. However, it allows determining RI/Sw relationship under every circumstance (such as a "non-Archie" behaviour).

Last, WiRI simulations have shown a deviation of the n exponent depending on the sample characteristics (K , P_c). Two experiments have shown the limitations of the method and why it should be used only under the assumptions (homogeneity and Archie behaviour) described in [9] otherwise the possibility to estimate a wrong n exponent is quasi-certain. Furthermore, homogeneity needs to be assessed quantitatively through X-CT in order to use a cut off value [21] and also to direct studies towards the most appropriate method. However, the WiRI experiment is an asset of real interest when it comes to quickly determine P_c/Sw and n exponent on homogeneous samples. Fig. 13 is a summary of durations of each experiment for each sample of this study. The graph clearly shows that WiRI proved to be much shorter to determine P_c/Sw and n exponent for all samples.

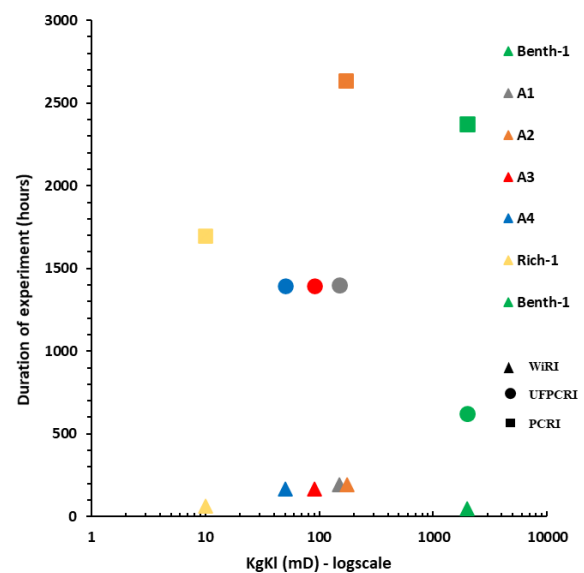


Fig. 13. Total duration of experiment versus Klinkenberg corrected gas permeability for each sample presented in this paper. WiRI is the shortest experiment (10 days maximum for the presented samples). UFPCR duration is about 2 months and PP about 4 months. For the Richemont sample Sw_i was not reached neither for PP nor for WiRI

The authors thank Cyril Caubit and Pierre-Edouard Schreiber for their involvement in the management and the development of this project.

REFERENCES

- [1] C. McPhee, J. Reed, I. Zubizarreta, "Core analysis: a best practice guide", Elsevier, 2015.
- [2] D. Tiab, E.C. Donaldson, "Petrophysics: theory and practice of measuring reservoir rock and fluid transport properties", Gulf professional publishing, 2015.
- [3] G.E. Archie, "The Electrical Resistivity Log as an Aid in Determining Some Reservoir Characteristics." Trans 146: 54-62, (1942)

- [4] J.A de Waal, R.M.M Smits J.D. de Graaf, B.A. Schipper, "Measurement and evaluation of resistivity index curves". SPWLA Thirtieth Annual Logging Symposium, June 11-14, 1989
- [5] M. Fleury, "FRIM: A Fast Resistivity Index Measurement Method," in SCA, paper 29, (1998)
- [6] M. Fleury, "Advances in resistivity measurements using the FRIM method at reservoir conditions. Application to carbonates" in SCA, paper 31, (2003)
- [7] N. Bona, E. Rossi, B. Bam, "Ultrafast Determination of Archie and Indonesia m&n Exponents for Electric log Interpretation: a Tight Gas Example", IPTC-17446-MS, (2014)
- [8] P. Faurissoux, A. Colombain, G. Pujol, O. Fraute, B. Nicot, "Ultra Fast Capillary Pressure and Resistivity Index measurements (UFPCRI) combining Centrifugation, NMR Imaging, and resistivity Profiling" in SCA, paper 2, (2017)
- [9] Q. Danielczick, P. Faurissoux, B. Nicot, "Wireless Acquisition for Resistivity Index in Centrifuge – WiRI: A new method to estimate Archie's law Parameters", in SCA, paper 18, (2021)
- [10] D. Green, J. Dick, J. Gardner, B. Balcom, B. Zhou, "Comparison Study of Capillary Pressure Curves Obtained Using Traditional Centrifuge and Magnetic Resonance Imaging Techniques", in SCA, paper 30, (2007)
- [11] D. Green, J. McAloon, P. Cano-Barrita, J. Burger, B. Balcom, "Oil/Water Imbibition and Drainage Capillary Pressure Determined by MRI on a Wide Sampling of Rocks", in SCA, paper 1, (2008)
- [12] W. Krauth, "Introduction to Monte Carlo algorithms" summer school in Beg-Rohu (France) and Budapest 1996, 2006. cel-00092936
- [13] <https://scores-panterra.nl/>
- [14] J.G. Maas, B. Flemisch, A. Hebing, "Open Source Simulator DuMu^X Available for SCAL Data Interpretation", in SCA, Paper 8, (2011)
- [15] <http://www.cydarex.fr/>
- [16] R. Lenormand, K. Lorentzen, J.G. Maas, D. Ruth, "Comparison of Four Numerical Simulators for SCAL Experiments" in SCA, paper 6, (2016)
- [17] CYDAR-SCAL User Manual – April 2021– p.43 on: http://cydarex.fr/files/CYDAR_SCAL.pdf
- [18] "Randn function"
<https://fr.mathworks.com/help/matlab/ref/randn.html>
- [19] F. Pairoys, "Rock Electrical Properties from Porous Plate and Resistivity Experiments: Tips to Maximize Data Quality", in SCA, Paper 38, (2018)
- [20] J.G. Maas, A. Hebing, "Quantitative X-ray CT for SCAL Plug Homogeneity Assessment", in SCA, Paper 4, (2013)
- [21] J.G. Maas, N. Springer, A. Hebing, "Defining a sample heterogeneity cut-off value to obtain representative Special Core Analysis (SCAL) measurements", in SCA, paper 24, (2019)
- [22] M. Han, M. Fleury, P. Levitz, "Effect of the pore structure on Resistivity Index curves" in SCA, paper 34 (2007)
- [23] M.H. Waxman, L. J. M. Smits, "Electrical Conductivities in Oil-Bearing Shaly Sands", Society of Petroleum Engineers Journal, SPE-1863-A, June (1968)
- [24] M.H. Waxman, E.C. Thomas, "Electrical Conductivities in Shaly Sands-I. The Relation Between Hydrocarbon Saturation and Resistivity Index; II. The Temperature Coefficient of Electrical Conductivity", Journal of Petroleum Technology, SPE-4094-PA, February. (1974)

Unraveling electrokinetics – a brand new and innovative workflow for the quantification of electrokinetic properties of siliciclastic rocks

Matthias Halisch^{1,*}, Stephan Kaufhold², and Christian Weber²

¹Leibniz Institute for Applied Geophysics (LIAG), Dept. 5 Petrophysics & Borehole Geophysics, 30655 Hannover, Germany

²Federal Institute for Geosciences and Natural Resources (BGR), Dept. B2.1 Technical Mineralogy, 30655 Hannover, Germany

Abstract. Electrokinetic properties have been measured, assessed and quantified for a very long time, mostly for classic colloidal systems (e.g., soils) or suspensions (e.g., clay-water-mixtures). Electrokinetic effects are used for both, fundamental investigations, such as the quantification of quadrature electrical conductivity and polarization processes, as well as for applied research, such as the systematic investigation of fluid stabilities (e.g. of solvents and proppants). Nevertheless, the quantification of electrokinetic parameters is extremely challenging. First, because they cannot be measured directly. Common techniques utilize the measurement of electrokinetic effects, which can be transferred to distinct electrokinetic parameters. Second, because electrokinetic properties depend on a high number of material and fluid quantities, such as the type of mineral and fluid phase, grain size, grain shape, grain roughness, ion content of the fluid, ion valence, ion mobility and pH-value. Although it is possible to quantify these properties on a general base for different formation, they can differ widely within natural rocks. Furthermore, specimen need to be crushed for the analysis. By doing this, the in-situ grain geometry and surface topology is destroyed. Even worse, milling causes the occurrence of amorphous mineral phases, which are mineralogical equivalent to the originating phases, but which may greatly differ in terms of electrokinetic properties. Hence, the value of the so derived data is very questionable. Within this case study, we will present a brand new and highly innovative methodical approach to overcome the issues as mentioned before. We will present and discuss both, very first electrokinetic data from a variety of siliciclastic rocks that have been processed as described in this manuscript, as well as the sample processing workflow.

1 Key Motivation

The key motivation for this innovative and new workflow lies within the fundamental research and understanding of the so-called “Induced Polarization effect” that was observed and published for the first time in 1920 by Conrad Schlumberger. Originally developed for prospecting ore deposits, the Induced Polarization (IP) or Spectral Induced Polarization (SIP) method is used to characterize natural solid and unconsolidated rocks, by covering many different approaches. Possibly more than any other geophysical method, SIP is able to build an important bridge between field and laboratory scale, i.e. between application and process and fundamental research [e.g., 1-6]. The main interest of basic research here is to comprehensively describe or characterize the causes of the IP effect in sedimentary rocks. In addition to investigating empirical correlations between SIP related parameters and classical petrophysical properties, such as specific surface area [e.g., 7], or permeability [e.g., 2], recent research has also focused on understanding the physical and electrochemical interaction between the rock-forming matrix and the fluid-filled pore space [e.g.,

8, 9]. Based on this, varieties of models have been developed in recent years to describe the IP effect phenomenological. In this context, these models are either grain-based [e.g., 10-13], or pore-space based [e.g., 14-17] and take into account, at least to some extent, corresponding characteristic geometric structures and sizes found at the pore scale.

1.1 IP-theory

If an external electric field E is applied, a current density (j) is formed in any material, which is composed of a conduction current (j_L) and a displacement current (j_V):

$$j = j_L + j_V. \quad (1)$$

The conduction current density is obtained directly from Ohm's law:

$$j_L = \sigma E, \quad (2)$$

where σ corresponds to the electrical conductivity of the material. Now, if - as is the case with SIP - a periodic alternating electric field is present (i.e., $E \sim \exp(i\omega t)$, with

* Corresponding author: matthias.halisch@leibniz-liag.de

$i = \sqrt{-1}$, ω = angular frequency = $2 \pi f$, t = time), the displacement current density is given by:

$$j_V = d/dt \epsilon E = i\omega \epsilon E. \quad (3)$$

The ϵ here corresponds to the so-called dielectric constant and is composed of the relative dielectric constant and the vacuum dielectric constant ($\epsilon = \epsilon_r \epsilon_0$). If we now consider the low, i.e., the SIP-typical frequency range (~ 1 mHz to ~ 10 kHz), the ratio of conduction to displacement current density becomes very large, i.e., the displacement current density - and thus the influence of the dielectric constant of the material - becomes negligible [18]:

$$|j_L| / |j_V| = \sigma / (\epsilon_r \epsilon_0 \omega) \gg 1. \quad (4)$$

Consequently, the electrical material behaviour in this frequency range is dominated by the conductivity, which is described as a frequency-dependent and, in the case of inhomogeneous, natural rocks, moreover as a complex quantity consisting of real (σ') and imaginary part (σ'') [19]:

$$\sigma(\omega) = \sigma'(\omega) + i\sigma''(\omega). \quad (5)$$

Due to different polarization mechanisms, there is a characteristic phase shift between the current and voltage signal by an angle ϕ :

$$\phi(\omega) = \arctan (\sigma''(\omega) / \sigma'(\omega)). \quad (6)$$

This measurable phenomenon is commonly referred to as the "IP effect". As listed in the introduction, quite a few variants and variations of phenomenological models (some mineral grain-based, others pore space-based) exist to describe, characterize, and reproduce the IP effect in a material-dependent, i.e., rock-specific, manner under ideal circumstances. The latter, however, is particularly challenging because, although there are recognized polarization mechanisms, their individual influence, integrated over the entire sample volume under investigation, is largely not understood. It is undisputed that the electrical conductivity ($\sigma(\omega)$) of a rock whose pore space is filled with electrolyte is largely determined by the electrical conductivity of the fluid (σ_w). That is, the rock-forming minerals behave relatively as "quasi-insulators" due to their very low electrical conductivity. However, electrochemical interactions cause the formation of a so-called interfacial conductivity ($\sigma_g(\omega)$) at the interface between the pore fluid and the rock matrix. Since this conductivity is also a complex quantity, the rock conductivity can be described using the so-called formation resistance factor F [20] as follows [21, 22]:

$$\sigma(\omega) = (\sigma_w / F) + \sigma_g'(\omega) + i * \sigma_g''(\omega) \quad (7).$$

Electrochemical processes and interactions result in a solid accumulation of ions on the surface of the mineral grain. This "solid" layer is called the Stern layer (or Helmholtz layer). The transition to the (free) pore fluid is formed by a region of diffusely distributed ions. The ion

concentration within this diffuse layer decreases exponentially with distance from the Stern layer. Together, this results in the so-called electric double layer (EDL, Figure 1). As it can be seen from (7), the imaginary part of the rock conductivity (quadrature conductivity, also denoted as σ'') is caused solely by the contribution of the interfacial conductivity. Hence, the EDL occupies a central role in research on the IP effect, which is expressed in particular in the mechanistic models for the so-called membrane and Stern layer polarization. In these models, cations from the electrolyte accumulate firmly and diffusely on the usually negatively charged mineral surface: an EDL is formed. If an external alternating electric field is now applied, charge accumulation occurs and consequently a concentration gradient in the ion distribution. This concentration gradient is dissipated by diffusion after the electric field is switched off [23].

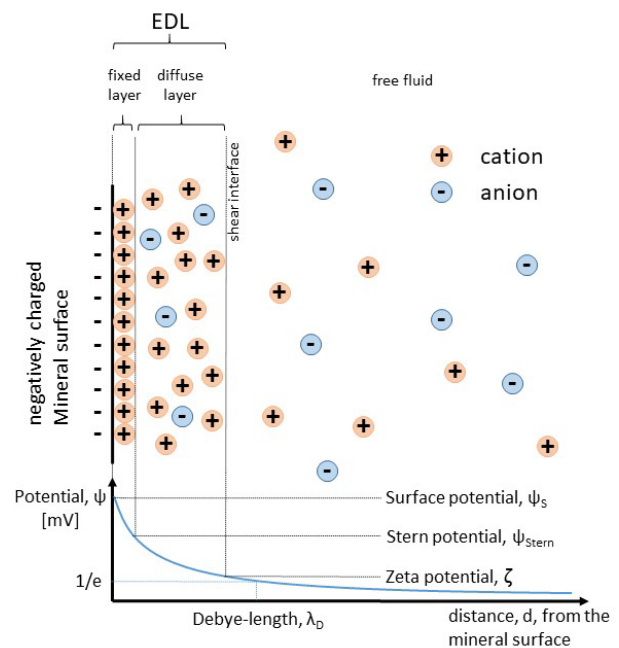


Fig. 1. Schematic representation of the charge carrier distribution at the interface between mineral grain (left) and electrolyte (right) without an externally applied electric field. At the negatively charged mineral surface (e.g., quartz) a fixed and a diffuse layer are formed, which together form the electrical double layer (EDL). The resulting potentials are shown in the lower part.

In addition to the dependence on the specific material surface, the research approaches based on the membrane polarization model focus primarily on the geometry or on the topology of the pore spaces, e.g. their diameter, their length, or their ratio to each other. Particularly noteworthy are the approaches to model membrane polarization by [24-28]. In addition, a few publications exist that attempt to include the influence of the electrical double layer in a highly generalized manner [e.g., 12, 29-31]. Nevertheless, all of these approaches lack systematically measured and validated, "in-situ" double-layer parameters of natural rocks and minerals. Closing this knowledge gap within the framework of this project is a key motivation.

1.2 Electrical double layer model

It is remarkable to note that research on the electrical double layer as well as on the IP effect has been carried out in parallel for almost a century, but that rudimentary efforts to link both research areas have only been made in the last 10 years. The characterization of the EDL has long been part of the standard repertoire in the fields of physical and inorganic chemistry as well as soil science and (clay) mineralogy, to name just a few of the disciplines with which rock physics or IP research could be synergistically linked. Comprehensive information on the formation, the dynamics, processes and applications around the EDL can be found in seminal textbooks [32, 33, 34].

However, crucial and linking for IP-related research on natural solid rocks is the formation of an EDL, so that when an external electric field is applied, the anions and cations in the diffuse layer as well as in the free fluid (cf. Fig.1) start to move according to the respective field direction. This leads to an accumulation of charge or to a "polarization effect" (Fig. 2), which in turn can be measured and interpreted as a contribution of the interfacial conductivity to the rock conductivity. The EDL is decisively characterized by the diffuse layer, i.e., as the dynamic part of itself.

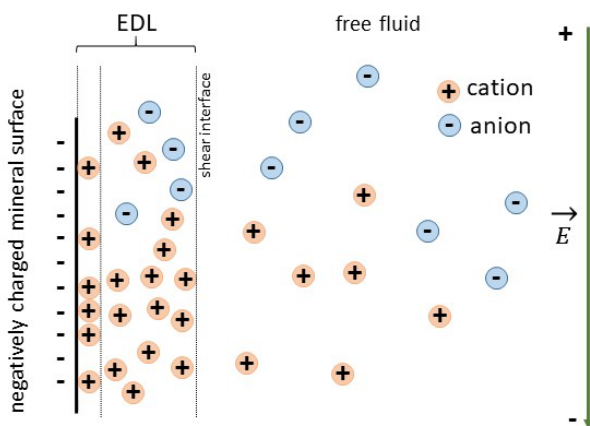


Fig. 2. Schematic representation of charge separation / accumulation with applied external alternating electric field (E). The EDL plays a decisive role for the polarization behaviour or for the IP effect.

The relevant parameter characterizing the diffuse part of the EDL is the so-called zeta potential [35, 36]. The zeta potential is defined as the electric potential at the shear layer of a moving particle in a suspension. Consequently, the zeta potential is an interfacial property (here at the solid-liquid interface) and depends on the surface potential (or surface charge) and thus on the mineral, its surface, and the properties of the electrolyte (see Table 1) [34]. In conclusion, there is a direct relationship between the interfacial conductivity (eq. 7) and the zeta potential. Moreover, the zeta potential is a main indicator of the electrostatic repulsion of ions in the dispersion medium, i.e., the higher the zeta potential, the greater the repulsion, i.e., the less likely is agglomeration of small charged

(mineral) particles. In classical EDL research, this relationship is used to characterize the stability of colloidal dispersions [37]. However, a look at the relevant EDL-related literature also shows that for decades almost exclusively only so-called colloidal systems have been the focus of research interest [e.g., 34, 35, 38-40].

Table 1. Summary of relevant dependencies of the zeta potential of solid and liquid phase.

solid phase (mineral)	liquid phase (electrolyte)
type of mineral	valency
surface	ion mobility
roughness	ion concentration
grain form	ph-value
grain size	temperature

A classical colloidal system consists of particularly finely dispersed, especially small (sub-micrometer range) particles (e.g. clay particles), which are contained in a dispersion medium. Thus, two main questions arise for SIP-related EDL characterization of natural solid rocks:

- 1.) How can the zeta potential be determined on a solid rock, taking into account the multiple dependencies as listed in Table 1?
- 2.) Does the necessary technology for the preparation and for the measurement exist at all?

2 Electrokinetic methods

In the course of our own preliminary work, we have investigated precisely these two questions. In order to be able to answer the first question, we will first take a brief look at the existing measurement methods. A variety of measurement techniques exist for determining the zeta potential, all of which are based on the measurement of an electrokinetic effect [36]. EDL properties themselves (as shown in Fig.1.) cannot be measured directly. One talks about an electrokinetic effect if the coupling of a mechanical and an electrical force is present in any combination. The only important thing is that two phases (here: solid-liquid) move relative to each other. In practice, one phase is moving while the other remains stationary.

Table 2 summarizes the main measurement techniques of electrokinetic effects and their sample requirements (Note: optical methods, such as laser scattering light microscopy, are neglected here because they are only considered for particularly highly dilute dispersions ($\ll 1$ vol.%) and small particle sizes ($< 0.1 \mu\text{m}$) and are thus generally unsuitable for EDL characterization of solid rocks.)

Thus, of the methods described in the literature, per se only the so-called streaming potential measurement is suitable for EDL characterization of solid rocks [34, 35]. However, this measurement has a significant disadvantage related to the systematic investigation of the EDL influence on the IP effect: the measurement on a solid rock sample provides only one value of the zeta

potential integrated over the entire sample volume, i.e., over all solid phase dependencies (table 1, left hand side). Thus, on the other hand, the systematic variations of the fluid dependencies (table 1, right hand side) lose significance or solely deliver basic descriptions of the EDL properties of the entire sample. Any other measurement technique for the determination of EDL parameters require particles in a dispersion medium, i.e., the "classical" colloidal systems as mentioned above.

Table 2. Overview of the main techniques for measuring electrokinetic effects.

electrical induced			
technique	measured effect	sample type	particle size
electrophoresis	electrophoretic mobility	colloidal	< 2 μm
electro-osmosis	electro-osmotic flow	colloidal	< 2 μm
electro-acoustic	electrokinetic sonic amplitude	colloidal	< 10 - 50 μm
mechanical induced			
technique	measured effect	sample type	particle size
sedimentation	sedimentation potential	colloidal	< 6,3 μm
fluid flow	streaming potential	solid	< 1 mm
acousto-electric	colloidal vibration potential	colloidal	< 200 - 300 μm

Of these methods, only electro-acoustic methods [41] thereby cover approximately the grain size range (particle size range) of a natural sedimentary rock [42]. Accordingly, this seems favourable in terms of the fundamental understanding of the IP-effect occurring at the solid-liquid-interface. In electroacoustic methods, the zeta potential is determined in two ways [36]: via the so-called "electrokinetic sonic amplitude effect" (ESA) and via the measurement of the so-called "colloid vibration potential" (CVP). The instrument available for this study uses the ESA measurement to determine the EDL parameters. Hence, this method is briefly described in the following. Figure 3 schematically shows the setup of the instrument. While the suspension is in continuous circulation in the system, an alternating voltage is applied between two plate electrodes (Fig. 3, D), which are in direct contact with the suspension. As the suspension passes through the alternating electric field, the dispersed particles are deflected toward the plates. This produces a measurable ultrasonic wave as all particles move in phase with each other. The ESA wave is decoupled by a silicate glass window (Fig. 3, B) and its amplitude converted into a signal by a piezoelectric transducer.

The ESA signal depends on the particle velocity and thus consequently on the particle charge and particle size. Larger particles are inert compared to small particles, causing a time delay between the change in direction of the electric field and the direction of particle motion (i.e., a change in sign of the particle velocity). By measuring the magnitude and phase of the ESA signal, both the zeta potential and the particle size can be determined [42]. The main advantage of the ESA method is that significantly larger particle (grain) sizes can be included for systematic investigations of natural rocks. Whereas classical methods are strictly limited regarding this parameter, ESA is able to include grains as large as up to 200-300 μm in diameter (i.e., at least 100 times larger grains than electrophoresis).

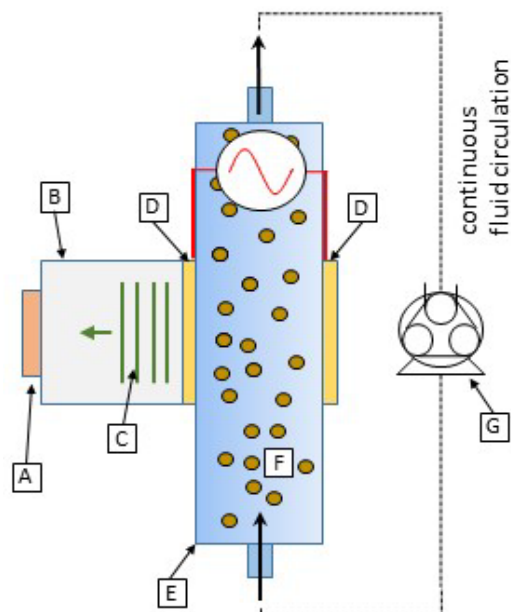


Fig. 3. Schematic illustration of the method used to measure the so-called electro-kinetic sound amplitude effect. (A) Piezoelectric transducer, (B) high-purity silicate glass, (C) ESA shaft, (D) plate electrodes, (E) measuring cell, (F) suspension, (G) peristaltic metering pump.

3 Sample preparation

At this point, it is obvious that a solid rock has to be turned back into an "unconsolidated material" if one wants to consider all relevant dependencies for EDL characterization (after completion of all further petrophysical, mineralogical, structural and topological investigations, of course). For the purpose of this new workflow, two different ways of doing this (the conventional, as well as the new approach) are presented in the following.

3.1 Conventional approach

The established standard procedure of sample crushing for (e.g.) geochemical analysis is to crush and grind up the material. However, not only are the mineral grains mechanically destroyed, but their surfaces in particular are transformed into an amorphous equivalent of themselves as the degree of grinding increases, i.e., as a result of greater pressure and rising temperature (Fig. 4). Chemically, the material does not change, but its surface and interfacial properties change, sometimes significantly, as a result, making it much more difficult to measure electrokinetic in-situ effects [34].

Furthermore, grinding destroys the original grain size distribution and creates a mono-modal grain size over time that does not exist in the original sample. Conclusively, mechanical crushing, milling and grinding of the material is (for obvious reasons) unsuitable to take the "in-situ" geometry and topology of the individual mineral grains of a clastic sedimentary rock during EDL characterization into account.

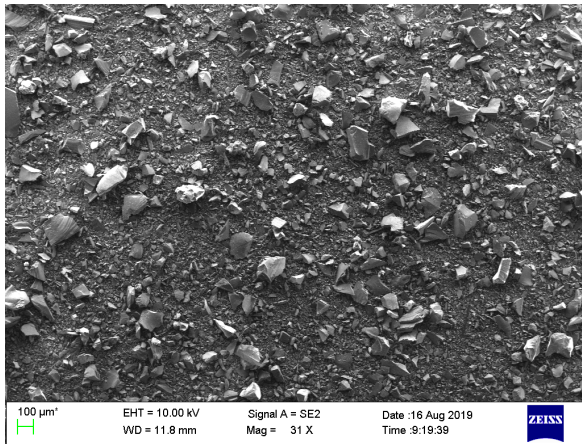


Fig. 4. SEM image showing the influence of conventional comminution (grinding) on the surface of quartz (originating from a Bentheimer sandstone). Clearly visible, sharp-edged fragments and mechanically destroyed surfaces that do not exist in the in-situ sample.

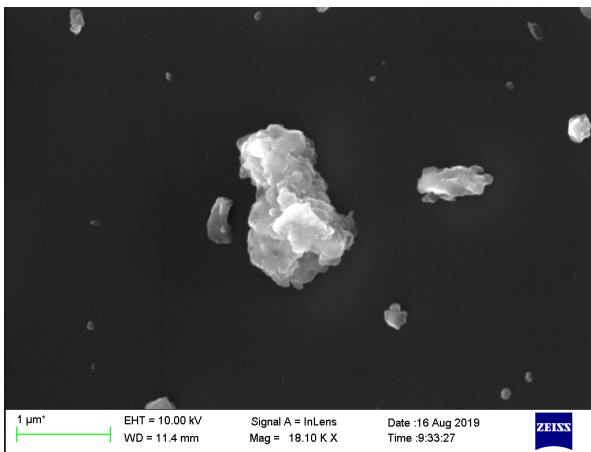


Fig. 5. SEM image showing that with increasing degree of comminution, the quartz surfaces are transformed by pressure and temperature into an amorphous equivalent (increasing "bubble formation" on the surface, grinding time 10 sec).

At this point, we would like to summarize the main issues, regarding the IP-related research of electrokinetic properties, shortly:

- For a deeper understanding of the IP-effect of silici-clastic rocks, unravelling the electrokinetics of the material is essential.
- For this purpose, we need to investigate the sample material as closely to its in-situ stage as possible. Both, solid, as well as fluid parameter, need to be taken into account.
- Classical methods for electrokinetic measurements allow systematic variations of the fluid properties, but are measured either in a volumetric state of the sample or have to be performed on a colloidal system (rock-fluid suspension). Accordingly, solid phase dependencies cannot be investigated, or are at least greatly falsified by amorphous phase transitions during the preparation process.

3.2 Advanced disaggregation technique

After extensive research, the so-called "electrodynamic disaggregation technique" was identified as a suitable method and is described amongst others in [43, 44]. This method allows the fragmentation of rocks, mineral agglomerates, mono-mineral crystals and glasses along grain boundaries or internal material discontinuities (e.g., fluid inclusions, structures caused by dissolution, etc.). In this process, an electrical discharge is directed towards a non- or low-conductive material (rock) while it is immersed in a dielectric fluid (e.g., water or oil). In general, the electrical resistance of a solid phase is greater than that of a liquid phase.

However, this physical behavior changes radically as soon as the applied electrical voltage becomes very large and is released in the form of short pulses. Under these conditions, the rock behaves as a "conductor" and the liquid as an "insulator," with the sample acting as a "discharge channel" between the cathode and anode of the fragmentation apparatus [43]. Thus, large amounts of energy are accumulated along the sample axis, generating pressures similar to those of an explosion or a low-energy plasma discharge (up to 10^{10} Pa, [45]). The resulting pressure wave refracts along grain boundaries or along grain surfaces, inducing tensile stresses that lead to disaggregation of the rock sample. Figure 6 shows a principle drawing as well as the originally used apparatus.

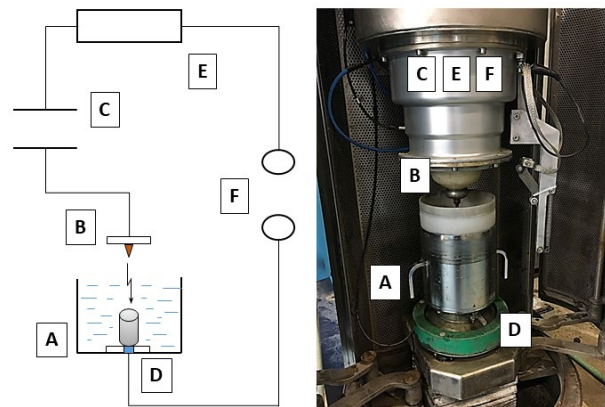


Fig.6. Schematic (left) and original (right) illustration of the setup and principle of the selfFrag apparatus used to fragment the sandstone samples. (A) Water-filled sample collector, (B) cathode, (C) plate capacitor, (D) anode and rock sample, (E) resistor, (F) toggle switch.

3.3 Approval of disaggregation results

The fragmentation grade and the degree of preservation of the mineral grains of sandstones fragmented by this advanced sample disaggregation technique, was the subject of a preliminary study. In total, 30 samples (cylindrical plugs with a diameter of 30 mm and a length of 40 mm) of three different sandstones (Bentheimer - BE, Obernkirchen - OK, and Flechtingen - FL), with widely differing structural and physical properties, were fragmented in the processing laboratory of the leading company for this technique (selfFrag).

The optimal, i.e., device and sample-specific fragmentation parameters, individually for each sandstone type, were systematically determined (Table 3). Following this work, the now processed and unconsolidated material was dried and further evaluated. Using scanning electron microscopy (SEM) and laser diffraction, the overall quality, degree of preservation and grain size distributions for each sample are assessed.

Table 3. Summary of optimal, unit-specific fragmentation parameters for each fragmented sandstone type.

rock	general sample characteristics	gap [mm]*	f [Hz]	U [kV]	pulses
BE	↓ clay; ↓↓ Fe; ↓↓ cement; ↑↑ Φ; ↑↑ k	40	5	150	10
OK	↓ clay; ↓↓ Fe; ↑ cement; ↑ Φ; ↓ k	40	5	150	30
FL	↑↑ clay; ↑ Fe; ↑↑ cement; ↓ Φ; ↓↓ k	35	5	150	40

*gap = distance cathode-sample;

↓ ↓ = very minor/low; ↓ = minor/low; ↑ = medium; ↑ ↑ = high.

Figure 7 shows an example of a Bentheim sandstone sample with a scanning electron micrograph before (Fig. 7, A) and after (Fig. 7, B) the fragmentation process. The significantly better degree of preservation of the individual mineral grains compared to grinding (see Fig. 4 & 5) is clearly noticeable. These are completely preserved in size and shape (Fig. 7B), as can be seen in direct comparison with the initial state (Fig. 7A). A temperature and pressure induced amorphous transformation of the grain surfaces is also not recognizable. Afterwards, the fragmented material was examined by laser diffraction with respect to its grain size distribution.

The result is shown in Figure 8. It can be clearly seen that the Bentheimer sandstone has a good sorting, i.e., a relatively narrow distribution of grain sizes. This distribution is dominated by grain sizes in the range 100 – 350 μm in diameter (about 90 % of all grains), which essentially reflects the matrix-forming mineral particles (primarily quartz and little feldspar). Grains smaller than 63 μm account for roughly 2 mass-% of all grain fractions of this sample, which is about 45 times less than the dominant size fraction.

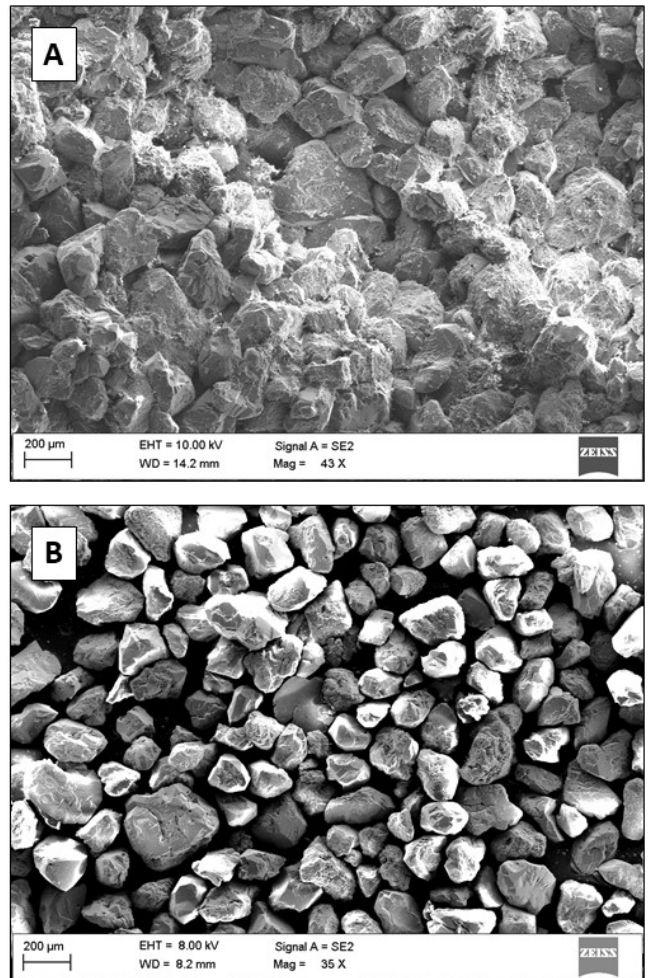


Fig. 7. Scanning electron image of a Bentheimer sandstone, before (A) and after (B) fragmentation using the selfFrag apparatus. The excellent degree of preservation of the mineral grains is clearly visible (please note: minor components < 63 μm such as clay minerals and cement have been separated for the SEM analysis).

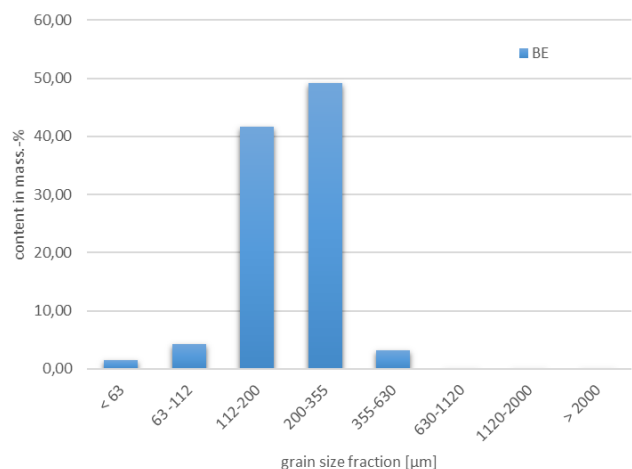


Fig. 8. Grain size distribution of the disaggregated Bentheimer sandstone sample (avg. of 10 samples).

4 Results

4.1 Petrophysics and SIP results

In advance to the disaggregation of the specimen, standard core analysis, as well as SIP-measurements have been conducted in order to characterize the different sandstones in terms of their basic petrophysical characteristics. Core analysis (here: grain density, porosity, permeability) followed protocols as referenced in [API RP40] and results are compiled in table 4. Results are presented for three different sandstones, originating from northern Germany: Bentheimer (BE), Obernkirchen (OK) and Flechtingen (FL) sandstone. As shown, the BE samples are characterized by an average porosity of 21 %, an average grain density of 2.65 g/cm³, and an average permeability of 575 mD, overall a “typical” cretaceous reservoir rock. The OK samples feature lower porosity (avg. 16.6 %) and permeability (avg. 19 mD), and slightly increased grain density due to the occurrence of carbonate cement within. FL samples feature lowest porosity (avg. 10.9 %) and permeability (avg. 6.2 mD), but also the highest average grain density due to the existence of Fe-oxides and a mixture of barite and carbonate cement within.

Table 4. Basic petrophysical properties of the investigated sandstones.

rock	porosity [%]			permeability [mD]		
	min	max	avg.	min.	max.	avg.
BE	20.2	22.2	21	529	653	575
OK	15.5	17.2	16.6	9	28	19
FL	6.5	16.6	10.9	0.3	32	6.2

For the SIP-measurements, samples have been saturated with a sodium-chloride solution, equivalent to an electrical conductivity of 100 mS/m (approx. 8 mmol/l NaCl). Measurements have been performed with a SIP-Quad device from Radic Research (Berlin, Germany) within a frequency range of 2 mHz to 10 kHz. For the SIP, averaged results of the quadrature conductivity (which is directly considered as a measure for the “IP-effect”, compare section 1) over the investigated frequency range are presented for each rock type (Figure 9).

Each curve represents the averaged signal of ten individual SIP-measurements. Though all three sandstone types show local maxima of quadrature conductivity at frequencies between 0.01 and 1 Hz, differences are clearly visible. The BE samples feature the smallest amplitude maximum (barely 0.06 mS/m), almost doubled by the OK samples (0.12 mS/m), whereas the FL sandstone indicates the highest amplitude maximum (almost 0.28 mS/m). Both, BE and OK samples indicate their maximum at more or less the same frequency (~ 0.25 – 0.3 Hz). For FL, the maximum conductivity values are located one order of magnitude in frequency below BE and OK (~ 0.03 Hz).

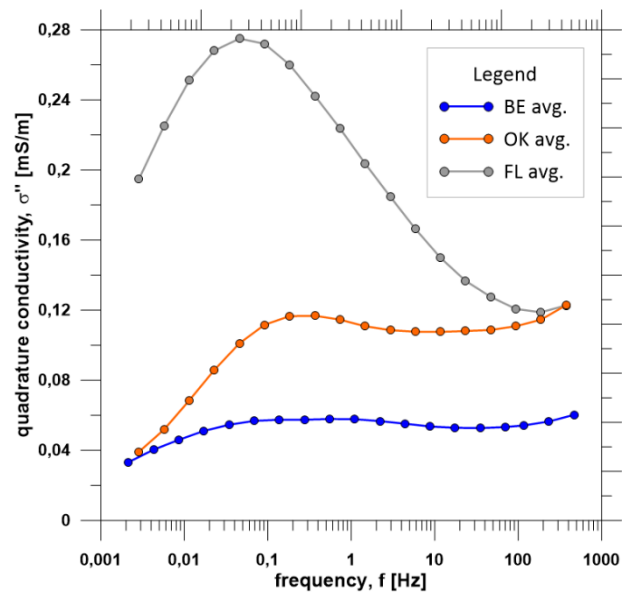


Fig. 9. Averaged results of the quadrature conductivity of the three investigated sandstones derived from SIP-measurements (top to bottom: Flechtingen - FL, Obernkirchen - OK, Bentheimer - BE).

4.2 Disaggregation results

Besides the already presented results for the Bentheimer sandstone (Fig. 7 & 8), SEM images and according grain size distributions for the OK and FL sandstones are presented.

Figure 10 shows a representative SEM image for the OK samples, showing a very good degree of preservation in terms of grain size and shape. The average grain sizes are smaller than for the BE samples. Nevertheless, some grains are still clearly cemented (Fig. 10, top right hand side), leading to larger, i.e., apparent grain sizes (Fig. 10, bottom) of 600 μm to > 2 mm. About 12 – 14 mass-% of the investigated sample material is affected. OK samples feature slight amount of carbonate cement, whereas BE samples are not cemented at all. This cement prevents a fragmentation of the OK samples as good as for the BE specimen. These grains have been sieved and removed for the ESA experiments. They are utilized for further investigation and optimization of the fragmentation process, respectively. Furthermore, OK sandstone features more grains < 63 μm than the BE type. This is in good accordance to the known mineralogy of both rocks, since the OK type features a higher content of clay minerals than the BE sandstone.

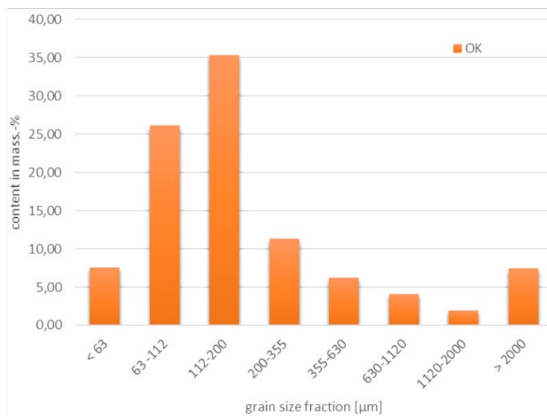
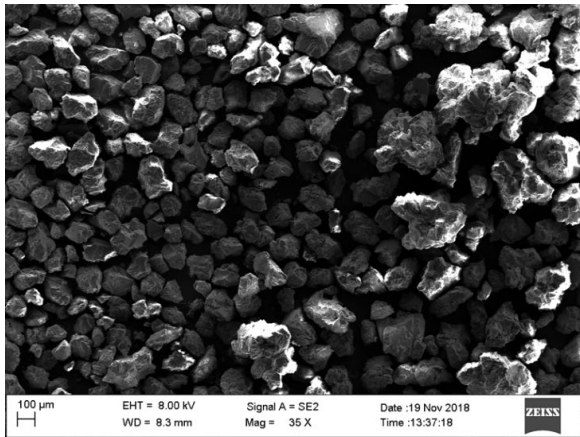


Fig. 10. Scanning electron image of the Obernkirchen sandstone (please note: minor components < 63 µm such as clay minerals and cement have been separated for the SEM analysis) after fragmentation using the selFrag apparatus (top), and the according grain size distribution (bottom, avg. of 10 samples).

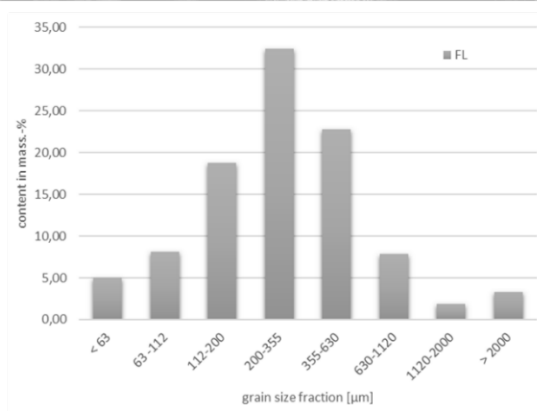
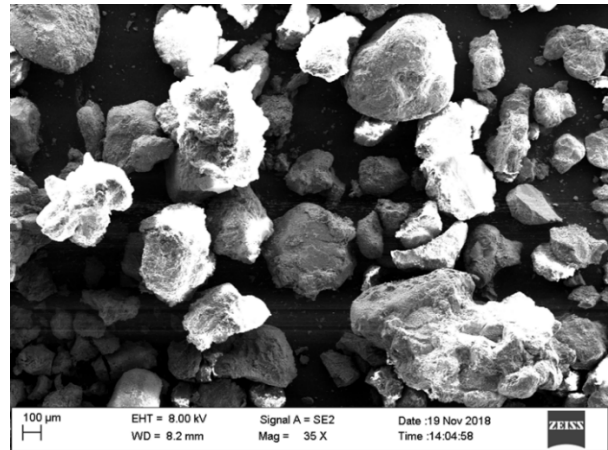


Fig. 11. Scanning electron image of the Flechtingen sandstone (please note: minor components < 63 µm such as clay minerals and cement have been separated for the SEM analysis) after fragmentation using the selFrag apparatus (top), and the according grain size distribution (bottom, avg. of 10 samples).

Figure 11 shows the results from disaggregation and grain size analysis for the FL samples. Again, a very good degree of grain preservation is observed. The average grain size is higher than for OK, but in range with the BE sandstone. Nevertheless, the overall width of the distribution is significantly larger than for the BE type. Again, still cemented grains exist (sizes > 600 µm), caused by insufficient fragmentation, as for the OK samples. The slight, left-skewed distribution may indicate a slightly better fragmentation of the barite cement within the FL specimen compared to the carbonate cement of the OK samples. As before, these grains have been sieved and removed for the ESA experiments.

Furthermore, FL sandstone features more grains < 63 µm than the BE type, but little less than OK. It is known from extensive mineralogical investigations on the FL samples that they do feature a distinct amount of clay minerals within (smectite), which is distributed as “coating” upon the larger quartz grains. This coating has been partially broken during the fragmentation, accumulating in this grain size region. Additionally, FL specimens contain hematite (up to 5 vol.-%) with typical sizes in range of 20 – 35 microns. Accordingly, grains < 63µm are a mixture of broken smectite and hematite for the FL sandstone.

4.3 Zeta potential results

The zeta potential measurements have been conducted on suspensions, consisting of 5 mass-% of the fragmented sample material and 95 mass-% of sodium chloride solution, acting as carrier medium. For each sample, two different grain size fractions have been prepared: 2µm and 63-100µm. Additionally, a pure quartz crystal was milled and separated into a 2µm and 2-20µm grain size cluster, to highlight the influence of the sample preparation upon measured results. Figure 12 highlights the results for these experiments.

As it can be seen, zeta potential values for the 63-100µm fraction for both BE and OK samples is more or less in the same range, averaging to -2.75 mV. This size fraction is dominated by idiomorphic quartz and minor content of feldspar, which both form the main components of the rock matrix. In contrast, the according FL fraction clusters at lower zeta potential values, averaging to -23 mV. Though the matrix also mainly consists of quartz, grains are distinctively coated with smectite, causing this effect. For the smallest size fraction (2µm), BE zeta potential averages to -10 mV, OK to -15 mV, still close to each other, but visually separated from each other.

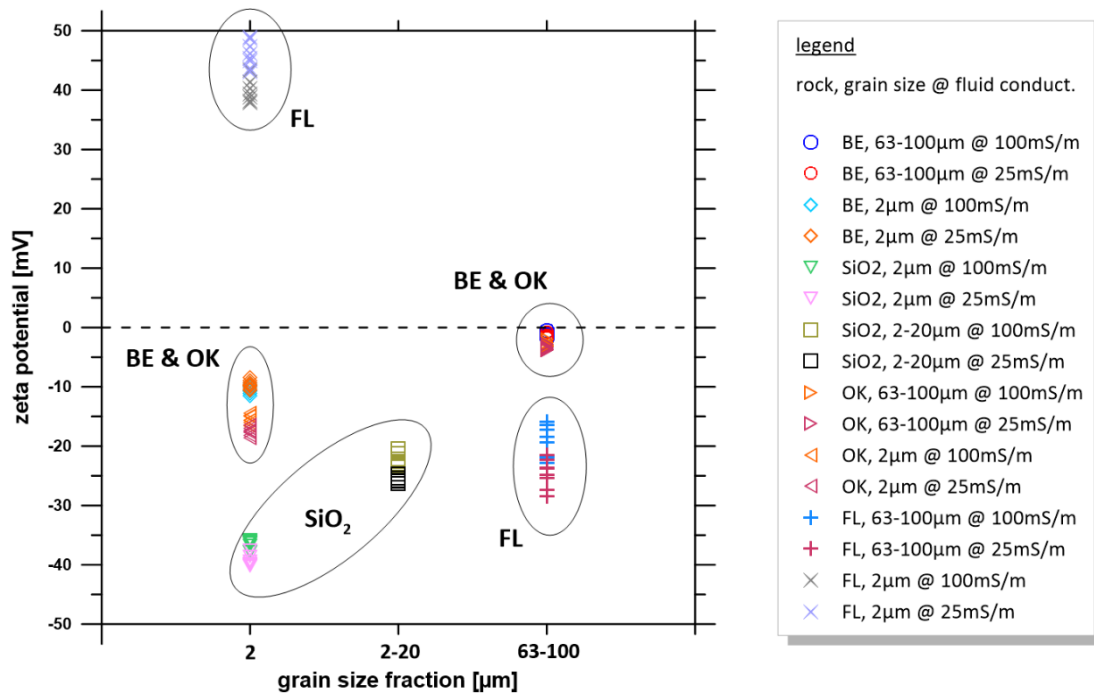


Fig. 12. Zeta potential versus selected grain size fractions for the three fragmented sandstones and a conventionally milled SiO₂ crystal.

In this grain size fraction, almost no quartz exist. Instead, this fraction is dominated by small clay mineral particles (mostly kaolinite and little illite), featuring a significantly larger surface area and electrokinetic potential. The separation indicates the difference in the clay types in between both samples: BE solely features kaolinite whereas OK inhibits a mixture of kaolinite and illite. For FL however, zeta potential values have turned into positive values for the 2µm grain size fraction, averaging to +43 mV. From mineralogical investigations, we know that parts of the smectite coating, originating from the large quartz grains, disaggregated into smaller pieces during fragmentation. However, smectite would lead to even larger negative zeta potentials than kaolinite and illite. According to our analysis, this result is caused by hematite, which originally exist as a fine dispersed phase within the Flechtingen sandstone. As Fe-oxide, hematite inhibits a very large and positive electro-kinetic potential, causing the observed effect.

The crushed and grinded SiO₂ indicates a significant increase of the zeta potential with decreasing grain sizes. As described in section 3.1, grinding and milling leads towards an amorphous phase transition of the SiO₂. Though the surface area increases compared to an idiomorphic crystal, this increase would not be sufficient to accumulate such a large electrokinetic potential. In fact, the “steepness” of the zeta potential increase for idiomorphic quartz is significantly smaller. However, the amorphous surface is able to “bind” more ions compared to the idiomorphic surface. This effect is described as an “apparent zeta potential” [46]. Here, it averages between -25 mV (for the 2-20 µm size fraction) and -37.5 mV (for the 2 µm fraction). These values are close to pure kaolinite and illite [33, 46, 47] and might lead to falsified

interpretations in terms of pore scale interface processes and mineralogical composition.

4.4 Joint interpretation: ESA and SIP data

The results of the ESA measurements are in very good accordance compared to the SIP data. The BE samples feature less amount of clay minerals and cementation, hence the SIP signal amplitude is less pronounced than for the other sandstones. This context is also clearly visible within the zeta potential data. For large and (more or less) pure, idiomorphic quartz grains of the rock matrix, zeta potential values are small or even close to zero. The OK samples clearly indicate the exact same behaviour for the 63-100µm size fraction. Since the OK sandstone features slightly more clay minerals (both, mineral type and volume content), zeta potential values are more pronounced than for the BE specimens. This is in very good accordance to the literature from which is known that kaolinite features the lowest zeta potentials, followed by illite and smectites. The almost doubled SIP signal maximum of OK compared to BE can be directly related to this change in clay volume and mineralogy.

The FL samples feature the highest SIP signal amplitude, as a direct result of the highly polarizable hematite grains, possibly acting as small capacitors upon the surface of the rock matrix. The existence of smectite coatings upon the grain matrix is clearly verified by the distinctively higher (= more negative) zeta potential values for the 63-100µm fraction. Accordingly, the increased polarizability of smectite amplifies the effect of the hematite upon the main surfaces. As a matter of fact we can assume that two polarization mechanisms exist for this type of sandstone: an electronically conductance mechanism for the Fe-oxides and a classical ohmic surface conductance mechanism for the smectites.

5 Conclusions

The presented innovative techniques for highly controlled rock sample fragmentation (the so-called electrodynamic disaggregation technique) and zeta potential measurements are key for the advanced understanding of processes and for fundamental research at the solid-liquid interface of natural (reservoir) rocks. It is possible to link mineralogy, core and special core analysis (SIP), and electrokinetic properties directly, enhancing joint data interpretation and mechanistic model assumptions derived on larger scales. The appraisal and assessment of characteristic length scales (grain sizes) for these mechanisms has now become possible for the first time in SIP-related research. Nevertheless, two drawbacks exist: first, heavily cemented parts of the rock might not fragment as good as less cemented volumes, and might falsify the interpretation of grain size fractions (if not removed in advance). Second, non-clastic materials, i.e., biogenic carbonates, or any other rock without any distinct grain edges within, are most likely not able to be processed by this workflow. For this, carbonates and very fine-grained rock types (clay- and mudstones) are part of the ongoing research.

Acknowledgements

The authors would like to thank Daniel Parvaz from selfFrag (Kerzers, Switzerland) for the support and fruitful discussions about the disaggregation technique. In addition, we would like to thank Prof. Dr. Helge Stanjek (RWTH Aachen, Germany) for his knowledge and time for discussing the ESA results, as well as Prof. Dr. Andreas Weller (TU Clausthal, Germany) for discussing the IP-effect theory.

References

- W.K. Sawyer, C.I. Pierce, and R.B. Lowe, *Petrophysics*, **42**, 71-82 (2001).
- D.P. Lesmes, and S.P. Friedman, in: Y. Rubin, and S.S. Hubbard, *Hydrogeophysics*, Springer Publishing (2005).
- J.B.T. Scott, and R.D. Barker, *Quarterly Journal of Engineering Geology & Hydrogeology*, **38**, 143-154 (2005).
- A. Hördt, R. Blaschek, A. Kemna, and N. Zisser, *Journal of Applied Geophysics*, **62**, 33-46 (2007).
- A. Weller, and L. Slater, *Geophysics*, **77** (5), 185-198 (2012), <https://doi:10.1190/geo2012-0030.1>.
- Z. Zhang, and A. Weller, *Geophysics*, **79** (6), 377-387 (2014), <https://doi:10.1190/geo2014-0143.1>.
- A. Weller, L. Slater, S. Nordsiek, and D. Ntarlagiannis, *Geophysics*, **75** (4), 105-112 (2010), <https://doi:10.1190/1.3471577>.
- A. Weller, L. Slater, and S. Nordsiek, *Geophysics*, **78**, 315-325 (2013), <https://doi:10.1190/geo2013-0076.1>.
- C. Weber, M. Halisch, and H. Stanjek, *Clays and Clay Minerals*, **66** (1), 86-95 (2018).
- K. Titov, V. Tarasov, and A. Levitski, *Journal of Applied Geophysics*, **50**, 417-433 (2002).
- L. Slater, and D.R. Glaser, *Geophysics*, **68**, 1547-1558 (2003).
- A. Revil, and N. Florsch, *Geophysical Journal International*, **181**, 1480-1498 (2010), <https://doi:10.1111/j.1365-246X.2010.04573.x>.
- K. Koch, A. Revil, and K. Hollinger, *Geophysical Journal International*, **190**, 230-242 (2012), <https://doi:10.1111/j.1365-246X.2012.05510.x>.
- J.B.T. Scott, and R.D. Barker, *Geophysical Research Letters*, **30**, 1450 ff. (2003).
- S. Kruschwitz, A. Binley, D. Lesmes, and A. Elshenawy, *Geophysics*, **75**, 113-123 (2010), <https://doi:10.1190/1.3479835>.
- K. Titov, A. Tarasov, Y. Ilyin, N. Seleznev, and A. Boyd, *Geophysical Journal International*, **180**, 1095-1106 (2010), <https://doi:10.1111/j.1365-246X.2009.04465.x>.
- Q. Niu, and A. Revil, *Geophysics*, **81**, 17-32 (2016), <https://doi:10.1190/GEO2015-0072.1>.
- H. Militzer, and F. Weber, *Angewandte Geophysik*, Bd.2, Springer Publishing (1985).
- J. Schön, *Petrophysik*, Ferdinand Enke Publishing (1983).
- G.E. Archie, *Transactions of the American Institute of Metallurgists and Petroleum Engineers*, **146**, 54-62 (1942), <https://doi:10.2118/942054-G>.
- J.R. Schopper, in: G. Angenheister, Landolt-Börnstein, Bd.1b/V, Springer Publishing (1982).
- J. Kuhlenskampff, and J.R. Schopper, in: SPWLA Transactions, Eleventh European Formation Evaluation Symposium (1988).
- D.J. Marshall, and T.R. Madden, *Geophysics*, **24**, 790-816 (1959).
- A. Blaschek, and A. Hördt, *Near Surface Geophysics*, **55**, 579-588 (2009).
- M. Bückner, and A. Hördt, *Geophysics*, **78**, 229-314 (2013a), <https://doi:10.1190/geo2012-9548.1>.
- M. Bückner, and A. Hördt, *Geophysical Journal International*, **194**, 804-813 (2013b), <https://doi:10.1193/gji/ggt136>.
- H. Stebner, M. Halisch, and A. Hördt, *Near Surface Geophysics*, **15**, 563-578 (2017), <https://doi:10.3997/1873-0604.2017054>.
- A. Hördt, K. Bairlein, M. Bückner, and H. Stebner, *Near Surface Geophysics*, **15**, 579-592 (2017), <https://doi:10.3997/1873-0604.2017053>.
- D.P. Leroy, A. Revil, A. Kemna, P. Coszena, and A. Ghorbani, *Journal of Colloid and Interface Science*, **321**, 103-117 (2008), <https://doi:10.1016/j.jcis.2007.12.031>.
- A. Revil, and M. Skold, *Geophysical Journal International*, **187**, 813-824 (2011), <https://doi:10.1111/j.1365-246X.2011.05181.x>.
- A. Revil, *Water Resources Research*, **48**, W02517 (2012), <https://doi:10.101029/2011WR011260>.
- J. Lyklema, and M. Minor, *Colloids and Surfaces A: Physicochemical and Engineering Aspects*, **140**, 33-41 (1998).
- K. Jasmund, and G. Lagaly, *Tonminerale und Tone – Struktur, Eigenschaften, Anwendung und Einsatz in Industrie und Umwelt*. Steinkopff Publishing (1993).
- J. Lyklema, *Fundamentals of Interface and Colloid Science*, Vol. II – Solid-Liquid Interfaces. Academic Press (2011).
- R.J. Hunter, *Zeta Potential in Colloid Science - Principles and Applications*. Academic Press (1981).
- Th. Luxbacher, *The Zeta Potential for Solid Phases Analysis*. 1. Edition, A48IP010EN-A (2014).
- B.J. Kirby, *Micro- and Nanoscale Fluid Mechanics: Transport in Microfluidic Devices*. Cambridge University Press (2010).
- S.S. Dukhin, and B.V. Derjaguin, in: *Surface and Colloid Science*, **7** (7), Wiley Publishing (1974).
- S.Y. Kang, and A.S. Sangani, *Journal of Colloid and Interface Science*, **165**, 195-211 (1994), <https://doi.org/10.1006/jcis.1994.1220>.
- A.V. Delgado, F. Gonzalez-Caballero, R.J. Hunter, L.K. Koopal, and J. Lyklema, *Journal of Colloid and Interface Science*, **209**, 194-224 (2007).

41. F. Hinze, S. Ripperger, and M. Stintz, *Chemie Ingenieur Technik*, **72**, 322-332, Wiley Publishing (2000).
42. R.W. O'Brian, A. Jones, and W.N. Rowlands, *Colloids and Surfaces A: Physicochemical and Engineering Aspects*, **218** (1-3), 89-111 (2003), [https://doi.org/10.1016/S0927-7757\(02\)00593-9](https://doi.org/10.1016/S0927-7757(02)00593-9).
43. U. Andres, J. Jirestig, and I. Timoshkin, *Powder Technology*, **104**, 37-49 (1999)
44. E. Gnos, D. Kurz, I. Leya, and U. Eggenberger, *Proceedings, Goldschmidt Conference* (2007).
45. N.S. Rudashevsky, B.E. Burakov, S.D. Lupal, O.A.R. Thalhammer, and B. Saini-Eidukat, *Trans. Inst. Mining Metal*, **104**, C25-C29 (1995).
46. H.C. Li, and P.L. De Bruyn, *Surface Science*, **5**, 203-220 (1966).
47. C.H. Hamann, and W. Vielstich, in : *Elektrochemie II – Elektrodenprozesse*, *Angewandte Elektrochemie*. Verlag Chemie (1981).

Analytical Models for Predicting the Formation Resistivity Factor and Resistivity Index at Overburden Conditions

Meysam Nourani*, Stefano Pruno, Mohammad Ghasemi, Muhamet Meti Fazlija, Byron Gonzalez and Hans-Erik Rodvelt

Stratum Reservoir AS, Stavanger, Norway

Abstract. In this study, new parameters referred to as rock resistivity modulus (RRM) and true resistivity modulus (TRM) were defined. Analytical models were developed based on RRM, TRM and Archie's equation for predicting Formation Resistivity Factor (FRF) and Resistivity Index (RI) under overburden pressure conditions. The results indicated that overburden FRF is dependent on FRF at initial pressure (ambient FRF), RRM and net confining pressure difference. RRM decreases with cementation factor and rock compressibility. The proposed FRF model was validated using 374 actual core data of 79 plug samples (31 sandstone and 48 carbonate plug samples) from three sandstone reservoirs and four carbonate reservoirs, measured under 4-6 different overburden pressures. The developed FRF model fitted the experimental data with average relative error of 2% and 3% for sandstone and carbonate samples respectively. Moreover, the applications and limitations of the models have been investigated and discussed. Further theoretical analysis showed that overburden RI is a function of RI at initial pressure, TRM and net confining pressure difference. The developed models supplement resistivity measurements and can be applied to estimate FRF, RI and saturation exponent (n) variations with overburden pressure.

Introduction

Archie's Formation Resistivity Factor (FRF) is one of the most essential petrophysical properties for log calibration and reservoir characterisation. The FRF is a dimensionless parameter defined as the ratio of the resistivity of rock fully saturated with brine (R_o [Ωm]) to the formation water resistivity (R_w [Ωm]). FRF is related to the porosity (ϕ [fraction]) by the Archie equation as follows:

$$FRF = \frac{R_o}{R_w} = \phi^{-m} \quad (1)$$

where m is the cementation factor which is also referred to as porosity exponent or cementation exponent.

The porosity of rock is the ratio between the pore space volume (V_p) to the bulk volume (V_b) of the rock and is expressed as a fraction. Considering electrical properties of rocks, the Resistivity Index (RI) is the second essential dimensionless parameter. RI is calculated as the ratio of the resistivity of rock when partially saturated with water (R_t [Ωm]) to the R_o . It is linked to the water saturation (S_w [fraction]), as follows:

$$RI = \frac{R_t}{R_o} = S_w^{-n} \quad (2)$$

where n is the saturation exponent [1]. Combining Equations (1) and (2) yields the following equation which is referred to as saturation equation:

$$S_w = \left(\frac{R_w}{\phi^m R_t} \right)^{\frac{1}{n}} \quad (3)$$

These empirical equations were derived for clean, clay-free, strongly water-wet sandstones with simple and unimodal pore geometry. Further assumptions are that the rock grains are non-conductive, and all the water contributes to electrical current flow [2–4]. The estimation of the volume of hydrocarbon initially in place at reservoir conditions ($HCIP$ [m^3]) is vital information for reservoir management and is determined by the water saturation, the porosity, and the volume of the reservoir (V [m^3]), as follows [5,6]:

$$HCIP = V\phi(1 - S_w) \quad (4)$$

The accuracy of predicting the volume of the reservoir is high for mature fields which have been produced through numerous wells for many years. In addition, reservoir porosity can be obtained by using logging tools, such as sonic and neutron devices. Calibrating logging data to core analysis results can provide more accurate data sets and increase confidence in estimated reservoir porosity values.

Various methodologies for obtaining R_w have been reported in literature, such as direct measurement in a resistivity cell, chemical analysis of produced water samples, use of spontaneous potential (SP) curves, water catalogues and numerous other empirical methods [7–10]. Moreover, R_t can be achieved from the electrical resistivity logs. Therefore, by determining Archie's exponents (m and n) through conducting laboratory measurements, the in-situ water saturation can be calculated using Equation (3). These empirical parameters must be obtained at representative pressure and temperature conditions. Hence, they are quantified based on the results of special core analysis (SCAL). Laboratory FRF SCAL tests are performed in such a way as to be as representative as possible of the reservoir

* Corresponding author: meysam.nourani@stratumreservoir.com

conditions, but typically they are performed at lower temperature and overburden pressure conditions. This is due to time constraints, the complexity of the measurements and higher expense. It is also common to perform FRF tests at a single overburden pressure due to limited SCAL program budget [11]. Thus, testing conditions are usually dissimilar to the actual conditions in the reservoir.

Overburden pressure is defined as the vertical stress or hydrostatic pressure exerted by all overlying layers of material (rock, salt, water) on a reference point or layer. The formation compresses once the overburden pressure increases beyond the limit of the fluid pressure in the pore space [12]. As a result of compression, the tortuosity of flow paths varies and the pore sizes and accordingly porosity, decreases. As porosity decreases, in accordance with Archie's law, FRF increases [13–16]. Many researchers have investigated the effect of confining pressure on the FRF of numerous rock samples. It has been reported convincingly that FRF increases with increasing confining stress and overburden pressure [13–24]. The effect of overburden pressure on FRF is dissimilar for different rocks depending on the pore size distribution, clay content, porosity, and permeability [8].

Since determination of cementation and saturation exponents is among the most uncertain parameters required for estimating *HCIIP* in Equation (4), without considering the effect of overburden pressure, the predicted saturation from resistivity logs can be a basis of uncertainties and subsequently leads to inaccurate estimations of hydrocarbon volumes initially in place.

To model the effect of overburden pressure in sandstone and carbonate cores a novel, theoretical investigation supported by experimental results is introduced. The objectives of this analytical-experimental research are to explore the relationship between FRF, RI and overburden pressure and to develop mathematical models for predicting FRF under different overburden pressures. The models are validated using actual core sample resistivity data at ambient temperature and different net confining pressure conditions from sandstone and carbonate reservoirs.

Development of the FRF Models

Rock resistivity modulus (RRM) is defined as the change in R_o per unit of R_o per change in pressure. Thus, RRM is a measure of the relative change in the rock resistivity of rock fully saturated with brine in response to a pressure change as follows:

$$\gamma_{R_o} = -\frac{1}{R_o} \frac{\partial R_o}{\partial P} \quad (5)$$

In addition, the water resistivity modulus (WRM) and the true resistivity modulus (TRM) can be defined by analogy to RRM as follows:

$$\gamma_{R_w} = -\frac{1}{R_w} \frac{\partial R_w}{\partial P} \quad (6)$$

$$\gamma_{R_t} = -\frac{1}{R_t} \frac{\partial R_t}{\partial P} \quad (7)$$

By separating the R_o in Equation (5) and integrating while assuming a constant RRM over the pressure interval of interest, the R_o at a given overburden pressure can be calculated as follows:

$$R_{o_2} = R_{o_1} e^{-\gamma_{R_o} \Delta P} \quad (8)$$

where R_{o_1} and ΔP are rock resistivity at initial pressure and net confining pressure difference respectively. Combining Equations (1) and (5), yields the following equation:

$$\gamma_{R_o} = -\frac{\varphi^m}{R_w} \frac{\partial (\frac{R_w}{\varphi^m})}{\partial P} \quad (9)$$

It has been shown that the variations in cementation and saturation exponents with overburden pressure are not significant [11,24,25]. The maximum change in the cementation and saturation exponents with overburden pressure for water-wet cores have been reported at around 2% and 8% respectively [24]. Hence, for the sake of simplicity in deriving the mathematical models, it was supposed that m and n coefficients do not vary with overburden pressure. Accordingly, by assuming a constant cementation exponent over the pressure interval of interest, taking the derivative of the term $(\frac{R_w}{\varphi^m})$ with respect to pressure in Equation (9) and rearranging it, the RRM can be calculated using the following formula:

$$\gamma_{R_o} = -\frac{1}{R_w} \frac{\partial R_w}{\partial P} + m \frac{1}{\varphi} \frac{\partial \varphi}{\partial P} \quad (10)$$

The variations in porosity of a porous rock due to changes in overburden pressure are related to the pore volume compressibility (C_p) and bulk compressibility (C_b) which are expressed in Equations (11) and (12) [26]:

$$C_p = -\frac{1}{V_p} \frac{\partial V_p}{\partial P} \quad (11)$$

$$C_b = -\frac{1}{V_b} \frac{\partial V_b}{\partial P} \quad (12)$$

Taking the derivative of the porosity with respect to pressure and replacing C_p and C_b from Equations (11) and (12) into it, yields the following equation:

$$\frac{\partial \varphi}{\partial P} = \varphi (C_b - C_p) \quad (13)$$

By combining Equations (6), (10) and (13), the following equation can be obtained:

$$\gamma_{R_o} = \gamma_{R_w} + m (C_b - C_p) \quad (14)$$

The water resistivity is independent of pressure, for pressure and temperature conditions below 58,000 psi (4,000 bar) and 170 °C. [27]. This pressure is much greater than those normally encountered in hydrocarbon reservoirs. Consequently, the water resistivity and WRM over the pressure interval of interest are assumed constant and zero respectively. By dividing both sides of Equation (8) by the water resistivity, the overburden FRF can be calculated as:

$$FRF_2 = FRF_1 e^{-\gamma_{R_o} \Delta P} \quad (15)$$

In addition, by disregarding WRM in Equation (14), a simplified formula for estimating the RRM is obtained:

$$\gamma_{R_o} = m (C_b - C_p) \quad (16)$$

By replacing the RRM in Equation (15), the FRF at a given overburden pressure can be calculated as follows:

$$FRF_2 = FRF_1 e^{m(C_p - C_b)\Delta P} \quad (17)$$

Thus, FRF can be predicted by two models. Measuring FRF under several overburden pressures is an essential requirement for applying the first model which is referred to as the Multi-FRF model. In the Multi-FRF model, Equation (15) is used to fit overburden FRF data. A plot of the ratio $\frac{FRF_2}{FRF_1}$ versus the net confining pressure difference on a semi-logarithmic scale passing through $\Delta P = 0$, when $FRF_2 = FRF_1$, gives a straight line of slope $-\gamma_{R_o}$, as:

$$\gamma_{R_o} = - \frac{\ln \frac{FRF_2}{FRF_1}}{\Delta P} \quad (18)$$

The obtained RRM can be used to predict FRF at any overburden pressure using Equation (15). When FRF is measured only at initial pressure, the second model which is referred to as the Single-FRF model can be used to estimate overburden FRF through Equation (17). It should be noted that the FRF models have been derived based on Archie's equation, thus Archie's assumptions apply to them. Accordingly, the developed FRF models are applicable only if Archie's equation is valid.

Validating the FRF Models

Two overburden FRF datasets comprising samples from three sandstone and four carbonate reservoirs were used to apply and validate the developed models. The first dataset includes 55 plug samples from five different North Sea reservoirs. The range of porosity, permeability and grain density of the samples have been investigated and listed in Table 1. Bulk mineral composition of the samples was measured by X-ray diffraction (XRD). The average tectosilicates, carbonate and phyllosilicate content of the samples are presented in Table 2.

Table 1. Overview of the range of porosity, water permeability (K_w), grain density of the samples.

Reservoir	Porosity (%)		Kw (mD)		Grain density (g/cc)	
	Min.	Max.	Min.	Max.	Min.	Max.
1	17.1	43.4	0.012	6.51	2.68	2.71
2	25.5	39.8	0.012	2.86	2.65	2.71
3	18.0	27.3	0.503	571	2.64	2.77
4	16.4	35.9	0.338	980	2.62	2.69
5	31.4	40.4	592	3890	2.65	2.79

Table 2. Overview of the average bulk mineral composition.

Reservoir	Tectosilicates (wt%)	Carbonates (wt%)	Phyllosilicates (wt%)
1	1	99	0
2	20	77	1
3	73	16	5
4	78	2	17
5	73	13	5

Equations (15) and (17) were fitted to the measured FRF data, and Figures 1 and 2 show examples of the best regression line and least square method statistical parameters. After applying the proposed models to the dataset, an excellent agreement has been observed ($R^2=0.9992$) between both the Multi-FRF and Single-FRF models and the measured data (Figure 1).

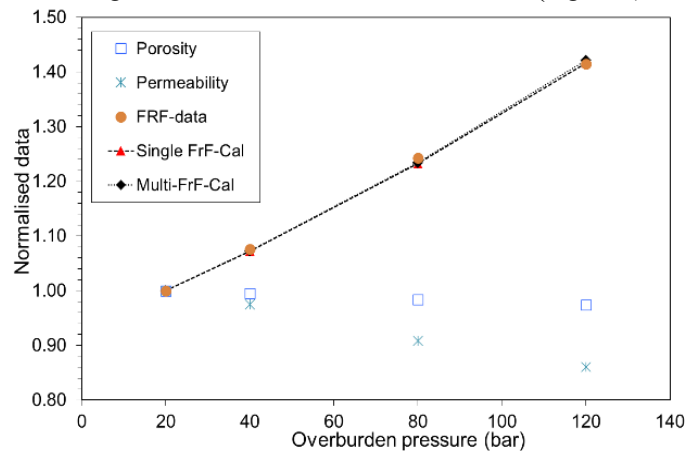


Fig. 1. Example 1, fitting of Equations (15) and (17) to FRF data; relation between the overburden pressure and normalized porosity, permeability and FRF.

Figure 2 shows a very good correlation with the Multi-FRF model ($R^2=0.9973$), whereas uncertainty in compressibility data causes the Single-FRF model to overestimate the FRF values at overburden pressures above the initial pressure. Although, the Single-FRF model has clearly deviated from the measured data, the maximum relative error between the measured and predicted FRF at 120 bar is only 12.6% as shown in Figure 2.

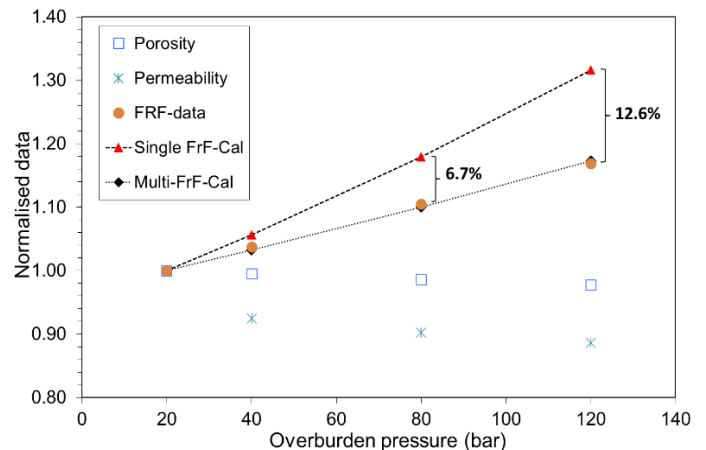


Fig. 2. Example 2, fitting of Equations (15) and (17) to FRF data; relationship between the overburden pressure and normalized porosity, permeability and FRF.

$\ln \frac{FRF_2}{FRF_1}$ is plotted versus the net confining pressure difference for six sandstone samples in Figure 3. As examples, the RRM_s were calculated from the slope of the lines in Figure 3 and listed in Table 3. As R_o increases with overburden pressure, the gradient of rock resistivity with respect to pressure becomes a positive number. Thus, according to Equation (5), RRM is a negative number as shown in Table 3.

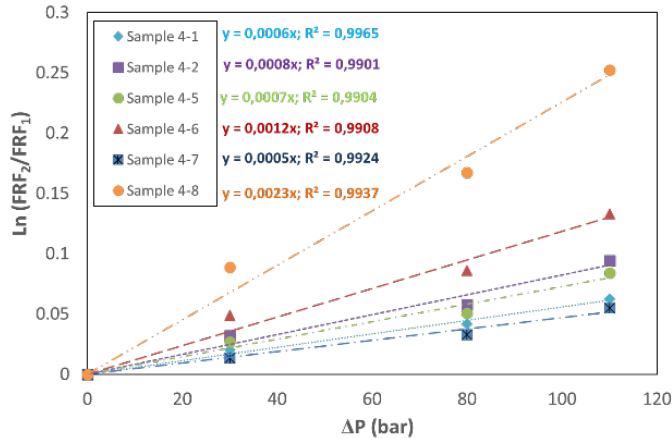


Fig. 3. $\ln \frac{FRF_2}{FRF_1}$ versus net confining pressure difference. According to Equation (18), the RRM_s were determined by the slope of lines for six North Sea samples.

Table 3. The calculated RRM_s from the slope of the lines in Fig.3.

Sample	FRF ₁ @ 20 bar	RRM (bar ⁻¹)
4-1	6.80	-5.57E-04
4-2	10.13	-8.21E-04
4-5	7.97	-7.27E-04
4-6	12.55	-1.18E-03
4-7	6.67	-4.68E-04
4-8	18.30	-2.26E-03

The modelled overburden FRF calculated by the Multi-FRF method is plotted versus the measured overburden FRF of the 55 samples from five North Sea reservoirs in Figure 4. A good fit between the model-predicted overburden FRF and the experimental measured laboratory data is observed.

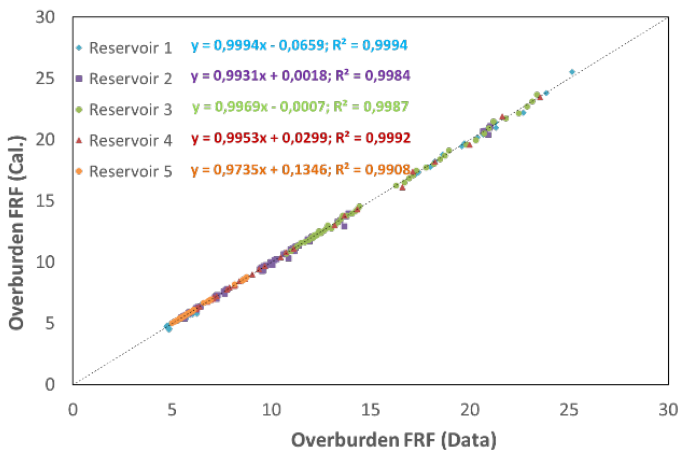


Fig. 4. Overburden FRF calculated using Equation (15) versus measured overburden FRF for five North Sea reservoirs.

The R² calculated by Single-FRF and Multi-FRF models for North Sea reservoirs are listed in Table 4. As expected, the Multi-FRF model shows a higher degree of accuracy than the Single-FRF model.

Table 4. Overview of the corresponding R² from model equations.

Reservoir	R ² (Single-FRF)	R ² (Multi-FRF)
1	0.9961	0.9994
2	0.9996	0.9984
3	0.9949	0.9987
4	0.9968	0.9992
5	0.9767	0.9908

The second dataset has been extracted from published literature [28,29] and includes 24 plug samples from two carbonate reservoirs. Figure 5 shows that the estimated overburden FRF from Equation (15) correlates with the experimental data for six samples from field S [28] with a maximum relative error of less than 8%.

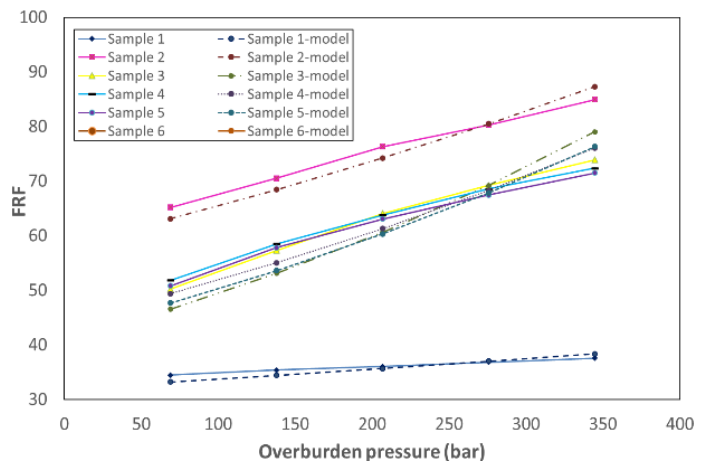


Fig. 5. Measured and calculated overburden FRF by Multi-FRF model versus overburden pressure for six samples from field S [28].

Figure 6 indicates a good correlation between the Multi-FRF model predicted and the measured overburden FRF data, with R² of 0.9869 and 0.9970 for the data from literature [28,29].

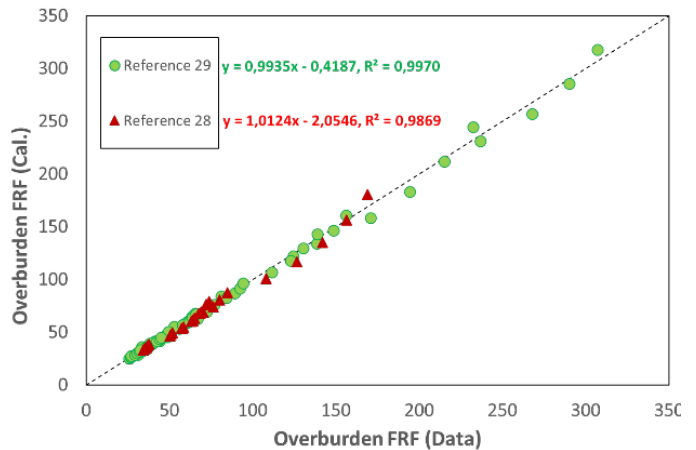


Fig. 6. Overburden FRF calculated using Equation (15) versus measured overburden FRF for two carbonate reservoirs [28,29].

As presented by Figure 7, a very good correlation is seen between the Multi-FRF model estimated values and the measured data. For overburden FRF, R^2 values are higher than 0.9975 for 153 sandstone and 221 carbonate data points.

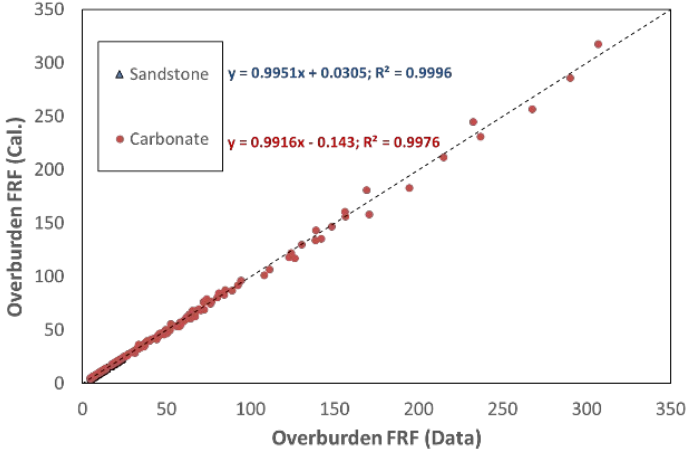


Fig. 7. Overburden FRF calculated using Equation (15) versus measured overburden FRF for sandstone and carbonate reservoirs.

Moreover, the average relative error for the 31 sandstone and 48 carbonate samples were calculated at 2% and 3% respectively. Overall, these results indicate that the general trend of the Multi-FRF model demonstrates very good correlation with the laboratory measurements for all the 79 sandstone and carbonate samples.

Development of the RI Model

A similar modelling approach can be applied to the calculation of RI and Archie's saturation n -exponent. If R_t is separated in Equation (7) and integrated while assuming TRM is constant over the pressure interval of interest, the overburden R_t can be obtained from Equation (19):

$$R_{t_2} = R_{t_1} e^{-\gamma_{R_t} \Delta P} \quad (19)$$

By dividing Equation (19) by Equation (8), the RI at a given overburden pressure can be predicted as follows:

$$RI_2 = RI_1 e^{(\gamma_{R_o} - \gamma_{R_t}) \Delta P} \quad (20)$$

Combining Equations (1), (2) and (7) yields the following equation:

$$\gamma_{R_t} = -\frac{\varphi^m S_w^n}{R_w} \times \frac{\partial(\frac{R_w}{\varphi^m S_w^n})}{\partial P} \quad (21)$$

Hence, by assuming constant cementation and saturation exponents over the pressure interval of interest and taking the derivative of the term $(\frac{R_w}{\varphi^m S_w^n})$ with respect to pressure in Equation (21) and rearranging it, the TRM can be calculated as follows:

$$\gamma_{R_t} = -\frac{1}{R_w} \frac{\partial R_w}{\partial P} + m \frac{1}{\varphi} \frac{\partial \varphi}{\partial P} + n \frac{1}{S_w} \frac{\partial S_w}{\partial P} \quad (22)$$

In addition, the formation brine compressibility; C_{fb} , is expressed as follows [30]:

$$C_{fb} = -\frac{1}{V_w} \frac{\partial V_w}{\partial P} \quad (23)$$

where V_w is the volume of the formation brine; this volume can be estimated through Equation (24).

$$V_w = \varphi V_b S_w \quad (24)$$

Combining Equations (23) and (24) and taking the derivative of the term $(\varphi V_b S_w)$ with respect to pressure and replacing C_p and C_b from Equations (11) and (12) into it, yields the following equation:

$$\frac{1}{S_w} \frac{\partial S_w}{\partial P} = C_p - C_{fb} \quad (25)$$

Thus, the TRM can be calculated by replacing Equations (6), (13) and (25) into Equation (22) as below:

$$\gamma_{R_t} = \gamma_{R_w} + m(C_b - C_p) + n(C_p - C_{fb}) \quad (26)$$

By replacing the RRM and TRM (from Equations (14) and (26) respectively) in Equation (20), the overburden RI can be calculated as follows:

$$RI_2 = RI_1 e^{n(C_{fb} - C_p) \Delta P} \quad (27)$$

From integration of Equation (25) with respect to pressure, the S_w at a given overburden pressure can be predicted as follows:

$$S_{w_2} = S_{w_1} e^{(C_p - C_{fb}) \Delta P} \quad (28)$$

Consequently, the saturation exponent at a given overburden pressure can be predicted by replacing Equations (27) and (28) into Equation (2) as below:

$$n_2 = -\frac{\ln RI_1 + [n_1 (C_{fb} - C_p)] \Delta P}{\ln S_{w_1} + (C_p - C_{fb}) \Delta P} \quad (29)$$

The compressibility of formation brine [psi^{-1}] containing no gas in solution and for pressures from 1,000 to 20,000 psi (69 to 2,844 bar), temperatures between 200 and 270°F (93 and 132°C) and salinities of 0 to 200 g/L NaCl equivalent can be estimated using the following correlation [30]:

$$C_{fb} = \frac{1}{7.033 P + 541.5 C - 5377 T + 403.3 \times 10^3} \quad (30)$$

where P , C and T are pressure [psi], salt concentration [g/L] and temperature [$^{\circ}\text{F}$] respectively. The more general forms of the Equations (27), (28) and (29) result from replacing the pressure steps 1 and 2 with i and $i + 1$ ($i \geq 1$), so:

$$RI_{i+1} = RI_i e^{n_i (C_{fb_i} - C_{p_i}) (P_{i+1} - P_i)} \quad (31)$$

$$S_{w_{i+1}} = S_{w_i} e^{(C_{p_i} - C_{fb_i}) (P_{i+1} - P_i)} \quad (32)$$

$$n_{i+1} = -\frac{\ln RI_i + n_i (C_{fb_i} - C_{p_i}) (P_{i+1} - P_i)}{\ln S_{w_i} + (C_{p_i} - C_{fb_i}) (P_{i+1} - P_i)} \quad (33)$$

Figure 8 illustrates an example of predicting saturation exponents at various overburden pressures using Equations (31), (32) and (33). The composite n-exponent was equal to 1.93 and was calculated from measurements conducted at 190 bar and 98°C on 12 SCAL plug samples from reservoir 3. The composite saturation exponents for net confining overburden pressures of 350 and 700 bar are predicted as 1.95 and 1.97 respectively.

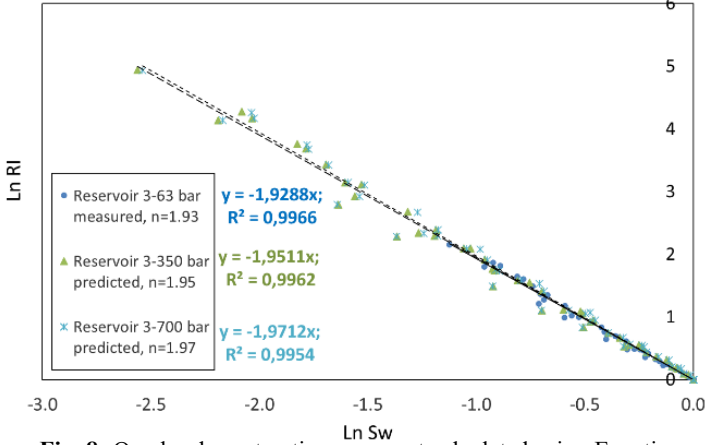


Fig. 8. Overburden saturation exponent calculated using Equations (31), (32) and (33).

Figure 9 shows the predicted composite n-exponent for reservoirs 1-4 versus overburden pressure (RI data is not available for reservoir 5). Linear relationships between the predicted composite saturation exponents and the overburden pressures have been developed. Saturation exponent increases linearly with overburden pressure, as shown in Figure 9.

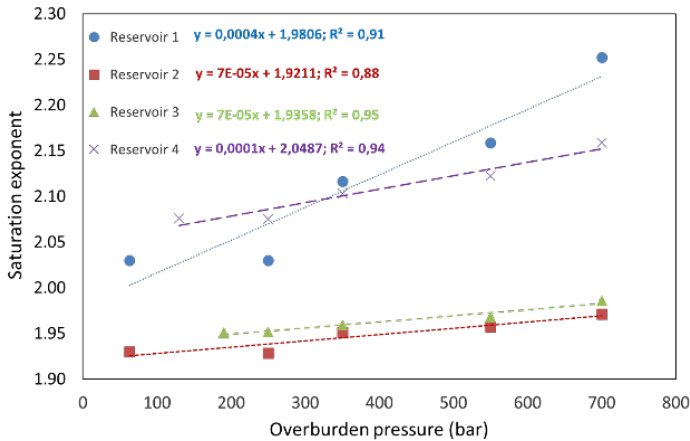


Fig. 9. Predicted composite n-exponent versus overburden pressure for reservoirs 1, 2, 3 and 4.

As shown in Table 2, reservoirs 2 and 3 are predominately carbonate and silicate reservoirs, respectively. The minimum rate of change in saturation exponent with respect to overburden pressure are observed for these two reservoirs with different lithologies (Figure 9). Also, the maximum gradient of saturation exponent with respect to overburden pressure is calculated for reservoir 1 which is the nearly pure (99%) carbonate reservoir. According to Equation (33), saturation exponent is dependent on the difference between the formation brine compressibility and the pore volume compressibility. When C_{fb} and C_p are almost identical and

consequently their difference is close to zero, the saturation exponent doesn't change significantly. Lewis et al. reported that changes in overburden pressures have a relatively minor effect upon the saturation exponent, but at the same time it slightly rises as the overburden pressure increases [24]. Although, experimental data was not available to support the theoretically developed model, but the predicted trends show consistency with the reported results by Lewis et al.

Development of the Apparent FRF Model

Conductivity is defined as the reciprocal of the electrical resistivity. Clay minerals in a rock play a role as a separate conductor. The effect of the clay on the conductivity of the rock is dependent upon the type, quantity, structure, and distribution in the rock [4]. As can be seen from the Table 2, the amount of clay in the investigated sandstone samples is low and varies between 0% and 17%. Figure 10 shows the conductivity behaviour of the shaly-sand as a function of brine conductivity, where C_w [$\Omega^{-1}\text{m}^{-1}$] and C_o [$\Omega^{-1}\text{m}^{-1}$] are the brine conductivity and the brine-saturated rock conductivity, respectively. The C_o is related to the C_w by the Waxman and Smits equation as follows [31]:

$$C_o = \frac{C_w}{F^*} + \frac{BQ_v}{F^*} \quad (34)$$

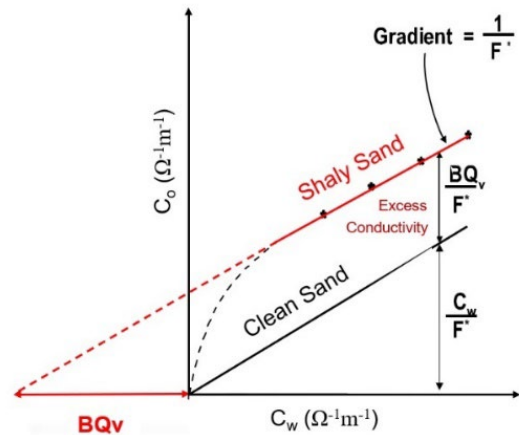


Fig. 10. Water-saturated rock conductivity (C_o) as a function of water conductivity (C_w). Adopted from [31].

where F^* , B [$(\Omega^{-1}\text{m}^{-1})/(\text{meq/ml})$] and Q_v [meq/ml] are the shaly-sand FRF (apparent FRF), the volume concentration of sodium exchange cations associated with the clay and the equivalent conductance of sodium clay exchange cations, respectively. Therefore, as shown in Figure 10, beyond the primary dilute area, C_o increases linearly with C_w . The term $(\frac{BQ_v}{F^*})$ is determined from the intercept of the regressed best-fit straight-line curve to the C_o - C_w data pairs [11]. The reciprocal of the shaly-sand FRF is calculated from the gradient (slope) of the plot C_o as a function of C_w as [31,32]:

$$\frac{1}{F^*} = \frac{dC_o}{dC_w} \quad (35)$$

By assuming that brine conductivity is independent of pressure and taking the derivative of Equation (35) with respect to pressure, yields the following equation:

$$\frac{\partial F^*}{\partial P} = -\frac{\frac{\partial(dC_o)}{\partial P} dC_w}{dC_o dC_o} \quad (36)$$

The rock conductivity modulus (RCM) can be defined as follows:

$$\gamma_{C_o} = -\frac{1}{dC_o} \frac{\partial(dC_o)}{\partial P} \quad (37)$$

Combining Equations (35), (36) and (37), yields the following equation:

$$\frac{\partial F^*}{F^*} = \gamma_{C_o} \partial P \quad (38)$$

From integration of Equation (38) with respect to pressure while assuming a constant RCM over the pressure interval of interest, the apparent FRF at overburden pressure can be calculated from Equation (39) as follows:

$$F^*_2 = F^*_1 e^{\gamma_{C_o} \Delta P} \quad (39)$$

For clean sands, excess conductivity which is the intercept of the line ($\frac{BQ_v}{F^*}$) in Figure 10 becomes zero. Thus, RCM can be simplified as below:

$$\gamma_{C_o} = -\frac{1}{C_o} \frac{\partial C_o}{\partial P} \quad (40)$$

Replacing the brine-saturated rock conductivity ($R_o = \frac{1}{C_o}$) in RRM's definition in Equation (5) and taking the derivative with respect to pressure and combining it with Equation (40), yields $\gamma_{R_o} = -\gamma_{C_o}$. As mentioned before, RRM values are negative since rock resistivity increases with overburden pressure. As the rock conductivity of clean sand is the reciprocal of the rock resistivity, the rock conductivity decreases with overburden pressure. Consequently, according to Equation (40), RCM becomes positive normally. Consequently, for clean sands, Equations (15) and (39) match as expected as the apparent FRF approaches FRF, and power coefficients reflect equal values. Figure 11 shows an example of predicting apparent FRF at different overburden pressures.

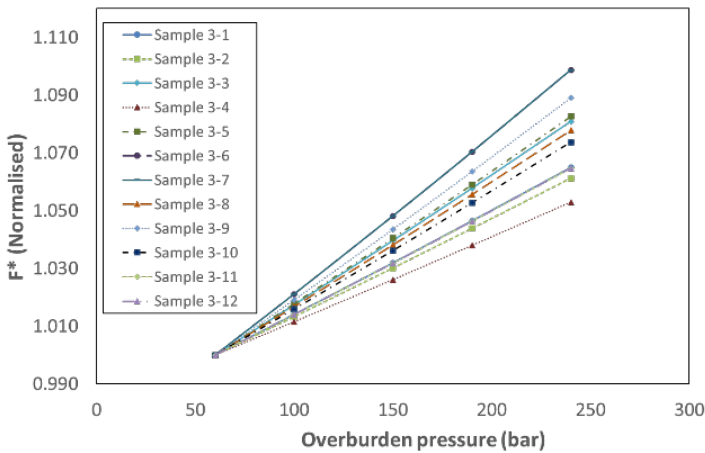


Fig. 11. Example predicting apparent FRF for 12 SCAL plug samples from reservoir 3, using Equation (39).

The apparent FRF data at stress are normalised to values at 60 bar for 12 samples from reservoir 3, as shown in Figure 11. Overburden FRF measurement has been conducted at

several overburden pressures on reservoir 3 samples, whereas C_o/C_w measurements have been performed only at one overburden pressure step. According to Table 2, the clay content of reservoir 3 samples is quite low. Thus, the absolute values of RRM and RCM can be assumed equal. The apparent FRF at 190 bar and 20°C was calculated based on the C_o/C_w measurement. The apparent FRF is predicted at overburden pressures of 60, 100, 150 and 240 bar, using Equation (39) and RRM obtained from the overburden FRF measurement.

Results and Discussion

A good correlation was observed between exponential models presented in equations (15) and (17) and FRF experimental results in Figure 1; also, for the investigated dataset the graphical trends appear to be a linear function of the increasing overburden pressure. This is mathematically reasonable as the power coefficients in Equation (15) and (17) are much less than one, thus the exponential function can be converted to a linear function as follows:

$$FRF_2 = aP_2 + b \quad (41)$$

where a and b are the slope and the intercept of the line, respectively as:

$$a = FRF_1 m_1 (C_p - C_b) \quad (42)$$

$$b = FRF_1 [1 - m_1 P_1 (C_p - C_b)] \quad (43)$$

As ΔP and consequently the power coefficients increase by pressure, the prerequisite condition needed for converting exponential function to linear function ($-\gamma_{R_o} \Delta P \ll 1$) becomes invalid. Accordingly, deviations from linearity between the FRF and the overburden pressure are observed for high pressures. Figures 12 and 13 illustrate examples of this behavior of the fitting of the Multi-FRF model to the FRF data measured at a high range of overburden pressure.

The effect of overburden pressure on the electrical resistivities has been attributed to the mechanical feature which comprises pore constriction alterations and pore volume deformations [16]. The grain framework compacts and deforms from an increase in overburden pressure and because of compaction. Framework grains become in inlaid contact with each other, instead of being in point or line contact [33].

Once a rock is exposed to overburden pressure, it experiences a variation in volume. This variation is called strain [34]. Until strain is proportional to the magnitude of the applied pressure, the rock shows elastic behaviour. Under such conditions if the pressure is removed, the volume of the rock sample returns to its original state. Plastic deformation occurs once the applied overburden pressure on a rock is beyond its elastic limit. Thus, plastic deformation is that deformation that generates a permanent alteration in the volume of a rock without that rock having failed by fracturing [35]. Sudden downward changes in the slope of the plot FRF as a function of overburden pressure at high overburden pressures could be related to the change from more elastic to more plastic or ductile failure behaviour (Figure 12).

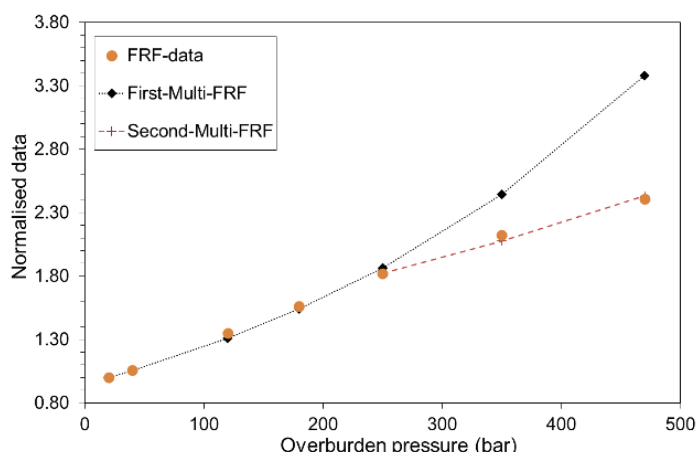


Fig. 12. Example fitting of Equation (15) to the normalised FRF data measured at a large range of overburden pressures when FRF shows a curving downward behaviour.

Micron-scale deformation mechanisms such as grain rotation and sliding, microcrack growth and closure, cement breakage, elastic grain-contact spreading and crystal plastic deformation in clay appear when the applied overburden pressure increases, and the load-bearing grain framework of the sample is extremely high [36]. Abrupt upward changes in the slope of the plot FRF as a function of overburden pressure at very high overburden pressures are indicative of suspected pore collapse, which causes grain rearrangement and repacking (Figure 13).

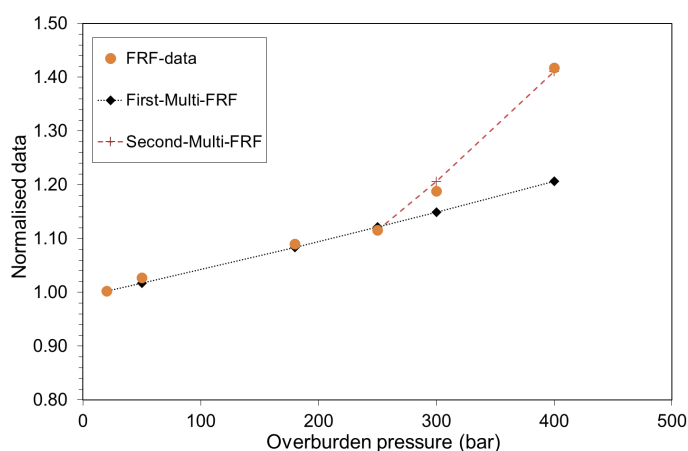


Fig. 13. Example fitting of Equation (15) to the normalised FRF data measured at a large range of overburden pressures when FRF shows curving upward behaviour [11].

When the confining compaction stress is sufficiently high, inelastic mechanisms such as intragranular cracks (contact spalling), grain rotation and grain sliding triggered by intergranular microcracks, and cement breakage are activated and dominated [11,36,37].

Upward or downward changes in the slope of the plot FRF as a function of overburden pressure leads to variation of the original trend of the FRF with the overburden pressure. This consequently causes deviations between the measured FRF data and the proposed model.

To improve the accuracy of the Multi-FRF model in predicting FRF data at a large range of overburden pressures, the second Multi-FRF model can be applied. It may be applied from the point that the trend of the graph of FRF

versus overburden pressure has started to change due to probable plastic behaviour (curving downward behaviour) or rearranged grains and pore structures (curving upward behaviour). Hence, due to the slope change at high overburden pressures, the first Multi-FRF models were not capable of predicting overburden FRFs properly for high overburden pressures in Figures 12 and 13. Moreover, Figures 12 and 13 display the second Multi-FRF models correlate well to the measured FRF data at high overburden pressures. The initial pressure has been set to 250 bar for the second Multi-FRF model in Equation (15); RRM has been calculated based on the FRF values measured at overburden pressures greater than and equal to 250 bar in Figures 12 and 13. R^2 of the plot $\ln \frac{FRF_2}{FRF_1}$ versus the net confining pressure

difference is a good diagnostic tool to verify the requirement of applying the second Multi-FRF model. As shown in Figure 3, R^2 greater than 0.9900 shows that the original trend of the FRF with the overburden pressure works accurately. Whereas R^2 lower than 0.9900 indicates that applying the second Multi-FRF model is most likely needed for more accurate predictions of FRF values at high overburden pressures.

Practically, FRF data at various overburden pressures are not always available. Porosity and water permeability measurements are the basic experiments that are usually measured on all the samples at initial pressure, normally 20 bar, before conducting any SCAL program. FRF can also be measured at initial pressure in conjunction with porosity and water permeability measurements for all the SCAL samples. According to Equation (17), in addition to initial FRF data, the difference between the pore volume compressibility and bulk compressibility is required for predicting overburden FRF by the Single-FRF model. If porosity has been measured under different overburden pressures, C_p-C_b can be estimated through Equation (13). When overburden porosity and compressibility data are not available, C_p can be calculated through empirical correlations such as the following equations [38]:

$$C_p = \frac{97.32 \times 10^{-6}}{(1+55.8721\varphi)^{1.42859}} \quad (44)$$

$$C_p = \frac{0.853531}{(1+2.47664 \times 10^6 \varphi)^{0.9299}} \quad (45)$$

Equations (44) and (45) were developed for consolidated sandstones and limestone, respectively. Also, the bulk compressibility can be related to the pore compressibility as follows [39,40]:

$$C_b \cong C_p \varphi \quad (46)$$

Consequently, the difference between the pore volume compressibility and bulk compressibility can be estimated through Equations (44), (45) and (46). Table 5 demonstrates the sensitivity of using the different methods and data to estimate C_p-C_b and overburden FRF for the sample plotted in Figure 2 at 120 bar where the maximum deviation from the measured FRF data has been observed. Using two overburden porosity values to calculate C_p-C_b through equation 13 leads to a 12.6% overestimation of FRF at 120 bar as shown in Figure 2 and listed in Table 5. Increasing the number of

overburden porosity values to four in calculation of C_p-C_b leads to a 10.3% underestimation of overburden FRF. That means the absolute value of the relative error improves 2.3% by using four overburden porosity values. Whereas using correlations (44), (45) and (46) for estimating C_p-C_b worsens the absolute value of the FRF relative error only 3.1%. The average relative error for predicting overburden FRF for samples from North Sea reservoirs by using the Single-FRF model and correlations (Equations 44-46) is less than 5%. Therefore, although it was shown that the Multi-FRF model is more accurate for predicting FRF in comparison with the Single-FRF model, the Single-FRF model can be applied for predicting overburden FRF if the prerequisites of the Multi-FRF model are unavailable.

Table 5. The sensitivity of using the different methods and data to estimate FRF at 120 bar for sample plotted in Figure 2.

FRF-Model	Used data/method to calculate C_p-C_b	C_p-C_b (bar ⁻¹)	$-\gamma_{Ro}$ (bar ⁻¹)	Rel. Er. (%)
Single	ϕ at 2 OB P./ Equation (13)	1.30E-03	2.82E-03	12.6
Single	ϕ at 4 OB P./ Equation (13)	2.24E-04	4.84E-04	-10.3
Single	Equations (44), (45) & (46)	5.57E-05	1.20E-04	-13.4
Multi	Equation (16)	7.57E-04	1.59E-03	0.4

Conclusions

Based on the developed FRF models and the application of the models to two overburden FRF datasets including sandstone and carbonate samples from seven reservoirs, the following conclusions can be drawn.

1-Two analytical FRF models referred to as the Multi-FRF model and Single-FRF model have been developed. Both exponential models can be converted to linear models for a range of low overburden pressures (for example for net confining overburden pressure $P < 150$ bar for this specific dataset) and include FRF at initial pressure and net confining pressure difference. In addition, the Multi-FRF model involves the rock resistivity modulus, whereas the Single-FRF model is dependent on the cementation exponent, the pore volume compressibility and bulk compressibility. The FRF models have been derived mathematically based on Archie's equation, thus they are expected to be valid within Archie's equation limitation, assumption, and boundary conditions.

2-The validity of the developed FRF models were verified through their applications on 374 actual core data of 79 plug samples (31 sandstone and 48 carbonate plug samples). The results of validation showed that the FRF models succeeded in predicting the behaviour of FRF for the investigated net confining overburden pressure range at ambient temperature with average relative error of 2% and 3% for sandstone and carbonate samples, respectively.

3-Theoretical models are proposed to predict RI, water saturation and saturation exponent behaviour under overburden pressure. In addition, a special Multi-FRF model has been developed to predict apparent FRF for shaly rocks. As RI and C_o/C_w experiments are normally performed only at current reservoir overburden pressure and temperature conditions, the developed models may help to predict RI and F^* behaviours at different overburden pressures - within the model boundary conditions and basic assumptions.

4-However, the model predicted trends, and the maximum change in the saturation exponent with overburden pressure shows consistency with the reported results in literature [24]. Experimental data and further investigations are required to validate the developed theoretical models (RI, S_w , saturation exponent and apparent FRF models).

Acknowledgment

The authors thank Aker BP ASA for granting the permission to publish this paper. Further we thank Reza Askarinezhad (NORCE Norwegian Research Centre AS, Norway) for the original idea that initiated this research paper. Min Cheng (Stratum Reservoir, USA) is acknowledged for fruitful discussions and constructive comments.

Nomenclature

- a Slope of the line in Equation (41), bar⁻¹
- b Intercept of the line in Equation (41), dimensionless
- B Volume concentration of sodium exchange cations associated with the clay, ($\Omega^{-1}m^{-1}$)/(meq/ml)
- C Salt concentration, g/L
- C_b Bulk compressibility, bar⁻¹
- C_{fb} Formation brine compressibility, bar⁻¹
- C_o Brine-saturated rock conductivity, $\Omega^{-1}m^{-1}$
- C_p Pore volume compressibility, bar⁻¹ (psi⁻¹ in Equations (44) and (45))
- C_w Brine conductivity, $\Omega^{-1}m^{-1}$
- ΔP Confining pressure difference, bar
- ϕ Porosity, fraction
- F^* Shaly-sand FRF (apparent FRF), dimensionless
- FRF Formation Resistivity Factor, dimensionless
- γ_{Co} Rock conductivity modulus, bar⁻¹
- γ_{Ro} Rock resistivity modulus, bar⁻¹
- γ_{Rt} True resistivity modulus, bar⁻¹
- γ_{Rw} Water resistivity modulus, bar⁻¹
- $HCIIP$ Volume of hydrocarbon initially in place at reservoir conditions, m³
- i Pressure step
- m Cementation factor
- n Saturation exponent
- P Pressure, bar (psi only in Equation (30))
- Q_v Equivalent conductance of sodium clay exchange cations, meq/ml
- RI Resistivity Index, dimensionless
- R_o Resistivity of rock fully saturated with brine, Ωm
- R_t Resistivity of rock partially saturated with brine, Ωm
- R_w Formation water resistivity, Ωm

S_w	Water saturation, fraction
T	Temperature, °F
V	Volume of the reservoir, m ³
V_b	Bulk volume, m ³
V_p	Pore space volume, m ³
V_w	Volume of the formation brine, m ³

References

- [1] Archie GE. The Electrical Resistivity Log as an Aid in Determining Some Reservoir Characteristics. Transactions of the AIME 1942; 146:54–62. <https://doi.org/10.2118/942054-g>.
- [2] Carter SL, Power HH. The Relationship Between Electrical Resistivity and Brine Saturation in Reservoir Rocks. The Log Analyst 1962;2.
- [3] Mungan N, Moore EJ. Certain Wettability Effects on Electrical Resistivity in Porous Media. Journal of Petroleum Technology 1968; 7:20–5. <https://doi.org/10.2118/68-01-04>.
- [4] Torsæter O, Abtahi M. Experimental Reservoir Engineering Laboratory Workbook. Norwegian University of Science and Technology 2003.
- [5] Masoudi P, Zahedi A, Ali M, Farshid A, Seyed Mohammad Z. Estimation of in Place Hydrocarbon Volume in Multi-Layered Reservoirs Using Deterministic and Probabilistic Approaches. Energy Exploration & Exploitation 2011;29:543–57. <https://doi.org/10.1260/01445987.29.5.543>.
- [6] Fleury M, Efnik M, Kalam MZ. Evaluation of Water Saturation From Resistivity in a Carbonate Field. From Laboratory to Logs. Proceedings of International Symposium of the Society of Core Analysts, SCA2004-22, Abu Dhabi, UAE, 2004, p. 5–9.
- [7] Tiab D, Donaldson EC. Petrophysics: Theory and Practice of Measuring Reservoir Rock and Fluid Transport Properties. Gulf Professional Publishing; 2015.
- [8] Moore EJ, Szasz SE, Whitney BF. Determining Formation Water Resistivity From Chemical Analysis. Journal of Petroleum Technology 1966; 18:373–6. <https://doi.org/10.2118/1337-pa>.
- [9] Dusenbery RA, Osoba JS. Determination of Formation Water Resistivity Using Shale Properties. Permian Basin Oil and Gas Recovery Conference, SPE-150306-MS; 1986. <https://doi.org/10.2118/15030-ms>.
- [10] Henry JD, Cunningham WA. A New Method for Determination of Formation Water Resistivity From the Spontaneous Potential Curve. Fall Meeting of the Society of Petroleum Engineers of AIME, SPE-437-MS; 1962. <https://doi.org/10.2118/437-ms>.
- [11] McPhee C, Reed J, Zubizarreta I. Core analysis: A Best Practice Guide. Elsevier; 2015. <https://doi.org/10.1016/b978-0-444-63533-4.00001-9>.
- [12] Baker RO, Yarranton HW, Jensen J. Practical Reservoir Engineering and Characterization. Gulf Professional Publishing; 2015. <https://doi.org/10.1016/b978-0-12-801811-8.00010-9>.
- [13] Fatt I. Effect of Overburden and Reservoir Pressure on Electric Logging Formation Factor. AAPG Bulletin 1957; 41:2456–66. <https://doi.org/10.1306/0bda59a8-16bd-11d7-8645000102c1865d>.
- [14] Brace WF, Orange AS, Madden TR. The Effect of Pressure on the Electrical Resistivity of Water-Saturated Crystalline Rocks. Journal of Geophysical Research 1965; 70:5669–78. <https://doi.org/10.1029/jz070i022p05669>.
- [15] Timur A, Hemphkins WB, Worthington AE. Porosity and Pressure Dependence of Formation Resistivity Factor for Sandstones. Trans CWLS 4th Formation Evaluation Symp., vol. 30, 1972.
- [16] Jing XD, Archer JS, Daltaban TS. Laboratory Study of the Electrical and Hydraulic Properties of Rocks Under Simulated Reservoir Conditions. Marine and Petroleum Geology 1992;9:115–27. [https://doi.org/10.1016/0264-8172\(92\)90084-r](https://doi.org/10.1016/0264-8172(92)90084-r).
- [17] Longeron DG, Argaud MJ, Feraud JP. Effect of Overburden Pressure and the Nature and Microscopic Distribution of Fluids on Electrical Properties of Rock Samples, SPE Paper 15383. 61st Annual Technical Conference, Society of Petroleum Engineers, New Orleans, LA, October 1986, p. 5–8. <https://doi.org/10.2118/15383-PA>.
- [18] Hashmy KH, Campbell JM. The Effect of Pore Configuration, Pressure and Temperature on Rock Resistivity. SPWLA 7th Annual Logging Symposium, SPWLA-1966-W; 1966.
- [19] Wyble DO. Effect of Applied Pressure on the Conductivity, Porosity and Permeability of Sandstones. Journal of Petroleum Technology 1958; 10:57–9. <https://doi.org/10.2118/1081-G>.
- [20] Glanville CR. Laboratory Study Indicates Significant Effect of Pressure on Resistivity of Reservoir Rock. Journal of Petroleum Technology 1959; 11:20–6. <https://doi.org/10.2118/1153-g>.
- [21] Brace WF, Orange AS. Electrical Resistivity Changes in Saturated Rocks During Fracture and Frictional Sliding. Journal of Geophysical Research 1968; 73:1433–45. <https://doi.org/10.1029/JB073i004p01433>.
- [22] Parkhomenko EI. Electrical Resistivity of Minerals and Rocks at High Temperature and Pressure. Reviews of Geophysics 1982; 20:193–218. <https://doi.org/10.1029/rg020i002p00193>.
- [23] Redmond JC. Effect of Simulated Overburden Pressure on the Resistivity, Porosity and Permeability of Selected Sandstones. The Pennsylvania State University; 1962. <https://doi.org/10.2118/461-pa>.
- [24] Lewis MG, Sharma MM, Dunlap HF. Wettability and Stress Effects on Saturation and Cementation Exponents. SPWLA 29th Annual Logging Symposium, SPWLA-1988-K; 1988.
- [25] Sondena E, Brattell F, Kolltvelt K, Normann HP. A Comparison Between Capillary Pressure Data and Saturation Exponent Obtained at Ambient Conditions and at Reservoir Conditions. SPE Formation Evaluation; SPE-19592-PA 1992; 7:34–40. <https://doi.org/10.2118/19592-PA>.
- [26] Zheng Z, McLennan J, Jones A. Pore Volume Compressibilities Under Different Stress Conditions. SCA-9005, 1990.
- [27] Quist AS, Marshall WL. Electrical Conductances of Aqueous Sodium Chloride Solutions from 0 to 800 d. and at Pressures to 4000 bars. The Journal of Physical Chemistry 1968; 72:684–703. <https://doi.org/10.1021/j100848a050>.
- [28] Behin R. Investigation on the effect of stress on cementation factor of Iranian carbonate oil reservoir rocks. International Symposium of the Society of Core Analysts held in Abu Dhabi, UAE, SCA 2004-41, 2004.

- [29] Eshraghi E, Moghadasi J. An Experimental Investigation on Archie Parameters at Ambient and Overburden Condition of Iranian Clean Carbonate Reservoir Rock and Developing a new Formation Resistivity Model for Limestone and Dolomite Samples. International Petroleum Technology Conference, IPTC-17223-MS; 2014. <https://doi.org/10.2523/IPTC-17223-MS>.
- [30] Osif TL. The Effects of Salt, Gas, Temperature, and Pressure on the Compressibility of Water. SPE Reservoir Engineering 1988; 3:175–81. <https://doi.org/10.2118/13174-PA>.
- [31] Waxman MH, Smits LJM. Electrical conductivities in oil-bearing shaly sands. Society of Petroleum Engineers Journal 1968; 8:107–22. <https://doi.org/10.2118/1863-a>.
- [32] Waxman MH, Thomas EC. Electrical Conductivities in Shaly Sands-I. The Relation Between Hydrocarbon Saturation and Resistivity Index, SPE-1863-A, 213–25. <https://doi.org/10.2118/4094-ms>.
- [33] Zhang S, Zhengwei F. Permeability Damage Micro-Mechanisms and Stimulation of Low-Permeability Sandstone Reservoirs: A Case Study, Bohai Bay Basin, China. Petroleum Exploration and Development 2020; 47:374–82. [https://doi.org/10.1016/S1876-3804\(20\)60054-4](https://doi.org/10.1016/S1876-3804(20)60054-4).
- [34] Aldrich Jr MJ, Lane KS. Pore Pressure Effects on Berea Sandstone Subjected to Experimental Deformation. Geological Society of America Bulletin 1969; 80:1577–86. [https://doi.org/10.1130/00167606\(1969\)80\[1577:ppeobs\]2.0.co;2](https://doi.org/10.1130/00167606(1969)80[1577:ppeobs]2.0.co;2).
- [35] Seyfert CK. Plastic Deformation of Rocks and Rock-Forming Minerals. Structural Geology and Tectonics, Berlin, Heidelberg: Springer Berlin Heidelberg; 1987, p. 495–502. https://doi.org/10.1007/3-540-31080-0_78.
- [36] Schutjens P, Hanssen TH, Hettema MHH, Merour J, de Bree P, Coremans JWA, et al. Compaction-Induced Porosity/Permeability Reduction in Sandstone Reservoirs: Data and Model for Elasticity-Dominated Deformation. SPE-88441-PA, 2004;7:202–16. <https://doi.org/10.2118/88441-PA>.
- [37] Kaye LN, Hacksma JD, Knudson S, Smith JE. Special Core Analysis Loading Conditions for a Friable, Stress-Sensitive Sandstone. Proceedings of 1st Society of Core Analysts European Core Analysis Symposium, London, vol. 21, 1990, p. 23.
- [38] Satter, Abdus, and Ghulam M. Iqbal. Reservoir Rock Properties. Reservoir Engineering, 2016; 29-79. <https://doi.org/10.1016/b978-0-12-800219-3.00003-6>.
- [39] Geertsma, J. The Effect of Fluid Pressure Decline on Volumetric Changes of Porous Rocks. Transactions of the AIME 210.01 1957; 331-340. <https://doi.org/10.2118/728-G>.
- [40] Ahmed, Tarek. Fundamentals of rock properties. Reservoir engineering handbook 2010;189-287. <https://doi.org/10.1016/B978-1-85617-803-7.50012-2>.

Innovations in low UCS core acquisition and quality assessment using digital rock physics

Dmitry Lakshantov¹, Jennie Cook^{1*}, Yuliana Zapata¹, Dave Saucier¹, Robin Eve¹, Mark Lancaster¹, Nathan Lane¹, Glen Gettemy¹, Kevan Sincock², Elizabeth Liu², Rosemarie Geetan³, Ian Draper⁴, and Tim Gill⁴

¹BP, Sunbury, UK & Houston, Texas, USA

²BP, now independent consultant

³BP, now Bifrost Energy

⁴Baker Hughes

Abstract. Digital rock physics was used to support development and deployment of a novel percussion sidewall coring technology that can enable a cost-effective reservoir characterization strategy. Subsurface samples acquired with percussion sidewall core often exhibit penetrative damage making them of limited use for subsurface characterization. We have evaluated a novel method of percussion sidewall core (PSWC) acquisition that minimizes acquisition damage and will provide intact samples of reservoir material for use in subsurface workflows. This paper details the benchmarking and validation workflow developed using laboratory experiments and digital rock physics on outcrop samples. A planned field trial of this technology is planned for 2022.

Six sandstones of known properties were used in the validation program, and these sandstones exhibit a range of low to medium unconfined compressive strengths (UCS). Reference plugs were cut from all materials. The sandstone samples were then used as the source material in laboratory testing of various novel designs of PSWC bullets. The PSWC bullets were shot in simulated downhole environments. Both reference plugs and test plugs were imaged with high-resolution X-ray microCT (Zeiss Versa), and digital rock analysis was conducted on all samples. Using images of reference and post-test material, damage could be identified and simulated petrophysical properties including porosity and permeability could be determined and directly compared.

Digital rock physics provide unique insight to evaluate and quantify changes (or lack of changes) to the sample material subjected to the PSWC acquisition. Damage encountered in the test samples includes grain crushing and compaction that degrades storage and transport properties, and dilatant zones that locally enhance transport properties. The presence, frequency and distribution of these zones are dependent on experimental parameters. In all cases, undisturbed rock fabric could be identified in each sample and intact texture was verified by comparison with reference material.

A novel and efficient method for acquiring and evaluating subsurface samples was developed and benchmarked. By optimizing PSWC bullet design and coupling this with a mature, image-based digital rock technology, this work demonstrates that the samples and results obtained by this method are representative. Based on encouraging results from the validation workflow, the novel percussion sidewall technology will be run in an upcoming carbon capture appraisal well. We will discuss preliminary observations from this field trial with the opportunity to compare the results against full bore and rotary coring.

1 Introduction

Rock samples are a key part of any subsurface workflow, whether traditional oil & gas or carbon capture & sequestration. Rock samples are used as ‘ground-truth’ in wireline analysis and inform the complete subsurface description. Full bore core offers the most comprehensive sampling strategy, but cost may make acquiring core difficult to justify.

Rotary sidewall core (RSWC) acquired on wireline offers a less costly mechanism to acquire core plugs for subsurface characterization. Although, RSWC may not be suitable for all analyses including relative permeability, recovered cores are generally of good quality and suitable for most routine and special core analysis. However, in weak or highly overbalanced formations, RSWC acquisition can have poor recovery (Jackson, 2021). In such cases, the only alternative is to acquire rock samples via percussion sidewall coring (PSWC). PSWC often has good recovery, but the

acquisition process and eventual sample extraction can result in sample damage affecting traditional laboratory analysis (Webster and Dawsongrove, 1959). In routine core analysis, typically the entire width of the PSWC or RSWC sample is used, but it may be trimmed for length. This is especially an issue for soft PSWC samples, where some of the extracted material is likely to be damaged further. Thus, any analysis of the whole extracted plug will likely include both damaged and undamaged regions which may impact analytical measurements.

To reduce the issues associated with PSWC damage, a novel bullet was designed. The main innovations consist in an optimized bullet profile and an X-ray transparent internal sleeve. The bullet profile was modified to reduce stress concentration and minimize damage ahead of the barrel during sample acquisition. The internal sleeve encapsulates the sample reducing the risk of damage during extraction from the barrel assembly. In addition, X-ray transparency allows direct high-resolution imaging of the acquired sample,

enabling the use of Digital Rock Physics (DRP) (Draper et al., 2022; Lakshtanov et al., 2022).

DRP is a technique that uses high-resolution three-dimensional imaging and numerical simulation to determine the static and dynamic properties of an imaged sample. Static properties from DRP can be used in the same way as traditional laboratory core analysis. Unlike laboratory core analysis, however, image-based simulations can be performed on a variety of subsurface samples, from whole and RSWC, but also end trims, offcuts, PSWC, and cuttings, where no other traditional analysis can be used. DRP analysis offers reduced cycle time over most laboratory special core analysis, often providing results within weeks once material is received.

In addition to DRP simulation results, the three-dimensional images can provide critical information, particularly where heterogeneity or sample quality may be an issue. Using DRP, the plug can be imaged, and undamaged regions can be selected, which is why DRP/PSWC for softer reservoirs has been a significant value driver over the last few years.

2 Sample Selection

Six sandstones of known properties were used in the novel PSWC testing program. These sandstones were chosen to cover a wide range of low and medium unconfined compressive strengths (UCS). Reference plugs were cut from all sandstones. The sandstone samples were then used as the parent material in laboratory testing of various designs of PSWC barrels. The novel PSWC barrels were shot in ambient and simulated downhole environments discussed further in section 3.2 (Lakshtanov et al., 2022).

Sandstones included in this study include Silver Sands (SS), Salt Wash South (SO), Salt Wash Red (SW), Castlegate (CG), Berea Buff (BB), and Berea Spider (BS). General rock properties for these formations were provided by the material supplier and are outlined in *Table 1*.

All formations are generally homogeneous clean quartz sandstones with variable amounts of cement and intergranular clay. Bedding is visible in some samples, particularly the SW formation. Where possible sample blocks were oriented to allow the plugs to be acquired parallel to bedding, as they would be in a typical downhole application (vertical well in horizontal bedding), but in some cases this was not possible, and some plugs were acquired across dipping beds.

Grain density for all samples is between 2.61 and 2.66 g/cm³ (*Table 1*), indicative of a quartzose grain framework. Cement, where present, typically consists of quartz overgrowths with minor carbonate. Sample porosity and permeability vary between 20% to 35%, and between 100mD to ~10 D, respectively. UCS ranges from weak (<100 psi) to hard (> 5000 psi). A common rule of thumb in the industry to select between RSWC and PSWC methods is to use the target formation expected UCS values. In target formations with UCS lower than 100psi, PSWC is often preferred because of greater sample recovery, whereas where UCS is greater than 1000psi RSWC is usually preferred. There are other considerations in selecting the best acquisition method, including downhole hydrostatic overbalance and intended use of the sample, but UCS is often the primary determining factor. In this study, rock types with UCS values above and below

1000psi were selected to explore the impact of rock properties on sample recovery and quality.

Table 1 : Rock properties for outcrop sandstones included in the novel PSWC evaluation program (Lakshtanov et al., 2022).

Formation	Sample Code	Grain Density (g/cm ³)	Porosity (%)	Permeability (mD)
Berea Buff	BB	2.64	21.4	273
Berea Buff		2.63	21.4	407
Berea Buff		2.63	21.4	402
Berea Buff		2.63	21.7	283
Berea Spider	BS	2.64	21.3	346
Berea Spider		2.63	21.7	428
Castlegate	CG	2.63	26.9	920
Castlegate		2.63	26.9	1100
Castlegate		2.63	27.2	876
Castlegate		2.63	25.6	764
Salt Wash Red	SW	2.63	24.3	1720
Salt Wash Red		2.62	25.4	2370
Salt Wash Red		2.62	24.1	1890
Salt Wash South	SO	2.63	30.2	6590
Salt Wash South		2.61	30.7	6320
Salt Wash South		2.60	31.9	7260
Salt Wash South		2.61	30.9	5550
Silver Sands	SS	2.64	32.1	9185
Silver Sands		2.66	33.8	9158
Silver Sands		2.65	33.1	8291

Porosity versus UCS for the six sandstones included in the testing program are shown in *Figure 1*. In these clean sandstones, porosity variation is primarily a function of grain packing and cementation, thus high porosity sandstones selected have a looser packing arrangement and less cement and are typically weaker than lower porosity sandstones. UCS was measured on samples from these formations, but we do not have UCS information for each sample evaluated. Because we see good correlation between porosity and UCS for these test plugs (*Figure 1*), for further analyses we use porosity as a proxy for rock strength in this sample suite.

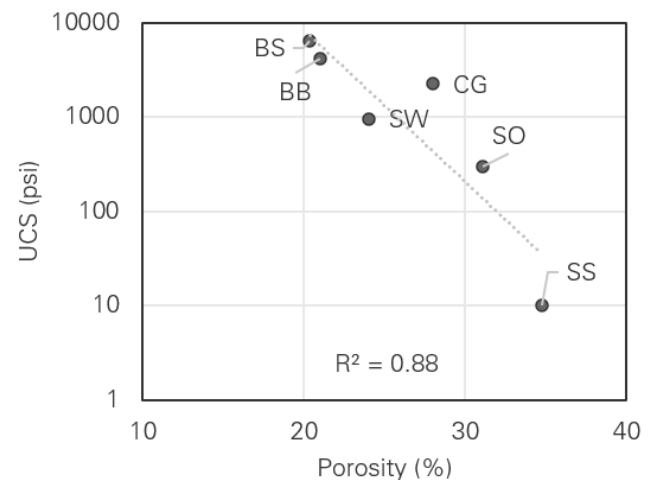


Figure 1 : Porosity and unconfined compressive strength (UCS) for outcrop sandstones included in the PSWC evaluation

3 Novel PSWC Design & Testing

3.1. Barrel & Sleeve Design

The objective of design and testing of the novel PSWC tool was to modify the traditional tool in such a way as to minimize damage to the extracted sample and to facilitate analysis of the recovered material. The design of the novel PSWC barrel was refined over multiple iterations, however all versions differed from conventional PSWC barrels in one key aspect: the addition of an X-ray transparent aluminum sleeve (Draper et al., 2022).

A conventional barrel typically consists of two parts, the driver, and the cutter (*Figure 2*). A key innovation was the addition of an aluminum sleeve (*Figure 2*). The aluminum material of the sleeve was deliberately chosen to be X-ray transparent to allow microCT scanning of the formation.

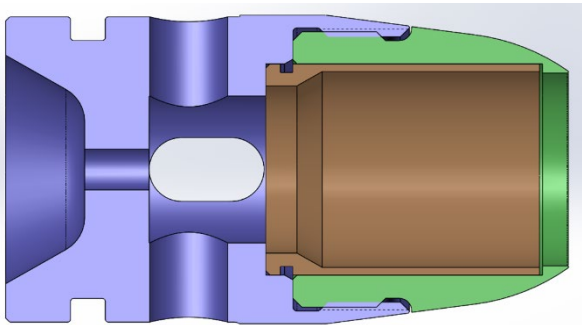


Figure 2 : Novel PSWC barrel assembly including driver (blue), cutter (green), and aluminum sleeve (brown)

When used downhole the three components are assembled as shown in *Figure 2*. After the core is recovered, the tool is disassembled to allow the sleeve to be removed without disturbing the sample material inside. The sleeve would then be returned to the lab for CT-scanning (Draper et al., 2022).

For this project, the quality of the resultant core was optimized, and a series of tests was conducted to refine the design of the cutter of the barrel to minimize observed damage. The design changes were guided by computer modelling of the formation behavior during the coring process, and several designs were developed and tested. The barrel design ultimately selected for testing and analysis has significantly less metal at the cutter edge than a traditional barrel (*Figure 2*), resulting in a narrower and sharper profile. Through testing, it was determined that this sharper profile significantly reduced damage to the cores.

3.2. Testing Program

Three phases of experimental tests were designed to evaluate the novel percussion sidewall coring tool and its performance and effectiveness under a variety of conditions:

Phase 1: Ambient quasi-static tests

Phase 2: Ambient dynamic tests

Phase 3: Reservoir-condition dynamic tests

3.2.1 Phase 1: Ambient Quasi-static

The objective of Phase 1 was to test the initial barrel assembly concept and design and calibrate penetration versus load data for subsequent dynamic tests. In Phase 1, PSWC barrels were pushed into blocks of outcrop sandstones (CG, SW, and BB) with a 100kN frame at velocities between 20 and 90 m/s. Sleeves and samples were then extracted from the test bullet and photographed and microCT-scanned (Lakshatanov et al., 2022).

3.2.2 Phase 2: Ambient Dynamic

Phase 2 tests were designed to test dynamic penetration of the barrel and improve the design to maximize recovery and minimize sample damage. These tests were conducted at ambient conditions with a transient overbalance applied to the sample face. The team wanted to evaluate the survivability of the barrel assembly, the effectiveness of the internal sleeve, ease of sample removal, and sample damage for different formations acquired at higher velocities (Lakshatanov et al., 2022).

3.2.3 Phase 3: Reservoir-Condition Dynamic

Phase 3 tests were designed to test the acquisition and recovery of sample material with dynamic penetration at reservoir conditions. An Overbalance Test Cell (OBTC) was designed where barrels were fired through pressurized water to evaluate the impact of charge, rock type, pressure, filter cake, and barrel design. Using this design, and adjustable overbalance between 0 – 1000 psi could be applied. All samples were saturated with either base oil or water (SS). Mudcake was simulated variously by layers of primer, paint, and silicone adhesive. Velocity of the bullet was directly measured for both phase 2 and phase 3 tests.

Several key variables were evaluated in Phase 3 test runs (3a, 3c, 3d, 3e), including cell pressure, cell velocity, gun pressure, muzzle velocity, barrel penetration, and length of recovered cores. These runs varied in the types of samples tested, the conditions tested, and test design including sleeve diameter and OBTC feed through. Most tests were conducted at 1000 psi cell pressure, with several tested at lower pressures (200 psi) to evaluate the impact of overbalance. Cell velocity is the velocity of the bullet prior to impact as measured in the OBTC by frangible pins recording the progress of the projectile over time. The gun pressure is the pressure at which the external airgun was fired, whereas the muzzle velocity is the velocity the projectile exiting the gun. Cell velocity is the speed of the barrel just before impact inside the OBTC. Penetration refers to the depth of penetration of the barrel into the sample material, which often correlates to the length of the recovered sample material (Lakshatanov et al., 2022).

4 Digital Rock Physics Imaging & Analysis

4.1. Imaging

High-resolution 3D micro-CT digital rock images of test and reference plugs were acquired using a Zeiss Versa microCT system located in BP's laboratories in Sunbury-on-Thames, United Kingdom. Micro-CT is ideally suited for

DRP imaging because it uses non-destructive X-ray scanning to generate 3D images. The Zeiss Versa micro-CT system enables imaging at multiple resolutions, facilitating sample characterization at multiple scales. Images were acquired at resolutions between 2 and 11 microns and image size was frequently greater than one billion voxels. Each voxel consists of a 16-bit grayscale attenuation value. These X-ray attenuation values are approximately proportional to the material density and chemistry and thus can be interpreted easily (Ketcham and Carlson, 2001; Cnudde and Boone, 2013).

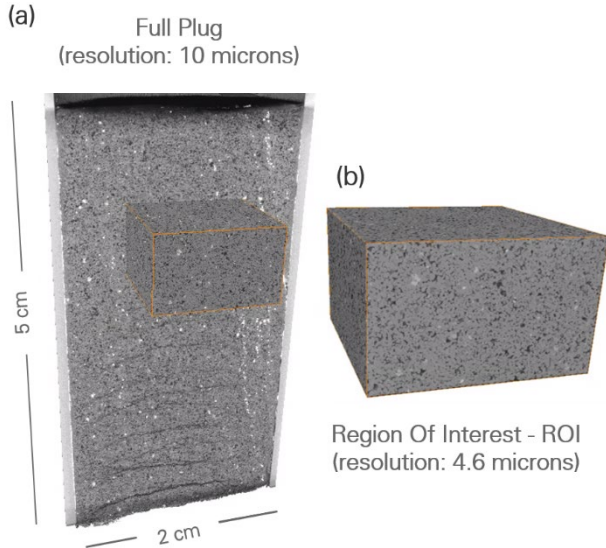


Figure 3: Micro-CT images of acquired sample material (CG). (a) Full plug image at 10 microns including sleeve, and region-of-interest (ROI) image location imaged at 4.6 microns (orange) acquired in an intact portion of the sample. The top of the image is the face of the sample. (b) Region-of-interest (ROI) image (Lakshtanov et al., 2022).

Material that had been tested and extracted as part of the novel PSWC testing program and control material were imaged from each sandstone formation. Where possible, both control and test samples were equally sized, and images were acquired at similar resolutions.

Two types of images were acquired as part of the validation program. Full plug images, where the entire width of the plug was imaged, were acquired typically at resolutions between 7 and 11 microns (Figure 3). This type of image is used to assess plug-scale damage, but resolution is not adequate for numerical simulation of rock properties such as porosity & permeability (Lakshtanov et al., 2022).

For numerical simulation of rock properties, region-of-interest (ROI) images were acquired at resolutions between 4 – 5 microns, with some higher resolution images also acquired (Figure 3). In conventional microCT imaging, image resolution is a function of sample size. ROI images are acquired using magnification objectives enabling higher resolution images to be acquired without subsampling the recovered cores. Where possible, these ROI images were acquired from zones identified within full plug images where visible damage was minimal or absent.

4.2. Damage Characterization

Full plug images were used to characterize visible damage to the plug and to locate intact, undamaged areas for ROI imaging and simulation. The damage typically encountered in the test plugs includes open fractures and zones of disaggregation, or grain crushing and zones of compaction. Often this damage occurs perpendicular to the plug axis and orthogonal to the direction of acquisition, but damage also occurs along the edge of the sample at the boundary of the PSWC bullet. This damage along the boundary between bullet and sleeve is often compactive and/or cataclastic and is referred to as a damage ‘rind’ (Lakshtanov et al., 2022).

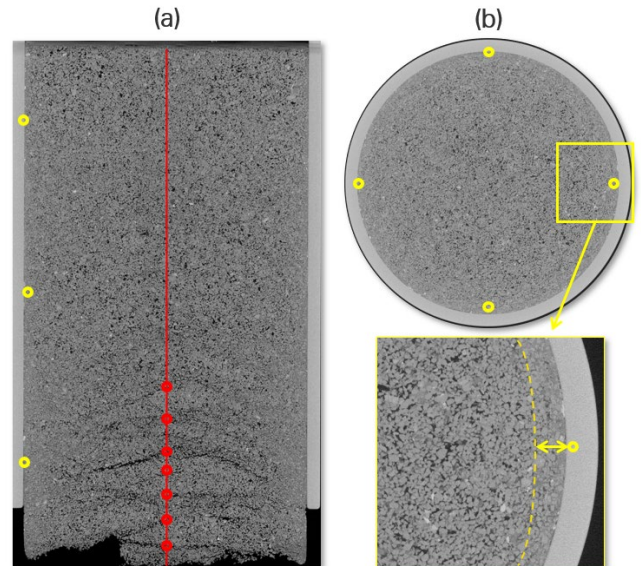


Figure 4: Damage characterization key metrics: (a) open fractures and cataclastic zones are identified along a transect (red line) along the plug’s (CG) length; (b) the rind thickness (compacted/crushed zone) is measured in several locations along the xy plane and the sample’s length (yellow circles) (Lakshtanov et al., 2022).

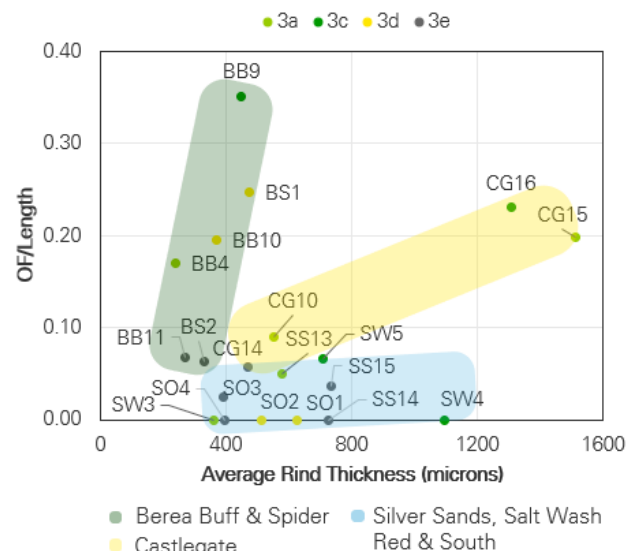


Figure 5: OF/length vs average rind thickness for Phase 3 (Reservoir-condition dynamic) test runs (Lakshtanov et al., 2022).

To characterize the observed damage, three indexes were compared across the various experiments. These indexes are: (1) average rind thickness, (2) open fracture ratio, and (3) cataclastic zone ratio. The average rind thickness is calculated as the average thickness of the visible damage at the sleeve boundary measured at three locations along the

plug's length (bottom, center, top) and the xy plane (north, south, east, and west). The open fracture and cataclastic zone ratios are computed as the number of fractures/ cataclastic zones encountered divided by the plug's length. The main damage metrics and occurrence in a test plug is shown in **Figure 4** and the two ratios are shown graphically in **Figure 5**. Clustering among formation samples is observed and highlighted by the colored clouds in the plot. The clustering trends are associated with similar rock properties among the formation samples such as porosity and UCS.

The effects of sample length on the observed damage at the boundary of the sample (average rind thickness) for various formations are explored in **Figure 6**, also shown clustered by formation. Longer samples within the same formation appear to exhibit a thicker damage rind around the edge. Some variation is evident where samples were tested with modified sleeve designs (i.e., CG14).

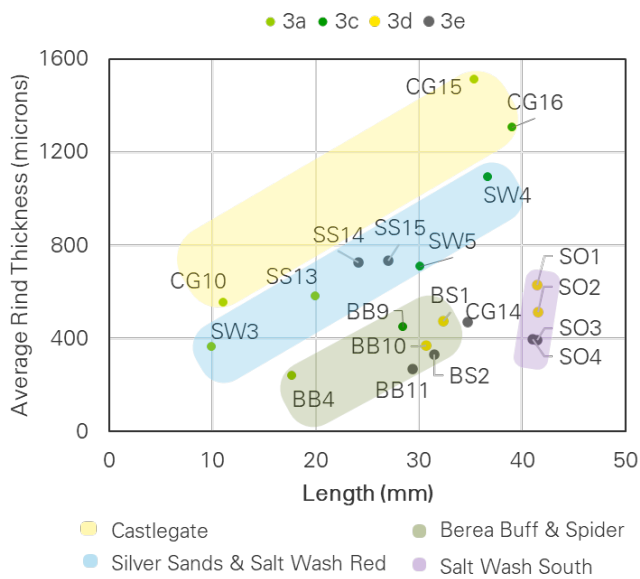


Figure 6: Average rind thickness vs. plug length for different series 3a, 3c, 3d, and 3e. The sample length and the observed damage exhibit a positive correlation associated with each formation (Lakshatnov et al., 2022).

Relationships between damage indices and select experimental parameters are explored in **Figure 7**. These plots show that plug velocity and penetration impact the amount of damage encountered in these plugs, but the type, amount, and distribution of damage is highly dependent on formation and rock properties.

Intact zones were chosen for high-resolution ROI imaging and DRP simulation. Intact zones were identified visually and characterized by the absence of cataclasis or open fractures and were often located near the center of the acquired sample.

4.3. Static Property Simulation

Prior to DRP numerical simulation, ROI images were processed to reduce noise, enhance coherence, and preserve grain edges. Post-filtering, the images were segmented based on the X-ray attenuation into pore and grain phases. To segment the image, we employed a region-growing thresholding algorithm (Caselles et al., 1997, Sheppard et al., 2004; Jones et al., 2007).

The segmented image is then used as a numerical grid for parallelized image-based Direct Numerical simulations

(Fredrich et al., 2014), part of BP's DRP workflow. Methods and results from our image-based petrophysical property simulations have gone through a rigorous verification and validation process as discussed in detail in Fredrich et al. (2014).

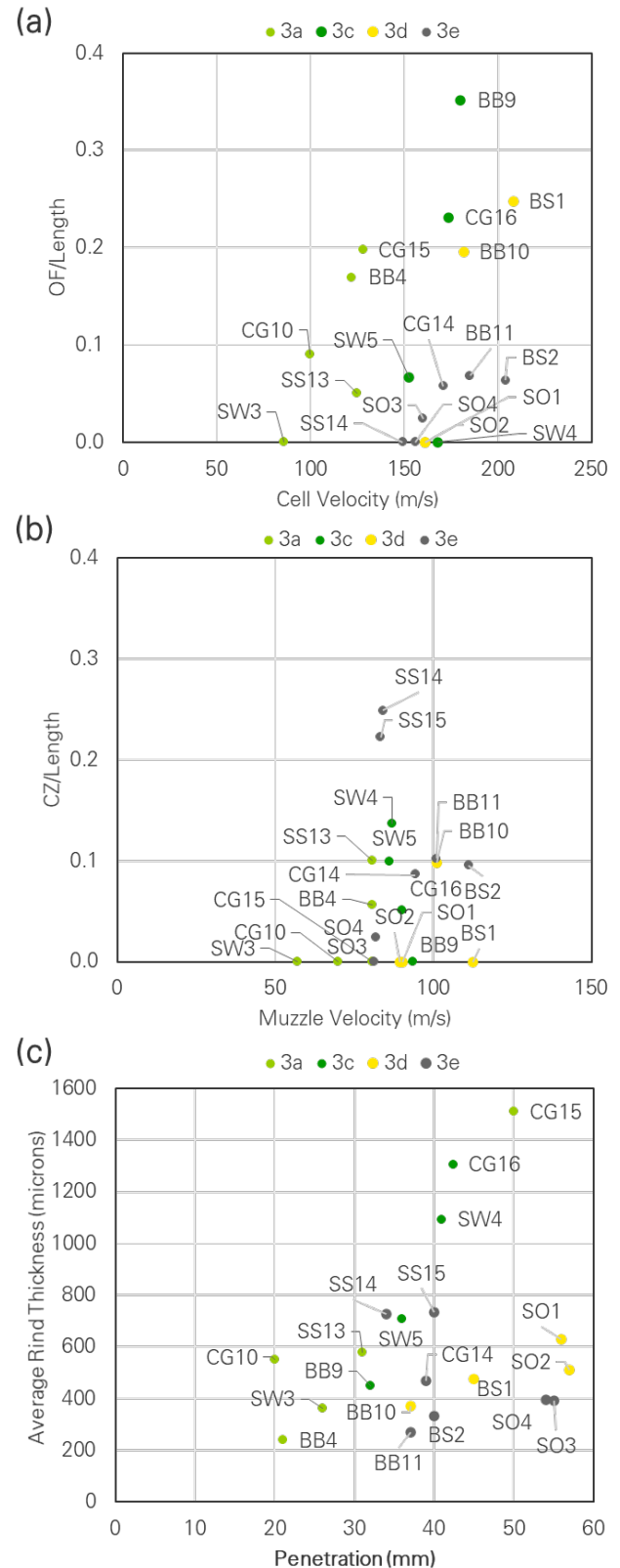


Figure 7: Damage metrics & experiment variable controls for various series of experiments. (a) open fracture ratio and cell velocity, (b) cataclastic zone ratio and muzzle velocity, (c) average rind thickness and penetration (Lakshatnov et al., 2022).

Both reference and test samples were imaged at high-resolution and processed through BP's internal DRP

workflow. Image-based porosity & permeability results were directly compared between reference and test samples, and routine core analysis results, where available.

DRP porosity versus permeability for both reference (control) and test samples are shown in **Figure 8**. Properties vary with formation and span a porosity range of over 15 porosity units and over two orders of magnitude permeability. SS and SO samples have the highest porosity & permeability whereas BS and BB have the lowest porosity & permeability. To compare results more directly from reference (control) and test plugs, we averaged porosity and permeability for each test series and formation and plotted it against averaged porosity and permeability for the reference sample results for the same formation. These averaged results are presented in **Figure 9** for Phase 3 tests.

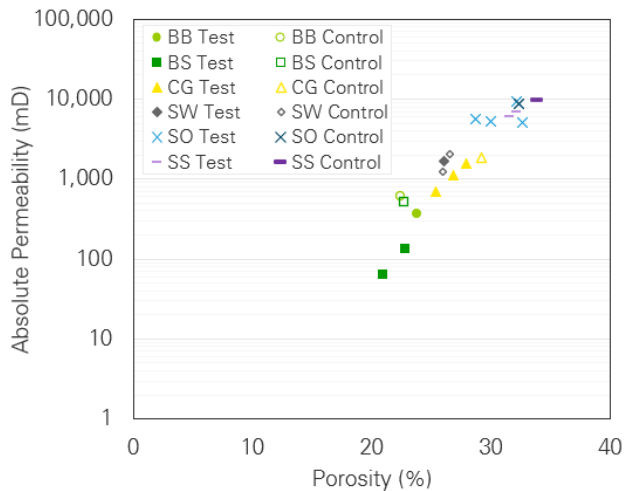


Figure 8: Permeability and porosity for various test and control plugs (Lakshatnov et al., 2022).

Digital rocks physics results for control samples and those acquired via test acquisition offer the best opportunity to compare changes to the sample fabric and texture. Although there is natural variability present in these samples that cannot be excluded, averaged results are within 5 porosity units and within one order of magnitude permeability between plugs extracted through the PSWC process and control plugs.

Routine core analysis was performed on reference material of all formations and provided in **Table 1**. Samples were dried at 105°C. Porosity was measured using a porosimeter at 1.3 MPa confining pressure. Permeability was measured with a porosimeter at 2.7 MPa confining pressure, whereas DRP properties were acquired at ambient conditions. Averaged RCA porosity and permeability versus DRP control and test sample porosity and permeability are shown in **Figure 10**.

5 Field Trialing the Novel PSWC Technology

Based on encouraging results from the laboratory testing and DRP evaluation, the next step in the novel PSWC development will be testing the tool in a downhole environment in a real formation. Wells targeting softer formations where this tool is likely to be used in the future have been prioritized.

Field trials of the novel percussion tool are scheduled to occur in 2022 and 2023. Where possible, multiple types of subsurface samples will be acquired including full bore core

and/or rotary sidewall core (RSWC) to provide a robust comparison. Traditional RSWC or full-bore core samples will be sent for both traditional routine laboratory core analysis (RCA) and digital rocks analysis. Novel PSWC will be analyzed with the Digital Rocks workflow and RCA where possible, and results compared to traditional core acquisition methods.

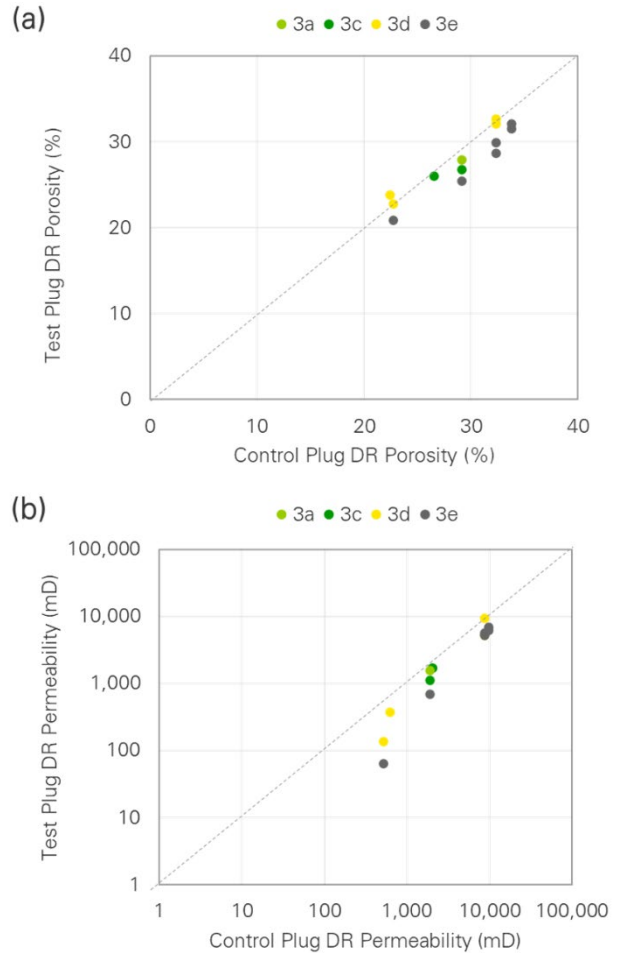


Figure 9: Control and test plug property comparison by experiment series: (a) porosity, (b) permeability (Lakshatnov et al., 2022).

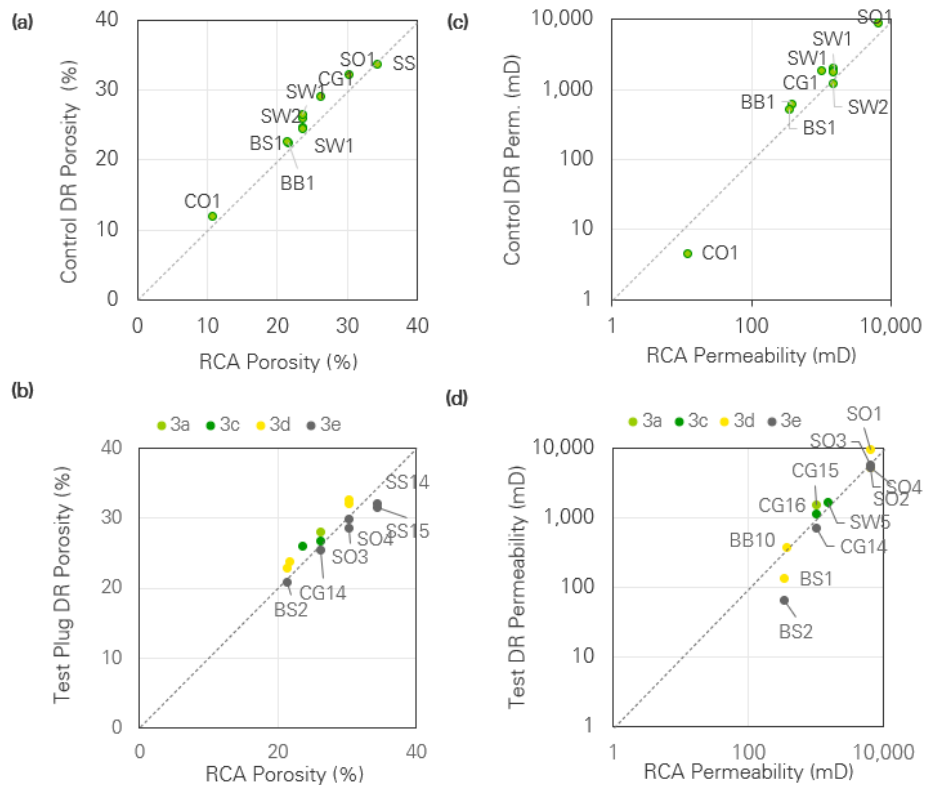


Figure 10: Control and test plugs comparison between laboratory (RCA) and DRP static properties. (a) Control DRP and RCA porosity, (b) Test DRP and RCA porosity, (c) Control DRP and RCA permeability, (d) Test DRP and RCA permeability.

6 Summary & Conclusions

Traditional PSWC have long been considered of limited value. However, with modification to the PSWC tool and barrel it is possible to acquire high quality cores that can be used as inputs into digital rock analysis. This solution is best suited for lower and moderate UCS formations.

In this paper we demonstrate ongoing validation and benchmarking of a novel percussion sidewall coring technique using DRP, a high-resolution three-dimensional image-based workflow. We characterize plug-scale damage with full plug imaging and introduce a semi-quantitative damage characterization scheme. We use these full plug images to identify areas with minimal visible damage for high-resolution ROI imaging to compute static rock properties for both test and control plugs.

The results show that although all samples tested with the novel percussion sidewall coring technique exhibit damage at the plug scale, internally, these plugs contain intact be analyzed in subsurface workflows with DRP.

The ability to couple percussion sidewall coring with DRP analysis in soft sands will enable a low-cost sampling strategy for traditional oil & gas and carbon capture & sequestration applications. BP has developed and maintained a mature DRP technology capability with in-house imaging and analysis capabilities for subsurface characterization workflows. This technology capability ensures that both the acquisition and analysis of PSWC is cost effective.

Next steps for this project include a field trial of the tool coupled with DRP analysis on plugs extracted from whole core and those extracted with the novel percussion sidewall coring technique. We anticipate these field trials occurring in 2022 & 2023.

References

1. Caselles, V., R. Kimmel, and G. Sapiro, 1997, Geodesic active contours, *International Journal of Computer Vision*, vol. 22, no. 1, p. 61-79.
2. Cnudde, V. and M. Boone, 2013, High-resolution X-ray computed tomography in geosciences: A review of the current technology and applications, *Earth-Science Reviews*, vol. 123, p. 1-17.
3. Draper, I., T. Gill, D. Lakshtanov, J. Cook, Y. Zapata, R. Eve, M. Lancaster, N. Lane, D. Saucier, G. Gettemy, and K. Sincock, Solving the challenge of acquiring low UCS cores for quantitative digital rock physics, *SPWLA 63rd Annual Logging Symposium*, <https://doi.org/10.30632/SPWLA-2022-0128>
4. Lakshtanov, D., Y. Zapata, D. Saucier, J. Cook, R. Eve, M. Lancaster, N. Lane, G. Gettemy, K. Sincock, E. Liu, R. Geetan, I. Draper, and T. Gill, 2022, Using digital rock physics to evaluate novel percussion core quality, *SPWLA 63rd Annual Logging Symposium*, <https://doi.org/10.30632/SPWLA-2022-0128>
5. Fredrich, J. T., D. Lakshtanov, N. Lane, E. B. Liu, C. Natarajan, D. M. Ni, and J. Toms, 2014, *Digital*

Rocks: Developing An Emerging Technology Through To A Proven Capability Deployed In The Business, SPE 170752.

6. Jackson, C. 2021. Tutorial: A Century of Sidewall Coring Evolution and Challenges, From Shallow Land to Deep Water. *Petrophysics* 62 (03), 230-243, <https://doi.org/10.30632/PJV62N3-2021t1>
7. Jones, A. C., C. H. Arns, A. P. Sheppard, D. W. Hutmacher, B. K. Milthorpe, and M. A. Knackstedt, 2007, Assessment of bone ingrowth into porous biomaterials using MICRO-CT, *Biomaterials*, vol. 28, no. 15, p. 2491-2504.
8. Ketcham, R. A. and W. D. Carlson, 2001, Acquisition, optimization and interpretation of X-ray computed tomographic imagery: applications to the geosciences, *Computers & Geosciences*, vol. 27, no. 4, p. 381-400.
9. Sheppard, A. P., R. M. Sok, and H. Averdunk, 2004, Techniques for image enhancement and segmentation of tomographic images of porous materials, *Physica A: Statistical mechanics and its applications*, vol. 339, no. 1, p. 145-151.
10. Webster, G. M., & Dawsongrove, G. E. 1959. The Alteration of Rock Properties by Percussion Sidewall Coring. Paper SPE 1159-G prepared for presentation at Fall Meeting of Los Angeles Basin Section in Los Angeles, California, October 16-17, <https://doi.org/10.2118/1159-G>

THz Imaging to Map the Microporosity Distribution in Carbonate Rocks

Shannon L. Eichmann^{1,*†}, Jacob Bouchard^{2†}, Hooisweng Ow³, Doug Petkie², and Martin Poitzsch³

¹Aramco Research Center – Houston, Aramco Services Company, Houston, TX

²Department of Physics, Worcester Polytechnic Institute, Worcester, MA

³Aramco Research Center – Boston, Aramco Services Company, Boston, MA

† Contributed equally to this work.

Abstract. Terahertz (THz) spectroscopy is a non-destructive tool used in many industries to analyze materials including measuring the water content and the distribution of water in biological samples. THz Time-Domain Spectroscopy (THz-TDS) measures the dielectric and structural properties of a sample by probing it with an ultrafast THz pulse and measuring the change in amplitude and phase. In this study we demonstrate the use of THz-TDS imaging to quickly map lateral variations in microporosity (ϕ_μ) using the THz attenuation due to water in the pores after clearing the large pores via centrifugation. Three carbonate rock samples with differing ϕ and pore size distributions were selected for this study. Three water saturation states were produced for each sample: saturated, centrifuged, and dry. At each saturation state, the sample is weighed and imaged using THz-TDS to spatially map and measure ϕ_μ . The results show that for each sample the ϕ_μ obtained using THz-TDS imaging is in excellent agreement with that obtained from both mass balance and MICP. In addition, the THz-TDS maps show significant differences in the spatial distribution of the microporosity for samples having similar composition. This method provides a means to measure ϕ and ϕ_μ while mapping the spatial distribution of ϕ_μ toward improved petrophysical characterization of carbonate reservoir rocks.

1 Introduction

Carbonate reservoirs hold up to 60% of the global petroleum reserves and contain a wide range of pore types and sizes which are non-uniformly distributed compared to sandstone reservoirs where the pores have a narrow pore size distribution (PSD) and are more uniformly distributed throughout the rock matrix [1, 2]. A suite of reservoir characterization methods covering the kilometer to nanometer length scales is required to guide production and reservoir management decisions. Of particular interest for carbonate reservoirs, is the amount of microporosity (ϕ_μ) (i.e., percentage of pores <1 μm diameter) and its distribution within the rock as these pore sizes are commonly linked to the residual and bypassed oil following primary and secondary depletion [3-7].

Using laboratory analyses, geologists and engineers gain an understanding of how the rock properties (i.e., porosity (ϕ), permeability, PSD, wettability, etc.) change with depth [8-10]. Typical methods of measuring ϕ include mercury intrusion, optical and scanning electron microscopy (SEM), computed tomography (CT), and gas porosimetry [2, 10-15]. While accurate, non-imaging methods may be destructive or make use of hazardous materials to provide bulk measurements of ϕ . Imaging methods, however, can be limited by a trade-off between field-of-view (FOV) and resolution to produce ϕ distribution maps.

X-Ray CT, optical microscopy, and SEM are common imaging methods used to evaluate ϕ and PSD in conventional and unconventional reservoir rocks. CT and micro-CT provide 3D images of whole core and core plugs at 100s to 10s of microns/pixel resolution. The resolution provided by CT and even micro-CT can be insufficient to effectively map ϕ_μ distributions in carbonate rocks. In some examples, heavy ion tracers have been used to dope imbibed fluids to track fluid mobility including forced displacement and diffusion within unresolved ϕ using x-ray CT [16, 17]. Petrography using optical and fluorescence microscopy provide resolutions ranging from a few hundred nanometers up to 10s of microns [3, 18-21]. These techniques are quite versatile and through detailed analyses geologist can provide information about mineralogy, depositional environment, ϕ and PSD. SEM provides the highest resolution of these imaging techniques, down to a few nanometers/pixel, where both 2D and 3D rock images can be produced, and ϕ and PSD be measured using image processing methods. While large tiled 2D SEM (pores larger than ~ 5 nm) and laser scanning confocal microscopy (pores larger than ~ 200 nm) images can be produced to maintain high resolution while maintaining the ability to image a plug face, these images are typically very large and challenging process leading to slow turnaround time between data collection and quantification.

* Corresponding author: shannon.eichmann@aramcoamericas.com

Terahertz (THz) time-domain spectroscopy (TDS) is a relatively new method with significant development in the past 30 years [22-25]. THz-TDS operates over the 100 GHz (~30 μm) to 10 THz (~3 mm) bandwidth where the spectrometer produces a THz pulse which transmits through the sample and different proportions of the pulse are scattered, reflected, absorbed, or transmitted depending on the material properties. A Fourier transform of the transmitted time-dependent signal provides the absorbed and scattered frequencies in the spectrum. This method has been used for the investigation of chemicals [26], restoration of artwork [27] [28], water content of tissues and plants [29-31], and imaging for security applications [32]. Previous work established that THz TDS is capable of measuring bulk porosity [33, 34]. More specifically measuring ϕ and ϕ_{μ} of carbonates by making use of the strong water absorption in the THz spectrum and its change during dehydration [14]. This prior study, however, did not demonstrate the ability to map the ϕ_{μ} distribution which is relevant to reservoir characterization.

As the field of THz spectroscopy has matured, turnkey benchtop setups have been made available that greatly simplify the application of this technique. By utilizing a turnkey system, THz TDS could be integrated into a core analysis workflow with very little difficulty. In this paper we demonstrate a method of using THz TDS of carbonate rocks at different water saturation states to generate 2D ϕ_{μ} maps. These maps show spatial variations in the ϕ_{μ} within each sample and allow comparisons of these distributions between samples. These micropores and their distributions are challenging or impossible to resolve at a large FOV with most core imaging techniques. The results show that when the THz TDS ϕ_{μ} map data are combined with mass balance, the relative amount of microporosity in each sample can be estimated and agree well with bulk measurements.

2 Materials and Methods

2.1 Samples

Three carbonate core plug samples 1.5" in diameter were used: one carbonate plug from a field (Sample 1) and two Indiana limestone core plugs from Kocurek Industries (Caldwell, TX) (Samples 2 and 3). Samples 2 and 3 were cut into 2 mm, 4 mm, and 6 mm thick wafers and Sample 1 was cut into 2 mm and 4 mm thick wafers which were then cut in half to produce half-moon shaped samples for THz TDS imaging. The remaining half plug of each sample was used for additional characterization. Each half-moon sample was pre-cleaned to remove any pore occluding dust from the cutting process by submerging the sample in water under vacuum for two days. The sample was then centrifuged and dried in an oven at 100 °C.

2.2 Terahertz Time Domain Spectroscopy (THz-TDS)

Terahertz time domain spectroscopy (THz TDS) probes samples with short pulses of terahertz radiation and the system monitors the amplitude and phase of the transmitted pulse. The small THz wavelengths can probe small features and interact with water molecules (Figure 1a). Water strongly absorbs THz radiation, thus intensity maps from the peak-to-peak pulse amplitude at collected at 0.5 mm/pixel across samples at different saturation states correspond to the water distribution in a sample (Figure 1b). A Toptica Teraflash system equipped with an imaging gantry extension was used to measure the peak-to-peak pulse amplitude over a 70 ps window with two measurements taken at each point and averaged together.

Porosity maps were generated from three intensity maps of the same sample at different saturation states: a) fully saturated, b) centrifuged to partial saturation, and c) dried. The maps are compared using a custom image analysis script written for IgorPro to align the sample within each map, compare the intensity at each pixel, and generate porosity maps. The map of the saturated ϕ was generated by comparing maps (a) and (c), the map of the ϕ_{μ} was generated from maps (b) and (c), and the map of macroporosity (ϕ_M) was generated from (a) and (b).

2.3 Workflow

Half-moon samples were measured in sequence using the workflow shown in Figure 1c. The dry sample was weighed to obtain the initial dry mass, $m_{dry,i}$, and then vacuum saturated for two days in the ion-saturated solution remaining from the pre-cleaning step to reduce calcium carbonate dissolution due to its solubility in water. The saturated sample was removed from the vacuum chamber and fluid, excess water blotted, and weighed again to obtain the saturated mass, m_{sat} , and a THz-TDS map (19 mm x 42 mm; 0.5 mm/pixel) was collected to map the saturated pores.

The sample was centrifuged using an Eppendorf 5801 with a FA-45-6-30 fixed angle rotor to clear large pores based on the applied capillary pressure assuming a contact angle of 45° and the interfacial tension of 72.8 mN/m. Following centrifugation, the sample was weighed to obtain the centrifuged mass, m_{cent} , and another THz TDS map collected to map the micropores. Finally, the samples are oven dried at 100 °C, weighed to obtain the final dry mass, $m_{dry,f}$, and the final THz TDS spectroscopy map collected.

The full workflow was repeated two to three times per 2 mm, 4 mm, and 6 mm samples to clear pore with pore diameter (d_p) greater than 1 μm . If samples fractured during centrifugation, the pieces were recovered from the centrifuge tube, weighed, and pieced back together for THz mapping.

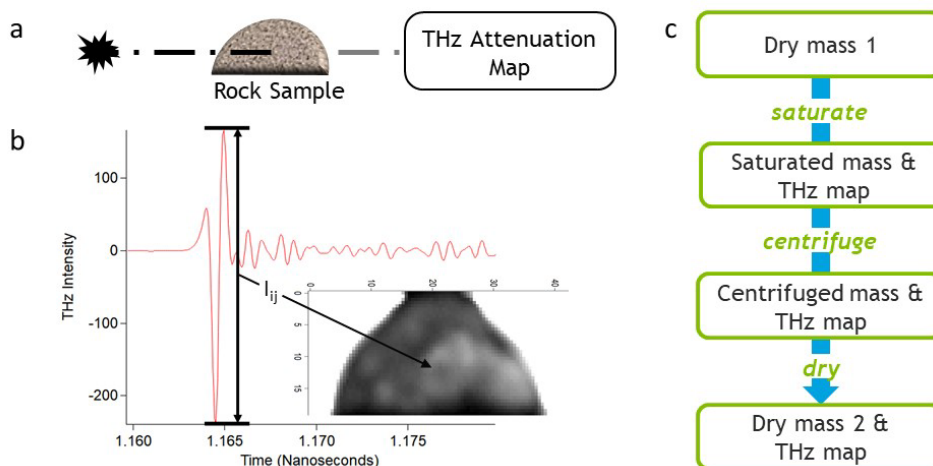


Figure 1. Schematic of the measurement scheme and workflow. (a) The Terahertz (THz) beam passes through the rock sample to produce a THz-TDS attenuation map. (b) The THz-TDS pulse (red) and the marked peak-to-peak amplitude (black) used to generate the attenuation map where the darkest pixels are the most attenuating and the brightest the least. (c) THz-TDS workflow.

2.3.1 Porosity and Microporosity by Mass

The mass data were used to calculate the total (ϕ_m) and microporosity ($\phi_{\mu,m}$). The total porosity was calculated as the ratio of the saturated pore volume, V_p , to the bulk volume, V_b , and V_p is calculated using the mass balance between the water saturated rock, m_{sat} , and dry rock, m_{dry} , and the density of water, ρ_w , as 1 g/cm^3 .

The bulk density, ρ_b , of each sample was calculated from the mass and dimensions of each plug. The bulk density of Samples 1 and 2 is 2.2 g/cm^3 and Sample 3 is 2.3 g/cm^3 .

The amount of $\phi_{\mu,m}$ is determined as the ratio of the volume of micropores, $V_{\mu,pores}$, to V_b where $V_{\mu,pores}$ is calculated from the mass balance using the mass of the rock after centrifugation, m_{cent} , and the final dry mass of the rock, $m_{dry,f}$.

2.3.2 Microporosity by THz

While the goal of the THz imaging is not to directly calculate microporosity but to provide maps of the spatial variations in the microporosity within the sample, the sensitivity of the measurement to the water in the sample does provide a means to estimate the microporosity from THz ($\phi_{\mu,THz}$) as shown in Eqn. 1

$$\phi_{\mu,THz} = avg \left(\frac{\left(\frac{THz_{cent,ij}}{THz_{sat,ij}} \right)}{\max \left(\frac{THz_{cent,ij}}{THz_{sat,ij}} \right)} \right) * avg \left(\frac{\left(\frac{THz_{sat,ij}}{THz_{dry,ij}} \right)}{\rho_b * \max \left(\frac{THz_{sat,ij}}{THz_{dry,ij}} \right)} \right) \quad (1)$$

where $THz_{cent,ij}$, $THz_{sat,ij}$, and $THz_{dry,ij}$ are the THz attenuation map intensity data at each ij pixel within a region of interest (ROI) selected around the rock boundary. The maximum of the ratio of the two maps was

used to account for power fluctuations that might occur due to fluctuations in the humidity of the air and changes in alignment. The relative amount of the relative amount of microporosity, $\phi_{\mu,THz}$, to total porosity from mass, ϕ_m was then calculated for comparison to mass balance and MICP.

2.4 Mercury Injection Capillary Pressure (MICP)

Remaining portions of the plugs sampled for THz imaging were used for mercury injection capillary porosimetry (MICP) analysis (MetaRock Laboratories, Houston, TX). A full description of the MICP technique and apparatus can be found in general petrophysics textbooks [12]. Plug samples were tested in the as-received state and then dried in an oven at $100 \text{ }^\circ\text{C}$. The maximum pressure applied in MICP is 60,000 psi. The microporosity from MICP $\phi_{\mu,MICP}$ were obtained from the cumulative PSD curve.

2.5 X-Ray Computed Tomography (CT)

CT scans were collected using a NSI X5000 Industrial CT scanner (North Star Imaging, Inc.) to observe the grain and large pores within the remaining half-plugs used for MICP. The scans were performed at 720 views per rotation where the reconstructed voxel size was $50 \text{ } \mu\text{m} \times 50 \text{ } \mu\text{m} \times 50 \text{ } \mu\text{m}$. The CT radiographs were reconstructed using the iTomoFDK software (iTomoography Corporation, Houston, TX). GeoDict (Math2Market) was used to generate 3D renderings of the CT scans and segment the large pores using a simple intensity cutoff.

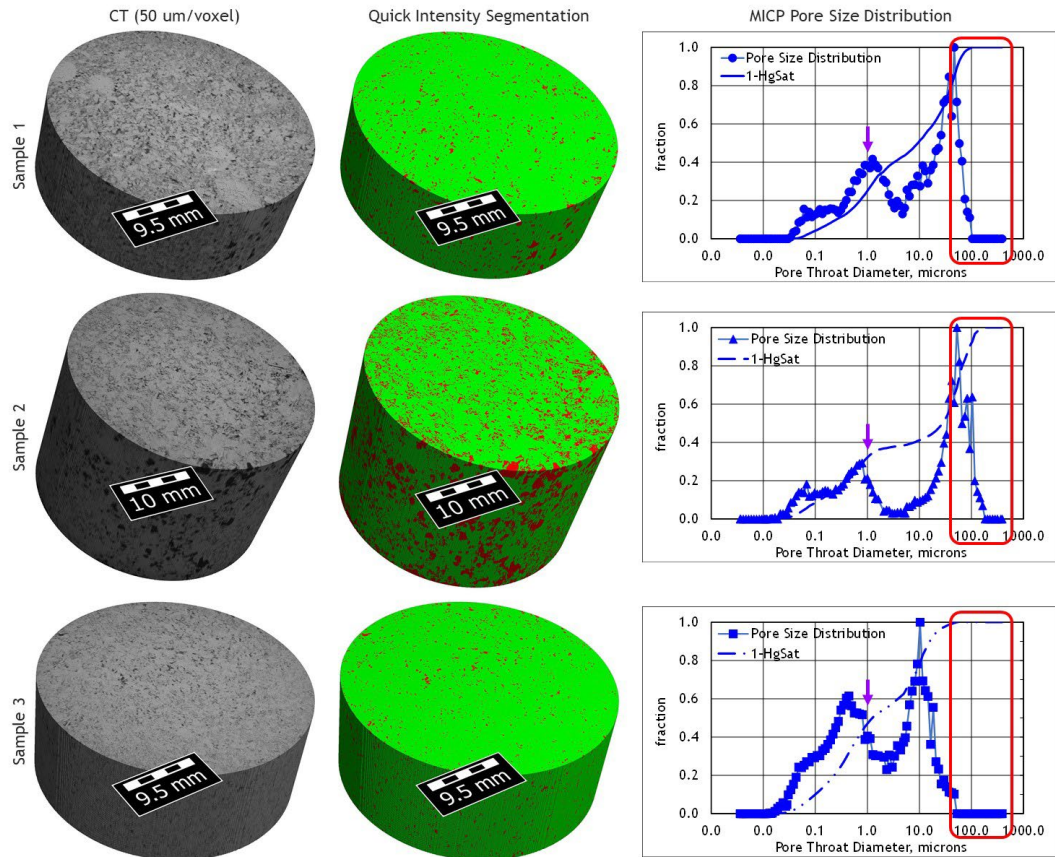


Figure 2. X-Ray CT Scans and MICP Pore Size Distributions. (left) CT scan renderings of the portions of each sample used for MICP analysis. The black to dark grey voxels are large pores and the light grey voxels contain matrix minerals and unresolved pores. (middle) Segmented CT scans showing resolvable pores (red) with pore sizes larger than the voxel size ($50\ \mu\text{m} \times 50\ \mu\text{m} \times 50\ \mu\text{m}$). (right) Normalized PSD and cumulative curves from MICP. Red box indicates the approximate pore size range of the segmented pores and the purple arrows indicate the pore size cutoff for micropores ($d_p < 1\ \mu\text{m}$).

3 Results and Discussion

3.1 THz Maps

Figure 2 shows CT scans of the samples used for MICP analysis in grayscale and segmented to show large pores. The normalized PSD obtained by MICP from each sample is also shown where the red box indicates the approximate range of pore sizes resolvable in the CT reconstructions. The MICP data confirm that few pores in the sample are on the order of 10s of microns and the relative amount of micropores with d_p smaller than $1\ \mu\text{m}$ varies between 20% and 50% of the total porosity (see also Figure 5).

Figure 3 shows a photo, THz TDS attenuation maps, and THz TDS difference maps of the 4mm thick section of Sample 2. The color variations in the photo (Fig. 3a) are due to variations in mineralogy, cementation, porosity, and surface roughness.

The attenuation maps shown in Fig. 3b-3d show grayscale intensity variations which change with the presence of water, scattering, and to a lesser extent with the rock composition. Thus, the darkest pixels in the saturated

(Fig. 3b) and centrifuged (Fig. 3c) maps are those that contain the most water where the intensity variations in the dry map (Fig. 3d) are related to compositional and structural variations. Edge artifacts, visible as a high-intensity ring along the edge of the sample in Figs. 3b-3d, are caused by the knife edge effect wherein the sharp edge of the sample causes some radiation to diffract around it and blurs the THz signal.

The difference maps in Figures 3e-3g show how the attenuation changed between steps. The areas of the difference map comparing the saturated versus dry attenuation maps (Fig. 3e) shows the regions of the sample that became saturated with water upon vacuum saturation. Similarly, the areas of difference maps comparing the saturated versus centrifuged attenuation maps (Fig. 3f) shows the regions of the sample that lost the most water during centrifugation, meaning those containing the pores larger than the cutoff (i.e., macropores). The areas of the difference map comparing the centrifuged versus dry attenuation maps (Fig. 3g) shows the regions of the sample that lost water during drying, meaning those regions containing the pores smaller than the cutoff (i.e., micropores). When

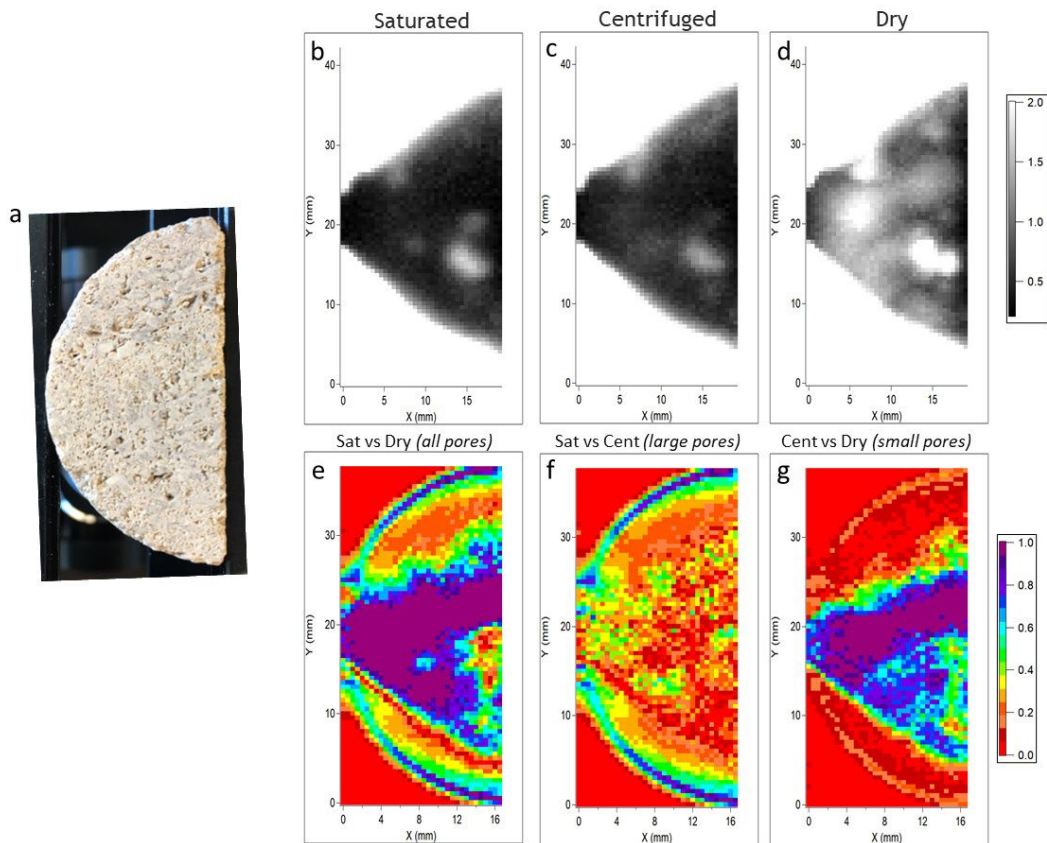


Figure 3. THz-TDS attenuation and attenuation difference maps of Sample 2 (4 mm thick) as representative data examples. (a) photo, (b-d) normalized attenuation maps of the saturated, centrifuged, and dry samples, and (e-g) difference maps between the saturated and dry, saturated, and centrifuged, and centrifuged and dry attenuation maps to represent the spatial variation of the saturated pores, macropores ($d_p > 1 \mu\text{m}$), and micropores ($d_p < 1 \mu\text{m}$).

comparing each of the difference maps, in Fig. 3e-3g, the locations of the macro- and micropores can be seen. In this example there appears to be a clear band of micropores through the center of the sample (Fig. 3g) whereas the macropores are more evenly distributed (Fig. 3f).

Figure 4 shows the photos and macroporosity and microporosity maps for all three samples. The maps show how the distribution of macro- and micropores vary in each of the samples. Sample 1 shows a concentration of micropores in the center of the sample (green and purple pixels) and concentrated micropores on the left. Sample 2 shows distributed macropores (orange, yellow, and green pixels) and a concentrated band and patches of micropores. Finally, Sample 3 shows distributed macro- and micropores. In each case the THz difference maps indicate regions of co-localized macro- and micropores as would be expected for carbonate rocks. Sample 3 appears to have more co-localization of the macro- and micropores where Sample 1 has less, and Sample 2 has the least. This will be confirmed in future work with thin section and high-resolution imaging studies of these samples.

3.2 Porosity and Microporosity Comparisons

Figure 5 compares the measured porosity and microporosity for each sample. The total porosity was measured on the half-plugs by MICP and on the THz samples by mass balance (mass) (Fig. 5a). The microporosity below the $d_p = 1 \mu\text{m}$ (purple data) pore clearing cutoff (Fig. 5a) was measured on the THz samples by mass balance (mass) and from the THz maps using Eqn. 1 (THz), and on half-plugs by MICP (MICP). Figure 5b shows the relative amount of the total porosity that is microporosity from the mass balance (mass) and THz maps on the THz sample (THz) compared to what was measured by MICP on half-plugs (MICP) for the $d_p = 1 \mu\text{m}$ (purple data) pore clearing cutoff. The mass balance and THz porosity and microporosity data are the average of the measurements and the error bars are one standard deviation. The mass balance and THz maps are measured on the same half-moon samples and include the 2mm, 4mm, and 6mm thick samples where the MICP data was measured on a half plug.

The porosity data (Fig. 5a) shows that the total porosity of the samples ranges from 20% to 17% and decreases from Sample 1 with the highest to Sample 3 with the lowest total porosity. Comparisons of the dry mass before and after each run showed some mass loss during the process

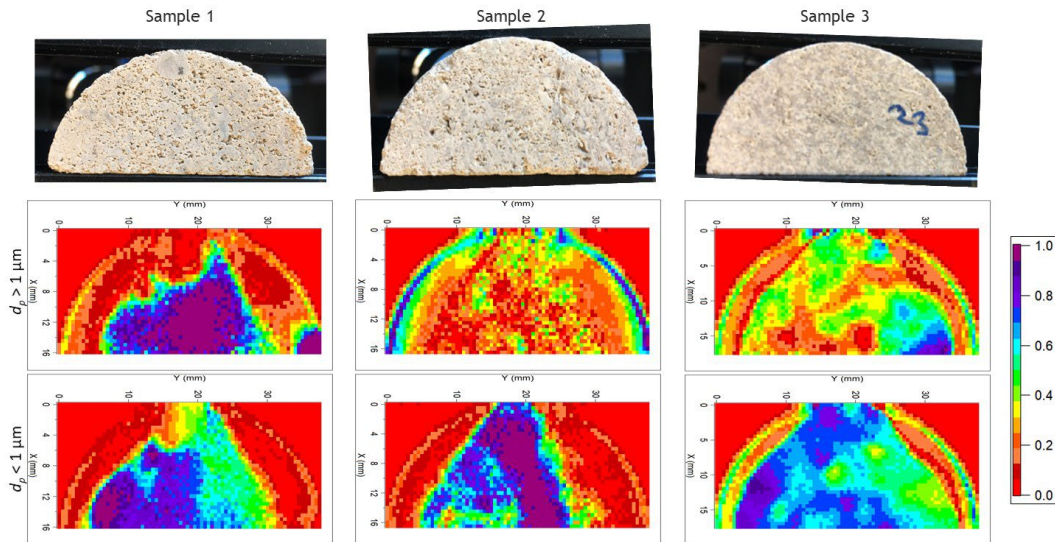


Figure 4. THz-TDS attenuation difference maps of each sample (4 mm thick) showing macro- and microporosity. (top) photo, (middle) macropores ($d_p > 1 \mu\text{m}$), and (bottom) micropores ($d_p < 1 \mu\text{m}$).

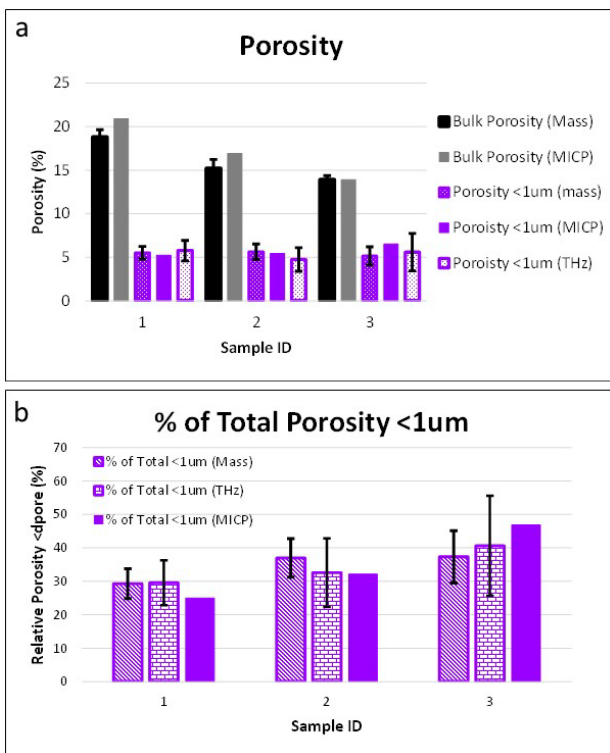


Figure 5. Porosity and microporosity comparisons. (a) Total porosity and microporosity for Samples 1-3. Total porosity from MICP (grey) and mass balance (black). The microporosity with $d_p < 1 \mu\text{m}$ from mass balance (white dots), MICP (solid), and THz-TDS maps (purple dots). (b) Relative amount of the total porosity attributed to the microporosity with $d_p < 1 \mu\text{m}$ from mass (diagonal lines), THz-TDS (brick), and MICP (solid). In both (a) and (b), the THz and mass data are the average of data collected on the half mood samples and the error bars represent one standard deviation.

which was attributed to erosion processes and potential loss of mechanical stability of small pores and rock material along the boundaries. Despite this, the comparison between the porosity and relative amount of microporosity measured for $d_p > 1 \mu\text{m}$ pore clearing

threshold are in excellent agreement between all methods, mass balance, THz maps, and MICP (Fig. 5a and 5b).

4 Conclusions

This paper demonstrates the use of THz TDS to map pore structure heterogeneity in carbonate rocks using the THz attenuation due to water-filled pores. Three carbonate rocks with varying ϕ and PSD were used to demonstrate the effectiveness of the method. When the samples are centrifuged to selectively displace water with air in pores larger than a selected pore size threshold, the THz TDS maps provide a unique capability to map large field-of-view ϕ_μ distributions (Fig. 3 and Fig. 4) within these bimodal pore systems.

The workflow presented also demonstrates the ability to quantify the percentage of the ϕ_μ using the data obtained from the THz and mass balance on the samples (Fig. 5). When compared to total and microporosity distributions obtained from MICP the results from the presented workflow are in good agreement.

In summary, the workflow presented in this paper provides a first demonstration of using THz TDS to map and quantify ϕ_μ in carbonate rocks which have a bimodal pore size distribution and contain a significant amount of ϕ_μ . Thus, given the excellent agreement between the relative amount of microporosity at $d_p < 1 \mu\text{m}$, the threshold for formation evaluation, obtained by the THz TDS workflow compared with that from MICP and the added ability to map microporosity spatial variations, we believe that this workflow provides valuable information for future incorporation into special core analysis workflows.

Acknowledgements

We would like to thank Ayrat Gizzatov, Gary Eppler, and Qiushi Sun for their help with sampling, sample preparation, and CT scanning.

References

1. Chopra, S., N. Chemingui, and R.D. Miller, *The Leading Edge*, **24** 488-489 (2005).
2. Schön, J.H., *Physical properties of rocks: Fundamentals and principles of petrophysics*. 2015: Elsevier.
3. Cantrell, D.L. and R.M. Hagerty, *GeoArabia*, **4** 129-154 (1999).
4. Clerke, E.A., *SPE Journal*, **14** 524-531 (2009).
5. Patzek, T.W., A.M. Saad, and A. Hassan, *Energies*, **15** 1243 (2022).
6. Pittman, E.D., *AAPG Bulletin*, **55** 1873-1878 (1971).
7. Stanley, R., S. Guidry, and H. Al-Ansi. *Microporosity spatial modeling in a giant carbonate reservoir*. in *International Petroleum Technology Conference*. 2015. OnePetro.
8. Ibrahim Khan, M. and M.R. Islam, *The Petroleum Engineering Handbook: Sustainable Operations*. 2007: Gulf Publishing Company.
9. Baker, R.O., H.W. Yarranton, and J.L. Jensen, *Practical Reservoir Engineering and Characterization*. 2015: Gulf Professional Publishing.
10. Ramsey, M., Schlumberger., (2019).
11. Conner, W., et al., *Langmuir*, **2** 151-154 (1986).
12. Dandekar, A.Y., *Petroleum reservoir rock and fluid properties*. 2013: CRC press.
13. Funk, J., et al. *Core imaging—twenty five years of equipment, techniques, and applications of X-ray computed tomography (CT) for core analysis*. in *International Symposium of the Society of Core Analysts*. 2011.
14. Heshmat, B., et al., *Optics express*, **25** 27370-27385 (2017).
15. Tiab, D. and E.C. Donaldson, *Petrophysics: theory and practice of measuring reservoir rock and fluid transport properties*. 2015: Gulf professional publishing.
16. Singh, K., et al., *Scientific data*, **5** 1-8 (2018).
17. Zhang, Y., et al., *Fuel*, **207** 312-322 (2017).
18. Hackley, P.C., et al., *International Journal of Coal Geology*, **241** 103745 (2021).
19. Hurley, N.F., K. Nakamura, and H. Rosenberg, *Journal of Sedimentary Research*, **91** 735-750 (2021).
20. Jobe, T., et al., *Petroleum Geoscience*, **24** 323-334 (2018).
21. Jobe, T.D., *Sedimentology, chemostratigraphy and quantitative pore architecture in microporous carbonates: Examples from a giant oil field offshore Abu Dhabi, UAE*. 2013: Colorado School of Mines.
22. Pahlevaninezhad, H., B. Heshmat, and T.E. Darcie, *IEEE Photon*, **3** 307-310 (2011).
23. Redo-Sanchez, A., et al., *Nature Communications*, 12665 (2016).
24. Heshmat, B., et al., *Nano Letters*, **12** 6255-6259 (2012).
25. Heshmat, B., H. Pahlevaninezhad, and T.E. Darcie, *IEEE Photonics Journal*, **4** 970-985 (2012).
26. Walther, M., et al., *Analytical and Bioanalytical Chemistry*, 1009-1017 (2010).
27. Abraham, E., et al., *Applied Physics A*, **100** 585-590 (2014).
28. Fukunaga, K. and M. Picollo. *Terahertz time domain spectroscopy and imaging applied to cultural heritage*. in *13th International Symposium on Nondestructive Characterization of Materials*. 2013. Le Mans, France.
29. Banerjee, D., et al., *Optics express*, **16** 9060-9066 (2008).
30. Castro-Camus, E., M. Palomar, and A. Covarrubias, *Scientific reports*, **3** 1-5 (2013).
31. Wang, Y., et al., *Optics Express*, **18** 15504-15512 (2010).
32. Kemp, M., et al. *Security applications of terahertz technology*. in *AeroSense 2003*. 2003. Orlando, Florida.
33. Bawuah, P., et al., *Journal of Infrared, Millimeter, and Terahertz Waves*, **41** 450-469 (2020).
34. Naftaly, M., et al., *MDPI Sensors*, **20** (2020).

Angle-dependent ultrasonic wave propagation in rocks for estimating high-resolution elastic properties of complex core samples

Daria Olszowska*, Gabriel Gallardo-Giozza, Domenico Crisafulli, and Carlos Torres-Verdín

The University of Texas at Austin, Austin, TX, USA

Abstract. Due to depositional, diagenetic, and structural processes, reservoir rocks are rarely homogeneous, often exhibiting significant short-range variations in elastic properties. Such spatial variability can have measurable effects on macroscopic mechanical properties for drilling and production operations. We describe a new laboratory method for acquisition of ultrasonic angle-dependent measurements of reflected waves that delivers high-resolution, continuous descriptions of P- and S-wave velocity and anisotropy along the surface of the rock sample. Reflection coefficient vs. incidence angle is the main source of information about rock elastic properties. The acquired measurements are matched to numerical simulations to estimate P- and S-wave velocity and density of the porous sample and their variations within the rock specimen, providing continuous descriptions of sample complexity. Data collected from various locations on the rock specimen are subsequently used to construct 2D models of elastic properties along the surface of the rock sample. P- and S-wave velocities estimated with this method agree well with acoustic transmission measurements for most homogeneous rocks. The spatial resolution of the method is limited by receiver size, measurement frequency, and incidence angle. At high incidence angles, the surface area sensitive to the measurements increases and, consequently, the spatial resolution of the corresponding reflection coefficient decreases across neighboring layers.

1 INTRODUCTION

Sedimentary rocks are rarely homogeneous, often exhibiting high degrees of spatial heterogeneity due to various geological processes such as deposition, diagenesis, and tectonics. As exemplified in Figure 1, alternating layers of stiff and compliant rocks, with thicknesses varying from millimeters to meters, pose challenges for drilling and production operations. Knowledge of the mechanical properties of rocks and their spatial variations is crucial for formation strength predictions, wellbore and perforation stability, sand production evaluation, and subsidence problems [1-3]. Presence of heterogeneities below the resolution of standard laboratory/field techniques leads to spatial averaging effects that mask true rock properties. This behavior can lead to significant consequences, such as wellbore failure, or critical differences between hydraulic fracturing models and actual field observations [4-6]. There is a great need to detect changes in rock elastic properties at a fine scale to mitigate exploration and development risks.

Most standard laboratory techniques fail to estimate small-scale variations of rock elastic properties (static and dynamic). Their resolution is often limited by sample size, yielding average values for thinly-laminated rocks. Presence of pre-existing fractures can also exacerbate measurement biases. The latter biases are commonplace in standard rock loading and ultrasonic transmission methods, which can give unreliable results for complex rock samples. A solution to this averaging problem is the introduction of continuous mechanical property measurements along the specimen, which yield more detailed information about sample

variability. Such methods already exist but have limited use in the industry.



Fig. 1. Mancos Shale samples. Different colors refer to compliant (dark) and stiff (light) layers.

The scratch test is a method that correlates the force applied to scratch a rock sample with its mechanical properties (unconfined compressive strength and fracture toughness). When compared to standard strength-testing methods, measurements exhibit much higher resolution (1-2 mm) than with conventional procedures. Measured properties, however, can be biased by both sample saturation and friction between the specimen and the cutter. Moreover, the scratch test leaves a small furrow at the tool-sample

* Corresponding author: daria.olszowska@utexas.edu

contact, raising concerns about possible core damage [7]. Another technique that enables high-resolution detection of mechanical property changes along a rock is the indentation test. Elastic properties of a rock sample are estimated using the relationship between load and depth of penetration. The resolution of this method depends on the tip size and ranges from the nano- to macro-scale. Presence of material “pile-up” or “sink-in” around the tip complicates the interpretation of indentation test results. As a consequence, there may be significant differences between true and apparent contact areas, leading to errors in estimated properties [8-10].

We introduce an alternative laboratory method to measure rock elastic properties via a spatially continuous and non-destructive method. Using angle-dependent ultrasonic reflection coefficients, high-resolution data are delivered for rock sample properties and their variability. In the sections that follow, we first describe the new laboratory system and the corresponding measuring technique. Next, angle-dependent ultrasonic reflection coefficients are used to estimate elastic properties along homogeneous and complex rocks (artificial and natural) and to generate 2D descriptions of the examined rock samples.

2 METHOD

The ultrasonic angle-dependent reflection coefficient method is a technique that offers improved resolution compared to standard laboratory measurements. It is a pitch-catch method, where the source and the receivers are positioned at an angle with the sample. Data are collected at multiple incidence angles and the measurements are normalized with a reference value. Continuous measurements performed along the sample mitigate spatial averaging effects. The resolution of our method is determined by both transducer diameter and signal frequency. Because the size of the acoustic beam is much smaller than the sample, the measurement is sensitive to a limited surface area. This area, owing to the nature of the measurement, increases with incidence angle (θ_i) and is proportional to $1/\cos(\theta_i)$. Data are collected at various locations across the sample surface, providing detailed information about rock property changes, and used to construct a 2D rock model.

2.1 Reflection-coefficient measurement system

Figure 2 shows the reflection-coefficient measurement apparatus. The initial design of this apparatus is well described in the literature [11,12]. An update in the design that distinguishes it from other similar devices is the receiver array. Instead of only one receiver and one transmitter, up to four ultrasonic receivers can be used at different locations. Multiple transducers allow the detection of the reflected and refracted P and S waves simultaneously, thereby reducing measurement time. Figure 3 shows the measurement geometry and illustrates a third type of wave that is detected by the system, i.e., the direct wave, which in some cases can interfere with reflected wave measurements. The direct wave, therefore, needs to be considered when calculating reflection coefficients.

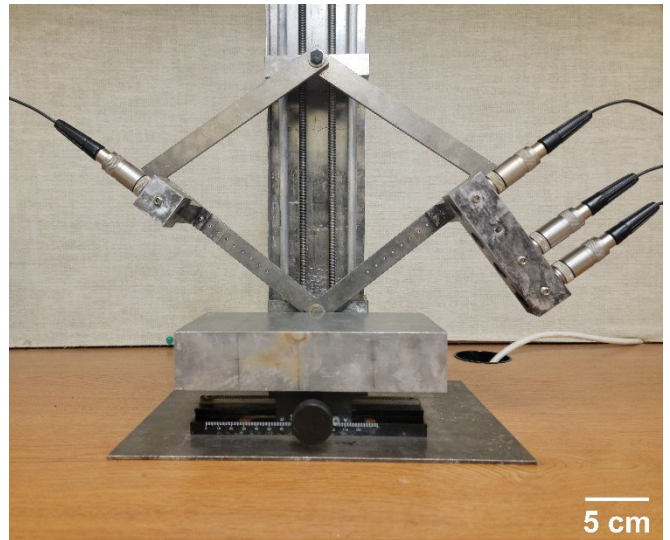


Fig. 2. Ultrasonic reflection coefficient apparatus. The sample (aluminum) is placed on a moving table, allowing changes in sample positioning during the experiment. Transmitter (on the left) and receiver array (on the right) are deployed on two arms with a common rotation axis. Two lead screws allow changes of incidence angle (on the left) and sample top positioning (on the right).

Transmitter and receivers are deployed on two arms with a common axis of rotation attached to two moving plates and lead screws. Such design allows the measurement of reflection coefficients at different incidence angles without moving the sample and while keeping the transducer-sample distance constant. This latter condition ensures that the acoustic beam center be located at the same point for all angle measurements. The rock sample is placed on a moving table allowing measurement-position changes throughout the experiment and continuous data collection along the sample. Two lead screws allow not only variations of incidence angle but also precise sample top positioning.

The laboratory system includes a wave transmission and acquisition module containing an HP 8116A pulse/function generator, Rigol DS1054Z oscilloscope, four Olympus V303 immersion transducers (1 MHz, 1.25 cm diameter), four Olympus V323 immersion transducers (2.25 MHz, 0.64 cm diameter) and watertight transmission cables. Depending on the transducer type, we use 500 ns (1 MHz transducer) or 222 ns (2.25 MHz transducer) pulse signals with 100 Hz repetition frequency and 8 V peak-to-peak amplitude. Each waveform is recorded after performing an average of 256 stacks of measurements in order to mitigate acquisition noise. All measurements are performed with the transducers and the sample submerged in a fluid (water/castor oil).

2.2 Data acquisition, processing, and modeling

The amplitude of the reflected wave and its variation with incidence angle becomes the primary source of rock elastic property information. Reflection coefficients are calculated by comparing the amplitudes of reflected and reference waves. The amplitude of the reference wave is measured by placing the transmitter and receiver face-to-face and

recording the waveform without the presence of the rock sample. This procedure mitigates measurement effects due to transducer size and fluid attenuation. Reflection coefficients are calculated as the ratio of the reflected and reference wave amplitudes. Because the distance traveled by the wave at different incidence angles remains constant, there is no need to correct the measured amplitudes for the effects of attenuation and beam spreading.

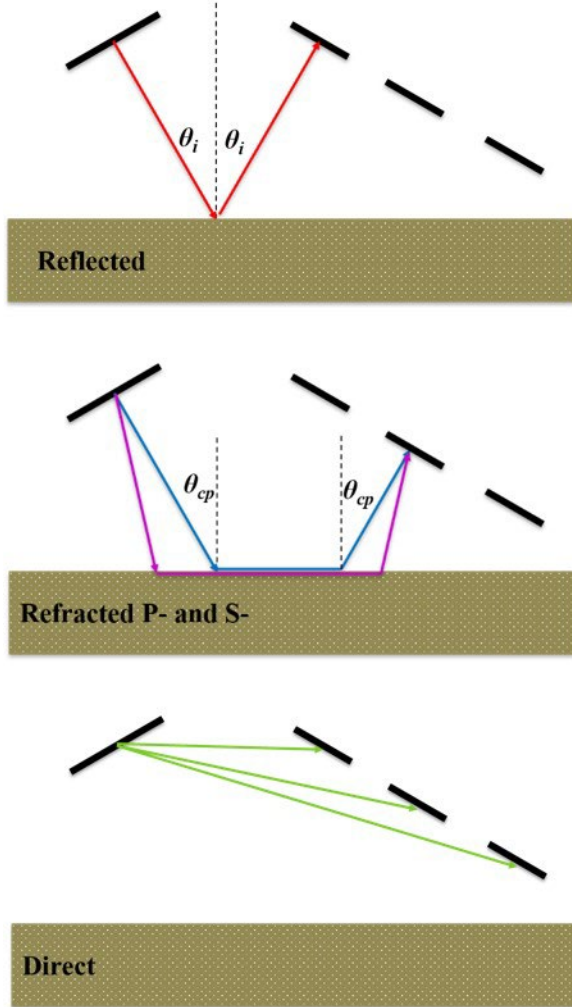


Fig. 3. Wave arrival geometry. A reflected wave propagating at incidence angle θ_i is captured by the first transducer in the receiver array. Measurements are sensitive to a limited surface area. Refracted waves occurring at and beyond P- and S-wave critical angles, θ_{cp} and θ_{cs} (not shown in the figure), respectively, are captured by receivers at positions 2 and 3. Because of the nature of the refracted wave, measurements cover larger surface areas on the rock sample compared to reflection measurements, hence are subject to spatial averaging effects across complex rock samples. Direct waves propagate from the transmitter to the receivers.

Variations of ultrasonic reflection coefficient with angle are then used to estimate rock elastic properties. Measured reflection coefficients are matched with numerical simulations (semi-analytical and numerical models) to estimate P- and S-wave velocities, V_p and V_s , respectively, and density, ρ , of the examined sample. While the semi-

analytical model assumes a homogeneous rock sample, the numerical model considers variations in rock elastic properties within the sample. Because of the finite transducer size and source-rock-receiver distance, plane-wave theory cannot be used to describe wave behavior at the interface between two media. Instead, we use a bounded beam model representing the wavefront as a superposition of multiple infinite plane waves traveling in different directions [13]. The acoustic wave is propagated from the source toward the fluid-solid interface using the phase advance technique [14,15], given by

$$P(k_x, k_y, z) = P(k_x, k_y, 0) e^{ik_z z}, \quad (1)$$

where $P(k_x, k_y, 0)$ is the source ($z = 0$) acoustic wavefield, $P(k_x, k_y, z)$ is the acoustic wavefield calculated anywhere in the space, k_x , k_y , and k_z are the wavenumbers in the x , y , and z directions, respectively, and $i = \sqrt{-1}$. At the interface ($z = h$), each plane wave component of the wavefield is modified by the reflection coefficient $R(k_x, k_y)$ in the form

$$P(k_x, k_y, h) = P(k_x, k_y, 0) e^{ik_z h} R(k_x, k_y). \quad (2)$$

We use an inhomogeneous wave reflection coefficient model to predict the acoustic wave behavior at the solid-fluid interface [16]. It follows that

$$R(k_x) = \frac{(k_s^2 - 2k_x^2)^2 + 4k_x^2 k_{pz} k_{sz} - \frac{\rho_w}{\rho} k_s^4 k_{pz}/k_z}{(k_s^2 - 2k_x^2)^2 + 4k_x^2 k_{pz} k_{sz} + \frac{\rho_w}{\rho} k_s^4 k_{pz}/k_z}, \quad (3)$$

where $k_{pz} = \sqrt{k_p^2 - k_x^2}$, $k_p = \frac{\omega}{V_p}$, $k_{sz} = \sqrt{k_s^2 - k_x^2}$ and $k_s = \frac{\omega}{V_s}$; k_p and k_s are the P and S wavenumbers in the solid, respectively, ω is the angular frequency, and ρ_w/ρ is the density ratio between the upper and lower media; $R(k_y)$ is calculated using the same equation but changing k_x to k_y . Subsequently, the acoustic wavefield modified by the fluid-solid interface is propagated toward the receiver using the same phase advance technique. Both measurement and modeling schemes, including refracted waves, have been verified with a water-aluminum interface [17]. Results obtained from the latter verification confirmed a good match between measurements and their numerical simulation. Differences between P- and S-wave velocities estimated with the reflection-coefficient method and those measured with a standard acoustic transmission procedure did not exceed 1%. Density, however, was underestimated, with a 7% difference with respect to standard laboratory measurements. The refracted wave method further validated the measurement, yielding an error below 4%.

Complementary to the semi-analytical model, we use SOFI2D (finite-difference viscoelastic time-domain forward modeling algorithm [18,19]) to model reflection coefficients obtained from homogeneous and spatially complex rock samples for their comparison to laboratory measurements. We assume that sample properties change only in one direction. Therefore, in order to reduce computational time, we use a 2.5D model (2D model space with an 3D azimuthal explosive source). The geometry of the laboratory system is replicated by the software. Each reflected wave is normalized

by the reference wave, where the maximum absolute amplitude is the value of the reflection coefficient at a given incidence angle.

3 CASE STUDIES

This section documents the results obtained with the angle-dependent ultrasonic reflection coefficient method using natural and synthetic samples exhibiting homogeneous and heterogeneous elastic properties. Prior to performing the measurements, each sample is first dried in the oven to remove residual fluid saturation and then saturated with water using a vacuum pump. The sample, source, and receiver are submerged in water during the experiment. Based on low-angle reflection coefficient measurements collected at various locations on the sample surface, small-scale variations in reflected wave amplitude are detected and used to construct 2D rock models of reflection coefficient. Likewise, it is shown how angle-dependent reflectivity curves change from one location to another, and how the presence of rock spatial heterogeneity affects the measurements. For the sake of simplicity but without sacrifice of generality, we assume that the sample top is flat and perfectly horizontal and that the distance traveled by the wave remains constant throughout the experiment. Dynamic elastic properties of the tested samples are estimated using a nonlinear inversion algorithm to match measurements with their numerical simulations based on trust-region least-squares minimization [20-22] and compared to standard laboratory measurements when available. The inversion algorithm uses only the absolute value of reflection coefficients to estimate the elastic properties of the rocks. In the following analysis, we assume that rocks are purely elastic/non-dispersive. Phase estimation and modeling requires further analysis of poroelastic rock properties and of their effect on reflected waves. Two types of anisotropic samples are considered for analysis: (1) when layer properties are known before acquiring the measurements (synthetic sample), and (2) when there is no prior information about the sample, layer geometry, and properties.

3.1 Homogeneous samples



Fig. 4. Homogeneous rock samples. Berea Sandstone (left) and Texas Cream Limestone (right).

This section describes measurements performed on homogeneous rock samples: Berea Sandstone and Texas

Cream Limestone. The same rocks are subsequently used to construct synthetic layered samples. Both rock samples are 10x10 cm blocks with a flat surface (Figure 4). Measurements acquired with angle-dependent ultrasonic reflection coefficients are compared against acoustic transmission measurements (Table 1), where source and receiver are placed on opposite ends of the sample and the arrival time of P- and S- waves is measured and translated into V_p and V_s , respectively. For homogeneous samples, we expect the results obtained with both methods to give similar results.

Table 1. Homogeneous samples. Elastic properties measured with the acoustic transmission and ultrasonic reflection coefficient methods and their percentage differences.

Sample	Method	V_p [m/s]	V_s [m/s]	ρ [kg/m ³]
Berea Sandstone	Transmission	2714	1129	2050
	Ultrasonic Reflection Coefficients	2849	1180	1950
	% Difference	5	4.5	5
Texas Cream Limestone	Transmission	3355	1775	1920
	Ultrasonic Reflection Coefficients	3402	1649	1845
	% Difference	1.4	7.1	3.9

3.1.1 Berea Sandstone

Figure 5 shows the laboratory results obtained from the water-saturated Berea Sandstone interface. Because of higher data quality and larger signal-to-noise ratio, we choose to only show measurements acquired with 1 MHz transducers. Dashed and dotted lines describe the results obtained with the bounded beam and numerical model, respectively. Table 1 shows the values used to generate both models. The match between measurements and numerical simulation is very good, except at angles from 30 to 35 deg. This discrepancy is related to the P-wave critical angle (31 deg), where the modeled receiver response does not follow the laboratory data trend (increase in measured values); instead, the curve smoothly transitions from an almost horizontal to an inclined orientation. The P-wave becomes inhomogeneous at the longitudinal critical angle, hence part of the energy propagates parallel to the sample surface, while part is converted into a leaky mode, causing disruptions to the wavefield [23]. Differences between properties estimated with the ultrasonic reflection coefficient and the acoustic transmission methods do not exceed 5%.

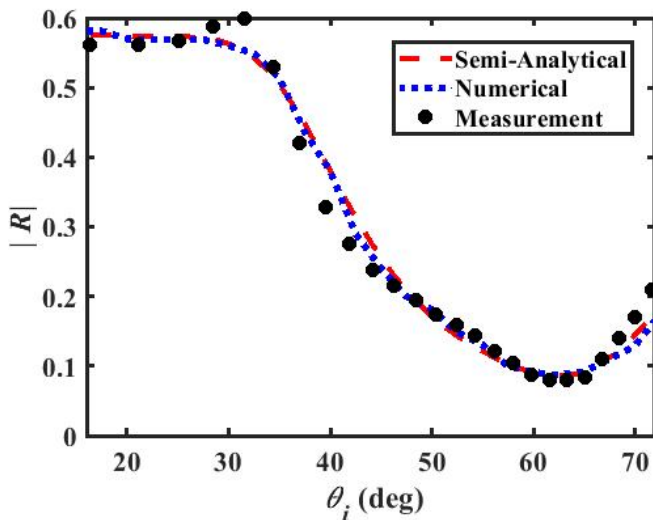


Fig. 5. Berea Sandstone. Measured (dots) and modeled (dashed line – semi-analytical, dotted line - numerical) ultrasonic reflection coefficients with respect to angle of incidence. Measurements performed with a 1-MHz immersion transducers (source and receiver).

3.1.2 Texas Cream Limestone

Figure 6 compares laboratory measurements of ultrasonic reflection coefficients for the Texas Cream Limestone acquired at different incidence angles (dots) against the results obtained with the bounded beam model (dashed lines) and numerical model (dotted lines). Overall, the match between measurements and numerical simulations obtained with both models is good, with some exemptions around 25-30 degrees. Similarly, for the case of Berea Sandstone, results obtained with both numerical models show a discrepancy with laboratory measurements around the P-wave critical angle (23 deg). Numerical simulations show a better fit near the longitudinal critical angle; the amplitude of reflection coefficients increases following the experimental measurements, but their values are lower than those of laboratory measurements. Semi-analytical results exhibit a smooth transition near the P-wave critical angle. Differences between numerical and semi-analytical results are also noticeable at angles above 65 degrees: while the former fit the measurements well, the latter fail to match the experimental data. This behavior coincides with the S-wave critical angle which takes place at 64 degrees. Table 1 describes the elastic properties estimated with the reflection coefficient method, where the results are compared to acoustic transmission measurements. The difference of measurements between the two techniques does not exceed 4%, except for S-wave velocity, which exhibits a difference of 7.1%.

3.2 Complex rock samples

This section describes results obtained for synthetic Berea Sandstone – Texas Cream Limestone and natural complex carbonate samples. A 2D model of the sample is constructed (assuming constant properties within each layer) and the study focuses on how angle-dependent reflectivity curves

vary from one data collection location to another and what the effect of the neighboring layers is. In this section, we compare results obtained with two types of transducers, 1 MHz and 2.25 MHz. The difference between the transducers is not only their central frequency of operation but also their size: the 2.25 MHz transducer is half the size of the 1 MHz transducer. We assess the effects of transducer size and frequency on measurement resolution and their ability to estimate properties of a single layer without spatial averaging effects.

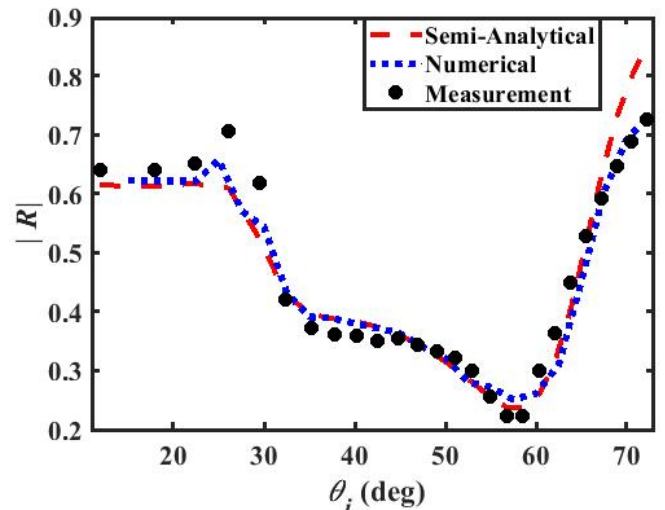


Fig. 6. Texas Cream Limestone. Measured (dots) and modeled (dashed line – semi-analytical, dotted line - numerical) ultrasonic reflection coefficients as a function of angle of incidence. Measurements performed with a 1-MHz immersion transducers (source and receiver).

3.2.1 Berea Sandstone – Texas Cream Limestone

Berea Sandstone – Texas Cream Limestone is an artificial composite stack made of alternating layers of both rocks glued together with epoxy. The thickness of the layers is not constant and varies between 12.5 mm and 21.8 mm. Figures 7A and 7B describe the sample geometry, and the expected reflection coefficients at different locations. For visualization purposes (better color resolution), reflection coefficients are normalized: values range from 0 (for clean Texas Cream Limestone) to 1 (for clean Berea Sandstone). Panels C and D show normalized ultrasonic reflection coefficients obtained at different locations and at very low incidence angles (4 deg) with 1 MHz and 2.25 MHz transducers, respectively. Measurement locations are at the center of each layer and at the boundaries between them as indicated by the black dots. Measurements acquired with both types of receivers indicate variations in the normalized reflection coefficients related to changes in sample property. We observe that numerically simulated reflection coefficients and laboratory measurements do not agree. When the measurement collection point is located at the center of the layer, the reflection coefficient tends to the expected value. On the other hand, at the interface between layers, the measurement is sensitive to both types of rock (averaging effect), whereby the discrepancy with the expected reflection coefficient increases. In general, measurements acquired with higher-frequency transducers show a better match with the Berea

Sandstone/Texas Cream Limestone layered sample model. Differences between the two sets of measurements are caused primarily by transducer size and measurement frequency: the smaller the transducer the higher the resolution.

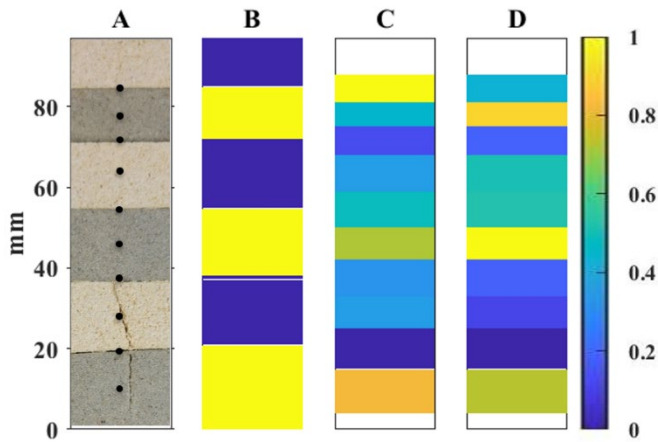


Fig. 7. Artificial complex rock. Panel A shows the sample made of alternating layers of Berea sandstone (grey) and Texas Cream Limestone (light) with measurement locations (dots). Panel B shows expected values of normalized reflection coefficients at different sample locations. Panels C and D show normalized low-angle ultrasonic reflection coefficients measured with 1 MHz and 2.25 MHz transducers, respectively.

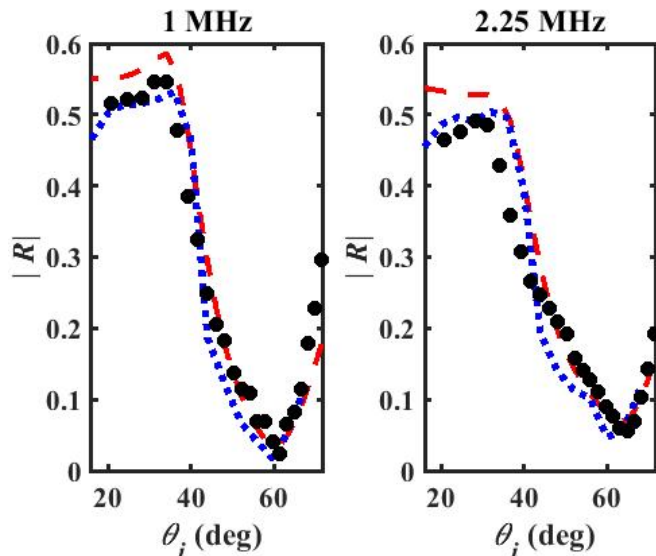


Fig. 8. Center of Berea Sandstone layer (located between 40-55 mm). Measured (dots) and modeled (dashed line – semi-analytical, dotted line - numerical) ultrasonic reflection coefficients as functions of angle of incidence for the cases of 1 MHz (left) and 2.25 MHz transducers (right).

Because angle-dependent reflectivity curves for Berea Sandstone and Texas Cream Limestone have a distinctive shape, we expect to observe differences between the angle-dependent ultrasonic reflection coefficients measured at specific sample locations. Figure 8 compares laboratory measurements acquired with 1 MHz and 2.25 MHz ultrasonic transducers at the center of the 17.3 mm Berea Sandstone layer and their match with semi-analytical numerical simulations. Results obtained with both pairs of transducers

have a very similar shape, with small differences between them. Note that the semi-analytical reflection coefficients do not match laboratory measurements performed at low angles for both cases, but the deviation is higher for 2.25 MHz measurements. The numerical model, which contrary to the semi-analytical model includes information about sample heterogeneity, gives a better match at low angles, but deviates from experimental measurements at high angles. Interestingly, we observe that the numerically simulated reflection coefficients change depending on the measurement frequency, even when layer thickness (17.28 mm) is greater than transducer size, confirming the laboratory observations. Elastic properties estimated with both measurements yield similar values when compared to homogeneous Berea Sandstone properties estimated with standard laboratory methods. The difference does not exceed 5%, except for V_s estimated from 2.25 MHz measurements (5.4%). In general, in this case, the 1 MHz measurement yields a smaller difference with respect to homogeneous sample properties.

Figure 9 shows how the measured angle-dependent ultrasonic reflection coefficients change from one measurement location to another. In this example, the center of the beam was placed either in the center of the Berea Sandstone layer (BS2 stands for the second Berea Sandstone sample counted from the bottom) or at the border with Texas Cream Limestone. We describe two cases: when Texas Cream is either on the right (BS2/TX2) or the left side (TX1/BS2) of Berea Sandstone. TX1 and TX2 stand for the first and the second Texas Cream Limestone layer counted from the bottom of the sample, respectively. We observe that reflectivity curves measured with 1 MHz and 2.25 MHz transducers differ, although, they all have a shape that is close to that of the homogeneous Berea Sandstone, without much visible effect due to the Texas Cream Limestone. We expected to observe a greater deviation from the homogeneous sample behavior, especially at the Berea Sandstone/Texas Cream Limestone interface. Measurements acquired with the 1 MHz transducers almost overlap, except between 20 - 40 degrees, where we observe additional discrepancies between the acquired measurements. We know that the area sensitive to the measurement increases with the incidence angle, thereby increasing the sample averaging effect. Therefore, the resolution of the measurement is the highest possible at low angles. We observe more variability in the measurements acquired with 2.25 MHz transducers than with 1 MHz transducers. The increase in amplitude below 40 degrees is much more significant for the measurements acquired at the interface. Additionally, the location of the minimum reflection coefficient is shifted toward higher angles at the center of the layer. When we compare homogeneous Berea Sandstone and Texas Cream Limestone angle-dependent reflectivity curves, we notice that the location of the minimum value changes from 65 degrees to 59 degrees, respectively. The measurement acquired from the center of the Berea Sandstone layer with the 2.25 MHz transducer is sensitive mostly to the properties of the single material, with minimal effect due to neighboring layers. This behavior confirms our previous observations that smaller-diameter and higher-frequency transducers provide enhanced resolution when estimating changes in the sample elastic properties. Although the differences in reflection coefficient plots obtained at different sample locations can be subtle, they

are related to changes in the material density or P/S-wave critical angle. It is also important to note that epoxy used to glue the components has a measurable effect on reflection coefficient measurements. We do not record a smooth transition between the layers; instead, we observe a mechanical discontinuity causing internal reflections and backscattering, thereby increasing the difficulty of interpretation and data-model match.

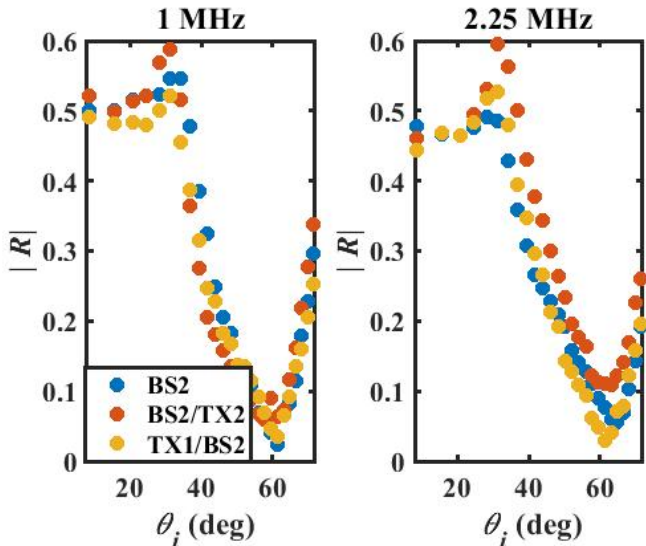


Fig. 9. Angle-dependent ultrasonic reflection coefficients obtained at the center of the Berea Sandstone layer (blue), and at the interface with Texas Cream Limestone (red and yellow). Measurements performed with 1 MHz (left) and 2.25 MHz transducers (right).

3.2.2 Complex carbonate

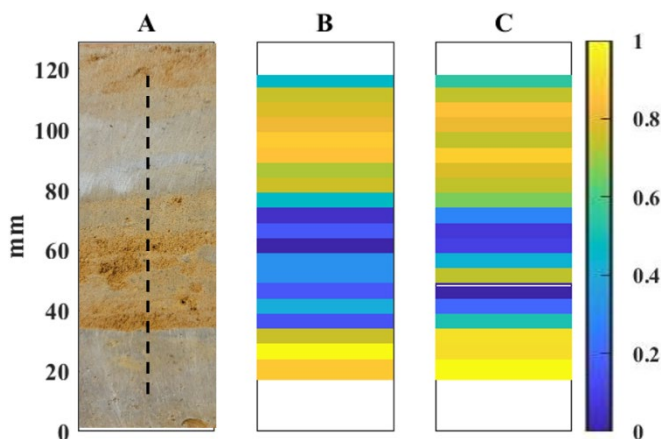


Fig. 10. Complex carbonate. Panel A shows the sample with the measurement axis (dashed line). Measurements are acquired every 5 mm between 10 mm and 110 mm. Panel B shows normalized low-angle ultrasonic reflection coefficients obtained with the 1 MHz transducer. Panel C shows normalized low-angle ultrasonic reflection coefficients obtained with 2.25 MHz transducers.

As shown in Figure 10, the complex carbonate sample is a natural rock with visible layering. Contrary to the artificial sample, there is no prior information about layer elastic properties. From macroscopic observations, we notice that the light gray layers are very tight, with low porosity, while the brown layers have small vugs. Low-angle reflection coefficients measured between 20 mm and 120 mm at 5 mm intervals along the samples show variability across the sample, hence suggesting changes in rock elastic properties. Normalized reflection coefficient plots show regions with high and low values, which correspond to the light grey and brown layers, respectively. This behavior confirms our macroscopic observations: tight areas exhibit higher impedance (higher velocity and density) compared to the vuggy zone. Similar to the previous case, measurements acquired with 2.25 MHz transducers exhibit better resolution; we also observe more variability in the measurements across the sample.

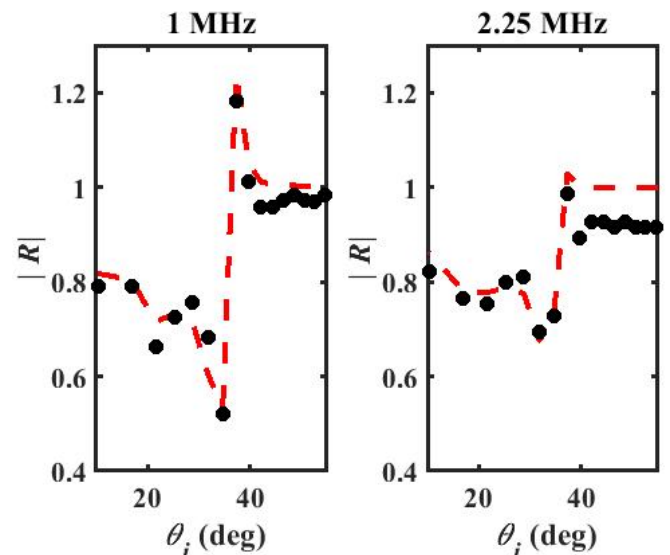


Fig. 11. Complex carbonate. Measured (dots) and modeled (dashed line) ultrasonic reflection coefficients as a function of angle of incidence for 1 MHz (left) and 2.25 MHz transducers (right). The center of the beam is located at 90 mm (approximately the center of the light-gray layer).

Measurements acquired at the center of the light-gray layer (100 mm) with 1 MHz and 2.25 MHz transducers are matched with numerical simulations performed with the semi-analytical model (Figure 11). Angle-dependent ultrasonic reflection coefficients measured with both types of transducers have a similar shape but with a smaller range in the values for the higher-frequency measurements. The bounded beam model has difficulties matching the 2.25 MHz measurements at angles above 40 degrees, and simulated reflection coefficients are higher than the measured reflection coefficients. Despite differences in the experimental angle-dependent reflection coefficients, both measurements yield similar values of P- and S-wave velocities; V_p ranges from 5906 m/s (1 MHz) to 6158 m/s (2.25 MHz), with a 3% difference between the estimated values. S-wave velocity estimated with both measurements gives 2882 m/s and 2893 m/s, for the 1 MHz and 2.25 MHz transducers, respectively (0.3% difference). Density estimations, however, exhibit a

significant difference (28%) between the lower (2434 kg/m³) and the higher frequency measurements (3114 kg/m³). Based on a better model-laboratory match obtained for 1 MHz measurements and the expected density of tight carbonate rocks, we conclude that the lower sample density is a more reliable outcome.

Figure 12 shows how angle-dependent reflection coefficients vary across the complex carbonate sample. Measurements are centered at 35, 60, 75, and 100 mm; locations are selected based on both low-angle reflection coefficients (minimum, maximum, and the transition zone) and macroscopic variations in sample properties (visible layers/alteration zones). We observe a significant change in the angle-dependent reflectivity curves between measurement locations related to changes in rock elastic properties. Variations in wave velocities estimated for different sample locations range from 5061 m/s to 6158 m/s for V_p and from 2700 m/s to 2893 m/s for V_s . Those values yield a percentage change of 17.8% and 6.7% in P- and S-wave velocities, respectively.

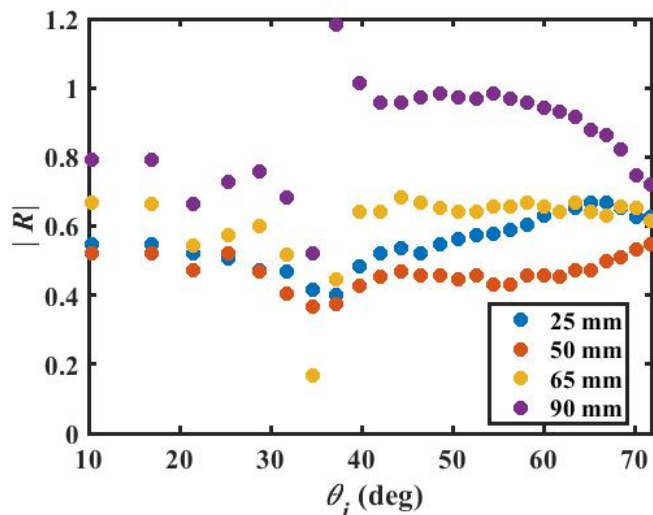


Fig. 12. Angle-dependent ultrasonic reflection coefficients measured at different locations across the complex carbonate sample. Measurements acquired with the 1 MHz transducer.

4 CONCLUSIONS

Ultrasonic angle-dependent reflection coefficient measurements enable high-resolution estimation of rock elastic properties under laboratory conditions. Comparison between measurements, semi-analytical and numerical simulations in homogeneous media show good agreement. Analysis of heterogeneous media shows that the spatial resolution of reflection coefficient measurements increases with increasing frequency and decreasing transducer diameter. This behavior is due to the acoustic beam spread (lower for higher-frequency signals) and the active area of the sensor.

The angle-dependent ultrasonic reflection coefficient method was implemented to estimate elastic properties of four water-saturated samples: (1) homogeneous Berea Sandstone, (2) Texas Cream Limestone, (3) heterogenous synthetic sample made of alternating layers of Berea Sandstone and Texas Cream Limestone, and (4) a complex

carbonate with visible layers/alterations. Measurements performed on homogenous rocks were matched with semi-analytical and numerical simulations. Estimated elastic properties compared against standard laboratory methods showed a good agreement, with differences not exceeding 5% for most of the cases. This result confirms the reliability of the ultrasonic angle-dependent reflection coefficient measurements as an alternative method to estimate rock elastic properties.

The method was tested on synthetic and natural complex samples. Low-angle (4 degrees) reflection coefficients measured at different locations across the sample showed variations related to local changes in sample elastic properties. As expected, measurements acquired with smaller transducers exhibited greater spatial variations in the estimated rock properties. Because the measurement is sensitive to a surface area limited by the receiver size, the smaller the transducer the lower the averaging effect in heterogeneous samples. The effect of transducer size on the measurements was also noticeable in the angle-dependent reflection coefficient curves; measurements acquired with a larger diameter receiver exhibited a very similar shape at different locations when the layer thickness was below the sensor resolution. On the other hand, we observed that laboratory measurements acquired with smaller-diameter transducers were in general more difficult to match with semi-analytical or numerical simulations. The drawback of having small transmitter and receivers is the system sensitivity to sample imperfections (e.g. cracks, fractures, not a flat surface) and requires higher precision in sample positioning (the acoustic beam needs to be centered directly at the top of the sample). With this condition, one can estimate the properties of a single layer in a complex sample with an error below 5% when compared to a homogeneous rock of the same type.

5 NOMENCLATURE

- h = source – interface distance
- i = imaginary unit
- k = wavenumber in fluid
- k_x = x -component of the wavenumber in fluid
- k_y = y -component of the wavenumber in fluid
- k_z = z -component of the wavenumber in fluid
- k_p = compressional wavenumber in solid
- k_{pz} = z - component of the compressional wavenumber in solid
- k_s = shear wavenumber in solid
- k_{sz} = z -component of the shear wavenumber in solid
- P = acoustic wavefield
- R = ultrasonic reflection coefficient
- V_p = compressional-wave velocity in solid
- V_s = shear-wave velocity in solid
- x, y, z = coordinates of a cartesian coordinate system
- θ_i = incidence angle
- θ_{cp} = compressional-wave critical angle
- θ_{cs} = shear-wave critical angle
- ρ_w = density of the upper medium (water)
- ρ = density of the lower medium (sample)
- ω = angular frequency

6 ACKNOWLEDGMENTS

This work reported in this paper was funded by the University of Texas at Austin's Research Consortium on Formation Evaluation, jointly sponsored by Aramco, Baker Hughes, BHP Billiton, BP, Chevron, CNOOC International, ConocoPhillips, Eni, Equinor ASA, Halliburton, INPEX Corporation, Occidental, Oil Search, Petrobras, Repsol, Schlumberger, Todd Energy, TotalEnergies, and Wintershall Dea.

7 REFERENCES

1. W.A.M. Wanniarachchi, P.G. Ranjith, M.S.A. Perera, Q. Lyu, B. Mahanta, R. Soc. Open Sci., **4**, 1-10 (2017)
2. E. Fjaer, R.M. Holt, A.M. Holt, P. Horsrud, *Petroleum Related Rock Mechanics* (Elsevier, Oxford, 2008)
3. D.K. Sethi, *SPE/DOE Low Permeability Gas Reservoirs Symposium*, SPE-9833-MS (1981)
4. J.L. Miskimins, R.D. Barree, *SPE Production and Operations Symposium*, SPE-80935-MS (2003)
5. B.V.V. Cherian, S. Higgins-Borchardt, G.A.A. Bordakov, A. Yunuskhajayev, Z. Al-Jalal, D. Mata, J. Jeffers, *SPE Energy Resources Conference*, SPE-169960-MS (2014)
6. R. Suarez-Rivera, W.D. Von Gonten, J. Graham, S. Ali, J. Degenhardt, A. Jegadeesan, *Unconventional Resources Technology Conference*, URTEC-2460515-MS (2016)
7. G. Schei, E. Fjaer, E. Detournay, C.J. Kenter, G.F. Fuh, F. Zausa, *SPE Annual Technical Conference and Exhibition*, SPE 63255 (2000)
8. S. Suresh, A.E. Giannakopoulos, J. Alcalá, *Acta Mater.*, **45**, 1307-1321 (1997)
9. A.E. Giannakopoulos, S. Suresh, *Scr. Mater.*, **40**, 1191 – 1198 (1999)
10. J. Alcalá, A.E. Giannakopoulos, S. Suresh, *J. Mater. Res.*, **13**, 1390 – 1400 (2011)
11. T. Pialucha, P. Cawley, 1994, *J. Acoust. Soc. Am.*, **96**, 1651 – 1660 (1994)
12. J.D. Sagers, M.R. Haberman, P.S. Wilson, 2013, *J. Acoust. Soc. Am.*, **134**, EL271 – EL275 (2013)
13. L.M. Brekhovskikh, *Waves in Layered Media* (Nauka, Moscow, 1960)
14. Y. Bouzidi, D.R. Schmitt, 2008, *IEEE Trans. Ultrason. Ferroelectr. Freq. Control*, **55**, 2661 – 2673 (2008)
15. R. Malehmir, N. Kazemi, D.R. Schmitt, *Ultrasonics*, **80**, 15-21 (2017)
16. S. Vanaverbeke, F. Windels, O. Leroy, *J. Acoust. Soc. Am.*, **113**, 73 – 83 (2003)
17. D. Olszowska, G. Gallardo-Giozza, C. Torres-Verdin, *SPWLA 62th Annual Logging Symposium*, SPWLA-2021-0058 (2021)
18. T. Bohlen, *Comput. and Geosci.*, **28**, 887–899 (2002)
19. T. Bohlen, D. De Nil, D. Köhn, S. Jetschny, *SOFI2D seismic modeling with finite differences: 2D—elastic and viscoelastic version. Users guide* (Karlsruhe Institute of Technology, Karlsruhe, 2016)
20. K. Levenberg, *Q. Appl. Math.*, **2**, 164–168 (1994)
21. D. Marquardt, *SIAM J. Appl. Math.*, **11**, 431–441 (1963)
22. J.J. Moré, *Conference on Numerical Analysis* (1977)
23. T.P. Pialucha, *The reflection coefficient from interface layers in NDT of adhesive joints* (Imperial College of Science, Technology and Medicine, University of London, 1992)

Pore network simulations coupled with innovative wettability anchoring experiment to predict relative permeability of a mixed-wet rock

Mohamed Regaieg^{1*}, Franck Nono², Titly Farhana Faisal³, Clément Varloteaux⁴ and Richard Rivenq¹

¹ TotalEnergies SE

² Modis

³ Inria

⁴ Computational Hydrocarbon Laboratory for Optimized Energy Efficiency

Abstract. Since the pioneering work of Oren et al. [1] several attempts have been made to predict relative permeability curves with Digital Rock Physics (DRP) technique. However, the problem has proved more complex than what researchers have expected, and these attempts failed. One of the main issues was the high number of uncertain parameters especially for the wettability input and this gets worst in mixed-wet scenario as the number of parameters is higher than in water-wet and oil-wet cases. In fact, Sorbie and Skauge stated that wettability assignment is the most complex and least validated stage in DRP simulation workflow. Similarly, Bondino et al. [2] concluded that “genuine prediction” of multi-phase flow properties will remain not credible until important progress is achieved in the area of wettability characterization at the pore scale.

In this work, we propose a pragmatic approach to tackle this problem. First, we develop an innovative fast anchoring experiment imaged by microCT scanner, that helps to determine several wettability parameters needed for the DRP simulation (including the fraction of oil-wet /water-wet pores, any spatial or radius correlation of oil wet pores ...). This experiment also provides an estimation of residual oil saturation that is an important parameter and helps to anchor the pore scale simulations and further reduce the uncertainty. In addition to help reducing the uncertainty of the simulation, this experiment provides a fast (compared to Amott Harvey test) estimation of the wettability of the system. Images representing large volumes with low resolution are, first, improved with Enhanced Super Resolution Generative Adversarial Networks (ESRGAN) to obtain a large image with high resolution. Then, a pore network is extracted, and TotalEnergies parallel pore network simulator is used for multiphase flow simulations considering the constraints from the anchoring experiment to reduce the uncertainty. Finally, we compare our simulations against high quality SCAL experiment performed in-house and we assess the predictive power of our DRP workflow.

1- Introduction

Wettability input is key for DRP simulation as it controls the capillary forces and hence the invasion order. Unfortunately, it is not easy to characterize, and things become more complicated in mixed-wet scenario where fraction of oil-wet, water-wet, the spatial distribution of oil-wet pores and their correlation to the radii of the pores are important parameters needed to be indicated to the model. If one fails to do so, the model would have too many degrees of freedom and genuine predictions are not easy to achieve. In fact, [3] have stated that wettability assignment is the most complex and least validated stage in DRP simulation workflow. Similarly, [2] have concluded that “genuine prediction” of multi-phase flow properties will remain not credible until important progress is achieved in the area of wettability characterization at the pore scale.

Contact angle measurements from Micro-CT images of multiphase flow experiment has been very attractive recently [4]. However, as these measurements use the 3-phase contact line for the computations, they are very sensitive to the image resolution and insufficient image resolution leads to contact angle values close to 90 degrees with very large standard deviation [5]. Furthermore, automated contact angle measurements take into consideration the pinned menisci which are different from the contact angle input needed by a PNM simulator.

Recent observations [6,7] showed that wettability is correlated in space, and the pores having similar wettabilities are likely to be at a close spatial location. However, verifying that this correlation exists for a particular system and measuring the correlation length is not straightforward, requires one to perform a multiphase flow experiment and have several menisci in

* Corresponding author: mohamed.regaieg@totalenergies.com

neighboring pores which is not always easy to achieve. Then, image processing is needed in order to quantify the correlation length [7] which is not ideal for an industrial workflow.

Dixit et al. [8] proposed that wettability could be correlated to the size of the pores and proposed three models: Fractional-Wet model (i.e. contact angles are not correlated to the size of the pores), Mixed-Wet Large (i.e. where large pores are oil wet and small pores are water-wet) and Mixed-Wet Small (i.e. small pores are oil-wet and large pores are water-wet). They used this theory and PNM simulations to better interpret the differences between Amott-Harvey and USBM indices and proposed that the differences between these indicators could give an indication of the type of the wettability model.

[9] have demonstrated that fractional wet, mixed-wet large and mixed-wet small models are all possible theoretically. They also acquired Scanning Electron Microscopy (SEM) and Environmental Scanning Electron Microscopy (ESEM) images used to analyze mineralogy and local wetting properties. The ESEM used condensation of water to visualize if water appeared as drops on the surface (less water-wet), or as a water film condensed on the surface (water-wet). The water film was seen as whitening of the edges of the solid surface due to refraction of the water films. They also mentioned that they needed to analyze many images to be conclusive. Again, this is not practical in an industrial workflow where we aim to have a fast wettability characterization and feed it to a DRP model to be able to predict relative permeability curves quickly.

To solve the issues described above, we propose an innovative DRP simulation anchoring fast experiment that is easy to implement in an industrial workflow. It allows us to characterize the wettability of the sample, the fractions of OW and WW pores, determine the type of the wettability correlation to the radius of the pores, if there is any, and finally identifies if there is a wettability spatial correlation and allows the computation of this correlation length.

In this paper, we first describe TotalEnergies's DRP workflow based on 1) ESRGAN method to enhance the resolution of an image with a large field of view 2) GNM technique to extract a pore network with conductivities computed on the rock image, 3) a network stitching code that allows the extraction of large networks and 4) TotalEnergies' fully parallelized inhouse tool DynaPNM that can simulate flow in networks with several million pore elements.

Subsequently we describe and present the results of our wettability anchoring experiment that allows us to find the simulation wettability input as well as measure

experimental parameters, such as S_{or} and K_{rw} at S_{or} that allow us to constrain our simulations.

Then, we present the sensitivity study where the uncertain simulation parameters are varied and only the realisations in agreement with the wettability anchoring experiment results are kept. Hundreds of different realizations are used to produce P10, P50 and P90 relative permeability sets.

Finally, the simulated relative permeability curves are compared to an in-house SCAL experiment to assess the predictive potential of our simulation workflow.

2- Description of the simulation workflow

2.1. Enhanced Super resolution Generative Adversarial Networks (ESRGAN)

Acquiring micro-CT images of a rock is the first step in DRP simulation. This is then followed by segmenting the images to distinguish the rock from the pore space, and finally flow simulations are performed to compute advanced rock properties such as relative permeability and capillary pressure. [10] have proved that when the geometry of the pore space is well characterized, the flow simulators perform well.

However, the geometry of a real rock is not always well characterized, notably due to the lack of image resolution which in turn introduces uncertainty in the pore/throat geometry and consequently introduces errors in rock properties computation. Furthermore, during image acquisition a compromise is often made between the speed of the image acquisition, the size of the scanned volume and the resolution obtained: generally, increasing the resolution decreases the field of view, in turn limiting the quantity of information obtained from the image and thus making DRP simulations less representative.

In this work, we have implemented the ESRGAN method proposed by Wang et al. [11]. This method is based on two phases of training: PSNR step where the L1 loss function is minimized during the training of the generator. In this stage, the borders of the pores are improved but the texture of the rock is not captured. The weights of the trained generator are used as the starting point of the second stage of the training that we call GAN training. Pretraining with PSNR helps the GAN to have more visually pleasant results. The loss function of the second stage has three terms: the adversarial loss, the perceptual loss and the content loss. For the adversarial loss, Wang et al [11] proposed to use a relativistic average GAN [12] where loss function does not optimize discriminator to distinguish data real or fake. Instead, RaGAN's discriminator distinguishes that "real data isn't like average fake data" or "fake data isn't like average real data". According to Wang et al [11], this helps to learn sharper edges and more detailed textures. The perceptual loss helps the network to

capture perceptually relevant differences like textures or the clays in the rock images. These are determined from features maps obtained from VGG19 before the activation. We do not use the weights of the pre-trained VGG19 network, instead we re-train it with rock micro-CT images in order to have more relevant features and we have observed an improvement of the results after that. Finally, the content loss is the L1 pixel-by-pixel between the generated and the high-resolution images.

The loss for the generator is therefore

$$L_G = L_{percep} + \lambda L_G^{Ra} + \eta L_1$$

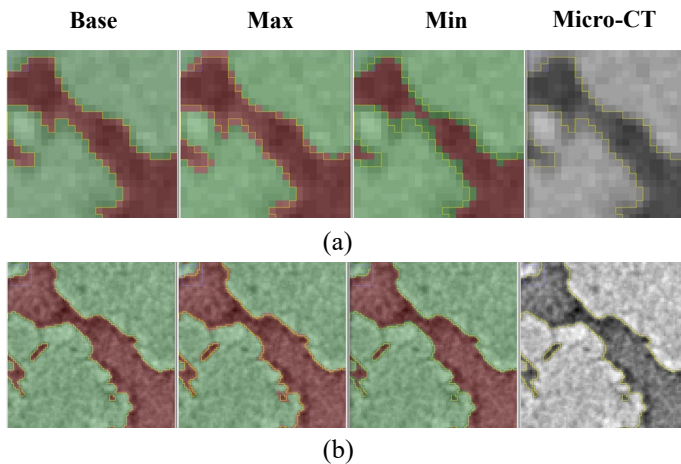
where L_{percep} is the perceptual loss, L_1 is the 1-norm distance between recovered image $G(x_i)$ and the ground-truth y , and λ (equal to 5×10^{-3}), η (equal to 1×10^{-2}) are the coefficients to balance different loss terms.

We have made the training parallel using multiple nodes and multiple GPUs in each node. The training is performed using two scans of the same small volume (1.45 microns image and 5.8 microns image), 3000 crops of 384*384 pixels images are made to form the training dataset. Training was performed using 36 GPUs and took 2 days. Afterwards, the trained model was applied to a second full low-resolution dataset of Bentheimer from another acquisition. An up-sampling in the Z direction was done on the low-resolution image that was next passed to the trained neural network. The generator was applied slice by slice on 2D images with 796 x 820 pixels to generate a 3D image of 3184 x 3280 x 12928 with voxel size of 1.45 microns. Then, we consider a subset from super resolution image, and we compare it to a high-resolution zoom of the same volume. Very good agreement was obtained when compared super resolution to high resolution images visually (Fig 2). Fig 3 presents permeability and porosity computations for low resolution, high resolution and super resolution images for an ensemble of realistic segmentations.

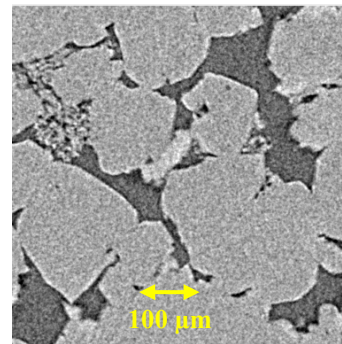
Fig 1 : Example of the several segmentation hypotheses considered in this work for a low-resolution image (a) and a high resolution image (b)

As segmenting the images could bias the results, we propose to perform for each image three realistic segmentations that a user is likely to consider. We choose a ‘Min’ segmentation with slightly underestimating the pore space comparing to the other segmentations, a ‘Max’ segmentation where pores are larger and a ‘Base’ segmentation between the ‘Min’ and ‘Max’ cases. We use machine learning based trainable Weka segmentation [13] where several classifiers are trained according to the scenarios defined above Fig 1

We observe that permeability and porosity computations are closer and have less uncertainty with super resolution. Next, we check the bodies and throat sizes distributions for high resolution, low resolution, and super resolution images. We clearly observe that the estimation of pore and throat radii is considerably improved with super resolution (Fig 4). Fig 5 presents simulated capillary pressure curves using low resolution, high resolution and super resolution images. We note we have tried to use several realistic segmentations for each case to illustrate the uncertainty related to this step and therefore we present envelopes of capillary pressure curves. We can clearly notice that ESRGAN makes our simulated primary drainage capillary pressure curves more accurate. Having validated the ESRGAN approach we propose to use it in the next part of the paper. However, these large images are challenging to handle in DRP simulation, and we expose in the next sections our strategy to enable using them in our numerical study.



(a)



(a)

(b)

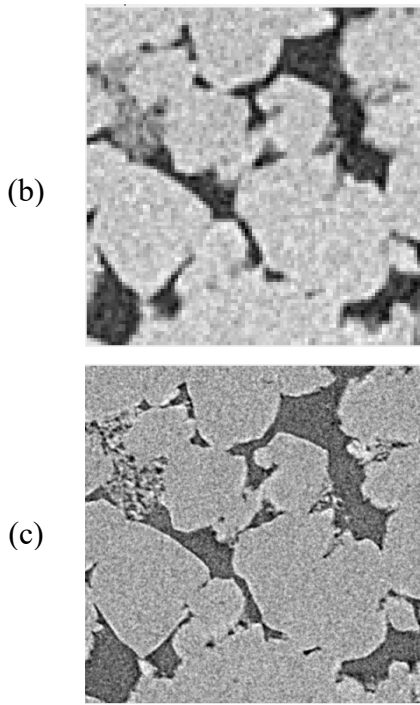
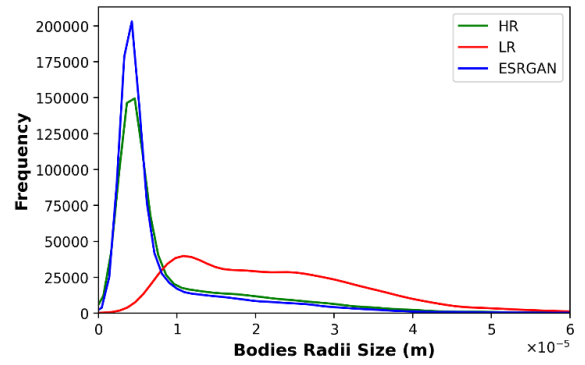
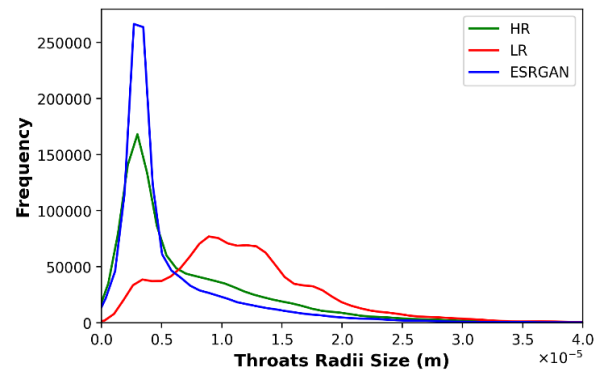


Fig 2 : comparison between super resolution (a), low resolution (b) and high resolution (c) images



(a)



(b)

Fig 4 : Comparison between pore size distribution for bodies using Maximum Ball Algorithm (a) and throats (b) using 3 images: low resolution (red), super resolution (blue) and high resolution (green)

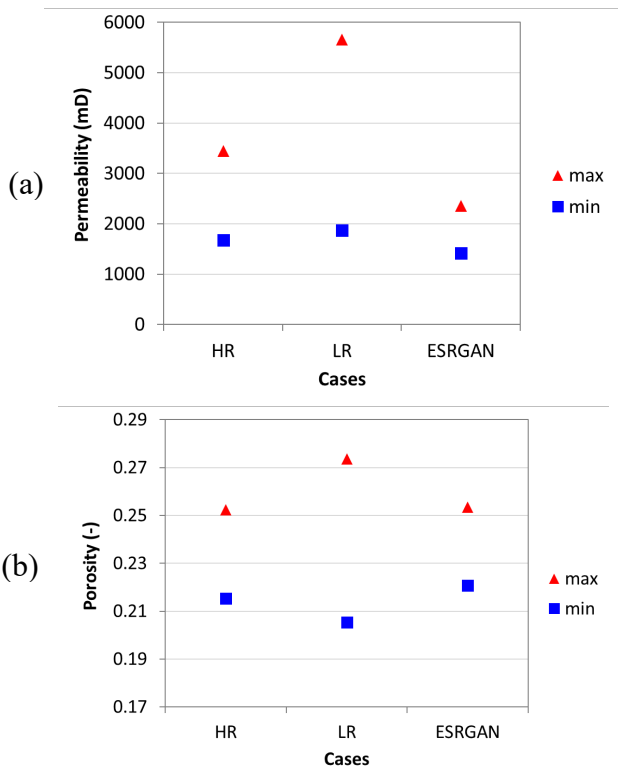


Fig 3 : Comparison of permeability using Openfoam (a) and porosity (b) for low, high and super resolution images for several realistic segmentations (max and min segmentation for each case)

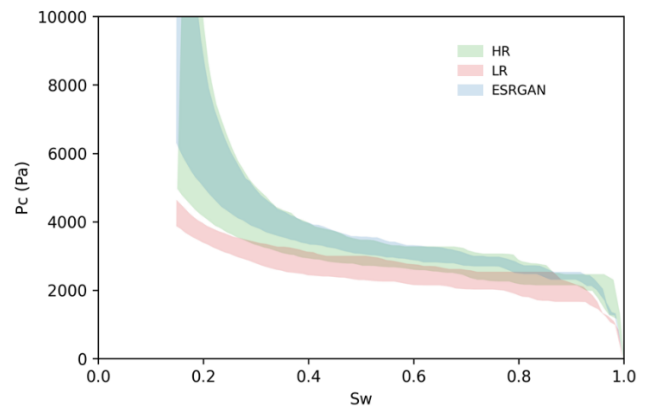


Fig 5 : Comparison between computed capillary pressure curves with TotalEnergies DRP simulation tools and using 3 images with several realistic segmentation: low resolution (red), super resolution (blue) and high resolution (green)

2.2. Pore Network Extraction

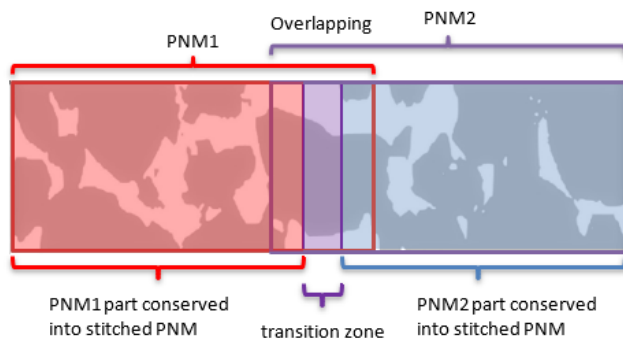


Fig 6 : An illustration of the pore network stitching process

In contrast to some digital rock physics methods, pore network models do not involve two-phase direct flow simulation in a 3D digital rock. Instead, it needs a pore network that is extracted from 3D reconstructions. Various algorithms exist to extract the skeleton of the 3D model that carries the essential geometric and topological information of the underlying pore system. In this work, we use a pore network extraction platform called GNextract developed with Imperial College, London [14]. GNextract is first used to reconstruct an upscaled version of the 3D segmented image of a rock in the form of a network of pore elements where the single-phase flow conductances in each pore are derived by solving the Stokes equation in the original geometry using OpenFOAM. Unfortunately, the extraction code needs a large amount of memory to extract large images (more than 60 GB of RAM for 1500³ voxels image). Therefore, to overcome this limitation, a stitching process has been developed on networks extracted from overlapped sub-volume of a given image. Error! Reference source not found. illustrates the stitching process and shows that the stitched network is formed by a first part conserved from PNM1, a second part conserved from PNM2, and a third part obtained on a transition zone where rules inspired from the ones used by GNextract are defined to choose the elements. More details of the stitching process could be found in [15].

2.3. Pore network flow simulator

Once a pore network is extracted with the corresponding conductance values from single phase DNS simulation, we go on to perform two-phase flow simulations. These simulations are performed using DynaPNM, TotalEnergies' inhouse pore network simulator [16], that we use in quasi-static mode as all the cases that we study in this paper are capillary dominated.

The physical rules implemented in the simulator are broadly similar to the ones used in [1,17] with the exception of a major change in the film flow model [15]. The geometry of the pore network is simplified into an ensemble of pore bodies connected through pore throats

during the pore network extraction step. As the invasions are totally controlled by the geometry, there is no need to compute the pressure gradients. The invasion order is determined through the capillary entry pressure of each element and the trapping is determined through a clustering algorithm. For every relative permeability point computation, the phases are isolated, and a pressure gradient is applied to the network. The pressure on each node is calculated, the corresponding production rate at the outlet is computed, and effective permeability of each phase is determined through Darcy's law.

The network is initially filled with water. A primary drainage is first simulated to establish irreducible water saturation, S_{wi} . As the network is assumed water-wet, oil injection follows an invasion percolation regime. Water layers in pore elements with corners make water trapping very difficult and allow to achieve very low S_{wi} values.

Primary drainage is then followed with a waterflood after an aging process where oil filled pore wettability is changed. First, water spontaneously fills the water-wet part of the network through piston like displacement and snap-off. In this phase the smallest pores are filled first, then the next smallest are filled, and so on. The defending oil phase can escape by flowing through oil-filled pores. Once spontaneous imbibition ends, the invading water is over pressured by applying a negative capillary pressure. Now, the largest pore elements are filled first, and oil can escape to the outlet either by flowing through the center of oil filled pores or through oil films. Once all the oil is trapped, the simulation stops.

The simulator has been parallelized to allow the simulation of large systems. First, the domain is decomposed, each processor has allocated memory and performs the computations of a subdomain. Each processor also needs information from the neighboring subdomains. The pore bodies and throats inside each subdomain of a processor are named local elements while the pore bodies and throats from neighbor subdomains are named ghost elements. Synchronization of the information of the ghost elements is performed after each capillary pressure step or after a maximum change in the network phases saturations. This communication is made using Message Passing Interface library MPI [18]. Furthermore, a parallel clustering algorithm has been implemented in order to determine if the defending phase is trapped and parallel linear solver library [19] is used for permeability and relative permeability computations. This parallelization allows us to simulate large networks with tens of million elements in few hours [15].

2.4. Statistical analysis

Several input parameters of pore network simulation are uncertain, especially the ones linked to the wettability input. These uncertainties have been used by some researchers in the past to “tune” the simulation results to SCAL relative permeability curves. However, if one wants to be predictive, she/he should not know the result *a priori* and this makes choosing the uncertain parameters tricky. Therefore, we have designed a wettability anchoring experiment (described in the next section) to help us better estimate these wettability parameters. Subsequently, we have developed a statistical uncertainty workflow [15] in which we vary the uncertain pore network simulation parameters within the ranges determined from the experiment. First, thousands of DynaPNM input files are generated in an experimental design phase using WSP method [20]. Subsequently, flow simulations are run on TotalEnergies’ supercomputer PANGEA. Then, a selection exercise is performed on these realisations to only keep the ones in agreement with S_{or} and K_{rw} at R_{os} measured from the wettability anchoring experiment. This is followed by a simulation ranking exercise based on the oil production after a given amount of water injected corresponding to each Kr curve and allows us to define three scenarios:

- P10: an optimistic scenario in which only 10% of the simulations produce more than this case
- P50: a median scenario in which 50% of simulations produce more than this case
- P90: a pessimistic scenario in which 90% of the simulations produce more than this case

3- Wettability anchoring experiment

Wettability is one of the main inputs of PNM simulation and unfortunately it is difficult to characterize *a-priori*. Moreover, even if a qualitative assignment of wettability is done and water-wet, oil-wet, or mixed-wet scenario is identified, a high number of uncertain parameters remains especially for mixed-wet case as the contact angles, the fractions of OW and WW pores, wettability spatial correlation and wettability correlations to pore radii (i.e., Do we have MWS, MWL or FW model) are all important parameters that could impact the simulation results. Considering all the possible values of these simulation inputs results in large simulation uncertainty which is not satisfactory.

Besides, performing a classical wettability test like the Amott Harvey or USBM needs a lot of time and does not provide all the information needed by the simulation.

Therefore, we have designed a fast wettability anchoring experiment imaged by micro-CT scanner that provides us with crucial data for our wettability input as

well as some measurements that will help us constrain our simulation and thus reduce the uncertainty. We first test this approach on a Bentheimer sample as described in the next section.

3.1. Description of the experiment

We start our experiment by mounting a 6 mm diameter Bentheimer sample in a flow cell with confining pressure of 50 Bars, the experimental set-up is illustrated in **Fig 7**. First, we establish S_{wi} using viscous displacement using mineral oil (Marcol52) where the same conditions (e.g., capillary number, same fluids ...) are used comparing to the validation SCAL experiment described in the next section. This is followed by replacing the mineral oil with toluene then with dead crude oil and aging the sample for 2 weeks at 80° C in a similar protocol (e.g. injected pore volumes, rate, ...) used by the SCAL laboratory. After the aging, $K_{ro}(S_{wi})$ was measured and a decrease of 30% of the K_{ro} was obtained. This was followed by injection of 2.5 Pore volumes of decaline to remove the dead oil without impacting the actual plug’s wettability. Next, mineral oil (Marcol52) was injected to replace decaline. We note that fluids replacement was performed at low flow rates to ensure that we do not change the initial water saturation. An image acquisition is performed after aging at S_{wi} and this is followed by the start of a spontaneous imbibition phase. We use one end opened protocol where water enters the sample and oil leaves it from the same side in counter-current imbibition process. Very low capillary number ($8E-09$) was used for the leaching process that aims to remove the produced oil from the diffuser without forcing the flow of water into the sample.

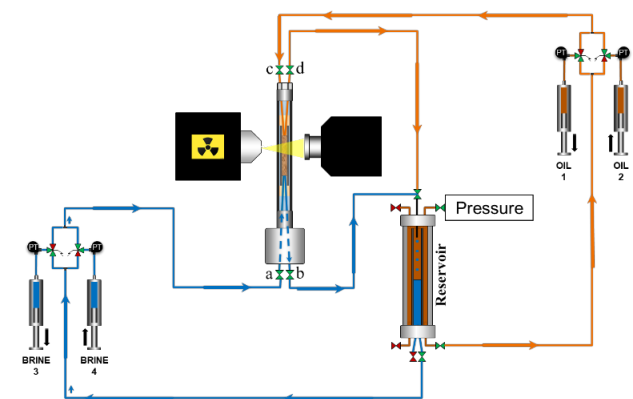


Fig 7 : Experimental set-up of the wettability anchoring experiment. In spontaneous imbibition c and d are closed, a and b are opened. In spontaneous drainage a and b are closed, c and d opened.

We only perform the spontaneous imbibition process for a week as we have observed that it was sufficient for water to imbibe in the first part of the sample to have a

fast experiment, but if time permits it can be interesting to continue the process for a longer time. Then, water is injected into the sample in a forced imbibition with the same maximum capillary number used in our SCAL lab. Finally, using a similar protocol we perform a spontaneous drainage in the other face of the sample. Micro-CT acquisitions are made at the end of each phase of the experiment.

The main objective of this test is to identify water-wet and oil-wet pores. It is obvious that water would imbibe to the water-wet pores in spontaneous waterflood and to the oil-wet pores in spontaneous drainage. This helps to map these pores and as a consequence analyze the volumes imbibed, the spatial correlation of wettability and the wettability correlations to the radii of the pores.

3.2. Analysis of the results

3.2.1- Wettability characterization and quantification of OW fraction

Fig 8 shows that water has imbibed during spontaneous imbibition and the comparison between the S_{wi} image and the image at the end of spontaneous imbibition clearly shows some of the water-wet pores. Similarly, **Fig 9** shows that oil has imbibed during spontaneous drainage and the comparison shows some of the oil-wet pores. We point out here the water/oil have only access to the connected water-wet/oil-wet pores and that we did stop the spontaneous imbibition/drainage phase on purpose after a week as discussed previously.

Water has imbibed until the middle of our sample during spontaneous imbibition and oil entered to a length of 800 slices during the spontaneous drainage. In order to have a consistent analysis and to compare the imbibed volumes, we perform our analysis on the first 800 slices of the sample (i.e. from inlet side in spontaneous imbibition and from outlet side in spontaneous drainage) as we would like to compare the imbibed volumes.

We observed that in the first 800 slices of the sample the water saturation increased by 7.5%. Similarly, we observed that the oil saturation has increased by 2.3% on the same length from the outlet side. This confirms that we have a mixed-wet sample. However, it can be misleading as oil advances in spontaneous drainage meaning that receding contact angles will be the effective angles in this process. We may have a situation where a pore has an oil-wet advancing contact angle but a lower than 90° receding contact angle. These would not be accounted for in the imbibed oil volume. Furthermore, oil has not access to the already oil-filled pores at S_{or} that could be oil-wet. The analysis of the imbibed volumes demonstrates that the system is mixed-wet but we cannot yet compute the oil-wet fraction in the system.

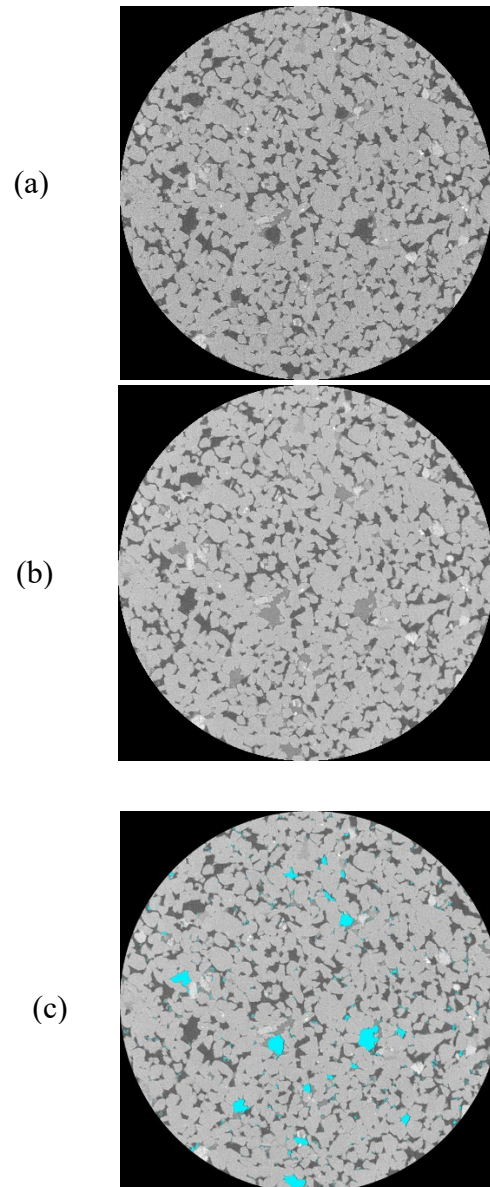
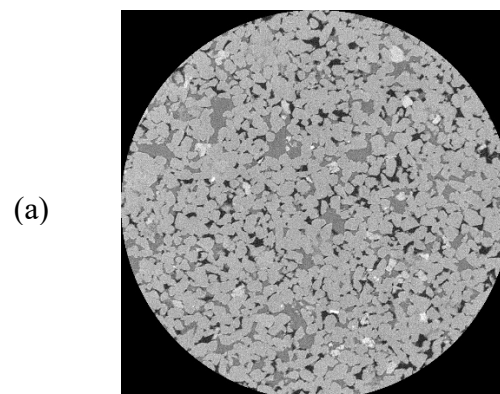


Fig 8 : Image of a slice from the experiment at S_{wi} (a), after spontaneous imbibition (b) and the image after spontaneous imbibition with some water-wet pores highlighted in blue (c)



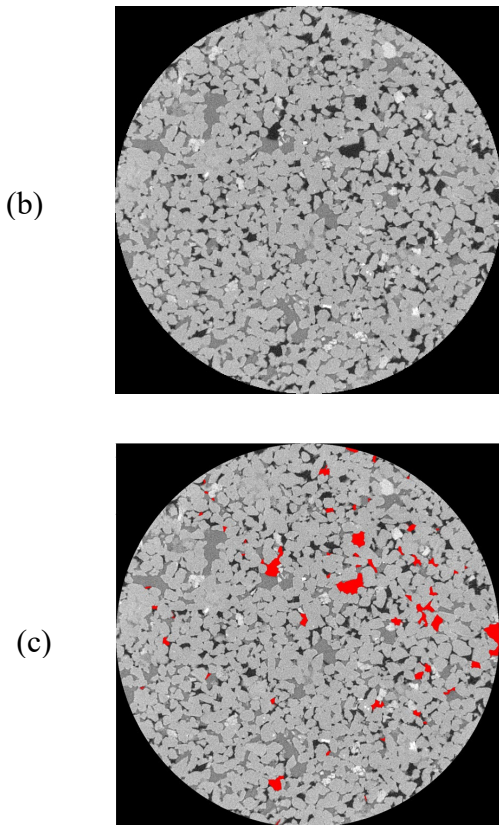


Fig 9 : Image of a slice from the experiment at Sor (a), after spontaneous drainage (b) and the image after spontaneous drainage with some oil-wet pores highlighted in red (c)

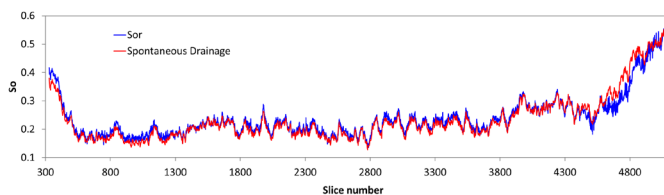


Fig 10 : Oil saturation profile at Sor (blue) and after spontaneous drainage (red). Injection performed from left to right.

The saturation profile of the oil at Sor **Fig 10** shows a capillary end effect which is an indication that the system is not water-wet. Furthermore, this provides us with important information about the oil saturation at P_c equal to zero that was 55%. This helps us to characterize the oil-wet fraction in the system that is needed to achieve this. We estimate it to 53-63% of oil-wet fraction after a fast PNM sensitivities study where the $P_c=0$ was reached at $S_w \sim 0.45$. We also note that by considering the oil profile at the center we are able to estimate the residual oil saturation that we use in the selection exercise later. Moreover, we have measured the K_{rw} at ROS in this experiment that should be close to K_{rw} at Sor. We then add an uncertainty to this measurement and use it as a constraint in the selection exercise described later.

Finally, the fact that the imbibed water volume was much higher than the imbibed oil volume for the same duration and at the same sample length gives us an indication that the receding contact angle was lower than 90° in a considerable amount of the oil-wet pores. This is an interesting information that we keep in mind when we choose the oil-wet contact angles input of the simulation.

3.2.2- Wettability correlation to the radii of the pores

As discussed previously, [7] proposed that wettability could be correlated to the size of the pores and proposed 3 models: Fractional-Wet model (i.e. contact angles are not correlated to the size of the pores), Mixed-Wet Large (i.e., where large pores are oil wet and small pores are water-wet) and Mixed-Wet Small (i.e., small pores are oil-wet and large pores are water-wet). Identifying the wettability model (i.e. FW, MWS or MWL) is important for PNM simulation as it impacts the invaded pores and the residual oil saturation [9]. Oil that imbibes into the system in spontaneous drainage does not have access to the full rock as a part of the porosity is already filled with oil. Therefore, we propose to perform this analysis on the water-wet pores that had access to all the pore space during the spontaneous imbibition.

A pore network has been extracted from the images and used to analyze the experimental results. **Fig 11** presents the pore radii distribution of the water-wet pores and **Fig 12** shows the volumetric fraction of water-wet pores as a function of the pore radii. We can observe a clear correlation between the pore radius and the percentage of water-wet pores in the system that demonstrates that for this system large pores are more likely to be water-wet. We conclude then that we are in a MWS wettability model.

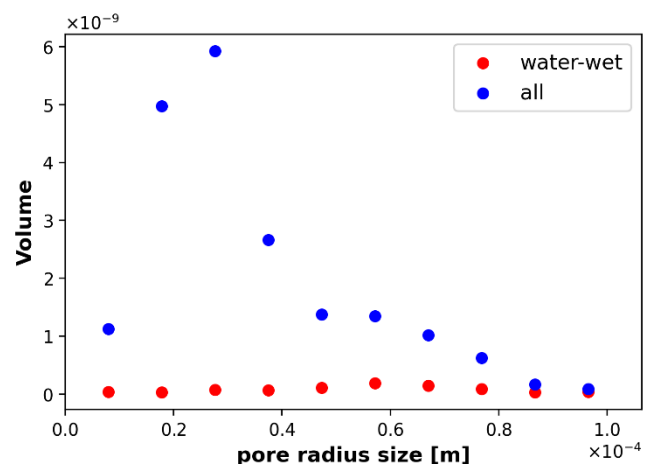


Fig 11 : The pore radii distribution obtained after extracting a pore network (blue) and the water-wet pore size distribution obtained from analyzing the pores occupancy (red)

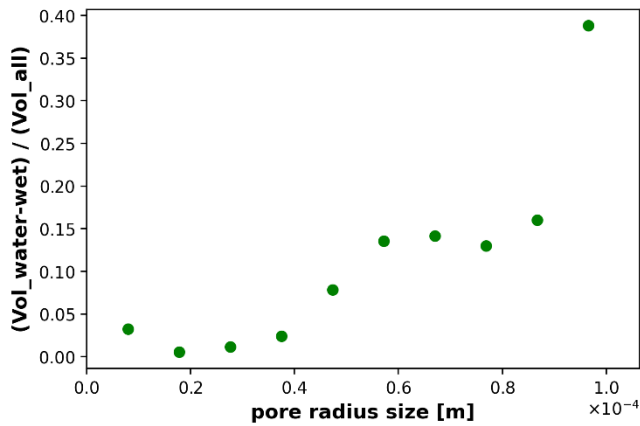


Fig 12 : The water-wet volumetric fraction as a function of the pore radius obtained after extracting a pore network and analyzing the fluids occupancies

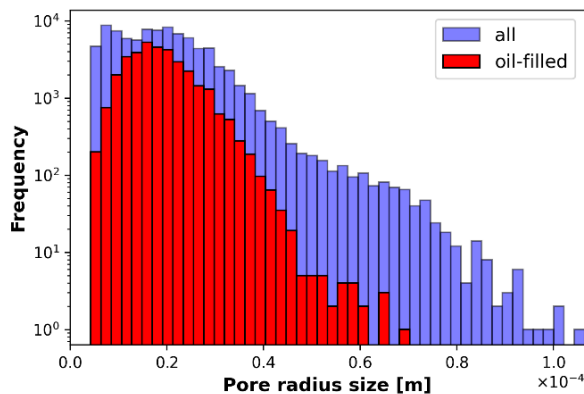


Fig 13 : Radii of oil filled pores at residual oil saturation, oil remains in the small pores

Fig 13 shows the oil filled pores at residual oil saturation, we observe that oil remains in the small pores which is what we expect in a MWS scenario as during waterflood water will first invade the water-wet pores then the larger oil-wet pores as the fluids will enter first the pores with lower capillary entry pressure in a drainage process [9]. This makes us more confident in the results of our analysis.

3.2.3- Spatial correlation of wettability

In this section, we investigate whether the wettability is correlated in space with clumps of more oil-wet and water-wet pores. This is an important parameter for the simulation and could have significant implications of the phase's connectivity especially through the flow in layers which would impact the relative permeability curves and the residual oil saturation. We propose to analyze spatial correlation using the water-wet pore's location determined from the extracted pore network because water had access to the full pore space during the spontaneous imbibition as explained in the previous section.

A common way of visualizing the spatial autocorrelation of a variable is a variogram plot (**Fig 14**) The correlation length can be regarded as a measure for the stationarity of a specific parameter distribution in space. In this case, the semi variance becomes stationary at a correlation length of 500 μm that represents for this rock 6 node to node lengths. This could be an important parameters for the simulations and in some cases it is not possible to match experimental observations if spatial correlation is not quantified properly [6]

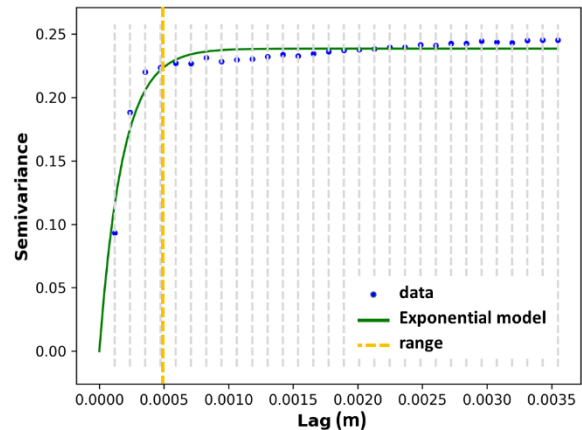


Fig 14 : Variogram plot for the water-wet pores using scikit-gstat [21]. It shows a correlation length of 500 μm

To summarize, the wettability experiment provides us with:

- 1- The fractions of oil-wet and water-wet pores obtained from the analysis of the capillary end effect
- 2- An indication of the contact angles in the oil-wet pores from the comparison of the volumes imbibed during spontaneous waterflood and spontaneous imbibition. For instance, if there is 50% oil-wet pores but nothing imbibes in spontaneous drainage it means that advancing contact angles are higher than 90° and receding contact angles are lower than 90° . Then, when we choose our contact angles we will select angles not too far from 90° . Similarly, if we have 50% oil-wet pores and similar volumes imbibed in the spontaneous imbibition and spontaneous drainage this means that even the receding contact angle in all pores is still higher than 90° then we know that we need higher contact angles in the oil-wet part.
- 3- The mapping of the water-wet pores provides us with a computation of the spatial correlation length
- 4- The mapping of the water-wet pores provides us with information of the wettability correlation to the pore radii (i.e.: MWS, MWL or FW)

4- Validation of DRP simulation workflow

Having built the DRP workflow, we proceeded to its validation. First, we took a low-resolution Bentheimer image at 5.8 microns that we enhance using ESRGAN to improve its resolution by a factor 4 and obtain an image with 3184x3280x12928 voxels. This image has the same aspect ratio as the SCAL experiment described below to avoid any differences created by different aspect ratios. Then, a stitching process was applied on the super-resolution image described previously. The image was divided into several subvolumes (2*2*9 along X, Y and Z) and networks were extracted from each sub-volume and stitched together. A network with 3.6 million elements was generated. After that, we create our experimental design to vary the simulation parameters within the uncertainty ranges. The input of the wettability anchoring is key at this stage and allows us to reduce the ranges of our parameters and hence have a smaller dispersion in our simulation results. In our experimental design, 3000 realizations have been generated and simulated (with varying the seeds numbers, the parameters of the contact angle distributions as described in table 1 and wettability spatial correlation parameters...) and mixed-wet small wettability model has been used in all the simulations. More details of our simulation input parameters can be found in **Table 1**. We note that we have used two contact angle distributions: the first in the oil-wet part of the sample and the second in the water-wet pores. The choice of these pores was made to be consistent with a mixed-wet small wettability model and considering spatial auto-correlation of pores with similar wettability. The wettability anchoring experiment did not provide us with direct information about contact angles. However, it gave indirect information about the oil-wet contact angles. In fact, imbibed water volume was much higher than the imbibed oil volume for the same duration and at the same sample length gives us an indication that the receding contact angle was lower than 90° in a considerable amount of the oil-wet pores. Therefore, we chose medium to low oil-wet contact angles to be consistent with this observation.

Table 1 : Simulation parameters used in Mixed-Wet Bentheimer simulations

Parameters	Value/Range
PD receding contact angle distribution	Normal distribution
PD receding contact angle standard deviation	4°-8°
Mean receding PD distribution	20°-30°
WF dist1 (oil-wet) advancing contact angle distribution	Normal distribution

WF dist1 (oil-wet), advancing contact angle standard deviation	4°-8°
Mean advancing WF dist1 (oil-wet) contact angle	115°-135°
WF dist 2 (water-wet) advancing contact angle distribution	Normal distribution
WF dist2 (water-wet), advancing contact angle standard deviation	4°- 8°
Mean advancing WF dist2 (water-wet) contact angle	70°-89°
Fraction of distribution 2 (water-wet fraction)	0.37-0.47
Correlation length	5-7 pores
Wettability model	Mixed-Wet Small
Initial water saturation	0.12-0.13

We observed that after aging in the anchoring experiment, several water droplets appeared on the center of the pores (**Fig 15**). We think that these correspond to some water layers that got disconnected after aging and that fall in the center of the pores. We measured that the oil relative permeability decreased by 30% during the aging, we apply therefore this reduction by scaling our simulated oil relative permeability. This reduction of permeability would not impact the water relative permeability since pores are filled with a single phase after the water invades them during waterflood.

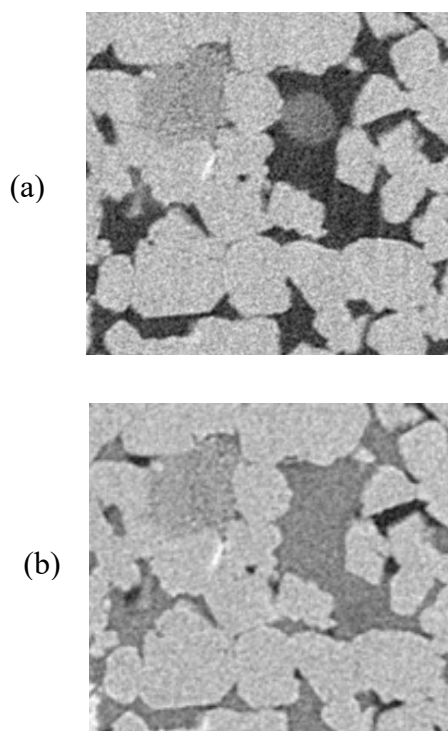


Fig 15 : Multiphase CT images at Swi after aging (a) and at Sor (b). It shows that water (dark grey) droplets were blocking an oil (black) filled pore at Swi and that the same pore becomes fully filled with water at the end of waterflood.

In order to reduce the uncertainty further, we use the measured parameters in the anchoring experiment and only keep the realizations that agree with the measurements from the wettability anchoring experiment. Therefore, we only keep simulations that have:

- $P_c=0$ between $S_w=0.4$ and $S_w=0.5$
- $0.1 < K_{rw} (S_{or}) < 0.2$
- $0.18 < S_{or} < 0.26$

After performing our blind simulation test, we compare the results to a high quality unsteady-state experiment performed in-house. The SCAL experiment was performed on a 5 cm diameter Bentheimer plug with 20 cm length. The plug had a porosity of 24% with an absolute brine permeability of 2.3D. Primary drainage was achieved through oil flooding using a displacement with viscous oil to target a low S_{wi} exempted from capillary end-effect. A homogeneous S_{wi} profile of average 12.1% was obtained. To make the plug mixed-wet, the same dead oil used on the anchoring wettability experiment was used to replace the mineral oil and perform 15 days of dynamic ageing process at 80°C to alter wettability of the SCAL plug. Afterwards, multi-rates waterflood at 80°C was performed. Initial flow rates were sized to fit Hagoort criteria [22] to avoid viscous fingering. It started at around 0.3ft/day. Oil production-pressure gradient vs time, and transient to equilibrium saturation profiles through 2D X-ray imaging internal devices were acquired during the experiment and numerical interpretation was performed using the software CYDAR® to find the best couple (K_r/P_c) matching oil production, pressure gradient and saturation profiles (transient and equilibrium).

Fig 16 shows our simulated relative permeability curves with all realizations and the P10, P50 and P90 scenarios obtained after ranking the oil production after 1 pore volume injected. We observe that our curves were in very good agreement with SCAL relative permeability that was presented by an envelope to consider the associated uncertainty. In fact, in an unsteady-state relative permeability experiment, the production data are then inverted in order to determine relative permeability curves. This inversion is non-unique and therefore we represent the SCAL relative permeability curve with an envelope of possible inversions of production data. This makes us confident about the predictive potential of DRP simulation when well informed with experimental data.

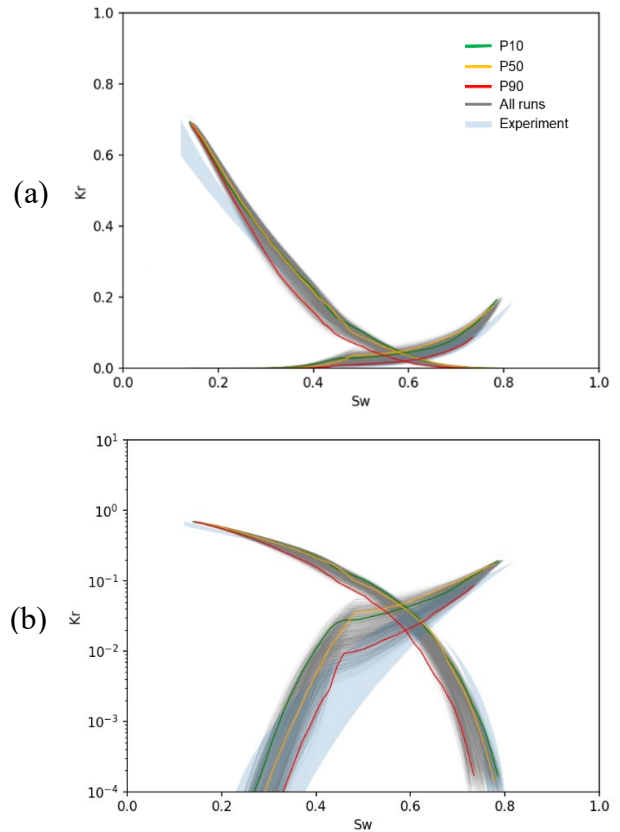


Fig 16 : Comparison between the simulated relative permeability curves: all realization (grey), P10 (green), P50 (yellow) and P90 (red) and experimental data (blue). We present the plots in linear (a) and log scales (b)

5- Conclusions

In this study we have applied TotalEnergies' DRP simulation workflow to predict the relative permeability in a Mixed-Wet Bentheimer. First, we augmented a low-resolution image using ESRGAN in order to have an image with a large field of view and fine resolution. Then, we extracted a pore network from this image using a stitching methodology.

Wettability input has been the weakest point of DRP simulation in the last few decades as it is difficult to quantify the values of contact angles, the wettability model and the spatial distribution of contact angles leading to having high number of degrees of freedom. Therefore, we have designed an innovative fast experiment that helps us to characterize wettability and have more reliable PNM simulations. With this experiment we could characterize that we have a mixed-wet system and identify the wettability model. In fact, we clearly observed that wettability in our sample was correlated to the radius and that the large pores were water-wet and the small oil-wet. The pore radii of the oil filled pores at residual oil saturation confirmed our observation as oil remained in the small pores which is a characteristic of mixed-wet small model. We could

also observe a spatial correlation of wettability and the correlation length had 6 pores length.

Having obtained all this information, we could run several hundreds of realizations of our simulations using our parallel PNM simulator where we varied the parameters within the identified uncertainty ranges. Furthermore, this experiment provided us with important measurements that helped us better constrain our simulations and we only kept the realizations that agreed with the measured data. Afterwards, our simulations were compared to a high quality in-house SCAL experiment performed with the same rock, same fluids and similar conditions. A very good agreement was obtained between the simulated and experimental data.

This study provided very promising results that, if confirmed by similar validation tests, would indicate that DRP simulation coupled with our pragmatic approach to characterize wettability is ready to be used in operational studies.

Acknowledgements

The authors would like to thank TotalEnergies management for the authorization to publish this work. Régis Brugidou is acknowledged for the fruitful discussions about the experimental set-up.

References

- [1] Oren P-E, Bakke S, Arntzen OJ. Extending predictive capabilities to network models. *SPE journal* 1998;3(04):324–36.
- [2] Bondino I, Hamon G, Kallel W, Kac D. Relative Permeabilities From Simulation in 3D Rock Models and Equivalent Pore Networks: Critical Review and Way Forward. *SPWLA-2012-v53n6a2* 2013;54(06):538–46.
- [3] Sorbie KS, Skauge A. Can Network Modeling Predict Two-Phase Flow Functions? *SPWLA-2012-v53n6a2* 2012;53(06):401–9.
- [4] AlRatrouf A, Raeini AQ, Bijeljic B, Blunt MJ. Automatic measurement of contact angle in pore-space images. *Advances in Water Resources* 2017;109:158–69.
- [5] Sun C, McClure JE, Mostaghimi P, Herring AL, Meisenheimer DE, Wildenschild D, Berg S, Armstrong RT. Characterization of wetting using topological principles. *J Colloid Interface Sci* 2020;578:106–15.
- [6] Foroughi S, Bijeljic B, Lin Q, Raeini AQ, Blunt MJ. Pore-by-pore modeling, analysis, and prediction of two-phase flow in mixed-wet rocks. *Phys. Rev. E* 2020;102(2):23302.
- [7] AlRatrouf A, Blunt MJ, Bijeljic B. Spatial correlation of contact angle and curvature in pore-space images. *Water Resour. Res.* 2018;54(9):6133–52.
- [8] Dixit AB, Buckley JS, McDougall SR, Sorbie KS. Empirical measures of wettability in porous media and the relationship between them derived from pore-scale modelling. *Transport in Porous Media* 2000;40(1):27–54.
- [9] Skauge A, Spildo K, Høiland L, Vik B. Theoretical and experimental evidence of different wettability classes. *JOURNAL OF PETROLEUM SCIENCE AND ENGINEERING* 2007;57(3-4):321–33.
- [10] Yang J, Bondino I, Regaieg M, Moncorgé A. Pore to pore validation of pore network modelling against micromodel experiment results. *Computational Geosciences* 2017;21(5):849–62.
- [11] Wang X, Yu K, Wu S, Gu J, Liu Y, Dong C, Qiao Y, Change Loy C. Esrgan: Enhanced super-resolution generative adversarial networks. In: *Proceedings of the European conference on computer vision (ECCV) workshops*. p. 0.
- [12] Jolicoeur-Martineau A. The relativistic discriminator: a key element missing from standard GAN. *arXiv preprint arXiv:1807.00734* 2018.
- [13] Arganda-Carreras I, Kaynig V, Rueden C, Eliceiri KW, Schindelin J, Cardona A, Sebastian Seung H. Trainable Weka Segmentation: a machine learning tool for microscopy pixel classification. *Bioinformatics* 2017;33(15):2424–6.
- [14] Raeini AQ, Bijeljic B, Blunt MJ. Generalized network modeling: Network extraction as a coarse-scale discretization of the void space of porous media. *Phys. Rev. E* 2017;96(1):13312.
- [15] Regaieg M, Bondino I, Varloteaux C, Farhana Faisal T, Yang J, Rivenq R (editors). *Large two phase Digital Rock Physics simulations for relative permeability uncertainty assessment*; 2021.
- [16] Regaieg M, Moncorgé A. Adaptive dynamic/quasi-static pore network model for efficient multiphase flow simulation. *Computational Geosciences* 2017;21(4):795–806.
- [17] Valvatne PH, Blunt MJ. Predictive pore-scale modeling of two-phase flow in mixed wet media. *Water Resour. Res.* 2004;40(7).
- [18] Gropp W, Gropp WD, Lusk E, Lusk, Argonne Distinguished Fellow Emeritus Ewing, Skjellum A. *Using MPI: portable parallel programming with the message-passing interface*. MIT press; 1999.
- [19] Balay S, Abhyankar S, Adams M, Brown J, Brune P, Buschelman K, Dalcin L, Dener A, Eijkhout V, Gropp W. *PETSc users manual* 2019.
- [20] Sergeant M. *Contribution de la Méthodologie de la Recherche Expérimentale à l'élaboration de matrices uniformes: Application aux effets de solvants et de substituants*. Aix-Marseille 3; 1989.
- [21] Mälicke M. *SciKit-GStat 1.0: a SciPy-flavored geostatistical variogram estimation toolbox written in Python*. *Geoscientific Model Development* 2022;15(6):2505–32.
- [22] Hagoort J. Displacement stability of water drives in water-wet connate-water-bearing reservoirs. *Society of Petroleum Engineers Journal* 1974;14(01):63–74.

ElRock-Net: Assessing the Utility of Machine Learning to Initialize 3D Electric Potential Simulations

Bernard C. Chang^{1,*}, Javier E. Santos², Rodolfo Victor³, and Maša Prodanović¹

¹Hildebrand Department of Petroleum and Geosystems Engineering, The University of Texas at Austin, Austin, TX 78722, USA

²Center for Nonlinear Studies and Computational Earth Science Group, Earth and Environmental Sciences Division, Los Alamos National Laboratory, USA

³Petrobras, Rio de Janeiro, Brazil

Abstract. Advancements in imaging technology are enabling accurate simulations of transport properties through the pore space of an imaged rock sample, albeit at a computational cost. Meanwhile, machine learning has emerged as an alternate tool for modelling transport properties that, once trained, use a fraction of the computational resources that traditional simulations require. However, machine learning models often fail to strictly enforce physical constraints of the system, leading to solutions that are less accurate than that of traditional solvers. Here we propose a novel hybrid workflow that combines machine learning and conventional simulation methods to combine their speed and accuracy. The workflow begins with a 3D, binary image of a sample. A trained convolutional neural network learns spatial relationships between a porous medium geometry and predicts the electric potential field through the medium. A validated finite difference solver uses the predicted field as input and fine-tunes it to obtain a deterministic result. The proposed workflow provides reductions in computational cost without sacrificing solution accuracy on unseen samples despite not having a fully trained model.

1 Introduction

Quantifying electrical properties in porous media is an important method for characterizing and monitoring subsurface systems. It has applications in hydrocarbon reservoirs, carbon capture and storage [1], hydrogeology [2], and mineral exploration [3]. The electrical response of these systems aids in inferring the composition of the material and its phase distributions.

For example, in well-log interpretation of hydrocarbon reservoirs, the resistivity log is a particularly useful indicator of *in situ* fluid saturation estimations because of its sensitivity to the varying phase conductivities [4]. Conventional interpretation models generally rely on the assumption that saline formation water is the only conductive phase — that hydrocarbon and the solid matrix do not readily allow electric current to flow. Correlating the resistivity to fluid saturations are crucial to accurately assessing the viability of a reservoir.

Fundamentally, electrical resistivity is an intrinsic property of a material that quantifies how strongly it conducts electric current. The overall resistivity response is subject to depositional and diagenetic processes that dictate the structure of the pore space and the phases that fill the pore space (assuming that the grains are not conductive). More specifically, resistivity measurements are most impacted by the electric tortuosity of the connected conductive region and variations in cross-sectional area of the conducting path [5]. The physical processes that result in these geometric heterogeneities can exist on multiple length scales, extending down to the nano- and micron-scales.

Small scale (i.e., nanometer-to-micron-scale) heterogeneities can have a significant impact on the total electrical response of the system, arguably more so than for fluid flow [6]. Physical interpretations of larger length-scale correlation components, such as the Winsauer tortuosity factor [7] or the cementation exponent in Archie's equations [8], often attempt to account for these pore-scale heterogeneities [9]. However, quantifying electrical behavior on the pore scale is critical to making inferences on larger domains.

Recent improvements in imaging technology have led to the observation of many porous media processes. Digital, 3D image data acquired through high-resolution imaging, such as computed tomography (CT), micro-computed tomography (μ CT), and focused ion beam scanning electron microscopy (FIB-SEM) reveal details of porous media structures on various length scales. Analyzing rock properties based on these digital images are collectively known as *digital rock physics*. Assuming a minimum representative elementary volume (REV) and sufficient resolution, direct simulations on these image samples provide an accurate picture of physical processes on the pore scale and the ability to upscale to larger length scales. Further, breakthrough innovations in storage, hardware, and software have provided the capability to process data, run simulations, and analyze results on increasingly large images. Digital Rocks Portal (DRP) [10] is highlighted here as an open repository that contains a wide range of porous media samples. It provides simulation and machine learning training data used in this work and many others [11, 12, 13].

* Corresponding author: bcchang@utexas.edu

Although imaging advancements have contributed to improved understanding of pore-scale processes, the computational resources required to handle the enlarged image sizes are likewise increasing. Conservatively, computational demands scale to the cube of the side length of the discretized domain. This becomes problematic when performing simulations on structurally heterogeneous samples, such as in carbonate rocks. Oftentimes, achieving a minimum REV (if possible) necessitates increasing the size of the image sample beyond a system's hardware capabilities. This renders performing direct simulations on REV's of complex systems exceedingly difficult, typically resulting in long compute times on supercomputers.

Meanwhile, deep learning has emerged as an alternate tool for recognizing patterns from observational data. These algorithms have widespread applications in subsurface systems, including reservoir characterization, production optimization, and lithology interpretation and rock classification [14, 15, 16]. In the context of digital rocks physics, machine learning workflows have also been successful modeling some transport properties such as permeability and flow velocity [13, 17, 18]. However, these workflows often fail to strictly enforce the physical constraints of the system, leading to solutions that are less accurate than that of traditional solvers. Training accurate neural network models also require large quantities of data and are not easily generalized to complex, heterogeneous reservoir rocks.

Here we propose a framework similar to that of Wang et. al [19] for combining machine learning workflows and direct simulation methods (Fig. 1). A trained neural network extracts spatial relationships between a porous medium geometry and predicts the electric potential field through the medium. The predicted field is used as the initial condition for a validated Laplace equation solver and fine-tunes it to obtain a deterministic result. This framework combines the benefits of machine learning and direct simulation to reach a solution quickly without sacrificing accuracy. We also provide some guidelines and metrics for assessing the model predictions on unseen samples.

2 Methods and Materials

2.1 Dataset

Porous media in the subsurface is comprised of a wide range of lithologies. Because most traditional resistivity correlations were developed for clastic, sedimentary rocks, we direct assessment of the proposed framework to predictions on such lithologies.

To generalize our findings, we sample from open data benchmark on Digital Rocks Portal (DRP) [20, 21]. The catalog consists of 217 binary images spanning over 50 rock types and lithologies and were processed from 125 projects currently hosted on DRP. The catalog also includes results from flow and electrical simulations in addition to geometric and structural characterizations of the pore space. Subvolumes of 256^3 and 480^3 were extracted from the center of the original samples and oriented such that the direction of flow is parallel to the z-axis. The images were then preprocessed to ensure percolation and to eliminate all but the largest connected component of the pore space.

As part of this study, we sample four numerically-dilated sphere packs and four sandstone samples. The original, discretized sphere pack was reconstructed using the locations of the Finney packing of spheres [22]. Subsequent morphological operations (erosion and dilation) were performed to vary the porosity from 0.10 – 0.42. The five sandstone samples selected for this study originated from Neumann et al. on DRP [23] and include Parker, Leopard, Kirby, and Bentheimer sandstones with porosity values summarized in Table 1. We assume that the sandstone samples are clay-free. For both sandstones and sphere packs, we assume the solid matrix is non-conductive and the void space is fully saturated with conductive brine.

Direct simulations often perform calculations on volume sizes exceeding 1000^3 voxels. However, memory constraints on the available graphical processing units (GPUs) severely limited the size of viable training data. The 200^3 subvolumes are therefore used for training data.

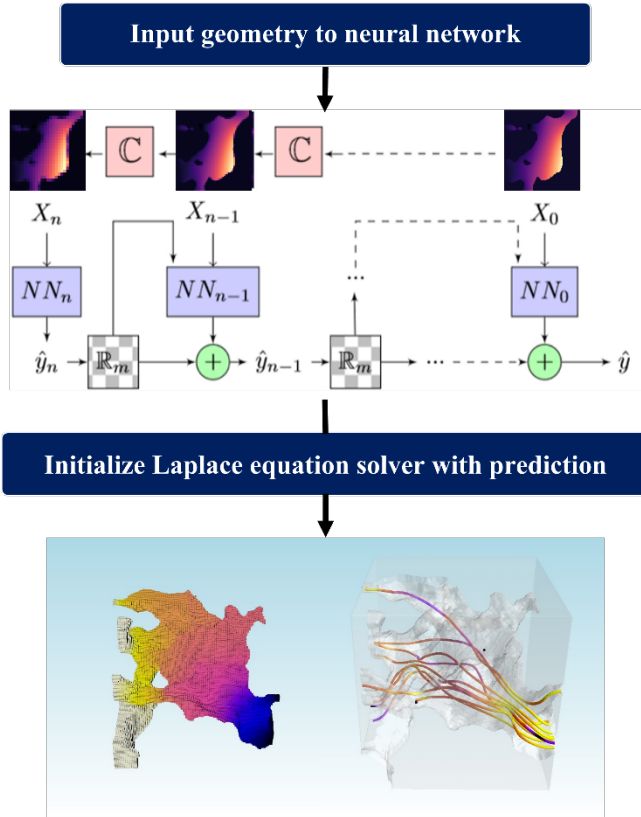


Fig. 1. Conceptual figure of the proposed framework. A trained neural network predicts the electric potential distribution through the pore space. A validated solver is then initialized with the prediction and obtains the potential and current fields through the medium.

Table 1. Nomenclature, porosity, and simulated formation factor for sphere pack and sandstone samples.

Sample	Description	ϕ	F
SP0	Eroded SP	0.418	$3.57 \pm 2.21\text{E-}04$
SP2	Dilated SP	0.293	$6.48 \pm 3.91\text{E-}04$
SP4	Dilated SP	0.182	$15.38 \pm 4.42\text{E-}02$
SP6	Dilated SP	0.099	$98.71 \pm 9.64\text{E-}01$
SS4	Parker SS	0.268	$11.00 \pm 6.33\text{E-}02$
SS8	Leopard SS	0.273	$11.05 \pm 2.22\text{E-}02$
SS9	Kirby SS	0.211	$21.91 \pm 1.23\text{E-}1$
SS11	Bentheimer SS	0.088	$174.95 \pm 4.12\text{E}0$

2.2 Electrical Simulations

Traditional methods of relating electrical resistivity to fluid saturation (S_w) in clay-free reservoirs are commonly based on Archie's empirical equations [8].

$$R_t = R_w \frac{a}{\phi^m S_w^n}, \quad (1)$$

where R_t and R_w are the total resistivity and resistivity of formation water, a is the Winsauer tortuosity factor [7], ϕ is porosity, S_w is the brine saturation, and m and n are experimentally obtained cementation and saturation exponents.

The formation resistivity factor, F , is derived from Archie's equation and relates the sample's resistivity to its ϕ and a :

$$F = \frac{\sigma_w}{\sigma_o} = \frac{a}{\phi^m}, \quad (2)$$

where σ_w and σ_o are the conductivities of the brine and the fully brine-saturated formation, respectively. Physically, F can be considered a normalized conductivity that measures the influence of the pore structure on the conductivity of the sample.

We assume a reliable segmentation of a porous medium into solid and void space and use it to solve the generalized Laplace equation for the electric potential distribution through the medium,

$$\nabla \cdot (\sigma \nabla \varphi) = 0, \quad (3)$$

where φ is the scalar electric potential field.

The volume-averaged currents in the three coordinate directions are found using the solution to the finite difference representation of the Laplace equation. The total electric current, I , through the rock is defined as

$$I = \oint \sigma \nabla \varphi \cdot \hat{n} \, dA. \quad (4)$$

The electric current is then used to calculate the macroscopic conductivity of the rock

$$\sigma_{\text{rock}} = \frac{LI}{A\Delta V}, \quad (5)$$

where L is the sample length, A is the area of a slice orthogonal to the flow of electric current, and ΔV is the difference in macroscopic electric potential applied at the inlet and outlet. Finally, we use σ_{rock} in equation 2 to calculate F .

Every sample chosen for this dataset consists of one non-conductive grain phase and one conductive fluid phase. We, therefore, assign the conductivities of the grain and fluid phases to be 0 and 1, respectively. The potential value at the inlet and outlet slices are fixed and the electric potential is initialized as a linear gradient through the pore space. The normal component of the electric current density is set to zero at pore-grain boundaries.

We perform electrical simulations using Digital Rock Suite (DRS) [24]. To validate the code, we numerically calculated the electrical conductivities of 14 fluid configurations in a periodic, random, close-packing of spheres of uniform radius. The datasets, authored by McClure et al. [25], used the lattice Boltzmann method to determine equilibrium fluid configurations at different initial fluid saturations. We compare the DRS solution to that of DC3D.f, a similar, open-source code from the National Institute of Standards and Technology [26]. The reported porosity of the sphere pack is 0.369 and has a computational domain size of 900^3 voxels. The code was validated using samples containing multiple fluids occupying the pore space. However, the scope of this study is limited to samples with a single occupying fluid. While electrical predictions in partially-saturated domains are desirable, accurate single-phase electrical property prediction has remained a challenge and must be better understood first.

As Fig. 2 shows, both solvers showed good agreement in their results. Generally speaking, as the wetting phase saturation decreases, the bulk wetting phase becomes disconnected and a negative deviation from Archie's law would be observed [27]. However, in this saturation regime, we would expect the resistivity to follow a linear trend in log-log space (Archie's law). The power law fit further supports validation of DRS as the fitting parameters, a and n , matched the expected values for a packing of spheres.

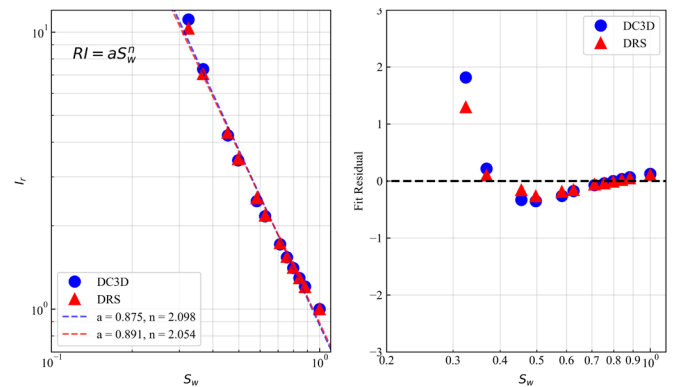


Fig. 2. Comparison of resistivity calculation results on a 900^3 -voxel packing of spheres at various brine saturations. Both results follow a linear trend as described by Archie's equation; however, Digital Rock Suite performed better at smaller saturations. Each simulation uses 64 processors on the Stampede2 cluster in the Texas Advanced Computing Center (TACC).

In terms of run times, DRS was generally faster than DC3D.f and saw considerable improvement at smaller water saturations.

2.3 Machine Learning Model

Direct numerical simulations on images can accurately describe physical phenomena through complex geometries. However, fully deterministic calculations are often computationally demanding, particularly for large domains.

Another promising avenue is using data-driven models to estimate properties from 3D images. Machine learning (ML) has emerged as an effective tool for finding complex relationships in structured data. Making predictions with ML models is computationally inexpensive compared to traditional simulations.

For any neural network, the training phase is the most resource-intensive task. Typically, models are trained on GPUs because their hardware architecture enables them to handle more parallel processes than their CPU counterparts. However, most commercially-available GPUs host memory ranging from 2 – 24 GB, resulting in a constraint on the size of viable training data. This presents a bottleneck for network training in that training on images larger than the required minimum REV is often difficult or impossible with current hardware resources.

To circumvent this constraint, previous networks often employed patch-based learning [13, 19] in which the image is divided into small subvolumes. This was advantageous in that the network could train and predict on any arbitrarily-sized volume. However, patch-based learning assumes stationarity of the flow statistic and, therefore, depends on the statistical homogeneity of the pore space.

For the proposed framework, we adopt the MultiScale Network for hierarchical regression (MS-Net) [18], which is the first convolutional neural network (CNN) that successfully predicted permeability of imaged samples that included heterogeneities such as fractures and vugs. The network architecture was designed to capture morphological information across entire 3D volumes by using a hierarchical set of models, each responsible for learning increasingly coarse realizations of the input data. Santos et al. [18] originally used this network to predict the fluid flow velocity field and absolute permeability from a 3D binary image. Preliminary results indicate that the same network architecture can be adopted to predict the electric potential field.

The coarsening process involves averaging each group of 8 neighboring pixels (in 3D) to obtain a new image that is 8 times smaller than the original (Fig. 3). In this fashion, the model can see the image in its entirety, allowing it to recognize heterogeneity in the pore space. The hierarchical network architecture consists of a system of smaller neural networks. The individual neural networks train and predict on the same input domain, but at different resolutions. The features that each network learns at its associated scale are used to inform the next refined scale. As such, the coarsest image and each prediction is subsequently passed to increasingly fine resolution scales until the original image resolution is recovered.



Fig. 3. Example coarsening of the ground-truth image, in this case the detrended electric potential. Average pooling is performed on each successive layer to reduce the size of the preceding image by 2^3 . A system of networks are trained on each scale, with coarser images informing finer images.

The ground truth data for training comes from the output of the numerical solver, DRS. DRS initializes the electric potential through each slice of the image using a linear gradient between the inlet and outlet slice values (2 and 1, respectively). We would expect the final solution to present similarly, except with deviations due to the configuration of the input geometry and the applied boundary conditions. The underlying gradient can be removed (detrended) to aid in improving machine learning model performance by subtracting the initial linear gradient and only training with residual values of the electric potential. From a machine learning perspective, the underlying trend can distort the relationship between the explanatory and response variables, hindering a model’s ability to learn. By detrending the data, we eliminate the need for the model to learn the underlying trend. This highlights anomalous regions where the potential value deviates from the underlying linear gradient initialization. The model then predicts these residual values to which the linear trend can then be re-added (retrended) to recover the original potential distribution.

In this framework, we train the neural network using only the binary image as input.

2.4 Assessment Metrics

Neural networks have difficulty generalizing to features they have not seen before [28]. Common approaches for remedying this are by either increasing the diversity of the training data or by developing more robust relationships by including more information about the data (e.g. geometric features, physics-informed learning, etc.). Additionally, predictions of transport fields do not necessarily obey the physical laws that govern such processes. Whether providing the network with more training data or employing the proposed framework, traditional simulations are still a necessary component to scientific research.

The assessment of the proposed framework leverages a phenomenon known as overfitting. Overfitting occurs when the network depends on specific details of the training set — in essence, the model fits to the noise of the training data. Theoretically, a completely overfit model will predict the training data with 100% accuracy. Overfitting is generally undesirable because it only performs well on the training data while making relatively poor predictions on unseen data.

The scope of this study is not to produce a generalizable model, but to assess the degree to which a model should be trained to see benefits in simulation run time. We, therefore, perform a sensitivity analysis in which models are

intentionally overfitted to the provided training data. These models are intended as the “best case” scenario in which the error in prediction for the supplied training sample is minimal. They are not intended to be generalized models that can be applied to predict on other domains. Each model is provided one training sample, is trained for approximately 30,000 epochs, and predicts on the same training sample. Intermediate model states are saved throughout training to track the model’s progression. The intermediate and final predictions are supplied to DRS and the run times to simulation convergence are compared.

We explore nine metrics to assess the training-data prediction accuracy of the model throughout training. We calculated each metric directly on the predicted detrended field (model output) and on the manually re-trended field (input field supplied to DRS). These metrics are evaluated against the simulation run times to gain insights into the components important to the success of the proposed framework. When the ground-truth is known, such as in training and validation data for supervised learning, the most important metrics can be included as additional penalization criteria. When generalizing to unseen data, metrics that do not require a known solution can also be calculated to evaluate the quality of the prediction.

2.4.1 Norms

Neural network training is an optimization problem in which a loss function is minimized. Because loss functions are measures of prediction error, the vector norms of the difference between the labeled data and the predictions are commonly employed in loss functions. MS-Net uses the Mean Squared Error (MSE) loss function between the ground-truth (Y_i) and predicted (\hat{Y}_i) fields,

$$MSE = \frac{1}{n} \sum_i^n (Y_i - \hat{Y}_i)^2. \quad (5)$$

The use of MSE causes MS-Net to preferentially penalize larger magnitudes of $|Y_i - \hat{Y}_i|$. In other words, the network pays more attention to model parameters that cause predictions to diverge further from the true field. For comparison, we also calculate the L_2 distance between Y_i and \hat{Y}_i ,

$$L_2 = \sqrt{\sum_i^n (Y_i - \hat{Y}_i)^2}. \quad (6)$$

Alternatively, one may choose to use the mean absolute error (MAE), based on the L_1 distance, as the loss function. This loss function is less sensitive to outliers than MSE because the values are not squared. We, therefore, calculate the L_1 distance to the ground truth,

$$L_1 = \sum_i^n |Y_i - \hat{Y}_i|. \quad (7)$$

2.4.2 Peak Signal-to-Noise Ratio

Peak signal-to-noise ratio (PSNR) is commonly used to quantify the “closeness” of an image to being an exact copy of another such as when filtering images. It is a voxel-by-voxel calculation, derived from MSE, that determines imperceptible differences between two images and is defined as

$$PSNR = 20 \log_{10} \frac{MAX_I}{MSE(Y_i, \hat{Y}_i)}, \quad (8)$$

where MAX_I is the maximum possible voxel value of the 3D image. The PSNR value decreases as the MSE increases, implying large differences between the input images.

2.4.3 Histograms

Analyzing the histogram of \hat{Y}_i reveals important information about the training progression and areas that the model has difficulty training. Comparing the distributions of \hat{Y}_i and Y_i can also help to confirm error metrics.

Detrending a field helps the network train by eliminating the need to learn the variance due to an underlying trend. As previously stated, detrending the potential field highlights anomalous regions in which the potential deviates from the underlying linear trend. These residuals are approximately normally distributed about a mean close to zero. Here we track the mean of \hat{Y}_i , which should approach the expected value of Y_i as training progresses.

2.4.4 D-2 Score

The result of both patch-based networks and multiscale networks are predictions made up of perceptible blocks. These are unphysical artifacts of the network algorithm due to the convolution operation. When analyzing these types of images for mass conservation or slice-wise flux continuity, the boundaries between blocks manifest as large jumps in otherwise continuous behavior. If unresolved, these can negatively impact calculations of properties, such as F or permeability. MS-Net appears to refine these blocks as training continues; however, they are still seen even after the model is severely overfit.

We quantify the smoothness of the image using a value derived from taking the Laplacian of the image — the D-2 score. First, the Laplacian of the image is taken,

$$\nabla \cdot \nabla \hat{Y} = \frac{\partial^2 \hat{Y}}{\partial x^2} + \frac{\partial^2 \hat{Y}}{\partial y^2} + \frac{\partial^2 \hat{Y}}{\partial z^2}. \quad (10)$$

The Laplacian of the image is calculated by convolving the predicted image with a 27-point Laplacian stencil [29]. We sum the Laplacian over all pore voxels to calculate the D-2 score. When compared to the D-2 score of the labeled training image, intermediate predictions with more pronounced boundary effects will have a larger D-2 score. The D-2 score

begins to decrease throughout the training progress as the artificial boundary effects are refined.

2.4.5 Formation Factor

Finally, we calculate the formation factor of \hat{Y} . The average current flux in the direction of flow is used for calculating F , so evaluating this property and its associated uncertainty in the predicted image is an indication of flux continuity through the image.

The uncertainty (standard deviation) in the current flux across every slice orthogonal to the flow direction is used as a convergence criterion in DRS simulations. Therefore, calculating the uncertainty in F in the prediction provides a direct comparison to DRS convergence.

Here, we convolve the prediction with a finite difference kernel to calculate the component of the current density parallel to the direction of flow. We then implement a masking scheme to respect the pore-grain boundary conditions outlined in the DRS algorithm. Like DRS, this component of current density is summed over each orthogonal-to-flow slice to find the current flux. Finally, the average and standard deviation of these fluxes are used to evaluate the macroscopic conductivity and formation factor.

3 Results and Discussion

MS-Net is trained using single 3D, binary images of 200³ sphere packs and clean sandstones. The models' accuracy of predicting the potential field of the training samples is evaluated. The accuracy metrics are compared against the predicted formation factor. Finally, we investigate possible relationships between these metrics and accelerating simulation results by using the predicted field as input.

Training was performed using Nvidia 16 GB V100 GPUs on Longhorn — a Texas Advanced Computing Center (TACC) resource. Each model was trained for ~30,000 epochs, requiring ~16 hours of training time. This illustrates the cost balance between machine learning training and simulation that must be considered. Though models can require long training times (order of hours to days), making predictions are effectively instantaneous when compared to simulations. For example, in this study, testing is performed on a local desktop machine with 64 GB RAM and required only a few seconds to make a prediction. Using this framework with generalized models can lead to reaching accurate solutions far more quickly for a limitless number of unseen samples. This framework can also be extended to more complicated solvers that generally require longer run times for more immediate run-time reduction benefits.

3.1 Evaluation of Training Performance

The training progress of machine learning models are commonly tracked using the models' loss functions. Common examples of loss functions are MAE (L_1 loss) and the MSE (L_2 loss).

The L_1 norm (Fig. 4) of the detrended field monotonically decreases as training progresses, an indication

that intermediate predictions are approaching the labeled data.

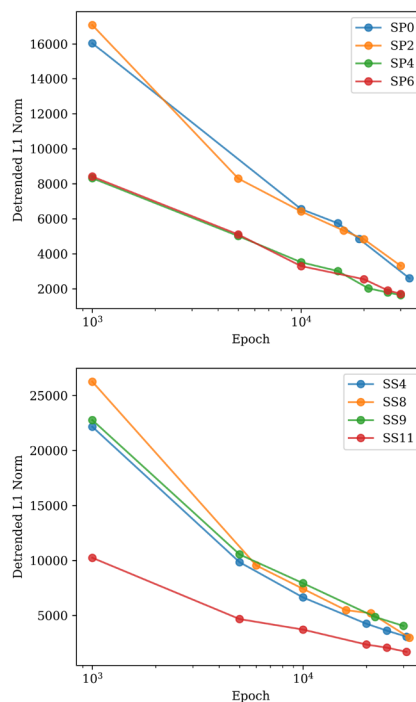


Fig. 4. L_1 distance to ground truth of various models saved through training. The L_1 distance, or MAE, is a common training performance metric. For both the sphere pack samples (left) and sandstone samples (right), we see that the MAE monotonically decreases as training progresses.

The L_2 loss (Fig. 5) shows similar behavior. The L_1 and L_2 losses follow the same general curve for a particular sample. SP2 and SS4 maintain the largest error throughout training among their respective sphere packs and sandstone

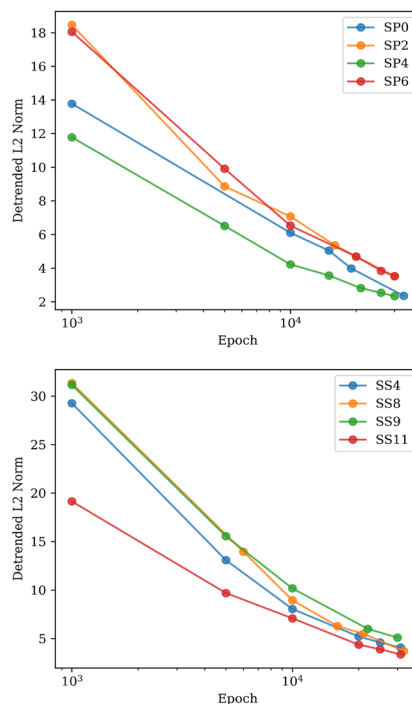


Fig. 5. L_2 distance to ground truth of various models saved through training. Similar to the MAE (Fig. 4), the MSE monotonically decreases as training progresses for both the sphere pack samples (left) and sandstone samples (right).

samples. SP6 and SS11 tend to have the smallest error during training, though this could be an artifact of their small porosity values.

As previously discussed, the MS-Net architecture trains convolutional neural networks on multiple resolution scales. Making predictions using this architecture involves a refinement operation, which results in blocky predictions. These blocks are artificial discontinuities within the pore space and will negatively impact calculations of macroscopic properties, such as F .

The Laplacian of the image (Fig. 6) highlights regions where rapid changes in intensity occur. Naturally, this occurs near the pore-grain boundary, where boundary conditions must be enforced. The potential within grains is assigned to be zero while the potential values in the pore space change gradually and with an approximately linear underlying trend. Therefore, the Laplacian should be close to zero within the pore and the grain space.

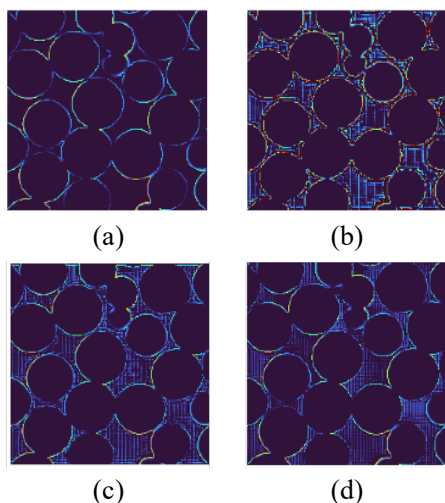


Fig. 6. Example slice (200 x 200) of the Laplacian transform of a) DRS output, Laplacian of the model predictions after b) 1000, c) 15000, d) 30000 training epochs. The Laplacian highlights sharp contrasts in voxel values (grain-pore boundaries and block artifacts). As training progresses, the boundary effects gradually disappear, which, when summed, results in decreasing D-2 scores approaching that of the simulation output.

Evaluating the Laplacian of the prediction captures the large change in image intensity near the pore-grain boundary and along the artificial discontinuities. As training progresses, MS-Net tends to refine these blocks. Nonetheless, they are still prevalent in the model predictions, even in highly overfit models. This highlights the need for more intelligent masking operations to refine the resolution of the prediction from the coarsest scale. One could also incorporate smoothing operations, such as median filtering, into model training.

3.2 Evaluation of Predicted Formation Factor

To compute the current density, we convolve the predicted electric potential field with a finite difference kernel and sum the result over each slice. The average of the slice-wise sum is used to calculate the predicted formation factor (\hat{F}).

\hat{F} of the final model matches closely with the simulation results for both the sphere packs and the sandstone samples (Fig. 7). In general, the model underpredicts the value of F ,

particularly at smaller values of porosity. Likewise, the uncertainty in \hat{F} , calculated from the standard deviation in the sum of the slice-wise current flux, increases with decreasing porosity. These observations can be attributed to the potential value discontinuities at the boundaries of the block artifacts.

Fig. 7 also shows a clear relationship between the uncertainty of \hat{F} and the simplicity of the pore system — the uncertainty in \hat{F} of the sandstone samples is larger than that of the sphere packs. The uncertainty in \hat{F} stems from local heterogeneities of the pore space. Structural details, such as tortuosity and constriction factor, nonuniformly affect the current flux and are not directly accounted for when evaluating F . Therefore, the uncertainty in \hat{F} is generally small for more homogeneous samples like sphere packs and in samples with large porosity.

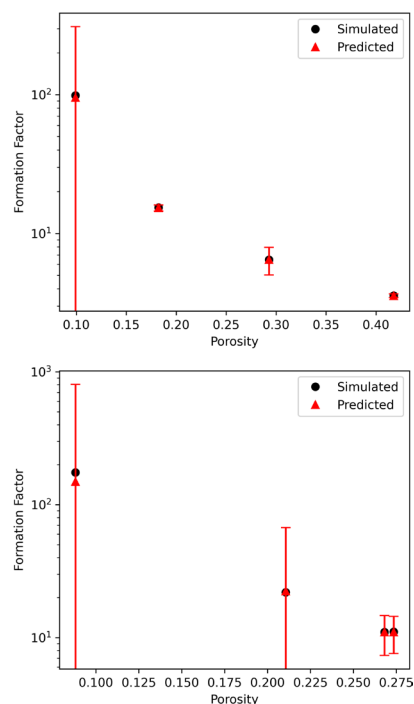


Fig. 7. Formation factor comparison between the simulated result (black circles) and the final model prediction (red triangles). The predicted values of formation factor are fairly accurate for both sphere packs (left) and sandstones (right) but tend to underpredict the ground truth. The uncertainty of the prediction is much larger than that of the simulation.

Although the MSE monotonically decreases with training epoch, the relative error in \hat{F} does not follow the same trend (Fig. 8). Several samples show good early \hat{F} and are only slightly improved by the final prediction, at the smallest MSE. Broadly speaking, this is indicative of the fact that F is a macroscopic quantity and does not account for the exact microscopic details of the pore space. The implications of this are that undertrained models are still serviceable as F estimators. Nevertheless, additional training generally still results in a decrease in the relative error of \hat{F} . This is apparent in the sandstone samples where later \hat{F} are closer to the expected result than early \hat{F} .

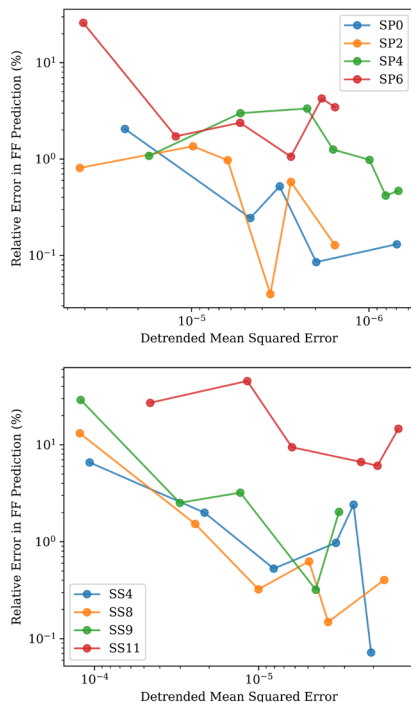


Fig. 8. Relative error in the formation factor prediction versus MSE (decreasing MSE to the right to reflect training progression) of the sphere pack samples (left) and the sandstone samples (right). Decreasing MSE does not necessarily indicate improved formation factor prediction.

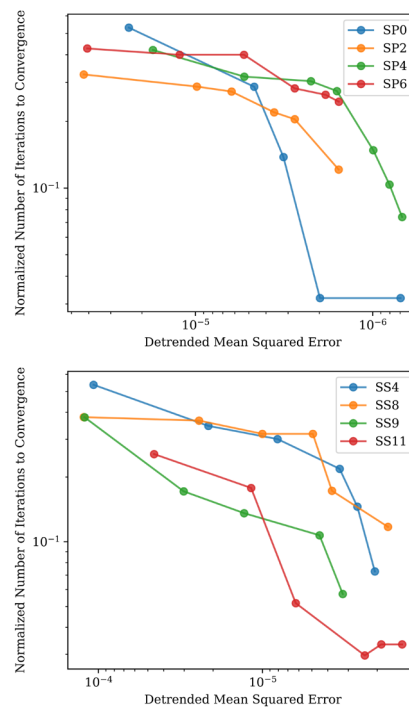


Fig. 9. Normalized number of iterations to convergence error versus MSE (decreasing MSE to the right). The framework improves the run time of both sphere packs (left) and sandstones (right) to less than 10% of the original.

3.3 Evaluation of Simulation Time Improvement

To assess the proposed framework, we save the re-trended predictions of intermediately trained models and feed them to DRS as initial conditions. We note the number of iterations that DRS requires to reach convergence and normalize it by the number of iterations required when assuming a linear potential gradient.

Typical simulations used for this study required between 800 – 2000 iterations to converge (more porous and well-connected samples generally required fewer iterations). The actual wall-clock run time for the simulations are largely hardware dependent. Because the images used in this study are relatively small, the total simulation run time only lasted

Here, we report the most illuminating metrics. We first investigate metrics associated with supervised learning — those that compare predictions with labeled data. We then look for relationships between unsupervised metrics and run time improvements to provide example diagnostics that can be included in future model training.

3.3.1 Supervised Metrics

Using \hat{Y} as the initial condition for DRS results in a drastic improvement in the required run time to convergence (Fig. 9). In the best cases, the proposed framework saw over an order of magnitude improvement, reducing the number of iterations to convergence to less than 10% of that of the linear gradient assumption.

MSE is a decent predictor of the run time improvement, where the number of iterations to convergence decreases with decreasing MSE. However, the plateau in iterations at large MSE indicates that the model needs to achieve a threshold accuracy before seeing a significant improvement in run time. Nevertheless, even under-trained models with large MSE still sees over a 50% improvement in run time, implying that models do not necessarily need to make entirely accurate predictions to seeing benefits in run time. This has important implications for the use of the proposed framework, particularly when applying a trained model to unseen data. We also expect to see more significant improvements as the size and complexity of the image increases. For example, the 900^3 spherepack samples used for code validation required simulation times upwards of 10 hours for the smallest saturation points. This could feasibly be reduced to a run time of only a few minutes if supplied an extremely accurate prediction result. If one assumes that the simulation run time approximately scales to the cube of input image side length [13], we hypothesize that one could feasibly start seeing significant run time benefits when predicting on $\sim 500^3$ images (2+ hours of simulation time reduced to several minutes).

Because PSNR is derived from MSE, it exhibits similar predictive capability of run time improvement as MSE (Fig. 10). The curves also show slow improvement in run time at small values of PSNR. At a PSNR value of ~ 40 , we begin to see drastic improvement in run time. Except for SP0 and SS11, we do not see the run time curves level off in this PSNR range, implying that further run time improvement is possible.

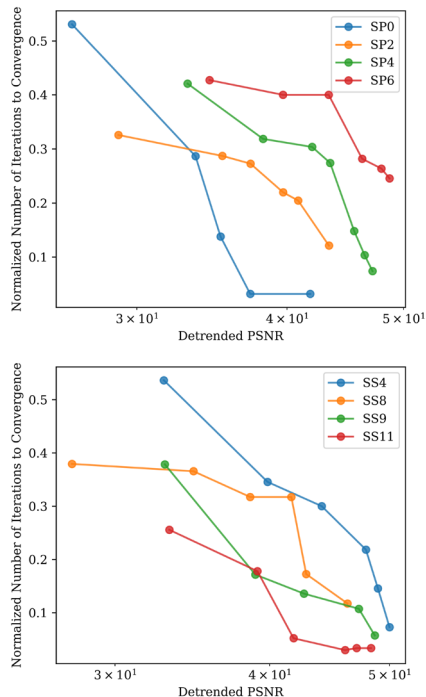


Fig. 10. Normalized number of iterations to convergence error versus PSNR. At PSNR of ~ 40 , we begin to see large improvements in run times in both sphere packs (left) and sandstone (right) samples.

3.3.2 Unsupervised Metrics

Thus far, the discussed metrics for run time improvement have required labeled data against which the prediction is evaluated. When extending models to unseen samples, the test data does not yet have a labeled ground truth. Unsupervised learning is advantageous in this respect where the model learns from patterns in unlabeled data. Here, we discuss a few performance metrics that can be calculated on the prediction itself, without the need for labeled data. These metrics are suggestions for diagnostic tools that can be used to assess whether the solver will see a significant run time improvement by initializing using the model prediction.

We first explore the uncertainty in the slice-wise current flux — the solver’s primary convergence criterion (Fig. 11). We compute the uncertainty using the method outlined for computing F , but stop short of calculating the macroscopic conductivity. The uncertainty in the current flux is a direct point of comparison to the convergence of DRS. We, therefore, expect a direct relationship between the decrease of the number of iterations to convergence and the decrease of uncertainty in current flux. Fig. 11 confirms this hypothesis, where we see three distinct regimes of run time improvement.

First, the improvement in run time is somewhat gradual at large current flux uncertainties. The run time speed-up in

this uncertainty range can be substantial in relatively open geometries such as in SP0 and SS4, with run times accelerating by over 20%. In tighter or more heterogeneous samples, such as SP6 and SS8, the initial run time improvement is not as significant. This is because the solver needs to fix prediction errors that occupy a larger fraction of the computational domain.

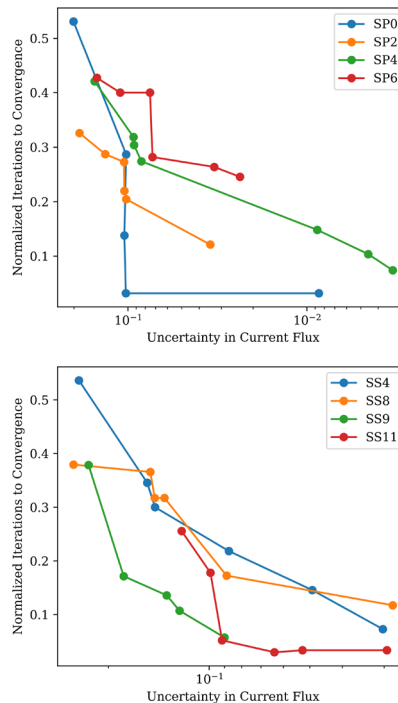


Fig. 11. Normalized number of iterations to convergence error versus uncertainty in current flux (decreasing to the right). The uncertainty in current flux provides a direct point of comparison to the solver. We see a large drop in run time at uncertainty $\sim 10\%$ for both sphere packs (left) and sandstones (right).

Next, when the uncertainty in current flux is reduced to 0.1-0.2, we see a sudden drop in the necessary iterations to convergence. In some cases, such as in SP0 and SS11, the number of required iterations drops to under 10% of that of the linear gradient assumption. The size of the drop is not necessarily dependent on the porosity or complexity of the sample. In the sphere pack samples, where the sphere locations remain constant, smaller porosity geometries do not tend to see the same level of run time improvement as their larger porosity counterparts. However, the amount by which the tightest sample improves is larger than some of the more open samples.

After the large drop, the run time improvement curve either levels off or continues a more gradual decrease. The curves appear to approach a theoretical run time limit, constrained by the solver itself and the level to which the model can resolve the blocks in the prediction. We cannot report further run time improvement in samples that have already reached this limit (SP0 and SS11), even with further training and error reduction. In the cases where the theoretical limit has not yet been reached, it appears the geometric complexity of the pore space dictates the rate by which the run time continues to improve. Using porosity as a proxy for complexity, we see that larger porosity samples tend to improve more rapidly after the initial drop than smaller porosity samples. This is consistent for both sphere pack and sandstone samples. We also observe that for similar porosity

samples (~ 0.2), the run time in this regime improves more slowly for more geometrically complex samples (sandstones) than for simpler samples (sphere packs).

Finally, we discuss the Laplacian of the image as an indicator tool of solver run time improvement. During training, we identified the refinement block artifacts as the largest source of errors. As training progresses, the block artifacts tend to become more refined and the D-2 score decreases. We mask the pore space immediately adjacent to grain-pore boundaries (Euclidean distance = 1) to mitigate the effects of these boundaries on the D-2 score. We also found that normalizing the D-2 score by the solid volume raised to the $2/3$ power helped to overlap the curves for better comparison. Physically, the D-2 score accounts for phase discontinuities at the solid-pore boundary, so raising the solid volume to the $2/3$ power provides a value dimensionally consistent with surface area.

We see behavior in the sphere pack samples like that of the uncertainty in current flux where a large drop in run time precedes more gradual improvement (Fig. 12). However, we also see non-unique values of iterations to convergence for a singular D2 score, indicating that it may not be as good of a predictor as the uncertainty in current flux.

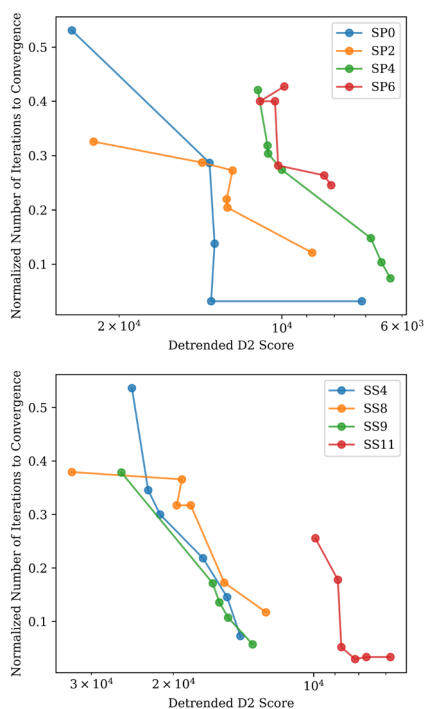


Fig. 12. Normalized number of iterations to convergence error versus normalized D2 score (decreasing to the right). The D2 score is normalized by $(1 - \phi)^{\frac{2}{3}}$. While we see similar behavior as Fig. 11, several D2 scores exhibit non-unique iterations to convergence. However, it is still a good indicator of how blocky the prediction is.

In the sandstone samples, we see that the normalized curves agree with each other quite well, except for the tightest sample (SS11). In the other three cases, we observe a well-behaved decrease of run time in this normalized D-2 score range. This indicates that a non-trainable Laplacian filter or D-2 score could be implemented in a neural network as a performance metric and could help guide model training.

4 Conclusions

This study confirms that the proposed framework of initializing a solver with a machine learning prediction can drastically reduce the run time needed to achieve a deterministic result. Here, we limit the samples to a size of 200^3 due to GPU limitations and we observed over an order of magnitude run time improvement.

Throughout this study we also conclude the following:

- Commonly used error metrics (i.e., MAE and MSE) do not always provide adequate detail of the predictive performance of the model.
- An initial ML prediction does not need to be exact to result in an accurate formation factor prediction
- Supervised metrics, such as MSE and PSNR, are good indicators of run time improvement.
- Achieving a convergence metric of $\sim 0.1 - 0.2$ drastically decreases the number of iterations to convergence.
- The D2 score can be incorporated into the model loss to help smooth the predictions.

This framework has important implications for training predictive models. These metrics can serve as performance criteria when the model is extended to unseen data. It is clear that even overfit models struggle to make perfect predictions and that solvers are still needed to enforce the conservation laws the solution is required to obey.

The sizes of the image data used in this study are admittedly small because we predicted on the same set of images as was used to train the models. The intent was to assess the sensitivity of the run time improvement to the proposed error metrics. Because testing can be performed on CPUs, the prediction samples are not limited to the same sizes as the training data. We expect more significant run time improvements if applying the framework to larger image samples where any gains are a balance between the reduced accuracy when predicting on unseen images and a model's ability to make predictions effectively instantaneously.

Future work will emphasize the development of more generalizable models and assessing these metrics on larger images. Because the actual prediction space accounts for less than 30% of the entire image (only pore space), training on larger images could possibly be achieved by supplying the network with a sparse representation of the pore space during training. Incorporating findings from this study, we plan to implement the finite difference kernel used to find the current flux as a hard constraint, thereby limiting the prediction space to more physical solutions. We also plan to incorporate the Laplacian filter into the cost function to mitigate the block effects of the refinement process. More robust models can be developed by including morphological feature maps (e.g., Euclidean distance map, time of flight, maximum inscribed sphere, etc.) as extra training channels, instead of only using the binary image.

Acknowledgements

We gratefully acknowledge the Digital Porous Media (formerly Digital Rocks Petrophysics) Industrial Affiliates Program for their support and technical expertise (B.C., M.P).

J.S. gratefully acknowledges the support of the U.S. Department of Energy through the LANL/LDRD Program and the Center for Non-Linear Studies.

The Texas Advanced Computing Center provided high performance computing resources used to perform the simulations and training reported in this study.

References

1. P. Glover. *Treatise on Geophysics*, vol. 11, 477–89–137, 10.1016/B978-0-444-53802-4.00189-5 (2015).
2. A. Revil, M. Karaoulis, T. Johnson, and A. Kemna. *Hydrogeol. J.* 20, 617–658, (2012).
3. P. Egbelehulu, M. Abu, N. Abdulsalam, and A. Taiwo. *Pak. J. Geol.* 4, (2020).
4. J.E. Carothers and C.R. Porter. *The Log Analyst* 12, no. 01 (January 1, 1971).
5. C.F. Berg. *Physical Review. E, Statistical, Nonlinear, and Soft Matter Physics* 86, no. 4 Pt 2 (October 2012): 046314.
6. J. H. Norbistrath, G.P. Eberli, B. Laurich, G. Desbois, R.J. Wegeer, and J. L. Urai. *AAPG Bulletin* 99, no. 11 (2015): 2077–98.
7. W.O. Winsauer, H. M. Shearin Jr., P. H. Masson, and M. Williams. *AAPG Bulletin* 36, 2, 253–277 (1952).
8. G.E. Archie, *Transactions of the AIME* 146 01, 54–62 (1942)
9. Q.F. Niu and C. Zhang. *Geophysical Research Letters* 45, 4, 1870–1877 (2018).
10. M. Prodanović, M. Esteva, J. McClure, B. C. Chang, J. E. Santos, A. Radhakrishnan, A. Singh, and H. Khan. *Society of Core Analysts* (2022).
11. A. Mehmani, R. Verma, and M. Prodanović. *Marine and Petroleum Geology* 114 (2020): 104141.
12. B. Bijeljic, A. Raeni, P. Mostaghimi, and M.J. Blunt. *Physical Review E* 87, no. 1 (January 10, 2013): 013011.
13. J. E. Santos, D. Xu, H. Jo, C.J. Landry, M. Prodanović, and M.J. Pyrcz. *Advances in Water Resources* 138 103539 (2020).
14. S. Mohaghegh. *Journal of Petroleum Technology - J PETROL TECHNOL* 52 (September 1, 2000): 64–73.
15. J. Pollock, Z. Stoecker-Sylvia, V. Veedu, N. Panchal, and H. Elshahawi. “Machine Learning for Improved Directional Drilling.” In *Offshore Technology Conference*, 2018.
16. L.P. Zhu, H.Q. Li, Z.G. Yang, C.Y. Li, and Y.L. Ao. *Petrophysics-The SPWLA Journal of Formation Evaluation and Reservoir Description* 59, no. 06 (2018): 799–810.
17. Sudakov, E. Burnaev, and D. Koroteev. *Computers & Geosciences* 127, 91–98 (2019).
18. J.E. Santos, Y. Yin, H. Jo, W. Pan, Q. Kang, H.S. Viswanathan, M. Prodanović, M.J. Pyrcz, and N. Lubbers. *Transport in Porous Media* 140, 1, 241–272 (2021).
19. Y.D. Wang, T. Chung, R.T. Armstrong, and P. Mostaghimi, arXiv, (2020).
20. J.E. Santos, B.C. Chang, Q. Kang, H.S. Viswanathan, N. Lubbers, A. Gigliotti, and M. Prodanović. *Digital Rocks Portal*, (2021).
21. J.E. Santos, B.C. Chang, A. Gigliotti, Y. Yin, W. Song, M. Prodanović, Q. Kang, N. Lubbers, and H.S. Viswanathan, *Scientific Data*, (Under Review).
22. J. Finney, *Digital Rocks Portal*, (2016).
23. R. Neumann, M. Andreetta, and E. Lucas-Oliveira. *Digital Rocks Portal*, (2020).
24. R.A. Victor, *Pore Scale Modeling of Rock Transport Properties* (2014).
25. J. McClure, James, *Digital Rocks Portal*, (2016).
26. R. Bohn and E. Garboczi. *User Manual for Finite Element and Finite Difference Programs: A Parallel Version of NISTIR 6269 and NISTIR 6997* (2003).
27. M. Han, S. Youssef, E. Rosenberg, M. Fleury, and P. Levitz. *Physical Review E* 79, no. 3 (March 30, 2009): 031127.
28. K. Kawaguchi, L.P. Kaelbling, and Y. Bengio, arXiv, (2020).
29. H. O’Reilly and J. M. Beck. *International Journal For Numerical Methods in Engineering* 0, 1-16 (2006).

A Bayesian optimization approach to the extraction of intrinsic physical parameters from T_2 relaxation responses

Rupeng Li¹, Igor Shikhov¹, and Christoph H. Arns^{1,*}

¹ UNSW, School of Minerals & Energy Resources Engineering, Sydney 2052 NSW, Australia

Abstract. NMR transverse relaxation responses in porous media provide a sensitive probe of the micro-structure yet are influenced by a set of factors which are not easily detangled. Low-field T_2 transverse relaxation measurements can be carried out quickly and are frequently used to derive pore size distributions and determine derivative parameters like movable fluid volumes or permeability. Here we present an inverse solution workflow extracting related intrinsic physical parameters of the system by tightly fitting experiment and numerical simulation(s). We propose a Bayesian optimization approach that determines five T_2 related properties associated with two values of temperature simultaneously. This concurrent optimization (CO-OPT) utilizes Gaussian process regression to determine the intrinsic physical parameters leading to a match to experiment with a minimal number of function evaluations. A multi-modal search strategy is employed to identify non-unique solution sets of the problem. The workflow is demonstrated on Bentheimer sandstone, identifying five intrinsic physical parameters simultaneously, namely the surface relaxivity of quartz and the effective diffusion and relaxation times of the clay regions at 20°C and 60°C, providing the temperature-dependent quartz surface relaxivity and effective clay parameters. Given the generality of the method, it can easily be adapted to transverse relaxation experiments, or dynamic conditions where e.g., a change in wettability is monitored by intrinsic NMR parameters.

1 Introduction

NMR relaxometry has proven its high value both for laboratory and field petrophysical applications for estimation of pore size distributions [1], saturation of fluids [2], wetting conditions [3] and permeability [4].

The underlying assumption behind – relaxation occurs in fast diffusion regime (a surface governed process) in isolated or weakly coupled pores – must be valid, which is typically the case. This allows representing the observed relaxation rate in saturated rocks $1/T_2$ as a linear sum of three rate processes: bulk fluid relaxation rate $1/T_{2b}$, surface relaxation rate $1/T_{2s}$ and diffusion in the internal field $1/T_{2D}$ [5]

$$\frac{1}{T_2} = \frac{1}{T_{2b}} + \frac{1}{T_{2s}} + \frac{1}{T_{2D}}. \quad (1)$$

Here ρ_2 is transverse surface relaxivity, S and V are surface area and volume of an individual pore. In diamagnetic and weakly paramagnetic rocks, the surface relaxation term, i.e.,

$$\frac{1}{T_{2s}} = \rho_2 \frac{S}{V}, \quad (2)$$

is the primary relaxation mechanism, thus relating the T_2 distribution to pore-sizes. Typically, surface relaxivity is evaluated by matching a T_2 distribution's mode to that of a pore-aperture distribution obtained using mercury intrusion

capillary pressure analysis. However, this approach is not entirely problem free, since pore-space geometry and the mode value are practically insensitive to temperature variations in the order of 50°C, while the value of T_2 relaxation distribution mode would noticeably change. It is well known that surface relaxivity is sensitive not only to pore geometry, but also to types of solid and fluid pair, wetting state, and temperature. The latter is also important in the context of calibration of field data with laboratory acquired data. Godefroy et al. [6] developed, and supported experimentally, a theoretical framework describing a surface relaxivity temperature dependency. They established that with increase of the temperature the surface relaxivity of quartz to water in a water-wet sandstone is increasing. Similar observations were reported by [7]. In this work we seek to test further the rarely reported temperature-dependent surface relaxivity behavior in sandstone rocks with the aid of an inverse problem formulation enabling to deduce surface relaxivity and accounting for several temperature effects unaccounted for in the past.

Micro-CT based random walk NMR relaxation simulation allows to easily incorporate effects of faster fluid diffusion at higher temperature, accounts for corresponding change of diffusion governed magnetization exchange, longer bulk water relaxation time etc., as long as corresponding inputs are known (measured). We here exclude from consideration the temperature effect on magnetic susceptibility primarily for the sake of simplicity, but also reasonably assuming

* Corresponding author: c.arns@unsw.edu.au

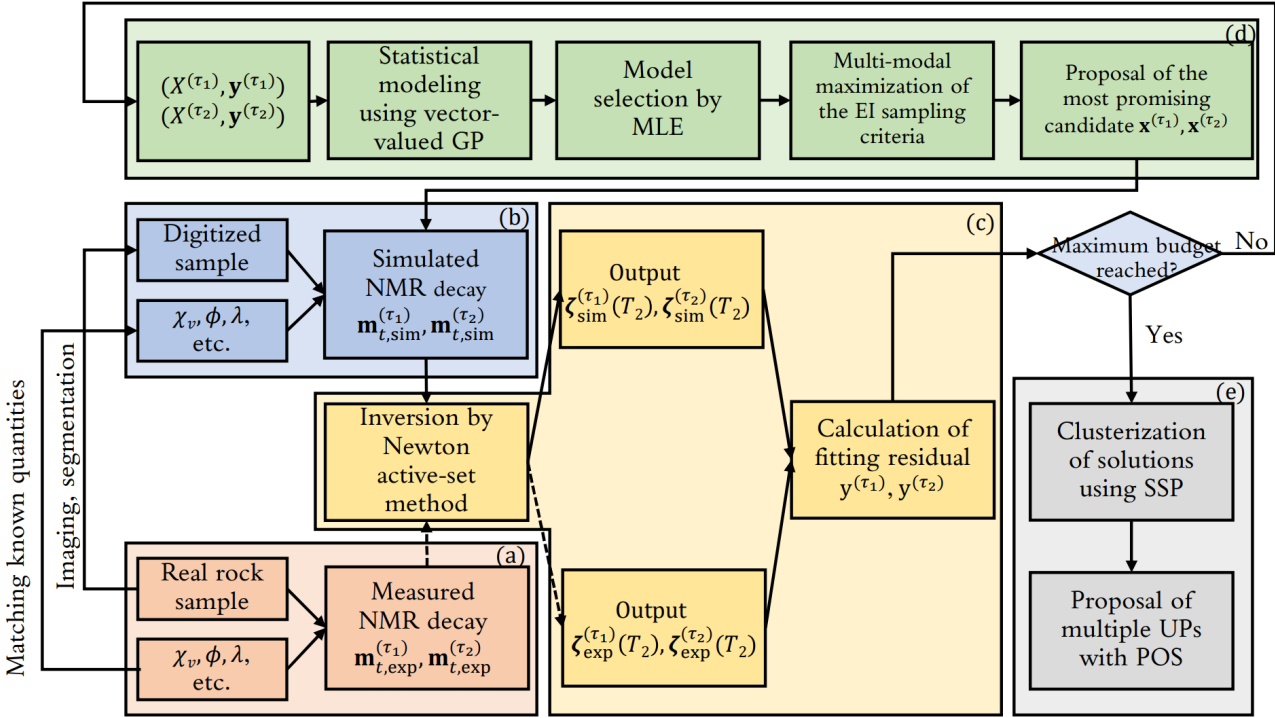


Fig. 1. Flowchart of CO-OPT for the estimation of intrinsic physical parameters from T_2 relaxation responses at two different temperatures.

insignificance of associated effects since the sample rock is diamagnetic, made of mostly of quartz. The magnetic susceptibility of the latter is practically constant in the temperature interval of interest [8]. We note that numerical simulations assign mineral-specific intrinsic properties like surface relaxivity at the pore scale [9-11] while matching distribution modes of experiments results in an effective [12] or apparent surface relaxivity [13; 14].

Given the significant advances in numerical techniques, the temperature-dependent intrinsic parameters can be regarded as unknown and later determined when good matches are achieved between simulations and measurements but is hindered by a practical issue: expensive function evaluations prohibit the enumeration of all configurations of unknown physical parameters in the multi-dimensional solution space. Luckily, the issue of computational burden has been successfully addressed by Bayesian optimization, for which only statistically optimum solutions are proposed for function evaluations, while balancing exploration and exploitation in the solution space. The advantage of Bayesian optimization has been leveraged to recover physical, geometrical, or structural parameters where expensive cost functions are involved [15-17], and in particular, complex multi-physics, multi-parameter, multi-modal problem arising in NMR relaxometry [11]. Furthermore, Bayesian optimization has been integrated with transfer learning for multi-objective optimization, and in particular, for by simultaneous optimization of T_1 and T_2 distributions [18]. In both studies, a multi-modal search strategy, comprising a multi-start L-BFGS-B optimizer searching for local optimum solutions, and a global optimizer social-learning particle swarm optimizer (SL-PSO) for global optimum solutions, are applied to recover all (major) local optimal solutions, i.e., potentially identifying multiple physically valid solution sets.

In this study, we adapt the dual-task inverse solution workflow (DT-ISW) developed for simultaneous fitting of T_1 and T_2 distributions in [18] to the context of simultaneous optimization of T_2 distributions associated with various values of temperature, referred to as concurrent optimization (CO-OPT). We demonstrate the performance of CO-OPT on a Bentheimer sandstone sample by the identification of five intrinsic parameters controlling the NMR relaxation response: one shared quantity, i.e., the tortuosity in clay regions, together with four unique quantities, i.e., transverse surface relaxivity of quartz and effective transverse relaxation time in clay regions, at two values of temperature τ_1 and τ_2 . We also provide the SEP as the reference for which the physical quantities related to two values of temperature are separately identified ignoring the constraints that tortuosity is a constant value for a given structure. Finally, we provide the Pareto optimal solutions (POS), which allows operators to balance the preference of T_2 data fits at two values of temperature for the slightly conflicting objectives.

2 Methodology

2.1. Concurrent optimization

As adapted from DT-ISW introduced in [18], CO-OPT is composed of five components: (a) observables, (b) NMR forward solver, (c) cost-function, (d) Bayesian optimization, and (e) solution analysis. Fig. 1 demonstrates CO-OPT using two values of temperature as an example. We briefly summarize these components as itemized list below, while detailed descriptions follow in the next section:

- Measure the NMR transverse relaxation decays $\mathbf{m}_{t,exp}^{(\tau_1)}$ and $\mathbf{m}_{t,exp}^{(\tau_2)}$ at temperatures τ_1 and τ_2 .

- b) Simulate the decays $\mathbf{m}_{t,\text{sim}}^{(\tau_1)}$ and $\mathbf{m}_{t,\text{sim}}^{(\tau_2)}$ for the chosen sets of unknown intrinsic parameters $\mathbf{x}^{(\tau_1)}$ and $\mathbf{x}^{(\tau_2)}$ on the segmented tomographic images (example: transverse surface relaxivities of the resolved phase: quartz, tortuosity of clay region, effective transverse relaxation times of clay regions), while honoring known quantities like porosity ϕ , volumetric magnetic susceptibility χ_v , bulk physical properties of water, and matching the physical kernel (see Eq. (3)) and regularization parameter λ .
- c) Acquire the T_2 distribution using both simulated and measured decays, i.e., $\zeta_{\text{sim}}^{(\tau_1)}(T_2)$ and $\zeta_{\text{exp}}^{(\tau_2)}(T_2)$. Evaluate the cost-function and calculate the sum of the L₂ norm of the fitting residuals for the T_2 distributions.
- d) Jointly model the T_2 objective functions at the two values of temperature using the vector-valued Gaussian Process (GP) with correlation captured, followed by inference of model hyperparameters using maximum likelihood estimation; then the EI acquisition function is maximized to identify the promising candidates $\mathbf{x}^{(\tau_1)}$ and $\mathbf{x}^{(\tau_2)}$. Finally, solutions within sparsely explored regions are evaluated using exact simulation.
- e) Model the objective functions with the updated model hyperparameters upon depletion of the optimization budget and divide the solution space into various unique partitions (UPs) associated with different modes of the objective function using the solution space partitioning (SSP) introduced in [11]. For each UP the top three solutions and the POS are reported.

2.2 Materials, measurements, and NMR simulations

2.2.1 Rock Sample

Experimental reference NMR responses were obtained for a Bentheimer sandstone cylindrical core plug (25 mm diameter and 50 mm long) of 23.9% porosity saturated with 3 wt.% NaCl brine. This rock is composed primarily by quartz (96%) with remaining fraction represented equally by feldspar and kaolinite. The sample has volumetric magnetic susceptibility -7.45×10^{-6} (SI units).

2.2.2 T_2 Reference Data

We acquire transverse relaxation response of saturated sandstone rock using the standard Carr, Purcell, Meiboom and Gill (CPMG) pulse sequence [19; 20]. The NMR measurements were carried out using a Magritek Rock Core Analyzer operating at 2 MHz proton resonance frequency. Acquired echo-trains were 40,000 echoes long, with echo-time interval 250 us. Summation of 4 scans following phase cycling sequence resulted in a signal-to-noise ratio of around 50. The magnetization decays are treated as multi-exponential sum with unknown distribution of amplitudes $\zeta(T_2)$ representing a Fredholm integral equation of the first kind:

$$m_{T_2}(t) = \int_0^\infty \zeta(T_2) e^{-t/T_2} dT_2 + \eta_n(t), \quad (3)$$

where $m_{T_2}(t)$ is the transverse magnetization decay as function of time t and η_n is additive white noise, and the objective is the estimation of the probability density function of T_2 , i.e., $\zeta(T_2)$.

Practically, the T_2 distribution are obtained using a non-negative least squares (NNLS) algorithms, which minimizes the residual sum between the known left-hand side signal and right-hand side prediction, at the same time retaining a degree of control over distribution shape (smoothness) with a penalty/weight term (known as regularization parameter) [21-23]. All experimental and simulated decays were inverted using the algorithm [21] with resulting solutions identically binned across 256 logarithmically spaced T_2 intervals.

2.2.3 Digitized Image

A Bentheimer sandstone plug of 5mm diameter was imaged in double helix mode on the UNSW Tyree X-ray CT facility with a total acquisition time of 12h, resulting in a reconstructed tomogram with a resolution of $\epsilon = 2.16 \mu\text{m}$. The grey-scale tomogram was segmented into pore-space, quartz, clay region (a micro-porous effective phase), feldspar and an iron-rich dense mineral phase. For details of the segmentation process see [25], which uses the same sample. Fig. 2 depicts a slice through the tomogram and resultant phase segmentation. Statistics of the Bentheimer sandstone segmentations for the calculation of the internal magnetic field at lattice resolution ϵ that follows are listed in Table 1 and Table 2. The micro-CT image was segmented taking into account XRD data reported in [24], though there is a slight difference in between possibly due to mineralogy variation at the mm scale. Basic mineral composition from XRD data and segmented CT image (in brackets) are quartz 96% (96.6%), feldspar 2.4% (1.7%), kaolinite 1.4% (1.6%), others 0.2% (0.15%).

Table 1. Statistics of the Bentheimer sandstone segmentations. Segmented image porosity used in simulation (ϕ_{sim}) is calculated as $f_p + 0.5f_c$ [24], domain size is in voxel, ϵ denotes voxel size, and f_i are phase fractions (f_p : resolved porosity, f_c : clay region, f_q : quartz, f_f : feldspar, f_h : high-density).

ϕ_{sim}	phase fractions				
	f_p	f_c	f_q	f_f	f_h
0.2373	0.2252	0.0241	0.7369	0.0126	0.0011

Assuming quartz, feldspar and kaolinite are all iron-free and having similar elemental composition are likely to exhibit similar magnetic susceptibility, susceptibility of bulk sandstone is decomposed into four separate values. Quartz and feldspar are indeed typically reported in a similar range, e.g., Hunt reported $-13 \sim -17 \times 10^{-6}$ SI for both [25]. We measured χ_v of fluid and bulk rock only. In particular, χ_v for distilled water and 3% NaCl brine are -8.90 and -9.12×10^{-6} SI, respectively, while for convenience we typically use in simulations -9.0×10^{-6} SI for aqueous phase [26]. The balance value required to match the average bulk is attributed to a volumetrically small fraction of the high-density minerals assumed to be iron-rich.

Table 2. Measured average volumetric magnetic susceptibilities χ_v , known values for NaCl brine, clay region, quartz, feldspar, and inferred value for high-density using material balance.

volumetric magnetic susceptibilities (SI, multiply by 10^6)					
χ_v	$\chi_{v,w}$	$\chi_{v,c}$	$\chi_{v,q}$	$\chi_{v,f}$	$\chi_{v,h}$
-7.45	-9	$(\chi_{v,w} + \chi_{v,k})/2$	-12	-12	1900

2.2.4 T_2 Simulation

Given the naturally discretized segmented tomogram, the NMR responses are simulated via a lattice random walk algorithm following [9-11]. The simulation is carried out in multiple stages: first, the internal magnetic field is calculated in the dipole approximation via a convolution of the susceptibility field as defined by the individual phase susceptibilities given in Table 1 with a dipole field; second, the random walks are carried out on the segmented tomogram with a sub-lattice spacing of $\epsilon/10$ (low temperature) or $\epsilon/15$

(high temperature); random walks are started with a probability linearly related to the porosity of each voxel with each simulation consisting of about 80,000 random walks, dephasing according to the internal fields, with surface interactions lumped into the surface relaxivity for resolved phases, or into a local effective relaxation time for clay regions. Local internal magnetic field values at the required discretization level are derived via tri-linear interpolation from the coarse-scale internal field (resolution of ϵ). Third, the resultant magnetization decay is transformed to the T_2 distribution via an inverse Laplace transform (ILT) [22]. In the optimization framework the phase susceptibilities and the bulk properties of the saturation brine (diffusion coefficient and T_2 bulk relaxation time, see Table 3) are considered as

Table 3. Bulk diffusion coefficient and transverse relaxation time of water for the two temperatures considered.

τ / Celsius	D_0 /(cm ² /s)	$T_{2b,w}$ / s
20	2.03×10^{-5}	2.27
60	4.76×10^{-5}	5.26

constants. The other pore-scale physical parameters, namely the surface relaxivity of quartz $\rho_{2,q}$, the effective T_2 relaxation time of clay regions ($T_{2e,c}$), and the effective diffusion coefficient of clay regions ($D_{e,c}$) at different temperatures, in the following noted by superscripts (τ_1) and (τ_2), are the target of the proposed optimization effort. The surface relaxivity of minority phases is set to the surface relaxivity of quartz.

2.3 Minimization of T_2 objective under various temperatures

For notational simplicity we describe only two temperatures here, i.e., τ_1 and τ_2 . The problem of minimization of the sum of the L2 norm of the fitting residuals for T_2 distributions acquired at τ_1 and τ_2 can be formulated as:

$$\text{minimize } f^{(\text{obj})}(\mathbf{x}) = f^{(\tau_1)}(\mathbf{x}^{(\tau_1)}) + f^{(\tau_2)}(\mathbf{x}^{(\tau_2)}), \quad (4)$$

$$\text{where } \mathbf{x} = [\mathbf{x}^{(\tau_1)}, \mathbf{x}^{(\tau_2)}], \quad (5)$$

$$\mathbf{x}^{(\tau_1)} = [\rho_{2,q}^{(\tau_1)}, T_{2e,c}^{(\tau_1)}, D_{e,c}^{(\tau_1)}], \quad (6)$$

$$\mathbf{x}^{(\tau_2)} = [\rho_{2,q}^{(\tau_2)}, T_{2e,c}^{(\tau_2)}, D_{e,c}^{(\tau_2)}], \quad (7)$$

$$\text{subject to } D_{e,c}^{(\tau_1)}/D_0^{(\tau_1)} = D_{e,c}^{(\tau_2)}/D_0^{(\tau_2)}, \quad (8)$$

$$\mathbf{x}_l \leq \mathbf{x} \leq \mathbf{x}_u. \quad (9)$$

where \mathbf{x}_l and \mathbf{x}_u are the lower and upper bounds of the pre-specified search domain and $f^{(\tau_1)}$ and $f^{(\tau_2)}$ are L2 norm of the fitting residuals for T_2 distributions acquired at temperatures τ_1 and τ_2 , respectively, expressed as

$$f^{(\tau_1)}(\mathbf{x}^{(\tau_1)}) = \|\zeta_{\text{sim}}^{(\tau_1)}(T_2|\mathbf{x}^{(\tau_1)}) - \zeta_{\text{exp}}^{(\tau_1)}(T_2)\|_2^2, \quad (10)$$

$$f^{(\tau_2)}(\mathbf{x}^{(\tau_2)}) = \|\zeta_{\text{sim}}^{(\tau_2)}(T_2|\mathbf{x}^{(\tau_2)}) - \zeta_{\text{exp}}^{(\tau_2)}(T_2)\|_2^2, \quad (11)$$

with weights for all data points of the T_2 distribution being equally 1. Each lower-dimension component $\mathbf{x}^{(i)}$, $i \in \{1,2\}$ is associated with a specific temperature and therefore Eq. (5) specifies the complete solution. The constraints Eq. (8) apply due to Archie's Law, i.e.,

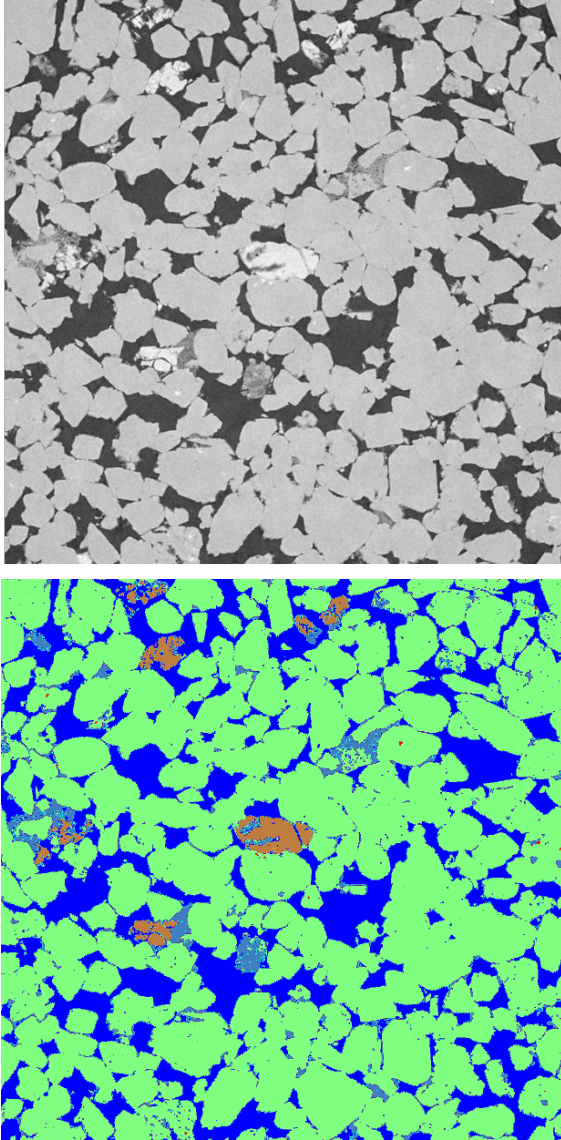


Fig. 2. Slice through the grey-scale tomogram and corresponding five-phase segmentation. Domain size: 1240^3 voxel, voxelsize $\epsilon = 2.16 \mu\text{m}$. Blue: pore, indigo: clay, green: quartz, brown: feldspar, red: high-density phase.

$$\frac{1}{\mathcal{T}} = \frac{D_e}{D_0} \quad (12)$$

where \mathcal{T} is the tortuosity. We assume that for a given structure the \mathcal{T} is independent of temperature and Eq. (12) holds under both values of temperature.

2.3.1 Scalar-Valued Gaussian Processes

GP is a distribution over functions, and is characterized by its mean function $m(\mathbf{x})$ and covariance function $k(\mathbf{x}, \mathbf{x}')$ as [11; 27]

$$f(\mathbf{x}) \sim \mathcal{GP}(m(\mathbf{x}), k(\mathbf{x}, \mathbf{x}')), \quad (13)$$

where $x = (x_1, x_2, \dots, x_D)^\top$ is a candidate in \mathcal{X} of dimension $D \times 1$, $f(\mathbf{x})$ is the process evaluated at location x . In GP, the prior distribution over f is expressed as

$$\mathbf{f} | X \sim \mathcal{N}(\mathbf{m}_0, K_f(X, X)), \quad (14)$$

where \mathcal{N} denotes normal distribution, $\mathbf{m}_0 \in \mathcal{R}^{n \times 1}$ denotes the mean vector for observations, $(X, \mathbf{y}) = \{\mathbf{x}_i, y_i\}_{i=1}^n$ and (\mathbf{x}^*, y^*) denotes observed and predicted candidates respectively, and $K_f(X, X)$ denotes the $n \times n$ covariance matrix for \mathbf{f} , with the (p, q) entry expressed by $k(\mathbf{x}_p, \mathbf{x}_q)$. Accommodating the noise using Gaussian likelihood function yields $\mathbf{y} | \mathbf{f} = \mathcal{N}(\mathbf{f}, \sigma_n^2 I)$, and the posterior distribution for a single predicted candidate becomes

$$y^* | \mathbf{x}^*, X, \mathbf{y}, \theta_s \sim \mathcal{N}(\mu(\mathbf{x}^*), \sigma^2(\mathbf{x}^*)), \quad (15)$$

where \mathcal{N} is normal distribution, θ_s is the model hyperparameters for the scalar-valued GP, and

$$\begin{aligned} \mu(\mathbf{x}^*) &= m_0^* + K_f(\mathbf{x}^*, X) [K_f(X, X) + \sigma_n^2 I]^{-1} (\mathbf{y} \\ &\quad - m_0), \\ \sigma^2(\mathbf{x}^*) &= K_f(\mathbf{x}^*, \mathbf{x}^*) + \sigma_n^2 \\ &\quad - K_f(\mathbf{x}^*, X) [K_f(X, X) \\ &\quad + \sigma_n^2 I]^{-1} K_f(X, \mathbf{x}^*). \end{aligned} \quad (16)$$

2.3.2 Vector-Valued Gaussian Processes

GP with multiple outputs can be represented by the vector-valued GP indicates. $Q = 2$ applied throughout this study, indicating that there are two correlated tasks. The GP kernel in Eq. (13) has to be replaced by a vector-valued GP kernel taking into account the correlation between the Q outputs of \mathbf{f} , with \mathbf{f} expressed as [28; 29]

$$\mathbf{f}(\mathbf{x}) \sim \mathcal{GP}(\mathbf{m}(\mathbf{x}), \mathbf{K}(\mathbf{x}, \mathbf{x}')), \quad (17)$$

where $\mathbf{m}(\mathbf{x}) \in \mathcal{R}^{Q \times 1}$ denotes the stacked mean function $\{\mathbf{m}_q(\mathbf{x})\}_{q=1}^Q$ for each output and K denotes a matrix-valued function whose entries $(\mathbf{K}(\mathbf{x}, \mathbf{x}'))_{q, q'}$ express the correlation between the input-pairs \mathbf{x} and \mathbf{x}' , and between the outputs-pairs $f_q(\mathbf{x})$ and $f_{q'}(\mathbf{x})$. We account for the noisy observations using a Gaussian likelihood, i.e., $\mathbf{y} | \mathbf{f} = \mathcal{N}(\mathbf{f}, \Sigma_n \otimes I)$, where $\Sigma_n = \text{diag}(\sigma_n^2)$ is a $Q \times Q$ diagonal matrix incorporating task-dependent noise levels, and $\sigma_n^2 = (\sigma_{n,1}^2, \dots, \sigma_{n,Q}^2)^\top$ is a vector of noise variances. Similar with

the case of scalar-valued GP, the predicted distribution for a single predicted candidate \mathbf{x}^* is expressed as

$$\mathbf{y}^* | \mathbf{x}^*, X, \mathbf{y}, \theta_v \sim \mathcal{N}(\boldsymbol{\mu}_{\mathbf{x}^*}, \Sigma_{\mathbf{x}^*}), \quad (18)$$

where $\mathbf{y}^* = [y_1^*, \dots, y_Q^*]^\top$ concatenates Q outputs for \mathbf{x}^* , θ_v is a vector of model hyperparameters (v stands for vector-valued GP), and

$$\begin{aligned} \boldsymbol{\mu}_{\mathbf{x}^*} &= \mathbf{m}_0^* + \mathbf{K}_f(\mathbf{x}^*, X) [\mathbf{K}_f(X, X) + \Sigma_n \otimes I]^{-1} (\mathbf{y} \\ &\quad - \mathbf{m}_0), \\ \Sigma_{\mathbf{x}^*} &= \mathbf{K}_f(\mathbf{x}^*, \mathbf{x}^*) + \Sigma_n \\ &\quad - \mathbf{K}_f(\mathbf{x}^*, X) [\mathbf{K}_f(X, X) + \Sigma_n \\ &\quad \otimes I]^{-1} \mathbf{K}_f(X, \mathbf{x}^*). \end{aligned} \quad (19)$$

2.3.3 Candidate Proposal and Solution Analysis

We use the standard EI acquisition function, which for the q^{th} task is

$$a_{\text{EI}, \tau_q}(\mathbf{x}^*) = \int_{-\infty}^{y_q(\mathbf{x}_q^-)} (y_q(\mathbf{x}_q^-) - u) p(u) du, \quad (20)$$

where \mathbf{x}_q^- is the current best observed candidate for the q^{th} objective and $u = y_q^* | X, \mathbf{y}, \mathbf{x}^*, \theta_v$ is the Gaussian distributed variable given by Eq. (18).

A promising candidate is proposed by joint maximization of a_{EI, τ_1} and a_{EI, τ_2} in the form of $\sum_{q=1}^2 a_{\text{EI}, \tau_q}$ under equality constraints using sequential quadratic programming (SQP) [30]. The initial guesses are placed randomly in the feasible domain, ensuring that the multi-modal nature of the objective function is captured.

When the optimization budget depletes, the model hyperparameters are updated and the T_2 objectives associated with various values of temperature are jointly modelled using new hyperparameters settings. The solution space of Eq. (4) is then divided into various unique partitions (UPs) corresponding to various modes of the objective function. We referred to the solution with the lowest fitness value in each UP is as the local minimum (LM). For details see [11]. Meanwhile, the two objectives are expected to be slightly conflicting since measurements are corrupted by noise so that there is no solution that simultaneously achieves good matches for each objective. As a result, we provide the POS of the T_2 data fits for the slightly conflicting objectives, which is defined as the set of solutions that is not dominated by any other solutions. Mathematically, \mathbf{x}_1 dominates \mathbf{x}_2 if \mathbf{x}_1 beats or ties \mathbf{x}_2 for each of the two objectives, i.e., $f^{(i)}(\mathbf{x}_1) \leq f^{(i)}(\mathbf{x}_2)$, $\forall i \in \{1, 2\}$, and $f^{(i)}(\mathbf{x}_1) < f^{(i)}(\mathbf{x}_2)$, $\exists i \in \{1, 2\}$.

3 Results

In this study, we determined the surface relaxivity of quartz and the effective transverse relaxation time and tortuosity for the clay region at two temperatures: $\tau_1 = 20^\circ\text{C}$ and $\tau_2 = 60^\circ\text{C}$, respectively. We compared the speed of convergence, non-unique solution sets as well as the optimum solutions provided by CO-OPT, where tortuosity is a shared parameter for both temperatures and SEP - tortuosity at each

Table 4. The top three candidates in terms of $f^{(obj)}$ (or $f^{(\tau_1)}$ and $f^{(\tau_2)}$ if $f^{(obj)}$ does not exist) within each UP, identified using the two approaches. UPs are sorted in ascending order of the best identified $f^{(obj)}$ within the UP. T_2 distributions corresponding to the LMs are displayed Fig. 3. Both $\log_{10} \mathcal{J}$ and \mathcal{J} are reported for convenience. Numbers in the R column indicate the rankings of the solutions out of 200 evaluated candidates in terms of $f^{(obj)}$, whereas numbers in the $Step$ column indicate at which step those solutions are proposed.

UP	R	$\rho_{2,q}^{(\tau_1)}$ ($\mu\text{m/s}$)	$\rho_{2,q}^{(\tau_2)}$ ($\mu\text{m/s}$)	$\log_{10}[T_{2,e,c}^{(\tau_1)}(\text{s})]$	$\log_{10}[T_{2,e,c}^{(\tau_2)}(\text{s})]$	$\log_{10} \mathcal{J}$	\mathcal{J}	$f^{(\tau_1)}$ $\times 10^{-4}$	$f^{(\tau_2)}$ $\times 10^{-4}$	$f^{(obj)}$ $\times 10^{-4}$	Step
CO-OPT											
1	1	11.169	9.820	-1.889	-2.304	0.535	3.424	2.52	24.23	26.75	131
	2	11.509	10.132	-1.722	-2.143	0.697	4.980	5.61	28.49	34.10	97
	3	9.744	9.978	-1.811	-1.905	0.901	7.956	10.54	27.12	37.66	141
2	4	12.075	9.398	-1.934	-2.530	0.341	2.194	6.45	32.15	38.61	140
	5	12.058	12.103	-2.445	-2.602	0	1	13.13	27.03	40.16	60
	6	12.042	12.100	-2.449	-2.602	0	1	13.31	27.03	40.34	58
SEP, $\tau_1 = 20^\circ\text{C}$											
1	1	10.892	-	-1.923	-	0.625	4.213	2.87	-	-	84
	2	11.008	-	-1.943	-	0.593	3.919	3.44	-	-	74
	3	10.895	-	-1.875	-	0.643	4.393	3.85	-	-	196
2	29	11.915	-	-2.406	-	0	1	9.91	-	-	72
	30	11.949	-	-2.397	-	0	1	9.91	-	-	67
	31	12.005	-	-2.389	-	0	1	9.95	-	-	69
SEP, $\tau_2 = 60^\circ\text{C}$											
1	1	-	9.068	-	-2.085	0.783	6.067	-	22.64	-	174
	2	-	10.061	-	-1.916	0.895	7.848	-	23.11	-	142
	3	-	8.741	-	-2.101	0.786	6.112	-	24.75	-	195
2	6	-	12.089	-	-2.601	0	1	-	27.03	-	169
	7	-	12.130	-	-2.594	0	1	-	27.05	-	149
	8	-	12.003	-	-2.606	0	1	-	27.08	-	172

temperature is an independent parameter for optimization. Practically the base-10 logarithm of the effective relaxation time and of the tortuosity are employed since they usually vary across orders of magnitude. The solution space is subject to the following bounds:

$$\begin{aligned}
 0 &\leq \rho_{2,q}^{(\tau_1)} / (\mu\text{m/s}), \rho_{2,q}^{(\tau_2)} / (\mu\text{m/s}) \leq 24, \\
 -3 &\leq \log_{10} (T_{2,e,c}^{(\tau_1)} / \text{s}), \log_{10} (T_{2,e,c}^{(\tau_2)} / \text{s}) \leq 0, \\
 0 &\leq \log_{10} \mathcal{J} \leq 1.6.
 \end{aligned}$$

The solution space \mathcal{X} composed by such constraints is so large that a grid search or random search is intractable in consideration for the expensive simulation. The optimization budget is 200 function evaluations.

For both approaches here, the multi-modal nature of the objective functions is well-catered, and the non-unique solution sets are identified using solution space partitioning (SSP), clustering all solutions to different UPs. Table 4 shows identified parameter values of the LMs for the two approaches. LMs with $f^{(obj)}$ above 1×10^{-2} are not listed. The problem of non-unique solution sets is encountered in both methods: UP 2 is identified as a mathematically sound solution set, though it is physically less likely since the inferred value for tortuosity reaches the lower bound of 1. Within the physically valid solution set, UP 1, we observe two

trends for the variation of surface relaxivity with temperature: Both CO-OPT and SEP consistently show two different response patterns to increase of temperature. Group 1 shows a decrease of surface relaxivity $\rho_{2,q}$ by about 15%, while group 2 shows a nearly constant surface relaxivity (increase of about 1%). Specifically, for CO-OPT there is a noticeable decrease in $\rho_{2,q}$, as shown by UP 1, e.g., a decrease from 11.6 $\mu\text{m/s}$ to 9.8 $\mu\text{m/s}$ (averaged over three solutions) while there is a light to no increase in $\rho_{2,q}$, as shown by the UP 2, e.g., an increase from 12.0 $\mu\text{m/s}$ to 12.1 $\mu\text{m/s}$. SEP shows the same trend, with surface relaxivity decreasing from 10.9 $\mu\text{m/s}$ to 9.3 $\mu\text{m/s}$, or increasing from 11.3 $\mu\text{m/s}$ to 11.4 $\mu\text{m/s}$. We note that the solutions are of low fitness value for both objective functions and thus are considered mathematically correct. The trend is similar for SEP for which there is no constraint to keep tortuosity constant with temperature. As a result, the uncertainty in non-unique solution sets cannot be reduced by examining the quality of fit or the fitness value.

Fig. 3 shows the fit corresponding to the LMs in Table 4. From appearance, the fits for the T_2 distribution at $\tau_1 = 20^\circ\text{C}$ are better than $\tau_2 = 60^\circ\text{C}$ for both methods, leading to approximately 10 times larger fitness values at higher temperature. We assume that the larger misfit at higher temperature is mainly a function of increasing diffusion coupling emphasizing the effect of small micro-structural

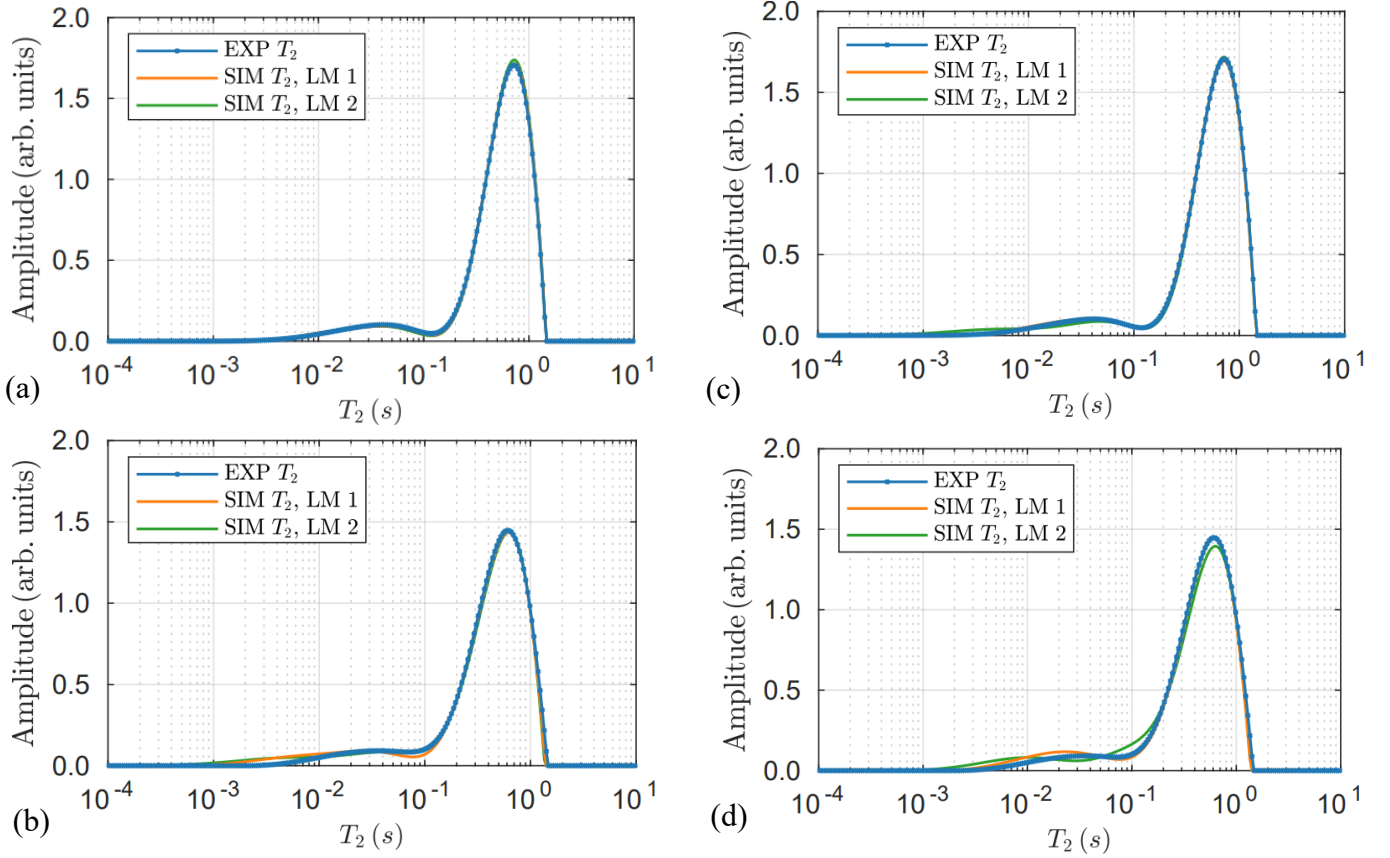


Fig. 3. The T_2 distributions corresponding to the LMs listed in Table 4: (a) CO-OPT, $\tau_1 = 20^\circ\text{C}$, (b) CO-OPT, $\tau_2 = 60^\circ\text{C}$, (c) SEP, $\tau_1 = 20^\circ\text{C}$ and (d) SEP, $\tau_2 = 60^\circ\text{C}$.

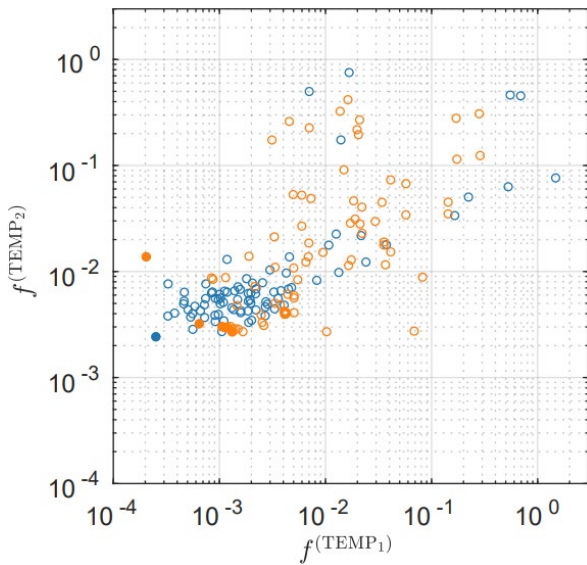


Fig. 4. Minimization of $f^{(\tau_1)}$ and $f^{(\tau_2)}$ using CO-OPT. Candidates in the bottom-left corner are preferred. Solid dots are Pareto optimum solutions; blue and orange dots correspond to UP 1 and UP 2 of CO-OPT in Table 4, and the circles are the dominated solutions.

features in the model.

Here we did not address the mathematical validity for the selection of an optimum solution since the two objectives are slightly conflicting: the $f^{(\tau_1)}$ value of LM 2 is inferior to the second-best solution though it achieves better value for $f^{(\tau_2)}$, as shown in Fig. 4, where candidates in the bottom-left corner

are preferred and considered as feasible solutions. Such conflict is also reflected in the result of SEP from Table 4 that if $f^{(\tau_1)}$ and $f^{(\tau_2)}$ are individually optimized, $\mathbf{x}^{(\tau_1)}$ and $\mathbf{x}^{(\tau_2)}$ will neither recover the same value of $\log_{10} \mathcal{J}$ nor satisfy the constraints of Eq. (7). As a result, in situations where the uncertainty in measurement is high, or the conflict between the two objectives cannot be neglected, an optimum solution cannot be solely determined mathematically.

Since it is difficult to visualize the possible solution sets in five-dimensional space, we show in Fig. 5 the isosurface plot of the two objective functions $f^{(\tau_1)}$ and $f^{(\tau_2)}$ for the CO-OPT solution both in the three-dimensional space, as well as the correlation plot between $\rho_{2,q}$ and $\log_{10} T_{2e,c}$. From both isosurface plots and correlation plots we observe that there are multiple solution sets corresponding to both $f^{(\tau_1)}$ and $f^{(\tau_2)}$, which needs additional physical constraints to reduce such uncertainties.

4 Discussion and Conclusions

In this paper we analyzed the temperature dependent NMR relaxation responses and associated intrinsic physical properties of Bentheimer sandstone, namely the surface relaxivity of quartz and two effective clay parameters, the effective bulk relaxation time $T_{2e,c}$ and the effective diffusion coefficient $D_{e,c}$ of clay, the latter of which was reported as tortuosity to account for its geometric origin and accounting for the expectation that tortuosity remains a constant with respect to temperature. To achieve these aims we introduced

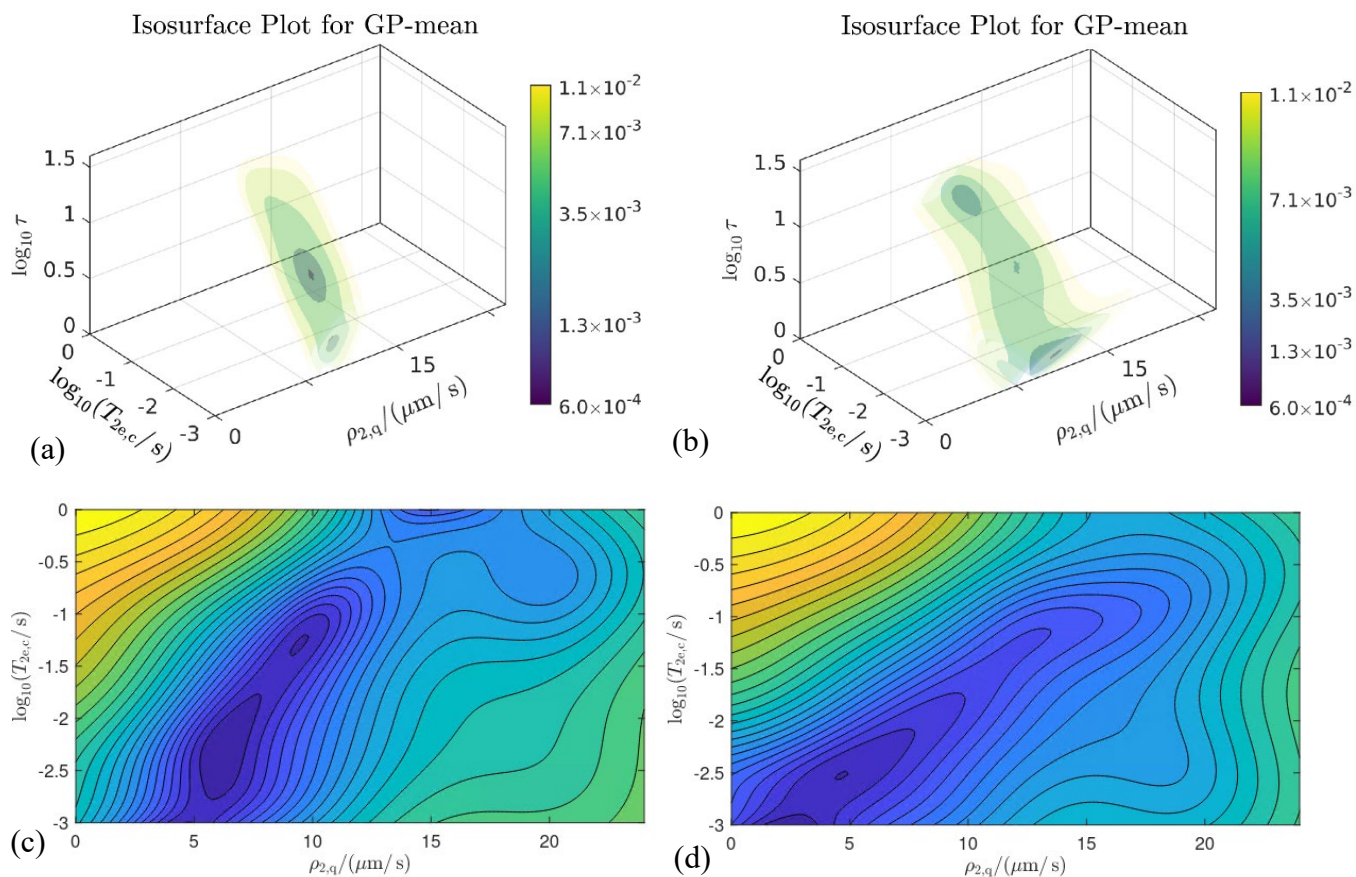


Fig. 5. The isosurface plot of (a) $f(\tau_1)$ and (b) $f(\tau_2)$ each in the three-dimensional space evaluated after the budget of 200 function evaluations is depleted, with contour plots (c) and (d) showing the correlation between $\rho_{2,q} - \log_{10} T_{2e,c}$ as projections of the iso-surface plot on to the $\rho_{2,q} - \log_{10} T_{2e,c}$ plane. We display five levels of isosurfaces, corresponding to the minimum 0.01%, 0.1%, 1%, 3%, 5% of the scalar field. Blue colors indicate regions with higher probability that mathematically good solutions can be found.

the CO-OPT workflow, which determines the temperature dependent transverse surface relaxivities and effective transverse relaxation time by joint minimization of the deviation between simulated and measured T_2 distributions at two values of temperature: five parameters were identified by computationally producing T_2 distributions almost identical with experiments for two values of temperature.

The experimentally observed enhanced relaxation in Bentheimer sandstone with temperature increase agrees with literature reports. However, contrary to these reports, the mechanisms behind the observed faster relaxation does not require the involvement of a higher surface relaxivity of quartz. We established two solutions, one is that of practically constant surface relaxivity of quartz and another is negatively correlating to temperature (15% lower if temperature is 40 °C higher). Both solutions enable matching the shift between experimental T_2 distributions, apparently either solely due to faster bulk water diffusion or additionally aided by magnetization coupling between micro- and macro-porosity.

The effective relaxation time of clay decreases by 30-40% with temperature increase. Though we are unable to conclude on specific values since multiple values within a fairly wide interval seem possible (approximately 3 to 15 ms), depending on the analysis method utilized.

The prediction of clay tortuosity is the least certain out of five properties, primarily due to an inherent difficulty of the effective medium approach when applied to dispersed clay in sandstone (in particular for smaller clay pockets/regions).

The effect of incorrect magnetization exchange due to unrealistic discontinuity between effective and bulk diffusion at the clay-macropore interface increases with faster diffusion, i.e. is also “temperature-dependent”, and may require a further refinement of numerical simulation.

The results of this study are contrary to what we expected upon starting on this analysis, the target of which was the derivation of the temperature dependence of intrinsic physical properties relevant to NMR relaxation-diffusion responses in rock samples.

We plan to further analyze this behavior in the future with resolved clay [29] and feldspar model structures and increase the resolution of micro-CT images, avoiding the introduction of an effective diffusion coefficient entirely. This should allow us to understand sensitivities and pinpoint the mechanism responsible for the observed behavior. We remark that resolving this issue may have direct implications to the interpretation of NMR responses in the context of wettability alteration, a subject of current intensive study [30].

CHA acknowledges the Australian Research Council for funding through ARC discovery project DP200103548. This work was supported by computational resources provided by the Australian Government through gadi under the National Computational Merit Allocation Scheme (grant m65).

References

1. M. G. Prammer, SPE Annual Technical Conference and Exhibition (1994).
2. W. F. J. Slijkerman, J. P. Hofman, W. J. Looyestijn, Y. Volokitin, *Petrophysics - The SPWLA Journal of Formation Evaluation and Reservoir Description*, **42**(04) (2001).
3. M. Fleury, F. Deflandre, *Magn. Reson. Imaging*, **21**(3), 385-387 (2003).
4. A. Timur, SPWLA 9th Annual Logging Symposium (1968).
5. H. C. Torrey, *Phys. Rev.*, **104**(3), 563-565 (1956).
6. S. Godefroy, M. Fleury, F. Deflandre, J. P. Korb, *J. Phys. Chem. B*, **106**(43), 11183-11190 (2002).
7. K. Katika, H. Fordsmand, I. L. Fabricius, *Microporous Mesoporous Mater.*, **269**, 122-124 (2018).
8. A. Ali, D. K. Potter, *Geophysics*, **77**(3), WA211-WA221 (2012).
9. C. H. Arns, T. AlGhamdi, J.-Y. Arns, *New J. Phys.*, **13**(1), 015004 (2011).
10. Y. Cui, I. Shikhov, R. Li, S. Liu, C. H. Arns, *J. Pet. Sci. Eng.*, **202**, 108521 (2021).
11. R. Li, I. Shikhov, C. H. Arns, *Phys. Rev. Appl.*, **15**(5), 054003 (2021).
12. J. Chen, G. J. Hirasaki, M. Flaum, *J. Pet. Sci. Eng.*, **52**(1), 161-171 (2006).
13. M. Müller-Petke, R. Dlugosch, J. Lehmann-Horn, M. Ronczka, *Geophysics*, **80**(3), D195-D206 (2015).
14. S. Costabel, C. Weidner, M. Müller-Petke, G. Houben, *Hydrol. Earth Syst. Sci.*, **22**(3), 1713-1729 (2018).
15. J. Mockus, *J. Glob. Optim.*, **4**(4), 347-365 (1994).
16. D. R. Jones, M. Schonlau, W. J. Welch, *J. Glob. Optim.*, **13**(4), 455-492 (1998).
17. J. Snoek, H. Larochelle, R. P. Adams (2012), in *Proceedings of the 25th International Conference on Neural Information Processing Systems - Volume 2*, edited, pp. 2951-2959, Curran Associates Inc., Lake Tahoe, Nevada.
18. R. Li, I. Shikhov, C. H. Arns, *SPE J.* (2022).
19. H. Y. Carr, E. M. Purcell, *Phys. Rev.*, **94**(3), 630-638 (1954).
20. S. Meiboom, D. Gill, *Rev. Sci. Instrum.*, **29**(8), 688-691 (1958).
21. C. L. Lawson, R. J. Hanson, Prentice-Hall Inc.
22. P. C. Hansen, *Inverse Probl.*, **8**(6), 849-872 (1992).
23. D. P. Bertsekas, *SIAM J. Control Optim.*, **20**(2), 221-246 (1982).
24. I. Shikhov, D. S. Thomas, C. H. Arns, *Energy & Fuels*, **33**(9), 8184-8201 (2019).
25. C. P. Hunt, B. M. Moskowitz, S. K. Banerjee (1995), in *Rock Physics & Phase Relations*, edited, pp. 189-204.
26. I. Shikhov, Phd Thesis (2015).
27. C. E. Rasmussen, C. K. I. Williams (2005), The MIT Press.
28. E. V. Bonilla, K. M. A. Chai, C. K. I. Williams (2007), in *Proceedings of the 20th International Conference on Neural Information Processing Systems*, edited, pp. 153-160, Curran Associates Inc., Vancouver, British Columbia, Canada.
29. K. Swersky, J. Snoek, R. P. Adams (2013), in *Proceedings of the 26th International Conference on Neural Information Processing Systems - Volume 2*, edited, pp. 2004-2012, Curran Associates Inc., Lake Tahoe, Nevada.
30. P. T. Boggs, J. W. Tolle, *Acta Numer.*, **4**, 1-51 (1995).

Shale Characterization Using Magnetic Resonance

Mohammad Sadegh Zamiri^{1,2}, Jiangfeng Guo^{1,3}, Florea Marica¹, Laura Romero-Zerón², and Bruce J. Balcom^{1,*}

¹UNB MRI Research Centre, Physics Department, University of New Brunswick, Fredericton, NB E3B 5A3, Canada

²Department of Chemical Engineering, University of New Brunswick, Fredericton, NB E3B 5A3, Canada

³State Key Laboratory of Petroleum Resources and Prospecting, China University of Petroleum (Beijing), Beijing, 102249, China

Abstract. Shale characterization while important is complicated by low porosity and low permeability. Nanoporosity and a high degree of heterogeneity present further difficulties. Magnetic resonance (MR) methods have great potential to provide quantitative and spatially resolved information on fluids present in porous rocks. The shale MR response, however, is challenging due to short-lived signals that deter quantitative signal detection and imaging. Multicomponent signals require high resolution methods for adequate signal differentiation. MR methods must cope with low measurement sensitivity at low field. In this paper, T_1 - T_2^* and Look-Locker T_1^* - T_2^* methods were employed to resolve the shale signal for water, oil, and kerogen at high and low field. This permits fluid quantification and kerogen assessment. The T_1 - T_2^* measurement was employed to understand and control contrast in the SPRITE imaging method. This permitted imaging that gave separate images of water and oil. Water absorption/desorption, evaporation, step pyrolysis, and water uptake experiments were monitored using T_1 - T_2^* measurement and MR imaging. The results showed (1) the capability of the T_1 - T_2^* measurement to differentiate and quantify kerogen, oil, and water in shales, (2) characterization of shale heterogeneity on the core plug scale, and (3) demonstrated the key role of wettability in determining the spatial distribution of water in shales.

1 Introduction

There are vast untapped hydrocarbon reserves in shale formations worldwide. Accurate rock characterization is essential for economic hydrocarbon production from such formations. Shale characterization includes, but is not limited to, quantification of pore-filling fluids, kerogen assessment, and understanding fluid storage and transport [1]. Shale fluid quantification methods are essential to estimate hydrocarbon reserves and to help guide reservoir and well development plans. Furthermore, kerogen, the solid organic matter in shale rocks, is commonly assessed due to a positive correlation between kerogen content in shales and reservoir quality [2]. Shale rocks commonly exhibit low porosity and permeability, nano-scale pores, and a high degree of heterogeneity which present challenges for characterization methods for such rocks. Conventional core analysis methods, such as retort, two-phase extraction, and Dean Stark method for fluid quantification, and pyrolysis and elemental analysis for kerogen assessment are cumbersome and sample destructive. They commonly rely on volumetric measurements which may be erroneous and provide no spatial information.

Shales exhibit a multiscale heterogeneity that controls fluid storage and transport [3-5]. These heterogeneities include laminated structure on millimetre and centimeter scale. On the micro-meter scale, inclusion of minerals and organic matter, and microfractures are evident. The shale pore network can only be detected at nanoscale. These features are commonly studied using imaging methods. However, available imaging methods [6-9], such as scanning electron microscopy (SEM) and nano-computed tomography (nano-CT), have limited field of view (FOV), are sample

destructive, and are principally sensitive to the morphology and topology of the rock rather than the pore-filling fluids. Therefore, extensive computational methods are required not only to convert the spatial information to fluid flow and storage but also to upscale this information to accurately measure petrophysical quantities at a representative elementary volume (REV) [10].

Alternatively, 1H magnetic resonance (MR) methods are non-destructive, robust, detect signal directly from fluid in nanopores of shale rocks, and provide images with centimeter scale FOV. MR methods rely on measurement of signal relaxation lifetimes (T_1 , T_2 , and T_2^*) and molecular diffusion. These variables are sensitive to molecular dynamics and molecular environment. MR methods for shale rocks present several challenges. (1) MR signal for shales is short-lived which hinders signal detection and quantification. (2) Several shale species such as brine, oil and kerogen contain hydrogen that gives rise to a multicomponent MR signal. (3) The short-lived signal prevents application of most MR imaging methods. (4) Current MR measurements are not compatible with instruments available for shale characterization. Most common MR scanners dedicated to rock core plug analysis operate at low field which provides a low sensitivity for shale measurements compared to high field measurements.

The best-known MR methods for shale characterization include T_1 - T_2 relaxation correlation measurement [11-20] and Diffusion- T_2 measurement [15,19,20], commonly implemented at high field. These methods are limited by the echo time, often on the order of hundreds of microseconds, which is inadequate for resolving the fast-relaxing shale signal. This prevents quantitative signal detection and spatial encoding. Furthermore, shale signal peaks commonly overlap in relaxation correlation measurements which prevent signal

* Corresponding author: bjb@unb.ca

quantification. For example, at low field, the oil signal component overlaps with that of water [15,21]. Therefore, shale measurements are commonly performed at high field. To overcome the issue of signal overlap, it was proposed to (1) use the field dependency of oil to identify oil phase in shales [21], (2) use Diffusion- T_2 measurement to resolve oil and water signals at low field. However, the former requires special instrumentation, and the latter is only sensitive to free fluid in shale rocks [15].

In this paper, MR measurements on outcrop shale samples from Eagle Ford, Marcellus, and Barnett Formations are presented. 2D T_1 - T_2^* relaxation correlation measurement [22,23] was introduced for shale characterization [24,25]. It was shown that the T_1 - T_2^* technique can overcome some of the issues inherent in shale measurements by resolving the multicomponent shale signal and quantifying signal peaks at low and high field. The high resolution of the T_1 - T_2^* method allows usage of a reference sample that helps produce consistent signal quantification between measurements. The T_1 - T_2^* resolved signal was exploited in conjunction with water adsorption/desorption and evaporation experiments to quantify oil and water content in shale samples. A step pyrolysis measurement coupled with T_1 - T_2^* measurement showed that the short transverse relaxation signal component was dominated by the kerogen content. Resolved kerogen signal was used to evaluate kerogen hydrocarbon generation potential. The Look-Locker T_1^* - T_2^* method [26], a variation of T_1 - T_2^* technique, was used at low field to give quantitative water and oil content in shales, and kerogen assessment with high-sensitivity. The Look-Locker T_1^* - T_2^* technique permitted fast and quantitative shale measurement at low field. The centric-scan SPRITE imaging method [27,28] with magnetization preparation was employed to give 1D and 3D oil and water images on a core plug scale. The images acquired using this method showed that sample scale heterogeneities are commonly imposed by the shales' lamina. The natural water and oil distribution in shale samples was greatly influenced by the samples' bedding structure. Water uptake experiments were monitored using T_1 - T_2^* measurement and the SPRITE imaging method with oil suppression. The results illustrated the wettability control of spatial water distribution in shales during spontaneous imbibition.

2 Theory

Molecules in liquids have fast tumbling motion through which the average magnetic perturbations caused by dipolar interactions vanishes. Therefore, these interactions are not responsible for relaxation in liquids. For solids, slow molecular motion results in residual dipolar interactions. Solid echo techniques can partially refocus these dephasing effects. In these techniques, large spin systems and molecular motion still lead to irreversible decay of the transverse magnetization [29].

The transverse magnetization decay is characterized by the spin-spin relaxation time, T_2 . However, the primary time domain MR signal in this work is a free induction decay (FID), described by the effective spin-spin relaxation time, T_2^* . As a result of inhomogeneity in the magnetic field, transverse relaxation measured by the FID decays more

rapidly than that solely due to only T_2 effects [30]. These field inhomogeneities can arise from (1) inhomogeneity in the underlying magnetic field, B_0 and (2) diamagnetic susceptibility mismatch between the sample's compositions, $\Delta\chi$. The effective spin-spin relaxation time, T_2^* is a combination of the spin-spin relaxation time, T_2 and the two inhomogeneity effects mentioned above and can be expressed using Eq. 1 [31].

$$\frac{1}{T_2^*} \approx \frac{1}{T_2} + \gamma\Delta B_0 + \gamma\Delta\chi B_0 \quad (1)$$

where ΔB_0 is the breadth of the magnetic field distribution, B_0 .

T_2 relaxation of liquids is commonly of the order hundreds of milliseconds whereas for solids such as kerogen in shales decay will occur in a few tens of microseconds. This prevents signal discrimination and quantification of fast-relaxing solid kerogen. In this regime, Eq. 1 for the T_2^* is dominated by the T_2 lifetime. Therefore, T_2^* contrast measured by FID can be used to estimate T_2 contrast. T_2^* can be measured with a greater accuracy compared to the T_2 lifetime in shales. Employment of T_2^* instead of T_2 in the 2D MR correlation measurements results in a better resolution of signal species.

3 Experimental section

3.1 Pulse sequences

3.1.1 2D relaxation correlation methods

T_1 - T_2 relaxation correlation measurements were performed according to the pulse sequence shown in Figure 1a. The pulse sequence consists of two parts, a T_1 recovery stage and an acquisition part. During the saturation in the T_1 recovery stage, longitudinal magnetization is reduced to zero. This magnetization then partially recovers during the variable time τ_r . In the acquisition part, the signal is recorded using CPMG which collects data with an echo time, τ_e time spacing. The pulse sequence in Figure 1a is repeated with various τ_r values logarithmically spaced to cover the T_1 recovery of the sample magnetization.

T_1 - T_2^* relaxation correlation measurements [22,23] were performed according to the pulse sequence shown in Figure 1b. The T_1 recovery stage is similar to that of T_1 - T_2 measurement. In the acquisition part, the 90° pulse brings the recovered magnetization into the transverse plane to be detected in time by the FID with a short dwell time, dw , spacing between data points after a short deadtime, t_d . Multiple FIDs are acquired at various τ_r values logarithmically spaced to cover the T_1 recovery of the sample magnetization.

The pulse sequence for the Look-Locker T_1^* - T_2^* relaxation correlation measurement [26] is shown in Figure 1c. The effective longitudinal relaxation time, T_1^* is measured when a Look-Locker sequence is used. T_1^* is closely related to the T_1 relaxation time, according to Eq. 2a This measurement, by contrast to the T_1 - T_2^* measurement, does not require performing various T_1 recoveries. Multiple FIDs are acquired by employing multiple low flip angle pulses, α during a single longitudinal magnetization recovery. These pulses are separated by a time τ . Therefore, T_1 recovery times

in this measurement are linearly spaced. A Look-Locker T_1^* - T_2^* measurement can be acquired substantially faster than a T_1 - T_2^* measurement. Signal averaging can be performed to improve signal-to-noise ratio (SNR) and sensitivity of the measurement. This technique enables fast and quantitative measurements at low field. The signal intensities obtained using the Look-Locker T_1^* - T_2^* measurement should be corrected using Eq. 2b to give signal proportional to the hydrogen content [26].

$$\frac{1}{T_1^*} = \frac{1}{T_1} - \frac{\ln(\cos \alpha)}{S^* \tau} \quad (2a)$$

$$S = \frac{S^* \tau}{(\tau + T_1^* \ln(\cos \alpha)) \cdot \sin \alpha} \quad (2b)$$

where S and S^* are signal proportional to the hydrogen content and signal obtained from Look-Locker T_1^* - T_2^* measurement, respectively. T_1^* is determined from the coordinate of the signal peak on the T_1^* - T_2^* correlation plot.

3.1.2 Imaging method

The imaging measurements were performed using the scheme presented in Figure 1d. The pulse sequence consists of a magnetization preparation stage and a readout part [32,33]. In the first part, the combination of 90° pulse and the spoiling gradient brings the longitudinal magnetization to zero. This magnetization partially recovers during the variable T_1 recovery time, τ_r . In the second part, the recovered magnetization is acquired using a centric-scan SPRITE readout. This gives the image signal according to Eq. 3.

$$S(r, \tau_r, t_p) = M_{\text{Prep}}(r, \tau_r) \cdot \exp\left(-\frac{t_p}{T_2^*}\right) \cdot \sin \alpha \quad (3)$$

where M_{Prep} is a series of T_1 -weighted images acquired for each τ_r , r is the position and t_p is the image encoding time. The FID decays for oil (red), water (blue), and kerogen (black) in shales are shown separately in Figure 1d for illustration purposes. The fast-decaying kerogen signal can be excluded from the image by choosing a long t_p . The t_p can be short enough to acquire oil and water signal. The prepared magnetization, M_{Prep} at each position is a superposition of all T_1 signal components recovered during τ_r . Therefore, M_{Prep} is described by the integral in Eq. 4 to give $\rho(r, T_1)$, the image signal resolved in the T_1 relaxation time.

$$M_{\text{Prep}}(r, \tau_r) = \int \rho(r, T_1) \cdot \left(1 - \exp\left(-\frac{\tau_r}{T_1}\right)\right) \cdot dT_1 \quad (4)$$

3.2 Shale samples and experiments

Table 1 presents a summary of experiments performed on various shale samples at different magnetic fields. Shale samples were outcrop, provided by Kocurek Industries Inc. (Caldwell, TX), and were cylindrical in shape. Shale samples from the Eagle Ford Formation, the Marcellus Formation, and the Barnett Formation are referred to as EG, M, and B, respectively, followed by a sample index number.

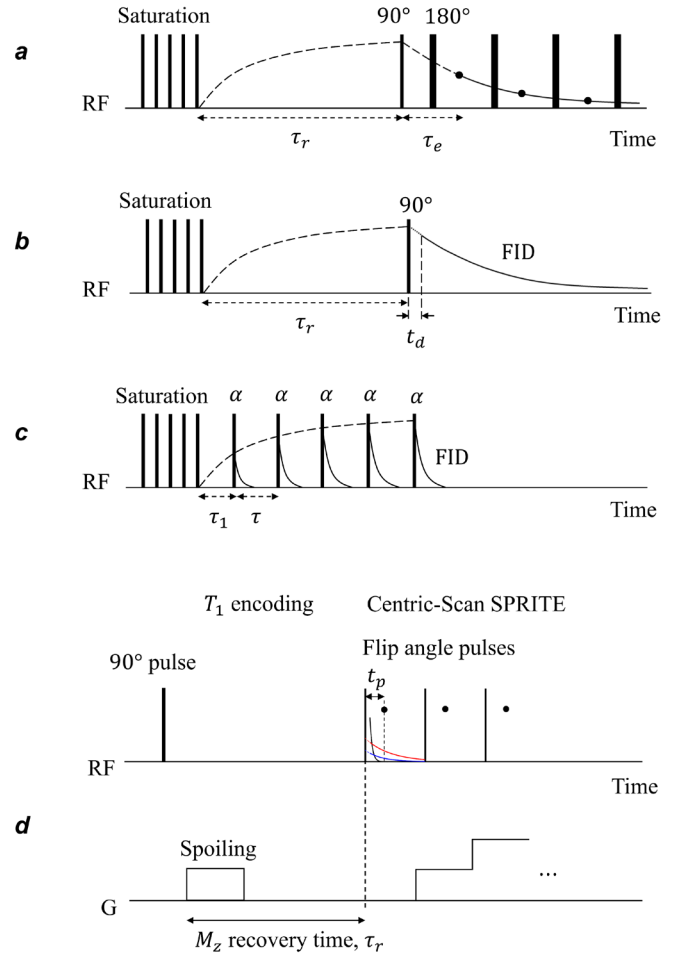


Fig. 1. Schematic diagrams of pulse sequences for (a) T_1 - T_2^* measurement, (b) T_1 - T_2^* measurement, (c) Look-Locker T_1^* - T_2^* measurement, and (d) centric-scan SPRITE with magnetization preparation. The FID decays for oil (red), water (blue), and kerogen (black) are shown separately for illustration purposes. The kerogen FID fully decays before signal detection in the Centric scan SPRITE measurement. T_1 - T_2^* measurement provides a better resolution in time compared to T_1 - T_2^* measurement. Look-Locker T_1^* - T_2^* measurement acquires multiple FIDs during a single T_1 recovery and is therefore drastically faster than T_1 - T_2^* measurement.

Water adsorption and desorption experiments were performed at a controlled relative humidity of 0.75 and near 0, respectively, in a desiccator at a temperature of 24 °C. This allowed manipulation of the water content in shale samples, leaving oil and kerogen content intact. Evaporation experiments were conducted by placing the samples in an oven that was set to 60 °C. This caused the oil and water content of the samples to decrease, leaving kerogen content intact. Step pyrolysis experiments were performed by exposing the samples to elevated temperatures up to 850 °C in the presence of helium. This caused kerogen content to decrease and thermally dissociate to generate hydrocarbon. The water uptake experiments were performed by bringing the bottom face of the sample in contact with 3 wt% KCl brine. This initiated water imbibition into the samples.

Table 1. Summary of experiments conducted on various shale samples.

Sample ID	Formation	Field (T)	Experiment
EG4	Eagle Ford	2.4	Comparison of T_1 - T_2^* and T_1 - T_2 measurement
EG13	Eagle Ford	0.2	
EG4	Eagle Ford	2.4	Water adsorption/desorption and evaporation coupled with T_1 - T_2^* measurement
EG12	Eagle Ford	4.7	Step pyrolysis coupled with T_1 - T_2^* measurement
EG12	Eagle Ford	4.7	Comparison of T_1 - T_2^* and Look-Locker T_1^* - T_2^* measurement
EG13	Eagle Ford	0.2	
EG10 EG11	Eagle Ford	2.4	1D and 3D imaging of natural fluid content
M5	Marcellus		
B5	Barnett		
EG10 EG11	Eagle Ford	2.4	Water uptake

3.3 Instrumentation

The MR measurements were conducted using three instruments. (1) A Nalorac (Martinez, CA) horizontal bore superconducting magnet with magnetic field strength of 2.4 T, equipped with a custom-built birdcage RF probe, 4.5 cm id, driven by a 2 kW Tomco (Tomco Technologies, Stepney, Australia) RF amplifier. The RF probe had a 90° pulse duration of 10.5 μ s and probe deadtime of 24 μ s. The water-cooled Nalorac gradient set driven by Techron (Elkhart, IN) 8710 amplifiers provided maximum gradient strengths of 25 G/cm in the three principal directions. The console was a Tecmag (Houston, TX) Redstone. (2) A vertical bore 4.7 T superconducting magnet (Cryomagnetics, Oak Ridge, TN) was driven by a Redstone console (Tecmag, Houston, TX). The RF probe was a Doty DS1-874 (Doty Scientific, Columbia, SC) birdcage with 2.1 cm id driven by a 2 kW Tomco RF amplifier (Tomco Technologies, Stepney, Australia), with a 90° pulse duration of 23 μ s and probe deadtime of 20 μ s. (3) A MARAN DRX-HF (Oxford Instruments Ltd, Abingdon, Oxford, UK) vertical bore permanent magnet provided a magnetic field of 0.2 T. The RF probe was a custom-built solenoid 12 cm in length with a 4.5 cm id with a 90° pulse duration of 15 μ s and probe deadtime of 43 μ s. MR measurements performed using instruments (1) and (2) are referred to as high field measurements throughout the text, whereas those conducted using instrument (3) are considered low field measurements.

4 Results and discussions

4.1 Resolving shale signal species using T_1 - T_2 and T_1 - T_2^* measurements

T_2^* can be measured with a much better time resolution compared to T_2 . Figure 2 compares FID and CPMG measurements for shale sample EG13. The FID measurement offered a significant improvement in time resolution compared to the CPMG measurement. CPMG measurement is limited by the echo time, τ_e , which is commonly in the order of hundreds of microseconds. The transverse magnetization in Figure 2 was measured with an echo time of 200 μ s and is sampled at intervals of the echo time. In the FID, however, data acquisition started after a deadtime, t_d of 43 μ s with sampling at a dwell time, dw of 1 microsecond. Data sampling frequency in FID is improved by at least two orders of magnitude compared to CPMG, which results better time resolution of the decay. Figure 2 demonstrates that (1) the CPMG approaches FID decay curve for samples with fast-decaying signal components, as indicated in Eq. 1, (2) FID gives a higher resolution in time compared to CPMG. The fast-relaxing kerogen signal is completely missed in the CPMG measurement while it was acquired in the FID.

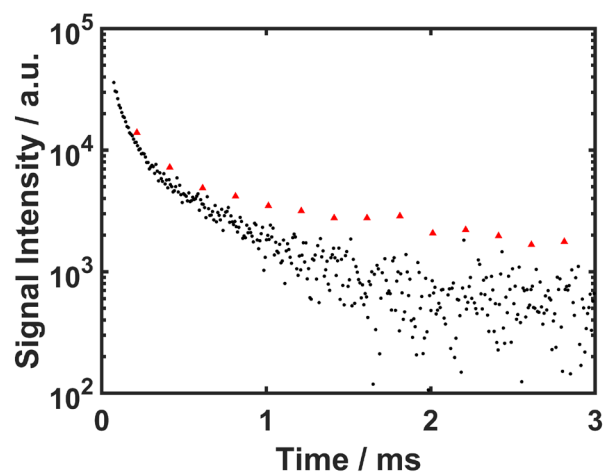


Fig 2. Comparison of FID (circles) and CPMG (triangles) measurements at low field for shale sample EG13. The FID approaches the CPMG at early times. Better time resolution is achieved using the FID compared to the CPMG. Kerogen signal is missed by the CPMG because of the echo time limitation.

Figure 3 shows 2D T_1 - T_2 and T_1 - T_2^* relaxation correlation measurements of two shale samples at high and low field. Signal components in Figure 3 are marked with their corresponding shale species, integrated signal intensity, and log-mean relaxation times.

Water in shale undergoes a strong surface relaxation. Its signal peak yielded a short T_1 of \sim 1 ms and low T_1/T_2 and T_1/T_2^* ratios. The coordinates of the water signal peaks in the T_1 - T_2 and T_1 - T_2^* relaxation correlation maps did not depend on the field strength. Oil in the shale samples had large T_1/T_2 and T_1/T_2^* ratios which yielded a long T_1 of \sim 159 ms at high field and a T_1 of \sim 38 ms at low field measured using T_1 - T_2^* measurement, as shown in Figures 3b and 3d. The oil T_1 was significantly affected by the field strength. Such effects of field strength on the T_1 of water and oil in shales has been reported elsewhere [15,21]. Kerogen relaxation is dominated by dipolar interactions which causes very short transverse relaxation times and large diagonal value peak (T_1/T_2 and T_1/T_2^* ratios). Kerogen yielded a T_2^* of \sim 10 μ s, and a long T_1 of \sim 250 ms at high field and T_1 of \sim 30 ms at low field. Kerogen also showed a significant T_1 variation with the field strength. Figures 3b and 3d provide evidence of T_1

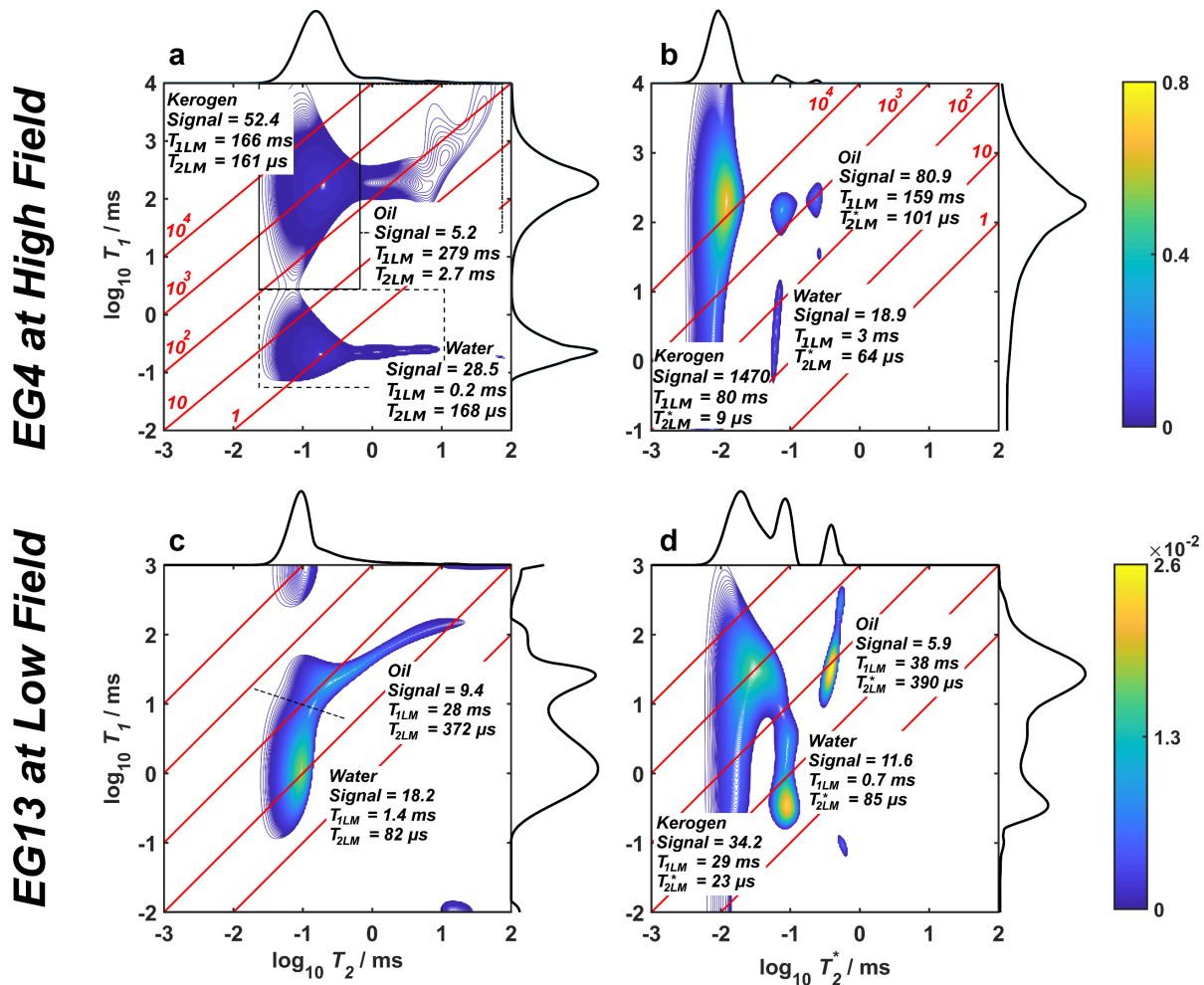


Fig. 3. Comparison of T_1 - T_2 measurement (a and c) and T_1 - T_2^* measurement (b and d) performed at 2.4 T and 0.2 T. Shale signal species, oil, water, and kerogen are better resolved and quantified using T_1 - T_2^* measurement. Integrated signal intensity and T_2 log-mean for each signal peak is shown next to the peak. The diagonal lines show relaxation time ratios (T_1/T_2^* or T_1/T_2) of 1, 10, 10^2 , 10^3 , and 10^4 . The values of the diagonals are the same in all subfigures.

dependency on the field strength for kerogen, similar to that for oil. This is consistent with the BPP relaxation model of dipolar interaction for solid like materials.

Shale signal components overlap in the T_1 - T_2 relaxation correlation plot. The overlap of shale signal deters fluid quantification. As shown in Figure 3a, at high field, the kerogen signal peak overlaps with that of oil and water. Furthermore, the T_1 dependency of oil in shales on the field strength caused oil and water signal peaks to overlap at low field in the T_1 - T_2 relaxation correlation plot of Figure 3c. T_1 - T_2^* relaxation correlation measurement, by contrast, provides the adequate resolution to discriminate kerogen, oil, and water signal peaks at both high and low fields as shown in Figures 3b and 3d.

A significantly better time resolution of transverse relaxation lifetime is achieved using the T_1 - T_2^* method compared to the T_1 - T_2 method. In T_1 - T_2^* measurement, signal detection begins a few microseconds after the RF pulse, unlike T_1 - T_2 measurement in which that starts after an echo time of hundreds of microseconds. Furthermore, the rate of data collection in the T_1 - T_2^* measurement is improved by at least two orders of magnitude. This improved time resolution allows better discrimination of signal components.

As shown in Figure 3c, the kerogen signal was not visible in the T_1 - T_2 relaxation correlation plot at low field due to the echo time limitation. At high field, in Figure 3a, the kerogen signal peak was shifted to a higher T_2 value and its detected integrated signal intensity was reduced significantly in T_1 - T_2 relaxation correlation map. This leads to overlap of signal peaks in the T_1 - T_2 relaxation correlation map, which hampers signal differentiation and quantification. Therefore, Shale signal components are better resolved and quantified using the T_1 - T_2^* relaxation correlation measurement. Moreover, comparing Figure 3b and 3d, the kerogen signal contribution to the total shale signal is reduced for the measurement at low field. This is due to the long deadtime of 43 μ s for the low field instrument compared to the decay lifetime of kerogen. It is worth mentioning that this is not a characteristic of all low field measurements. In principle, a low field measurement with a short deadtime should be capable of giving correct signal contributions for all shale signal species.

4.2 Fluid quantification using T_1 - T_2^* measurement

In this section, water and oil content of a shale sample is manipulated systematically to calibrate the MR signal with the fluid content. This helps not only to unambiguously

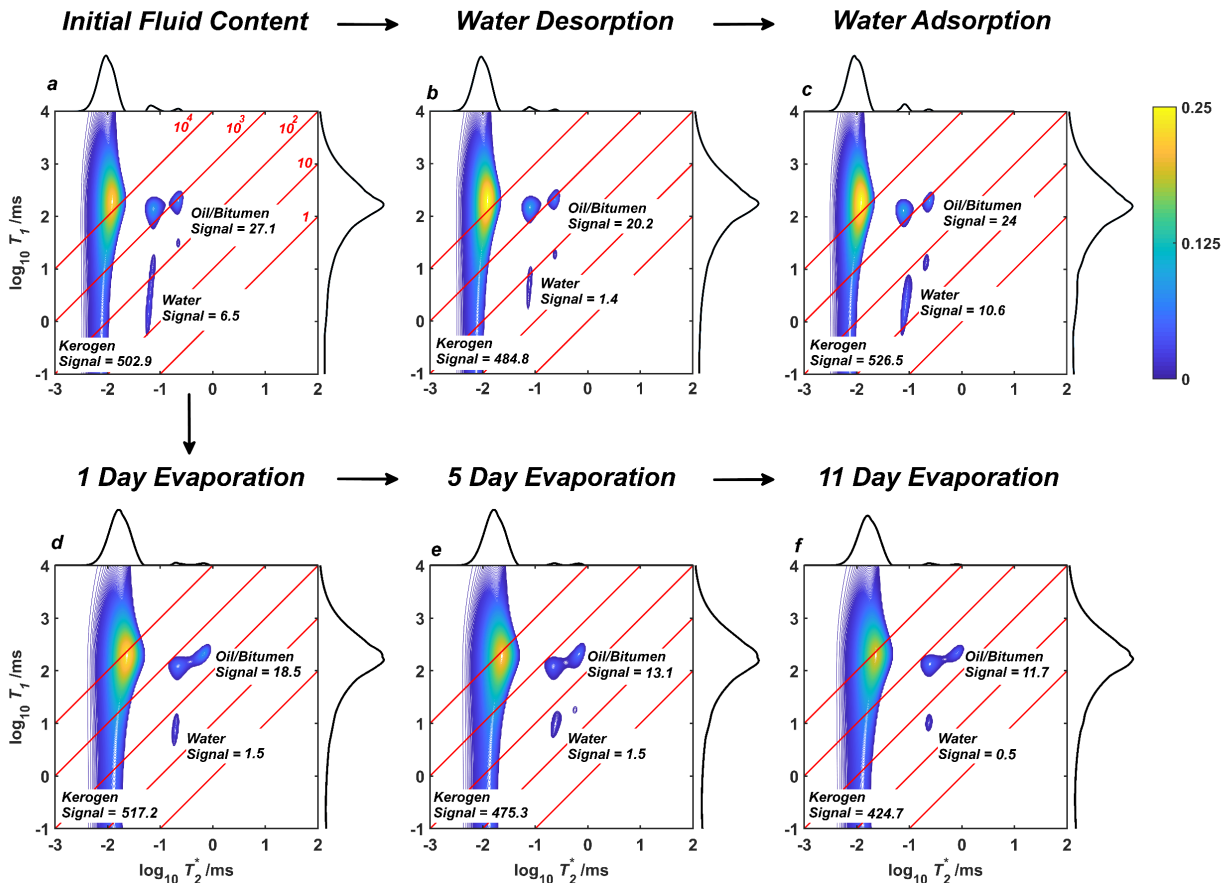


Fig. 4. T_1 - T_2^* measurement for sample EG4 undergoing water adsorption/desorption and evaporation experiments. T_1 - T_2^* measurement (a) at the as-received condition, (b) after water adsorption (c) after water desorption (d) after 1 day of evaporation (e) after 5 days of evaporation (f) after 11 days of evaporation. Water peak signal intensity varied when shale water content was manipulated during water adsorption/desorption experiments. Kerogen and oil signal intensities remained constant. Water and oil signal intensities decreased during evaporation experiments. Kerogen intensity remained constant.

distinguish water, oil, and kerogen signal components in the relaxation correlation plot but also to quantify shale fluid content. Figure 4a shows the T_1 - T_2^* measurement of a shale sample in its as-received condition. This shale sample was subjected to two sets of experiments (1) water adsorption/desorption and (2) evaporation experiments.

The water adsorption/desorption experiments were performed using 40.84 gr crushed shale sample in desiccator with controlled relative humidity at room temperature to manipulate water content of the shale sample. Figure 4b and 4c show the T_1 - T_2^* relaxation correlation measurement of the shale sample after water desorption and after water adsorption, respectively. Water integrated signal intensity decreased from 6.5 to 1.4 after water desorption and increased to 10.6 after water adsorption. Oil signal intensity decreased slightly, while kerogen signal intensity remained relatively constant. Some light oil components may have evaporated in the desiccator and left the sample, resulting in the 20% reduction in the oil signal.

During the evaporation experiments, water and oil content in 10.46 gr of crushed shale sample decreased. Figures 4d-f show the T_1 - T_2^* measurement after 1, 5, and 11 days. The integrated signal intensity of the signal peaks associated with water and oil reduced while kerogen integrated signal intensity remained relatively unchanged. The slight decrease

in the kerogen signal intensity is likely due to loss of a minor amount of the powered sample between measurements.

The integrated signal intensity of the resolved MR signal of shale species in the T_1 - T_2^* relaxation correlation plot gives linear relationships with their corresponding shale species. This is a foundation for fluid quantification in shales. In Figure 5a, the water integrated signal intensity is calibrated for water content in the shale sample by a plot of the sample's mass change due to change in the sample's water content with the resolved integrated signal intensity of water in the T_1 - T_2^* measurement. The initial water content of the sample is calculated to be 0.24 gr water / 100 gr rock. Having the water calibration curve, the mass loss due to water vaporization, in the evaporation experiment, can be calculated to give sample's mass loss due to oil evaporation. This allows calibration of oil signal in Figure 5b. The initial oil content of the sample is calculated to be 0.98 gr oil / 100 gr rock.

4.3 Kerogen characterization

A step pyrolysis experiment coupled with T_1 - T_2^* relaxation correlation measurements were performed to manipulate kerogen signal in the shale samples. The integrated signal intensity of kerogen, oil, and water resolved using the T_1 - T_2^* relaxation correlation measurement was determined after

each pyrolysis step. The integrated signal intensities were then converted to hydrogen content of shale species in moles using a reference sample which had a known hydrogen content.

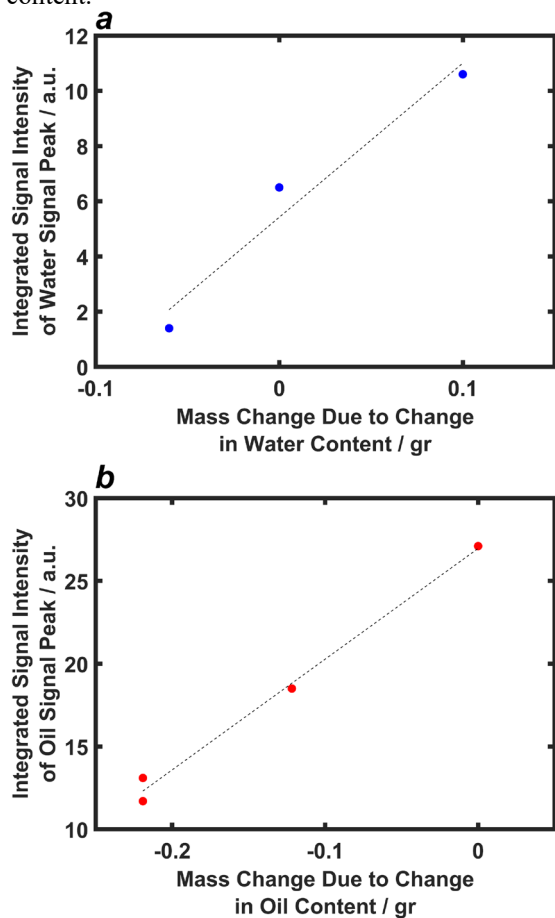


Fig. 5. (a) Water and (b) oil integrated signal intensity obtained from T_1 - T_2^* measurement versus sample mass change due to change in the respective fluid content shows a linear relationship that is used to calibrated signal and give shale water and oil content.

Figures 6a show the hydrogen contents of kerogen, oil, and water relative to its initial values. Figure 6b shows a thermogravimetric analysis (TGA) and its derivative (DTG) for the shale sample. The water vaporization from the sample is evident in the DTG analysis at 100 °C. The water evaporation in TGA is consistent with the hydrogen water content determined using the T_1 - T_2^* measurement. The short relaxation signal component in the T_1 - T_2^* measurement decreased at a temperature range that is similar to that of kerogen pyrolysis. Furthermore, hydroxyls in clay minerals are commonly pyrolyzed at 600-1000 °C [34]. Therefore, the short relaxation signal component is dominated by the hydrogen content of the shale sample in the form of kerogen.

The hydrogen content in kerogen was calculated to be 1.05 mol/100 gr rock. The kerogen hydrogen content in shales is the most important chemical benchmark to determine its hydrocarbon potential. A kerogen class I to IV has decreasing amount of hydrogen in its structure. Additionally, comparing shale samples from the same formation, an immature kerogen has greater hydrogen quantity [35].

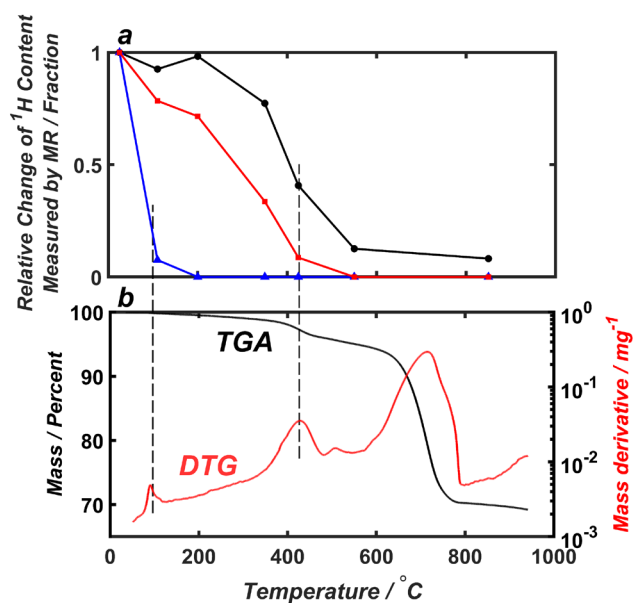


Fig. 6. (a) Change of hydrogen content relative to its initial value as a function of pyrolysis temperature. The hydrogen contents of kerogen (black), oil (red), and water (blue) in the shale sample are determined using calibration of signal from T_1 - T_2^* measurement. (b) thermogravimetric analysis (TGA) of shale sample measuring mass loss versus pyrolysis temperature. DTG shows the derivative of the TGA curve that distinguishes peaks. Water peak in DTG at temperature ~100 °C is consistent with the water content measured using MR. The decrease in kerogen hydrogen content from the short transverse relaxation lifetime of T_1 - T_2^* measurement is consistent with the DTG kerogen peak at 425 °C.

4.4 Look-Locker T_1^* - T_2^* relaxation correlation at low field

Figure 7 compares Look-Locker T_1^* - T_2^* and T_1 - T_2^* relaxation correlation measurements for two nominally similar shale samples. 10.8 gr of sample EG12 and 134.62 gr of sample EG13 were measured at low and high field, respectively. The instrument sensitive volume for the high field measurements was smaller than that for the low field measurements. Therefore, a smaller quantity of shale sample was used for the high field measurements. This should be considered when comparing low and high field measurements presented here. Since signal strength is proportional to the amount of hydrogen present for the measurement. In the Look-Locker T_1^* - T_2^* plots, the integrated signal intensities in arbitrary units are corrected based on Eq. 2b and are shown next to each signal peak.

Shale species are adequately resolved in both Look-Locker T_1^* - T_2^* and T_1 - T_2^* relaxation correlation plots. Integrated signal intensities for oil and water signal peaks measured by T_1 - T_2^* measurement are close to those obtained by Look-Locker T_1^* - T_2^* measurement for both samples. The signal intensities shown in Figure 7a-d are calibrated using a reference sample with known hydrogen content to give the oil and water content in gr per 100 gr of rock. It is assumed that water and oil have the same hydrogen density. Figure 7e shows that the fluid content obtained using Look-Locker T_1^* - T_2^* and T_1 - T_2^* measurements are similar. This allows quantifying fluid content in shales using Look-Locker T_1^* - T_2^* measurement. Kerogen signal intensity is underestimated at

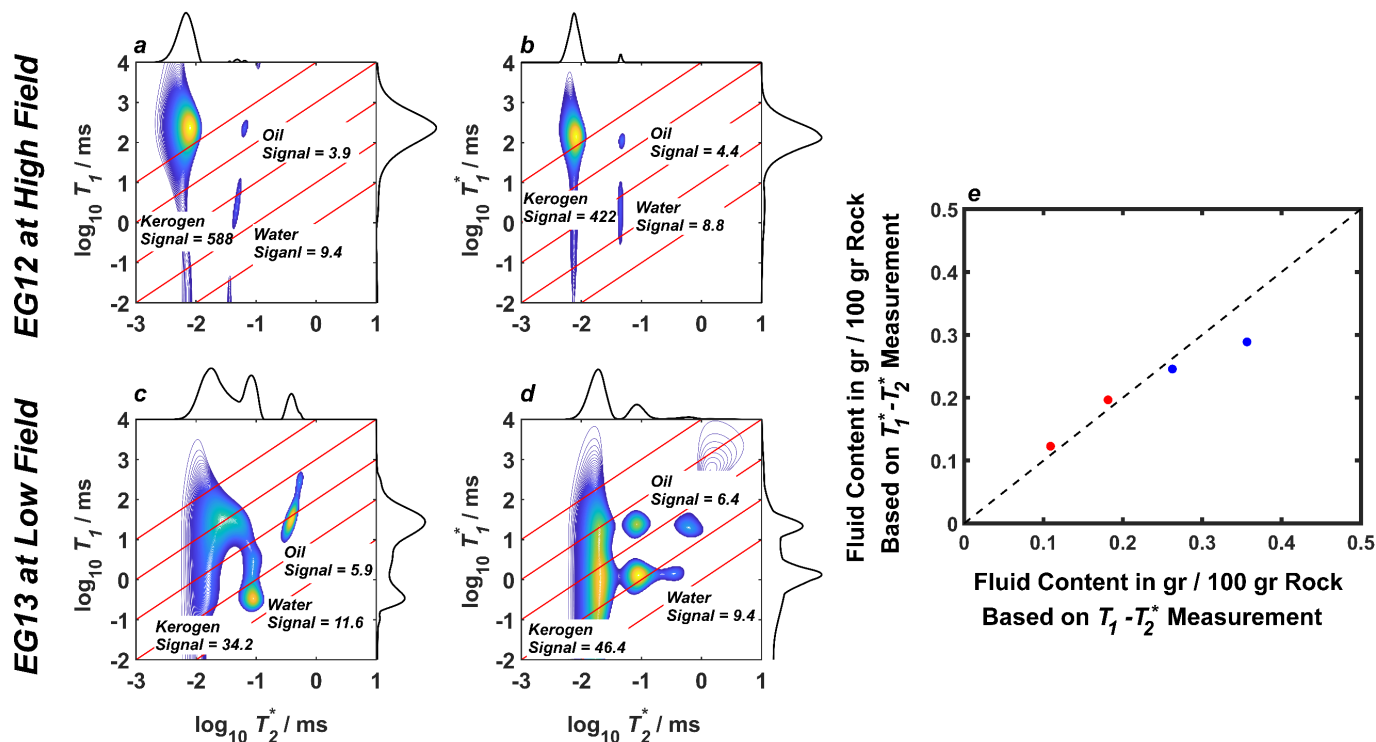


Fig. 7. Comparison of $T_1-T_2^*$ measurement (a and c) and Look-Locker $T_1^*-T_2^*$ measurement (b and d) performed at 4.7 T and 0.2 T for samples EG12 and EG13, respectively. Shale signal species, oil, water, and kerogen are resolved and quantified using both measurement methods. $T_1^*-T_2^*$ measurement is much faster compared to $T_1-T_2^*$ measurement. The integrated signal intensities next to each signal peak for the $T_1^*-T_2^*$ measurement are corrected using Eq. 2b. (e) Fluid quantities determined using $T_1-T_2^*$ measurement versus that measured using $T_1^*-T_2^*$ measurement. Similar values for fluid quantities are determined. The blue and red data points represent water and oil content, respectively. The dashed line is the simple diagonal.

low field since it was measured using a long deadtime compared to the kerogen decay lifetime.

In comparison with the $T_1-T_2^*$ method, the Look-Locker $T_1^*-T_2^*$ method provides sufficient resolution to resolve and quantify shale fluids while reducing measurement time significantly. Application of Look-Locker $T_1^*-T_2^*$ method becomes especially beneficial at low field due reduced sensitivity. Measurement time for the $T_1-T_2^*$ method was 30 min giving a SNR of 453, and 2.5 hr with a SNR of 81 at high and low field, respectively. Look-Locker $T_1^*-T_2^*$ measurement took 1 min at high field yielding a SNR of 93 and 17 min at low field giving a SNR of 40.

In Figure 1c, FIDs are acquired at linearly spaced T_1 recovery times. Therefore, this measurement is suitable for samples that yield sufficiently close T_1 relaxation times. Shale signals meet this requirement. The Look-Locker $T_1^*-T_2^*$ method is able to resolve and quantify shale signal components.

The Look-Locker $T_1^*-T_2^*$ method using more common low field MR scanners will give fast, non-invasive, and accurate shale fluid content for shale drill cuttings at the wellsite and core plugs in the laboratory.

4.5 Imaging shale samples

Shale signal components resolved in the $T_1-T_2^*$ measurement can be employed to understand and guide the invoked contrast in the SPRITE imaging method. The kerogen signal can be excluded from the image signal by choosing a sufficiently long t_p to allow kerogen signal to fully decay but

short enough to acquire the shale fluid signals. The remaining signal can be resolved for oil and water based on their T_1 contrast detected by the $T_1-T_2^*$ measurement. Application of this imaging technique gives separate oil and water images in core plug size samples.

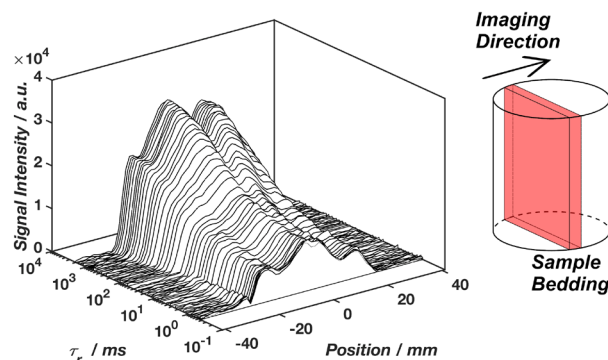


Fig. 8. T_1 -weighted 1D images of sample EG11 perpendicular to the sample beddings. The images show T_1 recovery of magnetization during τ_r with position. Reproduced with permission from Chemical Engineering Journal (2022) 428, 131042 [25].

Figure 8 shows a series of T_1 -weighted images of shale sample EG11 acquired using 1D centric-scan SPRITE method described in Section 3.1.2. The images were acquired perpendicular to the bedding structure of the samples to reveal contrast in their oil and water content. Figure 8 shows T_1 recovery of magnetization as T_1 encoding time, τ_r increases.

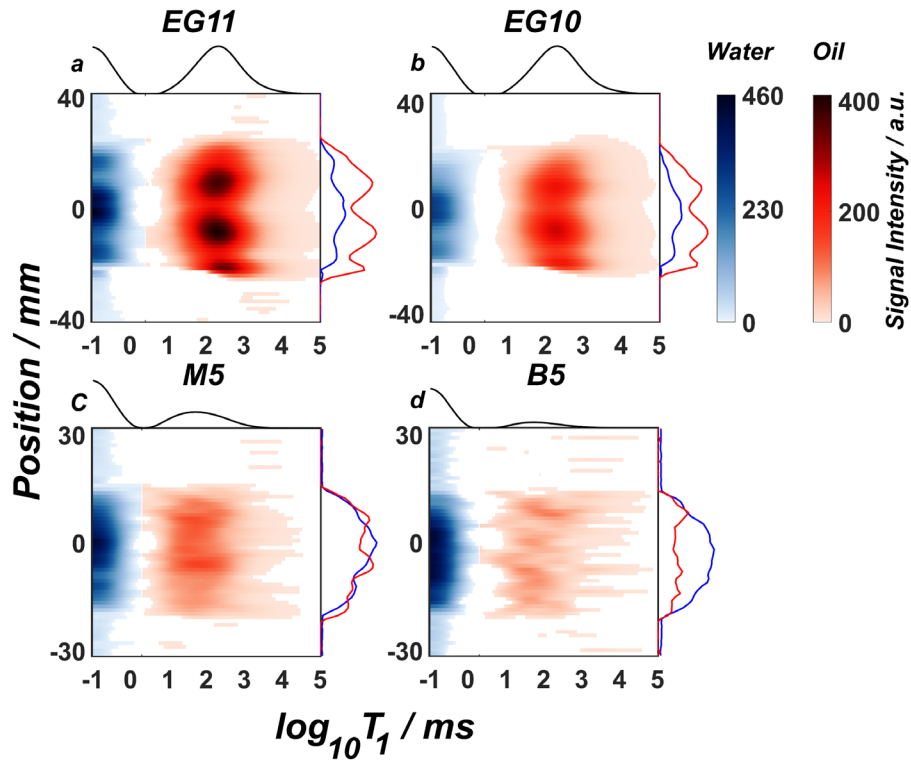


Fig. 9. T_1 resolved 1D images for (a) EG11 from Eagle Ford Formation, (b) EG10 from Eagle Ford Formation (c) M5 from Marcellus Formation, and (d) B5 from Barnett Formation. The projections on the horizontal axes is the bulk T_1 distribution of the sample after kerogen signal was excluded. The blue projection on the vertical axes is the projection of short T_1 component indicating water image, and the red one is the projection of long T_1 component representing oil image. The oil and water profiles spike alternatively. Reproduced with permission from Chemical Engineering Journal (2022) 428, 131042 [25].

4.5.1 Natural fluid storage in shales – wettability

The data shown in Figure 8 was processed using Eq. 4 to resolve the image signal for oil and water in the T_1 relaxation time. Three more shale samples, EG10, M5, and B5 from different formations in their as-received condition, were processed using the same method. Figure 9 shows the spatially resolved T_1 after exclusion of kerogen signal. The

long T_1 signal component is attributed to the oil in the shale samples, and the short T_1 signal species is associated with the shale water content. The projection of the signal on the horizontal axis gives the bulk T_1 relaxation time of the sample after exclusion of kerogen signal. The integrated signal intensity of the long T_1 signal peak shown on the vertical axis in red gives the oil image in the sample, and the integrated signal intensity of the short T_1 signal component on the same axis in blue yields the water image.

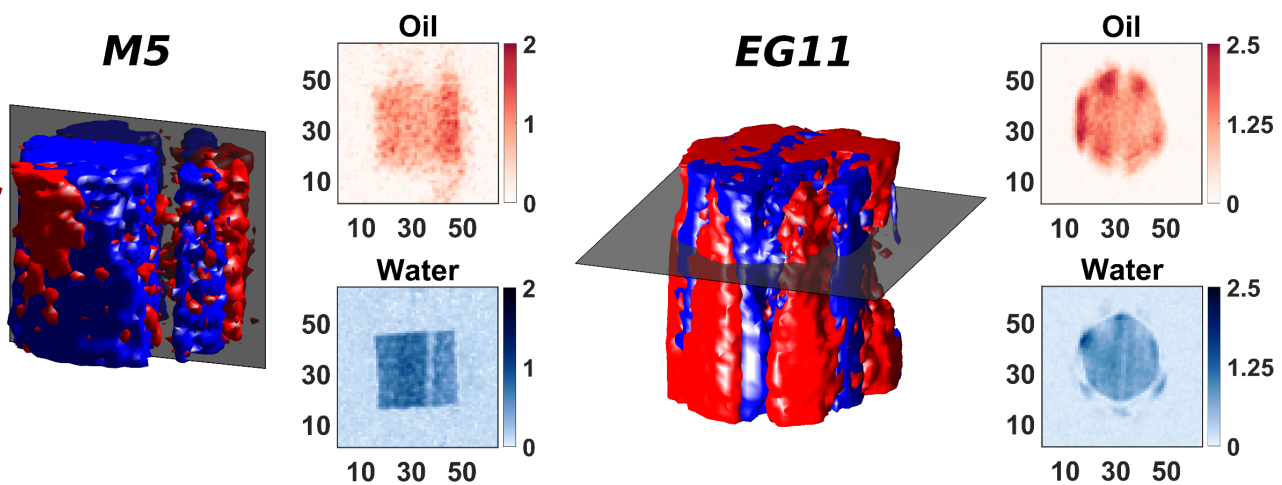


Fig. 10. Superimposed 3D images of water and oil in shale samples M5 and EG11. The cross sections show signal intensity converted to fluid content in porosity unit (p.u.). Fluid distribution is controlled by the bedding structure of the samples. The signal void in sample M5 is indication of a low porosity layer. Axis for cross sections show pixel numbers. Image FOV was 80 mm. Reproduced with permission from Chemical Engineering Journal (2022) 428, 131042 [25].

The high degree of shale heterogeneity demands 3D imaging. The imaging scheme in Figure 1 was also employed using 3D centric-scan SPRITE to give 3D images of oil and water. The superimposed 3D images of oil and water for samples EG11 and M5 in their as-received condition are shown in Figure 10. The 3D images were calibrated using a reference sample to give quantity of fluids. The oil hydrogen index was assumed to be similar to that of water. The cross sections of the 3D images in Figure 10 show the water and oil content in porosity unit (p.u.).

The core plug scale heterogeneity of shale samples is commonly characterized by their bedding structure. The 1D images of oil (red) and water (water) in various shale samples in Figure 9 show alternating oil-rich and water-rich layers. The oil images show a crest at the trough of the water images. This means the pore space in some layers is mostly occupied by water, while the pore space in other layers is largely prone to oil.

The degree and nature of the shale heterogeneity can be characterized by how it manifests as variation in the fluid saturation. A 1D image of a sample with homogenous fluid saturation acquired with an image direction shown in the schematic core plug in Figure 8 yields a semicircle. Figure 9d shows such characteristics in the 1D image of sample B5. Alternating oil-rich and water-rich layers indicates spatial wettability variation. A layer with a higher clay content is more likely to be water-rich since it is naturally water-wet, while a layer with more organic kerogen content may be more favourable to the oil phase. The superimposed 3D image of oil and water in the sample EG11 also shows the sample's layered structure. The image intensity of the cross sections in Figure 10 is calibrated to give oil and water content in porosity unit. For sample M5, in Figure 10, the signal void in

the oil and water images is due to a low porosity layer, since no fracture is visible on the periphery of the core plug.

4.6 Water uptake

The key role of shale core plug scale heterogeneity on the fluid storage, discussed in Section 4.5, motivates study of its impact on the fluid flow in shales. This was investigated by performing water uptake experiments on two nominally similar samples, EG10 and EG11. The water uptake experiments were monitored using gravimetric measurements, T_1 - T_2^* method, and 3D centric-scan SPRITE imaging method with T_1 suppression for 30 days.

4.6.1 T_1 - T_2^* measurements

Figure 11 shows T_1 - T_2^* measurements of samples EG10 and EG11 before and after water uptake experiment. Water integrated signal intensity increased for both samples during water uptake experiment.

The high resolution of T_1 - T_2^* method allowed measuring the sample EG11 with a reference sample. The reference sample composition was 17.0 wt% H₂O, 82.9 wt% D₂O and 0.07 wt% CuSO₄ and contained 3.1 mmol of ¹H. The signal peak from the reference sample of known hydrogen content is shown in green in the T_1 - T_2^* measurements of Figure 11. The position of the signal peak from the reference sample in the T_1 - T_2^* relaxation correlation plot was adjusted by varying the concentration of CuSO₄. This signal peak was well-resolved from the shale signal species. Therefore, it did not interfere with quantification of shale signal components. The employment of a reference sample (1) aids in production of consistent results between measurements because the signal

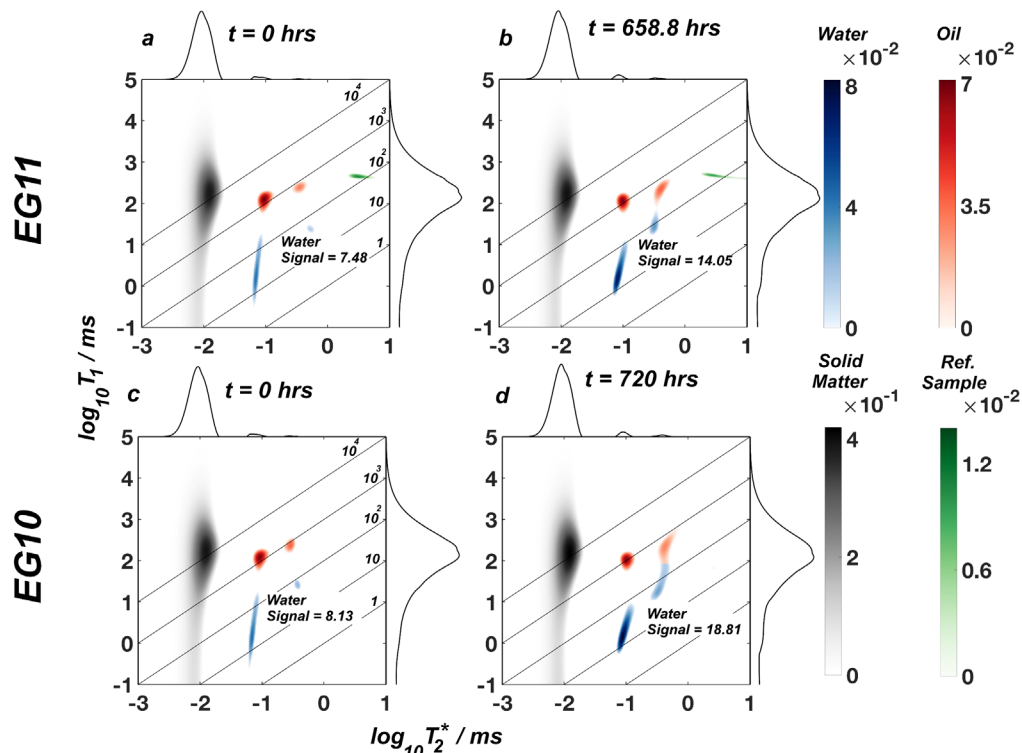


Fig. 11. 2D T_1 - T_2^* relaxation correlations of sample EG11 and EG10 (a and c) before and (b and d) after water uptake, respectively. Kerogen, water, oil, and reference sample signals are resolved and are shown in gray, blue, red, and green, respectively. The water peaks show an increase in signal intensity with water uptake. Reproduced with permission from Chemical Engineering Journal (2022) 428, 131042 [25].

properties of the reference sample remain constant between measurements. This becomes particularly significant when T_1 - T_2^* measurements of multiple samples are to be compared or when T_1 - T_2^* responses of a sample are measured during a process. (2) A reference sample can be used to convert MR signal for shale signal species to their hydrogen content. It should be noticed that the poor signal differentiation by the T_1 - T_2 method prevents application of such reference sample. Signal discrimination is hampered in the T_1 - T_2 method compared to T_1 - T_2^* method for shales. Therefore, the overlap of signal components will further impair quantification of shale signal intensities using T_1 - T_2 methods. As shown in Figure 11, the T_1 - T_2^* method was capable of resolving and quantifying multicomponent signals, even when four signal components are present.

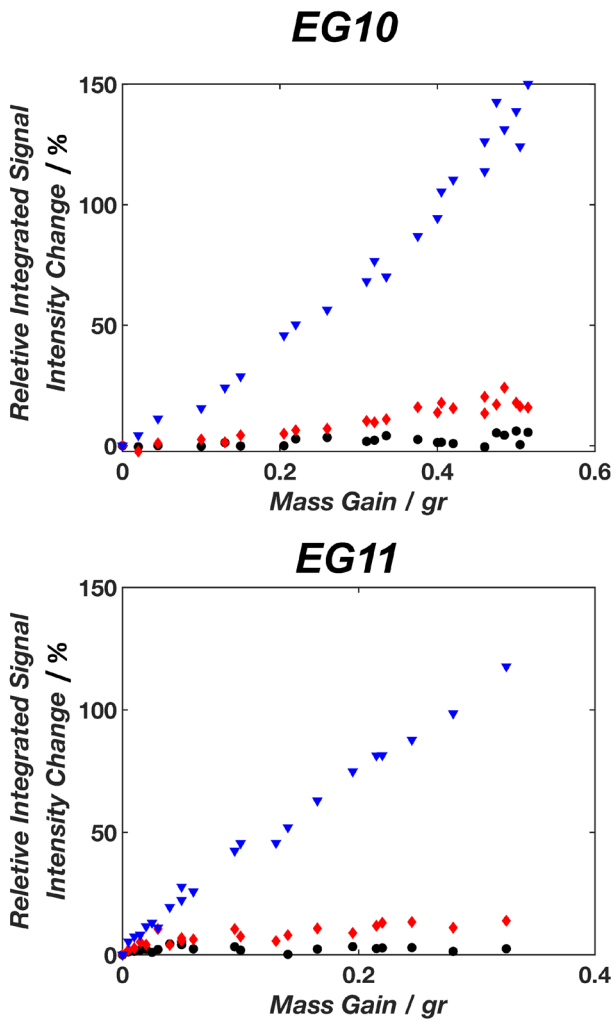


Fig. 12. Relative signal change of water peak (\blacktriangledown), oil (\blacklozenge), and kerogen (\bullet) signal peaks versus mass gained by (a) sample EG10 and (b) sample EG11, based on the T_1 - T_2^* measurements during water uptake experiments. Kerogen and oil signal intensities remained essentially unchanged. Water signal intensity in the T_1 - T_2^* relaxation correlations showed a linear relationship with shale water content.

Relative integrated signal intensity change ($\frac{S(t)-S(t=0)}{S(t=0)} \times 100$) in Figure 12 for oil and kerogen shale signal components remained constant, while that of water changed

during water uptake experiments for both shale samples. Water signal component showed a linear relationship with the sample mass gain due to water uptake. This not only confirms the identification of water signal peak, but also allows accurate quantification of water content in the shale samples.

4.6.2 Imaging during water uptake

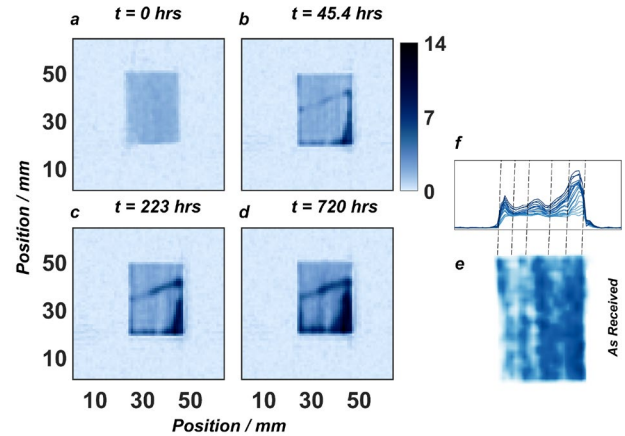


Fig. 13. 2D cross sections (a to d) extracted from oil suppressed 3D centric-scan SPRITE measurements perpendicular to the beddings of EG10 sample with time during water uptake experiment. The signal intensity is calibrated to the water content in porosity units. 2D cross section (e) from oil suppressed 3D centric-scan SPRITE image shows sample EG10 in its as received condition. 1D water profiles (f) are projections of the water content in the 2D cross sections as water uptake proceeds. The dashed lines demonstrate that beddings identified in the as received condition control the water transport during water imbibition. Water uptake in the EG10 sample reveals the layered structure of the sample and the fracture across the sample. Reproduced with permission from Chemical Engineering Journal (2022) 428, 131042 [25].

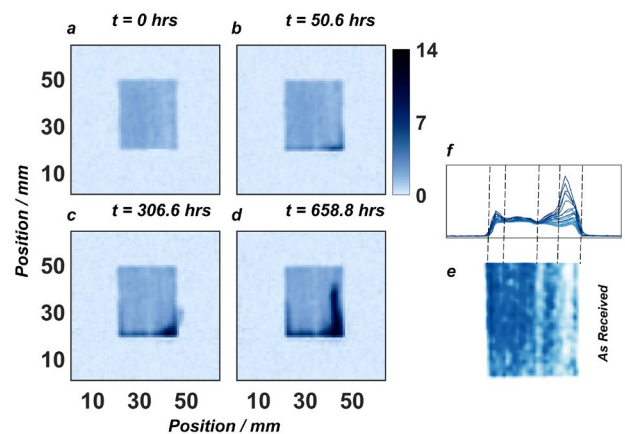


Fig. 14. 2D cross sections (a to d) extracted from oil suppressed 3D centric-scan SPRITE measurements perpendicular to the beddings of EG11 sample with time during water uptake experiment. The signal intensity is calibrated to the water content in porosity units. 2D cross section (e) from oil suppressed 3D centric-scan SPRITE image shows sample EG11 in its as received condition. 1D water profiles (f) are projections of the water content in the 2D cross sections as water uptake proceeds. The dashed lines demonstrate that beddings identified in the as received condition control the water transport during water imbibition. Water uptake in the EG11 shale sample reveals the layered structure of the sample. Reproduced with permission from Chemical Engineering Journal (2022) 428, 131042 [25].

Figure 13 and Figure 14 show 2D slices from 3D images acquired using centric-scan SPRITE imaging method with T_1 suppression for samples EG10 and EG11, respectively, undergoing water uptake. The image intensity was converted to water content in porosity unit using a reference sample. The water imbibition, in Figures 13 and 14, followed the bedding structure of the sample. This shows that wettability variation between the sample beddings, also detected for shale samples in their as-received condition, plays an important role in the fluid flow. Figure 13 shows a visible fracture that was filled with water as water uptake continued.

5 Conclusion

This work presents magnetic resonance methods and their application for quantitative signal detection for shale characterization. It was shown that T_1 - T_2^* relaxation correlation measurement differentiated and quantified the short-lived multicomponent MR signal in shales. The Look-Locker T_1^* - T_2^* measurement was demonstrated to give quantitative shale signal with high sensitivity even at low field. The SPRITE imaging method with magnetization preparation was used to give 1D and 3D images with a field of view of 8 cm. Millimetre scale heterogeneities in shale samples were identified using the imaging technique. These heterogeneities were imposed on water and oil content by the samples' laminae. Water absorption/desorption and evaporation experiments were used to calibrate MR signal to give oil and water content. Step pyrolysis experiments showed that the short transverse signal lifetime is dominated by the kerogen content. Water uptake experiments coupled with MR imaging and T_1 - T_2^* measurement demonstrated the key role of wettability in determining transport in shales.

Application of these methods for shale core analysis in the laboratory and for shale drill cuttings enhances estimation of reservoir quality and ensures economic hydrocarbons production from shale reservoirs.

S. Zamiri thanks the New Brunswick Innovation Foundation for a scholarship and University of New Brunswick for the Gerald I. Goobie Chemical Engineering Scholarship. Bruce J. Balcom acknowledges NSERC of Canada for a Discovery grant [2015-6122] and the Canada Chairs program for a Research Chair in Material Science MRI [950-230894].

References

1. R. Rezaee, *Fundamentals of Gas Shale Reservoirs* (John Wiley & Sons, Inc, Hoboken, 2015)
2. Y. Zee Ma, S.A. Holditch, *Unconventional Oil and Gas Resources Handbook* (Elsevier, 2016)
3. Y. Wang, S. Xu, F. Hao, B. Zhang, Z. Shu, Q. Gou, et al., *Geol Soc Am Bull* 132, 1704–21 (2020)
4. R.G. Loucks, R.M. Reed, S.C. Ruppel, U. Hammes, *AAPG Bull* 96, 1071–98 (2012)
5. L. Zhang, B. Li, S. Jiang, D. Xiao, S. Lu, Y. Zhang, et al., *Int J Coal Geol* 195, 250–66 (2018)
6. T. Saif, Q. Lin, A.R. Butcher, B. Bijeljic, M.J. Blunt, *Appl Energ* 202, 628–47 (2017)
7. M. Akbarabadi, S. Saraji, M. Piri, D. Georgi, M. Delshad, *Adv Water Resour* 107, 160–79 (2017)
8. S. Chen, J. Jiang, B. Guo, *Chem Eng J* 417, 129210 (2021)
9. Y. Wu, P. Tahmasebi, C. Lin, L. Ren, C. Dong, *Mar Petrol Geol* 109, 9–21 (2019)
10. S. Kelly, H. El-Sobky, C. Torres-Verdín, M.T. Balhoff, *Adv Water Resour* 95, 302–16 (2016)
11. M. Fleury, M. Romero-Sarmiento, *J Petrol Sci Eng* 137, 55–62 (2016)
12. P.M. Singer, Z. Chen, X. Wang, G.J. Hirasaki *Fuel* 280, 118626 (2020)
13. P.M. Singer, Z. Chen, G.J. Hirasaki *Petrophysics* 57, 604–19 (2016)
14. R. Kausik, CC. Minh, L. Zielinski, B. Vissapragada, R. Akkurt, Y. Song, et al., *SPE, SPE-147198-MS* (2011)
15. R. Kausik, K. Fellah, L. Feng, G. Simpson, *Petrophysics* 58, 341–51 (2017)
16. R. Kausik, K. Fellah, E. Rylander, P.M. Singer, R.E. Lewis, S.M. Sinclair, *Petrophysics* 57, 339–50 (2016)
17. B. Sun, E. Yang, H. Wang, S.J. Seltzer, V. Montoya, J. Crowe, et al., *SPWLA 57th Annual Logging Symposium* (2016)
18. C. Minh, S. Crary, L. Zielinski, C.B. Liu, S. Jones, S. Jacobsen, *SPE, SPE-161578-MS* (2012)
19. Y-Q. Song, R. Kausik, *Prog Nucl Mag Res Sp* 112–113, 17–33 (2019)
20. R. Kausik, C.C. Minh, L. Zielinski, B. Vissapragada, R. Akkurt, Y-Q. Song, et al., *SPE, SPE-147198-MS* (2011)
21. J-P. Korb, B. Nicot, I. Jolivet, *Micropor Mesopor Mat* 269, 7–11 (2018)
22. R. Enjilela, J. Guo, B. MacMillan, F. Marica, A. Afrough, B.J. Balcom, *J Magn Reson* 326, 106961 (2021)
23. J. Guo, B. MacMillan, M.S. Zamiri, B.J. Balcom, *J Magn Reson* 328, 107005 (2021)
24. M.S. Zamiri, B. MacMillan, F. Marica, J. Guo, L. Romero-Zerón, B.J. Balcom, *Fuel* 284, 119014 (2021)
25. M.S. Zamiri, F. Marica, L. Romero-Zerón, B.J. Balcom, *Chem Eng J* 428, 131042 (2022)
26. J. Guo, M.S. Zamiri, B.J. Balcom, *J Magn Reson* 335, 107123 (2022)
27. B.J. Balcom, R.P. Macgregor, S.D. Beyea, D.P. Green, R.L. Armstrong, T.W. Bremner, *J Magn Reson A* 123, 131–4 (1996)
28. M. Halse, D.J. Goodyear, B. MacMillan, P. Szomolanyi, D. Matheson, B.J. Balcom, *J Magn Reson* 165, 219–29 (2003)
29. R. Kimmich, *NMR Tomography, Diffusometry, Relaxometry* (Springer Berlin Heidelberg; 1997)
30. P.T. Callaghan, *Translational Dynamics and Magnetic Resonance* (Oxford University Press, 2011)
31. J. Mitchell, *J Magn Reson* 240, 52–60 (2014)
32. I.V. Mastikhin, B.J. Balcom, P.J. Prado, C.B. Kennedy, *J Magn Reson* 136, 159–68 (1999)
33. L. Li, F. Marica, Q. Chen, B. MacMillan, B.J. Balcom, *J Magn Reson* 186, 282–92 (2007)
34. M. Labus, I. Matyasik, *J Therm Anal Calorim* 136, 1185–94 (2019)
35. B. Tissot, B. Durand, J. Espitalie, A. Combaz, *AAPG Bull* 58 (1974)

The effect of nanoconfinement on the phase behavior of ethane/n-propane binary mixture: An experimental study at varying pore sizes and compositions

Keerti Vardhan Sharma^{a,*}, Rami M. Alloush^a, Kareem Al-Garadi^a, and Mohammad Piri^a

^aCenter of Innovation for Flow through Porous Media, Department of Petroleum Engineering, University of Wyoming, Laramie, Wyoming, USA, 82071

Abstract. Enhanced fluid-solid and fluid-fluid interactions due to nanoconfinement in unconventional gas reservoirs can translate to the hydrocarbon components showing different phase behaviors than those observed during the bulk phase analysis. Furthermore, desorption of fluids from nanopores during production from unconventional reservoirs results in reduced reservoir pressure, strengthening the effect of capillarity on the phase behavior of the hydrocarbons. Efforts are being made to develop and improve phase behavior models to predict the effect of confinement on phase equilibria of hydrocarbon mixtures in nanopores. Nonetheless, the scarcity of experimental data revealing the effects of factors such as pore size distribution on adsorption and desorption behaviors of the hydrocarbon components poses a major impediment to improving the accuracy of the models. This experimental study investigates the effect of confinement on the phase equilibria of binary mixtures of Ethane/n-Propane with different compositions in MCM-41 nanoporous material at three different pore sizes of 6 nm, 8 nm, and 12 nm. The condensation pressures of the mixture for these pore sizes are determined from the mass-pressure isotherms obtained during the adsorption process using a patented gravimetric apparatus. The variations in the condensation pressures with respect to pore sizes for different compositions of the binary mixture manifest the effect of capillary pressure and molar fraction on the vapor-liquid equilibrium. Furthermore, a direct proportionality with the pore size was evident from the results, which agrees with the trends available in the literature. The results also demonstrate that the relative quantities of the components play a significant role in the shifting of the phase envelopes of hydrocarbon mixtures. Additionally, the degree of selective adsorption in the nanopores decreases with an increase in the molar fraction of heavy components. This study presents a new dataset that improves the current understanding of the phase behavior of hydrocarbon mixtures in nanopores. Moreover, this investigation can be of great interest to the researchers developing phase behavior models to study vapor-liquid equilibria of the confined fluids.

1 Introduction

Hydrocarbons have been a vital part of modern human life for the past century and will continue to satiate the ever-growing global energy demand in the near future [1]. Hydrocarbons such as ethane (C_2H_6) and propane (C_3H_8) are the most significant natural organic deposits available in geological formations, along with methane [2]. In addition, they are essential for numerous industrial and domestic applications [3,4]. For example, they are used as a fuel [5-10], sources for hydrogen and methane production [11,12], solvents [13], fluids for cooling and heating in the petrochemical industry [14-16], and catalysts [17].

The bulk thermodynamic properties of pure ethane, propane, ethane/propane mixture, and their mixtures with

other fluids in the gaseous or liquid states have been studied extensively [18-29]. For example, the bulk phase behaviors of ethane and propane gases were determined using statistical thermodynamic approaches for a wide range of temperatures (0 to 1,500 K) at atmospheric pressure [30]. In addition, phase behaviors of various mixtures containing ethane, propane, or both and other fluids such as Xenon [31], hydrogen [32], water [33,34], CO_2 [35,36], hydrate [37], sunflower oil [38], bitumen [39], and other hydrocarbons [40-45] have been evaluated at different conditions. However, only a few studies investigated the phase behavior characteristics of ethane and propane and their mixtures in confined spaces, which significantly differ from those observed in bulk conditions [46,47]. This difference is attributed to the effects of confinement, which are governed by intensified fluid-fluid and solid-fluid interactions. Such interactions control the

* Corresponding author: ksharmal@uwyo.edu

flow of confined fluids in porous media, resulting from altered phase behavior due to nanoconfinement.

Understanding the phase behavior of fluids in nanoconfinement is critical for several disciplines in science and engineering, such as geochemistry [48], hydrogen storage [49], catalysis [50], heat transfer [51–53], and drug delivery [54]. An example from the oil industry is shale reservoirs, where nanopores make up a significant portion of the hydrocarbon-bearing matrix compared to those of the macropores and fractures [55,56]. It is paramount to carefully characterize the confined phase behavior of hydrocarbons stored in nanopores for effective development and recovery optimization from unconventional resources such as shales [57–59].

Several researchers have made notable efforts to develop numerical models that can account for the fluid-fluid and solid-fluid interactions in confined fluid systems. Ma and Jamili [59] used the Simplified Local-Density (SLD) theory to modify the Peng-Robinson equation of state (PR-EOS) to probe the fluid-wall interactions under nanoconfinement. They calculated the density profiles as a function of pore width for ethane and propane in a 5-nm wide slit pore under conditions of 3,043 psi and 80 °C. This work was based upon the modified model (SLD-PR). The density profiles for ethane and propane were distinct from each other such that propane had higher bulk densities and adsorbed layer densities than those of ethane. In addition, ethane showed a significant difference between its adsorbed and bulk densities than that exhibited by propane. Therefore, they concluded that the confinement effects are more pronounced on lighter fluids than on heavier ones in the same pore size and at similar temperature and pressure conditions. Dong et al. [58] coupled the cubic Peng-Robinson (PR) equation of state (EOS) with the multicomponent potential theory of adsorption (MPTA) to study and model the confined behavior of pure ethane, propane, and ethane/methane and propane/methane mixtures in organic nanopores. In addition, the thermodynamic properties of ethane and propane hydrates were investigated in porous silica gels of four different pore sizes 100, 30, 15, and 6 nm [60]. Sugata and Piri developed a modified equation of state (EOS) to evaluate the thermodynamic properties of fluids under nanoconfinement. The authors combined the perturbed chain-statistical associating fluid theory (PC-SAFT) EOS with the Young-Laplace equation to account for the effect of capillary pressure in predicting the phase behavior of confined fluids [61].

Barsotti et al. [62] presented experimentally measured isotherms of pure propane in mesoporous silica MCM-41 of various pore sizes (8.08, 4.19, and 2.90 nm) over a wide range of temperatures, from 5 to 50 °C. They found that propane's capillary condensation pressure increased with an increase in temperature and pore size. In addition, the adsorption branch of the propane isotherms showed a concave shape, reflecting the effect of fluid-solid interactions. Furthermore, these isotherms followed the common capillary condensation trend, and exhibited hysteresis and the effect of supercriticality (see [62] for more details). Other studies observed that the capillary condensation of propane in crushed shale could result in significant swelling of kerogen that can in turn induce fractures and pore deformation [63,64].

Zhao and Jin [65] studied methane/propane mixture phase behavior in nanopores connected to the bulk regions (i.e.,

nanopores connected to macropores and natural/hydraulic fractures) using density functional theory (DFT). They determined that a two-phase region could form inside the nanopores, and its size grows with increasing pore size. However, this study employed a uniform pore size model and did not consider the effect of the pore size distribution (PSD). In another study by the same authors [66], they used the DFT and the same fluid mixture (methane/propane) to investigate the effect of PSD on capillary condensation in nanopores during constant composition expansion (CCE) and constant volume depletion (CVD) processes. They considered the impact of the interplay between nanopores and macropores/fractures, which was overlooked in other studies that focused only on the effect of the PSD [65, 67]. To this end, two different pore sizes (5 nm and 10 nm) were numerically generated, and three PSD models with varying ratios of nanopores and bulk region volumes were constructed. The simulated media represented oil-wet pores of carbon slits, while the macropores/fractures denoted the bulk region where the confinement effects did not exist. They concluded that when pressure declines (i.e., desorption of fluids), the phase transitions occur first in bulk, then in the larger pores, followed by smaller pores. In addition, the composition of the heavier component decreases in the phase transition region but increases in the other areas with no phase transition. The trend mentioned above is due to the influence of PSD, which becomes more pronounced as the pressure goes below the dew point pressure, and propane inside the nanopores can be released in this pressure region. As the proportion of the smaller pores in the system becomes larger, the confinement effect in these media becomes stronger. And the communication between the nanopores and bulk induces the accumulation of heavier components. Thus, the recovery of the heavier molecules is suppressed.

It is evident from the literature that most studies probed the confined phase behavior of fluids using numerical techniques. Only a limited number of investigations have been dedicated to experimentally probing the effects of confinement, and these have mostly used a single component and employed a narrow range of pore sizes. To the best of our knowledge, no experimental study probed the effects of composition and pore sizes on the phase behavior of the ethane/propane mixture in nanopores. In this study, we employed an advanced gravimetric technique to study the phase behavior of confined ethane/propane mixture for two different compositions in three different sizes of nanopores (7, 10.2, and 12.3 nm). The two compositions used were (M1) 46.6% and 53.4% and (M2) 37.3% and 62.7% of ethane and propane, respectively. The adsorption isotherms were measured at -18 °C.

The remainder of this paper is organized as follows. **Section 2** provides details about the materials and methods used to conduct the experiments. This section briefly discusses the specifications of the materials and fluids used as adsorbents and adsorbates, preparation of the nanoporous materials and apparatus, experimental procedure, and the data acquisition and processing techniques. The experimental results, such as adsorption isotherms for both compositions in all three pore sizes, are presented and analyzed in **Section 3**. Finally, the conclusions and final remarks are listed in **Section 4**.

2 Materials and methods

2.1 Materials and sample preparation

Three different sizes of the mesoporous silica material known as MCM-41 were acquired from Glantreo, Ltd. This material is known for its controlled pore shapes and sizes. The nanopores of MCM-41 are unconnected, cylindrical in shape, and possess a uniform pore size distribution [68]. The provider-specified pore sizes of the MCM-41 samples used in this work are 6, 8, and 12 nm. The non-local density functional theory (NLDFT) analysis was performed on these samples to determine the average pore size of the material. **Table 1** shows the pore diameters of the MCM-41 samples calculated by using the NLDFT.

Table 1: Pore diameter of various MCM-41 samples used in this study. The pore size distributions for all samples are provided in **Appendix I**.

MCM-41 samples	NLDFT Pore diameter (nm)
MCM-41 (60 A)	7
MCM-41 (80 A)	10.2
MCM-41 (120 A)	12.3

We observed a certain degree of discrepancy in the pore diameters given by the provider and those obtained through the NLDFT calculations. The latter generated pore diameter values that were larger than those provided by the manufacturer. Samples were packed into different titanium sample holders using a standard procedure (see Ref. [62] for details). Research grade ethane and propane gases were obtained from Airgas Inc. Both gases possessed 99.8% purity. The fluid mixture was prepared in-house using a mixing setup consisting of a two-cylinder ISCO pump, a high-accuracy balance, a vacuum pump, and an accumulator.

2.2 Apparatus

A patented gravimetric nanocondensation apparatus [69] was employed to measure the adsorption isotherms. The schematic diagram of the apparatus is shown in **Figure 1**. It consisted of an environmental chamber from Thermotron, sample holders, and four Mettler Toledo mass comparators. Different samples of the nanoporous material were packed inside the sample holders, which were housed inside the environmental chamber. The chamber could operate over a wide range of subzero and high-temperature conditions and maintain the desired temperature with an accuracy of ± 0.1 °C. The highly advanced XPE 505 C mass comparators possessed an accuracy of ± 0.00001 g. They were located above the environmental chamber on an anti-vibration platform and suspended the sample holders inside the enclosure through thin metal wires. The changes in the mass of the adsorbed fluid were directly measured using these balances during the experiment. The apparatus allows for the measurement of four isotherms simultaneously. Other key components and configurations of the apparatus, such as pumps, pressure transducers, and different valve assemblies, are shown in **Figure 1**. The original nanocondensation apparatus was recently improved with incorporation of an advanced automation module [70], which increased the efficiency of

the data acquisition process and enhanced the accuracy of the measurements. To this end, automation hardware and data acquisition boxes were installed in the system, which controlled the opening and closing of the valves and monitored the pressure of the sample holders in real-time.

2.3 Experimental procedure

To prepare the nanocondensation apparatus for the adsorption experiments, an accumulator containing the compressed hydrocarbon mixture was connected to the adsorption inlet valves of the system. Next, the whole instrument was vacuumed for 48 hours to remove any air or humidity from the samples and fluid lines. The temperature of the system was then brought to the experimental condition (i.e., -18 °C) while it was being subjected to a vacuum. The process was stopped once the chamber temperature was stabilized, and a good vacuum condition was observed at the Leybold low-pressure gauge. Subsequently, the adsorption mode was activated on a customized automated LabView software that had been loaded on the computer. In this mode, all Vindum valves that connect the fluid source to the sample holders were opened to allow a gradual injection of fluids into the nanoporous material. During the experiments, the ethane/propane mixture was introduced into the medium in small doses to ensure a slow and consistent buildup of the system pressure. The fluid injection parameters, such as (i) injection time or pulse time and (ii) equilibrium time (i.e., the time difference between two consecutive dosages), were then set on the Labview software (see **Figure A(d)** in Appendix for an illustration of this procedure). The injection time (i.e., dosage time) signifies the duration over which the adsorption valves remain open for the fluid to flow into the material under a certain pressure. The equilibrium time was chosen such that the pressure, after introducing each dose, could reach equilibrium within that time frame. The Rosemount pressure transducers connected to the sample holders recorded the pressure variations in real time. Additionally, a customized Python script plotted this data and facilitated the visual verification of the equilibrium conditions. These two time-related parameters significantly influence the accuracy of the measurements. They can be changed throughout the experiments (as needed) to ensure that a subsequent injection is performed only when the system pressure has attained equilibrium after every dose of fluid is injected. In this work, the initial injection and equilibrium times were fixed at 100 ms and 120 minutes, respectively. The mass and pressure of the sample holders were recorded every second during the adsorption process, and the raw data were logged and plotted throughout the experiment to check for the accuracy. The adsorption isotherm data points, which show mass vs. pressure, were acquired at each equilibrium state (i.e., every two hours). These points were plotted in real-time during the tests to monitor the trend and identify capillary condensation and bulk saturation regions. The adsorption process was stopped once the pressure inside the sample holders reached the bulk saturation pressure of the fluid mixture. Finally, the complete mass-pressure data was processed, and capillary condensation and saturation pressures were determined.

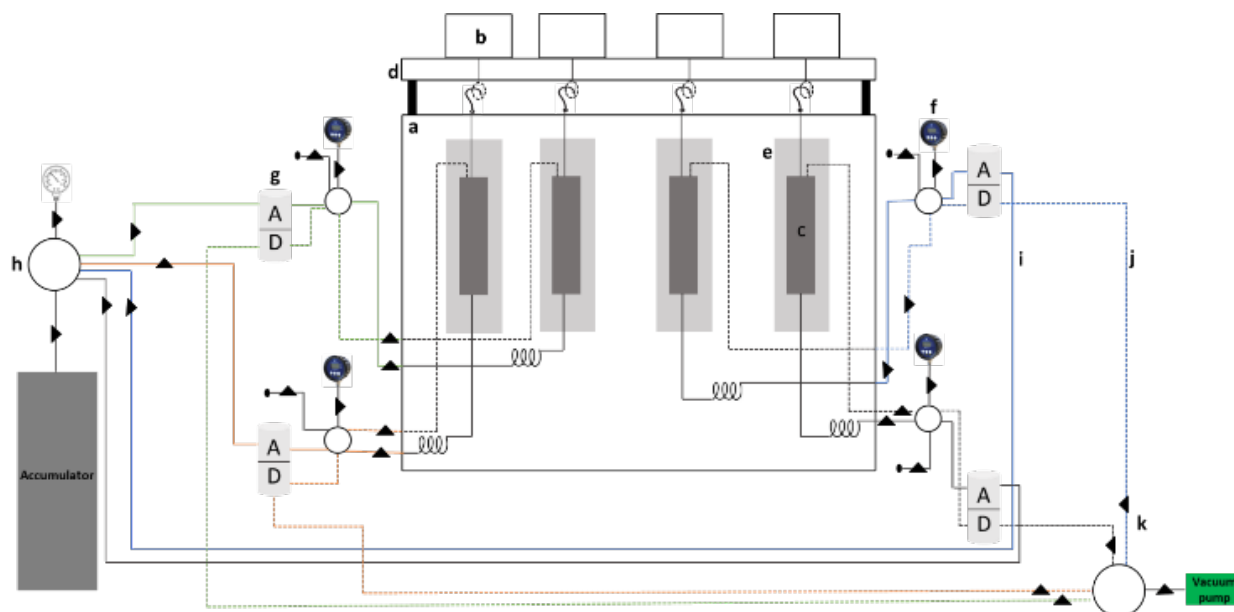


Figure 1. Schematic diagram of the components and configuration of the nanocondensation apparatus: (a) environmental chamber, (b) mass comparator or balance, (c) sample holder, (d) antivibration table, (e) sample holder cover, (f) Rosemount pressure transducers, (g) Vindum valves, (h) manifolds, (i) adsorption fluid lines, and (j) desorption fluid lines.

3 Results and discussion

In this section, we present and discuss the results of the confined phase behavior tests that used ethane/propane mixtures in model nanoporous material MCM-41. We provide the adsorption isotherms for two different ethane/propane mixture compositions in three pore sizes, 7, 10.2, and 12.3 nm, at -18 °C temperature. We calculate the capillary condensation pressures for each pore size by fitting the first derivatives of the mass with respect to pressure (i.e., dm/dP) to a Lorentzian function. The peak of the Lorentzian function indicates the fastest rate of increase in the mass of the adsorbed fluid at a certain pressure and is identified as the capillary condensation pressure [69]. The first inflection point on the adsorption isotherm represents the vapor-liquid phase transition due to nanoconfinement. When the system's pressure is below the saturation pressure of the fluid, an abrupt increase in the adsorbed mass corresponds to the condensation of the fluid inside the nanopores due to enhanced solid-liquid interactions. As the system pressure increases gradually and reaches the bulk saturation pressure, the vapor-liquid phase transition occurs throughout the sample holders and causes a significant increase in the mass of the sample holders. This is identified as a steep increase in the mass on the adsorption isotherms (the vertical-like section of the isotherm), also known as bulk condensation or bubble pressure. Therefore, on an adsorption isotherm, the first inflection point corresponds to the beginning of condensation due to nanopores, and the second abrupt jump in the mass reflects the bulk vapor-liquid phase transition. The bulk vapor-liquid equilibrium (VLE) for various mole fractions of ethane/propane mixture at the experimental temperature of -18 °C is shown in **Figure 2**. The adsorption isotherms for compositions M1 and M2 are presented in **Figures 3** and **4**.

At this temperature, for composition M1, the bulk saturation pressure is expected to be approximately 112 psi (see **Figure 2**). The experimentally measured adsorption isotherms for this mixture are shown in **Figure 3**. The results indicate that the experimental bulk bubble pressure (highlighted by the double-dashed line) for this composition is approximately 94 psi, which is lower than the theoretically calculated bulk bubble pressure highlighted by the single-dashed line. This difference in the saturation pressure of the hydrocarbon mixture can be attributed to the selective adsorption inside the nanopores. The suppression in the saturation pressure indicates higher adsorption of the lighter component, which is ethane in this study. However, more experimental studies are needed to establish and quantify this phenomenon for this mixture. The capillary condensation pressures were calculated for all three pore sizes and are listed in **Table 2**. Additionally, examples of the Lorentzian curve fitting for the dm/dP vs. pressure for both compositions are given in **Figure 5**. It is observed that the effect of nanoconfinement is profound in the smallest pore sizes used here (7 nm), and it decreases with an increase in the pore size. The capillary condensation pressure of ethane/propane mixture for M1 composition in nanopores of 7 nm pore size was measured to be 54.75 psi. However, this pressure increases significantly (73.82 psi) as the pore size scales to 10.2 nm. Furthermore, for the largest pore size used in this study (12.3 nm), a slight increase was observed in the capillary condensation pressure (79.5 psi). This trend is in agreement with those presented in the literature, which shows that the capillary condensation pressure increases with an increase in the pore size. In other words, the degree of suppression of the saturation pressure for vapor-liquid phase transition due to confinement is larger in the tighter nanopores owing to enhanced wall-fluid interactions.

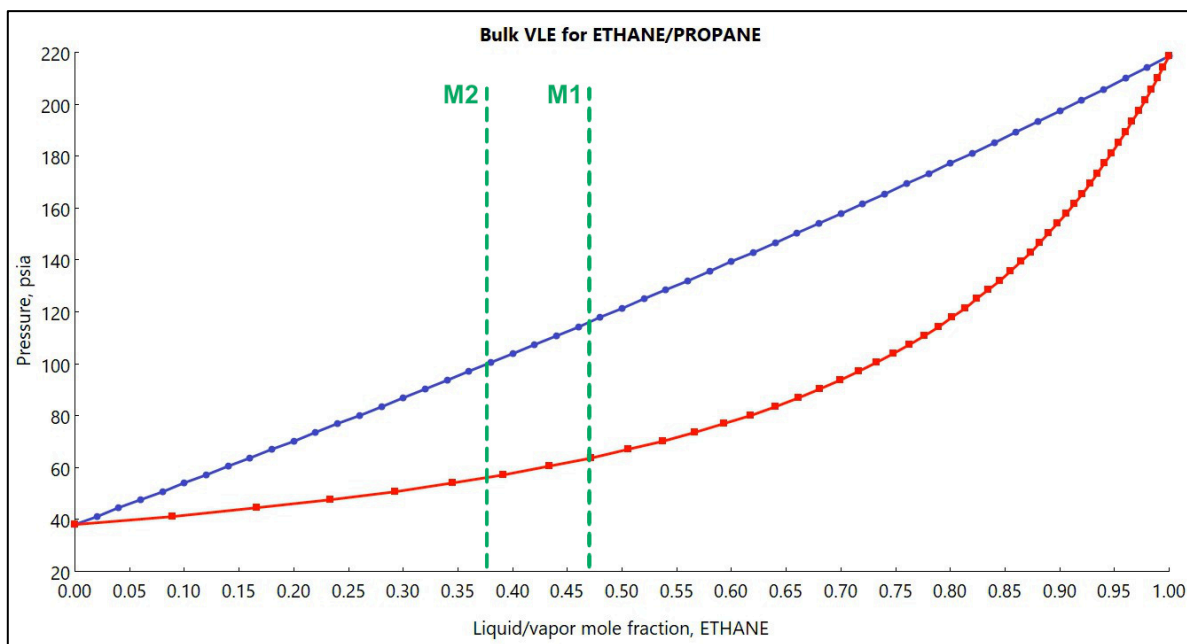


Figure 2. Bulk vapor-liquid equilibrium (VLE) for ethane/propane mixture for various mole fractions of ethane calculated using the Peng-Robinson equation of state. The blue line indicates the bubble point pressure while the orange line shows the dew point pressure.

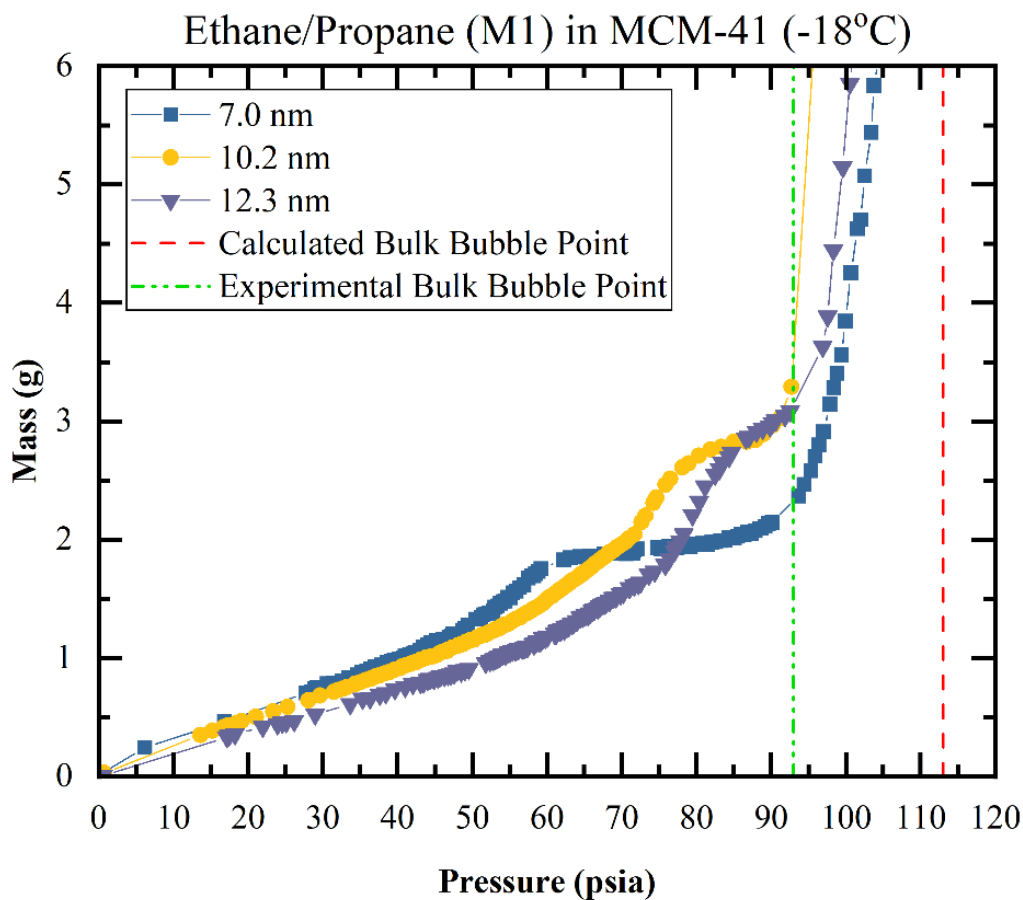


Figure 3. Experimentally measured adsorption isotherms for the mixture M1 (46.6% ethane and 63.4% propane) in MCM-41 of different pore sizes of 7, 10.2, and 12.3 nm at -18 °C. See **Table 1** for the original pore sizes and those calculated using the NLDFT.

The second ethane/propane mixture denoted as M2 was prepared such that the mole fraction of the lighter component (ethane) was lower than that in the first mixture (M1). The M2 mixture contained 37.3 mol% of ethane and 62.7 mol% of propane. This composition included approximately 10

mol% less ethane compared to that in M1, which had 46.6 mol% ethane. The experimentally measured adsorption isotherms for the composition M2 at a similar temperature (-18 °C) are presented in **Figure 4**.

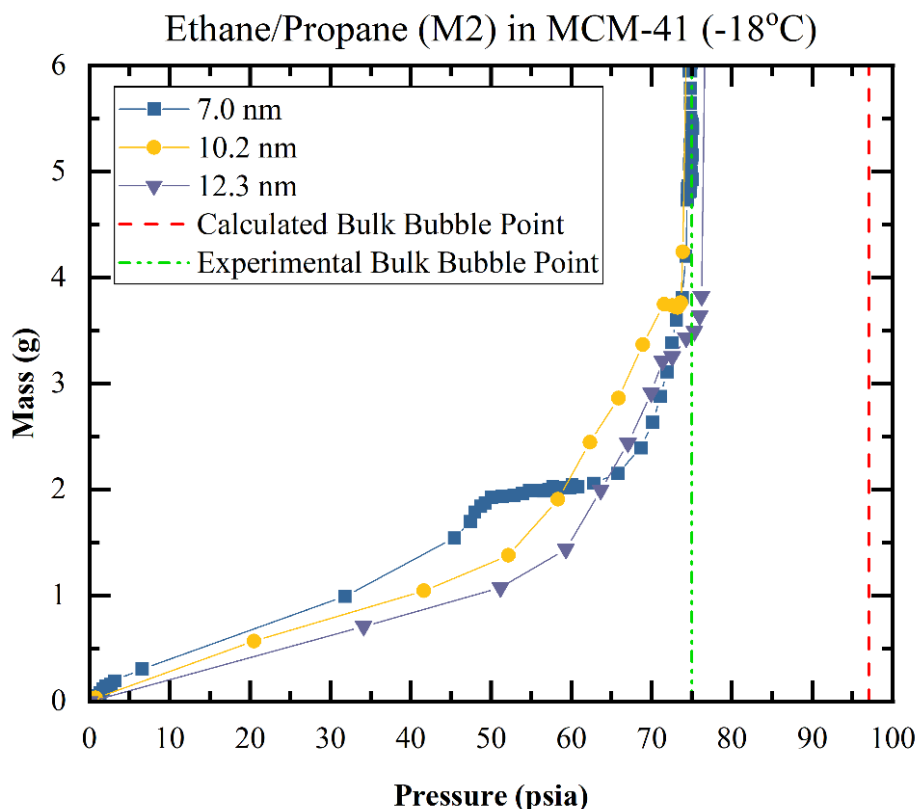


Figure 4. Experimentally measured adsorption isotherms for the composition M2 (37.3% ethane and 62.7% propane) in MCM-41 of different pore sizes (7 nm, 10.2 nm, and 12.3 nm) at -18 °C.

This composition's theoretical bulk saturation pressure is expected to be around 97 psi, which is lower than that of M1 due to less ethane present in the mixture. However, experimentally measured bulk bubble pressure was found to be approximately 75 psi, which is significantly lower than its theoretical counterpart. This again indicates that selective adsorption inside the nanoporous material can cause a decrease in the bulk saturation pressure. In other words, the predominant adsorption of ethane in nanopores compared to propane leaves less ethane in the mixture and changes the composition of the mixture, which results in reduced saturation pressure due to propane's relative heaviness and lower saturation pressure. Similarly, this needs further investigation (proposed later) by performing experiments using compositions with stark differences in the molar fractions. As mentioned earlier, the capillary condensation pressures were calculated from the Lorentzian fits.

An example of the Lorentzian fit of the experimental data for the M2 mixture has been provided in **Figure 5**.

The measured capillary condensation pressures for M2, also provided in **Table 2**, confirm the trends from the experimental results of the M1 mixture. The capillary condensation pressure increases with an increase in the pore size. However, for M2, which has less ethane than mixture M1, the capillary condensation pressures were lower than what was calculated for mixture M1 for all pore sizes. This indicates that the higher is the molar fraction of the lighter component, the lower becomes the adsorption of the heavier component. When the molar fraction of the heavier component increases, the capillary condensation pressures are decreased as the heavy component faces less competition from the lighter one during adsorption. This is supported by the fact that the confinement pressures are not similar for both compositions due to the selective adsorption's dependency on the composition.

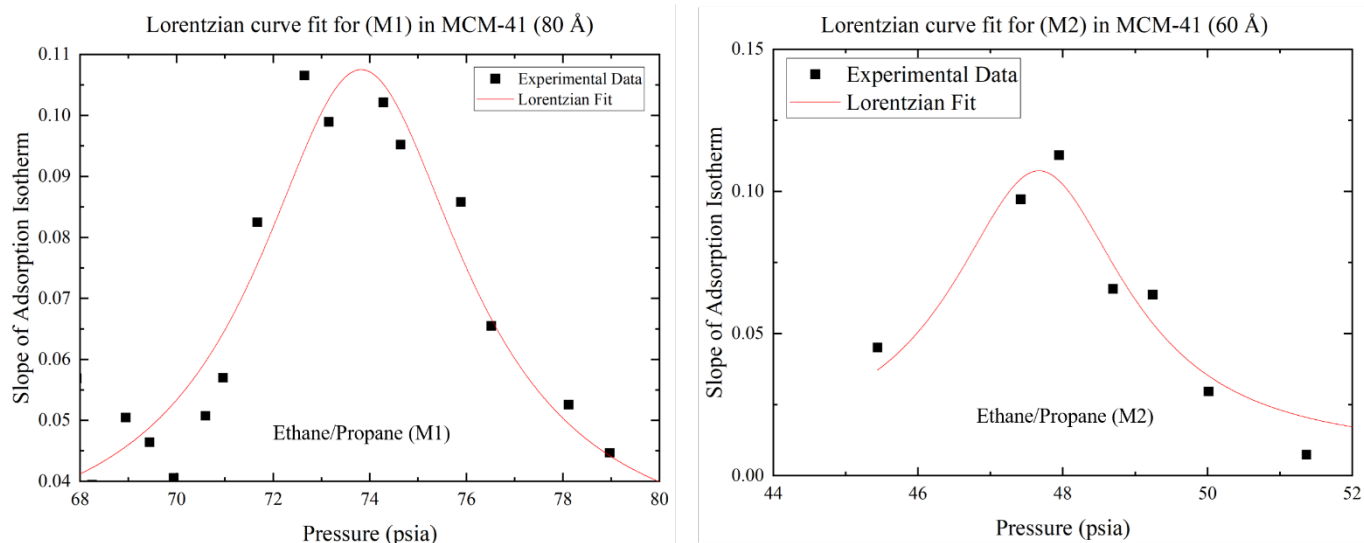


Figure 5. Examples of the Lorentzian curve fit of the first derivative of mass with respect to pressure (i.e., the slope of adsorption isotherm) for ethane/propane mixture of compositions M1 and M2 for two different pore sizes: 80 Å (10.2 nm from NLDFT) for M1, and 60 Å (7 nm from NLDFT) for M2. The peak of the Lorentzian curve corresponds to the fastest rate of fluid adsorption and is defined as the capillary condensation pressure.

Table 2. Experimentally measured capillary condensation pressures of ethane/propane mixture from the adsorption isotherms for different pore sizes of MCM-41 samples and two different compositions, M1 and M2.

Adsorbent	Temperature (°C)	Mixture	Capillary Condensation Pressure (psia)
MCM-41 (60 Å)	-18	M1	54.75
MCM-41 (80 Å)	-18	M1	73.82
MCM-41 (120 Å)	-18	M1	79.58
MCM-41 (60 Å)	-18	M2	47.67
MCM-41 (80 Å)	-18	M2	62.55
MCM-41 (120 Å)	-18	M2	65.11

Therefore, one may state that the selective adsorption of the hydrocarbon components is relative and is influenced by their molar fractions. Interestingly, the experimentally measured capillary condensation pressures for both compositions conform to the calculated bulk pressures and not the experimental counterparts. It is known from the Young-Laplace equation that the capillary pressure is proportional to the surface tension and inversely related to the pore diameter. Therefore, the capillary pressures may vary linearly with the inverse of the pore size. It is evident from **Figure 6**, which shows the plots of bulk and capillary condensation pressures versus the reciprocal of the pore sizes, that the calculated bulk pressures (representing a pore of infinite diameter) fall on a straight line with capillary condensation pressures, abiding by the Young-Laplace equation.

The diamond symbols in **Figure 6** for both compositions at 0 nm⁻¹ correspond to calculated bulk pressures at the inverse of infinite pore diameter. The results strongly agree with the literature and deliver important insights regarding the effect of the composition of the hydrocarbon mixtures on their confined phase behavior. It is indicated that mole percents of either light or heavy components push the occurrence of the confinement-induced phase transitions inside the two-phase region of the mixture. Furthermore, new tests will be conducted using the empty sample holders, i.e., in the absence of nanopores, to determine the experimental bulk saturation pressure of the mixture with different compositions. This will further enrich the inferences drawn from the present results regarding selective adsorption and the shifts in the vapor-liquid phase transition due to confinement.

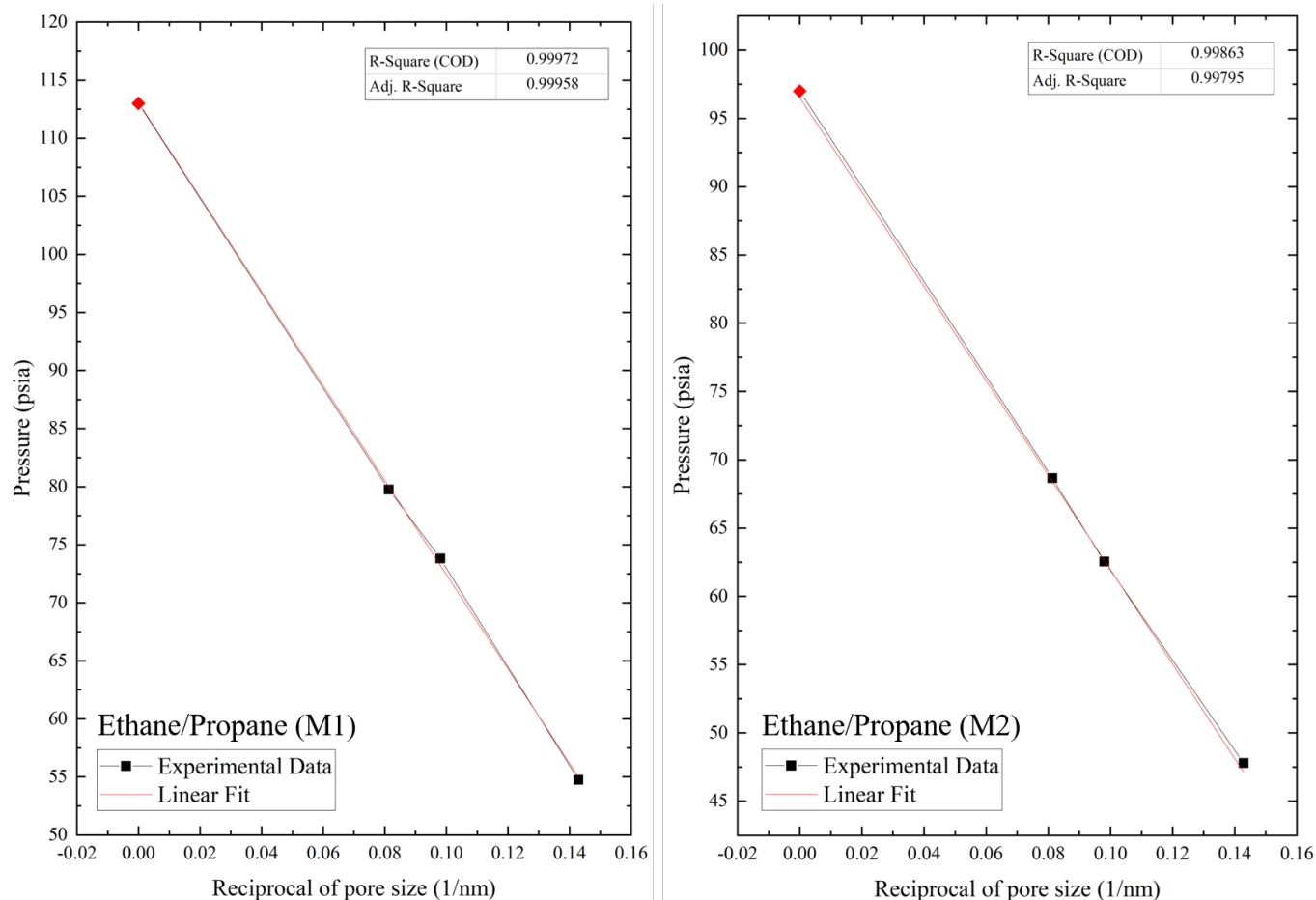


Figure 6. Variation in the experimentally measured capillary condensation pressure with respect to the reciprocal of the pore diameter for both compositions, M1 (left) and M2 (right), of the ethane/propane mixture. The diamond symbol represents the bulk saturation pressure calculated using the PC-SAFT equation of state, and square symbols represent the experimental data of capillary condensation pressure.

4 Conclusions

Ethane and propane are two of the most critical components of typical hydrocarbon mixtures and have numerous applications in several industrial sectors. However, their thermodynamic properties under confinement are still poorly understood and therefore need to be carefully characterized, particularly under mixture conditions. In this study, we experimentally investigated the phase behavior of ethane/propane mixture with different compositions in nanopores of varying pore sizes. To this end, mesoporous material MCM-41 with different pore sizes varying from 7 nm to 12.3 nm was utilized. All experiments were conducted at a temperature of -18 °C. The capillary condensation pressures were calculated from the experimentally measured adsorption isotherms for each composition. The results showed that the confinement effect weakens in larger pores and the vapor-liquid phase transition due to the confinement occurs at much lower pressure in tighter nanopores. In addition, it was also observed that selective adsorption takes place and causes the experimentally measured saturation pressure to be lower than the bulk saturation pressure calculated using an equation of state. It was noticed that the higher mole fraction of the lighter component prohibits the

adsorption of the heavier component in the nanopores up to some degree. However, when the mole fraction of the lighter component is decreased, the capillary condensation pressure decreases, and the degree of selective adsorption is also suppressed. The calculated bulk pressure and experimentally measured capillary condensation pressure results showed conformance to the Young-Laplace equation and exhibited a linear proportionality to the reciprocal of the pore size. This confirmed the accuracy of the measurements. A more in-depth investigation is warranted to characterize the relationships between selective adsorption and mole fractions of the lighter and heavier components at different temperature conditions. To this end, new experiments will be conducted for a wide range of temperatures using a mixture of varying compositions. In conclusion, the results from this research enrich the literature with the new experimental data for ethane/propane binary mixtures. In addition, the insights from this work can inform the development decisions made when exploiting unconventional reservoirs in which enormous quantities of hydrocarbons are stored in nanopores. Furthermore, the new results can also facilitate the development of advanced simulation models and rigorous

equations of state that can accurately predict the phase behavior of the confined fluids.

The authors gratefully acknowledge the financial support of Hess Corporation and the University of Wyoming during the course of this research.

References

1. C. Hall, P. Tharakan, J. Hallock, C. Cleveland, and M. Jefferson, "Hydrocarbons and the evolution of human culture," *NATURE*, vol. 426, pp. 318–322, Nov. 2003.
2. M. Podsiadło, A. Olejniczak, and A. Katrusiak, "Why propane?," *Journal of Physical Chemistry C*, vol. 117, no. 9, pp. 4759–4763, Mar. 2013.
3. X. Y. Chen, A. Xiao, and D. Rodrigue, "Polymer-based Membranes for Propylene/Propane Separation," *Separation and Purification Reviews*, vol. 51, no. 1. Taylor and Francis Ltd., pp. 130–142, 2022.
4. A. J. Sundararaj, B. C. Pillai, G. K.R, A. N. Subash, A. P. Haran, and P. Kumar, "Investigation of Ignition Delay for Low Molecular Weight Hydrocarbon Fuel by Using Shock Tube in Reflected Shock Mode," *Journal of the Geological Society of India*, vol. 93, no. 2, pp. 218–222, Feb. 2019.
5. W. A. Daniel, "Engine Variable Effects on Exhaust Hydrocarbon Composition (A Single-Cylinder Engine Study With Propane as the Fuel)," *SAE Transactions*, vol. 76, pp. 774–795, 1968.
6. K. Andersson, R. Johansson, F. Johnsson, and B. Leckner, "Radiation intensity of propane-fired oxy-fuel flames: Implications for soot formation," *Energy and Fuels*, vol. 22, no. 3, pp. 1535–1541, May 2008.
7. P. F. Bryan, "Removal of propylene from fuel-grade propane," *Separation and Purification Reviews*, vol. 33, no. 2. pp. 157–182, 2004.
8. X. Su, F. Zhang, Y. Yin, B. Tu, and M. Cheng, "Thermodynamic analysis and fuel processing strategies for propane-fueled solid oxide fuel cell," *Energy Conversion and Management*, vol. 204, Jan. 2020.
9. E. Antolini, "Direct propane fuel cells," *Fuel*, vol. 315., May 01, 2022.
10. M. Aydin *et al.*, "Recent decreases in fossil-fuel emissions of 10. ethane and methane derived from firn air," *Nature*, vol. 476, no. 7359. pp. 198–201, Aug. 11, 2011.
11. Y. Sawama *et al.*, "Stainless Steel-Mediated Hydrogen Generation from Alkanes and Diethyl Ether and Its Application for Arene Reduction," *Organic Letters*, vol. 20, no. 10, pp. 2892–2896, May 2018.
12. N. Shah, Y. Wang, D. Panjala, and G. P. Huffman, "Production of hydrogen and carbon nanostructures by non-oxidative catalytic dehydrogenation of ethane and propane," *Energy and Fuels*, vol. 18, no. 3, pp. 727–735, May 2004.
13. J. P. Cason and C. B. Roberts, "Metallic copper nanoparticle synthesis in AOT reverse micelles in compressed propane and supercritical ethane solutions," *Journal of Physical Chemistry B*, vol. 104, no. 6, pp. 1217–1221, Feb. 2000.
14. H. Sun, H. Zhu, F. Liu, and H. Ding, "Simulation and optimization of a novel Rankine power cycle for recovering cold energy from liquefied natural gas using a mixed working fluid," *Energy*, vol. 70, pp. 317–324, Jun. 2014.
15. B. Zühlsdorf, J. K. Jensen, S. Cignitti, C. Madsen, and B. Elmegaard, "Analysis of temperature glide matching of heat pumps with zeotropic working fluid mixtures for different temperature glides," *Energy*, vol. 153, pp. 650–660, Jun. 2018.
16. S. Douvartzides and I. Karmalis, "Working fluid selection for the Organic Rankine Cycle (ORC) exhaust heat recovery of an internal combustion engine power plant," in *IOP Conference Series: Materials Science and Engineering*, vol. 161, no. 1, Dec. 2016.
17. O. Demoulin, B. le Clef, M. Navez, and P. Ruiz, "Combustion of methane, ethane and propane and of mixtures of methane with ethane or propane on Pd/ γ -Al₂O₃ catalysts," *Applied Catalysis A: General*, vol. 344, no. 1–2, pp. 1–9, Jul. 2008.
18. M. Benedict, G. B. Webb, and L. C. Rubin, "An empirical equation for thermodynamic properties of light hydrocarbons and their mixtures. I. Methane, ethane, propane and n-butane," *The Journal of Chemical Physics*, vol. 8, no. 4, pp. 334–345, 1940.
19. K. S. Pitzer, "Thermodynamics of gaseous hydrocarbons: Ethane, ethylene, propane, propylene, n-butane, isobutane, 1-butene, cis and trans 2-butenes, isobutene, and neopentane (Tetramethylmethane)," *The Journal of Chemical Physics*, vol. 5, no. 6, pp. 473–479, 1937.
20. X. Cao *et al.*, "Phase diagrams for clathrate hydrates of methane, ethane, and propane from first-principles thermodynamics," *Physical Chemistry Chemical Physics*, vol. 18, no. 4, pp. 3272–3279, Jan. 2016.
21. H. Tanaka, "The thermodynamic stability of clathrate hydrate. III. Accommodation of nonspherical propane and ethane molecules," *The Journal of Chemical Physics*, vol. 101, no. 12, pp. 10833–10842, 1994.
22. K. S. Pitzer, "The molecular structure and thermodynamics of propane: The vibration frequencies, barrier to internal rotation, entropy, and heat capacity," *The Journal of Chemical Physics*, vol. 12, no. 7, pp. 310–314, 1944.
23. A. H. Mohammadi, W. Afzal, and D. Richon, "Experimental data and predictions of dissociation conditions for ethane and propane simple hydrates in the presence of distilled water and methane, ethane, propane, and carbon dioxide simple hydrates in the presence of ethanol aqueous solutions," *Journal of Chemical and Engineering Data*, vol. 53, no. 1, pp. 73–76, Jan. 2008.

24. A. H. Mohammadi, W. Afzal, and D. Richon, "Gas hydrates of methane, ethane, propane, and carbon dioxide in the presence of single NaCl, KCl, and CaCl₂ aqueous solutions: Experimental measurements and predictions of dissociation conditions," *Journal of Chemical Thermodynamics*, vol. 40, no. 12, pp. 1693–1697, Dec. 2008.
25. E. W. Lemmon, R. T. Jacobsen, "A Generalized Model for the Thermodynamic Properties of Mixtures," *International Journal of Thermophysics*, vol. 20, pp. 825–835, 1999.
26. J. Gregorowicz, "Solid-fluid phase behaviour of linear polyethylene solutions in propane, ethane and ethylene at high pressures," *Journal of Supercritical Fluids*, vol. 43, no. 2, pp. 357–366, Dec. 2007.
27. L. Djordjević, R. A. Budenholzer, "Vapor-Liquid Equilibrium Data for Ethane-Propane System at Low Temperatures," *Journal of Chemical & Engineering Data*, vol. 15, no. 1, pp. 10-12, 1970.
28. J. B. Ott, P. R. Brown, and J. T. Sipowska, "Comparison of excess molar enthalpies and excess molar volumes as a function of temperature and pressure for mixtures of (ethane, propane, and butane) with (methanol, ethanol, propan-1-ol, and butan-1-ol)," *The Journal of Chemical Thermodynamics*, vol. 28, pp. 379-404, 1996.
29. I. M. Abdulagatov, S. B. Kiselev, L. N. Levina, Z. R. Zakaryayev, and O. N. Mamchenkova, "Experimental and Theoretical Studies of the Crossover Behavior of the Specific Heat $C_{v,x}$ of Ethane, Propane, and Their Mixture at Critical Isochores," *International Journal of Thermophysics*, vol. 17, pp. 423-440, 1996.
30. J. Chao, R. C. Wilhoit, and B. J. Zwolinski, "Ideal Gas Thermodynamic Properties of Ethane and Propane," *Journal of Physical and Chemical Reference Data*, vol. 2, no. 2, pp. 427–438, 1973.
31. E. J. M. Filipe *et al.*, "Thermodynamics of liquid mixtures of xenon with alkanes: (Xenon + ethane) and (xenon + propane)," *Journal of Physical Chemistry B*, vol. 104, no. 6, pp. 1315–1321, Feb. 2000.
32. R. B. Williams, and D. L. Katz, "Vapor-Liquid Equilibria in Binary Systems. Hydrogen with Ethylene, Ethane, Propylene, and Propane," *Industrial & Engineering Chemistry*, vol. 46, no. 12, pp. 2512-2520, 1954.
33. L. Lue, and D. Blankschtein, "Liquid-State Theory of Hydrocarbon-Water Systems: Application to Methane, Ethane, and Propane," *The Journal of Physical Chemistry*, vol. 96, no. 21, pp. 8582-8594, 1992.
34. Q. Cui and V. H. Smith, "Analysis of solvation structure and thermodynamics of ethane and propane in water by reference interaction site model theory using all-atom models," *Journal of Chemical Physics*, vol. 115, no. 5, pp. 2228–2236, Aug. 2001.
35. I. Velasco, C. Rivas, J. F. Martínez-López, S. T. Blanco, S. Otín, and M. Artal, "Accurate values of some thermodynamic properties for carbon dioxide, ethane, propane, and some binary mixtures," *Journal of Physical Chemistry B*, vol. 115, no. 25, pp. 8216–8230, Jun. 2011.
36. S. Horstmann, K. Fischer, J. Gmehling, and P. Kólař, "Experimental determination of the critical line for (carbon dioxide + ethane) and calculation of various thermodynamic properties for (carbon dioxide + n-alkane) using the PSRK model," *Journal of Chemical Thermodynamics*, vol. 32, no. 4, pp. 451–464, 2000.
37. K. Yasuda and R. Ohmura, "Phase equilibrium for clathrate hydrates formed with methane, ethane, propane, or carbon dioxide at temperatures below the freezing point of water," *Journal of Chemical and Engineering Data*, vol. 53, no. 9, pp. 2182–2188, Sep. 2008.
38. C. B. de la Fuente Juan, D. M. Guillermo, A. B. Esteban, B. B. Susana, "Phase equilibria in binary mixtures of ethane and propane with sunflower oil," *Fluid Phase Equilibria*, vol. 101, pp. 247-257, 1994.
39. Y. Dini, M. Becerra, and J. M. Shaw, "Phase behavior and thermophysical properties of peace river bitumen + propane mixtures from 303 K to 393 K," *Journal of Chemical and Engineering Data*, vol. 61, no. 8, pp. 2659–2668, Aug. 2016.
40. G. W. Billman, B. H. Sage, and W. N. Lacey, "Phase Behavior in the Methane-ethane-n-pentane System," *Trans*, vol. 174, no. 1, pp. 13-24, 1948.
41. H. C. Wiese, H. H. Reamer, and B. H. Sage, "Phase Equilibria in Hydrocarbon Systems. Phase Behavior in the Methane-Propane-n-Decane System," *Journal of Chemical & Engineering Data*, vol. 15, no. 1, pp. 75-82, 1970.
42. N. G. Tassin, V. A. Masciotti, and M. Cismondi, "Phase behavior of multicomponent alkane mixtures and evaluation of predictive capacity for the PR and RKPR EoS's," *Fluid Phase Equilibria*, vol. 480, pp. 53–65, Jan. 2019.
43. M. Benedict, G. B. Webb, and L. C. Rubin, "An empirical equation for thermodynamic properties of light hydrocarbons and their mixtures: II. Mixtures of methane, ethane, propane, and n-butane," *The Journal of Chemical Physics*, vol. 10, no. 12, pp. 747–758, 1942.
44. J. Vairogs, A. J. Klekers, and W. C. Edmister, "Phase Equilibria in the Methane-Ethane-Propane-n-Pentane-n-Hexane-n-Decane System," *AIChE Journal*, vol. 17, no. 2, pp. 308-312, 1971.
45. A. R. Price and R. Kobayashi, "Low Temperature Vapor-Liquid Equilibrium in Light Hydrocarbon Mixtures: Methane-Ethane-Propane System," *Journal of Chemical & Engineering Data*, vol. 4, no. 1, pp. 40-52, 1959.
46. E. Lowry and M. Piri, "Effect of Surface Chemistry on Confined Phase Behavior in Nanoporous Media: An Experimental and Molecular Modeling Study," *Langmuir*, vol. 34, no. 32, pp. 9349–9358, Aug. 2018.

47. P. H. Nelson, "Pore-throat sizes in sandstones, tight sandstones, and shales," *AAPG Bulletin*, vol. 93, no. 3, pp. 329–340, 2009.
48. D. R. Cole, S. Ok, A. Striolo, and A. Phan, "Hydrocarbon behavior at nanoscale interfaces," *Reviews in Mineralogy and Geochemistry*, vol. 75, pp. 495–545, 2013.
49. M. Hirscher, B. Panella, and B. Schmitz, "Metal-organic frameworks for hydrogen storage," *Microporous and Mesoporous Materials*, vol. 129, no. 3, pp. 335–339, Apr. 2010.
50. J. Li *et al.*, "Hypercrosslinked organic polymer based carbonaceous catalytic materials: Sulfonic acid functionality and nano-confinement effect," *Applied Catalysis B: Environmental*, vol. 176–177, pp. 718–730, Oct. 2015.
51. H. W. Hu, G. H. Tang, and D. Niu, "Wettability modified nanoporous ceramic membrane for simultaneous residual heat and condensate recovery," *Scientific Reports*, vol. 6, Jun. 2016.
52. M. M. Awad, A. S. Dalkiliç, and S. Wongwises, "A critical review on condensation heat transfer in microchannels and minichannels," *Journal of Nanotechnology in Engineering and Medicine*, vol. 5, no. 1, 2014.
53. S. Zarei, H. R. Talesh Bahrami, and H. Saffari, "Effects of geometry and dimension of micro/nano-structures on the heat transfer in dropwise condensation: A theoretical study," *Applied Thermal Engineering*, vol. 137, pp. 440–450, Jun. 2018.
54. M. Thommes and K. A. Cychoz, "Physical adsorption characterization of nanoporous materials: Progress and challenges," *Adsorption*, vol. 20, no. 2–3, pp. 233–250, Feb. 2014.
55. Y. Zhao and Z. Jin, "Hydrocarbon mixture phase behavior in multi-scale systems in relation to shale oil recovery: The effect of pore size distributions," *Fuel*, vol. 291, May 2021.
56. E. Barsotti, S. P. Tan, S. Saraji, M. Piri, and J. H. Chen, "A review on capillary condensation in nanoporous media: Implications for hydrocarbon recovery from tight reservoirs," *Fuel*, vol. 184. Elsevier Ltd, pp. 344–361, Nov. 15, 2016.
57. E. Barsotti, "Capillary Condensation in Shale: A Narrative Review," in *SPE Annual Technical Conference and Exhibition*, SPE-199768-STU, September 2019.
58. X. Dong, H. Liu, W. Guo, J. Hou, Z. Chen, and K. Wu, "Study of the confined behavior of hydrocarbons in organic nanopores by the potential theory," *Fluid Phase Equilibria*, vol. 429, pp. 214–226, Dec. 2016.
59. Y. Ma and A. Jamili, "Using Simplified Local Density/Peng-Robinson Equation of State to Study the Effects of Confinement in Shale Formations on Phase Behavior," SPE-168986-MS 2014.
60. Y. Seo, S. Lee, I. Cha, J. D. Lee, and H. Lee, "Phase equilibria and thermodynamic modeling of ethane and propane hydrates in porous silica gels," *Journal of Physical Chemistry B*, vol. 113, no. 16, pp. 5487–5492, Apr. 2009.
61. S.P. Tan and M. Piri, "Equation-of-State Modeling of Associating-Fluids Phase Equilibria in Nanopores," *Fluid Phase Equilib.*, vol. 405, 157–166, 2015.
62. E. Barsotti, S. P. Tan, M. Piri, and J. H. Chen, "Phenomenological Study of Confined Criticality: Insights from the Capillary Condensation of Propane, n -Butane, and n -Pentane in Nanopores," *Langmuir*, vol. 34, no. 15, pp. 4473–4483, Apr. 2018.
63. E. Barsotti, E. Lowry, M. Piri, and J. H. Chen, "Using Capillary Condensation and Evaporation Isotherms to Investigate Confined Fluid Phase Behavior in Shales," in *E3S Web of Conferences*, vol. 146, Feb. 2020.
64. E. Barsotti, S. P. Tan, M. Piri, and J. H. Chen, "Capillary-condensation hysteresis in naturally-occurring nanoporous media," *Fuel*, vol. 263, Mar. 2020.
65. Y. Zhao and Z. Jin, "Hydrocarbon-phase behaviors in shale nanopore/fracture model: Multiscale, multicomponent, and multiphase," *SPE Journal*, vol. 24, no. 6, pp. 2526–2540, 2019.
66. Y. Zhao, Y. Wang, J. Zhong, Y. Xu, D. Sinton, and Z. Jin, "Bubble Point Pressures of Hydrocarbon Mixtures in Multiscale Volumes from Density Functional Theory," *Langmuir*, vol. 34, no. 46, pp. 14058–14068, Nov. 2018.
67. B. Jin, R. Bi, and H. Nasrabadi, "Molecular simulation of the pore size distribution effect on phase behavior of methane confined in nanopores," *Fluid Phase Equilibria*, vol. 452, pp. 94–102, Nov. 2017.
68. K. Jean Edler, "Template Induction of Supramolecular Structure: Synthesis and Characterisation of the Mesoporous Molecular Sieve, MCM-41," Ph.D. Thesis, 1997.
69. E. Barsotti, S. Saraji, and M. Piri, "Nanocondensation Apparatus", *US Patent*, US15/588,094, 2017.
70. R. Alloush, E. Lowry, and M. Piri, "Automated Apparatus for Characterization of Fluid-Solid Systems," *US Patent*, US63/186,366, Filed May 10, 2021.

Appendix I

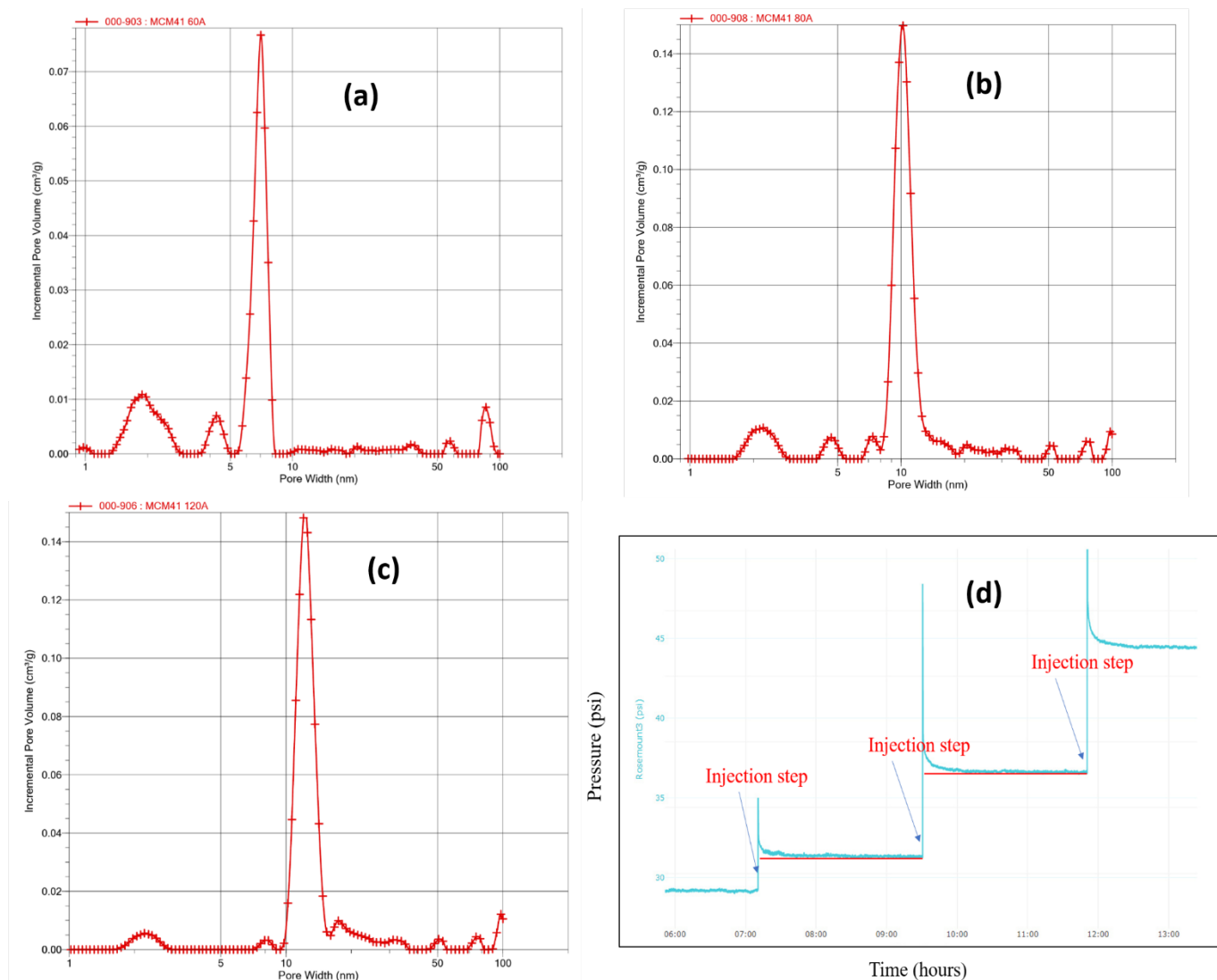


Figure A. (a) – (c): The NLDFT calculated pore size distributions obtained for the MCM-41 samples with pore diameters of 60 Å, 80 Å, and 120Å, respectively. (d): An example from the pressure vs. time raw data for a sample holder packed with MCM-41 material (7 nm NLDFT) exhibiting the establishment of equilibrium conditions after each injection step. The red horizontal lines are reference lines added to show the equilibrium (stabilization of the pressure) occurring within the two hours windows after each dosage of fluid.

Forced Imbibition and Uncertainty Modelling using the Morphological Method

Pit Arnold^{1,*}, Mario Dragovits¹, Sven Linden², Fatime Zekiri³, and Holger Ott^{1,†}

¹Montanuniversität Leoben, Chair of Reservoir Engineering, 8700 Leoben, Austria

²Math2Market GmbH, 67655 Kaiserslautern, Germany

³OMV E&P GmbH, 1020 Vienna, Austria

Abstract. The morphological approach is a computationally attractive method for calculating relative permeability and capillary pressure saturation functions. In the workflow, morphological operations are used to calculate the fluid phase distribution in the pore space of a digital twin. Once the pore space is occupied, the fluid-phase conductivity and thus the relative permeability can be calculated by direct flow simulations on the phase occupied pore space. It therefore combines computational advantages that are used in pore network modeling with direct flow simulations on the digital twin. While the morphological operations conceptually correctly describe the primary drainage process, the imbibition process is described less obviously. So far, the method has delivered good results for drainage, but showed limitations in terms of imbibition processes and uncertainty modeling. In this work, we implement contact angle distributions in a deterministic and stochastic way in the approach. With this, we extend the simulated saturation range from purely spontaneous to forced imbibition, resulting in a full range imbibition relative permeability. Furthermore, by introducing stochastic contact angle distributions, different fluid phase distributions are obtained which allow for an uncertainty analysis. To verify the simulation results, we check (a) whether the simulation results agree with experience from SCAL measurements, and (b) compare the morphologically derived results and experimentally determined. Due to the newly introduced modifications, the imbibition process now behaves as physically expected and is in better agreement with experimental data compared to earlier studies.

1 Introduction

Digital Rock Physics (DRP) becomes increasingly attractive for computing multi-phase flow properties. Compared to classical Special Core Analysis (SCAL) experiments, DRP appears as less time and labor intensive, and hence as cost competitive. Furthermore, just small rock samples are required and therefore DR analysis can be applied to situations in which there are no suitable SCAL samples available.

DRP may be categorized in full physics models and reduced models. Full physics models provide deep insights in displacement physics, yet are typically computationally expensive and therefore possess limited use for upstream developments [1–3]. Methods such as Lattice Boltzmann are able to model the actual visco-capillary effects on the pore scale and therefore can reproduce experimental displacement results also outside capillary limits [4]. Yet their limitation lies within the possibility to vary petrophysical parameters such as the wettability of a system, as the simulations are highly time consuming.

Reduced models on the other hand are often computationally attractive, allowing for a larger number of simulations and hence for uncertainty analysis. Prominent examples are pore network models (PNM) which handle displacement physics in a rule-based fashion on idealized pore networks. The phase conductivities are computed by solving simplified analytical

solutions rather than the underlying differential equations [5–7]. In PNM, the idealized pore networks are extracted by calculating the skeleton of the network, pore volumes and pore throat sizes from digital rock structures, with different authors using different algorithms [8–11]. All these algorithms are based on morphological operations.

The morphological method (MM), as presented in the following, makes use of morphological operations to calculate the fluid phase distribution directly in the digital twin, rather than to extract an idealized network. With this, the MM is bridging between both worlds; it makes use morphological operations to populate the as-measured pore space with the fluid phases, and solves the Navier-Stokes equation directly on the pore space to simulate effective permeability.

The morphological operations are applied in a rule-based, quasi-static manner, so that no time scale is associated with the displacement process. Since they are applied to the pore structure, the modelled displacement processes refer to a capillary-dominated flow – viscous processes are not considered. However, the fact that the displacement processes are purely calculated on basis of image processing makes the MM very time-competitive.

When simulating drainage processes, liquid invasion is controlled by the dilation of the mineral phase of the digital twin; pore throats are then identified and connectivity to

* Corresponding author: pit.arnold@unileoben.ac.at, holger.ott@unileoben.ac.at

neighboring pores is tested for each dilation step. Assigning an interfacial tension to fluid-fluid interfaces and a contact angle to mineral-fluid-fluid three-phase contact lines allow the capillary pressure to be calculated for each dilatation step, i.e., for different saturations by the Young-Laplace equation. Comparison with experimental data shows close agreement with experimental drainage data, while there are significant discrepancies for imbibition reported [12].

The relative permeability is then simulated by solving the Navier-Stokes equation in the pore space connected by the individual fluid phase. This limits the two-phase flow to the connected phase volume. Ganglion dynamics, which can contribute to the mobility of the non-wetting phase, especially in the case of high wetting phase saturations, are therefore not considered [13, 14].

So far, the method has delivered good results for drainage, but showed limitations in terms of imbibition processes and uncertainty modeling. In particular, imbibition processes were limited, since only individual processes could be modelled, either forced (drainage) or spontaneous (imbibition) processes. The forced part of the imbibition was therefore not previously incorporated. In this work, we implement contact angle distributions in a deterministic and stochastic way. With this, we extend the imbibition process from purely spontaneous to forced imbibition, resulting in full range imbibition capillary pressure ($p_c(S_{WP})$) and relative permeability ($k_r(S_{WP})$) saturation functions. Furthermore, by introducing stochastic contact angle distributions, different fluid phase distributions are obtained, which allows for uncertainty analyses. To verify the simulation results, we check (a) whether the simulation results agree with experience from SCAL measurements, and (b) compare morphologically with experimentally derived results.

2 Numerical Methods and Developments

2.1. The Morphological Method

The morphological method (MM) is based on mathematical morphology and applies morphological operations to pore-scale rock images. It was originally developed by Matheron and Serra in 1964 in the frame of Serra's PhD thesis and later published in Serra et al. 1982 [15]. The basic operations dilation and erosion applied to the rock's pore structure enable the quantitative analysis of pore geometries with regard to the drainage displacement thresholds – the pore throats. The morphological identification of thresholds links the pore structure to capillarity and hence to fluid displacement physics. The mathematical fundamentals are discussed in detail in Hilpert and Miller's paper from 2001 [16]. Initially, the approach was limited to binary images, but can also be applied to greyscale images. A derivative, the pore MM, also known as maximum inscribed spheres [11], predicts the distribution of a wetting phase (WP) and a non-wetting phase (NWP) inside a porous medium.

In general, the MM predicts saturation changes on basis of geometrical rock properties and therefore intrinsically assumes that capillary forces are dominating compared to viscous forces, i.e., the capillary number is low. The method therefore distributes the two fluid phases by using

morphological operations rather than solving partial differential equations. A criterion for a displacement event is the disconnection to the respective wetting and non-wetting reservoir attached to the system boundaries. For imbibition and drainage, we are (thoroughly) referring to the invasion of the WP and the NWP, respectively. The image operations change the topology of the fluid phases, which corresponds to the physical event of a capillary pressure change, where the extend of the dilation operation corresponds to the pore throat radius in the Young-Laplace equation. Figure 1 shows the displacement of the wetting phase (blue) by the non-wetting phase (green), for a solid phase with a single contact angle (grey) and multiple contact angle materials (grey and brown). The number of voxels dilated describes the radius r , which in a drainage process corresponds to the pore throat size. Different process angles are introduced after Schulz, by scaling the dilation radius with the $\cos(\theta)$, with θ being the contact angle [17]. This method slightly overestimates the actual contact angle and does not work for contact angles close to 90° .

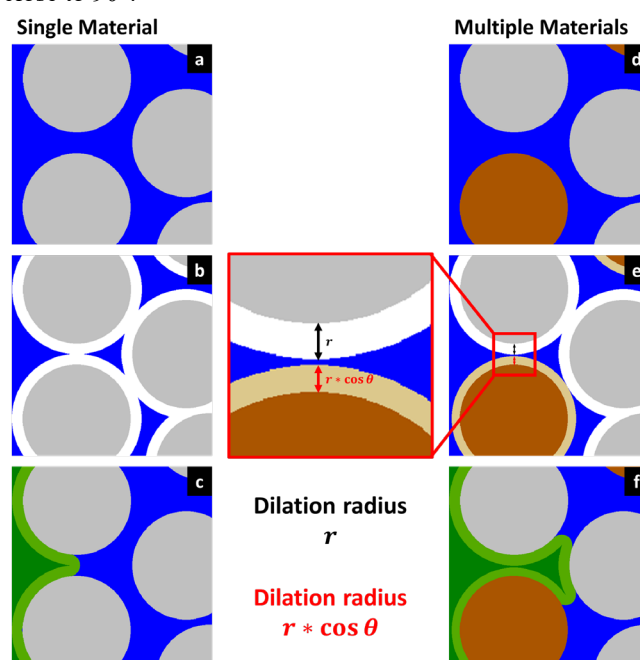


Fig. 1: Simplified illustration of a drainage invasion step for a single contact angle material (a-c) and dual contact angle materials (d-f). Solid phases are colored grey and brown, the wetting phase is colored blue and the non-wetting phase green. Dilated volumes are indicated in the respective lighter color.

2.2 Initial drainage and spontaneous imbibition implementations

A primary drainage is defined as the displacement of the wetting by the non-wetting phase. The process is described by a sequence of equilibrium steps, which mimic the invasion as a consequence of an applied differential pressure. A sequence of three operations corresponding to a single displacement event is shown in Figure 1. It illustrates a simplified 2D porous structure with circular grains in grey and the pore space filled with a wetting phase (blue). In the steps from images (a) to (b), grains are dilated to identify and close the narrowest pore throats. Defining the NWP reservoir on the left-hand side of the image, the invaded NWP is

connected to the NWP reservoir and recolored (dark green). In a next step, the NWP is dilated (light green) by the same voxel radius as the grains were dilated in the prior step. Since in a drainage process, the NW fluid invades first the larger pore throats, the invading fluid (green) phase cannot overcome the first pore throat which is indicated in image (c). The right-hand side of Figure 1 (d-f) shows that the approach can be modified by the introduction of a different mineral with a modified contact angle (brown). When applying multiple contact angles for the same scenario, the invading phase can overcome the same pore throat, since the dilation is scaled by $\cos(\theta)$ (light brown), which results in different invasion pathways for the same applied pressure. In this process, the invading NWP must in every step be connected to the inlet phase, which is the NWP “reservoir”, and the wetting phase to the outlet, the WP reservoir.

The algorithm of the above-described morphological drainage process consists of four steps:

1. Dilation of the grains into the WP pore space by a voxel radius r , which can be scaled by $\cos(\theta)$.
2. Recolor the pore space, which is connected to the NWP reservoir and label it as NWP.
3. Dilate the NWP by the initial (non-scaled) voxel radius from step one.
4. Recolor all WP, which is disconnected from the WP reservoir as residual. It will no longer be considered for further dilation steps.

The last step allows for a residual saturation and may be ignored when simulating mercury injection capillary pressure experiment [18]. Performing the drainage algorithm by gradually decreasing the radius r (number of voxels), results in a quasi-stationary invasion of the non-wetting phase. Scaling the dilation radius in step 1 by $\cos(\theta)$ alters the invasion pathway with regard to the wetting condition. When contacting non-wetting material, the pore space would immediately be populated by the approaching NWP. The interfacial tension is only accounted for in post-processing for calculating p_c and therefore results only in a up or down shift of the (resulting) p_c curves, but does not influence the (resulting) fluid distribution. A drainage process is either stopped when the WP is entirely disconnected from the outlet, or the dilation reaches a sub-voxel value.

The basic algorithm for drainage can be modified to simulate imbibition processes, by interchanging step 2 and 3. An imbibition front stops, when either the NWP is disconnected from the NWP reservoir or the dilation radius exceeds the size of the largest pores, i.e., allowing no fluid phase changes anymore or non-wetting material cannot be bypassed by the WP anymore, acting as a barrier.

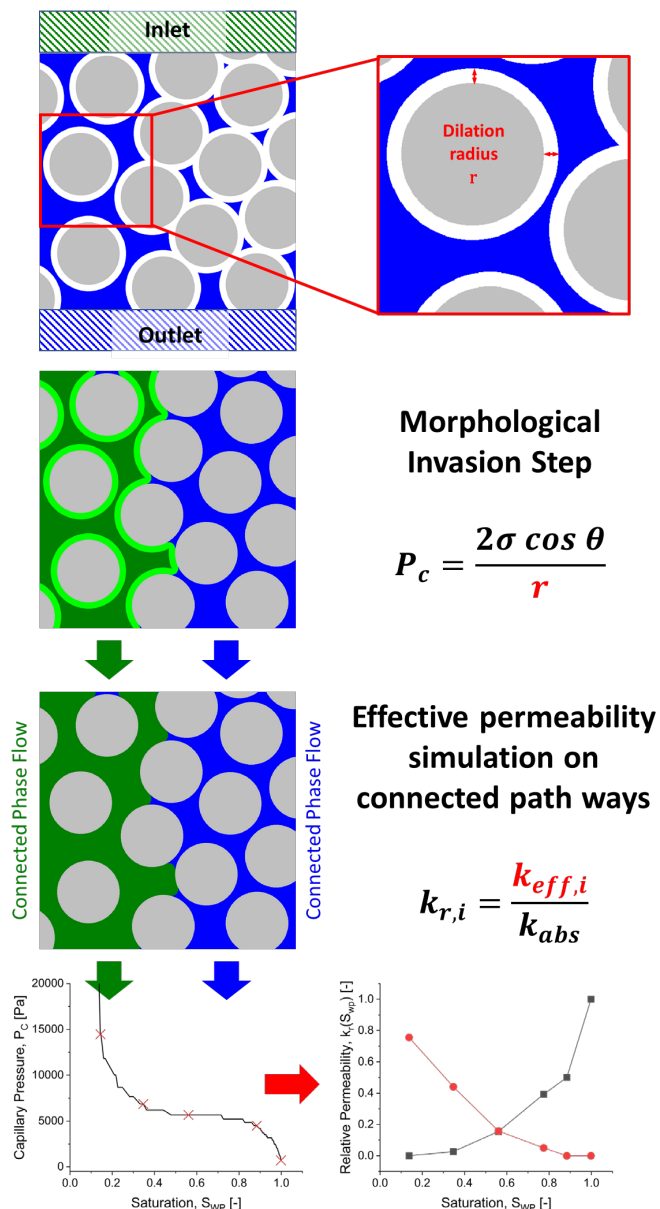


Fig. 2: Simplified 2D illustrated phase population by the MM, resulting in two connected pathways for the given saturation state. The bottom image, shows the simulated $k_r(S_{WP})$ on basis of individual saturation steps acquired from a capillary pressure drainage simulation on a Berea sandstone.

2.3 Simulation of effective permeability

The $p_c(S_{WP})$ saturation function is a direct result of the MM, i.e., a purely structural property. Furthermore, the MM delivers the fluid distribution in the pore space for each simulated saturation state and hence, information on the connectivity of both phases. The MM, however, does not deliver permeability and $k_r(S_{WP})$ directly. While the absolute permeability (K) is simulated by solving the Stokes equation on the total pore space, assuming single phase flow for a small constant pressure drop in flow direction ($\Delta p = 0.02 \text{ Pa}$) and periodic boundary conditions in the tangential direction. Since we are having very slow flows, due to the small pressure drop, we solve the Stokes instead of the Navier-Stokes equation as it delivers the same results while

being computationally less demanding. The effective permeability ($k_r(S_{WP})/K$) is simulated for each fluid phase separately, considering the respective connected pathways only. This means that $k_r(S_{WP})$ simulations consider the respective other phase as immobile, i.e., all internal boundaries as rigid and fixed. Furthermore, $k_r(S_{WP})$ can only be calculated in cases the respective fluid phase is connected throughout the simulation domain at the given saturation state, otherwise it is zero. A snap-off event can therefore lead to the loss of phase conductivity, while the phase is still accessible for a displacement event, as it is connected to the outlet.

2.4 Limitations of the initial implementation

As described earlier, the MM is based on geometric operations on the digital rock structures and is therefore entirely governed by the porous structure and, if present, residual fluid phases. This describes the nature of a primary drainage process quite well, as the non-wetting phase intrusion is restricted by the pore throat radii, which inversely scale to the capillary pressures. However, processes like imbibition are partly spontaneous and rather driven by interfacial properties like wetting state and contact-angle distribution. How well does the MM capture the physical process? For a single contact angle, the invading fluid always takes the same pathway through the porous domain independent of the contact angle. This means that a contact angle variation will not alter the invasion sequence and the resulting fluid distribution and is therefore not changing the relative permeability curves.

The implementation of multiple contact angles was addressed by Schulz et al. [17]. Hereby the invasion process is altered by scaling the dilation radii with $\cos(\theta)$, however limiting the system to contact angles below or above 90° – for contact angles in a range between 60° and 120° the simulations are likely to fail. The introduction of multiple contact angles allows for varying displacement pathways.

After all, the imbibition process as given above is still limited to the spontaneous part of the capillary pressure curve, i.e., to the positive P_c range, which results in a limited saturation range. So far one of the stopping criteria is a disconnection of the NWP from the NWP reservoir. We typically describe the flow in a single direction and therefore assign the lateral boundary conditions as periodic, while the inlet as connected to an WP reservoir and the outlet connected to the NWP reservoir. Hence, the invasion process can result in an early snap-off of the NWP, while leaving a larger part of the saturation as residual. This results in a drastic reduction of the NWP effective permeabilities, respectively increase for the WP.

2.5 Full-scale imbibition

While the drainage process is defined as the invasion of the non-wetting phase, i.e., indicated by an entirely positive capillary pressure, imbibition processes can show an early saturation range of positive and a late saturation range of negative capillary pressure. A negative capillary pressure indicates a forced process, which actually can be understood

as drainage process. Therefore, in order to simulate the full saturation range with the pore MM, we first couple the imbibition process with a subsequent drainage process.

The stopping criteria of the spontaneous imbibition (SI) process is the disconnection of the NWP from the outlet – the NWP is trapped and cannot be displaced neither by an imbibition nor by a drainage algorithm. In order to switch from a spontaneous to a forced process, a non-wetting material must be introduced, which prevents access of parts of the pore space by the spontaneous process. This may be physically correct, because it reflects the meaning of a negative capillary pressure. A straightforward implementation is the introduction of non-wetting material before the start of the SI modelling. Depending on the topology and volume of non-wetting material introduced, the SI stops at different saturation stages. In this work, the non-wetting material is introduced in two alternative ways:

1. Introduction of non-wetting material on basis of stochastic field before the drainage process. This ensures that the non-wetting material is in contact with the NWP at the end of the drainage process.
2. Introduction of non-wetting material at the end of the drainage process in NWP filled pores only, prioritizing the biggest pores first.

In the stochastic approach the volumetric percentage and region size considered for the stochastic field are defined. The material is then implemented on basis of an isotropic gaussian random field. Figure 3 shows the exemplary implementation of non-wetting material with two different region sizes. In both cases the same random seed was chosen, whereas one region size is smaller and the other bigger than the average grain size visible. Depending on the region size and solid volume percentage (SVP) considered, unavoidably the introduced material can be interconnected throughout the structure. The volume percentage of material changed equals the surface area percentage between the pore and solid materials with minor deviations.

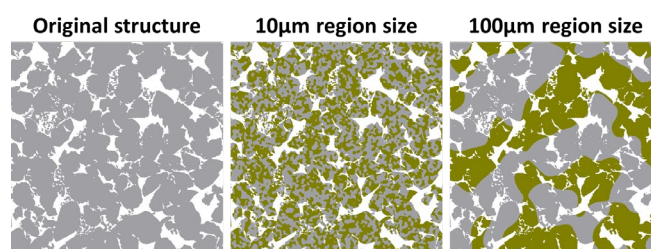


Fig. 3: A second material introduced on basis of a stochastic field in a digital twin (left) of the size of $1472 \times 1472 \mu\text{m}$. The yellow material corresponds in both cases to a solid volume percentage (SVP) of 50% of the structure, with different region sizes of $10 \mu\text{m}$ (middle) and $100 \mu\text{m}$ (right).

The deterministic approach is based on the natural process of a wettability alteration during an ageing process, where mineral surfaces in contact with the NWP can change their initial wetting state [19–21]. It applies an algorithm at the end of a drainage process, analyzing the pore size distribution and introducing non-wetting material in the biggest pores first, only at contacts of the mineral and NWP. In the algorithm we define the volume of pores considered for the

implementation. The volume considered does not equal the surface area, as only a part of the pore material is changed. Figure 4 illustrates the algorithm on a simplified structure. The different pore sizes are displayed as volume field scaled by a hue-saturation-lightness color legend, where blue represents the smallest and red the biggest pores. In the second illustration the pore space, which is considered by the algorithm is marked as red. The pore space considered is a user input so far and can be varied between 1% to 99%. The last two images show the resulting material changes, where only material in contact with the previous marked pores is considered, while prioritizing the material in the bigger pores. This algorithm has the advantage that different non-wetting contact angles can be introduced at the end of the drainage.

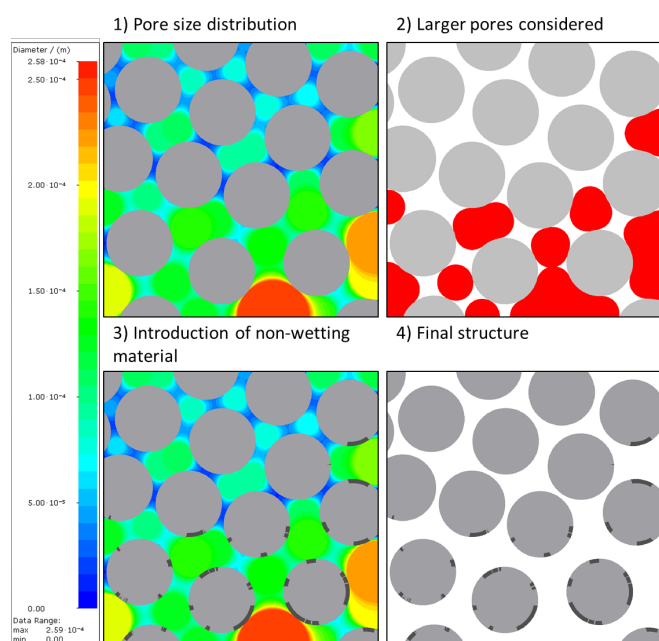


Fig. 4: Simplified illustration of the deterministic algorithm for introduction of non-wetting material, assuming the pore space is entirely filled with the NWP. After the pore-throat size distribution (1), 50% of the largest pores (2) are considered for the implementation of non-wetting material, resulting in a change of the structure (4). In image (3) it can be seen that bigger pores are prioritized for the implementation of the new material. The structure has a size of 1000×1000 voxels and resolution of $(1 \mu\text{m})^2/\text{voxel}$.

The forced imbibition (FI) part is then modelled with the drainage algorithm where the contact angles and the role of the phases are inverted. This means that a non-wetting contact angle is considered to be wetting (i.e. $180^\circ - \alpha$) for the FI drainage process, while swapping the role of the WP and NWP. This corresponds to a turnover of the menisci between the WP and NWP at the transition from the spontaneous to the forced displacement process.

2.6 Comparison to experimental data

A steady-state experimental data set [12] was used as reference for benchmarking. The data set consists of a time series of pore-scale-resolved fluid distributions on which NWP and WP effective permeability can be simulated and directly compared to the respective results from the MM. This benchmark was carried out by Berg et al. and is repeated in the present work with and without the described

modifications in the MM. While in the earlier study relative permeability simulated on the numerical and experimental fluid distributions show a substantial mismatch, with the embedded innovations, a much closer match could be achieved as discussed in the result part.

2.7 Simulation input

The uncertainty analysis for the contact angle distributions was performed on a Berea Sandstone with the dimensions of $800 \times 800 \times 800$ voxels and a voxel size of $1.84 \mu\text{m}$. The digital rock sample has a resolved porosity of 19.6% and a simulated permeability of 780 mD.

The synchrotron experiment by Berg et al. was conducted on a Gildehauser sandstone, with an average resolved porosity of 20% and a permeability of 1.5 ± 0.3 D. For the comparison to simulations on the experimentally derived fluid distributions, the pre-segmented dataset from the digital rocks portal were used [22]. The digital twin has a resolution of $(4.4 \mu\text{m})^3/\text{voxel}$ and consists of a cylindrical domain with the dimension of $830 \times 830 \times 566$ voxels. The digital twin has a porosity of 20.3% and a simulated permeability of 1.55 D.

3 Results

In order to test the innovations introduced with this work, we use the new degrees of freedom to define the wetting state and simulate different scenarios. First, we simulate capillary pressure curves on a digital twin for Berea sandstone. With this, we compare the results for the stochastic and deterministic implementation and for different wetting states in order to assess the trends in the $p_c(S_{WP})$ on a physical basis. Second, we compare the new approaches with experiments by simulating $k_r(S_{WP})$ for experimentally and morphologically determined fluid distributions, while varying the simulated wetting states.

3.1 Full-scale imbibition and introduction of non-wetting material

In the previous section, we introduced two principally different algorithms for the implementation of non-wetting material, a stochastic and a deterministic algorithm. For the stochastic algorithm, the non-wetting material is introduced prior to the drainage process, which ensures that the non-wetting pores are filled with the NWP at connate WP saturation. With regard to the subsequent imbibition process, the higher the SVP of the non-wetting region the earlier the spontaneous imbibition is stopped and the bigger is the contribution of the forced part to the total imbibition process. Furthermore, the region size chosen is critical as it influences the drainage and imbibition. In Figure 5 we can observe these changes, where an increasing SVP and decreasing region size result in a more non-wetting state of the system. The dark yellow symbols, which partly overlay with the newly modelled data sets, show the results of the initial drainage and spontaneous imbibition implementation. In this case, there is only one wetting contact angle assigned, and therefore only spontaneous imbibition can be modelled. To make the systems comparable for all combinations the same contact

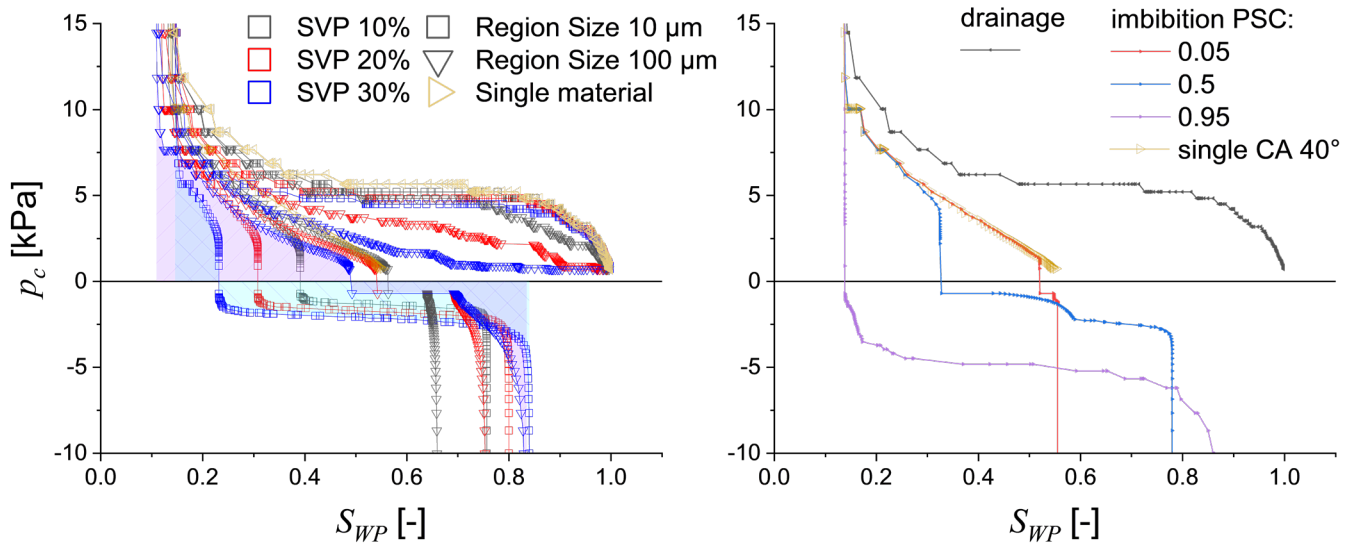


Fig. 5: Data modelled with the stochastic approach: Influence of the region size and solid volume percentage (SVP) on the drainage and imbibition curve (left). The marked areas underneath the curve indicate the wetting conditions of the SVP 30% case for a region size of 10 μm (cyan) and 100 μm (magenta), indicating non-wetting and wetting conditions respectively, when comparing the positive and negative areas below the curves. The yellow line represents the single material base case, without a forced imbibition. Data modelled with the deterministic approach: Influence of the pore space considered (PSC) on the imbibition curve (right).

Three different non-wetting volume changes (10%, 20%, 30%) with two different region sizes (10 and 100 μm) were modelled, resulting in additional 6 scenarios. While the residual WP saturation is rather unaffected, the residual NWP saturation decreases with increasing SVP and decreasing region size, which is coherent with the proportion of spontaneous to forced imbibition. An increasing volumetric proportion of non-wetting material results in a more non-wetting trend. The region size on the other hand displays the opposite, where a decrease of the region size leads to an earlier inhibition of the spontaneous imbibition. This is a result of the spatial distribution of non-wetting material, even though the surface area of non-wetting material is approximately the same for both region sizes, we do have more pores which are affected by non-wetting material. Consequently, the available pore space for the invasion during the spontaneous process is reduced. The effect of the region size, respectively the contact angle spatial distribution is large. It can make the overall system water wet or oil wet, which is directly recognized by comparing the positive and negative areas under the curve (indicated by the shaded areas for the SVP 30% cases in Figure 5), which links directly to the work the system does to the environment (spontaneous and positive) and the work the environment does to the system (forced and negative) – the ratio corresponds to the wettability index. When taking the logarithm of that ratio, similar to the U.S. Bureau of Mines (USBM) wettability index, positive values indicate a wetting behavior, as the spontaneous work is larger than the forced work and vice-versa. This makes the 30% SVP system with the 10 μm region size non-wetting and the one with 100 μm wetting, as indicated by the indices of -0.51 and 0.34 respectively.

It is worth mentioning that also the drainage curves are affected. For the smaller region sizes, more work is required to desaturate the system, if the region size is smaller. The reason may be that with larger region sizes, some pores are

wetting to the NWP and therefore a fraction of the volume can be invaded by the NWP without effort.

In the deterministic approach the non-wetting material is implemented at the end of the drainage process, which leaves the drainage process itself unaffected. Therefore, unlike in the stochastic approach, all imbibition scenarios start from the same point (drainage endpoint). Despite the substantial differences of both algorithms, the trends are similar with regards to the forced imbibition part and the residual NWP saturation. However, as discussed above, the exact NWP distribution after drainage determines the non-wetting material distribution. The right panel of Figure 5 shows the results, when assigning non-wetting material, while considering 5%, 50% and 95% of the entire pore space; the more pore space is considered for turning to non-wetting material, the more the system behaves non-wetting. This is displayed by lower residual NWP saturations and larger areas under the negative p_c branch. When considering almost the entire pore space (the 95% case in Figure 5), we do not have any spontaneous imbibition, as the WP front does not have any available space for advancing spontaneously, since it is immediately confronted with non-wetting material. For systems with low pore volume considered, the spontaneous imbibition follows the original trend, as only a small portion of the system is unavailable for the invasion sequence. Generally, both algorithms display similar trends with an increasing volume of non-wetting material introduced.

A difference of the imbibition p_c curves simulated with the MM and laboratory p_c curves, is the abrupt p_c drop at the transition from the spontaneous to the forced part of the curves across the $p_c = 0$ condition. We believe that this jump is physically correct and is a result of (a) a discrete contact angle distribution, and (b) a result of the finite size of the digital twin. We anticipate at this point that it has no influence on the simulated relative permeabilities:

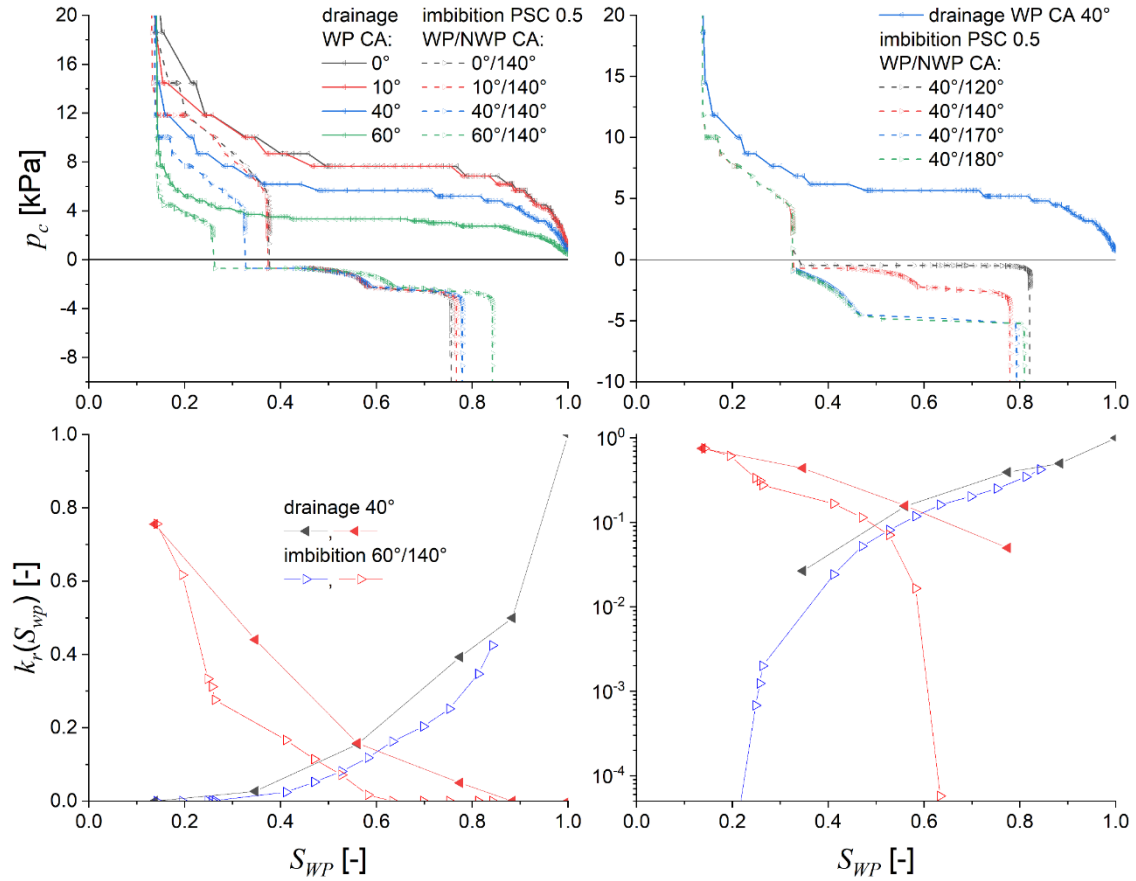


Fig. 6: Capillary pressure curves (top) when applying the deterministic modelling approach, while considering 50% of the pore space for the non-wetting material implementation. Sensitivities to the wetting (left) and non-wetting (right) contact angles. The relative permeability curves show the effective extension of the connectivity of the wetting and non-wetting phase on a linear (left) and logarithmic (right) scale beyond the spontaneous imbibition

At the point at which Imbibition changes from spontaneous to forced, all the pore space that can be spontaneously invaded is invaded. At that point, the interfacial curvature locally flips from concave (from the perspective of the wetting phase) to convex with only a neglectable saturation change. During the flip, the system crosses the $p_c = 0$ condition. Therefore, this discontinuity may be mitigated (a) by a continuous contact angle distribution, and (b) by investigating macroscopic system sizes as for classical p_c measurements. With respect to (a) it depends very much on the reason for contact angle variation – is it due to mineral-to-mineral variation or due to aging, or both. In all cases, the contact angle distribution may be discontinuous. With regards to (b), the MM as well as p_c measurements are based on fluid invasion processes. We assume that locally one process dominates, i.e., spontaneous or forced imbibition. However, for larger sample domains it may be that at a given time at different positions, there are slightly different saturation states. This would smoothen experimentally derived p_c curves for an average saturation state.

3.2 Sensitivity to the contact angle

To study the sensitivities to the implemented contact angles on imbibition p_c and k_r , the deterministic approach is used, where the material is implemented at the end of the drainage process. This guarantees a better comparability, as the

drainage process is not affected by the non-wetting contact angle.

In contrast to the initial implementation, two contact angles are assigned, resulting in a material distribution with the initially assigned wetting contact angle and with a modified contact angle. The modified areas are those prioritized by the primary drainage process to be in contact with the non-wetting phase material. A certain volume percentage of the prioritized area was then assigned to non-wetting contact angles. While drainage is determined by the wetting contact angle only, imbibition is sensitive to both. Unless otherwise stated and for comparability, the chosen pore space considered, 50%, is the same for all simulations. The left panel of Figure 6 shows the results by variation of the WP contact angle by leaving the NWP contact angle constant. Both curves, drainage and imbibition are affected. With increasing WP contact angle, less pressure is required for the NWP to enter the pore space – the p_c curve is lowering. Referring to imbibition, a contact angle increase lowers the saturation range for the SI and decreases the residual NWP saturation. These are clear indications of a less wetting behavior of the system, which is expected when applying a higher contact angle to the wetting phase. Furthermore, it can be observed that the shape of the forced imbibition curve is not influenced as it is governed entirely by the non-wetting contact angle. The earlier the forced imbibition is started, the larger the overall saturation range. This behavior is expected

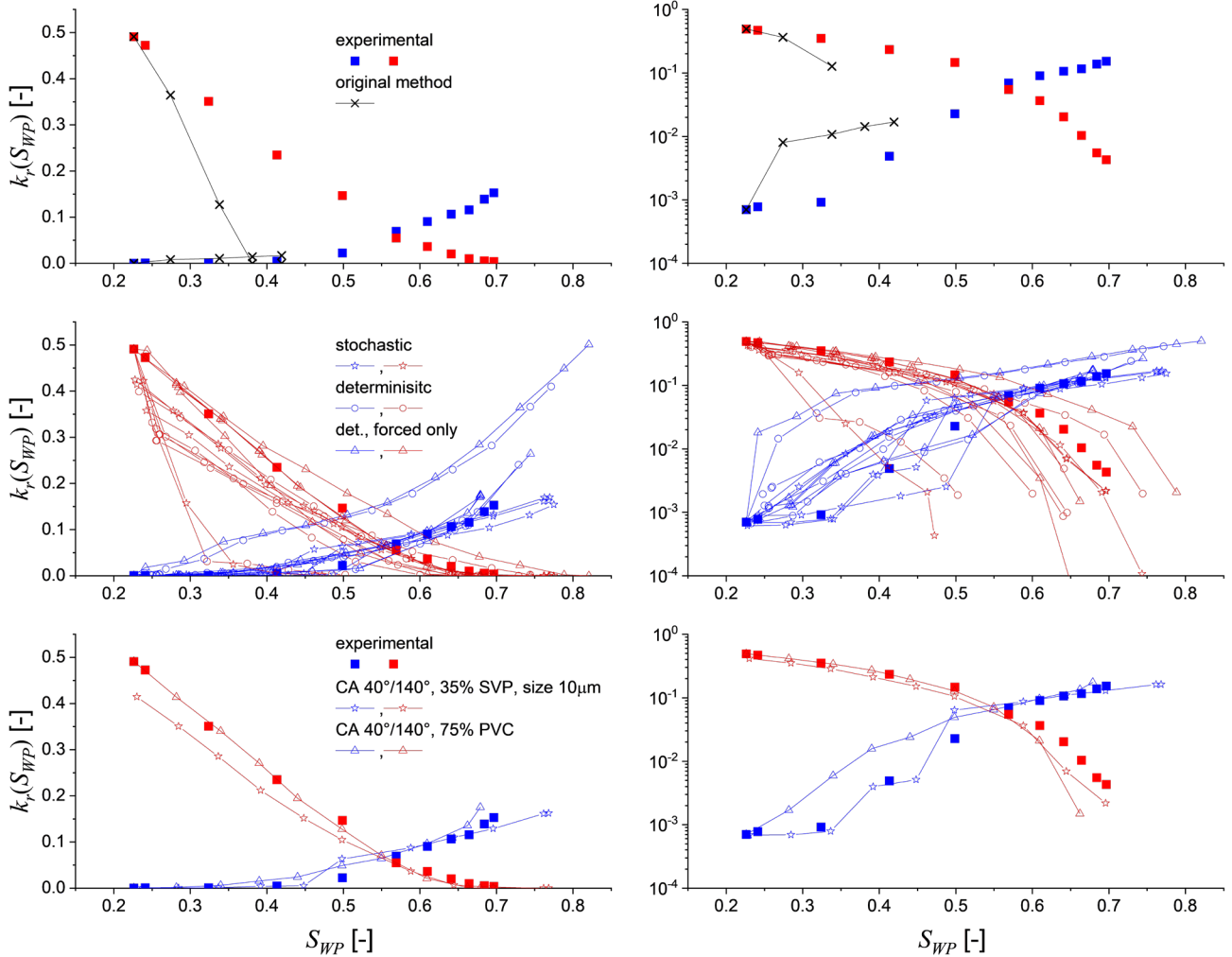


Fig. 7: Relative permeability curves on a linear (left) and logarithmic (right) scale. The experimental data is displayed by solid squares (\blacksquare). In the top panel the experimental data is compared with the original populated models. The middle shows a cloud of relative permeabilities modelled for different wetting and non-wetting contact angle combinations. The last panel shows the best matches for the deterministic and stochastic modelling approach.

from SCAL experience and is also reflected in the subsequent simulation of the relative permeability curves.

The right panel of Figure 6 shows the influence of the non-wetting contact angle. As the wetting contact angle is kept constant, only the forced imbibition is influenced. It can be observed that not only residual saturations, but also the shape of the curve is changing. Except for 120° , an increasing non-wetting contact angle results in a lower residual NWP saturation. However, the effects are minor compared to those of the wetting contact angle, which effect both parts of the curve. As seen in Figure 6 not only the cross-over at $p_c = 0$ but also the saturation endpoints are changing, which is resulting from the nature of the spontaneous and forced imbibition algorithms. Since the forced imbibition is modelled like a drainage process, the residual saturations are governed by the preexisting fluid phase distributions and the pore throat structure of the medium. As the starting point, namely the end of the SI is the same for all configurations the curves are only influenced by the scaling with the $\cos(\theta)$ during the dilation process. This results in slightly altered pathways, with similar final states.

Generally, we observe that the trends of the capillary pressure curves show physical trends with regard to contact angles and

associated wettability index. The most influential parameter has proven to be the way, the non-wetting material is introduced as displayed in Figure 5, where here the size and volume are of essence, as is acts as stopping criteria for the advancing SI front.

3.3 Relative permeabilities from morphological vs. experimental fluid distributions

A previous study by Berg et al. [12] has shown that imbibition relative permeability curves simulated morphologically and experimentally determined fluid distributions greatly disagree. In this section, we make the same comparison with the modified morphological approach and the respective extended imbibition saturation range. Furthermore, in the modified morphological approach, there are tuning parameters to (a) fit the numerical to the experimental results, and (b) to determine an uncertainty range. Since the experimental data refer to a water-oil displacement, we refer in this section to water and oil instead of WP and the NWP, without losing generality. We predominantly applied the deterministic algorithm to investigate the sensitivity of the

relative permeabilities with respect to different wetting states of the system. To minimize numerical capillary end effects, which can highly influence relative permeability, we mirrored the domain in flow direction. For the flow simulations, we cropped the domain back to its original size. The procedure proved to have only minor influences on the saturations, but improved the connectivity of the phases as a premature disconnection at the end of the domain is avoided.

As a starting point for the imbibition simulations, the experimental fluid phase distribution was used at connate water saturation of $S_{w,c} = 0.21$. The experimental residual oil saturation ($S_{o,r} = 0.29$) served as a reference end point to choose the right parameters for the algorithm. The imbibition simulations were performed considering 75% of the pore space for conversion, which resulted in a residual oil saturation ranging from 0.25 to 0.35 for non-wetting material contact angle of 180° and 140° respectively. With the initial implementations already shown in the study of Berg et al. [12] a $S_w = 0.41$ was reached at the end of the spontaneous imbibition process. In the top row of Figure 7, we show the experimental relative permeability curves in comparison with the initial morphological modelling approach. When applying the new algorithm, we reduce the spontaneous imbibition saturation ranges to between 0.25 to 0.32 depending on the chosen water-wet contact angle. These are only minor saturation changes with respect to the starting saturation, which is a result of the relatively high amount of pore space considered for the implementation of the non-wetting material. In the middle row of Figure 7 the range of resulting relative permeability curves are plotted, showing that we successfully extended the saturation range while reducing the offset to the experimental data.

The water wetting contact angle mainly influences the oil relative permeability, while the non-wetting contact angle influences both. The lower the water wetting contact angle, the lower the oil relative permeability is, this effect is very prominent especially at the early stage of the imbibition. Since the reduced connectivity of the oil comes from the spontaneous imbibition, the effect is more prominent for strongly wetting contact angles around $\theta = 0^\circ$. This results from the trends shown in Figure 6, where the SI part of the curve is larger for low contact angles, respectively the forced part smaller. This is a consequence of NWP clusters, which have been disconnected during the SI process and will not be reconnected during the forced imbibition process. Therefore, we get more of a water wet trend, with regard to the oil relative permeability, the less is modelled spontaneously. Especially since the NWP cannot be reconnected during any further displacement events. On the first view this may appear counter intuitive. On the other hand, in a flow experiment, water may invade with a higher rate than being spontaneous, i.e., imbibition may be forced.

The middle row in Figure 7 shows the simulation results for different contact angle combinations. In the different relative permeability realizations of our system, the outliers from the experimental data are from simulations using contact angle of 120° for the NWP, where we have already seen in the p_c

curves that this contact angle does not act in accordance with the other trends. Furthermore, one of the datasets is modelled with a large region size, which results in a strong SI and therefore a mismatch to the experimental data.

The best matches were achieved, as shown at the bottom of Figure 7, when modelling the imbibition process by a forced imbibition only. For both, the stochastic and deterministic implementation, avoiding extreme contact angles, i.e., contact angles close to 0°, 90° and 180°, proved to work best. To make sure the deterministic and stochastic approach are comparable, the same volume of introduced non-wetting material and a small region size (10 μm) for the later was chosen. Even though the residual saturations for both approaches differ, the trend and results for the $k_r(S_w)$ are similar. This could be an indication that for the displacement of the non-wetting phase the pore throat radii, hence the pore structure itself is more dominating than the wetting conditions implied.

Using the degrees of freedom as discussed above, leads to a cloud of relative permeability curves, which represents an uncertainty interval with respect to the wetting condition. This data can now be compared to the simulation results on the experimental fluid distribution by Berg et al. The experiments were performed under steady-state conditions, where the system was imaged at different fractional flow conditions. Since for each fractional flow step a steady state was reached, the flow must correspond to a process forced by injection. In addition, Berg et al. observed water film swelling by saturation changes at the beginning of imbibition, without significant displacement events taking place. Assuming this film swelling represent the spontaneous imbibition process, it would only account for a limited saturation range, whereas further displacement is connected to a forced displacement. This would correlate with the large number of pores where non-wetting material was introduced (PSC = 75%), and hence an only small SI range to match the experiment.

4 Summary and Conclusion

We successfully combined morphological algorithms for spontaneous and forced processes to describe the full-range imbibition capillary pressure and relative permeability curves. For this, distributions of wetting and non-wetting regions were introduced. With this, a premature stopping criterium for the spontaneous process was introduced, maintaining the connectivity of both phases at the end of the spontaneous process. As both phases are still connected, a subsequent forced imbibition process can be modelled by using the drainage MM.

For the implementation of the non-wetting regions, two approaches were developed, a deterministic and a stochastic approach. Capillary pressure curves were modelled for both approaches. By varying the nonwetting-region sizes and distributions and the contact angles and their combinations, we could show that the p_c follows physical trends and SCAL experiences [19,21,23-25].

Relative permeability curves were then calculated by solving the Stokes equations on the connected pathways for different saturation states. Varying the wettability-related parameters

results in an uncertainty interval that may be used for stochastic reservoir modeling. Relative permeability was predominantly calculated on a data set by Berg et al., which allowed a comparison between the original MM, the MM as modified in the frame of this work, and experimentally determined fluid distributions. A good match between morphological and experimental data could be achieved by avoiding strong wetting conditions, while modelling the imbibition process with a forced imbibition only. This is potentially due to the actual nature of the imbibition process under injection conditions, which may rather be forced than spontaneous.

In summary, with the made modifications, the morphological method can be used to model imbibition over the full saturation scale. We were able to demonstrate realistic physical trends and to deliver realistic results in comparison to pore-scale experiments. The wettability-related parameters can be used for uncertainty modeling and to match morphological to experimental results. However, we are still lacking the possibility to implement true neutral wetting conditions, as simulations with contact angles between 60° and 120° fail, or result in saturation end points opposing the actual physical trends. Being able to model contact angles in this interval would mitigate or even remove the sharp transitions between spontaneous and forced imbibition. Further investigation is needed to explain the best match by assuming a pure forced imbibition. This may be a result of potentially high viscous forces during the injection experiment, which may make the imbibition forced across the full saturation scale. This is the definition of a drainage process. The remaining questions are how to narrow down the input parameters in cases where no experimental data are available, and to a certain extent their physical interpretation of the best matches.

References

- [1] C. Pan, M. Hilpert, and C. T. Miller, "Lattice-Boltzmann simulation of two-phase flow in porous media," *Water Resour. Res.*, vol. 40, no. 1, 2004, doi: 10.1029/2003WR002120.
- [2] C. Chukwudozie and M. Tyagi, "Pore scale inertial flow simulations in 3-D smooth and rough sphere packs using lattice Boltzmann method," *AIChE J.*, vol. 59, no. 12, pp. 4858–4870, 2013, doi: 10.1002/aic.14232.
- [3] E. S. Boek, I. Zacharoudiou, F. Gray, S. M. Shah, J. P. Crawshaw, and J. Yang, "Multiphase-Flow and Reactive-Transport Validation Studies at the Pore Scale by Use of Lattice Boltzmann Computer Simulations," *SPE Journal*, vol. 22, no. 03, pp. 940–949, 2017, doi: 10.2118/170941-PA.
- [4] F. O. Alpak, S. Berg, and I. Zacharoudiou, "Prediction of fluid topology and relative permeability in imbibition in sandstone rock by direct numerical simulation," *Advances in Water Resources*, vol. 122, pp. 49–59, 2018, doi: 10.1016/j.advwatres.2018.09.001.
- [5] M. J. Blunt, "Flow in porous media — pore-network models and multiphase flow," *Current Opinion in Colloid & Interface Science*, vol. 6, no. 3, pp. 197–207, 2001, doi: 10.1016/S1359-0294(01)00084-X.
- [6] B. Zhao et al., "Comprehensive comparison of pore-scale models for multiphase flow in porous media," *Proceedings of the National Academy of Sciences of the United States of America*, vol. 116, no. 28, pp. 13799–13806, 2019, doi: 10.1073/pnas.1901619116.
- [7] V. Joekar-Niasar and S. Majid Hassanizadeh, "Effect of fluids properties on non-equilibrium capillarity effects: Dynamic pore-network modeling," *International Journal of Multiphase Flow*, vol. 37, no. 2, pp. 198–214, 2011, doi: 10.1016/j.ijmultiphaseflow.2010.09.007.
- [8] H. Dong and M. J. Blunt, "Pore-network extraction from micro-computerized-tomography images," *Phys. Rev. E*, vol. 80, 3 Pt 2, p. 36307, 2009, doi: 10.1103/PhysRevE.80.036307.
- [9] J. T. Gostick, "Versatile and efficient pore network extraction method using marker-based watershed segmentation," *Physical review. E*, vol. 96, 2-1, p. 23307, 2017, doi: 10.1103/PhysRevE.96.023307.
- [10] W. B. Lindquist and A. Venkatarangan, "Investigating 3D geometry of porous media from high resolution images," *Physics and Chemistry of the Earth, Part A: Solid Earth and Geodesy*, vol. 24, no. 7, pp. 593–599, 1999, doi: 10.1016/S1464-1895(99)00085-X.
- [11] D. Silin and T. Patzek, "Pore space morphology analysis using maximal inscribed spheres," *Physica A: Statistical Mechanics and its Applications*, vol. 371, no. 2, pp. 336–360, 2006, doi: 10.1016/j.physa.2006.04.048.
- [12] S. Berg et al., "Connected pathway relative permeability from pore-scale imaging of imbibition," *Advances in Water Resources*, vol. 90, pp. 24–35, 2016, doi: 10.1016/j.advwatres.2016.01.010.
- [13] M. Rücker et al., "From connected pathway flow to ganglion dynamics," *Geophys. Res. Lett.*, vol. 42, no. 10, pp. 3888–3894, 2015, doi: 10.1002/2015GL064007.
- [14] R. T. Armstrong, J. E. McClure, M. A. Berrill, M. Rücker, S. Schlüter, and S. Berg, "Beyond Darcy's law: The role of phase topology and ganglion dynamics for two-fluid flow," *Physical review. E*, vol. 94, 4-1, p. 43113, 2016, doi: 10.1103/PhysRevE.94.043113.
- [15] J. P. Serra, J. Serra, and N. Cressie, *Image Analysis and Mathematical Morphology*: Academic Press, 1982. [Online]. Available: <https://books.google.at/books?id=6pZTAAAYAAJ>
- [16] M. Hilpert and C. T. Miller, "Pore-morphology-based simulation of drainage in totally wetting porous media," *Advances in Water Resources*, vol. 24, 3-4, pp. 243–255, 2001, doi: 10.1016/S0309-1708(00)00056-7.
- [17] V. P. Schulz, E. A. Wargo, and E. C. Kumbur, "Pore-Morphology-Based Simulation of Drainage in Porous Media Featuring a Locally Variable Contact Angle," *Transport in Porous Media*, vol. 107, no. 1, pp. 13–25, 2015, doi: 10.1007/s11242-014-0422-4.

- [18] B. Ahrenholz *et al.*, “Prediction of capillary hysteresis in a porous material using lattice-Boltzmann methods and comparison to experimental data and a morphological pore network model,” *Advances in Water Resources*, vol. 31, no. 9, pp. 1151–1173, 2008, doi: 10.1016/j.advwatres.2008.03.009.
- [19] M. Rücker *et al.*, “Relationship between wetting and capillary pressure in a crude oil/brine/rock system: From nano-scale to core-scale,” *Journal of colloid and interface science*, vol. 562, pp. 159–169, 2020, doi: 10.1016/j.jcis.2019.11.086.
- [20] G. J. Hirasaki, J. A. Rohan, S. T. Dubey, and H. Niko, “Wettability Evaluation During Restored-State Core Analysis,” in *All Days*, New Orleans, Louisiana, 09231990.
- [21] Wael Abdallah, Jill S. Buckley, Andrew Carnegie, John Edwards, Bernd Herold, Edmund Fordham, Arne Graue, Tarek Habashy, Nikita Seleznev, Claude Sighner, Hassan Hussain, Bernhard Montaron, Murtaza Ziauddin, “Fundamentals of Wettability,” pp. 44–61, 2007.
- [22] Steffen Berg, Ryan Armstrong, and Andreas Weigmann, “Gildehauser Sandstone,” 2018. <https://doi.org/10.17612/p7ww95>
- [23] W. Anderson, “Wettability Literature Survey- Part 2: Wettability Measurement,” *Journal of Petroleum Technology*, vol. 38, no. 11, pp. 1246–1262, 1986, doi: 10.2118/13933-PA.
- [24] X. Zhou, N. R. Morrow, and S. Ma, “Interrelationship of Wettability, Initial Water Saturation, Aging Time, and Oil Recovery by Spontaneous Imbibition and Waterflooding,” *SPE Journal*, vol. 5, no. 02, pp. 199–207, 2000, doi: 10.2118/62507-PA.
- [25] S. Zou and R. T. Armstrong, “Multiphase Flow Under Heterogeneous Wettability Conditions Studied by Special Core Analysis and Pore-Scale Imaging,” *SPE Journal*, vol. 24, no. 03, pp. 1234–1247, 2019, doi: 10.2118/195577-PA.

Initial states of core flooding techniques evaluation: a global pore-scale investigation

Franck Nono^{1,*}, Cyril Caubit², and Richard Rivenq²

¹Modis, Pau, France

²TotalEnergies, Pau, France

Abstract. Initial water saturation (S_{wi}) preceding waterflooding experiments is an important factor because it impacts multiphase flow properties and the degree of wettability reached after ageing. There exist various techniques aiming to achieve S_{wi} on core plugs but there is scarce data which compare them and size their differences down to the pore-scale and considering wettability. The available data show large quantitative discrepancies with the best choices often not clear. In fact, already obtaining homogeneous profiles with average values comparable to reservoirs states in reasonable time is not so straightforward. Relying only on both these aspects to judge the quality of an initialization technique may hide possible pore scale artifacts.

In this work, we used 3D X-ray microtomography to compare at the pore scale different targets of S_{wi} achieved using porous-plate, viscous displacement, and centrifuge techniques. We used mini plugs from Bentheimer sandstone with different initial wettabilities. Pore-scale properties such as pore occupancy, fluids connectivity, etc., were investigated. Multiphase flow properties were also measured during tests. Our study is mainly focused on: (i) the impact of the initialization technique, (ii) the Impact of rock's initial wettability.

For water-wet plugs, all techniques exhibit similar pore-scale results for low targets of S_{wi} . In the other hand, capillary end-effects are the crucial artefacts for higher S_{wi} targets. Recirculation or reverse spinning to flatten saturation profiles generates disconnected oil clusters. The porous plate method delivered robust results. For oil-wet plugs, viscous displacement generates large brine ganglia trapped in big pores and difficult to mobilize thus leading to unwanted high S_{wi} . These observations are made despite suitable rocks permeabilities. The trends are confirmed by investigations of core cleaning efficiency. For identical primary drainage protocols before and after cleaning, we observed a repeatable increase of S_{wi} after cleaning. Nevertheless, in our experiments the after-cleaning oil-wetness was so low that brine occupied smaller pores as wanted.

These experimental observations clearly highlight the possible non-negligible impacts of primary drainage techniques, the protocols associated and the rock wettability on establishing a representative S_{wi} prior to multiphase flow experiments.

1 Introduction

In order to understand multiphase flow processes at the field scale for various important purposes (soil remediation, oil recovery, CO₂ injection, etc.) flow experiments are conducted at the core scale in laboratories with conditions very close to reservoirs conditions. It implies having the same initial fluids distribution as in specific locations of the reservoir. Unfortunately, there is no direct initial pore-scale in situ observation to rely on, but it is stated that all reservoir rocks were initially water-wet before oil migration and the initial water saturation (i.e. in oil-water transition zone) or irreducible water saturation (S_{wirr}) was first located at the pores surface (films) [1], in small pores, corners and crevices. After what, an ageing process occurred through millions of years and impacted the affinity of the reservoir rock with the reservoir fluids. In laboratories, this process is then repeated prior to oil recovery experiments on smaller time scales. S_{wi} is an important parameter as it sets the departure of various flow properties measurements [2] which will depend not only on its average value but also on

its distribution within the pore network. To resume, it is important to set S_{wi} alike a water wet state so for its distribution after ageing to be close to that of the reservoir, keeping in mind that there is a big assumption on the fact that the ageing time in laboratories will be able to achieve the same wettability of the reservoir that was achieved during millions of years.

From core flooding laboratory perspective, experimental investigations need a start on almost water-wet cores. To do so, drilled reservoir plugs are cleaned with specific solvents before achieving S_{wi} in order to restore the initial water-wet state [2, 3]. Nevertheless, cleaning is known to not always being efficient [4] and can lead to non-water-wet plugs prior to SCAL experiments. In these cases, wettability may play an important role on S_{wi} distribution [5]. The long-time concept of phases distribution during a non-water-wet primary drainage is always hypothesized to explain behaviours such as low effective oil permeability at S_{wi} [5]. Moreover, pore occupancy is meant to be inversed to that of a water-wet case, meaning large blobs of brine trapped in big pores and oil in small pores. There are no direct pore

* Corresponding author: franck.nono@modis.com

scale observations of this trapping on real rocks. The only experimental observations are those coming from micromodels or artificial porous media (acrylic bead packs) [6]. The authors observed significant larger brine blobs population in oil-wet bead packs than in water-wet cases with slight changes of saturation, although over one order of magnitude increase in flowrate.

The three most used techniques [3] to achieve initial water saturation on core plugs in laboratories are: (i) dynamic displacement, (ii) porous-plate and (iii) centrifuge. These methods are well documented at the macro-scale and their theoretical and practical advantages and drawbacks seem to be known. In one hand, the porous plate method generally delivers robust results and can target a wide range of S_{wi} but is time consuming. In addition, limitation of the ceramic maximum capillary pressure [4] or experimental artefacts such as poor capillary contact with rock may introduce significant errors [7] and render S_{wi} difficult to obtain. Improvements of this method are mainly focused in reducing the measurement time, by modifying the geometry and/or the intrinsic properties of the porous plate [2, 8]. In the other hand, both dynamic displacement and centrifuge methods are faster to implement but generate gradient of saturation profiles along the plug because of the capillary end-effect [9]. In these cases, plugs sometimes undergo reverse flow injection or reverse spinning [2, 10] to flatten saturation profiles. Limitations in terms of set-up limits such as maximum flowrates, maximum pressures or maximum spinning rates can emphasize the difficulty of reaching low S_{wi} , specifically when dealing with low permeable rocks [1]. In general case the main point of control for quality check of an experimental S_{wi} in comparison with that of the reservoir is its average value. For laboratories equipped with In-situ saturation monitoring (ISSM) set-ups, both the average value and homogeneous profile are the main criteria to attest for a good departing point for flooding experiments. Meanwhile large inconsistencies and discrepancies are still observed on multiphase flow properties even after achieving almost the same S_{wi} on the same rock-type, with same fluids but different initializing methods [7]. The consensus about the best method to use (fast and accurate) is not clear. Macro-scale properties seem to not be sufficient to identify the source of these discrepancies. Recent studies [11, 12] specifically compared the flooding and centrifuge techniques till the nanoscale on a dual porosity carbonate rock (Ketton limestone). It appeared that samples which went through centrifuge experiments became finally more oil-wet than samples which underwent oil flooding. The difference was ascribed to reachable level of capillary

pressure and the pore network structure. During flooding, in a section brine fills the pores and throats located on the easiest path while for centrifuge all the pores and throats with radius above the applied capillary pressure radius are filled. Moreover, if the water-wet network is made of two distinct paths (micro and macro porosity) not well connected like Ketton limestone; oil flooding would likely miss the micro-porosity invasion. Nevertheless, some questions remain on how capillary end effect was considered, its impact on the results or the impact of dopants on wettability as it was used on final water-wet experiments and not used on final oil-wet experiments.

In this study, we used 3D X-ray microtomography to investigate and compare fluids dispositions at the pore scale after S_{wi} achievement using the three methods discussed above with exactly the same fluids and experimental conditions. In order to eliminate any issue related to set-up limits, we decided to work on suitable unimodal rocks enabling a large range of S_{wi} to be targeted by any method. We focused our study on two main axes:

- (i) Water-wet S_{wi} comparisons at the pore scale using different initializing method: It will help us to settle thoroughly the crucial differences and point out drawbacks of some routines in primary drainage protocols
- (ii) Impact of rock's initial wettability on primary drainage: This point is investigated via two different strategies: first by performing primary drainage on artificially made non-water wet outcrops and second by performing primary drainage on outcrops that were cleaned after their wettability was modified using crude oil.

2 Materials and methods

2.1. Porous media: Bentheimer sandstone

Primary drainage experiments till S_{wi} were performed on fresh cylindrical Bentheimer sandstones. The mineralogy is reported in Table 1.

Table 1. Mineralogy of the rock-type used in this study

Bentheimer	96% Quartz, 3% Clays, feldspar.
------------	---------------------------------

Bentheimer mean pore throat diameter averages 30 μ m to 40 μ m. It is known to be homogeneous with an absolute permeability around 1 to 3 Darcy and a porosity around 20% to 25%. This outcrop is initially water wet. Experiments performed in this study also include achieving S_{wi} on Bentheimer plugs which had their initial water wettability

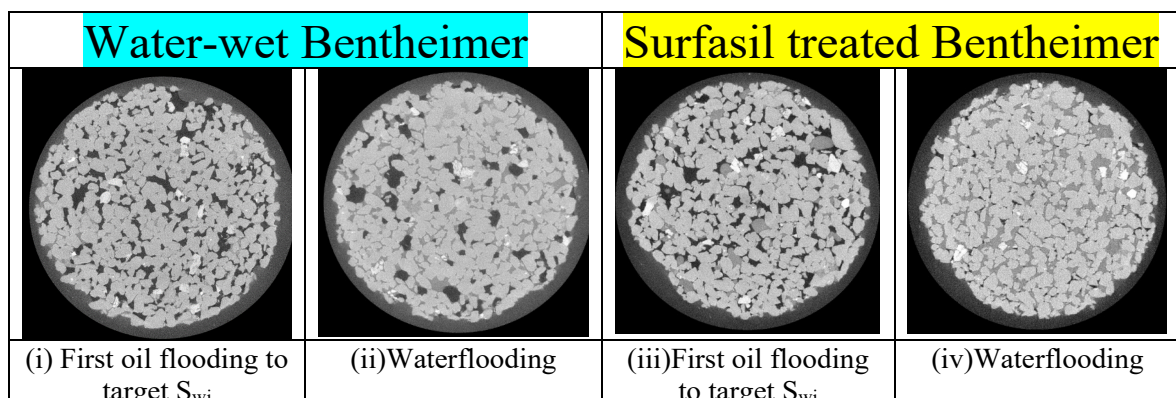


Figure 1 : Comparisons of pore-space occupancy between water-wet Bentheimer at S_{wi} (ii) and S_{or} (ii) and Surfasil treated Bentheimer at S_{wi} (iii) and S_{or} (iv).

altered. Two different procedures were used to alter Bentheimer sandstones wettability prior to flooding. For some plugs, a chemical alteration was used and consisted in saturating under vacuum the water-wet pore space with a mixture of toluene (95%) and Surfasil® (5%), directly followed with 3 min of ageing at room temperature. After that, the samples were flushed with 100% toluene, then cleaned and dried in an oven. A proof of wettability alteration through this chemical protocol is shown in figure 1. This chemical treatment tends to artificially homogenize the oil wetness behaviour of the pore space while for natural rocks, wettability may vary within the pore space. In this study, we have to think about the micro-plugs as part of larger size plugs. The goal is to focus on the impact of a well identified wettability on the trapping process. We achieved quick flooding test, coupled with 3D X-ray imaging to compare the visual differences between water-wet and altered wettability greyscale images on Bentheimer during primary drainage and waterflooding with same fluids. One can refer to Nono et al., 2019 [9], section 3.5, to understand the colour code of the greyscale reconstructed data. As we can see, oil flooding and waterflooding images between water-wet media and Surfasil-treated media are

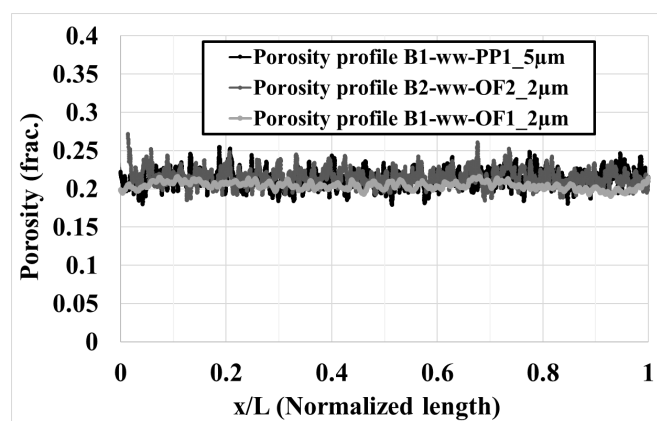


Figure 2. Examples of Bentheimer plugs porosity profiles obtained through 3D image processing.

totally different, especially the end of the waterflooding processes. We observe large blobs of oil in big pores for water-wet media (as expected), while oil remains in very small pores for Surfasil-treated media. Thus, we were confident that our Surfasil-treated media were not water-wet. For other plugs, we altered wettability by a more or less efficient cleaning that followed an ageing process (at very low S_{wi}) of 15 days with dead oil (crude oil A) at 80°C. Bentheimer plugs were selected with a homogeneous porosity profile (examples on figure 2), permeabilities ranging from 1.45D to 2D and porosities ranging from 20.5% to 22%. Note that the porosities here are obtained through image processing and represent the porosity that is directly visualized on 3D images. 97-99% of this porosity is connected and the rest made of disconnected porosity clusters is attributed to image processing uncertainties. This visualized porosity can be 1p.u to 3p.u less than the true porosity because it does not account the pore volume in clays which is under the resolution of the images. An experimental protocol exists to account for the sub-resolved

porosity [13, 14] but in this case, we had access to almost the entire pore volume. It was then not necessary.

2.2. Fluids

We focus our study on oil/brine displacements. In order to be able to distinctly distinguish oil phase, brine phase and grains on 3D images, there is a need of a clear atomic density contrast between them. In our case, we doped brine with 7%wt of potassium iodide (KI) essentially.

Decane was used as mineral oil ($\mu_D = 0.93\text{cP}$, and $\rho_D = 0.73\text{g.cc}^{-1}$ at 25°C). For ageing processes at 80°C to alter wettability, we replaced Decane with a dead oil [Dead oil A] with following characteristics: $\mu_A = 6\text{cP}$ (2cP at 80°C), and $\rho_A = 0.845\text{g.cc}^{-1}$ at 25°C.

2.3. Image acquisition and processing

3D images were acquired using a Zeiss Xradia Versa 520. Energy settings were chosen between 80kV and 100kV while power varied between 7W and 9W. Voxel size varied from 4µm for 4mm diameter plugs to 5µm for 1cm diameter plugs. Samples were analyzed on the total sample's length and we had to stitch a maximum of 9 segments (3cm length) which would take up to 22h in total acquisition time (~ 2h30 per segment).

Image processing was realized using Avizo 2020.3® and the open-source software ImageJ. Greyscale color code for the reconstructed data and Image processing sequences used are identical to the one used by Nono et al. [9].

2.4. Experimental set-ups

The cells designed in this study were used under same experimental conditions in terms of confining pressure, pore pressure and temperature during ageing if necessary. These parameters are fixed as follows: Confining pressure = 30 bars, Pore pressure = 10 bars and ageing temperature = 80°C. Different types of cells were developed for this study.

2.4.1. Oil flooding cell

Oil flooding experiments were achieved using the same set-up than that used by Berthet et al. [15], with end faces diffusers made of grooves. For this cell, samples were automatically 4mm diameter and almost 3cm length. The flow is achieved vertically, and the injections are started by respecting gravity direction. It means injecting the lighter fluid from top to bottom and the denser fluid from bottom to top. In this cell, the sample's end faces are in contact with only one flow line each. Pressure gradients are not measured at the rock end faces but on the flow lines outside the cell. A correction is made to take into account the pressure gradient they generate.

2.4.2. Porous-plate cells

We designed an in-house porous-plate cell with almost the same technical improvement as for Pentland et al. (2014) [16] enabling both the possibility to perform a porous plate experiment and to perform core flooding with flow

properties measurements (absolute/effective permeabilities). This cell entirely made of Peek® also enables 3D X-ray imaging for pore scale analysis. In these cells, samples are automatically 1cm diameter. The porous plate is made with a center hole enabling flooding. When the center hole is isolated, the flow is operated through the porous plate. During porous-plate experiments, oil invades the total volume of the center aperture at breakthrough because the capillary pressure there is lower than the capillary pressure needed to displace water in the porous-plate. Porous-plate experiments could also be achieved on the 4mm diameter plugs using the 4mm flooding cell described above (section 2.4.1). For this case, a full ceramic cylinder of 4mm diameter is placed between the sample's bottom face and the diffuser. No measurement of effective permeability is possible here because the ceramic is a full material without a center cylindrical aperture.

2.4.3. Centrifuge cell

At the very end, we also designed an in-house centrifuge cell enabling both the possibility to achieve centrifuge experiments and to acquire 3D X-ray images of the sample in it. With this cell, centrifuge experiments are performed under confining pressures. Samples used are automatically 1cm diameter.

In this way, the dry samples are initially loaded in the cell before any saturation and flooding steps. We avoid having the saturated plugs in contact with air or having to mount saturated plugs in jackets and air-filled cells which can increase the level of uncertainty on the experimental processes. By this way we also control the length of our samples and the end faces surface quality.

2.5. Experimental procedures

The overall experimental procedure is depicted in figure 4. The first part of the procedure (proc.1) aims to directly compare: porous plate (PP), centrifuge (CF) and oil flooding (OF) experiments during the first primary drainage for the same S_{wi} targeted. The overall procedure (proc.2) aims to investigate cleaning efficiency and its impact on primary drainage. In this paper, wettability assessment is achieved through ROS (remaining oil saturation) profiles. In this study, we focus on 14 samples in which 12 underwent only proc.1 while 2 samples underwent proc.2. The flowrates used in this study are reported in terms of capillary number (Ca) expressed in equation 1:

$$Ca = v \cdot \mu / \gamma \quad (1)$$

Where v represents the superficial fluid velocity ($m \cdot s^{-1}$), μ the displacing phase viscosity ($P_a \cdot s$) and γ the interfacial tension ($N \cdot m^{-1}$).

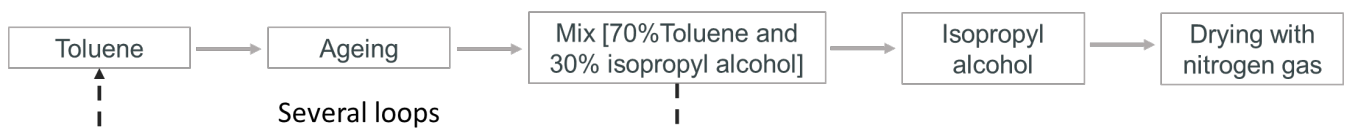


Figure 4. Classic cleaning sequence in core flooding laboratory

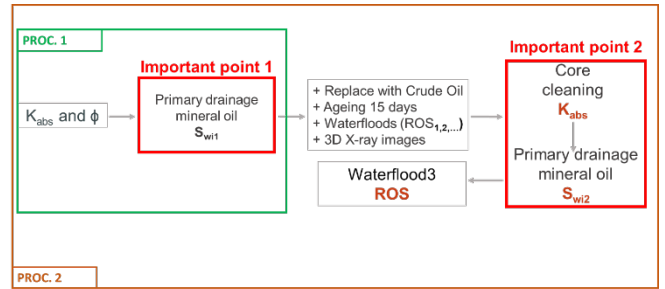


Figure 3. Experimental procedures used in this study. The green domain is proc.1 which aims in comparing first primary drainage data. Proc.2 (brown domain) starts with proc.1.

Proc.2 which includes proc.1 is performed as follows:

- (i) Dry 3D scan of the whole sample mounted in the cell with a confining pressure of 30 bars, at 4 or 5 μm of voxel size (depending on the sample's diameter, respectively 4mm and 10mm diameter). Then the cell with the sample in it is moved from the micro-CT to the flooding stage.
- (ii) Vacuum saturation and flushing at low rate (30 $\mu l/min$) with 40 pores volumes (PVs) of brine with a pore pressure of 10 bars and a confining pressure of 40 bars. For the rest of the protocol, we maintained 30 bars of effective pressure. Measurement of the absolute permeability is achieved with rates varying from 10 $\mu l/min$ to 100 $\mu l/min$ (5 to 6 rates).
- (iii) Primary drainage with Decane using either the porous plate (PP), the centrifuge (CF) or the oil flooding (OF) technique to target a known initial water saturation (S_{wi}). A multistep approach is used and corresponds to a gradual increase in capillary number for OF in unsteady-state mode, gradual increase in capillary pressure for PP and gradual increase in rotational speed for CF. Values of capillary number or capillary pressures or spinning rates depend on the target of initial water saturation. Here we monitor the DP for OF, the injecting syringe volume VS time for PP and the production for CF.

After the maximum rate/spin used, reverse the flow (only for CF and OF) using the maximum rate/spin to flatten saturation profiles. At the end of primary drainage, we perform a 3D scan of the whole sample and measure oil permeability at S_{wi} ($K_o(S_{wi})$). A close attention is done on measuring effective permeability especially when high S_{wi} values are targeted. We used oil flooding and 5 rates to measure effective permeability. For the OF method, the maximum rate used corresponds to a value less than the maximum rate used to achieve S_{wi} . For The PP method, we made sure that the pressure gradient during each oil flooding rate did not surpass the maximum capillary pressure implemented during the porous-plate displacement to achieve S_{wi} . Here, during the measurements we focused on how quick we obtained the plateau of gradient pressure for each rate and 2D X-ray projections of the outlet during permeability measurements. No brine was produced during these stages, and the pressure gradient stabilizations were fast. [This is the end of proc.1]

- (iv) If ageing with crude oil is expected (only performed on 4mm diameter samples): replacement of the mineral oil with 5 PVs of toluene (at 10 μ l/min) then with 5 PVs of dead oil A (at 4 μ l/min) at 80°C in an oven to avoid wax appearance. Dynamic aging at very low rate (0.05 μ l/min) with dead oil A for 15 days. During ageing time, the flow is reversed after 7 days.
- (v) After ageing, we perform a waterflooding of the sample at 50 μ l/min and 80°C till gradient pressure equilibrium then 3D scans of the sample at remaining oil saturation (ROS) and at 28°C which is the temperature of the micro-CT.
- (vi) Sample cleaning: the cleaning process is depicted in figure 3. Two different approaches are tested: Cleaning at ambient temperature and cleaning at 80°C. The goal is to try to mimic an inefficient and an efficient cleaning. Cleaning consists in several loops, injecting toluene, then azeotropic mix of toluene and isopropyl alcohol (70%/30%) with an ageing time between both steps (in general 5 to 6 hours). When the sample is cleaned enough (colorless effluents), we inject 4 pore volumes of isopropyl alcohol and dry the sample using Nitrogen gas. The rate of injection is held constant at 40 μ l/min.
- (vii) We restart the steps (i) to (iii) using exactly the same inputs (flowrates, pressures, injection time, time of reversal, etc.).
- (viii) Waterflooding of the sample with brine and 3D scan to visualize fluids distribution. [**This is the end of proc.2**]

It is important to note that during all these steps (with OF, CF and PP methods) the plugs remained under confining and pore pressure in their initial cell from (i) to (viii).

To ease the reading of the paper and the identification of the samples we use the following formula for Bentheimer samples names:

B(a)-(b)-(c)(d) where: (a) stands for the protocol number (1 for proc.1 and 2 for proc.2), (b) stands for the initial wettability (ww for water-wet and sw for altered wettability using Surfasil®), (c) stands for the primary drainage method (PP: porous plate, CF: centrifuge or OF: oil flooding) and (d) stands for the number of the sample if there are many. An example of Bentheimer sample name can be: **B2-ww-CF3** meaning that this Bentheimer sample has undergone proc.2 with an initial water-wet wettability, using Centrifuge as main primary drainage method and is the third sample to undergo these steps.

The different plugs used with their geometry, porosity, permeability, average S_{wi} values, are given in Table 2. Due to the fact that our mini-plugs pore volumes were very smaller than the system dead volumes, we could not achieve a direct measurement of the produced volume. Material balance is achieved here by image processing on the part of the network that is visible. Image segmentation applied in this study is partly operator dependent. A variation of +/- 2% can be added as the variability of image segmentation.

Table 2. Bentheimer samples properties

		Sample name	Porosity μ CT (%)	Perm. (D)	D (mm)	S_{wi} (%)	$K_{ro}(S_{wi})$
B E N T H E I M E R	Low S_{wi} targeted	B1-ww-OF1	21.3	1.53	3.92	7.5	0.84
		B1-ww-PP1	20.5	1.45	9.87	8	0.88
		B1-sw-OF1	21	1.7	3.92	35	0.1
		B1-sw-OF2	22	1.65	3.78	18.5	0.32
		B1-sw-PP	20.6	/	3.88	10.5	/
		B2-ww-OF1	20.5	2	3.85	5.3	0.75
	High S_{wi} targeted	B2-ww-OF2	21.1	1.98	3.88	4	0.86
		B1-ww-OF2	20.5	1.62	3.94	31	0.29
		B1-ww-OF3	21.5	1.68	3.85	47.5	0.22
		B1-ww-PP2	21	1.9	9.88	35.4	0.53
		B1-ww-CF	22	2.1	9.85		

3 Results and discussions

Results are divided into three topics:

i. Low targets of S_{wi} : In this section, we focused only on OF and PP methods. Experimental investigations are achieved on targets below 10% of initial water saturation. The same experimental inputs and chronology are used for each sample to target the same S_{wi} , disregarding wettability. For the OF method, a final capillary number of $Ca = 1.5 \times 10^{-4}$ is used. For PP method, a maximum capillary pressure of $P_c = 100$ mbars was used.

ii. High targets of S_{wi} : In this section, high targets of S_{wi} are implemented. OF, PP and CF are used for Bentheimer. The maximum capillary number used during OF was $C_a = 1.5 \times 10^{-5}$. For PP experiments, we used a maximum capillary pressure of $P_c = 35$ mbars and for the CF method, we achieved a single experiment using a spinning rate of 400rpm corresponding to an entry capillary pressure of 35 mbars.

iii. Cleaning efficiency impact: In this section, two Bentheimer samples underwent the overall proc.2 (figure 4) till the last waterflooding. As the two previous topics above will highlight the importance of wettability on S_{wi} , it is therefore mandatory to understand in which manner the wettability obtained after cleaning impacts our processes.

It is important to note that for low and high S_{wi} , effective permeabilities are measured using multi-rates injections of oil only. As shown by [9], disconnection of water and perturbations of the outlet water saturation occurred during primary drainage once oil breakthrough happened. These perturbations increase with rate and partly contribute to highly decreasing the actual outlet saturation and decreasing the impact of capillary end-effect on gradient pressure.

3.1. Low targets of S_{wi}

3.1.1. Low S_{wi} on water-wet porous media

Samples concerned: **B1-ww-OF1** and **B1-ww-PP1** for proc.1, **B2-ww-OF1** and **B2-ww-OF2** for proc.2.

We focus in this section on the first primary drainage. Everything that comes after the first primary drainage (B2's samples) will be discussed in the cleaning efficiency paragraph.

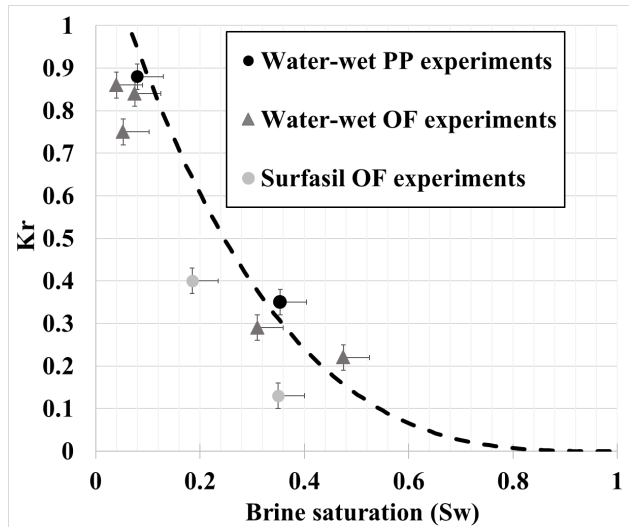


Figure 5. Synthesis of $K_{ro}(S_{wi})$ after primary drainage for low and high S_{wi}

Oil flooding experiments lasted ~ 2 h to reach S_{wi} while the porous plate experiment lasted 3 days. In figure 5 we plotted primary drainage relative permeability values obtained at S_{wi} for all samples. We also plotted a Bentheimer sandstone primary drainage K_r curve taken from the literature [9] which is the result of a Corey fit of the experimental points reported in [19] and was successfully used for experiments on plugs [9] coming from the same batch as the samples used in this study.

Almost all the experimental values of oil relative permeability at low S_{wi} (from 4% to 8%) are close to the literature curve and no clear distinction can be made between each initialization method (figure 5) a part one OF point at $S_{wi} = 5\%$ with $K_{r_{ow}}$ measured at 0.75 which is a bit below low S_{wi} cloud. Saturation profiles obtained by 3D image segmentation on each sample (figure 6) show homogeneous profiles without noticeable capillary end-effects while expected for water-wet porous media. Beyond the high Rapoport number used which reduces C.E.E, Nono et al. [9] also shown that the oil outlet saturation may increase with rate.

For both PP and OF, oil is connected from inlet to the outlet with 100% connectivity. At these low targets, brine remains in clays, corners, and films layers. No direct distinction at this stage is made between oil flooding and porous plate experiments at the macroscale based on the accessible pore scale observations made in this study. Both methods give similar results in terms of pore occupancy, oil global connectivity with reproducible values of S_{wi} and effective oil permeabilities. Based on Rucker et al. [11] we know that at

the nanoscale, differences could arise regarding surface coverage and lead to different wettability after ageing. The authors observed for very close values of S_{wi} between CF and OF, very different wettability with the OF method being inefficient beside CF method.

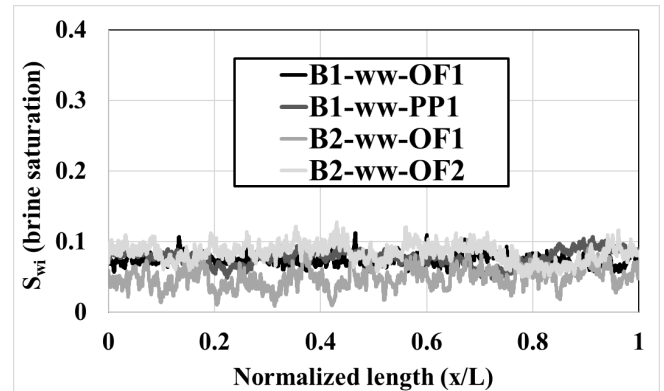


Figure 6. Saturation profiles for low targets of S_{wi} on Bentheimer

Regarding their conclusions, the CF method with high spinning rates to achieve low S_{wi} would have led to the same macro-scale observations on Bentheimer sandstones. Unfortunately, we could not access nanoscale properties and did not perform spontaneous displacements comparisons. As films layers are not visible due to the limits of the imaging set-up, we cannot draw the same conclusions of equity between the different methods at the nanoscale, specifically on surface coverage by films layers.

3.1.2. Low S_{wi} on non-water-wet porous media

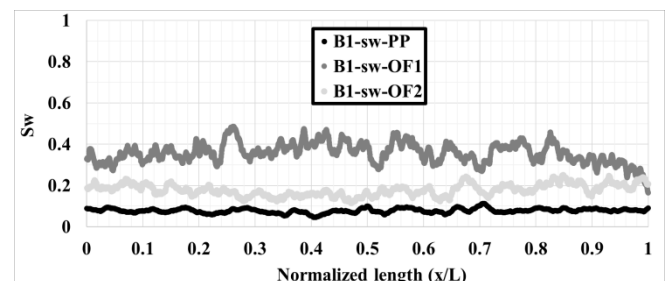


Figure 7. Water saturation profiles of surfasil-treated Bentheimer plugs, targeting low S_{wi} .

Samples concerned: **B1-sw-OF1, B1-sw-OF2, B1-sw-PP,**

On **B1-sw-OF1 and B1-sw-PP**, oil flooding and porous-plate were performed respectively under the same conditions of capillary number and capillary pressure than that of water-wet Bentheimer plugs in section 3.1.1. On **figure 7** are plotted final saturation profiles. We observe a non-neglectable ~ 20 -25 p.u higher average saturation for oil flooding (B1-sw-OF1) than water-wet samples but also with the porous-plate experiment at the same wettability. Both samples will be investigated distinctly.

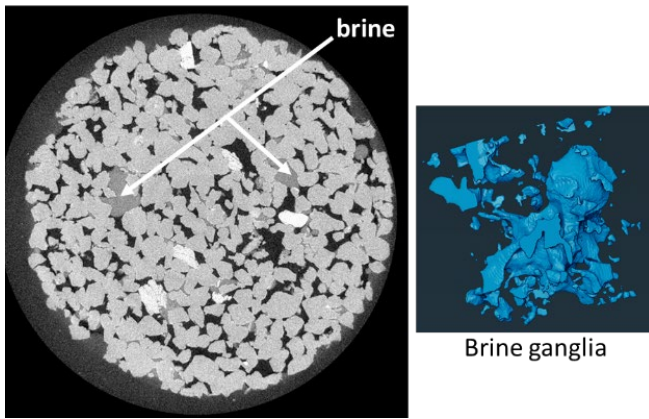


Figure 8. On the left: 2D slice of a Surfasil-treated Bentheimer at S_{wi} , on the right: isolated ganglia of brine

- **B1-sw-OF1**: OF pore scale investigations on **B1-sw-OF1** highlight small pores and big pores filled with brine after oil flooding whereas for water-wet case, brine does not fill at all the big pores (figure 1, image (iii)). 3D segmentation shows big ganglia of brine connecting many pores and been surrounded and trapped by oil (figure 8). The geometries of ganglia highlight a clearly more oil-wet trend. Without dynamic imaging, we were not sure if snap-off could occur in these cases, but we believed trapping through snap-off of the brine phase should normally be very limited as there are no initial oil layers in the system. The sample is initially 100% brine saturated.

S_{wi} obtained on **B1-sw-OF1** being finally high, we could quantitatively compare the pore occupancy with a water-wet Bentheimer on which we achieved a high S_{wi} with close values. We choose **B1-ww-OF2** (Table 2) from which S_{wi} are close to each other (35% and 31%). To investigate pore occupancy, we used a pore network extraction code called GNexttract developed with Imperial college of London [17] which was used to satisfactorily validate TotalEnergies' DRP workflow for multiphase flow simulation and relative permeability estimation against experimental core flooding experiments [18].

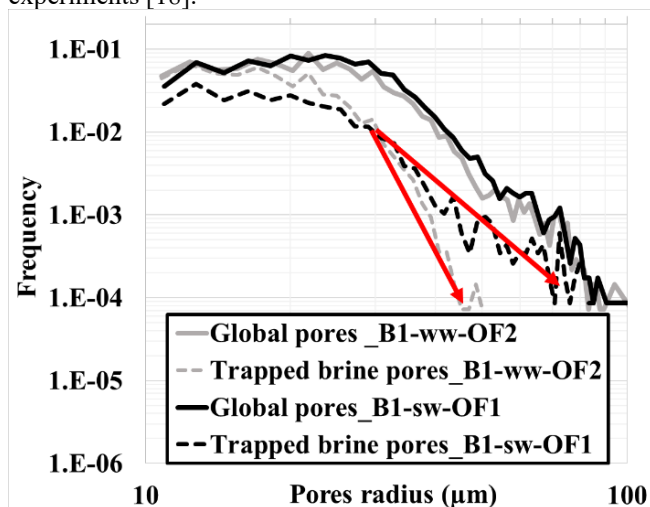


Figure 9. Comparison between water pore occupancy of a water-wet Bentheimer (B1-ww-OF2) and a Surfasil-treated Bentheimer (B1-sw-OF1) at same S_{wi} .

Results are depicted in figure 9. Continuous lines refer to total pores radius distribution and the dashed lines refer to distribution of pores radius in which at least 50% of brine is present.

Due to image segmentation uncertainties, we choose to remove all pores radius below $10\mu\text{m}$ so that the minimum pore diameter investigated is at least five times the pixel resolution ($5 \times 4\mu\text{m} = 20\mu\text{m}$). We consider that this is the minimum size detectable by our segmentation process without large uncertainties. For both samples, we analyzed approximately the entire pore volumes. As expected, both samples exhibit the same total pore radius distribution curves confirming the good similar pore network of different Bentheimer plugs.

At S_{wi} for the water-wet case (grey color), there is 100% water in the smallest pores and the number of these pores decreases sharply when increasing pores radius. Above $50\mu\text{m}$ of radius, no more water pore exists. For surfasil-treated sample at S_{wi} , a higher fraction of small pores than the water wet case are filled with oil whereas the sample is initially 100% water saturated as the water-wet case. It means that oil displaced water in small pores and throats more easily than the water-wet case. When we increase in pores/throats radius, pores filled with water decrease but less quickly than the water-wet case. The contrast due to wettability is less abrupt than the water-wet case. At $30\mu\text{m}$, there is a cross. The fraction of water pores become greater in the surfasil-treated case than in the water-wet case, till very big pores. There are larger pores/throats occupied by water for the surfasil-treated samples than the water-wet plugs.

Maximum water pores radius is around $90\mu\text{m}$, almost 2 times higher than the water-wet case.

- **B1-sw-OF2**: The experiment done on **B1-sw-OF1** was repeated on **B1-sw-OF2** but this time the maximum capillary number used was 4 times greater than the previous one. S_{wi} was decreased down to 18.5% but still remained 10p.u higher than water-wet cases at lower capillary numbers. On figure 10, we achieved pore occupancy comparisons between **B1-sw-OF2** and the water-wet case **B1-ww-OF2** ($S_{wi} = 18.5\%$ and $S_{wi} = 31\%$ respectively).

For the surfasil-treated sample (black color), some smallest pores are filled with oil. When pore radius increases, we observe a progressive and linear trend which is a decrease of water pores till $\sim 30\mu\text{m}$ meaning that water mobilization affects all pores radius between $10\mu\text{m}$ and $30\mu\text{m}$. Whereas for the water-wet case, the curvature confirms that the decrease is a function of size: big pores first before the small ones. After $37\mu\text{m}$, Surfasil-treated curve (dashed black in figure 10) shows a sharp decrease, but the largest pore remains larger than the water-wet case (red circle in figure 10).

It confirms that even at moderate to lower water saturation, the pore occupancy dynamic remains affected, and the sequence of filling or trapping is totally different from a water-wet case. Lower targets of S_{wi} will be difficult to obtain in these cases because of the initial wettability.

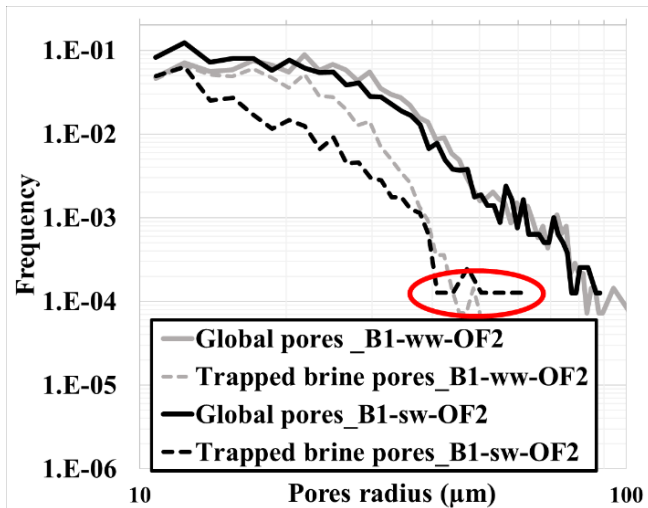


Figure 10. Comparison between water pore occupancy of a water-wet Bentheimer (B1-ww-OF2) and a Surfasil-treated Bentheimer (B1-sw-OF2).

To highlight the impact of this pore occupancy, we measured the effective permeabilities of oil for the surfasil treated samples for S_{wi} 's = 18% and 35% (figure 5). The effective permeabilities calculated are clearly under the trend with differences up to 0.2 units. The oil phase network has its effective permeability reduced by the presence of water trapped in many big pores.

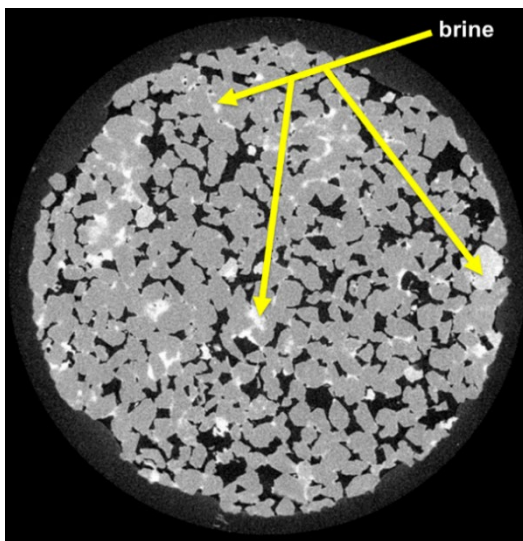


Figure 11. 2D slice of B1-sw-PP at S_{wi} . Water remains in small pores, crevices, corners, and clays.

- **B1-sw-PP:** This experiment was achieved on a 4mm diameter plug without the possibility to measure effective permeability as the cell was not available. Porous plate primary drainage is operated in this case with a full porous plate without any center hole to measure flow properties. A highly doped brine was used in this case. The capillary pressure applied was 100 mbars as for the maximum capillary pressure applied on water-wet cases in section 3.1.1. Surprisingly, the S_{wi} obtained was low (figure 7), almost with same visual occupancy (figure 11) than the water-wet case. Water remained in clays and in very narrow pores. If the system is completely oil-wet, we expect the

filling sequence to be reversed with oil filling preferentially the small pores before the big pores and we expect to see disconnected blobs of brine trapped in some big pores as we observed on B1-sw-OF1. The results obtained then raised some questions:

(i) Does the surfasil treatment in this case was not done properly? – Samples were prepared through a series of batches. The Surfasil-treated samples used in this study come from the same batch. The probability that this sample followed a process different from the others is very low regarding waterflooding results on which the observations made were similar to what observed on figure 1 for surfasil treated samples.

(ii) Is there a difference between the trapping occurring during OF and PP? – Trapping may differ. For a water-wet case, at high pressures, S_{wi} is finished to be achieved by films drainage no matter if we are performing OF or PP method. High pressures will always lead to decrease S_{wi} as water layers remain connected. For a non-water-wet case, no initial layer flow is available to decrease S_{wi} with increasing pressure. In addition, the frontal invasion evolves with a constant pressure during PP method whereas it varies for the OF method meaning the invasion patterns could differ and so could be the trapping behind the front. The OF capillary pressure distribution is not homogeneous at S_{wi} whereas PP capillary distribution is.

(iii) Wettability obtained with surfasil treatment is close to an intermediate wettability? – If the system is neutral wet ($\theta \sim 90^\circ$), water production is maximized at breakthrough during primary drainage as capillary forces are very low and very low S_{wi} value is expected. But it should also be the case during oil flooding. We observed that it is not (figure 1). Further investigations are needed on this topic. The next step will be to observe the filling sequence at the pore scale through X-ray imaging of the intermediate equilibrium capillary pressures stages.

3.2. High targets of S_{wi}

3.2.1. High S_{wi} on water-wet porous media

Samples concerned: **B1-ww-OF2, B1-ww-OF3, B1-ww-PP2 and B2-ww-CF.**

In this section capillary end-effects (C.E.E) are expected to be the main issue to cope with. For OF and CF experiments,

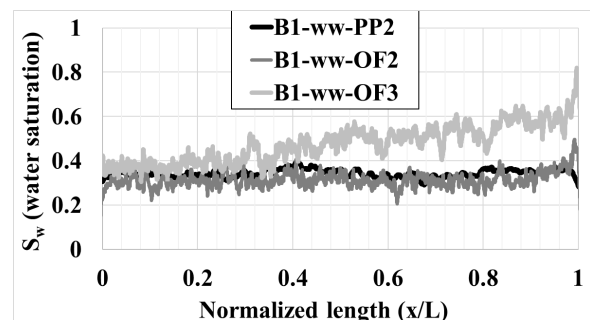


Figure 12. Saturation profiles of water-wet Bentheimer samples at the end of primary drainage (after reversals), targeting high S_{wi}

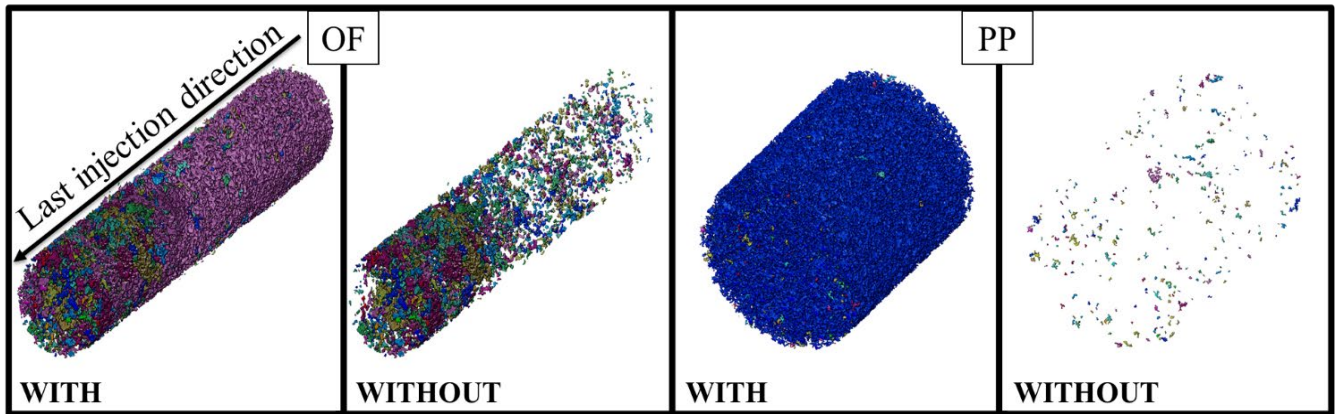


Figure 13. Example of oil disconnected clusters after primary drainage with and without the percolating cluster. We observe less disconnected and well distributed clusters for the PP method and the opposite for the OF method (**B1-ww-OF2** and **B1-ww-PP2**)

reversal flooding and spinning were achieved to flatten saturation profiles impacted by C.E.E. Effective permeabilities at S_{wi} on PP and OF experiments are available.

For the CF experiment, due to its latest arrival into the experimental pipe, we just achieved a quick test to confirm the dynamic and crucial observations that were observed especially during the OF experiment. Thus, saturation profiles which are reported on figure 12 do not concern CF experiment. As expected, for OF profiles, we observe gradients of saturation, especially near the outlet end face of plugs even after reversal flows. PP gives very homogeneous results.

Despite saturation gradients, the $K_o(S_{wi})$ reported on figure 5 are in a cloud which is near the literature curve. Capillary end-effect should normally highly impact effective permeabilities, and more when the sample is so permeable [9, 20]. A lot more experiments must be achieved to be able to detect a trend.

The crucial differences come from pore scale investigations. 3D images at S_{wi} were segmented and oil total volume was isolated. We observed a lot of disconnected oil clusters for samples gone under OF method. The principal oil cluster is connected from the inlet to the outlet, but the fraction of the disconnected clusters which are not taking part to the flow varied from 5% (very flat saturation profiles with little C.E.E as **B1-ww-OF2**) to almost 15% of the total oil volume (high saturation gradient as **B1-ww-OF3**) whereas the PP method gave a maximum of 0.1% of disconnected cluster mainly ascribed to segmentation uncertainties. For example, on figure 13, we show an entire OF sample and an entire PP sample with and without the percolating cluster. Each colored cluster is a disconnected cluster. When capillary end-effect is involved, a lot of clusters are disconnected because of the reversal flow. This is due to the brine held at the outlet by C.E.E which is being re-injected back-into the sample through oil injection from outlet to inlet. From a water-wet perspective, this causes a partial imbibition process with trapping of an important amount of oil. Afterwards, the pressure needed to access pores where there is trapped oil and reconnect these disconnected clusters will be higher than if no oil phase was trapped in these pores. Another observation is made on the clusters

size. In figure 14, we plotted clusters size (total volume in μ l) in function of their center of geometry on B1-ww-OF2.

In this graph, we do not represent the percolating cluster. We observe a general increasing trend of cluster size (red ellipse) when we go from inlet to outlet. Larger clusters are found near the outlet. This could be due to the decrease of capillary pressure towards the outlet end of the sample which causes disconnection of larger oil clusters during the re-imbibition process, on a few throats by snap-off or cooperative pore filling.

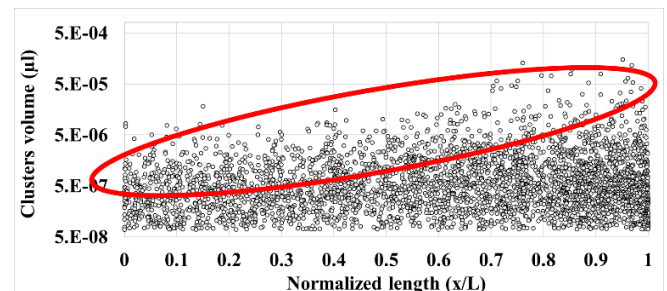


Figure 14. Disconnected oil clusters size distribution

A quick test was achieved with the CF cell and a small length plug (1cm) to confirm that this disconnection also happens on CF method when we do reverse the flow in the sample. Before the reverse, we will consider for the CF method that the drainage is done from the “first inlet” to the “first outlet”. Then when afterwards we turn the sample into the CF device to reverse the drainage, we consider that we go from the “last inlet” to the “last outlet”. Last inlet is the same location as the first outlet and last outlet is the same location as the first inlet. Without measuring multiphase flow properties, we first performed a quick primary drainage at low spinning rate to keep a large brine saturation at the outlet. Then, before the end of primary drainage we returned the sample and achieved another quick primary drainage at the same rate. We wanted to observe if:

- (i) The first inlet (which is the last outlet) had a lot of disconnected clusters?
- (ii) The last inlet had more connected clusters?

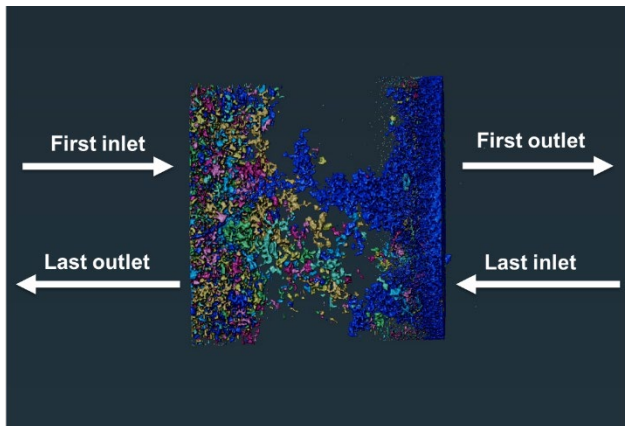


Figure 15. Clusters distribution at the end of the CF experiment. Each disconnected oil cluster has a different color.

In figure 15, we show oil clusters distribution at the end of the CF experiment. We observe a large cluster (blue) at the last inlet which is oil re-invading the pores from drainage process. This cluster seems connected with very few disconnected clusters around. Initially, as it was the first outlet, there was a high saturation of brine.

At the opposite, we observe a lot of disconnected oil cluster at the last outlet which was the first inlet before the reverse spinning. The oil that invaded initially this first inlet was then connected as the blue cluster. Because of the reverse spinning, the displacement of brine from the capillary end-effect zone to the inlet generated trapping of oil. With this quick experiment, it is now evidenced that the trapping observed is mainly due to re-imbibition processes and not image analysis uncertainties or something else.

For OF and CF, there can be a non-neglectable number of disconnected clusters at the end of flooding or spinning even if the saturation profiles seem flat after reversals. These disconnected oil clusters have a good probability to not be reconnected during replacements with crude oil or after ageing. Thus, the wettability in these pores after ageing may be different from the other pores crossed by the percolating cluster.

The variation of clusters size towards the outlet can affect wettability homogeneity within the sample. Despite a flat saturation profile, the disconnected oil acts apart from the principal channel of flow. In this case, wettability may be well altered at the inlet and less at the outlet.

3.3. Cleaning efficiency impact

Samples concerned: **B2-ww-OF1** and **B2-ww-OF2**

In this section we choose two samples that underwent the overall proc.2. Ageing achieved with crude oil changed the wettability of the plugs from water-wet to weakly water-wet or mixed-wet behaviour. An example of ROS profile is depicted in figure 16. The ROS was around 20% while for water wet Bentheimer sandstone, residual oil saturation is around 30% to 45% [9]. We also could clearly identify a slight capillary end effect to oil near the outlet which confirms that the wettability of the samples was altered using dead oil A.

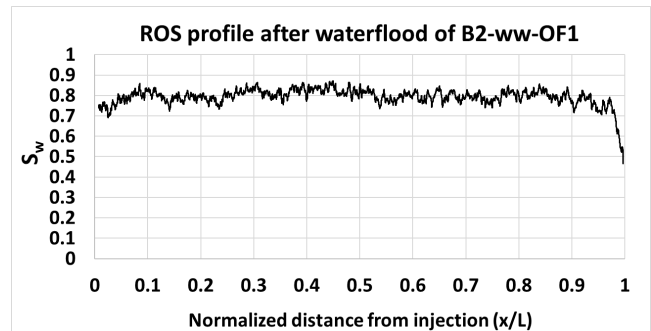


Figure 16: ROS profile obtained after the first waterflood of B2-ww-OF1 following 2 weeks of ageing with dead oil A.

The only difference between the two samples used in this section is that **B2-ww-OF1** was cleaned using only one loop (figure 3) and **B2-ww-OF2** was cleaned with a multi-loop process. The goal is to compare the two primary drainages: before and after cleaning, which are performed using identical flooding conditions.

In table 3, we reported experimental properties measured on both samples during proc.2.

Table 3. Properties measured on Bentheimer samples during proc.2 achievement.

Sample name	K_w before cleaning (D)	S_{wi} before cleaning (%)	S_{wi} after cleaning (%)	K_w after cleaning (D)
B2-ww-OF1	2	5.3	10.6	1.4
B2-ww-OF2	1.98	4	22	1

We do observe a reproducible increase of S_{wi} after cleaning despite identical capillary numbers and pore volumes injected to the initial primary drainage before cleaning and a reproducible decrease of absolute permeability after cleaning.

An illustration of this increase is presented on a 2D slice of B2-ww-OF1 in figure 17. We observe that in general, the increase of S_{wi} is principally located in very narrow pores.

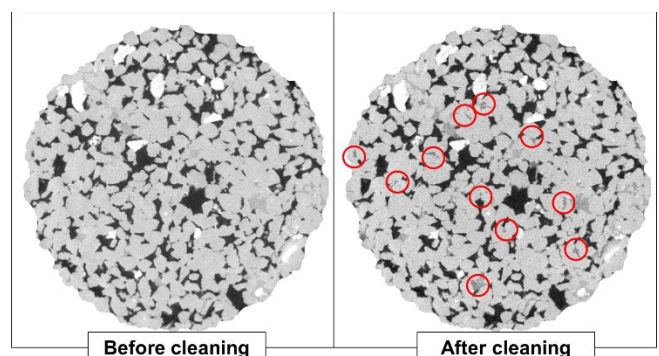


Figure 17. Comparisons of 2D slice at S_{wi} before cleaning and After cleaning of B2-ww-OF1

We also observed an important reproducible decrease of permeability after cleaning, which can lead to almost 50% loss of absolute permeability without any observable change on 3D images. Additional experimental investigations showed that this decrease happens when the mix of the two solvents (Toluene and isopropyl alcohol) is injected into the samples. The physical reasons are not yet understood and

are still under investigations but if the pore-network is conserved, then the issue is probably under resolution thus maybe in clays.

Regarding these results, we had two possibilities of explanations:

- (i) The increase of S_{wi} after cleaning is not linked with the loss of permeability: then it means that despite the cleaning, the final wettability may not come back to its initial state. We could be in presence of a weakly water-wet pore network with less strongly water-wet pores thus water trapped in more and more narrow to intermediate pores-throats sizes.
- (ii) The increase of S_{wi} after cleaning is linked with the loss of permeability: which is also likely to happen as at constant wettability, a loss of permeability increases the displacement pressure needed to invade pores (capillary forces). As we used the identical protocol of primary drainage before cleaning, we can only reach higher values of S_{wi} as viscous forces are not enough to counterbalance this increase in capillary forces.

4 Conclusions

This paper presents a detailed analysis at the pore-scale of different methods to achieve S_{wi} considering wettability. Bentheimer sandstone was used with different initial wettability.

What lessons can be learned about this experimental investigation?

- The porous plate method remains the most robust technique at almost all points of view. The only drawback is about the time needed to achieve an experiment.
- For low S_{wi} on water-wet plugs, we observe no distinction on fluids connectivity, pore occupancy and no capillary end effects between these initialization methods. However, a special caution must be required for the OF method. As shown by Rucker et al. [11, 12], clear distinctions can arise at the nanoscale on surface coverage. The lack of capillary pressure and the trend to bypass parts of the pore network for the OF method decreases the capacity to change wettability than the CF and the PP methods where we have control of the applied capillary pressure thus the invaded pore/throat sizes. When possible, one should clearly privilege PP method as it maintains a constant capillary pressure through the sample's length. It has the advantage that it can be used for short or long cores, in jackets with pore pressures and at temperature. It is directly adapted for oil flooding set-ups. Some systems also exist coupling the PP method with flooding experiments [16]. If not possible, it is generally better to rely on the CF method to achieve S_{wi} . The main advantage of CF regarding OF is that we avoid bypassing pore network structures and control the real capillary pressure versus length applied on the sample. Controlling capillary pressure distribution is a real advantage as one can size the threshold pressure which can counter-balance sufficiently the water films disjoining pressure so as to much better alter wettability. However, CF also suffers of capillary end-effects and there are some important constraints such as the samples length which is

limited, the experimental pressure and temperature which is most of the time at ambient conditions and the sample handling. Therefore, the coupling between PP and OF may be the best option taking into account all different constraints.

- For non-water-wet plugs, a conclusion is quite difficult to draw. According to our results that are to be confirmed with a lot more experiments, low initial water saturation is achieved with the porous plate method. We observed different sequence of trapping which may be due to the invasion patterns difference between methods. Oil flooding technique generates a lot of disconnected water clusters with a lower oil effective permeability. The pore occupancy (brine in large pores) is different from what is wanted.

- When targeting high S_{wi} (i.e. transition zone) on water-wet plugs, we must deal with capillary end-effect linked to a gradient of capillary pressure on the sample's length. It affects essentially OF and CF methods. If no porous plate is used then we should at least find a way to avoid saturation gradients, disconnecting oil clusters and more over homogenize water film thickness in the overall volume. As it is shown in this study, without optimized set-ups (coupling of OF and PP [16] for example) it is clearly impossible to avoid trapping when achieving reversals. But we can try to decrease its impact. Some ways forward to investigate can be suggested: (i) the first suggestion would be to start reversing the flow after the maximum capillary (OF) or bond number (CF) to be used for unidirectional injection. We can expect that it limits the water volume held at the outlet (C.E.E) that will be re-injected in the sample and the reverse will act to thicken the large water films left near the outlet volume because of the capillary end effect. (ii) the second suggestion which should come after achieving the first one would be to perform several reversals at maximum capillary and bond number to avoid heterogeneity in terms of clusters size towards sample's length for the disconnected clusters. The goal here would be to reconnect the maximum of possible clusters to the principal percolating oil cluster and to homogenize disconnected clusters sizes towards the sample's length. Then a nano-scale study of surface coverage as done by [11, 12] has to be achieved to clarify whether these reversals help to homogenize the potential of having wettability altered through the overall length of the sample.

We thank TotalEnergies for their financial support and the permission to publish this paper. We also acknowledge Dr. M. Regaieg, Dr. F. Pairoys, Mr Q. Danielczick, Mr R. Brugidou and Mr M. Bizeau for their insightful discussions and contributions.

References

1. Z. Zubo, L. Manli and C. Weifeng, "An Experimental Study of Irreducible Water Saturation Establishment", International Symposium of Core Analysts, Avignon, France, 2014 [SCA2014-070]
2. M. Fleury, "The spinning porous plate (SPP) method: a new technique for setting irreducible water saturation on core samples", International Symposium of Core Analysts, Noordwijk, Netherlands, 2009 [SCA2009-08]
3. C. McPhee, J. Reed and I. Zubizarreta, "Core analysis: a best practice guide", Amsterdam: Elsevier, 2015.
4. R. Farokhpoor, L. Sundal, A. Skjaerstein, A. Hebing, X. Zhang and L. Pirlea, "Core cleaning and wettability restoration – selecting appropriate method", International Symposium of Core Analysts, 2021 [SCA2021-016]
5. O. Vizika, J.P. Duquerroix, "Gas injection and Heterogeneous Wettability: what is the relevant information that petrophysics can provide", International Symposium of Core Analysts, Calgary, Canada, 1997 [SCA-9708].
6. C. J. Landry, Z. T. Karpyn and M. Piri, (2011). Pore-scale analysis of trapped immiscible fluid structures and fluid interfacial areas in oil-wet and water-wet bead packs. *Geofluids*, 11(2), 209-227. <https://doi.org/10.1111/j.1468-8123.2011.00333.x>. De Lillo, F. Cecconi, G. Lacorata, A. Vulpiani, *EPL*, **84** (2008).
7. C.A. McPhee, and K.G. Arthur. "Relative Permeability Measurements: An Inter-Laboratory Comparison." Paper presented at the European Petroleum Conference, London, United Kingdom, October 1994. doi: <https://doi.org/10.2118/28826-MS>. C.A. McPhee & K.G. Arthur SPE 28826 October 25-27 1994.
8. Wilson O.B., Tjetland B.G. and Skauge A., "Porous plates influence on effective drainage rates in capillary pressure experiments", International Symposium of Core Analysts, Edinburg, Scotland 2001 [SCA2001-30].
9. F. Nono, P. Moonen, H. Berthet and R. Rivenq, "Multiphase flow imaging through X-ray microtomography: Reconsideration of capillary end-effects and boundary conditions", International Symposium of Core Analysts, Pau, France 2019 [SCA2019-019].
10. F. Pairoys, C. Caubit, M. Alexander and J. Ramos, "Comparing Centrifuge, Steady-State and Semi-Dynamic methods for relative permeability and capillary pressure determination: New Insights", International Symposium of Core Analysts, Online, 2021 [SCA2021-019].
11. M. Ruecker, W.-B. Bartels, G. Garfi, M. Shams, T. Bultreys, M. Boone, S. Pieterse, G. C. Maitland, S. Krevor, V. Cnudde, H. Mahani, S. Berg, A. Georgiadis, P. F. Luckham, Relationship between Wetting and Capillary Pressure in a Crude Oil/Brine/rock system: From Nanoscale to Core-Scale *Journal of Colloid and Interface Science* 562(7), 159-169, 2020.
12. M. Rücker, W.-B. Bartels, T. Bultreys, M. Boone, K. Singh, G. Garfi, A. Scanziani, C. Spurin, S. Yesufu, S. Krevor, M. J. Blunt, O. Wilson, H. Mahani, V. Cnudde, P. F. Luckham, A. Georgiadis and S. Berg, "Workflow for upscaling wettability from the nano- to core-scales", International Symposium of the Society of Core Analysts, Pau, France, 2019 [SCA2019-07]
13. Q. Lin, Y. Al-khulaifi, B. Bijeljic and M.J. Blunt, (2016). Quantification of sub-resolution porosity in carbonate rocks by applying high-salinity contrast brine using X-ray microtomography differential imaging. *Advances in Water Resources*. 96. 10.1016/j.advwatres.2016.08.002. A. Mecke, I. Lee, J.R. Baker jr., M.M. Banaszak Holl, B.G. Orr, *Eur. Phys. J. E* **14**, 7 (2004)
14. Q. Lin, B. Bijeljic, H. Rieke and M. J. Blunt, (2017). Visualization and quantification of capillary drainage in pore space of laminated sandstone by a porous plate method using differential imaging X-ray microtomography. *Water Resources Research*, 53, 7457–7468. <https://doi.org/10.1002/2017WR021083>
15. H. Berthet, P. Andriamananjaona, S. Barboutreau, M. Hebert, R. Farwati, R. Meftah, G. Quenault, J.P. Chaulet, R. Brugidou, and R. Rivenq, "Capillary desaturation curves and insights on trapped oil at the pore-scale, in water-wet and oil-wet sandstones," International Symposium of the Society of Core Analysts, SCA2018 Trondheim, Norway, (2018) [SCA2018-036].
16. C.H. Pentland, R.M. El-Maghraby, S. Iglauer and M.J. Blunt, "The toroidal porous plate: A new method to facilitate waterflooding", International Symposium of the Society of Core Analysts, SCA2014, Avignon, France 2014 [SCA2014-068].
17. A.G. Raeini, B. Bijeljic, M.J. Blunt: Generalized network modeling of capillary-dominated two-phase flow. *Physical review*.E97(2-1), 23308 (2018). Doi:10.1103/PhysRevE.97.023308. De Lillo, F. Cecconi, G. Lacorata, A. Vulpiani, *EPL*, **84** (2008)
18. M. Regaieg, I. Bondino, C. Varloteaux, T.F. Faisal, J. Yang and R. Rivenq, "Large two phase Digital Rock Physics simulations for relative permeability uncertainty assessment", International Symposium of the Society of Core Analysts, SCA 2021, Online, [SCA2021-007].
19. M.J. Blunt, "Multiphase Flow in Permeable Media: A Pore-Scale Perspective," Cambridge University Press. doi: 10.1017/9781316145098, 2017
20. S.K. Masalmeh, " Impact of capillary forces on residual oil saturation and flooding experiments for mixed to oil-wet carbonate reservoirs", International Symposium of the Society of Core Analysts, Aberdeen, Scotland, 2012 [SCA2012-11].

Numerical study of NMR relaxation responses in synthetic clayey sandstone by dual-scale modeling

Yingzhi Cui, Igor Shikhov, and Christoph Arns*

School of Minerals and Energy Resources Engineering, University of New South Wales, Sydney, Australia

Abstract. Nuclear Magnetic Resonance (NMR) relaxometry is a common technique for petrophysical characterization of sedimentary rocks. The standard interpretation of NMR relaxation response assumes that the fast diffusion limit is valid for the whole pore space, allowing to translate transverse relaxation components into pore apertures. However, porous media naturally exhibit multiple length scales. The diffusion between different sized pores may modify the transverse relaxation rate, weakening the relationship with corresponding pore size populations. Focusing on sandstones, we investigate the impact of diffusion coupling on transverse relaxation depending on kaolinite amount, spatial distribution and temperature. A series of synthetic clayey sandstone models with different clay amounts and morphological distributions (pore-lining, pore-filling and laminated) are generated based on a micro-CT image of an actual Bentheimer sandstone. A dual-scale random walk NMR relaxation simulation with resolved multi-porosity kaolinite models is utilized to avoid problems in near to interface exchange regions typical for effective medium representations. Simulations provide spatially resolved dynamics of magnetization exchange between different porosity populations. The results indicate that increased temperature and kaolinite clay amount with lower micro-porosity allows higher magnetization exchange between micro- and macro-porous regions. Pore-lining clay demonstrates stronger diffusional coupling effects, leading to an overestimation of micro-porosity. We further discuss the impact of diffusion coupling on NMR-estimated permeability via SDR and Coates models.

1 Introduction

Nuclear magnetic resonance (NMR) well logging is an important formation evaluation technique widely utilized for estimation of reservoir petrophysical properties, such as fluid types, saturations, and permeability. The interpretation of NMR data assumes that diffusing protons sample isolated pores (the so-called fast diffusion limit), in which case the observed relaxation rate is related to the surface-to-volume of individual pores [1]. However, molecular diffusion between different pore populations, referred to in literature as diffusional coupling, may lead to erroneous predictions if being unaccounted for. In fact, diffusional coupling appearing as magnetization exchange in NMR data is closely related to the connectivity between micro- and macro-porosity. It has been shown that depending on spatial distribution in rocks, microporosity may be a significant contributor to transport properties and may be responsible for a significant increase of the electrical conductivity [2], higher than anticipated hydraulic flux [3], and may control grain dissolution [4] or wettability alteration through asphaltenes deposition rate. While in this work we focus on the impact of diffusional coupling in the context of NMR interpretation, specifically on the relationship between magnetization exchange and transverse relaxation (T_2), the developed analysis is applicable to all mentioned transport problems.

The diffusional coupling phenomenon in respect to NMR data analysis has been extensively studied in synthetic porous media [5, 6], or sedimentary rocks, namely carbonate [7 - 10] and shaly sandstone [6, 11]. It has been reported in literature

that two key petrophysical properties estimated from T_2 responses (irreducible water saturation and permeability) are affected if magnetization exchange between distinctive pore populations is significant. The standard practice in NMR core analysis is to relate T_2 values to pore size, i.e. the short relaxation time components of the T_2 distribution can be attributed to irreducible or capillary bound water (CBW), while the longer time components separated by the cutoff value ($T_{2,cutoff}$) correspond to mobile fluid in larger pores (known also as free fluid index FFI) [12]. However, it was demonstrated that calculated BVI values from NMR T_2 responses of sedimentary rocks exhibiting a well-coupled pore system are prone to large errors approaching 50% [15]. Interestingly, it was observed that at high temperature these effects were far less severe than at ambient temperature. The exact reason of this observation was not established since temperature dependence of governing physical properties (increase of self-diffusion coefficient of fluids and surface relaxivity [16]) suggests exactly the opposite. It is fair to acknowledge the limitation of the numerical simulation model used by [15], excluding internal field gradients effects from consideration. In addition, the temperature dependence of surface relaxivity is still poorly understood – both increases and decreases with temperature are reported in literature [6]. In the case of complete coupling, the micro- and macro-pores cannot even be identified from T_2 distribution resulting in the erroneous estimation of irreducible saturation [11].

NMR based permeability is estimated using one of two correlations: T_{2m} - based SDR equation (after Schlumberger

* Corresponding author: c.arns@unsw.edu.au

Doll Research) [17] and $T_{2,cutoff}$ - based Coates model [18]. The magnetization exchange tends to shift one of the two coupled components – the one having a longer relaxation time – towards a shorter relaxation time [19], affecting NMR-related components of both models (T_{2lm} , CBW/FFI) and creating poor estimates. For instance, [8] demonstrated that permeability estimations based on SDR model for different rocks could exhibit relative errors up to 15%. [20] shows that T_2 shifts to shorter times because of intermediate diffusion coupling between micro- and macro-pores in chlorite-coated sample leading to inaccurate permeability estimation. In addition, a pore-connectivity parameter, introduced for the Coates model, offers more precise permeability and movable fluid volume estimates in complex coupled pore geometry [21]. The study [22] further extended to directional pore-connectivity factor to accurately characterize anisotropic directional permeability of sedimentary rock with NMR measurements.

Numerically diffusional coupling was analyzed in the context of relaxation in ideal pore networks [23]. Three geometrical models were presented to describe magnetization decay in carbonates with mixed intra- and intergranular porosity [24]. They reported that diffusional coupling may cause a shift of the longer relaxation peak and distort the amplitudes of the T_2 distributions. [7] further investigated coupling effects based on a 3D sphere model; constant internal magnetic gradient assumed. The results indicate that inter-pore diffusion has a strong impact on NMR measurements. More recently, simulations based on 3D periodic micro-porous grain consolidation models support the interpretation of NMR measurements in terms of magnetization exchange between dual-scale pore system [25 - 27]. The simplified models miss the morphological and geometrical information of the sedimentary rocks. To have an explicit representation of porous media, the X-ray micro-CT tomography was employed. Pore-pore coupling was analyzed by tracking random walkers within the partitioned pore space, which demonstrates that diffusion between pores occurs to a significant degree [28]. A numerical study on fractured carbonates [29] established that diffusional coupling may lead to underestimation of intergranular porosity by more than 10%. Although micro-CT images can offer more accurate internal structures of rock, micro-porosity often cannot be fully resolved due to either resolution limitations or simultaneous requirements of resolution and field of view. The non-resolved intermediate phase is then treated either as effective medium [28] or merged into the solid phase [30]. Yet, scanning electron microscopy (SEM) micrographs even of relatively simple rocks like Bentheimer sandstone (Fig. 1) indicate that the realistic micro-structure is complicated. Clay particles may fully or partially fill the pore space with heterogeneous local micro-porosity for each clay pocket. More generally, clay may also coat solid grains or appear as thin laminations [31]. These differences in the spatial distribution of clay as well as varying clay porosity and connectivity invite more complex coupling effects.

In this work we consider the impact of the spatial distribution and amount of clay on NMR relaxation responses. A simulation-based methodology is employed, which enables the quantification of the diffusional coupling phenomenon, in particular the evolution of magnetization across clay interface and impact on NMR relaxation derived

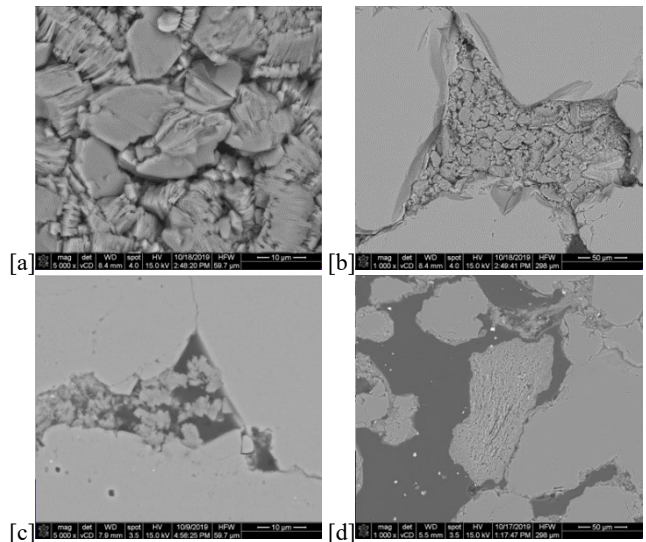


Fig. 1. [a] SEM image of kaolinite pocket in Bentheimer Sandstone; [b] Low porosity full-filled kaolinite pocket. [c] Medium porosity partial-filled kaolinite pocket. [d] Coated clay around quartz.

petrophysical properties such as irreducible water saturation (BVI) and permeability. A series of synthetic clayey sandstone models are generated with different clay amounts (6 vol% - 16 vol%) and synthetic morphological distributions (loosely termed coated, laminated, pore-lining and pore-filling) combined with resolved multi-porosity kaolinite models to track magnetization exchange between macro- and micro-pores. The evolution of magnetization exchange between different porosity populations is captured as function of observation time and penetration depth, together with the increase in the diffusion coefficient due to temperature; other intrinsic physical parameters like mineral-specific surface relaxivities are set constant in this fundamental study. Accounting for these effects from clay consequently improves NMR-estimated permeability via SDR and Coates models and enables more robust petrophysical interpretations.

2 Methodology

The objectives of this study require generation of clay distributions at different scales ranging from dispersed (pore-lining and pore-filling) to coated and laminated clay types. In the following we first introduce the methods for the coarse-scale distribution of clay regions, followed by fine-scale clay structure modeling, associated NMR simulations, and regional analysis fields embedded in the NMR solver enabling the local tracking of magnetization exchange. This is followed by a recapturing of NMR permeability correlations and the determination of permeability from tomographic images using the lattice Boltzmann technique.

2.1 Synthetic Clayey Sandstone

The synthetic clayey sandstones 3D models utilized in this study are based on the micro-CT image of Bentheimer sandstone shown in Fig. 2 and the SEM images (Fig. 1). The latter shows that pores of the original rock can be either fully or partially filled with kaolinite aggregates. Furthermore, those clay pockets exhibit different aggregate density and

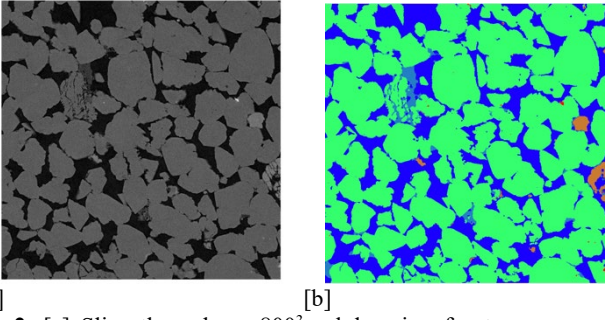


Fig. 2. [a] Slice through an 800^3 subdomain of a tomogram of Bentheimer sandstone at a resolution of $2.2 \mu\text{m}$ voxel and [b] corresponding five phase segmentation. The colors are: dark blue - pore, green - quartz, cyan - clay, brown - feldspar, red - high-density minerals.

thus clay region porosity. This translates to clay regions with different intensity in the micro-CT images, where clay particles are not resolved (Fig. 2a). It is assumed that the intensity of kaolinite particles is similar to quartz. Therefore, the intensity in each clay region (I_c) is volume-weighted by the pore intensity (I_p) and quartz intensity (I_q). The intensity distribution of clay pockets (Fig. 3a) shows that the major values are around 1.2×10^4 to 1.3×10^4 . The porosity of each clay pocket is estimated by $\phi_k = (I_q - I_c)/(I_q - I_p)$. The corresponding distribution shows that clay region porosity falls mainly into the range of 0.3 - 0.6 (Fig 3b). Consequently, we allowed for four discrete clay porosity labels corresponding to clay porosity of $\phi_c \in \{0.3, 0.4, 0.5, 0.6\}$.

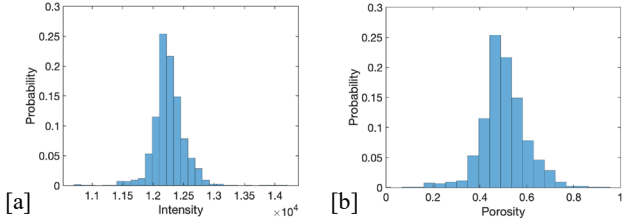


Fig. 3. [a] Intensity probability distribution of all clay pockets in the Bentheimer micro-CT images; [b] corresponding porosity distribution of clay pockets.

Four different clay distributions are constructed: pore-filling, pore-lining, coated and laminated. The models are generated with different clay volume fractions of 6 vol%, 11 vol% and 16 vol% to investigate the effects from clay amount. For pore-filling clay pockets we divided the resolved pore space into convex regions or pores. This is achieved by performing a watershed transformation [33] on the Euclidean distance map [34, 35] (Fig. 4a). We randomly assign the clay phase to the partitioned pores until the clay volume fraction meets the requirement. For pore-lining clay pockets, we determine the center for each pore (Fig. 4b) and preserve the pore fraction corresponding to the maximal inscribed sphere as pore space.

The remaining pore space is assigned as clay, resulting in a partial-filled clay layer of varying thickness. The coated clay phase is assigned only based on the distance threshold of EDT map. For laminated clay, we generated different layered system according to kriging interpolation method with random range, sill, and nuggets for mimicking the clay distribution.

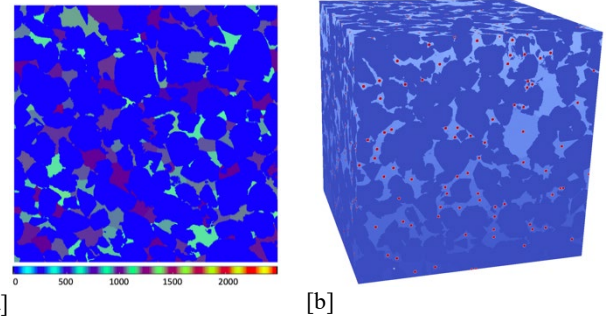


Fig. 4. [a] Slice through the 800^3 watershed pore partitioning - region boundaries are the watersheds of the EDT, and [b] a 3D visualization of the centers in 800^3 watershed pore partitioning. Resolution: $2.2 \mu\text{m}/\text{voxel}$.

To satisfy the clay volume fraction, the mean thickness values of each horizon are different. To reduce discretization effects from the image and force an accurate calculation of the internal magnetic fields [32], a tri-linear interpolation is applied with factor 4 refinement. Thus, the original 800^3 domain is refined to 3200^3 voxels with voxel size of $0.55 \mu\text{m}/\text{voxel}$ and smoother solid surface shown in Fig 5.

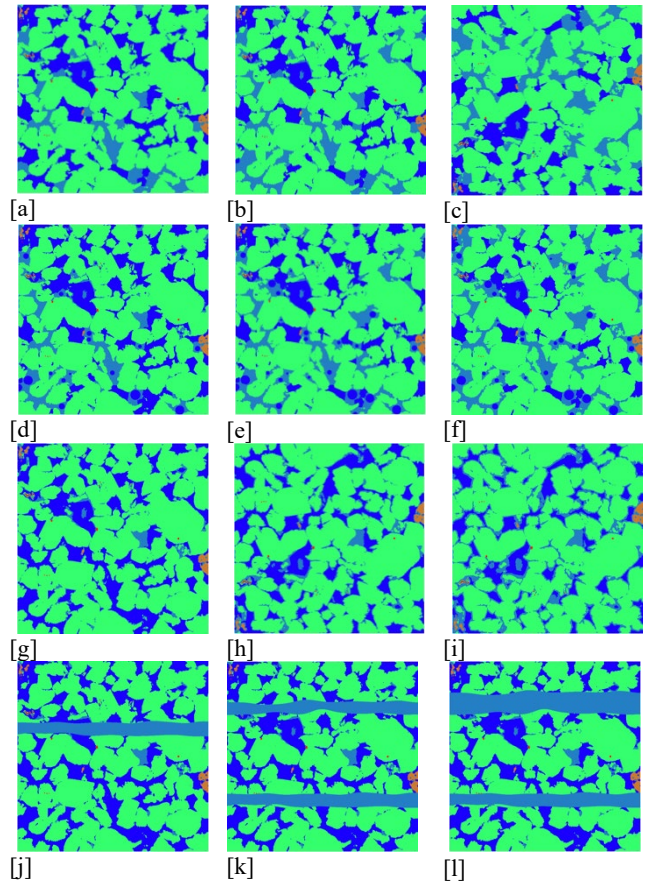


Fig. 5. Slices of 3200^3 synthetic clayey sandstone (resolution $0.55 \mu\text{m}/\text{voxel}$). [a-c] pore-filling clay; [d-f]: pore-lining clay; [g-i]: coated clay; [j-l]: laminated clay. The left column with 6 vol% clay phase, the middle column with 11 vol% clay phase and the right column with 16 vol% clay phase. The colors are: dark blue - pore, green - quartz, cyan - clay, brown - feldspar, red - high-density minerals.

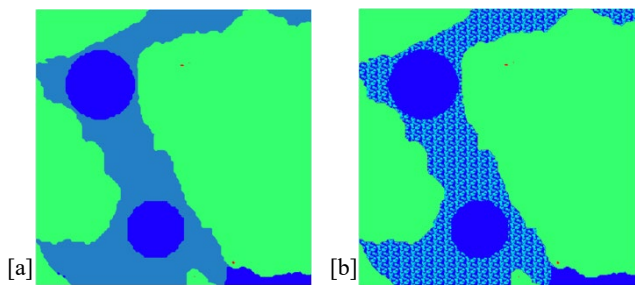


Fig 6. [a] A 400^2 subsection of the 3200^3 synthetic clayey sandstone (16 vol%) with unresolved clay phase and voxel size of $0.55 \mu\text{m}$. [b] Corresponding 10000^2 cross-section of [a] where each clay pocket is replaced by the corresponding kaolinite model. The resolution of the fully resolved model is 22 nm/voxel. The color schemes is: dark blue - pore, green - quartz, cyan - clay, brown - feldspar, red - high-density minerals.

2.2 Kaolinite Model

Kaolinite is one of the most common clay mineral constituents of sedimentary rocks, especially in sandstones. However, the microstructure cannot be fully resolved in the micro-CT image due to resolution limitations (Fig. 2). To resolve the microstructure within kaolinite pockets, we reconstruct 3D volumetric kaolinite models following the method detailed in [36]. In this study, we discretize the kaolinite microstructure as a periodic domain of 400^3 voxel with resolution of 22 nm, which is 1/100 of micro-CT image resolution. Four realizations with average porosity $\phi_c \in \{0.3, 0.4, 0.5, 0.6\}$ are constructed. Surface area S_v and $T_{2\text{eff}}$ of the clay models are reported in Table 1 and are in agreement with published surface area measurements [6, 37] and T_2 values [38]. Here, the density for kaolinite we used is 2.6 g/cm^3 . The surface relaxivity (ρ_2) is $1.2 \mu\text{m/s}$. For NMR simulations the unresolved clay regions of the micro-CT images are replaced by the corresponding kaolinite model according to clay porosity. Fig. 6 depicts a subsection of the coarse scale model with unresolved clay regions, and the corresponding high-resolution model with fully resolved structure and different clay pocket porosity.

Table 1. Surface area (S_v) and effective relaxation time ($T_{2\text{eff}}$) of different porosity kaolinite model.

ϕ_c	$S_v (\text{m}^2/\text{g})$	$T_{2\text{eff}} (\text{ms})$
0.3	23.5	13.2
0.4	19.7	18.7
0.5	15.1	24.5
0.6	12.3	30.3

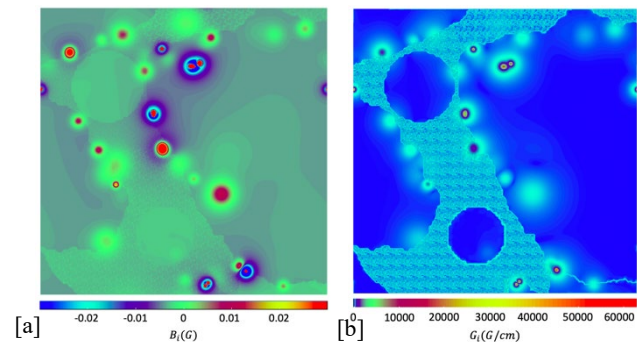


Fig 7. Cross-section of Fig 6 corresponding 10000^2 subset of [a] internal magnetic field distribution $B_i(\mathbf{r})$ and [b] internal magnetic gradient distribution $G_{\text{in}}(\mathbf{r})$ at 22 nm/voxel.

2.3 Dual-scale NMR Relaxation Simulation

The dual-scale NMR relaxation response simulation has been described in detail previously [32]. In this work the simulation approach is extended to clay regions with different porosity. Furthermore, we implement the tracking of magnetization for dual-scale simulations, following the approach of [39]. In the previous section we detailed our approach of combining the resolved clay regions with the micro-CT based segmented tomogram. This resulted in a micro-structure where the interpolated coarse-scale segmentation ($0.55 \mu\text{m}$ resolution) is mapped to a voxel size of 22nm, the same as the clay region models. Thus, a random walk could now in principle be carried out completely in the resolved pore space. However, for the simulation of the NMR transverse relaxation response the internal magnetic field at every location is required. The calculation of high-resolution internal magnetic fields (B_i) is achieved by a separation of near- and far-field effects in a dipole-approximation of the internal field with dual-scale samples [32]. This allows calculating the coarse-scale internal magnetic fields via Fourier methods. The fine-scale internal magnetic fields of the periodic clay models are calculated separately. Then, the fine resolution internal magnetic field can be calculated as a combination of the coarse scale field interpolated to a voxel size of 22nm and a perturbation from the fine-scale field. The latter is calculated by deducting the coarse scale trend from the fine-scale fields (ensuring zero mean at tomogram scale). Like the fine-scale microstructure, B_i is never stored in memory at full resolution (at $80,000^3$ voxel it would be prohibitively large) but constructed locally when required for either a random trajectory during NMR simulations, to visualize parts of the high-resolution internal magnetic field, or to extract statistics. An example of high-resolution B_i distribution and corresponding spatial internal gradient distribution (G_i) is shown in Fig. 7.

Once the magnetic field distribution is generated, the random walk algorithm is carried out on a regular cubic lattice with fine-scale resolution ($\epsilon = 22 \text{ nm}$). The corresponding time step τ_i of a step i is given by $\tau_i = 6D_0/\epsilon^2$, where D_0 is the free diffusion coefficient of water, which we here vary with temperature. Bulk and surface relaxation are implemented as signal weighting factors for each step, with $S_i = S_b S_s$. Here $S_b = \exp(-\tau_i/T_{2,b})$ is the contribution by bulk relaxation, and $S_s = 1 - 6\rho_2\tau_i/(\epsilon A)$ the contribution by surface relaxation, where ρ_2 is the surface relaxivity of solid. For steps within the same fluid $S_s = 1$. A is a correction

factor of order 1, which accounts for the details of the random walk implementation [40]. For imaged structures, this value is typically close to $A = 3/2$. Besides, the contribution of the internal field to dephasing is calculated explicitly written as $\Delta\phi$. The bulk relaxation, surface relaxation and phase variation caused by diffusive relaxation are then incorporated into the calculation of each walker's magnetization, which becomes

$$M_w(t_j) = M_w(0) \cos [\Delta\phi(t_j)] \prod S_i \quad (1)$$

Averaging over random walks and recording at $t = nt_E$ ($n=1,2,\dots,N$) results in the magnetization decay $M(t)$. The relaxation time distribution is obtained by fitting a multi-exponential decay to $M(t)$.

In this study, the NMR transverse relaxation response is simulated for a given Larmor frequency of $f = 2\text{MHz}$ and echo time $t_E = 200 \mu\text{s}$. For synthetic clayey sandstone, the surface relaxivity ρ_2 of the solid and the magnetic susceptibility χ of each phase are reported in Table 2.

Table 2. The surface relaxivity (ρ_2) and magnetic susceptibility (χ) of each phase assigned for NMR relaxation response simulation.

Phase	ρ_2 ($\mu\text{m/s}$)	χ (μSI)
Water	-	-8.9
Kaolinite	1.2	-11.0
Quartz	9.0	-12.0
Feldspar	9.0	-12.0
High-Density	60.0	5270

2.4 EDT Based Regional Magnetization Exchange

The magnetization exchange (or coupling) refers to a fraction of the spin population, which originates in one of the porosity types (e.g. macro-porosity) at the beginning of NMR signal acquisition, and found after a specific time interval (exchange time) in another porosity type (e.g. micro-porosity). The spin population in question should possess a measurable magnetization, thus defining a process sensitive to porosity types morphology and inter-connectivity.

Measuring the magnetization exchange between porosity partitions using random walk simulations is achieved by adding a phase label to the start and end positions of the walkers and employing the Euclidean distance transform (EDT). The former labeled phase can identify the diffusion of magnetization as macro-micro (start at macro-pore and end at micro-pore) and micro-macro (start at micro-pore and end at macro-pore). The latter EDT refers to a process that generates Euclidean distance fields for a 3D voxelized representation of samples. Valid distance values for each phase are calculated by assigning each voxel of the phase of interest the shortest distance to a voxel of another phase using distances between voxel centers. The implementation is a parallel version of algorithm 4 of [34]. An example of high-resolution EDT maps for macro- and micro-porous regions is depicted in Fig. 8. Given the distance information and phase labels, the quantification of the local magnetization evolution can now

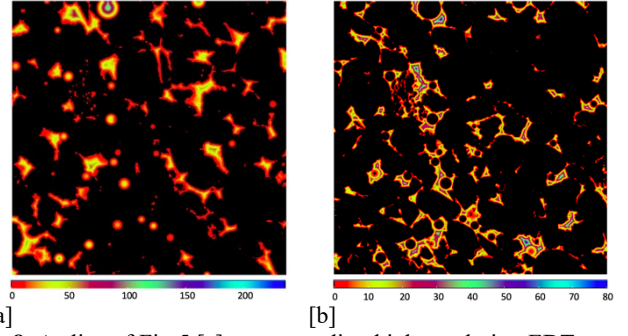


Fig 8. A slice of Fig 5 [c] corresponding high-resolution EDT map for [a] macro-pores in voxel unit, 3200^2 in $0.55 \mu\text{m/voxel}$; [b] micro-pores in voxel unit, 3200^2 in $0.55 \mu\text{m/voxel}$.

be achieved by counting the walker strength in respect to a particular shell and phase. This information allows tracking the penetration depth (d) of magnetization diffusing across different pore populations. In addition, the magnetization exchange is counted at different observation time $t = nt_E$ ($n=1,2,\dots,N$). Therefore, The magnetization exchange can be characterized as a function of penetration depth and observation time $M_{ex}(d,t)$.

2.5 Permeability Estimation

In this section we briefly overview common NMR permeability correlations as well as the lattice Boltzmann technique to calculate permeability directly from tomographic images. Together these techniques are utilized to quantify the effect of clay content and spatial distributions with associated diffusion coupling on permeability predictions.

2.5.1 NMR Correlated Permeability Model

The NMR-estimated permeability by SDR [17] and the Coates models [18] are given by the following equations

$$k_{SDR} = a_s \phi^b T_{2lm}^c \quad (2)$$

$$k_{Coates} = a_c \phi^b \left(\frac{FFI}{BIV} \right)^c \quad (3)$$

where k is permeability in μm^2 (approx. mD), ϕ is porosity in %, with b and c exponents typically set to 4 and 2, respectively. For the SDR model (Eqn. 2), a_s is a parameter accounting for formation lithology. The SDR estimates mean hydraulic radius through the logarithmic mean relaxation time T_{2lm} and despite apparent limitations has proven applicable to fully water saturated water-wet formations. For the Coates Model (Eqn. 3), a_c is the Coates permeability coefficient, which is often used as denominator of porosity. The fixed $T_{2,cutoff}$ divides the T_2 distribution into two fractions corresponding to bound water (BVI, shorter relaxation times) and free fluid (FFI, longer relaxation times). Generally, cut-off times of 33 ms and 92 ms are appropriate for sandstones and carbonates, respectively [18]. However, our previous study shows that $T_{2,cutoff}$ values determined based on the irreducible water saturations S_{wirr} vary in different sandstones [36]. The primary assumption behind these correlations is that the fast diffusion limit condition applies to all components of the relaxation spectrum.

The SDR correlation is essentially based on a general relationship between permeability k , characteristic length scale of a pore system L , and porosity ϕ , $k \propto \phi^m L^2$, reported by many authors [41 - 43]. We note that the definitions of the characteristic length scale are different. L can be obtained from capillary pressure measurements in the study [41]. On the other hand, L is defined as dynamically connected pore size in the study from [42]. While the length scale offered from NMR T_2 distribution is related to pore volume-to-surface ratio V_p/S . $k \propto \phi^{1.8} (V_p/S)^2$ for the grain consolidation model is presented in [43]. More recently, the correlation between permeability and four different types of pore diameters is demonstrated as $k \propto \phi^4 \langle d \rangle^2$ based on micro-CT image [35]. Eqn. 2 can be easily expressed in the latter form noting in the fast diffusion limit $T_2 \sim L/(6\rho)$. Since the observable physical property is relaxation time and numerical simulation offers (and requires as input) surface relaxivity, we apply the squared proportionality factor 6ρ to the lithological parameter a_s , making it dimensionless: $a'_s = a_s/(6\rho)^2$. Typically, in laboratory core analysis the only unknown in the SDR equation is the lithological parameter, which has to be established for log calibration. Below we discuss the effect caused by the diffusional coupling in presence of different amount of clay on the modified lithological parameter a'_s .

2.5.2 Lattice Boltzmann Method

The Lattice Boltzmann Method (LBM) is a mesoscopic approach to fluid mechanics utilizing particle densities via a collision and streaming algorithm. The LBM has become an effective method for estimation of fluid flow in porous media because of its simplicity and flexibility to various flow geometries [44 - 46]. It is employed in this study to provide reference permeability values evaluate the enhancements in the NMR permeability estimations. The fluid is treated as continuous medium, and the solution of a discretized Boltzmann equation can match the Navier-Stokes equation. The D3Q19 (3-dimensional lattice with 19 possible velocity directions) lattice [47] is selected. The method starts with the initialization of distribution functions. The macroscopic fluid properties can be computed by

$$\rho(\mathbf{x}, t) = \sum_{i=1}^{19} f_i(\mathbf{x}, t) \quad (4)$$

$$\rho \mathbf{v}(\mathbf{x}, t) = \sum_{i=1}^{19} \mathbf{e}_i f_i(\mathbf{x}, t) \quad (5)$$

where ρ is the macroscopic fluid density, \mathbf{v} is the velocity, \mathbf{e}_i are the microscopic velocity vectors and f_i is the particle density distribution function. After applying boundary conditions, the algorithm for density evolution which includes the stream and collide operation is given by

$$f_i(\mathbf{x} + \mathbf{e}_i \delta t, t + \delta t) = f_i(\mathbf{x}, t) - \frac{f_i(\mathbf{x}, t) - f_i^{eq}(\mathbf{x}, t)}{\tau} \quad (6)$$

where f_i^{eq} is the equilibrium distribution function and τ is the relaxation time. In the simulation, the BGK (Bhatnagar-

Gross-Crook) collision kernel is applied to simulate the single phase fluid behavior with bounce-back condition at the fluid-solid interface [48] The pressure gradient is simulated by a body force [46].

3 Magnetization Exchange Analysis

In this section we analyze the exchange of magnetization between different compartments of the clayey sandstone samples as function of clay distribution, clay region porosity, and temperature. Change in those parameters affects the main observables, namely the shape of the T_2 distribution, the position of individual modes of the distribution, as well as the size of the spatial regions active in magnetization exchange, which are discussed in the following. Consequences for permeability estimation are analyzed in the section thereafter.

3.1 Clay Distribution and Micro-porosity Effects

Consider first the relationships between diffusional coupling, clay distribution, clay content, and clay region porosity (ϕ_c) at ambient conditions. NMR simulations were conducted on both the pore-lining and pore-filling samples for a range of clay fractions, where kaolinite clay models with constant porosity ϕ_c (average over the 400³ clay model) are mapped to the respective clay regions. The corresponding T_2 distributions are given in Fig. 9. Stronger diffusional coupling effects can be observed for the coated and pore-lining clay distributions with higher clay porosity (ϕ_c). The part of the T_2 distribution associated with coated type of clay morphology exhibits faster relaxation time than other three clay morphology despite equal volumetric fraction in sandstone. Especially, with increasing clay amount, the T_2 distribution of the coated clay becomes unimodal and no longer represents pore size distribution. Diffusional coupling enhanced the relaxation rate and the slow relaxation time peak shifts to short time.

The correlation between clay amount and the transverse relaxation rate ($1/T_{2lm}$) is demonstrated in Fig. 10. $1/T_{2lm}$ of four clay morphological types demonstrate a linear relationship with clay content in different slopes. The micro-porosity has more impact on the relaxation rate of grain-coating and pore-lining clay morphology when the amount surpasses 10 vol% (Fig 10 [b, c]). The higher clay porosity and stronger coupling effects lead to the fast relaxation peak shifts for the longer relaxation times, resulting in a decreased slope and vice versa. The distortion of relative amplitudes of the fast relaxation peak and slow relaxation peak due to diffusional coupling may break down the correlation between the peak area ratio and the porosity fraction of micro-pores and macro-pores [24]. The micro-porosity may be overestimated with increasing clay amount. We note that both grain-coating and pore-lining clay morphological types with higher clay porosity exhibit larger errors. This is because of two effects -- the higher clay porosity (ϕ_c) allows more protons to diffuse between micro- and macro-pores and the pore-lining clay distribution pattern offers more clay-region to macro-pore interface area and thus lead to a higher diffusion

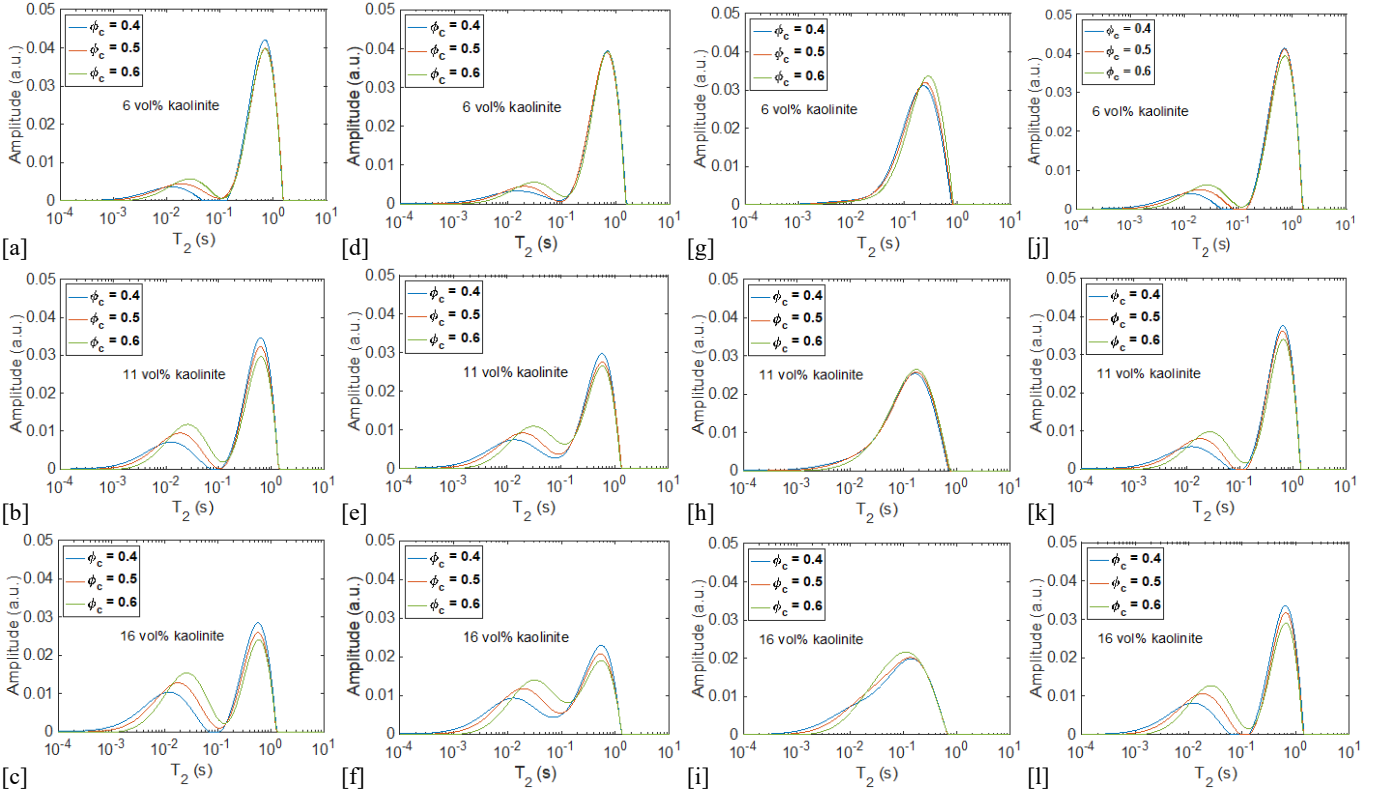


Fig. 9 The T_2 distribution of [a-c] pore-filling; [d-f] pore-lining; [g-i] coated; [j-l] laminated synthetic sandstone with different clay amount. Top row: 6 vol%, middle: 11 vol%, bottom: 16 vol%. $\phi_c \in \{0.4, 0.5, 0.6\}$ denotes the micro-porosity of kaolinite

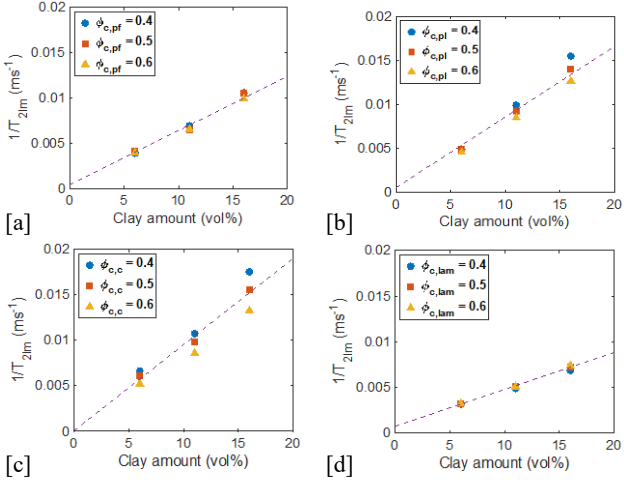


Fig. 10 Linear relationship between clay volume fraction and T_{2lm} for different clay distributions. [a] pore-filling, [b] pore-lining, [c] coated, [d] laminated. The purple dashed lines are the linear trend between T_{2lm} and clay amount.

3.2 Diffusional Exchange Between Different Compartments

We demonstrate the correlation between magnetization exchange ($M_{ex}(d,t)$) and time as well as Euclidean distance. Since the samples containing different clay amounts indicate the same trends, we chose a system with 11 vol% clay amounts as a representative example. $M_{ex}(d,t)$ as function of observation time is shown in Fig. 11, where $\sum d$ is the distance integration over each EDT shell. Similar magnetization exchange profiles are presented in both macro-micro and micro-macro directions. At the beginning, a growing number of walkers diffuse between micro- and macro-porous regions with time increasing. The diffusional

exchange of magnetization reaches a maximum value at around 10-30 ms. After that, magnetization exchange decreases and there is almost no leaked magnetization between two pore populations when time exceeds 1s as defined by compartment association at start and end position of the exchanging spin packet. The magnetization exchange is significantly affected by micro-porosity for coated and pore-lining clay morphology when diffusion occurred in both two directions. These two clay distribution patterns with higher micro-porosity allow protons diffusing between micro- and macro-pores more frequently. For grain-coated morphological pattern, the magnetization exchange when $\phi_c = 0.6$ is two times stronger than $\phi_c = 0.4$. While, the $M_{ex}(\sum d,t)$ for pore-filling and laminated samples are much closer. Overall, the coated clay type exhibits five times higher magnetization exchange compared to other samples. The magnetization exchange of pore-lining clay type demonstrates two-fold compared to pore-filling and laminated one when clay porosity is 0.5 and 0.6. However, if porosity of the compared clay types reduced to 0.4, the difference in exchanged magnetization diminishes. This can be explained by stronger surface relaxation in the clay region due to an increase in surface-to-volume ratio.

Consider now the correlations between magnetization exchange and Euclidean distance presented in Fig 12. Here, we take examples of pore-filling and pore-lining samples. The overall trend demonstrates that magnetization exchange presents approximately exponential decay with Euclidean distance for both directions. The leaked magnetization from two porosity populations towards the other is reduced as the walkers moving far from the interface boundary.

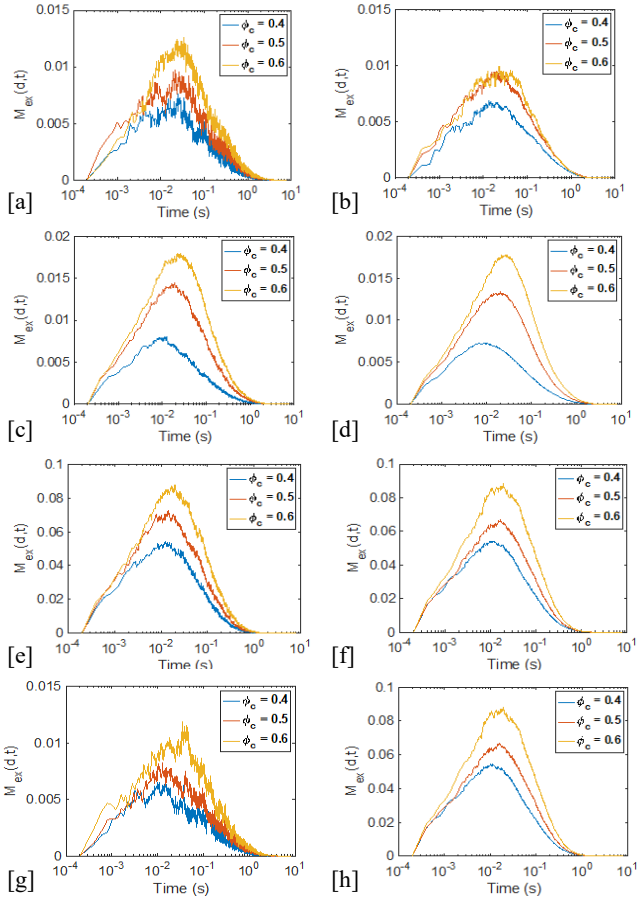


Fig. 11 The magnetization exchange $M_{ex}(d,t)$ as function of observation time for [a, b] pore-filling, [c, d] pore-lining, [e, f] coated, [g, h] laminated samples with clay amount 11 vol% in diffusion direction: left column: macro-micro; right column: micro-macro. Here, the distance is the integration of each EDT shell $d = \sum d$. ϕ_c is the micro-porosity for clay phase.

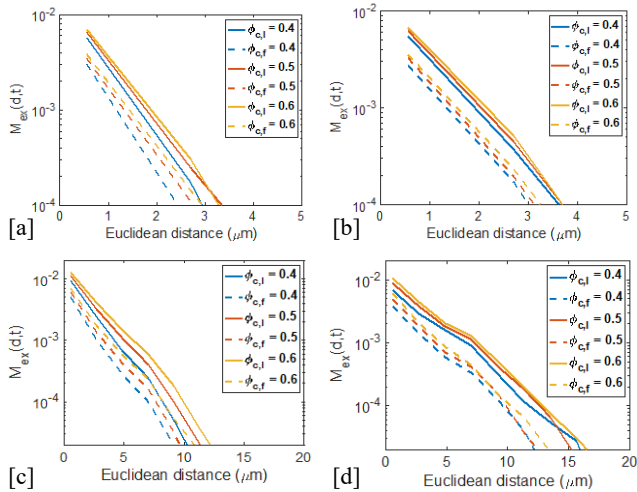


Fig. 12 The magnetization exchange $M_{ex}(d,t)$ of samples with 11 vol% clay from macro- to micro-pore (left column) and from micro- to macro-pore (right column) at various times [a, b] $t = 5 t_E$; [c, d] $t = 50 t_E$. The solid line and dash line represent for pore-lining and pore-filling clay distribution respectively.

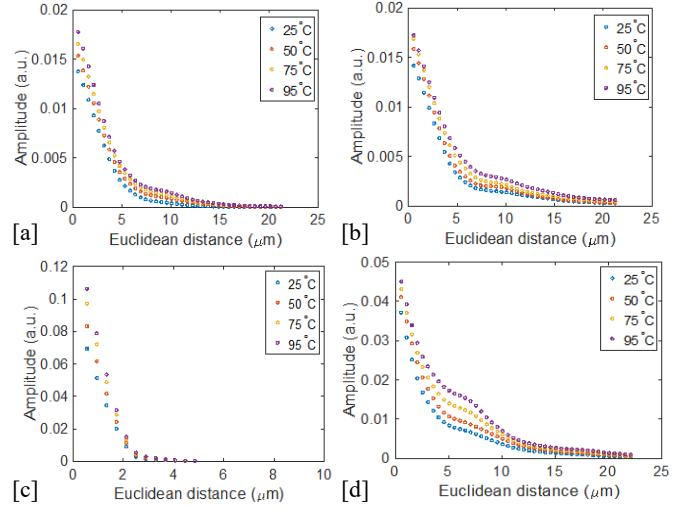


Fig. 13 The correlation of the fitting amplitude at each EDT shell and Euclidean distance in different directions macro-micro (left column) and micro-macro (right column) for [a, b] pore-lining samples, [c, d] coated samples at temperature 25 °C, 50 °C, 75 °C and 95 °C.

The corresponding maximum distance at short time ($t = 5 t_E$) is close to 3-4 μm . The distance increases to 10-15 μm at $t = 50 t_E$. The higher clay porosity allows more walkers travel to longer distance between micro- and macro-porous regions. The pore-lining sample with lower clay porosity presents less diffusion of magnetization than pore-filling with higher clay porosity. The reason for that may be, that strong surface relaxation is dominant in tight clay pockets. On the contrary, the pore-lining sample always presents higher $M_{ex}(d,t)$ values when walkers travel from micro-pore to macro-pore (Fig. 12b, d).

3.3 Temperature Effects

The diffusional coupling effects can be enhanced with the temperature increasing due to alteration of diffusion coefficient and surface relaxivity [6, 7]. In this section, we noted that we only focus on the contribution of diffusion to magnetization exchange. We simulated the NMR relaxation response at 25 °C, 50 °C, 75 °C and 95 °C with diffusion coefficient $2.15 \times 10^{-5} cm^2/s$, $3.97 \times 10^{-5} cm^2/s$, $6.10 \times 10^{-5} cm^2/s$ and $8.07 \times 10^{-5} cm^2/s$, respectively. The magnetization exchange between micro- and macro-porous regions with integrated time are recorded in respect to particular EDT shell $M_{ex}(d, \sum t)$, that provides the local magnetization evolution in approximate Gaussian distribution. The correlation of the fitting amplitude for $M_{ex}(d, \sum t)$ and Euclidean distance at different temperatures is presented in Fig. 13. Here we demonstrate pore-lining and grain-coated clay morphological types due to their stronger diffusional coupling effects.

As expected, the diffusion of magnetization is enhanced with increased temperature. For pore-lining sample, the diffusion of magnetization becomes weak when distance exceeds 20 μm , the maximum Euclidean distance employed here is 22.05 μm (around 40 voxels) from macro-pore to micro-pore. The amplitude of the magnetization exchange at 95 °C is around 1.3 - 1.4 times higher than that at 25 °C within the short distance. While, in the opposite direction, the walkers can penetrate slightly deeper into the macro-pore

space. For the grain-coated type, since the distance values around the solid are small, the corresponding penetration distance from macro-pore to micro-pore is around 5 μm . On the contrary, the walkers can still invade macro-pores with distance around 22 μm .

4 Permeability Estimation

In this section, we analyze the coupling effects on permeability estimation for pore-filling and pore-lining samples which are the most common clay patterns in sandstones.

Table 3. The permeability simulated by LBM for pore-lining (K_l) and pore-filling (K_f) samples with different clay amount.

Clay (vol%)	K_l (mD)	K_f (mD)
6	639.35	746.41
11	226.59	355.07
16	63.91	109.79

We first calculated permeability by LBM for synthetic clayey sandstones, assuming the clay regions provide no contribution to transport (Table. 3). The permeability values decrease with increasing clay amount. The pore-filling samples exhibit higher permeability than corresponding pore-lining samples of same clay amount. The following analysis of coupling effects on permeability estimate using SDR and Coates models is performed in respect to corresponding prefactors.

4.1 SDR Model

The implications of temperature on the shape of the relaxation time distributions are shown in Fig. 14 [a-f]. We calculated the dimensionless lithological parameter a'_s following Eqn. 2 for both coupling-on and coupling-off scenarios by employing the absolute permeability in Table 3. We report the prefactor $a'_{s,l}$ for pore-lining sample and $a'_{s,f}$ for pore-filling sample with different temperatures in Table 4. The temperature effects are weak when the clay amount is small leading to limited contrast between the coupling-on and coupling-off scenarios. However, as clay amounts increase the temperature effects are enhanced, resulting in a prefactor change of around 1.6 times for the pore-lining sample with clay amount of 16 vol%. While, for pore-filling samples, $a'_{s,f}$ presents weak dependency of temperature due to less shifts and distortion of the T_2 distribution due to diffusion between micro- and macro-porous regions.

4.2 Coates Model

Consider now the permeability estimation via Coates model. According to the coupling-off T_2 distributions (Fig. 15 blue-dashed line), the separated fast relaxation peak corresponds to the bounded irreducible water ($S_{w,irr}$). The normalized BVI is obtained by plotting the cumulative T_2 curves of $S_{w,irr}$ in Fig. 15. The $T_{2,cutoff}$ is determined by horizontal projection of $S_{w,irr}$ curve for $S_w = 100\%$. The cross-point is then project down to the x axis with relevant T_2 value, which is $T_{2,cutoff}$ [18]. The correlation between $T_{2,cutoff}$ and temperature for pore-lining and pore-filling samples as function of clay amount is given

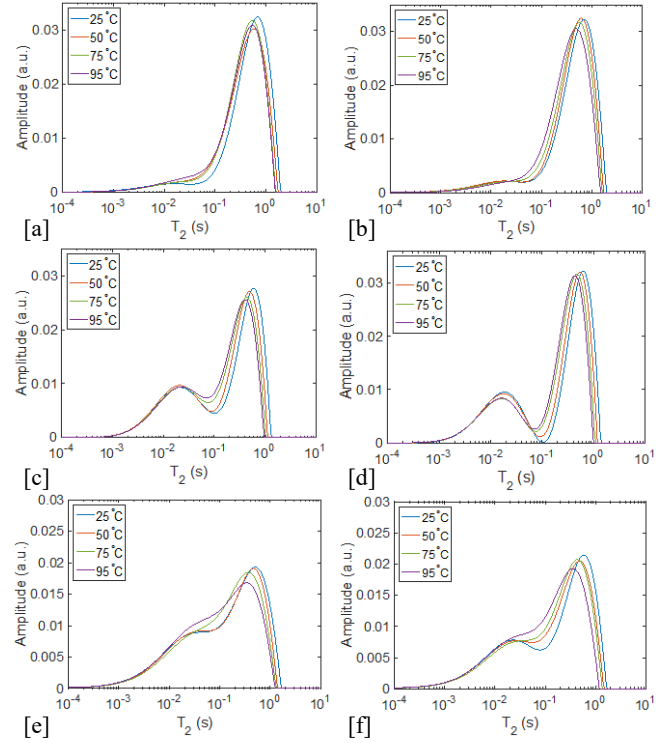


Fig. 14 The comparison of T_2 distributions of pore-lining (left column) and pore-filling (right column) for samples with clay amount [a, b] 6 vol%, [c, d] 11 vol%, [e, f] 16 vol% at the temperature 25 °C, 50 °C, 75 °C and 95 °C.

Table 4. The SDR model prefactor for pore-lining sample ($a'_{s,l}$) and pore-filling sample ($a'_{s,f}$) at temperature 25°C, 50°C, 75°C and 95°C with different clay amount.

Clay (vol)	T (°C)	$a'_{s,l}$		$a'_{s,f}$	
		Coupling-on	Coupling-off	Coupling-on	Coupling-off
6	25	1.06	0.94	1.22	1.07
	50	1.34	0.94	1.54	1.09
	75	1.47	0.98	1.67	1.10
	95	1.66	0.98	1.91	1.10
11	25	3.66	1.89	4.36	2.96
	50	5.03	1.94	5.27	3.13
	75	5.39	2.03	5.50	3.16
	95	5.93	2.04	6.39	3.17
16	25	3.97	1.37	6.06	2.28
	50	4.44	1.40	6.47	2.28
	75	4.62	1.41	6.81	2.35
	95	6.51	1.41	7.10	2.37

in Fig 16. The overall trend shows that $T_{2,cutoff}$ values decrease as temperature increase. This may result from the decrease in amplitude of the slow relaxation peak, and the tendency of the bimodal T_2 distribution towards becoming more unimodal with increasing temperature, especially for higher clay amounts (Fig. 14). Since pore-lining clays exhibit stronger

coupling effects, the related $T_{2,cutoff}$ values are lower than for pore-filling clays. As clay amounts increase, the contrast

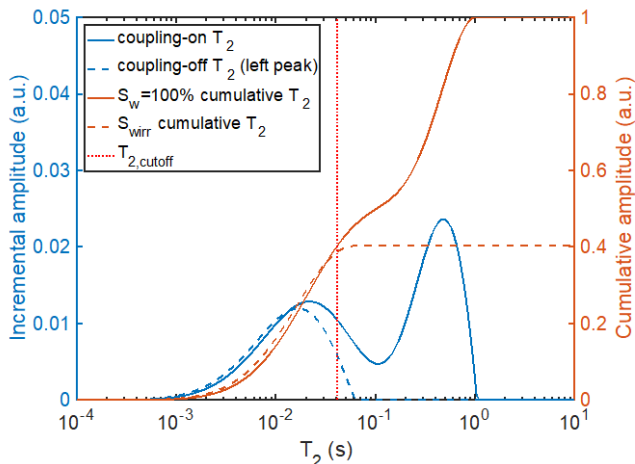


Fig. 15 The cumulative T_2 curves on fully saturated ($S_w = 100\%$) sample with 11 vol% clay amount and on irreducible saturation S_{wirr} are utilized to establish a $T_{2,cutoff}$ via BVI.

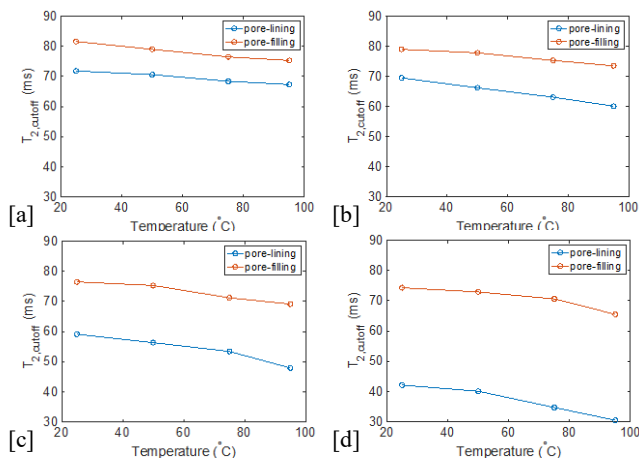


Fig. 16 The correlation between $T_{2,cutoff}$ and temperature for pore-lining and pore-filling samples in different clay amount [a] 2 vol% (original clay amount within Bentheimer sandstone), [b] 6 vol%, [c] 11 vol %, [d] 16 vol%.

Table 5. The Coates model prefactor for pore-lining sample ($a_{c,l}$) and pore-filling sample ($a_{c,f}$) at temperature 25 °C, 50 °C, 75 °C and 95 °C with different clay amount.

Clay (vol%)	T (°C)	$a_{c,l}$	$a_{c,f}$
6	25	10.03	10.09
	50	9.58	10.03
	75	8.85	9.71
	95	8.64	9.59
11	25	45.77	66.55
	50	43.42	63.01
	75	40.59	58.25
	95	36.13	50.73
16	25	92.37	114.82
	50	86.53	107.67

	75	77.39	99.19
	95	72.38	95.14

between the two clay distribution scenarios is growing. When clay amount reaches 16 vol%, the $T_{2,cutoff}$ for pore-lining sample decrease from 42 ms to 30 ms at temperature range from 25 °C to 95 °C. While the reduction for pore-filling samples is from 74 ms to 65 ms.

By applying various $T_{2,cutoff}$, the FFI/BVI ratio can be obtained via T_2 distribution of each sample. With known permeability, porosity and FFI/BVI ratio, we derived prefactor a_c in Coates model according to Eqn. 3. The a_c values are reported in Table 5. The results indicate that the prefactors are not affected much by temperature when little clay is present in the rocks. However, when the clay amount is higher than 10 vol%, both pore-lining and pore-filling samples show dependency on temperature. The smaller $T_{2,cutoff}$ values lead to higher FFI/BVI ratio, resulting in decreased a_c as temperature increasing. Therefore, the permeability may be overestimated if only fixed $T_{2,cutoff}$ is utilized without prefactor compensation.

5 Conclusion

This study evaluates the magnitude of diffusional coupling effects on petrophysical evaluation of clayey sandstone based on NMR transverse relaxation depending on clay volume fraction, distribution pattern, local porosity, and temperatures. The magnetization exchange between micro- and macroporous regions with aid of EDT map is employed to characterize the diffusion as function of time and penetration depth. This in turn enabled an analysis of potential impacts on permeability predictions. We draw the following specific conclusions:

1. The rocks with coated and pore-lining clay distribution present stronger diffusional coupling effects than pore-filling and laminated one. The distortion of T_2 distribution can result in an overestimation of micro-porosity.
2. The magnetization exchange between micro- and macroporous regions due to diffusion is demonstrated as exponential function of penetration depth (Euclidean distance) and Gaussian function of observation time.
3. The log-mean of transverse relaxation time demonstrates linear dependency on clay amount. The slope can be altered by different micro-porosity, especially for rocks with pore-lining clay distribution.
4. The diffusional coupling effects are magnified with increasing temperature. The prefactors of SDR model and Coates model exhibit temperature dependency in higher clay amount rocks. The NMR-related permeability can be overestimated if fixed $T_{2,cutoff}$ is utilized without consideration of prefactor compensation.

References

- [1] K. Brownstein and C. Tarr, "Importance of classical diffusion in NMR studies of water in biological cells," *Phys. Rev. A*, vol. 19, p. 446–2453, 1979.
- [2] H. Dai, I. Shikhov, R. Li, J. Arns and C. Arns, "Mechanisms of confining pressure dependence of

- resistivity index for tight sandstones by digital core analysis,” *SPE J.*, vol. 26, p. 883–896, 2021.
- [3] S. Apourvari and C. Arns, “Image-based relative permeability upscaling from pore scale,” *Adv. Water Res.*, vol. 95, pp. 161–175, 2016.
- [4] J. Qajar, N. Francois and C. Arns, “Microtomographic characterization of dissolution-induced local porosity changes including fines migration in carbonate rock,” *SPE J.*, vol. 18, p. 545–562, 2013.
- [5] E. Grunewald and R. Knight, “A laboratory study of NMR relaxation times and pore coupling in heterogeneous media,” *Geophysics*, vol. 74, p. 215–221, 2009.
- [6] V. Anand and G. Hirasaki, “Paramagnetic relaxation in sandstones: distinguishing T_1 and T_2 dependence on surface relaxation, internal gradients and dependence on echo spacing,” *J. Magn. Reson.*, vol. 190, p. 68 – 85, 2008.
- [7] E. Toumelin, C. Torres-Verdin, S. Chen and D. Fischer, “Analysis of NMR diffusion coupling effects in two-phase carbonate rocks: comparison of measurements with Monte Carlo simulations,” in *SPWLA 43rd Annual Logging Symposium*, Oiso, Japan, 2002.
- [8] E. Toumelin, C. Torres-Verdín, S. Chen and D. Fischer, “Reconciling NMR measurements and numerical simulations: assessment of temperature and diffusive coupling effects on two-phase carbonate samples,” *Petrophysics*, vol. 44, 2003.
- [9] N. Gomaa, A. Al-Alyak, D. Ouzzane, O. Saif, M. Okuyiga, A. Opco, D. Allen, D. Rose, R. Ramamoorthy and E. Bize, “Case study of permeability, Vug quantification, and rock typing in a complex carbonate,” in *SPE Annual Technical Conference and Exhibition*, San Antonio, Texas, 2006.
- [10] W. Trevizan, P. Netto, B. Coutinho, V. Machado, E. Rios, S. Chen, W. Shao and P. Romero, “Method for predicting permeability of complex carbonate reservoirs using NMR logging measurements,” *Petrophysics*, vol. 55, p. 240–252, 2014.
- [11] M. Fleury and J. Soualem, “Quantitative analysis of diffusional pore coupling from T_2 -store- T_2 NMR experiments,” *Journal of Colloid and Interface Science*, vol. 336, p. 250–259, 2009.
- [12] C. Morriss, J. Maclnnis, R. Freedman, J. Smaardyck, C. Straley, W. Kenyon, H. Vinegar and P. Tutunjian, “Field test of an experimental pulsed nuclear magnetism tool,” in *SPWLA 34th Annual Logging Symposium*, Calgary, Alberta, 1993.
- [13] C. Straley, D. Rossini, P. Tutunjian, H. Vinegar and C. Morriss, “Core analysis by low-field NMR,” in *The Log Analyst* 38, 1997.
- [14] G. Coates, J. Galford, D. Mardon and D. Marschall, “A new characterization of bulk-volume irreducible using magnetic resonance,” in *The Log Analyst* 39, 1998.
- [15] E. Toumelin, C. Torres-Verdín and S. Chen, “Modeling of multiple echo-time NMR measurements for complex pore geometries and multiphase saturations,” *SPE Reser. Eval. Eng.*, vol. 6, p. 234–243, 2003.
- [16] S. Godefroy, M. Fleury, F. Deflandre and J. Korb, “Temperature effect on NMR surface relaxation in rocks for well logging applications,” *J. Phys. Chem. B*, vol. 106, p. 11183–11190, 2002.
- [17] E. Kenyon, I. Day, C. Straley and F. Willemsen, “A three-part study of NMR longitudinal relaxation properties of water-saturated sandstones,” *SPE Formation Evaluation*, vol. 3, p. 622–636, 1988.
- [18] G. Coates, L. Xiao and M. Prammer, *NMR logging: principles and applications*, Houston: Haliburton Energy Services, 1999.
- [19] G. Carneiro, A. Souza, A. Boyd, L. Schwartz, Y. Song, R. Azeredo, W. Trevizan, B. Santos, E. Rios and V. Machado, “Evaluating Pore Space Connectivity by NMR Diffusive Coupling,” in *SPWLA 55th Annual Logging Symposium*, Abu Dhabi, United Arab Emirates, 2014.
- [20] M. Jácomo, R. Trindade, E. de Oliveira, C. Leite, E. Montrazi, M. Andreeta and T. Bonagamba, “Nuclear magnetic resonance and pore coupling in clay-coated sandstones with anomalous porosity preservation, ŷgua Grande Formation, Rec & ocirc;ncavo Basin, Brazil,” *Petrophysics*, vol. 59, p. 136–152, 2018.
- [21] S. Chen, D. Jacobi, H. Kwak, M. Altunbay and J. Kloos, “Pore-connectivity based permeability model for complex carbonate formations,” in *SPWLA 49th Annual Logging Symposium*, ustin, Texas, 2008.
- [22] L. Chi and Z. Heidari, “Directional-permeability assessment in formations with complex pore geometry with a new nuclear-magnetic-resonance-based permeability model,” *SPE J.*, vol. 21, p. 1436–1449, 2016.
- [23] M. Cohen and K. Mendelson, “Nuclear magnetic relaxation and the internal geometry of sedimentary rocks,” *J. Appl. Phys.*, vol. 53, p. 1127–1135, 1982.
- [24] T. Ramakrishnan, E. Fordham, W. Kenyon, L. Schwartz and D. Wilkinson, “Forward models for nuclear magnetic resonance in carbonate rocks,” in *The Log Analyst* 40, 1999.
- [25] Z. Zhang, D. Johnson and L. Schwartz, “Simulating the time-dependent diffusion coefficient in mixed-pore-size materials,” *Phys. Rev. E*, vol. 84, p. 031129, 2011.
- [26] L. Schwartz, D. Johnson, J. Mitchell, T. Chandrasekera and E. Fordham, “Modeling two-dimensional magnetic resonance measurements in coupled pore systems,” *Phys. Rev. E*, vol. 88, p. 032813, 2013.
- [27] J. Mitchell, A. Souza, E. Fordham and A. Boyd, “A finite element approach to forward modeling of nuclear magnetic resonance measurements in coupled pore systems,” *J. Chem. Phys.*, vol. 150, p. 154708:1–12, 2019.
- [28] C. Arns, A. Sheppard, R. Sok and M. Knackstedt, “NMR petrophysical predictions on digitized core

- images,” in *46th Annual Logging Symposium, Society of Petrophysicists & Well Log Analyst*, New Orleans, Texas, 2005.
- [29] L. Chi and Z. Heidari, “Diffusional coupling between microfractures and pore structure and its impact on nuclear magnetic resonance measurements in multiple-porosity system,” *Geophysic*, vol. 80, pp. 31–42, 2014.
- [30] C. Arns, Y. Melean, A. Sheppard and M. Knackstedt, “A comparison of pore structure analysis by NMR and Xray-CT techniques,” in *9th Annual Logging Symposium, Society of Petrophysicists & Well Log Analyst*, Edinburgh, 2008.
- [31] M. Tankiewicz, “Experimental Investigation of Strength Anisotropy of Varved Clay,” *Procedia Earth Planet. Sci.*, vol. 15, p. 732–737, 2015.
- [32] Y. Cui, I. Shikhov and C. Arns, “NMR relaxation modeling in porous media with dual-scale resolved internal magnetic fields,” *Transport in Porous Media*, 2022.
- [33] A. Sheppard, R. Sok and H. Averdunk, “Techniques for image enhancement and segmentation of tomographic images of porous materials,” *Physica A*, vol. 339, p. 145–151, 2004.
- [34] T. Saito and J. Toriwaki, “New algorithms for Euclidean distance transformation of an n-dimensional digitized picture with applications,” *Pattern Recognition*, vol. 27, p. 1551–1565, 1994.
- [35] C. Arns, A. Sakellariou, T. Senden, A. Sheppard, R. Sok, W. Pinczewski and M. Knackstedt, “Digital core laboratory: Reservoir core analysis from 3D images,” *Petrophysics*, vol. 46, no. 260–277, 2005.
- [36] Y. Cui, I. Shikhov, R. Li, S. Liu and C. Arns, “A numerical study of field strength and clay morphology impact on NMR transverse relaxation in sandstones,” *J. Pet. Sci. Eng.*, vol. 202, p. 10852, 2021.
- [37] J. Mbey, F. Thomas, A. Razafitianamaharavo, C. Caillet and F. Villieras., “A comparative study of some kaolinites surface properties,” *Applied Clay Science*, vol. 172, p. 135–145, 2019.
- [38] A. Matteson, J. Tomanic, M. Herron, D. Allen and W. Kenyon, “NMR relaxation of clay-brine mixtures,” *PE Reser. Eval. Eng.*, vol. 3, p. 408–413, 2000.
- [39] Y. Zheng, I. Shikhov, L. Gbayan, J. Arns and C. Arns, “About the connectivity of dual-scale media based on micro-structure based regional analysis of NMR flow propagators,” *J. Contam. Hydrol.*, vol. 212, p. 143–151, 2018.
- [40] D. Bergman, K. Dunn, L. Schwartz and P. Mitra, “Self-diffusion in a periodic Porous medium: a comparison of different approaches,” *Phys. Rev. E*, vol. 51, p. 3393–3400, 1995.
- [41] A. Katz and A. Thompson, “Quantitative prediction of permeability in porous rock,” *Phys. Rev. B*, vol. 34, p. 8179–8181, 1986.
- [42] L. Johnson, J. Koplik and L. Schwartz, “New pore size parameter characterizing transport in porous media,” *Phys. Rev. Lett.*, vol. 57, p. 2564–2567, 1986.
- [43] J. Banavar and L. Schwartz, “Magnetic resonance as a probe of permeability in porous media,” *Phys. Rev. Lett.*, vol. 58, p. 1411–1414, 1987.
- [44] U. Frisch, B. Hasslacher and Y. Pomeau, “Lattice-gas automata for the Navier-Stokes equation,” *Phys. Rev. Lett.*, vol. 56, p. 1505–1508, 1986.
- [45] D. Rothman, “Cellular-automaton fluids: A model for flow in porous media,” *Geophysics*, vol. 53, p. 509–518, 1988.
- [46] B. Ferreol and D. Rothman, “Lattice-Boltzmann simulations of flow through Fontainebleau sandstone,” *Trans. Porous. Med.*, vol. 20, p. 3–20, 1995.
- [47] N. Martys and J. Hagedorn, “Multiscale modeling of fluid transport in heterogeneous materials using discrete boltzmann methods,” *Materials and structures*, vol. 35, p. 650–658, 2002.
- [48] N. Martys and H. Chen, “Simulation of multicomponent fluids in complex three-dimensional geometries by the lattice Boltzmann method,” *Phys. Rev. E*, vol. 53, p. 743–750, 1996.
- [49] M. Elsayed, G. Glatz, A. El-Husseiny, A. Alqubalee, A. Adebayo, K. Al-Garadi and M. Mahmoud, “The effect of clay content on the spin–spin NMR relaxation time measured in porous media,” *ACS Omega*, vol. 5, p. 6545–6555, 2020.
- [50] D. Johnson and L. Schwartz, “Analytic theory of two-dimensional NMR in systems with coupled macro- and micropores,” *Phys. Rev. E*, vol. 90, p. 032407, 2014.

Artificial Intelligence Assisted Quantitative Petrophysical Properties Analysis using Core Images and Well Logs

Tao Lin^{1,*}, Mokhles Mezghani², Chicheng Xu¹, and Weichang Li¹

¹Aramco Americas: Aramco Research Center - Houston, 16300 Park Row Dr., Houston, TX 77084, USA

²Saudi Aramco, Dhahran Heights, Building 9172, 31311 Dhahran, Saudi Arabia

Abstract. Reservoir characterization requires petrophysical properties, such as porosity and permeability, to be populated in a 3D reservoir model. It is critical to quantitatively estimate the vertical profiles of petrophysical properties in each well. Traditional approaches are time consuming and labor intensive, and sometimes invasive to the core. To overcome these issues, we propose to apply image analysis and automated artificial intelligence (AI) workflow to improve high-resolution quantitative petrophysical characterization. The workflow estimates the continuous vertical profiles of petrophysical properties in each well, by integrating core plug measurements, core images and well logs with computer vision (CV) and machine learning (ML) techniques. We achieved reasonably good correlation and accuracy from the models. The approach enables core digitization, core preservation and reduces exploration risk, as well as providing petrophysical insights to assist core description.

1. Introduction

Rock properties including petrophysical properties (porosity and permeability), geomechanical properties (Poisson's ratio and Young's modulus), and geochemical properties (Total organic carbon and kerogen volume) are critical for subsurface reservoir modeling. A critical step is to estimate the vertical profiles of petrophysical properties in each well based on core measurements and well logs [1, 2]. Traditionally, qualitative visual observations of depositional and diagenetic features are routinely recorded by geoscientists for geologic interpretation and petrophysical characterization. Quantitative core measurements are typically acquired in laboratory from core plugs at discrete depth levels. Both approaches are time consuming and labor intensive, and sometimes invasive to the core. Those petrophysical properties are then used to calibrate petrophysical models together with well logs. In very heterogeneous reservoirs, petrophysical properties can exhibit large variability on very small scale to be resolved by well logs. In addition, core analysis and other relevant information generate a large number of heterogeneous formats data, which can be difficult to integrate effectively into a single modeling framework. Therefore, integrating higher resolution measurements such as core scans or core images in an automated quantitative analysis workflow can improve petrophysical characterization at the cored interval resolution [3].

Core images are often used by geologists only on a descriptive basis for sedimentary (bedding, grain size, lithology), structural (dipping, deformation), and diagenetic features (fractures, vugs). It also has rich information about the subsurface rocks that can be extracted for quantitative characterization purposes. For example, different lithologies are often present in different brightness or colors. Shale or clay-rich rocks often appear darker in color than sandstones or limestones. For the same lithology, coarse-grained and porous intervals often exhibit different textures from the tight and fine-grained intervals, which is sometimes observable by human eyes. However, core-based visual information has not been routinely integrated into petrophysical models. Recent advances in computer vision and machine learning enable more quantitative use of core images in petrophysical characterization workflows with improved performances [3].

In this paper, we introduce an AI assisted quantitative workflow that estimates the continuous vertical profiles of petrophysical properties in each well, by integrating core plug measurements, core images and well logs with computer vision (CV) and machine learning (ML) techniques. We demonstrate that core images and well logs can be quantitatively integrated into petrophysical workflows to enhance estimation of petrophysical properties in cored intervals.

* Corresponding author: tao.lin@aramcoamericas.com

2. Data Preparation

While drilling exploration or development wells, cores are extracted from the subsurface. These cores are an important source of information for subsurface characterization. After cores are extracted, they are placed in cylinders, usually 3-ft long, and then sent to the core laboratory for further analysis and visual examination. Some of these analyses are performed before slabbing the core and others are done after the slabbing.

Before the slabbing, one of the core analyses is provided by the Gamma Ray measured with relatively small spacing ranging from 0.05 ft to 0.1 ft. Some of the analyses require the extraction of several samples (called plugs) from each core of 3 ft long. Plugs are generally used to measure different properties such as porosity, permeability, and grain density with a spacing ranging from 0.5 ft to 1.0 ft. An example of slabbed and plugged cores is shown in **Figure 1**.



Figure 1. Slabbed and plugged geological cores.

For visual examination, the core is slabbed in two parts, for example, 1/4 and 3/4 for 4 inches core diameter. On the slabbed core, a handwritten text is added to the slabbed face of the core to mark the extracted plug identifier and the core depth at every foot. Finally, a high-resolution photo (approximately 100 pixels per centimeter) of the slabbed core is taken, as shown in **Figure 2**.

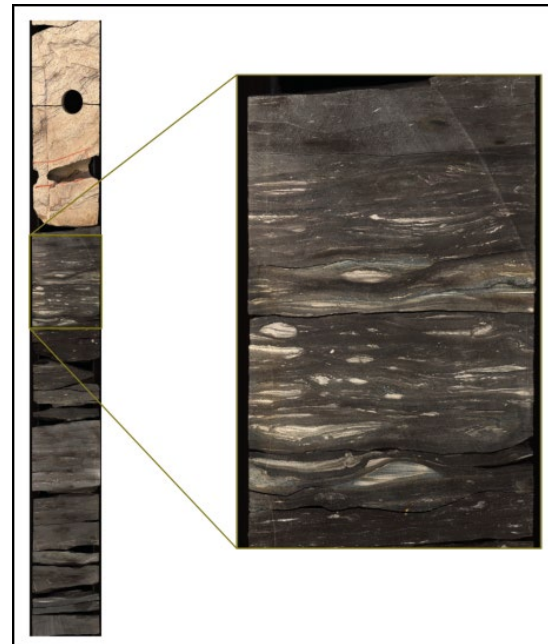


Figure 2. High resolution core image.

3. Core image features extraction

Firstly, we want to prepare some image features from the core images, to model the petrophysical properties quantitatively. Hence, we pre-process and analyze the core images using computer vision (CV) techniques.

Feature extraction is a core component of CV, both in traditional image processing, as well as the more recent deep learning frameworks. The traditional CV techniques have developed several approaches to extract image features from digital images or videos, so that a set of salient representations of the object of interest can be quantitatively captured. The features are chosen in a way sensitive to the target variables, to gain high-level understanding and perform model building and subsequent prediction. For instance, the color models provide simple yet useful characteristics about a rock description from image, represented in terms of the red/green/blue (RGB) color channels, as shown in **Figure 3**. In addition, the color model can be converted to the hue/saturation/brightness (HSV) model, to emphasize different characteristics of the same image, as shown in **Figure 4**. In addition, image entropy such as the Shannon entropy can be computed as a statistical measure of randomness that can be used to characterize the texture of the input core image.

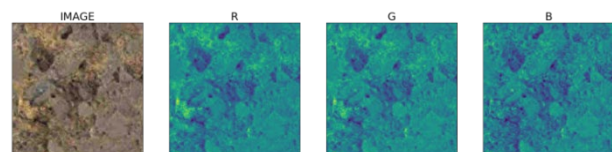


Figure 3. RGB color representation of a core image. (left) original core image in white color; (R/G/B) separated color channels of core image, R=red, G=green, B=blue.

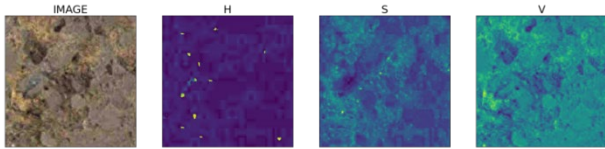


Figure 4. HSV color representation of a core image. (left) original core image in white color; (H/S/V) separated color channels of core image, H=hue, S=saturation, V=value/brightness.

The petrophysical properties can also correlate to the texture of the core, thus it is desirable to further include the core image texture representation in the analytic. We represent the core image texture through the Haralick texture features [4]. These features are computed from the Gray Level Co-occurrence Matrix (GLCM), which counts the co-occurrence of neighboring gray levels in an image [5]. Haralick then introduced 14 statistics calculated from the GLCM to describe the texture of an image. Typically, the maximum correlation coefficient is not calculated due to computational instability, so this feature is skipped in our analysis. The core images are partitioned into patches before calculating the GLCM and extracting the Haralick features from each image patch. **Figure 5** shows an example of Haralick texture features extracted from the core image. Although the Haralick textures are not straightforward to human, they are very informative to the machine learning data analytics.

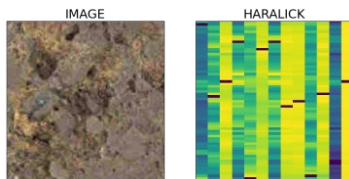


Figure 5. Haralick texture features a core image. (left) original core image; (right) Haralick texture features at each depth strips, each column represents one calculated coefficient in sequence of depth.

Each one of the image features described above are then aggregated horizontally into a profile in depth, resampled and aligned with well logs and core analysis data. To eliminate potential local artifacts in the core image, such as plug holes or markers, each feature depth profile is smoothed with box-car windows that can cover those artifacts, as shown in **Figure 6**. The smoothed profiles are then used subsequently in the model building. An example of core images and extracted image features in depth profile is shown in **Figure 6**.

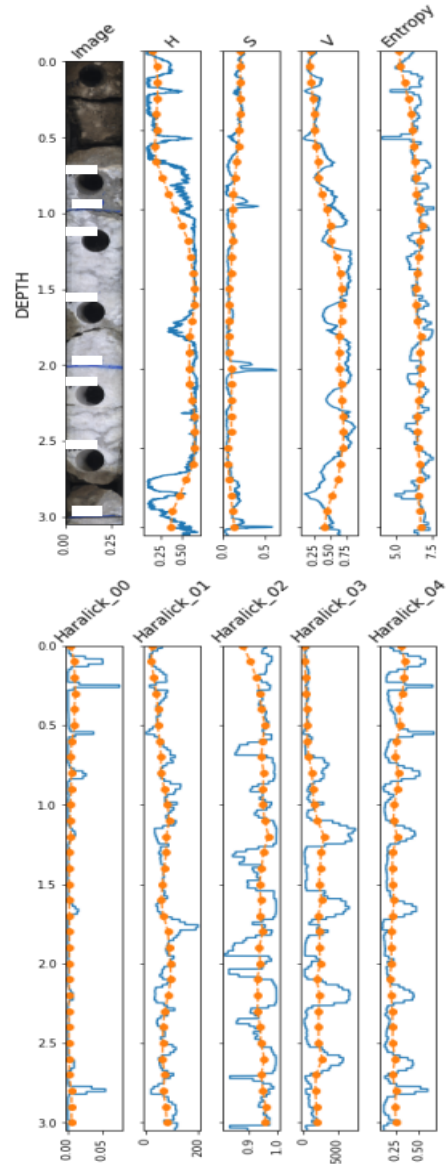


Figure 6. Example of core image (left) and extracted image features (right & bottom). Only a few of image features are shown here, from left to right: hue (H), saturation (S), value (V), Shannon entropy (Entropy), angular second moment (Haralick_00), contrast (Haralick_01), correlation (Haralick_02), sum of squares variance (Haralick_03), inverse difference moment (Haralick_04). The blue curves are the depth-wise aggregation of raw computation, and the orange curves are smoothed features profile for model building.

4. Machine learning modeling

We formulate the task of petrophysical property prediction as a supervised regression problem. The core image features described in the previous section and the well logs, such as core gamma log, are used as the input features for model building. The target properties from core analysis are used as the ground truth labels. In this paper, we investigate the prediction of three properties including grain density, porosity, and permeability.

The image features are first extracted from quality-checked and cleaned core images. Then the extracted

features are combined with well log data to create the ensemble feature profile. The core analysis data is used as the ground truth label set. The features are fed into selected machine learning regression algorithms to train the corresponding models, test on new image data, and for performance evaluation. The overall workflow is shown in **Figure 7**.

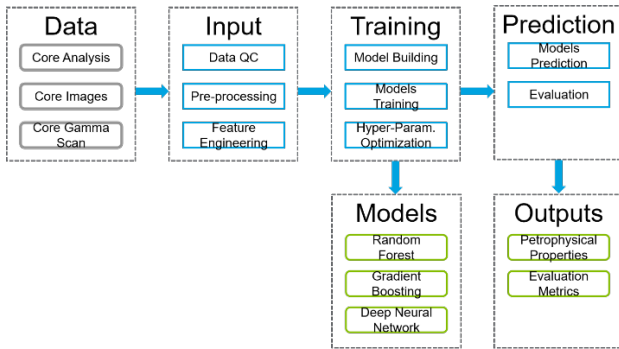


Figure 7. Workflow of AI-assisted petrophysical properties regression based on core images and well logs

4.1. Classification and Regression Tree

Classification and Regression Trees (CART) are among the most popular machine learning algorithms given their intelligibility and simplicity [6]. CART is a decision tree-based prediction model. Each decision tree is a set of internal (non-leaf) nodes and leaves. Each internal nodes are associated with an input feature, and the selected feature is used to make decision on how to divide the data set into two separate sets with certain criteria. Each leaf of the tree is labeled with a class or regression function, and the algorithm walks through the tree by making decisions at each node from input features and arrives at the corresponding leaf to compute the classification or regression. The procedure is shown as the sub-trees in **Figure 8(a)**.

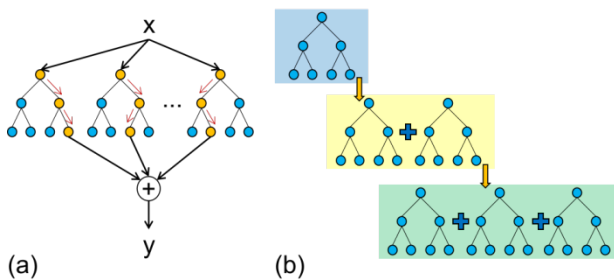


Figure 8. Diagram of classification and regression trees (CART) based regression models: (a) Random Forest; (b) Gradient Boosting.

In this work, two ensemble techniques are used to build the regression models, which effectively construct more than one CART. The random forest (RF) technique is one type of bootstrap aggregating or bagging ensemble, which builds multiple weak CART with repeatedly resampled training data and averages the trees for a consensus prediction [7]. The gradient boosting (GB) technique incrementally builds an ensemble by training

new weak CART to minimize the residual of previous iteration [8]. **Figure 8(a)&(b)** shows the diagrams of both RF and GB algorithms.

4.2. Deep Neural Network

Among the recent advances of machine learning, deep learning (DL) has attracted broad attention [9]. DL technology is based on deep neural networks (DNN), which are networks composed of layers of artificial neurons [10]. The neuron receives input signals from other neurons or external sources, sums them up with weights in transfer function, and produces output with non-linear activation function. The model is trained by learning optimal weights from training data.

In this work, the feed-forward network topology is adopted to model the petrophysical properties. The network consists of multiple layers of neurons, and connections between neighboring layers. The neurons in each layer are shown in **Figure 9**, and the last layer has a linear activation to output the target variable. Three individual networks are trained to model each petrophysical properties, grain density, porosity, and permeability respectively.

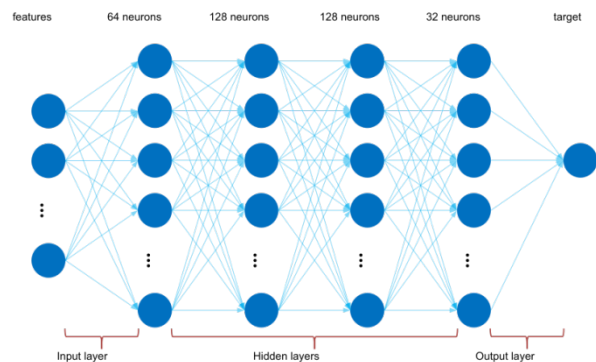


Figure 9. Diagram of deep neural networks. The image features and well logs data are fed as input to the network. The network consists of 4 hidden layers and output one target petrophysical property. Individual networks are trained to model each petrophysical property.

5. Field example

We tested the workflow of AI-assisted petrophysical properties prediction in a field from Saudi Arabia. The workflow is described in the previous section. The machine learning models used in this study are Random Forest, Gradient Boosting (GB) and Deep Fully Connected Neural Network (NN).

We plot the cross plots of the predicted against the actual values for each petrophysical properties **Figure 10**, to visualize the performance of the model prediction. All values are normalized to [0, 1] for the visualization. A guideline of $y=x$ is plotted in a red line to represent a perfect match. The prediction results from each model (NN, RF, GB) are reasonably close to the ground truth.

The grain density has a small dynamic range and almost discrete values related to rock types. The porosity has a good distribution, and all models can capture the property very well. The permeability is more challenging to predict due to weaker correlation between the physics of the rock and the image. Despite that, the models are still able to capture the overall trend with slightly higher level of variances than those of density and porosity prediction.

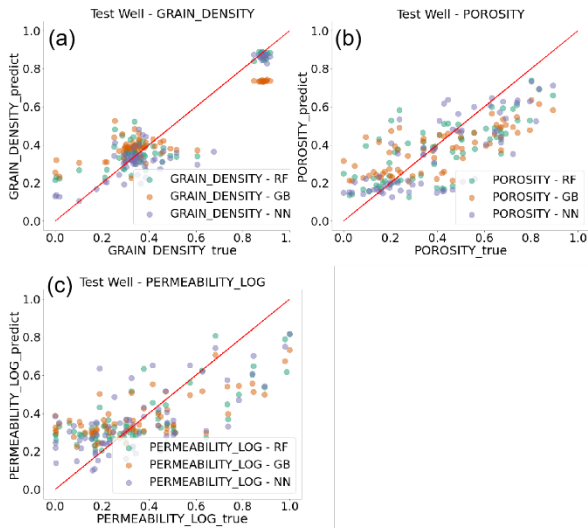


Figure 10. The cross plot of predicted against actual petrophysical properties. The target properties are: (a) grain density; (b) porosity; and (c) permeability (logarithmic). The regression algorithms are color-coded: (1) random forest as green dots; (2) gradient boosting as orange dots; and (3) deep neural network as purple dots. The red line represents the guide of $y=x$. All values are normalized to $[0, 1]$.

The depth tracks of predicted and actual petrophysical properties are shown in **Figure 11**. All values are normalized to $[0, 1]$ for the visualization, and the depth is represented in sample index. In grain density estimation, NN and RF models' predictions have very good performance and similar accuracy, while GB model prediction is also reasonable. In porosity estimation, all three models can track the trend well, while NN performs slightly better on capturing low porosity and RF performs slightly better on capturing high porosity. In permeability estimation, the prediction error is also reasonable with more challenging on lower and higher ends, while RF is slightly better at the average trend, and NN and GB are slightly better at providing the overall correlation between the prediction and ground truth.

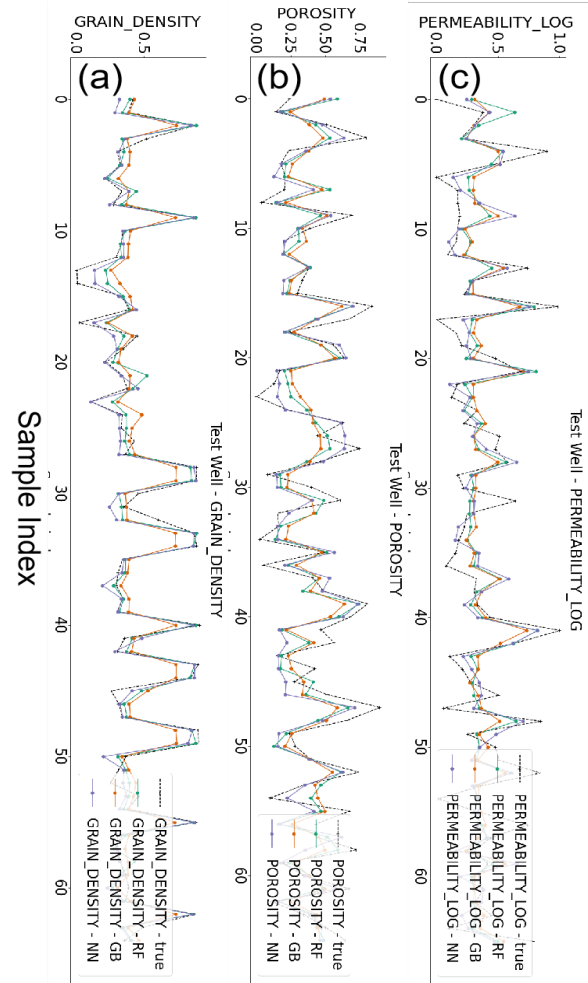


Figure 11. The depth track of predicted and actual petrophysical properties. The target properties are: (a) grain density; (b) porosity; and (c) permeability (logarithmic). The regression algorithms are color-coded: (1) random forest as green lines; (2) gradient boosting as orange lines; (3) deep neural network as purple lines; and (4) ground truth labels as black dash lines. All values are normalized to $[0, 1]$.

We also derived the feature importance from RF models respecting to each petrophysical properties, as shown in **Figure 12**. The feature importance describes which features are relevant in the modeling, where the relative scores are effective. It can help domain experts with better understanding of the core characteristics, by providing insights into the data set and models. The relative scores can highlight which features may be more relevant to the target property and model building, and which features are less relevant. Such knowledge can be interpreted by petrophysicists and data scientists as the basis for gathering more or different data. We can also improve the predictive models by selecting more significant features using feature importance. Such feature selection can simplify the modeling problem, speed up the modeling process, and sometimes improve the model performance. In this case study, we note that grain density is more relevant to hue, which is correlated to the rock type. For example, shale rocks often appear darker in color than sandstones or limestones, where correlates to distinguishable grain density. Meanwhile, porosity and permeability are relevant to both image

features and textures, especially some Haralick textures, due to the complex correlations between core images and physical properties.

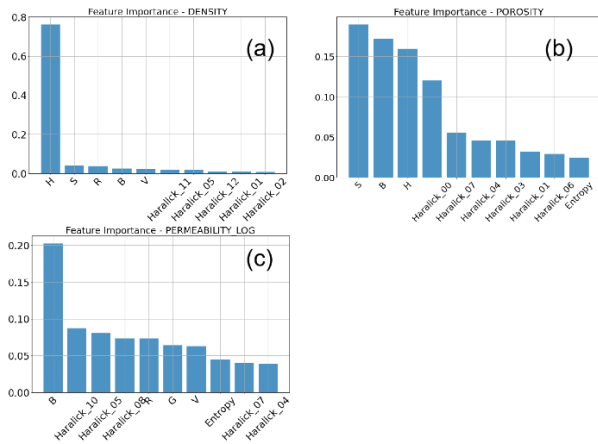


Figure 12. The feature importance of modeled petrophysical properties by Random Forest. The target properties are: (a) grain density; (b) porosity; and (c) permeability (logarithmic). The features are sorted by their importance to the prediction, and only the top 10 most important features are shown.

The overall performance is summarized in Table 1. In the table, y denotes the ground truth measurements and \hat{y} denotes the model prediction. The R^2 denotes the coefficient of determination and is defined by:

$$R^2 = 1 - \frac{\sum(y - \hat{y})^2}{\sum(y - \text{avg}(y))^2}$$

The full-scale error (FSE) is defined by:

$$\text{FSE} = (y - \hat{y})/\text{max}(y)$$

And the zero-normalized cross-correlation (CC) is defined by:

$$\text{CC} = \frac{1}{n} \frac{\sum(y - \text{avg}(y))(\hat{y} - \text{avg}(\hat{y}))}{\sqrt{\sum(y - \text{avg}(y))^2} \sqrt{\sum(\hat{y} - \text{avg}(\hat{y}))^2}}$$

Table 1. Evaluation metrics of all models to target petrophysical properties

Target	Model	R ²	FSE	CC
Grain Density	NN	70.4%	8.4%	86.0%
	RF	68.3%	8.7%	82.6%
	GB	56.6%	12.2%	77.5%
Porosity	NN	40.6%	14.3%	69.2%
	RF	40.7%	15.1%	68.1%
	GB	37.8%	16.0%	69.2%
Permeability (LOG10)	NN	33.2%	16.5%	62.9%
	RF	37.0%	16.4%	61.5%
	GB	34.4%	16.9%	62.2%

In this case study, NN has overall slightly better performance in terms of metrics of accuracy and correlation, while RF and GB also provide reasonable prediction. However, it should be noted that prediction accuracy depends on many factors including feature engineering, hyper-parameter tuning, and training vs. validation vs. testing data splitting.

6. Conclusion

We have demonstrated that it is feasible to integrate core images and well logs into quantitative petrophysical characterization workflow, with the assistance of computer vision and machine learning technology. We successfully applied the workflow on data from several heterogeneous reservoirs in Saudi Arabia. The core images are preprocessed and analyzed with CV techniques to extracted features as a depth profiles. The features are aligned with core gamma logs and plug analysis. Image features such as RGB and HSV provide more information related to lithology while entropy and Haralick provide more information regarding rock textures. The integrated features vector is imported in ML models building and training with difference ML regression algorithms, such as CART and DNN. The models produce high-resolution profiles of petrophysical properties that can be very useful for up-scaling. We evaluated the importance of each feature from CART model for individual target, to provide petrophysical insights of core characteristics and help in future model building. We also evaluated the model performances and achieved reasonably good correlation and accuracy from the models.

The AI-assisted workflow leverages machine learning techniques to automate the process of core data analysis, reduces human effort and cost, and provides fast core petrophysical properties prediction. The approach enables core digitization and core preservation, and reduces exploration risk, as well as provides petrophysical insights to assist core description. Machine leaning algorithms add value to business cases with workflow automation and improved efficiency.

References

1. F. J. Lucia, *Carbonate Reservoir Characterization* (Springer-Verlag Berlin, Heidelberg, 2007)
2. C. Xu, Z. Heidari, C. Torres-Verdín, SPE ATCE (2012)
3. A. Gonzalez, L. Kanyan, Z. Heidari, L. Olivier, *Petrophysics*, **61** 495–518 (2020)
4. R. M. Haralick, K. Shanmugam, I. Dinstein, *IEEE Trans. on Systems, Man, and Cybernetics* **SMC-3**, **No.6**, 610-621.(1973)
5. M. Partio, B. Cramariuc, M. Gabbouj, A. Visa, *Norsig2002* (2002)
6. M. Krzywinski, N. Altman, *Nat Methods* **14**, 757-758 (2017)

7. L. Breiman, *Machine Learning* **45(1)**, 5–32 (2001)
8. J. H. Friedman, *Computational Statistics and Data Analysis* **28**, 367-378 (2002)
9. J. Jiang, R. Xu, S. C. James, C. Xu, *SPE Res Eval & Eng* **24**, 250–261 (2021)
10. Y. LeCun, Y. Bengio, G. Hinton, *Nature* **521**, 436–444 (2015)

Combining high-resolution core data and machine learning schemes to develop sustainable core analysis practices

Christophe Germy^{1,*}, Tanguy Lhomme¹, Luc Perneder¹, and John Cummings²

¹EPSLOG, Liege, Belgium

²Stratum Reservoir, UK

Abstract. Traditional core analysis methods rely on extensive rock testing programs and require large numbers of plug samples. Numerous stakeholders compete for intact core material and often do not take the time to base their selection of samples on objective and reliable information. As a consequence, samples dedicated to core analysis programs consume a significant fraction of the material available and their selection is based on very little *a-priori* information. In an attempt to change this paradigm, we promote the CoreDNA workflow: a more sustainable approach of core analysis with the objective to optimize the value of cores by increasing the quantity of high-quality data extracted while keeping the analyst footprint to a minimum. The first step of this approach consists of combining several non-destructive tests to produce a multi-disciplinary set of continuous profiles of rock properties, as early as possible in the core analysis workflow, without causing any irreparable damage to the cores. Using fully mobile technology, continuous high-resolution and high-fidelity rock property data can be generated, immediately upon barrel-opening, prior to modification by slabbing and plugging. The technique can also be successfully mobilised on legacy core datasets. Multi-disciplinary data tracks ranging from textural and colour features of the rock, to grain size distribution statistics, elemental concentrations, elastic wave velocities and rock strength are generated. These tracks are integrated under a unique format and used as a road-map to guide core analysts during more complex and expensive discipline-specific tasks such as SCAL or RMT. These cost-efficient, non-destructive tests are designed to produce high-density multidisciplinary databases, providing data for targeted follow-on studies by not only core analysts but also geologists and petrophysicists. This data acquisition philosophy is completed by high-end data analytics using the latest developments in Machine Learning, with the objective to build and properly train predictive models for geological and petrophysical descriptions. Predictive AI models need to be trained with labelled data. CoreDNA provides multidisciplinary input data and output data constrained by rock/lithofacies, physical rock properties, elemental geochemistry data and possible diagenetic features, all concisely labelled and linked to high-resolution depth-referenced ultra-high resolution photographs. We describe cases in which supervised machine learning has been applied to CoreDNA analysis, and how this has improved the application of multidisciplinary core data in reservoir characterisation studies. The compatibility of CoreDNA data to support the classification of rocks with a convolutional neural network has been established. This represents a first step towards an Artificial Intelligence framework for the identification and classification of rock facies. The deployment of the iterative; multistage approach described above to real-world examples from extractive industries will further refine this novel approach. Such a coordinated effort will require extensive resources to create unambiguous labels for training sets. In turn, this will clear the path and lay the foundation for the building of robust AI models dedicated to the task of predicting rock properties from high quality, non-destructive core data.

1 Introduction

In a recent publication [1] we presented an integrated core analysis solution combining transdisciplinary, high resolution, non-destructive measurements on whole cores, for an early yet objective description of cores and the rapid estimation of formation properties.

Results of these fast tests are analysed real-time and turned into high resolution, continuous profiles of properties (petrophysical, geomechanical and geochemistry). This data is fed into (unsupervised) machine learning algorithms for the automated identification of lithofacies, the design of fit-for-purpose

plug selections and the programming of subsequent steps in core analysis programs.

This unsupervised machine learning scheme enables the identification of a number of facies utilising a cluster analysis which establishes ‘groupings’ of data points with similar physical, visual and elemental characteristics. This approach does not presently enable sorting into pre-existing classes. To achieve this requires the development of an iterative, multi-stage approach, involving supervision, which is the focus of this paper.

* Corresponding author: tanguy.lhomme@epslog.com

2 Methodology

2.1 Workflow

Acquire CoreDNA data: CoreDNA data acquisition and analysis methods produce the input data to be fed into AI models. These cost-efficient, non-destructive tests are designed to produce high-density multidisciplinary databases, forming the input for predictive expert geologist and petrophysicist systems.

Construct a predictive model using a neural network: Predictive AI models need to be trained with labelled data. This implies the creation of training data sets for which CoreDNA input data is available together with output data, *i.e.* highly detailed geological descriptions with facies, diagenetic features and other geological markers already identified and labelled in ultra-high resolution photographs, together with accurate petrophysical properties.

Optimize the performance of the predictive model: Creating such a training set is a highly resource-intensive task and should be anticipated as an iterative improvement cycle. The data set used to train the AI model is meant to grow over time, as more and more CoreDNA input data become available along with corresponding standardized geological labels. This continuous optimization ensures that the AI model prediction performances increase with the number of projects.

2.2 Data acquisition and integration

As a core data acquisition principle, CoreDNA combines transdisciplinary, high-resolution, non-destructive measurements for a rapid and objective description of cores and the quantitative estimation of formation properties. Core samples, which may be whole cores still in their half-open liners, or fractions of legacy cores, are scanned with multiple sensors interfaced to one single table-top equipment. These smart sensors share the same depth reference and compatible resolution ranges. The complete CoreDNA test series includes the following tests:

- Portable XRF measurements for elemental composition,
- High-resolution photo for panoramic viewing of the cores, under white and UV lights,
- Laser scan for surface rugosity and grain properties
- Ultra-high-resolution (UHR) photos (1.8 μ m/pixel) for the rock texture and grain properties,
- Probe permeability,
- P- and S-wave ultrasonic velocity logging,
- Strength log from the scratch test,
- Grain size and grain fabric data.

CoreDNA data sets are designed to be used as a single source, unified format platform to unravel the complexity of tested cores. The basic analysis concept for such multi-dimensional data sets involves data checking and augmentation routines that prepare for unsupervised and supervised machine learning schemes.

2.3 Supervised Machine Learning

The relevance of CoreDNA data to train neural networks was established with a dedicated study. The findings are summarized in this section.

Data set: This study uses ultra-high-resolution photos together with physical data such as elemental compositions from pXRF, grain size, and strength, acquired on a series of 27 outcrop samples (17 sandstones and 10 carbonates), each of 20cm in length, with known labels (Figure 1 and Table 1).



Figure 1: Panoramic photos of the 27 outcrop samples used to train a supervised machine learning scheme for rock classification purposes.

Table 1: Class labels

Class	Label
1	Alabama Marble
2	Bandera Brown
3	Bentheimer
4	Berea Buff
5	Berea Gray
6	Berea Sister Gray
7	Boise
8	BonneTerre Dolomite
9	Burlington (Carthage Marble)
10	Carbon Tan
11	Castlegate
12	Colton

13	Crab Orchard
14	Edwards White
15	Edwards Yellow
16	Idaho Gray
17	Indiana High Perm
18	Indiana Low Perm
19	Kentucky
20	Kirby
21	Leapord
22	Nugget
23	Parker
24	Rocheron
25	Sans Saba
26	Silurian Dolomite
27	Wisconsin

Using standard augmentation techniques [2] the number of 600x600 pixel photos of samples was brought to 479. The multidimensional data set was completed with 16 CoreDNA vectors including strength, mean grain size derived from laser topographical maps, and elemental compositions from XRF measurements (Figure 2, Figure 3, Table 1, Table 2).

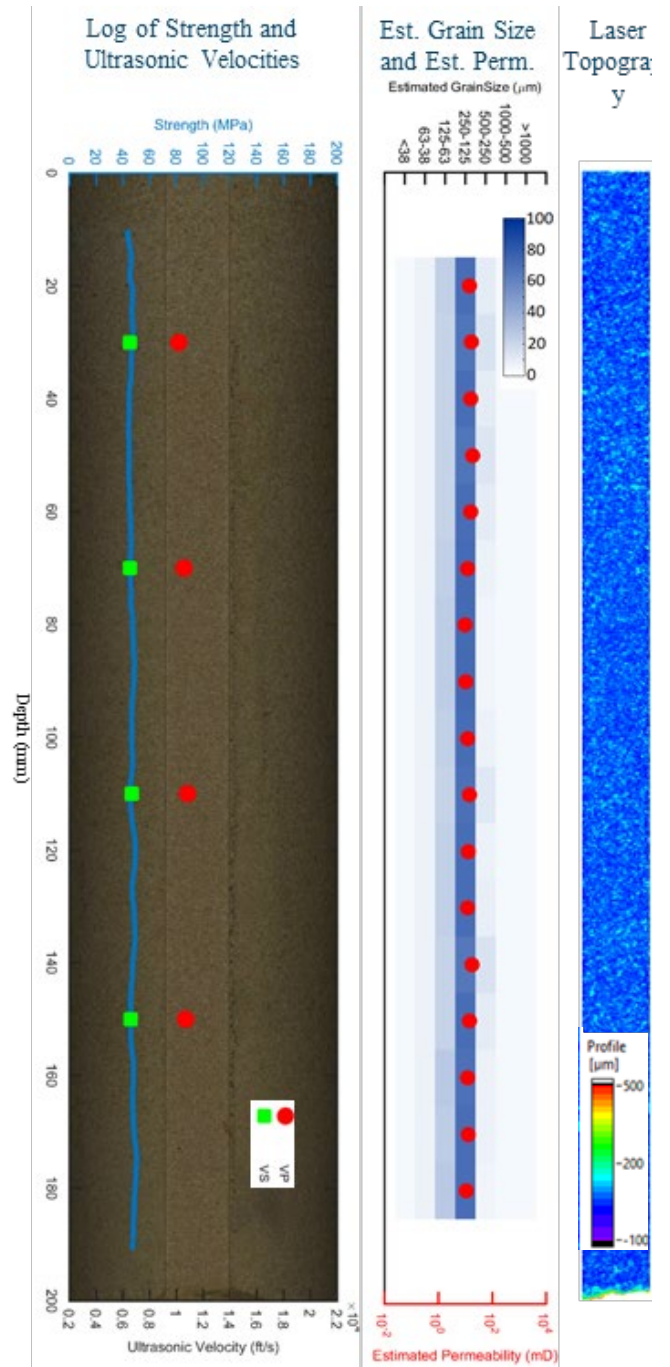


Figure 2: CoreDNA data for the San Saba outcrop sample: Strength and ultrasonic velocity profiles, high resolution

panoramic core photo, rugosity map and permeability index estimated from grain size distributions.

Ultra High Resolution Pictures

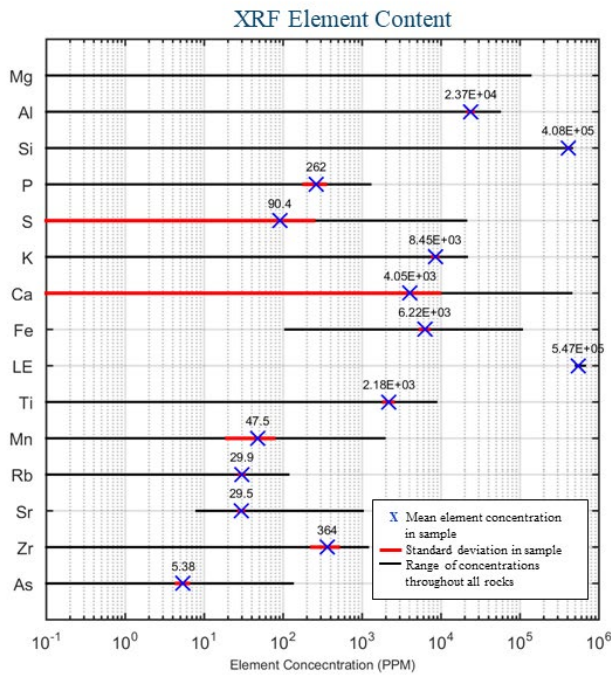
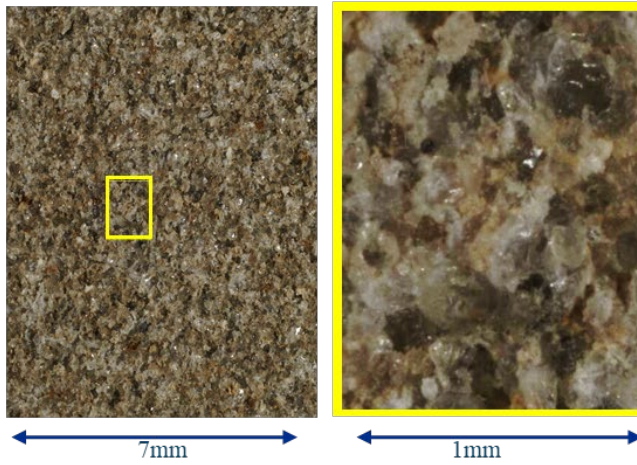


Figure 3 : CoreDNA data for the San Saba outcrop sample: high and ultra-high definition photographs; elemental composition from XRF measurements.

Table 2 : CoreDNA data for the Sans Saba outcrop sample: geomechanical properties.

Test Results	Rock Strength [MPa]	Ultrasonic Wave Velocity [ft/s]		
		Vp	Vs	
Sample A	Mean	45	11,053	7,044
	STD	3	582	87
	Min	37	10,572	6,944
	Max	53	11,581	7,118
Sample B	Mean	47	10,572	6,568
	STD	2	280	72
	Min	44	10,192	6,518
	Max	50	10,842	6,671

Table 3: CoreDNA data for the Sans Saba outcrop sample: petrophysical properties.

Test Results	Est. Grain Size [mm]	Est. Perm. [mD]	
			Sample A
	STD	5.8	3.3
	Min	135.3	8.0
	Max	154.5	18.9
Sample B	Mean	146.4	13.7
	STD	4.2	2.5
	Min	139.6	9.9
	Max	153.9	18.5

This data set was split in training, validation and test sets according to the proportion shown in Figure 4.

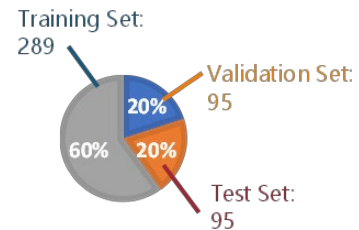


Figure 4: Data set proportions for neural network training and validation.

Convolutional Neural Network: A version of the convolutional neural network EfficientNet pre-trained with 14 million images from the ImageNet database corresponding to 20,000 categories, was used for transfer learning [3].

Results. After training the neural network with 60% of the multi-dimensional input data set (Figure 5), we tested its ability to match tested rock with existing labels.

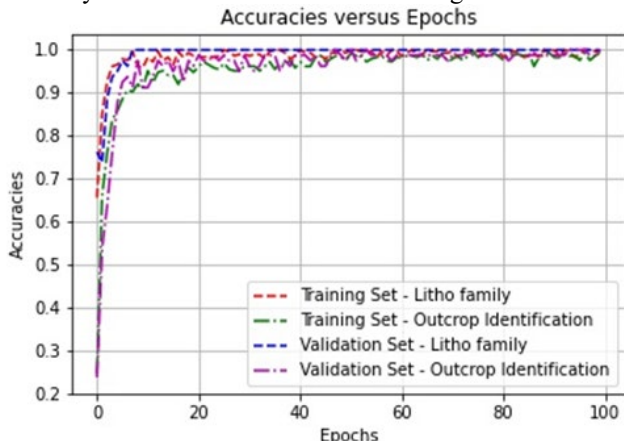


Figure 5: Neural network training phase.

The current classification performances of the network reach an accuracy of 99%, as seen in Figure 6 showing the numbers of actual samples in the test set which were properly identified for each class.

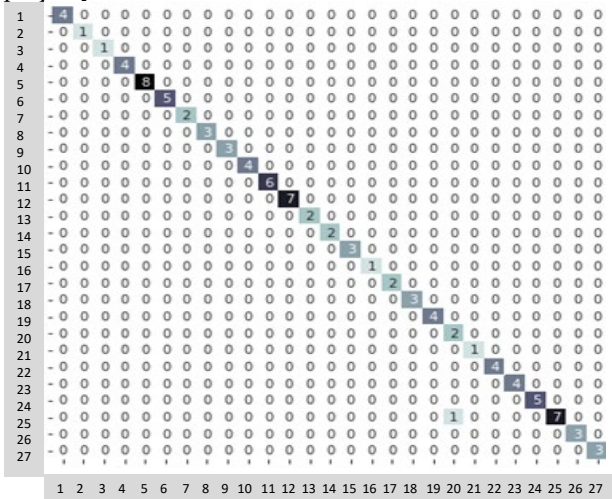


Figure 6: Actual vs predicted labels by the trained EfficientNet convolutional neural network.

Only one data point (corresponding to the Sans Saba rock sample) out of 95 was mislabelled and confused with another rock (Kirby) with very similar physical properties and visual aspect. This represents an exciting first step towards executing CoreDNA analysis, and in particular, ultra-high resolution image analysis, with the aim of automated identification and classification of rock types.

2.4 Optimizing the performance of the predictive model

Creating such a training set is a highly resource-intensive task and should be anticipated as an iterative improvement cycle described in Figure 7.

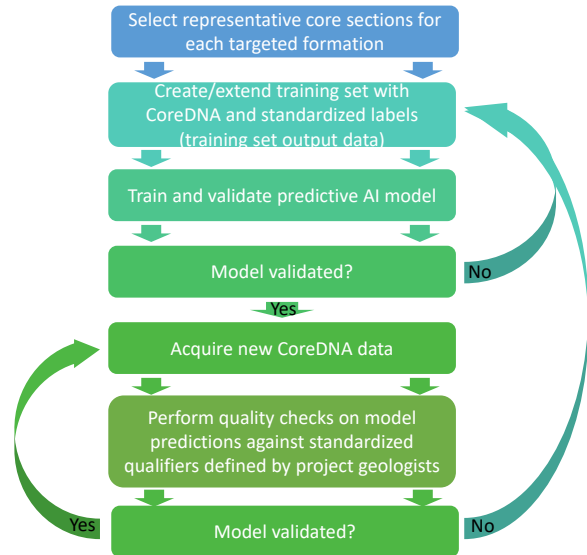


Figure 7: Iterative AI model improvement loop.

The value of the multistage approach described above comes from the significant reduction of the effort required by the quality checks to validate the AI model predictions compared to the requirements for the extension of the training set. The deployment of such an approach to real-world examples from extractive industries will require significant resources to create extensive sets of digital core data and strictly repeatable standards, if this data is to be transformed into unambiguous digital labels used in training sets. In an attempt to enhance the coherence and reduce the subjectivity of man-made observations and interpretations, which can often be applied in conjunction with objective physical data, we designed a software tool dedicated to the registering of such information into shared multidisciplinary databases.

2.5 LithoLog

LithoLog software is a product developed with input from expert sedimentologists, with the goal of digitalising sedimentological information using standardized qualifiers to minimise subjectivity and inconsistency in the description process, while also generating robust, fully quantitative sedimentological data at a scale normally reserved for detailed petrographic analysis/optical microscopy. It is designed to simplify navigation through large multiscale datasets composed of (i) core data logs with centimetre resolution, (ii) panoramic high-resolution pictures covering 1m (3 feet) of core sample, and (iii) ultra-high resolution pictures of each centimetre of core. The software ergonomics and accessibility have been prioritized to create a user-friendly platform, suitable for a diverse range of disciplines/contributors, thereby accelerating the creation of large databases for AI model training.

Digital core description: The main features of LithoLog software include visualisation panels for high (35µm/pixel) and ultra-high (1.8µm/pixel) resolution pictures. The resolution enables detailed sedimentological core description, which provides hugely important information and data on the fabric and texture of reservoir rocks, while providing input into the interpretive elements

of core description such as depositional process *and environment assignments*.

Standardized qualifiers: Functionalities are built in the software so that users can edit primary lithology and qualifiers at a centimetre scale. The introduction of a single set of standardized qualifiers shared among multiple users is taking one step towards standardized workflows and methodologies for core descriptions, which are lacking compared to RCA/CCA/SCAL type studies.

Visualizing Grain size distributions: Graphic tools are included to visualize and perform quality checks on grain size distribution data from CoreDNA laser scans for entire cored sections, with a resolution of a centimetre. A UHR photo (1.8 μ per pixel) is loaded with a digital grain size overlay, with 1 image per cm. The digital grain size overlay can be selected from pre-defined Wentworth-scale grainsize bins [4] until the circles match visible grains. Individual grain diameter can be measured with micron scale accuracy, meaning even poorly sorted sediments can be accurately quantified (Figure 8).

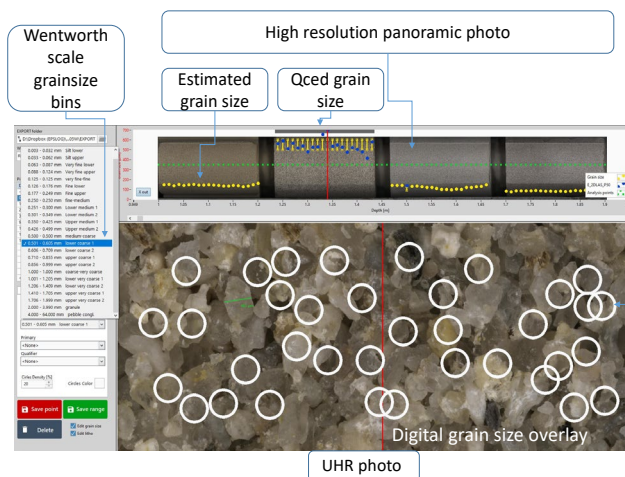


Figure 8: Grain size distributions visualisation and quality checking in LithoLog.

Third-party data visualization: Data can be imported from any *.las or *.csv file, ensuring applicability across industry. This provides further assistance to select appropriate qualifiers to label the formation under study.

3 Conclusions

CoreDNA is a technology that can be applied on fresh cores as soon as barrels are opened but also on legacy cores. Its main objective is to assist core analysts with continuous, high-resolution profiles of high fidelity properties measured directly on cores, before the core has been permanently modified by slabbing and plugging. For this, we create multi-disciplinary data tracks, which can be all integrated under one unique format and used as a road-map to guide core analysts during more complex and expensive discipline-specific tasks such as SCAL or RMT.

CoreDNA arrays of transdisciplinary, high-resolution, non-destructive tests were deployed as an integrated core analysis package in conjunction with unsupervised and supervised machine learning schemes.

The compatibility of CoreDNA data to support the classification of rocks with convolutional neural network was established. The development of an Artificial Intelligence framework for the identification and classification of rock facies is a piece of work in progress. Next steps will require the deployment of the iterative, multistage approach described above to real-world examples from extractive industries. Such a coordinated effort will require extensive resources to create unambiguous labels for training sets. In turn, this will clear the path and lay the foundation for the building of robust AI models dedicated to the task of predicting rock properties from high quality non-destructive core data.

References

- [1] C. Germy, T. Lhomme and P. Bisset, “Combining high-resolution core data with unsupervised machine learning schemes for the identification of rock types and the prediction of reservoir quality” in The 34th International Symposium of the Society of Core Analysts, 2021.
- [2] C. Shorten and T. Khoshgoftaar, “A survey on Image Data Augmentation for Deep Learning” *Journal of Big Data*, vol. 6, no. 60, 2019.
- [3] M. Tan and Q. V. Le, “EfficientNet: Rethinking Model Scaling for Conventional Neural Networks” in International Conference on Machine Learning, Long Beach, 2019.
- [4] C. K. Wentworth, “A Scale of Grade and Class Terms for Clastic Sediments” *The Journal of Geology*, 1922.

Prediction of centrifuge capillary pressure using machine learning techniques

Brandon Jeremy Bursey¹, Erfan Mohagheghian¹, Edison Sripal¹ and Lesley Anne James^{1,*}

¹Department of Process Engineering, Memorial University of Newfoundland, St. John's, NL, Canada

Abstract. In current literature in the petroleum industry, machine learning has been used to predict capillary pressure only on the centrifugal data points and not the complete capillary pressure curves generated from existing correlations after analysis. This paper will present novel information that will benefit the petroleum industry as it shows machine learning techniques can be used to obtain the complete capillary pressure curve which is the end goal in undertaking an SCAL centrifuge experiment.

This research involves testing core samples using a centrifuge set up to produce capillary pressure data points. Then, using a commercial SCAL interpretation software, the collected data is utilized to generate complete capillary pressure curves based on developed literature correlations. RCAL data for the core samples is also obtained to be used with the machine learning techniques. The machine learning models are then applied to the collected data to predict the capillary pressure curves. Optimization of the different machine learning techniques is done to improve the predictions.

The results show the machine learning techniques perform very well on the validation set after being trained on the training set. The machine learning models also provide reasonable prediction of the complete capillary pressure curves on the testing data set. Changing of the machine learning technique parameters also shows the effect on the overall precision and the improvements that can be made. Further research can be done to see the effectiveness of using machine learning techniques to predict other SCAL properties such as relative permeability. This can then greatly reduce the time needed to obtain these extremely important properties for reservoir characterization.

1 Introduction

Researchers continue to find new ways to reduce the time and improve the accuracy of reservoir characterization [1]. Specialized core analysis (SCAL) examines important reservoir characteristics such as capillary pressure and relative permeability to estimate incremental oil recovery during secondary water or gas flooding and tertiary enhanced oil recovery. Arguably, SCAL is more time consuming and has more uncertainty compared to routine core analysis and fluid characterisation. Capillary pressure (P_c) is the pressure between two immiscible phases in a capillary tube or, in this case, within the rock's pores [2]. Capillary pressure is measured in a lab through spontaneous imbibition, gravity drainage, and forced imbibition tests. P_c is used directly in reservoir simulators to account for unrecoverable oil and it is further used to estimate relative permeability or the relative conductivity of the rock to more than one fluid phase simultaneously. The three main test methods used to determine capillary pressure curves are centrifuge, porous plate, and mercury injection [2]. The advantages and disadvantages of these methods are summarized in Table 1. It is worth pointing out that mercury injection capillary pressure (MICP) does not respond to wettability components in the pores since Hg is an ideal non-wetting fluid. Hence MICP reflects only the pore geometry and therefore differs slightly from other tests that use oil/brine/gas.

The oil and gas industry has always been highly competitive and somewhat unpredictable. In recent years, companies have

begun using machine learning techniques to combat several challenges and issues in data processing and handling in various oil and gas activities such as reducing risk factors and cost of maintenance [3]. In current literature, machine learning has been used to predict the experimental capillary pressure data points obtained from centrifugal and mercury injection tests with varying results [4-6]. For the case that did use centrifugal data, correlations were not applied to the experimental results to obtain a complete capillary pressure curve. This research aims to obtain complete capillary pressure curves generated from existing correlations after analysis of centrifugal data and then test the novelty in using machine learning techniques to predict the experimental capillary pressure curve and water saturation. Three machine learning techniques, including the artificial neural network, support vector regression and random forest regression were used to predict the capillary pressure from centrifuge test samples with routine core analysis data (porosity, permeability, grain density, and irreducible water saturation) being used as inputs. ML-based approaches generate a multi-point capillary pressure curve as a function of fluid saturation using the provided input parameters. The ML prediction is not just a single value just as the experimentally measured and calculated capillary pressure values are recorded at discrete fluid saturation points. Although experimental techniques are broadly used to generate the capillary pressure curve of core samples, they are expensive and require core samples to be in reservoir conditions that is very difficult to achieve. As a result, researchers ponder whether data-driven

* Corresponding author: ljames@mun.ca

methods can estimate SCAL data. Can one develop accurate machine learning methods to predict SCAL data such as capillary pressure of core samples from routine core analysis data without a need for time consuming and finicky laboratory experiments?

Table 1. Pc Methods – Advantages and Disadvantages [2]

Method	Advantages	Disadvantages
Centrifuge	<ul style="list-style-type: none"> - Applicable to most rock types - Simple and quick - Non-destructive test - Uses synthetic reservoir fluids 	<ul style="list-style-type: none"> - Most expensive method - Raw production data needs to be corrected by the test lab
Porous Plate	<ul style="list-style-type: none"> - Best method to achieve a uniform saturation profile - Uses synthetic reservoir fluids - Non-destructive test 	<ul style="list-style-type: none"> - Time consuming to achieve complete Pc curve - Time allowed to achieve equilibrium can completely govern resultant curve
Mercury Injection	<ul style="list-style-type: none"> - Low-cost technique - Rapid tests 	<ul style="list-style-type: none"> - Not representative of reservoir fluids - Test is destructive (mercury remains in sample)

1.1 Machine Learning Technique Types

Machine learning is the broad study of programming algorithms that can learn through experience from the use of a variety of data [7]. Machine learning techniques are categorized into either supervised or unsupervised learning with supervised learning being further broken into classification and regression as shown in Fig. 1.

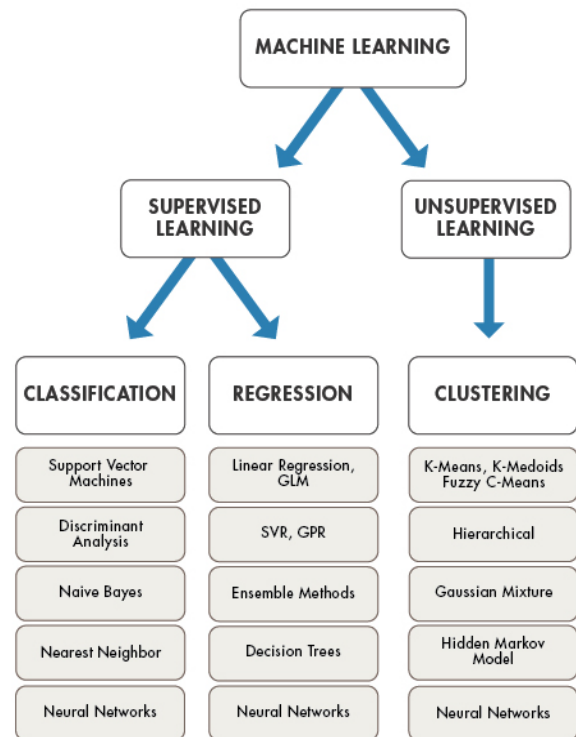


Fig. 1. Machine Learning Algorithm Breakdown [8]

For the purposes of this research, supervised learning regression techniques that were used are briefly explained as follows.

1.1.1 Support Vector Regression

Support vector regression (SVR) is a popular technique where support vector machines are adapted for regression with a quantitative response [9]. The technique provides flexibility in defining the acceptable error for the model and determines an appropriate line or hyperplane fit to the data [10]. For SVR, the objective function is to minimize the L2-norm of the coefficient vector. One strength of SVR is a variety of kernel functions being available to select or modify depending on the requirements for your own predictions [11]. The kernel function transforms data that are not linearly separable to linearly separable in a higher dimensional space. As well, given its dependence on support vectors, not all training data is needed for predictions. The support vectors determine the decision boundaries between the data from different trends that are used to do regression. SVR is a supervised technique in which data are fed into the model in (input, output) pairs.

1.1.2 Artificial Neural Network

Artificial neural network (ANN) is another regression technique that learns from processing (input, output) data pairs supplied during the training-testing split of input data. The more examples and variety of inputs the model is given, the more accurate the model typically will predict outputs [9]. Fig. 2 below shows the architecture of an ANN model, where the X nodes are the input layer, the Z nodes are the hidden layer, and the Y nodes are the output layer. For this study, X consists of porosity, permeability, grain density, and irreducible water saturation and Y consists of capillary pressure and water saturation. The number of hidden layers

and epochs (number of cycles through the training data) can be varied to see their effect on the predictions. The input to every hidden layer is the linear combination of the outputs of the previous layer passed through a non-linear function, also called the activation function. Activation function can be one of hyperbolic tangent (tanh), sigmoid, Rectified Linear Unit (ReLU), linear, etc.

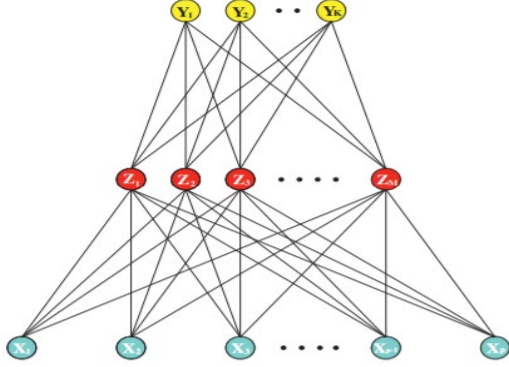


Fig. 2. Single Hidden Layer ANN [8]

1.1.3 Random Forest Regression

Random forest regression (RFR) is a supervised learning technique that utilizes ensemble learning for regression analysis. The method uses predictions from multiple learning algorithms to obtain a more accurate prediction [12]. RFR is also one of the most powerful regression techniques and is useful for non-linear relationships. A typical setup of a RFR model is where multiple decision trees are constructed on training data and the mean of the trees is outputted as the prediction. Each tree processes the input parameters, including the porosity, permeability, grain density, and irreducible water saturation to predict capillary pressure and water saturation. Therefore, capillary pressure and water saturation are the output of each tree. The final output will be the average of all trees outputs in the forest.

However, it should be pointed out that capillary pressure curves generated by machine learning methods and experimental methods are often not accurate and seldom match the distribution of wetting and non-wetting phases sensed by imaging techniques. An ML-based method can predict water saturation and capillary pressure curve much faster than laboratory methods and potentially with no more uncertainty. Also, ML-based methods can be generalized to different fields if enough samples are used to train the models. In this manner, the need for core samples from new fields in reservoir conditions is mitigated.

2 Literature Review

2.1 Centrifuge Capillary Pressure Correlations

The centrifuge capillary pressure problem involves solving the challenge of determining local saturations along the length of the core based on the averaged saturations measured during the centrifuge experiment [13]. To solve the centrifuge capillary pressure problem numerous correlations have been developed that take on the general form of Eq. 1.

$$S(P_{c1}) = a_1 \hat{S}(P_{c1}) + a_2 P_{c1} \frac{d\hat{S}(P_{c1})}{dP_{c1}} + E \quad (1)$$

where a_1 , a_2 , and E will vary depending on the correlation used [14]. The main assumptions are hydrostatic equilibrium being reached at each phase and the boundary condition of the capillary pressure being zero at the outflow face [13]. $S(P_{c1})$ is the local saturation and $\hat{S}(P_{c1})$ is the average saturation measured during the centrifuge experiment. P_{c1} is determined from Eq. 2.

$$P_{c1} = \frac{1}{2} \Delta\rho \omega^2 (r_2^2 - r_1^2) \quad (2)$$

Where $\Delta\rho$ is the difference in the fluid densities and r_1 and r_2 are the radii at the inner and outer faces of the sample in the centrifuge core holder and ω is the rotation speed.

2.1.1 Hassler Brunner Method

The simplest solution for the centrifuge capillary problem was developed by Hassler and Brunner and it is also the poorest solution as it neglects both radial and gravity effects [15]. These assumptions can be satisfied for very short and narrow samples spun far from the rotation axis. In the case of the general centrifuge capillary problem, the Hassler-Brunner equation reduces to the following:

$$S(P_{c1}) = \hat{S}(P_{c1}) + P_{c1} \frac{d\hat{S}(P_{c1})}{dP_{c1}} \quad (3)$$

where $a_1 = 1$, $a_2 = 1$ and $E = 0$.

Forbes first solution demonstrated that this solution is always significantly lower, in terms of saturation, than the true $S(P_c)$ solution [14].

2.1.2 Forbes First Solution

Forbes built upon previous solutions to the centrifuge capillary problem and came up with his own solution that still neglects both radial and gravity effects but incorporates the difference in the centrifuge core radii [13]. Forbes solution took the form shown in Eq. 4.s

$$S(P_{c1}) = \hat{S}(P_{c1}) + \frac{1}{1+\alpha} P_{c1} \frac{d\hat{S}(P_{c1})}{dP_{c1}} \quad (4)$$

where $a_1 = 1$, $a_2 = \frac{1}{1+\alpha}$ and $E = 0$.

$$\alpha = \frac{1 - \sqrt{1-B}}{1 - 2\sqrt{1-B}} \quad (5)$$

$$B = 1 - \left(\frac{r_1}{r_2}\right)^2 \quad (6)$$

2.1.3 Spline Functions

Nordtvedt and Kolltvelt were first to approximate the wetting phase saturation as a function of the capillary pressure whereby the capillary pressure curve is approximated piecewise by a polynomial [16]. This parameter estimation technique is usually related to functions which are too simplistic to describe the shape of capillary pressure curves [15]. A linear system of equations is then obtained and the piecewise approximation polynomial takes on the form shown in Eq. 7.

$$S(P_{c1}) = a_{i,0} + a_{i,1}P_{c1} + a_{i,2}P_{c1}^2 \quad i = 1, 2, \dots, n_I \quad (7)$$

Where i indicates the interval number and n_I refers to the total number of intervals.

2.2 Current Machine Learning Applications

Busaleh et al. used several types of machine learning techniques to predict capillary pressure in carbonate oil reservoirs from data comprised of mercury injection drainage capillary pressure data [4]. Their data consisted of 202 carbonate core samples that contained at minimum 70 capillary pressure versus saturation points in addition to the corresponding porosity, permeability, and grain density for the core. For their machine learning techniques, the inputs used were porosity, permeability, grain density, and water saturation with their output being capillary pressure. They used a training-testing split of 70-30 of the core sample data. With the variety of machine learning techniques came with mixed results. ANN-trainbr, ANN-trainlm, ANN-trainscg, ANN-trainoss refer to neural networks using Bayesian regularization backpropagation, Liebenberg-Marquardt optimization, scaled conjugate gradient, and one-step secant methods, respectively.

The decision tree algorithm performed the best on the training data however this is likely due to overfitting as it performed considerably worse on the testing set. The ANN-trainbr method performed the best overall; however, there is still significant room for improvement [4].

Jamshidian et al. obtained centrifuge capillary pressure data for 15 core samples each of which having 27 capillary pressure data points totalling 405 data points. They completed seven cases to see the effects of additional input parameters on the final predictions [5]. An ANN model with a Cuckoo optimization algorithm was used to predict capillary pressure as the only output which was then compared against the experimental centrifuge values. The training set consisted of 8 cores with the remaining 7 used for validation.

Table 2. ANN Models with Input Parameters [5]

ANN Modelling Case	Contributing Input Parameter(s)
Case 1	S_w
Case 2	S_w, k_{air}
Case 3	S_w, k_{air}, ϕ
Case 4	$S_w, k_{air}, \phi, S_{w,irr}$
Case 5	$S_w, k_{air}, \phi, S_{w,irr}, k_w$
Case 6	$S_w, k_{air}, \phi, S_{w,irr}, k_w, k_o @ S_{w,irr}$
Case 7	$S_w, k_{air}, \phi, S_{w,irr}, k_w, k_o @ S_{w,irr}, \rho_{grain}$

Table 2 above shows the different cases modelled with the addition of input parameters. Water saturation, air permeability, porosity, irreducible water saturation, water permeability, oil permeability at irreducible water saturation, and grain density were the contributing input parameters.

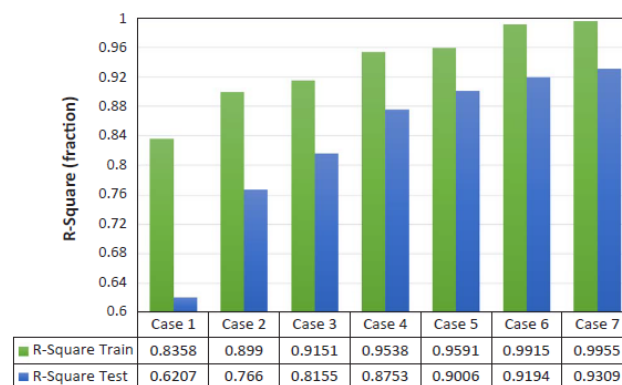


Fig. 3. Correlation Coefficients for the Different Cases [5]

From Fig. 3 the increase of input parameters correlates with an increase in the correlation coefficient for both the training and testing data sets. Case 1 through 7 correlates to the ANN modelling case and contributing input parameters shown in Table 2. Also, the greatest prediction comes with all the input parameters being used. Fig. 4 below highlights the accuracy of the predictions for core number 9 under the case 7 scenario.

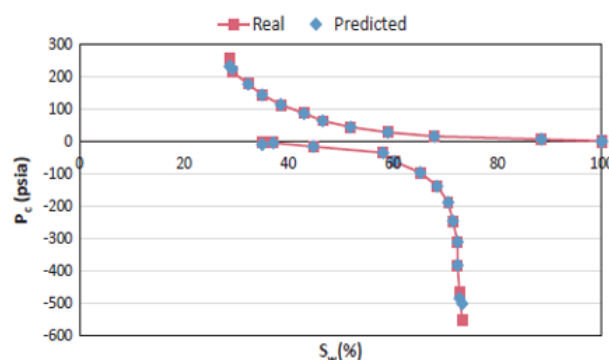


Fig. 4. Core Number 9 Experimental versus Predicted Values [5]

Kasha et al. developed a new method for capillary pressure estimation based on the Leverett J-function as shown in Eq. 8. This is a dimensionless function of water saturation describing capillary pressure also considering pore size and interfacial tension [6].

$$J(S_w) = \frac{P_c(S_w) \sqrt{\frac{k}{\phi}}}{\gamma \cos \theta} \quad (8)$$

$$r = 900.33 \sqrt{\frac{k}{\phi}} \quad (9)$$

Eq. 9 above is the Carman-Kozeny equation which was used to determine the average pore size. The data consisted of 214 samples of mercury injection data with permeability and porosity data and the J versus water saturation for each curve was calculated. The workflow consisted of the formulation of grouping features from porosity, permeability, and pore throat-radius. The formed grouping features can be seen in Eq. 10 and 11.

$$F_1 = 0.01(\ln k \ln r^{0.5} - 3.23) \quad (10)$$

$$F_2 = 0.39 \left(\frac{\phi^{0.5} \ln k}{\ln r^{0.5}} - 0.11 \right) \quad (11)$$

This approach was compared against the flow zone indicator (FZI) method, which is a rock typing method grouping capillary pressure data into different rock types [6].

$$F_{1(FZI)} = 0.37 \left(\log \frac{\phi}{1-\phi} + 2.71 \right) \quad (12)$$

$$F_{2(FZI)} = 0.28 \left(\log \sqrt{\frac{k}{\phi}} + 1.71 \right) \quad (13)$$

Next an unsupervised machine learning technique (clustering) was used to group each sample based on the grouping features. A technique called the within-cluster sum of squares (WCSS) was used to determine the optimum number of clusters.

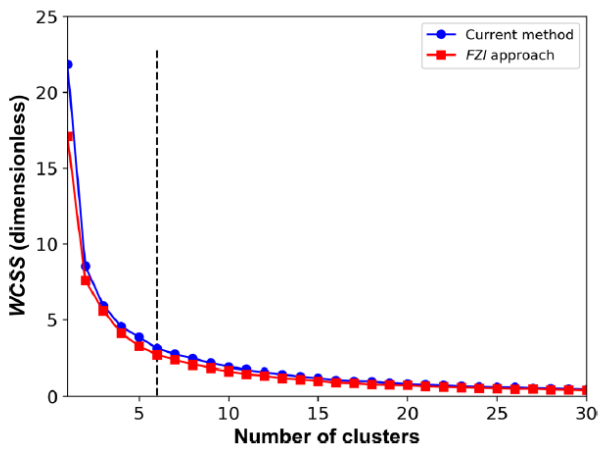


Fig. 5. WCSS Optimum Clusters [6]

The WCSS is the sum of squared deviations between each cluster's data points and the cluster's centroid. In this case, as shown in Fig. 5, four scenarios were considered based on the maximum curvature of 6 and three higher cluster scenarios of 10, 15 and 20 clusters.

The results of the cluster scenarios based on the grouping features can be seen in Fig. 6.

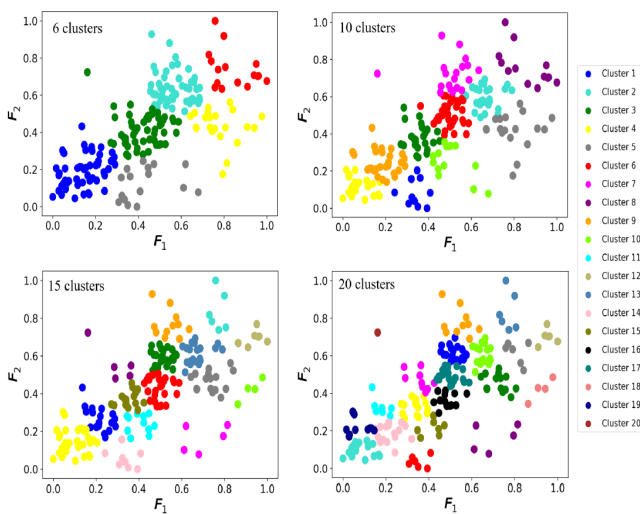


Fig. 6. Clustering Scenarios Based on Grouping Features [6]

From these generated clusters in each of the scenarios, an average J curve was calculated based on the J curves for each

sample that were identified in the specific cluster as seen in Fig. 7.

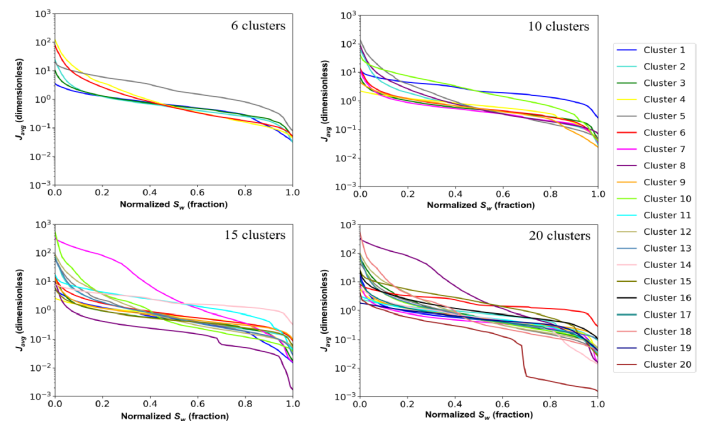


Fig. 7. Average J Curves Based on Clustering Scenarios [6]

An example of the average J curves calculated against the J curves for each sample identified in a cluster is shown in Fig. 8. This is showing the curves for cluster 1 and 2 for the 6 clusters scenario.

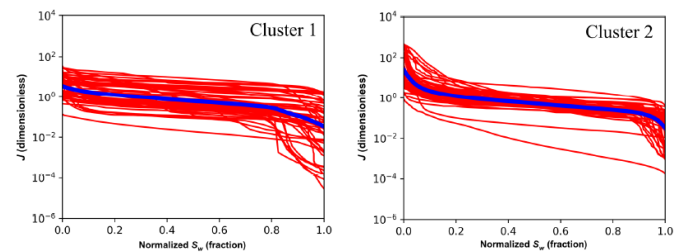


Fig. 8. Cluster 1&2 J Curves for 6 Cluster Scenario [6]

Next, classification algorithms (supervised machine learning) were used to develop maps for the prediction of corresponding clusters for new samples. The algorithms used were K-nearest neighbours (KNN), kernel support vector machine (KSVM), decision tree (DT), and random forest (RF) which were validated by using six carbonate rocks and comparing with the respective experimental data. The best predictions were for the 6 and 10 cluster scenarios with the accuracy for each algorithm found below in Table 3.

Table 3. Classification Algorithm Results [6]

Classification Algorithm	Current Method	
	6 Clusters (%)	10 Clusters (%)
KSVM	97.09	91.24
KNN	95.95	90.62
RF	95.29	87.75
DT	94.12	81.90

As shown, KSVM provided the highest accuracy in the predictions. This algorithm was then subsequently used to classify the validation set (6 carbonate rocks). The rock properties and the grouping features for each can be seen in Table 4 along with the identified cluster for each rock.

Table 4. Summary of Rock Properties and Validation Results [6]

Rock Information				Grouping Feature		Identified Cluster	
Rock Type	k (md)	Φ (%)	r (μm)	F1	F2	6 Clusters (KSVM)	10 Clusters (KSVM)
1	124.350	1.21	91271	0.91	0.10	4	5
2	26.710	11.87	13506	0.69	0.44	4	5
3	5.580	10.05	6709	0.57	0.39	3	6
4	0.586	8.64	2345	0.43	0.35	3	3
5	0.041	6.12	737	0.28	0.27	1	9
6	0.003	4.51	232	0.16	0.20	1	9

Busaleh et al. presented work completed on mercury injection data from carbonate rocks. Although they used a variety of machine learning techniques, results were poor, and more emphasis could have been placed on obtaining better results from a few techniques.

The work from Jamshidian et al. used centrifuge experimental data and an ANN with a Cuckoo optimization algorithm being used to predict capillary pressure with varying inputs. It is important to note here the predictions were completed on capillary pressure experimental centrifuge points with water saturation being used as an input. 7 different cases were conducted with each case involving an additional input parameter which in turn increased the accuracy of the predictions. The limitation here however was the use of the raw centrifuge experimental points. The use of an interpretation software was not used to apply literature correlations to obtain a complete capillary pressure curve.

Kasha et al. took a different approach in using an unsupervised algorithm, clustering, first followed by classification algorithms. The limitation here being the need for an abundance of mercury injection data for many samples to be clustered together and an accurate average J curve for those types of rocks to then be developed. Other approaches could have been taken as well with regards to the pore size distribution such as the Winland r_{35} values.

This research aims to show the novelty of using machine learning techniques to predict complete capillary pressure curves developed from conducting centrifuge tests followed by using SCAL interpretation software to apply literature correlations. This in turn can reduce the time to obtain a complete capillary pressure curve and help improve reservoir characterization which is the end goal in undertaking a SCAL centrifuge experiment. Although several researchers have used ML methods to predict SCAL data, they have focused on predicting a single value of the quantity of interest (relative permeability, capillary pressure, water saturation, etc.). This study assesses the capability of three machine learning algorithms in generating the capillary pressure curves that consists of both capillary pressure and water saturation. Therefore, the novelty of this paper is to simultaneously predict capillary pressure and water saturation values to generate the capillary pressure curve.

3 Methodology

3.1 Centrifuge Capillary Pressure Tests

For this research, multiple centrifuge capillary pressure tests were conducted. The setup consisted of a VINCI RC 4500 – capillary pressure refrigerated centrifuge along with a computer with the appropriate recording and interpretation software. The interpretation software used was CYDAR which offers a powerful solution for the interpretation of conventional and specialized core analysis experiments. CYDAR is also used to record the water saturation and speed versus time during the experiment. A separate VINCI software is used to set the rotational speeds and block times for the centrifuge as well as setting up the camera interfaces for the holding cups.

Core samples were first cleaned followed by drying out in an oven for approximately 1-2 days. Following drying the core samples, their length and diameter were recorded using a Vernier calliper. Next, the dry weight of the cores were recorded. The petrophysical properties of the cores used in the machine learning can be seen in Table 5 below.

Table 5. Core Petrophysical Properties

Core #	Porosity	Permeability (mD)	Grain Density (g/mL)	Swirr
Core 1	0.222	300	2.011	0.045
Core 2	0.217	180	2.089	0.098
Core 3	0.317	2300	1.761	0.033
Core 4	0.316	2300	1.736	0.064
Core 5	0.308	2300	2.034	0.068
Core 6	0.308	2173	1.811	0.2
Core 7	0.285	2216	1.627	0.23
Core 8	0.265	2557	1.844	0.162
Core 9	0.261	1631	1.864	0.066
Core 10	0.296	2868	2.032	0.306
Core 11	0.2828	3591	1.792	0.058
Core 12	0.267	2900	2.033	0.185
Core 13	0.27	2200	1.686	0.23

Next, a synthetic brine was prepared for the simulation of formation water, the composition is shown in Table 6 below.

Table 6. Synthetic Brine Formulation

Synthetic Brine Formulation		
NaCl	50.397 g/kg	96.96 g/L
CaCl ₂ *2H ₂ O	13.202 g/kg	14.16 g/L
MgCl ₂ *6H ₂ O	2.760 g/kg	2.96 g/L
KCl	0.439 g/kg	0.46 g/L
Na ₂ SO ₄	0.345 g/kg	0.37 g/L
Subtotal	107.132 g/kg	114.91 g/L
Add Water	892.868 g/kg	957.69 g/L
Total	1000 g/kg	1072.60 g/L

The cores were then loaded into a vessel where the approximately 1 L of brine was pumped in to saturate the cores for approximately one day. Due to the high permeability of the cores one day proved sufficient in saturating the cores. After saturation had occurred, the wet weight of the cores was measured. This data was then used to calculate the porosity and grain density of each sample.

The cores were then loaded into centrifuge core holders where the top, bottom pipe, and sleeve were determined from the core length as shown in Fig. 9a.

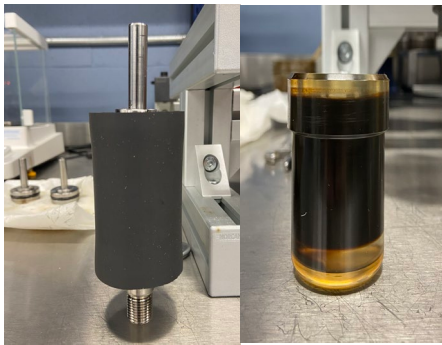


Fig. 9a) Assembled Core Sample (left) **9b)** Holding Cup (right)

The core holders were pressurized to 2000 psi using a hand pump and silicone oil. Small amounts of deionized water and oil were put into the holding cups to create an interface as seen in Fig. 17b. The core holders were also weighed to ensure symmetrical weight before being loaded in the centrifuge.

Once loaded in the centrifuge, the recorded data was inputted in CYDAR, and the recording software was loaded. Multi-step speeds (between 500 to either 3500 or 4500 rpm in increasing 500 increments) as well as step durations were specified, and the camera was set to record the oil-water interface for the respective cups as shown in Fig. 10. This figure shows an oil-water system with the right arrow indicating the water side and the left arrow indicating the oil side. The arrow pointing between the two indicates the oil-water interface. Throughout the drainage experiment as the oil is forced into the core and the water out, the interface will gradually move towards the left. The camera was also checked periodically to ensure it was still properly recording the interface.

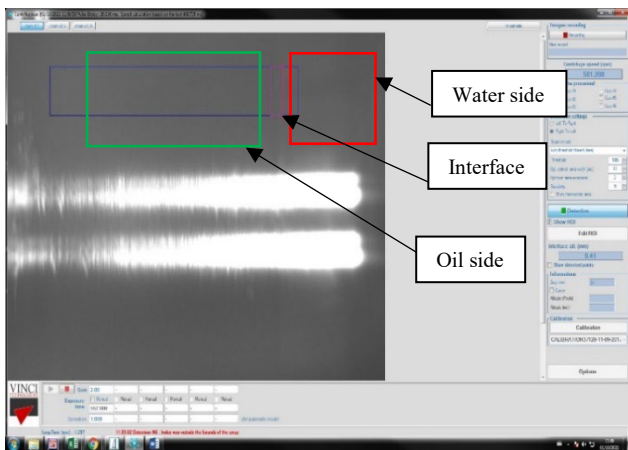


Fig. 10. Camera Interface

Upon completion of the centrifuge test, the next step was to process the recorded data. This required the use of CYDAR interpretation software. The water saturation versus time data was cleaned to exclude any outlier data that the camera may have recorded, and the block times and durations were recorded and entered for CYDAR to calculate the capillary pressure based on the step speeds. For each core, an analytical fit was calculated for the experimental data and Forbes first solution correlation [13] was applied to the experimental data. An example of a complete capillary pressure curve for a

sample after processing can be seen in Fig. 11. A bi-exponential fit was the analytical method used in this case. As shown, both analytical and Forbes methods lack rigor to fit the experimental data.

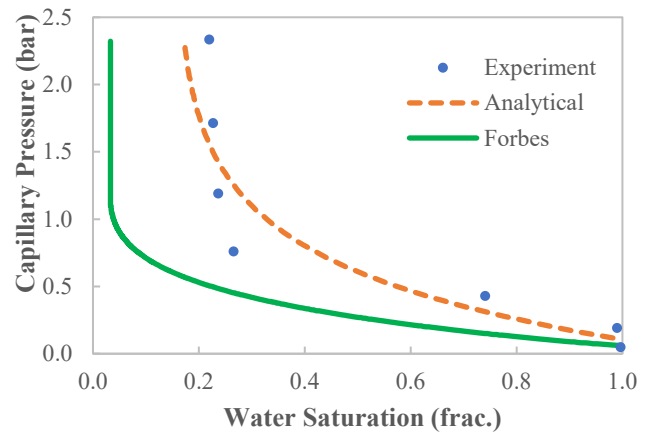


Fig. 11. Core 3 Processed Data (drainage capillary pressure)

For each of the 13 cores the Forbes first solution was applied to the experimental data. Using CYDAR, data from the Forbes curves was discretized to be used for the machine learning techniques in order to predict the Forbes curves.

3.2 Machine Learning Techniques

A spreadsheet was developed to collect all the test data for the machine learning techniques before pre-processing of the data from 13 core samples. The machine learning workflow followed in this case can be seen in Fig. 12.

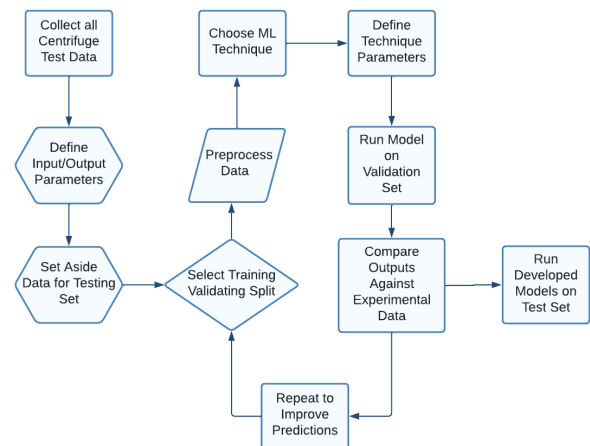


Fig. 12. Machine Learning Workflow

The inputs for the machine learning techniques as mentioned previously were the routine core analysis data of porosity, permeability, grain density, and irreducible water saturation. The outputs were water saturation and capillary pressure; subsequently, multi-output regression models were developed. Data for 2 core samples were put into a separate file to be used as a test set after model development. Note that for these 2 samples, 1995 (input, output) data points were recorded. For the remaining 11 cores, a training-testing split of 70-30 was used to train the models. Using these 11 cores,

10,955 (input, output) data points were recorded and used to train and validate the ML models. Depending on the technique used, the parameters were defined for each; for ANN the epochs, activation function, hidden layers, and neurons, for RFR the number of trees, and for support vector regression the tolerance and max iterations. Standardization and normalization feature scaling were also implemented to see how they would affect overall performance. Eqs. 14 and 15 show the methods for standardization and normalization, respectively.

$$X' = \frac{X - \mu}{\sigma}, \quad (14)$$

where μ is the mean of the feature values and σ is the standard deviation of the feature values.

$$X' = \frac{X - X_{min}}{X_{max} - X_{min}}, \quad (15)$$

where X_{min} and X_{max} are the minimum and maximum of the feature, respectively.

Once the models were run on the training and testing data, their performance was measured using 2 measurements, including the mean squared error (MSE) and correlation coefficient (R^2) where n corresponds to the total number of data points.

$$MSE = \frac{1}{n} \cdot \sum (actual - predicted)^2 \quad (16)$$

Finally, once all models were developed on the validation data set, they were then tested and evaluated on the unseen data set. All machine learning methods were implemented using Python 3.7 programming language along with Keras library with Tensorflow 2.3 backend.

4 Results and Discussion

The results from all ML algorithms on the validation data is shown in Table 7.

Table 7. ML Models Results – Test Data

ML Algorithm	MSE	R ² (Validation Data)
Random Forest	2.09×10 ⁻⁵	0.9997
Neural Network	0.00222	0.9937
Support Vector	0.00436	0.9543

All models performed well with random forest being the best with a correlation coefficient of 0.9997. Figs. 13 and 14 show the prediction versus experimental data for ANN for capillary pressure and water saturation, respectively.

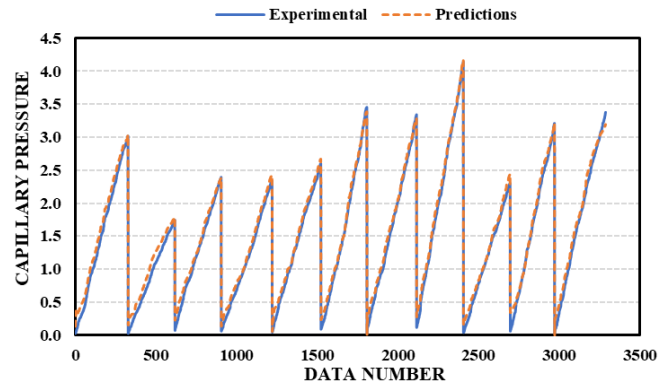


Fig. 13. ANN Validation Data Results – Capillary Pressure

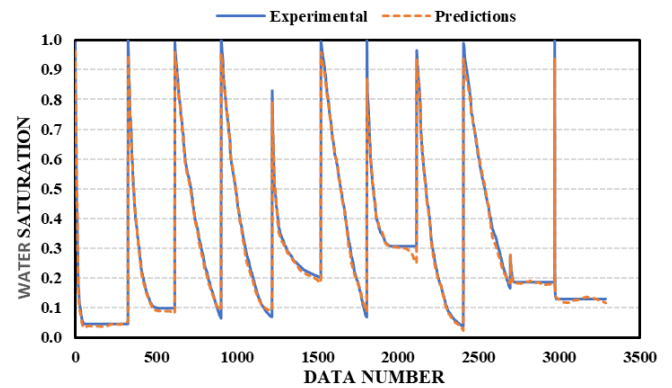


Fig. 14. ANN Validation Data Results – Water Saturation

Similarly, Figs. 15 and 16 highlight the results for the SVR model and Fig. 17 and 18 are the results for the RFR model on the testing data.

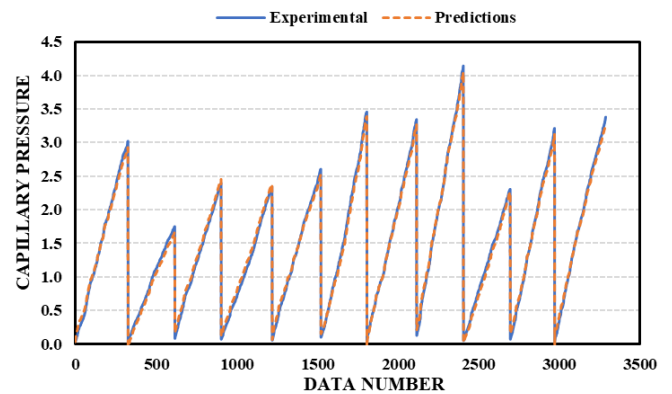


Fig. 15. SVR Validation Data Results – Capillary Pressure

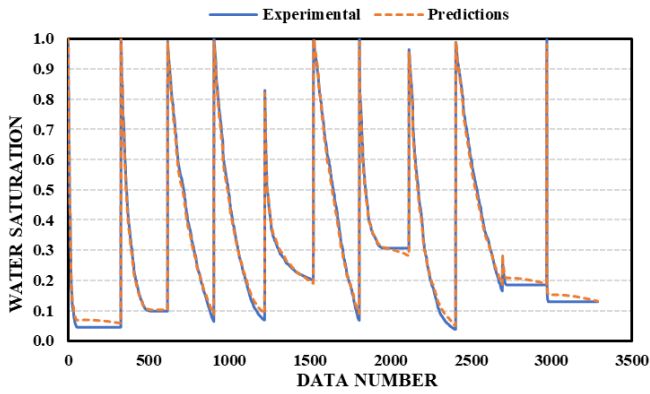


Fig. 16. SVR Validation Data Results – Water Saturation

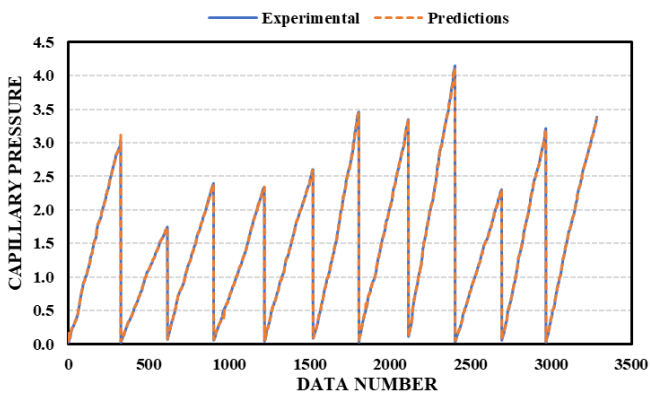


Fig. 17. RFR Validation Data Results – Capillary Pressure

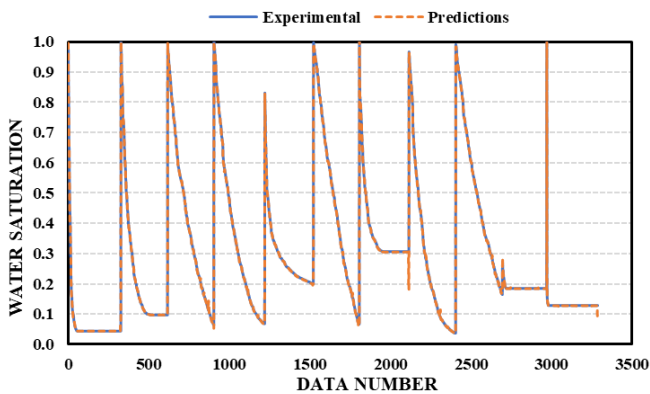


Fig. 18. RFR Validation Data Results – Water Saturation

A sensitivity analysis was also completed on the ANN parameters of hidden layers, neurons, and activation functions. The base case for the following graphs is a model with 32 neurons, 2 hidden layers and a rectified linear unit (ReLU) activation function (i.e. when seeing the effects of changing neurons, 2 hidden layers and ReLU activation function is used).

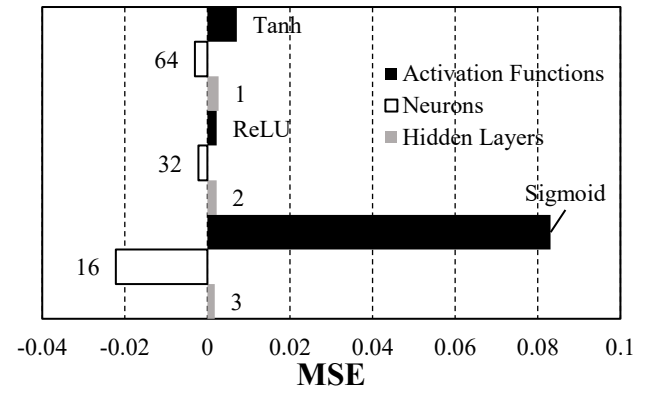


Fig. 19. Varying ANN MSE Results

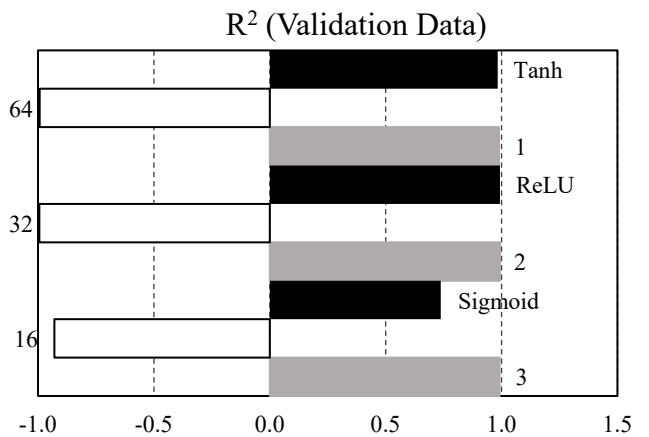


Fig. 20. Varying ANN R² Results

As can be seen from Figs. 19&20 the biggest change in prediction accuracy comes with the change in using Tanh as the activation function. Minimal changes occurred in the prediction accuracy with varying the hidden layers with 2 hidden layers performing the best. Finally, for the varying of neurons, the greatest error occurred when using 16, while the greatest prediction happened using 32.

With the ML models developed, the test set of the 2 cores that was set aside was then given to the models for predictions. The following graphs highlight the accuracy of each model showing the test data results with the results on the test set when using normalized and standardized feature scaling.

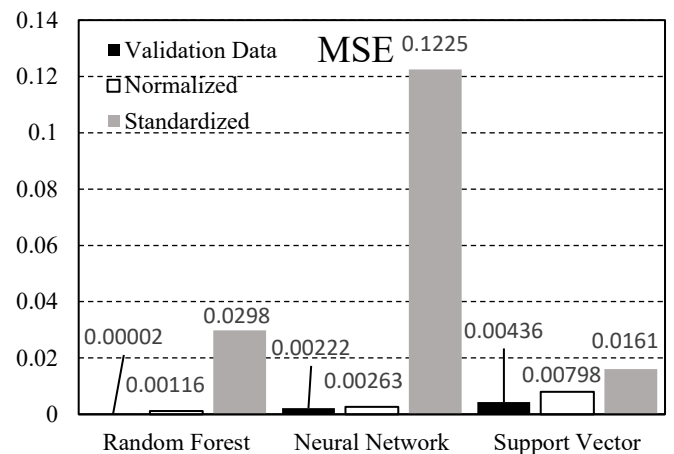


Fig. 21. MSE Results of Models for Test and Validation Data

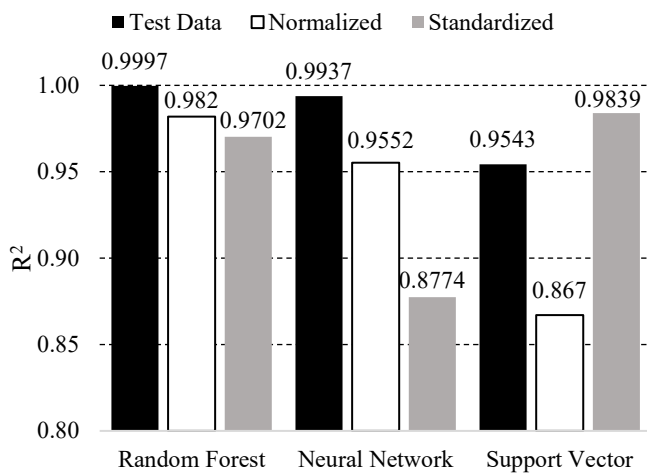


Fig. 22. R² Results of Models for Validation Data

Following the evaluation of the validation data, unseen data consisting of 2 cores was used to test the accuracy of the models. The results for each of the models can be seen in Table 8.

Table 8. ML Models Results – Unseen Data

ML Algorithm	MSE	R ² (Unseen Data)
Random Forest	0.0248	0.9734
Neural Network	0.1034	0.8886
Support Vector	0.0438	0.9527

As shown in Fig. 23, although RFR performed the best overall on the validation data and unseen data with regards to the performance metrics, it is very noisy when predicting unseen data. SVR performed the greatest overall with a smoother curve, however the entry capillary pressure was predicted higher.

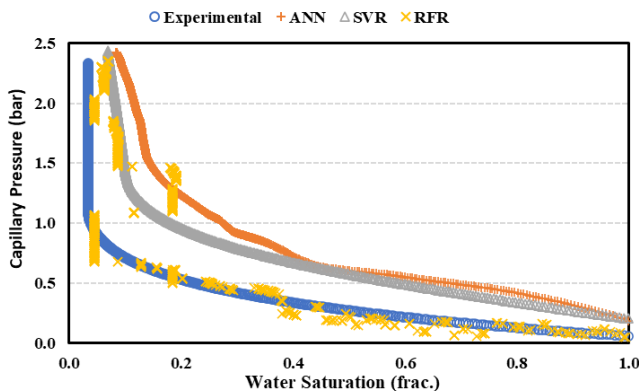


Fig. 23. Unseen Data Model Results – First Core

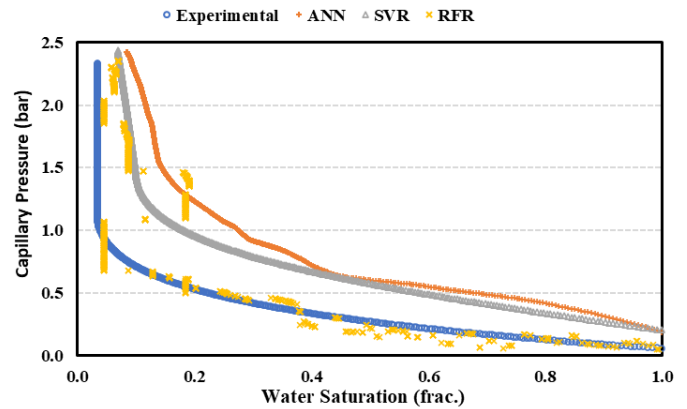


Fig. 24. Unseen Data Model Results – Second Core

Similar to the first core, RFR was noisy again in predictions for the second core. ANN and SVR curves were smoother but showed differences in the entry capillary pressure.

5 Conclusions

This work investigated various machine learning techniques in predicting complete drainage capillary pressure curves. Centrifuge capillary pressure tests were conducted with SCAL interpretation software being used to apply the Forbes First solution correlation. Data for 13 cores was obtained along with the respective RCAL data of porosity, permeability, grain density, and irreducible water saturation for each core. Once all the data was collected, three machine learning models were developed using training and validation data sets with some of the collected data set aside to be used as a test data set. Some of the key findings from this work were that the three techniques used all performed very well on the validation data set as evident from the performance metrics used. Another takeaway is the effectiveness of conducting a sensitivity analysis as evident in the results from the ANN model when changing the neurons, hidden layers, and activation function used.

Some recommendations for future work are to conduct centrifuge experiments on more cores of different rock types to see how the models will perform when using a variety of rock types. As well as, incorporating additional input data such as pore size distribution to see the effects. Additional cores could also be added to the unseen data for the models to increase the accuracy of the predictions. With the success of applying machine learning techniques to capillary pressure, future work can also be to conduct other SCAL tests such as relative permeability to see the effectiveness of machine learning techniques in predicting other reservoir characteristics.

Acknowledgements

The authors would like to thank the Hibernia Management and Development Company (HMDC), Chevron Canada Ltd, Energy Research and Innovation Newfoundland and Labrador (ERINL), the Natural Sciences and Engineering Research Council of Canada (NSERC), the Province of Newfoundland and Labrador, and Mitacs for financial support.

References

1. S.B. Suslick, D. Schiozer, M.R. Rodriguez. Uncertainty and Risk Analysis in Petroleum Exploration and Production. *Terrae* **6**(1): 30-21 (2009).
<https://www.ige.unicamp.br/terrae/V6/PDF-N6/T-a3i.pdf>
2. C. McPhee, J. Reed, I. Zubizarreta. Core Analysis – A Best Practice Guide.
<https://app.knovel.com/hotlink/toc/id:kpCAABPG03/core-analysis-best-practice/core-analysis-best-practice>
3. A. Sircar, K. Yadav, K. Rayavarapu, N. Bist, H. Oza. Application of machine learning and artificial intelligence in oil and gas industry. *Petroleum Research* **6**, 379-391, (2021).
4. Y.R. Busaleh, A. Abdulraheem, T. Okasha. Prediction of Capillary Pressure for Oil Carbonate Reservoirs by Artificial Intelligence Technique. SPE Asia Pacific Oil and Gas Conference Exhibition. (2016).
<https://doi.org/10.2118/182173-MS>
5. M. Jamshidian, M. Mansouri Zadehm M. Hadian, R. Moghadasi, O. Mohammadzadeh. A Novel Estimation Method for Capillary Pressure Curves Based on Routine Core Analysis Data Using Artificial Neural Networks Optimized by Cuckoo Algorithm – A Case Study. (2018). *Fuel*, **220**, 363–378.
<https://doi.org/10.1016/j.fuel.2018.01.099>
6. A.A. Kasha, A. Sakhaee-Pour, I.A. Hussein. ‘Machine Learning for Capillary Pressure Estimation.’ *SPE Res Eval & Eng* **25**. (2022): 1-20. doi: <https://doi-org.qe2a-proxy.mun.ca/10.2118/208579-PA>
7. T. Mitchell. *Machine Learning*. New York: McGraw Hill. (1997). OCLC 36417892.
8. Mathworks Help Center. *Machine Learning in MATLAB*
<https://www.mathworks.com/help/stats/machine-learning-in-matlab.html>
9. T. Hastie, R. Tibshirani, J. Friedman. *The Elements of Statistical Learning*. Springer New York.
https://doi.org/10.1007/978-0-387-84858-7_12
10. A. Shmilovici. Support Vector Machines. In : O. Maimon, L. Rokach. (eds) *Data Mining and Knowledge Discovery Handbook*. (2005). Springer, Boston, MA.
https://doi-org.qe2a-proxy.mun.ca/10.1007/0-387-25465-X_12
11. Rodríguez-Pérez, R., Bajorath, J. Evolution of Support Vector Machine and Regression Modeling in Chemoinformatics and Drug Discovery. *J Comput Aided Mol Des* (2022). <https://doi-org.qe2a-proxy.mun.ca/10.1007/s10822-022-00442-9>
12. K. Fawagreh, M.M. Gaber, E. Elyan. Random forests: from early developments to recent advancements. *System Science and Control Engineering*. Volume 2. (2014).
<https://doi-org.qe2a-proxy.mun.ca/10.1080/21642583.2014.956265>
13. P. Forbes. Simple and Accurate Methods for Converting Centrifuge Data into Drainage and Imbibition Capillary Pressure Curves. *SPWLA-1994-V35n4a3*, 35(04), 13. (1994).
14. Z.A. Chen, D.W. Ruth. Measurement and Interpretation of Centrifuge Capillary Pressure Curves-The SCA Survey Data. *The Log Analyst*, 36(05), 13. (1995).
15. P. Forbes. Centrifuge Data Analysis Techniques : An SCA Survey on the Calculation of Drainage Capillary Pressure Curves from Centrifuge Measurements. 20. (1997).
16. J.E. Nordvedt, K. Kolltvelt. Capillary Pressure Curves From Centrifuge Data by Use of Spline Functions. *SPE-19019-PA*, 6(04), 497–501. <https://doi.org/10.2118/19019-PA> (1991).

Digital rock workflow to calculate wettability distribution in a reservoir rock

Ashraful Islam^{1,*}, Rafael Tio Salazar¹, and Bernd Crouse¹

¹Dassault Systèmes Simulia, USA

Abstract. Wettability has a strong influence on multi-phase flow behavior through reservoir rock. Reservoir rocks tend to have spatially varying wettability. Prior to contact with oil, rocks are almost always naturally water-wet. As oil invades the pore-space over geologic time, the initial water-wet state may be altered in certain locations due to adhesion of substances within the oil phase to the grains. Mechanisms of wettability alteration depend on various properties such as pressure, temperature, mineral chemistry, surface roughness and fluid composition. In this study wettability alteration in a reservoir rock is studied through direct simulation using multiphase Lattice Boltzmann method where the computational grid is constructed from segmented micro-CT images of the rock sample. The pore-grain interface is defined by a triangulated surface mesh for accurate fluxes near boundary and local curvature calculation. A capillary pressure drainage simulation is conducted in a water-wet Berea sandstone sample initially filled with water. When oil invades the pore space as the capillary pressure is increased, a fraction of the pore-grain surface is altered towards an oil-wet condition, as determined by a novel wettability alteration process. This process calculates local curvature at every surface element of the rock, obtains local capillary pressure from the simulation and assumes a disjoining pressure to determine water-film breakage at every location of the pore-grain surface. As a result, a spatially varying rock wettability is created. Using this new wettability distribution, the simulation is continued to allow the fluid phases to redistribute accordingly. The process is iteratively carried out until both fluid saturation and wettability distribution converged at a given applied capillary pressure. Afterwards, the pressure is ramped up to the next stage and the process is repeated again. It has been found that the wettability alteration is a slow dynamic process where the non-wetting phase can gradually invade finer pore space as the surrounding grain wettability is altered. In this study, it has also been found that wettability alteration of the reservoir rock produces lower connate water saturation during primary drainage compared to the simulation results without alteration. The resulting spatially varying wettability distribution from primary drainage is used for a subsequent water flooding simulation to calculate water-oil relative permeability curves. The methodology presented in this work can be leveraged to better understand and predict an improved mixed wetting conditions found in the reservoir rocks which is needed for more accurate displacement tests such as relative permeability simulations.

1 Introduction

Two-phase relative permeability describes how easily one fluid can be moved through a porous medium in the presence of another fluid. It is an important characteristic of hydrocarbon reservoir rocks and a crucial input to oil and gas reservoir simulation modeling. Relative permeability, and multiphase flow through porous media in general, is dependent on various characteristics of the fluid-fluid-rock system, including rock surface properties, physical properties of each fluid, and flow conditions. They can be expressed as dimensionless numbers such as viscosity and density ratio, capillary number, wettability and geometric state function [1]. Wettability is a measure of a fluid's tendency to adhere to a solid surface in the presence of other immiscible fluids. Macroscopically, it can be measured by the contact angle at the three-phase contact line and classified as water-wet (minimum 0°, maximum 60 to 75°), neutral-wet (minimum 60 to 75°, maximum 105 to 120°) and oil-wet (minimum 105 to 120°, maximum 180°) in the petroleum engineering context. Microscopically, it can be related to the molecular energy difference between the energy of the combined system

and the combined bulk energies of the individual components.

The physics of multiphase flow at pore scale is very different for water-wet and oil-wet rocks and its impact can be found in capillary pressure or relative permeability curves [2-6], both critical inputs for reservoir simulation forecasting. Thus, an accurate wettability condition is an important input parameter for multiphase fluid displacement simulations and impacts the overall productivity of the hydrocarbon reservoir [7].

Reservoir rocks, unlike man-made materials, tend to have spatially varying wettability, i.e., the contact angle varies from location to location on the surface of the grains in contact with the fluids in the pore space of a rock [8-10]. The contact angle distribution is a result of the mineral composition and the geological history of a hydrocarbon-bearing rock as well as surface texture, chemical composition of fluids (e.g., water, oil) in contact with the different crystalline planes of the grain minerals present in the rock, etc. Prior to contact with crude oil, rocks are almost always naturally water-wet. As oil invades the pore-space over geological time, the initial water-wet character may be altered

* Corresponding author: ashraful.islam@3ds.com

in certain locations due to adhesion of surface-active materials from the oil phase. Mechanisms of wettability alteration depend on various local system properties such as pressure, temperature, mineral type, and fluids composition.

When rock samples are extracted from oil/gas reservoirs during the drilling process, they are often contaminated with mud and other fluids and chemicals. When those rock samples are subject to laboratory experiments to obtain two-phase relative permeability curves or capillary pressure curves, a common lab preparation procedure is to first clean the rock of fluids using solvents and then attempt to restore the rock's natural wettability. This process of attempting to reestablish fluid phase distribution and wettability distribution (e.g. contact angles) representative of the subsurface reservoir conditions is referred to as "aging". A typical aging procedure would involve cleaning the rock sample of original fluids and contaminants and treating the rock sample with chemicals that induce a water-wet condition. Next, the sample is saturated with brine, and in a "drainage" procedure oil is pushed in (hence brine is pushed out) using estimated reservoir conditions of temperature and pressure. The rock sample is then "aged" for a period of time, e.g. 4 weeks, allowing wettability alteration to occur, presumably in a fashion similar enough to what had occurred in the real subsurface rock formation so that a realistic wetting condition is restored.

With the advancement of imaging and computational fluid dynamics, it is now possible to perform a relative permeability or capillary pressure analysis numerically for rock samples. But the accuracy of these simulations also depends on the spatial distribution of the wetting condition of the grains among many other inputs [5]. Using x-ray micro-tomography (micro-CT), it is possible to measure in-situ contact angles [11-16] in an aged rock sample from laboratory procedure and use as input for numerical relative permeability analysis. Observations of the relative fluid coverage of rock mineral surfaces can also be used to create a 3D map of the wetting state of the rock [8-9]. However, establishing an initial fluid distribution and wetting conditions using numerical simulation remain challenging. It includes understanding the role of thin films in porous media. The type and thickness of films coating pore walls determines a reservoir rock wettability and whether or not a reservoir rock can be altered from its initial state of wettability [5, 17]. Thin film physics also depends on the grain surface mineralogy and the fluid pair. It is interrelated with the pore shape, especially pore curvature and surface roughness. As a result, the solution scope to this problem spans from molecular to microscopic scales, where molecular interactions determine the Derjaguin-Landau-Verwey-Overbeek (DLVO) forces [18, 19], and interfacial tension, while microscopic pore topology determines candidate surfaces for wettability alteration.

In this work, we describe a numerical Digital Rock workflow starting from pore scale 3D image acquisition to relative permeability fluid flow simulation, including a novel wettability alteration process. Wettability alteration is carried out in a digitally reconstructed 3D pore-grain model, paying attention to the micro scale interactions. The resulting spatially varying wettability distribution is used for relative permeability simulation. The next section describes the methodology, including image processing, an overview of the

numerical modeling approach, and detailed description of the wettability alteration process. Afterwards, wettability alteration and relative permeability results for a Berea sandstone can be found in the results section, which is followed by conclusions to shed some light on future research in this regard.

2 Methodology

2.1 Sample imaging

This study uses a Digital Rock workflow [15] that starts with the acquisition of a 3D image of a Berea Sandstone sample using an x-ray micro-tomography (micro-CT). Fig 1(a) shows a 2D slice of the 3D scans captured perpendicular to the fluid displacement direction. Emphasis was given to acquiring images that are free of x-ray imaging artefacts such as beam-hardening, shadowing, ring artefacts etc. Next, a segmentation workflow is applied to that image to identify the pores and grains as shown in black and white respectively in Fig 1(b). This segmentation uses differences in grey values and intensity gradients to identify voxels along the solid-pore boundary and produce the resolved pore structure to be used in the flow simulation. Further reference for image acquisition and processing can be found in [20].

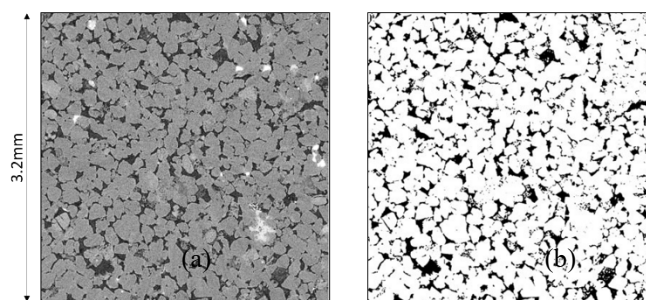
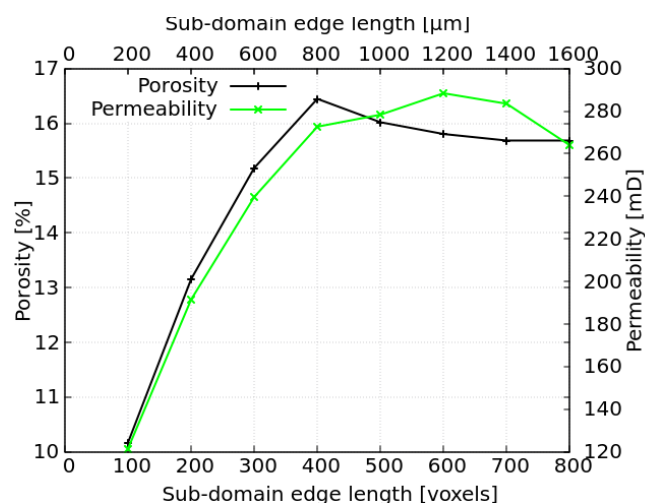


Fig. 1. Two-dimensional section of 3D scans for the Berea Sandstone used in this work: (a) original grey scale, (b) segmented image.

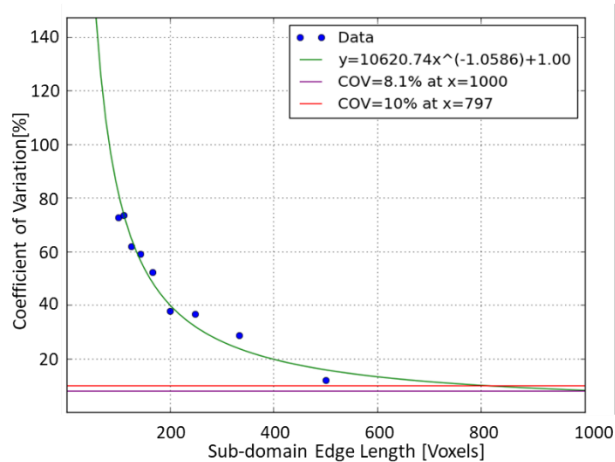
The stack of micro-CT images of a Berea sandstone was captured at $2.0\mu\text{m}$ per voxel resolution to ensure good mesh quality for subsequent fluid flow simulation. At this resolution, the resulting 3D image shows sufficient pore connectivity in all three directions. The pore bottleneck radii, which is defined by the radius of the largest rigid sphere that can be percolated across the 3d rock pore space without getting stuck, were calculated to be 3.0, 3.6 and 3.2 voxels in the x, y and z directions respectively. Note that the bottleneck radius needs to be large enough to ensure sufficient accuracy of the fluid flow simulation and that requirement is solver specific. In a previously published work [20], it has been demonstrated that the Lattice Boltzmann method (LBM) solver used for this study can provide accurate results at this resolution.

Attention was also paid to ensure that the field of view of the 3D image is large enough to capture a representative elementary volume. A size growing analysis was performed, where the entire analysis domain is divided into

incrementally bigger, overlapping, and centered subdomains of equal aspect ratio. For each of the sub-domains, porosity and single-phase permeability values are calculated as shown in Fig. 2(a). Additionally, a coefficient of variation of permeability as a function of sub-domain size is calculated in Fig. 2(b) [21]. This chart represents likelihood that a certain subdomain permeability value will be one standard deviation of the mean value. Based on these results, we chose a subdomain of 800 voxels (corresponding to 1.6 mm) cubic size for subsequent multiphase simulation.



(a)



(b)

Fig. 2. Representative elementary volume calculation: a) size growing analysis for porosity and permeability b) Permeability coefficient of variation, defined as the ratio of standard deviation to mean value.

2.2 Numerical modelling approach

The multiphase fluid flow numerical simulation is conducted in the segmented 3D pore-space voxels of the selected rock domain using a multiphase LBM solver. The LBM is based on mesoscopic kinetic theory and solves a discrete form of the Boltzmann transport equations instead of Navier-Stokes equations [22-26]. In this method, most of the operations can be performed locally on a cubic lattice, resulting in highly parallel computational performance [27]. This simulation performance quality makes LBM an ideal candidate for

porous media applications where typically a large domain with complex pore network needs to be simulated. The LBM has been successfully used for various porous media applications such as in hydrocarbon bearing rocks [20, 28], gas diffusion layers in fuel cells [29, 30], porous electrodes in lithium-ion batteries [31, 32] etc.

The LBM implementation used in the current study is based on the multiphase framework presented by Shan and Chen [33] that later went through various improvements for simulating porous media applications with sufficiently high accuracy at low resolution and small viscosity [27, 34]. This is a diffuse interface method where different particle species are used to generate separated fluid phases, and the interaction between the different particle species determines the inter-component interfacial tension. Thus, the interfaces between different components are automatically determined once the species' interactions are defined. As a result, the complexity of explicit interface tracking such as in traditional volume-of-fluid or level-set approaches can be avoided.

In order to capture correctly the physics of multi-component fluid flow, even at low resolution, the current LBM implementation uses, in addition to the voxel elements, triangulated surface elements also known as surfels, to accurately capture the pore-grain boundary as demonstrated in [35-37]. The use of surfels to define the exact wall location results in more accurate fluxes near boundaries, and increased accuracy at lower numerical resolution compared with operating directly on the voxel grid of the micro-CT scan. Usage of surfels also improves the accuracy of local curvature and curvature-based pressure calculation as described in section 2.3.3.

2.3 Numerical model setup

2.3.1 Capillary pressure displacement

A capillary pressure driven primary drainage (oil displacing water) simulation is performed in the selected rock domain to establish a fluid phase (oil/water) distribution for subsequent

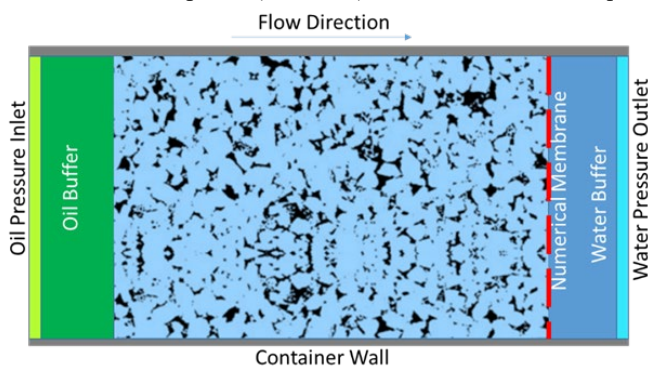


Fig. 3. Schematic of a capillary pressure drainage simulation setup mimicking a porous-plate method.

water flooding simulation. Initially, the simulated domain pore space is fully saturated with water and a uniformly distributed strong water-wet wetting condition is applied to all pore-grain boundary surfaces. In all previous Digital Rock multiphase flow studies, the initial wettability condition is maintained constant along the simulation. In the current

study, the wetting condition is altered during this drainage simulation using a process described in section 2.3.5 and compared with a traditional no-alteration scenario.

As shown in Fig. 3, the rock sample is placed inside a container box. The container has solid walls in the x and y direction, while in z direction (flow direction), oil and water buffers are placed in the opposite sides of the rock domain to control the capillary pressure. In addition, a numerical membrane acting as a porous plate is placed in between the rock domain and water buffer. This numerical membrane behaves as a volume-free and massless barrier that prevents oil from entering into the water buffer. Water on the other hand, can flow through the membrane without any resistance. Thus, the usage of this numerical membrane serves as a capillary pressure barrier for the non-wetting phase, similar to the porous plate in capillary pressure lab analysis [38]. It is worth mentioning that this numerical membrane is a unique feature of the current LBM implementation we use, and that can practically replace the modeling of a finely resolved porous plate which can be computationally expensive and can potentially raise numerical issues.

During primary drainage, the pressure at the oil buffer is gradually ramped up so that oil starts to invade the pore space filled with water. At each pressure level the simulation continues until the saturation change is within a preset convergence value and a static equilibrium is achieved.

2.3.2 Relative permeability displacement

Using the initial fluid distribution, obtained from the previous capillary pressure drainage simulation, a multiphase unsteady-state k_r relative permeability fluid flow simulation is carried out. In this unsteady-state k_r method, a periodic boundary conditions and a driving force are applied in the flow direction, while no-flow boundary conditions are used in the directions perpendicular to flow. Further details of this procedure can be found in [20].

2.3.3 Curvature calculation

The pore-grain boundary, which consists of triangular surface elements, is used for both mean curvature calculation and to define wall boundary conditions for fluid flow. As described in [39], from a theoretical point of view, triangular meshes do not have any curvature at all, since all faces are flat and the curvature is not properly defined along edges and at vertices because the surface is not C^2 differentiable. One possible alternative is to think of a triangular mesh as a piecewise linear approximation of an unknown smooth surface and calculate mean curvature at the vertex. In the current study, we use an open-source, freely available tool “Visualization Toolkit” (VTK) [40] to calculate the mean curvature at every vertex:

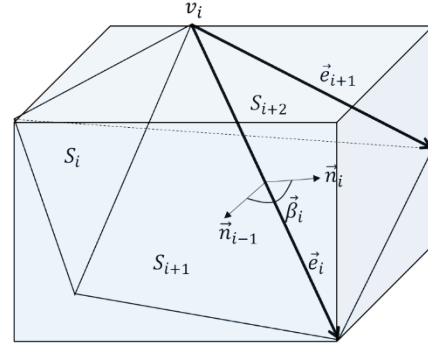


Fig. 4. Curvature calculation: cubic lattice voxel with more than one triangular surface elements inside.

$$|\bar{H}| = \int_S |H| = \frac{1}{4} \sum_{i=1}^n \|\vec{e}_i\| |\beta_i| \quad (1)$$

where, $|H|$, \vec{e}_i and β_i represent absolute mean curvature, edge shared by two triangular surface elements and dihedral angle between the normals of the adjacent triangles at an edge \vec{e}_i , respectively, as shown in Fig. 4. This integral value is then normalized by the surrounding area of a vertex to calculate the curvature at the vertex.

In the current workflow, since we need to calculate the curvature for every voxel in the computational domain, the curvature at the triangular surface element is calculated by:

$$|H|_{S_i} = \frac{1}{3} [|H|_{v_i} + |H|_{v_{i+1}} + |H|_{v_{i-1}}] \quad (2)$$

where, S_i and v_i represent the triangular surface element and one of the vertex in that element respectively. Since the surface elements do not cross over from one cubic lattice voxel to another, curvature for every voxel can be calculated by area weighted averaging:

$$|H|_{\text{voxel}} = \frac{1}{\sum_{i=1}^n A_{S_i}} [|H|_{S_1} A_{S_1} + |H|_{S_{i+1}} A_{S_{i+1}} + \dots + |H|_{S_n} A_{S_n}] \quad (3)$$

where, A_{S_i} and $|H|_{S_i}$ represent area and curvature of a triangular surface element while n represents number of elements in a given voxel.

2.3.4 Force balance

The basic mechanism that drives wettability alteration is related to achieving a local force balance in the fluid-fluid-solid interfaces. It involves three forces:

- 1) Capillary pressure (P_c), i.e. the pressure difference between non-wetting (oil) and wetting (water) fluids. Since the capillary pressure measurement and subsequent wettability alteration takes place when both of the fluid phases achieve static equilibrium, the difference between inlet oil pressure and outlet water pressure can also be considered as the capillary pressure of the system.

$$P_c = P_{inlet} - P_{outlet} \quad (4)$$

- 2) Curvature based pressure (P_v) is the pressure caused by solid geometry forcing the shape of the oil/water interface into the shape of the pore geometry:

$$P_v = \sigma |H|_{voxel} \quad (5)$$

where, σ is the interfacial tension coefficient.

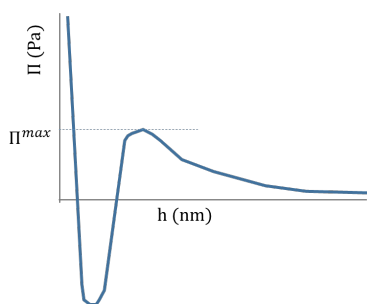


Fig. 5 Schematic of a disjoining pressure isotherm

- 3) Disjoining pressure (Π) is the pressure that prevents a thin water film from rupturing. As explained in [17], when oil invades a water-wet pore space, a thin water film is developed which coats and adheres to the solid surface. Disjoining pressure is a function of film thickness, h as shown in the schematic in Fig. 5. Positive disjoining pressure can be seen as the repulsive stabilizing force that keeps the oil away from the water-wet interface. Depending on the film thickness, either one of the following two repulsive forces can contribute to positive disjoining pressure: The first one is the electrostatic force that originates from the electrical double layers present at the solid/water and water/oil interfaces. The second one is a strong hydration force that plays dominant role when film thickness approaches molecular dimensions. On the other hand, dispersive van der Waals forces, are usually attractive and destabilizes thin water films contributing to the negative disjoining pressure.

The shape of the disjoining pressure isotherm, Fig. 5, suggests the existence of a local maximum disjoining pressure. When the applied capillary pressure exceeds the sum of the local curvature-based pressure and maximum disjoining pressure, the local thin water film can be considered ruptured making the adjacent grain surface a candidate for wettability alteration:

$$P_c > P_v + \Pi^{max} \quad (6)$$

It should be emphasized that Eq. (6) i.e. the augmented Young-Laplace equation, considers both disjoining pressure and local pore shape for wettability alteration [5]. To illustrate the local pore shape dependency, consider a non-wetting fluid flowing through two separate micro channels, one with circular cross-section and other with star shaped cross-section. If they have the same bottleneck radius, as per Eq.

(6), the thin film in a star shaped pore is more likely to be ruptured, even though the disjoining pressure and applied capillary pressure in star shaped pore is the same as the circular pore. Also, disjoining pressure is a necessary ingredient to explain capillary equilibrium for saturation high enough where only a smaller fraction of interfaces are really “free” interfaces but the majority of the oil-water interface follows the shape of the solid. In some instances the interfaces can even be flat, i.e. zero curvature. In order to sustain a force balance (Eq. 6), the phase pressure difference has to be taken up by the disjoining pressure.

2.3.5 Wettability alteration

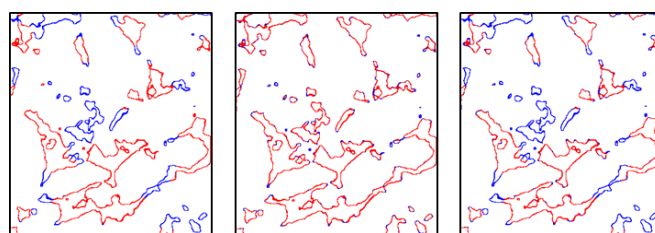


Fig. 6. Surface selection (red) for wettability alteration: (a) selection is adjacent to a non-wetting phase, (b) selection satisfies $P_c > P_v + \Pi^{max}$ condition and (c) selection is subset of (a) and (b).

The wettability alteration workflow starts by creating a digital representation of the pore-grain surface and setting up the scenario for capillary pressure drainage simulation as described earlier. Afterwards the following steps are implemented to change the local wettability within a multiphase fluid flow simulation:

- 1) The simulation is continued until static equilibrium is achieved for a certain capillary pressure (P_c).
- 2) The surface elements in contact with the non-wetting phase are identified as shown by the red lines in Fig. 6(a)
- 3) The curvature-based pressure, (P_v) is also calculated using Eq. (5) at every voxel containing the pore-grain surface boundary as described in section 2.3.3 and 2.3.4.
- 4) Then Eq. (6) is used to determine whether a local water-film breakage may occur as represented by the red lines in Fig 6(b).
- 5) Afterwards, a subset of surface elements from step 2) and 4) is identified as the candidate location for wettability alteration as shown by the red lines in Fig 6(c).
- 6) The wettability alteration can be a slow, dynamic process that occurs over many small discrete time intervals. In order to facilitate further change in fluid saturation, the simulation is continued with the updated wetting condition maintaining same capillary pressure until static equilibrium is achieved.
- 7) Afterwards the pressure is ramped up to the next value and the above steps are repeated again.

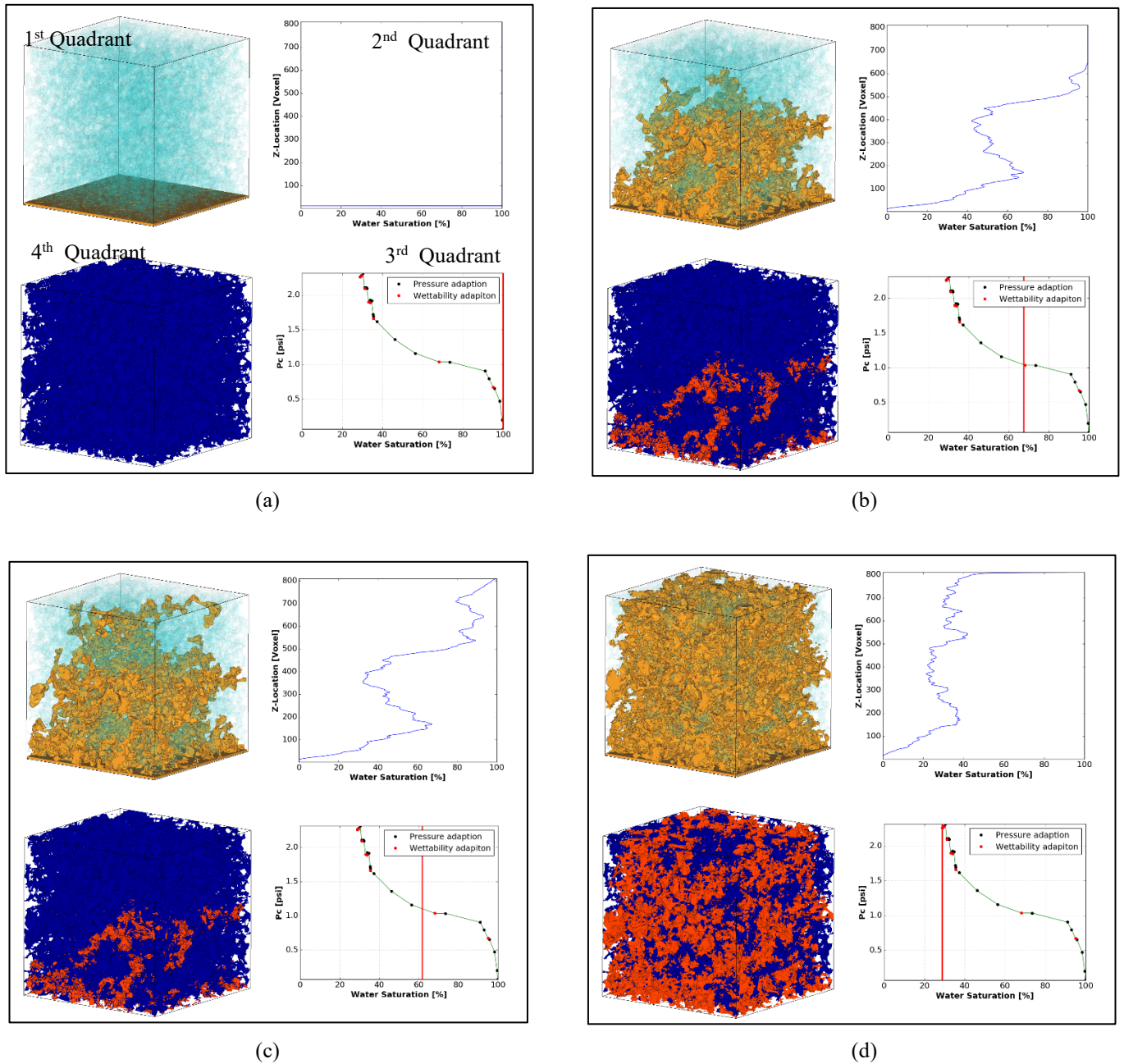


Fig. 7. Various stages of wettability alteration simulation. The 1st quadrant in each figure shows an iso surfaces of oil (beige) and a volume rendering of water (blue), 2nd quadrant shows the water saturation profile along the flow direction, 3rd quadrant shows capillary pressure versus water saturation chart and 4th quadrant shows oil wet (red) and water wet (blue) surface within the pore space in 3D.

Thus, it is ensured that the fluid saturation is converged not only for certain applied pressure but also due to the corresponding change in wetting condition. It should be noted that the above procedure takes disjoining pressure for different minerals and fluid pair as an input. In the current study, we assumed a positive, repulsive disjoining pressure of 5000 Pa. As a next step, the workflow can be extended to calculate disjoining pressure using Molecular Dynamics simulation or from the experiments.

3 Results

3.1 Wettability alteration in a Berea sandstone

Fig. 7 shows capillary pressure drainage simulation results for an oil/water system in a strongly water-wet Berea sandstone initially filled with water. The black and red measurement points in Fig. 7, 3rd quadrants represent equilibrium states after pressure and wettability adaption respectively. At the beginning of the simulation, the water saturation changes are small in response to the increase in oil pressure. But as the pressure is ramped up enough to overcome the capillary pressure imposed by the local pore throat radii, oil rapidly invades the pore space as can be seen in between 90% and 70% of the water saturation, which is a phenomena called “Haines Jump” [41]. As reported in [42], the Reynolds number calculated during Haines Jump are estimated to be in the order of one, indicating laminar flow, but the inertial

forces are still relevant. The current simulation uses a Lattice Boltzmann formulation that represents the full transient Navier-Stokes equation which is essential to capture this phenomenon [18]. However, not all the pore space is filled during Haines jump, especially during a slow convergence to static equilibrium. Even though Haines Jump process is far from quasi-static, during the subsequent slow convergence stage the phase pressure difference is not significantly large enough for the non-wetting phase to rapidly invade and the flow of oil can be described as quasi static and capillary dominant. In such a scenario, oil droplets can be snapped off when passing through a narrow pore-throat, similar to “Roof snap off” phenomena as described in [43,44] which can also be seen in current simulation as illustrated in Fig 8.

As can be seen in Fig. 7(c), oil breakthrough occurs for this rock sample at around 60% of water saturation, when the numerical porous plate stops further advancement of oil into the water buffer. Thus, it allows the oil pressure to build up, so that the oil non-wetting phase can intrude smaller pores too. As a result, having porous plate also helps achieving higher pressure-saturation points as shown in Fig. 7(d).

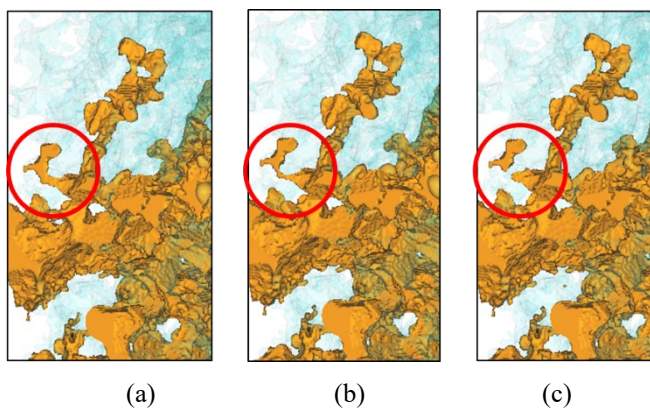


Fig. 8. Oil blob “Roof” snap off during drainage simulation.

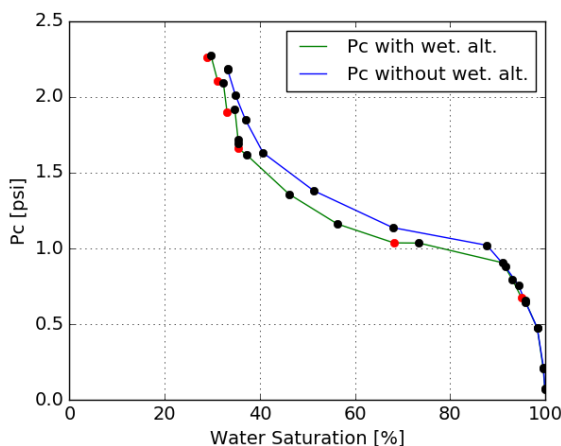
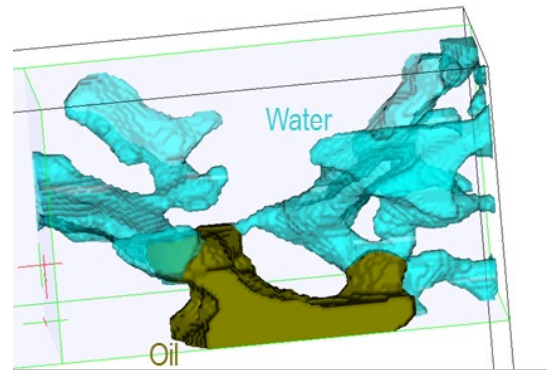
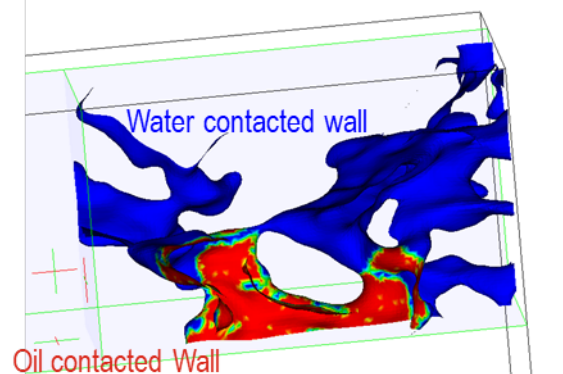


Fig. 9. Capillary pressure curves with (green) and without (blue) wettability alteration.

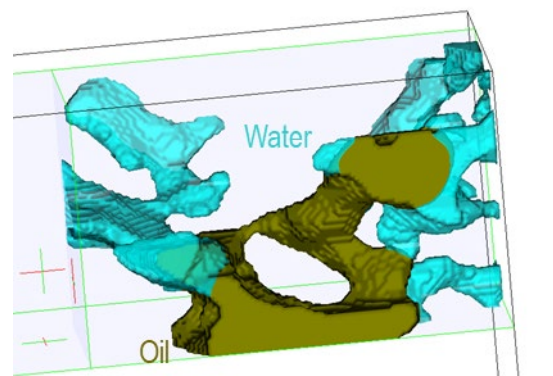
For this simulation we carry out the wettability alteration after every four pressure steps by following the methodology



(a)



(b)



(c)

Fig. 10. A pore scale event showing the slow dynamics of wettability alteration: (a) flow of oil is blocked by a narrow pore-throat, (b) local surface wettability alteration, and (c) updated fluid distribution in response to the wettability alteration.

described in section 2.3.5. In Fig 7, the 4th quadrants show the water wet (blue) and oil wet (red) surfaces at different stages of the simulation. Only a small fraction of the surface area in contact with the oil non-wetting phase is subjected to alteration at low capillary pressures, because the applied capillary pressure is not large enough to overcome the repulsive disjoining pressure for thin film rupture. In contrast, alteration at higher capillary pressures creates larger fraction of oil-wet surface. By the end of simulation, almost 70% of

the pore-grain surface is altered from strongly water-wet to oil-wet condition.

Fig. 9 shows a comparison between two capillary pressure curves with and without wettability alteration. Drainage with wettability alteration exhibits smaller capillary entry pressure. Fig. 9 also confirms that the inclusion of the wettability alteration mechanism in the multiphase flow simulation leads to an overall lower water saturation in the drainage displacement. It can be hypothesized that for a given topology, the degree of observed difference between with and without alteration depends on the rock mineralogy. Different mineral and fluid pair can result in much higher or lower or even negative disjoining pressure which can potentially make the wettability alteration effect more pronounced.

This phenomenon can be explained by the slow dynamic impact of wettability alteration that allows non-wetting fluid to intrude into very small pores, as the wettability can be changed in such a way that capillary pressure does not need to be overcome. In other words, the iterative process between wettability alteration, the consequential change of capillary pressure and establishing a new capillary equilibrium from the updated capillary pressure allows the contact line to move into smaller pores than without wettability alteration. Fig. 10 illustrates an example of a local pore scale displacement where the flow of oil is blocked by a narrow water-wet pore-throat at certain applied capillary pressure. Next, the mechanism of wettability alteration of the pore-grain surface is carried out and certain portion of the surface in contact with oil is altered to more oil-wet condition, as shown in Fig 10(b). As the simulation is resumed with the updated wetting condition, but still at the same applied capillary pressure, the new oil wet surface helps oil to push through the small pore-throat and displace more water as shown in Fig 10(c). Wettability alteration shown in 10(b) is an outcome of procedure described in 2.3.5 that implements a steady-state solution of the augmented Young-Laplace equation. Once the wettability of the candidate surface is altered, the transient fluid flow simulation is resumed and the slow dynamic impact of alteration such as in Fig 10(c) is simulated in time domain.

From this study, it is clear that wettability alteration has an impact on the overall displacement, but the alteration has been modeled as a discrete event happening every after certain pressure interval. We plan to investigate further the impact of discrete pressure interval of alteration as a next step.

3.2 Relative permeability analysis

The initial fluid and wettability distributions obtained from the capillary pressure drainage simulation are used as inputs for a subsequent relative permeability simulation where water displaces oil (imbibition). Fig. 11 shows the relative permeability simulation results in the Berea Sandstone model, for both altered and un-altered wettability conditions. Wettability alteration creates a mixed wet condition that allows oil to penetrate deeper into the pore space. As a result, the initial water saturation is lower than the un-altered

wettability case (water-wet). For the mixed wet case, a thin oil film develops onto the grains where wettability alteration took place and the flow of water during water-flooding kr simulation may not be in direct contact with the grain wall. As a result, water relative permeability is higher for the altered wettability than the unaltered case where there is no oil film. The film also creates persistent oil connectivity even at higher water saturation which leads to more oil recovery for the alteration induced mixed wet case.

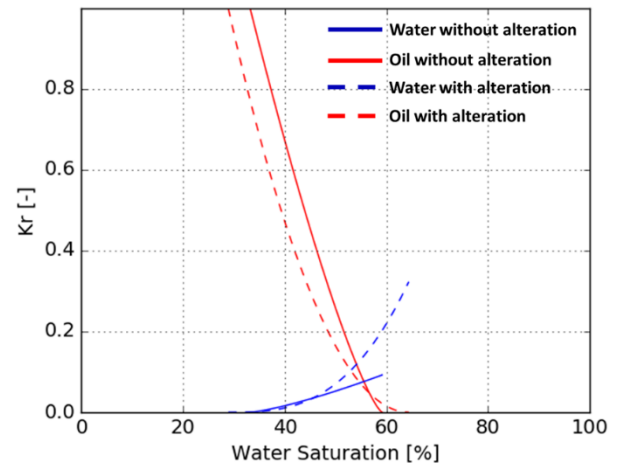


Fig. 11. Oil/water relative permeability curves with and without wettability alteration.

4 Conclusion

A numerical wettability alteration methodology based on a provided disjoining pressure isotherm has been established and implemented using a multiphase Lattice Boltzmann Method. In particular –

1. An iterative process for wettability alteration has been developed based on force balance between curvature-based pressure, applied pressures and disjoining pressure.
2. This work also offers a secondary oil displacement mechanism based on slow dynamic wettability alteration process. This theory can be helpful to understand how oil can get inside into very fine pore space even though capillary pressure is not sufficient.
3. The effect of wettability alteration on overall oil production has also been illustrated by performing a subsequent relative permeability simulation.

In the future, this work can be extended to encompass molecular models of thin film physics, mineralogy and fluid pairs. Using Molecular Dynamics simulation, it is feasible to calculate interfacial tension and wettability on first principles basis as demonstrated in [45-47]. Current Lattice Boltzmann workflow to calculate spatial wettability distribution can be integrated with a Molecular Dynamics workflow to obtain

interfacial tension, contact angle and disjoining pressure isotherm inputs.

References

1. J. E. McClure, R.T. Armstrong, M. A. Berril, S. Schlüter, S. Berg, "A geometric state function for two-fluid flow in porous media," *Phys Rev Fluids* **3**, 084306 (2018)
2. W.G. Anderson, "Wettability literature survey-part4: Effects of wettability on capillary pressure," *J Pet Technol* **39**, 1283 (1987)
3. W.G. Anderson, "Wettability literature survey-part 5: The effects of wettability on relative permeability," *J Pet Technol* **39**, 1453 (1987)
4. Q. Lin, B. Bijeljic, S. Berg, R. Pini, M.J. Blunt, S. Krevor, "Minimal surfaces in porous media: Pore-scale imaging of multiphase flow in an altered wettability Bentheimer sandstone", *Phys. Rev. E*, **99**, 6 (2019).
5. M. Rücker , W.-B. Bartels , G. Garfi, M. Shams, T. Bultreys, M. Boone, S. Pieterse, G.C. Maitland, S. Krevor, V. Cnudde, H. Mahani, S. Berg, A. Georgiadis, P.F. Luckham, "Relationship between wetting and capillary pressure in a crude oil/brine/rock system: From nano-scale to core-scale", *J Colloid Interface Sci.*, **562**, 159(2020)
6. M. Rücker, W.-B. Bartels, K. Singh, N. Brussee, A. Coorn, H. A. van der Linde, A. Bonnin, H. Ott, S. M. Hassanizadeh, M. J. Blunt, H. Mahani, A. Georgiadis, S. Berg, " The effect of mixed wettability on pore-scale flow regimes based on a flooding experiment in Ketton limestone," *Geophys. Res. Lett.* **46**, 3225-3234 (2019).
7. N.R. Morrow, "Wettability and its effect on oil recovery," *J Pet Technol* **42**, 1476 (1990)
8. G. Garfi, C.M. John, M. Rücker, Q. Lin, C. Spurin, S. Berg, S. Krevor, "Determination of the spatial distribution of wetting in the pore networks of rocks", *J Colloid Interface Sci.*, **613**, 786 (2022).
9. G. Garfi, C.M. John, Q. Lin, S. Berg, S. Krevor, "Fluid surface coverage showing the controls of rock mineralogy on the wetting state," *Geophys. Res. Lett.* **47** (8) (2020).
10. S. Foroughi, B. Bijeljic, Q. Lin, A.Q. Raeini, M.J. Blunt, "Pore-by-pore modeling, analysis, and prediction of two-phase flow in mixed-wet rocks," *Phys. Rev. E* **102**, 02330 (2020).
11. Q. Lin, B. Bijeljic, S. Berg, R. Pini, M.J. Blunt, S. Krevor, "Minimal surfaces in porous media: Pore-scale imaging of multiphase flow in an altered wettability Bentheimer sandstone", *Phys. Rev. E*, **99**, 6 (2019).
12. A. Scanziani, K. Singh, M.J. Blunt, A. Guadagnini, "Automatic method for estimation of in situ effective contact angle from X-ray micro tomography images of two-phase flow in porous media", *J. Colloid Interface Sci.* **496**, 51 (2017).
13. W.-B. Bartels, M. Rücker, M. Boone, T. Bultreys, H. Mahani, S. Berg, S.M. Hassanizadeh, V. Cnudde, "Imaging spontaneous imbibition in full Darcy-scale samples at pore-scale resolution by fast X-ray tomography", *Water Resour. Res.*, **55** 7072 (2019).
14. A.M. Alhammadi, A. AlRatrou, K. Singh, B. Bijeljic, M.J. Blunt, "In situ characterization of mixed-wettability in a reservoir rock at subsurface conditions", *Sci. Rep.*, **7**, 10753 (2017).
15. M. Andrew, B. Bijeljic, M.J. Blunt, "Pore-scale contact angle measurements at reservoir conditions using X-ray microtomography", *Adv. Water Resour.*, **68**, 24 (2014).
16. M. Prodanović, W.B. Lindquist, R.S. Seright, "Residual fluid blobs and contact angle measurements from X-ray images of fluid displacement," *XVI International Conference on Computational Methods in Water Resources*, (2006).
17. C.J. Radke, A.R. Kovscek, H. Wong, "A pore-level scenario for the development of mixed wettability in oil reservoirs," SPE 24880, *SPE Ann. Tech Conf. and Exhib.*, Washington, D.C. USA, Oct, 1992.
18. B.V. Derjaguin, E.V. Obukhov, "Anomalous properties of thin polymolecular films V.," *Acta Physicochim. URSS*, **10**(1), 25-44 (1939a).
19. B.V. Derjaguin, E.V. Obukhov, "Anomalous properties of thin polymolecular films V.," *Acta Physicochim. URSS*, **10**(2), 153-174 (1939b).
20. G.R. Jerauld, J. Fredrich, N. Lane, Q. Sheng, B. Crouse, D.M. Freed, A. Fager, and R. Xu, "Validation of a workflow for digitally measuring relative permeability," SPE 188688, *SPE Abu Dhabi Int. Pet. Exhib. & Conf.*, Abu Dhabi, U.A.E., Nov., 2017.
21. M. A. Al Ibrahim, N. F. Hurley, W. Zhao, D. Acero-Allard, "An automated petrographic image analysis system: capillary pressure curves using confocal microscopy," SPE 159180-MS, *SPE Annual Technical Conference and Exhibition*, San Antonio, Texas, USA, Oct, 2012.
22. S. Chen and G. Doolen, "Lattice Boltzmann method for fluid flows," *Annu. Rev. Fluid Mech.*, **30**, 329 (1998).
23. S. Chen, H. Chen, D. Martinez, and W. Mattheus, "Lattice Boltzmann model for simulation of magnetohydrodynamics," *Phys. Rev. Lett.*, **67**, 3776 (1991).

24. H. Chen, S. Chen, W. Matthaeus, "Recovery of the Navier - Stokes equations using a lattice-gas Boltzmann method," *Phys. Rev. A*, **45**, R5339 (1992).
25. Y. Qian, D. d'Humieres, P. Lallemand, "Lattice BGK models for Navier-Stokes equation," *Europhys. Lett.*, **17**, 479 (1992)
26. H. Chen, "Volumetric formulation of the lattice Boltzmann method for fluid dynamics: Basic concept," *Phys. Rev. E*, **58**, 3955(1998)
27. H. Otomo, H. Fan, R. Hazlett, Y. Li, I. Staroselsky, R. Zhang, R., and H. Chen, H., "Simulation of residual oil displacement in a sinusoidal channel with the Lattice Boltzmann method," *Comptes Rendus Mécanique*, **343**, 559 (2015).
28. H. Andrä, N. Combaret, J. Dvorkin, E. Glatt, J. Han, M. Kabel, Y. Keehm, F. Krzikalla, M. Lee, C. Madonna, M. Marsh, T. Muketji, E. H. Saenger, R. Sain, N. Saxena, S. Ricker, A. Wiegmann, X. Zhan, "Digital rock physics benchmarks—part II: Computing effective properties," *Comp. Geosci.*, **50**, 33 (2013)
29. J. Wu, J.J. Huang, "Dynamic behaviors of liquid droplets on a gas diffusion layer surface: Hybrid lattice Boltzmann investigation," *J. App. Phys.*, **118**, 044902 (2015)
30. M.A. Safi, N.I. Prasianakis, J. Mantzaras, A. Lamibrac, F.N. Buchi, "Experimental and pore-level numerical investigation of water evaporation in gas diffusion layers of polymer electrolyte fuel cells," *Int J Heat and Mass Trans.*, **115**, 238 (2017).
31. L. Martin, P. Benedikt, K. Benjamin, W. Julius, D. Timo, S. Volker, L. Arnulf, "Understanding electrolyte filling of Lithium-ion battery electrodes on the pore scale using the Lattice Boltzmann Method," *Batteries and Supercaps*, **e202200090**, (to be published)
32. D.H. Jeon, "Wettability in electrodes and its impact on the performance of Lithium-ion batteries," *Energy Storage Materials*, **18**, 139 (2019)
33. X. Shan and H. Chen, "Lattice Boltzmann model for simulating flows with multiple phases and components," *Phys Rev E*, **47**, 1815 (1993).
34. H. Otomo, H. Fan, Y. Li, M. Dressler, I. Staroselsky, R. Zhang, and H. Chen, "Studies of accurate multicomponent Lattice Boltzmann models on benchmark cases required for engineering applications," *Jour. Comp. Sci.*, **17**, 334 (2016).
35. H. Otomo, B. Crouse, M. Dressler, D.M. Freed, I. Staroselsky, R. Zhang, H. Chen, "Multi-component Lattice Boltzmann models for accurate simulation of flows with wide viscosity variation," *Computer Fluids*, **172**, 674 (2018)
36. H. Chen, C. Teixeira, and K. Molvig, "Realization of fluid boundary conditions via discrete Boltzmann dynamics," *Int. J. Mod. Phys. C*, **9**, 1281 (1998).
37. B. Crouse, D. M. Freed, N. Koliha, G. Balasubramanian, R. Satti, D. Bale, and S. Zuklic, "A Lattice-Boltzmann based method applied to Digital Rock characterization of perforation tunnel damage," SCA 2016-058, *Int. Symp. Soc. Core Analysts*, Snow Mass, CO, USA., (2016).
38. C. McPhee, J. Reed, I. Zubizarreta, *Core Analysis: A best Practice Guide*, **64**, 449 (2015).
39. N. Dyn, K. Hormann, S-J. Kim, D. Levin, "Optimizing 3D triangulations using discrete curvature analysis," *Mathematical methods for curves and surfaces*, **1**, 135 (2001)
40. *The VTK User's Guide*, (11th Edition, Kitware Inc., 2010)
41. W.B. Haines, "Studies in the physical properties of soil : the hysteresis effect in capillary properties and the modes of moisture distribution." *J Agric Sci*, **20**, 97 (1930)
42. R. T. Armstrong, N. Evseev, D. Koroteev, S. Berg, "Modeling the velocity field during Haines jumps in porous media," *Adv Water Resour*, **77**, 57-68, (2015).
43. J.G. Roof, "Snap-Off of oil droplets in water-wet pores," *SPE J.*, **10**, 85 (1970)
44. R. T. Armstrong, S. Berg, O. Dinariev, N. Evseev, D. Klemm, D. Koroteev, S. Safonov, "Modeling of pore-scale two-phase phenomena using density functional hydrodynamics,"
45. V. Khosravi, S.M. Mahmood, D. Zivar, H. Sharifigaliuk, "Investigating the applicability of molecular dynamics simulation for estimating the wettability of sandstone hydrocarbon formations", *ACS Omega*, **5**, 22852 (2020).
46. M.P. Anderson, M.V. Bennetzen, A. Klamt, S.L.S Stipp, "First principles prediction of liquid/liquid interfacial tension," *J. Chem. Theory Comput.*, **10**, 3401 (2014).
47. M.P. Anderson, T. Hassenkam, J. Matthiesen, L.V. Nikolajsen, D.V. Okhrimenko, S. Dobberschutz, S.L.S Stipp, "First-principles prediction of surface wetting," *Langmuir*, **36**, 12451 (2020).

Fast wettability assessment on small rock samples using a 3D, high-resolution, image-based Amott-like test

Maria Repina*, Regis Brugidou, Alexandre Dufour and Richard Rivenq

TotalEnergies OneTech, CSTJF 64000 Pau, France

Abstract. In this paper, we propose a new experimental set-up to carry out a full Amott-like cycle on small core samples (4 mm. diameter, 15 mm. length), imaged with a high-resolution micro-CT scanner. We conduct this experiment on two core samples from a carbonate reservoir. Each step of the cycle was followed by a 3D high-resolution scan along the entire sample length and analysed using digital image-processing algorithms. The characterization of wettability is based on multiple criteria: a) a pseudo-wettability index, analogous to the Amott-Harvey index, calculated from both resolved and unresolved pores; b) experimental observations during the spontaneous phases, and c) analysis of the spatial fluid distribution in the pore space. This new type of experiment has several advantages: a) it respects the experimental sequence of the industry standard Amott test, yet with a significantly reduced test duration; b) it provides complementary information describing the spatial distribution of the fluids in the visible pore network during spontaneous and forced phases; c) it is less sensitive to imaging resolution than existing approaches based on topological characteristics and contact angles.

1 Introduction

Wettability is a key factor controlling multi-phase flow in porous media. The standard and well-established laboratory procedures used to characterize the wettability of an oil/brine/rock system in the O&G industry are the Amott and USBM tests. They provide wettability indexes based on a combination of spontaneous and forced displacement properties of the oil/brine/rock system. They are very valuable for petrophysicists and reservoir engineers but take long to perform, up to several months, often even more than a year, and thus often come too late during reservoir pre-development evaluations.

In the last few years, there has been a growing interest in the assessment of wettability within the pore space, often associated with estimates of contact angles, interfacial curvature, or topological functions. These estimates have the advantage of considering millions of resolved pores. However, most of the calculated image-based wettability estimates often suffer from the lack of image resolution. Additionally, they might be influenced by the pore structure complexity.

In this paper, we explore the possibility of acquiring a qualitative wettability indicator, similar to that obtained using the conventional wettability characterization via Amott tests on centimeter-sized samples, using instead millimeter-sized samples imaged with a high-resolution micro-CT scanner. Following the idea presented in [6], also reported in [7] as a means of rapidly characterizing the wettability input required for Digital Rock Physics simulation, we used a similar experimental set-up to realize a full Amott-like cycle on small core samples (4mm diameter, 15mm long) with fluid

saturations determined from micro-CT image analysis. It is also expected that pore scale imaging, at least in the part of pore network that can be fully resolved, will provide additional information on the wetting properties of the system. This approach was tested on two carbonate samples from the same reservoir.

2 Materials and methods

2.1 Rock samples and fluid properties

Two cylindrical samples of a reservoir carbonate rock were used in this study, their mineralogical composition is shown in Fig. 1.

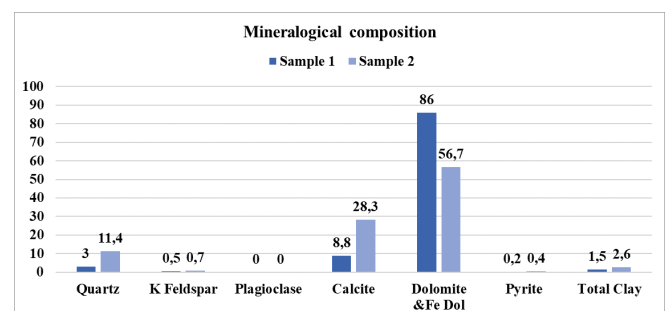


Fig. 1. Mini core samples mineralogical composition

Their main geometrical characteristics are provided in Table 1.

* Corresponding author: repina.maria@totalenergies.com

Table 1. Samples characteristics.

Sample	Length, mm	Diameter, mm	Porosity of the big parent plug, %	Permeability of the big parent plug, mD
1	13.95	3.91	20	20
2	14.50	3.90	8	16

The oil phase used was Marcol 52 (M52). The brine used for drainage and imbibition stages is a formation water doped with KI, its composition is presented in Table 2.

Table 2. Brine composition.

Sel	C (g/L)
KI	100.0
NaCl	81.1
CaCl ₂ , 2H ₂ O	14.5
MgCl ₂ , 6H ₂ O	3.9
KCl	3.7
Na ₂ SO ₄	1.5

For the characterization of the pore space with the Differential Imaging technique [3, 5], potassium iodide concentration was multiplied by three, following the example of [5].

The dead oil used for the ageing comes from the field from which the carbonate reservoir samples were taken. This oil was centrifuged before being received; it was not filtered before the injection into the core.

1.2 Experimental program

The experimental program presented below, was applied to two samples.

Table 3 summarizes experimental temperature and pressure parameters.

Table 3. Experimental parameters.

Ageing temperature (°C)	95
Temperature during spontaneous and forced phases (°C)	28
Pore pressure during imaging (bar)	11
Confining pressure during imaging (bar)	50
Maximum confining pressure during forced phases (bar)	120
Maximum pore pressure during forced phases (bar)	100

2.2.1 Sample cleaning (carried out separately for both samples)

1. Sample was put in the Viton sleeve before being placed in a carbon flow cell
2. Confining pressure of 25 bars was applied and maintained within the cell to compress the Viton sleeve

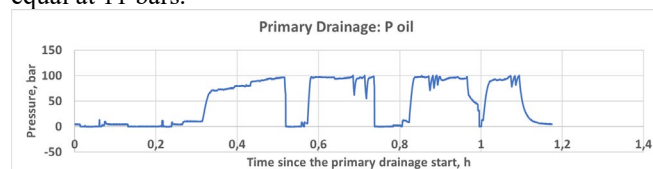
around the core sample to avoid fluid bypass. Temperature was raised to 65°C

3. 30 PV of 30 g/L NaCl/CaCl₂ (mass 90%/10%) brine was injected to wash out salts present in the sample
4. 95PV of toluene was injected at 5 µL/min
5. It was followed by the cyclic injection of toluene and mix of toluene and isopropanol in both directions. The cycles were composed of two phases: 30 PV at 5 µL/min toluene or toluene + isopropanol injection followed by maceration lasting between 2 and 8 hours. During the maceration period, the pore pressure was kept at 5 bars
6. Cleaning was finished with the injection of 78 PV of isopropanol at 10 µL/min
7. Sample was blown with the N₂
8. Temperature was lowered from 65°C to 28°C

2.2.2 Experimental protocol for porosity, saturation, and wettability characterization

For each sample, the experiment was performed as follows:

1. Core holder with the vertical flowing cell was installed into the micro-CT scanner
2. Four continuous tomograms “Dry scans” were taken for the whole sample with a voxel size 2.07 µm. The overlap of approximately 30% was used to stitch the four scans together
3. Vacuum was installed.
4. 25 PV of 300 g/L KI brine was injected into the rock sample to ensure that it was fully saturated with the highly contrasted brine. This step was necessary to characterize the sub-resolution pore space by applying the Differential Imaging method [3]. For more details, refer to the next section
5. Four continuous “KI 300” scans were taken for the whole sample with a voxel size 2.07 µm. Acquisition parameters were kept the same as for the dry scans.
6. High salinity brine was replaced by 48 PV of KI 100g/L brine. During the replacement brine injection, pressure was maintained close to 10 bars.
7. The primary drainage was effectuated by injecting 715 PV of the mineral oil M52 at 250µL/min. The direction was changed four times starting in a downwards direction. During the primary drainage, the confinement pressure was raised to 120 bars. SWi was fixed at 20-25%, with the most uniform SWi saturation profile. Fig. 2 shows the pressure recording during the primary drainage. The recovery pressure stayed equal at 11 bars.


Fig. 2. Sample 1: Pressure monitoring during the primary drainage

8. Confinement pressure was decreased to 50 bars. The sample was moved to the oven.
9. 6 PV of toluene was injected to serve as a buffer between M52 and the dead oil.
10. M52 was replaced by the dead oil.
11. Four weeks ageing began. The temperature of the oven was kept at 95°C, pore pressure - at 6 bars. At the beginning of the second week, 6 PV of dead oil was injected at 0.6 µL/min in a downwards direction. One week after the

direction of oil injection was changed, 700 μL of dead oil was injected at 0.6 $\mu\text{L}/\text{min}$. At the beginning of the last week of ageing, 6 PV of dead oil was injected at 0.6 $\mu\text{L}/\text{min}$ one more time.

12. The temperature was progressively decreased to 65°C.
13. 6 PV of toluene was injected to serve as a buffer between dead oil and M52.
14. Dead oil was replaced by the mineral oil M52.
15. Four continuous “SW_i aged” scans were taken for the whole sample with a voxel size 2.07 μm . Acquisition parameters were kept the same as for the dry scans.
16. Flow cell was connected to the imbibition experimental set-up shown in Fig. 3.

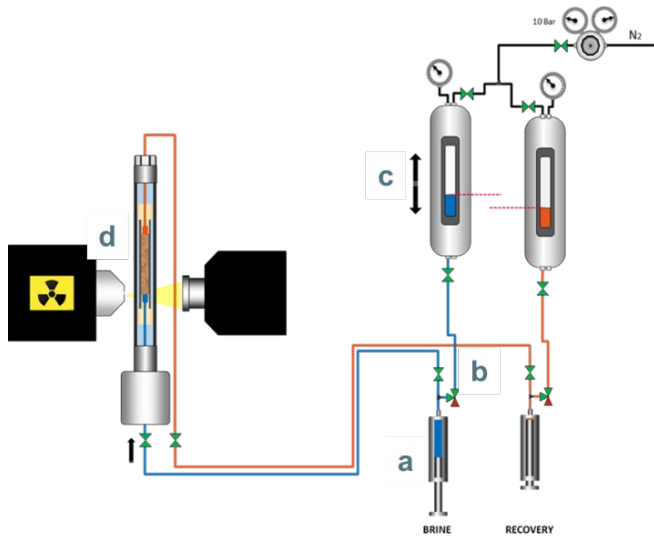


Fig. 3. Experimental set-up for the spontaneous imbibition: water level is controlled by the height of the water bottle. Steps indicated by a, b, c, d are detailed in the following paragraph.

17. The spontaneous imbibition was conducted as follows:
 - a) 5 PV of brine was injected at 0.6 $\mu\text{L}/\text{min}$ to put the brine level at the inlet entrance, the brine arrival was controlled with the radio, as shown in Fig. 4

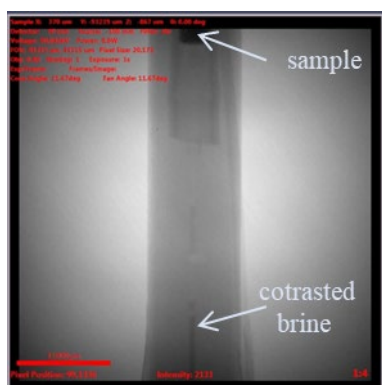


Fig. 4. Radio view: water rise in the tubing.

- b) Injection was stopped, and the valve was switched. At that stage, the brine from the bottle started to interact with the sample and the recovery valve stayed opened.
 - c) Water bottle height was progressively adapted so that water pressure was sufficient to keep the brine level at the sample entrance, see Fig. 5.

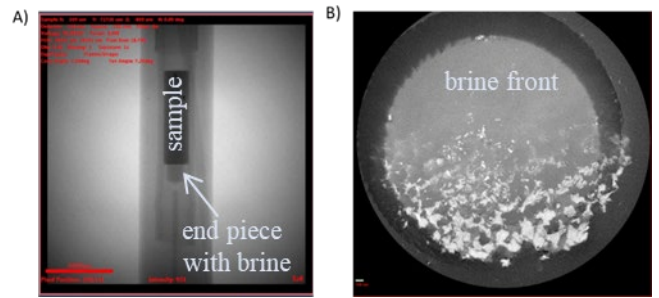


Fig. 5. Sample 1 A) Radio view: water in contact with the sample; B) image view: water in contact with the sample at the inlet

- d) Over the next 6 days, the brine invasion was checked regularly with the radio and with the high-resolution acquisitions.
18. Four continuous “Spont_Imbib” scans were taken for the whole sample with a voxel size 2.07 μm . Acquisition parameters were kept the same as for the dry scans.

19. The line connected to the water bottle was closed. The forced imbibition began. It consisted of injecting:
 - a) 610 PV of the brine at the progressively increasing flow rate from 0.6 $\mu\text{L}/\text{min}$ to 700 $\mu\text{L}/\text{min}$ in the upward direction.
 - b) 350 PV of the brine at 700 $\mu\text{L}/\text{min}$ in the downward direction.

The recovery and the confinement pressures were fixed at 11 and 120 bars respectively.

20. Confinement pressure was decreased to 50 bars. Brine pressure was regulated at 10 bars. The recovery valve was closed. Four continuous “Forced_Imbib” scans were taken for the whole sample with a voxel size 2.07 μm . Acquisition parameters were kept the same as for the dry scans.

21. The flow cell was connected to the drainage experimental set-up shown in Fig. 6

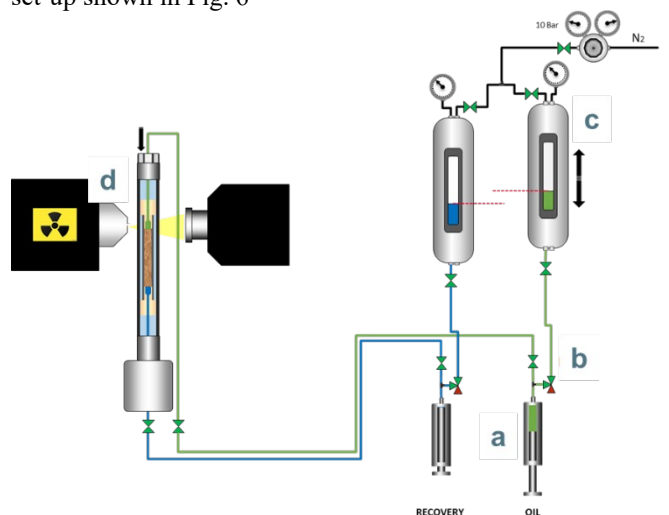


Fig. 6. Experimental set-up for the spontaneous drainage: M52 level is controlled by the height of the M52 bottle. Steps indicated by a, b, c, d are detailed in the following paragraph.

22. Spontaneous drainage was conducted as follows:
 - a) 15 PV of M52 was injected at 1 $\mu\text{L}/\text{min}$ to fill the line connected to the sample and thus, put the M52 level at the inlet entrance. The arrival of the M52 was controlled with the

X-ray monitoring in radio mode. Fig. 7 shows two stages: before and after M52 front arrival.

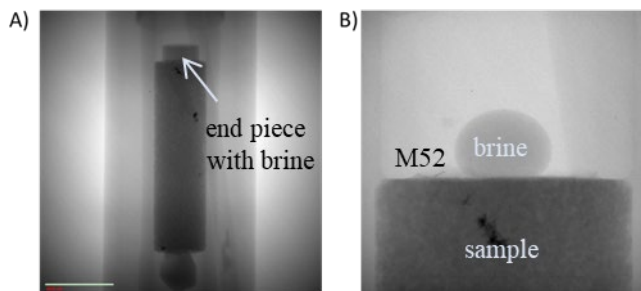


Fig. 7. A) Before: water in contact with the sample; B) After: zoom at the top of the sample: M52 pushed the water, however one water droplet stayed attached.

- b) The injection was stopped, and the valve was switched. At that stage, M52 from the bottle started to interact with the sample and the recovery valve stayed opened.
- c) Water bottle height was progressively adapted so that the M52 column pressure was sufficient to keep M52 level at the sample entrance.
- d) Over the next 6 days, M52 spontaneous invasion was regularly checked in radio mode and with the high-resolution acquisitions.

23 Four continuous “Spont_Drain” scans were taken for the whole sample with a voxel size 2.07 μm . Acquisition parameters were kept the same as for the dry scans.

24. The line connected to the M52 bottle was closed. The forced drainage was started. It consisted of injecting:

- a) 300 PV of M52 at the maximal possible flow rate in a downwards direction. The flow rate limitation was due to the max pressure limit equal to 100 bars. The max. constant injection flow rate that did not provoke the pump to shut down was equal to 60 $\mu\text{L}/\text{min}$
- b) 300 PV at 60 $\mu\text{L}/\text{min}$ in the upward direction
- c) 325 PV at 55 $\mu\text{L}/\text{min}$ in the downward direction.

The recovery and the confinement pressures were fixed at 10 and 120 bars respectively.

25. Confinement pressure was decreased to 50 bars. M52 pressure was regulated at 10 bars. The recovery valve was closed. Four continuous “Forced_Drain” scans were taken for the whole sample with a voxel size 2.07 μm . Acquisition parameters were kept the same as for the dry scans.

1.3 Imaging methods and processing

2.3.1 Imaging method

The images were taken by an Xradia Versa 520 high-resolution microCT. The X-ray energy was 90 kV and the power was 8W. The number of projections for each radio was 2001. The pixel size of all images was equal to 2.07 μm . All tomograms were reconstructed into 3D images using Zeiss reconstruction software.

Dry, KI_300, SWi_aged, Spont_Imbib., Forced_Imbib., Spont_Drain., Forced_Drain. images were first stitched together to cover the whole length of the sample. After, they were registered to the dry images to have the same orientation and to be easily comparable. A nonlocal means filter was used to remove noise. The image analysis was performed with the help of software packages: Mango [8] for the routine actions, ImageJ for the trainable Weka segmentation [2].

2.3.2 Characterization of the pore space and fluids inside

Differential imaging [3, 4] was used to quantify both resolvable and sub-resolution porosity. This method relies on the observation that the difference image between the KI saturated scan and the dry scan maximizes the phase contrast between grain, macro pores and zones containing sub-voxel porosity phases (Fig.8A – Fig.8C, zones 1-3 contain sub-resolution porosity) and consequently, provides a good input for image segmentation.

We clearly observe some sub-resolution pores with intermediate grey scale values in Fig. 8C. Results of the Weka trainable segmentation of the difference image can be found in Fig. 8D. Fig. 8E illustrates how good a trainable Weka segmentation is at capturing complex textures of the dual pore network.

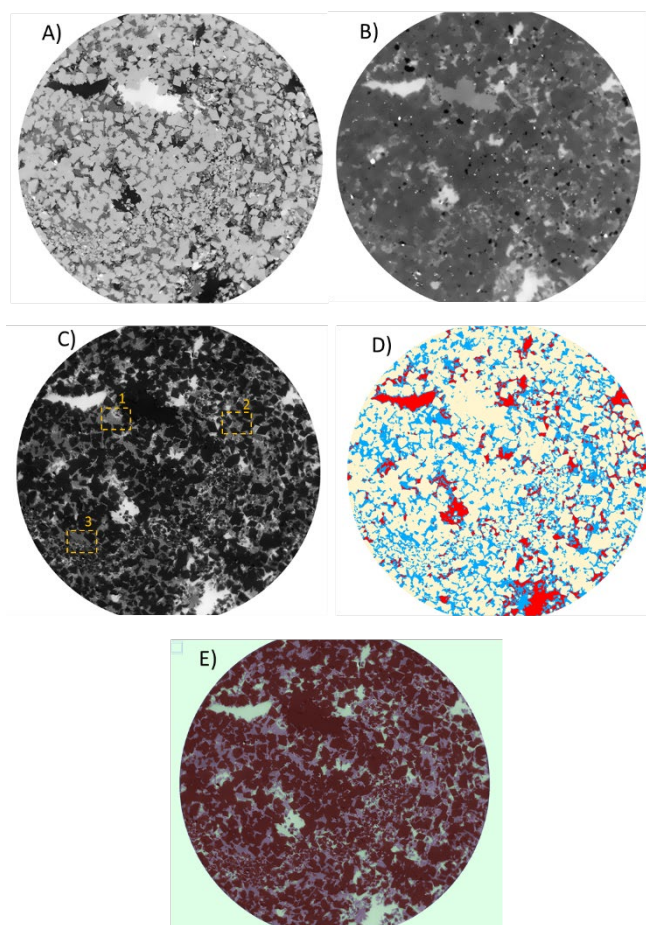


Fig. 8. Sample 2: two-dimensional cross-section of three-dimensional micro-CT images at the same location (13.18 mm from the sample inlet). A) dry scan; B) 300 g/L brine saturated scan; C) difference image between A and B; D) segmented difference image

(resolved pores in red, unresolved porous zones in blue and tight grains in yellow); E) overlay of C and D images. Boxes 1-3 give examples of the zones containing sub-resolution porosity

Porosity of the sub-voxel zones was estimated based on the linear interpolation between two reference values (grey value of tight grains and grey value of brine in macro pores).

Fig.9 illustrates the profiles of total, macro and micro porosities for the second sample. As can be seen, the sample is heterogeneous in porosity. The mean total porosity slightly increases towards the outlet of the second examined mini core sample. As expected from the visualization of the pore network, a big part of the total porosity comes from the sub-voxel porosity.

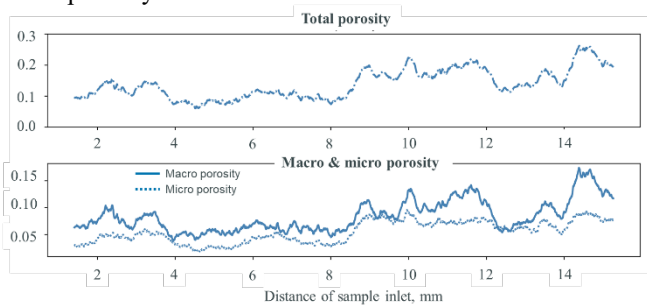


Fig. 9. Sample 2: porosity profiles along the sample length

Porosity quantification for samples 1 and 2 is given in Table 4.

Table 4. Porosity average values.

	Sample 1	Sample 2
Sub-resolution porosity	0.06 ± 0.01	0.06 ± 0.01
Resolved porosity	0.04	0.08
Total porosity	0.10 ± 0.01	0.14 ± 0.01

Two examples of the maps of the total (resolved and sub-voxel) porosity are illustrated in Fig.10.

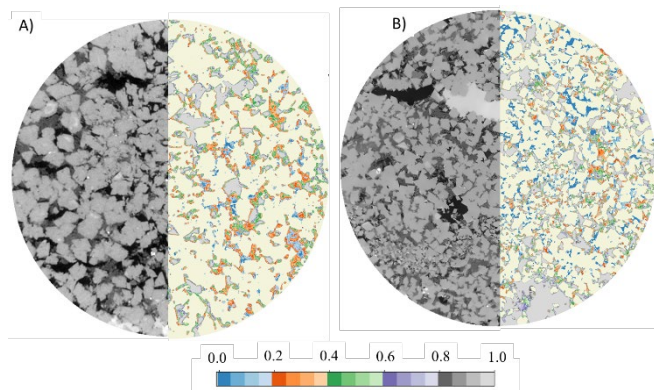


Fig. 10. Porosity map for A) Sample 1, slice is located at 12.68 mm from the inlet; B) Sample 2, slice is located at 13.18 mm from the inlet.

Grey-scale multiphase images for all stages of the second experiment are illustrated in Fig. 11 – Fig. 12. The black is mineral oil, the dark grey is grains, the light grey is doped brine.

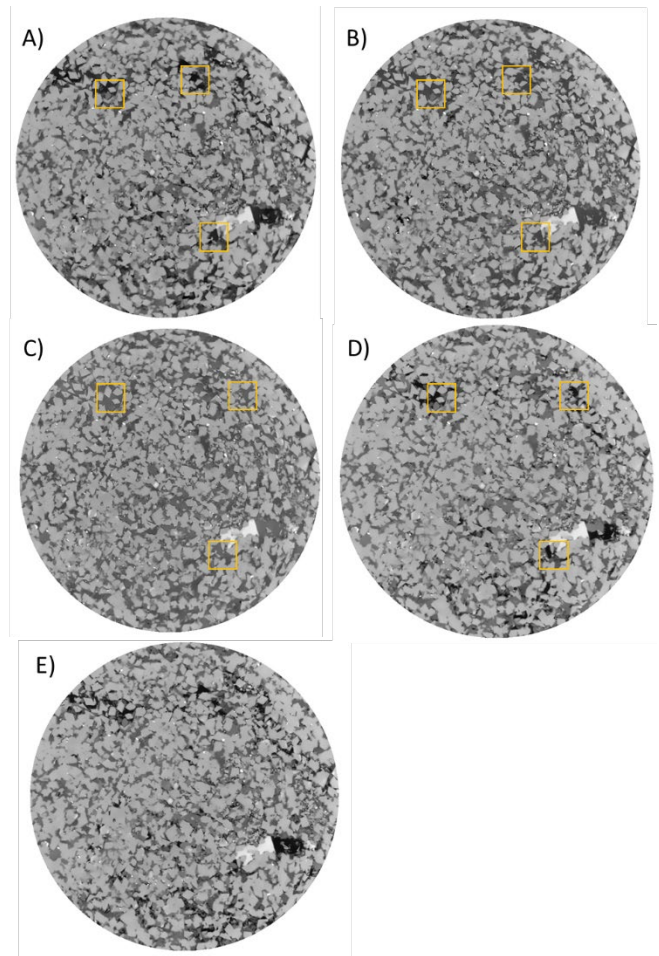


Fig. 11. Sample 1. Two-dimensional cross sections of three-dimensional micro-CT images. Slices are located at 1.56 mm from the bottom of the sample. Radius of each slice is equal to 1.53 mm. A) SWi aged scan; B) Sp_Imbib scan; C) For_Imbib scan; D) Sp_drainage scan; E) For_Drainage scan. The yellow boxes indicate regions where fluid occupation was changed in comparison with the previous or the following saturation state

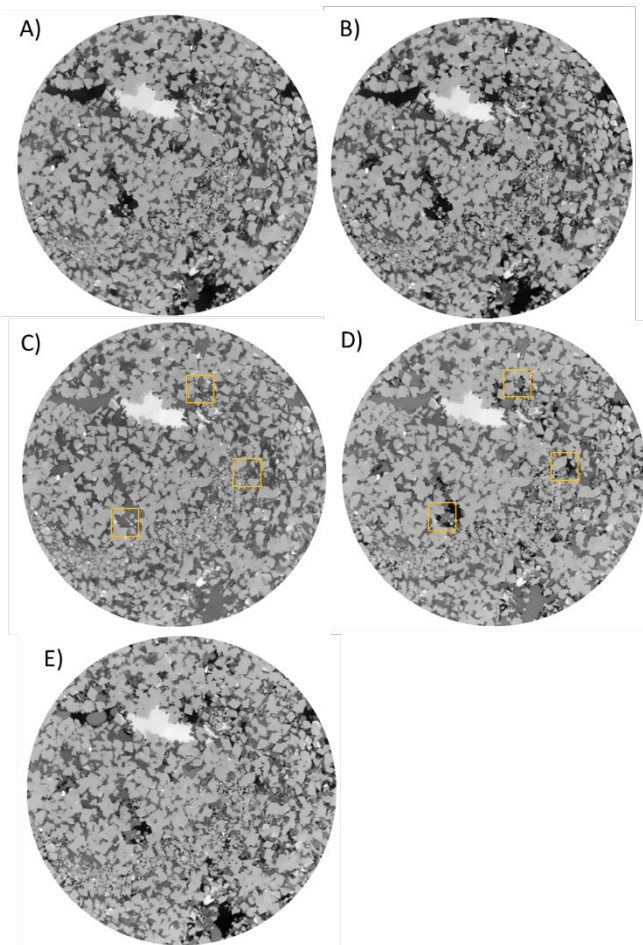


Fig. 12. Sample 2. Two-dimensional cross sections of three-dimensional micro-CT images. Slices are located at 13.18 mm from the bottom of the sample. Radius of each slice is equal to 1.53 mm. A) SWi_aged scan; B) Sp_Imbib scan; C) For_Imbib scan; D) Sp_drainage scan; E) For_Drainage scan. The yellow boxes indicate regions where fluid occupation was changed in comparison with the previous or the following saturation state

Fluid occupancy in the macro pores was identified by the direct two-phase segmentation using the converging active contour method with Mango software. Water saturation characterization in the sub-resolution pores was carried out following the principals of the differential imaging method.

The brine saturation profiles across the second sample are shown in Fig. 13.

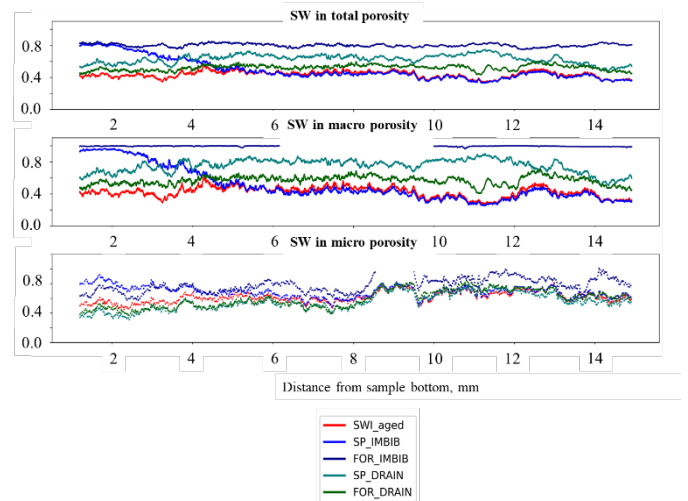


Fig. 13. Brine saturation profiles along the second sample from bottom to top: total; in macro pores; in sub-voxel zones. Brine access during the spontaneous imbibition was at the bottom, mineral oil access during the spontaneous drainage was at the top

It is apparent from Fig. 13 that the spontaneous imbibition of water happened only at the bottom, only one quarter of the sample had seen the increase of the water saturation coming principally from the macro pores. As for the spontaneous drainage, it was of higher intensity. Water saturation profiles suggest that it occurred along the entire sample, both macro and sub-resolution pores participated in the spontaneous drainage. Similar behaviour was seen for the first sample.

Average brine saturation values for both samples are presented in Table 5 – Table 6.

Table 5. Sample 1: water saturation average values.

	Ageing	Sp. Imb.	For. Imb.	Sp. Drn.	For. Drn.
Sub-resolution pores	0.60	0.48	1	0.86	0.80
Resolved pores	0.18	0.29	0.99	0.90	0.58
Total	0.46	0.48	0.99	0.87	0.72

Table 6. Sample 2: water saturation average values.

	Ageing	Sp. Imb.	For. Imb.	Sp. Drn.	For. Drn.
Sub-resolved pores	0.45	0.47	0.50	0.44	0.44
Resolved pores	0.42	0.50	0.99	0.75	0.57
Total	0.44	0.49	0.80	0.63	0.52

Table 5 and Table 6 illustrate that for both samples water saturation after the secondary drainage is higher than after the primary drainage. This increase of the water saturation was expected: during the secondary drainage it was much more difficult to inject M52 than during the first drainage. As a reminder, during the first and second drainage, the maximum accepted injection pressure was limited to 100 bars. During the second drainage, the maximum injection flow rate was divided by 4-5 vs. the primary drainage to respect the pressure

limitation. This could suggest that during the four-week ageing, the initial wettability was shifted to a more oil-wet wettability, provoking more intensive water trapping that was noticed during the secondary drainage.

It should be noted that water saturation of the resolved porosity after the forced imbibition might be overestimated. In fact, the volume of oil films on the rock surface cannot be quantified with a high degree of precision, because it is below image resolution. The uncertainty of the saturation after this step is the highest, it is estimated at 3-5 %.

1.4 Wettability analysis results and discussions

To characterize the wettability behavior, we proposed to conduct the Amott-like test on two mini-core samples. This test includes a four-displacement sequence, similar to that of an Amott test, starting from the irreducible saturation state after ageing. It assumes that each sample is subjected to spontaneous and forced flows, first by water (imbibition) and afterwards by oil (drainage). The spontaneous flows are capillary driven. The forced flows are implemented by viscous displacement.

A pseudo-wettability index is proposed to be calculated by the following Eq. 1:

$$I_w - I_o = \frac{S_w^{sp,imb} - S_w^{Swi}}{S_w^{for,imb} - S_w^{Swi}} - \frac{S_o^{sp,dr} - S_o^{for,imb}}{1 - S_w^{for,dr} - S_o^{for,imb}} \quad (1)$$

Where I_w – is imbibition index, I_o – is drainage index, sp.imb and sp.dr are spontaneous imbibition and drainage, for.imb and for.dr are forced imbibition and drainage. This index is comprised between +1 and -1, it refers to the quantitative degree of wettability like the Amott-Harvey index [1].

Table 7 shows the results of pseudo-wettability index calculation for two samples.

Table 7. Result of pseudo-wettability index calculation.

	Sample 1		Iw- Io	Sample 2		Iw- Io
	Iw	Io		Iw	Io	
All pores	0.04	0.44	-0.41	0.14	0.61	-0.47

Results obtained from the pseudo-wettability index calculation suggest that the studied rock-fluids systems are most probably oil wet, for both samples the drainage index is systematically much higher than the imbibition index.

Moreover, this conclusion is supported by the following experimental observations:

- 1) Difficulty in setting S_{wi} : for both samples, total initial water saturation remains high, suggesting capillary trapping of water
- 2) For both samples, the spontaneous imbibition remains limited to the lower part of the sample. The increase of water saturation after the spontaneous imbibition might be even attributed to the initial water advancement provoked under the initial non-stabilized pressure of the water bottle. For this reason, it was advised to adapt the experimental set-up to rule out, or at least substantially reduce the probability of the accidental forced imbibition at the sample inlet
- 3) Spontaneous drainage, on the other hand, happened over the entire length of the sample. We found a clear oil saturation increase in both resolved and the sub-resolution porosity across two samples. Moreover, we even recorded in the radio

mode M52 production at the bottom of the second sample during the first 6 days, as shown in Fig. 14

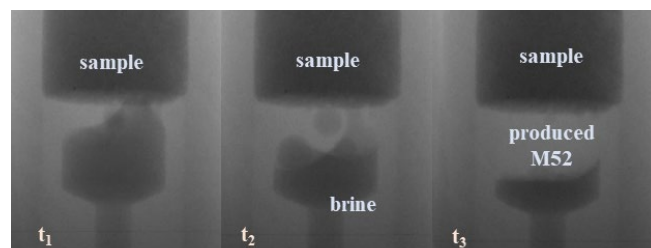


Fig. 14. Bottom of the second sample imaged in the radio mode during the spontaneous drainage: M52 production over time

4) Distribution of oil and brine visible interfaces within the resolved pores also suggests oil wettability, Fig. 15

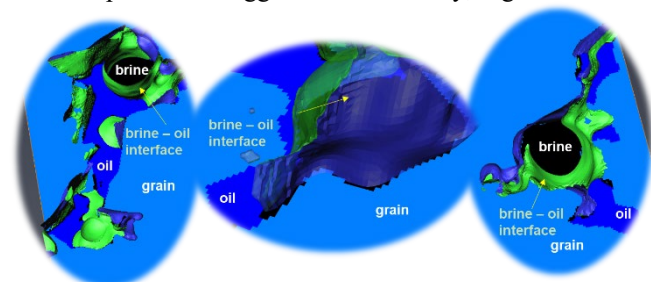


Fig. 15. Examples of some resolved pores of the first sample with brine-oil interfaces having negative curvature and occupying the large pore spaces

2 Conclusions

To assess the wettability of reservoir samples in a quick and physically meaningful manner, we designed a new experimental set-up allowing us to carry out a full Amott-like cycle on a small core sample imaged with a high-resolution micro-CT scanner.

The advantage of this kind of experiment is that it provides global wettability characterization based on multiple experimental observations, the analysis of the fluid distribution in the porous space and the result of the pseudo-wettability index calculation. Moreover, it respects the experimental sequence of the industry standard Amott test, yet with a significantly reduced test duration. Thanks to the high-quality 3D imaging, it provides complementary information describing the spatial distribution of the fluids in the visible pore network during spontaneous and forced phases. On top of that, it is less sensitive to imaging resolution than existing approaches based on topological characteristics and contact angles.

Comparison with the results of conventional Amott test on neighbour centimeter-sized core samples was planned and initiated in parallel to the Amott-like image-based tests on small core samples. These standard tests are still in progress. Future work should involve the comparison of the results of the wettability characterization on small core samples with the proposed experimental design to the results of the standard Amott ones.

References

- [1] Amott, E. 1959. Observations Relating to the Wettability of Porous Rock. *Trans.* 216, 01, 156–162.
- [2] Arganda-Carreras, I., Kaynig, V., Rueden, C., Eliceiri, K. W., Schindelin, J., Cardona, A., and Sebastian Seung, H. 2017. Trainable Weka Segmentation: a machine learning tool for microscopy pixel classification. *Bioinformatics (Oxford, England)* 33, 15, 2424–2426.
- [3] Gao, Y., Lin, Q., Bijeljic, B., and Blunt, M. J. 2017. X-ray Microtomography of Intermittency in Multiphase Flow at Steady State Using a Differential Imaging Method. *Water resources research* 53, 12, 10274–10292.
- [4] Gao, Y., Raeini, A. Q., Selem, A. M., Bondino, I., Blunt, M. J., and Bijeljic, B. 2020. Pore-scale imaging with measurement of relative permeability and capillary pressure on the same reservoir sandstone sample under water-wet and mixed-wet conditions. *Advances in Water Resources* 146, 2, 103786.
- [5] Lin, Q., Al-Khulaifi, Y., Blunt, M. J., and Bijeljic, B. 2016. Quantification of sub-resolution porosity in carbonate rocks by applying high-salinity contrast brine using X-ray microtomography differential imaging. *Advances in Water Resources* 96, 306–322.
- [6] Regaieg M, Brugidou R and Nono, F. 2022. *A porous sample wettability parameter determining method and related system*, US Patent No. 63/342,923.
- [7] Regaieg M, Nono F, Farhana Faisal T, Varloteaux C and Rivenq R. 2022. Pore network simulations coupled with innovative wettability anchoring experiment to predict relative permeability of a mixed-wet rock. *Symposium of the Society of Core Analysis* (2022).
- [8] Sheppard, A. *MANGO*. ANU.

Hybrid Technique for setting initial water saturation on core samples

Victor Fernandes^{1,2,*}, Cyril Caubit¹, Benjamin Nicot¹, Fabrice Pairoys¹, Henri Bertin² and Jean Lachaud²

¹TotalEnergies CSTJF, Avenue Larribau, 64000 Pau, France

²I2M-Université de Bordeaux, CNRS, 351, Cours de la Libération, 33405 Talence, France

Abstract. Relative permeability and capillary pressure are important parameters in reservoir simulations because it helps in understanding and anticipating oil and/or gas production scenarios over the years. They are both obtained in laboratory after establishing the required initial conditions. As a matter of fact, before measuring imbibition relative permeability and capillary pressure, it is recommended to set initial rock reservoir conditions by establishing appropriate initial water saturation (S_{wi}) and by ageing the core to restore the reservoir wettability. There are several conventional techniques to establish S_{wi} . The Viscous Flooding is a fast technique, but it may create a non-uniform saturation profile and, in some cases, be inefficient to reach low S_{wi} targets. Centrifugation is a capillary-driven technique that is also very fast, however the possibility of not desaturating the outlet face is a significant constraint. In both cases, reversing flow direction is generally performed to flatten the saturation profile, however this phenomenon is poorly controlled. The application of capillary pressure by Porous Plate allows targeting a specific value of S_{wi} and generates a uniform saturation profile, however it is a very time-consuming method. In this paper we present the Hybrid Drainage Technique, which couples Viscous Flooding and Porous Plate approaches, significantly reducing the experimental duration when setting S_{wi} . Another advantage of the method is the possibility of setting a uniform saturation profile at the targeted S_{wi} . A specific core holder, adapted to NMR imaging, and allowing to perform both Viscous Flooding and Porous Plate testing without unloading the rock, was designed. Using this core holder enables performing ageing and imbibition coreflood testing, with no further manipulation of the core sample. Monitoring saturation profiles was made possible by using a NMR imaging setup. The method has been tested and validated on two outcrop samples from Bentheimer (sandstone) and Richemont (limestone), drastically reducing the experimental time of the primary drainage step in comparison to a classical Porous Plate drainage, but also leading to uniform water saturation profiles. The experiment duration is reduced, and it enables the realization of coreflooding, therefore this technique may be used for larger samples classically used in relative permeability experiments. This approach is preferred as it provides faster and more reliable measurements of saturation.

1 Background and state of the art

For the prediction of a hydrocarbon's reservoir production, numerical simulations are performed. The simulation models rely on two important petrophysical parameters: the relative permeability (K_r) and the capillary pressure (P_c). These are parameters that can only be obtained in the laboratory by performing Special Core Analysis (SCAL) studies. The workflow for the definition of both parameters contains several steps in which the original condition of the reservoir is expected to be reproduced as closely as possible to in situ conditions, in a technique known as wettability restoration.

The restored state method consists of coring a rock sample from the reservoir, sampling and plugging in the appropriate dimensions (usually cylindrical samples, varying from 1" and 1.5" in diameter and up to 3" in length [1]). The first step of the conventional procedure for reproduction of reservoir conditions consists in taking the sample to its initial state in terms of wettability. For that matter, the sample is cleaned with the objective of removing native oil, mud filtrates, precipitated salts and connate water. In this process, water, CO_2 and a variety of organic non-polar and polar solvents may be used to ensure appropriate cleaning intended to

produce a water-wet sample. The sample is then submitted to conventional or vacuum oven-drying as well as flow through drying (by using, for instance, N_2).

The next step consists in setting the fluids' initial saturation. This phase is called primary drainage (PD) and mimics the migration phase of hydrocarbons from the source rock to the reservoir [2]. It begins with a fully brine-saturation state, followed by the injection of oil (in the case of an oil/water experiment). After reaching the target value of S_{wi} , which is defined by the response of the reservoir logging relative to the region where the sample was cored, a wettability restoration phase is performed by ageing the core sample in its own crude oil at high temperature (typically $80^\circ C$) and pore (or back) pressure, which prevent water loss. After these steps, the sample may be considered as restored to its original state of wettability and fluid settings.

The following step is called imbibition, which consists in injecting brine in the core for oil recovery. This phase is performed to reproduce and experimentally simulate the production phase of the reservoir. During this phase, the oil production rate, the saturation profile dynamics and the pressure drop between the sample's inlet and outlet allow the determination of K_r and P_c by inverse analysis. However, any

* Corresponding author: victor.de-oliveira-fernandes@totalenergies.com

error committed when setting fluids initial saturation and restoring rock's wettability will impact the sample's response during imbibition, leading to uncertainties on Kr and Pc estimations.

As primary drainage is a key step in restoring the rock's true conditions in the reservoir, several techniques may be used, each of them carrying advantages and drawbacks. Variations have been proposed by different authors to benefit from the best features of each technique.

As all experimental steps in SCAL are supposed to reproduce the reservoir behaviour, experimental artefacts must be avoided. The main artefact impacting the establishment of a homogeneous Swi profile is capillary end effects (CEE) that is defined as a gradient of the wetting phase saturation along the sample longitudinal axis. This effect is originated from a capillary pressure drop between inlet and outlet faces of the sample during oil injection. It must be corrected before any SCAL tests as it does not represent a real behaviour of fluids during migration in the reservoir.

Because relative permeability and capillary pressure are related to fluid saturations in a non-linear way, the presence of a saturation gradient will prevent their direct determination. However, by means of numerical simulation based on an extended form of Darcy's law with appropriate boundary conditions, the effect of a non-uniform saturation profile on Kr and Pc determination may be mitigated [3, 4, 5, 6, 7].

Whereas the direct impact of CEE on the determination of Kr and Pc may be corrected, the impact of CEE on wettability restoration, thus on Kr and Pc calculation, is a more complicated issue. One of the hypotheses is that the wettability of the core is homogeneous, so that Kr and Pc will behave in the same way along the core. However, as wettability change during ageing is dependent on fluid saturations, a non-uniform wettability profile will result from a sample for which capillary end effects have not been removed [8]. Furthermore, maintaining a homogeneous saturation profile during ageing is a necessary but insufficient condition. It has been shown that a heterogeneous wettability profile may result even when a homogeneous saturation profile is ensured during ageing [9, 10].

Nonetheless, capillary end effects are not always a phenomenon that need to be minimized. Some experiments have been designed to take advantage of this effect, for example, to speed up the measurement of capillary pressure curve [11, 12, 13, 14].

There are three major primary drainage techniques in SCAL experiments, which main advantages and drawbacks are presented in Table 1:

Table 1 – Advantages and Drawbacks of PD techniques

	Advantages	Drawbacks
Viscous Flooding	Fast method	Non-uniform saturation profile
	Standard injection rig and equipment	Difficult to reach low Swi values
	Provides primary drainage Kr	Fines migration under high flowrate

Centrifuge	Faster than Porous Plate	Friable samples can be easily damaged
	Capillary pressure driven technique	Specific equipment needed
	Lower CEE than Viscous Oil Flooding	Manipulation needed for further SCAL steps
Porous Plate	Homogeneous saturation profile	Time consuming
	Good method for friable samples	Capillary contact may be a problem
	Capillary pressure driven technique	Manipulation needed for further SCAL steps

The principal technique used in SCAL experiments with large samples (typically D = 50 mm; L = 200 mm) is Viscous Oil Injection that consists in injecting oil at constant flowrate steps in the sample while measuring the pressure drop between inlet and outlet as well as fluid productions. At first, only water will be produced as oil percolates in the sample and expels water from the pores. After oil breakthrough, both phases will be produced until no more water is recovered. This is a fast technique that does not require any particular setup, being possible to be carried out in the same cell used for the following steps in SCAL (ageing and flooding) and by a simple injection rig. However, capillary end effects (CEE) due to the capillary pressure drop along the sample is an important constraint (as seen in Fig. 1), as well as reaching low values of Swi (<10%) in some specific cases. This problem may be solved by injecting at higher flowrates. Nonetheless, it may cause irreversible damage in the core, such as fines migration and additional pore volume creation, impacting further measurements once the rock matrix has been modified.

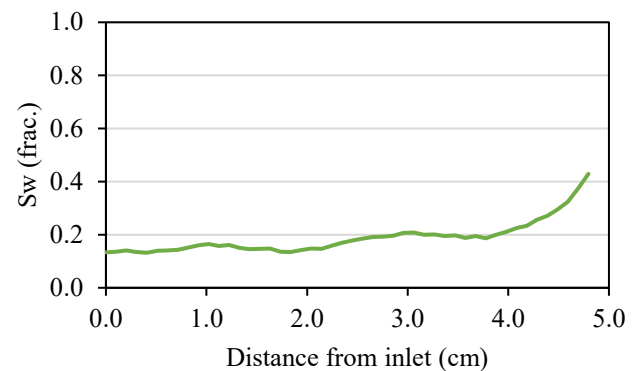


Fig. 1. Water saturation profile of a Bentheimer sandstone measured by NMR after a Viscous Flooding primary drainage. Capillary end effects are clearly visible close to the sample's outlet.

One method of dealing with capillary end effects is to reverse the direction of injection. Although this method may generate a homogeneous saturation profile, two major issues may result:

- Brine placed in the outlet of the sample is mobilized and displaced towards the inlet, generating an imbibition and increasing water saturation at these points. This phenomenon can be seen in Fig. 2.
- Formation of disconnected oil clusters that will adversely affect wettability restoration and impact effective permeability measurements [15].

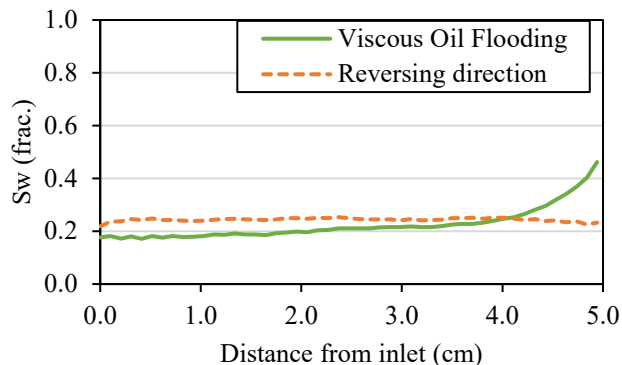


Fig. 2. Bentheimer sandstone submitted to Viscous Oil Flooding (VOF) followed by flow direction reversal – NMR profiles imaging. It is possible to observe a general imbibition of the brine present in the last cm after the last step of VOF (green line) on the final profile (orange-dotted line).

Centrifugation is another technique for setting initial oil saturation. This technique was introduced by Hassler and Brunner [16]. It consists in placing a rock sample inside a centrifuge machine that will induce an injection pressure through centripetal forces from high speed rotation. Ignoring any two dimensional effects, the expression that defines the capillary pressure at a radius r is given by Eq. 1:

$$P_c(r) = \frac{1}{2} \Delta \rho \omega^2 (R^2 - r^2) \quad (1)$$

where, P_c is the capillary pressure, $\Delta \rho$ is the density difference between the resident brine and the injected fluid, ω is the rotational speed of the centrifuge and R is the distance between the centrifuge central axis and the sample outlet.

The issues of this technique are not only the presence of capillary end effects (as seen in Fig. 3), but also the possibility of not desaturating the outlet face of the sample. This effect comes from the boundary condition when r is equal to R in Eq. 1, which gives $P_c = 0$, then, $Sw = 1$. The solution for these problems is to reverse injection direction; however, it potentially induces the same issues as presented for the viscous oil injection. In addition, by using Centrifuge as primary drainage method, manipulation is generally needed to unload the sample from the centrifuge machine and to load it into the cell adapted for further flooding, such as ageing and imbibition steps.

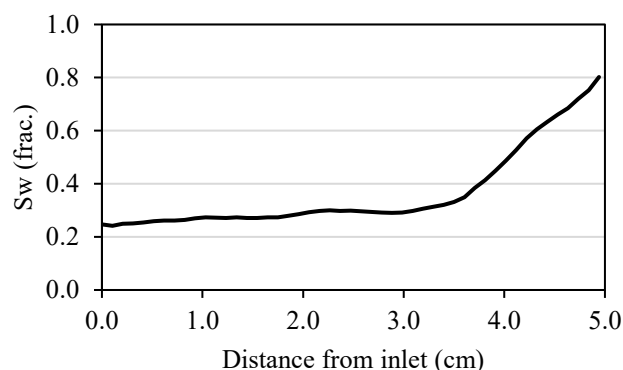


Fig. 3. Water saturation profile acquired by NMR after a Centrifuge primary drainage of a Bentheimer sandstone. Once again, the presence of CEE is clearly noticed close to the outlet.

The last fraction of the saturation profile in Fig. 1 and Fig. 3 showing an increase from 4 cm and 3.5 cm, respectively, is called the capillary foot. It is characterised as the remaining capillary end effect at the end of primary drainage for methods which do not prevent this effect by means of a semi-permeable membrane or plate.

The Porous Plate technique is considered the reference method for establishing initial water saturation. It was first introduced to measure capillary pressure versus water saturation in a water/gas system [17], further being extended to water/oil systems. This technique of primary drainage consists in placing a semi-permeable ceramic plate at the outlet of the sample. As a consequence of its small pore sizes and strong water-wetness, a high entry threshold pressure is needed for the non-wetting fluid to invade the ceramic. For a primary drainage cycle, the porous plate is essentially water-wet, allowing exclusively water to flow. The oil phase is directly injected by means of a volumetric pump, with continuous phase connection from the inlet to the porous plate. As capillary pressure is equally distributed along the sample, this technique generates a uniform saturation profile along the core, as seen in Fig. 4. However, as the porous plate permeability is extremely low to avoid oil invasion, this experiment may be highly time consuming depending on the targeted Sw_i . Another drawback is the need of unloading the porous plate from the overburden cell to perform further SCAL steps.

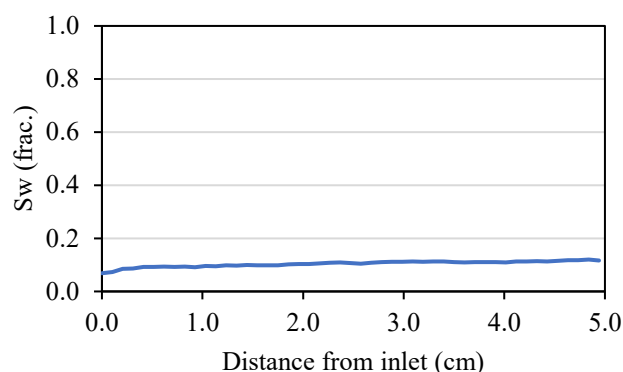


Fig. 4. Water saturation profile of a Bentheimer sandstone after a Porous Plate primary drainage. The profile, acquired by NMR imaging, shows a homogeneous saturation profile.

Some solutions to generate homogeneous saturation profile in reduced experimental time were proposed by some authors. The Spinning Porous Plate basically consists in placing a sample in contact with a multi-perforated porous plate to spin in a centrifuge [18]. It presents satisfactory results regarding the homogeneity of the saturation profile in sandstones of permeability around 70 mD at low Swi targets. However, it fails in achieving the same homogeneity quality for tighter samples and at higher levels of Swi. By performing the primary drainage cycle in the centrifuge, the following SCAL steps also demand additional handling. To overcome the combined issues of setting homogeneous profile and reducing handling, a by-pass to the porous plate was proposed [19] in the Toroidal Porous Plate. However, this proposition does not deal with experimental duration of the primary drainage step, as classic Porous Plate is performed in this case.

From these challenges, we propose a new Hybrid Drainage Technique (HDT) that is capable of not only reducing experimental time in comparison to a classic Porous Plate primary drainage, but also generating a homogeneous saturation profile without reversing flow direction as in Viscous Flooding and Centrifugation. By performing such a technique, we will prevent problems related to saturation profile heterogeneity, wettability restoration and disconnected oil clusters formation, as discussed earlier.

2 Methodology

2.1 The Hybrid Drainage Technique

The principle of the Hybrid Drainage Technique consists of coupling Viscous Flooding and Porous Plate for performing a fast, capillary-driven primary drainage, free from capillary end effects.

For this matter, the rock sample is inserted in an overburden cell together with a mono-perforated porous plate placed at the sample's outlet. This perforated porous plate is then mounted on a base-plate - called platen in what follows - constituted of two isolated outlets: one directly connected to the porous plate bypass (hereafter called Outlet 1), and one positioned immediately behind the porous plate (called Outlet 2). The presence of an O-ring ensures the isolation between both outlets that are connected to valves out of the cell.

The design of the overburden cell and the platen housing the porous plate, as well as the Hybrid Drainage Technique were filed for patent. A schematic drawing of the overburden cell is shown in Fig. 5.

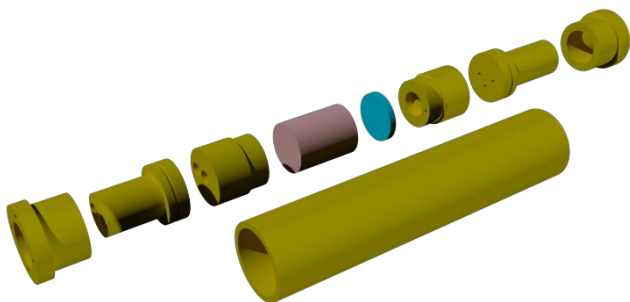


Fig. 5. Representation of the overburden cell.

As well as in other capillary-driven techniques (e.g., Porous Plate and Centrifuge) knowing the target Pc is mandatory for reaching a correct Swi value in the Hybrid Drainage Technique.

The HDT is composed of two phases: an initial oil injection similar to the Viscous Flooding technique and a second part similar to the Porous Plate technique, where capillary foot produced during Phase 1 will be eliminated.

Phase 1:

At first, oil is injected in the sample at constant pressure keeping Outlet 1 opened and Outlet 2 closed. Oil displaces water initially in place through the bypass of the porous plate (Outlet 1). This phase will generate a non-uniform saturation profile due to capillary end effects, such as in a classic Viscous Flooding. The end of Phase 1 is achieved when no more water is produced after oil breakthrough. At this moment, the goal is to minimise capillary foot by imposing a constant pressure on the whole sample that will homogenise fluid saturations, which will be performed in Phase 2.

Phase 2:

The transition to Phase 2 consists in swapping outlet's valves: Outlet 1, previously opened, is closed, and Outlet 2, previously closed, is opened. Therefore, a transition to a capillary-driven injection is initiated, where capillary pressure will be controlled by the porous plate. This will impose the same Pc along the core, eliminating the capillary foot. No modification is made regarding the injection pump once it is set in pressure regulation mode at the target inlet pressure. A schematic showing both outlets and the way they are distributed is shown in Fig. 6.

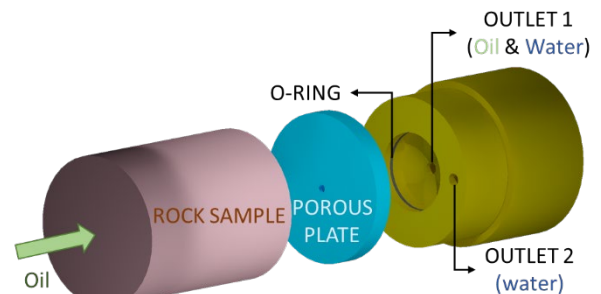


Fig. 6. Schematic representation of the method, showing both fluid outlets.

The main benefits of this technique are experimental time reduction and a homogenous saturation profile generation. The time reduction is due to fast water production from Viscous Oil Flooding while the latter results from a very quick transition to Porous Plate drainage without removal from the cell. In addition, the sample is immediately ready for further testing as it always remains in the experimental cell with confining stress.

2.2 Experimental Setup

The experimental setup used for performing HDT's proof of concept is shown in Fig. 7. The arrows indicate flow direction and fluid type in each line: red represents oil flow and blue represents brine flow.

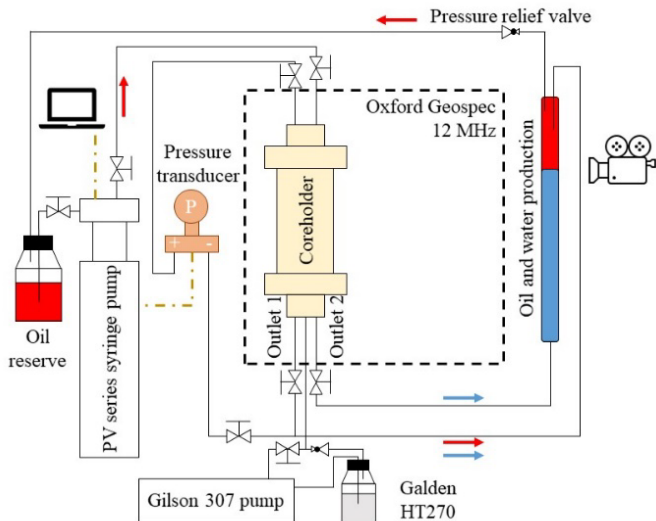


Fig. 7. Schematic of the experimental apparatus used for performing the HDT with *in situ* monitoring by NMR.

Oil injection was performed by a PV-Series low pressure syringe pump by FloxLab, which allows either constant flowrate or constant pressure fluid injection. The confinement pressure was maintained by a Gilson 307 pump directly connected to the overburden cell and to a pressure relief valve.

The NMR setup consists of a GeoSpec 12 MHz low-field DRX spectrometer by Oxford Instruments, equipped with magnetic field gradients on the vertical axis. This equipment allowed monitoring of saturation profiles and produced volumes during flooding by 1D saturation profiles and 1D T_2 relaxation times distribution NMR pulse sequences, respectively.

For double verification of produced volumes, a high-resolution camera is used for monitoring a graduated burette (± 0.03 cc) that receives volume production from the sample. A pressure reduction valve is placed downstream of the burette to keep the system under pressure during the experiment.

The overburden cell used for the experiments is metallic-free, being entirely made in PEEK[®], as well as all flow lines. This is important as this material produces no NMR signal. The porous plate used for the experiments is made of porous alumina, with a typical pore radius of 90 nm.

2.3 Metrics used for comparing results

In order to perform a fair comparison between methods, metrics have been established for when water production during primary drainage would indicate the end of this step. For this matter, a sample is considered to have reached S_{wi} when the rate of production is lower than 0.1 % per day.

Regarding the homogeneity of the saturation profile, a standard deviation of water saturation values in profiles was calculated after the end of each phase of primary drainage. In addition, a “max – min” parameter was established to indicate the maximum deviation in water saturation of a given profile.

3 Results

3.1 Solid and fluids properties

For the validation of this new method, cylindrical plugs ($D = 38$ mm per $L = 50$ mm) from two facies were chosen: Bentheimer sandstone (BEN) and Richemont limestone (RCH). The Richemont samples were extracted from the Thénac Block, which presents lower permeability and porosity compared to the conventional LCT block more commonly used in other works. For petrophysical characterisation, a Conventional Core Analysis (CCA) routine was performed and the results are shown in Table 2.

Table 2 - CCA data for Bentheimer and Richemont samples

Sample	V_p (Φ)	K_w
BEN-HD-LS	13.45 cc (23.69 %)	1832 mD
BEN-PP-LS	15.35 cc (26.94 %)	1857 mD
BEN-HD-HS	15.48 cc (27.22 %)	1996 mD
BEN-PP-HS	14.73 cc (25.35 %)	2034 mD
RCH-HD-LS	9.36 cc (16.38 %)	0.76 mD
RCH-PP-LS	8.94 cc (15.60 %)	0.78 mD
RCH-HD-HS	9.36 cc (16.38 %)	0.76 mD
RCH-PP-HS	9.95 cc (17.55 %)	0.80 mD

In order to allow an unambiguous detection of hydrocarbon by NMR, deuterium oxide (D_2O) was used for the aqueous phase since this fluid is not detected by NMR acquisitions. In addition, Potassium Iodide (KI) was added to the aqueous solution (7 wt.%) to improve the X-ray Microtomography imaging of the sample. Marcol-52, a synthetic oil manufactured by ExxonMobil, was used as non-wetting phase during primary drainage. Base properties of the fluids used in the experiments are presented in Table 3.

Table 3 - Basic properties of fluids used in experiments

Fluid	Composition	Density	Viscosity
Brine	$D_2O + KI @ 70$ g/l	1.16 g/cc	1.19 cP
Mineral Oil	Marcol-52	0.83 g/cc	12.00 cP

Furthermore, Galden HT270 fluorinated oil from Solvay was used as confinement fluid, as it produces no NMR signal.

3.2 Hybrid Drainage tests

In order to perform an exhaustive proof of concept of the Hybrid Drainage Technique, two S_{wi} target values were defined for two rock samples with different scales of permeability – Low S_{wi} (LS) and High S_{wi} (HS) as in Table 2. Twin samples were submitted to the same levels of capillary pressure by the Hybrid Drainage Technique and by the conventional Porous Plate method – HD and PP in Table 2, respectively. In that way, a clear comparison of experiment duration between the HDT and PP primary drainage was achieved.

The Porous Plate experiments were performed in conventional Hassler Cells, and brine production was monitored by a burette connected to a pressure transducer that measures the pressure imposed by the produced brine column, which is then converted into a volume.

HDT tests were conducted in the new overburden cell suitable for NMR measurements. 1D T_2 relaxation times distribution allowed production monitoring and 1D saturation profiles provided the visualization of the saturation profile dynamics of the HDT. Furthermore, the latter showed the presence of capillary end effects at the end of Phase 1 and their elimination during Phase 2.

Both Porous Plate and HDT experiments were conducted at a confining pressure of 30 bar at ambient controlled temperature of 20 °C.

Moreover, a Darcy-scale simulation of the relative permeability and capillary pressure for the Richemont limestone during Phase 1 of the HDT was performed using CYDAR[®]. CYDAR[®] is a numerical simulator for design and interpretation of petrophysical laboratory experiments. It is a product from the French Institute of Petroleum and New Energies (IFPEN) and is commercialized by Cydarex.

3.2 High S_{wi} (30 – 40%) Bentheimer sandstone

Taking into consideration Bentheimer’s capillary pressure curve, as shown in Fig. 8, targeted P_c for high S_{wi} in Bentheimer was set to $P_c = 80$ mbar.

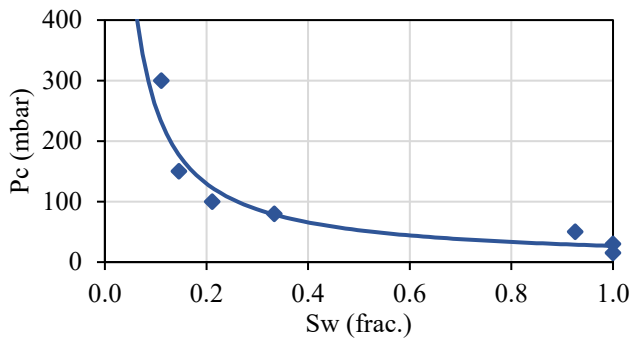


Fig. 8. Primary drainage P_c versus S_w curve for the Bentheimer sandstone.

In Fig. 9 it is possible to observe water saturation profiles advancing at Phase 1 of the method.

At the end of this step, it’s possible to notice the presence of the capillary end effect at the sample outlet originated from the pressure drop between inlet and outlet.

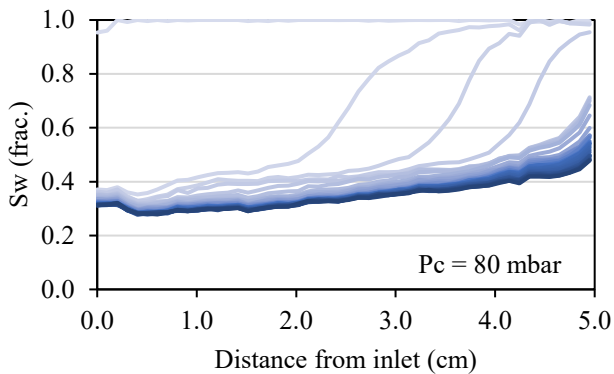


Fig. 9. Saturation profiles advancing during Phase 1 of BEN-HD-HS ($P_c = 80$ mbar).

At the end of this step, we observe for the water saturation profile:

- Std-dev (S_w): 4 %

- Max-min (S_w): 20 %

As no further motion was observed in saturation profiles, Phase 2 begins and water saturation profile dynamics are visible in Fig. 10. At this point, it is possible to notice more important changes in water saturation at the last fraction, as capillary pressure becomes homogeneous along the sample.

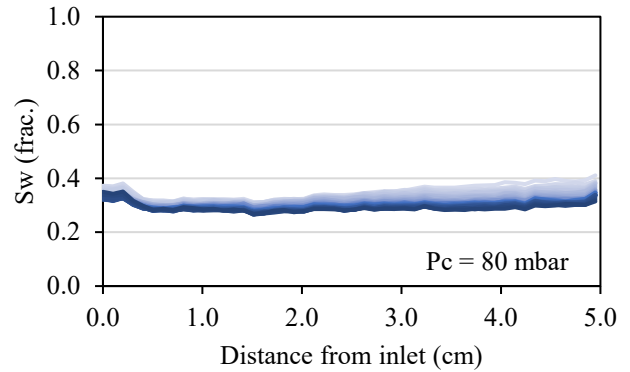


Fig. 10. Saturation profiles advancing during Phase 2 of BEN-HD-HS ($P_c = 80$ mbar).

At the end of the Hybrid Drainage Technique, we obtain:

- Std-dev (S_w): 1 %
- Max-min (S_w): 8 %

3.3 Low S_{wi} (20 – 25%) Bentheimer sandstone

In order to reach a lower value of S_{wi} in the Bentheimer sandstone, a P_c of 110 mbar was used. From Fig. 8, at this capillary pressure, S_{wi} is around 22%. In Fig. 11 it is possible to observe a behaviour comparable to the behaviour of BEN-HD-HS (notation given by Table 2), as an oil shock front invades the sample quickly desaturating it to a value close to S_{wi} .

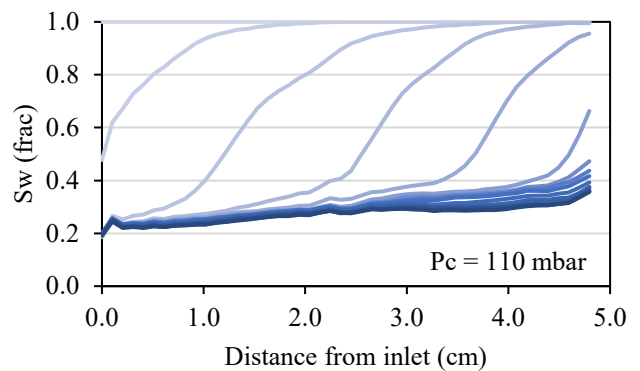


Fig. 11. Saturation profiles advancing during Phase 1 of BEN-HD-LS ($P_c = 110$ mbar).

At this point, we have:

- Std-dev (S_w): 3 %
- Max-min (S_w): 20 %

After transition to Phase 2, once again it is possible to observe a decrease in capillary end effects close to the outlet (Fig. 12).

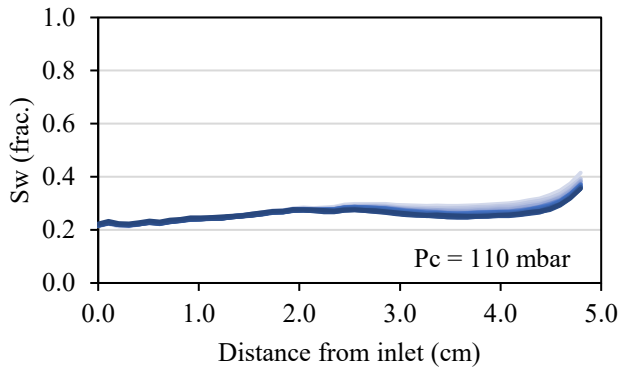


Fig. 12. Saturation profiles advancing during Phase 2 of BEN-HD-LS ($P_c = 110$ mbar).

At the end of the PD for BEN-HD-LS, we have:

- Std-dev (Sw): 2 %
- Max-min (Sw): 13 %

In Fig. 12 it is still possible to observe a small CEE in the last half cm of the sample. As fully saturated NMR imaging shows no abnormal saturation behaviour in this end, this effect does not represent a heterogeneity issue. Even though this test has respected the production cessation criteria, a longer Phase 2 would probably have homogenized the saturation profile, eliminating the CEE.

During Phase 1 of both experiments, it is possible to notice the shock front on the saturation profile as oil enters the sample at high velocity, quickly decreasing water saturation to a value close to S_{wi} . It is also possible to observe a piston-like behaviour of the oil phase.

The monophasic dispersion allows the characterization of the dispersive behaviour of the porous media. This measurement consists of a miscible replacement of fluids, usually brines with different salinities (C the concentration of the injected brine and C_0 the concentration of the resident brine). Density (or resistivity) is monitored downstream the sample during the experiment, which allows tracing the evolution of the relative concentration between the resident and the injected brine over time. Knowing the flowrate used for the experiment, it is possible to obtain the C/C_0 versus injected Pore Volume (PV).

The behaviour of the monophasic dispersion curve of the Bentheimer sandstone [20], as observed in Fig. 13, is in good agreement with the saturation profiles dynamic during Phase 1 of HDT.

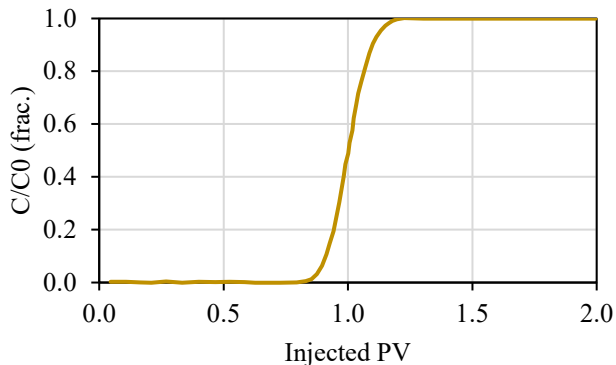


Fig. 13. Bentheimer's dispersion curve (extracted from Satken et al. 2021).

3.4 High S_{wi} (40 - 45%) Richemont limestone

The Richemont P_c versus S_w curve is shown in Fig. 14.

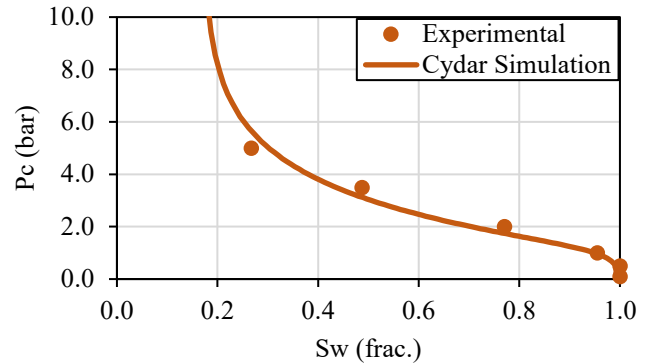


Fig. 14. Primary drainage P_c versus S_w curve for the Richemont limestone.

As the Richemont sample is a much less permeable rock, capillary pressure for high values (HS) of S_{wi} was set to 3.875 bar.

In this case, Phase 1 was performed at a constant flowrate ($Q = 3$ cc/h), in order to allow the numerical simulations needed to infer K_r and P_c by inverse analysis. For that matter, the pressure drop between inlet and outlet, water production and S_w profiles advancing were measured. S_w profiles advancing are shown in Fig. 15.

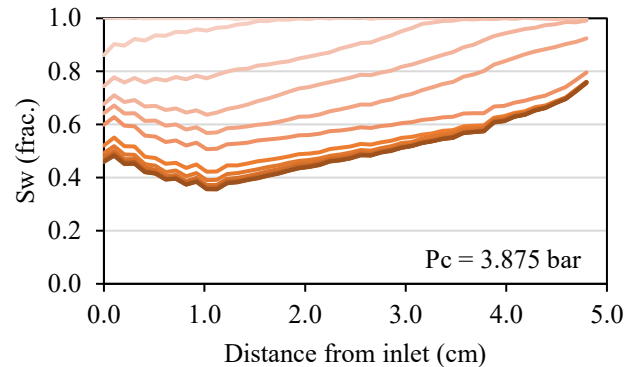


Fig. 15. Saturation profiles advancing during Phase 1 of RCH-HD-HS ($P_c = 3.875$ bar).

In the transition from Phase 1 to Phase 2, we had:

- Std-dev (Sw): 9 %
- Max-min (Sw): 40 %

After the transition to Phase 2, it was possible to observe the equilibration of the saturation profiles as capillary pressure was equalized along the sample (Fig. 16). However, an effect observed in the inlet of the sample was not corrected after the transition. This effect will be further discussed in the "Discussion" section.

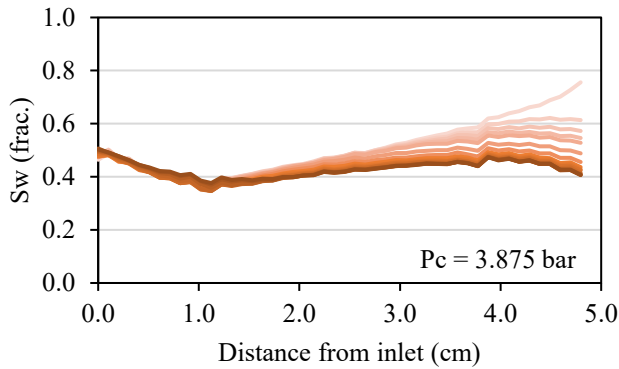


Fig. 16. Saturation profiles advancing during Phase 2 of RCH-HD-HS ($P_c = 3.875$ bar).

At the end of RCH-HD-HS primary drainage, we have:

- Std-dev (Sw): 2 %
- Max-min (Sw): 13 %

3.5 Low Swi (25 - 30%) Richemont limestone

Observing the P_c versus S_w curve for the Richemont sample, in order to achieve a S_{wi} of around 25 %, a P_c of 5 bar was applied. Therefore, Phase 1 has been performed at a constant inlet pressure of 5 bar with open bypass, and the saturation profiles advancing may be seen in Fig. 17.

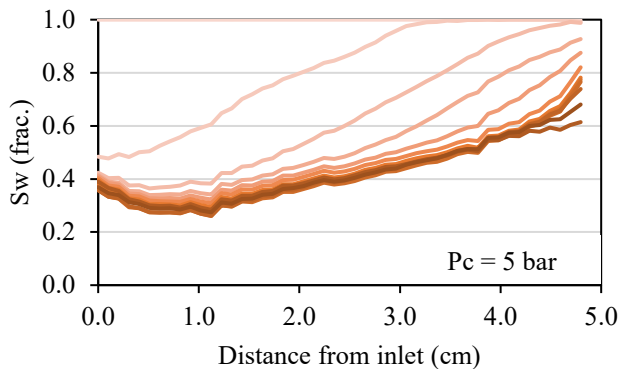


Fig. 17. Saturation profiles advancing during Phase 1 of RCH-HD-LS ($P_c = 5$ bar).

After Phase 1 of RCH-HD-LS primary drainage:

- Std-dev (Sw): 10 %
- Max-min (Sw): 41 %

After closing the bypass and performing the transition to Phase 2, a clear homogenization of the saturation profiles is observed in Fig. 18 by the elimination of the CEE. Nonetheless, the same effect in the saturation profile close to the inlet, as observed in the RCH-HD-HS, is present for this sample.

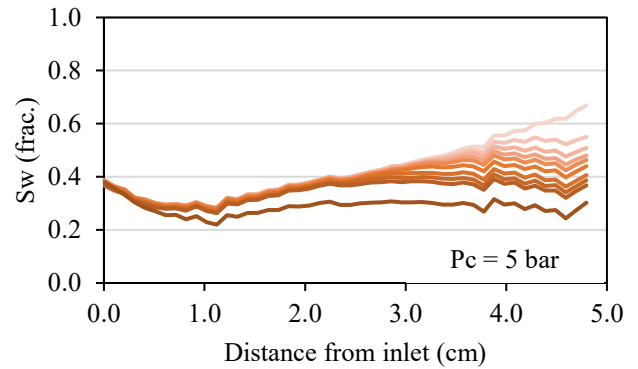


Fig. 18. Saturation profiles advancing during Phase 2 of RCH-HD-LS ($P_c = 5$ bar).

At the end of Phase 2, we have:

- Std-dev (Sw): 2 %
- Max-min (Sw): 16 %

In the Richemont case, the saturation profile dynamics behaves differently from Bentheimer's, as an earlier breakthrough and a much more dispersive behaviour takes place. This phenomenon was expected from the dispersion test presented in Fig. 19.

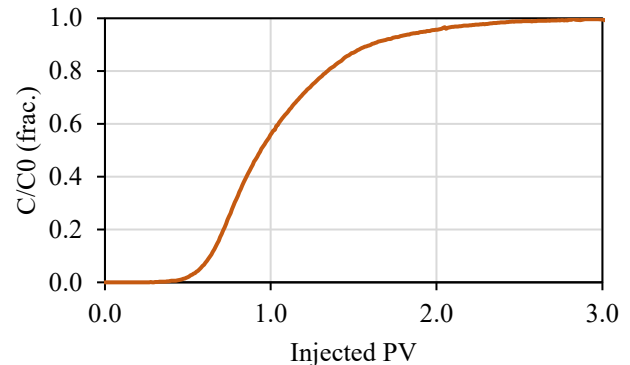


Fig. 19. Monophase dispersion for the Richemont sample.

3.6 Experimental time saving between HDT and Porous Plate

In this section, we present a comparison between the duration of the Hybrid Drainage Technique tests and the associated Porous Plate tests. The aim is to show the potential time reduction by using this technique over the classical Porous Plate.

As discussed before, equivalent Porous Plate tests were conducted by imposing the same inlet pressure in Bentheimer and Richemont sister plugs. Bentheimer's and Richemont's S_w versus time curves are shown in Fig. 20 and Fig. 21.

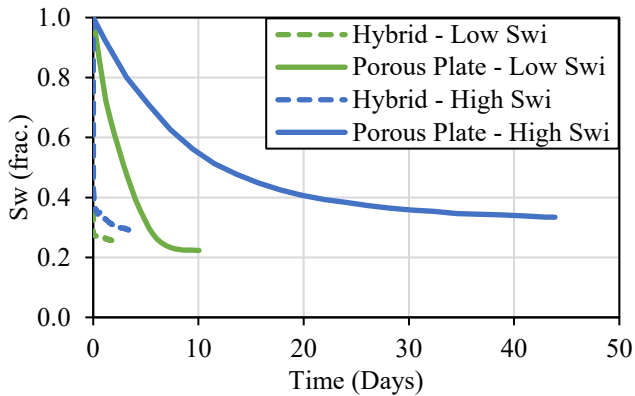


Fig. 20. Comparison between experimental duration for Porous Plate and Hybrid Drainage Technique on Bentheimer samples.

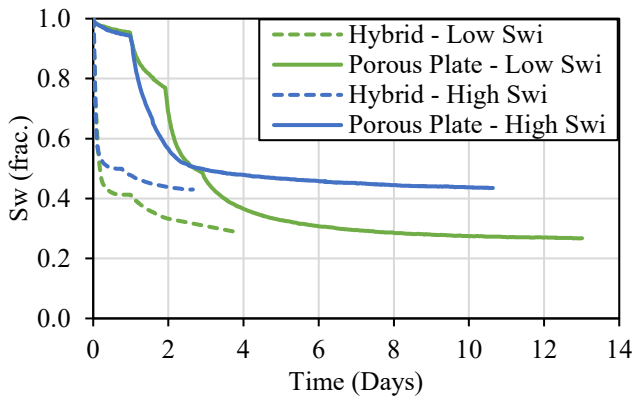


Fig. 21. Comparison between experimental duration for Porous Plate and Hybrid Drainage Technique on Richemont samples.

3.7 Simulation

A history match of the pressure drop (dP), water production (Vw) and Sw profiles was performed for the Richemont sample to define primary drainage Kr and Pc curves. The results are presented in Fig. 22, Fig. 23 and Fig. 24.

In addition, a Mean Absolute Percentage Error (MAPE) between the experimental data and the simulated results is presented for dP, water production and Sw profiles. This approach allows a validation of the match quality between experimental and simulated results. For calculating the MAPE, Eq. 2 was used:

$$MAPE (\%) = 100 * \frac{1}{N} * \sum_{i=1}^N \left| \frac{x_{exp} - x_{sim}}{x_{exp}} \right| \quad (2)$$

where N is the number of experimental and simulated points compared, x_{exp} are each experimental point and x_{sim} are each simulated point.

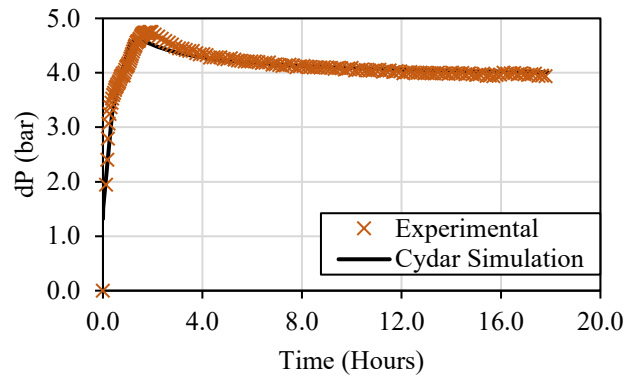


Fig. 22. History match of the pressure drop of the Richemont sample during Phase 1 of HDT.

- MAPE (dP): 1.9 %

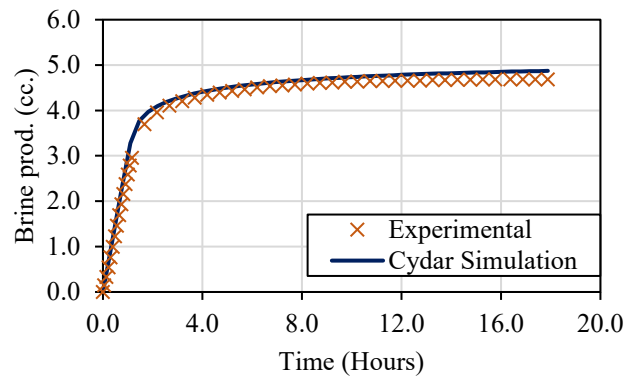


Fig. 23. History match of the produced brine volume of the Richemont sample during Phase 1 of HDT.

- MAPE (Vw production): 3.0 %

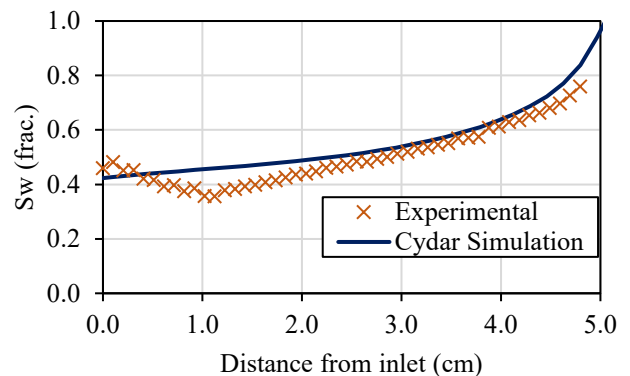


Fig. 24. History match of the water saturation profile imaged by NMR of the Richemont sample during Phase 1 of HDT.

- MAPE (Sw Profile): 8.5 %

Furthermore, Kr and Pc curves were obtained by optimization of the three parameters presented above and follow analytical functions of Corey and Logbeta, respectively.

Corey expressions [21] are useful for describing the relative permeability behaviour between residual end points

based on normalised phase saturation. In the case of primary drainage, the normalised oil relative permeability is defined by Eq. 3:

$$k_{ron} = S_{on}^{No} \quad (3)$$

The analogous equation for the water phase is given by Eq. 4:

$$k_{rwn} = S_{wn}^{Nw} \quad (4)$$

When experimental artifacts are prevented, N_o and N_w exponents carry important information regarding the rock's wettability, as they define the dynamic behaviour of fluids flow.

The Logbeta is an analytical function used for defining the shape of the capillary pressure versus water saturation curve based on the experimental data.

The K_r and P_c curves are shown in Fig. 14 and Fig. 25.

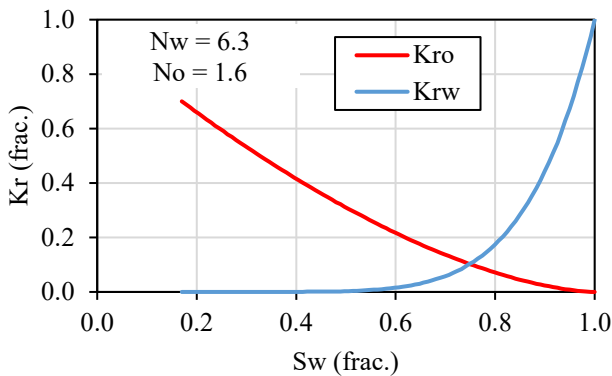


Fig. 25. Computed primary drainage K_r curve for the Richemont sample after optimization of production, dP and S_w profiles.

The experiences described in this paper represent a proof of concept and a validation of the Hybrid Drainage Technique. As this method was conceived to be used on larger samples, generally preferred for SCAL tests, two primary drainage simulations were performed on CYDAR[®]: one Porous Plate and one HDT. The aim of this test is to compare the experiment duration of both techniques and understand the potential time saving of performing HDT over the Porous Plate on a full-size core. Basic properties, P_c and K_r inputs used for these simulations are presented in Table 4:

Table 4 – Basic, K_r and P_c inputs for CYDAR[®] simulation

Basic properties	D	50 mm
	L	200 mm
	K_{abs}	2000 mD
	Φ	0.249
	V_p	97.782 cc
K_r	K_{rw} max	0.902
	K_{ro} max	0.800
	S_w min	0.117
	S_w max	1.000
	N_w	5.428
	N_o	4.792
P_c	S_w min	0.117
	S_w max	1.000
	P_0	7.782 mbar
	$P_{threshold}$	51.469 mbar

Both simulations were performed at inlet pressure equal to 110 mbar and equilibration time for both tests are presented in Fig. 26:

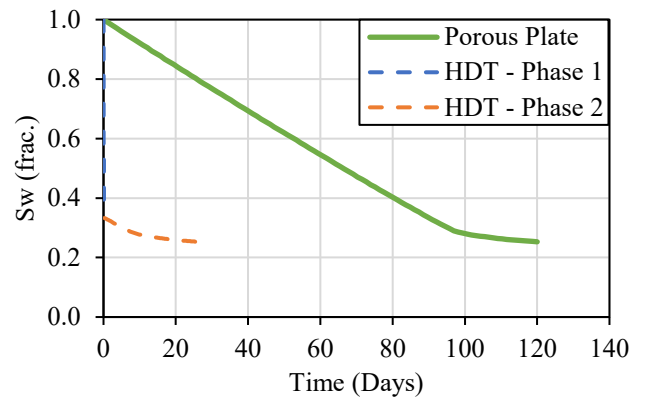


Fig. 26. Comparison between equilibration times for numerical simulations of a conventional Porous Plate and Hybrid Drainage primary drainage.

4 Discussion

Analysis of the HDT imaged by NMR, PP results and saturation profiles from both Centrifuge and Viscous Flooding highlight several important points:

1. The Hybrid Drainage method is effective in eliminating capillary end effects in reduced experimental time compared to a classic PP primary drainage. This has shown to be true in both high and low target S_{wi} on water-wet sandstone and limestone presenting substantially different permeability. This represents a new finding regarding the existing techniques. On the other hand, time reduction appears to be more effective when targeting values of S_{wi} farther from the irreducible water saturation asymptote.
2. In addition, when observing HDT curves for a lower permeability sample (the Richemont case, presented in Fig. 21), it is possible to expect further reduction of the experiment duration as the transition between Phase 1 and Phase 2 could have been performed earlier.
3. The CYDAR[®] simulation of Porous Plate and HDT on full-size cores agrees with experimental data on smaller plugs. They show that experiment duration reduction is also expected for large SCAL samples.
4. With respect to the saturation profiles obtained in HDT for the Richemont samples, an effect in saturation at the inlet face is observed, which results in a higher MAPE than expected for the saturation profile match. This effect is possibly due to the inlet diffuser format. The diffuser used for these experiments was a classical “bulls-eye”, which may concentrate current flow lines bypassing a portion of the inlet face of the sample. Further experiments on a modified-double-spiral diffuser will be performed in order to reduce this effect.
5. Regarding a comparison to the Viscous Flooding method (considered as Phase 1 of the Hybrid Drainage

Technique in this research), the impact on Standard Deviation and “Max-Min” data indicates the effectiveness of the transition to Phase 2 in reducing capillary end effects and producing a homogeneous saturation profile. In addition, as HDT does not remove capillary foot by reversing injection direction, no disconnected oil cluster formation and unwanted imbibition during the primary drainage phase is expected. In Viscous Flooding, this effect has shown to be an obstacle to proper wettability restoration and Kr determination.

6. Moreover, when observing the final saturation profile in Phase 1 for Low Swi – Bentheimer, BEN-HD-LS from Fig. 11, one could state that capillary end effects may have been eliminated by injecting at a higher flowrate. However, this solution is not optimal as this may damage the sample, which could alter its petrophysical properties, such as absolute permeability and porosity, and risk missing the targeted Swi. Using the HDT results in elimination or reduction of the capillary end effects by homogenising the Pc with a porous plate therefore removing any risk of damage to the sample.
7. This methodology has also shown a good agreement when comparing it with the expected fluid dynamics for the first oil flooding from dispersion tests. The Bentheimer samples had a piston-like behaviour and the Richemont samples have shown a much more dispersive shape.

5 Conclusions and perspectives

After analysis of all the experimental data generated by this proof of concept and its advantages and drawbacks, both goals regarding the new method have been attained: 1) the production of a homogeneous saturation profile in 2) a reduced experimental time.

More thorough examination of the results indicates a clear advantage when performing experiments which target higher Swi values; those which have not reached the asymptotic portion of the Pc curve. However, experimental time reduction has been also systematically observed in the lower Swi targets.

As this method has been developed to be applied on Kr experiments, that are generally performed on full-size cores, a test on samples of such dimensions composes one of the next steps of the method’s validation. In this case, we expect a greater time saving when comparing to a full-size core Porous Plate primary drainage.

In addition, in order to confirm that the Hybrid Drainage Technique does not induce the generation of disconnect oil clusters during primary drainage, as seen in classic Viscous Oil Flooding, a Hybrid Drainage test imaged by high resolution Micro-tomography will be further performed.

To conclude, a test on reservoir core samples (neutral to oil-wet) may complete the deployment of the method.

6 References

1. C. McPhee, J. Reed and I. Zubizarreta, *Core analysis: a best practice guide*, vol. 64, p. 106 (2015)
2. D. Tiab and E. Donaldson, *Petrophysics: theory and practice of measuring reservoir rock and fluid transport properties*, vol. 3, p. 47-50 (2012)
3. T.S. Ramakrishnan and A. Cappiello, CES, *A new technique to measure static and dynamic properties of a partially saturated porous medium*, vol. 46, p. 1157-1163 (1993)
4. E. J. Fordham, L. D. Hall, T. S. Ramakrishnan, M. R. Sharpe and C. Hall, AICHE journal, *Saturation gradients in drainage of porous media: NMR imaging measurements*, vol. 39, no 9, p. 1431-1443 (1993)
5. R. Lenormand, A. Eisenzimmer and C. Zarcone, *A novel method for determination of water/oil capillary pressure of mixed-wettability samples*, SCA1993-22 (1993)
6. D. Huang and M. Honarpour, JPSE, *Capillary end effects in coreflood calculations*, vol. 19, p. 103-117 (1998)
7. K. Romanenko and B. Balcom, JPSE, *An assessment of non-wetting phase relative permeability in water-wet sandstones based on quantitative MRI of capillary end effects*, vol. 110, p. 225-231 (2013)
8. M. Lombard, S. Gautier, P. Egermann, O. Vizika and E. Tachet, *Petrophysical parameter measurements: comparison of semi-dynamic and centrifuge methods for water-wet and oil-wet limestone samples*, SCA2006-09 (2006)
9. A. Graue, E. Aspenes, T. BOGNØ, R. W. Moe and J. Ramsdal, JPSE, *Alteration of wettability and wettability heterogeneity*, vol. 33, p. 3-17 (2002)
10. M. Mascle, S. Youssef, H. Youssef and O. Vizika, *In-situ investigation of ageing protocol effect on relative permeability measurements using high throughput experimentation methods*, SCA2018-016 (2018)
11. D. Green, J. Dick, J. Gardner, B. Balcom and B. Zhou, *Comparison study of capillary pressure curves obtained using traditional centrifuge and magnetic resonance imaging techniques*, SCA2007-30 (2007)
12. M. Fleury, *FRIM: a fast resistivity index measurement method*, SCA1998-29 (1998)
13. P. Faurissoux, A. Colombain, G. Pujol, O. Fraute and B. Nicot, *Ultra Fast Capillary Pressure and Resistivity Index measurements (UFPCRI) combining centrifugation, NMR imaging, and resistivity profiling*, SCA2017-02 (2017)
14. Q. Danielczick, P. Faurissoux and B. Nicot, *Wireless acquisition for Resistivity Index in Centrifuge – Wiri: a new method to estimate Archie’s Law parameters*, SCA2021-18 (2021)
15. F. Nono, C. Caubit and R. Rivenq, *Initial states of coreflooding techniques evaluation: a global pore-scale investigation*, SCA2022-T016 (to be published)
16. G. L. Hassler and E. Brunner, AIME 160, *Measurement of capillary pressures in small core samples*, (1945)

17. J. J. McCullough, F. W. Albaugh and P. H. Jones, DDP, *Determination of the interstitial-water content of oil and gas sand by laboratory tests of core samples*, (1944)
18. M. Fleury, *The Spinning Porous Plate (SSP) method: a new technique for setting irreducible water saturation on core samples*, SCA2009-08 (2009)
19. C. H. Pentland, R. M. El-Maghraby, S. Iglauer and M. J. Blunt, *The toroidal porous plate: a new method to facilitate waterflooding*, SCA2014-068 (2014)
20. B. Satken, H. Bertin and A. Omari, EAGE, *Adsorption/Retention of HPAM polymer in polymer flooding process: effect of molecular weight, concentration and wettability*, p. 1-14, IOR2021-111 (2021)
21. A. T. Corey, *et al.* JPT, *Three-phase relative permeability*, **vol. 8**, no 11, p. 63-65 (1956)

Water-Gas Imbibition Relative Permeability: Literature Review, Direct versus Indirect Methods and Experimental Recommendations

Fabrice Pairoys¹, Cyril Caubit¹

¹TOTALENERGIES CSTJF, Pau, France

Abstract. When an active aquifer encroaches into a gas bearing reservoir or when an oil rim sweeps gas during late depletion of the gas cap, gas displacement by liquid is important for estimating the gas recovery. In the water displacing gas condition, the viscosity ratio is extremely favorable, resulting in a sharp waterfront in the reservoir matrix: it results that changing the relative permeability K_r shape has negligible effect, while endpoints water relative permeability K_{rw} Max and residual gas saturation S_{gr} are much more important to understand gas flow performance for estimation of gas recovery with active aquifer or productivity decline after water breakthrough. Three main methods are used to determine water/gas relative permeability curves: imbibition unsteady-state, imbibition steady-state or indirect approaches such as co-current spontaneous imbibition if transient data are available. One of the other popular indirect methods is called Brooks-Corey approach: by measuring the drainage P_c curve using centrifuge or porous plate methods, it is possible to calculate a pore size distribution index λ . This coefficient is used in a Brooks-Corey model to determine the drainage K_r curve. It is also required to measure and determine the relationship between the residual gas saturation S_{gr} and the initial gas saturation S_{gi} relationship. Finally, it is accepted that there is no hysteresis on the water relative permeability K_{rw} curve, as water is always the wetting phase in the gas/water couple. As non-wetting phase, gas exhibits strong hysteresis between drainage and imbibition curves: it is therefore necessary to apply a correction on the drainage K_{rg} curve to build the imbibition one using correcting models. The aim of this paper is to compare gas/water relative permeability of elastic rocks using direct waterflooding information and indirect approach using Brooks-Corey model. It is shown that using the indirect approach leads to results like those experimentally obtained. Also, additional numerical simulations are proposed to discuss the relevance of measuring the entire water-gas imbibition relative permeability curve using the steady-state approach.

1 Introduction

Trapping mechanisms at pore scale of non-wetting fluids such as gas (versus liquids) have been mainly investigated through observations using glass micromodels or transparent glass bead systems. Micro-CT recently started 3D imaging of trapped gas in rocks to better understand this trapping phenomenon. Both techniques have shown that gas phase is trapped as discontinuous phase at the middle of the large pores while water occupies smaller pores as shown by [1].

Different types of displacement mechanisms in imbibition cycle have been put in evidence on glass micromodels by [2]: it is shown that, in liquid-wet domain, the imbibition is mainly dependent on pore size distribution and contact angle. Later, [3], [4] and [5] showed that:

- The ratio between pore throat and pore diameters (aspect ratio) matters, with more trapping at larger aspect ratio
- The number of pore throats connected to a given pore is also very important on trapping, with large coordination numbers tending to lead to less trapping
- An increase in contact angle suppresses snap-off, leading to less trapping

If these results have been observed on glass micromodels and pore network models, micro-CT should confirm the above-mentioned trends. Today, the resolution of micro-

CT systems limits these investigations to fair to very good quality rocks.

At the macroscopic scale, in most cases, the displacement of gas by liquid occurs at favorable to extremely favorable viscosity ratios. During laboratory experiments, there is no or negligible variation of gas saturation after the water breakthrough. In the field, flood is almost piston-like in the reservoir matrix, with no mobile gas behind the waterfront. It is finally concluded that attention is devoted to S_{gr} and maximum K_{rw} value at S_{gr} rather than the shape of the K_r curve. Nevertheless, imbibition relative permeability bounding curve, measured or derived, is still required for reservoir numerical simulations.

In this paper, we made a literature review on the methods to estimate the residual gas saturation, looking at the parameters that can affect S_{gr} , providing tips for the waterflooding tests. Also, the indirect Brooks-Corey approach, coupled with the Land's hysteresis model, was tested and compared to the experimental data results. It confirmed the findings and conclusions from [6].

2 Background

2.1 Experimental Methods to estimate S_{gr}

Several gas/water imbibition experimental methods can be used to determine S_{gr} :

* Corresponding author: fabrice.pairoys@totalenergies.com

- Porous plate method: after a primary drainage of water displaced by humidified nitrogen at highest capillary pressure, P_c is then gradually decreased in a stepwise manner allowing controlled imbibition of gas-saturated water. Residual gas is obtained by material balance when the capillary pressure $P_c=0$. This test is time-consuming, especially on low permeability rocks. On very low permeability samples, mercury imbibition can be attempted to obtain trapped non-wetting phase saturation, but it is not recommended.
- Unsteady-state method; it is a forced displacement of gas by water at constant low rate Q_w or low differential pressure dP . Residual gas saturation S_{gr} is obtained at the end of the flood when the gas production ceases (generally right after the water breakthrough). In situ saturation monitoring is recommended: it generally confirms the sharp front with no variation of the gas saturation behind the front
- Steady-state method: it is a co-injection of gas and water, but it is not the best appropriate approach to determine S_{gr} , except maybe on heterogeneous rocks and gas/condensate studies. It can be used to obtain the full Kr curve
- Spontaneous imbibition by water or capillary rise method: it is the most popular technique to determine S_{gr} . The spontaneous imbibition test requires a strongly wetting liquid to achieve a non-wetting residual saturation. Two configurations exist: co-current and counter-current displacements, respectively with the liquid touching the bottom of the rock (capillary rise test) and with the rock fully immersed in the liquid

Based on the past literature, there is no ideal technique and decision of choosing such or such method: it is case dependent. [7] and [8] reported very similar trapped gas saturations using steady-state, unsteady-state and spontaneous imbibition. More recently, some studies from [9] put in evidence some significant differences on S_{gr} computed from the different methods. Based on the above observations, it is recommended to make a combination of techniques during a study. Important to note that large uncertainty in results is anticipated for very tight gas reservoirs with porosity ϕ below 5% and permeability K below 0.01 mD. In this specific case we won't develop in this work, non-standard approach such as evaporation method may be tested.

2.2 Various Potential Effects on S_{gr} (Literature review and in house experience)

Regarding the types of liquid, [10] showed that same trapped gas saturation is found using different imbibing fluids, provided the liquids strongly wet the rock.

For the forced displacements, it is recommended to perform the liquid injection at low rate despite most of the past studies show no S_{gr} dependency on displacement rate ([7], [8], [11]: only [9] showed significant differences in S_{grw} values between porous plate method and unsteady-state coreflooding tests.

Fluid pressure or temperature do not affect residual gas saturation ([11], [12]), [13], [14]).

Regarding the effect of wettability, it is always assumed that gas is the non-wetting phase and liquid the wetting phase. However, it was early observed by [7] that some cores could imbibe oil but not water. It was confirmed by in house tests, showing that water is not always strongly wetting the rock in respect to gas. When water is not imbibing the rock, other fluids can be tested, such as toluene or refined oil: in house experience and literature have showed that these liquids are sometimes more wetting the rock than water ([15], [16]). When poor water wetness is observed, it can either result from true original reservoir wettability or from core contamination.

Effect of S_{gi} on S_{gr} :

Residual gas saturation S_{gr} strongly depends on initial gas saturation, both on sandstones ([7], [10], [14], [17]) and on carbonates ([18]). Several formulas can be used to capture this effect: the most used is the Land's formula ([17]):

$$\frac{1}{S_{gr}^*} - \frac{1}{S_{gi}^*} = C = \frac{1}{S_{gr}(S_{wi})} - \frac{1}{1-S_{wi}} \quad \text{Eq 1}$$

$$S_{gi}^* = \frac{S_{gi}}{1-S_{wi}} \text{ and } S_{gr}^* = \frac{S_{gr}}{1-S_{wi}} \quad \text{Eq 2}$$

Other ones like [18] or [19] are available.

[21] measured the residual gas saturation S_{gr} as function of initial gas saturation S_{gi} on 60 sandstone samples. Their porosity and permeability ranged from 0.06 to 0.25 and from 0.1 to 2000 mD. S_{grm} values ranged from 0.04 to 0.65. It was confirmed that the piecewise linear relationship from [19] is the best relationship to describe S_{gr} - S_{gi} curves. None of the hyperbolic laws can correctly describe the observed experimental behavior. The relationship from [20] gave the poorest estimates of S_{gr} as a function of S_{gi} .

The existence of S_{gr} plateau as S_{gi} decreases is linked to the absence of gas trapping inside micropores. Assuming pores are drained in order of size while S_{gi} increases, the lowest S_g value of the piecewise linear and horizontal relationship between residual and initial gas saturation may be defined as the limit between drained pores that trap gas and pores too small to trap gas. It indirectly confirms that there is no gas trapping in micropores.

Despite it was observed that model from [19] best captures experimental relationships between S_{gr} and S_{gi} , the industry and particularly numerical codes continue using Land's model.

Effect of rock properties, S_{gr} versus porosity with or without clays:

It has been observed large S_{gr} variations in a given field with decreasing S_{gr} trend as porosity increases ([14]) but several in house and external studies have shown more complex trends ([9]). [22] has collected data results from the literature showing wide dispersion of the maximum residual gas saturation S_{grm} /porosity cross plot:

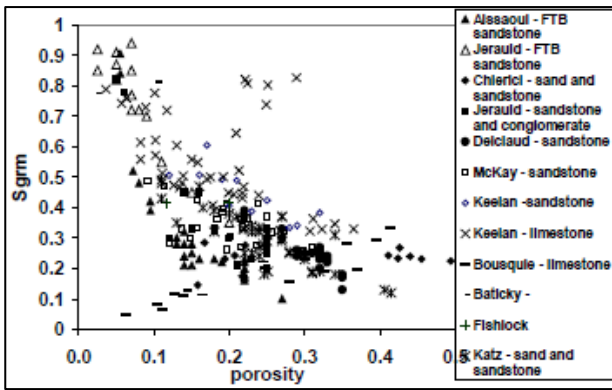


Fig. 1. Literature review 1 of maximum trapped gas saturation versus porosity, in absence of irreducible water saturation

Despite some studies concluded that S_{gr} increases as porosity decreases, Figure 1 shows the difficulty that encountered [13] to find, in vain, a general correlation between porosity (permeability and S_{gi} too) and S_{gr} . The largest investigation was performed by [22] and [23] with more than 300 S_{gr} measurements on sandstones:

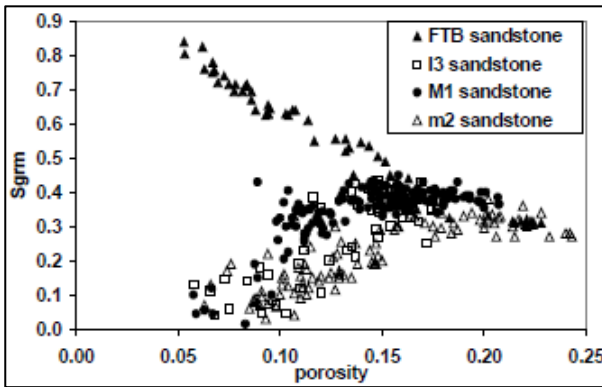


Fig. 2. Literature review 2 of maximum trapped gas saturation versus porosity in absence of irreducible water saturation

For porosity values below 15%, Figure 2 shows that S_{grm} decreases for I3, M1, M2 sandstones and increases for FTB (Fontainebleau outcrops) as porosity decreases. Above 15% of porosity, the data results from all reservoirs converge, with S_{grm} values varying from 25% to 35%.

The difference between the Fontainebleau sandstone and the other ones was explained by the presence of microporosity or clays, the Fontainebleau sandstone being mesoporous and clay-free.

Later, [24] provided the following plot of S_{grm} versus porosity, adding the clay %. It shows that greater microporosity in the clay mineral assemblage enhances water imbibition and limits gas trapping.

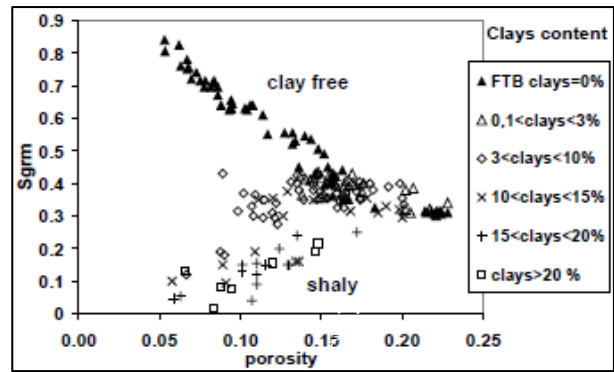


Fig. 3. Literature review 3 of maximum trapped gas saturation versus porosity with clay %, in absence of irreducible water saturation

The observations show that assessing the variability of S_{gr} within a reservoir and finding clues to explain it from a sedimentological point of view are key objectives.

Based on the literature review, it is obvious that laboratory work is required to guess a trapped gas saturation. Any estimation should be given ± 10 s.u. at minimum, with larger uncertainty when dealing with carbonate rocks and sandstone rocks with less than 15 p.u. porosity.

2.3 Waterflood tips:

In water displacing gas tests, most of the studies show no additional gas production post breakthrough, whatever the displacement rate as expected from a liquid-wet system. During laboratory waterflood, 1 to 2 PVs injected are enough. Moreover, as the viscosity ratio is extremely favorable, resulting in a very sharp waterfront in conventional matrix, the endpoints S_{gr} and K_{rw} at S_{gr} are more important than the K_r shape by itself.

Some cautions are required when performing waterflood, such as equilibrating the phases to avoid any mass transfer, avoiding compressing gas in the pore network during the test. Coreflooding tests can be performed with a low solubility gas such as nitrogen, at ambient temperature and ambient or reduced pore pressure.

2.4 Deriving water/gas imbibition K_r curves from S_{gr}/S_{gi} experiments:

In strongly water wetting conditions, it is stated that the shape of the imbibition relative permeability is not important while the S_{gr}/S_{gi} relationship and K_{rw} Max value are. Nevertheless, imbibition K_r curves are still needed as input in reservoir simulations.

They are few developed methods to obtain this K_r curve in water-wet conditions. The approach proposed by [17] is generally used when drainage gas/water K_r and S_{gr}/S_{gi} relationship are available. It assumes that:

- The water wetting phase does not exhibit any hysteresis, meaning that drainage and imbibition K_{rw} overlay
- The gas non-wetting phase exhibits a strong hysteresis between drainage and imbibition, but imbibition K_{rg} can be derived from drainage K_{rg}

- The gas non-wetting phase can be treated as two separate saturations, one trapped that does not contribute to the flow, another one mobile used to calculate $K_{rg}(S_g)$

2.5 Calculation $K_{rg}(S_g)$:

- 1- Imbibition starts from the maximum gas saturation post drainage
- 2- S_{gr} is derived from the experimental S_{gr}/S_{gi} relationship using Land's formula (Equation 1 and Equation 2)
- 3- Mobile non-wetting phase saturations S_{gF}^* are calculated for various gas saturations using the following equation:

$$S_{gF}^* = \frac{1}{2} \left(S_g^* - S_{gr}^* + \sqrt{(S_g^* - S_{gr}^*)^2 + \frac{4}{c} (S_g^* - S_{gr}^*)} \right) \text{Eq 3}$$

Where S_g^* is the effective total gas saturation, including trapped gas.

- 4- Imbibition relative permeability to gas is then calculated using:

$$K_{rg} = S_{gF}^{*2} \left(1 - (1 - S_{gF}^*)^{\varepsilon-2} \right) \text{Eq 4}$$

Where the exponent ε corresponds to the drainage exponent of the wetting phase Brooks-Corey exponent detailed later ($K_{rw} = S_w^{*\varepsilon} = S_w^{*\frac{(2+3\lambda)}{\lambda}}$).

The above method implies that drainage relative permeability curve has been measured, which is, unfortunately, not always the case. Nevertheless, if primary drainage capillary pressure has been measured, drainage relative permeability can be inferred from capillary pressure.

2.6 Deriving water/gas imbibition Kr curves from water/gas drainage capillary pressure:

Assuming that the rock is strongly wetted by the liquid in the gas/liquid system, the effect of different wettability on relative permeability curves is nil. Therefore, several methods of estimation can be used to estimate gas/liquid Kr, such as [25], [26], [27], [28]. In this study, the Brooks-Corey approach ([28]) is used to determine the drainage relative permeability from the drainage capillary pressure.

The tested procedure is made several steps:

- 1- Obtaining drainage capillary pressure either from MICP, centrifuge or porous plate tests. It first allows to determine the various rock types and saturation function per rock type. Capillary pressure averaging is necessary to provide one single Pc curve, using Leverett J-function for instance ([29])
- 2- For each rock type, plot of Pc versus saturation on a log-log scale and fit the curve using a Brooks-Corey equation:

$$P_c = P_{ce} (S_w^*)^{-\frac{1}{\lambda}} \text{Eq 5}$$

Where P_{ce} is the entry capillary pressure, S_w^* the reduced water saturation and λ the pore size distribution index

- 3- Build the drainage Brooks-Corey relative permeability curves using the above λ fitting parameter and the below equations:

$$K_{rw} = S_w^{*\frac{(2+3\lambda)}{\lambda}} \text{Eq 6}$$

$$K_{rg} = (1 - S_w^*)^2 \left[1 - (S_w^*)^{\frac{(2+\lambda)}{\lambda}} \right] \text{Eq 7}$$

- 4- The resulting Brooks-Corey K_{rg} curve must be fitted with a simple Corey function to determine the water Corey exponent n_w for K_{rw} , the water Corey exponent n_w is directly calculated $n_w = \frac{2+3\lambda}{\lambda}$: the curve is now following a Corey model
- 5- The indirect calculated drainage Corey coefficients can be compared to the cloud of Corey coefficients from drainage Kr experimental results stored in our database
- 6- In parallel, plot the S_{gr}/S_{gi} relationship: in our example, the Land's method was tested, obtaining a Land's coefficient for each rock type
- 7- Using the drainage K_{rg} , the K_{rg} correction is performed to calculate K_{rg} imbibition using Equation 4 ($K_{rg} = f[S_{gF}^*]$), imbibition K_{rw} being similar to the drainage one, ranging from S_{gi} to S_{gr}

3 Experimental Program

We present in this paper an example taken from a real gas field, with an active aquifer encroaching into the reservoir. The reservoir rock is a sandstone with low to medium clay content. Only data results from the best rock type RT1, containing no clay, are presented as example.

To validate the indirect Brooks-Corey method for inferring the imbibition relative permeability curve for a specific rock type, the experimental program consisted in:

- Measuring nitrogen/brine primary drainage porous plate capillary pressure with measurement of the maximum gas permeability K_{gMax} at S_{wi}
- Low imbibition waterflooding rate tests to establish S_{gr}/S_{gi} relationship with measurement of the maximum brine permeability K_{wMax} at S_{gr}
- Final Dean-Stark quality check

The experimental program was performed at 3145 psi of net confining pressure and ambient temperature. To avoid gas compression, the design of the waterflooding test was done such a way the differential pressure was less than 2% of the 10 bars fluid pressure. Nitrogen and brine of 130 kppm NaCl equivalent salinity were equilibrated at the test pressure to avoid any mass transfer.

4 Experimental Results

Table 1 represents all data results collected during the program.

Table 1. RT1 core analysis properties

Id	ϕ (%)	Kkl (mD)	Swi (%)	Kg (Swi) (mD)	Sgr (%)	Kw (Sgr) (mD)	Krw (Sgr)
1	23.0	238	14.6	202	20.6	22,8	0,113
2	22.4	263	18.9	204	19.3	29,9	0,146
3	23.4	413	15.0	323	19.8	34,9	0,108
4	22.9	491	13.3	388	21.6	43,3	0,112
5	23.7	143	16.7	128	19.9	23,5	0,184
6	23.0	602	12.1	474	19.4	110	0,233
7	23.7	466	17.7	418	20.8	113	0,272

Important to note that the rock has no complex pore structure and negligible clay content.

For the rock type RT1, an averaged capillary pressure curve was obtained using the J-Leverett approach. Figure 4 represents the J-function versus water saturation Sw on a log-log plot with two “framing/bounding” functions, pessimistic and optimistic respectively:

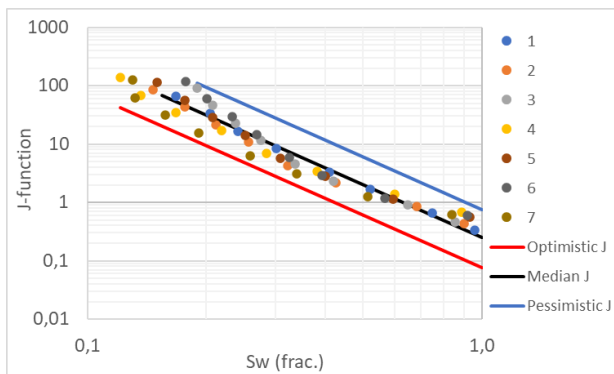


Fig. 4. Median J-function versus Sw with envelope

A power law type function $J=aSw^{-b}$ is used to fit the J-data points and to frame the data point cloud. In addition to the mean function plot, a pessimistic and optimistic cases were positioned to frame the J-data points. This approach results in finding associated Pc envelope in addition to the averaged Pc curve (Figure 5).

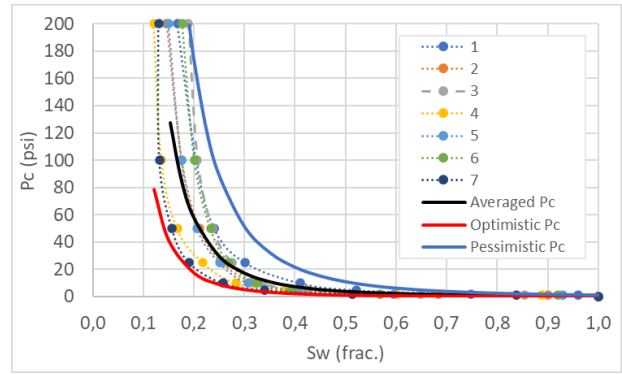


Fig. 5. Average capillary pressure Pc curve (in black) with its envelope (optimistic Pc in red, pessimistic Pc in blue)

Note that the transformation from the mean J-function to the averaged capillary pressure Pc was obtained using arithmetic average of the porosity and permeability. The Pc envelope helps the reservoir engineer to understand the uncertainty on the measured Pc and adjust its saturation’s law for static reservoir modeling with observed logging information if needed.

Then, by plotting the log-log plot Pc versus effective water saturation Sw* and by using a power regression $Y=aX^b$, the respective values of entry pressure Pce ($Pce=a$) and pore size distribution index λ ($\lambda=-1/b$) from Equation 5 can be determined. Note that low Sw values may be discarded to obtain an acceptable correlation coefficient R².

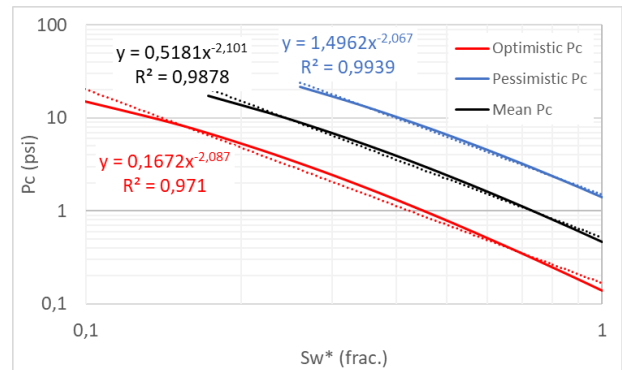


Fig. 6. Log-log plot of averaged capillary pressure Pc

The Brooks-Corey parameters can be computed from the regressions, for the averaged Pc and its envelope.

Table 2. Brooks-Corey parameters for Pc

	Optimistic Pc	Pessimistic Pc	Averaged Pc
Pce (psi)	0.17	1.50	0,52
λ	0.479	0.483	0,476
Swi (%)	12.1	18.9	15.4

The obtained low λ values result from the good grain sorting and size, high permeability/porosity of this sandstone reservoir rock type. λ values from Table 2 are then substituted in Equations 6 and 7 to build the Kr curves. It is shown that the three λ values obtained from low case, high case and mean case are very close together. The resulting Kr curves have same curvature. The only difference is the value of S_{wi} , according to the case.

The Sgr versus Sgi plot is then built to determine the C Land parameter that will be later used in the model.

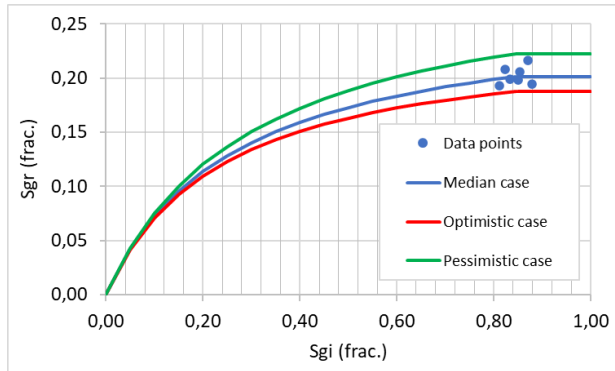


Fig. 7. Log-log plot of averaged capillary pressure Pc

The uncertainty on Sgr values may be captured by bounding the data points cloud. For RT1, the Sgr value may vary from 18.8% to 22.3% (Figure 7). The equivalent and median C parameter was found to be equal to 3.2.

The following step shows only the median case. Using Equations 3 and 4, with the C and λ parameters determined earlier (respectively $C=3.2$ and $\lambda=0.476$), the imbibition Krg is then calculated. The Sgr value was taken as the average of the seven measured Sgr from Table 1. Also, the Krw Max values measured at the end of the respective waterflooding tests are plotted in Figure 8.

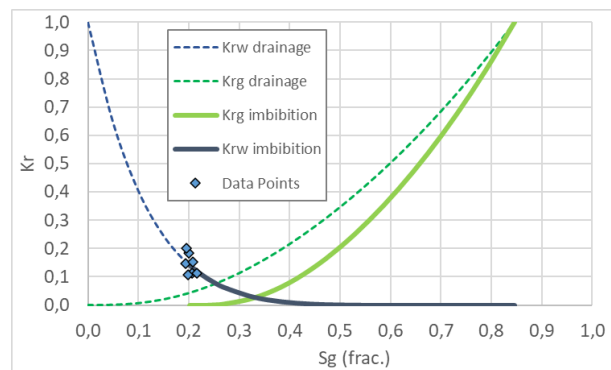


Fig. 8. Imbibition relative permeability curves from the median Pc curve and measured Krw Max at Sgr

As explained earlier, the shape of Kr curves and respective equivalent imbibition Corey exponents ($N_w=7.2$ and $N_g=2.1$) are not of high importance, only Krw Max and Sgi/Sgr relationship are. In Figure 8, it is observed that the indirect Brooks-Corey method falls in the cloud of Krw Max experimental data points. In our example, the indirect Brooks-Corey Krw Max value was

equal to 0.142 while the averaged Krw Max values measured on the seven samples was 0.145.

For the indirect Sgr value, all can understand that it must match because the value is calculated from the average of the individual and experimental Sgr values.

Note that, in our example, the nitrogen Corey exponents for drainage and imbibition modes were found to be equal, though there is a hysteresis on the Krg.

At the end of the imbibition cycle, the water saturations measured by material balance on the seven samples during the waterflooding tests are compared with the saturation measured by Dean-Stark.

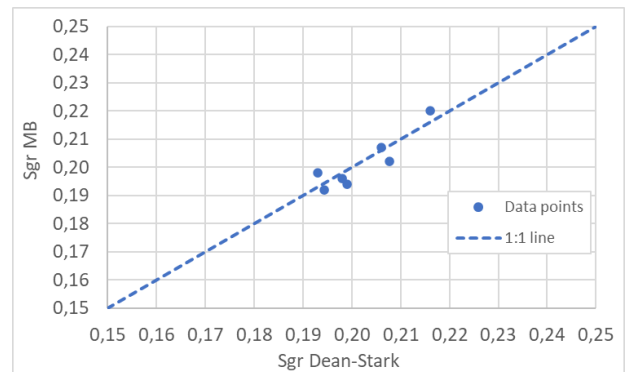


Fig. 9. Comparison between Dean-Stark Sgr and Sgr determined by material balance (Sgr MB)

Both methods lead to close Sgr values ($\pm 1\%$ S.U. max.), validating the measured production by material balance during the waterfloods.

5 Discussion

In gas-liquid imbibition cycle, it is often attempted to measure the relative permeability curve using steady-state approach. It consists in co-injecting water and gas at a total constant flowrate but varying ratios, increasing the water fractional flow.

In the case of water-gas test, where the viscosity ratio is extremely favorable and where the water is strongly wetting, we can question the relevance of performing this kind of experiment. As a matter of fact, the imbibition water-gas relative permeability curves are defined on a small range of saturation. This is because it requires extremely low water ratio to obtain data points at low water saturation. Due the experimental limitations, it may be impossible for the laboratories to design and perform such test. This statement can be proven by using numerical simulations.

CYDAR 1D numerical simulations were performed to design a steady-state relative permeability test. In our example, we used the same parameters than those presented earlier on RT1 (rock geometry and properties, fluid properties, Brooks-Corey Kr parameters, initial and final conditions).

Table 3. Simulation parameters

Rock		
L	6,60	cm
D	3,81	cm
ϕ	23,2	%
Kkl	388	mD
Fluids		
μ_w	1,38	cP
μ_g	0,017	cP
ρ_w	1,1	g/cc
ρ_o	0,001	g/cc
Kr parameters		
Nw	7,2	
Ng	2,1	
Sgi	84,6	%
Sgr	20,2	%
Krg Max	1	
Krw Max	0,142	

Note that:

- The rock properties come from the average of core plug dimensions, porosity and Klinkenberg permeability
- The fluid properties were measured for the brine, calculated for the nitrogen
- The Kr parameters come from the experimental program and Brooks-Corey Kr coefficients discussed above

A first design was tested, with no imbibition capillary pressure ($P_c=0$), a total constant flow rate of 100cc/h with 8 ratio and an additional bump rate at 450cc/h.

Table 4. Design for simulation

Time (day)	Qw (cc/h)	Qg (cc/h)
25	0,01	99,99
2	0,1	99,9
2	1	99
2	10	90
2	50	50
2	80	20
2	100	0
2	450	0

The minimum flow rate for a high precision pump is around 0,01 cc/h. This rate value corresponds to the first fractional water rate applied in the simulation. Even on the large permeability sample, the first ratio requires 25 days before obtaining equilibrium but:

- More than 50% of the produced gas is produced during this first ratio
- The dP stabilization is attained at 5 mbar, which may be readable with the resolution of the dP transducers but the confidence in the measurement is poor (high uncertainty)
- The transient saturation profiles simulated are vertical, showing no additional production after breakthrough

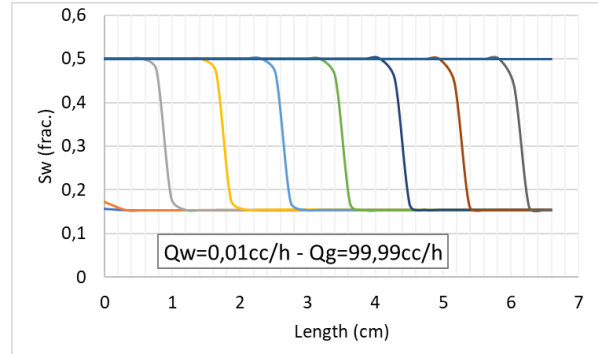


Fig. 10. Saturation profiles during the first ratio ($Q_t=100$ cc/h)

The simulated data results with the above experimental design are presented in Figure 11.

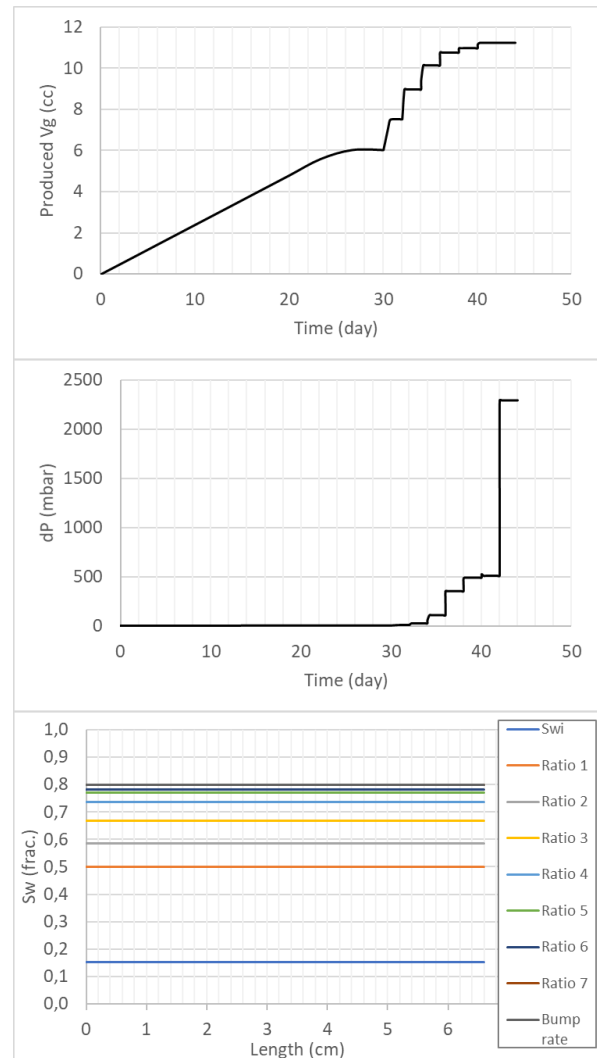


Fig. 11. Gas production, dP signal and saturation profiles at equilibrium

The simulated results presented in Figure 11 show that it is extremely difficult to measure the imbibition water-gas relative permeability. Even at the lowest water rate, the first ratio leads to more than 50% of the gas production. It is impossible to get Kr data points between Swi (=15.4%) and Sw=50%.

It is also extremely difficult to ensure good dP reading before the third ratio because of dP values at equilibrium below 30 mbars, resulting in high kr data points uncertainty too.

The Kr data points can only be defined in a reduced water saturation range $0.585 < S_w < 0.798$, equivalent to $0.415 < S_g < S_{gr} = 0.202$.

3 additional simulations were run to observe the impact of capillary pressure, considering 3 different cases:

- Case 1 is considered as an extreme case with a strongly water-wet rock, using the positive primary drainage curve. In this case, the corresponding Amott water index Iw is equal to 1
- Case 2 is a median case, less water-wet, using a log(beta) function to build a curve with a positive and negative parts. The choice was to impose a value of Sw(Pc=0) equal to 0.5. It results in Iw close to 0.5
- Case 3 is another extreme case with a significant and non-realistic negative Pc (chosen for the sensitivity study), considering the rock is not water-wet. The Sw(Pc=0) value is then equal to Swi, with no spontaneous imbibition of water. The resulting Iw is nil.

For relative permeability, same parameters than those from Table 3 were taken. Obviously, there is a problem of consistency between Kr parameters and Pc parameters for case 3 mainly (water-wet Kr vs non-water-wet Pc), but it helps in understanding the impact of Pc on the simulations thus on the steady-state experimental design.

The averaged primary drainage curve was taken to build the case 1, rescaled in the imbibition cycle saturation range. As explained previously, it is an extreme case.

A log(beta) function was used to build case 2 and case 3. It is a 3 input-parameter function [Po, β, Sw(Pc=0)] as shown in Equation 8:

$$Pc = c.Po.ln\left(\frac{(1-S_w^{*\beta})}{S_w^{*\beta}}\right) - b \quad \text{Eq 8}$$

With Po a pressure coefficient to control the magnitude of the Pc curve, Sw* the reduced/normalized water saturation, β coefficient to control the asymmetry of the function, b, a function dependent on the water saturation at Pc=0, and c parameter calculated as a function of β to impose a slope equal to Po at the middle of the Pc curve (Sw*=0.5).

The Kr simulation parameters detailed in Table 3 were taken, in addition to the Pc parameters for case 1 from

Table 2 (Brooks-Corey Pc) and Pc parameters for case 2 and 3 indicated in Table 5.

Table 5. Simulation parameters for Pc

CASE 1, Brooks-Corey Pc parameters		
Pce	0.52	psi
λ	0.476	
Iw	1,0	
CASE 2, log(beta) Pc parameters		
Po	11.6	psi
β	5	
Sw(Pc=0)	0,50	frac.
Iw	0,5	
CASE 2, log(beta) Pc parameters		
Po	11.6	psi
β	5	
Sw(Pc=0)	0,16	frac.
Iw	0,0	

The resulting Pc curves are shown in Figure 12 below:

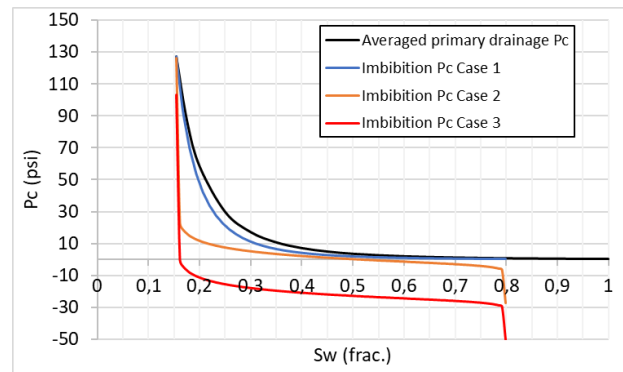


Fig. 12. Primary drainage (black) and imbibition capillary pressure curves for case 1 (blue), case 2 (orange) and case 3 (red)

The results from the three simulations are presented in Figure 13.

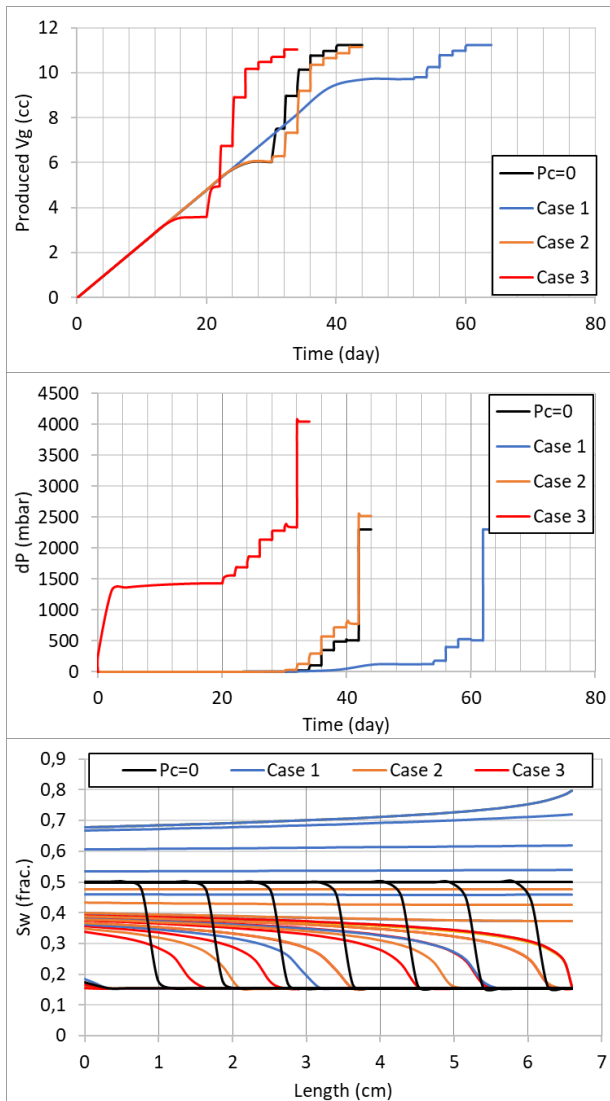


Fig. 13. Gas production, dP signal and saturation profiles during the first ratio ($Q_w=0.01\text{cc/h} - Q_g=99.99\text{cc/h}$)

The results from the simulations show that:

- The Pc effect is visible on the extreme cases in term of experimental durations, with shorter experiment with the least water-wetness condition and longer experiment with strongly water-wet condition
- More water-wet condition, longer and higher gas production at the first rate, but also lowest level of dP making the experiment almost not useable and uncertain, confirming that the steady-state Kr curve cannot be described over the full saturation range
- Case 2 and case with Pc=0 are very close regarding dP and produced Vg. Even with $I_w=0.5$, case 2 Pc curve remains flat, close to Pc=0 over a large range of saturation. Nevertheless, the saturation profiles are different (case 2 profiles tilted compared to “front like displacement” profiles at Pc=0)
- Case 3 results in short experimental duration, with readable high dP value and less produced Vg at the first ratio, allowing to potentially design an acceptable test. But the non-water wet Pc curve is not consistent

with the measured Kr curve on the specific presented experiment. But it shows that, if the rock is not strongly water-wet compared to gas (as observed in the literature on some CO₂-brine coreflooding studies), it may be possible to measure the relative permeability curve

As explained in the last bullet point, imbibition gas-water Kr could be measured. But additional limitations can be encountered. As steady-state approach requires dP and produced Vg stabilization to calculate the relative permeability point at equilibrium, a lot of PVs must be injected through the sample: it may lead to some gas diffusion in water. Moreover, at high measured dP, gas compressibility and expansion may affect the in-situ saturation at ambient conditions: it is then preferable to perform more complex experiments at high pore pressure, with live fluids and specific HPHT separators and so on. Again, it only makes sense if the rock is not strongly water-wet.

6 Conclusions and Recommendations

In addition to a bibliography review on gas-water relative permeability and trapping relationship, experimental results from a consolidated sandstone reservoir study were compared with an indirect method to determine imbibition relative permeability. It is concluded that, after properly defining rock types using the measured primary drainage capillary pressure, the Brooks-Corey approach coupled with Land’s hysteresis model is a good proxy for providing both drainage and imbibition gas-water relative permeability when water is strongly wetting the rock compared to gas. Due to the strong water wettability to the rock, it is extremely difficult or even impossible to experimentally determine imbibition relative permeability with unsteady-steady or steady-state coreflooding tests. The key parameters for the imbibition cycles are Krw Max and the Sgr-Sgi relationship: the shape of the Kr curve has negligible influence on the microscopic efficiency in imbibition cycle at strongly water-wet conditions, with very favorable viscosity ratio resulting in piston like displacement (no mobile gas behind the front).

It is not required to perform steady-state experimental test to attempt obtaining the imbibition gas-water Kr curve on water-wet rock. Numerical simulations confirmed this statement using the presented experimental case. Now, considering a non-water-wet system, as observed in some CO₂-brine studies at HPHT conditions, unsteady or steady-state coreflooding tests may be performed to capture the relative permeability curves.

All these observations confirm the findings in [6]: they will help in defining experimental protocols and interpretation of petrophysical parameters Kr and Pc in gas reservoirs with aquifer encroachment but also in saline aquifers that are identified as suitable storage formations for carbon dioxide (CO₂): in this last example, as the CO₂ plume rises upward in the formation due to the density contrast, the re-imbibition of water in the CO₂ flooded area will trap CO₂ as discontinuous non-wetting

phase: assessing the capacity of the aquifer to trap the CO₂ is obviously of high importance.

The authors would like to thank TOTAL ENERGIES for permission to publish this work and Gerald Hamon for his knowledge sharing throughout his career.

Nomenclature

C: Land's coefficient

CT: computed tomography

D: diameter, cm

dP: differential pressure, mBar

FTB: Fontainebleau outcrops

K: permeability, mD

K_g: gas permeability, mD

K_{kl}: Klinkenberg gas permeability, mD

K_w: water permeability, mD

K_{w Max}: maximum water permeability, mD

K_r: relative permeability

K_{rg}: gas relative permeability

K_{rg Max}: maximum gas relative permeability

K_{rw}: water relative permeability

K_{rw Max}: maximum water relative permeability

L: length, cm

MB: material balance

MICP: mercury injection capillary pressure

N_g: gas Corey exponent

N_w: water Corey exponent

P_c: capillary pressure

P_{ce}: entry capillary pressure

p.u.: porosity unit

Q_g: gas flow rate

Q_w: water flow rate

S_g: gas saturation

*S_g**: normalized/reduced gas saturation

*S_{gF}**: free and normalized/reduced water gas saturation

S_{gi}: initial gas saturation

*S_{gi}**: normalized/reduced initial gas saturation

S_{gr}: residual gas saturation

*S_{gr}**: normalized/reduced residual gas saturation

S_{grw}: residual gas saturation post waterflood

S_{grm}: maximum residual gas saturation with *S_{gi}=1*

S_w: water saturation

*S_w**: normalized/reduced water saturation

S_{wi}: irreducible water saturation

s.u.: saturation unit

V_g: produced gas volume

ε: function of *λ*, with $\varepsilon=(2+3\lambda)/\lambda$

φ: porosity

λ: pore size distribution index

ρ_g: gas density

μ_g: gas viscosity

ρ_w: water density

μ_w: water viscosity

References

1. Kumar, M. et al.: "Imaging of pore scale distribution of fluids and wettability", SCA 2008-16.
2. Lenormand, R. et al.: "Mechanisms of the Displacement of One Fluid by Another in a Network of Capillary Ducts", (1983), J. Fluid Mech., 135, 337-353.
3. Wardlaw, N.C.: "Fluid topology, pore size and aspect ratio during imbibition", Transport in Porous Media, 1988, V3,17-37.
4. Jerauld, G. et al.: "The effect of pore-structure on hysteresis in relative permeability and capillary pressure: Pore-level modeling", Transport in Porous Media, vol. 5, no. 2, pp. 103-151, 1990.
5. Blunt, M. et al.: "Pore-level modeling of wetting", Physical Review E, vol. 52, no. 6, pp. 6387- 6403, 1995.
6. Cense, A. et al.: "SCAL for gas reservoirs: a contribution for better experiments", SCA 2016-023.
7. Geffen, T. et al.: "Efficiency of gas displacement from porous media by liquid flooding", Transactions AIME, vol 195, 1952, p 29-38.
8. Legatski, M. et al.: "Displacement of gas from porous media by water", SPE 899, 1964.
9. Bull, O. et al.: "The quest for the true residual gas saturation- An experimental Approach", SCA 2011-03.
10. Pickell, J. et al.: "Application of air-Mercury and oil-air capillary pressure data in the study of pore structure and fluid distribution", SPEJ, March 1966, p 55-61, also SPE 1227.
11. MacKay, B.: "Laboratory studies of gas displacement from sandstone reservoir having strong water drive", APEA Journal 1974.
12. Handy, L.: "Determination of effective capillary pressure for porous media from imbibition data", Petroleum Transactions AIME, 1960, vol 219, p 75-80.
13. Chierici, G. et al.: "Experimental research of gas saturation behind the waterfront in gas reservoirs subjected to water drive", World Petroleum congress Frankfurt, 19-26 June 1963.
14. Delclaud, J.: "Laboratory measurements of the residual gas saturation", SCA 1991-23 EURO, 1991.
15. Keelan, D.: "A critical review of core analysis techniques", JCPT, April-June 1972, p 42-55.
16. Fahes, M. et al.: "Wettability alteration to intermediate gas-wetting in gas-condensate reservoirs at high temperatures", SPEJ, December 2007, p 397-407.
17. Land, C. S.: "Calculation of Imbibition Relative Permeability for Two- and Three-Phase Flow from Rock Properties", SPEJ, (June 1968), 149.
18. Keelan, D.K. et al.: "Trapped-gas saturation in carbonate formations", SPE 4535, (1975).

19. Aissaoui, A.: "Etude théorique et expérimentale de l'hystérésis des pressions capillaires et des perméabilités relatives en vue du stockage souterrain de gaz", PhD thesis, Ecole des Mines de Paris, 1983.
20. Jerauld, G.: "General three phase relative permeability model for Prudhoe Bay", *SPERE* 12(4) p 255-263, 1997
21. Suzanne, K. et al.: "Residual gas saturation of sample originally at residual water saturation in heterogeneous sandstone reservoirs", SCA 2003-14.
22. Suzanne, K. et al.: "Distribution of trapped gas saturation in heterogeneous sandstone reservoirs", SCA 2001-14.
23. Hamon, G. et al.: "Field-wide variations of trapped gas saturation in heterogeneous sandstone reservoirs", SPE 71524, 2001.
24. Suzanne, K. et al.: "Experimental relationships between residual gas saturation in heterogeneous sandstone reservoirs", SPE 84038, 2003.
25. Purcell, W. R.: "Capillary Pressures – Their Measurement Using Mercury and the Calculation of Permeability" *Trans. AIME*, (1949), 186, 39.
26. Burdine, N. T.: "Relative Permeability Calculations from Pore Size Distribution Data" *Trans. AIME*, (1953), 198, 71.
27. Corey, A. T.: "The Interrelation between Gas and Oil Relative Permeabilities", *Prod. Mon.* (1954), 19, 38.
28. Brooks, R. H. and Corey, A. T.: "Properties of Porous Media Affecting Fluid Flow", *J. Irrig. Drain. Div.*, (1966), 6, 61.
29. Leverett, M.C.: "Capillary behavior in porous solids". *Transactions of the AIME* (142): 159–172, 1941.

Geomechanical Deformation of Saturated Porous Media under Various Wettability Conditions: A Pore-scale Investigation

Ahmed Zankoor^{1, *}, Rui Wang¹, Maziar Arshadi¹, and Mohammad Piri¹

¹ Center of Innovation for Flow through Porous Media, Department of Petroleum Engineering, University of Wyoming, Laramie, WY, USA.

Abstract. Geomechanical deformation may occur during various engineering processes that involve fluid flow in the subsurface, such as hydrocarbon recovery, groundwater withdrawal, and CO₂ sequestration. However, its impact on multiphase flow in porous media is still poorly understood due to the limited research on this topic at the pore scale level. In this study, we investigate the effects of pore space deformation on pore-scale fluid occupancies and in-situ capillary pressures of two companion miniature sand packs under different wettability conditions. To this end, the samples were first subjected to drainage (oil-displacing-water) processes, one using Soltrol and other with dead crude oil, to establish different wettability states in the samples. The mediums were then contracted by increasing the hydrostatic (radial and axial) stresses. The fluid occupancies and the fluid-fluid interfacial curvatures under different stress conditions were acquired using high-resolution x-ray computed tomography and advanced image analysis techniques. The results of our investigations showed that as the pore space contracted due to the hydrostatic stress, a decrease in the oil saturation was observed in both samples but to a lesser extent and less uniformity in the oil-wet case. Similarly, the in-situ capillary pressure measurements showed a more uniform and significant reduction after the compression in the water-wet sample. Nonetheless, local increases in the in-situ capillary pressure were observed in the oil-wet sample. Capillary pressure reductions or increases were attributed to interfaces being displaced or hinged in place in response to the compression process.

1. Introduction

Fluid extraction or injection from/into subsurface reservoirs causes variations in the effective stresses which in turn may cause geomechanical deformation. The deformation of porous media has critical impacts on the multiphase flow phenomena at micro- and macro-scale levels and, under certain circumstances, may result in field-scale implications such as land subsidence and induced fractures and fissures [1, 2].

Over the decades, one of the most common methods used to investigate the impacts of the pore space deformation on multiphase flow and fluid distribution in porous media was measuring the saturation-relative permeability data under various stress conditions. However, inconsistent or even contradictory results have been reported in the literature. By increasing the hydrostatic confining pressure and maintaining the pore pressure constant, multiple researchers reported that the relative permeability of the non-wetting phase decreased significantly, whereas that of the wetting phase was nearly remained unchanged [3, 4, 5]. By contrast, a different trend was also reported in the literature [6, 7, 8]. In these studies, the relative permeabilities of the wetting and non-wetting phases were found to decrease and increase, respectively, as the confining pressure was increased. In addition to these two dominant viewpoints, some other conclusions have been reached, such as that neither the wetting nor the non-wetting phase relative permeabilities were sensitive to the changes in the stress [9, 10].

The lack of consensus on the impacts of geomechanical deformation on fluid flow is partly due to the limited understanding of the pore-scale mechanisms accompanying this phenomenon, because the previous – predominantly Darcy scale – experiments do not provide insight into underlying pore-scale physics that govern the macroscopic behavior of such systems.

The recent advances in x-ray microtomography imaging have provided a new window of opportunity to directly observe the multi-phase flow phenomena in such systems and further advance the understanding of the flow behavior on the pore-scale level. However, the application of these technologies to investigate geomechanical deformation is still at its early development stages and pore-scale studies in such area are scarce at best. The impacts of the pore space deformation on the fluid occupancy were studied by Torrealba et al. (2016) [11]. They observed that primary drainage established different initial water saturation profiles along a glass bead pack under various stress conditions even though the average saturations were similar. Moreover, they reported that the residual oil saturation decreased when waterflooding was performed simultaneously with the sample's compression, whereas it was negligibly affected if the sample was compressed after the residual oil was trapped.

* Corresponding author: azankoor@uwoyo.edu

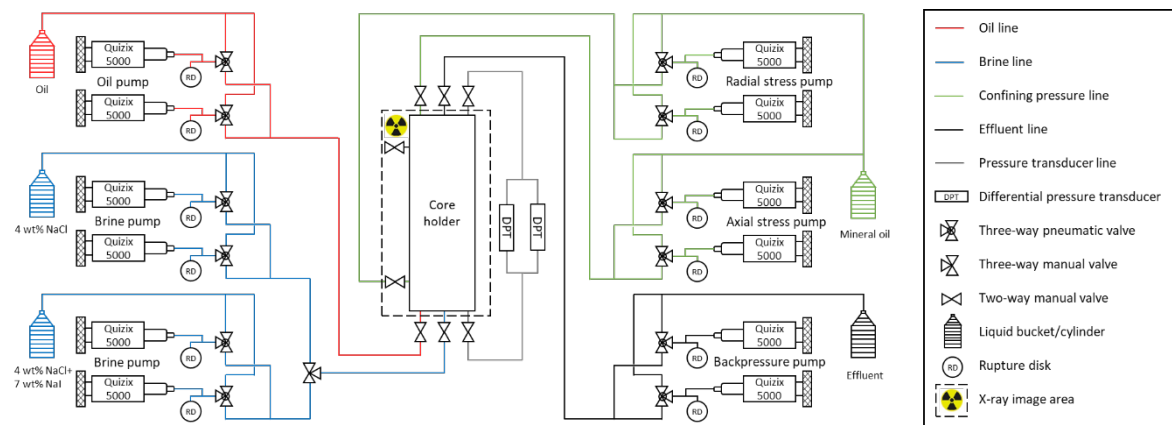


Fig.1. Schematic diagram of the experimental setup used in this study.

In the current research, we provide, to our best knowledge, the first pore-scale investigations of the impact of wettability on the response of the fluids in porous media to geomechanical deformation. We provide an improved understanding of such processes by extending our previous investigations [12, 13] to probe the interrelationship between pore-scale capillary pressure and fluid occupancy when pore space is compacted.

2. Experiments and data acquisition

The experimental data used in this study was generated by Wang et al. [12, 13] during a set of micro-scale core flooding experiments. In this section, we provide brief descriptions of the rock sample and fluids as well as the experimental apparatus and procedure used to obtain the data. More details can be found in the original work.

2.1. Sample and fluids

Two miniature sandpack samples, each with a diameter of 10 mm and a length of 75 mm, were used as the samples in the water- and oil-wet experiments to observe remarkable pore space deformation at lower stress conditions. Such deformation was necessary to observe significant impacts on the pore-scale fluid configuration and flow properties compared to less significant responses of other porous media (e.g., consolidated rocks). Moreover, the sandpack sample could represent unconsolidated reservoirs, which are expected to deform prominently as stress varies. The sandpack grains were the high-roundness and high-sphericity Northern White monocrystalline sands (100 weight % SiO₂) with the diameters varying from 106 to 300 microns (100 mesh). To ensure the two samples had similar properties, the two sandpacks were prepared using an identical preparation technique, which was developed based on the method proposed by the University of Alberta [14, 15, 16]. Instead of raining the sands into liquid, we densified the dry sands by vibrating for 2 hours to eliminate any bedding or sedimentary sequence caused by the different settling rates of large and small grains during the deposition process [17]. This is because the resistance of air is negligible compared to liquid, and grains with different sizes and shapes are more likely to deposit with the similar speed in air [18]. Afterward, the sands

were partially filled by distilled water through spontaneous imbibition and frozen in liquid nitrogen. This allowed for preventing the samples from collapsing and maintaining their properties unchanged when they were transported to the core holder.

The aqueous phase used in the water- and oil-wet experiments was a 4 wt% NaCl + 7 wt% NaI brine solution. The purpose of adding NaI was to increase the x-ray attenuation in the brine and obtain a better contrast between the brine and oil in the two-phase fluid occupancy images. The oil phases used in the water- and oil-wet experiments were Soltrol 170 mineral oil and dead crude oil recovered from the Permian Basin in Texas, respectively. The Soltrol 170 was passed through layers of silica gel and alumina multiple times before the main tests to remove all the polar components that might alter the wettability of the sandpack sample. All the solid particles that were larger than 5 micrometer were filtered from the crude oil in advance to avoid blocking the pore space during the flow tests. The properties of the sandpack and fluids used in this study are listed in Tables 1 and 2.

Table 1. Porosities and permeabilities of the two sandpack samples used in the water- and oil-wet experiments at the effective stress of 100 psi.

Sample	Porosity	Permeability (D)
A (water-wet)	0.302	6.59
B (oil-wet)	0.306	7.58

Table 2. Properties of the fluids used in this study at ambient temperature and pressure.

Fluid	Density (g/cc)	Viscosity (cp)	Oil/Brine IFT (mN/m)
Brine	1.07	1.06	
Sotrol 170	0.78	2.92	41.3
Crude oil	0.83	5.60	14.9

2.2. Experimental setup and procedure

The experimental setup used for the water- and oil-wet experiments is comprised of the following components: a high-resolution x-ray micro-CT scanner used to scan the sample and acquire the fluid occupancy during the experiment and a high-pressure and high-temperature core-flooding system, which consisted of an X-ray transparent miniature core holder made of carbon fiber, multiple Quizix pumps, two differential pressure transducers, and tubing. The schematic of the apparatus is shown in **Fig.1**.

Before starting the experiments, the sandpack sample was left in the core holder at an effective stress of 100 psi for three hours until it was completely thawed. It was then dried by blowing CO₂ at 30 psig for another three hours and vacuumed overnight. After the sample was 100% saturated by the doped brine (4 wt% NaCl + 7wt% NaI) both the pore pressure and the hydrostatic confining pressure were gradually increased to the target values by the backpressure regulation pump and the confining pumps (the radial and axial stress pumps). The initial permeability was measured by performing a series of brine flow tests at various flow rates and recording the pressure drops using the differential pressure transducers. To obtain the pore network before the compression, a high-resolution scan was performed after the doped brine was displaced by the one without the NaI. Then the pore space was filled by the doped brine again before the oil phase was introduced into the pore space. Note that the doped brine must be used to saturate the sample and fill the dead volumes after the system was vacuumed. It aimed to avoid diffusion caused by the concentration difference of iodine ions between the dead volumes and the sandpack sample. Otherwise, oil/water interfaces may become blurry during the experiment.

During the main experiments, oil was initially injected into the sandpack sample at 0.01 cc/min. The oil flow rate was then gradually increased until a target initial water saturation ($S_{wi}= 20$ to 30%) was confirmed by the fluid occupancy images acquired by micro-CT scans. At this stage, we stopped the oil injection and increased the hydrostatic confining pressures to the pre-determined value in 8 hours, which was expected to be longer than the normal relaxation time after a change in phase saturation in a unconsolidated porous medium [19], in the water-wet experiment. Stopping the oil injection aimed to eliminate the impacts of fluid flow on fluid occupancy. In other words, any fluid redistribution observed in the new fluid occupancy acquired after the compression could be ascribed to the pore space contraction.

In the oil-wet experiment, dynamic aging was performed before stopping the flow and increasing the confining pressure to alter the wettability of the sandpack sample. We heated the sample at 50 °C and simultaneously injected the dead crude oil at a low flow rate of 0.002 cc/min. This allowed for making up for the loss of the polar components that reacted with the solid surfaces. During the dynamic aging, we injected 0.1 to 0.5 pore volume of brine every 7 to 10 days (partial waterflooding) to mobilize the oil-water interfaces and measured the in-situ contact angles on the fluid occupancy images. After each measurement, the initial fluid occupancy was restored by oil injection. **Fig. 3** shows oil-water interfaces in both the water- and oil-wet cases during

the partial waterflooding processes. Overall, the average in-situ contact angle at the end of primary drainage was 41.7° in the water-wet case while in the oil-wet case it increased with time during the dynamic aging process and stabilized at 107° after 5 weeks. More details about the in-situ wettability measurements can be found elsewhere [12, 13].

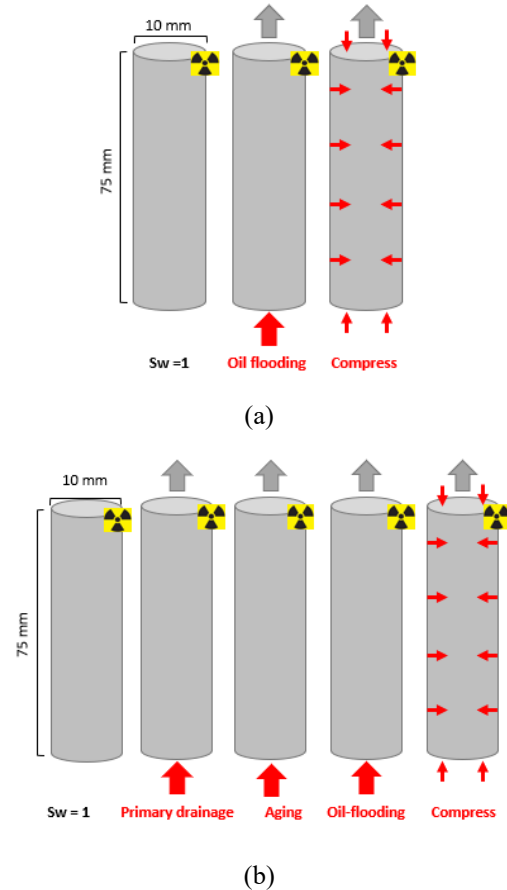


Fig. 2. Schematic diagrams of the experimental procedures followed in the (a) water-wet and (b) oil-wet experiments (replotted after Wang et al. (2022) [12, 13]).

3. Image analysis

The raw grayscale images acquired during the core-flooding experiments were processed using Avizo software [20]. They were first filtered using 3D non-local means and median filters to improve the signal-to-noise ratio, registered and superimposed by the corresponding pore map (before or after the compression), and subsequently segmented using the interactive thresholding method to generate the pore-scale fluid occupancy maps, i.e., images with unique labels assigned to the oil, aqueous, and solid phases. The fluid occupancy maps were then used to quantify the fluid volume/saturation along the flow direction. We also characterized the in-situ capillary pressure using the interfacial curvature analysis method described by Zankoor et al. [21]. In this method, the pore-scale oil-water interfaces were first extracted from the segmented images and then

smoothened to reduce the impact of voxelization on curvature analysis. Subsequently, the local curvature values were computed at each point of the interface, and the average of all curvature values was found to calculate the local capillary pressure using the Young-Laplace equation:

$$P_{c_{ow}} = P_o - P_w = \sigma_{ow}K_T \quad (1)$$

where $P_{c_{ow}}$ is the oil-water capillary pressure in Pa, P_o and P_w are the oil and water pressures, respectively, in Pa, σ_{ow} denotes the interfacial tension between the oil and water phases in N/m, and K_T is the average total curvature of the interface in m^{-1} (i.e., summation of the principal curvatures).

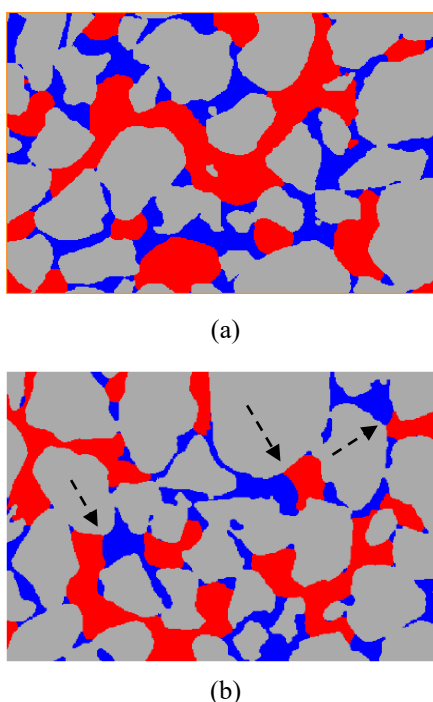


Fig. 3. Pore-scale fluid occupancy during partial waterflooding processes on the (a) **water-wet** and (b) **oil-wet** samples. Oil-water interfaces bulging in the oil-phase (black arrows in (b)) confirm the establishment of the oil-wet conditions.

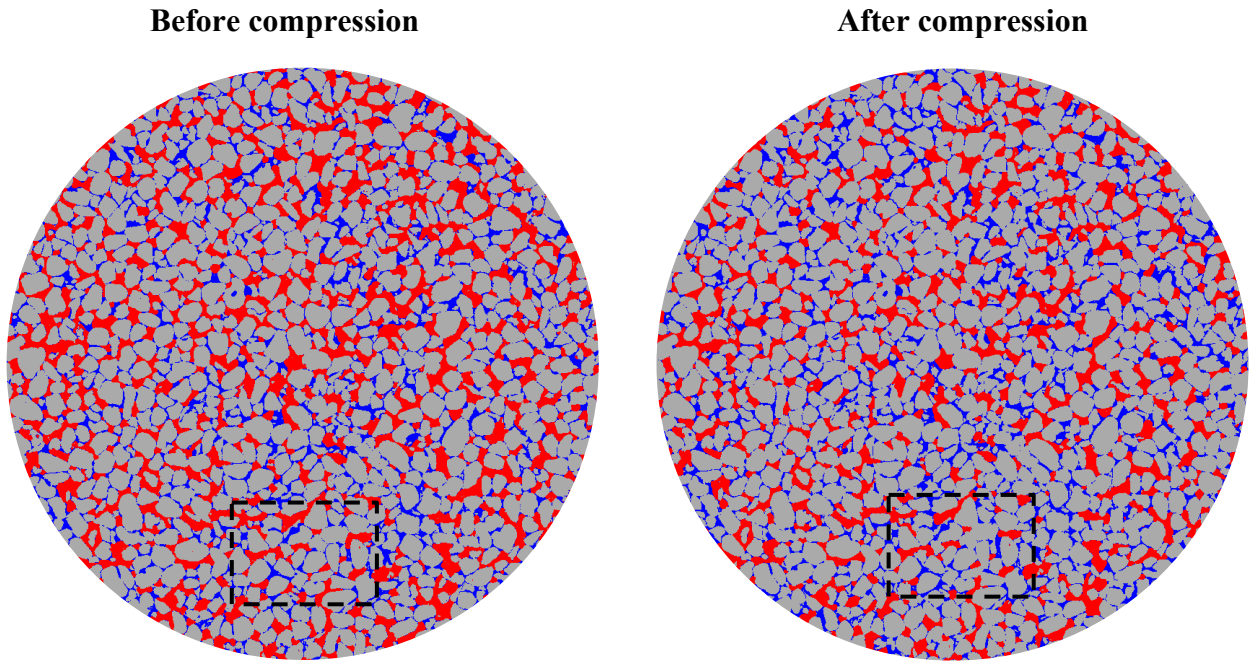
4. Results and discussion

As explained in the materials & method section, the two sandpack samples were subjected to oil flooding and then compression processes. The first sample was flooded with filtered Soltrol to maintain a water-wet medium. The second sample was desaturated with and dynamically aged using the dead crude oil to alter the wettability of the medium to non-water-wet states. The initial water saturations (S_{wi}) established after these processes were found to be 0.31 and 0.2, respectively. The lower S_{wi} in the oil-wet case was attributed to the lower interfacial tension and higher viscosity

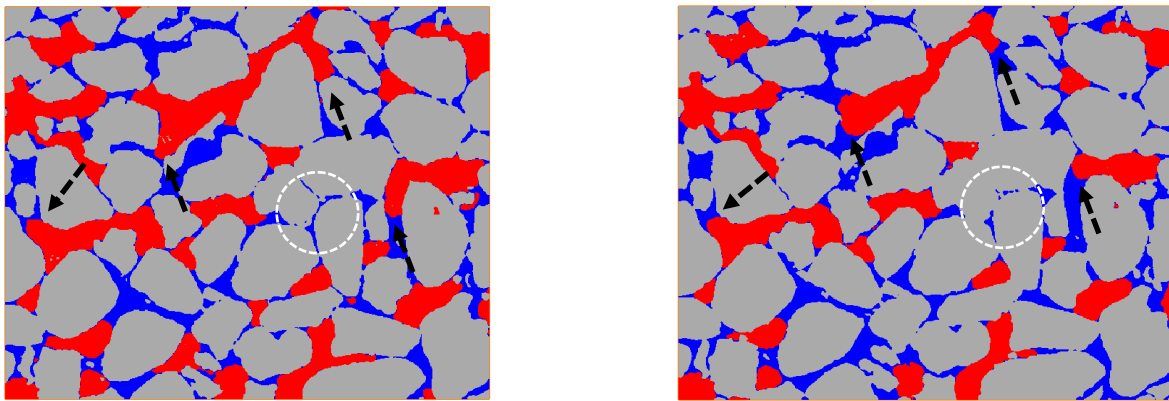
of the crude oil which improved the water displacement efficiency (see Fig. 4(a) and Fig. 5(a)). The subsequent compression processes squeezed the samples causing contraction of the pore space and the close-up of some pore elements, as illustrated by the dashed circles in Fig. 4(b) and Fig. 5(b), and, in turn, expelled fluid(s) out of the samples. Fig. 6(a) and Fig. 7(a) show the oil volume profiles along the flow direction before and after compression for the water- and oil-wet samples, respectively. In the water-wet sample, the oil volume reduced significantly and uniformly across the medium. In addition to pore space contraction, this reduction was found to be partly induced by water flow from outside the field of view (FOV) displacing oil from the FOV. This imbibition-like process caused considerable water-to-oil displacements. Therefore, interfaces were pushed toward wider regions in the pore space, as indicated by the black arrows in Fig. 4(b). These displacements were associated with significant reductions in the interfacial curvatures and the respective capillary pressure values as shown in Fig. 6 (b).

In the oil-wet sample, the response to the compression process was relatively more heterogeneous across the sample compared to the water-wet case. As displayed in Fig. 7(a), the oil volume reduction was less compared to that in the water-wet case. In particular, the volume and relative volume changes (ΔV_o and $(\Delta V_o/V_o) \times 100$) in the oil-wet sample were $-1.26E+06 \mu m^3$ and -6% compared to $-2.96E+06 \mu m^3$ and -18% in the water-wet case. This is attributed to the lower affinity of the porous medium to expel the oil phase in the oil-wet sample. It is also observed that in the oil-wet sample, the oil volume reduction at the two ends of the FOV is more significant compared to the middle which requires further investigations.

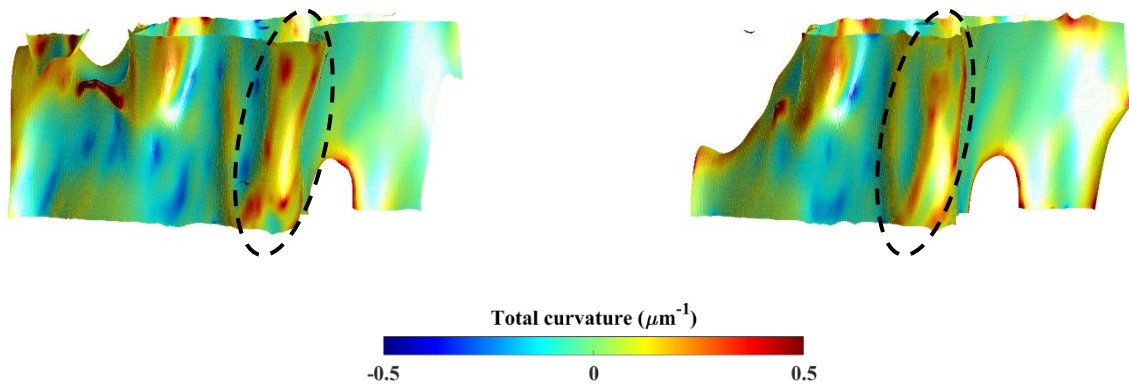
The in-situ capillary pressure profile along the z-axis of the oil-wet sample (flow direction within FOV) is shown in Fig. 7(b). First, it can be noted that the capillary pressure values in the oil-wet sample are smaller than those in the water-wet case (by around one order of magnitude). This is consistent with the oil-wet condition established after the dynamic aging process since more interfaces are expected to have negative curvatures. The profile revealed that the compaction of the oil-wet sample caused the local capillary pressure to change nonuniformly across the medium. The local capillary pressure slightly decreased or remained unchanged at the two ends, while it increased at the middle part. The behavior at the two ends can be attributed to the significant reduction in the oil volume at these locations (as shown in Fig. 7(a)), which implies that oil was displaced, and interfaces moved toward wider regions in the pore space. On the other hand, the behavior in the middle part of the sample may imply less significant displacement of the interfaces accompanying the compression process. As a result, the pore space contraction may cause the interfaces to hinge in place and become more curved. In Fig. 5(b), yellow point to locations where oil-water interfaces experienced insignificant displacements and hinged in-place in response to the compression process. In other words, interfaces may bear part of the stress caused by the compression process. These hypotheses will be further investigated in future studies.



(a) Pore-scale fluid occupancy maps of the entire FOV with oil, brine and grains shown in red, blue and grey, respectively.



(b) Magnified view of the dashed areas in (a). The black arrows point to oil-water interfaces displaced through water-to-oil displaced through water-to-oil displacements in response to the compression process.

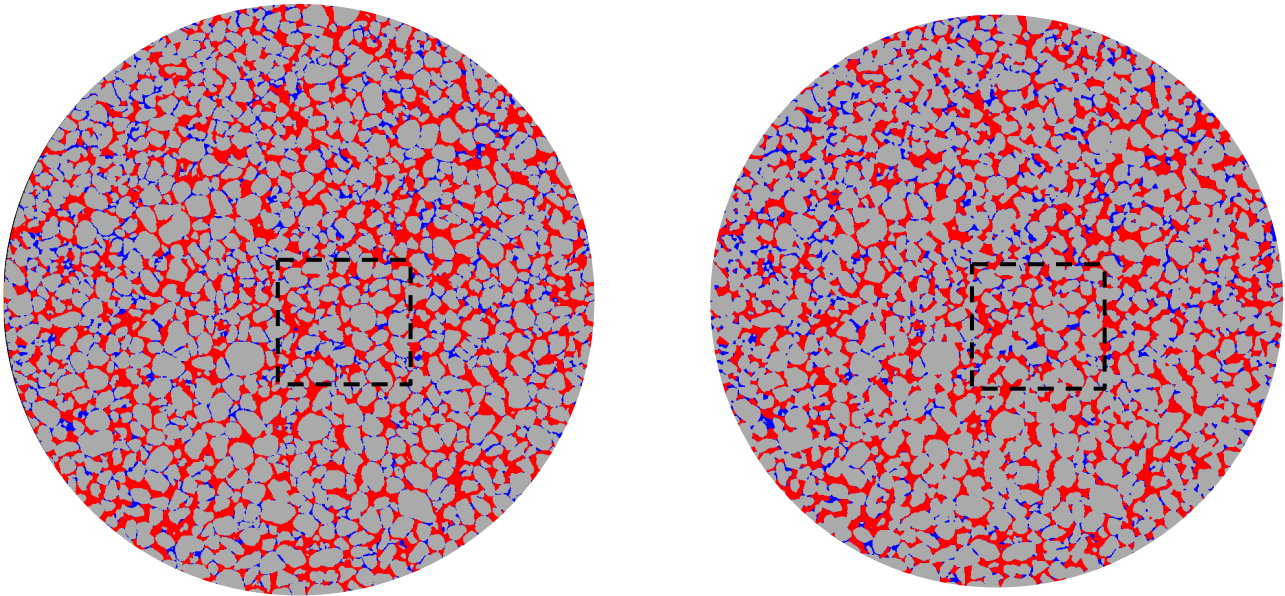


(c) Example of oil interfaces color-coded based on the curvature values. The dashed areas show reduction in the interfacial curvature due to the compression process.

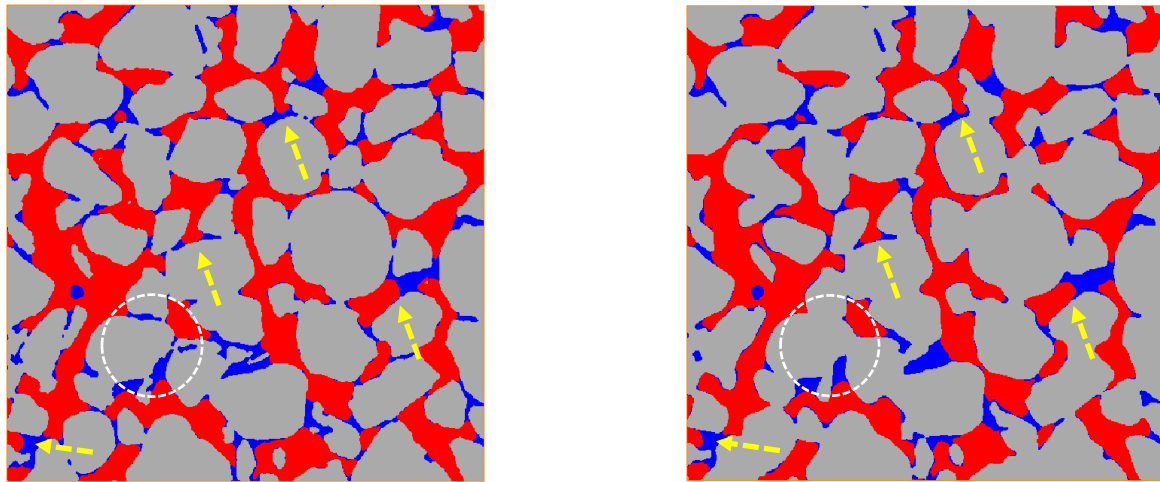
Fig. 4. Two and three dimensional visualizations of the **water-wet** sample before (left column) and after (right column) compression.

Before compression

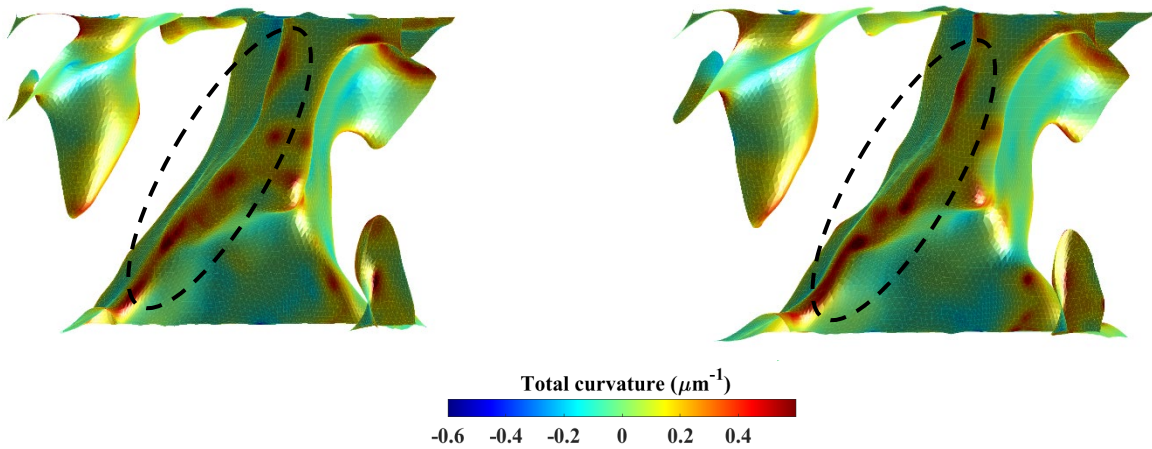
After compression



(a) Pore-scale fluid occupancy maps of the entire FOV with oil, brine and grains shown in red, blue and grey, respectively.

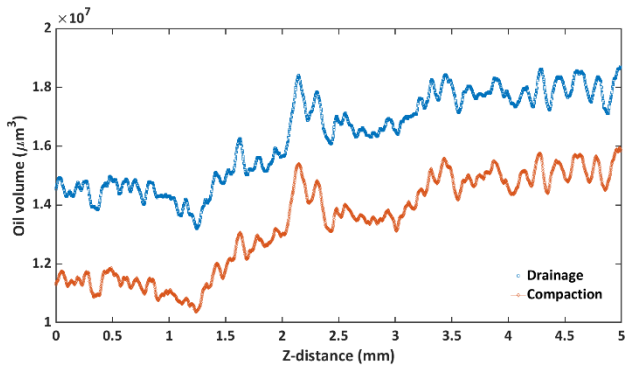


(b) Magnified view of the dashed areas in (a). The yellow arrows point to oil-water interfaces hinging in place in response to the compression process.

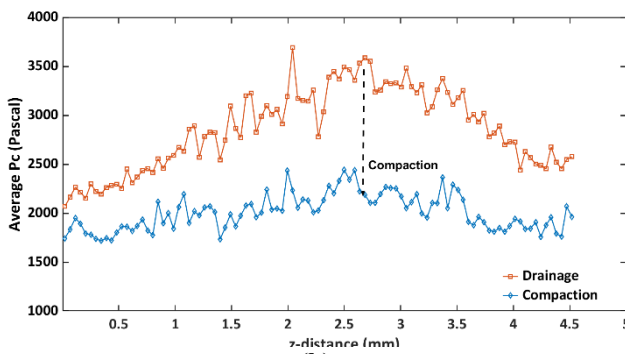


(c) Example of oil interfaces color-coded based on the curvature values. The dashed areas show increases in the interfacial curvature due to the compression process.

Fig. 5. Two and three dimensional visualizations of the **oil-wet** sample before (left column) and after (right column) compression.

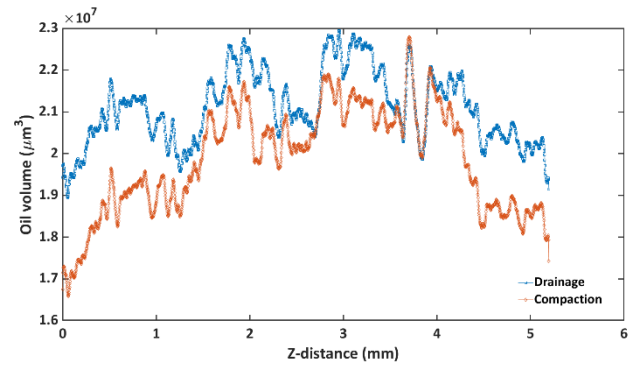


(a)

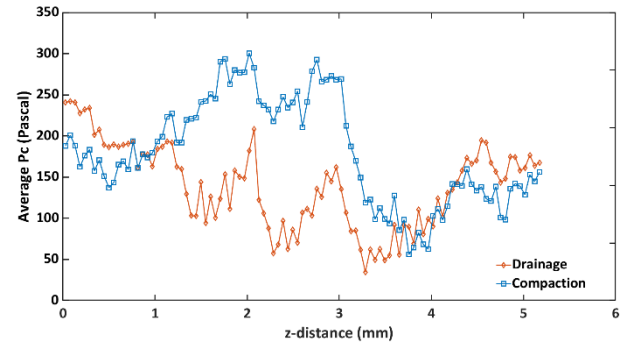


(b)

Fig. 6. Oil volume (a) and in-situ capillary pressure (b) profiles along the flow direction of the water-wet sample during oil flooding and compaction processes.



(a)



(b)

Fig. 7. Oil volume (a) and in-situ capillary pressure (b) profiles along the flow direction of the oil-wet sample during oil flooding and compaction processes.

4. Conclusions

Pore-scale images of water- and oil-wet miniature sandpack samples were acquired under low and high stress conditions. The two samples were subjected to oil drainage processes and then compressed hydrostatically to similar stress levels. The acquired images were analyzed to obtain fluid volume and in-situ capillary pressure profiles across the imaging FOV. The results of this study showed that the pore space contraction caused reduction in the oil volume in both samples indicating oil desaturation. However, unlike the water-wet sample, this reduction was less uniform in the oil-wet sample with less significant changes in the middle region of the FOV. The in-situ capillary pressure measurements also showed a general reduction trend which is attributed to displacement of interfaces to wider regions in the pore space due to the contraction. Nevertheless, local increases in capillary pressure were observed in the middle part of the oil-wet sample which was associated with pinned interfaces hinging in place and experiencing increase in their curvature accompanying the pore-space contraction.

We gratefully acknowledge the financial support of Thermo Fisher Scientific, Hess Corporation, and the University of Wyoming. We also thank the reviewers Dr. Steffen Berg and Dr. Will Richardson for their detailed revision and constructive comments.

References

- [1] G. Gambolati and P. Teatini, "Geomechanics of subsurface water withdrawal and injection," *Water Resources Research*, vol. 51, 2015.
- [2] G. Alexander E. and C. George V., "Subsidence over producing oil and gas fields, and gas leakage to the surface," *Journal of Petroleum Science and Engineering*, vol. 9, 1993.
- [3] H. S. Ali, M. A. Al-Marhoun, S. A. Abu-Khamsin and M. S. Celik, "The Effect of Overburden Pressure on Relative Permeability," *Middle East Oil Show, Bahrain*, 1987.
- [4] C. Jones, A. Al-Quraishi, J. Somerville and S. A. Hamilton, "Stress sensitivity of saturation and end-point relative permeabilities," *Society of core analysts, Edinburgh, Scotland*, 2001.
- [5] A. Gawish and E. Al-Homadhi, "Relative permeability curves for high pressure, high temperature reservoir conditions," *Oil Gas Bus*, vol. 2, 2008.
- [6] D. Chen, Z. Pan, J. Liu and L. D. Connell, "An improved relative permeability model for coal reservoirs," *International Journal of Coal Geology*, 2013.
- [7] M. K. Dabbous, A. A. Reznik, J. J. Taber and P. F. Fulton, "The Permeability of Coal to Gas and Water," *Society of Petroleum Engineers Journal*, vol. 14.
- [8] J. W. Wilson, "Determination of relative permeability under simulated reservoir," *AIChE Journal*, vol. 2, 1956.
- [9] I. Fatt, "The Effect of Overburden Pressure on Relative Permeability," *Journal of Petroleum Technology*, vol. 5, 1953.
- [10] R. D. Thomas and D. C. Ward, "Effect of Overburden Pressure and Water Saturation on Gas Permeability of Tight Sandstone Cores," *Journal of Petroleum Technology*, vol. 24, 1972.
- [11] V. A. Torrealba, Z. T. Karpyn, H. Yoon, K. A. Klise and D. Crandall, "Pore-scale investigation on stress-dependent characteristics of granular packs and the impact of pore deformation on fluid distribution," *Geofluids*, vol. 16, 2016.
- [12] R. Wang, M. Arshadi, A. Zankoor and M. Piri, "Pore space deformation and its implications for two phase flow through porous media: A micro scale experimental investigation," (*Submitted*), 2022.
- [13] R. Wang, M. Arshadi and M. Piri, Impacts of pore space deformation on two-phase flow in unconsolidated porous media under various wettability conditions, In preparation, 2022.
- [14] M. Hamoud, "Influence of geomechanical processes on relative permeability," (*Mater's thesis*). Retrieved from [*ProQuest*]. Edmonton, Alberta: University of Alberta., 2012.
- [15] M. Pazouki, "An experimental study on oil sand lump ablation," (*Doctoral dissertation*). Retrieved from [*ProQuest*]. Edmonton, Alberta: University of Alberta., 2013.
- [16] X. Wang, R. Chalaturnyk, H. Huang and J. Leung, "Permeability Variations Associated with Various Stress State during Pore Pressure Injection.," *Paper presented at 49th U.S. Rock Mechanics/Geomechanics*

Symposium, San Francisco, California.,
2015.

- [17] R. Ferguson and M. Church, "A Simple Universal Equation for Grain Settling Velocity," *Journal of Sedimentary Research*, vol. 74, no. 6, p. 933–937, 2004.
- [18] E. Farrell and D. Sherman, "A new relationship between grain size and fall (settling) velocity in air. ," *Progress in Physical Geography: Earth and Environment.*, vol. 39, no. 3, pp. 361-387, 2015.
- [19] S. Schlüter, S. Berg, T. Li, H.-J. Vogel and D. Wildenschild, "Time scales of relaxation dynamics during transient conditions in two-phase flow," *Water Resources Research*, vol. 53, no. 6, pp. 4709-4724, 2017.
- [20] M. Khishvand, A. Alizadeh and M. Piri, "In-situ characterization of wettability and pore-scale displacements during two- and three-phase flow in natural porous media," *Adv. in Water Res.*, 2016.
- [21] A. Zankoor, M. Khishvand, A. Mohamed, R. Wang and M. Piri, "In-situ capillary pressure and wettability in natural porous media: Multi-scale experimentation and automated characterization using x-ray images," *Journal of Colloid and Interface Science*, 2021.

A Combinational NMR and Dielectric Technique Using Spectral NMR Mapped Distributions of Dielectric Relaxation

James Funk^{1,*}, Michael Myers¹, and Lori Hathon¹

¹University of Houston, Department of Petroleum Engineering, 5000 Gulf Freeway, Houston, Texas, 7723

Abstract. Combinations of NMR and dielectric measurements frequently address challenging saturation determinations and wettability in conventional reservoirs. When pore structure effects are addressed, the NMR characteristics are well documented. However, the dielectric measurement response is attributed to the “texture” of the rock matrix. This simple pore structure descriptor can be improved if the electromagnetic constitutive equations and the governing physics in both measurements are considered. Similar to the dipolar relaxation equivalence of NMR and dielectric correlation time measurements in the BPP model, we develop a relaxation time correlation assuming representative Maxwell-Wagner relaxations. The key carbonate pore components demonstrated by Myers are used along with diffusion measurements and analyses to relate the Maxwell-Wagner effect to the Brownstein and Tarr model for surface relaxivity. The distributions of dielectric relaxation times in carbonate dispersion curves from 1 – 300 MHz are quantified using the Havriliak-Negami (HN) model. The quantifications are used to evaluate characteristic dielectric dispersions curves from a dielectric carbonate model with multiple pore systems. The modeled pore system fractions are spectrally mapped to the NMR T_1 or T_2 distributions based on enhanced Debye shielding distances correlated with the conductivity. The characterized NMR distributions provide additional petrophysical insight for the frequently used Archie exponent combination (MN) associated with the water tortuosity.

1 Introduction

One of the fundamental ideas expressed in the classic paper by Bloembergen, Purcell, and Pound [1] focused on using molecular autocorrelation functions to compare dielectric and nuclear magnetic resonance (NMR) relaxation. In their quantification of “the effect of the thermal motion of the magnetic nuclei upon spin-spin interaction” they observe;

Values of t_c for ice, inferred from nuclear relaxation measurements, correlate well with dielectric dispersion data.

Applications of this comparative approach have been used extensively in polymer chemistry [2] and in bio-molecular protein conformational studies [3] [4]. Recent dielectric and NMR comparative approaches in the macromolecular chemistry field have incorporated the technique of fast-cycled cycling NMR that looks at dispersion in a magnetic field [5].

The exclusive use of the individual NMR and dielectric techniques for critical petrophysical parameters such as saturation, wettability, and pore morphology has been successful and well documented. The optimal combination techniques have been in the lower frequency range (spectral induced polarization, (SIP))[6, 7] and the

low-frequency limit[8], where combinations of Archie’s law conductivity and NMR surface relaxivity dominate.

Combinational use of dielectric and NMR measurements in petrophysics usually considers the two techniques as distinct processes that provide selective choices for different petrophysical parameter such as porosity or “water tortuosity”. Comparisons of derived parameters and mechanisms of the two tools are infrequent except in the evaluation of wettability[9-11].

Our focus on the combinations of dielectric and NMR tests employs a basic distributional model to address petrophysical characterizations using relaxation dynamics that emphasize the pore and water structure interactions [12, 13].

In this comparative approach we map dielectric dispersion time constants onto an NMR distributional structure. We use NMR measurements at 2 MHz and 23 MHz, along with dielectric measurements in the frequency range dominated by the Maxwell-Wagner effect. Results of the experiments are modeled with a hybrid relaxation-effective medium model, validated with petrophysical imaging techniques, and correlated with existing saturation and diffusion models.

* Corresponding author: manager.coreimaging@gmail.com

1.1 Autocorrelation and Molecular Motion Induced Relaxation Mechanisms

A typical dielectric dispersion experiment relies on the establishment of a frequency varied electric field, whose Fourier transform provides a distribution of molecular motion-induced time decay constants reflecting electromagnetic (EM) polarization. A typical NMR experiment also shows a molecular motion-induced decay, in this case decay of EM magnetization.

Although characterized decay constants between the two phenomena are orders of magnitude different, they are both tied intimately to the autocorrelation time for molecular motion (protons in NMR, bound dipoles in Debye water relaxation, hydrated ions in Maxwell-Wagner relaxation). Confusingly, in NMR where T_1 times are in seconds, the dielectric time constant is in pico-seconds. As Callaghan [14] mentioned:

Nothing quite so baffles the general physics community as the idea of motional averaging and its consequence of slow NMR signal decays arising from fast motion.

The mathematical models that describe and incorporate motional averaging time constants in NMR T_1 and T_2 values or dielectric τ_c are described in following sections.

1.1.1 NMR

In the Bloembergen, Purcell, and Pound paper the quantitative characterization of NMR relaxation in terms of autocorrelation time constants gives:

$$\frac{1}{T_1} = K \left[\frac{\tau_c}{1 + \omega_0^2 \tau_c^2} + \frac{4\tau_c}{1 + 4\omega_0^2 \tau_c^2} \right] \quad (1)$$

$$\frac{1}{T_2} = \frac{K}{2} \left[3\tau_c + \frac{5\tau_c}{1 + \omega_0^2 \tau_c^2} + \frac{2\tau_c}{1 + 4\omega_0^2 \tau_c^2} \right] \quad (2)$$

Where the constant K is, $K = \frac{3\mu_0^2}{160\pi^2} \cdot \frac{\hbar^2 \gamma^4}{r^6}$

Each term is characteristic of a particular frequency dependent, polarization direction, molecular motion induced relaxation. Relaxation rate variations with autocorrelation time are illustrated in Figure 1 for higher and lower fields exemplified with our 2 and 23 MHz systems.

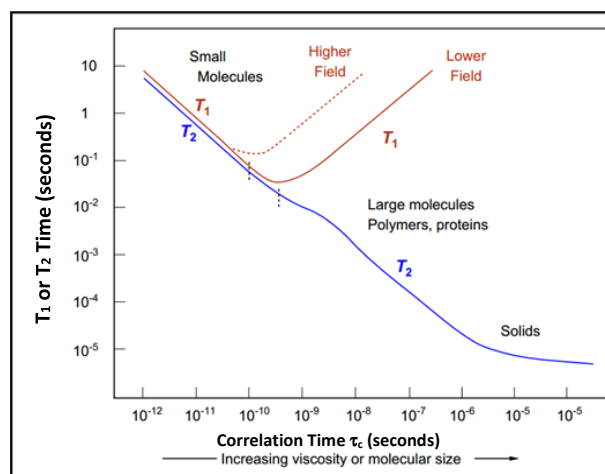


Figure 1 - Plot of the BPP model calculations showing the T_1 and T_2 response and departures from the "line narrowing" range ($T_1=T_2$) as a function of autocorrelation time τ_c .

1.1.2 Dielectrics

Similar to the additive relaxation (magnetization) mechanisms in NMR, dielectric processes can be described by their fundamental polarization mechanisms. Total polarization in the frequency range of this study can be characterized by three components correlated with the rock matrix, the fluids in the system, and the interface between the matrix and the fluids.

1.1.3 Rock Matrix - Electronic and Ionic Polarization - High-Frequency Limit

Distortion of the electron cloud around an atom and its return to equilibrium is a short, fast process extending into the electromagnetic spectrum's ultraviolet region. In crystalline materials and other solids, ionic polarization due to the relative displacement or vibrations of ionic lattice charges provides an additional relaxation mechanism extending into the EM spectrum [15]. These characteristics are the basis for the standards used in dielectric measurements and the termed "high-frequency limit" characteristics incorporated in most dielectric models.

1.1.4 Pore Fluids - Dipolar Relaxation - Water Structure

The interaction of EM energy with materials containing permanent dipoles has been a significant basis for work with dielectrics [13, 16-19]. The founding ideas are based on the original work of Debye on the dipole moment of water. Although induced dipoles in non-polar materials are significant in applied spectroscopic fields, for work with natural materials, the primary concern is with the permanent dipole moment of water. Although it is categorized differently as a bound charge effect [20], an orientational effect, or a surface effect [21], the process of dipolar orientation and relaxation describe an essential characteristic of the structure of water [12, 19].

Debye's work in 1929 resulted in an expression for the dielectric constant of water based on the relaxation time constant as,

$$\varepsilon^* = \varepsilon_\infty + \frac{(\varepsilon_s - \varepsilon_\infty)}{(1 + i\omega\tau_c)} \quad (3)$$

1.1.5 Interfacial Polarization – Maxwell-Wagner Effect

Restricted charge movement in complex structures adds to the dielectric storage through a structure-dependent polarization process. These complex systems exhibit non-Debye relaxation described empirically as distorted Cole-Cole plots. A frequently used representation of this and the one used in this study is the Havriliak-Negami (HN) model [22],

$$\varepsilon^* = \varepsilon_\infty + \frac{(\varepsilon_s - \varepsilon_\infty)}{(1 + (i\omega\tau_c)^\alpha)^\beta} \quad (4)$$

2 Experimental

2.1 Petrophysical Imaging and Measurement Sequence

Micro-CT images were acquired on the samples using a XTekCT micro-CT scanner operating at 110 KeV and 130 micro-amps. The flat panel detector provided an image resolution of 34.7 microns on a one-inch diameter sample. Samples were scanned in a cleaned and dried state with x-ray projections taken at 0.119-degree increments.

Image analyses were performed using Dragonfly software (Object Research Systems, Montreal, Canada). X-ray micro-CT images and Otsu segmented vugs of two of the samples are seen in Figures 2 and 3.

A set of eleven (11) carbonate samples consisting of a dielectric segment (6-8 mm thick) and a plug segment (~36 mm thick) were sliced from the scanned one-inch diameter plugs. These were cleaned and saturated with brines of various salinities in some, first by spontaneous imbibition, and in all by vacuum saturation. As brine saturations changed, sequential dielectric and NMR T₂ measurements were made on the thin samples. Multi-dimensional NMR measurements were made on the plug segments.

All plug samples were saturated with 10% sodium chloride brine prior to NMR testing. For the smaller dielectric samples, two separate sequences of saturation and measurement were employed.

In one group of samples, spontaneous imbibition steps identified by changes in the slope of weight increase with time were used to pull samples for concurrent dielectric and NMR T₂ measurements. A final saturation

was achieved using cycles of vacuum and pressure. Salinity changes were made by soaking samples in successively higher sodium chloride concentrations for periods in excess of two weeks. The other group of samples were handled similarly but without the incremental imbibition steps.

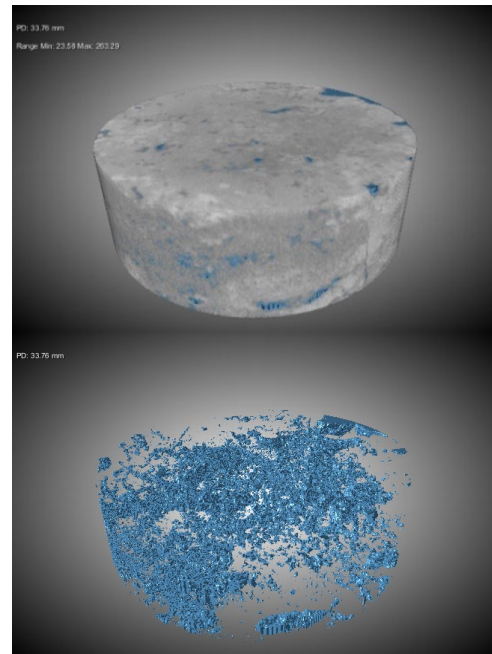


Figure 2 - Sample A4_D micro-CT image with Otsu threshold segmented vug fraction. Vug fraction is 4.27% of the bulk volume.

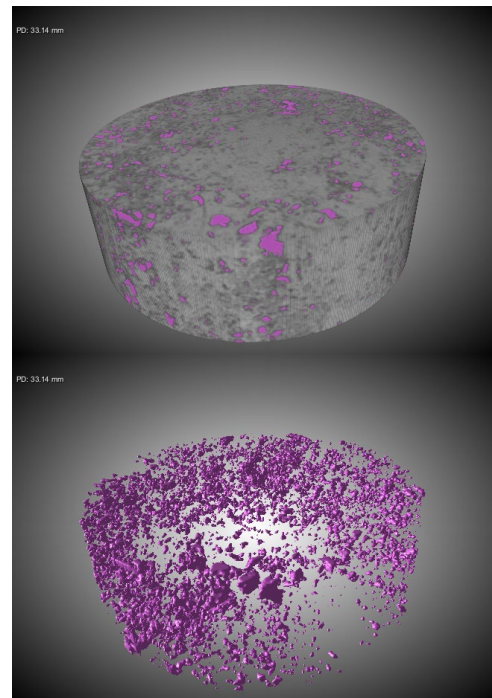


Figure 3 - Sample B1_D micro-CT image with Otsu threshold segmented vug fraction. Vug fraction is 1.48% of the bulk volume.

2.2 Dielectric Measurements

In the frequency range of 1 to 300 MHz, the most accurate technique for impedance measurements uses a calibrated capacitance cell. The cell is configured to minimize electrode potentials with gold plated contacts. Thin, brine saturated cellulose interfaces provide contact coupling with the samples. In our experiments, an HP 4291A impedance analyzer is in series with an HP 4289 bridge, an HP 4291B high impedance head test port, and a robust GenRad sample holder. The system communicates via an GPIB connection with a desktop workstation running National Instruments VISA software. The system is controlled and the recorded data is analyzed with a MATLAB acquisition and processing program.

Following an initial multi-step calibration of the HP 4291A and HP 4289 for open, short, load, and electrical length, the calibration is repeated at each sampling frequency with the sample holder in place. The measurement, commonly described as the RF-IV method, uses two sensitive high-speed voltmeters in the HP 4291A to measure the source voltage and the reflected current.

2.3 NMR Measurements

NMR measurements were made on Oxford Instruments (Maran Ultra) 2 MHz and an Oxford MQC 23 MHz system. The 2 MHz systems were equipped with 1D gradients enclosing a 50 mm diameter probe. Typical 90° pulse widths were 20 microseconds and CPMG echo spacings ($2 \cdot \tau$) were 200 microseconds. The 23 MHz system used a 30mm probe with τ values from 30 to 1000 microseconds. Recycle delays for both systems ranged from 7.5 to 15 seconds depending on the sample. Standard CPMG and inversion recovery pulse sequences were used for the T_1 / T_2 measurements.

NMR T_1/T_2 measurements were done on fully saturated and selected samples in both the 2 MHz and the 23 MHz systems. Pulse sequences followed the parameters used in the T_2 measurements for 30 T_1 τ values logarithmically spaced from 1 msec to 3 seconds.

3 Results and Discussion

3.1 Dielectric and NMR Distributions of Relaxation Times

Dielectric dispersion in carbonates scales with conductivity[23, 24] such that the normalized dielectric dispersion results shown in Figure 4 are consistent for all brine concentrations. The corresponding 23 MHz NMR T_2 distributions are shown in Figure 5.

In Figure 4 the lower dielectric constant values for samples A1_D and A2_D provide no direct information on the bi-modal nature of the pore system that is apparent in the NMR response shown in Figure 5. However, imbibition results do provide an indicator of NMR and

dielectric associated responses. For sample B1_D there was no measurable change in saturations between the first imbibition and second imbibition cycles, However, there were slight changes in the dielectric dispersion curves in Figure 6 and the corresponding NMR T_2 distribution curves in Figure 7.

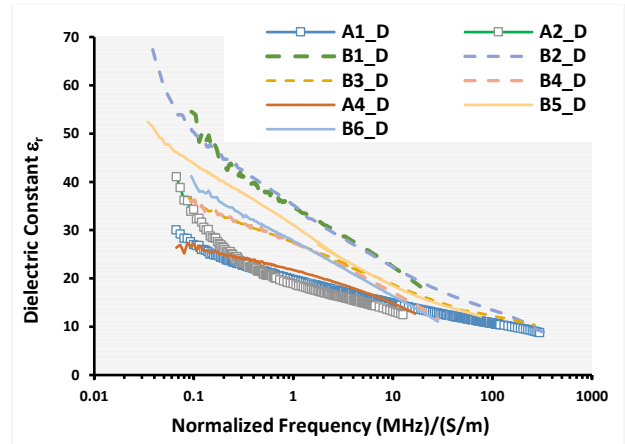


Figure 4 - Conductivity normalized dielectric constant dispersion for brine saturated Michigan carbonate samples.

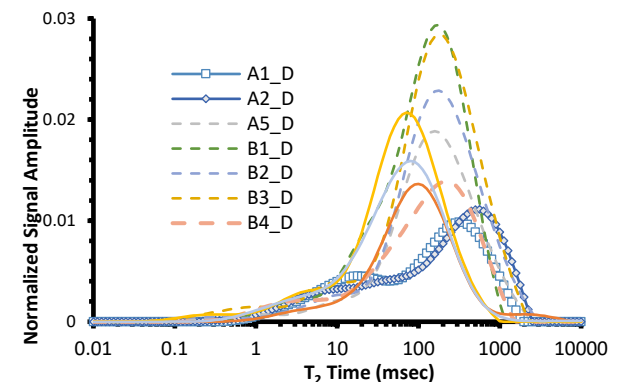


Figure 5 - 23 MHz Normalized NMR T_2 distributions for brine saturated Michigan carbonate samples.

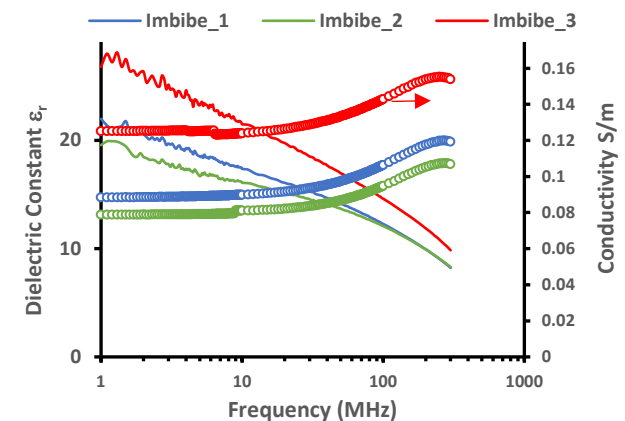


Figure 6 -Sample B1_D imbibition stage $\phi \cdot S_w$ dielectric dispersion data. Second imbibition step shows lower dielectric response between first and second imbibition.

One inference from the NMR distributions is that the brine imbibed in the first cycle has re-distributed to slightly smaller pores by the end of the second cycle. As we shall see in our τ_{PCM} model this type of change would result in the slightly reduced dielectric dispersion results seen in the test.

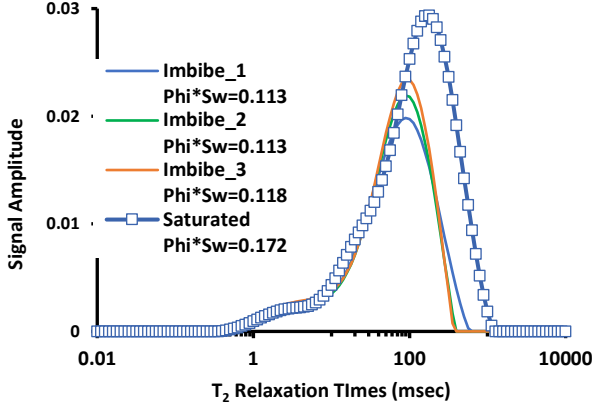


Figure 7 - Sample B1_D imbibition T_2 distributions showing shift to lower T_2 times between the first and second imbibition cycles.

3.2 Dielectric and NMR Pore Combination Model (τ_{PCM})

The carbonate pore components that contribute to the overall dielectric response are illustrated in Figure 8. These components, identified by Myers [24] using thin-section discriminators for the vug and matrix components, have proven to be durable, physics-based combination.

Extending this concept to a more finely defined pore structure combination was an enticing opportunity. Frequency normalization of the measured dielectric response by conductivity of the brine focuses the model, eliminating salinity variability. A subsequent fit of the matrix and vug components to the HN equation, provides a rapid object function fit for the dispersion data. These fits for the real components of the dielectric constant for the matrix and vug components $\epsilon_{r_{matrix}}$ and $\epsilon_{r_{vugs}}$, are used to determine the matrix ϕ_{Agm} , and vug, ϕ_{Agv} porosity in the linear pore combination for ϵ_r where:

$$\epsilon_r = \epsilon_{r_{matrix}} \cdot \phi_{Agm} + \epsilon_{r_{vugs}} \cdot \phi_{Agv} + \epsilon_{\infty} \quad (5)$$

The individual pore component dispersion curves are shown in Figure 8. The HN model values for τ in the two systems were: 1.93×10^{-10} sec. for the vug system and 5.47×10^{-9} sec. for the matrix system. Using Equation (2) from the BPP model these give T_1 values of 101.5 msec and 3.6 msec for the vug and matrix systems respectively.

A linear fit of Equation (5) for the fully saturated frequency normalized dielectric response of Sample B3_D is shown in Figure 9.

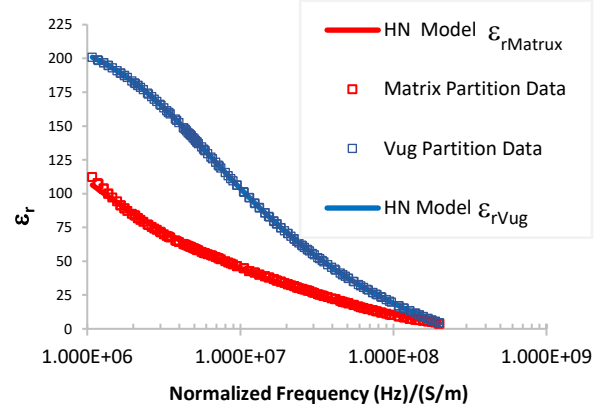


Figure 8 - Myers pore combination model matrix and vug dielectric dispersion curves with HN model fit.

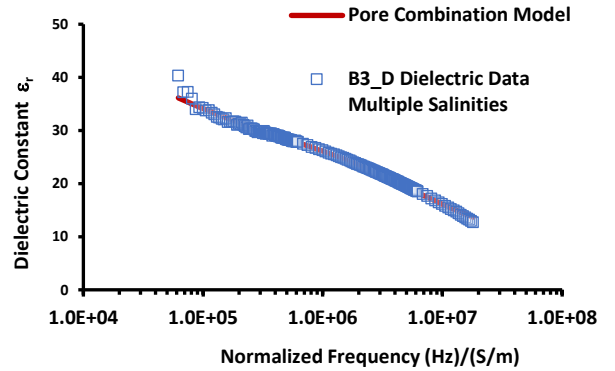


Figure 9 - Pore combination components and example fit using $\phi_{Vug} = .065$, $\phi_{matrix} = .055$, $\epsilon_{\infty} = 6.862$

The τ_{PCM} model essentially distributes the matrix fraction derived from the PCM fit onto the T_2 distribution. Attempts to use a simple T_2 cutoff failed to accurately capture a consistent size or size differential throughout the data set pointing to the need for a “spectral” distribution similar to that used for Swi evaluations in NMR data.

The proposed model assumes that the fractional matrix contribution to the dielectric intensity and dispersion starts first with the fastest relaxing NMR regions in the sample. It also assumes that the intensity of the interaction falls off with distance in a manner consistent with Debye shielding described in Equation (6).

$$\psi_V = \psi_S e^{-r/\lambda_D} \quad (6)$$

Substituting incremental T_2 values for r and constraining the matrix response to the pore combination model matrix fraction (ϕ_{AGM}), the derived spectral distribution parameter is the best fit for τ_{PCM} based on Equation (7). T_2 signal amplitudes at each T_2 are then

linear combinations of $M_{A_{gm}}$ and $M_{A_{gv}}$ determined from Equations (8) and (9).

$$\frac{\phi_{A_{gm}}}{\phi_T} = \sum_{i=n}^{i=1} \left[\frac{M(T_{2_i})}{M_T} \right] e^{-T_{2_i}/\tau_{PCM}} \quad (7)$$

$$M_{A_{gm}}(T_{2_i}) = M(T_{2_i}) e^{-T_{2_i}/\tau_{PCM}} \quad (8)$$

$$M_{A_{gv}}(T_{2_i}) = M(T_{2_i})(1 - e^{-T_{2_i}/\tau_{PCM}}) \quad (9)$$

Comparative results showing the range of distributions and their variability in the dielectric data are seen in the two dielectric samples shown in Figure 10 with distributions highlighted in Figures 11 and 12.

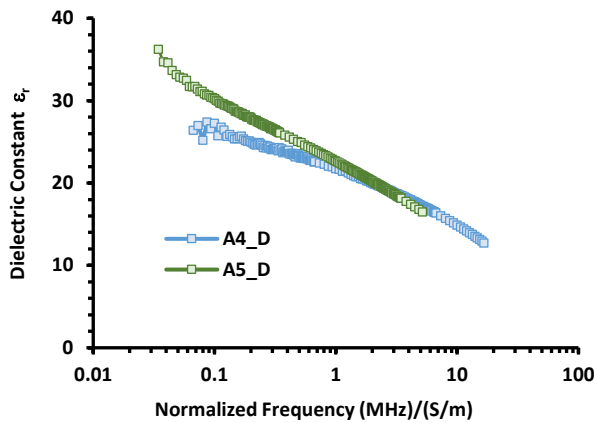


Figure 10 - Dielectric constant dispersion results for saturated samples A4_D and A5_D.

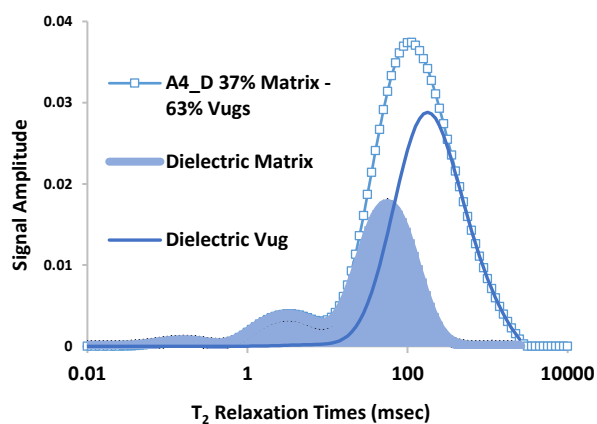


Figure 11 - T_2 mapped dielectric matrix and vug pore combinations for Sample A4_D. Matrix volume fraction 37%, Vug volume fraction 63%.

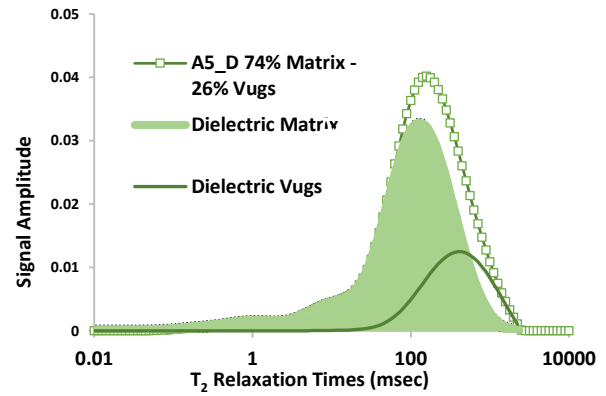


Figure 12 - T_2 mapped dielectric matrix and vug pore combinations for Sample A5_D. Matrix volume fraction 74%, Vug volume fraction 26%

T_2 mapped dielectric matrix and vug distributions for all samples are shown in Figures 13 and 14 and listed in Table 1.

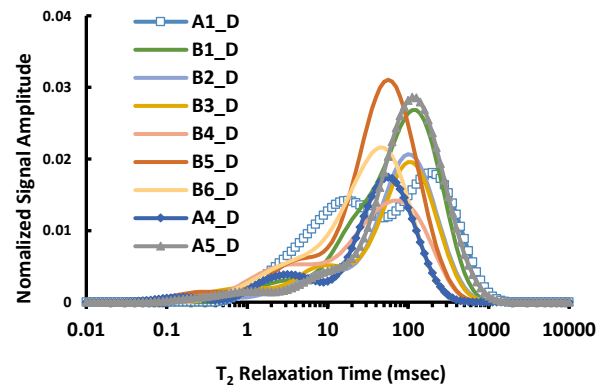


Figure 13 - Normalized T_2 mapped dielectric matrix components for brine saturated Michigan carbonate samples.

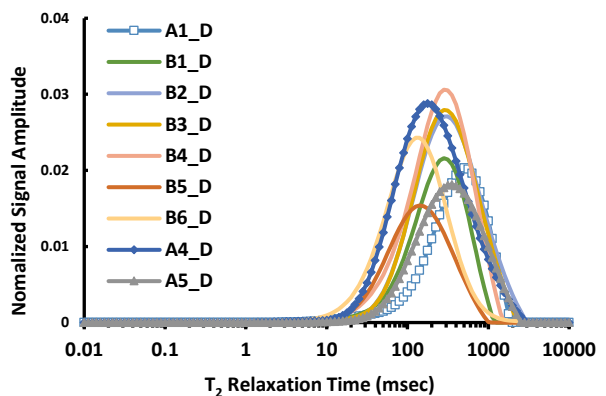


Figure 14 - Normalized T_2 mapped dielectric vug components for brine saturated Michigan carbonate samples.

Table 1 - Matrix and vug fractions determined from the normalized dielectric response and corresponding τ_{PCM}

Sample	τ_{PCM}	Fraction		
		Matrix	Vugs	Phi
A1_D	420	0.652	0.348	0.083
A4_D	96	0.370	0.630	0.081
A5_D	395	0.610	0.340	0.098
B1_D	315	0.638	0.362	0.172
B2	282	0.526	0.474	0.143
B3	190	0.455	0.545	0.13
B4_D	132	0.426	0.574	0.098
B5	221	0.703	0.297	0.119
B6_D	104.5	0.531	0.469	0.113

The mapping parameter for the dielectric matrix distributions, τ_{PCM} , was developed using exclusively the real component of the complex dielectric equation. The fundamental Kramer’s-Kronig relationship states that there should also be a relationship with the complex part of the dielectric equation. In this case the conductivity. Figure 15 shows this relationship. Here the formation factor was calculated using the 10 MHz value for conductivity. The dielectric pore combination model works well but breaks down with samples that show a single vug connection that covers the width of the sample such as Sample A2_D, which is not included in the analysis.

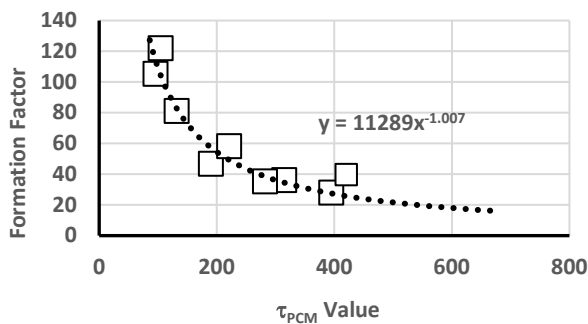


Figure 15 - Formation factor Correlation for τ_{PCM}

Tableau 2 - Sample Formation factor and corresponding Tau-PCM values

Sample	τ_{PCM}	FF		
		Phi	C_w/C_{10MHz}	m
A1_D	420	0.083	39.83	1.48
A4_D	96	0.081	105.24	1.85
A5_D	395	0.098	28.00	1.55
B1_D	315	0.172	36.16	2.04
B2_D	282	0.143	35.31	1.83
B3_D	190	0.13	46.65	1.88
B4_D	132	0.098	81.17	1.89
B5_D	221	0.119	58.25	1.91
B6_D	104.5	0.113	122.00	2.20

Spectral mapping of dielectric dispersion onto T_2 distributions provides a unique phenomenological model for linking two petrophysical tools and measurements. It shows clearly that "one size does not fit all" when defining a vug. The model supports the idea that the electromagnetic interactions are not size specific. It suggests that variations in the electric fields in a sample are related to the size of an inclusion and to the size of any surrounding inclusions. An ideal first step to validate the model and to establish theoretical support is to "look at the rocks".

4 Results

4.1 Imaging Carbonate Structure

Partitioning pore space using size and descriptive parameters is a fundamental practice in petrology and petrophysics. Introducing dielectric measurements to the mix is relatively new.

Early work in machine learning applied to thin sections and SEM backscattered images provides a qualitative tool to assess the duality in size related dielectric constants for the τ_{PCM} model.

Carbonate pore typing described by Ross [25] illustrates end-member characteristics that quantify the "rough" and "smooth" pore characteristics seen in SEM images. The areas are determined by erosion and dilation sequences associated with the number of size correlated cycles. Quantitative results are shown in Figure 16. The largest two end members listed are typical of the thin section and micro-CT porosities visible in this set of samples.

SEM Image	Rough Area		Smooth Area	
	Size	%	Size	%
	0-12	10	0-8	90
	0-12 12-23	50 8	0-8 8-31	19 23
	0-12 12-23 23-42	19 32 20	8-31 31-69	12 15
	12-23 23-42 42-76 76-210	2 19 38 10	31-69 69-134	4 20
	23-42 42-76 76-210	2 12 50	69-134 134-210	2 22

Figure 16 – SEM - Smooth and Rough areas based on erosion-dilation cycles. All sizes are in microns.

All sizes have some smooth and some rough areas. Overlaying the SEM sizes with the T_2 distributions puts smooth and rough areas in the 50 – 1200 msec T_2 range.

where there exists both matrix and vug components in relative ratios similar to the rough to smooth ratios of the SEM.

4.2 Saturation Effects

In addition to describing the dielectric dispersion of the pore combinations, Figure 8 illustrates differences in the dielectric constant for matrix and vug components at the NMR frequencies of 2 and 23 MHz. At 2 MHz the vug/matrix dielectric factor is 2.07 and 2.34 at 23 MHz.

These differences suggest that any measured dielectric value is sensitive to the distribution of fluids between matrix and vugs. Even to the extent where spatial variation can override saturation changes. This was indeed the case as shown by the Imbibe_1 dielectric and NMR response compared to Imbibe_2 for Sample B1_D shown in Figures 6 and 7 and for Sample B6_D in Figures 17 and 18.

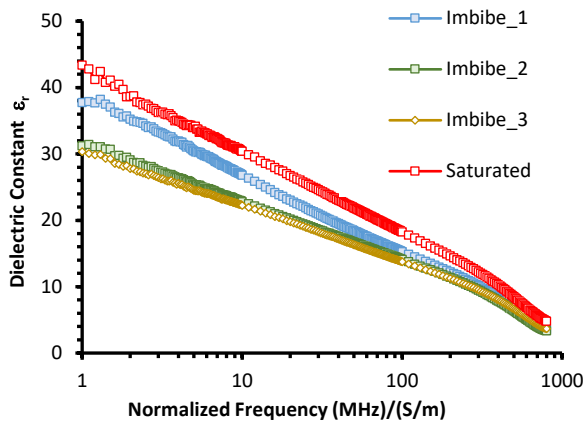


Figure 17 - Dielectric dispersion for imbibition cycles in Sample B6_D.

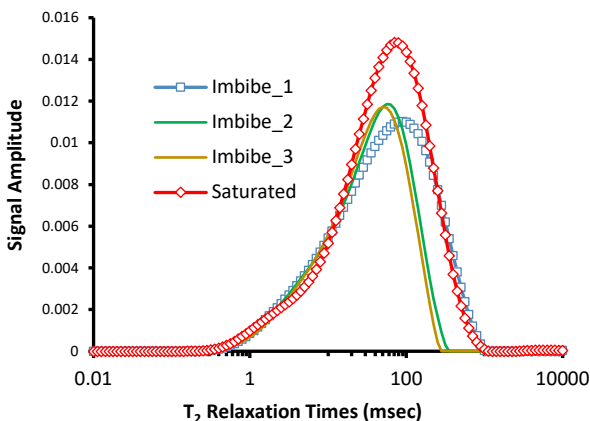


Figure 18 - Imbibition cycle NMR T₂ distributions for Sample B6_D.

The use of Equations (7) thru (9) and the correlation shown in Figure 15, was adapted based on samples with $\phi Sw = \phi$. Results for imbibition samples provided a convenient check on the model for lower values of ϕSw .

After partitioning the dielectric response for the partially saturated samples using matrix and vug dispersion functions shown in Figure 8, corresponding τ_{PCM} terms were determined and evaluated for their formation factor dependence. Values for four saturations established in sample B4_D are listed in Table 3. Higher saturations generally show better agreement due to the data density. Adding lower saturation values into the Figure 15 correlation should improve the model.

Table 3-Sample B4_D Imbibition Cycles- τ_{PCM} results

Imbibition	Tau_Pcm	Phi*Sw	Formation Factor	
			Experimental	Model
Imbibe_1	55.8	0.050	252	197
Imbibe_2	52.6	0.048	248	209
Imbibe_4	65.1	0.064	175	168
Saturated	132	0.098	81.2	79.6

5 Diffusion Correlations

The close connection of τ_{PCM} with the formation factor indicates that diffusion effects may be quantifiable with this technique. Based on ratios of restricted and unrestricted mean squared distance the equation,

$$\frac{D_{eff}}{D_0} = \frac{1}{FF \cdot \phi} \quad (10)$$

where D_{eff} is the effective diffusion, D_0 is the molecular self-diffusion, FF and phi are the formation factor and porosity, can be considered along with the equation relating the enhanced T₂ relaxation times at variable inter-echo times.

$$\frac{1}{T_{2D}} = \frac{1}{3} (\tau \gamma G)^2 D \quad (11)$$

In combination with the τ_{PCM} distributions, the variable tau technique can provide information on the relative diffusivity or internal gradients (G) in both the matrix and vug systems. Just as plots of the log mean T₂ values versus tau can be used for the entire sample, shifts for the matrix and vug distributions can provide comparative results for the effective diffusion in the two systems or for estimates of their internal gradients. An example of different shifts (matrix versus vug) for one of the samples is shown in Figures 19. Agreement between the sample and the dielectric determined formation factor is shown in Figure 20. The best agreement between the techniques used sample T_{2D} values with $G_{Sample}=68.1$ Gauss/cm or $G_{vug}=67.8$ Gauss/cm and $G_{Matrix}=120$ Gauss/cm.

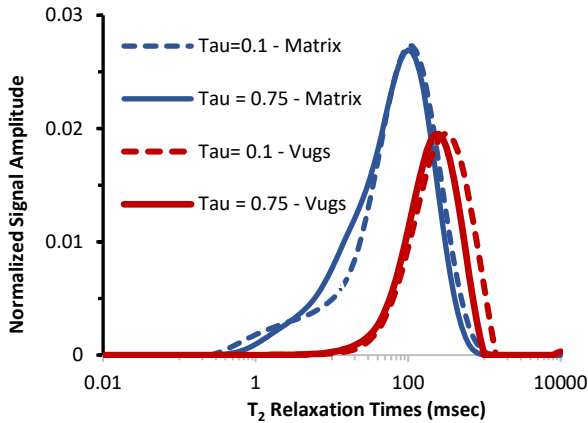


Figure 19 - Tau-pcm distributions with variable inter-echo spacing for Sample B1_D with $D_{eff}=4.18 \text{ e-}10 \text{ m}^2/\text{sec}$

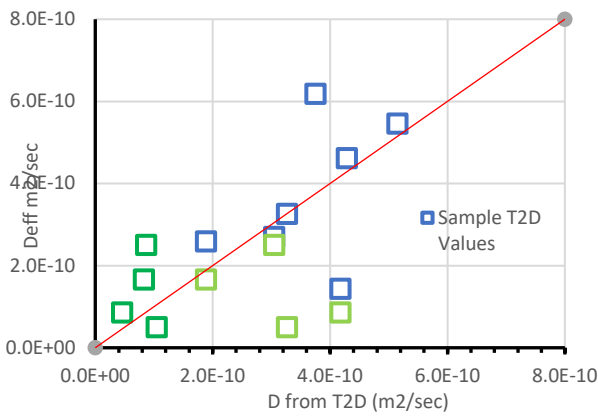


Figure 20 - Diffusion coefficients determined for dielectric from formation factor and variable tau measurements. Optimized with G determined as 68.1 Gauss/cm or Sample T2D.

5.1 T₁/T₂ Variations

Initial comparisons of 2 MHz and 23 MHz T₁/T₂ plots shown in Figure 21 and Figure 22 indicated that greater separation of relaxation mechanisms predicted by the BPP model (Figure 1) may be accessible.

Comparisons of Figure 22 with Figure 23 show the development of a secondary, horizontally developed, T₂ independent peak at long T₁ times. This peak is pronounced in Sample B4_D but develops in other samples as the vug fraction increases. The plots highlight different matrix fractions and relative differences in the build-up of the vug component in Samples B2_D and B4_D.

T₁/T₂ response differences would not be predicted simply by comparison of the T₁ or T₂ distributions. However, the application of the mapped dielectric partitioning (Figures 24 and 25) highlights the vug T₂ differences that are distinct and identifiable in long relaxing T₁ components (Figures 21 and 22).

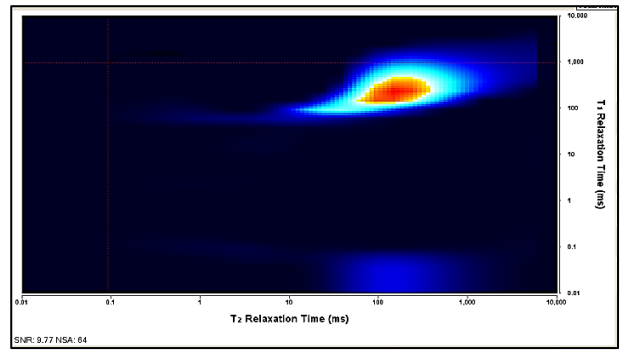


Figure 21 - 2 MHz T₁/T₂ plot for Saturated sample B2_D. As expected from BPP model there is less separation in the T₁ and T₂ peaks.

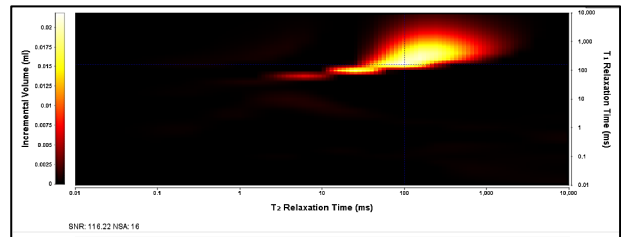


Figure 22 - T₁/T₂ plots at 2 MHz and 23 MHz for Sample B2_D. Better separation of the T₂ and T₁ elements reflects the T₁ and T₂ vertical separation seen in BPP model.

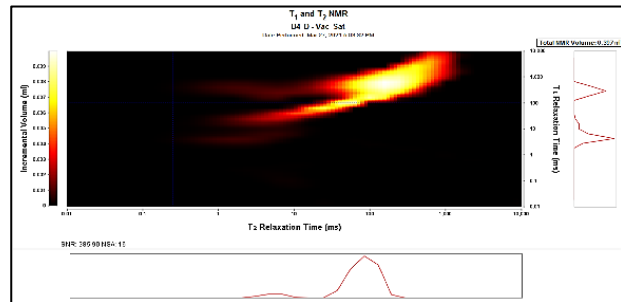


Figure 23 - T₁/T₂ plot for Sample B4_D, (Matrix Fraction = .426) showing the development of T₂ independent peak in the vug partition.

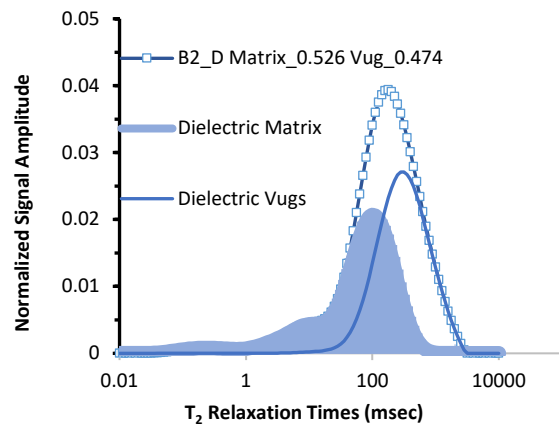


Figure 24-Partitioning of dielectric matrix and vug components for Sample B2_D under the normalized T₂ distribution.

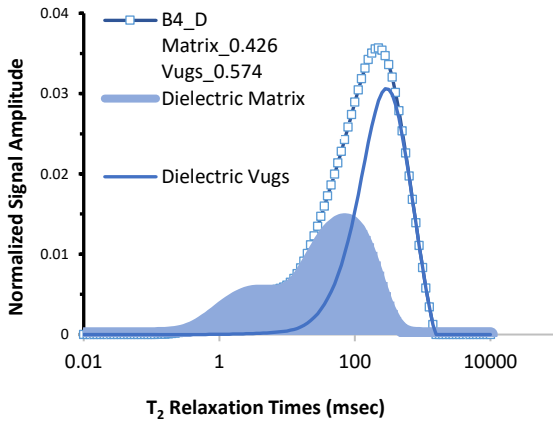


Figure 25 - Partitioning of dielectric matrix and vug components for Sample B4 under the normalized T_2 distribution.

6 Discussion

Dielectric analyses that follow the ideas of Maxwell-Garnet model focus on defining the electric field in an assortment of pore space geometries that incorporate geometrical orientation in the field. Although successful in practice a viable alternative is to use a fundamental measurement that reflects the geometry of the pore space. NMR T_2 distributions provide that information in an integral form. Our τ_{PCM} model allows us to differentiate the integral with respect to the dielectric constant and quantify the relative geometrical contributions of the matrix and the “vug” system.

Pore space imaging and specific petrophysical measurements for formation factor, resistivity index, and restricted diffusion provide validation and quantification for the differential mapping of dielectric responses to the T_2 spectrum. NMR T_1/T_2 dimensional measurements provide additional information that elucidate possible selective relaxation mechanisms for the different geometrical contributors.

The good agreement of saturation dependence with τ_{PCM} supports the linear relationship established by the technique and the established linear relationship between vug porosity and formation factor inherent in the pore combination model. It suggests that τ_{PCM} provides a modeled saturation discriminator for the matrix and vug systems more easily applied than the geometric terms used in the derivation of water tortuosity.

7 Conclusions

Spectral mapping of the dielectric response onto the NMR T_2 distributions provides a quantitative petrophysical tool useful for pore space characterization and saturation

mapping. The model provides a dielectric description of the T_2 relaxation spectrum constrained by the surface to volume correlations of the Brownstein and Tarr model.

The ability to distinguish the matrix and vug contributions in a system dominated by surface relaxivity (fast diffusion limit) is an essential step, comparable to that seen with D_2O displacement studies, to characterizing bi-modal fluid transport in conventional carbonates.

The utility of our τ_{PCM} application to the magnetization components of the T_2 distribution indicates that location characteristics of the dielectric constant are captured in our normal pulse sequences applied during a CPMG experiment.

The comparisons and agreements with previous and current work confirm the applicability of the technique and suggest that a progression beyond that of a phenomenological model is warranted.

8 Nomenclature

Physical Constants

τ_c – Autocorrelation time (nanoseconds)

\hbar – Planck's constant 1.05457×10^{-34} (J · s)

μ_0 – Permeability of free space 1.256637×10^{-6} (H / m)

ω_0 – NMR resonant frequency (radians / sec)

γ – Proton gyromagnetic ratio 267.515×10^{-6} (rad / s · T)

ψ_v – Electric potential (microvolts)

ψ_s – Surface potential (microvolts)

λ_D – Potential shielding distance (nanometers)

Dielectric Terms

ε^* – Complex relative permittivity

ε_∞ – high frequency relative permittivity limit

ε_s – low frequency relative permittivity

ε_r – Real component of the complex relative permittivity

ω – frequency for dielectric dispersion

τ_{PCM} – Dielectric to NMR mapping constant (microseconds)

ϕ_{Agm} – Porosity of the matrix component

ϕ_{Agv} – Porosity of the vug component

NMR Terms

T_1 – Spin – lattice relaxation time (msec)

T_2 – Spin – Spin relaxation time (msec)

T_{2D} – Relaxation time due to diffusion (msec)

$M(T_{2i})$ – Signal amplitude (magnetization) at T_2 time

D_{eff} – Effective diffusion coefficient (m^2/sec)

D_0 – Liquid diffusion coefficient (m^2/sec)

G – Magnetic gradient strength (Gauss/cm)

τ – CPMG interecho spacing (msec)

9 Bibliography

- [1] N. Bloembergen, E.M. Purcell, R.V. Pound, Relaxation effects in nuclear magnetic resonance absorption, *Physical Review* 73(7) (1948) 679-712.
- [2] K. Kabara, V. Madhurima, A.C. Kumbharkhane, A.V. Sarode, Study of H1 spin lattice relaxation and dielectric relaxation in Poly(propylene glycol) system, *Materials Chemistry and Physics* 209 (2018) 16-22.
- [3] M. Fukuzaki, N. Miura, N. Shinyashiki, D. Kurita, S. Shioya, M. Haida, S. Mashimo, Comparison of water relaxation time in serum albumin solution using nuclear magnetic resonance and time domain reflectometry, *Journal of Physical Chemistry*® 99(1) (1995) 431-435.
- [4] D. Kruk, E. Masiewicz, M. Wojciechowski, M. Florek-Wojciechowska, L.M. Broche, D.J. Lurie, Slow dynamics of solid proteins - Nuclear magnetic resonance relaxometry versus dielectric spectroscopy, *J Magn Reson* 314 (2020) 106721.
- [5] S. Godefroy, J.P. Korb, M. Fleury, R.G. Bryant, Surface nuclear magnetic relaxation and dynamics of water and oil in macroporous media, *Phys Rev E Stat Nonlin Soft Matter Phys* 64(2 Pt 1) (2001) 021605.
- [6] E. Müller-Huber, F. Börner, J.H. Börner, D. Kulke, Combined interpretation of NMR, MICP, and SIP measurements on mud-dominated and grain-dominated carbonate rocks, *Journal of Applied Geophysics* 159 (2018) 228-240.
- [7] Z. Zhang, S. Kruschwitz, A. Weller, M. Halisch, Enhanced pore space analysis by use of μ -CT, MIP, NMR, and SIP, *Solid Earth* 9(6) (2018) 1225-1238.
- [8] E. Toumelin, C. Torres-Verdin, N. Bona, Improving Petrophysical Interpretation With Wide-Band Electromagnetic Measurements, *SPE Journal* 13(02) (2008) 205-215.
- [9] E. Toumelin, Pore-scale petrophysical models for the simulation and combined interpretation of nuclear magnetic resonance and wide-band electromagnetic measurements of saturated rocks, ProQuest Dissertations Publishing, 2006.
- [10] F. C. Ferreira, M. Stukan, L. Liang, A. Souza, L. Venkataramanan, A. Beletskaya, D. Dias, M. Dantas da Silva, New Model for Wettability Change with Depth in Mixed-Wet Complex Carbonates, Abu Dhabi International Petroleum Exhibition & Conference, Society of Petroleum Engineers, Abu Dhabi, UAE, 2018, p. 28.
- [11] B. Sauerer, A. Valori, D. Krinis, W. Abdallah, NMR Wettability of Carbonate Reservoir Cores: Best Practices, SPE Middle East Oil and Gas Show and Conference, Society of Petroleum Engineers, Manama, Bahrain, 2019, p. 17.
- [12] Y. Marcus, Effect of Ions on the Structure of Water: Structure Making and Breaking, *Chemical reviews* 109(3) (2009) 1346-1370.
- [13] E. Levy, A. Puzenko, U. Kaatz, P.B. Ishai, Y. Feldman, Dielectric spectra broadening as the signature of dipole-matrix interaction. II. Water in ionic solutions, *The Journal of chemical physics* 136(11) (2012) 114503-114503-6.
- [14] P.T. Callaghan, *Translational Dynamics and Magnetic Resonance: Principles of Pulsed Gradient Spin Echo NMR*, OUP Oxford 2011.
- [15] C.P. Poole, H.A. Farach, CHAPTER 20 - Dielectric Relaxation, in: C.P. Poole, H.A. Farach (Eds.), *Relaxation in Magnetic Resonance*, Academic Press 1971, pp. 319-350.
- [16] J.P. Poley, J.J. Nooteboom, P.J. De Waal, Use Of V.h.f Dielectric Measurements For Borehole Formation Analysis, *SPWLA-1986-vXXVIIIn1a4 19(03)* (1978) 35.
- [17] M. Sliwinski-Bartkowiak, J. Gras, R. Sikorski, R. Radhakrishnan, L. Gelb, K.E. Gubbins, Phase Transitions in Pores: Experimental and Simulation Studies of Melting and Freezing, *Langmuir* 15(18) (1999) 6060-6069.
- [18] W.T. Coffey, Dielectric relaxation: an overview, *Journal of Molecular Liquids* 114(1) (2004) 5-25.
- [19] Y. Feldman, A. Puzenko, P. Ben Ishai, A. Gutina Greenbaum, The dielectric response of interfacial water—from the ordered structures to the single hydrated shell, *Colloid and Polymer Science* 292(8) (2014) 1923-1932.
- [20] N. Cassidy, Electrical and magnetic properties of rocks, soils and fluids, *Ground Penetrating Radar* 2009, pp. 41-72.
- [21] T.L. Chelidze, Y. Gueguen, Electrical spectroscopy of porous rocks: a review—I.Theoretical models, *Geophysical Journal International* 137(1) (1999) 1-15.
- [22] S. Havriliak, S. Negami, A complex plane representation of dielectric and mechanical relaxation processes in some polymers, *Polymer* 8 (1967) 161-210.
- [23] W.E. Kenyon, Texture effects on megahertz dielectric properties of calcite rock samples, *Journal of Applied Physics* 55(8) (1984) 3153-3159.
- [24] M.T. Myers, Pore Combination Modeling: A Technique for Modeling the Permeability and Resistivity Properties of Complex Pore Systems, SPE Annual Technical Conference and Exhibition, Society of Petroleum Engineers, Dallas, Texas, 1991, p. 11.
- [25] C.M. Ross, C.A. Callender, J.B. Turbeville, J.J. Funk, Modeling of Capillary Pressure Behavior Using Standard Open Hole Wireline Log Data: Demonstrated on Carbonates from the Middle East, SPE Annual Technical Conference and Exhibition, Society of Petroleum Engineers, Dallas, Texas, 1995, p. 12.

Experimental time-lapse visualization of mud-filtrate invasion and mudcake deposition in complex rocks using X-ray radiography

Pierre Aéréns^{1,*}, Carlos Torres-Verdín¹, and Nicolas Espinoza¹

¹The University of Texas at Austin

Abstract. Accurate description and modeling of multiphase fluid flow is of paramount importance for subsurface resource engineering. The main source of information to quantify *in situ* rock properties are borehole geophysical measurements, which are very often riddled with uncertainty ensuing from both rock heterogeneity/anisotropy and mud-filtrate invasion effects. Therefore, experimental methods are needed to accurately describe and quantify the physics of mud-filtrate invasion and mudcake deposition and its effects on borehole geophysical measurements. We develop a new high-resolution experimental method to investigate the invasion of water- and oil-base drilling muds into air-, brine- or oil-saturated rock samples using X-ray radiography. During mud injection, rock samples are scanned using high-resolution X-ray radiography, enabling the time-lapse visualization of both mud-filtrate invasion and external/internal mudcake deposition. Our experimental method successfully examines the effects of rock heterogeneity, bedding plane orientation, and anisotropy on the spatial distribution of fluids and mudcake formation resulting from mud-filtrate invasion. It also emphasizes the importance of initial fluid saturations and mud properties on the final fluid saturation state once mudcake seals the borehole. The procedure is fast, accurate, and reliable to quantify the process of mud-filtrate invasion at the core scale, enabling improved understanding of invasion effects on borehole geophysical measurements following drilling operations, especially in spatially complex rocks such as laminated sandstones and carbonates.

1 Introduction

Spatially heterogeneous reservoirs continue to be challenging for subsurface energy specialists. Appraisal of petroleum reservoirs and quantification of reserves rely heavily on borehole geophysical measurements, which remain the main source of data from the subsurface. However, borehole geophysical measurements are known to be greatly affected by uncertainty arising from rock heterogeneity and mud-filtrate invasion effects. It is therefore extremely important to properly understand and characterize the physical processes governing mud-filtrate invasion and mudcake deposition, in order to correct for their effects and accurately interpret borehole measurements, especially in heterolithic rocks. Description of multiphase flow in highly heterogeneous rocks during drilling operations requires experimental and numerical methods that integrate all information available on rock formations, *in situ* or drilling fluids, and their interactions. Given that it cannot be measured directly, numerical methods have been developed to estimate the radius of mud-filtrate invasion, from borehole measurements [1]. Unfortunately, these numerical methods remain subject to uncertainty and require comprehensive understanding of the physics of invasion and mudcake deposition, which can only be attained from experimental results.

Mud-filtrate invasion has been the focus of experimental research since the 1930s; numerous researchers have since expanded the scope of this research to include more and more complex cases and mechanisms [2, 3]. However, most of the available technical literature on the subject remains limited to

homogeneous rocks and/or unrealistic rock properties or configurations. At the same time, recent experimental procedures introduced industrial CT scanners to examine more realistic rock and borehole conditions during invasion, and to quantify *in situ* mud-filtrate invasion and mudcake deposition using X-ray computed tomography (CT) [4]. Historically, *in situ* visualization of fluids or flow inside opaque structures, such as rock samples, has been technically challenging. Over time, several methods have been explored and tested to determine *in situ* fluid distributions during coreflooding, including the use of transparent models, electrical resistivity, or nuclear magnetic resonance measurements, with each of these techniques presenting limitations [5]. Nevertheless, none of these methods rival X-ray CT when it comes to providing a fast and accurate measurement of fluid saturations or their spatial distribution. X-ray CT is a powerful tool with a vast range of applications that enables the non-destructive visualization of internal structures within objects. A CT scanner generates detailed three-dimensional (3D) images by relying on the difference in X-ray absorption resulting from the difference in atomic structure (density) of different materials present in the sample. CT imaging in the geosciences has gained considerable attention over the last decades, with modified medical X-ray CT scanners being an integral part of core analysis laboratories around the world. A more recent addition to the list of available tools was the introduction of industrial microfocus X-ray CT scanners, referred to as microCT scanners. Industrial microCT scanners rely on the same physical phenomenon to generate 3D images similar to

* Corresponding author: pierre.aerens@utexas.edu

those delivered by medical CT scanners. However, contrary to medical CT scanners that rotate the X-ray source and detector around the (typically) live specimen being scanned, microCT scanners are built such that the X-ray source (called the X-ray gun) and the detector are fixed, while the sample is placed on a rotating stage. Moreover, microCT scanners can be used at higher powers, hence at greater spatial resolution, because they are not bound by radiation limits [6, 7, 8].

We describe a new experimental procedure to monitor and study mud-filtrate invasion and mudcake deposition under conditions that resemble those typically encountered in a borehole. The experimental system is composed of an X-ray microCT scanner and an automated injection pump, enabling mud injection to take place inside the shielded cabinet of the microCT scanner. Instead of using a traditional cylindrical geometry, rectangular slabs are used to monitor the process of invasion [9]; slab dimensions are such that they can be assumed two-dimensional (2D) because fluid transport within the sample can be considered negligible in the direction perpendicular to its main plane, making the invasion front homogeneous in this direction too. Such a condition makes 2D X-ray radiography viable to monitor the experiment and eliminates the need for micro-computed tomography and data reconstruction. Mud-filtrate invasion takes place when drilling mud is forced into the diffuser at the inlet of the custom-made flow cell while the outlet is vented to atmospheric pressure. During mud injection, the rock core sample is scanned quasi-continuously using high-resolution X-ray radiography to capture and quantify both mud-filtrate invasion and mudcake deposition as a function of time.

2 Materials and methods

This section describes (1) the physics of X-ray CT as well as the imaging technique used during mud injection, (2) the experimental procedure, and finally (3) how the X-ray radiographs were processed to visualize mud-filtrate invasion.

As described above, a microCT scanner produces a spatial distribution of mass density of an object by acquiring 2D X-ray projections (each of them consisting of an X-ray radiography) that are then combined into a 3D image through the mathematical process known as reconstruction. Each X-ray radiography measures X-ray attenuation while X-rays propagate through the sample, with X-ray attenuation being a function of atomic number, density, and X-ray energy [10]. Depending on the energy of X-rays, the physical phenomenon mainly responsible for attenuation will be different: at low X-ray energy, photoelectric absorption is the main contributor to attenuation, whereas at high X-ray energy, Compton scattering (related to electron density) is the predominant effect [11]. Therefore, it is important to reach a sufficient X-ray energy level while scanning rocks saturated with fluids to ensure that X-ray attenuation, hence X-ray imaging, relies on substantial density and atomic number contrasts between the different phases present in the rock (solid and liquids). The 3D image of the sample is generated from the collection of 2D radiography images acquired at different angles through the process of image reconstruction. This computationally expensive mathematical process is the most crucial step for obtaining high-resolution 3D images; various algorithms can

be implemented, each with pros and cons, but all potentially affected by artifacts. Modern measurement techniques, however, help to remove these artifacts almost entirely. Despite the more common use of X-ray CT in the literature, especially in recent mud-filtrate invasion experimental research, some authors have preferred to reduce the scope of their studies to 2D X-ray radiography for a wide range of application. These includes visualization and characterization of multiphase flow [12, 13, 14], gravitational flow of particles [15], and monitoring of the frontal advance of fluids using gravity-led flow [16] or forced imbibition [17].

In our work, we chose to rely only on 2D radiography images, referred to as radiographs, to visualize the complexity/heterogeneity of each sample, and study and quantify mud-filtrate invasion in the pore space as well as mudcake deposition. This choice allows us to circumvent the reconstruction altogether, eliminating the need to correct for mathematical artifacts. Additionally, the flow cell no longer needs to be placed on a rotating stage during mud injection, eliminating challenges associated with the coupling of rotating and stationary elements. Nevertheless, the lack of reconstruction does not only bring about benefits: it also implies that we can only use 2D radiographs to quantify changes as a function of time in the rock sample as mud is being injected. Consequently, instead of using traditional, cylindrical cores, we employ thin rectangular-shaped rock samples. All experiments were carried out using 14 cm-long, 7 cm-wide, 0.6 cm-thick rock slabs. Because the thickness of each slab is one order of magnitude smaller than its width and length, the variability of rock properties perpendicular to the sample can be regarded negligible. For this reason, flow variability across the smallest dimension is considered negligible and the experiment becomes two-dimensional. In the case of laminated clastic rocks, some slabs were cut parallel to bedding planes while others were cut perpendicular to bedding planes, allowing us to study the effects of different heterogeneities on mud-filtrate invasion and mudcake deposition.

Table 1. Summary of petrophysical properties for the rock samples considered in this paper. Porosity was measured using the imbibition method. Permeability is brine permeability, while k_H and k_V refer to permeability parallel and perpendicular to laminations, respectively. The typical core used was approximately 1" in diameter and 5" long. Permeability was also measured using rock slabs. Each range was established using at least three data points.

Rock Core	Porosity	Permeability
ANTOLINI SANDSTONE laminated	11-14%	85-120 mD (k_H) 30-50 mD (k_V)
BEREA SANDSTONE	18-21%	25-80 mD
ESTAILLADES LIMESTONE	25-29%	110-190 mD
GRAY BERA	19-21%	74-78 mD
LEOPARD SANDSTONE	20-21%	160 – 300 mD
NUGGET SANDSTONE laminated	10-12%	55-65 mD (k_H) 0.5-1 mD (k_V)
SILURIAN DOLOMITE	16-17%	0.01-50 mD
UPPER GRAY BERA	20-22%	220-240 mD
“VUGGY” DOLOMITE	10-15%	0.04 mD-10 D

A wide range of rocks were examined for our study, ranging from homogeneous clastic rocks to complex carbonates with dual porosity. **Table 1** summarizes the rock samples used and their measured petrophysical properties. Slab permeability was measured using a probe permeameter. Each rock sample was dried at 100 °C for at least 24 hours prior to being embedded in the flow cell. Then, the sample was either used as is, for injection into air-saturated rocks, or saturated with either mineral oil or brine. The “vuggy” dolomite rock is a dolomite of unknown origin which exhibits zones of very low permeability and large vugs. Traditional, Hassler-type core holders are not suitable for this experimental procedure because they are typically made of stainless steel, a material that would interfere with X-ray attenuation. They are also designed for cylindrical cores in linear flow experiments. Instead, rock samples were embedded in rectangular flow cell made of polycarbonate, a material transparent to X-rays. High-strength epoxy was used to affix the slabs to their respective custom-made flow cells. **Figure 1** shows such a custom-made flow cell inside the microCT scanner cabinet. The flow cell is connected to the injection system that is also placed inside the shielded cabinet and controlled remotely.

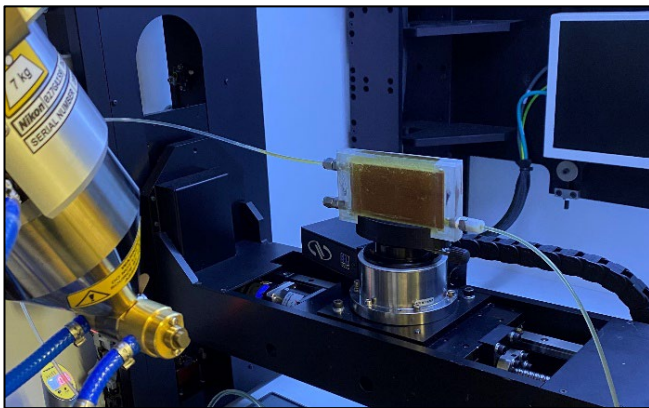


Fig. 1. Flow cell inside the microCT scanner cabinet. The custom-made flow cell is placed on the manipulator, between the X-ray gun (left) and the detector (back). The injection system is not visible on the photograph.

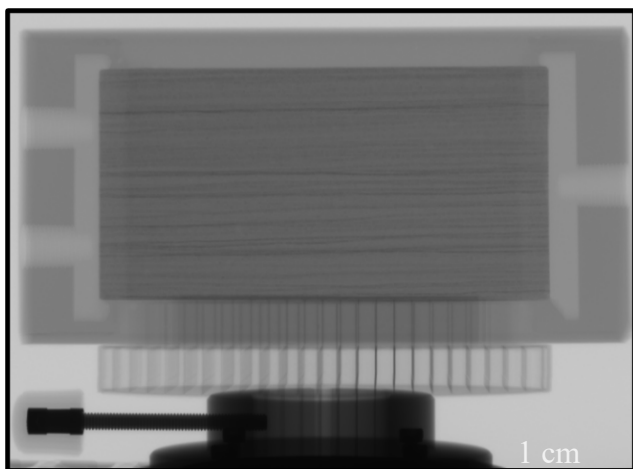


Fig. 2. X-ray radiography of a Nugget sandstone rock slab. The rock core is epoxied inside the polycarbonate frame that was designed for “two-dimensional” coreflood experiments.

Figure 2 shows an X-ray radiography of a Nugget sandstone rock slab epoxied into its plastic flow cell. On this radiograph, one can observe the rock slab itself, the polycarbonate frame (mostly transparent to X-rays, although the difference in plastic thickness is noticeable and the epoxy adds some material on top of the frame), the diffusers on both sides of the core (allowing each core to be used for two injection experiments), and the threaded ports (connections and tubing are not connected to the flow cell on this radiograph). On each end of the flow cell, inlet and outlet ports connect the tubing to diffusers, ensuring both a uniform flow on the surface of the slab and enough room for the mudcake to build up unrestrictedly. One can also observe the manipulator on which the flow cell is placed; the manipulator is used to position the rock sample perpendicularly to the incoming X-ray beam to satisfy the 2D assumption. When initiating an experiment, drilling mud is forced into the diffuser, the filter cake begins to form on the surface of the sample and mud filtrate, which cannot bypass the rock sample due to the epoxy, flows through the rock, invading the pore space. The flow is regarded to take place in the plane of the X-ray radiography.

Figure 3 shows a radiograph of two rock samples cut from the same block: one of the samples with bedding planes parallel to flow while the other exhibits bedding planes perpendicular to flow. By performing experiments with samples cut with laminations/bedding planes parallel and perpendicular to the pressure drop direction, it is possible to quantify the effects of rock anisotropy and heterogeneity on mud-filtrate invasion and mudcake buildup.



Fig. 3. X-ray radiographs of a laminated rock sample cut with bedding planes parallel (left panel) and perpendicular (right panel) to flow, respectively.

A Nikon XT-H 225 ST microCT scanner was used in this study, which includes a 225 kV microfocus source and a reflection target offering a 3 μm X-ray focal spot. Because the objective is to visualize flow at the core scale, and not at the pore scale, scan parameters were carefully selected such that acquisition time (i.e. time resolution) was optimized without affecting image resolution and/or noise. Depending on the rock sample being imaged, we achieved a resolution ranging from 17 to 50 μm. The typical scanning parameters responsible for this result are a beam energy of 110 kV, a beam current of 300 μA, and an exposure time of 708 ms. Copper filters of different thicknesses were employed to counterbalance image brightness resulting from the relatively high exposure time needed to attain acceptable resolution. X-ray radiographs are acquired quasi-continuously as drilling mud is being injected into the rock sample and mudcake is forming on the face of the core. Each pixel in a radiograph is assigned an X-ray attenuation number by the scanner, referred to as a grayscale number, which is related to the

average absorption coefficient of the different materials being imaged. As opposed to computed tomography, there is no automatic flux normalization available when using X-ray radiography. A correction factor is calculated based on grayscale fluctuations in pixels where no change is expected (such as the polycarbonate frame) and used to calibrate for variation of image brightness over time. This setting prevents offsets of grayscale number (due to flux oscillations) from producing non-physical values.

The experimental system, i.e. the X-ray gun, the detector, and the sample, is fully enclosed in a radiation shielding cabinet when the microCT scanner is energized, as per X-ray safety regulations. Therefore, a custom-made syringe pump is used to inject drilling mud into the rock samples; the pump is fully contained within the cabinet, is powered by batteries, and is operated remotely by a microcontroller connected via Bluetooth. Overbalance pressure, injection rate, and injected volume are the three quantities recorded and transmitted in real time to a computer during the experiment. The pressure is measured at the inlet with a high-accuracy pressure transducer. At the beginning of each experiment, drilling mud is injected into the sample by applying a pressure gradient; injection pressure is held constant by means of a proportional-integral-derivative control loop while the outlet is vented to ambient pressure.

Two drilling muds were used in this study: a water-base mud (WBM) and a synthetic oil-base mud (OBM). Both were characterized using API recommended practices; **Table 2** describes their measured properties. To secure an optimal contrast between the different fluid phases when the initial saturating fluid is not air, mineral oil and 30 wt% potassium iodide brine were used to initially saturate the samples with non-wetting and wetting phases, respectively.

Table 2. Summary of fluid properties for water-base mud (WBM) and synthetic oil-base mud (OBM).

Mud Properties	WBM	OBM
Mud specific gravity	1.3532	0.9334
Plastic Viscosity [cP]	24.4	18.9
Yield Point [lb _f /100 ft ²]	19	2.5
Gel Strength (10 sec.) [lb _f /100 ft ²]	2.9	1.8
Gel Strength (10 min.) [lb _f /100 ft ²]	4.3	2.3
API Loss @ 150°F [mL/30 min]	4.1	0.5
API Wet Cake Thickness [1/32 in.]	1.92	2.5
Solid Volume [%]	14	24
Water/Oil Ratio [v/v]	-	0.27

For each experiment, a baseline radiograph is acquired prior to starting the coreflood; at this point of the experiment, the sample is saturated with either a non-wetting phase (air or mineral oil) or a wetting phase (brine) depending on whether WBM or OBM is used, respectively. A second baseline radiograph is acquired after mud is injected to fill up the inlet diffuser, but before the system is pressurized. Baseline scans are used during data processing to make mud-filtrate invasion easily observable. MATLAB® was used to run the post-processing algorithm. Injection of drilling mud begins promptly after the acquisition of the baseline scans. A

pressure differential of 100 psi is applied to the sample by means of the syringe pump. This pressure differential, maintained constant throughout the experiment, induces mudcake formation on the face of the rock slab and mud-filtrate invasion inside the pore space of the sample.

Figure 4 illustrates both the baseline subtraction method and image processing technique with an Upper Gray Berea sample. The top left panel shows the raw radiograph of the baseline, air-saturated sample. One can observe the sample and the inlet diffuser on the left side of the image, filled with air. The radiograph shows a very homogeneous rock, as expected for an Upper Gray Berea. Any apparent heterogeneity is the result of the epoxy, not the sample (more visible on the bottom left panel). The top right panel shows the raw radiograph of the sample after 5.8 minutes of WBM injection at 100 psi overbalance pressure. One can already notice the mudcake deposition on the left face of the sample. It is also possible, albeit difficult, to distinguish a change in grayscale values inside the sample resulting from mud-filtrate invading the pore space and displacing air. The image in the bottom left panel is the heat, or color map of the top right panel, with a custom scale, making it easier to discern the invaded from the virgin zone. Finally, the bottom right panel shows the result of the baseline subtraction algorithm: the air-saturated radiograph (top left panel) is subtracted from the *in situ* scan acquired after 5.8 minutes of injection (top right panel).

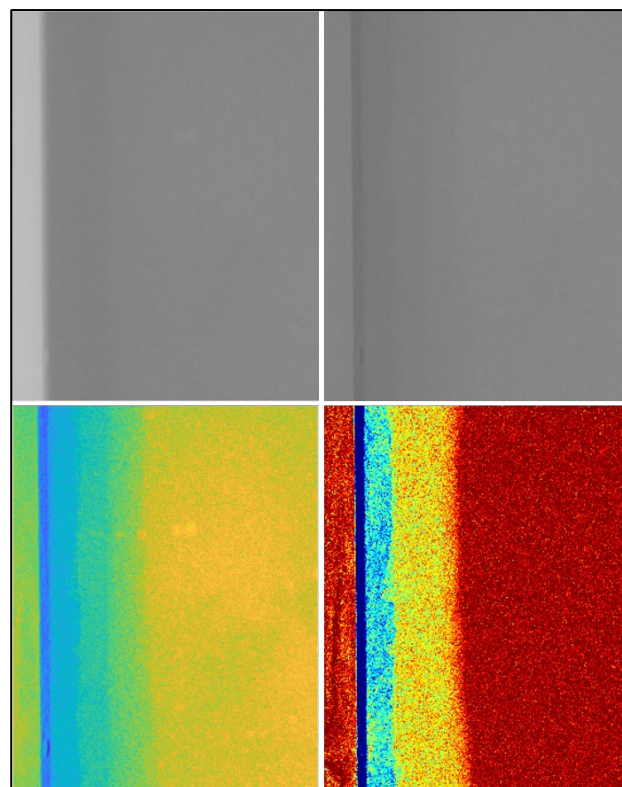


Fig. 4. Example of an WBM injection into an Upper Gray Berea sample illustrating the image processing method. Top left panel shows the baseline scan, acquired when the sample was air saturated. Top right panel shows the sample after 5.8 min of WBM injection at 100 psi overbalance. Bottom left panel shows the same scan with a different grayscale when loaded into MATLAB®. Bottom right picture shows the result of the baseline subtraction for the same time. The width of each image is 35 mm. No filter was applied to the images.

The red parts of the image correspond to zones where no change had occurred at this point in time during the experiment, while other colors, from yellow to dark blue, denote changes with respect to the initial state of the sample. As mudcake is being deposited on the face of the rock slab, the density of this area increases significantly, making it easy to determine its position and thickness. Mud-filtrate invasion inside the pores does not generate such a large density difference compared to the deposition of solid mud particles; therefore, changes with respect to the baseline radiograph are not as intense and shown in yellow in the processed image. This simple difference makes it easy to differentiate between mudcake and invaded zone. In this example, one notices that the invaded-zone color scale varies from yellow (as expected) to blue near the left face, a color that is supposed to indicate mudcake. This behavior is due to the geometry of the sample and how it is embedded in the plastic frame: at such early phase of the flow cell prototype, the rock slab protrudes from the epoxy coat and in the inlet diffuser in a way that makes 3 sides of it to be exposed to fluids in the diffuser (left face, as well as bottom and top face when looking at the image). Therefore, mudcake builds up not only on the left face of the sample, but also on the sides of the slab. However, the deposition is not unobstructed, as it is rapidly contacting the plastic frame, making the blue color on the image less deep than for mudcake building up on the left face of the rock slab. This instrumental drawback was fixed for subsequent cell flow prototypes, making sure that mudcake deposition occurred only on one face of the sample.

Because of the good resolution provided by this imaging method, the stacking of frames performed by the scanner to generate each radiograph (8 frames per image in this paper), and the natural good contrast between air and water-base mud filtrate, the locations of the invaded zone and mudcake are clearly visible in **Fig. 4**. Nevertheless, for other samples, determination of the precise location of the interface between virgin and invaded zones can be difficult because of the combined effects of random instrumental noise and small-scale heterogeneities; such effects are exacerbated by the image subtraction step. A 2D median filter was applied to each radiograph to circumvent the latter problem and improve the location of the invasion front while preserving edges when needed.

3 Results and discussion

This section describes several examples of drilling-mud injection experiments, starting from the simplest case, a homogeneous and isotropic Upper Gray Berea sandstone, to more complex rock samples such as heterogeneous and anisotropic clastic rocks, and highly heterogeneous carbonates. We also stress WBM injection experiments over OBM injection experiments, as the former is generally associated with deeper invasion and thicker mudcake, as expected from previously published studies [4, 18]. Likewise, we emphasize WBM invasion into air saturated samples, i.e., a connate fluid state seldom encountered in practice. The reason behind this choice was to simplify the proof of concept, as the density contrast between both types of drilling mud and air enables an easy observation of density variations within the flow cell (both inside the rock and in the diffuser).

As explained in the previous section, a 2D median filter was applied to every radiograph for all experiments; the filter is the same across all cases to facilitate image comparison. The spatial resolution and image length (i.e. in the direction of flow) are also consistent across all experiments described in this paper and equal to 29 microns and 35 millimeters, respectively. Drilling mud was injected at 100 psi overbalance for all experiments, and pump measurements (i.e. pressure, injected volume, and rate of injection) were recorded every 100 milliseconds.

Figure 5 shows the time-lapse mud-filtrate invasion and concurrent mudcake deposition of the same Upper Gray Berea experiment examined in the previous section. However, contrary to **Fig. 4**, a filter was applied in **Fig. 5**, making its effects on the data more conspicuous. The order of panels is from left to right, and top to bottom. Radiographs shown in **Fig. 5** were acquired after 0.5, 1, 3, 7, 32 and 75 min of WBM injection into the air-saturated sample. Upper Gray Berea is a very homogeneous, isotropic, and high permeability clastic rock; therefore, the observed front is almost vertical, and the displacement front is quasi piston-like, consistent with the Buckley-Leverett theory [19]. Such a behavior also explains why the invading front reaches the outer right edge of the image, indicating that the entire area displayed in the images has been invaded with drilling mud at approximately 75 minutes after the onset of the experiment. Nevertheless, one should note that the area displayed in **Fig. 5** does not correspond to the entirety of the sample: processed images were cropped to focus on the most relevant zones, and mud filtrate did not reach the other boundary of the rock slab.

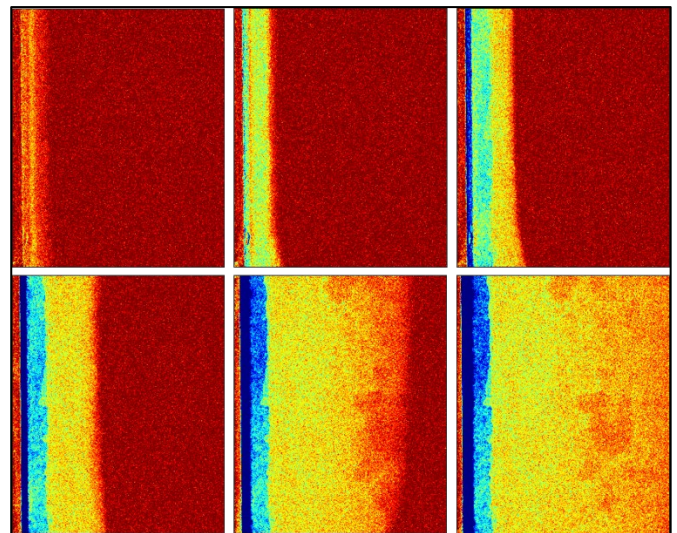


Fig. 5. WBM injection into an Upper Gray Berea sandstone sample. Each panel (from left to right and top to bottom) represents a radiograph acquired after 0.5, 1, 3, 7, 32 and 75 min of WBM injection into the air-saturated sample, respectively. The last radiograph was acquired at the time the saturation front reached the right edge of the image. Image width is 35 mm.

Figure 6 shows the mud-filtrate volume loss, i.e. invasion volume, as a function of time for both WBM and OBM injection into a Leopard sandstone core. The WBM injection experiment was carried out first on one side of the rock slab and, upon completion, OBM injection was initiated using the other side of the flow cell. The right panel shows the invasion volume in milliliters plotted against elapsed time in minutes,

while the left panel describes the same invasion volume, but plotted against the square-root of elapsed time. Plotting the mud-filtrate injected volume versus square-root of elapsed time is the standard approach to describing filtrate invasion data; obtaining a quasi-linear trend in the square-root of time domain is consistent with the filtration theory that governs the mud-filtrate invasion process [20]. The instantaneous volume of mud (filtrate and suspended particles) that flowed unobstructed at the beginning of both experiments before filter cake was formed, referred to as spurt loss, is visible on the left plot for both injections. This spurt effect is eliminated from the second plot by shifting the data in time before applying the square root.

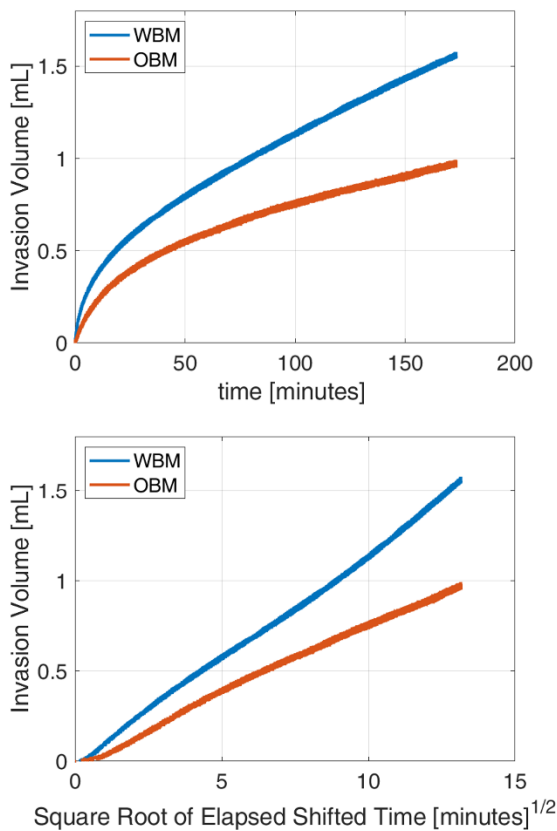


Fig. 6. Volume vs. time (top panel) and volume vs. square root of time (bottom panel) for an injection experiment into a Leopard sandstone sample using WBM and OBM.

As shown in **Fig. 6**, OBM injection is associated with a smaller cumulative mud-filtrate loss compared to WBM injection. However, the difference is not as large as expected, given previously reported results [4, 18], and field knowledge. The geometry of the sample might play an important role in this outcome and the geometrical factor should be investigated further.

Cases of application highlighted in this paper so far have been examples of homogeneous rocks. From this point onward, attention is switched to heterogeneous and anisotropic rocks, starting with a Nugget sandstone sample, i.e., a finely laminated clastic rock. **Figure 7** shows the time-lapse mud-filtrate invasion and concurrent mudcake deposition of the Nugget sandstone experiment. The sample was cut so that bedding planes were parallel to the flow direction. As opposed to **Fig. 5**, the first panel (top left) shows the radiograph of the dry sample in order to facilitate the

visual comparison of sample heterogeneity and the ensuing spatial distribution of fluids. The same format is adopted for all the subsequent figures. The next five panels shown in **Fig. 7** describe radiographs acquired after 1, 7, 14, 60 and 142 min of WBM injection into the air-saturated sample, respectively. Another notable difference with the previous example is the way in which the rock slab was embedded inside the plastic flow cell: instead of contacting different slab surfaces, the mud only contacts the left surface of the sample because of the slightly different design, making it impossible for mudcake to form anywhere else. The location of mudcake is therefore easier to determine compared to **Fig. 5**, and the 2D nature of the experiment is no longer affected by mudcake deposition outside of the plane of the sample. From the time-lapse radiographs, we observe that the evolution of the invasion front is not piston-like anymore and remains highly influenced by the thin laminations present in the sample. Despite some crossflow occurring during injection, the invasion front becomes more and more irregular as additional mud is injected into the sample, while the thickness of the mudcake is not constant along the direction perpendicular to flow.

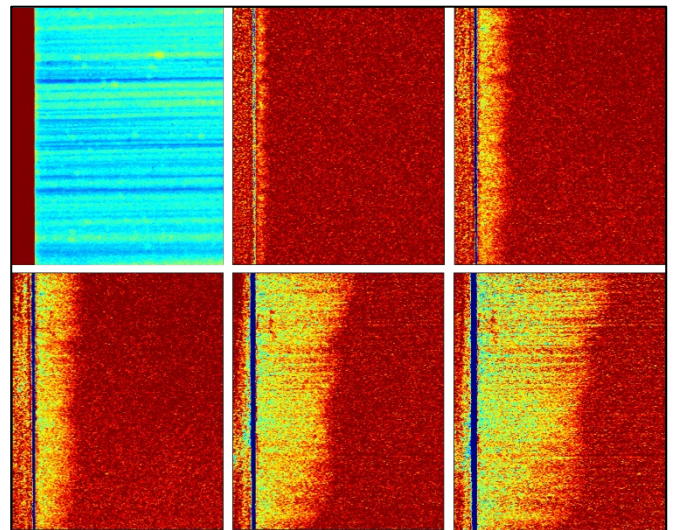


Fig. 7. WBM injection into a Nugget sandstone sample. The first (top left) panel is a grayscale map (with enhanced colors) of the sample, showcasing the heterogeneity of the rock sample. Each subsequent panel (from left to right and top to bottom) represents a radiograph acquired after 1, 7, 14, 60 and 142 min of WBM injection into the air-saturated sample, respectively. Image width is 35 mm.

Figure 8 shows the time-lapse mud-filtrate invasion and concurrent mudcake deposition for an Antolini sandstone experiment. In this experiment, the rock slab was also cut such that the laminations were parallel to the flow direction. As mentioned above, the first panel shows the grayscale map of the sample. Notice from the grayscale map that the round feature present is not a rock feature, but an air bubble trapped in epoxy. This situation does not affect the baseline subtraction results, as the bubble is present in every radiograph and is subtracted out in the process. The next five panels show time-lapse radiographs acquired after 1, 6, 16, 27 and 62 min of WBM injection into the air-saturated sample, respectively. Even when the Nugget and the Antolini sandstones can both be described as laminated clastic rocks the thickness of their laminations is different. Contrary to the

previous example that featured a thinly laminated Nugget sandstone, the Antolini sandstone exhibits thicker layers, each consisting of different petrophysical properties, while crossflow only takes place at the edges of these layers. One can notice that the unevenness of the invasion front at early times of injection is progressively leveled out, thanks to both crossflow and the smaller sample anisotropy compared to the Nugget sandstone. This observation correlates well with the information of **Table 1**, which indicates that the permeability of Antolini sandstone perpendicular to laminations (i.e. the “perpendicular” permeability) is only half the value of the “parallel” permeability, whereas the “perpendicular” permeability of the Nugget sandstone is one order of magnitude smaller than its “parallel” permeability. Finally, one can readily correlate the higher permeability streaks with the thickness of mudcake.

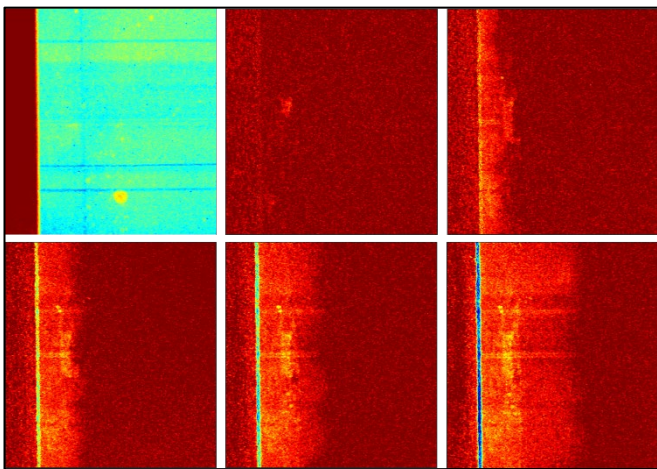


Fig. 8. WBM injection into a Antolini sandstone sample, with laminations parallel to the flow direction. The first panel is a grayscale map (with enhanced colors) of the sample, showcasing the heterogeneity of the rock sample. Each subsequent panel (from left to right and top to bottom) represents a radiograph acquired after 1, 6, 16, 27 and 62 min of WBM injection into the air-saturated sample, respectively. Image width is 35 mm.

Figure 9 shows the time-lapse mud-filtrate invasion and concurrent mudcake deposition for an Antolini sandstone experiment. In this experiment, the rock slab was cut such that the laminations were perpendicular to flow, and the rock sample was cored out of the same block as the sample described in **Fig. 8**. Once again, the first panel shows the grayscale map of the sample while the next five panels correspond to time-lapse radiographs acquired after 1, 6, 20, 97 and 300 min of WBM injection into the air-saturated sample, respectively. As expected, given the constant overbalance pressure applied to the sample for all experiments, it takes a longer injection time to reach approximately the same length of invasion compared to the previous example, due to the lower permeability of the sample with laminations perpendicular to the flow direction. The invasion front is also expected to be more uniform and approaching a piston-like displacement. However, such is not the case for this example, as mud filtrate bypasses low-permeability layers because the latter layers are not continuous across the sample. This behavior takes place in areas of the rock sample that are outside the zone of interest shown in the images. It becomes conspicuous in the last two

panels, showing changes with respect to the baseline scan ahead of the main front (a behavior also well represented in the last two cases examined in this paper, showcasing carbonate rocks). Apart from this observation, mudcake deposition is very uniform in **Fig. 9**.

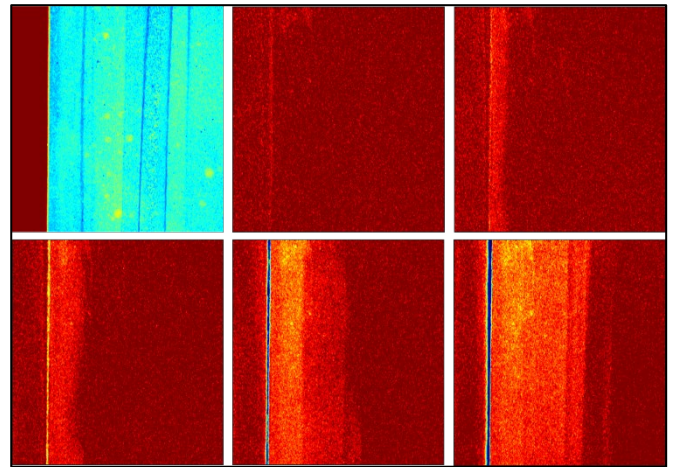


Fig. 9. WBM injection into a Antolini sandstone sample, with laminations perpendicular to the flow direction. The first panel is a grayscale map (with enhanced colors) of the sample, showcasing the heterogeneity of the rock sample. Each subsequent panel (from left to right and top to bottom) represents a radiograph acquired after 1, 6, 20, 97 and 300 min of WBM injection into the air-saturated sample, respectively. Image width is 35 mm.

Figure 10 shows the time-lapse mud-filtrate invasion and concurrent mudcake deposition for a “Vuggy” dolomite sample. The sample is of unknown origin and exhibits relatively large vugs, spanning from a few millimeters to the centimeter scale. The top left panel shows the grayscale map of the sample, where the vug structure is highlighted.

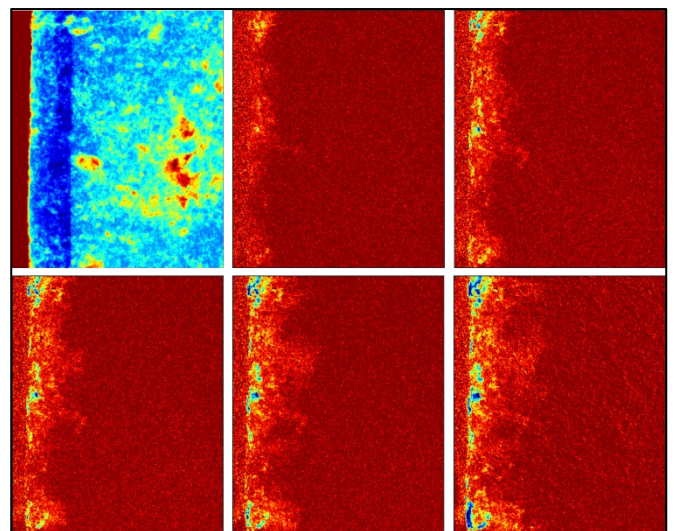


Fig. 10. WBM injection into a “Vuggy” Dolomite sample. The first panel is a grayscale map (with enhanced colors) showcasing the heterogeneity of the rock sample. Each subsequent panel (from left to right and top to bottom) represents a radiograph acquired after 1, 5, 8, 16 and 72 min of WBM injection into the air-saturated sample, respectively. Image width is 35 mm.

It should be noted that, because of the way the sample was epoxied inside the plastic frame, some vugs might be filled with resin, making them impermeable to any fluid. It is

difficult to assess beforehand the effect of epoxy on the sample, especially in vuggy carbonates. However, by monitoring the change in density with respect to the baseline and recording the volume injected as a function of time, we are able to describe fluid flow in vuggy carbonates as shown in this example and the next one. The next five panels of **Fig. 10** show time-lapse radiographs acquired after 1, 5, 8, 16 and 72 min of WBM injection into the air-saturated sample, respectively. As expected for a carbonate sample, some parts of the core are virtually impermeable to flow at this pressure, and mudcake cannot be deposited uniformly on the face of the slab. Mudcake deposition and mud-filtrate invasion occur only within segments of the sample that are permeable, i.e., in vugs. Contrary to previous examples, internal mudcake deposition is evident in this case. External mudcake is also discontinuous and the depth of invasion is significantly smaller than in clastic rocks. This behavior is attributed to the fact that existing pores are not well connected, and mud filtrate must fill internal vugs before invading the next section of the sample. Finally, the change of density with respect to the baseline scan is smaller compared to previous cases, hence the darker, reddish tinge of the “area of invasion”, compared to the more yellowish ones present in clastic rock samples.

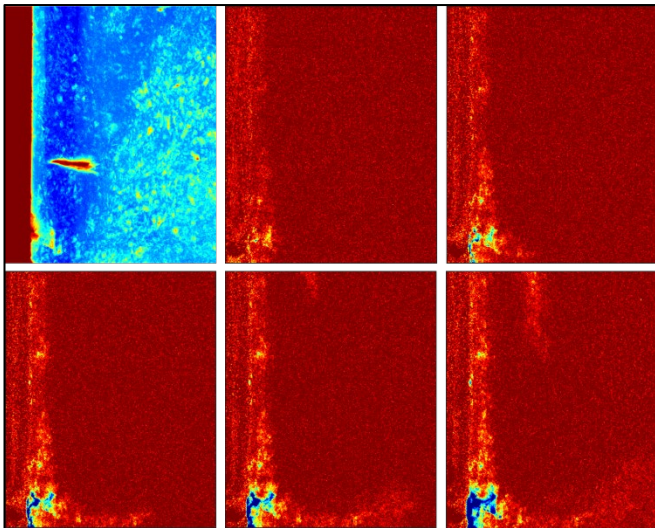


Fig. 11. WBM injection into a Silurian Dolomite sample. The first panel is a grayscale map (with enhanced colors) showcasing the heterogeneity of the rock sample. Each subsequent panel (from left to right and top to bottom) represents a radiograph acquired after 1, 5, 8, 17 and 68 min of WBM injection into the air-saturated sample, respectively. Image width is 35 mm.

Figure 11 describes the time-lapse mud-filtrate invasion and concurrent mudcake deposition for a Silurian dolomite experiment. This carbonate sample also exhibits vugs, but in a smaller extent compared to the previous case. Once again, the top left panel shows the grayscale map of the sample, where the vug system is visible. The next five panels of **Fig. 11** show time-lapse radiographs acquired after 1, 5, 8, 17 and 68 min of WBM injection into the air-saturated sample, respectively. Very similarly to the “Vuggy” dolomite sample, most of the mud-filtrate invasion and mudcake deposition take place where vugs are present. However, contrary to the previous example, most of the borehole face is impermeable and the vast majority of the invasion processes, including the

formation of external and internal mudcake, take place at the bottom of the image, where a substantial vug is present. Nevertheless, it can be noticed that some mud-filtrate invasion occurs at late times at the top of the radiographs too, following a permeable streak present in the rock. This behavior originates from the presence of a very similar vug located just above the window of interest displayed in **Fig. 11**, allowing for mudcake formation and mud-filtrate invasion to take place.

4 Summary and conclusions

We developed and verified a new high-resolution imaging technique to evaluate mud-filtrate invasion and mudcake deposition using “two-dimensional” injection experiments and X-ray radiography. The relevance of the experimental method was tested using a wide range of rock samples, from homogeneous clastic rocks to spatially complex carbonates exhibiting dual porosity. Injection experiments were performed using rectangular rock samples, an automated drilling mud injection system, and a microCT scanner. Water- and oil-base drilling muds were injected using a custom-made polycarbonate flow cell at a constant inlet pressure while the cores were quasi-continuously scanned using high-resolution X-ray radiography. Because rock slabs have a width one order of magnitude smaller than the remaining two dimensions, all invasion processes are regarded as two-dimensional and only X-ray radiographs are used to monitor them. By using reference radiographs acquired before mud pressurization, mud-filtrate invasion and mudcake deposition on the borehole wall were examined as a function of time and the effects of different rock heterogeneities on mud-filtrate invasion and mudcake formation were examined in detail.

Experimental results confirmed that 2D imaging using a microCT scanner enables the *in situ* visualization of the space-time distributions of (1) mud filtrate and (2) external and internal mudcake deposition, as already described for coreflood experiments of immiscible fluids in Aérens et al. [21]. Estimation of the time-lapse precise position and, more importantly, shape of the interface between the virgin zone and the mud-filtrate invaded zone is one, if not the most crucial contribution of this experimental method, along with the *in situ* measurement of mudcake buildup. Contrary to two-phase coreflood experiments, it is not possible to reach a state where the pore space has been mostly swept by mud filtrate (i.e., saturation of connate fluids approaches residual saturation), due to the very low permeability of mudcake and, therefore, the very low associated flow rate. This behavior means that explicit saturations cannot be directly calculated from the radiographs. However, the interface between mud filtrate and saturating fluids, and the 2D area corresponding to the invaded zone are both measurable physical quantities. Results are consistent with the theory of mud-filtrate invasion into porous rocks: injection of WBM results in longer mudcake deposition period, thicker mudcake, and higher filtrate invasion volume when compared to OBM. Our method yields a spatial resolution up to one order of magnitude higher than methods involving traditional medical X-ray scanners (conventional medical CT scanners have a resolution of 0.5 to 1 mm for decimeter-scale samples while micro-focus scanners have a resolution of approximately a

few tens of microns for centimeter-scale samples) and enables a better time resolution than with computed tomography experiments. Finally, data processing for this new method is also faster than with traditional CT scanners due to the lack of an image reconstruction step.

Furthermore, our experimental data unveil the strong correlation between the spatial distribution of mud filtrate (and mudcake deposition) and rock heterogeneity. Results indicate that spatial heterogeneity and anisotropy in both clastic and carbonate rocks remarkably influence the spatial distribution of fluids in the pore space and indicate that rock transmissibility has a significant impact on fluid-saturation distribution at high injection volumes. At early times of injection, mud filtrate preferentially follows higher permeability/porosity layers or veins. However, heterogeneous fluid distributions become homogenized as additional mud is injected when vertical transmissibility is significant, i.e., mainly in clastic laminated rocks. In the case of vuggy carbonates, lack of vertical transmissibility prevents this homogenization process to take place, leading to very “patchy” spatial distributions of filtrate, even at late times of injection. The latter observation has important consequences in the interpretation of borehole geophysical measurements is affected by the spatial distribution of fluids around the wellbore. More notably, results provide guidance to estimate fluid saturation from resistivity measurements acquired in spatially complex rocks.

Finally, our results show noteworthy differences in the invasion process whether water-based or oil-base mud is employed during drilling; differences are observed for mud-filtrate invasion in the pore space itself but also during mudcake deposition on the borehole wall. Results agree with field and previously reported laboratory observations: mudcake thickness and mud-filtrate volume loss are consistently higher in WBM experiments compared to OBM experiments. The peculiar geometry of the rock samples examined in this paper also enables the study of the effect of anisotropy on invasion processes by cutting rock slabs parallel and perpendicular to laminations. Overall, our method is fast and reliable to assess the influence of rock heterogeneity, anisotropy, and more generally, rock and fluid properties on mud-filtrate invasion and mudcake deposition.

We restate that the work reported in this paper emphasized WBM injection into air-saturated samples to streamline the validation and verification of the experimental methods. Future work includes performing additional experiments on spatially complex rocks to scrutinize the effect of different connate fluids on the final state of the rock sample and increasing overbalance pressures to bring this experimental procedure closer to field conditions.

Acknowledgements

The work reported in this paper was funded by The University of Texas at Austin’s Research Consortium on Formation Evaluation, jointly sponsored by Anadarko, Aramco, Baker Hughes, BHP, BP, Chevron, China Oilfield Services Limited, CNOOC International, ConocoPhillips, DEA, Eni, Equinor ASA, ExxonMobil, Halliburton, INPEX, Lundin Norway, Occidental, Oil Search, Petrobras, Repsol, Schlumberger, Shell, Southwestern, Total, Wintershall Dea, and Woodside Petroleum Limited.

X-ray scanning was performed at the Chevron Digital Petrophysics Laboratory (Hildebrand Department of Petroleum and Geosystems Engineering at The University of Texas at Austin).

List of Acronyms

CT	Computed Tomography
microCT	microfocus computed tomography
2D	two-dimensional
3D	three-dimensional
WBM	water-base mud
OBM	synthetic oil-base mud
MICP	Mercury Intrusion Capillary Pressure
NMR	Nuclear Magnetic Resonance

References

1. B. Voss, C. Torres-Verdín, A. Gandhi, G. Alabi, M. Lemkecher. *Common stratigraphic framework to simulate well logs and to cross-validate static and dynamic petrophysical interpretations*. Paper presented at the 50th SPWLA Symposium. (2009)
2. P. Jones, E. Babson, *Evaluation of rotary-drilling muds*, Drilling and Production Practice, pp. 22-33. (1935)
3. M. Chenevert, J Dewan. *A model for filtration of water-base mud during drilling: determination of mudcake parameters*. *Petrophysics*, **42**(03): 237-250. (2001)
4. C. Schroeder, C. Torres-Verdín. *Experimental Method for Time-Lapse Micro-CT Imaging of Mud-Filtrate Invasion and Mudcake Deposition*. *Petrophysics*, **60**(05): 620-630. <https://doi.org/10.30632/PJV60N5-2019a6>. (2019)
5. M. Honarpour, F. Koederitz, A. Herbert. *Relative Permeability of Petroleum Reservoirs*. Boca Raton, Florida: CRC Press. (1986)
6. S. Wellington, H. Vinegar. *X-Ray Computerized Tomography*. *J. Pet. Technol.*, **39**(08): 885–898. <https://doi.org/10.2118/16983-PA>. (1987)
7. R. Ketcham, W. Carlson. *Acquisition, Optimization and Interpretation of X-Ray Computed Tomographic Imagery: Applications to the Geosciences*. *Comp. & Geosc.*, **27**(04): 381-400. [https://doi.org/10.1016/S0098-3004\(00\)00116-3](https://doi.org/10.1016/S0098-3004(00)00116-3). (2001)
8. D. Wildenschild, A. Sheppard. *X-Ray Imaging and Analysis Techniques for Quantifying Pore-Scale Structure and Processes in Subsurface Porous Medium Systems*. *Advances in Water Resources*, **51**: 217-246. <https://doi.org/10.1016/j.advwatres.2012.07.018>. (2013)
9. J. Luo, D. Espinoza, Q. Nguyen. *X-Ray Micro-Focus Monitoring of Water Alternating Gas Injection in Heterogeneous Formations*. Paper presented at the SPE Impr. Oil Recov. Conference. <https://doi.org/10.2118/190223-MS>. (2018)
10. R. Ketcham, G. Iturrino, *Nondestructive High-Resolution Visualization and Measurement of Anisotropic Effective Porosity in Complex Lithologies Using High-Resolution X-Ray Computed Tomography*.

- Journal of Hydrology, **302**(1-4): 92-106. (2005).
<https://doi.org/10.1016/j.jhydrol.2004.06.037>.
11. J. Hsieh, *Computed Tomography: Principles, Design, Artifacts, and Recent Advances*. Bellingham, Washington: SPIE Press (2003)
 12. T. Heindel, J. Gray, T. Jensen, *An X-ray System for Visualizing Fluid Flows*. Flow Meas. Instr., **19**(2): 67–78.[\(2008\)](http://dx.doi.org/10.1016/i.flowmeasinst.2007.09.003)
 13. T. Heindel, *A Review of X-Ray Flow Visualization with Applications to Multiphase Flows*. J. Fl. Eng., **133**(7): 074001. <https://doi.org/10.1115/1.4004367>. (2011)
 14. A. Skauge, P. Ormehaug, T. Gurholt, B. Vik, I. Bondino, I., G. Hamon. *2-D Visualisation of Unstable Waterflood and Polymer Flood for Displacement of Heavy Oil*. Paper presented at the SPE Improved Oil Recovery Symposium. <https://doi.org/10.2118/154292-MS>. (2012)
 15. A. Romanowski, P. Luczak, K. Grudzien, *X-ray Imaging Analysis of Silo Flow Parameters Based on Trace Particles Using Targeted Crowdsourcing*. Sensors, **19**(15): 3317. <http://dx.doi.org/10.3390/s19153317>. (2019)
 16. V. Cnudde, M. Dierick, J. Vlassenbroeck, B. Masschaele, E. Lehmann, P. Jacobs, L. Van Hoorebeke. *High-speed Neutron Radiography for Monitoring the Water Absorption by Capillarity in Porous Materials*. Nuclear Instruments & Methods in Physics, **266**(1):155–163.<https://doi.org/10.1016/j.nimb.2007.10.030>. (2008)
 17. M. Zambrano, F. Hammed, K. Anders, L. Mancini, E. Tondi. *Implementation of Dynamic Neutron Radiography and Integrated X-Ray and Neutron Tomography in Porous Carbonate Reservoir Rocks*. Frontiers in Earth Science, **7**:329.<https://doi.org/10.3389/feart.2019.00329>. (2019)
 18. C. Schroeder, C. Torres-Verdín. *In-Situ Visualization and Characterization of Filter-Cake Deposition Using Time-Lapse Micro-CT Imaging*. Petrophysics, **63**(02): 199-217. <https://doi.org/10.30632/PJV63N2-2022a4>. (2022)
 19. S. Buckley, M. Leverett. *Mechanism of Fluid Displacement in Sands*. Trans. of the SPE, **146**, Part I, 107-116. <https://doi.org/10.2118/942107-G>. (1942)
 20. W. Chin. *Formation Invasion: With Applications to Measurement-While-Drilling, Time-Lapse Analysis, and Formation Damage*. Gulf Professional Publishing. (1995)
 21. P. Aérens, C. Torres- Verdín, N. Espinoza. *Experimental Investigation of Two-Phase Flow Properties of Heterogeneous Rocks for Advanced Formation Evaluation*. Paper presented at the SPE ATCE conference <https://doi.org/10.2118/206334-MS>. (2021)

Causal protocols to assess the viability of native state or restored state preparation

Jules Reed^{1}, Stefano Pruno², Izaskun Zubizarreta³ and Rolf Johansen⁴*

¹Premier Oilfield Group, Aberdeen, Scotland

²Stratum Reservoir (Norway) AS, Stavanger, Norway

³Indar Ltd, Aberdeen, Scotland

⁴Stratum Reservoir (Norway) AS, Trondheim, Norway

Abstract. Wettability is the fundamental attribute controlling reservoir rock-fluid properties such as capillary pressure and relative permeability. It is essential that a core study wettability represents the reservoir wettability and thus, one must decide whether native state or restored state analysis should be employed. There remains debate in our industry regarding which of these conditions should be more representative: some preferring native state (as recommended by Anderson's pivotal literature survey), whilst others favour the control and repeatability of restored state procedures. Recent increased use of wettability-altering mud additives, such as; asphaltic bridging agents, emulsifying agents, surfactants, etc., does not automatically preclude native state analysis, but inevitably complicates the process. Some consider native state analysis to be a simpler experimental method, assuming representative conditions and directly employing "as-received" core samples. However, "as-received" wettability and saturation may be altered during coring, wellsite core handling and laboratory processes, thus preventing native state analyses. If determining to employ native state core analysis, it is paramount, at an early stage in the program, to assess the impact of possible changes during coring through to laboratory processes; considering aspects such as: core damage, potential invasion of mud additives, saturation hysteresis, compositional change of the reservoir fluids, experimental conditions, laboratory methodologies, etc. In this paper, we show that rigorous native and restored state processes can give equally viable data and provide a suggested decision tree to guide considerations regarding the use of native or restored state analyses.

1 Introduction

Wettability is a fundamental attribute controlling reservoir rock-fluid properties such as capillary pressure and relative permeability [1-8]. Representative reservoir wettability is thus essential when performing most multi-fluid special core analysis experiments, such as: wettability, capillary pressure, core resistivity, relative permeability, etc. There are three main test states commonly used to represent wetting conditions for advanced core analyses: native (or alternatives), clean, and restored state. It is essential to be able to perform analyses under either one or all these conditions and understand when each may best represent the reservoir being studied.

It is important, early in this paper, to define "native state", because there are a few different terms with similar but slightly variant meaning: fresh, native and "as-received". This paper will employ the term "native" to describe the general state where it is deemed that the innate reservoir wettability has been sufficiently maintained in the core plugs until the point of testing, as defined by Anderson [3].

Anderson [3] provides more information about native state coring, core packing and preservation. He recognised, from the coring procedures and fluids of the time, that the biggest challenge to native state, without altering wettability or saturation, was during the trip to surface. The changes in pressure and temperature during the process of bringing core to surface can alter the composition and saturation of pore filling fluids: light-end oil components (gas) can liberate from the oil phase causing alteration of the reservoir oil composition; gas components may be lost from the system; gas movement will cause saturation redistribution, potentially of both water and oil, leading to uncertainties in the composition, saturation and rock-fluid contacts of pore filling fluids; heavy oil components (asphaltenes) may deposit; waxes may form; salt may precipitate from the water; solubility of wettability altering components may be changed, leading to both fluid-fluid and fluid-rock reassociations of those chemicals. In summary, any of these possible changes may alter authentic wettability.

There thus remains some debate on whether native state or restored state best represents original reservoir wettability, especially for liquid hydrocarbon reservoirs.

* Corresponding author: jules.reed@pofg.com

Native state core material, fundamentally, must maintain the original (native), yet most often unknown, reservoir wettability. It also should maintain fluid saturations from the reservoir depth to surface to laboratory, and ensure that those fluids are free from precipitates and/or contaminants, since these would be non-native and may influence results. In reality, change is difficult to avoid and many, if not all, fluids within received cores may have been altered.

Results of several cleaning pre-studies performed in recent years, indicated that oil-based mud invasion had irreversibly altered wettability, creating strongly oil-wet core material. Cleaning did not render these plugs water-wet (see Figure 1). Many samples continued to exhibit strong oil wettability, even after employing alternative cleaning methods and solvent mixes. For some cases where water-wet state was achieved, the core mineralogy and pore structure were altered or damaged by the cleaning/drying process and became unrepresentative of reservoir petrophysical properties. Consequently, there may be high uncertainty of achieving representative reservoir wettability by later restoration ageing protocols and neither native nor restored state analyses would be viable. So, to minimise contamination and alteration, it is strongly advocated to use low invasion protocols for all coring operations. **Note:** Some rocks contain structural organic matter such as coal or pyrobitumen, and would not be expected to achieve water-wetness. Thus, rock compositional analysis is a vital step to aid understanding of the wetting complex to support design of appropriate preparation procedures.

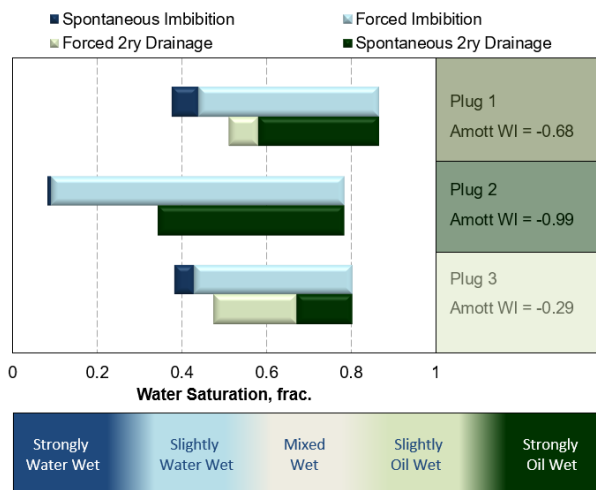


Figure 1. Clean state plugs showing oil-wetness (Mud-invaded)

A summary of wettability data from a North African Field is shown in Figure 2 - Amott wetting index versus permeability. Restored state (RS) plugs exhibited mixed wet results across the entire permeability range (ca. 100 to 2000 mD). The native state (NS) plugs with a similar permeability range, showed similar wetting indices, except a low permeability outlier (20 mD). The invaded plugs (INV) exhibit evidently more oil-wet results.

A low invasion coring program can be designed to reduce some of the changes by controlling the trip to surface rate thus minimising gas liberation rates and

excessive expulsion of fluids, but generally, some alteration is unavoidable. Therefore, it is not a given that “as-received” samples may be considered to represent the native reservoir wettability, saturation or properties. If either wettability has altered or fluid saturations have changed, the core cannot be considered native state, nor fresh state, and using such samples as-received, could produce incorrect and misleading results.

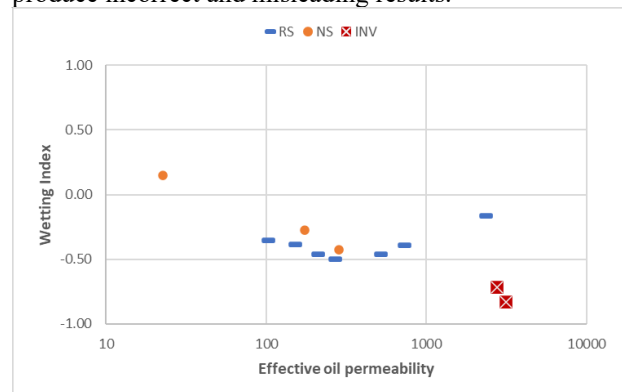


Figure 2: Amott wetting index as a function of permeability

As a case in point, Table 1 shows data from a core plug used for an as-received wettability study, with no pre-test preparation. The core had been acquired using water-based mud (WBM). Initially, Amott wettability results suggested a slightly oil-wet nature (Amott index = -0.121) but upon back-calculating initial water saturation ($S_{wi} = 0.557$) from final saturation checks and production volumes, it was realised that it did not compare to other saturation datasets (capillary pressure and well log data). After cleaning and establishing representative S_{wi} using relevant capillary pressure (P_c), from height above free water level (HAFWL) data, a corrected Amott index was calculated to be +0.253 (slightly water-wet). It was concluded that 32.3 saturation units (s.u.) of water mud filtrate had spontaneously imbibed before laboratory tests were initiated; during coring, wellsite core handling and shipment to the laboratory. This implies that core may not be merely used as-received but, to regard received core as native state, requires consideration of potential fluid changes and may need procedures to check and verify that connate saturations are present or can be re-established without significant hysteresis.

Table 1. Potential error in assuming as-received = native

Stage	As-Received	Corrected
Swi	0.557	0.234
Amott Imbibition Sw	0.634	0.634
Centrifuge Imbibition Swf	0.746	0.746
Spontaneous imbibition	0.077	0.4
Forced imbibition	0.112	0.112
Iw	0.407	0.781
Amott 2nd Drainage Sw	0.523	0.523
Centrifuge 2nd Drainage Swr	0.324	0.324
Spontaneous 2nd drainage	0.223	0.223
Forced 2nd drainage	0.199	0.199
Io	0.528	0.528
Amott Index	-0.121	0.253

Subsequently, the main requirements for ensuring representative native state core plugs would be:

unaltered wettability, unchanged saturation, no contamination and no change to fluid composition.

In contrast, Anderson [3] describes restored state core as a three-step process: cleaning, saturation with brine then oil, and ageing. Restored state procedures must: remove the connate fluids, precipitated solids and any invaded contaminants, whilst maintaining sample integrity (particularly clay/mineral structures) and without altering the capacity of pore-lining surfaces to associate with the correct fluid components that were involved in the in-situ wettability. The restoration process must then replace fluids: first, with a representative formation water, then re-introducing hydrocarbon to re-establish correct connate saturations at the equivalent pressure for HAFWL, and finally, restore the original reservoir wettability by ageing with representative reservoir oil under correct reservoir pressure and temperature. This assumes that the reservoir history is mimicked in this laboratory processes. So, designing a suitable procedure will benefit significantly from cross-disciplinary discussions to understand the history of the reservoir in question. General reservoir theory considers most reservoirs to have formed by deposition in a water-filled environment, thus being water-wet prior to the migration of oil into the system (primary drainage). Hence, it is largely accepted that cleaning should create water-wet conditions, except where naturally oil-wet matrix components may be present, e.g. organic material, chamosite, halite, etc. (note: this list is not exhaustive).

Preparation criteria are also important for digital rock properties (DRP), particularly when performing multi-phase corefloods on micro-plugs. Lin et al [9] stated the need for best practice preparation to initiate wettability, recommending a centrifuge method for establishing initial water saturation in a restored state protocol. Also, it must be noted that information gained from DRP show wettability to be more complex than is commonly understood, variable within a pore space and thus, a core plug merely captures an average of all the varying wetting states with the plug porosity.

2 Coring and Wellsite Core Handling

2.1 Native Wettability

It is well documented and accepted that oil-based mud (OBM) filtrates can alter wettability upon invasion into the reservoir pore system [2,10,11,12]. However, employing a low invasion OBM coring procedure could enable core acquisition with minimal or limited invasion [7,13,14,15]. Invasion is controlled by aspects like coring overbalance pressure, bit geometry, coring speed, mud circulation velocity, trip to surface rate, mud composition and rheological properties, petrophysical properties, reservoir fluids properties and compositions, reservoir wettability, initial fluids saturations, chemical concentration gradient and fluid connectivity to promote chemical diffusion. The key elements of low invasion coring deliberate all these parameters and set protocols to optimise as many as possible.

Success can only be known by determining the level of filtrate invasion in the core, which is most commonly

accomplished by adding tracer chemicals into the mud filtrate and measuring for their presence within the core plugs to be used in native state testing, or within offcut trim sub-samples. Some authors suggest that mud chemicals may be used as a tracer when no specific tracer additive was used during coring. If low invasion is successful, the core centre will contain filtrate saturation below the detection limit of the tracer in most samples. This uninvaded centre is expected to be large enough to obtain a 1.5" diameter core plug.

SCA 2014-094 [16] highlighted the need for coring mud properties and components to be available to all involved in the core analysis program. It suggests that the base oil of an OBM or certain salts in the water phase of a WBM, may be used as tracing agents in lieu of traced additives. Glycols, which are often added to WBM, can dissolve both in oil and water phases, and can be easily detected in the oil phase. Also this mud type often has large quantities of salts (usually KCl) which could be analysed.

SCA 2016-32 [17] used centrifugation to extract oil from the core plugs. It demonstrated that properties of effluent oil can be different from those of oil remaining in the core: polar components and asphaltenes seem to be retained in the core, perhaps because these components, deemed to be significant in wetting, could adhere to core surfaces. This is aligned with published data within the geochemical community, Bennett et al [18], which also observed that mud filtrate appeared to be more easily removed than the in-situ crude oil. The work also demonstrated that mud components could be used as "natural" tracers, potentially eliminating the need to add specific tracers. Besides reducing cost, this approach has the following possible advantages:

- works for small fluid samples,
- can be acquired from cores of any shape,
- both oil and water samples may be analysed,
- preliminary identification of oil type,
- detect major differences in produced and in-place oil composition.

If analysis clearly indicates no significant mud invasion has occurred, native state wettability tests may represent the in-situ reservoir conditions, assuming that changes have not occurred from other sources. If not confirmed, any test and subsequent analysis data that are wettability sensitive, may be compromised and could be a waste of resources (finance, personnel and time).

2.2 Native Saturation

The second important aspect to assess native state is fluid saturation; especially initial water saturation. As discussed by Bennion, et al. [19], coring operations can result in significant flushing of the core, particularly higher permeability, by the mud fluids from injection ports at the bit. If the coring fluid is water based, this will obviously result in an undesirable increase in the measured water saturation (S_w). If the coring fluid is purely oil based, irreducible water saturation (i.e., immobile) will be unaltered but mobile water (such as in a transition or aquifer zone) may be displaced from the core by oil filtrate, reducing the apparent (measured) S_w . Oil-based coring fluids, therefore, usually provide a

good estimate of “irreducible” S_w , but not necessarily the innate water saturation in a reservoir. Pure oil-based muds (often diesel based) are less common in recent years, due to HSE concerns of its benzene content. Currently, most oil-based muds, particularly for offshore wells, are synthetic, low toxicity oil-based muds (LTOBM), containing at least 5% water content and once called invert emulsion muds. Surfactants are necessary for LTOBMs to hold the oil, water and other additives together in suspension but will alter pore space wettability if invaded.

Gas, occasionally, has been used as a coring fluid but heat generated during the coring process, combined with the dehydrating nature and high rate of gas circulation, often results in desiccation of the core and artificially low saturations. This is not recommended for native state core.

Selection of an appropriate coring fluid is thus essential for obtaining representative core that can be used for saturation and special core analysis measurements. The specific data requirements, hence, measurement program, should determine the optimal coring fluid for any given situation. Table 2 summarizes some advantages and disadvantages of various types of coring fluids with respect to in-situ saturation determination and wettability effects [19,20].

Wellsite handling of native state cores must focus on rapid processing because low invasion coring may not fully inhibit invasion. Figure 3 shows CT evidence of an invaded zone, seen as the denser “halo” at the outer edges. At the very least, the outer surface of the core will be exposed to the mud during coring, core handling and shipment to the lab. Whilst exposed, there is the potential for mud chemicals to be transported through diffusion gradients within the interconnected pore fluids. This process was shown to happen at very early stages, by Zhang et al. [21].

Table 2. Mud types: pros and cons

Fluid Type	Effect of InSitu Saturation	Effects of Wettability
Water Based Mud	Good for Immobile S_o	Possible Wettability Alterations
	May increase S_w	(pH changes and/or ionic interactions)
	May reduce mobile S_o and S_g	Polymers effects
Pure Oil Mud (Diesel based no surfactants)	Good for Immobile S_{wi}	Possible Wettability Alterations
	May increase S_o	Higher potential for asphaltenes precipitation
	May reduce mobile S_w and S_g	
Pure Gas	May reduce mobile S_g (solubility effects)	
	Good for Immobile S_o	Unknown
	May reduce mobile S_o and S_w	
Invert Emulsion Mud	May reduce immobile S_w (desiccation)	
	May reduce mobile/immobile S_w	Wettability Alterations
	May reduce mobile/immobile S_g	due to surfactants (emulsifier or wetting agent) and other chemicals
Low Toxicity Oil based Mud	May increase S_o	Wettability Alterations
	May reduce mobile S_w and S_g	due to surfactants (emulsifier or wetting agent) and other chemicals
	May reduce mobile S_g (solubility effects)	

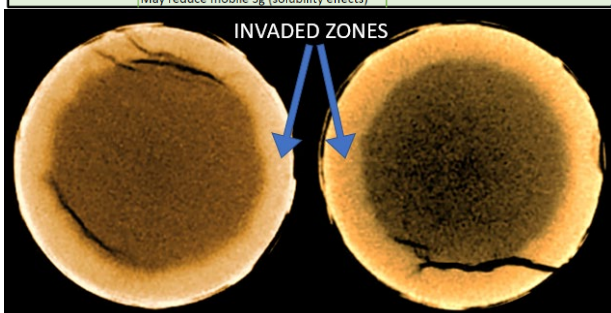


Figure 3: Outer layer mud invasion CT scan image

It is not normally recommended to cut plugs at wellsite, particularly SCAL plugs, owing to difficult conditions and impaired ability to see important sampling features, such as layer changes, bedding orientation and heterogeneities. But the rapid diffusion potential [20] and oxidation (atmospheric exposure) potential to alter wettability, Unsal et al [22] may necessitate rapid handling (wellsite plugging, trimming & preservation) for native state core, to separate the inner core material from an invaded outer layer or from surface fluids. Therefore, a decision must be made whether to process at wellsite (which pragmatically may not be possible) or to transport the core quickly to the lab for processing (recommended within 24 h, 48 h maximum).

If electing to process the core at wellsite, plugs should be cut with an appropriate fluid to minimise wettability and saturation alteration. Trim off the ends to create a 2” (5cm) long, right-cylinder plug. Weigh both the plug and both trim sections. Immediately preserve the plugs in Saran wrap, aluminium foil and wax. Weigh the wax-sealed plugs. The wax seal should be sufficient preservation, but further preservation could be to place the wax-sealed plug into a laminated aluminium (Mylar) sealable bag. If selecting to use sealable bags, the bag plus plug should be weighed once sealed. Trim sections should be wrapped in Saran wrap, aluminium foil, weighed and sealed within Mylar bags. Plug number and depth should be marked on wax coating and on the Mylar bags, McPhee et al [23].

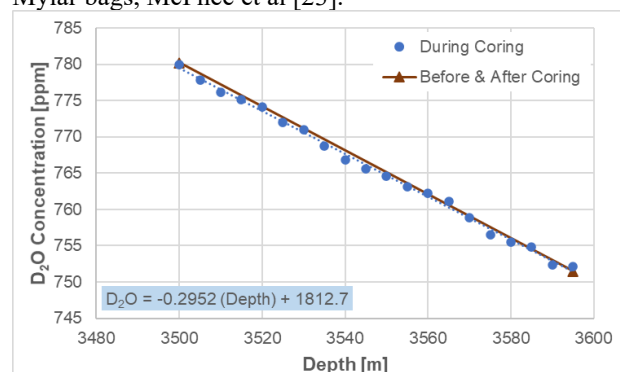


Figure 4: Tracer concentration in mud filtrate versus depth

To investigate the level of invasion, chemical tracers (e.g. tritiated or deuterated fluids, 1-bromonaphthalene or other halogenated fluids, hexadecane, specific salts, etc.) should be added to the mud filtrate (either oil, water or both, dependent upon which phase is of interest) at known concentrations. Alternatively, as mentioned above, mud chemicals which can be detected and are not native to the reservoir may be used. The traced mud should be circulated around the full system three times, to ensure reasonable mixing before coring. Samples of the mud, 0.3 – 1 litre volume, should be taken at regular depth intervals throughout coring, approx. 10 – 20 samples across the cored reservoir section, plus a sample immediately prior to and after coring. The mud samples should be analysed to measure the tracer concentration as a function of depth, since this may change due to mixing with reservoir fluids. Data should be interpreted as a function of depth and regressed to obtain a depth-

based equation of average tracer concentration in the mud (see example shown in Figure 4).

3 Laboratory

As mentioned previously, the main requirements for ensuring native state would be unaltered wettability (which is unknown in most cases), unchanged saturation, no contamination, and no change to fluid composition. Whilst some aspects of change can be minimised and partially controlled, some cannot and laboratory protocols must be designed merely to verify whether or not as-received properties exhibit values that can evidence little or no alteration. Since reservoir wettability is unknown it is recommended to study all three states; native, clean and restored, to check water wet conditions can be achieved (clean state) and to compare native and restored state data. Laboratory wettability measurements are time consuming which often prohibits their use as a preassessment tool. The lab protocols discussed below will therefore largely focus on assessing and/or controlling saturation, contamination, and fluid composition.

3.1 Modified Routine Core Analysis

Since most core programs begin with routine core analysis (RCA), early assessment can begin with evaluating possible contamination from mud chemicals, by tracer analysis as part of a Dean-Stark (DS) analysis program. As a standard procedure, to avoid diffusive invasion, it is recommended to cut DS plugs at wellsite from the centre of the core (least invaded region), parallel to the length axis, McPhee et al [23]. However, in the laboratory, the experimental procedures of the DS program may require a re-design dependent upon the specific tracer used. For example, DS extraction is standardly employed as a method to measure water content; extracting the water from each plug in an individual apparatus in a few days, followed by batch hydrocarbon and salt extraction. If hydrogen isotopes (deuterium or tritium) were added to the water phase, then standard DS extraction may be viable. However, if hydrocarbon tracers or water-based salt tracers were used, batch processing cannot be used. Procedures must be adjusted to collect the used solvents for tracer concentration measurements, and solvent volumes should be minimised to increase the concentration of tracer extracted into its volume, reducing uncertainty in the tracer measurements.

The results of a DS tracer study will give an overview of invasion; the first evidence whether native state core material (uninvaded or minimally invaded) may be possible. It may show if little or no invasion occurred, or if specific reservoir layers have been invaded, or if generally high invasion has happened. The information may be used to optimise selection of native state SCAL samples. Only plugs in uninvaded depths can be selected as native state, otherwise restored state testing must be considered.

3.2 SCAL plug selection

Initial selection should be performed to obtain plugs having representative petrophysical properties aligned to

rock types determined from RCA and well log data interpretation (and other reservoir information), ensuring the important zones of interest are captured. Comparison of RCA and SCAL data can be improved by cutting twin (or sister) plugs, i.e. the RCA plugs are cut as close as possible to the SCAL plugs, within the same rock layer. Selection should avoid any invaded depths, determined during RCA tracer analysis. CT images are recommended to support assessment of the selected plugs, Maas et al [24], avoiding undesirable attributes, such as: heterogeneity, fractures, etc. It is advisable to select more plugs than required, anticipating that some will be abandoned due to unrepresentative features and/or properties. This part of the selection process should be performed without opening the plug preservation materials, wax and/or Mylar bags.

End Trim Analysis

Analyses can be performed on the end trims to provide additional information to improve assessment of the SCAL plug selection and provide more relevant estimated properties (since basic properties cannot be performed on a native state plug, these properties must be estimated). It is important that the end trim material is comparable to the main plug. End trim measurements can be compared against RCA sister plug data for additional QC selection checks, since the end trim material is from the same depth and possibly a closer analogue of the core plug. Cutting plugs of approximately 5 cm long should provide sufficient end trim material to perform these suggested analyses for either 4" or 5¼" diameter core (see Figure 5). However, smaller diameter core (such as wireline core) is unlikely to have sufficient material to do this. As depicted in Figure 5, it is recommended to cut a 1" diameter trim plug from the offcut material. This supplies a SCAL core plug (1.5" diameter), a trim plug (1" diameter), plus additional trim material. The trim plug can undergo Dean-Stark extraction and routine analyses, to obtain basic rock properties, water and oil saturation, followed by high-pressure mercury injection to obtain pore throat size distribution and capillary pressure data. The remaining trim material might be used for petrographic analyses such as, x-ray diffraction (XRD), thin section analysis (TSA) and scanning electron microscopy (SEM), towards understanding the mineralogy and improved reservoir characterisation.

The following program is suggested for the end trim (plug offcut) material:

- Receipt and checking of trim preservation integrity and "as-received" weight
- Modified Dean-Stark extraction (Trim Plug)
 - measure water volume to determine saturation (equivalent to plug)
 - collect extracted oil in the toluene effluent
 - collect salt in methanol effluent (or consider the leach technique)
 - determine water saturation
 - determine oil saturation
- Measure tracer levels (compare to tracer levels in the plug)
 - from toluene effluent for hydrocarbon tracers

- and/or in the water volume (for water isotope tracers)
- and/or determine ionic composition of salt content and subsequent tracer concentration (if salt tracers were used)
- Measure grain volume, helium pore volume, porosity, grain density and gas permeability (if sufficient material is available)
- Measure mercury injection capillary pressure (trim plug, as depicted in Figure 5)

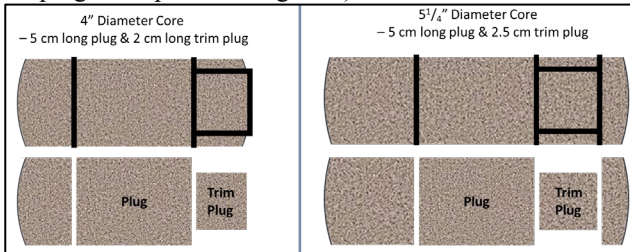


Figure 5: Schematic of possible cuts to obtain plug and trims (note: the black lines in the upper images denote cutting transections. The lower images show resulting material)

Contiguous end trim data can provide significant information about the core plug, if the material is relatively homogeneous. The properties of the end trim can be assumed as an estimate of the plug properties to ascribe estimated permeability, porosity, grain density and original water saturation and can be compared to the RCA (sister plug) data as additional quality control and verification of the comparability of the RCA to the SCAL plug data.

3.3 SCAL plug preparation

Native state preparation may require a customised program based on a variety of parameters, such as available laboratory techniques, core characteristics, degree of consolidation, core petrophysical properties, fluid types, pressure changes, temperature conditions and complex reservoir saturation history, such as paleocontacts. For instance, in their recent paper (Unsal et al [22]) highlighted the importance of the redox state, especially iron-rich minerals, on special core analysis, where oxidation from ferrous to ferric content could alter some basic rock properties, as well as wettability and dynamic properties. The paper recommends pre-studies to include the impact of different reducing agents on coreflood properties and suggests that reducing agents should always be considered particularly where core and fluids may have been oxidised. This is not widely considered in general SCAL procedures, where core and fluids are often exposed to atmosphere (though may be degassed and sometimes nitrogen purged). We have not addressed this in the following protocol but recommend that labs consider these chemical aspects.

The remainder of this section proposes one possible approach designed for plugs that might be considered “average” for a liquid hydrocarbon reservoir, for instance oil saturated above the transition zone at immobile water saturation, reasonably consolidated (not friable or unconsolidated), having permeability ranging 10 – 2000 mD and porosity ranging 0.15 – 0.30 v/v. Assuming this and assuming the core was cut using low

invasion protocols based on Rathmell et al [13], oil is expected to be the mobile phase so that filtrate invasion might be considered to mix with the reservoir oil. This would replace an unknown amount of oil and alter composition. In addition, degassing will occur as the core is brought to surface, displacing the mobile oil phase. At a minimum, protocols must replace the altered oil and expanded gas volumes with a controlled oil. Dead crude oil (stock tank oil) is often used as a laboratory surrogate for live reservoir oil and would constitute a controlled oil. It is vital that the controlled oil has been appropriately prepared and checked that it is not contaminated by mud chemicals. PVT fluid analysis should include spectrographic analysis of the stock tank oil (STO) to be used, mud filtrates, and any other hydrocarbon additives to the wellsite fluid vessels (such as the stock tank or separator units, where test fluids were obtained). Spectrographic comparison should assess any reservoir oil samples for potential contamination and only uncontaminated fluids should be used in testing.

In some circumstances, refined mineral oil might be used as a controlled oil, so long as it can be shown that it is compatible with the reservoir oil without precipitating asphaltenes (Buckley et al. [25]). Where necessary, fluid compatibility testing should be performed and buffering fluids considered to understand what would constitute “controlled oil”.

Water saturation may change due to invasion, depending upon the water content of the mud filtrate, but if invasion is detected within plug fluids, native state is not possible. However, salts may have precipitated dependent upon changes to temperature and pressure from reservoir to ambient conditions and upon water chemistry. The ionic composition of formation water should be reviewed for its potential to precipitate salts at ambient conditions. If salts precipitate, the composition and salinity of the autochthonous water will be altered.

Therefore, to ensure native state, any pore space saturated with evolved gas must be replaced with controlled, representative fluids. The autochthonous fluids, which may be contaminated with mud additives or particulates, or have altered during the trip to surface, must be replaced with controlled, uncontaminated fluids. It is then imperative to re-achieve original reservoir saturation after this exchange process, else significant saturation hysteresis will negate native state.

Native state preparation may thus include the following fluid protocols: exchange of altered connate water with synthetic formation water (SFW), collection and measurement of produced water for tracer analysis, replacement of altered oil with controlled oil, collection and measurement of produced oil for tracer analysis. Fluid exchange is achieved by centrifugation and/or flooding (see below protocols and bulleted summary).

After considering the fluids and possible changes to composition or saturation, if it is decided that both fluids must be replaced, flooding is not recommended because the exchanges will involve immiscible displacements to attempt to achieve residual fluid saturations, which are almost never achieved by flooding due to comparatively large capillary end effects, McPhee et al [23]. A mix of

centrifugation and flooding is recommended but must evidence that connate water saturation is re-established. To improve the probability of achieving residual saturations, it is recommended to use inert gas (nitrogen) as the displacing fluid owing to more favourable density difference, interfacial tension and contact angle than liquid-liquid centrifuge displacements. Simultaneously, it achieves residual saturation in both liquid phases, thereby minimising the volume of any particulates that may have precipitated and could be held as a colloid in these liquids. Another advantage of using an inert gas, such as nitrogen, is to reduce atmospheric exposure and potential oxidation, which can influence wettability. The centrifuge and plug storage equipment should be purged with nitrogen throughout the plug handling and loading process, to minimise exposure to air.

The rotational speeds for the centrifuge stages should be designed to apply a capillary pressure equivalent to a representative height above free water level (HAFWL), or apply a force expected to achieve a water saturation consistent with other water saturation data in similar rock types and similar HAFWL of the same reservoir. This requires discussions between the laboratory and oil company representatives, to review any relevant available reservoir data, such as well-logs, fluid properties, previous core data, etc. If end trim mercury injection was performed, these data can be used to support the comparison of reservoir to laboratory data. Care should be taken to consider the differences in fluid properties between reservoir and laboratory (surface tensions and contact angles), particularly the conversion from an oil-water to gas-water system, since nitrogen will be used as the displacing fluid.

The core plugs should be placed into a centrifuge and spun at the predetermined speed(s). Produced fluid volumes should be collected and recorded. Water production may imply that the applied centrifuge force was too high or that water has invaded from mud filtrate or that wettability has been altered. Tracer concentration of the liquid volumes should be measured. Volumes produced should be checked against the weight change to ensure agreement and verify fluid density values.

After each centrifuge step, nitrogen should be replaced by flooding with an appropriate controlled fluid, either degassed SFW, STO or refined oil, against a back-pressure of at least 10 bar (150 psi). Gas will be dissolved into the pressurised, undersaturated fluid. There is an option to obtain additional data during these floods by performing a miscible displacement, which will give information about the homogeneity of the pore space saturated by the mobile fluid and an estimate of mobile fluid volume. After replacing nitrogen with a controlled fluid, weight checks can be performed to determine the volume of fluids exchanged.

Added wettability information also may be gained by performing nuclear magnetic resonance (NMR) tests at liquid-filled residual saturation stages (see description later).

A cartoon representing the native state preparation process is given in Figure 6, and is described in bullet point form below:

- Remove from preservation

- Weigh “as-received” plug
 - weight check against wellsite recorded weight
- Measure NMR T1 and T2 (if possible T2-D analysis)
- Centrifuge under nitrogen to residual water (S_{wr}) and residual oil (S_{or}) saturation
 - Collect & measure fluid volume(s)
 - Analyse fluid(s) for tracer
- Remove from centrifuge and weigh
 - Compare weight change with produced fluid volume
- Load to a coreholder under nominal confining stress and saturate with synthetic formation water (SFW) by waterflooding against 20 bar (300 psi) pore pressure for at least 5 pore volumes injection (PVI), until stable differential pressure (dP)
 - One method to verify removal of the gas volume, would be to carefully de-apply and re-apply back pressure whilst continuing injection. If no gas is present, differential pressure should be equivalent in both regimes.
- Measure effective water permeability at S_{or}
 - There is an option to perform miscible dispersion analysis using a doped SFW. Dispersion can provide an estimate of the mobile water volume, hence water saturation (S_w), in turn an indication of S_{or} .
- Remove from the coreholder and weigh
 - Determine fluid volume exchange from weight change
- Measure NMR T1 and T2 (if possible T2-D analysis)
- Centrifuge under nitrogen to S_{wr} and S_{or}
 - Collect & measure fluid volume(s)
- Remove from centrifuge and weigh
 - Compare weight change with produced fluid volume
- Load to a coreholder under nominal confining stress and saturate with controlled STO by flooding at 20 bar (300 psi) pore pressure for at least 5 PVI, until stable dP. Verify gas removal.
- Measure effective oil permeability at S_{wr}
 - There is an option to perform miscible dispersion analysis using a doped oil. Dispersion can provide an estimate of the mobile oil volume, hence oil saturation (S_o), in turn an indication of S_{wr} .
- Remove from the coreholder and weigh
 - Determine fluid volume exchange from weight change
- Measure NMR T1 and T2 (if possible T2-D analysis)

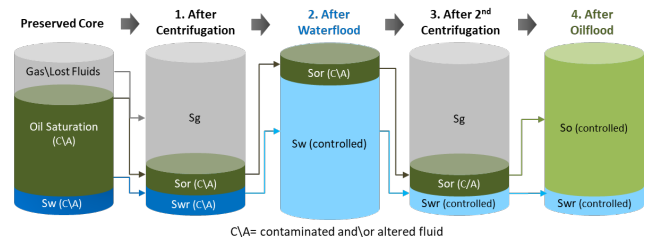


Figure 6. Cartoon of the process stages

Tracer analysis on fluid extracted by centrifugation

The fluid volumes extracted under the first centrifugation should be analysed for tracer content. In general, tracer concentrations measured on volumes produced under centrifugation will be more accurate than DS data because they are not diluted by solvent extraction volumes. Ideally, these should demonstrate that no tracer was detected or, at least, that concentrations are below the measurement limit. The measurement limit will be dependent upon the type of tracer and the test procedure used to measure its concentration. Therefore, it is wise to consider these measurement limits before selecting the tracer to be used. Any plug showing tracer concentration above the minimum measurable limit, should be disqualified due to invasion (hence, possible change to wettability). Invaded plugs cannot be used as native state and restored state must be considered for any wettability sensitive analyses. If this is the case, a cleaned state wettability analysis also should be performed to verify that water-wet conditions are achieved by cleaning before employing restored state protocols.

If no invasion is observed, the in-situ wettability is believed to have not been altered by mud filtrate invasion and protocols can continue to saturation checks to verify that connate water saturation can be re-established.

Table 3 shows the data from five (5) samples from a North African field study, where core was acquired using low invasion methods. Estimated tracer concentration within the hydrocarbon (HC) phase of the plugs is shown between 0.1 to 0.4 % for 4 plugs, across a permeability range of 100 to 2300 mD. However, the fifth (1500 mD permeability) shows high tracer content, 8.1 % and was subsequently disqualified from native state analysis. In this study, approximately 10% of all plugs were disqualified due to high invasion. Most of these plugs were from the top or bottom of individual core runs, where the rock is exposed for longer, or from zones where fracturing had occurred.

3.2 Saturation estimation

Dean-Stark saturation data, either from routine core analysis, or the trim plug, is useful to support estimations of irreducible water saturation, by estimating the “as-received” oil saturation ($S_{o,AR}$). S_w and S_o data obtained on the trim plugs can be used as a direct estimate of the “as-received” saturations of the SCAL plug. Otherwise, S_o from Dean-Stark of RCA plugs can be used to derive a correlation to gas permeability and thereby estimate $S_{o,AR}$ in each SCAL plug based on effective permeability measurements (either effective oil permeability at S_{wi} or water permeability at S_{or}). **Note:** the native state permeability is always effective permeability since absolute permeability can only be measured once cleaning has been performed and the sample saturated with a single fluid phase. $S_{o,AR}$ values are used to estimate residual oil saturation (S_{or}) after the first centrifugation under gas, which then can be used to estimate S_{wi} .

$$S_{or} = S_{o,AR} - \frac{V_o}{V_p}$$

where V_o is the oil volume produced during centrifugation and V_p is pore volume.

During the second centrifugation the sample is mostly water saturated (after displacing nitrogen with SFW) but contains residual oil content. The second centrifugation should re-establish initial water saturation under nitrogen, whilst the S_{or} remains constant. Thus S_{wi} can be calculated by:

$$S_{wi} = 1 - S_{or} - \frac{V_w}{V_p}$$

where V_w is the water volume produced during the second centrifugation under nitrogen gas.

Table 3 provides data from five (5) plugs undergoing a native state preparation for a large North African field. It does not show all measured or calculated values, but it indicates some of the important information pertinent to estimating saturations and for quality control.

Table 3: Table of measured properties for some samples

Estimated Permeability	(mD)	100	350	850	2300	1550
Estimated Porosity		0.135	0.175	0.191	0.221	0.210
Estimated pore volume		6.9	8.5	9.4	11.3	9.6
Centrifugation to Sor+Swi						
Weight before centrifuge	(g)	109.84	107.02	108.10	108.06	97.66
Weight after centrifuge	(g)	107.50	104.40	106.00	105.38	95.70
Volume water produced (burette)	(ml)	0	0	0.1	0	0
Volume oil produced (burette)	(ml)	2.5	2.7	2.1	1.8	2
Tracer concentration	(ppm)	0.1	0.1	0.4	0.6	11.3
Tracer in mud at sample depth	(ppm)	140.1	139.3	139.8	139.4	139.9
Filtrate Percentage in HC phase	%	0.1	0.1	0.3	0.4	8.1
Water saturation by flooding SFW						
kw(Sorg) - SFW	(mD)	59	367	1543	2458	1607
Weight after kw(Sorg)	(g)	113.46	113.40	114.95	115.46	104.73
Volume water replaced	(ml)	5.18	7.83	7.78	8.77	7.85
Establish Swr (gas-water centrifuge)						
Weight after centrifuge	(g)	107.58	104.53	106.26	105.64	96.09
Wt difference at centrifuge endpoints	(g)	0.08	0.13	0.26	0.26	0.39
Change in water saturation	(frac)	0.010	0.012	0.023	0.019	0.033
Oil saturation by flooding STO - 60°C						
ko(Swi)	(mD)	89	341	802	2269	1531
Weight after ko(Swi)	(g)	111.73	110.65	112.08	113.21	102.48
Volume oil exchanged	(ml)	5.17	7.63	7.26	9.44	7.97
Estimated Swi	(ml)	0.246	0.103	0.226	0.165	0.173

Estimated porosity and pore volume are shown. In this study, porosity was estimated from grain density and porosity properties of sister routine core plugs (similar depth and sand layer) and using measured calliper plug dimensions to calculate bulk volume. Bulk volume from calliper measurements assume a core plug to be a perfect cylinder and thus incorporate a higher potential error margin than the recommended ± 0.5 porosity units (p.u.) in API RP40[26]. These uncertainties will be reduced at the end of testing, when measurements of grain, bulk, and/or pore volume can be performed, but in the meantime a higher error margin potential must be allowed – possibly ± 1 p.u. In turn, saturation uncertainty will increase from the recommended ± 3 saturation units (s.u.). However, we would recommend a limit of ± 6 s.u. at this initial stage of preparation for selecting viable plug samples. **Note:** this limit is partly arbitrary, based on the understanding that most of the saturation error is derive from the porosity error, which varies between approximately 2 - 10 s.u. for $\pm 0.5 - 1$ p.u. error in the porosity range of 0.100 – 0.300. Volumetric production measurement error contributes far less to the overall saturation error, usually between 0.3 – 1 s.u.

Regarding quality control considerations, weight changes should compare to equivalent fluid production

volumes during centrifuge displacement steps, and to the subsequent replacement volumes when re-saturating with water or oil by flooding. It is recommended to calculate the difference between volumetric and weight measurements to saturation difference and apply the recommended limit of ± 6 s.u. Any plug outside this limit should be discontinued from native state testing.

From the first centrifugation under gas to S_{wi} and S_{or} , produced fluid volumes should be recorded. Water production should be minimal, preferably zero, since any water production indicates a change in initial saturation conditions (hence, no longer native state). Any observed water production should be calculated as saturation change and should not exceed ± 6 saturation units (s.u.).

The weight after the two centrifugation steps should be approximately equal, although some differences might be expected if the autochthonous fluids and controlled replacement fluids have different density. In Table 3, the weight after centrifugation to $S_{or}+S_{wi}$ and the weight after centrifugation to establish S_{wr} should be equal. Assuming no difference in S_{or} (since centrifugation was performed under equal displacement force), the weight difference between these two centrifugations (neglecting measurement error) can be assumed as possible change in water saturation. Any change outside ± 6 s.u. should disqualify the plug from native state testing. **Note:** this is a worst-case error scenario, since it assumes that the total weight change is attributed to water; however, changes in oil saturation and grain loss may also contribute to weight errors. It is therefore important to observe, record and account for any visible grain loss. For this North African field, the 5 plugs shown in Table 3 show a change in water saturation between 1 and 3.3 s.u., implying that change is minimal and might be considered as native state.

Estimated S_{wi} values can be compared to DS S_w data from sister RCA plugs and/or trim plugs and to any well log petrophysical data available for the field under analysis, as another QC step.

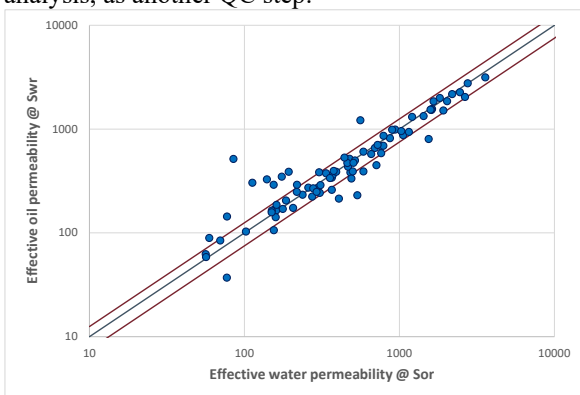


Figure 7: Effective oil versus effective water permeability

Although a weaker correlation, effective permeability data also may be used when considering selection and viability of core plugs. Figure 7 shows the correlation of a study from a large North African field; red lines indicating a 25% uncertainty. In this study, effective oil and effective water permeability was approximately equal but other reservoir systems and different wetting behaviour may result in different correlations, such as

effective oil permeability being higher, or vice versa. Outliers may not require exclusion but must be deliberated whether or not to exclude.

3.2 Wettability measurements

Nuclear Magnetic Resonance (NMR) measurements (T1/T2 and Diffusion) can be performed at different stages during native state preparation process. 2D D-T2 intensity maps can provide additional semi-quantitative information about wettability for fresh state or restored state cores. Existing restricted diffusion models allow the estimation of surface relaxivity, tortuosity, and wettability from the diffusivity and T1 or T2 data in the D-T2 maps measured on partially saturated plugs, without the need for separate NMR measurements of the bulk fluids and fully water-saturated rocks. [27,28,29,30]

Comparison of T1-T2 maps at different initial or irreducible saturation stages (S_{wi} , S_{or} , S_{gr}) could provide added information of fluids type and distribution within the rock pore structure, at fresh state conditions and after the native state preparation procedure.

The first set should select non-invaded core plugs and perform native state followed by restored state wettability analysis. This is to investigate the native state wettability of the acquired, low-invasion core and also to compare against restored state wettability. Using the same plug, although increasing experimental time, allows direct comparison of results. Plugs should also be selected from a range of lithofacies, petrophysical properties and height above free water level, to aid understanding of wettability distribution within the reservoir.

A second set should select known invaded plugs to show any differences to non-invaded plugs, thus exhibiting the effect of mud filtrate invasion on in-situ wettability.

A third set should select both invaded and non-invaded plugs. These should undergo typical cleaning and drying procedures followed by clean state wettability. Data from this set should exhibit strongly water-wet behaviour in both invaded and non-invaded plugs (except where mineralogy may dictate other behaviour), thereby indicating that filtrate components can be removed, and restored state procedures may be considered viable. Like the first set, these plugs should be chosen from a range of rock properties. If results are not strongly water-wet, mineralogy should be analysed for known non-water-wet components, such as: organic material (coal, kerogen, pyrobitumen, etc.), halite, chamosite, etc.

Most commonly, wettability is studied using the combined Amott-USBM method. Wettability results from the North African field are shown in Figure 8, indicating wettability indices of non-invaded native state plugs (NS), invaded native state plugs (INV) and restored state plugs (RS). These indicate similar mixed-wet data in native and restored state plugs, but alteration to strongly oil-wet behaviour of the invaded plugs.

4 Discussion

Core Preparation Discussion

Native state core preparation should not use fixed, or standard, procedures, nor is it guaranteed to result in viable plugs for use in a native state SCAL study. Instead, process control must regard the various factors influencing wettability and wettability alteration during coring and core preparation, and experimental procedures should be designed accordingly with decision gates in place to determine whether or not native state analyses can be used. This will be reservoir and well specific, since lithology, fluid types and coring procedures have a direct impact on wettability. Figure 10 gives an example flow diagram with decision gates that might be used when assessing native state protocols. It cannot be exhaustive, since there may be other controlling variables that have been omitted.

The flow diagram indicates some of the important decision factors:

- Wettability altering mud components
 - If present (or unknown), then invasion must be investigated and will either exhibit; no invasion, whereby NS is viable, or invasion, in which case NS is unviable.
 - If not present, then other alteration factors need consideration (e.g. saturation change)
- Were tracers used in the mud system during coring?
 - If not, consider using isotope analysis to investigate mud components
 - Else, if mud invasion is unknown, native state may be unviable
- Is there potential for asphaltene precipitation?
 - If asphaltenes are unstable and likely to precipitate, then an asphaltene study must be performed to confirm or discount precipitate in the cores.
 - Presence of precipitate may exclude NS analyses, or further study must determine if asphaltenes can be removed without altering original wettability
- Is water saturation unchanged?
 - If changed, can S_{wi} be re-achieved?
 - If S_w has been altered and cannot be re-achieved, NS analysis is unviable
- Is water composition unchanged, or is salt precipitation likely?
 - Salt precipitate must be removed, usually by replacing the autochthonous water with controlled formation water
 - This requires change to saturation and hence, re-establishment of S_{wi} must be achieved

It is possible that old, preserved core (either wax-coated or Mylar-sealed) may be selected for use in a native state SCAL study. In such a case, the preservation must be scrutinised. Seal integrity must be investigated. Have fluids been maintained within the sealed material? Are the properties of the core congruous with previous data from the core? Assessing the viability of old, preserved core will require a rigorous process including all the aspects for investigating fresh core, described in

this paper, but also ensuring comparison to previous study data. Any incongruity in reservoir properties should be deemed to negate native state analysis.

Wettability Discussion

Figure 8 shows data implying a distinct difference in the wetting index of invaded material (strongly oil-wet, Amott wettability indices between -0.72 and -0.83), compared to native and restored state core material (mixed-wet). Native and restored state plugs showed generally similar results with an index range between -0.16 to -0.50, in general. One native state sample, however, showed a slightly positive index (+0.15), but this may have been a function of poorer permeability. In general, poorer permeability will result in higher S_{wi} and hence, less oil present and less chance for wetting to be altered away from water wet. Figure 2 summarised the data as a function of permeability further supporting the evidence of invasion causing a change to wettability.

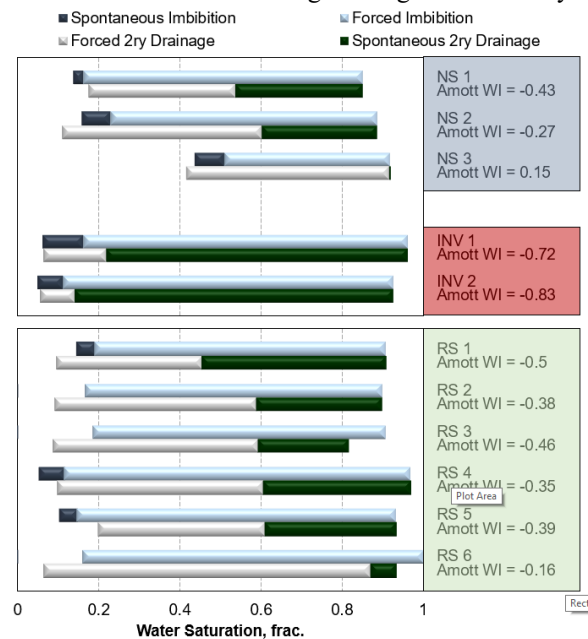


Figure 8: Wettability indices for native state (NS), invaded (INV) and restored state (RS) plugs

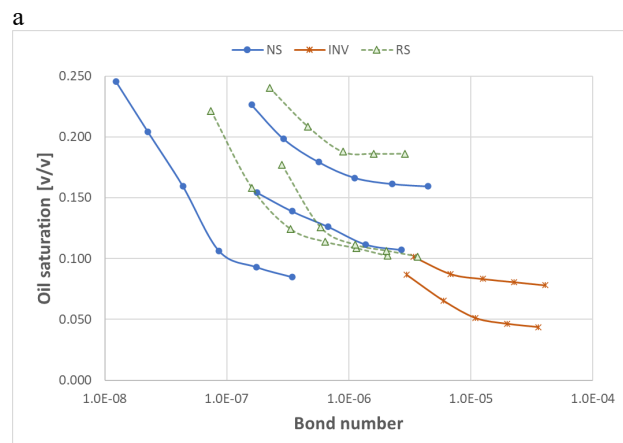


Figure 9: Centrifuge wettability data, S_o versus N_b

Remaining oil saturation was plotted against bond number (Figure 9) from centrifuge forced imbibition data, also indicating similar behaviour between the NS

and RS plugs (S_{or} stabilising between 10^{-7} to 10^{-6}), whilst invaded plugs did not stabilise before 10^{-5} and at generally lower residual oil saturation.

5 Conclusions

As-received core is probably not native state and SCAL should never be performed on as-received core without first considering the potential changes from coring, retrieval, wellsite handling and shipment.

Wettability analysis is an important stage in determining native and/or restored state feasibility.

We have defined a decision tree (illustrated in Figure 10) that could be used as an example process guide for considering whether native or restored state core should be used, though individual reservoirs should consider individual process design.

Data from the large North African field imply that native state preparations, for most of the plugs and the specific rock-water-oil combination in that particular reservoir system, were largely successful and that restored state procedures could be equally viable where invasion had occurred. Plugs were disqualified from native state testing where high invasion was seen whilst the majority of plugs showed low invasion.

Native state and restored state samples exhibited broadly similar behaviour, but invaded plugs exhibited strongly oil-wet characteristics.

The viability of a restored state process is largely determined by the ability of core cleaning to achieve strongly water-wet behaviour, except where certain organic and/or non-water wet mineral content exists naturally.

Acknowledgements

The authors thank Steffen Berg and Einar Ebeltoft for their useful input and recommendations to improve the paper.

References

1. J. Newcombe, J. McGhee, M. J. Rzas, "Wettability Versus Displacement in Water Flooding in Unconsolidated Sand Columns", *Trans. AIME*, **204**, 227–232, SPE 511-G (1955)
2. J.E. Bobek, C.C. Mattax, M.O. Denekas "Reservoir Rock Wettability - Its Significance and Evaluation", *Trans. AIME* **213**, 155-160 (1958)
3. W.G. Anderson, "Wettability Literature Survey-Part 1: Rock/Oil/ Brine Interactions and the Effects of Core Handling on Wettability", *JPT*, **38**, 1125-1144, SPE-13932-PA (1986)
4. Anderson, W.G. 'Wettability Literature Survey-Part 2: Wettability Measurement', (1986), SPE 13933
5. Anderson, W.G. 'Wettability Literature Survey-Part 3: The Effects of Wettability on the Electrical Properties of Porous Media', (1986), SPE 13934
6. Anderson, W.G. 'Wettability Literature Survey-Part 4: Effects of Wettability on Capillary Pressure', (1987), SPE 15271
7. Anderson, W.G. 'Wettability Literature Survey-Part 5: The Effects of Wettability on Relative Permeability', (1987), SPE 16323
8. Anderson, W.G. 'Wettability Literature Survey-Part 6: The Effects of Wettability on Waterflooding', (1987), SPE 16471
9. Lin, Q., Bijeljic, B., Krevor, S., Blunt, M.J., Rücker, M., Berg, S., Coorn, A., van der Linde, H.J., Georgiadis, A., & Wilson, O.B. (2018). A New Waterflood Initialization Protocol With Wettability Alteration for Pore-Scale Multiphase Flow Experiments. SCA2018-032
10. J.H. Stiles, J.M. Hutfilz, "The Use of Routine and Special Core Analysis in Characterizing Brent Group Reservoirs, U.K. North Sea", *JPT*, **704**, SPE 18386 (1992)
11. Ballard, T.J., Dawe, R.A., "Wettability Alteration Induced by Oil-Based Drilling Fluid", SPE 17160 (1988)
12. Jia, D., Buckley, J.S., Morrow, N.R., "Alteration of Wettability by Drilling Mud Filtrates", SCA1994-08 (1994)
13. Rathmell, J.J., Atkins, L.K., Kralik, J.G., "Application of Low Invasion Coring and Outcrop Studies to Reservoir Development Planning for the Villano Field", SCA1992-02 (1992)
14. Denney, D. "Development Planning with Low-Invasion Coring and Outcrop Studies." *JPT* 51 (1999): 54–55
15. Rathmell, J.J., Atkins, L., & Kralik, J.G. (1999). Application of Low Invasion Coring and Outcrop Studies to Reservoir Development Planning for the Villano Field.
16. Årland, K.S., Pruno, S., Skjæveland, O., (2014). ADVANCED RCA—Bridging the Gap between Routine and Special Core Analysis, SCA2014-094
17. Årland, K.S., Bastow, M., (2016). Quantifying Mud Contamination Without Adding Tracers, SCA 2016-32
18. Bennett, B., Buckman, J., Bowler, B.F., & Larter, S. (2004). Wettability alteration in petroleum systems: the role of polar non-hydrocarbons. *Petroleum Geoscience*, **10**, 271 - 277.
19. Bennion, D.B., Thomas, F.B., & Ma, T. (2001). Determination of Initial Fluid Saturations Using Traced Drilling Media. *Journal of Canadian Petroleum Technology*, **40**.
20. Buckley, J.S., Morrow, N. R., 2006: Wettability and Prediction of Oil Recovery from Reservoirs Developed with Modern Drilling and Completion Fluids, Report for the United States Department of Energy (DOE), BC-15164
21. Zhang, J., Chen, J., Thorsen, A.K., Constable, M., Nwaneri, N.S. 'NMR Investigation of Invasion Process of Formate Mud in Sandstone Cores', (2011), SCA2011-52

22. Unsal, E., van der Linde, H.J., & Wilson, O.B. (2020). Redox effects on relative permeability in Fe-rich clay bearing sandstones. *Marine and Petroleum Geology*, 115, 104251.
23. Mcphee, C., Reed, J., Zubizarreta, I.: *Core Analysis: A Best Practice Guide*. Elsevier, (2015), ISBN: 9780444635335
24. Mass, J. G., Springer, N., & Hebing, A. (2019). Defining a sample heterogeneity cut-off value to obtain representative Special Core Analysis (SCAL) measurements. [SCA2019-024].
25. Buckley, J.S., Fan, T., Tong, Z., & Morrow, N.R. (2006). Mixing Small Amounts of Crude Oil with Large Amounts of Asphaltene Precipitant. [SCA2006-02]
26. API RP40, "Recommended practices for core analysis", Second Edition. Feb. 1998.
27. Looyestijn, W.J. (2019). Practical Approach to Derive Wettability Index by NMR in Core Analysis Experiments. *Petrophysics V60*, 4
28. Minh, C.C., Heaton, N.J., Ramamoorthy, R., Decoster, E., White, J., Junk, E., Eyvazzadeh, R.Y., Al-Yousef, O., Fiorini, R., & McLendon, D. (2003). Planning and Interpreting NMR Fluid-Characterization Logs.
29. Minh, C.C., Crary, S., Valori, A., Bachman, N., Singer, P., Hursan, G., Ma, S., Belowi, A., Kraishan, G., (2016) Determination of Wettability from magnetic resonance relaxation and diffusion measurements on fresh-state cores ICE, Barcelona, Spain, April 2016, 211-211
30. Chen, J., Hirasaki, G.J., & Flaum, M. (2006). NMR wettability indices: Effect of OBM on wettability and NMR responses. *Journal of Petroleum Science and Engineering*, 52, 161-171.

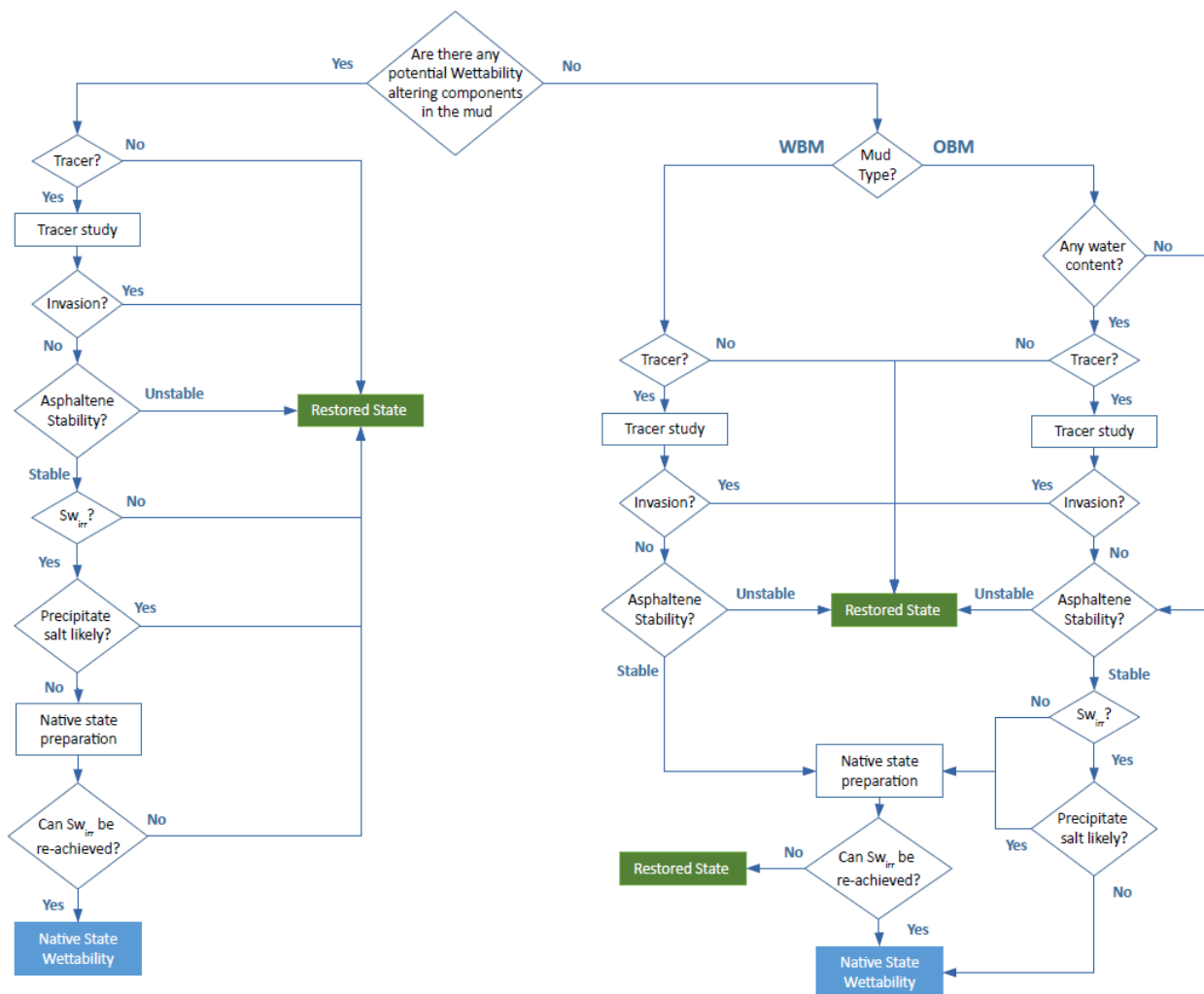


Figure 10. A suggested decision tree to determine viability of native state SCAL

Carbonated Water Injection for Heavy Oil Recovery

Jinxun Wang*, Abdulkarim M. AlSofi, Hassan Behairy, Abdullah M. Boqmi and Sinan Caliskan

Saudi Aramco, Saudi Arabia

Abstract. Coreflooding studies were performed at reservoir conditions using a 560-cP heavy crude oil and carbonate core samples. The CO₂-enriched injection water was applied after waterflooding for evaluating its potential for improving heavy oil recovery. Results showed that the carbonated water injection achieved an incremental oil recovery of 15.5% of original oil in core (OOIC). This evident incremental production suggests that CO₂ effectively diffuses into oil from water, which helps reduce oil viscosity and improve oil mobility. A few tiny dissolved holes were observed at the inlet end face of the core sample after the carbonated water injection. The CT image analysis showed that the rock dissolution was shallow, indicating that the carbonated water injection may not cause evident impact on the carbonate reservoir. For comparison, a hot water flooding test was conducted at 40°C above the reservoir temperature, which achieved an additional oil recovery of 21.0% OOIC. This indicates that the non-thermal technique of carbonated water flooding can achieve a comparable oil recovery enhancement as the hot water flooding for the studied heavy oil reservoir. The results from this work demonstrate the promising potential of the carbonated water flooding for improving the waterflooding performance for heavy oil carbonates.

1 Introduction

Reducing water/oil mobility ratio by enhancing oil mobility and/or lowering water mobility is among the most efficient solutions to improve heavy oil recovery. Thermal methods can effectively lower the heavy oil viscosity, leading to significant increase in oil mobility. Therefore, the steam based techniques, such as steam flooding, steam assisted gravity drainage (SAGD) and cyclic steam stimulation (CSS), are the most commonly used methods for heavy oil production. However, many reservoir conditions restrict the application of steam injection, such as thin pay thickness or deep reservoir. Hot water flooding is an alternative thermal option, although it might be less effective than steam injection in terms of heat delivery [1]. Polymer flooding has been recognized as a viable and efficient non-thermal technique to increase heavy oil recovery by reducing water mobility, and successfully applied in many heavy oil reservoirs worldwide [2-5]. Delivering CO₂ to heavy oil reservoir is another potential non-thermal solution, which can help remarkably improve oil mobility.

CO₂ flooding for enhanced oil recovery has been actively studied and successfully implemented in many fields. The effective oil mobilization by CO₂ flood is mainly attributed to the oil viscosity reduction, oil swelling, and/or miscibility [6]. However, some field conditions may restrict its practical application, for instance, the offshore reservoirs, or lack of adequate CO₂ supply. Carbonated water flood, injecting CO₂-enriched injection water as the displacement fluid instead of the conventional water, is an alternative method to utilize CO₂ for improving oil recovery. Except for lack of miscibility, carbonated water injection (CWI) retains most of other benefits of CO₂ flood. The carbonated water can interact with

both reservoir oil and rock, leading to beneficial changes to their properties for oil mobilization. Compared to direct CO₂ injection, the CWI can avoid the gravity segregation, which helps to achieve higher sweep efficiency. Compared to conventional waterflooding, the carbonated water injection helps to achieve more favorable mobility ratio. The carbonated water injection reduces oil viscosity due to the diffusion of CO₂ from water phase to oil phase. The dissolution of CO₂ in oil also causes oil swelling, which leads to higher relative permeability to oil. The oil swelling increases oil saturation, and improves oil phase continuity by reconnecting the isolated oil drops to larger oil ganglia.

Successful field trials of CWI were reported during 1950s to 1960s [7-9]. More than 40% additional oil recovery above the conventional waterflooding was achieved, and evident injectivity improvement was observed. Laboratory studies on CWI were active from 1950s to 1980s [10-13]. In recent years there is a growing interest in reducing carbon foot print, while the energy demand keeps increasing. The researches in CWI are gaining attentions again because it provides a safe and effective CO₂ storage solution as well as improving oil recovery [14-16]. The potential of oil recovery improvement by CWI was mainly evaluated by coreflooding studies. Despite the reported incremental oil recovery above the waterflooding had a wide range from 5% to 70% [14], in general, results showed that the CWI can substantially improve oil recovery compared to the conventional waterflooding. It was also revealed that applying CWI in secondary mode was more efficient than in tertiary mode [14-15]. An imbibition study also showed that compared to the unaltered water, the carbonated water accelerated production rate and significantly improved oil recovery [17]. Studies on bulk phase fluid properties, such as solubility, viscosity and volume expansion are commonly conducted to demonstrate the beneficial effects of CO₂ injection. High-pressure

* Corresponding author: jinxun.wang@aramco.com

micromodel experiments have also been used to help understand the mechanisms of oil recovery improvement by CWI [15, 16, 18]. The oil viscosity reduction, oil swelling, oil reconnection and redistribution were visually observed during the CWI processes. In addition to altering oil properties, the CWI may also induce interactions between the carbonated water and reservoir rock. An experimental study by contact angle measurements [19] showed that the carbonated water caused varied degrees of wettability alteration depending on the rock properties and test conditions. Laboratory studies on the rock dissolution by carbonated water were also reported for both sandstones and carbonates [20-21].

Most of the studies on CO₂ flooding and CWI are for conventional oil. An experimental by Millerand Jones [22] showed that the dissolution of CO₂ in heavy oil significantly reduced the oil viscosity, and the viscosity reduction effect tends to be more significant for heavier oil. For a heavy oil with API gravity of 10, the dissolution of CO₂ reduced the oil viscosity by a factor of 90 at 2,000 psi and 60°C. Although the swelling effect for viscous oil might be less evident than for light oil [18], the substantial viscosity reduction will help significantly improve oil mobility. With very few studies for heavy oil, and especially for carbonates, in this work we present a laboratory study to evaluate the potential of the carbonated water flooding for carbonate heavy oil reservoirs. A hot water flooding test was also conducted for comparison.

2 Experimental Materials

2.1 Brines

A synthetic connate water, with a total dissolved solids (TDS) of 136,954 mg/L, was prepared for saturating core plug samples. The waterflooding injection water for coreflooding tests was a synthetic brine with 11,582 mg/L TDS. This brine was also used for preparing carbonated water and for hot water flooding. The detailed brine compositions are presented in Table 1. Both brines were filtered through a 0.45 micron Millipore filter and deaerated for test use.

Table 1. Synthetic brine compositions.

	Synthetic Connate Water	Synthetic Injection Water
Na ⁺ , mg/L	41,355	3,410
Ca ²⁺ , mg/L	8,480	684
Mg ²⁺ , mg/L	1,453	113
K ⁺ , mg/L	1,184	261
Cl ⁻ , mg/L	82,982	5,756
SO ₄ ²⁻ , mg/L	1,500	1,130
HCO ₃ ⁻ , mg/L	/	228
Total Dissolved Solids, mg/L	136,954	11,582

2.2 Oil

A dead crude oil from a carbonate reservoir was used for the coreflooding tests. This heavy crude oil has very limited flow ability at room temperature, with oil viscosity of 58,600 cp at 25°C. At test temperature of 77°C, the oil viscosity was 565 cp.

2.3 Core samples

Four core plug samples from a carbonate reservoir were used in this study. The composite core sample, composed of two core plugs, was used for each coreflooding test for improving the material balance calculations. The ambient porosity and air permeability of these plugs ranged from 31.1% to 33.4% and 1,396 md to 1,454 md, respectively. Detailed properties of each core plug are presented in Table 2. The carbonated water flooding test was performed on the composite sample built by the first two plugs, while the other two plugs were used for the hot water flooding test.

Table 2. Properties of Core Plug Samples.

Sample	Length cm	Diameter cm	Ambient Porosity %	Ambient Air Permeability md
1	5.958	3.814	32.6	1494
2	5.369	3.732	33.4	1454
3	6.010	3.778	32.4	1408
4	5.896	3.784	31.1	1396

3 Experimental Methods

3.1 Coreflooding Experiment

Coreflooding experiments were performed to evaluate the potential of oil recovery improvement by the studied EOR strategies. Oil displacement experiments were conducted at a temperature of 77°C, with a backpressure of 2,600 psi and a confining pressure of 4,240 psi. Injection fluids, oil, brine and carbonated water, were loaded into the piston accumulators and injected into the core sample horizontally by a computer controlled Quizix pump. A constant injection rate of 0.25 ml/min was used for all the oil displacement processes. The pressure drop across the core sample was measured by digital differential pressure transducers. Both the carbonated water and the hot water floodings were performed in tertiary recovery mode to demonstrate the oil recovery improvement potential beyond the conventional waterflooding.

3.2 Core Preparation

Before saturating the core samples, computerized tomography (CT) scanning was performed on them to make sure there are no fractures or permeability barriers within the plug samples. Both the visual observation and the CT scanning confirmed that all the selected samples were homogeneous. Following that, the clean and dried core plug samples were first saturated with the synthetic connate water under vacuum, and then applying 2,000 psi pressure to make sure the core samples are fully saturated with the synthetic connate water. The centrifuge method was then used to establish the initial water saturation and saturate with oil. The maximum rotational speed was 4,500 RPM, and the prepared initial water saturation was at around 20% (Table 3). Finally, the oil-saturated core samples were then submerged under crude oil and put to age at reservoir temperature for four weeks.

3.3 Carbonated Water Flooding

The carbonated water flooding is an improved oil recovery (IOR) method, which improves the waterflooding performance by injecting CO₂-enriched water into the reservoir instead of the conventional injection water. Under the same temperature and pressure conditions, CO₂ is more soluble in oil than in water. Therefore, the CO₂ dissolved in water will transfer to oil phase after the injection of carbonated water. This will lead to oil viscosity reduction and favorable oil mobility enhancement. The oil volume expansion (swelling effect) is another beneficial effect, which also helps the oil recovery improvement. The oil recovery improvement potential of the carbonated water flooding for recovering heavy oil was evaluated by the coreflooding experiment conducted at reservoir conditions.

In this work, the carbonated water was prepared mainly by following the procedure presented by Dong et al. [14]. The CO₂ was mixed with the injection water at ambient temperature and elevated pressure. The CO₂ was first injected from a high pressure cylinder into a cylinder filled with the injection water. The sample cylinder was then mounted onto a rocker with a syringe pump connected to support pressure. After rocked for two hours, the CO₂-brine mixture was then left overnight to reach equilibrium. A small amount of the mixture sample was withdrawn at a constant pressure and flashed to two phases to measure the gas water ratio (GWR). Based on the correlation by Chang et al. [23], the estimated CO₂ solubility in the injection water at reservoir condition was around 20 scc CO₂/cc water. To make sure the injection fluid is single phase, the carbonated water was prepared at a lower CO₂/water ratio. The measured GWR of the prepared carbonated water before the coreflooding test was 18 scc CO₂/cc water.

After loaded into the coreflooding system, the core sample was first flushed with the oil at reservoir conditions to replace the oil in the core, and measure the oil permeability at initial water saturation (Table 3). The oil displacement was started with the conventional waterflooding using the injection water until the oil production was negligible. After that, 5.0 pore volumes (PV) of carbonated water was then injection, and finally followed by a post water flush using the injection water until the oil production was negligible. A

constant injection rate of 0.25 ml/min was used in all the displacement processes.

3.3 Hot Water Flooding

The major challenge for recovering heavy oil is the low oil mobility, and it is well recognized that thermal methods are among the most effective ways to tackle this problem. Oil viscosity usually decreases exponentially with increasing temperature. In this work, we conducted hot water flooding as a benchmark for the potential in improving heavy oil recovery. Hot water flooding can help significantly reduce oil viscosity, which will lead to remarkable improvement in oil mobility and sweep efficiency. In this study, we performed a water flooding at 120°C, around 40°C above the reservoir temperature, to mimic and evaluate the potential of hot water flooding on oil recovery improvement. The coreflooding procedure was generally the same as that for the carbonated water flooding, with both the hot water and the carbonated water applied in tertiary mode. The conventional waterflooding was first conducted at the temperature of 77°C. Following that, a second water flooding was then performed at 120°C to estimate the recovery potential from hot water flooding. The coreflooding was conducted until the oil production was negligible in each oil displacement stage.

4 Results and Discussion

4.1 Carbonated Water Flooding

The carbonated water flooding test was conducted on the composite sample composed of core plugs 1 and 2 (Table 2) to evaluate its potential in oil recovery improvement for the studied heavy oil. The carbonated water was injected after a conventional waterflooding, and then followed by a post water flush. Results showed that after around 1.2 PV of water injection, oil recovery reached 16.6% of original oil in core (OOIC) with 95.0% of water cut. After more than 20 PV of water injection, the waterflooding oil recovery reached 33.2% OOIC. Evident oil production improvement was achieved during the carbonated water flooding. After 5.0 PV of carbonated water injection, 13.4% OOIC additional oil was obtained. The final oil recovery reached 48.7% OOIC at the end of the post water flooding, with 15.5% OOIC incremental oil recovery achieved by the tertiary carbonated water flooding. The oil recovery curve and pressure response are plotted in Figure 1. It is noted that the capillary end effect might exist in this test due to the low injection rate. Generally, the carbonated water only has slight effects on water phase viscosity and the oil/water interfacial tension (IFT). At the same injection rate as for waterflooding, the carbonated water injection may not cause evident increase in capillary number. Therefore, the contribution of the end effect reduction to incremental oil might be slight. The evident incremental oil production in this test suggests that CO₂ effectively transfers out of the CO₂-saturated water and diffuses into the oil. The dissolution of CO₂ helps reduce oil viscosity and cause oil swelling, which yields more favorable water-oil mobility ratio. In terms of CO₂ utilization, injecting one litre (standard conditions) CO₂ produced around 1.3 ml incremental oil. This was consistent with the study results by Dong et al. (2011),

which ranged from 0.87 to 1.64 ml incremental oil per litre CO₂ injected. The encouraging oil recovery enhancement from this study shows a promising potential of the carbonated water flooding application for the studied heavy oil reservoir.

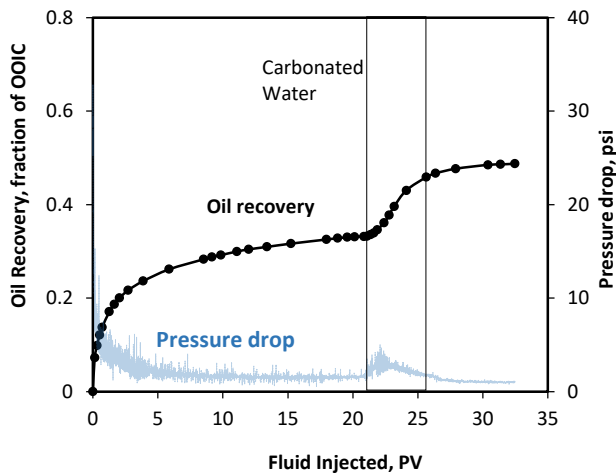


Fig. 1. Oil recovery and pressure drop as functions of injected pore volumes. Carbonated water flooding.

After the coreflooding test and unloaded the core sample from the core holder, it was observed that there were a few small holes at the inlet end face of the core sample. This was mainly attributed to the dissolution of rock by the carbonated water. The carbonated water has acidic nature, and it tends to dissolve the carbonate minerals of reservoir rock. The dissolution of the rock may lead to an increase in formation permeability, which can help improve the injectivity. However, it might be complex for sandstone because the dissolution may release cementing particles and cause later precipitation at pore throats. This might lead to the reduction in permeability [20]. For carbonates, the dissolution would generally improve pore connectivity because the carbonate minerals are the major components of the core. This effect was observed in a laboratory study using Middle Eastern carbonated rocks [21]. After large pore volumes of carbonated water injection, it was observed that the pore sizes became larger and some isolated pores were connected.

To help identify the dissolution effect by the carbonated water injection, we performed the CT image analysis on the core plug at the inlet end after the coreflooding test. Figure 2 compares the CT images before and after the coreflooding test. The first row shows four consecutive CT images scanned on the core plug before the coreflooding test. The left side image was the inlet face CT slice, and the thickness of each slice was 0.5 mm. It clearly showed that the core plug was homogeneous before the test. The second row images were the corresponding CT slices obtained after the carbonated water flooding test. The dissolved holes can be clearly observed from the left side two images. Figure 3 presents the CT images from varied view directions after the coreflooding. Generally, this CT image analysis indicated that the rock dissolution was relatively shallow (around 1.0 cm). The carbonated water injection may not cause evident effect on the carbonate reservoir. The similar phenomenon of slight

dissolution after carbonated water injection was also observed in a study by Mahzarl et al. [16].

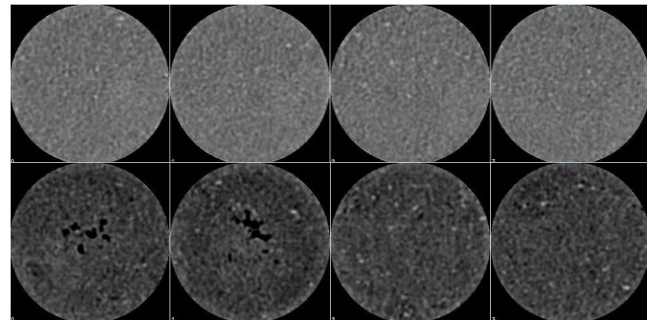


Fig. 2. Comparison of CT images before and after carbonated water flooding. The first row were four consecutive CT images scanned on the core plug before coreflooding, and the second row showed the corresponding images obtained after the coreflooding test. The left side image was the inlet face CT slice.

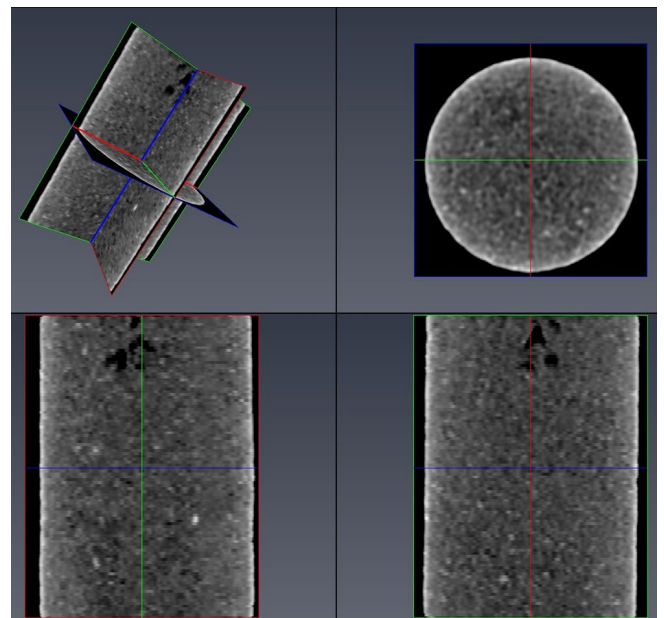


Fig. 3. CT images after carbonated water flooding.

4.2 Hot Water Flooding

The oil displacement test on the composite core sample 3&4 (Table 2) was performed to demonstrate the potential of hot water flooding in oil recovery enhancement. The conventional waterflooding was first conducted at 77°C. Following that, another waterflooding was then performed at 120°C to mimic the hot waterflooding. Results showed that after around 1.5 PV of water injection the water cut reached around 95.0%, and 20.2% OOIC was recovered. The waterflooding oil recovery after 20 PV of water injection reached 34.9% OOIC. The followed hot water flooding achieved significant additional oil production. The final oil recovery was 55.9% OOIC after 20 PV of hot water injection, with the incremental oil recovery reached 21.0% OOIC. Figure 4 shows the oil recovery and pressure drop as functions of pore volumes injected. Results clearly

demonstrate the remarkable potential of the hot water flooding for improving heavy oil recovery. Although it might be less effective than steam flooding in terms of heat delivery, hot water flooding does help evidently reduce oil viscosity. The extrapolated oil viscosity at 120°C based on the Arrhenius-type correlation was around 62 cp, which was only 11% of the original viscosity (565 cp) at 77°C. This dramatic oil viscosity reduction with increasing temperature contributes to the remarkable improvement in oil mobility. We conducted a simple calculation based on the Buckley-Leverett Equation to demonstrate the beneficial effect of oil viscosity reduction on accelerating oil production. All other parameters were kept the same except for the oil viscosity. The Corey correlation was used for relative permeability curves, and the exponents for oil and water phases were 3 and 2, respectively. The residual oil saturation was assumed to be 30%, and the end point water relative permeability was 0.15. Figure 5 compares the calculated oil recoveries for the 565 cp oil and the 62 cp oil. Results clearly showed the favourable effect of oil viscosity reduction on oil recovery improvement and acceleration. It is noted that a same residual oil saturation was used in the calculations. Some research studies [1, 24-25] indicates that oil viscosity reduction may also help reducing residual oil, which would further benefits the oil recovery improvement.

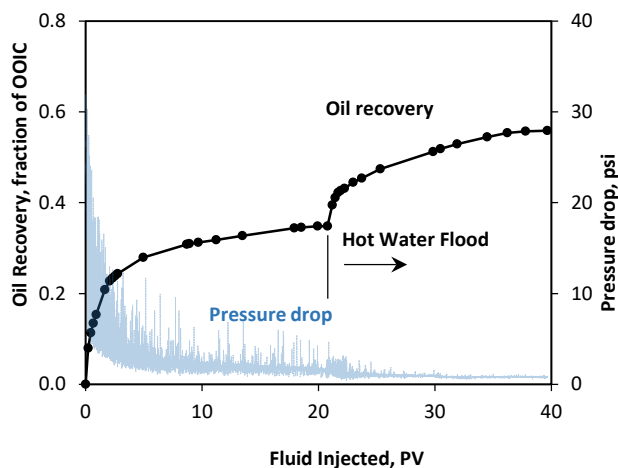


Fig. 4. Oil recovery and pressure drop as functions of injected pore volumes. Hot water flooding.

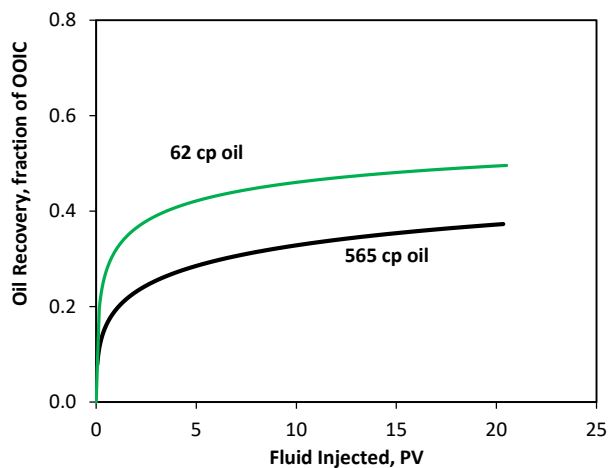


Fig. 5. Calculated (Buckley-Leverett Equation) oil recovery curves for 565 cp and 62 cp oils.

4.3 Discussion

Figure 6 compares the incremental oil recovery by the carbonated water flooding with that achieved by the hot water flooding during the tertiary production stage. The tertiary oil recovery in this figure was expressed in terms of the remaining oil in core after water flooding (ROIC). The detailed recovery data are summarized in Table 3. As shown in Figure 6, the incremental oil recovery at the end of the carbonated water injection was very close to the result by the hot water flooding after the same amount of water injection. Although hot water floodings at higher temperature will produce more incremental oil [1], the results from this study demonstrate that the carbonated water flooding has a potential to achieve encouraging oil recovery improvement. Delivering CO₂ by carbonated water into heavy oil reservoir is an effective solution to help evidently improve oil mobility.

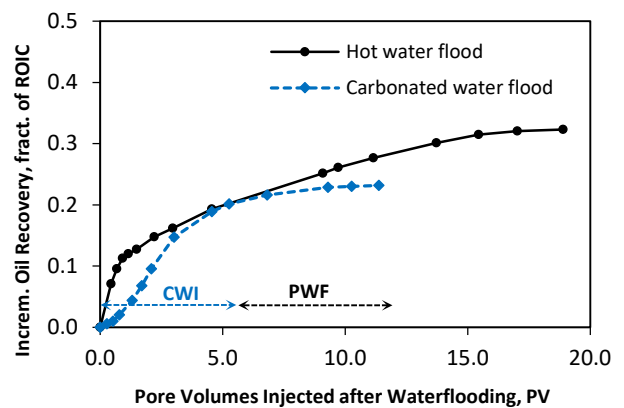


Fig. 6. Incremental oil recovery as functions of pore volumes injected after waterflooding. ROIC—remaining oil in core after waterflooding; CWI—carbonated water injection; PWF—post water flush.

Table 3. Summary of Oil Recovery Results.

	Carbonated Water Flooding	Hot Water Flooding
Core Sample	1&2	3&4
Ambient Porosity, %	33.0	31.7
Air Permeability, md	1475	1402
Initial water saturation, %	20.6	20.7
Oil permeability at Swi, md	1218	1032
Waterflooding oil recovery, %OOIC	33.2	34.9
Incremental recovery at 5.0 PV injection, %ROIC	19.7	19.9
Total incremental oil recovery, %ROIC	23.2	33.1
Final oil recovery, %OOIC	48.7	55.9

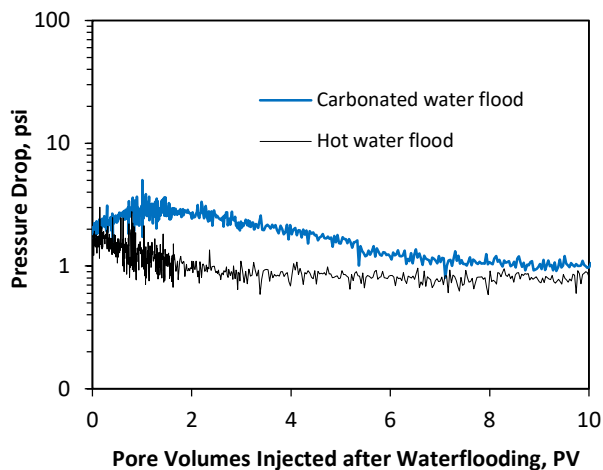


Fig. 7. Pressure drop as functions of pore volumes injected after waterflooding.

Figure 7 presents the pressure responses during the tertiary recovery process of both the carbonated water flooding and the hot water flooding. Results showed that when starting the carbonated water injection the pressure increased first, and then gradually decreased after more than 1.0 PV of injection. The pressure increase indicated that the carbonated water contacted with more remaining oil than the preceding plain injection water, which could positively contribute to oil mobilization. The diffusion of CO₂ from the carbonated water to oil phase is a relatively slow process. It might take some time or require certain amount of CO₂ delivered to achieve evident oil viscosity reduction. Therefore, the oil recovery enhancement by the carbonated water injection is relatively slow at the beginning. The delayed oil response at the earlier stage of the carbonated water injection can also be observed in Figure 6, where the slope of the oil recovery curve was relatively flat. On the contrary, as shown in Figure 7, the injection of hot water immediately led to significant pressure decrease. This indicated that the oil viscosity was effectively reduced at higher temperature, which would significantly enhance the oil mobilization. The steeper oil recovery curve at the earlier stage of hot water injection as shown in Figure 6 evidenced the remarkable response in oil production. In general, the carbonated water flooding can help evidently enhance heavy oil recovery, but the process of production improvement is relatively slower than hot water flooding.

It should be pointed out that the laboratory evaluations intend to study the ultimate potential in oil recovery improvement. The complex reservoir environment and operation processes usually have great impact on the actual results of field applications. For instance, the reservoir temperature is not constant during the hot water flooding. This would induce viscosity gradient and limit the efficiency of the process.

5 Conclusions

We evaluated carbonated water flood through a core flooding study for its potential application for a carbonate heavy oil reservoir. Hot water flooding was also conducted for

comparison. The following conclusions are drawn from this study:

- The carbonated water flooding applied in tertiary mode achieved 15.5% OOIC of oil recovery improvement for the studied heavy oil. This indicates that the oil viscosity is effectively reduced by the transfer of CO₂ from water to oil phase, and injecting carbonated water is more favorable than the conventional waterflooding.
- The hot water flooding performed at 120°C produced additional 21.0% OOIC incremental oil beyond waterflooding. This demonstrates the effectiveness of hot water flooding as well as the higher capacity of thermal techniques in oil mobility enhancement.
- Injecting carbonated water to carbonate core caused rock dissolution. The CT image analysis indicated that the rock dissolution was relatively shallow, and the carbonated water injection may not cause evident impact on the carbonate reservoir.
- The results from this work demonstrate the promising potential of the carbonated water flooding for improving the waterflooding performance for heavy oil carbonates. The incremental oil recoveries for both processes might be slightly overestimated due to the capillary end effect, but the general trend in oil recovery enhancement should be intact. Higher oil recovery enhancement is also expected upon further optimization studies.

References

1. J.K. Dietrich, The displacement of heavy oil from Diatomite using hot water and steam, Paper SPE-129705 presented at the 2010 SPE Improved Oil Recovery held in Tulsa, Oklahoma, USA, 24-28 April (2010).
2. D. Levitt, S. Jouenne, I. Bondino, E. Santanach-Carreras, M. Bourrel, Polymer flooding of heavy oil under adverse mobility conditions, Paper SPE-165267 presented at the SPE Enhanced Oil Recovery Conference held in Kuala Lumpur, Malaysia, 2-4 July (2013).
3. E. Delamaide, A. Zaitoun, G. Renard, R. Tabary, Pelican Lake Field: First successful application of polymer flooding in a heavy reservoir, SPE Res. Eval. & Eng. **17**(03): 340-354 (2014).
4. E. Delamaide, Polymer flooding of heavy oil – from screening to full-field extension, Paper SPE-171105-MS presented at the SPE Heavy and Extra Heavy Oil Conference – Latin America held in Medellin, Colombia, 24-26 September (2014).
5. R.S. Seright, D. Wang, N. Lerner, A. Nguyen, J. Sabid, R. Tochor, Can 25-cp polymer solution efficiently displace 1,600-cp oil during polymer flooding? SPE J. **23**(06): 2260-2278 (2018).
6. L.W. Holm, V.A. Josendal, Mechanisms of oil displacement by carbon dioxide, J. Pet. Technol. **26** (12): 1427-1438 (1974).
7. R.J. Christensen, Carbonated waterflood results—Texas and Oklahoma, Paper SPE-66 presented at the Seventh Annual Meeting of Rocky Mountain Petroleum Sections

- of AIME held in Farmington, NM, USA. 25-26 May (1961).
8. C.W. Hickok, H.J. Ramsay Jr., Case histories of carbonated waterfloods In Dewey-Bartlesville Field, Paper SPE-333 presented at the SPE Secondary Recovery Symposium held in Wichita Falls, Texas, USA. 7-8 May (1962).
 9. J.O. Scott, C.E. Forrester, Performance of Domes Unit carbonated waterflood - First Stage, *J. Pet. Technol.* **17**(12): 1379-1384 (1965).
 10. W.E. Johnson, Lab experiments with carbonated water and liquid carbon dioxide as oil recovery agents, *Producer Monthly*, November (1952).
 11. L.W. Holm, Carbon dioxide solvent flooding for increased oil recovery, *Trans. AIME.* **216**, 225-231 (1959).
 12. L.W. Holm, CO₂ requirements in CO₂ slug and carbonated water recovery processes, *Producer Monthly*, September (1963).
 13. E.H. Mayer, R.C. Earlougher Sr., A. Spivak, A. Costa, Analysis of heavy-oil immiscible CO₂ tertiary coreflood data, *SPE Res. Eng.*, **3** (01): 69-75 (1988).
 14. Y. Dong, B. Dindoruk, C. Ishizawa, E. Lewis, T. Kubicek, An experimental investigation of carbonated water flooding, Paper SPE-145380 presented at the SPE Annual Technical Conference and Exhibition held in Denver, Colorado, USA, 30 Oct-2 Nov (2011).
 15. M. Sohrabi, A. Emadi, S.A. Farzaneh, S. Ireland, A thorough investigation of mechanisms of enhanced oil recovery by carbonated water injection, Paper SPE-175159 presented at the SPE Annual Technical Conference and Exhibition held in Houston, Texas, USA, 28-30 September (2015).
 16. P. Mahzari, P. Tsohis, A. Farzaneh, M. Sohrabi, A. Enezi, A.A. Yousef, A.A. Eidan, A comprehensive experimental study of pore-scale and core-scale processes during carbonated water injection under reservoir conditions, Paper SPE-188142 presented at the SPE Kingdom of Saudi Arabia Annual Technical Symposium and Exhibition held in Dammam, Saudi Arabia, 24-27 April (2017).
 17. J.M. Perez, S.W. Poston, Q.J. Sharif, Carbonated water imbibition flooding: An enhanced oil recovery process for fractured reservoirs, Paper SPE/DOE-24164 presented at the SPE/DOE Eighth Symposium on Enhanced Oil Recovery held in Tulsa, Oklahoma, April 22-24 (1992).
 18. M. Sohrabi, M. Riazi, M. Jamiolahmady, S. Ireland, C. Brown, Mechanisms of Oil Recovery by Carbonated Water Injection, Paper SCA2009-26 presented at the International Symposium of the Society of Core Analysts held in Noordwijk, The Netherlands, 27-30 September (2009).
 19. M. Seyyedi, M. Sohrabi, A. Farzaneh, Investigation of Rock Wettability Alteration by Carbonated Water through Contact Angle Measurements, *Energy Fuels*, **29**(09): 5544-5553 (2015).
 20. S.G. Sayegh, F.F. Krause, M. Girard, C. DeBree, Rock/fluid interactions of carbonated brines in a sandstone reservoir: Pembina Cardium, Alberta, Canada. *SPE Form. Eval.* **5**(04):399-405 (1990).
 21. F. Kono, A. Kato, M. Shimokawara, K. Tsushima, Laboratory measurements on changes in carbonate rock properties due to CO₂-saturated water injection, Paper SPE-172013-MS presented at the Abu Dhabi International Petroleum Exhibition and Conference, 10-13 November (2014).
 22. J.S. Miller, R.A. Jones, A laboratory study to determine physical characteristics of heavy oil after CO₂ saturation, Paper SPE/DOE 9789 presented at the 1981 SPE/DOE Second Joint Symposium on Enhanced Oil Recovery of the Society of Petroleum Engineers held in Tulsa, Oklahoma, 5-8 April (1981).
 23. Y.B. Chang, B.K. Coats, J.S. Nolen, A compositional model for CO₂ floods including CO₂ solubility in water, *SPE Res. Eval. & Eng.* **1**(02): 155-160 (1998).
 24. S. Doorwar, K.K. Mohanty, Viscous-fingering function for unstable immiscible flows, *SPE J.* **22**(01): 19-30 (2017).
 25. C. Lamy, J. Botua, U. Granone, J. Hy-Billiot, A. Brisset, Temperature dependant relative permeabilities endpoint: laboratory experiments under reservoir conditions from hot-water flood to steamflood, Paper SPE-190422-MS presented at the SPE EOR Conference at Oil and Gas West Asia held in Muscat, Oman, 26-28 March (2018).

Carbonated Smart Water Injection for Optimized Oil Recovery in Chalk at High Temperature

Md Ashraful Islam Khan^{1*}, Sander Haaland Kleiberg¹, Ivan Dario Pinerez Torrijos¹, Tina Puntervold¹ and Skule Strand¹

¹Department of Energy Resources, University of Stavanger, 4036 Stavanger, Norway

Abstract. Finding cost-efficient ways of increasing oil production with a low carbon footprint is the new challenge for the petroleum industry that wants to meet the net-zero emission goals by 2050. Smart water injection is an EOR process that increases oil production and delays water breakthrough by wettability alteration. Seawater is a smart water in chalk reservoirs, being especially effective at high temperatures. Different studies have shown that the effectiveness of seawater can be further improved by modifying the ion composition before injection.

Carbonated water (CW) has been proposed as a potential EOR fluid. In addition to producing extra oil, reduction of greenhouse gas (CO₂) in the atmosphere can be achieved by using carbonated smart water as an injection fluid. The main mechanism behind increased oil recovery by injecting carbonated water is believed to be oil viscosity reduction and swelling, as the CO₂ is transferred from the aqueous phase to the oil phase. Wettability alteration has also been proposed as a possible mechanism, and this hypothesis is further investigated in this study along with other proposed mechanisms.

Stevens Klint outcrop chalk was used in this study, this material is recognized as an excellent analogue for North Sea chalk reservoirs. Optimized oil recovery by carbonated water in chalk was investigated at a high temperature (130°C) by flooding carbonated formation water (CFW) and carbonated sea water (CSW), to be compared with high saline formation water (FW) and sea water (SW) flooding. The oil/brine/rock/CO₂ interactions were tracked by measuring the pH of the produced water (PW) and by identifying any mineralogical changes by SEM (Scanning Electron Microscope) and EDX (Energy Dispersive X-Ray) analyses. The solubility of CO₂ in different brines was measured and compared with simulation data performed by PHREEQC. The diffusion of CO₂ from the aqueous phase to the oil phase was analysed to check if enough CO₂ can be diffused from the carbonated water into the oil phase.

By flooding CSW in both secondary and tertiary mode, a slight increase in the oil recovery was observed and was found to be the best performing brine. The oil recovery was also slightly increased using CFW in tertiary mode after FW which does not behave like smart water for carbonates.

The solubility of CO₂ was low and increased by increasing pressure and decreasing brine salinity. The acidity of CW did not increase by increasing pressure. No changes in pore surface minerals were observed after CW flooding, confirming limited mineral dissolution. A mass transfer of CO₂ from the brine phase to the oil phase was confirmed in the experimental work, but a significant amount of CO₂ remained in the brine phase.

The main mechanism behind this extra oil observed using CW is most likely not linked to oil swelling and viscosity reduction or mineral dissolution which could affect the porosity and the permeability of the rock system. Wettability alteration is a more likely explanation but needs to be looked further into for confirmation.

1 Introduction

The global energy demand is increasing more than 1% every year because of the growth of population and increase in per capita energy consumption in developing countries. Although energy production from renewable sources is showing strong growth in recent years, oil is still the biggest source of energy production [1]. Therefore, to meet the net zero carbon emission goal within 2050, it is important to find a better way to produce oil in an environmentally friendly manner. Carbon capture, utilization, and storage (CCUS) might be a solution where CO₂ will be captured and used as a product to produce

more oil, and therefore, CO₂ will be stored permanently in the reservoir after permanent plug and abandonment.

Previous lab experiments and field trials have shown that injection of CO₂ can increase oil recovery by reducing oil viscosity and increasing sweep efficiency [2]. The injected CO₂ was not fully recovered and thus shows storage possibility. However, direct CO₂ injection shows gravity segregation and viscous fingering effect that causes early CO₂ breakthrough along with technical difficulties in handling CO₂. These problems can be minimized by injecting carbonated water (CW) without sacrificing CO₂ storage potential [3].

* Corresponding author: sarjilsust09@gmail.com

Several mechanisms for CW EOR have been proposed in different literature [4]. The main mechanism behind extra oil recovery is believed to be the mass transfer of CO₂ from the water phase to the oil phase as the solubility of CO₂ is much higher in oil than in water [5-7]. This leads to oil swelling, reduction of interfacial tension (IFT) between oil and rock, and reduction of oil viscosity resulting in reconnection of isolated oil droplets, increases relative permeability of oil, and enhances the oil mobilization, thus increases sweep efficiency [3]. Wettability alteration due to CO₂ mass transfer was also proposed by Sohrabi et al. (2015). CO₂ dissolution into the oil phase destabilises the polar organic components of the oil attached to the rock surface and helps them to move. Decreases in the aqueous phase pH (in CW) also change the surface charges on the water/oil and water/rock interfaces which leads to subsequent changes in the wettability of the system and thus produces more oil [8].

The evolution of solution gas from the heavy oil caused by CO₂ dissolution is also considered one of the mechanisms for oil recovery by injecting CW [9]. The reaction between rock and CW resulting in rock dissolution and increase permeability by creating new a path to mobilize oil might also help to increase oil recovery [10].

Previously, our research has shown sea water (SW) works as smart water at high temperatures by changing the wettability of the reservoir. The effectiveness of SW can be further improved by removing NaCl from SW and spiking it with additional sulphate ions [11]. However, the preparation of this water demands additional energy to treat the water and obtain the desired compositions. Moreover, adding extra chemicals makes the injection less cost efficient. At high temperatures, non-stable sulphate concentration can lead to precipitation, affecting the porosity and permeability of the reservoir. Additionally, both the injection and the production facilities can experience severe scaling problems.

Therefore, there is a need for more environmentally friendly injection water that not only increases the oil recovery but also reduces the risk of precipitation. Injection of carbonated water can be a good alternative for the carbonate reservoir [4]. Many researchers reported extra oil recovery in carbonates by injecting carbonated water along with CO₂ storage possibilities [2].

Initial research done on carbonated water injection (CWI) in the 1940s by the Oil Recovery Corporation reported an extra 15% oil production when CW was injected after conventional water flooding [12]. Lake et al. (1984) have reported additional oil recovery of 26% in the tertiary mode by injecting CW in case of light oil. Recently, extensive research was conducted by Herriot Watt Institute of Petroleum Engineering Centre on CWI for oil recovery by core flooding and micro model which showed extra oil recovery both in the secondary and the tertiary mode [8]. Kilybay et al. (2016) performed a comparative oil recovery experiment by flooding different smart waters and carbonated smart water in carbonate reservoir core plugs and experienced extra oil recovery (~14%) for carbonated smart water injection. This extra oil recovery was attributed to the impact of CO₂ mass transfer from brine to oil inducing a viscosity drop, local flow diversion and trapped oil swelling. Carbonate dissolution and

pore enlargement were also proven through NMR porosity and ICP-MS studies [14]. Sand pack flooding experiments conducted by Mosavat (2014) showed it is possible to store CO₂ by injecting CW. Kechut et al. (2011) showed about 47 - 51% of total CO₂ injected can be stored by carbonated water injection through numerical simulations and laboratory experiments.

The objective of this work is to determine if CW can induce EOR effects in chalk and to determine which mechanisms may be behind such effects. Thus, we compared the oil recovery performance of different core floods by injecting different carbonated brines at high temperatures in equally restored chalk cores. The reasons behind the extra oil observed were discussed. The solubility of CO₂ in different brine was studied by experimental work and simulations. The mass transfer of CO₂ from the brine phase to the oil phase was also confirmed through experimental work.

2 Experimental sections

2.1. Core Material

Outcrop Chalk collected from Stevns Klint (SK) quarry, near Copenhagen, Denmark, was used in this experiment. Cores were drilled from the same chalk block in the same direction and cut and shaped to the desired diameter of 3.8 cm and the desired length of 7 cm. All cores were inspected visually, and no visible fractures and distinct heterogeneities were found. These outcrop chalk cores consisted of 98% pure biogenic CaCO₃ and are similar to North Sea chalk reservoir cores. SEM (Scanning Electron Microscope) and EDX (Energy Dispersive X-Ray) analyses were done to see the changes in the minerals before and after the exposure to different carbonated brines. The specific surface area, (BET), porosity, and permeability of the cores were measured, and the values measured were found to be similar to previously published data [11, 16-21]. The properties of the cores are given in Table 1.

Table 1. Physical properties of the SK cores.

Core #	BET m ² /g	Porosity (%)	Water Permeability k _w (mD)	Pore volume (mL)
SK-3	2.0	48.5	3.7	38.7
SK-4		49.5	3.8	40.9
SK-6		45.4	4.1	36.3
SK-11		47.2	3.8	38.3

2.2 Crude Oil

A low asphaltenic stock tank oil with an acid number (AN) of 2.90 mg KOH/g and a base number (BN) of 0.95 mg KOH/g was used as base oil. This base oil was diluted with 40 weights % of heptane, centrifuged, and filtrated through a 5 µm Millipore filter. The AN of that diluted oil is found to be

~2.1 mg KOH/g and no precipitation of asphaltenic material was observed during storage after filtration. The surface active polar organic components were removed from a batch of the base oil using silica gel that provided an oil of ~0 AN. When the diluted oil and silica-treated oil were mixed, an oil (Oil A) with AN of 0.58 mg KOH/g and BN of 0.30 mg KOH/g was obtained which was used in the experiments. AN and BN of the oil samples were analysed by potentiometric titration. The density and viscosity of the prepared oil were determined to be 0.81 g/cm³ and 2.4 cP, respectively.

2.3 Brines

Brines used in this experiment were made by mixing deionized water (DI) and reagent-grade salts. All the brines were mixed overnight by magnetic rotation and filtered through a 0.22 µm Millipore filter. SW composition is based on the sea water composition from the North Sea and the FW composition is based on the formation water from a North Sea Chalk reservoir. The properties of the brines are given in table 2.

Table 2. Properties of brines.

Ions(mM)/ Properties	SW	FW
[Na ⁺]	450.1	997.0
[K ⁺]	10.1	5.0
[Ca ⁺]	13.0	29.0
[Mg ²⁺]	44.5	8.0
[Cl ⁻]	525.1	1066.0
[HCO ₃ ⁻]	2.0	9.0
[SO ₄ ²⁻]	24.0	0.0
TDS (g/L)	33.34	62.83
Density (g/cm ³)	1.02	1.04
Bulk-pH	7.8	7.3

Carbonated sea water (CSW) and carbonated formation water (CFW) were prepared by equilibrating access CO₂ (g) with the respective brine in a pressure cylinder at 6-7 bar and 23 °C. The equilibrated carbonated brine was then moved to a separate cylinder at a higher pressure, so no gas cap was formed.

2.4 Core restoration

2.4.1 Establishing initial water saturation (S_{wi})

All cores were initially cleaned by flooding 5 PV of deionized (DI) water at room temperature to remove easily dissolvable salts, especially sulphate salts as described by Puntervold et al. (2007). The cores were then dried at 90°C to a constant weight. The initial formation water saturation (S_{wi}) of 10% was established by using the desiccator technique [22]. After they had reached 10% initial water saturation with formation water, the cores were stored in a sealed container for 3 days to allow an even ion distribution within the cores.

2.4.2 Oil exposure

The cores were then flooded with 4 PV of Oil (1.5 PV in each direction) at 50°C. Finally, the cores were wrapped in Teflon tape to avoid unrepresentative wetting on the outer surface and aged in the same oil for 2 weeks at 90°C to achieve a more homogeneous core wetting.

2.5 Oil Recovery by Spontaneous Imbibition

Spontaneous imbibition (SI) experiment was performed on a restored core to evaluate the degree of water wetness after core restoration. The experiment was performed at 110°C and 10 bar using formation water as the imbibing brine to avoid any chemical induced wettability alteration. The produced oil was collected in a glass burette that has a resolution of 0.1 ml. The volume of oil produced was calculated as % original oil in place (OOIP) versus time. The experimental setup is depicted in the following figure 1.

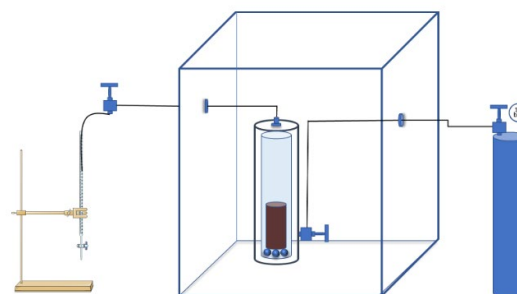


Fig. 1. Schematic of the setup used for spontaneous imbibition experiment.

2.6 Oil Recovery by Viscous Flooding (Forced Imbibition)

All experiments were performed at 130°C. The restored cores were mounted in the Hassler core holder with a confining pressure of 20 bar and a back pressure of 10 bar to prevent boiling. The cores were then successively flooded with different injection brines in secondary and tertiary mode at a constant injection rate of 1 PV/Day. When the recovery plateau was reached, the injection rate of the tertiary injection fluid was increased 4 times (4 PV/Day) to observe any end effects. The pressure drop was recorded during the experiment. Samples of produced water were collected during the experiment, and the pH of produced water were measured to catch any chemical reactions during the brine injections. The oil recovery, pressure drop, and the pH of the produced water was plotted against the PV brine injected. The experimental setup is illustrated in figure 2.

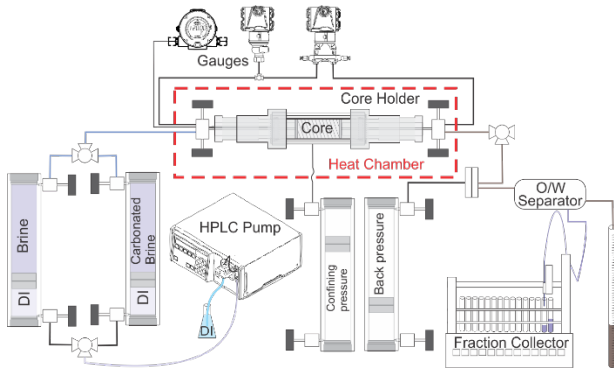


Fig. 2. Schematic of flooding setup.

2.7 Solubility of CO₂ in brines

The solubility of CO₂ in brines at 60°C was measured in the pressure range from 10 to 200 bar. 150 ml of a specific brine (DI, SW, FW) was mixed with 150 ml of CO₂ (g) at 10 bar in a pressured cylinder. The 2-phase system with a CO₂ gas cap above the brine was then temperature equilibrated overnight at 60°C. At each pressure stage the CO₂ – brine systems were mixed and allowed to equilibrate into 2 phases before a single flash of the equilibrated carbonated brine phase was performed. A small volume of the carbonated brine was flashed to standard conditions (SC). The pressure was maintained in the sample cylinder during the flash experiment. The mass of brine collected in the flash apparatus and liberated gas volume at SC was measured by a gasometer. The GOR as mg CO₂ per gram of brine was calculated based on the average of 3 flash experiments at each pressure stage. The pH of the carbonated brine was also measured in freshly taken samples after each flash experiment at ambient conditions.

2.8 Simulation of CO₂ solubility using PHREEQC

PHREEQC (version 3) software was used to simulate the solubility of CO₂ in different brines. The pH of the brines equilibrated with CO₂ was also simulated at specific pressure points at 60°C. The simulated data were then compared with the experimentally obtained data.

3 Results and discussion

3.1. Solubility of CO₂

To understand the potential of carbonated brine in EOR and the storage capacity of CO₂ in aquifers, it is important to understand the solubility of CO₂ in brines at pressure and temperature. Therefore, flash experiments were conducted to measure how much CO₂ is soluble in different brines at 60°C at a wide range of pressures. The amount of dissolved CO₂ in FW, SW, and DI water is presented in figure 3, as an average of the result from 3 flash experiments. The experimental data is also compared with simulated data obtained from PHREEQC.

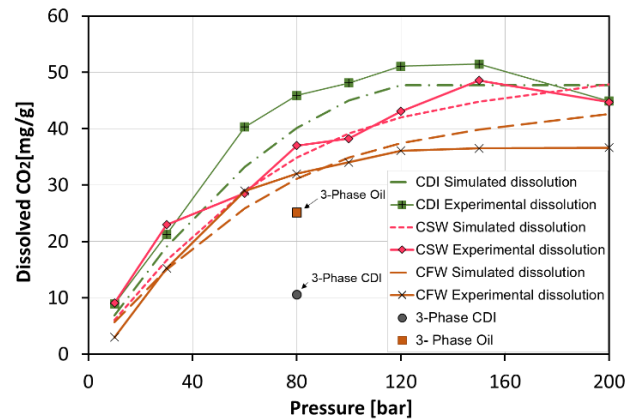


Fig. 3. Solubility of CO₂ in different brines at 60°C was plotted against pressure. Continuous lines are representing experimental data and dotted lines are representing the simulated data. 2 single points are representing the solubility of CO₂ in the water phase and the oil phase when both phases are present.

The experimental results show that the solubility of CO₂ gradually increases with the increase in pressure, but no significant increases are observed at pressures above 100 bar. CO₂ becomes a supercritical fluid when temperature and pressure exceed 31°C and 73 bar, without affecting the solubility of CO₂ in the brine phase. The solubility of CO₂ also depends on the salinity. The highest solubility is observed in DI water, and it decreases with increasing salinity. Thus, the formation water having the highest salinity (62830 ppm) showed the lowest solubility. However, the solubility difference was not more than 40% for FW and DI water at any pressure stages above the critical CO₂ pressure. The solubility of CO₂ in brines is low with maximum values of 50 mg/g in DI water. The solubility is less than 10 mg/g in all the brines at 10 bar which is the injection pressure for all the flooding experiments that will be presented in the next section.

The solubility of CO₂ in DI, SW, and FW has also been simulated using PHREEQC. The results from the simulations are presented in figure 3 and are in line with the experimental data, confirming the low CO₂ solubility at any pressure. This confirms that PHREEQC could be used to estimate CO₂ solubility in other brines or at other process temperatures.

The experimental data is aligned with simulated data and previously published experimental data by Duan et al. (2006) and Spycher and Pruess (2004).

The main mechanism behind extra oil recovery by carbonated water is the mass transfer of CO₂ from the water phase to the oil phase as the solubility of CO₂ is much higher in oil than in water. This phenomenon has been investigated in a 2-phase flash experiment at 80 bar and 60°C. CDI water at 80 bar and 60°C was equilibrated with the same amount of stabilized Oil A. Single flash experiments were performed from both equilibrated phases to SC.

At 80 bar and 60 °C, the CDI is able to dissolve 45 mg CO₂/g DI. After equilibrating with the same amount of crude oil, the amount of CO₂ in DI water was reduced 4 times down to 11

mg/g, while the amount of CO₂ transferred to the Crude oil Phase was 25 mg/g, giving a gas/oil ratio about 2.5 times higher than the gas/water ratio. Thus, this experiment confirms that CO₂ in carbonated water could be transferred to the oil phase as claimed by several researchers [5-7]. This transportation of CO₂ is because of the chemical potential difference between the two phases. But the amount of CO₂ that could be transported from carbonated water is very limited, so it is hard to believe that swelling and viscosity reduction of the oil phase could be the main mechanisms for enhancing oil recovery.

The brine phase collected from the single flash of carbonated water was collected, and the measured pH values for the individual brines at ambient conditions are presented in figure 4.

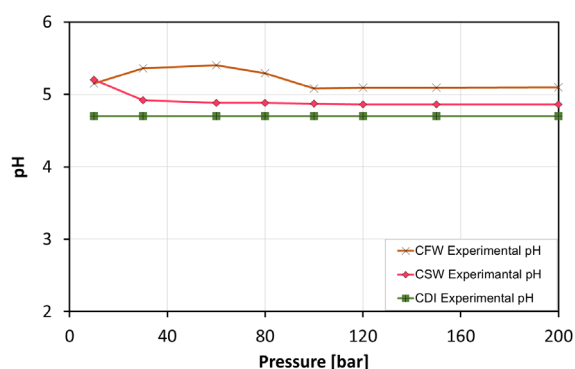
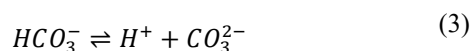
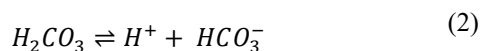
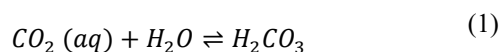


Fig. 4. The pH of different carbonated brines at different pressure and constant temperature (60°C). pH was measured at ambient conditions.

The pH was in the range of 4.7 to 5.2 for all brines and independent on the equilibrating pressure. CFW showed a slightly higher pH (~5) while CDI showed the lowest pH (~4.7).

Carbonic acid (H₂CO₃) is formed by dissolving CO₂ into different brine which is a weak acid (eq. 1). Carbonic acid is then rapidly separated into carbonate (CO₃²⁻) and bicarbonate (HCO₃⁻) (eq. 2 and 3) which provide hydrogen ions that give lower pH values (~5).



The constant pH values at different pressure points prove that the concentration of protons (H⁺) cannot be increased by increasing the amount of CO₂ in the brine phase as we observed by increased pressure. Simulation of the pH of different carbonated brine using PHREEQC confirmed the same trend, figure 5. The simulated pH is lower than the measured because the pH was measured in ambient

conditions.

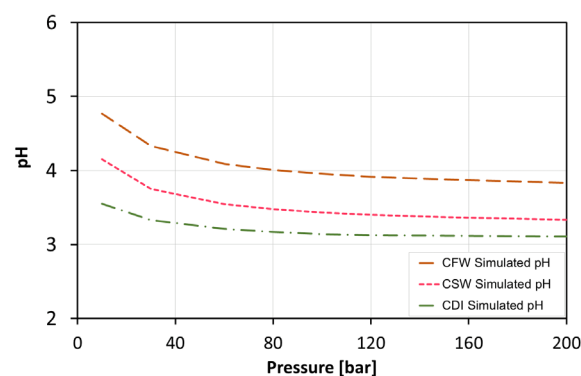


Fig. 5. Simulated pH of different carbonated brines at different pressure and constant temperature (60°C).

As the concentration of protons (H⁺) cannot be increased with an increase in pressure, the chemical effect of carbonated water in EOR cannot be increased by increasing pressure.

3.2. Initial wetting of the restored cores

All oil recovery studies performed on equally restored SK chalk cores were taken from the same block to minimize the variation in physical core properties. Spontaneous imbibition (SI) is a practical way to approach and quantify the wettability of oil/brine/rock systems [25]. Both the speed of imbibition and the ultimate recovery gives valuable information to describe the core wettability after the core restoration. SI experiments could easily be performed at reservoir temperature, to reduce uncertainties regarding physical fluid properties and temperature effects. A spontaneous imbibition test was performed on the restored core SK-3 at 10 bar at 110°C. FW was used as the imbibing brine to exclude the effect of chemical induced wettability alteration during the test. The result is presented in figure 6.

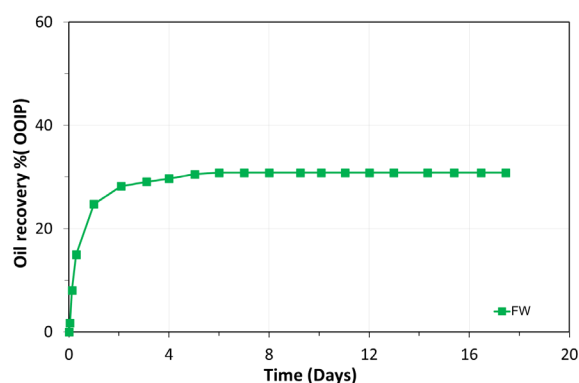


Fig. 6. Spontaneous imbibition into oil (AN=0.58 mgKOH/g) saturated (Swi=10%) chalk core at 110°C using FW as imbibing brine with a constant pressure of 10 bar. Oil recovery (% OOIP) was plotted against time (Days).

The Oil recovery reached its plateau at around 31% of OOIP on the 7th day, confirming positive capillary forces and that the core wettability is clearly on the water wet side.

A simplified wetting index only based on SI experiments can be used to calculate the wettability [26]. The degree of water-

wetness can be quantified by a modified Amott water index (I_{W-SI}^*) (eq. 4) using a very water-wet core as a reference core.

$$I_{W-SI}^* = \frac{SI_C}{SI_{WWC}} \quad (4)$$

SI_{WWC} is the oil recovery (% OOIP) by spontaneous imbibition from a strongly water-wet SK reference core which have not been exposed to any crude oil. The value of the modified Amott water index is 1 for a strongly water wet core and 0 for a neutral to strongly oil wet core.

To calculate the modified Amott water index for SK cores, we have used a strongly water-wet SK core as the reference core described by Piñerez Torrijos et al. (2019). The reference core was restored with FW, $S_{wi}=10\%$, heptane as oil phase, and FW was used as imbibing fluid at 23°C. A rapid oil production occurred, reaching a recovery of 68% OOIP after 40 minutes and an ultimate recovery of 71% OOIP after 4 hours. Therefore, the value of SI_{WWC} is 71. SI_C for the assessed SK-3 core is 31. I_{W-SI}^* for core SK-3 calculated by eq. 4 is then equal to 0.44 which suggests that the core has intermediate water wetness.

3.3. Flooding experiment

To evaluate the effectiveness of different types of injection brines on oil production, we have used equally restored sister cores of core SK-11, SK-6, and SK-4.

After core restoration, the cores were flooded at 130°C with different injection brines in both secondary and tertiary modes. The experiments were maintained by 20 bar confining pressure and 10 bar back pressure. The injection rate was constant and was 1 PV/D in all experiments performed. In the end, the injection rate was increased four times to evaluate any end effects. 4 different injection brines were used, formation water (FW), seawater (SW), carbonated formation water (CFW), and carbonated seawater (CSW). The carbonated brines were equilibrated with CO₂ gas at 6-7 bar, before the carbonated brine phase was transferred to a separate cylinder. The amount of CO₂ dissolved in the carbonated brines used for injection was then close to 5 mg CO₂/g of liquid. All injection brines were pressurized to 10 bar to match the back pressure of the system before injection.

In the first flooding experiment on core SK-11, FW was injected in secondary mode at a rate of 1 PV/D. The pressure difference between the inlet and outlet of the core was monitored. An ultimate oil recovery plateau of 68 %OOIP was reached after 2 PV was injected, figure 7a. The pressure drop (ΔP) gradually increased and reached the maximum value of 450 mbar after 0.5 PV was injected before it declined and stabilized at 150 mbar.

The pH in produced water samples was measured and compared with %OOIP in figure 7b. The first produced water was observed after 0.5 PV was injected (60 %OOIP). The produced water pH was close to 6.5, slightly lower than the bulk FW pH of 7.2.

After 3.5 PV injection, the injection brine was switched to CFW, figure 7. During the next 5 days (5 PV), 5% extra oil

was mobilized. The ΔP immediately increased from 150 mbar to 800 mbar which could not be explained by a change in the viscosity of CFW. With 4 times increase in ΔP it is difficult to pinpoint if the extra oil mobilized is a result of the CFW or increased viscous forces.

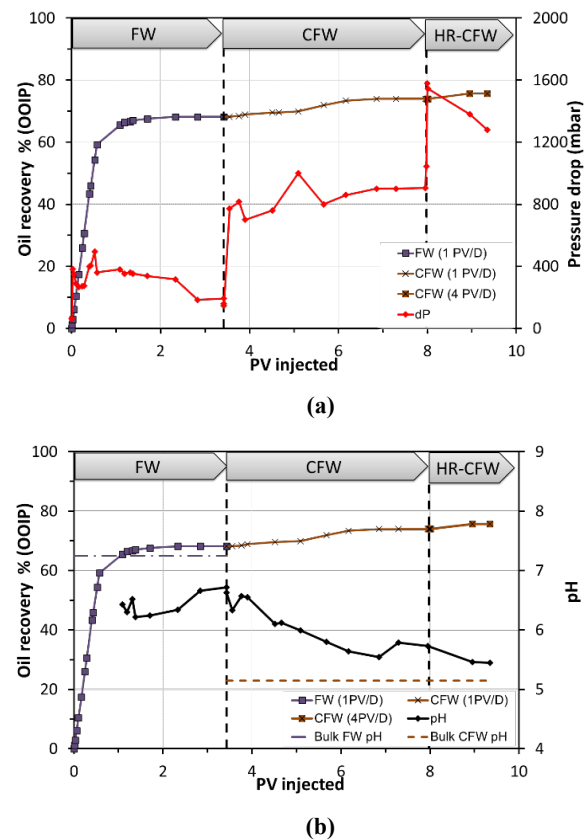


Fig. 7. Oil recovery tests on SK-11 core at 130°C. The flooding sequence was FW-CFW at a flooding rate of 1 PV/D. Oil recovery (%OOIP) was plotted against the PV injected and (a) average ΔP over the core, (b) pH of the produced water samples. At the end the injection rate was increased 4 times to 4 PV/D. Black dotted vertical lines are representing the change of injection fluid or change of injection rate. Coloured dotted horizontal lines represents the bulk pH of the injected fluids.

During CFW injection the pH in produced water samples went down below 6, confirming the presence of CFW which have a bulk pH of 5.2.

Since the chalk cores used in this experiment are mainly composed of calcite minerals, CaCO₃ dissolution could happen in presence of water, and CaCO₃ breaks into Ca²⁺ and CO₃²⁻ ions. CO₃²⁻ that take up a proton (H⁺) from water and becomes HCO₃⁻ leaving OH⁻ behind. On the other hand, CO₂ dissolved in water will form a weak Carbonic acid, H₂CO₃ which turns to H⁺ and HCO₃⁻. Then Ca²⁺ can take two ions of HCO₃⁻ and becomes soluble Ca(HCO₃)₂ while OH⁻ and H⁺ combine and become H₂O. Thus, the weak carbonic acid system is buffered in the porous media. This chemical process is illustrated simply in figure 8. The chemical equilibrium depicted in the figure does not change too much regardless of which brine (FW, SW, or DI) is being used.

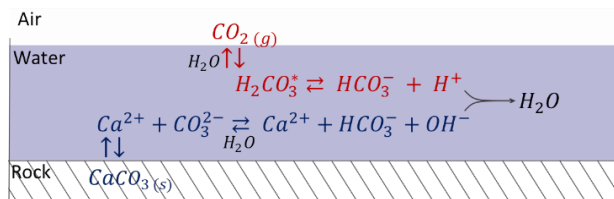
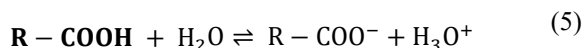


Fig. 8. Simple illustration of chemical processes happening inside the core in presence of both CaCO_3 (s) and CO_2 .

Therefore, the carbonate is working as a buffer to the injected CFW and increases its pH. Nevertheless, a change in pH can change the reactivity of the polar organic components (POC) towards the positively charged calcite rock surface as seen in the equations below.



Negative charged POC ($\text{R}-\text{COO}^-$) has the strongest affinity towards the positively charged calcite surface [28]. A reduction in pH could theoretically reduce the amount of $\text{R}-\text{COO}^-$ species and affect wettability, but the pK_a values for Naphthenic Acids described in Eq. 5 are typically below 4.5 [29] and will not significantly change the amount of non-protonated carboxylic acids.

However, the pressure difference during CFW was four times higher than FW. If viscous forces are important in the oil mobilization this could also cause higher oil recovery.

According to Wiebe and Gaddy (1940), the solubility of CO_2 reduces with an increase in temperature. In our experiment, the injection fluid was prepared at room temperature and then injected into the core at high temperature. The significant increase in pressure drop development is most likely linked to gas liberation and a third fluid phase in the pore system.

Many researchers have claimed that when carbonated water (CW) is injected into the carbonate reservoir, the acidic nature increases the dissolution of carbonate minerals which could promote an increase in porosity and permeability [31-34]. These changes in petrophysical properties help to increase oil recovery by creating a new flow path. CaCO_3 and MgCO_3 are carbonate minerals that can easily react with carbonated water. FW has a high concentration of both Ca^{2+} and Mg^{2+} ions which will limit the dissolution of carbonates even though the pH is somewhat reduced, as illustrated in figure 8. If there was a new flow path created during the oil recovery experiment in figure 7, the pressure drop should have been reduced.

After the oil production reached its plateau during CFW injection, the injection rate was increased from 1 PV/D to 4 PV/D to observe the effect of viscous forces and any end effects. A marginal extra oil mobilization of 1.5 %OOIP. The pH of the produced water was somewhat lower than at 1 PV/day, which could be explained by that the injection fluid has less time to interact with the minerals.

In the second oil recovery experiment on core SK-6, CSW was flooded in secondary mode followed by SW in tertiary

mode. Injection of CSW gave an ultimate oil recovery of 79 %OOIP which was reached after 2.5 PV injected, figure 9.

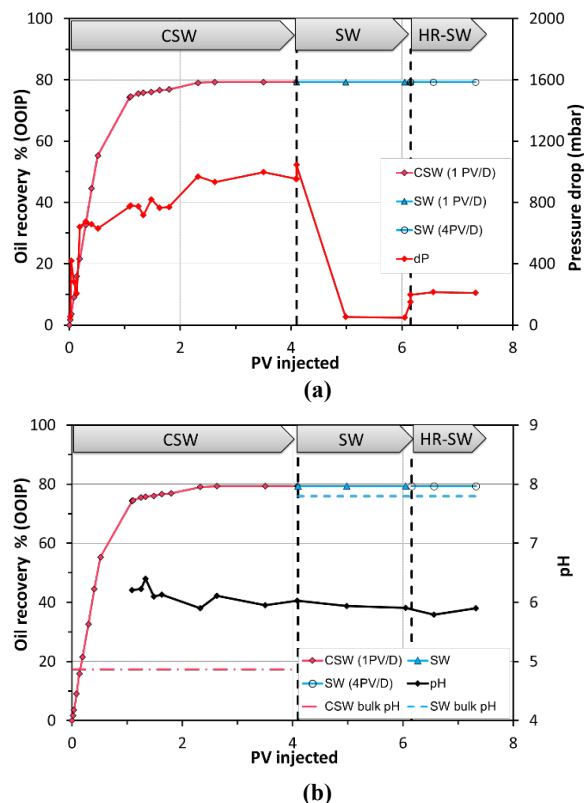


Fig. 9. Oil recovery tests on SK-6 core at 130°C with a back pressure of 10 bar. The flooding sequence was CSW-SW-HRSW. The flooding rate was 1 PV/D followed by a higher rate (HR) of 4 PV/D at the end. Oil recovery % (OOIP) was plotted against the PV injected of respective brine and (a) the average ΔP around the inlet and the outlet of the core, (b) the pH of the produced water. Black dotted lines are representing the change of injection fluid or change of injection rate. Colored dotted lines are representing the bulk pH of the injected fluid.

The ΔP was gradually increased during the hole CSW injection of 4 PV, even though water breakthrough took place after 0.5 PV injected. As previously discussed, the solubility of CO_2 reduces in higher temperatures and free CO_2 gas may promote the increase in ΔP .

After switching to SW, no extra oil mobilization was observed, but a significant decline in ΔP developed. This clearly indicates that free CO_2 liberated during CSW injection is taken up by SW and a new 2-phase flow system of Oil A and brine reestablished a more normal ΔP of 80 mbar. The results clearly indicate that CO_2 liberated from the brine phase trapped in the pore system is not easily diffusing into the residual oil but is being taken up in SW when that is passing through.

Increasing the injection rate 4 times did not mobilize any extra oil, but the ΔP increased to 200 mbar confirming typical pressure drop performance for a 2-phase fluid system in a heterogenous core. The pH of produced water is slightly acidic with a pH close to 6 during injection of both CSW and SW injection. This is slightly above the bulk pH of CSW and significantly below the bulk pH of SW.

Comparing the recovery results from FW-CFW injection (figure 7), and CSW- SW injection (figure 9), the CSW is significantly more efficient than FW in secondary mode. We know that SW behaves as a Smart Water and is able to change wettability and improve the sweep by inducing more positive capillary forces [11, 35]. To be able to evaluate if the significant improvement in the oil recovery during CSW injection is a result of wettability alteration by the ions present in the SW, or if the CO₂ present in the aqueous phase also contributes to the extra mobilized oil, a third core flooding experiment was performed on core SK-4 by injecting SW followed by CSW.

SW injection in secondary mode gave an ultimate oil recovery of 74 %OOIP after 2 PV injected. The water breakthrough was observed after 0.5 PV injected when 65 %OOIP was recovered. The experimental result is presented in figure 10.

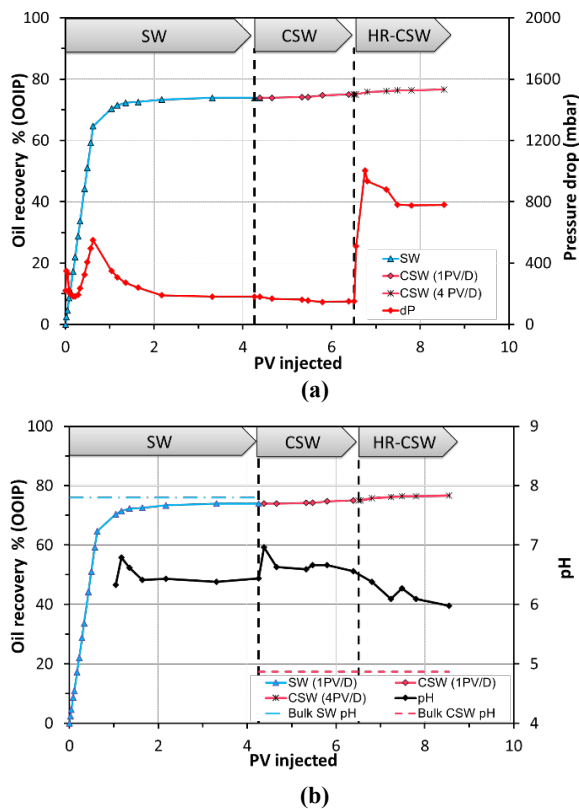


Fig. 10. Oil recovery tests on SK-4 core at 130°C with a back pressure of 10 bar. The flooding sequence was SW-CSW-HR CSW. The flooding rate was 1 PV/D followed by a higher rate (HR) of 4 PV/D at the end. Oil recovery % (OOIP) was plotted against the PV injected of respective brine, and (a) the average pressure drops around the inlet and the outlet of the core, (b) the pH of the produced water. Black dotted lines are representing the change of injection fluid or change of injection rate. Coloured dotted lines are representing the bulk pH of the injected fluid.

The ΔP profile is more normal and follows the same trend as observed during secondary FW injection when no gas phase is present, figure 7. The highest ΔP of 500 mbar was observed after 0.6 PV, gradually declining to 170 mbar when the oil recovery plateau was reached. The PW pH was almost constant and was around 6.5 during the SW injection.

After 4 PV, the injection brine was changed to CSW. During the next 3 PV, a slight increase of 1% OOIP extra oil was observed, indicating a tiny effect of the CO₂ present, supported by a slight decline in the PW pH towards 6. The ΔP during CSW injection indicated no free gas phase developing, and a low and stable ΔP of 150 mbar was observed, peaking at 1000 mbar during high-rate injection, before stabilizing again at 800 mbar. The significant increase in injection rate and ΔP had only a minor effect on oil mobilization, improving the recovery by only 2 %OOIP.

The overall recovery results confirm that by changing the chemistry of the injection brines, significant changes in ultimate oil recoveries could be observed. SW behaves as a Smart Water in mixed wet chalk, and the SW injection improved the ultimate oil recovery of 74% OOIP compared to baseline oil recovery using FW giving 68% OOIP. By adding CO₂ to the brine phase, carbonated brines could be formed. By injecting CSW in secondary mode an ultimate oil recovery of 79% OOIP was reached which is significant above SW recovery. Tertiary injection of CFW after FW and CSW after SW injection indicates smaller EOR effects.

The experimental results clearly demonstrate that the amount of CO₂ that could be dissolved in the brine phase is very limited. A significant amount of the CO₂ will still remain in the brine phase after equilibrium with the crude oil. The classical explanation linked to swelling and viscosity reduction of the oil phase is not likely the main mechanism for the extra oil mobilized during CW injection.

To evaluate the EOR mechanism of carbonated brines, we need to understand what could happen at the mineral surfaces linked to mineral dissolution processes and/or wettability alteration which we know could improve the sweep efficiency in water displacement processes in the presence of CO₂. We clearly observe a pH reduction during CW injection which due to mineral dissolution which was described in figure 8.

3.4. SEM and EDX analysis

Carbonated water will affect the mineral dissolution of calcite as described in figure 8. The effect of carbonate water exposure on mineral composition and pore surface minerals have been investigated by performing SEM and EDX analyses. In table 3, the mineral composition of SK Chalk in atomic weight % retrieved from EDX analyses before carbonated brine exposure is given in Table 3.

Table 3. Atomic weight % of SK cuttings retrieved from EDX before carbonated brine exposure.

Element	Na	Mg	Al	Si	S	K	Ca
Atomic %	0.02	0.13	0.19	0.81	0.54	0.23	98.06

The result confirms that SK chalk is very pure, consisting of more than 98% CaCO₃. The rest of the minerals are silicate minerals, Quartz, Clay, and/or Feldspars.

A Scanning Electron Microscopy (SEM) picture of the sample is given in figure 11.

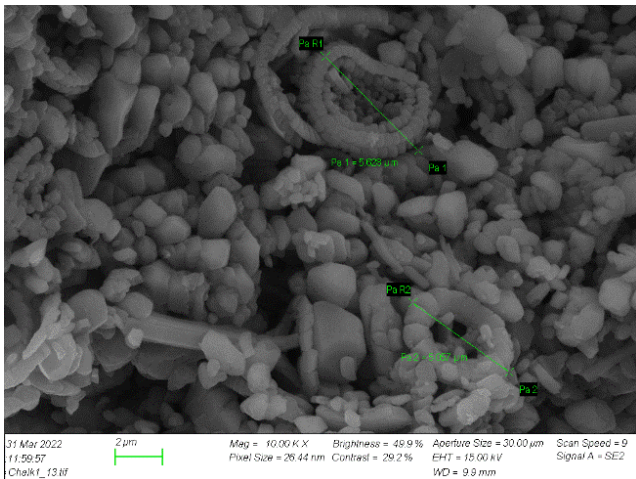


Fig. 11. SEM photo of the core sample before oil recovery test.

The presence of the intact coccolith ring confirms the biogenic origin of the Chalk.

After the core flooding experiments with carbonated brines, rock samples from the flooded cores were taken, dried, and analysed by SEM and EDX to track any mineralogical or visual changes in the mineral surfaces. Figure 12, 13, and 14 is representing the SEM photos from core SK-11, SK-4, and SK-6. Compared with figure 11, no visual changes on the mineral surfaces after carbonated brine exposure were detected. The coccolith rings are still intact and the grain sizes of the rock fragments are similar. No significant changes were found in the elements after the exposure by EDX.

The unchanged cation composition confirms negligible mineral dissolution by carbonated water. A few PV with carbonated brine is not enough to significantly affect the mineral surfaces when we have 2 m² of mineral surfaces in one gram of Chalk. At the same time, the calcite dissolution in brines with a high Ca²⁺ concentration as we have in FW and SW should be low due to the common ion effect.

However, Kono et al. (2014) observed significant dissolution of carbonate minerals by SEM. They reported smaller and smoother grains after carbonated water exposure and observed a significant increase of Ca²⁺ in the effluent brine. But in these core experiments, the total pore volume of fluid injected was several hundred, and without reporting injection rates. It is apparent that high injection volumes and rates could cause carbonate dissolution. Riazi (2011) found even sandstone is corroded by carbonated brine due to prolonged exposure to CWI for 2 weeks at the process conditions of 2000 psi and 38°C, which was a static exposure test, not a flooding experiment.

In our experiments, we have flooded SK cores with only about 4 PV which is more realistic to what could happen in the main part of the reservoir. Exposure with several PV with carbonated brines is more realistic to near wellbore effects for injection wells.

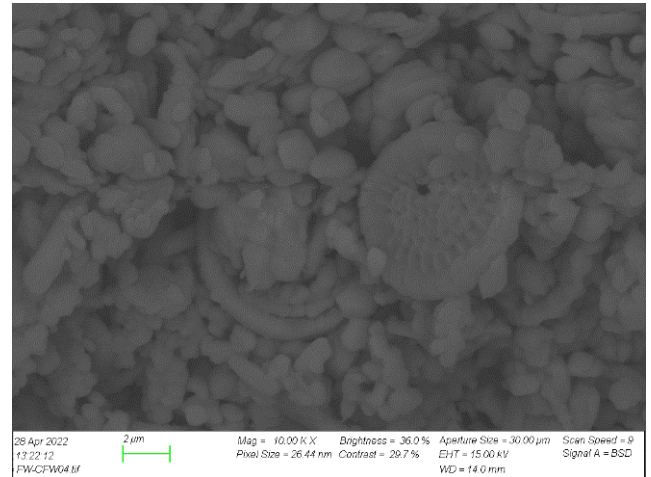


Fig. 12. SEM photo of chalk sample from core SK-11 after the oil recovery test by brine flooding (FW-CFW-HR CFW).

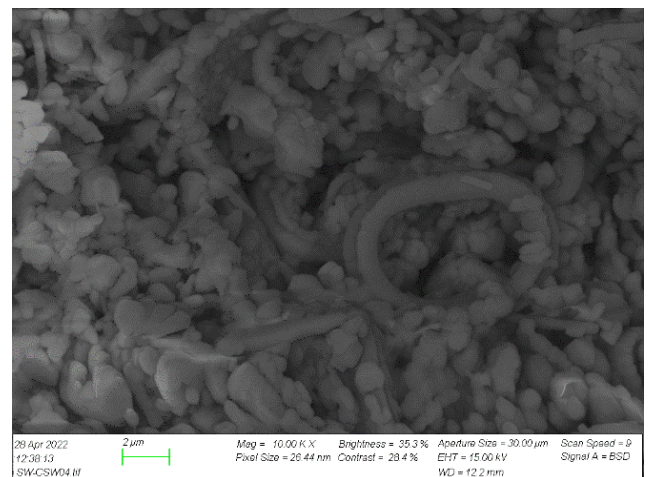


Fig. 13. SEM photo of chalk sample from core SK-4 after the oil recovery test by brine flooding (SW-CSW-HR CSW)

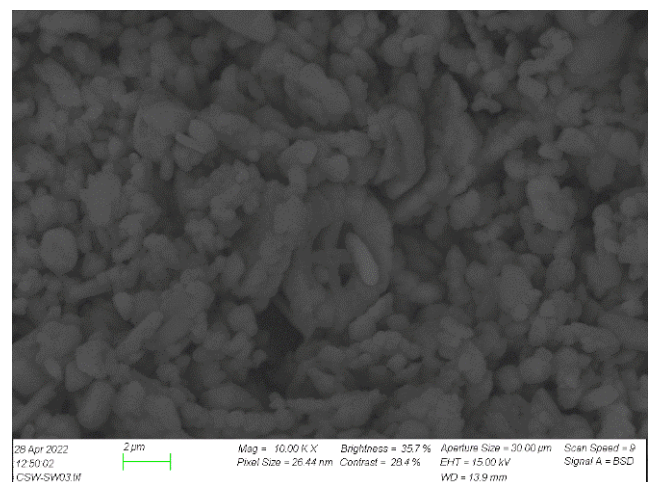


Fig. 14. SEM photo of chalk sample from core SK-6 after the oil recovery test by brine flooding (CSW-SW-HR SW)

4 Conclusions

Stevens Klint chalk was exposed to different carbonated brines at 130 °C to evaluate the effect of carbonated brines as an EOR fluid. The studies were coupled with CO₂ solubility experiments with 2 and 3 phases (CO₂, brines, and oil), as well as PHREEQC simulations. The main findings of this study were:

- The solubility of CO₂ in brine was low and depends on brine salinity. After reaching the super critical conditions of CO₂ the solubility did not increase significantly. The experimental solubility studies validated a relatively good performance of the PHREEQC simulator.
- Oil recoveries were slightly increased in chalk at high temperature both in secondary and tertiary mode. A mechanism linked to swelling and viscosity reduction of the oil phase is not likely to be a main mechanism for the extra oil.
- Dissolution of CaCO₃ in presence of carbonated brines can also contribute to change in petrophysical properties and thus produce extra oil. However, no changes on pore surface minerals after flooding with carbonated brines were observed by SEM and EDX analyses.
- Wettability alteration might play a vital role in increasing oil recovery but need further investigation.

The author gratefully acknowledges the financial support from the University of Stavanger and the laboratory work support from master's student Mahmood Fani and Saja H. A. Algazban.

References

1. BP. *Statistical Review of World Energy*. 2020 [cited 2022 20 May]; Available from: <https://www.bp.com/en/global/corporate/energy-economics/statistical-review-of-world-energy/oil.html>.
2. Esene, C., et al., *Comprehensive review of carbonated water injection for enhanced oil recovery*. *Fuel*, 2019. **237**: p. 1086-1107.
3. Riazi, M., et al. *Oil Recovery Improvement Using CO₂-Enriched Water Injection*. in *EUROPEC/EAGE Conference and Exhibition*. 2009.
4. Bisweswar, G., A. Al-Hamairi, and S. Jin, *Carbonated water injection: an efficient EOR approach. A review of fundamentals and prospects*. *Journal of Petroleum Exploration and Production Technology*, 2020. **10**(2): p. 673-685.
5. D. W. Green, a.G.P.W., *Enhanced oil recovery*. SPE Textbook Series., 1998: Society of Petroleum Engineers, Richardson, Texas.
6. Abedini, A. and F. Torabi, *Parametric Study of the Cyclic CO₂ Injection Process in Light Oil Systems*. *Industrial & Engineering Chemistry Research*, 2013. **52**(43): p. 15211-15223.
7. Dong, Y., et al. *An Experimental Investigation of Carbonated Water Flooding*. in *SPE Annual Technical Conference and Exhibition*. 2011.
8. Sohrabi, M., et al. *A Thorough Investigation of Mechanisms of Enhanced Oil Recovery by Carbonated Water Injection*. in *SPE Annual Technical Conference and Exhibition*. 2015.
9. Mosavat, N., *Utilization of Carbonated Water Injection (CWI) as a Means of Improved Oil Recovery in Light Oil Systems: Pore-Scale Mechanisms and Recovery Evaluation*, in *Faculty of Graduate Studies and Research*. 2014, University of Regina.
10. Kono, F., et al. *Laboratory Measurements on Changes in Carbonate Rock Properties due to CO₂-Saturated Water Injection*. in *Abu Dhabi International Petroleum Exhibition and Conference*. 2014.
11. Puntervold, T., et al., *Modified seawater as a smart EOR fluid in chalk*. *Journal of Petroleum Science and Engineering*, 2015. **133**: p. 440-443.
12. Adiputra, E., L. Mucharam, and S.D. Rahmawati. *Experimental Evaluation of Carbonated Water Injection to Increase Oil Recovery Using Spontaneous Imbibition*. in *Selected Topics on Improved Oil Recovery*. 2018. Singapore: Springer Singapore.
13. Lake, L.W., et al., *Isothermal, multiphase, multicomponent fluid flow in permeable media*. In *Situ*; (United States), 1984. **8:1**: p. Medium: X; Size: Pages: 1-40 2009-12-16.
14. Kilybay, A., et al. *Hybrid EOR Technology: Carbonated Water and Smart Water Improved Recovery in Oil Wet Carbonate Formation*. in *SPE Annual Caspian Technical Conference & Exhibition*. 2016.
15. Kechut, N.I., M. Jamiolahmady, and M. Sohrabi, *Numerical simulation of experimental carbonated water injection (CWI) for improved oil recovery and CO₂ storage*. *Journal of Petroleum Science and Engineering*, 2011. **77**(1): p. 111-120.
16. Parkhurst, D.A., C.A.J., *User's Guide to PHREEQC (Version 2)--A Computer Program for Speciation, Batch-Reaction, One-Dimensional Transport, and Inverse Geochemical Calculations*, U.S.G. SURVEY, Editor. 1999, U.S. DEPARTMENT OF THE INTERIOR.
17. Piñerez, I., et al., *Core wettability reproduction: A new solvent cleaning and core restoration strategy for chalk cores*. *Journal of Petroleum Science and Engineering*, 2020. **195**: p. 107654.
18. Hopkins, P., T. Puntervold, and S. Strand, *Preserving initial core wettability during core restoration of carbonate cores*, in *The International Symposium of the Society of Core Analysts*. 2015: St. John's Newfoundland and Labrador, Canada.
19. Shariatpanahi, S.F., S. Strand, and T. Austad, *Initial wetting properties of carbonate oil reservoirs: effect of the temperature and presence of sulfate in formation water*. *Energy & Fuels*, 2011. **25**(7): p. 3021-3028.
20. Fathi, S.J., T. Austad, and S. Strand, *Water-based enhanced oil recovery (EOR) by "Smart Water": optimal ionic composition for EOR in carbonates*. *Energy & Fuels*, 2011. **25**(11): p. 5173-5179.

21. Puntervold, T., S. Strand, and T. Austad, *New method to prepare outcrop chalk cores for wettability and oil recovery studies at low initial water saturation*. Energy & Fuels 2007. **21**(6): p. 3425-3430.
22. Springer, N., U. Korsbech, and H.K. Aage, *Resistivity index measurement without the porous plate: A desaturation technique based on evaporation produces uniform water saturation profiles and more reliable results for tight North Sea chalk*, in *Paper presented at the International Symposium of the Society of Core Analysts 2003*: Pau, France.
23. Duan, Z., et al., *An improved model for the calculation of CO₂ solubility in aqueous solutions containing Na⁺, K⁺, Ca²⁺, Mg²⁺, Cl⁻, and SO₄²⁻*. Marine Chemistry, 2006. **98**(2): p. 131-139.
24. Spycher, N. and K. Pruess, *CO₂-H₂O Mixtures in the Geological Sequestration of CO₂. II. Partitioning in Chloride Brines at 12-100°C and up to 600 bar*. 2004.
25. Anderson, W.G., *Wettability literature survey- part 1: rock/oil/brine interactions and the effects of core handling on wettability*. Journal of Petroleum Technology, 1986. **38**(10): p. 1125-1144.
26. Austad, T., et al., *Smart Water EOR: Beneficios y Aplicaciones en Reservorios Clásticos y Carbonatos*. 2017.
27. Piñerez Torrijos, I.D., et al., *Impact of Temperature on Wettability Alteration by Smart Water in Chalk*. 2019. **2019**(1): p. 1-11.
28. Standnes, D.C. and T. Austad, *Wettability alteration in chalk. 1. Preparation of core material and oil properties*. Journal of Petroleum Science and Engineering, 2000. **28**(3): p. 111-121.
29. Standal, S., et al., *Effect of polar organic components on wettability as studied by adsorption and contact angles*. Journal of Petroleum Science and Engineering, 1999. **24**: p. 131-144.
30. Wiebe, R. and V.L. Gaddy, *The Solubility of Carbon Dioxide in Water at Various Temperatures from 12 to 40° and at Pressures to 500 Atmospheres. Critical Phenomena**. Journal of the American Chemical Society, 1940. **62**(4): p. 815-817.
31. Bowker, K.A. and P.J. Shuler. *Carbon Dioxide Injection and Resultant Alteration of Weber Sandstone (Pennsylvania-Permian), Rangely Field, Colorado*. in *SPE Annual Technical Conference and Exhibition*. 1989.
32. Shiraki, R. and T.L. Dunn, *Experimental study on water-rock interactions during CO₂ flooding in the Tensleep Formation, Wyoming, USA*. Applied Geochemistry, 2000. **15**(3): p. 265-279.
33. Wellman, T.P., et al. *Evaluation of CO₂-Brine-Reservoir Rock Interaction with Laboratory Flow Tests and Reactive Transport Modeling*. in *International Symposium on Oilfield Chemistry*. 2003.
34. Grigg, R.B. and R.K. Svec. *CO₂ Transport Mechanisms in CO₂/Brine Coreflooding*. in *SPE Annual Technical Conference and Exhibition*. 2006.
35. Austad, T., et al., *Seawater as IOR fluid in fractured chalk*, in *Paper SPE93000 presented at the 2005 SPE International Symposium on Oilfield Chemistry*. 2005: Houston, TX, USA.
36. Riazi, M., *Pore scale mechanisms of carbonated water injection in oil reservoirs*, in *Petroleum Engineering*. 2011, Heriot-Watt University.

Nano-colloid based suspensions and emulsions used as means for enhanced oil recovery

Anastasia Strekla^{1,2}, Christina Ntente^{1,3}, Maria Theodoropoulou¹ and Christos Tsakiroglou^{1,*}

¹Foundation for Research and Technology Hellas - Institute of Chemical Engineering Sciences, 26504 Patras, Greece

²University of Patras, Department of Physics, 26504 Patras, Greece

³University of Patras, Department of Chemistry, 26504 Patras, Greece

Abstract. Aqueous solutions of polyphenols extracted from parsley leaves are mixed with solution of ferric chloride hexahydrate to synthesize suspensions of polyphenol-coated iron oxide nanoparticles, which are then used to prepare Pickering oil (n-decane)-in water emulsions. The performance of the nano-colloid suspensions and emulsions as agents of enhanced oil recovery (EOR) is assessed with secondary imbibition tests performed under constant flow rate on a glass-etched pore network, after a drainage / primary imbibition cycle for paraffin oil / brine (0.25M NaCl solution) system. The transient changes of the fluid saturation profile along with the pressure drop across the porous medium are recorded. Comparative analysis of the oil recovery efficiency attained with nano-colloid suspensions of varying iron concentration, and Pickering emulsion, enables us to classify them, and select the most efficient ones for further studies.

1 Introduction

The use of inorganic nanoparticles in petroleum engineering applications including enhanced oil recovery (EOR) has attracted the scientific interest in recent years [1]. An approach to improve the dispersibility of nanoparticles and tailor their properties for a particular application is to covalently attach polymers to the nanoparticle surface, resulting in polymer-coated nanoparticles (PNPs). While less work has been carried out with PNPs for EOR, recent work suggests they may be superior to unmodified nanoparticles for EOR [2]. PNPs can be tailored for a specific interface and application. PNPs can decrease the interfacial tension of oil and water or water and air, which can lead to more stable emulsions [3-6]. For example, silica nanoparticles coated with a polyelectrolyte were used to stabilize oil-in-water emulsions [7]. More recently, stable oil-in-water emulsions were generated by using silica nanoparticles coated with a pH responsive polymer, and it was found that the most stable emulsions were formed at lower polymer chain grafting densities [8,9]. Related studies on star polymers [10], bottlebrush polymers [11] and paramagnetic particles with adsorbed amphiphilic polymers found stable emulsions [12] and reductions in the oil-water interfacial tension at relatively low (0.1 wt %) particle contents [13]. PNPs can respond to temperature, pH, and light through a change in surface properties [6].

Moreover, significant progress has been done on the development of PNPs for the in-situ remediation of contaminated porous media (e.g. soils, sediments, and aquifers) by injecting zero-valent iron nanoparticles (nZVI) [14-16], and know-how obtained in the context of such environmental studies might be helpful in preparing stable

PNPs and designing efficient PNP-based EOR processes [17]. During the last years, green synthesis of NPs has been gaining importance in view of the advantages such as economic benefits, environment-friendly and recycling. Such 'greener' processes for obtaining various nanomaterials have been widely reported and are gathering attention in several nanotechnology-based applications [18]. As one of the green synthetic approaches, plant extracts were considered for the synthesis of nanoparticles through biosynthetic routes which involve primarily the extraction of polyphenols, which are natural polymers acting as reducing agents and stabilizers [19-21].

In the present work, aqueous solutions of polyphenols extracted from the leaves of parsley are mixed with solution of ferric chloride hexahydrate to produce suspensions of iron oxide nanoparticles, and an ultrasound probe is utilized to generate stable oil-in-water emulsions by mixing the suspensions with n-decane. The performance of the nano-colloid suspensions and emulsions as agents of enhanced oil recovery (EOR) is assessed with secondary imbibition tests performed after a drainage / imbibition cycle for paraffin oil / brine (NaCl solution) system. Displacement tests are conducted under constant flow rate in a transparent glass-etched pore network. The transient changes of the fluid saturation profile along with the pressure drop across the porous medium are recorded. The oil saturation is measured with image analysis of successive snap-shots captured by a CCD camera [22]. Comparative analysis of the oil displacement efficiency attained with nano-colloid suspensions and Pickering emulsions enables us to classify them and pre-select the most efficient ones for further studies.

2 Materials and Methods

* Corresponding author: ctsakir@iccht.forth.gr

2.1 Synthesis of nanoparticles suspensions and emulsions

Initially, 1000 mL of tri-distilled (3D) water were heated to 80 °C on a hot plate. Then, 50 g of chopped parsley were added in the water and left for 1 hr under stirring at constant temperature. Afterwards, the liquid extract was separated from the solid residue by vacuum filtration by using successively filters of pore size 4 µm, and 2.5 µm (Whatman) and centrifugation at 12000 rpm for 20 min (Heraeus Megafuge-16). The total polyphenol concentration (TPC) of extract was measured in terms of Gallic Acid Equivalent (g/L GAE), by using the Folin-Ciocalteu method [23] and UV-Vis spectroscopy (HITACHI U-3000).

The preparation of the iron oxide nanoparticles (IONP) was accomplished by adding, under stirring, the polyphenol extract (PPH) to a 0.1M FeCl₃ solution at a volume ratio 2:1 [24]. The reaction progress was monitored by recording continuously the pH and Redox Potential (ORP), Eh, of the solution with two probes (Vernier pH and ORP electrodes) connected with a data acquisition card (LabQuest Steam) (Fig.1a,b). When pH and Eh were stabilized, the solution colour changed to dark brown signifying the completion of the reaction. After having adjusted its pH to 6.0, the suspension was placed in a refrigerator and kept there until being used.

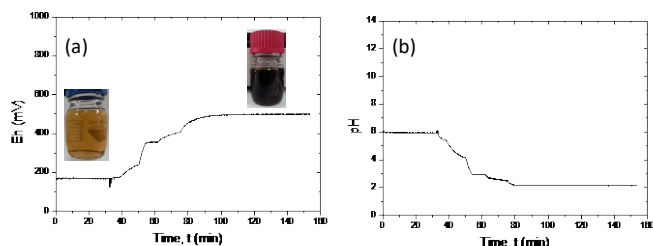


Fig.1. Transient response of the (a) Oxidation Reduction Potential, Eh, and (b) pH of solution, during the synthesis of iron oxide nanoparticles.

The preparation of emulsions was done by mixing 20 mL of aqueous phase (IONP suspension) with 20 mL of n-decane at a volume ratio 1:1 for 10 minutes inside an ultrasonic probe (Hielscher, UP400St).

2.2 Characterization of suspensions

Suspensions of PPH-coated IONPs were prepared at three iron (Fe) concentrations, 0.25, 0.5 and 0.75 g/L. The particle size distribution, and ζ-potential of all IONP suspensions were determined with Dynamic Light Scattering -DLS (Zetasizer Nano System, Malvern) after having diluted each suspension at ratio 1:50 with 3D water.

The surface tension of each solution/suspension, as well its interfacial tension with paraffin oil were measured at 25°C on a Sigma 702 (KSV Instruments) tensiometer by using the DuNouy Ring method.

The air/water and oil/water static contact angles were measured from images of drops of aqueous phase surrounded by air or oil on a glass plate, using a HY-2307 CMOS camera (Hayear) connected via USB with PC and equipped with image capturing software. The images were analyzed by the OpenDrop software [25].

2.3. Visualization tests

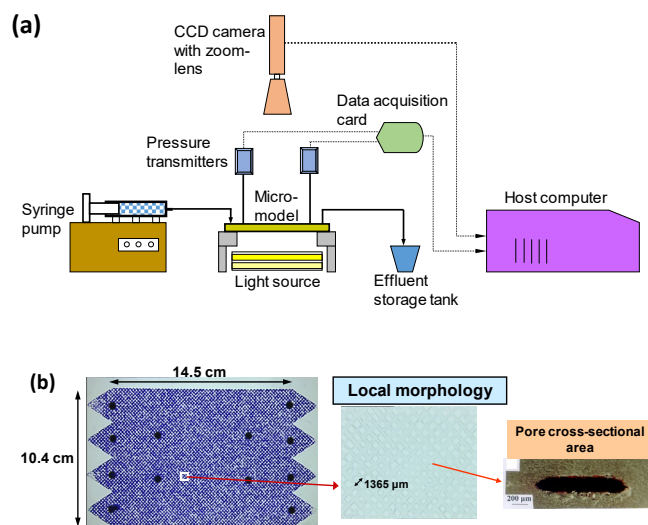


Fig. 2. (a) Schematic diagram of experimental setup. (b) Morphology of glass-etched pore network model.

Immiscible displacement tests were conducted on a glass-etched pore network model (Fig.2a,b). The visualization tests (Fig.2a) enable us to assess the capacity of the various types of NPs to reduce the residual oil remaining in the porous medium after primary drainage (flow rate, $q_o=0.08$ mL/min) primary imbibition (flow rate, $q_w=0.2$ mL/min), and secondary imbibition (flow rate, $q_w=0.2$ mL/min) cycles, where each displacement step started at the point that the previous step stopped, so that a continuous saturation history was recorded. Paraffin oil (Labkem, Spain) colored with oil red (concentration=1500 ppm) was selected as the model viscous oil phase. Aqueous solution of NaCl 0.25M was used as the brine in drainage and primary imbibition tests, and suspension of PPH-coated IONPs, along with its Pickering emulsion with n-decane were used as the displacing fluid in secondary imbibition tests. At each series of displacement tests, images were captured every 10-20 s by a CCD video camera (Panasonic AW-E300E). The pressures were measured continuously on two holes placed on the boundaries of visualized area (Fig.2a) through two pressure transmitters SGM (Electrosystems) properly connected with a data acquisition system (ADAMS-4561 & ADAMS-4117, Advantech). Recorded snap-shots of the flow pattern were processed with image analysis software (ImageJ) to determine the gradual variation of residual oil saturation. (Fig.2a,b).

The capillary number, Ca , and viscosity ratio, κ , are defined by

$$Ca = \frac{u_0 \mu_{inj}}{\gamma_{ow}} \quad (1)$$

$$\kappa = \frac{\mu_{inj}}{\mu_{disp}} \quad (2)$$

where u_0 is the superficial flow velocity ($=q/A$), μ_{inj} and μ_{disp} are the viscosities of injected and displaced fluid, and γ_{ow} is the oil/water interfacial tension. Moreover, the pore-scale, Ca_{L1} and network-scale, Ca_{LN} , capillary numbers [26] are defined by

$$Ca_{L1} = fCa \quad (2)$$

$$Ca_{LN} = Ca_{L1}(L_N/L_P) \quad (3)$$

$$f = \frac{L_P r_H}{k} \quad (4)$$

where L_N is the network length ($L_N=0.14$ m), L_P is the pore length ($L_P=1.365$ mm), r_H is the equivalent hydraulic pore radius ($r_H=60$ μ m) and k the absolute permeability of the porous medium ($k=20.5$ Da).

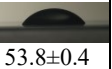
3 Results and discussion

The polyphenol concentration in parsley extract, measured by the Folin-Ciocalteu method, was found equal to 2.26 g/L GAE. The physicochemical and interfacial properties of all fluid systems are shown in Tables 1 and 2, respectively.

Table 1. Physicochemical properties of fluid systems

Solution / Suspension	Particle size distribution		ζ -potential (mV)	Density, ρ (g/cm ³)
	$\langle D_p \rangle$ (nm)	σ_p (nm)		
PPH-coated IONPs $C_{Fe}=0.25$ g/L	22.8	6.2	-22.1	0.993
PPH-coated IONPs $C_{Fe}=0.25$ g/L with 0.25 M NaCl	40.2	12.2	-	0.981
PPH-coated IONPs $C_{Fe}=0.5$ g/	55.0	21.7	-24.7	0.993
PPH-coated IONPs $C_{Fe}=0.75$ g/L	19.6	7.3	-10.3	0.990

Table 2. Interfacial properties of fluid systems

Solution / Suspension	Surface tension γ_s (mN/m)	Interfacial tension γ_{ow} (mN/m)	Air/water contact angle θ_a (°)	Oil/water contact angle θ_{ow} (°)
PPH solution	55.1	19.4	-	-
0.25M NaCl solution	72.5±0.5	44.0	 53.8±0.4	 54.5±1.3
PPH-coated IONPs $C_{Fe}=0.25$ g/L	62.8±0.5	27.9	 53.1±0.2	 39.2±5.9
PPH-coated IONPs with 0.25 M NaCl	57.4±0.25	20.7	 55±0.1	 43.9±0.4
PPH-coated IONPs $C_{Fe}=0.5$ g/	57.5±0.3	26.1	 51.2±1.2	 44.8±0.7
PPH-coated IONPs $C_{Fe}=0.75$ g/L	53.7±0.1	20.7	 35.2±2.7	 11.5±3.2

It is evident that the interfacial properties along with the contact angle are decreasing functions of the iron

concentration increases (Table 1), and the oil displacement efficiency is expected to be favoured when using IONP suspensions of progressively higher Fe concentration. On the other hand, the dynamic surface tension, measured by the pendant drop method is a decreasing function of time (Fig. 3a) revealing the capacity of the system to generate stable foams.

The relative volumes of the various phases as functions of time for a Pickering emulsion synthesized from IONP suspension with $C_{Fe}=0.25$ g/L and $C_{NaCl}=0.25$ M is shown in Fig.3b.

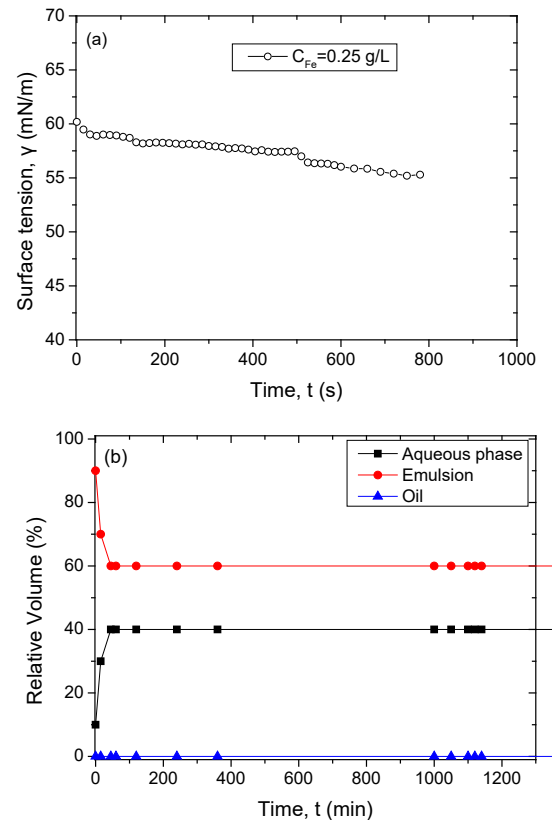


Fig.3. (a) Dynamic surface tension; (b) transient response of the relative volume of the various phases of emulsion.

Table 3. Experimental conditions

Injected fluid	q (mL/min)	$u_0 \times 10^5$ (m/s)	μ (Pa s)	$Ca \times 10^6$	κ	Ca_{L1}	Ca_{LN}
paraffin	0.08	0.94	0.026	8.0	26	0.032	3.32
NaCl 0.25M	0.2	2.35	0.001	0.77	0.038	0.0031	0.32
IONP $C_{Fe}=0.25$ g/L	0.2	2.35	0.001	0.84	0.038	0.0034	0.34
IONP $C_{Fe}=0.25$ g/L, $C_{NaCl}=0.25$ M	0.2	2.35	0.001	1.13	0.038	0.0046	0.47
Pickering	0.2	2.35	0.01246	14.1	0.48	0.057	5.86

emul-sion							
IONP $C_{Fe}=0.5$ g/L	0.2	2.35	0.001	0.9	0.03 8	0.00 36	0.38
IONP $C_{Fe}=0.7$ 5 g/L	0.2	2.35	0.001	1.13	0.03 8	0.00 46	0.46

Successive images of the drainage/ primary imbibition/ secondary imbibition steps are shown in Figs. 4-8. Drainage follows a frontal flow pattern (Fig.4a,5a,6a,7a,8a) due to the high viscosity ratio and high Ca_{LN} (Table 3, [26]). The primary imbibition flow pattern is dominated by capillary fingering (Fig.4b, 5b, 6b, 7b, 8b) due to the relatively low value of capillary number at pore, Ca_{LI} , and network, Ca_{LN} , scale (Table 3). Secondary imbibition by IONP suspensions is still dominated by capillary fingering (Fig.4c,5c,6c,7c. Table 3). However, the secondary imbibition by the emulsion transits to a frontal drive (Fig.8c) which is consistent with the increase of the viscosity ratio along with the pore & network scale capillary number by one order of magnitude (Table 3).

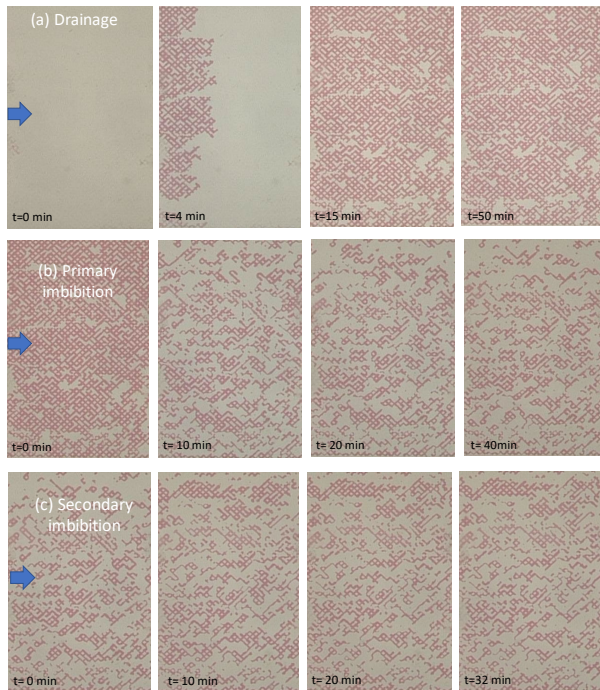


Fig.4. (a) Displacement of brine ($C_{NaCl}=0.25M$) by paraffin oil ($\mu=0.026$ Pa s). (b) Displacement of paraffin oil by brine ($C_{NaCl}=0.25M$). (c) Displacement of residual paraffin oil by IONP suspension ($C_{Fe}=0.25$ g/L, $C_{NaCl}=0.25M$).

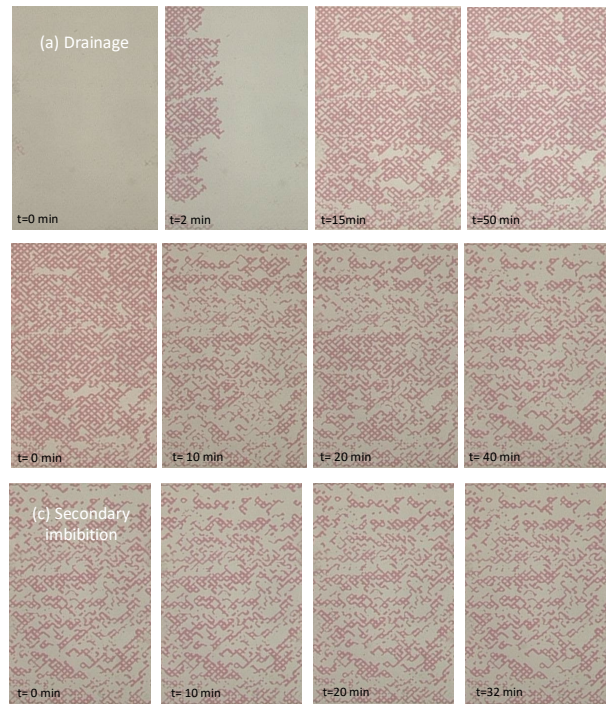


Fig.5. (a) Displacement of brine ($C_{NaCl}=0.25M$) by paraffin oil ($\mu=0.026$ Pa s). (b) Displacement of paraffin oil by brine ($C_{NaCl}=0.25M$). (c) Displacement of residual paraffin oil by IONP suspension ($C_{Fe}=0.25$ g/L).

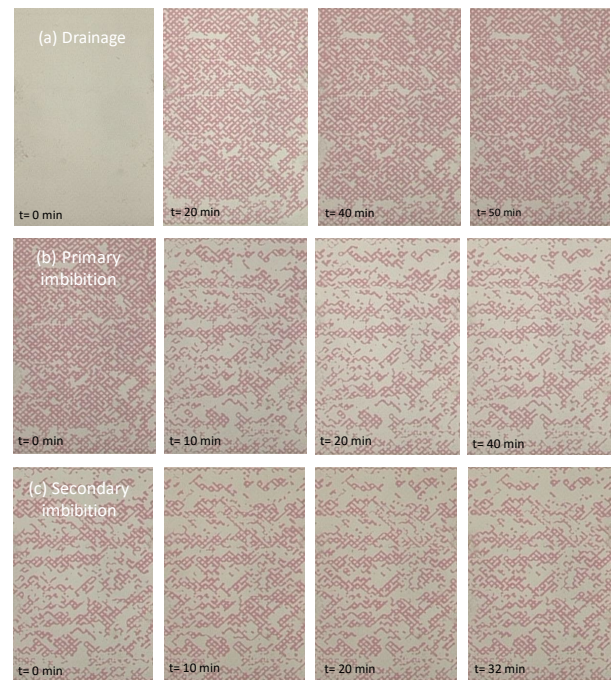


Fig.6. (a) Displacement of brine ($C_{NaCl}=0.25M$) by paraffin oil ($\mu=0.026$ Pa s). (b) Displacement of paraffin oil by brine ($C_{NaCl}=0.25M$). (c) Displacement of residual paraffin oil by IONP suspension ($C_{Fe}=0.50$ g/L).

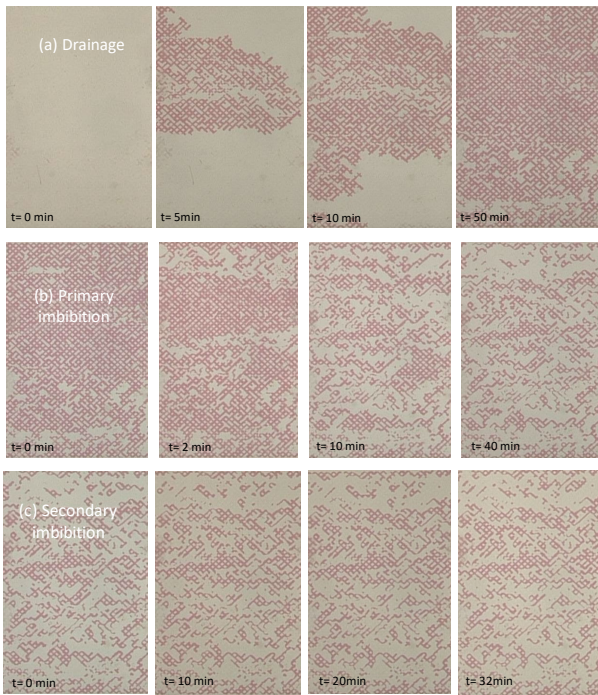


Fig.7. (a) Displacement of brine ($C_{NaCl}=0.25M$) by paraffin oil ($\mu=0.026$ Pa s). (b) Displacement of paraffin oil by brine ($C_{NaCl}=0.25M$). (c) Displacement of residual paraffin oil by IONP suspension ($C_{Fe}=0.75$ g/L).

the final stages of the process (Fig.9a,b,c,d). It is worth mentioning that during primary or secondary imbibition, oil mobilization is carried out via a mechanism of successive and locally occurring drainage / imbibition events. On the other hand, the displacement of residual oil by the emulsion follows a clearly frontal-like pattern and is a very efficient displacement, in terms of the percentage of residual oil recovery (Fig.8c).

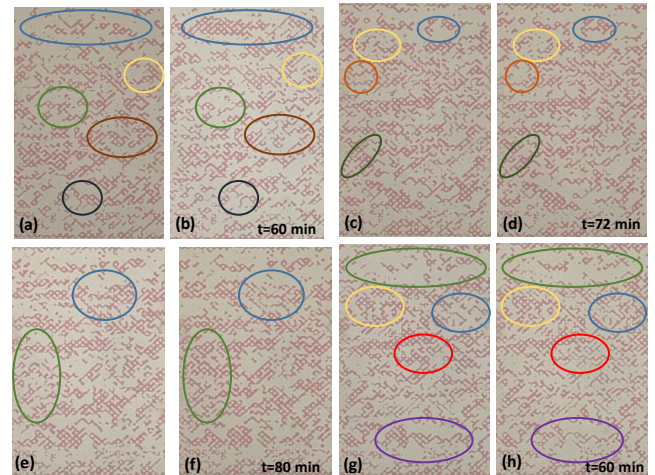


Fig. 9. Comparison between the final snap-shots of primary and secondary imbibition during the displacement of residual oil by (a,b) IONP suspension in brine with $C_{Fe}=0.25$ g/L, $C_{NaCl}=0.25M$, (c,d) IONP suspension with $C_{Fe}=0.25$ g/L, (e,f) IONP suspension with $C_{Fe}=0.50$ g/L, (g,h) IONP suspension with $C_{Fe}=0.75$ g/L.

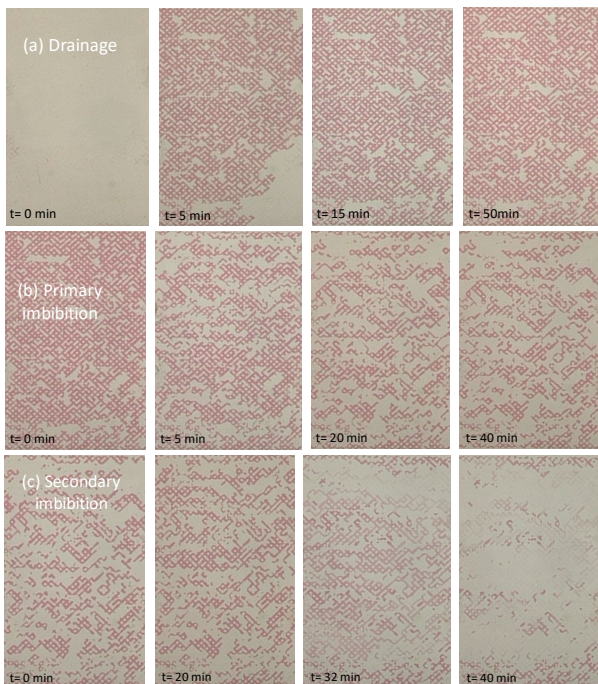


Fig.8. (a) Displacement of brine ($C_{NaCl}=0.25M$) by paraffin oil ($\mu=0.026$ Pa s). (b) Displacement of paraffin oil by brine ($C_{NaCl}=0.25M$). (c) Displacement of residual paraffin oil by Pickering emulsion.

During the injection of PPH-coated IONP suspensions oil trapped at the left of the visualized area (near the inlet ports) was mobilized and transferred towards the central area, leading to a temporary or permanent increase of oil saturation (Fig.9a-blue circles, Fig. 9b-blue circles, Fig. 9c-green circles, Fig.9d-blue circles). However, on average, the local oil saturation decreases over the majority of pore clusters, at

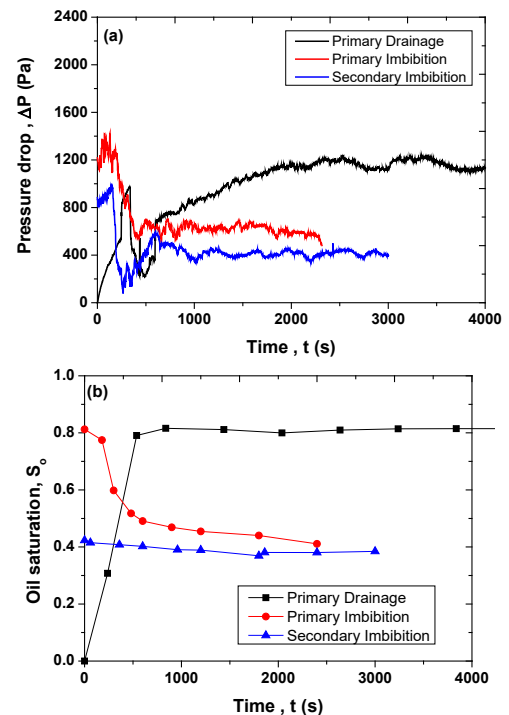


Fig.10. (a) Pressure drop, and (b) oil saturation, as a function of time. IONP suspension with $C_{Fe}=0.25$ g/L and $C_{NaCl}=0.25M$ was injected at the secondary imbibition step.

The transient response of the pressure drop across the central region of the glass micromodel along with the gradual change of oil saturation are shown in Figs.10-14.

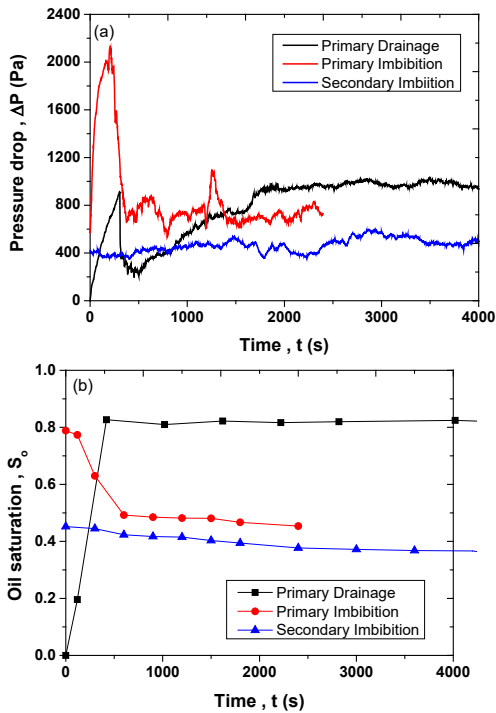


Fig.11. (a) Pressure drop, and (b) oil saturation, as a function of time. IONP suspension with $C_{Fe}=0.25$ g/L was injected at the secondary imbibition step.

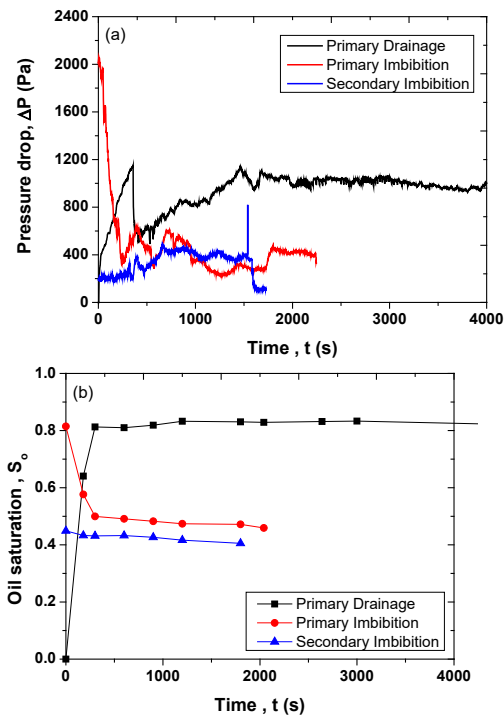


Fig.12. (a) Pressure drop, and (b) oil saturation, as a function of time. IONP suspension with $C_{Fe}=0.5$ g/L was injected at the secondary imbibition step.

The decrease of the residual oil saturation during the secondary imbibition step by IONP suspensions (Fig.10b,11b,12b,13b) is reflected in the relatively low pressure drop across the porous medium compared to the corresponding one of primary imbibition step (Fig.10a,11a,12a,13a). It is worth mentioning that during secondary imbibition with IONP suspensions, the residual oil

displacement efficiency seems to be higher without the presence of NaCl (Fig.11b, 12b, 13b, Table 4). In general, various mechanisms have been proposed in the literature to explain the higher oil recovery with low-salinity water-flooding [27]. Perhaps, oil recovery increases because of changes in the wettability of the porous medium toward more water-wet conditions [27]. On the other hand, it has been observed that at long term, the presence of NaCl favors the destabilization of IONP, their agglomeration, and subsequent precipitation. The high oil recovery efficiency of the secondary imbibition by the shear-thinning Pickering emulsion (Fig.14b) is associated with a relatively high pressure drop across the porous medium, also characterized by strong fluctuations (Fig.14a). The fluctuations are due to the broad range of the viscosity for a shear-thinning fluid (Fig. 15): (i) across a single pore [28], as the shear stress varies from zero (at the pore centre) to a maximum (at the pore walls); (ii) throughout the pore network [29,30] between the high and low flow rate regions.

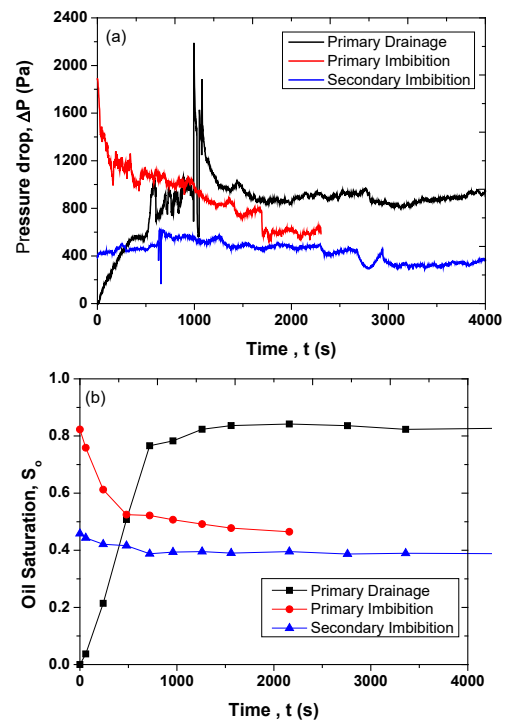


Fig.13. (a) Pressure drop, and (b) oil saturation, as a function of time. IONP suspension with $C_{Fe}=0.75$ g/L was injected at the secondary imbibition step.

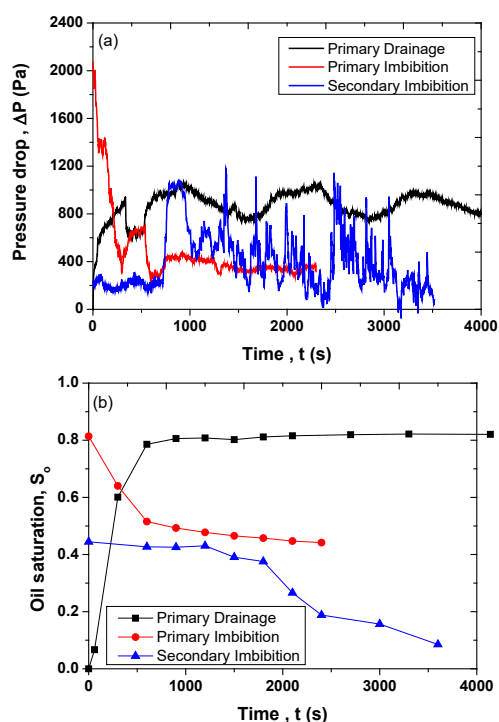


Fig.14. (a) Pressure drop, and (b) oil saturation, as a function of time. Pickering emulsion synthesized from IONP suspension with $C_{Fe}=0.25$ g/L and $C_{NaCl}=0.25$ M was injected at the secondary imbibition step.

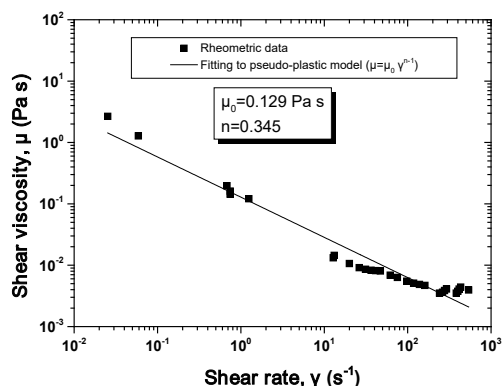


Fig.15. Shear viscosity of emulsion.

Table 4. Summary of results from EOR tests

Displacing fluid in secondary imbibition step	Drainage, S_o	Primary Imbibition, S_o	Secondary Imbibition, S_o	Oil recovery efficiency (%)
IONP $C_{Fe}=0.25$ g/L	0.815	0.453	0.36	20.5
IONP $C_{Fe}=0.25$ g/L, $C_{NaCl}=0.25$ M	0.815	0.410	0.386	6.1
Pickering emulsion $C_{Fe}=0.25$ g/L, $C_{NaCl}=0.25$ M	0.820	0.441	0.085	80.7
IONP $C_{Fe}=0.5$ g/L	0.818	0.459	0.405	11.7
IONP $C_{Fe}=0.75$ g/L	0.830	0.465	0.38692	16.7

4 Conclusions

The potential to increase the residual oil efficiency by injecting suspensions of iron oxide nanoparticles synthesized and stabilized by the polyphenols of plant extracts (parsley) is investigated with visualization tests on a glass-etched pore network. Over the investigated experimental conditions, imbibition with IONP suspensions is dominated by the capillary fingering flow pattern. The nanoparticles mobilize trapped oil by transferring it from upstream to downstream through a mechanism of successive steps of drainage (local increase of oil saturation) / imbibition (local decrease of oil saturation). It seems that the oil recovery efficiency of secondary imbibition tests is favored when using IONP suspensions without the presence of NaCl (Table 4). On the other hand, the oil recovery efficiency increases respectably when using Pickering emulsions stabilized by IONP.

Acknowledgements: The research project was supported by the Hellenic Foundation for Research and Innovation (H.F.R.I.) under the “1st Call for H.F.R.I. Research Projects to support Faculty members and Researchers and the procurement of high-cost research equipment” (Project Number: HFRI-FM17-361, acronym: EOR-PNP).

References

- M.S. Kamal, A.A. Adewunmi, A.A. Sultan, M.F. Al-Hamad, U. Mehmood. *J. Nanomat.* **2473175**, 1-16 (2017)
- H. ShamsiJazeyi, C.A. Miller, M.S. Wong, J.M. Tour, R. Verduzco. *Appl. Polymer Sci.* **131**, 40576, pp.1-13 (2014)
- T. Sharma, G.S. Kumar, J.S. Sangwai **129**, 221-232 (2015)
- T. Sharma, S.K. Govindarajan, J. Sangwai. *Ind. Eng. Chem. Res.* **54**, 1576-1584 (2015)
- N. Bizmark, M.A. Ioannidis, *Langmuir* **31**, 9282-9289 (2015)
- N. Kumar, T. Gaur, A. Mandal. *J. Ind. Eng. Chem.* **54**, 304-315 (2017).
- N. Saleh, T. Sarbu, K. Sirk, G.V. Lowry, K. Matyjaszewski, R.D. Tilton. *Langmuir* **21**, 9873-9878 (2005)
- T. Saigal, H. Dong, K. Matyjaszewski, R.D. Tilton. *Langmuir* **26 (19)**, 15200-15209 (2010)
- N. Bizmark, M.A. Ioannidis, *Langmuir* **33**, 10568-10576 (2017)
- T. Saigal, A. Yoshikawa, D. Kloss, M. Kato, P. L. Golas, K. Matyjaszewski, R.D. Tilton, *J. Coll. Interface Sci.* **394**, 284-292 (2013)
- X. Li, H. ShamsiJazeyi, S.L. Pesek, A. Agrawal, B. Hammouda, R. Verduzco. *Soft Matter* **10**, 2008-2015 (2014)
- K.Y. Yoon, Z. Li, B.M. Neilson, W. Lee, C. Huh, S.L. Bryant, C.W. Bielawski, K.P. Johnston. *Macromolecules* **45**, 5157-5166 (2012)

13. N.J. Alvarez, S.L. Anna, T. Saigal, R.D. Tilton, L.M. Walker. *Langmuir* **28**, 8052-8063 (2012)
14. C. Tsakiroglou, K. Terzi, A. Sikinioti-Lock, K. Hajdu, C. Aggelopoulos. *Sci. Total Env.* **563–564**, 866–878 (2016)
15. K. Terzi, A. Sikinioti-Lock, A. Gkelios, D. Tzavara, A. Skouras, C. Aggelopoulos, P. Klepetsanis, S. Antimisiaris, C.D. Tsakiroglou. *Coll. & Surf. A: Physicochem. & Eng. Aspects* **506**, 711-722 (2016)
16. C.D. Tsakiroglou, A. Sikinioti-Lock, K. Terzi, M.A. Theodoropoulou, *Chem. Eng. Sci.* **192**, 391-413 (2018).
17. D. Arab, A. Kantzas, S.L. Bryant *J. Pet. Sci. Eng.* **163** 217–242 (2018)
18. A. Sebastian, A. Nangia M.N.V. Prasad. *J. Clean. Prod.* **174**, 355-366 (2018)
19. J. Lin, X. Weng, R. Dharmarajan, Z. Chen. *Chemosphere* **169**, 413-417 (2017)
20. J. Fowsiya. G. Madhumitha. N.A. Al-Dhabi, M.V. Arasu, *J. Photochem. & Photobiol. B: Biology* **162**, 395–401 (2016)
21. M. Karavasilis, C.D. Tsakiroglou, *Emerging Science Journal* **3(6)**, 344-360 (2019)
22. M.A. Theodoropoulou, V. Sygouni, V. Karoutsos, C.D. Tsakiroglou, *Int. J. Multiphase Flow* **31**, 1155-1180 (2005)
23. M. Geremu, Y. B. Tola and A. Sualeh, *Chem. Biol. Technol. Agric.* **3:25**, pp.1-6 (2016)
24. V. Kamath, P. Chandra, G.P. Jeppu, *Int. J. Phytorem.* **22**, 1278-1294 (2020).
25. J.D. Berry, M.J. Neeson, R.R. Dagastine, D.Y.C. Chan, R.F. Tabor, *J. Coll. Inter. Sci.* **454** 226–237 (2015); <http://opencolloids.com>
26. C.D. Tsakiroglou, M. Theodoropoulou, V. Karoutsos, , *AIChE J.*, **49**, 2472-2486 (2003).
27. A. Katende, F. Sagala, *J. Molec. Liq.* **278**, 627-649 (2019)
28. C.D. Tsakiroglou, *J. Non-Newt. Fluid Mech.* **105**, 79-110 (2002)
29. C.D. Tsakiroglou, *J. Non-Newt. Fluid Mech.* **117**, 1-23 (2004).
30. C.D. Tsakiroglou, M. Theodoropoulou, V. Karoutsos, D. Papanicolaou, V. Sygouni, *J. Coll. Interface Sci.* **267**, 217-232 (2003).

Simultaneous Interpretation and Uncertainty Analysis of SCAL Data from Complex Rocks

*Omideza Amrollahinasab, Siroos Azizmohammadi and Holger Ott**

Department Petroleum Engineering, Montanuniversität Leoben, 8700 Leoben, Austria

Abstract

Relative permeability and capillary pressure saturation functions are key uncertainties in reservoir engineering. Many resources are spent on measuring these functions in special core analysis (SCAL) for field developments. Despite the effort and time invested, it is not yet common practice to numerically interpret SCAL data, nor is it common practice to study the resulting uncertainty to reliably extract these two-phase saturation functions. Further developments are particularly important for complex rock types such as microscopically and macroscopically heterogeneous carbonates.

Here, we present a MATLAB-MRST-based simulator for simultaneous matching of SCAL data sets from different experimental techniques. We focus on the most common SCAL techniques, namely, steady-state relative permeability and centrifuge capillary pressure. We discuss the implementation of the common parametrized relative permeability representations and their deficiency to describe data from rather complex rocks such as carbonates. To overcome this limitation, a point-by-point approach is developed and applied to an extensive carbonate data set. For uncertainty analysis, a Markov chain Monte Carlo (MCMC) sampling-based workflow is implemented and applied. The uncertainty is discussed in the frame of the individual data set, simultaneously analyzed data sets, and the sample-to-sample variation, which is an essential step toward stochastic reservoir modeling.

1. Introduction

Dynamic reservoir simulations require relative permeability ($k_r(S_w)$) and capillary pressure ($p_c(S_w)$) saturation functions when immiscible fluid displacement is of concern. Common examples are water flooding for oil production (water/oil), the production of deep geothermal systems (water/steam) and the geological storage of CO₂ (water/CO₂). In these operations, $k_r(S_w)$ and $p_c(S_w)$ decisively dominate the fluid displacement efficiency, sweep efficiency and injection/production pressure. History matching (HM) and predicting reservoir performance by numerical simulations therefore require an accurate input for those saturation functions. Classically, $k_r(S_w)$ and $p_c(S_w)$ are measured in laboratories by core flooding, which is subject to special core analysis (SCAL).

In SCAL, relative permeability is measured by the flooding experiments e.g. steady-state (SS) method, in which the two fluid phases, e.g., oil and water or CO₂ and water, are injected simultaneously at a constant total injection rate and at a certain fractional flow. By measuring the differential pressure and the water saturation after reaching steady-state conditions, Darcy's law can be used to calculate the relative permeability at that fractional flow point, and the scanning of the fractional flow curve allows us to measure the entire relative permeability curves. However, typically, the measured differential pressure cannot be assigned to a single S_w , since capillarity influences the fluid distribution in the rock—the so-called capillary end effect— $k_r(S_w)$ and $p_c(S_w)$ are coupled [1, 2]. Furthermore, in flooding experiments, the saturation

endpoints are typically not reached in a finite time. Toward endpoints, relative permeability measurements are often extended by other experimental methods, such as single-speed centrifuge experiments. In these examples, it turns out that single measurements may not describe a saturation function sufficiently, which means that measurements and analyses need to be combined. This is due to the natural inference of $k_r(S_w)$ and $p_c(S_w)$ in any type of two-phase flow experiments. For this reason, the classic analytical solutions to the SCAL experimental methods, such as using Darcy's law for SS, JBN analysis [3] for un-steady state (USS), and Hassler–Brunner [4] and Hagoort's [5] approaches for the analysis of centrifuge measurements, fail, as does the numerical description of individual data sets [6].

By numerical data interpretation, the full physical picture can be considered by a subsequent interpretation of $p_c(S_w)$ and $k_r(S_w)$ experiments or by a simultaneous interpretation of data sets [7, 8]. The latter case does not refer to the best match of the individual data set but to the best combined description, leading to a robust and reliable interpretation. Numerical SCAL interpretation refers to the inverse modeling approach, in which the simulation results are iteratively matched to the experimental data. However, inverse modeling is an ill-posed problem with intrinsic uncertainties [9]. Non-uniqueness and instabilities in part are the results of weighting assigned in the objective function, averaging methods applied and experimental uncertainties such as instrumental noise and systematic errors. It is also not necessarily given that the underlying physical model is sufficient to describe experimental observations. Examples may be simple, e.g., sample heterogeneity that is typically not accounted for in

SCAL interpretation, and pressure and saturation fluctuations by ganglion dynamics are not represented in the modeling approach using Darcy’s law [10, 11]. Additionally, the restriction to certain parametrized representations of $p_c(S_w)$ and $k_r(S_w)$, such as the Brooks Corey [12], modified Corey [13] or LET [14] representations, may be a threat for the interpretation of complex rocks such as carbonates [9]. As a result of this discussion, single representations of p_c and k_r saturation functions may not be sufficient for reliable reservoir flow predictions; uncertainty intervals should be included in modern stochastic reservoir modeling. The first promising attempts in this direction have been made in [9, 11, 15]. However, neither numerical interpretation nor uncertainty modeling is yet common practice in SCAL interpretation. A reason may be that the sophisticated SCAL simulation tools are proprietary, which hinders developments in this area.

With this paper, we provide an MRST-based open-source simulator running in MATLAB, for a comprehensive interpretation of SCAL experiments. The work focuses (a) on uncertainty modeling and probabilistic analysis following a Monte Carlo type of sampling with the goal of obtaining realistic intervals for early decision making and stochastic reservoir modeling. (b) Saturation functions are optionally constructed differently from common representations, depending on the complexity of the rock type under investigation. For the interpretation of rock types with a high complexity (the majority of carbonates), we introduce an optional point-by-point approach, which does not follow a specified mathematical function. With this approach, we overcome the limitations of the classic parametrization, which is demonstrated and discussed on a complex carbonate. The simulator runs forward simulations with the MATLAB Reservoir Simulation Toolbox (MRST) [16]. The gradient-based history matching used the MATLAB optimization toolbox. We also employed parallel high-performance delayed-rejection adaptive-metropolis Markov chain Monte Carlo (MCMC) (ParaDRAM) [17], all of which are open-source toolboxes built in MATLAB.

2. Experimental Materials and Methods

SCAL experiments were performed on Estailades limestone, a rather complex, dual porosity carbonate rock type. The SS and centrifuge (CF) data were published in [18]. The data set represents a primary drainage process on the original water-wet state of the rock.

Rock Samples: Experimental results from 5 rock samples taken from the same outcrop block of Estailades limestone are discussed in this paper. The average porosity was determined to be $\phi \sim 0.28$, and the average permeability was determined to be $K \sim 164$ mD. The sample properties are summarized in Table 1. The block showed overall porosity variations of 10% and permeability variations of 28% [18].

Table 1: Rock samples, rock properties and experimental process.

Sample ID	Porosity (fraction)	Permeability (mD)	Measurement
1	0.293	142.3	Steady-state relative permeability; primary drainage
2	0.271	141.8	
3	0.283	204.1	Multispeed centrifuge capillary pressure; primary drainage
4	0.283	141.2	
5	0.274	189.8	

The rock type was of dual porosity with a pure calcite mineralogy [18]. The samples were drilled and cut to dimensions of 3.75 cm diameter and 5 cm length for both types of experiments. Subsequently, the samples were cleaned, and $S_w = 1$ was established as the starting point for the drainage experiments.

Fluids: The SCAL experiments were performed at ambient pressure and temperature conditions (22 °C) using brine and decane as wetting and nonwetting fluids. The brine contained 3 wt% NaCl and 5 wt% CsCl as X-ray doping agents. Under experimental conditions, the brine viscosity was measured to be 0.993 cP, and the viscosity of decane was measured to be 0.827 cP.

Steady-State Experiments: Primary drainage SS relative permeability experiments were performed in vertical geometry by simultaneously injecting oil and water from top to bottom. The total injection rate was kept constant at 3 ml/min at different water fractional flow (f_w) steps.

The samples were initially saturated to $S_w = 1$ under vacuum conditions, followed by the first SS measurement at $f_w = 1$, delivering the absolute permeability. f_w was then stepwise decreased by keeping the total flow rate constant. For each f_w step, the differential pressure and the 1D saturation profile along the core were measured after reaching steady state.

The differential pressure was measured in two ways: (a) from injection to production end over the total porous domain (the data shown here) and (b) locally, over a length of 2.5 cm around the center of the plug over which the saturation profile was essentially flat (to exclude the capillary end effect). The local measurement allows us to analytically calculate the relative permeability point-by-point using Darcy’s law. The analytical solution serves as an initial guess for numerical interpretation. The saturation was monitored by measuring the X-ray attenuation profile along the core, which is sensitive to different X-ray absorption coefficients of the fluids and hence to the saturation state.

Multispeed Centrifuge Experiments: Centrifuge experiments were performed in drainage mode, starting from $S_w = 1$, established in the same way as for the SS experiments. The samples were desaturated in multiple steps of increasing centrifugal acceleration and angular frequencies. During the experiment, the cumulative water production was recorded by an automatic stroboscopic read-out system. At the end of each experimental step no further water production was observed. From the cumulative water production, the average water saturation (\bar{S}_w) can be calculated. From \bar{S}_w and the centrifugal

acceleration, $p_c(S_w)$ can be estimated by the Hassler–Brunner equations [4], which serve as a starting point for the numerical data interpretation further below.

3. Numerical Methods and Implementation

The forward modeling part is using the MRST to simulate the SS, unsteady-state (USS), and CF experiments both in an imbibition and drainage mode. We use the term “forward modeling” for the case in which we have the full set of rock and fluid properties available, and we numerically simulate SCAL experiments. Forward modeling is especially useful to design experiments and for quality control purposes of, e.g., third-party data, or to judge the validity of analytical solutions as starting point for numerical analysis; typically, analytical solutions serve as starting points of the numerical workflow.

The initial step in our methodology begins with calculating the saturation functions from the experimental measurements using the corresponding analytical solutions, i.e., the Darcy equation for SS experiments and the Hassler–Brunner equations [4] for CF experiments. Then, we implement an objective function with which we search for the least mean square error between the experimental measurements of the SS (pressure and saturation profiles) and CF experiments (average water saturation) and the corresponding simulation predictions. These errors are summed up in a single total error to be able to match both experiments simultaneously. This objective function is then fed into the MATLAB optimization toolbox *fmincon* function.

The *fmincon* function attempts to optimize the saturation functions by minimizing the least mean square error defined in the objective function. The variation in the saturation functions is done in a point-by-point fashion to overcome the limitations of saturation function parametrization functions, e.g., Corey [12] and LET [14], which is further explained in the section on the parametrization of saturation functions. The results of the history matching simulation are then input into the *ParaDRAM* package to run the Monte Carlo simulations, sampling variations of the saturation tables in the vicinity of the history match results, and quantify the uncertainty ranges around the history-matched solution.

As far as the convenience of use and the computational efficiency are concerned, MRST serves our purpose. Details, especially on the latter, are discussed further below.

Flow Equations and Solver: For the simulation of SCAL experiments, immiscible and incompressible fluid phases are assumed. Furthermore, fluid viscosities are assumed to be pressure independent and can be specified by the user. Under these conditions, two-phase flow can be described by the following governing equations: in the absence of source and sink terms, the material balance is expressed as:

$$\phi \partial_t(S_\alpha) + \nabla \cdot (\vec{v}_\alpha) = 0 \quad \alpha = w, o \quad (1)$$

Here, ϕ is the porosity and S_α is the phase saturation—both dimensionless—and \vec{v}_α is the Darcy phase velocity vector in units of m/s. Without the restriction to a specific

combination of fluids we refer the two phases α to oil (*o*) and water (*w*) in the following. The Darcy velocity \vec{v}_α is given by Darcy’s law:

$$\vec{v}_\alpha = - \left(\frac{k_{r\alpha}}{\mu_\alpha} \right) K (\nabla p_\alpha - \rho_\alpha \vec{g}) \quad \alpha = w, o \quad (2)$$

where $k_{r\alpha}$ are the dimensionless relative permeability saturation functions and μ_α are the phase viscosities in Pa · s. K is the absolute rock permeability in m², p_α are the phase pressures in Pa, and \vec{g} is the gravitational constant in m/s². Furthermore, the phase saturations satisfy $S_w + S_o = 1$, and incompressible flow is further restricted to $\nabla \cdot (\vec{v}_w + \vec{v}_o) = 0$.

The solver is based on the MRST automatic differentiation (AD) toolbox, including differentiation and divergence operators, automatic differentiation to compute the Jacobians, object-oriented framework, and state functions from which we make use in the simulator. The details on how these operators are implemented in the MRST framework can be found in [19].

The simulation time and the desired time stepping are managed by using the MRST *rampupTimesteps* function, which increases the simulations’ stability and accuracy since there are usually relatively larger changes in the saturation and pressure at the beginning of a simulation schedule. Then, the *simulateScheduleAD* function is used for simulations using fully implicit formulation and adaptive time step adjustments in case of convergence failures.

For the carbonate rock simulations shown in this paper, a maximum time step of ~20 hours with ~10 geometrically ramped-up time steps show the best tradeoff between the accuracy and the simulation speed for most of the cases.

Parametrization of Saturation Functions: SCAL data are numerically calculated by varying $k_r(S_w)$ and $p_c(S_w)$ to be compared with the experimental measurements e.g. pressure and saturation measurements. Traditionally, these saturation functions are constructed using parametrized power law functions. These functions are partly physically motivated [12] and partly designed to allow an effective description of a wide range of rock types [14]. The disadvantage of power laws is that they generally constrain the shape of the resulting saturation function. They also impact the history matching process, as they may cause highly non-unique response surfaces of the objective function that the optimizer is trying to minimize [9].

In this work, saturation functions are constructed point by point since a higher flexibility was needed to describe the specific carbonate rock type. In the point-by-point approach, we interpolate linearly between adjacent points using the MRST *interpTable* function. Derivatives are then computed by the piecewise linear interpolant. To find the overall best match of $k_r(S_w)$ and $p_c(S_w)$, the SS and multispeed CF data sets are interpreted pairwise and simultaneously. The saturation points are chosen on the basis of the experimental average water saturations after steady conditions were reached. The achieved saturation ranges of the individual data sets may be different. In the present case of primary drainage, S_{cw} may be reached by CF but typically not by SS. Therefore, outside the SS

saturation range, k_r is sensitive only to the CF measurement. The average of the saturation profiles at each fractional flow from SS defines the middle range water saturations, and the average water saturation from CF experiment defines the lower water saturations. In this way we define the water saturation vector on which the history matching process is performed. For simultaneous evaluation of $k_r(S_w)$ and $p_c(S_w)$, the MATLAB *fmincon* function automatically scales the input parameters to assist the optimization process. However, during the uncertainty quantification using the ParaDRAM package, no input parameter scaling is applied. To date, the point-by-point approach has not caused any numerical stability problems.

Steady-State and Unsteady-State Model: Steady-state and unsteady-state core flood experiments are modeled in a 1D linear domain as displayed in Figure 1 using the *tensorGrid* function in *MRST*. The domain size is adapted to the dimensions of the rock samples and regularly discretized in the flow direction with a grid size of 1 mm. This gridding scheme is inspired from the work of [6]. As typical in SCAL, the domain is considered homogeneous in all rock properties and is populated with the experimentally determined average values for K and ϕ .

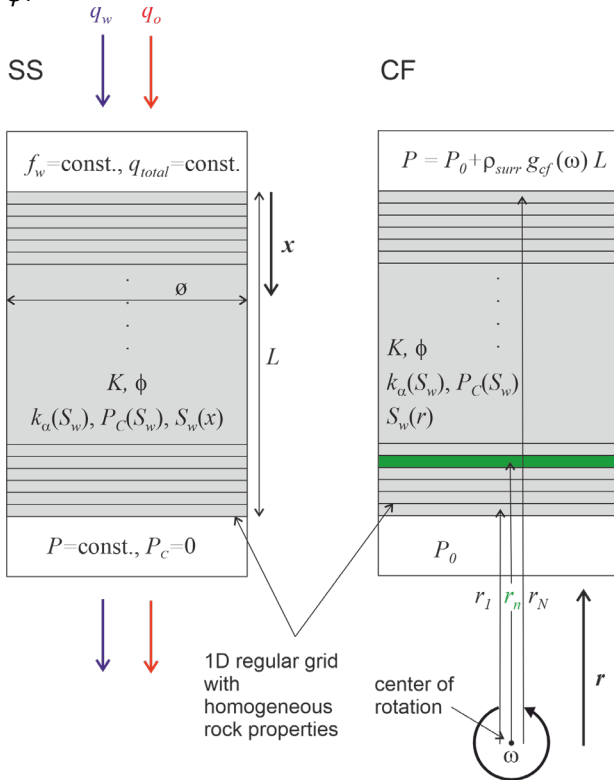


Figure 1: Modeling domains for matching steady-state (SS, left) and centrifuge experiments (CF, right). In this figure, f_w is the fractional flow of water, q_{total} total injected flow rate, ϕ porosity, P_c capillary pressure, K the absolute permeability, S_w water saturation, and P_0 initial pressure.

Extra grid blocks with the same volume are added to either end of the simulation domain to apply the inlet and outlet boundary conditions. By assigning $\phi = 1$, $P_c = 0$, and straight-line k_r functions, the discontinuity at the inlet and outlet boundary is introduced [6]. The experimental boundary conditions are also applied to these extra grids;

at the inlet boundary cell, constant flow rates, and at the outlet, constant pressure boundary conditions are applied by using the *fluxside* and *pside* functions in the *MRST*. The differential pressure is calculated as the pressure difference between the boundary cells at each end of the core. Since we assume the capillary pressure in these boundary cells to be zero, the water and oil pressures are the same in both cells, and the reported differential pressure applies to the respective connected fluid phase in the domain. For the calculations of average water saturations, these boundary cells are omitted from the water saturation profile outputs since the boundary cells are not a part of the main core body.

For the initialization of the primary drainage processes, the water saturations in the inlet and outlet boundary cells are set to one, and for the first imbibition process, they are set to zero. These settings follow the experimental layout, with the experiments starting at $f_w = 1$ for drainage and at $f_w = 0$ for imbibition.

By realizing the boundary conditions as described referring to the experimental settings of the injection pumps and the backpressure system, the experimental responses can be modeled and compared to the actual measurements. These are the differential pressure as measured by pressure transducers and the 1D saturation profiles, which are determined by X-ray absorption measurements.

Multispeed Centrifuge Model: For modeling centrifuge experiments, the modeling domain is set up as for the SS and USS core flood experiments. However, the driving force refers to the gravity term in equation (2). The model geometry is given on the right side of Figure 1. In centrifuge experiments, gravity is applied by centrifugal acceleration $g_{cf} = \omega^2 r$, in which r denotes the distance from the center of rotation; therefore, gravity varies along the modeling domain, i.e., along the core sample.

For the simulations of an individual experimental step at a constant angular frequency ω , both ends of the core are assigned a constant pressure boundary condition. The pressure boundary conditions in CF experiments are governed by the hydrostatic pressure in the surrounding fluid that invades during the CF experiment. At the boundary toward the center of rotation, the pressure is set to a constant $P_0 = \rho_{surr} \omega^2 r_0$, while on the opposite side of the modeling domain, the gravitational head amounts to $P = \rho_{surr} \omega^2 r_{N+1}$, with r_0 and r_{N+1} being the positions of the two boundary grid blocks and ρ_{surr} being the density of the surrounding/invasive fluid, which is oil in the case of drainage and water in the case of an imbibition process. Defining the boundary conditions as above allows us to establish the surrounding hydrostatic pressure and naturally account for the gravity-induced fluid flow in and out of the modeling domain.

A centrifuge device requires a certain time to reach the predefined angular velocity, which is called the startup time. This startup period affects the production profile, especially from cores with high absolute permeability. In the simulator, to account for the startup period we divide the startup rotation per minute (RPM) to the startup time and assume a linear increase in the centrifuge RPM to calculate a maximum rate at which the centrifuge RPM

can change over time (in the units of RPM/s). Then we scan through the CF rotation schedule and break it down into smaller RPM increase steps based on the maximum rate that the CF RPM can change. In the simulations, a startup period of 100 s to 2000 rpm is assumed, discretized in five 20-second steps.

4. History Matching

SCAL data interpretation by numerical history matching is well established but not yet common practice. A best practice is an assisted history matching procedure based on a user-defined objective function to be minimized, which also allows for a subsequent uncertainty analysis [9]. In this work, we go two steps beyond: first, similar to [20, 21], we analyze data sets of different measurements simultaneously instead of subsequently. Simultaneous analysis facilitates finding the best combined match of $k_r(S_w)$ and $p_c(S_w)$ by minimizing a common and normalized objective function. Second, in numerical HM, the $k_r(S_w)$ and $p_c(S_w)$ functions are typically represented by power laws, which is physically expected for simple rock types [13] [12]. The present module also allows a point-by-point description of $k_r(S_w)$ and $p_c(S_w)$ to match experimental data from highly complex rock types without the limitations of specific power-law representations.

In general, numerical HM is an underdetermined process, for which the Levenberg–Marquardt algorithm is used because of its robustness to the starting values [21] [22]. However, in contrast to the Levenberg–Marquardt approach, the *MATLAB fmincon* function implements interior-point or active-set algorithms in which a constrained nonlinear optimization algorithm allows for the implementation of inequalities; inequalities are essential for the aspired point-by-point approach to enforce monotonic behavior of k_r and p_c saturation functions, which is naturally the case by power-law representations. Monotonicity is demanded from a physical point of view, since we do not expect that, e.g., the phase permeability decreases with increasing saturation.

Inside the *fmincon* function, we set the optimization algorithm to be the *active set*, as it provides the best possible results by minimizing the following objective function:

$$K = \frac{1}{N_{obs}} \sum_{i=1}^{N_{obs}} \left(\frac{d_i - y_i}{d_i} \right)^2 \quad (3)$$

where d_i are the observed experimental values, y_i are the simulated responses, and N_{obs} is the number of parameters, which is equal to the number of measured data points. Various objective functions are reported in the relevant literature [11]. The convergence criteria for the *fmincon* function is the default 10^{-6} difference between the two last calculated objective function values. The χ^2 function is most commonly used as objective function for history matching purpose, however we found equation (3) to be more suitable for the simultaneous history matching of SS and CF experiments and point-by-point representation of the saturation tables. Simultaneous

experiments affect the data that we are matching (causing a different error surface) and the choice of representation affects the points that we are iterating on. This is because the measurements are at different scales (i.e., numerical values) and at different resolutions (i.e., point density), which is accounted for by the well-normalized objective function in equation (3). The available analytical solutions serve as a starting point for the HM process, which ensures that the solution is close enough to the optimal solution to minimize the chances of approaching a local minimum instead of the optimal solution.

4.1 Uncertainty modeling

After finding a match between the experimental and numerical responses, we explore the response surface around our optimal solution and determine its sensitivity. As also shown by [9], the history matching problem is ill-posed with local minima. In such cases, solutions through a Hessian matrix and a χ^2 analysis may fail. Instead, we opt for MCMC sampling.

In the traditional MCMC methods, manual tuning of parameters within the sampling algorithm may be required to ensure the convergence of the Markov chain to the target densities for the problem at hand. To avoid manual tuning, we use the ParaDRAM library, which offers a practical implementation of the delayed-rejection adaptive-metropolis MCMC or DRAM algorithm. DRAM is fully automated regarding the selection of the free parameters and is an extension of the traditional Metropolis–Hastings (MH) method [17].

The DRAM algorithm combines two algorithms, namely, the delayed-rejection (DR) and adaptive-metropolis (AM) algorithms. The AM algorithm, as opposed to the MH algorithm, adapts the proposal distribution based on the past history of the Markov chain (the points sampled thus far), and the DR algorithm improves the efficiency of the MCMC sampler, especially in higher dimensional problems; in high-dimensional domains, the number of rejections can become more significant than the acceptance, strongly compromising the efficiency of the sampler. Therefore, DRAM can be useful since the point-by-point construction of saturation functions refers to a high-dimensional space. Furthermore, this method is particularly useful for multimodal target density functions separated by deep valleys of low likelihood. Therefore, in the case of multiple local minima in the objective function response surface, this method can help us find them [23].

The MatDRAM algorithm [23] (existing in the ParaDRAM library) offers a practical variant of the generic DRAM algorithm relaxing the requirements for (a) a set of delayed-rejection-stage proposal distributions and (b) reduces the complexity of the acceptance probability. Symmetric proposal distributions with a fixed shape are used through the DR process, and the scales are determined through a user-defined schedule. To run the MCMC simulations, we use a likelihood estimation function as follows:

$$J = \frac{1}{N_{obs}} \sum_{i=1}^{N_{obs}} -\frac{1}{2} \left(\frac{d_i - y_i}{error \cdot d_i} \right)^2 \quad (4)$$

where *error* is a fixed value between 0 and 1 (expressed as a percentage below) and we multiply $-1/2$ to this function since here we aim to maximize the probability rather than minimizing as in equation (4). We assume a relative error of 2.5% for the pressure reading, 1% for the saturation profile of SS experiments, and 1% for the average water saturation of CF experiments. These fixed error values are simple assumptions coming from the experimental measurements' average standard deviation after steady state was reached. The experimental measurements act as observed (true) values, and through ParaMonte iterations, J is calculated from simulation predictions. During the MCMC simulations, $k_r(S_w)$ is hard bounded between zero and one, and $p_c(S_w)$ bounds are set to be half and double the optimum values (the minima – or the best saturation function - which is found in the history matching simulations) as lower and upper boundaries.

To force a monotonic behavior of the point-by-point saturation functions, we define a prior inequality function that checks if:

$$Ax \leq b \quad (5)$$

Where x is a vector, containing the parameters that are history matched, and the matrix A and vector b are defined in a way to have:

$$x_i \leq x_{i+1} \text{ or } x_i \leq x_{i-1} \quad (6)$$

based on the type of monotony that is forced on the parameters. This inequality is run before the likelihood estimation above (equation (4)), and if it is not valid we reject the sample before running the simulations to save computational time. In this function, we create the A and b matrix, in the same way the inequalities are forced in the MATLAB optimization toolbox [24], and reject the samples that are not monotonic prior to our main likelihood estimation function. This method saves computational time by not rejecting samples without running the main likelihood estimation function.

5. Benchmarking and Verification

The model's accuracy was verified by using synthetic data sets published by Lenormand et al. [25] and Loeve et al. [8] for the forward modeling and history matching modules, respectively. The simulator has been benchmarked with 5 simulation cases to the results of accepted SCAL simulators by comparing the results to [25]. Figure 2 shows (a) the $k_r(S_w)$ and (b) the $p_c(S_w)$ input and the comparison with the differential pressure and saturation data simulated by the SCORES simulator expressing $k_r(S_w)$ with a Corey model and $p_c(S_w)$ as tabulated values. Case 1 (c) represents the differential pressure during SS imbibition in a neutral-wet system. The synthetic data set includes bump floods as typically performed at the end of SS experiments to increase the accessible saturation window. Figure 2 (d) refers to a water-wet primary drainage process and the respective average water saturation from a CF experiment.

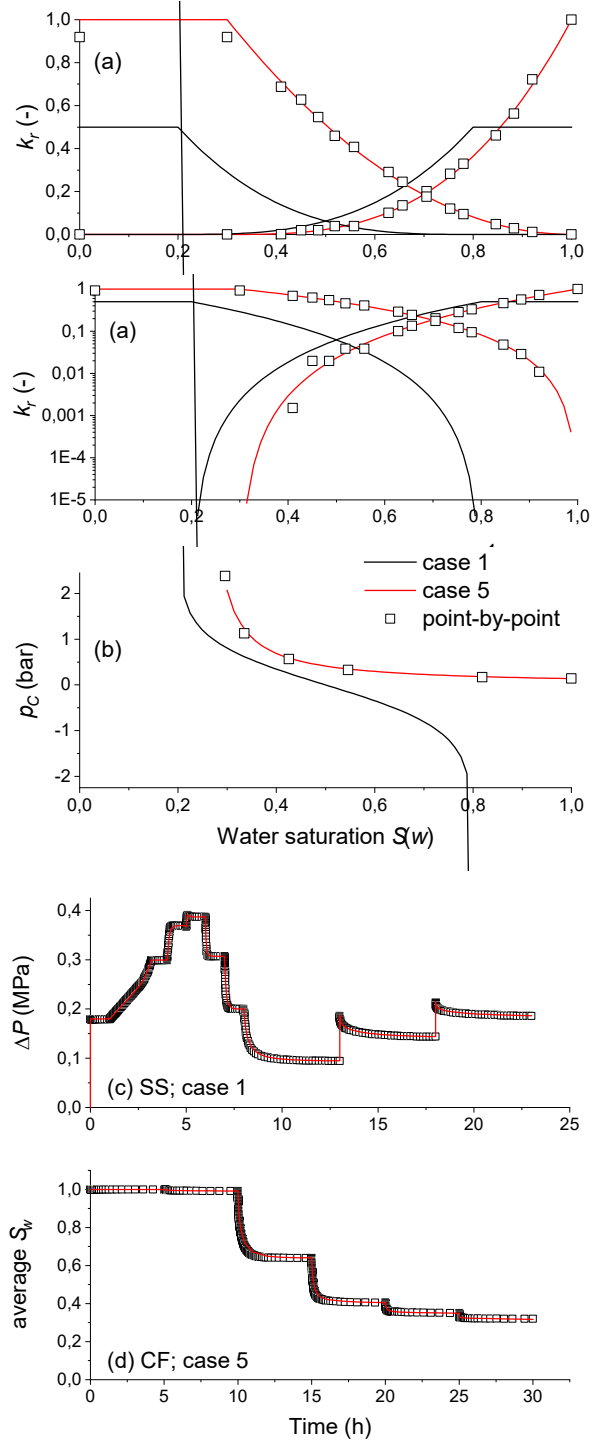


Figure 2: Verification by forward simulation using the reference data set presented by [25]. (a) and (b): Relative permeability and capillary pressure saturation functions, respectively, for primary drainage (case 5) and first imbibition (case 1). Panels (c) and (d) show the forward simulated differential pressure from SS (case 1) and the simulated average water saturation of the CF experiment of case 5, respectively. The symbols are simulated with SCORES, and the lines correspond to the simulator developed in the present work. The open squares in (a) and (b) refer to point-by-point matches of forward simulated experimental responses.

All simulation results show perfect agreement between all simulators, including the one developed in this work. For case 1, a domain discretized into 80 grid cells and a

maximum time step of 0.2 h lead to a runtime of ~16 s using a 9th series core i7 Intel CPU. For this benchmark we use *simulateScheduleAD* with the default parameters – fully implicit scheme and *LinearSolverAD* that calls standard MATLAB direct solver mldivide.

To benchmark the HM module and to demonstrate the MC uncertainty quantification, we use the synthetic data set by [8] to simultaneously match an USS and multi-speed CF imbibition experiment. The data set consists of unsteady-state (USS) and multispeed centrifuge simulated calculations (the synthetic pressure and production data). The Corey-type $k_r(S_w)$ [12] and the Skjaeveland-type [26] $p_c(S_w)$ input functions are shown in Figure 3 (a) and (b). The upper and lower bounds as well as the starting point of the HM are chosen as in [8]. The results are shown in the same panels. Deviations from the true values are found at connate water saturation and the oil endpoint relative permeability. The reason may be the limited information an USS imbibition experiment delivers at low water saturations. The uncertainty analysis is performed by assuming a 2.5% relative error for the pressure and production responses. Figure 3 (c) shows the resulting histograms and the two-parameter correlations for the relative permeability functions. On the contour plots, the Pearson’s correlation strengths are given in addition to red numbers [27]. Strong correlations are found between the endpoint relative permeability and endpoint saturations of the complimentary phase, as evident in the Pearson’s correlation matrix. The endpoint relative permeability also shows a strong correlation with the respective Corey exponents. This is a property of the specific mathematical representation of the saturation functions. For example, a change in the oil Corey exponent directly modifies the oil endpoint relative permeability at a given connate water saturation. The correlations may also provide a physical interpretation as far as the used function is physically motivated.

Above, the classic power-law representations are used to history match (HM) the synthetic datasets and benchmark the SCAL simulator HM module. In the point-by-point representation of the saturation functions, how many free history-matching parameters we have is determined by the count of the fractional flow steps implemented in the SS experiment, and the count of different rotational speeds implemented in the CF experiment. We use the $k_r(S_w)$ and $p_c(S_w)$ of [25] case 5 as input to simulate the primary drainage SS and CF experiments with 12 SS fractional flow (f_w) steps and 5 CF centrifugal speed steps. The simulated experimental responses are then matched with the point-by-point approach using the analytical solutions as starting points. The resulting saturation curves are shown as scatter graphs in Figure 2 (a) and (b). Naturally, the solution shows a certain scatter but describes the input saturation functions well. Deviations are found at the oil endpoint k_r . This may be expected since the SS drainage does not reach true S_{wc} and the centrifuge is missing sensitivity to k_r of the invading phase at that point.

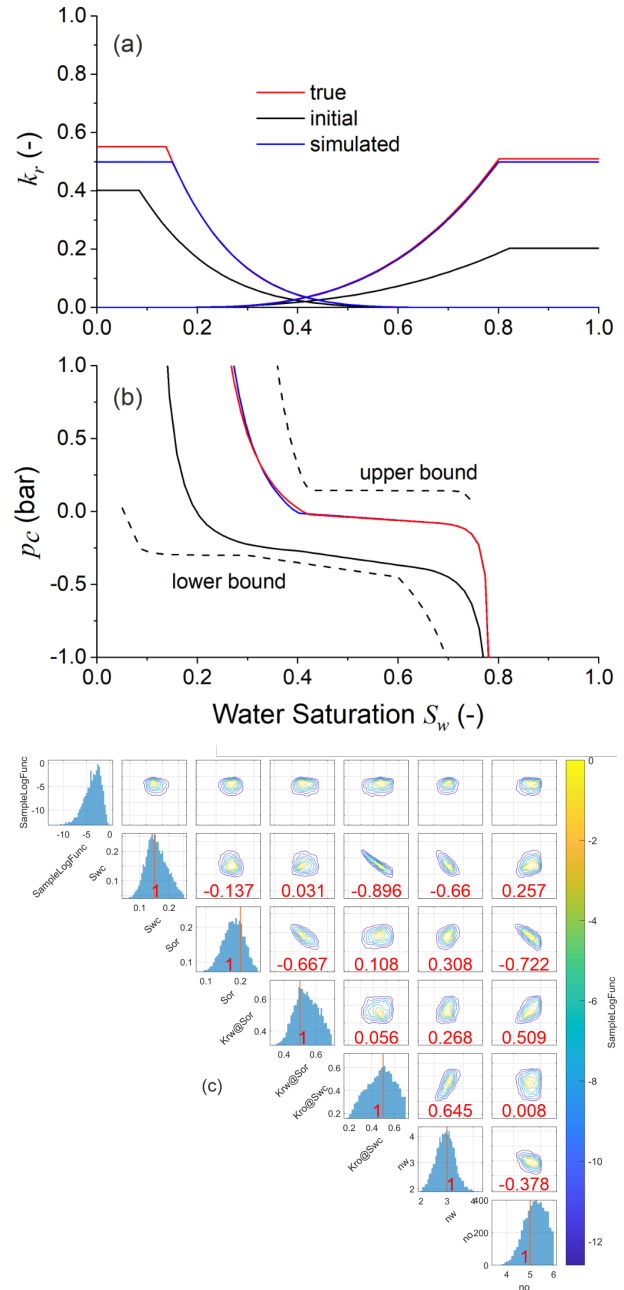


Figure 3: Simultaneous history matching and uncertainty quantification for benchmarking. Synthetic data sets of an unsteady-state and a multispeed centrifuge experiment [8] are matched with modified Corey and Skjaeveland parametrizations. True values, starting points and the matches are shown in (a) for relative permeability and (b) capillary pressure (see text for details). (c) shows the result of the MCMC uncertainty analysis. The diagonal shows the single parameter probability distribution (histograms). The off-diagonal elements (contour plots) show the two-parameter correlations for the relative permeability curves. The red numbers refer to the Pearson correlation strength matrix.

6. Results

The real case study is performed on an SCAL data set of Estailades limestone. The data set consists of two steady-state primary drainage relative permeability measurements and three multispeed centrifuge experiments. The experiments have been pair-wise simultaneously matched. Data from a CF/SS combination (samples 2 and 5) are shown in Figure 4. Details about the rock type and rock properties of the individual plugs are summarized in the Materials and methods section above.

At first, we simultaneously matched CF (average water saturations) and SS (pressure and saturation profiles) experimental measurements by using various power-law representations for $k_r(S_w)$, namely, Corey, LET and modified Corey, and the corresponding representations of $p_c(S_w)$. Since the data set refers to a primary drainage process, the water endpoint relative permeability is fixed to $k_{rw}(S_w = 1) = 1$. All the other parameters are left open. The residual water saturation is, however, a history matching parameter common for both $k_r(S_w)$ and $p_c(S_w)$ but matched separately from each other. This means that

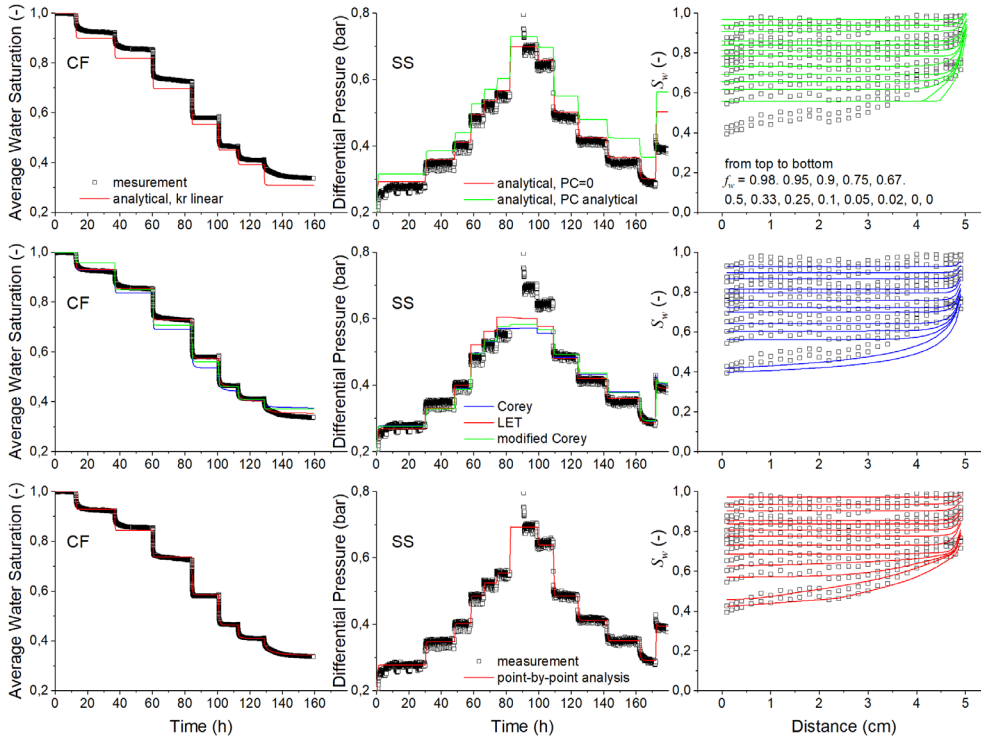


Figure 4 : Experimental data and analytical/numerical interpretations: CF average water saturation (left), SS differential pressure (middle), and SS saturation profiles (right). Top row: forward simulations using the analytical solutions. Middle row: automated and simultaneous history march using different $k_r(S_w)$ power-law input functions in combination with their corresponding $p_c(S_w)$ representations. Lower row: best match using the point-by-point approach.

6.1 Finding Solutions

The analytical solutions using Darcy’s law for SS and the Hassler–Brunner equations for CF experiments are shown in Figure 5 and are used as starting points for the numerical simulations. The quality of the analytical solutions is demonstrated by forward simulations and comparison of the results to the experimental data, as shown in the top row of Figure 4. The comparison of the SS differential pressure shows a reasonable match as capillary pressure is ignored. Including the Hassler–Brunner analytical solution in the forward simulation of the SS experiment, the data are no longer matched but rather an overestimation of the differential pressure. The Hassler–Brunner analytical solution itself underestimates the average water saturation of the CF experiment. The observed mismatches emphasize the importance of including both data sets in the analysis and even the importance of simultaneous history matching of $k_r(S_w)$ and $p_c(S_w)$, matching SS and CF experiments simultaneously.

S_{wc} can principally be different for both types of data sets. The starting point of the history match is the analytical solution shown in Figure 5.

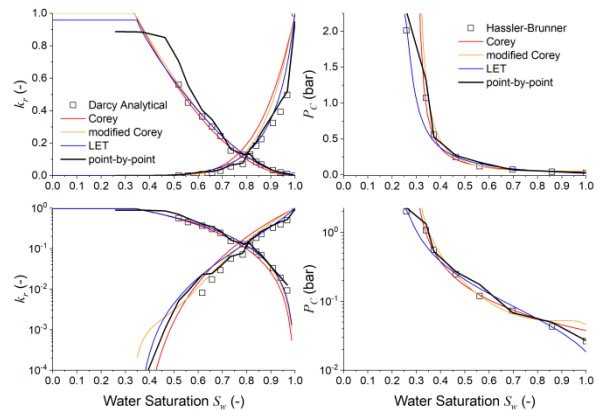


Figure 5 : Analytical solutions (symbols) and results of the history matching using various representations of $k_r(S_w)$ and $p_c(S_w)$, as indicated in the legends. Top: saturation functions on a linear scale. Bottom: the same functions on a logarithmic scale.

As shown in Figure 4, none of these models suitably describe the experimental data sets. Referring to the SS differential pressure, the deviation is strongest close to the crossing points of relative permeability, where the total fluid mobility is lowest, i.e., highest differential pressure values. However, referring to the combined data set of SS and CF, the overall deviations are unacceptably.

With the point-by-point HM approach, we give the system much more degrees of freedom. In this approach we used 17 points for water relative permeability, 17 for oil relative permeability and 8 points for the capillary pressure table. The points for the relative permeability tables are coming from the average of the saturation profiles at each fractional flow until the minimum water saturation measured in the SS experiment. Below this water saturation we get the points from average water saturations of the CF experiment. For the capillary pressure table, we get the points from the average water saturation of the CF experiment. Here we only vary the functional values and the saturation values are constant. The lower row of Figure 4 shows the resulting simulated versus experimental responses. With point-by-point matching, the $k_r(S_w)$ and $p_c(S_w)$ line shapes are not restricted to follow a certain functionality, and with this, complex rock structures may be described. In the present case of Estailades limestone, all responses can be well described, including the SS saturation profiles for all $f_w(S_w)$. The resulting $k_r(S_w)$ and $p_c(S_w)$ are shown in Figure 5, in which all solutions are compared. The point-by-point approach delivers rather irregularly shaped saturation functions but closely follows the irregularities directly observed in the experimental responses. Furthermore, all resulting saturation functions from the HM of the experimental measurements with the simulation predictions are within rather narrow intervals, which is surprising, considering the quality of the matched versus experimental responses. This opens up the important question about the uncertainty in the procedure and finally the resulting uncertainty in the saturation functions.

The results of the HM simulations depend on the optimization algorithm being used and for the point-by-point approach presented here we found the active-set algorithm in MATLAB *fmincon* function to be the most efficient. The Levenberg-Marquardt (LM) method which is used in the literature [9, 21] does not allow the implementation of inequalities (equation (3)) which is an integral part of the point-by-point approach to force the monotonic behavior for the saturation functions. Other algorithms e.g. interior-point can sometimes lead to a closer match to the experimental measurements in case power law representation for saturation functions are used.

6.2 Uncertainty Analysis

To quantify the uncertainties, we run Monte Carlo simulations using ParaMonte. We specify a chain size of 20,000, which is the number of unique points to be sampled from the likelihood estimation function. For this case it leads to ~1,5 million total likelihood estimation function calls or ~1.5% acceptance rate for the MCMC

algorithm. Considering the high-dimensional parameter space, the uncertainty analysis requires a large computational effort resulting in approximately a week of computational time on the used computer system. Figure 6 top shows the value of the likelihood estimation function, which reduces in the early iterations and then oscillates around a value of -15 . The adaptation measure is a real number between 0 and 1 with 0 implying no proposal adaptation and 1 implying extreme adaptation. The convergence of the adaptive Markov chain – the type of MCMC simulations that we are using in this study - to the target density is guaranteed, as long as the adaptation of the Markov chain monotonically decreases throughout the simulation. It is, therefore, important to monitor the amount of adaptation in ParaDRAM simulations to ensure the adaptation of the proposal distribution diminishes progressively throughout the simulation [28]. This value is shown in Figure 6 bottom and the moving average is shown to be monotonically decreasing. This is a healthy sign for the implemented Monte Carlo simulation, which shows a convergence in both the sampled likelihood estimation function and input parameters [17]. For the samples used in this study the point-by-point approach showed the best convergence and match with experimental data whereas; the power-law-like saturation functions do not well match the experimental data, which leads to convergence problems of the Monte Carlo simulation. In that case, the tracer chains overshoot to high values, making the uncertainty range larger. This behavior is sample specific and the saturation functions can be predicted using power law function with a high confidence level as shown in the literature [21].

Figure 7 shows the histograms of the simulated k_{ro} (a), k_{rw} (b), and p_c (c) points along the water saturation axis. These histograms can be used to quantify the uncertainty, which may be defined by calculating the P10 to P90 interval given in Figure 8. The interval refers to the probability of 10 to 90% that the quantity—in this case the fluid relative permeability—exceeds the given value. The P50, given in the same panel, refers to a best match from the Monte Carlo approach. In addition, Figure 7 shows the MCMC chain plots (the accepted Markov chain) at selected saturations along with the correlations between neighboring saturation points exemplarily for k_{ro} . The histograms and the MC line tracers show nearly Gaussian distributions except for the endpoint at connate water saturation. This means that the modeled drainage process is less sensitive to the endpoint, reflected in the elongated histogram shape. This leads to the large uncertainty range at the tail of the water relative permeability in Figure 8 (a). The same is true for the capillary pressure (c), as the centrifuge multistep simulation is less sensitive to the capillary pressure at residual water saturation, leading to a larger uncertainty at S_{wc} .

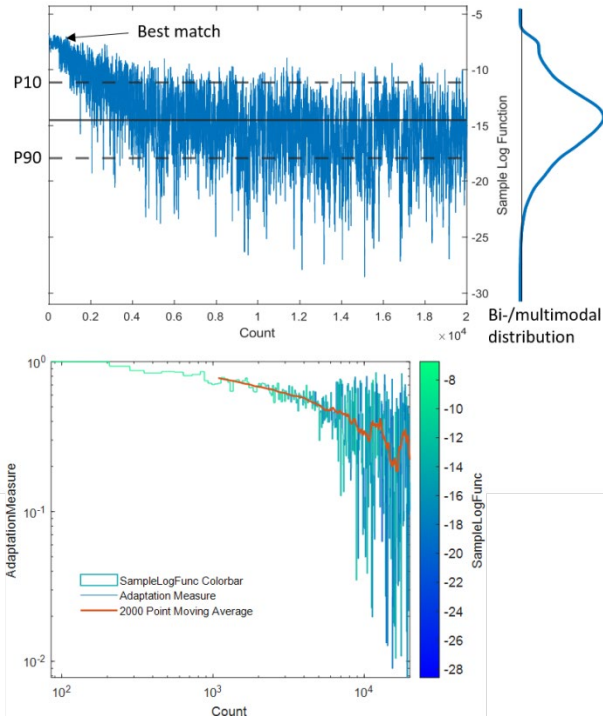


Figure 6: Top: the value of the sampled likelihood estimation function (equation (4)) during the MCMC for the accepted chain of samples. Bottom: the adaptation measure for the full Markov chain.

Although the histograms mostly show Gaussian behavior, the tracer in some chain plots does not always oscillate around a constant value (e.g., $k_{ro}(S_w = 0.97)$). Longer period temporary deviations may be caused by the relatively large parameter space and the respective degrees of freedom, in which the values of some parameters can deviate from the general trend and still be accepted. However, then because of the increased error in the likelihood estimation function, the rejection rate increases, and the chain returns to the previous trend that it was following before.

Figure 8 shows all relative permeability and capillary pressure curves calculated for the Estailades experimental data sets. It also shows the P10 and P90 range calculated from the earlier discussed data set referring to the histograms in Figure 7. The best history match lies within this range. However, it does not lie on the median of the interval. By performing a forward simulation of the experimental response in the boundary of the P10-to-P90 interval, the P10 and P90 pressure ranges are obtained, as shown in the inset of Figure 8(a). The measured pressure is well within the uncertainty range except around the highest-pressure points (lowest total fluid mobility) and around the pressure of the bump flood. These parts of the pressure plot are close to the boundaries of the calculated range.

The range here corresponds to the fixed relative error that we decided in the beginning before running the MCMC simulations. The resulting uncertainty range around the pressure is higher than the assigned 2.5%, since we also allocate 1% error to the saturation profile and 1% error to the average water saturation from the centrifuge experiment. Depending on the standard deviation of the experimental measurements, the error

assigned to the measurements in the equation (4) varies, which affects the calculated uncertainty range.

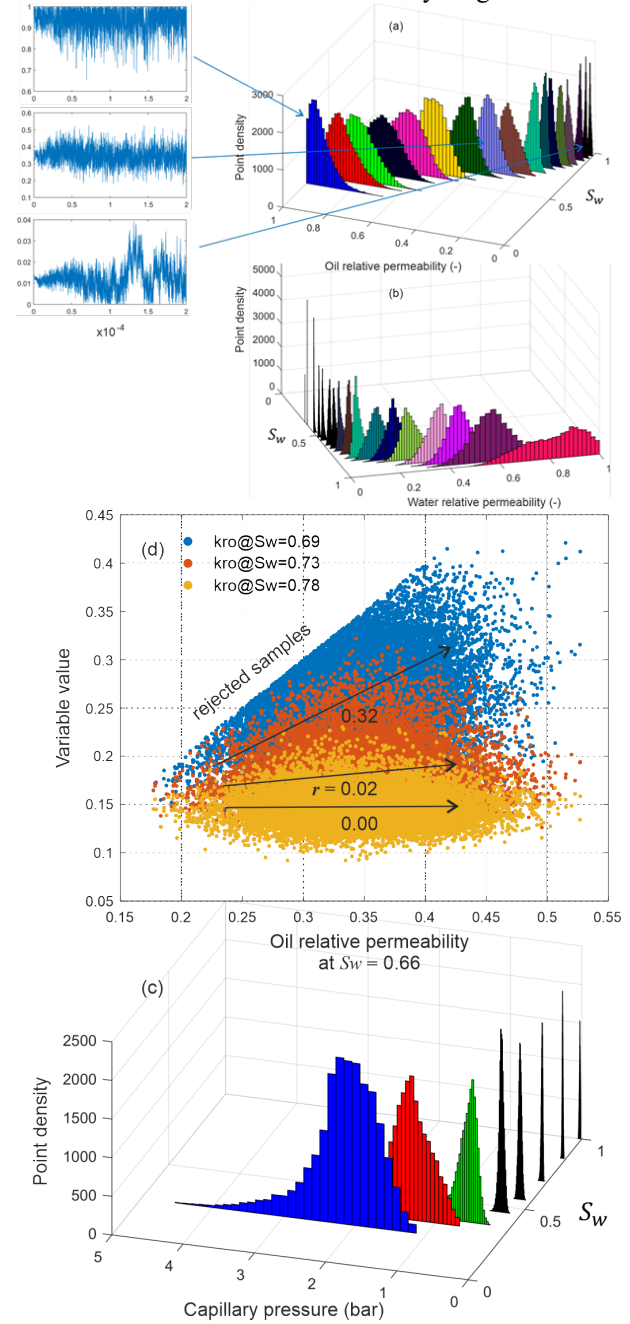


Figure 7: Histograms providing single parameter uncertainties of oil and water relative permeability, (a) and (b), respectively, and capillary pressure (c) saturation functions. MCMC chain plots are exemplarily given for oil relative permeability. (d) Correlation of oil relative permeability at the given water saturation with neighboring saturation points.

The reasoning behind this is intuitive since by doing so, we change the shape of the sampled response surface. The Pearson correlation matrix and the full grid plots for this analysis show the correlation strength between the history matched parameters. The map shows strong correlations between neighboring saturation points. This is partly caused by the forced monotonic behavior that we apply to our simulations. The relative permeability table shows positive correlation between the water saturation points next to each other (Figure 7 (d)) and this correlation is

negative for the capillary pressure table. At lower water saturations, the positive correlation between k_r saturation points span several next neighbors, which is the reason for the larger uncertainty interval at low S_w . At higher water saturations, there is a negative correlation between the water and oil relative permeability. This means that at higher water saturations, the total mobility (relative permeability at constant viscosity) is split between oil and water; as phase mobility increases, the mobility of the complimentary phase decreases—a behavior that we physically expect.

Figure 7 (d) illustrates the correlation strength between k_{ro} at $S_w = 0.66$ and its neighboring points. The Pearson's correlation strength r is labeled in the plot below the black arrows. This demonstrates that with increasing water saturation, the correlation vanishes.

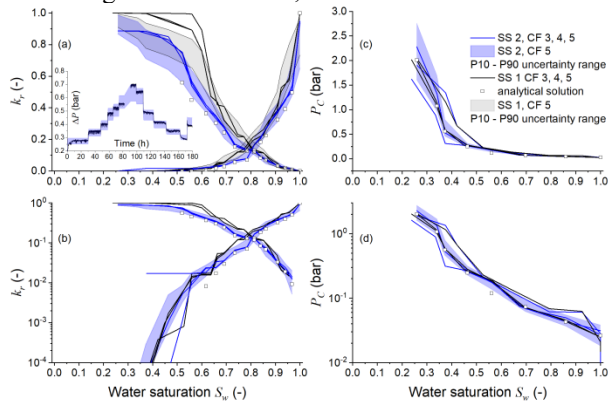


Figure 8: Panel (a) and (b): resulting relative permeability on a linear and logarithmic scale from experiment/sample SS 2 in combination with CF 2, 3 and 5. The uncertainty range is given for the combination SS2, CF 5. For comparison, the pair-wise analysis of SS1 with CF 3, 4 and 5 is given as well. Panel (c) and (d) provide the same information, but for the capillary pressure. The inset in (a) shows the P10 to P90 uncertainty interval for the differential pressure response during the SS 2 experiment as an example.

6.3 Sample-to-Sample Variation

It is a common problem that carbonates often show heterogeneity on various scales. In SCAL, we typically ignore heterogeneity on the plug scale, and SCAL data are numerically interpreted by assuming a simulation domain with homogeneous rock properties. However, sample-to-sample variations are common, even if the samples are drilled from locations close to each other. Therefore, it should be common practice to measure saturation functions on more than one plug from the region. In the present study on Estiallades, which is a common outcrop rock, the samples are from the same block and are therefore “twin plugs”. A natural question is whether measurements on twin plugs deliver results within the uncertainty range of the individual data set. [21] proposed a method to deal with the common data interpretation problems that rises from the heterogeneities of samples in SCAL experiments. They argued that by calculating the variability number (V) of the plugs using the X-Ray measurements one can decide on the significance of the heterogeneity based on the cut-off value for V . Their approach warrants further work to be looked into, also in

the framework of the reliability of the analysis provided from a small number of samples, in the future.

What we deliver in this study is an indication only because 5 plugs (a common number of samples available for SCAL) and 2 and 3 repeat measurements may or may not provide a solid statistical basis [21]. However, we use the two SS and the three CF experiments from [18] and simultaneously analyze all possible SS and CF combinations. The results are shown in Figure 8 (a) and (b) for relative permeability and (c) and (d) for capillary pressure. The simultaneous analysis shows a strong deviation between the SS results but a relatively small influence of the sample-to-sample variation in the CF experiments; the resulting curves split into two groups referring to the two SS experiments, which differ predominantly in the oil branch toward low water saturations, where the strongest point-to-point correlations are found as will be discussed further below. With respect to uncertainty, for simulations with a given SS data set, the k_r curves generated by combining with the different CF data lie within a narrow window compatible with the individual uncertainty range from MCMC. However, the two groups do not fall into the individual uncertainty ranges but show a certain overlap over the whole saturation range. In this specific case, it appears that sample-to-sample variation plays a stronger role than the uncertainty coming from individual data sets and their combinations.

6.4 Results: Bimodal Distributions

The samples from the likelihood estimation function shown at the top of Figure 6 show a rather multimodal histogram, indicating that there is no unique solution in the error surface. Figure 9 shows the histograms of $k_{ro}(S_w)$ for the SS 1/CF 5 case, where the best match lies partly outside the P10-P90 interval; in (c), the histograms are bimodal for water saturations below 0.6 and above 0.95, with a pronounced narrow maximum and an overlapping broad component. The global minimum is found using the MATLAB *fmincon* function—the best match, while the broad component dominates the uncertainty range in the MCMC sampling. Using equation (4) as the objective function in the *fmincon* function (without the $-1/2$ factor) leads to comparable results and trends when the *fmincon* function is used with equation (3) (see section 4.1), which excludes the influence of the specific choice of the objective function.

The complex bimodal histograms may be related to the following aspects: (a) At low S_w , the dataset is outside the range of the SS experiments. The information regarding k_r therefore comes exclusively from the centrifuge experiments. (b) Especially in the SS1 case, the HM result for k_{ro} is closely tied to 1 in this saturation range. If a monotonic behavior with $k_r \leq 1$ is required, most of the samples are rejected during HM in the respective range.

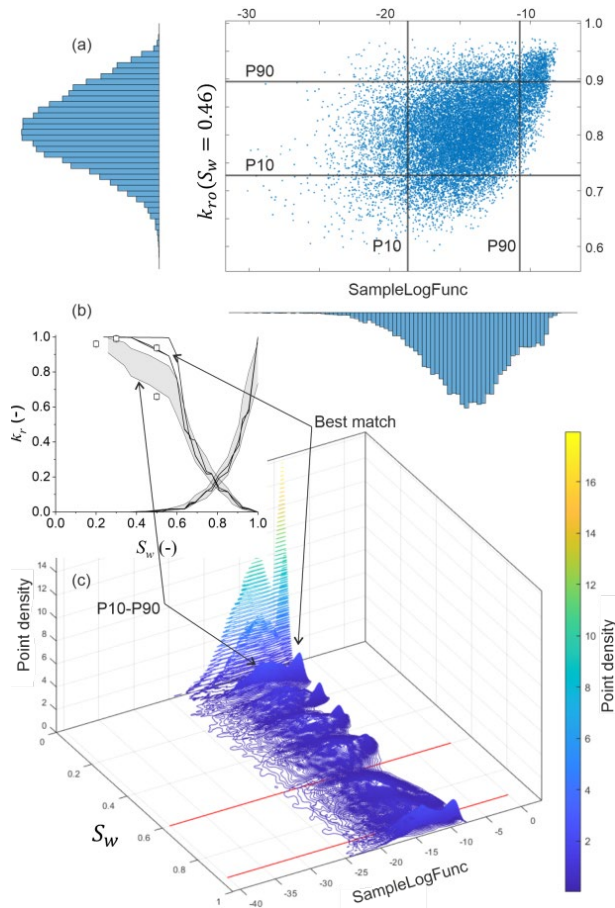


Figure 9: Sampled likelihood estimation function (equation (4)) versus oil relative permeability for the SS1 and CF5 combination. (a) for a single saturation state, $S_w = 0.46$; (c) for the full range of S_w . (b) Relative permeability and uncertainty interval from Figure 8 for comparison. The white symbols represent results from porous plate experiments, with errors of individual measurements in the order of the symbol size.

The symbols in Figure 9 (b) show the results of porous plate (PP) experiments [18]. By means of the PP method, samples are desaturated to a certain water saturation close to S_{wc} . Subsequently, the effective permeability is measured by multi-rate decane flooding (at $f_w = 0$). Assuming that the aqueous phase is largely immobile, k_{ro} was derived. However, also with the additional PP data, it is not possible to decide on the true k_{ro} . Due to the sample-to-sample variation—considering that the PP experiments were performed on different samples—the derived k_{ro} values vary in the full spread of generated data.

7. Summary and Conclusions

In the present study, we present a comprehensive way to interpret SCAL data. We apply a workflow starting from the well-known analytical solutions, directly derived from the individual data sets, as input for numerical history matching. The experimental data sets are described simultaneously and by means of a point-by-point parameterization - 34 points for the two relative permeability tables combined and 8 points for the capillary pressure table. With these innovations, a good description of complex saturation functions is possible.

Different parametrizations of the saturation functions are used. The study shows that using classic power-law representations is not sufficient to conclusively analyze data derived from more complex rock types, such as microscopically heterogeneous carbonates. For this purpose, the point-by-point approach, in which the saturation functions were evaluated at the individual saturation points defined by the experimental steps that serve as HM parameters. This approach allows us to match complex rocks since the functions are not restricted to power laws.

Furthermore, the simultaneous evaluation of SS and CF experimental data sets accounts for the fact that k_r and p_c are coupled. The results show that simultaneous rather than subsequent evaluation of those data sets leads to more objective results. With “objective” we mean to prefer a solution without manual, respectively personal intervention in the process. However, the massive increase in the free parameters in the simultaneous point-by-point approach substantially increases the required computational power, especially in cases where uncertainty analyses are performed.

The uncertainties are evaluated by MCMC simulations sampling the response surface of the likelihood estimation function of the combined data set. This allows the extraction of single parameter distribution functions and correlations between those parameters on the saturation scale. The study shows that despite the given high degree of freedom, the simultaneous point-by-point approach delivers a very robust description of two-phase flow in complex rock types. While the gradient-based HM reliably finds the best match, MCMC sampling demonstrates the complexity of the response surface. This results in one SS data set for a separation of the best match and the P10-P90 uncertainty interval (the best match is within the P01-P99).

By combining all available SS and CF experimental results for analysis, a comparison of the sample-to-sample variation with respect to the error of the individual data set could be made. For the specific rock type, the sample-to-sample variation seems to be dominant (as far as the limited data set allows for that statement). The results group around the individual SS curves with a narrow bandwidth by the various CF measurements. The P10-to-P90 uncertainty intervals of the two SS curves just marginally overlap apart from the saturation range around S_{wc} ; the individual data sets also show the greatest uncertainty around S_{wc} , which may have to do with the missing next-neighbor information toward lower water saturations.

The authors acknowledge valuable discussions with Jos Maas, Steffen Berg and Pit Arnold.

References

- [1] M. C. Leverett, "Capillary Behavior in Porous Solids," *Transactions of the AIME*, vol. 142, no. 01, p. 152–169, 1941.
- [2] D. D. Huang and M. M. Honarpour, "Capillary end effects in coreflood calculations," *Journal of*

- Petroleum Science and Engineering*, vol. 19, no. 1-2, p. 103–117, 1998.
- [3] E. Johnson, D. Bossler and V. N. Bossler, "Calculation of Relative Permeability from Displacement Experiments," *Transactions of the AIME*, vol. 216, no. 01, pp. 370-372, 1959.
- [4] G. L. Hassler and E. Brunner, "Measurement of Capillary Pressures in Small Core Samples," *Transactions of the AIME*, vol. 160, no. 01, p. 114–123, 1945.
- [5] J. Hagoort, "Oil Recovery by Gravity Drainage," *Society of Petroleum Engineers Journal*, vol. 20, no. 03, p. 139–150, 1980.
- [6] J. G. Maas and A. M. Schulte, "Computer simulation of Special Core Analysis (SCAL) flow experiments shared on the Internet," 1997.
- [7] J. G. Maas, B. Flemisch and A. Hebing, "Open Source Simulator for DuMux Available for SCAL Data Interpretation," p. 18–21, 2011.
- [8] D. Loeve, F. Wilschut, R. H. Hanea, J. Maas, P. Hooff, P. van den Hoek, S. G. Douma and J. Doren, "Simultaneous Determination of Relative Permeability and Capillary Pressure Curves by Assisted History Matching Several SCAL Experiments," *Society of Core Analysis Conference Paper SCA2011-35*, 2011.
- [9] S. Berg, E. Unsal and H. Dijk, "Non-uniqueness and uncertainty quantification of relative permeability measurements by inverse modelling," *Computers and Geotechnics*, vol. 132, p. 103964, 2021.
- [10] M. Rücker, A. Georgiadis, R. T. Armstrong, H. Ott, N. Brussee, H. van der Linde, L. Simon, F. Enzmann, M. Kersten and S. Berg, "The Origin of Non-thermal Fluctuations in Multiphase Flow in Porous Media," *Frontiers in Water*, vol. 3, 2021.
- [11] S. Berg, E. Unsal and H. Dijk, "Sensitivity and Uncertainty Analysis for Parameterization of Multiphase Flow Models," *Transport in Porous Media*, 2021.
- [12] R. H. Brooks and A. T. Corey, "Hydraulic Properties of Porous Media," no. 3, 1964.
- [13] A. T. Corey, "The interrelation between gas and oil relative permeabilities," p. 38–41, 1954.
- [14] F. Lomeland, E. Ebeltoft and W. Thomas, "A New Versatile Relative Permeability Correlation," *Society of Core Analysis Conference Paper SCA2005-32*, 2005.
- [15] A. R. Valdez, B. M. Rocha, G. Chapiro and R. Weber dos Santos, "Uncertainty quantification and sensitivity analysis for relative permeability models of two-phase flow in porous media," *Journal of Petroleum Science and Engineering*, vol. 192, p. 107297, 2020.
- [16] K.-A. Lie, *An Introduction to Reservoir Simulation Using MATLAB/GNU Octave*, Cambridge University Press, 2019.
- [17] A. Shahmoradi and F. Bagheri, *ParaDRAM: A Cross-Language Toolbox for Parallel High-Performance Delayed-Rejection Adaptive Metropolis Markov Chain Monte Carlo Simulations*, 2020.
- [18] H. Ott, C. H. Pentland and S. Oedai, "CO₂–brine displacement in heterogeneous carbonates," *International Journal of Greenhouse Gas Control*, vol. 33, p. 135–144, 2015.
- [19] S. Krogstad, K. Lie, O. Møyner, H. M. Nilsen, X. Raynaud and B. Skaflestad, "MRST-AD - an Open-Source Framework for Rapid Prototyping and Evaluation of Reservoir Simulation Problems," pp. SPE-173317-MS, 2015.
- [20] "Sendra," prores, [Online]. Available: <https://www.prores.no/solution/sendra>. [Accessed 08 06 2022].
- [21] J. G. Maas, N. Springer and A. Hebing, "Defining a sample heterogeneity cut-off value to obtain representative Special Core Analysis (SCAL) measurements," *Society of Core Analysts*, 2019.
- [22] S. Berg, E. Unsal and H. Dijk, "Impact of Relative Permeability Parameterization on the Uncertainty of Multiphase Flow Models," 2020.
- [23] S. Kumbhare and A. Shahmoradi, *MatDRAM: A pure-MATLAB Delayed-Rejection Adaptive Metropolis-Hastings Markov Chain Monte Carlo Sampler*.
- [24] MathWorks, *MATLAB optimization toolbox user's guide, R2020b ed.*, 2020.
- [25] R. Lenormand, K. Lorentzen, J. G. Maas and D. Ruth, "Comparison of Four Numerical Simulators for SCAL Experiments," *Petrophysics - The SPWLA Journal of Formation Evaluation and Reservoir Description*, vol. 58, no. 01, p. 48–56, 2017.
- [26] S. M. Skjaeveland, L. M. Siqveland, A. Kjosavik, W. H. Thomas and G. A. Virnovsky, "Capillary Pressure Correlation for Mixed-Wet Reservoirs," *SPE Reservoir Evaluation & Engineering*, vol. 3, no. 01, p. 60–67, 2000.
- [27] K. Pearson, "Notes on regression and inheritance in the case of two parents," *Proceedings of the Royal Society of London*, no. 58, pp. 240-242, 1895.
- [28] A. Shahmoradi, F. Bagheri and J. A. Osborne, "Fast fully-reproducible serial/parallel Monte Carlo and MCMC simulations and visualizations via ParaMonte: Python library," *arXiv preprint arXiv:2010.00724*, 2020.

Capturing the wetting state of an aged-carbonate core through pore-scale multiphase flow simulations

Tingting Wang¹, Ying Da Wang¹, Chenhao Sun², James E. McClure³, Peyman Mostaghimi¹, Ryan T. Armstrong^{1,*}

¹School of Minerals and Energy Resources Engineering, University of New South Wales, Kensington, New South Wales, Australia

²State Key Laboratory of Petroleum Resources and Prospecting, China University of Petroleum, Beijing 102249, PR China

³Advanced Research Computing, Virginia Polytechnic Institute and State University, Blacksburg, VA, USA

Abstract. Recent state-of-the-art Digital Rock (DR) technology is becoming an important workflow to complement and expand laboratory data with realistic simulations over a wider parameter space. With DR technology, X-ray computed microtomography (micro-CT) images of rocks are commonly used for relative permeability simulations. However, currently no clear approach exists for the integration of realistic rock surface wetting conditions into DR simulations, even though it is well known that multiphase flow is significantly influenced by the surface wetting properties of rocks. Realistic DR simulations requires a fundamental understanding of wetting at the length scale at which interfaces are well resolved, which is currently lacking in the literature. To address this issue, we conducted 2-phase Lattice-Boltzmann simulations in a carbonate rock using a developed effective wetting model that captures the multi-scale nature of the micro-porous and macro-porous regions, which allows for spatially variable wetting conditions that mimic an aged-state core. Simulation phase morphologies are then compared to experimental studies for a clean-state and aged-state core imaged with micro-CT to evaluate the wetting model and corresponding simulation results. Overall, the proposed research is tailored to investigate the fundamental processes of wetting in porous media needed for multiphase flow DR simulations.

1 Introduction

Wettability in a broad sense refers to a surface property where in the presence of two immiscible fluids, one fluid preferentially wets the surface [1]. It is a surface property of a substance, which exists widely in nature[2]. Wettability is an important characteristic of the interaction between rock and fluids, which reflects the distribution of oil and water in a reservoir. It plays an important role in multiphase flow and can significantly influence oil recovery [3].

The Lattice Boltzmann Method (LBM) works well for simulating single-phase and multi-phase flows [4]. However, when simulating multiphase flow, how to effectively consider surface wettability is a crucial factor affecting simulation results [5]. Wettability is an important factor that influences the flow characteristics of fluids in porous media. It can influence many physical parameters of reservoir rocks, such as irreducible water saturation, residual oil saturation, relative permeability, and capillary pressure [6]. How to assign a realistic wetting condition for direct multiphase flow simulations remains an open question.

In the early stage of wettability research, according to the fact that the minerals that make up reservoir rocks are mostly hydrophilic the wetting state was considered largely water wet. Later, it was found that after the formation of an oil reservoir, the rock surface will contact oil for geological time, and the active substances in crude oil will adhere to the rock surface, which changes the rock surface from water wet to oil wet or intermediate wet [7].

Assuming that the reservoir rock is homogeneous, the wetting tendency of water or oil would be uniform on the rock surface. Uniform wetting could be oil wet, water wet, or intermediate wet. However, due to the rock heterogeneity, distribution of fluids, and complexity of the crude oil, the actual rock could appear heterogeneous wetting, showing that parts of the surface are water wet, while others are rendered intermediate or oil wet [3].

There are two common lab methods to age cores to a ‘reservoir condition’. One is static aging [8], the other is dynamic aging [9]. After aging, the rock surface will have a wettability alteration and reach a more oil-wet condition than before. For either method the rock core is aged in crude oil at connate water saturation for an extended period. Rock surfaces in contact with oil are rendered oil wet or intermediate wet depending on the period of aging and properties of the crude oil. Of critical consideration is the acid content of the oil whereby more acidic oils are more active at rendering surfaces oil wet [10].

The wettability of rock is commonly characterized by an experimentally measured contact angle using the sessile drop technique [11]. However, this method can only describe the wettability of the pore surface at a specific location and cannot reflect the realistic wettability distribution in the pore space. In addition, contact angle measurements taken on a rock surface are an apparent contact angle at the length scale of the observation and do not necessarily reflect the intrinsic contact angle of a surface. Carbonate rocks, e.g., include micro-porous and macro-porous regions, apparent contact angle measurements are commonly taken at the macro-

* Corresponding author: ryan.armstrong@unsw.edu.au

pore length scale while the underlying microporous structure would influence the measurement [2].

Treiber et al. 1972 [12] show that approximately 80% of the more than 50 reservoirs they studied were moderately oil wet, i.e., contact angles from 120° to 140°. These moderately oil-wet systems are difficult to identify, and the wettability of core samples from these reservoirs can be easily altered inadvertently [13]. How to truly and completely reconstruct the pore space with its realistic wettability is still an important problem to be solved, which is more readily becoming a reality with the development of *in situ* contact angle measurements from X-ray computed microtomography images [14].

For carbonate rocks, AlRatrou et al. [15] measured *in situ* contact angles between immiscible fluids on segmented X-ray images, they found that for an aged sample, contact angles were more widely spread than water-wet conditions with values both less than and greater than 90°. They measured *in situ* contact angles of three samples (total of 595 million voxels) and reported a mean and standard deviation of 77°± 21° indicating a weakly water-wet condition with few oil-wet surfaces; 104°±26° showing a mixed-wet system with more oil-wet surfaces; and 94°±24° illustrating a mixed-wet system with contact angles ranging from water-wet to oil-wet. AlRatrou et al. [3] observed a wide range of contact angle values on flat calcite surfaces, the average contact angle values were 76°, 130°, and 141° for different wetting conditions.

Herein, we investigate a method to capture surface wettability in a digital rock model that mimics the realistic wettability of an aged-carbonate core. We take a targeted assignment of surface wettability, which can be changed from initially water wet to oil wet through the simulated contact of oil with the rock surface. After primary drainage, all rock surfaces in contact with oil are set to be oil wet, and all other surfaces remain water wet to mimic the aging process. Our proposition is that to what degree the oil-wet regions become oil-wet depends on the microporosity of the pore walls. Micropores retain water, and thus potentially remain water wet (to a degree) since the capillary pressure required to drain the microporosity is restrictively high. For validation, we compare pore-scale experimental images of fluids in an aged-carbonate core to those simulated under various wetting conditions. The Minkowski Functionals (MFs) are used to compare the fluid phase morphologies and contact angle measurements are used to understand the wetting condition and the influence that microporosity has on the apparent (effective) contact angle.

2. Materials and method

2.1 X-ray computed microtomography data

Two data sets were selected from the Digital Rocks Portal (<https://www.digitalrocksportal.org/>).

- Dataset 1: We used the Ketton image from DOI - 10.17612/P7HT11. The resolution of the image was 5 micrometres per voxel side using a laboratory-based X-ray micro-CT scanner [16].

- Dataset 2: We used the experiment data from the project DOI - 10.17612/3S3K-EE20. The images were obtained at a synchrotron facility during water injection in a mixed-wet sample [17]. The image resolution was 3.5 micrometres.

Dataset 1 comprises of greyscale and segmented multiphase images, but no images of experiments of mixed-wetting aged cores, while Dataset 2 does not contain an original greyscale image but does contain segmented multiphase images of an aged-carbonate core during an imbibition experiment. Dataset 2 was reported as a mixed-wet sample [17]; however, the experimental data shows an initial water saturation of 0.1% in the macropores.

2.2 Simulation

Two-phase Lattice Boltzmann Method (LBM) simulations were carried out on Dataset 1 and 2. The details of the implementation are provided by McClure et al. [18]. The mixed wetting nature of these cores was mapped onto the surface of the solid voxels by identifying whether solid voxels are in contact with water or oil after a primary drainage simulation. A workflow for the assignment of contact angles is provided in Figure 1. We assume that after primary drainage, the phase distributions are static, and over time, the wettability of the surfaces in contact with oil are altered, i.e., dynamic aging of the surface is not considered. The wettability of the domain thus becomes mixed wet, with surfaces in contact with water remaining water wet, and surfaces in contact with oil becoming oil wet. The exact contact angles to be assigned to the water-wet and oil-wet regions are discussed in Section 3.

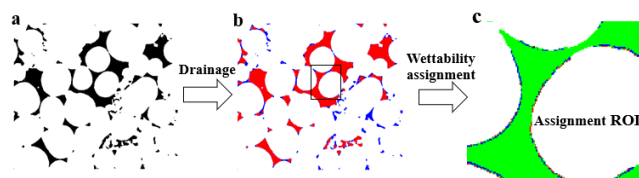


Fig. 1. The workflow for the assignment of contact angles; a is the binary image; b is the image after drainage; c is the Region-of-interest (ROI) image after wettability assignment.

In our implementation of LBM, the wetting of a surface to the two fluids present (defined as -1 and +1) can be defined as a scalar value α , ranging from -1 to +1. This is equivalent to assuming that the solid phase and surface of the solid is an immobile phase with an affinity to the two fluids proportional to the distance of α to fluid -1 and fluid +1. This automatically recovers the expected contact line and contact angle behaviour at both dynamic and static conditions [18]. On a flat surface of affinity α , the static contact angle can be defined as

$$\cos \theta = \alpha . \quad (1)$$

This angle can be considered as an effective (or apparent) contact angle at the pore scale.

All simulations were conducted at a Capillary number of 1×10^{-5} .

2.3 Contact Angle Models

We consider two methods for assigning the effective contact angle for the water-wet and oil-wet regions. Model (1) Uniform Wetting: we assume that the surfaces are smooth, impermeable, and homogenous. Therefore, a single effective contact angle is assigned to the oil-wet regions and likewise for the water-wet regions. Model (2) Cassie-Baxter Wetting: we assume that the grain surfaces are microporous and retain water which thereby influences the effective contact angle. This is reasonable for carbonate rocks given that the capillary pressure required to penetrate the microporosity during aging is typically not exceeded in experiments nor under geological conditions.

We follow the microporosity analysis method presented by Lin et al. [14]. The CT value of a voxel is proportional to the voxel density, in this way we can define the solid fraction on a per voxel basis as

$$\phi_s = \frac{CT_{\text{voxel}} - CT_{\text{macropores}}}{CT_{\text{grain}} - CT_{\text{macropores}}}, \quad (2)$$

where ϕ_s is voxel solid fraction, CT_{voxel} is the CT number of each voxel, $CT_{\text{macropores}}$ is the average CT value of macropores, and CT_{grain} is average CT value of the grains.

Based on the assumptions for Method (2) during aging the fraction of the carbonate rock surface that is exposed to oil depends on the microporosity. This means that only a fraction of a given voxel is rendered oil wet. The Cassie-Baxter model [2] provides a means to define this condition as

$$\cos \theta_E = \phi_s \cos \theta_Y + (1 - \phi_s), \quad (3)$$

where ϕ_s is the carbonate voxels solid fraction in contact with the oil surface, θ_Y is the intrinsic contact angle of a solid carbonate surface, and θ_E is the effective contact angle observed in a pore-scale image.

2.4 Minkowski Functionals

The Minkowski Functionals (MF) are geometric measures of size based on set theory (Serra 1983), which are commonly used in porous media research [19]. By considering the surface δX of phase (X) embedded in Euclidean space (Ω), the MFs are $d+1$ functionals, where d is the dimension of Ω . In three dimensional (3D) space, the MF are effectively volume, surface area, integral mean curvature, and Euler characteristic. M_0 is the first functional and represents the total volume of X . M_1 is the second functional and represents the integral measure of the surface area of X , defined as

$$M_1(X) = \int_{\delta X} ds, \quad (4)$$

where δX is the entire surface and ds is the surface element on X . M_2 is the third functional and represents the integral of mean curvature of the entire surface, which is defined as

$$M_2(X) = \int_{\delta X} \left[\frac{1}{r_1} + \frac{1}{r_2} \right] ds, \quad (5)$$

where r_1 and r_2 are the principal radii of curvature of surface element ds . M_3 represents the integral of Gaussian curvature of the entire surface, which is defined as

$$M_3(X) = \int_{\delta X} \left[\frac{1}{r_1 \times r_2} \right] ds = 4\pi\chi(X), \quad (6)$$

where $\chi(\delta X)$ is the Euler characteristic of the bounding surface and $\chi(X)$ is the Euler characteristic of phase X (Ohser and Mücklich 2000; Michielsen and De Raedt 2001). The Euler characteristic can also be described by isolated objects (N), redundant loops (L) and cavities (O), defined as

$$\chi(X) = N - L + O. \quad (7)$$

Equation (7) provides a more direct understanding of Euler number, i.e., a system with more loops has higher connectivity and more negative Euler number.

3. Results and discussions

For Model (2), we considered $\theta_Y = 130^\circ$ for oil-treated surfaces and $\theta_Y = 40^\circ$ of untreated surfaces. For Model (1), we considered a uniform contact angle of 130° for oil-treated and 40° for untreated surfaces. The reported average *in situ* contact angles for the experimental data was 110% degrees [16] while experimental sessile drop data provided by Treiber et al. 1972 [12] reported contact angles up to 160% for carbonate rocks. It is well known that the wetting conditions depend on the oil used, acid number, and treatment method used to age the core [20]. It has also been shown that direct *in situ* contact angle measurements can under predict the true contact angle by up to 20 degrees at high contact angle values [21]. Therefore, a contact angle of 130% was our best educated guess at a representative value for both Models (1) and (2).

Table 1. Summary of the conducted simulations. The drainage saturation corresponds to the saturation at which surface wettability was assigned.

Simulation Name	Dataset	Wetting Model	Oil-Wet Fraction
CB_0.65_1	1	Cassie-Baxter	0.65
CB_0.84_1	1	Cassie-Baxter	0.84
CB_0.99_1	1	Cassie-Baxter	0.99
Uni_0.99_1 CA90	1	Uniform	0.99
Uni_0.99_2	2	Uniform	0.99

In total five simulations were conducted as summarised in Table 1. Region-of-interest (ROI) images of these simulations are provided in Figure 2. The oil phase renderings are ordered from water wet to oil wet. Also, an image pair ($S_o = 0.5$, $S_o = 0.8$) is presented for each simulation. The final image pair (k, l) is the experimental data. Firstly, we observe that oil

connectivity improves with increasing oil saturation. Secondly, the oil adheres to the solid surface in both models but much less so in the Cassie-Baxter model than the uniform model. Thirdly, the initial oil saturation used to mimic the core aging procedure clearly impacted the simulation results. Overall, the rendering in Figures 2i and 2j qualitatively reflect the oil morphologies observed in the experimental data. These renderings correspond to simulation Uni_0.99_2 (see Table 1), which reflects an oil-wet state with oil coating the grain surfaces.

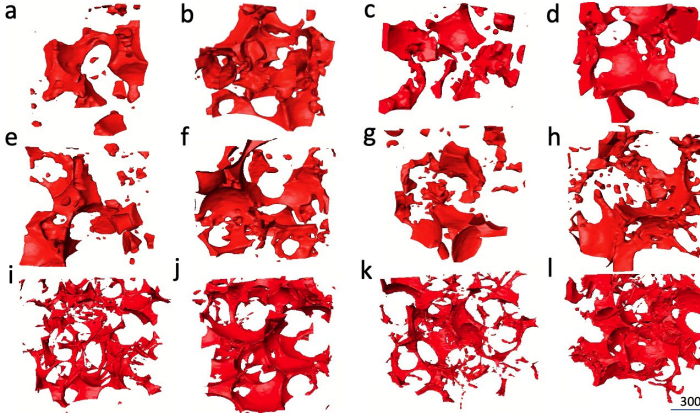


Fig. 2. Three-dimensional renderings of oil for five simulations and one experiment at oil saturations of 0.5 and 0.8; (a, b) are from simulation CB_0.65_1; (c, d) are from simulation CB_0.84_1; (e, f) are from simulation CB_0.99_1; (g, h) are from simulation Uni_0.99_1_CA90; (i, j) are from simulation Uni_0.99_2; and (k, l) are from the experimental data. See Table 1 for full details on each simulation case.

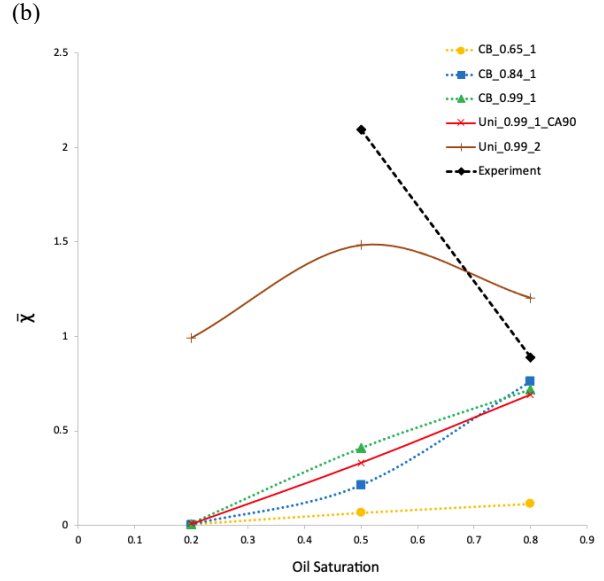
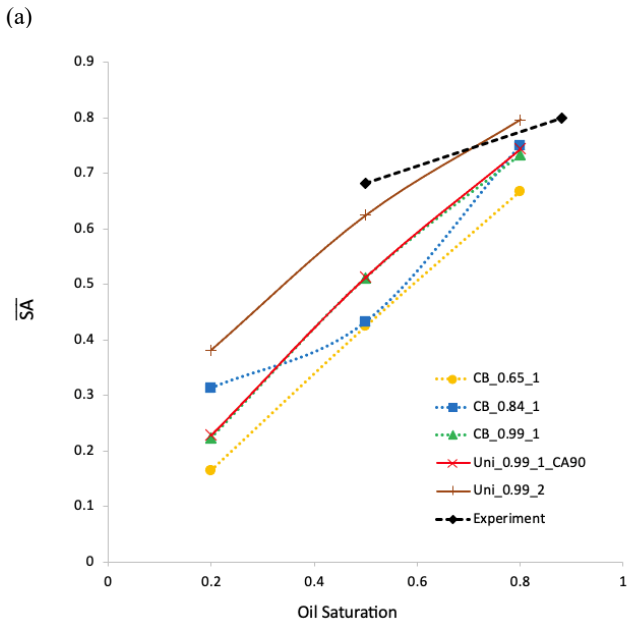


Fig. 3. (a) Surface area normalization (oil-grain surface area/total grain surface area) (b) Euler normalization (Euler of NWP/Euler of pore space) of 5 simulations and experimental data. The reported value at oil saturation of 0.2 is not the residual oil saturation.

In Figure 3, we provide quantitative measures of the oil morphology. These measures were taken at the length scale of the simulations and experimental images, which were equivalent. The reported surface area values were determined by

$$\overline{SA} = \frac{M_1\left(\frac{oil}{grain}\right)}{M_1(grain)},$$

where $M_1(Grain)$ is the total surface area of all grain surfaces and $M_1\left(\frac{oil}{grain}\right)$ is only the oil-grain surface area. In this way, we measure surface area coverage following the work of [22]. The reported Euler characteristic values were determined by

$$\bar{\chi} = \chi(oil)/\chi(pore\ space),$$

where $\chi(oil)$ is the Euler characteristic of the oil phase and $\chi(pore\ space)$ is the Euler characteristic of the pore space. As oil fills the pore space, $\bar{\chi}$ approaches 1. For oil-wet cases, however, as observed by our simulation results and the experimental data, the oil phase can become more connected than the pore space, i.e., $\bar{\chi} > 1$. This occurs due to the oil forming multiple loops along the grain surfaces.

Overall, as observed in Figure 3, the results from simulation Uni_0.99_2 provided the best morphological comparison to the experimental data. While the morphological values do not provide an exact match with the experimental data the values are arguably similar, and the overall trends are captured. An exact match would not be expected given that the model domain and boundary conditions are not 1:1 with the experiment. This occurs because the flow outside of the experimentally imaged region is unknown.

Given a particular wetting state it would be expected that the fluid/fluid interfacial curvatures between simulation and experiment would be comparable. These curvature distributions are presented in Figure 4 for the experimental and Uni_0.99_2 simulation datasets. For the simulation, 20.54% of the mean curvature distribution falls outside of the mean curvature distribution that was experimentally measured. In addition, the sub-distributions of the Gaussian curvatures are qualitatively comparable between simulation and experiment. This further suggests that the wetting state was represented by the Uni_0.99_2 simulation.

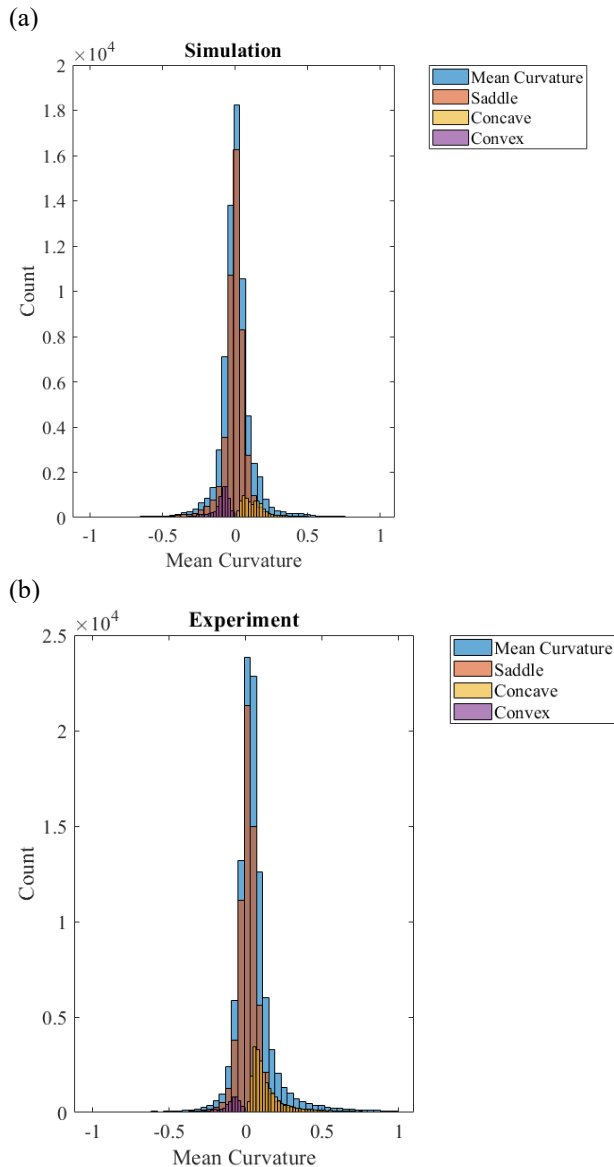


Fig. 4. (a) Curvature measurements of Uni_0.99_2 ($S_o=0.50$); (b) Curvature measurements of experimental data ($S_o=0.50$).

Overall, the simulation results suggested that a contact angle value of 130° for oil treated surfaces was representative of the experimental data while the Cassie-Baxter models created a too water-wet state. It can be assumed that the 130° uniform contact angle is an effective value and not the intrinsic contact angle of the

surface, as defined by Young's equation, since the carbonate surface is clearly rough with a dual porosity system whereby the microporosity is below the image resolution. However, measuring the surface microporosity of the carbonate grains with micro-CT is problematic and knowing what value to use for θ_Y in Equation (3) is difficult.

The difficulty with measuring the microporosity of grain surfaces is demonstrated in Figure 5. Two distributions of microporosity are presented: (1) all values within 3 voxels from a grain surface and (2) all other voxel microporosity values. Due to the partial volume effect during imaging, the grain surface voxels have CT values preferentially less than those values within the grains [23]. This results in high micro-porosity on the grain surface, which in turn results in water-wet conditions when Equation (3) is applied. A better representation of the microporosity could be the average microporosity value of those voxels at least 3 voxels from the surface. Based on the distribution presented in Figure 5, the average microporosity value would be 0.1268.

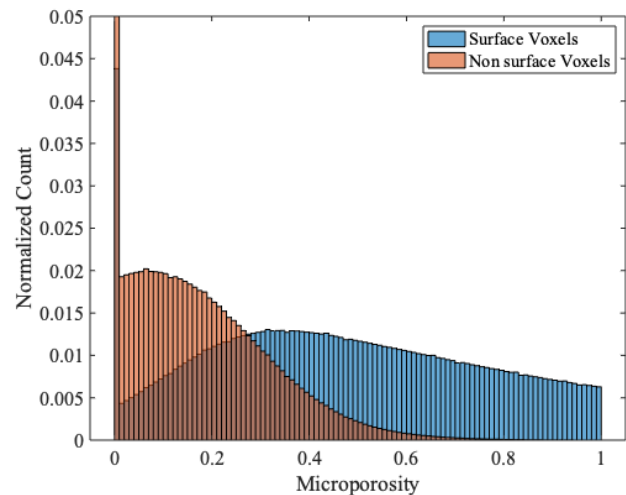


Fig. 5. Micro-porosity analysis. (1) Distribution of micro-porosity values for voxels that represent the grain surface. (2) Distribution of micro-porosity values that are at least 3 voxels from the surface.

An estimate of θ_Y can be obtained by using Equation (3). Based on simulation results, $\theta_E = 130^\circ$ provided the closest match to the experimental data. Based on Figure 5, the carbonate rock had an average microporosity of 0.1268. Therefore, θ_Y of the oil treated surfaces would have been approximately 160° . Such a contact angle is on the high-end of values reported by Treiber et al. 1972 [12] for oil treated pure (solid) calcite surfaces but remains within a reasonable range.

4. Conclusions

We conducted two-phase LBM simulations considering two different wetting models: (1) Uniform Wetting and (2) Cassie-Baxter Wetting. We then compared the resulting simulated morphological state of the oil to experimental data. Based on the oil phase images and morphological measures the Uni_0.99_2 model provided

the best approximation to the experimental data. This simulation case assumed a uniform contact angle of 130° for oil-treated and 40° for untreated surfaces. The experimental data was reported as being ‘mixed-wet’ even though the initial water saturation prior to imbibition was 0.1%. The impact that wettability heterogeneity could influence these results will need to be explored in future work.

We also highlighted the main difficulty with assigning surface wettability heterogeneity when working with micro-CT data. Due to the well-known partial volume effect, when applying Equation (2), surface voxels tend to have a lower solid fraction than expected based on solid fraction measurements taken far from an interface. Therefore, the Cassie-Baxter model resulted in more water-wet oil morphologies than that observed in the experimental data.

To best capture the wetting state, we provide the following suggestions for future work. Firstly, we should conduct more experiments with aging at different saturations. Secondly, we could consider dynamic aging by updating the contact angle values during the primary drainage process. Thirdly, we should consider the spatial distribution of the microporosity (at least three voxels from an interface) to assign a similar distribution to the model domain before applying the Cassie-Baxter model. This last suggestion would provide wettability heterogeneity to the surface and allow for a better understating to what degree this factor impacts the pore-scale morphology of oil.

References

- [1] W. Abdallah *et al.*, “Fundamentals of wettability,” *Technology*, vol. **38**, no. 1125–1144, p. 268, 1986.
- [2] A. B. D. Cassie and S. Baxter, “Wettability of porous surfaces,” *Trans. Faraday Soc.*, vol. **40**, p. 546, 1944, doi: 10.1039/tf9444000546.
- [3] A. AlRatrou, M. J. Blunt, and B. Bijeljic, “Wettability in complex porous materials, the mixed-wet state, and its relationship to surface roughness,” *Proc. Natl. Acad. Sci. U.S.A.*, vol. **115**, no. 36, pp. 8901–8906, Sep. 2018, doi: 10.1073/pnas.1803734115.
- [4] Y. Y. Yan, Y. Q. Zu, and B. Dong, “LBM, a useful tool for mesoscale modelling of single-phase and multiphase flow,” *Applied Thermal Engineering*, vol. **31**, no. 5, pp. 649–655, Apr. 2011, doi: 10.1016/j.applthermaleng.2010.10.010.
- [5] E. Ezzatneshan and H. Vaseghnia, “Evaluation of equations of state in multiphase lattice Boltzmann method with considering surface wettability effects,” *Physica A: Statistical Mechanics and its Applications*, vol. **541**, p. 123258, Mar. 2020, doi: 10.1016/j.physa.2019.123258.
- [6] W. Anderson, “Wettability literature survey-part 2: Wettability measurement,” *Journal of petroleum technology*, vol. **38**, no. 11, pp. 1–246, 1986.
- [7] R. Zhang, N. Qin, L. Peng, K. Tang, and Z. Ye, “Wettability alteration by trimeric cationic surfactant at water-wet/oil-wet mica mineral surfaces,” *Applied Surface Science*, vol. **258**, no. 20, pp. 7943–7949, Aug. 2012, doi: 10.1016/j.apsusc.2012.04.139.
- [8] X. Zhou and N. R. Morrow, “Interrelationship of Wettability, Initial Water Saturation, Aging Time, and Oil Recovery by Spontaneous Imbibition and Waterflooding,” *SPE Journal*, vol. **5**, no. 2, p. 9, 2000.
- [9] E. Sripal and L. A. James, “Application of an Optimization Method for the Restoration of Core Samples for SCAL Experiments,” p. 10, 2018.
- [10] D. C. Standnes and T. Austad, “Wettability alteration in chalk 1. Preparation of core material and oil properties,” p. 11, 2000.
- [11] D. Y. Kwok and A. W. Neumann, “Contact angle measurement and contact angle interpretation,” *Advances in Colloid and Interface Science*, vol. **81**, no. 3, pp. 167–249, Sep. 1999, doi: 10.1016/S0001-8686(98)00087-6.
- [12] L. E. Treiber and W. W. Owens, “A Laboratory Evaluation of the Wettability of Fifty Oil-Producing Reservoirs,” *Society of Petroleum Engineers Journal*, vol. **12**, no. 06, pp. 531–540, Dec. 1972, doi: 10.2118/3526-PA.
- [13] W. G. Anderson, “Wettability Literature Survey-Part 1: Rock/Oil/Brine Interactions and the Effects of Core Handling on Wettability,” *Journal of Petroleum Technology*, vol. **38**, no. 10, pp. 1125–1144, Oct. 1986, doi: 10.2118/13932-PA.
- [14] Q. Lin, Y. Al-Khulaifi, M. J. Blunt, and B. Bijeljic, “Quantification of sub-resolution porosity in carbonate rocks by applying high-salinity contrast brine using X-ray microtomography differential imaging,” *Advances in Water Resources*, vol. **96**, pp. 306–322, Oct. 2016, doi: 10.1016/j.advwatres.2016.08.002.
- [15] A. M. Alhammadi, A. AlRatrou, K. Singh, B. Bijeljic, and M. J. Blunt, “In situ characterization of mixed-wettability in a reservoir rock at subsurface conditions,” *Sci Rep*, vol. **7**, no. 1, p. 10753, Dec. 2017, doi: 10.1038/s41598-017-10992-w.
- [16] A. Scanziani, K. Singh, T. Bultreys, B. Bijeljic, and M. J. Blunt, “In situ characterization of immiscible three-phase flow at the pore scale for a water-wet carbonate rock,” *Advances in Water Resources*, vol. **121**, pp. 446–455, Nov. 2018, doi: 10.1016/j.advwatres.2018.09.010.
- [17] A. Scanziani, Q. Lin, A. Alhosani, M. Blunt, and B. Bijeljic, “Dynamics of displacement in mixed-wet porous media,” *Engineering*, preprint, Jan. 2020. doi: 10.31223/OSF.IO/JPMVC.
- [18] J. E. McClure, Z. Li, M. Berrill, and T. Ramstad, “The LBPM software package for simulating multiphase flow on digital images of porous rocks,” *Comput Geosci*, vol. **25**, no. 3, pp. 871–895, Jun. 2021, doi: 10.1007/s10596-020-10028-9.
- [19] R. T. Armstrong *et al.*, “Porous Media Characterization Using Minkowski Functionals: Theories, Applications and Future Directions,”

The 35th International
Symposium of the Society of Core Analysts

- Transp Porous Med*, vol. **130**, no. 1, pp. 305–335, Oct. 2019, doi: 10.1007/s11242-018-1201-4.
- [20] R. T. Armstrong, “Multiscale Characterization of Wettability in Porous Media,” p. 26.
- [21] C. Sun *et al.*, “Characterization of wetting using topological principles,” *Journal of Colloid and Interface Science*, vol. **578**, pp. 106–115, Oct. 2020, doi: 10.1016/j.jcis.2020.05.076.
- [22] G. Garfi, C. M. John, Q. Lin, S. Berg, and S. Krevor, “Fluid Surface Coverage Showing the Controls of Rock Mineralogy on the Wetting State,” *Geophys. Res. Lett.*, vol. **47**, no. 8, Apr. 2020, doi: 10.1029/2019GL086380.
- [23] D. Wildenschild and A. P. Sheppard, “X-ray imaging and analysis techniques for quantifying pore-scale structure and processes in subsurface porous medium systems,” *Advances in Water Resources*, vol. **51**, pp. 217–246, Jan. 2013, doi: 10.1016/j.advwatres.2012.07.018.

Comparison of Three-Dimensional Permeability Inversion from Positron Emission Tomography Experimental Data Using Convolutional Neural Networks and Ensemble Kalman Filter

Zitong Huang¹, and Christopher Zahasky^{1,*}

¹Department of Geoscience, University of Wisconsin-Madison, Madison, WI, USA

Abstract. In the field of core analysis, parameterization of permeability variation is the foundation for quantifying the role of geologic heterogeneity on a wide range of conservative, reactive, and colloidal transport processes. Recent utilization of *in situ* imaging, specifically positron emission tomography (PET), enables the measurement of three-dimensional (3-D) time-lapse radiotracer transport in geologic porous media. This experimental tool provides unprecedented spatial and temporal data that can capture millimeter-scale spatial variation in transport phenomena that enables the quantification of heterogeneous multiscale permeability in geologic cores. Using spatially and temporally resolved concentration measurements, an ensemble Kalman filter (EnKF) is first implemented for inverting for the subcore scale permeability in a sandstone core. In addition to this traditional inversion approach, an encoder-decoder based convolutional neural network (CNN) is trained to predict the 3-D subcore scale permeability map from the same PET experimental data. Through forward numerical models, the permeability inversion accuracy of the trained CNN is compared with the EnKF on an experimental PET imaging dataset acquired using a heterogeneous Berea sandstone core. The results indicate that, compared to the EnKF, a single trained CNN can capture the variable solute arrival time behavior in a core-flooding experiment with orders of magnitude improvement in computational efficiency. Finally, mild permeability perturbations are added to the CNN inverted permeability map as an approach for generating the initial EnKF ensemble to further examine the optimal balance between the inversion accuracy and computational efficiency. This experimental approach combined with deep learning and numerical workflows provides an unprecedented improvement in 3-D multiscale permeability determination in heterogeneous geologic core samples.

1 Introduction

Multiscale permeability heterogeneity is a fundamental challenge to quantitative analysis and interpretation of flow and transport observations during core-scale experiments. Permeability heterogeneity is present in all geologic materials, even the most uniform and well-characterized formations, such as Berea sandstone [1] and Bentheimer sandstone [2]. Improved understanding of multiphase flow processes, fines migration, and enhanced recovery technologies first requires the estimation of initial permeability conditions, potential permeability evolution, and spatial variation in permeability. Without rapid methods for 3-D permeability map determination, advanced understanding of these core-scale processes may be limited.

Medical, industrial, and synchrotron-based imaging methods applied to problems in the field of petroleum engineering and hydrogeology have revolutionized the understanding of physical processes from the nanometer to the meter scale [3–6]. Photon transmission imaging techniques such as X-ray computed tomography (X-ray CT) across a range of scales excel at characterizing materials with different electron densities. As a result, at the micrometer

scale, X-ray CT is ideal for mapping pore geometry and fluid interfaces [7, 8]. At the continuum scale—the scale at which Darcy's Law can be used to describe flow in a porous medium—X-ray CT can map the spatial distribution of fluids of different densities or variations in porosity [3, 9, 10]. More recently, positron emission tomography (PET) has emerged as a non-destructive imaging technique for quantifying conservative tracer and colloid transport in geologic materials [5, 11]. Using PET, it is possible to map 3-D time-lapse tracer distributions collected during core-flooding experiments. This has enabled studies of fundamental flow and transport processes such as solute tailing driven by diffusion into microporous carbonates [12], flow path alteration in fractured carbonates [13], fluid saturation [14, 15], fines migration in reservoir formations [11], and the rock compartmentalization driven by the presence of deformation bands [16].

Despite the aid provided by the high-resolution characterization of tracer and colloid transport, robust inversion of flow and transport parameters from image-based data remains challenging due to the intrinsic ill-posedness and high computational cost associated with the inversion problems. The non-linearity in the subsurface transport processes and the heterogeneity in the geologic materials

* Corresponding author: czahasky@wisc.edu

make subsurface image inversion problems often ill-posed [17]. Because of the ill-posedness, small uncertainties in the input observations due to imaging artifacts or measurement error can cause large uncertainties in the inversion results, and it is difficult for the inversion to converge to a unique maximum likelihood solution [18]. To reduce the ill-posedness of the numerical inversion problems, iterative regularization techniques based on certain prior information are explicitly imposed to only preserve the optimal set of features (or basis vectors) and prevent the amplification of the uncertainties in observations [17, 19]. However, previous studies have shown that the explicitly imposed regularization terms are either case-specific for over-simplified datasets or unable to incorporate all the prior information numerically for realistic datasets [20].

A PET image at a single timestep is often composed of over 10,000 voxel-level concentration measurements in a geologic core, and therefore the computational cost of utilizing all the information for 3-D permeability inversion can be high. Specifically, the high computational cost associated with the numerous forward modeling at every iteration can make the inversion of high-dimensional and geologically realistic permeability maps often unfeasible [21]. The need for a large number of forward models makes ensemble smoother and ensemble Kalman filter (EnKF) based inversion methods very computationally expensive [22–26]. For a 2-D inversion problem with less than 2,000 grid cells, the ensemble-based inversion methods would typically involve repeated flow and transport simulations on an ensemble of $O(10^2)$ models to get one complete inversion [27]. Development of high precision sub-core scale permeability inversion algorithms involving iterative J-Function characteristic calculations and coreflooding simulations is another core-scale permeability inversion approach [29]. Given the accurate porosity, saturation, and reasonable initial permeability maps, a convergence in sub-core scale permeability distribution generally took four to nine full iterations. Therefore, the reduction in computational time is often a trade-off with the reduction in experimental data collection time and resources.

In contrast, through a combination of weight decay, batch normalization, drop out, and early stopping, deep learning inversion methods can enforce the sparsity and smoothness in the solution spaces during the weight optimization process. Consequently, the encoder–decoder based convolutional neural networks (CNN) has been shown to address the ill-posedness problem by reducing the effects of noise [30], capturing features at a finer resolution [19], and learning a generalizable regularizer based on the training dataset without explicitly enforcing any constraints [20]. Moreover, instead of utilizing limited conditioning data, CNNs can be trained with large ensembles of flow and transport field characteristics (i.e. permeability) that span a diverse set of geologic materials in typical unfractured aquifers using classic methods such as Latin hypercube sampling. The representative set of training data allows CNNs to identify less significant features and capture the maximum amount of

variability with the minimum number of features [17], thus alleviating the ill-posedness of the inverse problem.

In this study, we first perform PET data dimension reduction, quantile-based analysis, and normalization procedures [31] to emphasize transport characteristic information that is most important for permeability distribution determination. This processing reduces the influence of experimental imaging noise, solute tailing behavior, variation in initial solute concentration, and solute dispersion. We then use this data to compare the inversion performance between the deep learning approach, specifically the recently developed encoder-decoder based CNN [31], and a traditional numerical inversion approach, specifically EnKF, in terms of computational cost and inversion accuracy. To further enhance these methods, we also demonstrate the use of a hybrid CNN with EnKF tuning to maximize the permeability inversion accuracy while minimizing the associated computational cost.

2 Methods

2.1 Experimental Data Acquisition

The details of the PET data acquisition, imaging system, and experimental platform can be found in previous work [5]. For this study, a 10 cm long Berea sandstone sample was loaded into a custom aluminium coreholder that enabled the application of confining pressure and thus no-flow boundary conditions on the cylindrical faces of the samples. The core was saturated with low-pressure CO₂ and then injected with water while applying backpressure at the outlet face to prevent gravity-driven desaturation during horizontal fluid injection. The differential pressure was monitored, and steady-state conditions were determined to have been reached when the differential pressure stabilized. Core-average permeability was calculated to be 23 mD using Darcy's Law based on measurements of steady-state differential pressure, core geometry, and fluid injection rate.

For the imaging experiment, the water injection rate was set to 2 mL/min (0.245 cm/min). The positron-emitting radiotracer—fludeoxyglucose (¹⁸F-FDG)—was diluted in water to a radio-concentration of 0.323 mCi/mL to reach the optimal radioactivity injected for minimizing imaging noise [5]. Fludeoxyglucose is a commercially available conservative tracer with a half-life of 109.7 minutes with high radioactive yields. High radioactive yields enable high signal radiotracer concentrations without altering aqueous fluid properties such as density—an advantage over X-ray computed tomography-based tracer approaches [5]. The PET scans were performed using a Siemens pre-clinical Inveon DPET scanner. Shortly after the scan started a 4 mL pulse of radiotracer (1.292 mCi) was injected into the core and displaced with water containing no ¹⁸F-FDG. An illustration of four frames of the time-lapse reconstructed PET image is shown in Figure 1.

The reconstructed PET data was further processed to reduce the dimensionality of the data for use in the permeability inversion workflows. In short, quantile analysis was performed on every voxel of the PET images to calculate the 0.5 quantile, equivalent to the median arrival time and therefore insensitive to potential tailing effects in more heterogeneous cores. This quantile calculation enables the reduction of the 4D PET data down to a 3D image that provides the necessary information of permeability inversion with added benefits of reducing image noise and reducing the influence of sample-specific dispersion. The resulting quantile arrival time map for the Berea sandstone core was then normalized by converting from time to pore volumes injected. Additional details of this dimension reduction can be found in previous work [31, 32]. The final data processing step was to remove the linear trend in quantile arrival times that results from the bulk 1D flow from one end face of the core to the other. This linear trend was removed from each voxel by subtracting the quantile arrival time that would occur in a homogeneous core based on the distance of each voxel from the inlet of the core. The result after this trend removal is termed the arrival time difference map. These difference maps highlight areas of faster advection, with values greater than zero, and areas of slower advection, with values less than zero. The experimental arrival time difference map serves as input into the inversion workflow. A plot of the arrival time maps is provided in the results section.

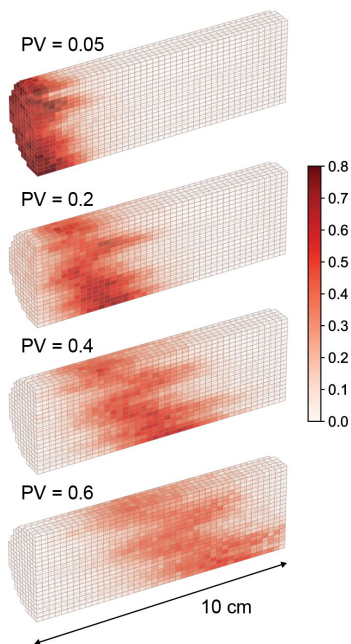


Fig. 1. Positron emission tomography time frames measuring radiotracer concentration distribution in the Berea sandstone core that was used in this study. The pore volumes injected (PV) are indicated above each image and fluid is injected from the left face of the core. The radiotracer was [¹⁸F]-FDG. The voxel size dimensions are 0.2329 x 0.2329 x 0.2388 cm³. These images highlight the permeability heterogeneity of the Berea sample that resulted in faster tracer breakthrough in the upper middle and lower portion of the core. Corresponding X-ray CT images confirm horizontal planar laminations in the lower portion of the core with subtle cross-bedding containing higher clay content in the upper portion of the core.

2.2 Training data generation

An encoder-decoder based CNN was constructed and trained on 16,000 pairs of synthetic permeability and arrival time difference maps. Specifically, 10,000 pairs were used as the training dataset—for providing learnable features, 5,500 pairs were used as the validation datasets—for monitoring and guiding the CNN during the training, and 500 pairs were used as the testing set—for verifying the CNN after the training. To account for the instrumental error during the PET imaging process, a Gaussian white noise with a mean of zero and a standard deviation of 1/70 of the range is applied to every arrival time map. A similar level of noise is observed in experimental arrival time maps.

The 3-D synthetic permeability maps were generated via the random field generation algorithm using the exponential covariance model using open-source package developed by [33]. The grid cells for all the synthetic permeability maps have dimensions of 0.25 × 0.25 × 0.25 cm³, and dimensions of 20 × 20 × 40 cells such that the model dimensions are nearly identical to the core samples and corresponding PET images. The synthetic permeability maps were sampled from parameters space with the mean ranging from 1 mD–20 D, log₁₀ variance ranging from −1.7 to 9.9. In each x, y, and z directions, the correlation length of all synthetic permeability maps spans from 0.25 to 12.5 cm—spanning sedimentological lengths scales contained in core-scale samples—and the angle of rotation spans from 0 to 90°. Three example permeability fields are shown in Figure 2. By using the Latin hypercube sampling algorithm [34], all the training, validating, and testing data were well-balanced and representative of this parameter space. Three example permeability fields are illustrated in the left column of Figure 2.

Using MODFLOW 2005 with MT3DMS [35], a set of arrival time maps were numerically simulated for each synthetic permeability map. The simulated arrival time map also has a dimension of 20 × 20 × 40, and it underwent the same pre-processing and dimension reduction procedures as the 3-D experimental PET data for calculating arrival time difference maps. Three example arrival time difference maps calculated from synthetically generated permeability fields are illustrated in the right column of Figure 2.

To further guide the training and preserve the uniqueness of the inversion, the average permeability (\bar{k}) for every synthetic core was calculated by Darcy's Law based on modeled pressure drop data for each synthetic permeability map.

$$\bar{k} = \frac{Q_t}{A} \cdot \frac{L}{\Delta P} \cdot \mu \quad (1)$$

Identical to the experimental conditions, all the synthetic cores had a length (L) of 10 cm and a cross-sectional area (A) of 78.5 cm². The flow rate through the synthetic core (Q_t) was set to 2 mL/min, and the pressure drop across the synthetic cores (ΔP) was calculated by subtracting the simulated

average pore pressure difference between the outlet slice and the inlet slice. The average permeability was expanded to a $1 \times 20 \times 20$ tensor and then concatenated to the inlet of the input arrival time map. Therefore, the overall dimension of the input is $20 \times 20 \times 41$.

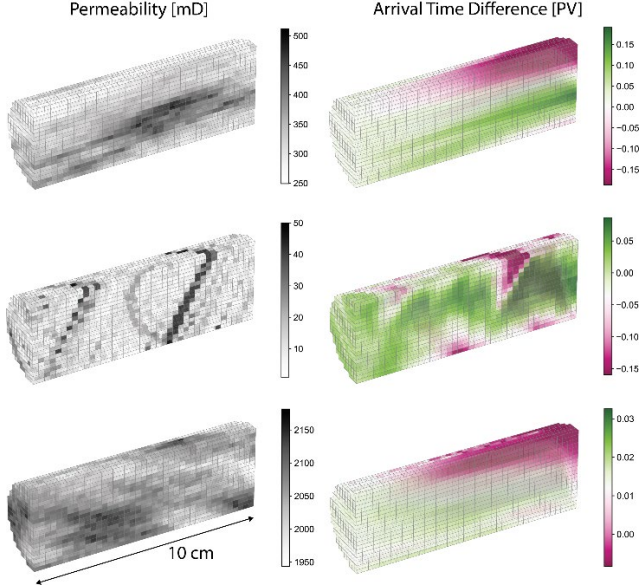


Fig. 2. Three example training data used for CNN training and test. The left column shows synthetically generated permeability field and the right column shows the corresponding arrival time difference map calculated from numerical simulation output.

2.3 Convolutional Neural Network Architecture

Convolution, sampling, and regression are the three main components of the encoder-decoder based CNN. The convolution blocks are composed of convolutional layers, that are used to gain an overall parameterization of the image. Sampling blocks are used to extract the high-frequency features of the input through downsampling and verify the learning through upsampling. The regression blocks are composed of a series of dense blocks connected in a residual-in-residual structure, which are used to perform deep regression over the sampled images.

A convolutional layer extracts features from input images through: $\mathbf{x}^{(l+1)} = \mathbf{f}_{l+1}(\mathbf{W}^{(l+1)}\mathbf{x}^{(l)} + \mathbf{b}^{(l+1)})$, where $\mathbf{W}^{(l+1)}$ is the weight matrix (or kernel), $\mathbf{b}^{(l+1)}$ is the bias vector, and \mathbf{f}_{l+1} is the nonlinear activation function that maps the input map $\mathbf{x}^{(l)}$ to a corresponding output map $\mathbf{x}^{(l+1)}$. In a convolutional layer, every neuron is linked to a receptive field, a region in the input that represents a particular feature. As the result, CNN captures smaller-scale features in the shallower layers and the more global information in the deeper layers. There are two main reasons for adopting CNN in the image-to-image regression problems. First, the parameter sharing features and sparse connectivity of CNNs require fewer parameters than the traditional neural networks [36], which reduces the computational cost of processing large datasets. Decompressing the input to latent spaces while learning further reduces the computational cost. Secondly, CNN is

highly capable of finding spatial correlations within a map by enforcing a local connectivity pattern between neurons of adjacent layers [36], which enables high accuracy in voxel-wise inversion.

By connecting each convolutional layer with all its subsequent layers, Densely Connected Convolutional Networks (DenseNet or dense block) fully leverage the hierarchical advantages of CNNs by encouraging feature propagation, sharing, and reuse among all the layers [37]. To increase the depth of the networks without the gradient-vanishing or gradient-exploding problem, a residual learning framework was adopted to connect the dense blocks in the networks. Instead of directly learning the unreferenced original mapping, the residual connection adopts a skip-connection between blocks that learn residual functions with reference to the layer input. Suppose \mathbf{x} is the input for the current layer and let \mathbf{x} denotes the residual. Let $\mathbf{F}(\mathbf{x})$ denote the optimal mapping of the current layer and let $\mathbf{R}(\mathbf{x})$ denotes the original mapping (or the residual function) of the current layer, and let $\mathbf{F}(\mathbf{x}) := \mathbf{R}(\mathbf{x}) + \mathbf{x}$. The $\mathbf{F}(\mathbf{x})$ is then passed to the next layer, so if the original $\mathbf{R}(\mathbf{x})$ of the current layer enlarges the error, the next layer could always refer back to the residual \mathbf{x} , which could be considered as skipping the layer that enlarges the error. To the other extreme, if the original mapping $\mathbf{R}(\mathbf{x})$ is optimal, the residual \mathbf{x} will be set to zero. Therefore, the deeper layer would produce no higher error than the upper layer. The residual-in-residual dense block (RRDB) are composed of a stack of residual dense blocks connected in another residual structure [38, 39]. Therefore, the residual learning was used in two levels, resulting in a residual-in-residual structure. For both of the two levels, the desired output is actually denoted as $\mathbf{F}(\mathbf{x}) := \beta \times \mathbf{R}(\mathbf{x}) + \mathbf{x}$, where $\beta \in (0, 1]$ is the residual scaling factor [38].

The inverted permeability map $\hat{\mathbf{x}}$ is then compared against the synthetic permeability map (or the ground truth) \mathbf{x} through loss functions, and the loss is going to be minimized by back-propagating the weights and bias through gradient descent. The overall loss function (Equation 2) is a combination of L1 loss (Equation 3) and KL-Divergence loss (Equation 4) weighted by α .

$$L_{total} = L_{L1} + \alpha L_{KL} \quad (2)$$

The L1 loss evaluates the absolute error between the synthetic (or ground truth) permeability map (\mathbf{x}) and inverted permeability map ($\hat{\mathbf{x}}$).

$$L_{L1} = \|\mathbf{x} - \hat{\mathbf{x}}\|_1 \quad (3)$$

The KL-Divergence loss measures the similarity between the synthetic (or ground truth) permeability distribution ($\mathcal{P}(\mathbf{x})$) and inverted permeability distribution ($\mathcal{Q}(\hat{\mathbf{x}})$).

$$L_{KL} = \mathcal{D}(\mathcal{P}(\mathbf{x}) \parallel \mathcal{Q}(\hat{\mathbf{x}}))_{KL} = \mathcal{P}(\mathbf{x}) \cdot \log \frac{\mathcal{P}(\mathbf{x})}{\mathcal{Q}(\hat{\mathbf{x}})} \quad (4)$$

The encoder of the CNN extracts the high-frequency features of the input through the convolutional block while compressing the input map down through the sampling block.

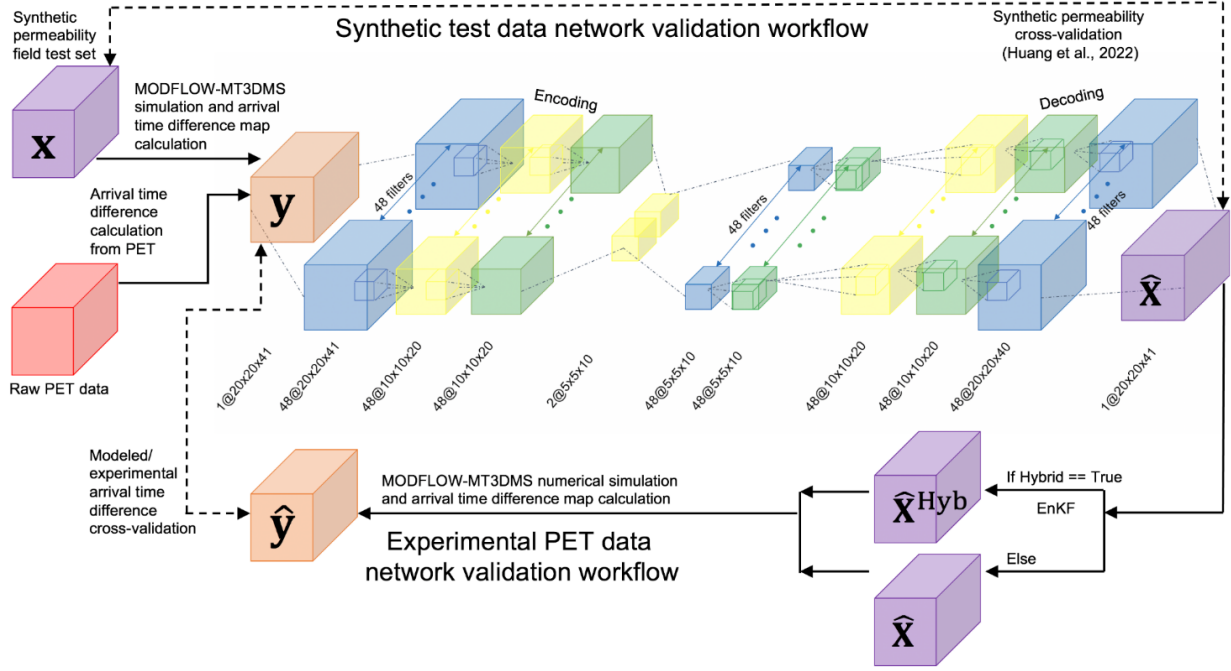


Fig. 3 Schematic of the overall inversion workflow. The top loop demonstrates the validation of the trained encoder-decoder based CNN using synthetic permeability maps [31]. The middle chain represents the CNN, including convolutional blocks (blue), up/down-sampling block (yellow), and residual-in-residual dense blocks (green). The bottom loop demonstrates the validation of the CNN using an experimental arrival time map collected from the Berea sandstone core. Note that the purple blocks correspond to synthetic (\mathbf{x}) or predicted ($\hat{\mathbf{x}}$) or EnKF tuned ($\hat{\mathbf{x}}^{\text{Hyb}}$) permeability maps, the red block is the PET data, and the orange blocks correspond to experimental (\mathbf{y}) and modeled ($\hat{\mathbf{y}}$) arrival time maps.

The compressed high-level features map is referred to as the latent space of the input map, which has a dimension of $5 \times 5 \times 10$. The decoder then up transposes the latent map based on the extracted high-frequency features. The inverted (or decoded) permeability map has a dimension of $20 \times 20 \times 40$.

To further validate the trained CNN performance under experimental settings, we run MODFLOW-MT3DMS flow simulations on the inverted permeability map $\hat{\mathbf{x}}$ to generate modeled arrival time map for direct comparison with the experimental arrival time map. The R2 score is used to evaluate the similarity between the modeled and experimental arrival time maps (R2 = 1 indicates perfect inversion). A detailed illustration of the overall training and validation workflow is illustrated in Figure 3. Additional details of the CNN architecture, training, and convergence performance can be found in [31].

2.4 Ensemble Kalman Filter

To compare the encoder-decoder based CNN with the most computationally efficient numerical inversion algorithm, an Ensemble Kalman filter [23] has been adopted and constructed for this study. The EnKF is the Monte Carlo approximation to Kalman filtering for sequential data assimilation. An advantage of the EnKF for this application is that uncertainty characterization of EnKF on the ensemble of inverted outcomes is computationally efficient [40] and the EnKF only requires the ensemble predicted error statistics to update the inverted parameters. The computational efficiency and inversion robustness of EnKF have been demonstrated by various hydrogeological data assimilation tasks, such as contaminant source identification [40] and history matching

[41]. In this study, we adopted the standard EnKF to characterize geologic core heterogeneity through continuum-scale permeability inversion.

To begin a standard EnKF inversion, an initial ensemble of augmented state vectors ($\mathbf{X}_{\text{init}} = [\mathbf{x}^{(1)}, \dots, \mathbf{x}^{(n_p)}]$) needs to be generated. In this study we performed EnKF inversion with three different types of ensembles. The first was generated by slightly perturbing the permeability prediction of the CNN permeability prediction as described in the following section. The second and third EnKF inversion were performed using a spatially correlated ensemble of permeability field based on the expected correlation in a layered sandstone (i.e., low-uncertainty ensemble) and using an ensemble of permeability fields that are generated assume less information is available (i.e., high-uncertainty ensemble). The ensemble of permeability fields was generated using the same algorithm as the CNN training data described in Section 2.2. A summary of the ensemble parameter space is given in Table 1.

According to previous studies, an assumption of the EnKF is that the true permeability map of the sample with unknown permeability lies in the linear span of the initial ensemble space [42]. If \mathbf{X} evolves with time, each \mathbf{X} contains the state vector (\mathbf{S}) with a dimension $n_s \times 1$ and a parameter vector (\mathbf{P}) with a dimension $n_p \times 1$. Through state operators (e.g., numerical model), the state vector (e.g., fluid pressure distribution) will vary with time based on the inverted parameter vector (e.g., permeability) at the corresponding time step. However, since \mathbf{X} in this study (i.e., the permeability map) is not varying with time and the observation operator (i.e., MODFLOW-MT3DMS model) does not require a state vector as input, \mathbf{X} only contains the

parameter vector with a dimension of $n_p \times 1$, where n_p equals the size of the 1-D flattened permeability map plus the average permeability calculated by Equation 1. Based on the corresponding state vectors, an ensemble of initial observation vectors ($\mathbf{Y}_{\text{init}} = [\mathbf{y}^{(1)}, \dots, \mathbf{y}^{(n_o)}]$), each with a dimension $n_o \times 1$, were simulated via Equation 5, where \mathbf{f} is the observation operator. All the dimension parameters used in this study are presented in Table 2.

$$\mathbf{Y}_{\text{init}} = \mathbf{f}(\mathbf{X}_{\text{init}}) \quad (5)$$

At iteration i , the standard EnKF involves two main steps. The first step is to compute the Kalman gain matrix \mathbf{G} for updating the parameter vector ensemble:

$$\mathbf{G} = \mathbf{P}_{xy} \cdot (\mathbf{P}_{yy} + \mathbf{R})^{-1} \quad (6)$$

Here \mathbf{P}_{xy} is the $n_p \times n_o$ cross-covariance matrix between the inverted permeability and simulated arrival time from the previous iteration (Equation 7), \mathbf{P}_{yy} is the $n_o \times n_o$ covariance matrix of the simulated arrival time from the previous iteration (Equation 8), and \mathbf{R} is the diagonal measurement error matrix created by projecting the measurement error at every voxel (or observation point) onto a $n_o \times n_o$ identity matrix.

$$\mathbf{P}_{xy} = (\underline{X}_{i-1} - \underline{X}_{i-1}) \cdot (\underline{Y}_{i-1} - \underline{Y}_{i-1})^T \quad (7)$$

$$\mathbf{P}_{yy} = (\underline{Y}_{i-1} - \underline{Y}_{i-1}) \cdot (\underline{Y}_{i-1} - \underline{Y}_{i-1})^T \quad (8)$$

Here, \underline{X}_{i-1} is a $n_p \times n_e$ matrix with each column containing the average of one vector in the parameter ensemble. Similarly, \underline{Y}_{i-1} is a $n_p \times n_e$ matrix with each column containing the average of one vector in the observation ensemble. Then, every parameter vector in the previous \underline{X}_{i-1} ensemble is updated with the Kalman gain matrix \mathbf{G} via Equation 9:

$$\mathbf{X}_i = \underline{X}_{i-1} + \mathbf{G} \cdot (\underline{Y}_{i-1} - \underline{Y}_{\text{true}}) \quad (9)$$

Here $\underline{Y}_{\text{true}}$ is the 1-D flattened experimental arrival time map measured from the Berea core. The vector $(\underline{Y}_{i-1} - \underline{Y}_{\text{true}})$ is used to quantify the new observational error. The combination of the Kalman gain matrix and observation error vector helps the Kalman filter to assimilate the observations for the new iteration of parameter updates.

The second step is to simulate the new observation ensemble \mathbf{Y}_i (i.e., arrival time maps calculated from MODFLOW-MT3DMS model output) based on the updated parameter ensemble \mathbf{X}_i via the observation operator for the new error statistics. By the end of every iteration, the ensemble average of all parameter vectors was generated as the permeability inversion result. The ensemble standard deviation provides an estimation of the inversion uncertainty.

2.5 Hybrid CNN with EnKF tuning

In the final permeability inversion approach, the CNN inversion results were used to generate an initial ensemble for

final tuning of the 3-D permeability prediction using the EnKF. The ensemble generation was performed by multiplying the CNN inverted permeability map by an ensemble of spatially correlated exponential covariance fields with a mean of 1 and variance ranging from 0.001 to 0.05; the correlation length and rotation angle of the fields were within the same range as the low-uncertainty parameter space presented in Table 1.

Table 1. The parameter space boundaries for generating the initial Berea EnKF permeability ensemble. Assuming no exact knowledge of the spatial information of the Berea permeability map, the permeability maps in the low-uncertainty ensemble are with a well-defined range of spatial information constrained by prior knowledge obtained from geologic knowledge and X-ray CT images on the core. In contrast, the permeability maps in the high-uncertainty ensemble are sampled from a larger parameter space. The mean permeability for both ensembles were calculated by Equation 1 using the data from core-flooding experiments.

Parameter Name	Low-uncertainty ensemble	High-uncertainty ensemble
Mean Permeability	23.2 mD	23.2 mD
log10 exponential variance	-3.0 - -2.0	-7.0 - -1.0
Correlation length in x, y directions	12.5 - 37.5 cm	0.25 - 25 cm
Correlation length in z directions	0 cm	0 cm
Rotation angle in x, y, z directions	0 Rad	0 - 3.14 Rad

Table 2. The dimension parameters used for EnKF.

Dimensional Parameter Name	Number of parameters
Number of ensemble (n_e)	400
Number of observation (n_o)	16,000
Number of parameters (n_p)	16,001

3 Results

For the encoder-decoder based CNN, each training took around 30 hours to complete on a Nvidia GeForce GTX980 GPU. All the 8,570,690 trained parameters were then stored in two separate path files (a 10.8 MB path file for the encoder model and a 22.1 MB path file for the decoder model). A summary of the training and validation loss is illustrated in Figure 4.

The EnKF inversion was an iterative process, and the time required to stabilize inversion accuracy heavily depends on the quality of the initial parameter ensembles. For the inversion via hybrid CNN with EnKF, the range of initial ensemble is very well-defined and constrained, and the

accuracy stabilization generally requires 3 to 4 hours. When the initial ensemble is less constrained, the range for the initial ensemble expands. The accuracy stabilization time was between 5 hours and 9 hours when sampling from low or high uncertainty ensemble parameter space.

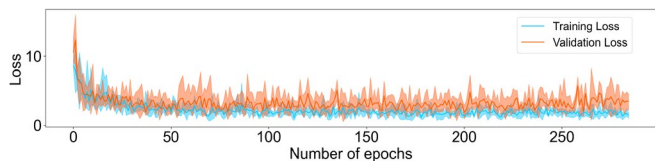


Fig. 4. An illustration of training and validation loss curves from five independent CNN training trails. At every epoch, the upper and lower bounds of the loss curve area indicate the maxima and the minima of the five loss curves. The bold middle line within the loss range represents the average loss of the five trials at every epoch.

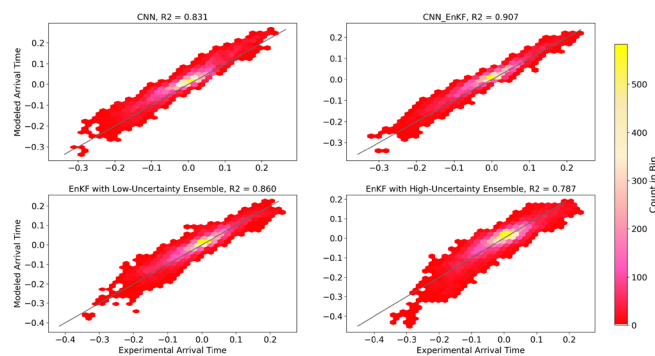


Fig. 5. Cross-plot of flattened experimental arrival time data (x-axis) and modeled arrival time difference based on the inverted permeability maps from CNN (top left), hybrid CNN with EnKF tuning (top right), EnKF with the low-uncertainty initial ensemble (bottom left), and EnKF with the high-uncertainty initial ensemble (bottom right). To illustrate the density of the correlations, the cross-plot is colored by the number of points in a local region of the cross-plot. The R2 correlation results indicate that the EnKF can bring significant improvement in permeability map prediction and the quality of the initial ensemble for the EnKF has a profound impact on the inversion accuracy.

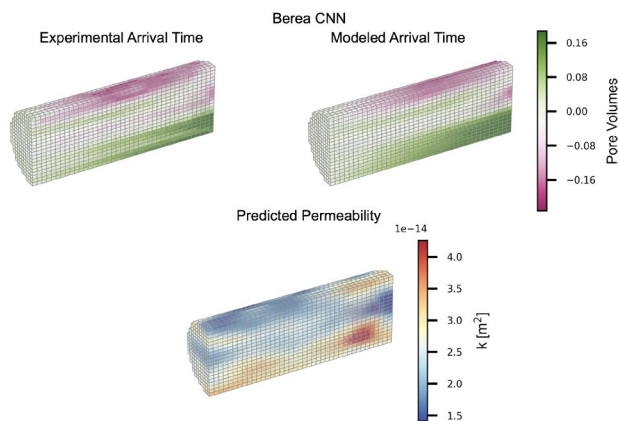


Fig. 6. Qualitative validation of the trained encoder-decoder based CNN using experimentally measured arrival time data measured with PET collected from the Berea sandstone core. The upper left subplots show the arrival time map calculated from the PET imaging data, the lower plot shows the predicted permeability by the network, and the upper right shows the modeled arrival time map based on the predicted permeability map. Note that the experimental and modeled arrival times have the same colorscale.

Three sets of initial ensembles with increasing levels of uncertainty (i.e., CNN-based, low uncertainty, and high uncertainty) were tested as the input for the EnKF inversion algorithm. Similar to the CNN validation workflow, modeled arrival time maps were generated based on the EnKF inverted permeability maps through MODFLOW-MT3DMS numerical simulation. As illustrated in Figure 5, the R2 correlation between the experimental and modeled arrival time decreases as the precision of the initial ensemble decreases. With an R2 accuracy of 0.891, the hybrid CNN with EnKF tuning excels both in terms of computational cost and inversion accuracy. As demonstrated in Figure 6 and 7, the EnKF algorithm captures more discrete heterogeneity that is more geologically realistic than the smoothed permeability map inversion produced by the CNN, resulting in higher inversion accuracy.

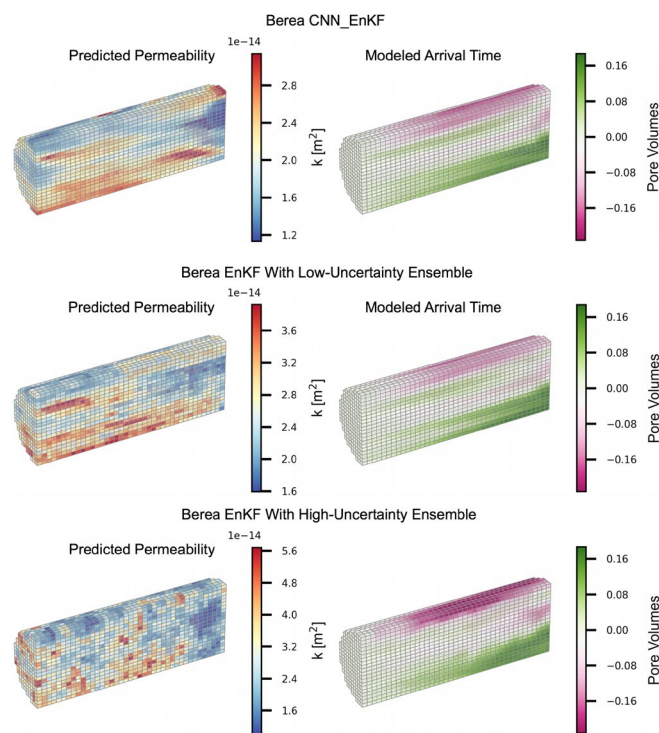


Fig. 7. A quantitative comparison of the inversion results for the hybrid CNN with EnKF tuning (top), the EnKF with the low-uncertainty initial ensemble (middle), and the EnKF with the high-uncertainty initial ensemble (bottom). The left subplots show the inverted 3-D permeability maps and the right subplots show the modeled arrival time maps.

4 Discussion

The high R2 correlation between the experimental and modeled arrival time maps illustrates that the trained encoder-decoder based CNN is capable of accurately determining the overall magnitude and local variations of 3-D permeability maps. With a reasonable initial ensemble, the Ensemble Kalman filter can achieve a similar or higher level of inversion accuracy as the encoder-decoder based CNN. As noted in previous inversion studies, the quality of the initial ensemble has a considerable impact on both the accuracy and computational efficiency of the inversion.

Trained CNNs are capable of describing the input imagery (e.g., PET data) in terms of dense and generalizable features, resulting in a significant reduction in computational time and memory requirements [43, 44]. Although the initial CNN training process is computationally intensive, the trained network can invert the permeability map of nearly any unfractured geologic core sample within 10 seconds. Furthermore, each path file that contains the trained parameters for the entire encoder-decoder network is only tens of megabytes.

Training of the encoder-decoder based CNN is purely data-driven, relying on statistical relationships instead of any iterative forward operator involved in the inversion process. Our work illustrates that the encoder-decoder based CNN is capable of learning a generalizable mapping function between the arrival time difference and permeability maps. The mapping function served as a pseudo-inverse operator [18], and it eliminates the need for numerically defining a forward operator, running iterative forward simulations, and computing covariance matrices. This significantly reduces computational time if inverting the permeability maps for multiple core samples.

As indicated by the inversion accuracy stabilization time, the EnKF requires high computational time and memory because of the iterative forward simulations and covariance matrices computations involved in the inversion process. For a system with $n = n_o = n_p$, the computational cost of the standard EnKF is at least in the order of $O(n_e^2 \cdot n)$ [45]. To mitigate this issue, both the ensemble size and the number of iterations need to be reduced by a well-constrained initial ensemble estimation.

Similar to CNN training data parameter space definition, the geologically reasonable EnKF ensemble definition is essential for accurate inversion results. Guided by the geologic knowledge and sedimentary structures present in X-ray CT core image obtained from previous experiments, the EnKF initialized with low-uncertainty permeability fields accurately capture the magnitude and variation of the Berea core's permeability map. Furthermore, the CNN inverted permeability map provides additional structural information that is difficult to defined manually to the EnKF inversion, resulting in the highest R2 inversion accuracy. In contrast, results of the EnKF initialized with the high-uncertainty permeability fields illustrate a lack of geologic realism.

In addition, if proper regularization techniques are not explicitly imposed, small uncertainties in the input observations arising from measurement error can result in large uncertainties in the inversion results due to the ill-posedness of the nonlinear inversion problem [17, 19]. For instance, as the uncertainty in the input ensemble increases, a clear reduction in the inversion accuracy is observed. This issue can be attenuated by using CNN to guide the generation of an initial ensemble with low uncertainty.

5 Conclusion

This study demonstrates the capability of both CNNs and traditional numerical inversion methods for determining subcore permeability maps from PET imaging data. The CNN can learn a generalizable relationship between the PET arrival time and permeability maps that allows a single trained network to invert for the permeability of any geologic sample represented by the training data parameter space. This enables an accurate 3-D permeability characterization of geologic cores. The data-driven nature of the CNN inversion approach has been shown to lead to an unprecedented reduction in computational time and memory requirements such that a single inversion can be run in seconds.

The EnKF numerical inversion algorithm requires more computationally intensive covariance calculations and observation operation that must be run for each sample-specific permeability field inversion. Similar to the CNN training data parameter space definition, the EnKF ensemble parameter space has a strong influence on inversion accuracy and computational efficiency. With a well-defined initial ensemble, the Ensemble Kalman filter may outperform the CNN results in terms of inversion accuracy. However, due to the variation and spatial complexity of different permeability fields in different reservoir rocks, prior knowledge about a specific geologic core will often be limited. As a solution, the CNN inverted permeability map with subtle perturbations that span the inversion uncertainty can serve as the starting point for generating a geologically realistic and sample specific ensemble with much lower uncertainty than traditional geostatistical ensemble generation methods. The hybrid CNN with EnKF tuning not only aids the EnKF to further improve its inversion accuracy but also broadens its capability at a larger scale or a finer resolution. Combined, this approach provides a transformational approach for rapid sub-core permeability characterization in complex geologic reservoir core samples.

Acknowledgments: Python scripts for training data generation, data analysis, CNN operation, and trained network parameters are permanently available at <https://doi.org/10.5281/zenodo.6354768>. The full training datasets and experimental data are permanently available at <https://doi.org/10.25740/gz610dt4642>. This work was supported as part of the Center for Mechanistic Control of Water-Hydrocarbon-Rock Interactions in Unconventional and Tight Oil Formations (CMC-UF), an Energy Frontier Research Center funded by the U.S. Department of Energy, Office of Science under DOE (BES) Award DE-SC0019165. Further support for this research was provided by the Office of the Vice Chancellor for Research and Graduate Education at the University of Wisconsin-Madison with funding from the Wisconsin Alumni Research Foundation and the University of Wisconsin-Madison Hilldale Undergraduate/Faculty Research Fellowship.

References

- [1] C. Zahasky and S. M. Benson, "Micro-Positron Emission Tomography for Measuring Sub-core Scale Single and Multiphase Transport Parameters in Porous Media," *Adv. Water Resour.*, vol. 115, pp. 1–16, 2018.

- [2] C. Zahasky, S. J. Jackson, Q. Lin, and S. Krevor, "Pore network model predictions of Darcy-scale multiphase flow heterogeneity validated by experiments," *Water Resour. Res.*, pp. 1–16, 2020.
- [3] S. Akin and A. R. Kovscek, "Computed Tomography in Petroleum Engineering Research," *Appl. X-ray Comput. Tomogr. Geosci.*, vol. 215, pp. 23–38, 2003.
- [4] M. J. Blunt *et al.*, "Pore-scale imaging and modelling," *Adv. Water Resour.*, vol. 51, pp. 197–216, 2013.
- [5] C. Zahasky, T. Kurotori, R. Pini, and S. M. Benson, "Positron emission tomography in water resources and subsurface energy resources engineering research," *Adv. Water Resour.*, vol. 127, no. March, pp. 39–52, 2019.
- [6] L. Leu, S. Berg, F. Enzmann, R. T. Armstrong, and M. Kersten, "Fast X-ray Micro-Tomography of Multiphase Flow in Berea Sandstone: A Sensitivity Study on Image Processing," *Transp. Porous Media*, vol. 105, no. 2, pp. 451–469, 2014.
- [7] R. T. Armstrong, M. L. Porter, and D. Wildenschild, "Linking pore-scale interfacial curvature to column-scale capillary pressure," *Adv. Water Resour.*, vol. 46, pp. 55–62, 2012.
- [8] C. Garing, J. A. de Chalendar, M. Voltolini, J. B. Ajo-Franklin, and S. M. Benson, "Pore-scale capillary pressure analysis using multi-scale X-ray micromotography," *Adv. Water Resour.*, vol. 104, pp. 223–241, 2017.
- [9] J. M. Minto, F. F. Hingerl, S. M. Benson, and R. J. Lunn, "X-ray CT and multiphase flow characterization of a 'bio-grouted' sandstone core: The effect of dissolution on seal longevity," *Int. J. Greenh. Gas Control*, vol. 64, no. September 2016, pp. 152–162, 2017.
- [10] C. Zahasky and S. M. Benson, "Spatial and temporal quantification of spontaneous imbibition," *Geophys. Res. Lett.*, vol. 46, no. 21, pp. 11972–11982, Nov. 2019.
- [11] C. Sutton and C. Zahasky, "An approach for image-based quantification of fines migration in geologic columns and core samples," in *SCA*, 2022.
- [12] T. Kurotori, C. Zahasky, S. A. Hosseinzadeh Hejazi, S. M. Shah, S. M. Benson, and R. Pini, "Measuring, imaging and modelling solute transport in a microporous limestone," *Chem. Eng. Sci.*, vol. 196, pp. 366–383, 2019.
- [13] B. Brattekas and R. S. Seright, "Implications for improved polymer gel conformance control during low-salinity chase-floods in fractured carbonates," *J. Pet. Sci. Eng.*, 2017.
- [14] Y. Hu *et al.*, "Unsteady-State Coreflooding Monitored by Positron Emission Tomography and X-ray Computed Tomography," no. July 2018, pp. 1–11, 2019.
- [15] M. A. Ferno *et al.*, "Combined positron emission tomography and computed tomography to visualize and quantify fluid flow in sedimentary rocks," *Water Resour. Res.*, vol. 51, no. 9, pp. 7811–7819, 2015.
- [16] C. R. Romano *et al.*, "Sub-core scale fluid flow behavior in a sandstone with cataclastic deformation bands," *Water Resour. Res.*, pp. 1–16, 2020.
- [17] E. K. Oware, S. M. J. Moysey, and T. Khan, "Physically based regularization of hydrogeophysical inverse problems for improved imaging of process-driven systems," *Water Resour. Res.*, vol. 49, no. 10, pp. 6238–6247, 2013.
- [18] J. Adler and O. Öktem, "Solving ill-posed inverse problems using iterative deep neural networks," *Inverse Probl.*, vol. 33, no. 12, pp. 1–24, 2017.
- [19] Y. Kim and N. Nakata, "Geophysical inversion versus machine learning in inverse problems," *Lead. Edge*, vol. 37, no. 12, pp. 894–901, 2018.
- [20] M. T. Mccann, K. H. Jin, and M. Unser, "Deep CNN for Inverse Problems in Imaging," *IEEE Signal Process. Mag.*, vol. 26, no. 9, pp. 4509–4522, 2017.
- [21] J. Fu and J. J. Gómez-Hernández, "A blocking markov chain Monte Carlo method for inverse stochastic hydrogeological modeling," *Math. Geosci.*, vol. 41, no. 2, pp. 105–128, 2009.
- [22] P. J. van Leeuwen and G. Evensen, "Data Assimilation and Inverse Methods in Terms of a Probabilistic Formulation," *Mon. Weather Rev.*, vol. 124, no. 12, pp. 2898–2913, Dec. 1996.
- [23] G. Evensen, "Sequential data assimilation with a nonlinear quasi-geostrophic model using Monte Carlo methods to forecast error statistics," *J. Geophys. Res.*, vol. 99, no. C5, 1994.
- [24] H. Zhou, J. J. Gómez-hernández, H. H. Franssen, and L. Li, "Advances in Water Resources An approach to handling non-Gaussianity of parameters and state variables in ensemble Kalman filtering," *Adv. Water Resour.*, vol. 34, no. 7, pp. 844–864, 2011.
- [25] A. A. Emerick and A. C. Reynolds, "Ensemble smoother with multiple data assimilation," *Comput. Geosci.*, vol. 55, pp. 3–15, 2013.
- [26] T. Xu and J. J. Gómez-Hernández, "Simultaneous identification of a contaminant source and hydraulic conductivity via the restart normal-score ensemble Kalman filter," *Adv. Water Resour.*, vol. 112, no. December 2017, pp. 106–123, 2018.
- [27] S. W. A. Canchumuni, A. A. Emerick, and M. A. C. Pacheco, "Towards a robust parameterization for conditioning facies models using deep variational autoencoders and ensemble smoother," *Comput. Geosci.*, vol. 128, no. January, pp. 87–102, 2019.
- [28] Q. Guo, X. Shi, X. Kang, S. Hao, L. Liu, and J. Wu, "Evaluation of the benefits of improved permeability estimation on high-resolution characterization of DNAPL distribution in aquifers with low-permeability lenses," *J. Hydrol.*, vol. 603, no. PB, p. 126955, 2021.
- [29] M. Krause, S. Krevor, and S. M. Benson, "A Procedure for the Accurate Determination of Sub-Core Scale Permeability Distributions with Error Quantification," *Transp. Porous Media*, vol. 98, no. 3, pp. 565–588, 2013.
- [30] G. Barbastathis, A. Ozcan, and G. Situ, "On the use of deep learning for computational imaging," *Optica*, vol. 6, no. 8, p. 921, Aug. 2019.

- [31] Z. Huang, T. Kurotori, R. Pini, S. M. Benson, and C. Zahasky, "Three-Dimensional Permeability Inversion Using Convolutional Neural Networks and Positron Emission Tomography," *Water Resour. Res.*, vol. 58, no. 3, pp. 1–21, 2022. *Commun. Pure Appl. Math.*, vol. 71, no. 5, pp. 892–937, 2018.
- [32] C. F. Harvey and S. M. Gorelick, "Mapping hydraulic conductivity: Sequential conditioning with measurements of solute arrival time, hydraulic head, and local conductivity," vol. 31, no. 7, pp. 1615–1626, 1995.
- [33] S. Müller and L. Schüler, "GeoStat-Framework/GSTools: v1.3.0 'Pure Pink.'" Zenodo, 2021.
- [34] J. L. Deutsch and C. V. Deutsch, "Latin hypercube sampling with multidimensional uniformity," *J. Stat. Plan. Inference*, vol. 142, no. 3, pp. 763–772, 2012.
- [35] C. Zheng and P. P. Wang, "MT3DMS - A Modular Three-Dimensional Multispecies Transport Model," *Strateg. Environ. Res. Dev. Progr.*, pp. 1–40, 1999.
- [36] I. Goodfellow, Y. Bengio, and A. Courville, *Deep Learning*. MIT Press, 2016.
- [37] G. Huang, Z. Liu, L. Van Der Maaten, and K. Q. Weinberger, "Densely connected convolutional networks," *Proc. - 30th IEEE Conf. Comput. Vis. Pattern Recognition, CVPR 2017*, vol. 2017-Janua, pp. 2261–2269, 2017.
- [38] X. Wang *et al.*, "ESRGAN: Enhanced super-resolution generative adversarial networks," *Lect. Notes Comput. Sci. (including Subser. Lect. Notes Artif. Intell. Lect. Notes Bioinformatics)*, vol. 11133 LNCS, pp. 63–79, 2019.
- [39] S. Mo, N. Zabarar, X. Shi, and J. Wu, "Deep Autoregressive Neural Networks for High-Dimensional Inverse Problems in Groundwater Contaminant Source Identification," *Water Resour. Res.*, vol. 55, no. 5, pp. 3856–3881, 2019.
- [40] Z. Chen, J. J. Gómez-Hernández, T. Xu, and A. Zanini, "Joint identification of contaminant source and aquifer geometry in a sandbox experiment with the restart ensemble Kalman filter," *J. Hydrol.*, vol. 564, no. August, pp. 1074–1084, 2018.
- [41] D. Erdal and O. A. Cirpka, "Preconditioning an ensemble Kalman filter for groundwater flow using environmental-tracer observations," *J. Hydrol.*, vol. 545, pp. 42–54, Feb. 2017.
- [42] N. K. Chada, M. A. Iglesias, L. Roininen, and A. M. Stuart, "Parameterizations for Ensemble Kalman Inversion," *Inverse Problems*, vol. 34, no. 10, pp. 1361–1392, 2018.
- [43] J. Masci, U. Meier, D. Cireşan, and J. Schmidhuber, "Stacked convolutional auto-encoders for hierarchical feature extraction," *Lect. Notes Comput. Sci. (including Subser. Lect. Notes Artif. Intell. Lect. Notes Bioinformatics)*, vol. 6791 LNCS, no. PART 1, pp. 52–59, 2011.
- [44] M. Norouzi, M. Ranjbar, and G. Mori, "Stacks of convolutional restricted boltzmann machines for shift-invariant feature learning," *2009 IEEE Conf. Comput. Vis. Pattern Recognition, CVPR 2009*, pp. 2735–2742, 2009.
- [45] A. J. Majda and X. T. Tong, "Performance of Ensemble Kalman Filters in Large Dimensions,"

Digital Rocks Portal (Digital Porous Media): connecting data, simulation and community

Maša Prodanović^{1,*}, *Maria Esteva*², *James McClure*³, *Bernard C. Chang*¹, *Javier E. Santos*⁴, *Anuradha Radhakrishnan*¹, *Ankita Singh*⁵, and *Hasan Khan*⁶

¹Hildebrand Department of Petroleum and Geosystems Engineering, The University of Texas at Austin, Austin, TX, USA

²Texas Advanced Computing Center, The University of Texas at Austin, Austin, TX, USA

³Advanced Research Computing, Virginia Tech, VT, USA

⁴Center for Nonlinear Studies & Earth and Environmental Sciences, Los Alamos National Laboratory, Los Alamos, NM, USA

⁵University of New South Wales alumna, Sydney, Australia

⁶Petroleum Engineering Department, King Fahd University of Petroleum and Minerals, Dhahran, Saudi Arabia

Abstract. Digital Rocks Portal (DRP, <https://www.digitalrocksportal.org>) organizes and preserves imaged datasets and experimental measurements of porous materials in subsurface, and beyond, with the mission to connect them to simulation and analysis, as well as educate the research community. We have over 150 projects represented in more than 200 publications, and an active community that reuses the data, most recently in multiple machine learning applications for automating image analysis as well as the prediction of transport. Such automation is at the core of ability to many formation evaluation tasks in near-real time. We present benchmark datasets that have played a role in recent machine learning prediction successes in the field. We further discuss the vision for further research advances, educational materials, as well as growth and sustainability plan of this digital rock physics community resource. In particular, we are in the process of expanding into a broader repository of engineered porous materials, specifically those for energy storage and the portal will transition to Digital Porous Media (DPM).

1 Introduction

The field of digital rock physics combines imaged porous media (such as rocks and soil) to simulations and other research methods such as machine learning (ML) and data analysis to understand transport and deformation in subsurface. Applications include formation evaluation, management of groundwater resources, carbon sequestration, enhanced oil recovery, and contaminant transport [1]. Typical geological systems are composed of a broad spectrum of porous media with properties such as permeability varying by orders of magnitude within an individual system. The advances in high-resolution imaging techniques (x-ray tomography, scattered electron and optical microscopy) have provided a wealth of 2D and 3D datasets that reveal the microstructure of rocks, soil or model media on scales ranging from nanometers to centimeters, and analysis and use of such images in simulation is computationally demanding [2]. Our practical questions nevertheless require upscaling to the field scale. Therefore, efficient connection of curated digital rocks data and scalable computing and machine learning (ML) applications is necessary for applications [3].

We here describe the organization of Digital Rocks Portal (DRP), a well-adopted portal for curation and visualization of large imaged datasets of geomaterials. DRP's mission is to organize and preserve imaged datasets and experimental measurements of porous materials in subsurface, connect them to research methods. We report on our efforts in

educating the research community by organizing workshops and mini-courses in data preservation, analysis and visualization.

Deep learning methods and convolutional neural networks (CNNs) have many applications in image processing and flow prediction [4]. For this, reliable "ground truth" benchmark datasets are needed because (1) supervised deep learning methods require a large amount of validated data to train models; and (2) the capabilities of the trained classifiers must be assessed quantitatively. Applying learning algorithms to the large volume of data stored within DRP is currently rendering scientific advances. We successfully applied deep learning algorithms on predicting 3D velocity fields in porous media images [5,6]. The implementation was done in TensorFlow [7] using high performance resources (HPC) at Texas Advanced Computing Center (TACC). The work in [5] sampled a wide variety of images from DRP as well as adding a benchmark collection [8], has specifically enabled deep learning training with geologic porous media whose heterogeneity (including fractures/cracks) likely surpasses any engineered porous materials, and, should data from energy storage materials become available, the results should immediately transfer. This exemplifies a workflow that can enable future real time permeability estimation based on imaged datasets, as the computational time of a deep learning prediction is in seconds compared to hours on HPC.

Visualization algorithms of cross-sections, volumes and surfaces of 3D data (e.g. marching cubes algorithm) are well-

* Corresponding author: masha@utexas.edu

known and available in a number of advanced visualizing platforms (e.g. ParaView, MayaVi, ImageJ, Dragonfly, to name a few that are open source). However, the complexity of the pore structure and processes captured within pose a challenge in visualizing the data, both from memory and computational perspective. That said, while this challenge is meant to reuse data from geosciences and subsurface engineering, all of the concepts that it is meant to educate students about are very much applicable to any scientific visualization endeavor: for instance, in biomedical field, heart or blood vessels in a human body, are often imaged using computed tomography (or simulated based on those images) and have particulate flow (blood flow, that is) within. In addition to the materials from the recent visualization contest reusing DRP datasets, we provide Jupyter Notebooks examples visualizing a 3D velocity field as well as porous media surfaces in multi-fluid situation.

Transitioning to renewable energy from the hydrocarbon-based sources that currently meet 65% of energy demands will require significant engineering effort on several fronts: (1) mitigating the effects of air pollution with solutions such as subsurface carbon dioxide sequestration; and (2) scaling up renewable energy based on the maturation of advanced energy devices, geothermal, and other solutions. Complex microstructure is a common element for many of these physical problems. We discuss our sustainability plan that includes the paid membership fees scheme for Digital Rocks Portal, thus ensuring its financial stability, (2) strengthening our visualization and analysis services and (3) generalizing and broadening the user base of DRP to Digital Porous Media (DPM) portal to energy storage materials. Geometric approaches developed to enhance digital rock images have excellent crossover potential to other complex material structures [9]. High performance methods to enhance experimental data collection workflows are also broadly generalizable [10].

for porous media as opposed to platforms such as Mendeley Data [12], Dryad [13] or Energy Data Exchange [14] that store data of any origin. The portal is specifically equipped with tools tailored to organize, visualize, analyze, and publish digital images of porous materials, Its data model shown in Fig.1. is the foundation for curating, describing and displaying the datasets. The data model enables imaged data curation workflows including adding provenance information and metadata used for rendering the images, and organizing the dataset in relation to its corresponding research activity such as observations, experiments, and simulations. Thus, the model is the basis for the datasets representations on the landing pages that displays provenance as material entities (samples) and processes (experimental or simulation) from which data derives. This tree like representation, which was evaluated through user studies [15], facilitates understanding of and access to complex and large datasets [16]. Example projects are shown in Fig.2. and Fig.3.

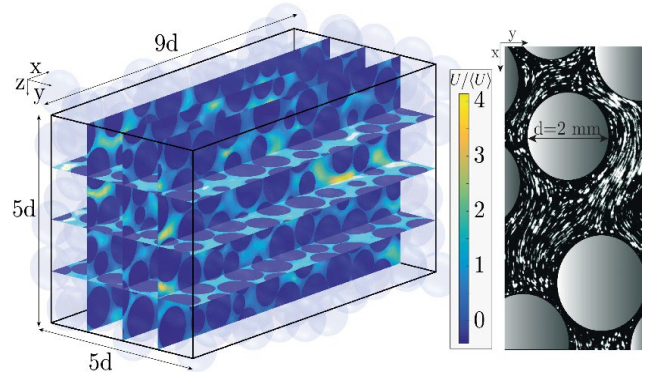
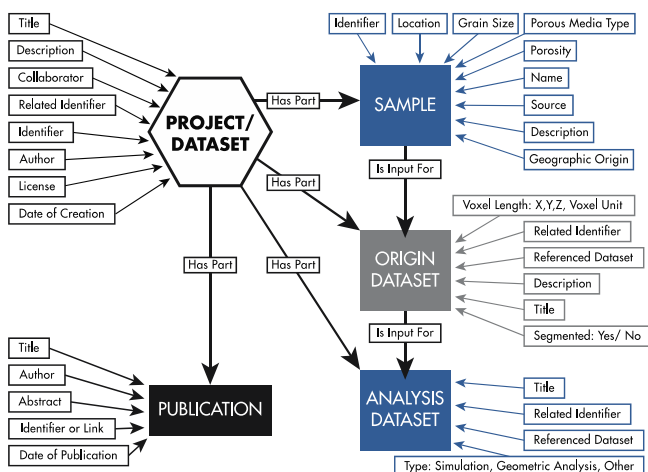


Fig.2. Example DRP project 3D experimental fluid velocity field within a sphere packing (model granular or soil structure) obtained particle velocimetry [17]. To our knowledge, this is the only open 3D velocimetry dataset, and has been the bases for the winning visualization entry in DRP visualization contest (see below).



2 Portal organization

Launched in September 2015 the DRP [11] is an established data repository, trusted by the community. DRP is specialized

Fig.1. DRP Data model is foundation for the database linking web content and files on HPC storage.

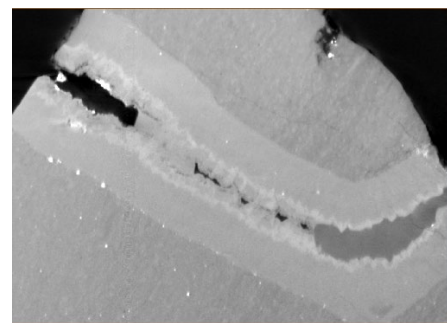


Fig.3. Example DRP project [18] with 3D x-ray microtomography images as well as XRF mineral maps of a partially mineralized vein contained from a core sample (depth of ~10,400 ft) in the Upper Wolfcamp formation. The sample was studied as part of the effort of the Department of Energy's Center for Nanoscale Controls on Geologic CO₂.

DRP does not assume a specific image format at this point. This is because subsurface porous media heterogeneity requires a variety of imaging modalities ranging from microscopy to x-ray microtomography to medical computed tomography with no commonly accepted data formats. As a result, DRP has built-in capabilities for translating and visualizing raw data after import, which distinguishes it from other imaged data repositories.

Data curation is assisted through the publication pipeline interface that carefully guides users through the process. Metadata collected during this process is essential for full documentation of the dataset. Images by themselves contain structural information collected at a certain time, but not more than that and this step is essential. Fig.4. and Fig.5. exemplify this information for an example project. Note that only part of the information collected is shown for brevity. Prior to publication and before assigning a digital object identifier (DOI), the datasets are verified for completeness and accuracy by a live curator, again unlike many data portals that allow upload of compressed archives. Current list of curators includes the majority of the authors of this publication and we are open to volunteers. DOIs are provided through The University of Texas Libraries subscription to DataCite Fabrica [19].

Particulate straining in carbonate proxy

Fig.4. Part of the metadata collected for an example dataset [20] including voxel length that relates the image to sample physical size.

Fig.5. Second part showing successful “ingestion” of two datasets of the same project as shown in Fig.4. ([20]) that are part of the same experiment (as proved by the image cross-sections. Action button allows download, shows a video of all slices (in 3D), and

basic image statistics such as histogram. “Action” button also has a button that allows connection to HPC cluster on TACC that opens ParaView for visualization. This software stack is however currently being updated.

DRP is implemented within the reliable HPC environment deployed and maintained by Texas Advanced Computing Center, and data storage is supported by The University of Texas System Research Cyberinfrastructure (UTRC) in the storage resource Corral. This infrastructure assures data security and persistence, interoperability with different HPC systems for visualization and analysis (TACC Analysis Portal, [21] currently on Lonestar6 and Stampede2 clusters) and continuing operation of the software stack, and thus it contributes to the portal’s sustainability.

3 Portal impact and user engagement

3.1. Metrics

Since 2015, DRP has published 154 projects and 200 related publications [22], ranging in size from 10MB to 728GB. DRP accepts international contributions. Our current query country of the institutional affiliation of the first author of the current DRP projects we find 48% from the U.S., 18.2% from UK, 9.5% from Australia, and the remainder from China, Belgium, Brazil, Canada, South Korea, Japan, Russia and Switzerland.

Since its launch, we have been keen in promoting DRP and in understanding its impact. We implemented Search Engine Optimization (SEO) strategies such as using schema.org vocabularies and Google-friendly metadata in the repository landing page. Using Google Analytics, we monitor an increase in total visits over the years as well as consistent spikes in usage, which coincide with academic events that we undertake (workshops, presentations, publications). We also implemented a data download count (of individual datasets) to each of our dataset pages: it is available under link “Usage Information” embedded in each project landing webpage. Through Google Scholar Alerts we follow mentions and citations to the repository and to individual datasets.

3.2 Digital Object Identifiers (DOIs) and increasing visibility of data

Journal publications have had DOIs for a long time, but providing them for research data or code is a relatively new adoption thanks to efforts such as Findable, Accessible, Interoperability, and Reusable (FAIR) data efforts launched in 2016 [23]. We have found that authors have variable or incomplete referencing styles for datasets in papers, whether they are referencing their own data or reusing someone else’s. Many, for instance, include only the name of the platform where the data is posted. Note that including the dataset DOI and a proper reference improves the findability, as **search engines presently do not find data as efficiently as they do papers (if at all)**. One reason for this is that datasets come in variable formats and are not easily searchable for information the way .pdf or text formats are. We thus next describe strategies that readers can use to improve other authors finding their data.

Increasingly, journals request that you publish your paper along with the data that supports your findings. For example, the AGU journals follow this FAIR data practice. Curating data for publication demands significant efforts on the part of

the researchers that have to organize and describe it so that others can recreate their results or reuse the data for a different purpose. At the same time, data publications can bring significant rewards in terms of citations and exposure of your work. To help you boost the discoverability and consequently the reuse of your data there are some basic strategies that you can follow:

To enhance discoverability:

- Add all the information (metadata) that DRP asks for, including your ORCID [24] ID (that uniquely identifies you in case you change affiliation or someone else shares your name) if you have it, and who funded your project.
- In your data description use terms that you consider people will search for when looking for this type of data. Highlight the unique characteristics of your dataset and suggest how your data could be useful to others and for what purposes.
- All these metadata are indexed by search engines such as Google, improving the possibilities that your data is discovered by broader audiences.

To facilitate data reuse:

- Add documentation in the form of readme files or reports to clearly explain how you obtained and processed the data. This stimulates the understandability of your publication and consequent data reuse.
- You can include code snippets as “Non-image data” to your datasets, or better yet, publish the code on GitHub and add it as a related publication in DRP.
- If you have them prior to publishing the data, add papers and proceedings that discuss the data as related publications. After your dataset is published you can request DRP curators to add your new publications by sending an email to masha@utexas.edu.

3.3 Newsletters, project highlights and educational material

Engaging the research community is necessary if the data will become reused and thus actively contribute to science and engineering. This can be done through (classical) conference presentations, but also contests, newsletters and social media activities that promote data sharing, and reuse, data cyberinfrastructure, and overall data education through the published materials.

To that end, we launched newsletters in October 2020 and have since published them at the rate of two to three per academic semester. See [22] for links to all newsletters as well as links to a various news articles written about DRP. YouTube playlist on Digital Rocks Portal Visualization [25] contains various visualizations of the datasets, as well as a growing list of interviews we recorded to highlight projects on DRP.

Data reuse contests is another activity whose goal was to stimulate engagement and demonstrate the research potential of these datasets. organized a successful a virtual visualization mini-course, followed by a visualization challenge in early 2021 with three categories (video, static image and 3D printed porous microstructure). This is described in the next section.

3.4. Visualization mini course and contest

In October 2020, a porous media visualization competition was organized which consisted of a mini course (taught using Jupyter Notebooks), followed by a challenge with three categories with monetary awards to promote data reuse and create visualization templates for porous materials (known for their complexity). The task was to reuse any 3D dataset from the DRP to create a static image, video, or 3D printed visualization. Porous media are challenging to visualize due to complexity of pore/grain/fluid surfaces and interfaces, and this creates a resource for those who wish to learn advanced 3D visualization. [Resources](#) and materials were stored in DRP to help the participants. The events were sponsored by [Southern Big Data Hub](#), [Object Research Systems](#), [Kitware](#) and [Dassault Systèmes](#). Tables 1 through 3 show the list of projects and the datasets that were reused from DRP.

Table 1. Winners of the static image category

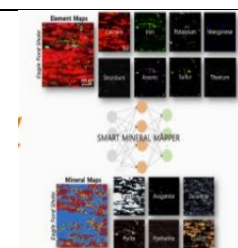
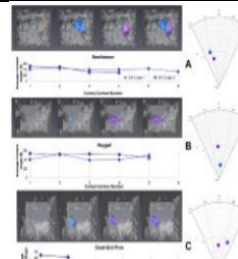
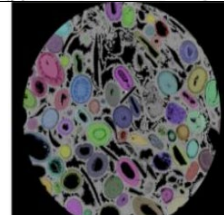
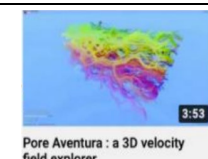
Title & winner	Dataset reused	Visualization
Smart mineral mapper, Julie Kim , Princeton University	Eagle Ford shale: synchrotron-based element and mineral maps	
Contact Angle Evolution, Laura Dalton , West Virginia University and National Energy Technology Laboratory	Bentheimer and nugget residual saturation micro-computed tomography data	
Identifying savonnieres carbonate oolites, Miral Tawfik , Pennsylvania State University	Savonnieres carbonate	

Table 2. Winners of the video category

Title & winner	Dataset reused	Visualization
Pore Aventura: 3D velocity field explorer, Dr. Mathieu Souzy, University of Twente	Experimental 3D velocity field in random sphere packing	

Flow visualization in porous media, Bin Wang , Louisiana State University	Experimenta l 3D velocity field in random sphere packing	
Fluid displacement in a fracture, Honggeun Jo , The University of Texas at Austin	Fractures with variable wettability and roughness	
Belgian fieldstone pores and solids, David Rippner , University of California, Davis	Belgian fieldstone	

Table 3. Winners of the 3D print category

Title & winner	Dataset reused	Visualization
Sphere pack juxtaposed with the non-wetting fluid at 40% saturation, Javier Santos , The University of Texas at Austin	Finney packing of spheres	
Visualization of sand/pore and a sphere packing surface, Yanbin Gong, University of Wyoming	Uniform quartz-Silver nanoparticle injection experiment and Finney packing of spheres	
Visualization of sandstone and carbonate pore space surface, Dr. Lingyun Kong, Energy and Environment Research Center	Doddington sandstone and Massangis Jaune carbonate	

4 Benchmark datasets

In order to push the state of the art for machine learning (ML) forward and provide comparisons between ML techniques, it would be very useful to have a large number of labeled data (the results of expensive full-physics simulations) to build models that work in the complexity of real-world pore structures. In other fields, large and diverse datasets [26,27] have sparked revolutions in ML by providing a common focal point that allows techniques to be compared against one another. Broadly speaking, this can be attributed to two factors. Firstly, unprecedented size and scale of data pushes the state of the art forward. Secondly, the public availability of these datasets makes easier the comparison of different modeling techniques, so that the relative advantages and disadvantages of different approaches can be more clearly

assessed. As an example, in porous media, the choice of fluid solver and numerical implementation thereof is a confounding variable with unknown effects on ML model characteristics.

We are working for DRP to become the a resource where benchmark tests that represent challenging, complex porous media in the context of image analysis, 3D simulation, empirical functional forms, and machine learning can be found. This diversity should include properties such as porous media lithology, boundary conditions, geometric resolution, and physical processes simulated. A large-scale collection of pore-scale data is critical for developing advanced ML algorithms that generalize to unseen samples from many real-life sources. Additionally, it (1) fosters advancement in our understanding of microscopic physics, (2) enables creation of new upscaling relationships, (3) provides a point of comparison to benchmark other simulators of physical processes, and (4) guides ML, which is still an up-and-coming field.

To that end, we have recently added a catalog of 3D geometries [8,28], as well as the companion collection of simulations [29,30], and structural properties of samples. The dataset includes 1736 flow and electrical simulation results on 217 digital samples, which required more than 500 core years of computation time. This data can be used for many purposes, such as constructing empirical models, validating new simulation codes, and developing machine learning algorithms that closely match the extensive purely-physical simulation. The dataset consists of simulations based on 217 digital rock samples, each containing two different domain sizes 256^3 and 480^3 . For each digital sample, there are five nanoconfinement simulations, one fluid flow simulation, ten geometric features, electrical conductivity data, topological descriptors, and .png files visualizing cross-sections of the 3D data. The companion SCA paper (Chang et al.) discusses how the simulations are used for training neural networks for prediction of electrical properties.

There are also benchmark datasets posted by other authors in the area of image analysis algorithms. Three sandstone and carbonate collections [31–33] have been used for improving resolution of micro-tomography images, especially in the presence of microporosity. Further, there is an extensive dataset [34] for comparison of both traditional and ML image denoising algorithms.

5 Visualization examples

We created two workflows for 3D visualization of surfaces and vector (velocity) fields and publish them in conjunction with this paper on GitHub of Dr. Prodanovic *(for the purpose of the review, they are available as a pdf alongside this manuscript)*. The workflows download and use the datasets from the portal.

In these examples we relied on Python-based PyVista visualization software and provide both regular Python code (that is somewhat more robust, as it allows PyVista to open a separate window with the plot) as well as Jupyter Notebook. Jupyter Notebooks are excellent teaching tool and embed the results into web browser. That makes them versatile, but an extension is needed to make it work. The figures below show

a glimpse into what is available within the worksheets; they can be adjusted to any other data on DRP.

Notably, while these worksheets are currently set up to download the data and visualize it, **they also work on TACC Visualization and Analysis portal [21], in particular on Lonestar6 HPC environment that can access DRP data storage directly without any download, and can analyze large datasets beyond the capability of an individual workstation.**

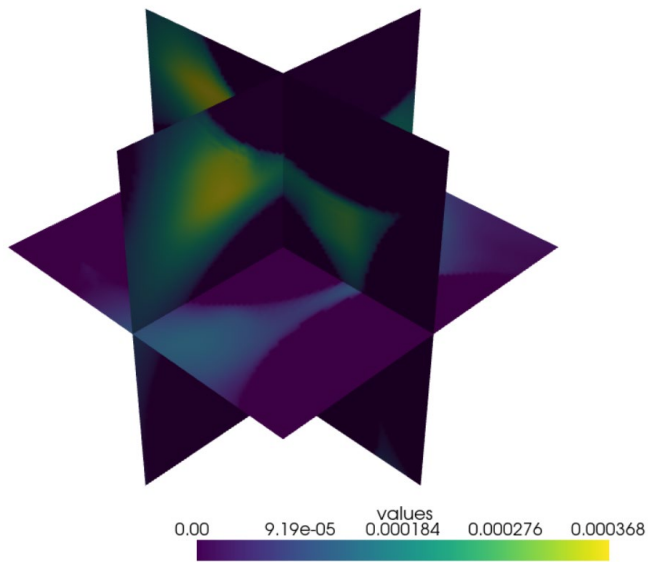


Fig. 6. Subset of the entire DRP velocimetry dataset from Fig.2 visualizing absolute values of velocities in PyVista.

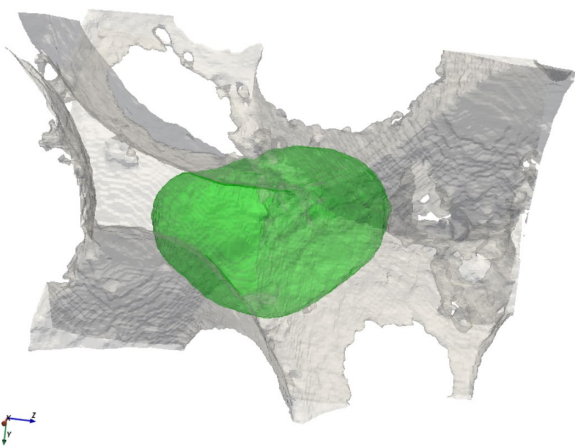


Fig. 7. Surface visualization in PyVista of an oil blob (in transparent green) within a Ketton limestone sample (transparent gray). The high resolution x-ray microtomography experimental data [35] was used in the example.

6 Related software

The data in Digital Rocks Portal can be characterized and visualized using various data analysis software, and previous section provides one example. Beyond that, open source

software such as ImageJ, ParaView, Visit or DragonFly is available, as well as commercial options (e.g. MATLAB, PerGeos).

Transport properties of porous materials, however, require simulation with different type of solvers. If segmented (binarized) images are available, then images can be direct input into simulation that produces a scalar or vector field of interest. The following table includes some open source example libraries.

Table 4. Example open source simulation software using DRP data.

Software	Application / method	Platform
LBPM [36]	Velocity fields, multiphase flow, lattice Boltzmann method	Unix, Parallel, C/C++ and MPI
Palabos [37]	Velocity fields, multiphase flow, lattice Boltzmann method	Unix, Parallel, C/C++ and MPI
MPLBM-UT [38]	Pre-processing and post-processing tools for single- and multi- phase flow with Palabos	Windows/Unix, Python
LSMPQS [39]	1.0 Capillarity dominated fluid displacement, level set method	Unix, Serial C & Fortran + OpenMPI
NIST Laplace Solver [40]	Generalized Laplace Equation Solver (e.g. utilized for el. conductivity)	Unix, Parallel
PoresPy [41]	Image analysis and pore network extraction, many algorithms	Unix/Windows, Python, Serial
OpenPNM [42,43]	Pore network modeling (extract network with PoresPy)	Unix/Windows, Python, Serial

7 Sustainability model

Sustainability is understood as a combination of technical and administrative strategies to ensure that users can rely on ongoing data infrastructure services that promote research innovation. While we support open science and specifically open data, neither is unfortunately free and a business model has to ultimately be developed for sustainability. The portal is on the way to scale up to a go-to location for benchmark datasets, and as such cannot be maintained in an ad-hoc manner and requires consistent financing to provide required services.

7.1. User fees

We formulated a business plan and begin adoption in 2021. Until that point users publishing data in DRP were not charged any fees as initial development (2015-2018) was supported by an NSF grant, and to this day rather limited support is available through Digital Porous Media Industry Affiliate Program at The University of Texas at Austin. In May and June 2021 DRP initiated a request for comments about establishing a funding model based on a) one-time publication fees or b) a DRP subscription plan to start in September of 2021. The community discussion was initiated via the DRP newsletter to all users (available on [22]) as well as through personal and email communications to the biggest DRP data providers. Documentation on DRP user agreement changes [44] has complete details of the proposed fee structure. Responses were publicly posted without personal identifiable information in DRP newsletter from July 13, 2021, linked to [22]. Five groups that publish regularly expressed support for the fee structure after the necessity was explained. The push back from the rest of the researchers came from the fact that they do not have open data fees built into their budgets. The fee structure is in Table 2 and the new user agreement is available on [11].

Table 5. The user fee structure implemented in September 2021.

Individual (one time per project)	< 2 GB	2-500 GB	500 GB – 1 TB
Open data publication fee	Free	\$1,500	\$ 3,000
Institutional membership (annual)	< 500 GB	500 GB - 1TB	1 – 3TB
Academic/non-profit	\$ 5,000	\$ 7,500	\$ 10,000
Company/private	\$ 7,500	\$ 10,000	\$ 12,500

7.2. Donations and sponsorships

Anyone can donate to or support Digital Rocks Portal: this is tax-deductible and easily done via credit card using UT Austin’s Giving platform. Contributions of \$100 or more are thanked with a promotional mug, mouse pad or a calendar. Table 6 below provides details on sponsorship levels.

Table 6. Donation and sponsorship levels.

Level	Type	Details
\$20+	Any time giving	Tax deductible and easily done via credit card .
\$500	Newsletter sponsor	You and/or your company will be featured in next newsletter.
\$1,500	Project sponsor	The donation will: (1) make one of the Folk McBride high resolution thin sections examples available for research, (2) permanently place a thank-you note to you/your company on the project landing page, and (3) make you an owner of promotional items with that

		project imagery. Check this presentation for suggested datasets. Any other (existing or new) project can be sponsored under the same terms.
\$3,000 or more	Student/fellow sponsor	Sponsor a student fellow (suggested \$3000-5000) who will help upload data from partner institutions and research groups and create advanced visualizations to accompany them in the semester following the donation.

7.3. Expanding the user base

Last but not the least, many energy storage and materials engineering samples are porous and require image analysis, simulation and ML techniques that are comparable to digital rocks physics. Technology transfer and change of the name to Digital Porous Media is imminent.

Acknowledgements

Foundational development of this portal was obtained through the National Science Foundation, NSF EAR CAREER grant 1255622 "Advanced interface methods in heterogeneous porous materials: a multi-disciplinary and multi-scale framework" as well as NSF EarthCube IA 1541008 from 2015-18. Since the end of 2018, limited support is available through the Digital Porous Media (formerly Digital Rock Petrophysics) Industry Affiliate Program at the University of Texas at Austin. All are gratefully acknowledged.

Programming support has been provided by the Texas Advanced Computing Center (Keith Strmiska) and the administrative support by Center for Petroleum and Geosystems Engineering (now Center for Subsurface Energy and the Environment).

References

- [1] M.J. Blunt, Multiphase flow in permeable media: a pore-scale perspective, Cambridge University Press, Cambridge, United Kingdom ; New York, NY, 2017.
- [2] A. Mehmani, R. Verma, M. Prodanović, Pore-scale modeling of carbonates, Marine and Petroleum Geology. 114 (2020) 104141. <https://doi.org/10.1016/j.marpetgeo.2019.104141>.
- [3] Y.D. Wang, M.J. Blunt, R.T. Armstrong, P. Mostaghimi, Deep learning in pore scale imaging and modeling, Earth-Science Reviews. 215 (2021) 103555. <https://doi.org/10.1016/j.earscirev.2021.103555>.
- [4] A. Krizhevsky, I. Sutskever, G.E. Hinton, ImageNet Classification with Deep Convolutional Neural Networks, in: F. Pereira, C.J.C. Burges, L. Bottou, K.Q. Weinberger (Eds.), Advances in Neural Information Processing Systems 25, Curran Associates, Inc., 2012: pp. 1097–1105. <http://papers.nips.cc/paper/4824-imagenet-classification-with-deep-convolutional-neural-networks.pdf> (accessed August 15, 2019).
- [5] J.E. Santos, Y. Yin, H. Jo, W. Pan, Q. Kang, H.S. Viswanathan, M. Prodanović, M.J. Pyrcz, N. Lubbers, Computationally Efficient Multiscale Neural Networks

- Applied to Fluid Flow in Complex 3D Porous Media, *Transp Porous Med.* (2021). <https://doi.org/10.1007/s11242-021-01617-y>.
- [6] J.E. Santos, D. Xu, H. Jo, C.J. Landry, M. Prodanović, M.J. Pyrcz, PoreFlow-Net: a 3D convolutional neural network to predict fluid flow through porous media, *Advances in Water Resources.* (2020) 103539. <https://doi.org/10.1016/j.advwatres.2020.103539>.
- [7] TensorFlow, TensorFlow. (n.d.). <https://www.tensorflow.org/> (accessed August 15, 2019).
- [8] J. Santos, Y. Yin, M. Prodanović, H. Khan, N. Lubbers, 3D Collection of Binary Images, (2021). <https://doi.org/10.17612/NXGK-K611>.
- [9] Y. Niu, Y. Da Wang, P. Mostaghimi, J.E. McClure, J. Yin, R.T. Armstrong, Geometrical-Based Generative Adversarial Network to Enhance Digital Rock Image Quality, *Phys. Rev. Applied.* 15 (2021) 064033. <https://doi.org/10.1103/PhysRevApplied.15.064033>.
- [10] J.E. McClure, J. Yin, R.T. Armstrong, K.C. Maheshwari, S. Wilkinson, L. Vlcek, Y. Da Wang, M.A. Berrill, M. Rivers, Toward Real-Time Analysis of Synchrotron Micro-Tomography Data: Accelerating Experimental Workflows with AI and HPC, in: J. Nichols, B. Verastegui, A. ‘Barney’ Maccabe, O. Hernandez, S. Parete-Koon, T. Ahearn (Eds.), *Driving Scientific and Engineering Discoveries Through the Convergence of HPC, Big Data and AI*, Springer International Publishing, Cham, 2020: pp. 226–239. https://doi.org/10.1007/978-3-030-63393-6_15.
- [11] M. Prodanovic, M. Esteva, M. Hanlon, G. Nanda, P. Agarwal, Digital Rocks Portal, (2015). <https://doi.org/10.17612/P7CC7K>.
- [12] Mendeley Data, (n.d.). <https://data.mendeley.com/> (accessed September 1, 2019).
- [13] Dryad, (n.d.). <http://datadryad.org/> (accessed February 22, 2017).
- [14] Energy Data Exchange (EDX), (n.d.). <https://edx.netl.doe.gov/> (accessed February 19, 2017).
- [15] S. Sweat, A. Ranganath, M. Esteva, M. Prodanović, User Guided Design: Building Confidence in Engineering Data Publication, in: University of Texas at Austin, Denver, CO, 2016. <https://doi.org/10.15781/T27940X4W>.
- [16] S. Fuchs, D. Crandall, M. Gill, J. Moore, B. Kutchko, Foamed Cement API RP 10B-4, (2018). <https://doi.org/10.17612/p7gd4q>.
- [17] M. Souzy, H. Lhuissier, Y. Méheust, T. Le Borgne, B. Metzger, Experimental 3D Velocity Field in Random Sphere Packing, (2020). <https://doi.org/10.17612/HDP8-0149>.
- [18] C. Peters, S. Hajirezaie, J. Kim, D. Crandall, Mineralized fracture in a mudrock shale, (2021). <https://doi.org/10.17612/P4WH-W011>.
- [19] DataCite Fabrica, DataCite Fabrica. (n.d.). <https://doi.datacite.org/> (accessed May 13, 2022).
- [20] H. Khan, M. Prodanovic, D. Dicarolo, Particulate straining in carbonate proxy, Digital Rocks Portal, 2018. <https://doi.org/10.17612/P7D96T>.
- [21] TACC Visualization Portal, (n.d.). <https://vis.tacc.utexas.edu/>.
- [22] Digital Rocks Portal About section, (n.d.). <https://www.digitalrockportal.org/about/>.
- [23] M.D. Wilkinson, M. Dumontier, I.J. Aalbersberg, G. Appleton, M. Axton, A. Baak, N. Blomberg, J.-W. Boiten, L.B. da Silva Santos, P.E. Bourne, J. Bouwman, A.J. Brookes, T. Clark, M. Crosas, I. Dillo, O. Dumon, S. Edmunds, C.T. Evelo, R. Finkers, A. Gonzalez-Beltran, A.J.G. Gray, P. Groth, C. Goble, J.S. Grethe, J. Heringa, P.A.C. ‘t Hoen, R. Hooft, T. Kuhn, R. Kok, J. Kok, S.J. Lusher, M.E. Martone, A. Mons, A.L. Packer, B. Persson, P. Rocca-Serra, M. Roos, R. van Schaik, S.-A. Sansone, E. Schultes, T. Sengstag, T. Slater, G. Strawn, M.A. Swertz, M. Thompson, J. van der Lei, E. van Mulligen, J. Velterop, A. Waagmeester, P. Wittenburg, K. Wolstencroft, J. Zhao, B. Mons, The FAIR Guiding Principles for scientific data management and stewardship, *Scientific Data.* 3 (2016) 160018. <https://doi.org/10.1038/sdata.2016.18>.
- [24] ORCID, (n.d.). <https://orcid.org/> (accessed May 14, 2022).
- [25] Digital Rocks Portal: Visualization - YouTube, (n.d.). <https://www.youtube.com/playlist?list=PL7QcRCNp33XA7B BvpNbwDZjLB-mezkUu> (accessed May 16, 2022).
- [26] ImageNet, (n.d.). <https://image-net.org/index> (accessed October 20, 2021).
- [27] Quantum-Machine.org: Home, (n.d.). <http://quantum-machine.org/> (accessed May 16, 2022).
- [28] J.E. Santos, M.J. Pyrcz, M. Prodanović, 3D Dataset of binary images: A collection of synthetically created digital rock images of complex media, *Data in Brief.* 40 (2022) 107797. <https://doi.org/10.1016/j.dib.2022.107797>.
- [29] J. Santos, Chang, Bernard, Gigliotti, Alex, Kang, Qinqun, Lubbers, Nicholas, Viswanathan, Hari, Prodanovic, Masa, 3D Dataset of Simulations, (2021). <https://doi.org/10.17612/93PD-Y471>.
- [30] J.E. Santos, Chang, Bernard, Gigliotti, Alex, Y. Yin, W. Song, Prodanovic, Masa, Q. Kang, Lubbers, Nicholas, H.S. Viswanathan, A Dataset of 3D Structural and Simulated Transport Properties of Complex Porous Media, *Nature Scientific Data.* Under Review (n.d.).
- [31] Y.D. Wang, R. Armstrong, P. Mostaghimi, A Diverse Super Resolution Dataset of Digital Rocks (DeepRock-SR): Sandstone, Carbonate, and Coal, (2019). <https://doi.org/10.17612/S3M9-E024>.
- [32] Y. Niu, Armstrong, Ryan, Mostaghimi, Peyman, Unpaired super-resolution on micro-CT sandstone by using cycle-consistent generative adversarial network, (2020). <https://doi.org/10.17612/VZTT-YX38>.
- [33] N. Alqahtani, P. Mostaghimi, R. Armstrong, A Multi-Resolution Complex Carbonates Micro-CT Dataset (MRCCM), (2021). <https://doi.org/10.17612/3T36-Q704>.
- [34] M. Tawfik, Z. Karpyn, S.X. Huang, scCO₂-Brine-Glass Dataset for Comparing Image Denoising Algorithms, (2022). <https://doi.org/10.17612/A1QA-2A25>.
- [35] K. Singh, M.J. Blunt, High resolution X-ray micro-tomography datasets for in-situ effective contact angle analysis in carbonate rocks, (2018). <https://doi.org/10.17612/P7D95F>.
- [36] J.E. McClure, Z. Li, M. Berrill, T. Ramstad, The LBPM software package for simulating multiphase flow on digital images of porous rocks, *Comput Geosci.* 25 (2021) 871–895. <https://doi.org/10.1007/s10596-020-10028-9>.
- [37] Palabos CFD and Complex Physics, (n.d.). <http://www.palabos.org/> (accessed January 16, 2014).
- [38] J.E. Santos, A. Gigliotti, A. Bihani, C. Landry, M.A. Hesse, M.J. Pyrcz, M. Prodanović, MPLBM-UT: Multiphase LBM library for permeable media analysis, *SoftwareX.* 18 (2022) 101097. <https://doi.org/10.1016/j.softx.2022.101097>.
- [39] R. Verma, M. Prodanovic, Level Set Method based Progressive Quasi-Static (LSMPQS) software 1.0, 2018. <https://github.com/rahulverma88/lsmpps-1.0>.
- [40] National Institute of Standards and Technology, NIST. (n.d.). <https://www.nist.gov/> (accessed May 17, 2022).
- [41] J.T. Gostick, Versatile and efficient pore network extraction method using marker-based watershed segmentation, *Phys. Rev. E.* 96 (2017) 023307. <https://doi.org/10.1103/PhysRevE.96.023307>.
- [42] OpenPNM | Home | An Open Source Pore Network Modeling Package, (n.d.). <http://openpnm.org/> (accessed November 1, 2015).
- [43] J. Gostick, M. Aghighi, J. Hinebaugh, T. Tranter, M.A. Hoeh, H. Day, B. Spellacy, M.H. Sharqawy, A. Bazylak, A. Burns, W. Lehnert, A. Putz, OpenPNM: A Pore Network Modeling

Package, *Computing in Science & Engineering*. 18 (2016)
60–74. <https://doi.org/10.1109/MCSE.2016.49>.

[44] Digital Rocks Portal User Agreement Documentation, (n.d.).
<https://www.digitalrocksportal.org/user-agreement-changes/>.

Pore-scale Analysis of CO₂-brine Displacement in Berea Sandstone and Its Implications to CO₂ Injectivity

Guangyuan Sun*, Zhuang Sun, Andrew Fager and Bernd Crouse

Dassault Systèmes, San Francisco, USA

Abstract. For storage in deep saline formations, where CO₂ is injected into the pore spaces of rocks previously occupied by saline groundwater (brine), relative permeability is a key input parameter for predictive models. CO₂ injectivity is considered to reach the maximum value at the CO₂ endpoint relative permeability when brine saturation becomes irreducible. The objective of this study is to investigate the effect of viscosity ratio, interfacial tension and wettability on relative permeability during CO₂-brine drainage. A multiphase lattice Boltzmann model (LBM) is employed to numerically measure pore-scale dynamics in CO₂-brine flow in the sample of Berea sandstone. CO₂/brine with interfacial tension from 30 to 45 mN/m and viscosity ratio from 0.05 to 0.17 (the range of values expected for typical storage reservoirs conditions) are carried out to systematically assess the influence on the relative permeability curves. Although CO₂ storage in sandstone saline aquifers is predominantly water wet, there are contradictory results as to the magnitude of the contact angle and its variation with fluid conditions. Therefore, the range of wetting conditions is studied to gain a better insight into the effect of wettability on supercritical CO₂ displacement. In this study, it is observed that interfacial tension variations play a trivial impact while both of viscosity ratio and wettability are likely to have a significant effect on relative permeability curves under representative condition of storage reservoirs. We also perform a near-wellbore scale geomechanics analysis to investigate the impact of relative permeability on CO₂ injectivity. The result shows that water-wet condition facilitates the CO₂ injection when there is no fracture induced.

1 Introduction

It is well accepted that global warming is due to the increase in atmospheric concentrations of greenhouse gases, such as carbon dioxide (CO₂). To achieve mid- and long-term targets in reducing CO₂ emissions and their intensity, various mitigation approaches are explored, foremost among them being CO₂ capture, utilization and storage (CCUS), which will play a significant role in the first half of this century if reduction targets are to be met [1-2]. Current methods to reduce atmospheric emissions of anthropogenic greenhouse gases often include the capture of CO₂ and subsequent injection into deep subsurface formations [3-5]. Such injection scenarios involve multiple fluids and lead to multiphase flow problems. Common approaches involve injection of CO₂ into deep formations, such that the CO₂ will be under sufficiently high pressure and temperature to remain in a supercritical state. For temperatures T and pressures P above the critical point ($T_c = 31.1^\circ\text{C}$ and $P_c = 7.38$ MPa), the injected CO₂ will have significantly higher density than that of gaseous CO₂, although still less than that of the resident formation water, usually brine. The viscosity of the CO₂ is also significantly less than that of the brine. Therefore, migration of the CO₂ away from the injection well involves both gravity override and unfavorable mobility ratio.

The potential for CO₂ storage in saline aquifers largely depends on the storage capacity and the CO₂ injectivity of the site. The storage capacity of aquifers is governed by aquifer

volume, porosity, and, most importantly, volumetric as well as microscopic displacement efficiencies. Injectivity, on the other hand, is governed by permeability, relative permeability, fracture characteristics of the rock, and rock compressibility [6].

The primary independent variables on multiphase flow, other than the rock structure, are pressure, temperature and salinity. The fluid properties such as viscosity, density, contact angle and interfacial tension can be described as secondary variables, depending on the first ones. Relative permeability, irreducible water and residual CO₂ saturations may be considered as tertiary variables, as these are in turn controlled by the fluid properties [7].

The viscosity ratio is defined as the ratio of the viscosity of the non-wetting phase to the wetting phase. The effect of viscosity ratio on relative permeability is not clear, as the observations reported in the literature are contradictory. Relative permeability is shown to be both independent of [8] or to increase with viscosity ratio [9-11] in experimental oil/water systems. However, Lefebvre du Prey et al. [12] showed that for a high viscosity ratio, the relative permeability of the lower viscosity fluid significantly decreases during drainage. Downie and Crane [13] suggest that a subsequent decrease in viscosity ratio does not return the relative permeability to its original value, thus concluding that viscosity ratio is not the only factor to change relative permeability. Bachu and Bennion [7] found that an increase of interfacial tension or a decrease in the viscosity ratio brings about similar changes of relative permeability of brine, irreducible water and residual CO₂ saturations that is,

* Corresponding author: Guangyuan.SUN@3ds.com

increasing relative permeability and decreasing residual saturations.

Interfacial tensions for the CO₂-brine system typically range from 25 to 55 mN/m at the conditions for subsurface storage [14]. The data to investigate the effect of interfacial tension on relative permeability for the CO₂-brine system is limited. Bennion and Bachu [7] measured relative permeability curves of drainage and imbibition with interfacial tensions in the range 19.8 to 56.2 mN/m in a water-wet sandstone. Unlike the oil-brine system, a significant increase in permeability is observed for decreasing interfacial tension. The imbibition curves become more linear with decreasing interfacial tension, suggesting there is an increase in total relative mobility and the flow at low interfacial tension behaves miscible. Both endpoint permeability of CO₂ and residual CO₂ saturation increase as interfacial tension decreases. However, they also suggested that the effects of viscosity ratio and interfacial tension cannot be separated, as the viscosity ratio simultaneously increases (0.02, 0.05 and 0.1) as interfacial tension decreases (56, 34, 20 mN/m). The discrepancy about the influence of interfacial tension could potentially result from the low viscosity ratio of the CO₂-brine system ($\ll 1$) as opposed to the high viscosity ratio of the oil-water system ($\gg 1$) [15]. The oil-water system is much more strongly controlled by viscous forces, which have the effect of decreasing the influence of interfacial tension on distribution of the wetting and non-wetting fluids.

For CO₂ storage in sandstone saline aquifers, the reservoirs under consideration are expected to be predominantly water-wet [16-18] but the results are contradictory as to the magnitude of the contact angle and its variation with fluid conditions. Espinoza and Santamarina [16] observed that quartz and calcite in CO₂-brine system is strongly water-wet with no impact of changing pressure and a weak dependence on salinity up to 3.5M NaCl. Chiquet et al. [19] have also observed the system to be water-wet on quartz with little impact of both pressure and salinity from atmospheric up to 10 MPa pressure and for 0.01-1M NaCl solutions. However, a transition was observed from water- to intermediate-wet with increasing CO₂ pressure and NaCl and the system appeared to be mixed-wet across the entire range of conditions during imbibition. In microfluidic experiments with silica micromodels, Kim et al. [17] found contact angles ranging from water- to mixed-wet for the supercritical CO₂-brine system, as the salinity increases from 0.01 to 5M NaCl.

In this work, we present the results of a numerical study that carefully characterizes relative permeability of CO₂-brine in Berea sandstone using the steady-state method. We study the effect of key fluid properties (viscosity ratio, interfacial tension and wettability) on drainage displacement of brine by CO₂ injection at different flow conditions of reservoir. We also perform a near-wellbore scale geomechanics analysis to investigate the impact of relative permeability on CO₂ injectivity.

2 Measurements and procedure

In this section, we present detailed information regarding the rock sample, flow conditions, and simulation setup and procedure used in this study.

2.1 Micro-CT imaging and processing

A Berea sandstone sample was selected in the study. Micro-CT scans were carried out on a cylindrical core sample of 5 mm inch diameter and 10 mm inch length to acquire 3D images of the pore structure with resolution of 2.02 μ m/voxel. As the attenuation of X-rays within the sample are associated to the material density, the micro-CT scans provide grey-scale images with color values related to the sample material (Figure 1 left). The resulting 3D image was denoised using typical image processing techniques including contrast enhancement and low-pass filtering (Figure 1 middle). Threshold segmentation was applied resulting in a binary image (Figure 1 right) suitable to be used as input to the numerical simulations. The resolved porosity is 15.7% and an absolute permeability of 235 mD was obtained from single-phase flow simulation. An imaging domain of 500 \times 500 \times 500 voxels is chosen for the multi-phase flow simulations.

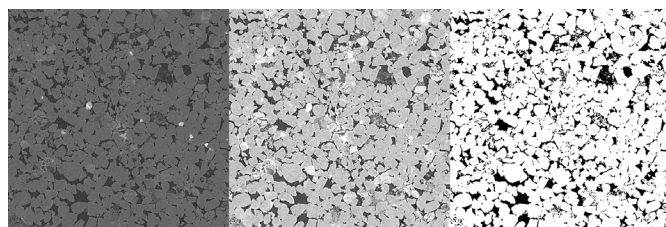


Fig. 1. Berea Sandstone micro-CT cross section: original (left), denoised (middle), and segmented (right) image slices.

2.2 Physical properties of system

To prepare for core flow condition, a primary drainage computation is performed to establish wettability distribution in pore space. It is assumed that during the drainage process, the smallest pores remain water-filled, while the non-wetting phase invades the remainder of the pore space. The pore surface can only become more repulsive to the water due to contact with non-wetting phase and the rock will achieve a “mixed wettability” state. More detail on these widely accepted mechanisms of aging or wettability alteration can be found in [20]. In the present numerical procedure, by assuming that 5% smallest pore volume still in contact with water after primary drainage, these pore surfaces are assigned a contact angle of 10°. The surfaces contacted by non-wetting phase are assigned a 30° and 170° contact angle for the water-wet and mixed-wet scenarios, respectively. The overall contact angle distributions are shown in Figure 2.

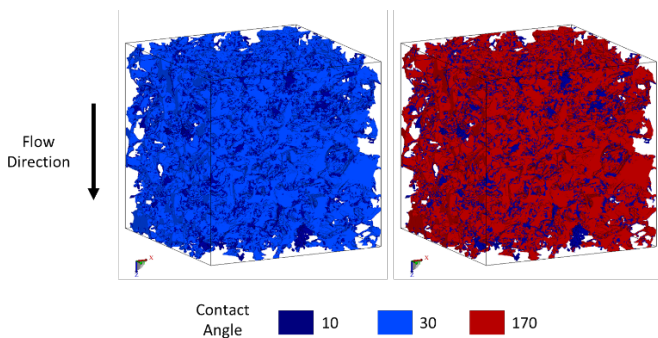


Fig. 2. Surface wettability in water- (left) and mixed-wet (right).

When it comes to fluid properties such as interfacial tension, viscosity and contact angle, it is straightforward to describe how these change with pressure, temperature and salinity. However, the design of a study to identify the individual contribution of each fluid property on the relative permeability remains a challenging exercise. As a result, the selections of fluid properties are at the same salinity (=1.98 mol/kg) and at the same time one or more of other parameters remain constant. It is common to use a dimensionless parameter such as capillary number (N_c) to combine these effects of interfacial tension and viscosity on relative permeability, which describes the ratio of viscous (governing flow) to capillary forces (governing trapping) acting in the pore space and is given by:

$$N_c = \frac{q\mu}{\sigma} \quad (1)$$

where q is the Darcy velocity, μ is the viscosity of the invading fluid and σ is the interfacial tension between CO₂ and brine. All the simulations reported in this study were performed under capillary dominated displacement regime with $N_c \sim 10^{-5}$ [21-22]. In section 3, the impact of the viscosity ratio, interfacial tension and wettability on relative permeability are discussed in more detail.

2.3 Multiphase numerical simulation

All flow simulations were performed using DigitalROCKTM, which uses a numerical solver based on the Shan-Chen multi-phase lattice Boltzmann model [23]. This solver has been validated on a variety of fundamental benchmarks and real reservoir rock test cases [23-28]. It also includes the ability to deal with high viscosity ratio of the immiscible fluid phases [29].

A steady-state displacement method is applied to measure relative permeability in this work. A displacement simulation starts at initial 100% brine saturation. Once the simulation proceeds until total flow rate is converged, the permeability is measured. Then the mixture of CO₂ and brine with increased CO₂ fraction is injected until the certain CO₂ saturation level is reached. The injection stops and waits until the flow rate is converged to achieve the equilibrium. At this point the permeability of CO₂ and brine is measured again at the current saturation. The same process will be repeated until the residual condition is reached when the brine phase barely moves. Periodic boundary conditions and a driving force are

applied in the flow direction. Additional details for this method can be found in [22, 25].

3 Pore-scale numerical simulation results

3.1 Interfacial tension effect

The interfacial tension of the CO₂-brine system at conditions covering the range relevant to CO₂ storage has been recently measured with the most comprehensive dataset provided by Li et al. [14]. As a thermophysical property, the interfacial tension is a function of pressure, temperature, and brine salinity. At conditions in subsurface storage, the interfacial tension ranges from 55 mN/m at high temperature, low pressure and high salinity to 20 mN/m at low temperature, high pressure and low salinity. Therefore, when it comes to evaluating the impact of interfacial tension on multiphase flow in the CO₂-brine system, the multi-dimensional nature of the relevant parameter space (density, viscosity and interfacial tension) are changing over the conditions of pressure, temperature and brine salinity. By holding one or more of these parameters (viscosity ratio and density ratio) constant, three values of interfacial tension chosen are applied within the range from 30 to 45 mN/m (Table 1) to examine the effect of interfacial tension on relative permeability (Figure 3).

Table 1. Conditions of relative permeability curves to assess the effect of interfacial tension [14].

Subsurface condition		Thermophysical fluid property		
Pressure [MPa]	Temperature [°C]	Interfacial tension [mN/m]	Viscosity ratio [-]	Density ratio [-]
7	62	45	0.04	0.14
8	35	37	0.04	0.63
20	72	30	0.08	0.63

The results illustrate that the dependence of the relative permeability displacement characteristics (end-point saturation and shape) on interfacial tension under the certain range of conditions in storage reservoirs. Endpoint relative permeability to CO₂ during drainage decreases with increasing interfacial tension, and residual brine saturation increases with increasing interfacial tension. This confirms that for lower interfacial tension it should be easier for the non-wetting phase (CO₂) to pass through pore throats, leading to higher relative permeability. However, this suggests that variations in interfacial tension alone (for the range of conditions expected in storage reservoirs) are still little and will not lead to significant variation in the relative permeability characteristics of a given rock.

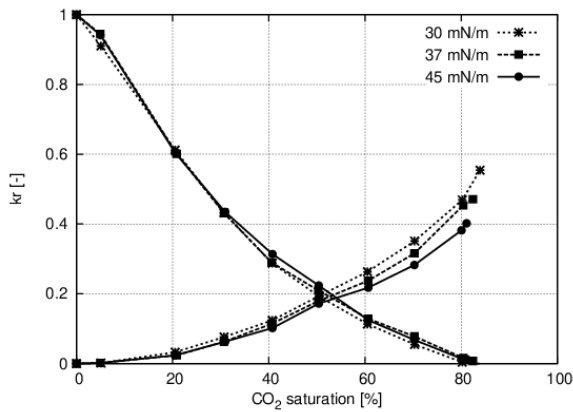


Fig. 3. Relative permeability curves measured for three different interfacial tensions.

3.2 Viscosity ratio effect

In this study, the viscosity ratio is defined as the ratio of the viscosity of CO₂ (non-wetting phase) to brine (wetting phase). CO₂ typically has lower viscosity than brine, and viscosity ratios from 0.02 to 0.2 are expected at geologically relevant conditions [30]. If injection of CO₂ into deep geological formations is considered, then the possible range of properties of the CO₂ can be estimated by considering typical conditions under which injection would occur. Because of the significant effect that the geothermal regime in a sedimentary basin has on CO₂-phase density and viscosity [31], we identify different basins in terms of magnitude of geothermal gradient and average land surface temperature. The average depth of the formation targeted for CO₂ storage range from about 1 km for shallow cold sites to 3 km for deep warm sites. Therefore, the properties of CO₂ and brine may vary, depending on pressure and temperature conditions. As representative condition of typical storage formations, surface temperature is 10 °C with geothermal gradient 25 °C/km for cold sites and 20 °C with geothermal gradient 45 °C/km for warm sites, respectively [30]. In both cases, a hydrostatic pressure gradient of 10.5 MPa/km is assumed that is typical for saline formation waters. Table 2 shows the conditions of pressure and temperature applied to study the effect of viscosity ratio. Under the conditions of deep cold formation, CO₂ injection is expected to be sufficiently deep to maintain the CO₂ in a supercritical state.

Table 2. Viscosity values for water and CO₂ at temperature (*T*) and pressure (*P*) conditions for representative deep old and shallow warm storage formation [30].

	Deep cold formation <i>P</i> : 31.5 MPa; <i>T</i> : 85 °C		Shallow warm formation <i>P</i> : 10.5 MPa; <i>T</i> : 65 °C	
	Viscosity [μPa·s]	Density [kg/m ³]	Viscosity [μPa·s]	Density [kg/m ³]
water	378	995	491	998
CO ₂	63	740	24	292
Ratio	0.17	0.74	0.05	0.29

Relative permeability curves of CO₂-brine with different viscosity ratios are shown in Figure 4. As the viscosity contrast between the two fluids increases, the less viscous fluid (CO₂) becomes more mobilized through the pore space and therefore has a higher permeability. This illustrates the advantage of deep aquifers that provides the injection conditions for CO₂ with higher mobility and thus more storage of CO₂.

Although it highlights that the individual effect of interfacial tension and viscosity ratio cannot be separated, interfacial tension does not play a significant role within certain storage conditions as suggested in this study. As seen previously, the interfacial tension for CO₂-brine systems decreases with increasing pressure and increases with increasing temperature and salinity. Water viscosity increases with pressure and salinity, and decreases with increasing temperature, while CO₂ viscosity also increases with pressure and decreases with increasing temperature. Considering that the variation of CO₂ viscosity is stronger than that of brine viscosity, the viscosity ratio of CO₂ to brine varies in the opposite manner as interfacial tension.

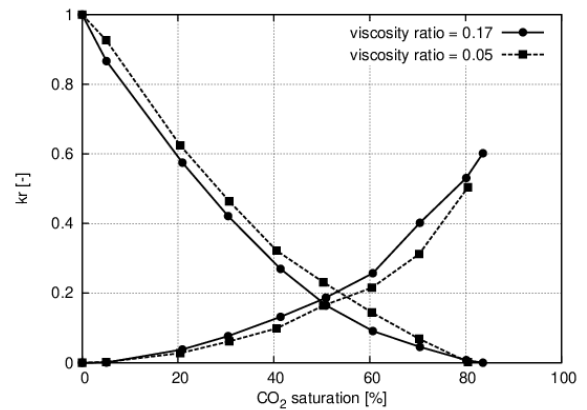


Fig. 4. Relative permeability curves measured for deep cold reservoir and shallow warm reservoir.

3.3 Wettability effect

Observations for CO₂-brine systems generally indicate a water-wet system for both sandstone and carbonate mineralogies, but there are contradictory results as to the magnitude of the contact angle and its variation with fluid conditions. In this study, two different wetting conditions (water-wet and mixed-wet) are chosen as defined in Section 2. The dependence of relative permeability on wetting condition are shown in Figure 5.

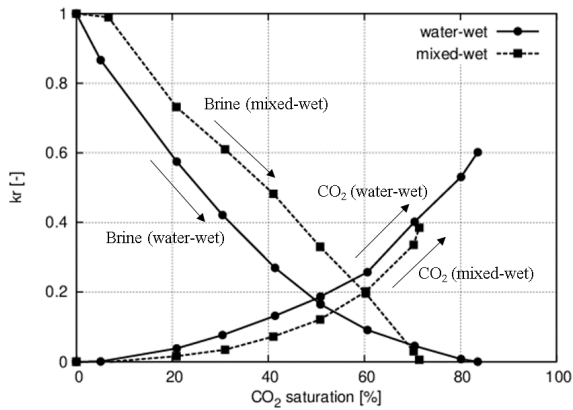


Fig. 5. Relative permeability curves measured for water-wet and mixed-wet condition.

During the displacement of water-wet system (drainage in this study), the rock is preferentially in contact with the water. As the nonwetting phase, CO₂ is generally located in the centers of the larger pores that forms continuous channels, while brine is found in the small pores and as a thin film on the rock surfaces. Eventually the remaining water is mainly found in three forms: (1) filling the smaller pores, (2) as a continuous film over the pore surface and (3) as trapped blobs surrounded by CO₂. In a mixed-wet system, the location of the two phases is reversed from the water-wet case. The injected CO₂ tends to imbibe into small and medium size pores, moving water into the large pores where it is easily displaced. The disconnected residual water remains in two forms: (1) small blobs in the centres of the larges pores, and (2) larger patches of water that are completely surrounding by CO₂. As above observed, the residual fluid distribution is shown in Figure 6.

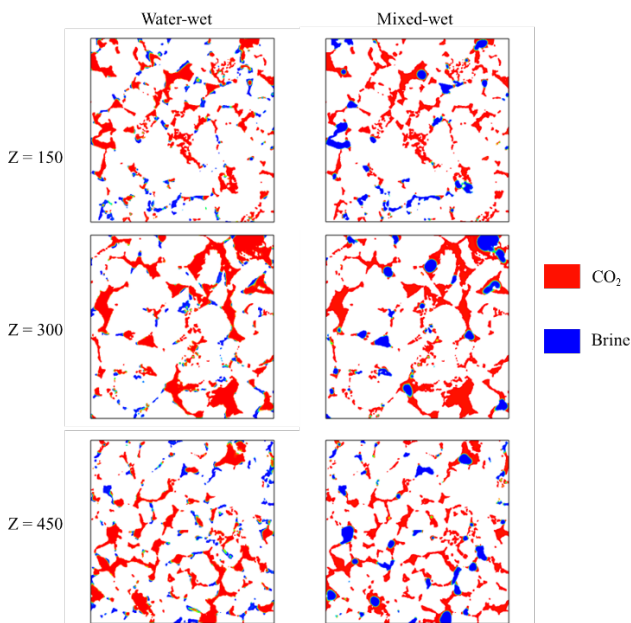


Fig. 6. Fluid distribution (red: CO₂; blue: brine) at residual stage along different depth in flow direction (Z) (left: water-wet; right: mixed-wet).

The differences in the relative permeability measured in water-wet and mixed-wet systems are caused by the differences in the fluid distributions. Consider a water-wet system, the brine does not significantly block the flow of CO₂, and the CO₂ permeability is relatively higher. This leads to a more efficient displacement than the one in a mixed-wet system and consequently lower residual water saturation. In contrast, the positions of the two fluids are reversed in mixed-wet system, CO₂ permeability is lower and brine permeability is higher because CO₂, as the wetting phase, tends to be located in the small pores and as a film on the surface, where it has little effect on the water flow. Therefore, the results of different wettability indicate that in CO₂-brine system, water-wet formation is able to store more CO₂ and more efficient injection is observed.

4 Near-wellbore analysis of CO₂ injectivity

We have shown the impact of wetting condition on the relative permeability curve in Section 3. In this section, we further perform a near-wellbore geomechanics analysis to investigate how the wettability impacts the CO₂ injectivity. The injectivity measures the ability of an injection well to receive injected fluid, and is a key parameter of CO₂ storage. It is defined as $\Pi = q_i / \Delta P$, where Π is the injectivity index, q_i is the injection rate, and ΔP is the pressure drop (bottom hole flowing pressure – reservoir pressure). CO₂ injectivity is considered to reach the maximum value at the CO₂ endpoint relative permeability when brine saturation becomes irreducible.

We set up the geomechanics model based on the finite element solver AbaqusTM. The porous formation is assumed isotropic and poroelastic following the Biot's theory [32]. Fluid flow in the pore space follows the Darcy's law. Governing equations of deformation and pore fluid flow are based on well-established theories and can be found in many textbooks and literatures [33-35]. Therefore, they are not repeated in this study.

A large CO₂ injection rate may induce fractures near the wellbore (e.g. In Salah CO₂ storage project) [36]. We model the fracture propagation and fluid flow in the fractures based on the cohesive zone method (CZM). CZM characterizes the fracturing process as the damage evolution between two initially bonded surfaces with zero thickness, and has been widely used in fracture mechanics. Detailed description of the CZM can be found in the Abaqus Documentation and many other literatures [37].

Figure 7 shows a schematic of the geomechanics model. We adopt a plane strain model (zero strain in the direction normal to the plane, a typical assumption for near-wellbore fracturing process) with a maximum principal stress σ_{\max} of 20 MPa and a minimum principal stress σ_{\min} of 10 MPa. We assign no normal displacement conditions to all the boundaries. The domain size is 50 × 50 m and the injection well is located in the center of the domain.

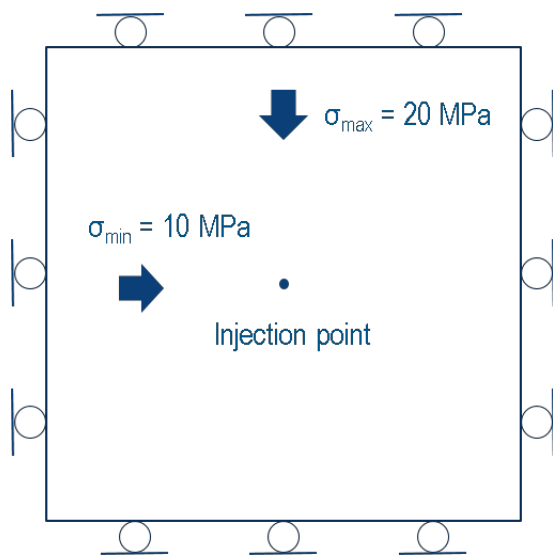


Fig. 7. Schematic of the geomechanics model. Domain size: 50 × 50 m.

In this section, we focus on the impact of wettability on the CO₂ injectivity. We consider two scenarios: water-wet and mixed-wet as presented in Section 3. Table 3 summarizes the geomechanics model parameters. The wetting condition will impact the relative permeability curve. All other parameters remain identical for these two case scenarios.

Table 3. Parameters of the geomechanics model

Parameters	Water-wet	Mixed-wet
Permeability (mD)	235	
Porosity	15.7%	
Residual water saturation (S_{wr})	16.4%	28.6%
Effective permeability of CO ₂ at S_{wr} (mD)	141.1	90.4
Young's modulus (GPa)	15	
Poisson's ratio	0.25	

We perform a baseline simulation with a CO₂ injection rate of 0.1 m³/s, water-wet condition. Figure 8 shows geomechanics simulation results including the pore pressure distribution at 100 s, the horizontal stress distribution at 100 s, and the evolution of injection pressure. CO₂ injection induces a fracture propagating perpendicular to the minimum principal stress direction. The injection pressure finally becomes stable at ~ 20 MPa.

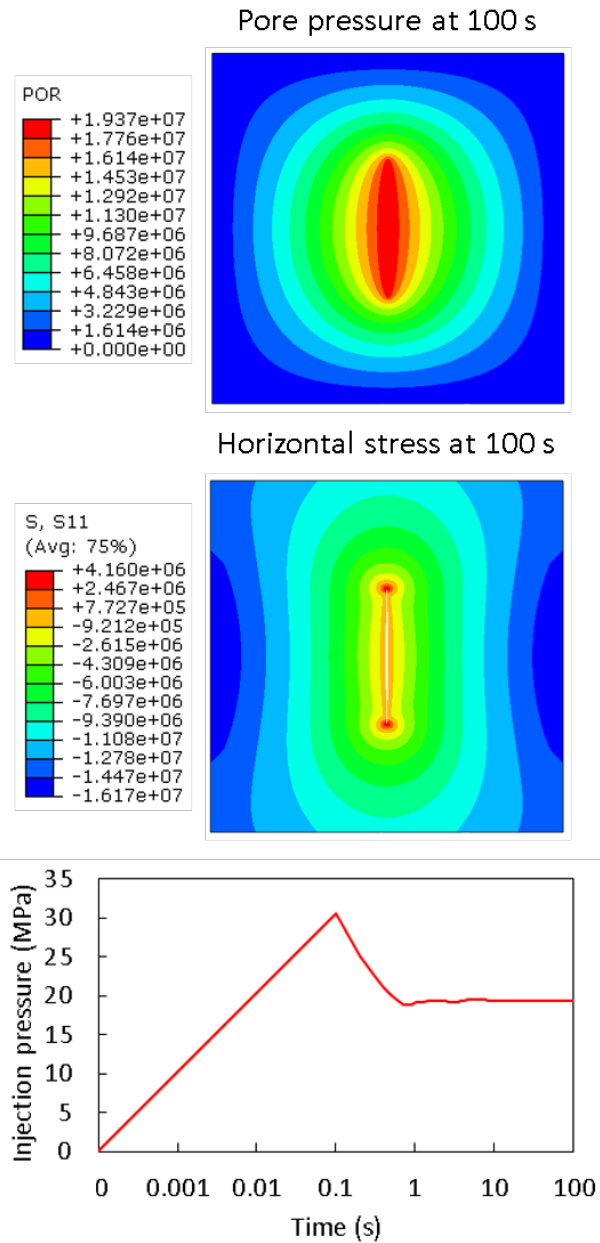


Fig. 8. Top: pore pressure distribution at the end of the numerical simulation (100 s). Middle: horizontal stress distribution at the end of the numerical simulation (100 s). Bottom: change of injection pressure over time. Time is plotted in a log scale to facilitate the visualization of pressure change. The injection pressure stabilizes at ~ 20 MPa. CO₂ injection rate is 0.1 m³/s and it is a water-wet condition.

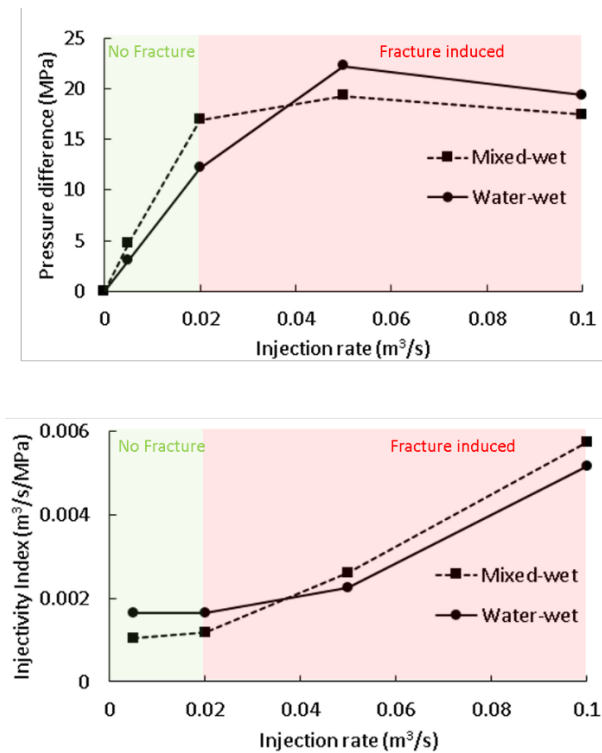


Fig. 9. Effect of wettability on CO₂ injectivity. The bottom figure is calculated from the top figure, where the injectivity index is defined as the injection rate over the pressure difference.

Figure 9 shows the geomechanics simulation results by varying the wetting condition and the injection rate. Each point corresponds to one geomechanics simulation. All other parameters remain identical. When the injection rate is relatively low (≤ 0.02 m³/s), there is no fracture and the fluid flow follows the Darcy's law. On the contrary, when the injection rate is high, a fracture is induced and the injectivity is significantly enhanced (manifested as a change in slope in the pressure difference - injection rate curve). Nevertheless, the induced fracture on the other hand may compromise the CO₂ containment, therefore, it is typically not favorable during a CO₂ injection.

We simulate two wetting conditions: water-wet and mixed-wet as discussed in Section 3. Water-wet condition facilitates the CO₂ fluid flow by offering the large pores and continuous flowing channels, which exhibits as a higher relative permeability of CO₂ on the relative permeability curve. Therefore, water-wet condition tends to have a higher injectivity compared to the mixed-wet condition when the injection rate is relatively low (no induced fracture). On the other hand, mixed-wet condition of a low CO₂ relative permeability facilitates the fracturing process. Therefore, mixed-wet condition tends to have a higher injectivity compared to the water-wet condition when the injection rate is high (with induced fracture), which indicates that the induced fracture starts to dominate the injectivity behavior. In summary, the wetting condition has an opposite impact on the CO₂ injectivity before and after the fracture was induced. Given that CO₂ injection generally tends to avoid fracturing process near the wellbore, a water-wet condition would be preferred from an injectivity perspective.

5 Conclusion

Using a DigitalROCK simulation approach, numerical simulation was carried out in Berea sandstone sample to study the impact of fluid properties (interfacial tension, viscosity ratio, and wettability) on steady-state relative permeability. As all these fluid properties depend on temperature, pressure and salinity, isolating the independent impact of them on relative permeability needs to hold one or more of other parameters constant. A weak dependency of displacement characteristics (end point relative permeability and shape of relative permeability and residual brine saturation) on interfacial tension was observed within typical range of storage formation condition. In contrast, viscosity ratio between CO₂ and brine shows clear dependency. Endpoint relative permeability to CO₂ decreases with increasing interfacial tension and decreasing viscosity ratio, while residual brine saturation increases with increasing interfacial tension and decreasing viscosity ratio. As it is common to consider storage formation as water-wet and the variation of contact angle observed in previous experiments, different wettability (water-wet and mixed-wet) are explored to investigate its impact on relative permeability. It turns out that the wettability has strong influences on relative permeability and there will be more CO₂ injected with higher CO₂ mobility in water-wet condition. A near-wellbore geomechanics model further demonstrates that a water-wet condition is preferred from an injectivity perspective.

References

1. IEA (International Energy Agency) Prospects for CO₂ Capture and Storage. IEA/OECD, Paris, 249 (2004)
2. IPCC (Intergovernmental Panel on Climate Change) IPCC special report on carbon dioxide capture and storage. In: Metz B, Davidson O, de Coninck HC, Loos M, Mayer LA, Cambridge University Press, Cambridge, 442 (2005)
3. S. Bachu, J. J. Adams, Energy Conversion and Management **44**(20), 3151-3175 (2002)
4. S. Holloway, Annual Review of Energy and the Environment **26**, 145-166 (2001)
5. S. M. Klara, R. D. Srivastava, and H. G. McIlvried, Energy Conversion and Management **44**, 2699-2712 (2003)
6. Y. Cinar, A. Riaz, & H. A. Tchelepi, SPE Journal, **14**(04), 588-594 (2009)
7. S. Bachu, B. Bennion, Environmental Geology, **54**(8), 1707-1722 (2008)
8. M.C. Leverett, Transactions of the AIME, **132**(1), 149-171 (1939)
9. S. T. Yuster, Proceedings of the 3rd World Petroleum Congress, **2**, 437-445 (1951)
10. A. S. Odeh, Trans., AIME, **216**, 346-353 (1959)
11. R. Ehrlich, Transport in Porous Media, **11**(3), 201-218 (1993)
12. E. J. Lefebvre du Prey, Society of Petroleum Engineers Journal, **13**(01), 39-47 (1973)

13. J. Downie, F. E. Crane, Society of Petroleum Engineers Journal, **1(02)**, 59-60 (1961)
14. X. Li, E.S. Boek, G.C. Maitland, J. M. Trusler, Journal of Chemical & Engineering Data, **57(5)**, 1369-1375 (2012)
15. B. Bennion, S. Bachu, SPE/DOE Symposium on Improved Oil Recovery, 1-10, January (2006)
16. D.N. Espinoza, J.C. Santamarina, Water Resources Research, **46**, 7 (2010)
17. Y. Kim, J. Wan, T.J. Kneafsey, T.K. Tokunaga Environmental Science and Technology, **46 (7)**, 4228-4235 (2012)
18. J. W. Jung, J. Wan, Energy & Fuels, **26**, 6053-6059 (2012)
19. P. Chiquet, J.L. Daridon, D. Broseta, S. Thibeau, Energy Conversion and Management, **48**, 736-744 (2006)
20. J. S. Buckley, Y. Liu, S. Monsterleet, Society of Petroleum Engineers Journal, **3(01)**, 54-61 (1998)
21. R. Xu, B. Crouse, D.M. Freed, et al. SCA **2018-066** presented at at the International Symposium of the Society of Core Analysts held in Trondheim, Norway (2018)
22. A. Fager, G. Sun, R. Xu, et al. Journal of Petroleum Science and Engineering, **208**, 109435 (2022)
23. X. Shan, H. Chen, Physical Review E, **47(3)**, 181 (1993).
24. B. Crouse, D. M. Freed, N. et al. SCA **2016-058** presented at the International Symposium of the Society of Core Analysts held in Snow Mass, Colorado, USA (2016)
25. G.R. Jerauld, J. Fredrich, N. Lane, Q. Sheng, B. Crouse, D. M. Freed, R. Xu, In SPE Abu Dhabi International Petroleum Exhibition & Conference. Society of Petroleum Engineers. November (2017)
26. H. Otomo, H. Fan, Y. Li, M. Dressler, I. Staroselsky, R. Zhang, H. Chen, Journal of Computational Science, **17**, 334-339 (2016)
27. H. Chen, C. Teixeira, K. Molvig, International Journal of Modern Physics C, **9(08)**, 1281-1292 (1998)
28. X. Shan, X.F. Yuan, H. Chen, Journal of Fluid Mechanics, **550**, 413-441 (2006)
29. H. Otomo, B. Crouse, M. Dressler, D. M. Freed, I. Staroselsky, R. Zhang, Chen, H, Computers & Fluids, **172**, 674-682 (2018)
30. J. M. Nordbotten, M. A. Celia, and S. Bachu, Transport in Porous Media, **58(3)**, 339-360 (2005)
31. S. Bachu, **Environmental** Geology, **44**, 277-289 (2003)
32. M.A. Biot, The Journal of the acoustical Society of america, **28(2)**, 179-191 (1956)
33. Jaeger, John Conrad, Neville GW Cook, Robert Zimmerman. *Fundamentals of rock mechanics* (John Wiley & Sons, 2009)
34. Zienkiewicz, Olgierd C., et al. *Computational geomechanics*, Vol. 613 (Chichester: Wiley, 1999)
35. E. Detournay, A.H.D. Cheng, *Fundamentals of poroelasticity*. In Analysis and design methods, 113-171 (Pergamon. 1993)
36. P. S. Ringrose, A. S. Mathieson, I. W. Wright, F. Selama, O. Hansen, R. Bissell, N. Saoula, and J. Midgley, Energy Procedia **37**, 6226-6236 (2013)
37. Abaqus. 2021. Abaqus 2021 online documentation.

Core Characterization of Patterson #5-25 Well for Carbon Capture and Storage in Western Kansas

Thomas Paronish^{1,2*}, Rhiannon Schmitt^{1,3}, Dustin Crandall², Franek Hasiuk⁴, Eugene Holubnyak⁴, Jingyao (Jenny) Meng⁵

¹ National Energy Technology Laboratory

² NETL Support Contractor

³ Oak Ridge Institute for Science and Education

⁴ Kansas Geological Survey

⁵ Virginia Division of Geology and Mineral Resources

Abstract. The computed tomography facilities and the Geotek Multi-Sensor Core Logger at the National Energy Technology Laboratory were used to collect data and characterize core from the Patterson #5-25 well. The Patterson #5-25 well was drilled as part of the Kansas Geological Survey led Carbon Storage Assurance Facility Enterprise (CarbonSAFE) Phase 2 project, the Integrated Midcontinent Stacked Carbon Storage Hub. As part of the CarbonSAFE project, permeability measurements of selected core were measured in zones of interest. Beyond the initial project work, we characterized the lithology utilizing non-destructive qualitative (multiscale CT images) and quantitative (X-ray fluorescence, P-wave velocity, gamma density, magnetic susceptibility) techniques to better characterize the reservoir quality and seal potential within the cored intervals. The core from the Patterson #5-25 well includes nearly 625 feet of core intermittently between the Pennsylvanian Atoka Shale and into Precambrian Basement. Core logger data and coarse resolution CT images were taken from 2/3 slab core along the entire length of the core. In addition to this macroscopic characterization of the core, potential reservoir facies along the length were examined at ten locations with high resolution CT images to examine reservoir pore systems and structural properties such as fractures. The Pennsylvanian Morrow Sandstone and Cambrian Reagan Sandstone had the best reservoir quality with high porosity and permeability. The Pennsylvanian Atoka Shale had the best seal potential with low permeability and few fractures. Throughout the Cambro-Ordovician Arbuckle Group zones of good reservoir conditions via secondary porosity were observed, with intervals of sub-mm to cm-scale vuggy porosity separated by relatively tight dolomitic zones. The Meramecian, Osage, and Viola carbonate units were observed to have generally thinner zones of good reservoir quality with some small baffles.

1 Introduction

The increase of CO₂ in the atmosphere has caused the climate to change and it has been essential to understand and develop ways to reduce atmospheric CO₂ [1]. The Integrated Midcontinent Stacked Carbon Storage Hub (IMSCS-HUB) was designed to develop a commercial-scale carbon capture, utilization, and storage project as part of a Phase II Carbon Storage Assurance Facility Enterprise (CarbonSAFE) project. The IMSCS-HUB is made up of ethanol, power plants, and other sources in Iowa, Kansas, and Nebraska and three stacked storage corridors: Sleepy Hollow Field (southwest-central Nebraska), Madrid (southwest Nebraska), and Patterson Site (Patterson, Heinitz, Hartland, and Oslo fields) (western Kansas) (Fig. 1) [2,3]. The Patterson site's Patterson #5-25 well is the focus of this study.

Understanding of the lithology, storage properties, and seal potential of the formations involved in this project is essential for optimized and environmentally safe long-term storage. By utilizing petrophysical logs, multi-scale CT imaging, and core characterization a multi-pronged understanding of these rocks has been developed.

1.1 Site Background

The Patterson #5-25 well was drilled in the spring of 2020 in the Patterson Field and with 625 feet of core recovered from target intervals between the Atoka to Precambrian Basement. A detailed breakdown of the cored intervals is available in

Table 1[2]. The Patterson Field, which was discovered in 1941 and still active has produced 3.14 Mbbls of oil from the Morrow Sand [4].

The Patterson Field sits atop a structural high within the Hugoton Embayment, that allows for four-way closure of the reservoir strata [2,3]. Initial estimates of storage potential following phase I showed the Patterson Field site could store up to 50Mt of CO₂ over 25 to 30 years based on simulations for storage in the Osage, Viola, and Arbuckle, and 200 Mt over the same period with the investigation of cored wells and seismic data in Phase II [2-4].

Table 1. Patterson #5-25 cored intervals and primary lithologies

Group/Formation	Cored depth (ft)	Primary lithology
Atoka Stage	4,615 to 4,751	Shale
Morrowan Stage (Morrow Sand)	4,751 to 4,880	Mixed (sand, shale, limestone)
Meramecian Stage	4,880 to 4,957	Limestone
Osage Stage	5,380 to 5,439	Limestone
Viola Formation	5,640 to 5,719	Limestone
Upper Arbuckle (Jefferson City-Cotter Fm.)	5,780 to 5,826	Dolomite
Lower Arbuckle (Roubidoux Fm and Bonnetterre Fm.)	5,959 to 6,200	Dolomite

* Corresponding author: thomas.paronish@netl.doe.gov

Reagan Sandstone and Granite wash	6,214 to 6,273	Sandstone
Precambrian Basement	6,278 to 6,300	Granite

The primary objective of this study is to build on the classification of the Patterson #5-25 well core utilizing non-destructive methods at NETL to understand the stratigraphy and sedimentology of reservoir units.

2 Methods

2.1 Core Characterization

The 625 feet of Patterson #5-25 Well core was examined and characterized to understand the lithologies present in the well and their storage potential. This was done by utilizing non-destructive experimental techniques at the NETL, which included core petrophysical measurements using a Geotek Multi-Sensor Corelogger and medical computed tomography (Medical CT) of the entire core length as well as micro-computed tomography (Micro-CT) image at selected reservoir zones. This data was compared to core data from the Kansas Geologic Survey (KGS) that includes porosity and permeability data and petrophysical logs (triple combo and NMR from Xaminer® Magnetic Resonance derived porosity and permeability). Halliburton estimated permeability at 6-inch intervals by utilizing the Coates Method with T2 peaks obtained from NMR. While details of this methodology are not provided, these permeability estimates are utilized for comparative analysis in the current work. Core-derived measurements were also provided by Premier Oilfield Group. Permeability and porosity were calculated from both full diameter core and core-plugs throughout the cored intervals and average permeability is displayed in log-plots [2]. The results show a discrepancy between the Coates modelled and core-measured permeability, in these cases the authors have more confidence in the core-measured result being it is a direct measure.

2.1.1 Multi-Sensor Core Logger (MSCL)

The MSCL provides core petrophysical measurements at high spatial resolution. The measurement suite includes gamma density, p-wave velocity, magnetic susceptibility, and X-Ray Fluorescence (XRF). This paper focuses on selected elements for the XRF and gamma density, and the data is available through the Energy Data eXchange portal [5].

The Patterson 5-25 Well was sampled using the MSCL at 6 cm resolution for the entire 625 feet of core. XRF data was collected using a portable handheld Olympus Delta Innov-X with a two-beam acquisition method at 60s exposure per beam. The two-beam mode provides a broad suit of elements including majors (Al, Si, P, S, Cl, Mg, K, and Ca), transition metals (Ti, Cr, Mn, Fe, Co), and trace metals (V, Ni, Cu, Zn, As, Mo, Ag, Cd, Sn, Sb, Hf, W, Pb, and Bi). We focus on major elements related to the dominant mineralogy which are shown on log plots as a percent of the total weight.

Gamma density was acquired by exposing the sample to gamma radiation and measuring the radiation attenuation. The attenuation is directly proportional to the density of the sample and is acquired by measuring the difference between radiation energy at the emission source and after it passes through the sample [6].

2.1.2 Medical CT images

Core scale CT scanning was done with a Toshiba® Aquilion TSX-101A/R medical scanner. The Medical CT generates images with a resolution in the mm-range, with a voxel resolution of 0.43 x 0.43 mm in the XY plane and 0.5 mm along the Z-axis. Scans were captured at energies of 135 KeV and 80 KeV. Radiographs are processed into a 3-D volumes and 2-D slices in ImageJ. For this study, the 2-D images were cropped to highlight the variation in the grayscale throughout the well.

Two CT scanning energies were used to enable determination of density using methods established in Siddiqui and Khamees, 2004; further details of the methodology used here can be found in Moore et al. (2018) [6,7]. Three homogenous standards with known bulk densities, similar to the core being interrogated, were used for calibration. Bulk density, or dual energy density was calculated using,

$$\rho_B = mCTN_{low} + pCTN_{high} + q \quad (1)$$

where [m, p, and q] are unknown coefficients that can be solved by setting up a system of equations with four 3x3 determinants and CTN are the CT numbers obtained at the low and high energies from the Medical CT [8].

In this study, the high and low energy images were processed by a Python script with a three dimensional 2-sigma gaussian blur to reduce noise. The scipy library in Python was used to solve for the m, p and q unknowns based on the calibration CTN values, which are then used to determine the ρ_B of each pixel in the 3-D volume. Any material with a density $<1.5 \text{ g/cm}^3$ was removed from determination of average density along the core length, which was calculated using the image processing program ImageJ [9].

2.1.3 Micro CT images

Micro-CT scans were acquired using a ZEISS Xardia MicroXCT-400 CT scanner. Micro-CT images are higher resolution scans that allow for more detailed investigation of mineralogy and porosity. Five micro-CT scans were acquired at a $2.36 \mu\text{m}^3$ voxel resolution. A small selection of samples were acquired in representative zones due to prolonged scanning times. Samples are listed in Table 2 and were 1-2 mm in diameter.

Table 2. Micro-CT images

Depth (ft)	Formation
------------	-----------

4,771.30	Morrow Sand
5,812.40	Upper Arbuckle/ Jefferson City-Cotter Fm
5,972.12	Lower Arbuckle/Roubidoux Fm.
6,213.50	Bonneterre-Reagan Sand Boundary
6,222.60	Reagan Sand

2.1.4 Ilastik thresholding

The five micro-CT images in Table 2 were segmented into relevant components using Ilastik, which is a supervised machine learning software that utilizes user training to determine feature classes based on a feature vector: color/intensity, edge type, and texture [10]. Training images is a time-intensive process where the user determines classes and identifies representative features in these, until uncertainty is adequately minimized between classes. For this study, feature classes were chosen to represent pore space (air) and mineralogical features (including quartz, dolomite, feldspar, and high attenuating minerals). Not all classes were used for every image and each image was trained on the feature classes separately due to different mineralogical compositions. Additionally, pre-processing of the Micro-CT images occurred in ImageJ prior to training to optimize the threshold results, which included a three-dimensional 2-sigma gaussian blur and adjustment of gray-scale levels.

Post-threshold images were brought back into ImageJ where a Look Up Table was applied to highlight the feature classes, and a histogram was calculated to show the distribution of feature classes within a Region of Interest (ROI) and subsequently give the porosity for the sample based on the percent of air within the sample.

3 Results and Discussion

Core characterization of the Patterson #5-25 well is separated into 3 zones designated spatially based on the continuously cored intervals, these include zone 1, the Atoka Stage, Morrowan Stage, and Meramecian Stage; zone 2, the Osage Stage, Viola Limestone, and Upper Arbuckle; and zone 3, the Lower Arbuckle, Reagan Sandstone, and Granite wash. These zones are classified based on petrophysical and geochemical characteristics with a focus on high quality reservoir features shown via the 5 micro-CT images and segmentations.

3.1 Core Characterization Zone 1: Atoka, Morrow, and Meramecian

Zone 1 represents the Pennsylvanian Atoka, Pennsylvanian Morrow, and Mississippian Meramecian stratigraphy (Fig. 1). The Atoka Stage is made up of interbedded black shale and

mudstone to wackestone (sometimes dolomitic). The Atoka has generally low permeability with some silty intervals exceeding 0.1 mD with similarly high porosity (10 to 20%). Although the Atoka Stage has 2-to-10-foot zones with increased porosity/permeability, the more dominant low permeability zones are comprised of approximately 30-foot intervals of black shale and tight limestones which act as low permeability seals.

The Morrowan Stage (4,751 to 4,880 ft) is comprised of a quartz-dominated medium- to coarse-grained sandstone and was oil-stained. Some pyrite can be seen throughout with some small interbedded mudstone and shale intervals. The base of the cored interval shows signs of increased amounts of shale, and logs show that this gradational effect continues to the top of the Meramecian Stage strata.

The Meramecian Stage strata (4,880 to 4,957 ft) is made up of primarily limestone with a small brecciation mudrock section. The limestone interval of the Meramecian stage was tight with little to no porosity or permeability but those vuggy sections did have significant porosity and permeability. The Meramecian is an ideal seal as it is comprised of massive tight carbonates with no local signs of vertical fractures.

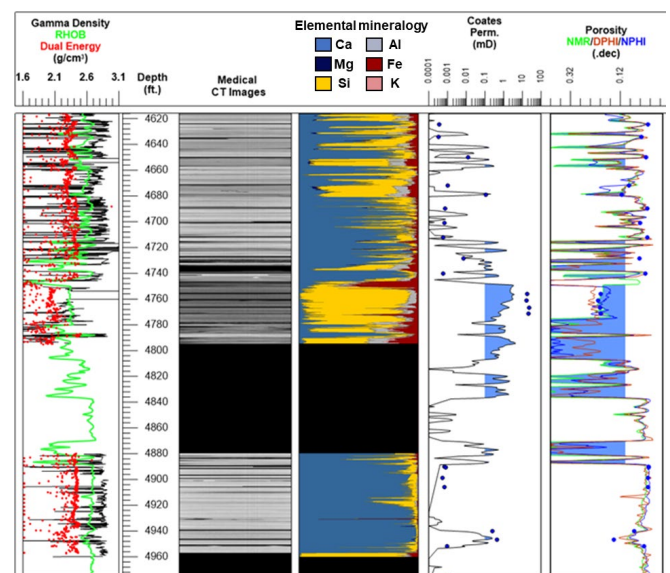


Fig. 1. Zone 1 log plot. Column 1 density (gamma density (black), dual energy density (red) and bulk density (green)); column 2, medical CT images; column 3, elemental mineralogy; column 4, Coates Permeability (line, fill represents zones of permeability greater than 0.1 mD) and core-derived permeability from KGS (dots)[2]; and column 5, porosity log (neutron porosity (NPHI, blue), density porosity (DPHI, red), NMR porosity (green, fill represents zones of porosity greater than .1)) and core-derived porosity from KGS (dots)[2].

3.1.2 Micro CT images

The micro-CT image for zone 1 was taken from the Morrow Stage which showed the best reservoir conditions in zone 1. Fig. 2. shows the results of the Ilastik threshold; a sample composition with 71.4% quartz, 7.2 % feldspar, and 1.7% high density minerals (including dolomite/calcite), with a porosity of 19.6%. The Morrow consists of generally well-sorted quartz with sub-angular to angular grains. Some quartz grains show intragranular fracturing which likely adds to the

overall porosity. Porosity in this sample mirrors the logs and KGS laboratory measurements for the sampled section. The feldspar grains are sparse but well sorted and show some intragranular fracturing similar to the quartz. The high-density mineral fraction was the lowest fraction of the volume analyzed and was mostly made up of pyrite and carbonate minerals.

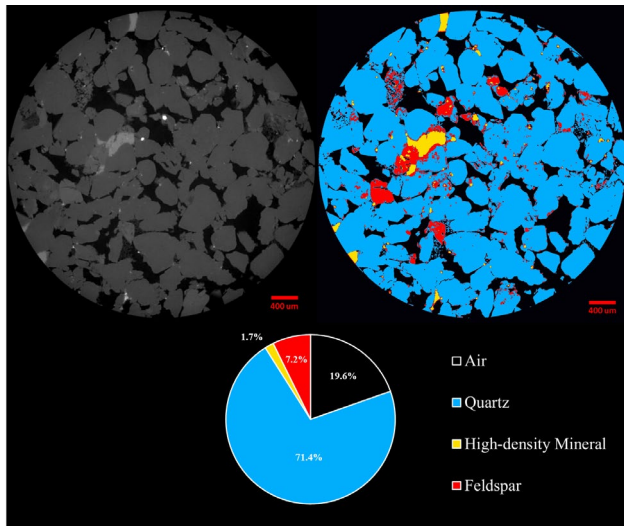


Fig. 2. Morrow sand micro-CT image with a slice of the volume showing the CT image unprocessed on left and threshold results on right (400 μm scale is shown on the bottom right of both images); below is the breakdown of feature classes from the volume.

3.2 Core Characterization Zone 2: Osage, Viola, and Upper Arbuckle

Zone 2 is represented by the Mississippian Osage Stage, Ordovician Viola Formation, and Upper Arbuckle (Jefferson City-Cotter Formations).

The Mississippian Osage Stage (5,380 to 5,439 ft) is made up of primarily limestone, with the upper 12 feet of core made up of a cherty limestone (seen in core and by the lack of clay elements (Al, Fe) and the enrichment of Si) (Fig. 3). This interval has excellent seal potential with porosities at about 5% or less and permeabilities less than 0.1 mD.

The Ordovician Viola Formation (5,640 to 5,720 ft) is the start of the Dolomitic dominated strata which continues to the base of the well (Fig. 4). The Viola Formation is made up primarily of dolopackstone in the upper portion of the formation with vugs and some mineralized fractures (5,640 to 5,654 ft) and brecciated intervals and chert-filled fractures and vugs at the bottom of the Viola Formation (5,658 to 5,720 ft). Vugs in the upper section of the Viola are open with some pin-point porosity becoming chert filled in the upper portion of the breccia. Porosity and permeability measurements from core and petrophysical logs show the Viola has between 5 to 10% porosity and 0.05 to 0.1 mD permeability (Fig.4), suggesting the Viola Formation would make a good reservoir unit.

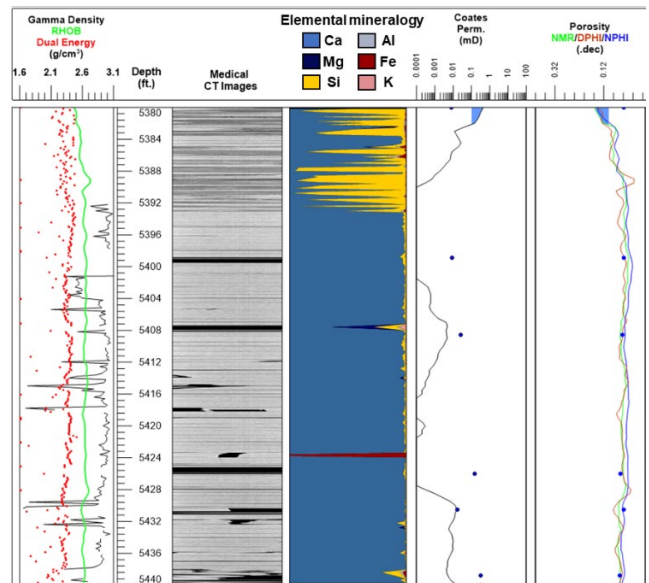


Fig. 3. Zone 2 Osage Stage log plot. See Fig. 1 for plot details

The Cambrian-Ordovician Upper Arbuckle (5,780 to 5,826 ft) is made up of the Jefferson City and Cotter Formations (Fig. 5). The Upper Arbuckle is primarily made up of Dolomite ranging between dolomudstone to dolograinstone. The dolomudstone intervals are generally tighter with some chert-filled vugs, and the dolograinstone have more porous features like vugs and pin-point porosity features. The Upper Arbuckle is also a good reservoir zone with an average porosity of about 9% and permeability between 0.01 and 0.1 mD.

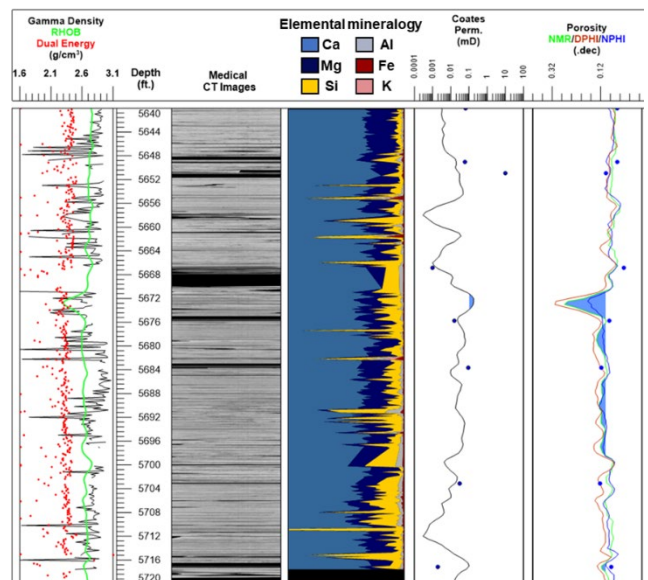


Fig. 4. Zone 2 Viola Stage log plot. See Fig. 1 for plot details

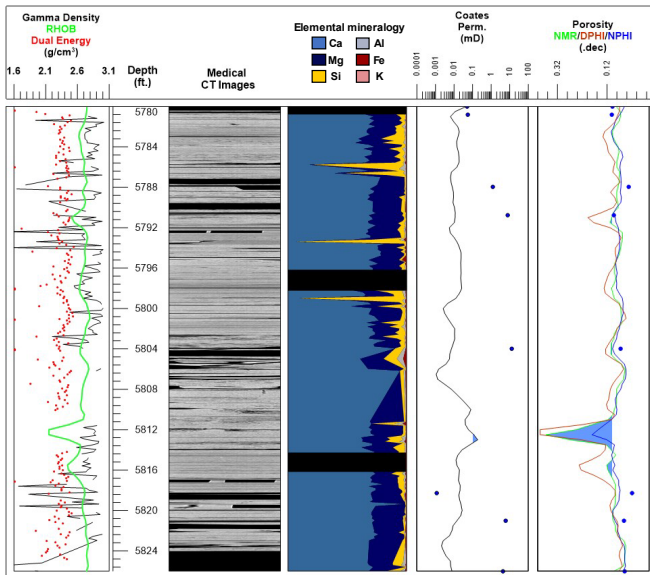


Fig. 5. Zone 2 Lower Arbuckle log plot. See Fig. 1 for plot details

3.2.1 Micro CT images

The sample examined with micro-CT in zone 2 was from the Upper Arbuckle (Jefferson City-Cotter Formation) at 5,812.4 ft (Fig. 6). This sample showed the best reservoir conditions in zone 2 and was taken from a section of dolograinstone with vuggy porosity surrounding the sample. The Ilastik segmentation shows the sample composition was dolomite and very minor amounts of high attenuating minerals (likely pyrite), with a porosity of 4.6%. The segmentation results miss some minor amounts of high-density minerals and quartz/feldspar grains; however, they are minor (<1%).

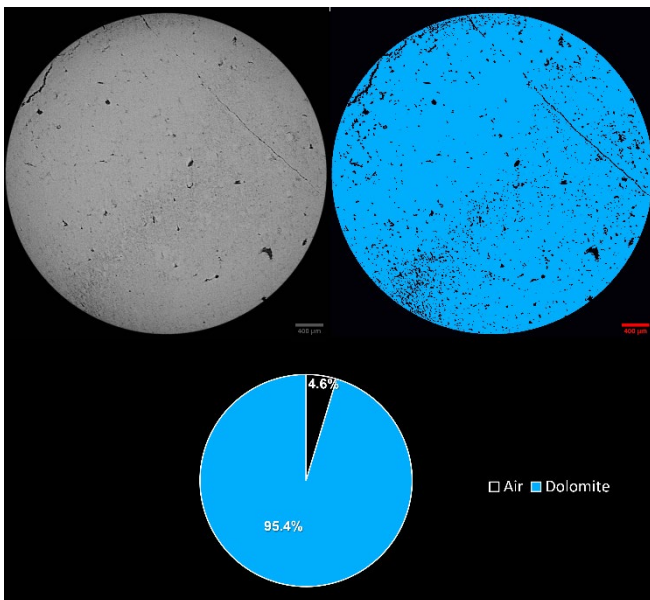


Fig. 6. Upper Arbuckle micro-CT image with a slice of the volume showing the CT image unprocessed on left and segmentation results on right (400 μm scale is shown on the bottom right of both images); below is a pie chart representing the portions of feature classes from the volume.

3.3 Zone 3: Lower Arbuckle, Reagan, and Granite wash

Zone 3 is made up of the Lower Arbuckle subgroup that includes the Roubidoux and Bonneterre formations, the Reagan Sandstone, and Granite wash (Fig. 7). The Lower Arbuckle subgroup is made of primarily of dolomitic facies. The Roubidoux Formation (5,959 to 6,042 ft) is made up of dolomudstone, dolograinstone, and doloboundstones. The dolomudstone intervals are generally tight with some vuggy porosity and open fractures, whereas the doloboundstone and dolograinstone facies contain more vuggy porosity and are highly fractured (mostly mineralized). At 6,016 to 6,025 ft, the Roubidoux becomes a sandy dolostone where the porosity increases to about 12% and permeability to about 10 mD.

The Bonneterre Formation (6,042 to 6,216 ft) is made up of dolomudstone and doloboundstone, both tighter than the Roubidoux Formation. Doloboundstone intervals are fractured with mineralized calcite. Doloboundstone in the lower portion of the formation were vuggier and more porous. The Bonneterre has more range in porosity (from 1 to 9%) and permeability (0.001 to 0.98 mD) but did show good reservoir characteristics.

The Reagan Sandstone and Granite wash (6,214 to 6,273 ft) consists of medium to fine-grained sandstones, siltstone, and conglomerates with mm- to cm-sized quartz clasts. The Reagan Sandstone portion (6,214 to 6,259 ft) is more dolomitic compared to the Granite wash interval (6,259 to 6,273 ft), which contains more feldspars and less dolomite. These intervals show good reservoir characteristics with porosity and permeability ranges between 9 to 15% and 0.01 and 2 mD.

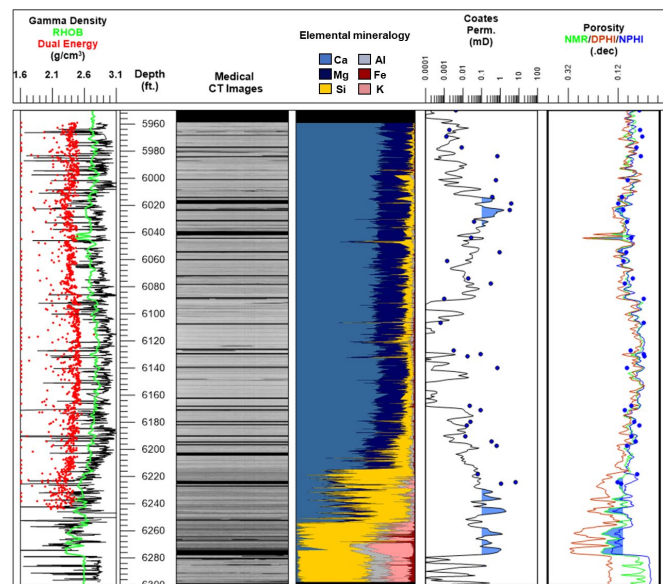


Fig 7. Zone 3 log plot. See Fig. 1 for plot details

3.3.1 Micro CT images

The micro-CT images examined in zone 3 were from the Lower Arbuckle (Roubidoux) at 5,972.12 ft (Fig. 8); Bonneterre-Reagan Sandstone boundary at 6,213.50 ft (Fig. 9); and from medium-grained sandstone from the Reagan

Sandstone at 6,222.60 ft (Fig. 10). All were chosen because they were representative sections of these zones in the core and log data.

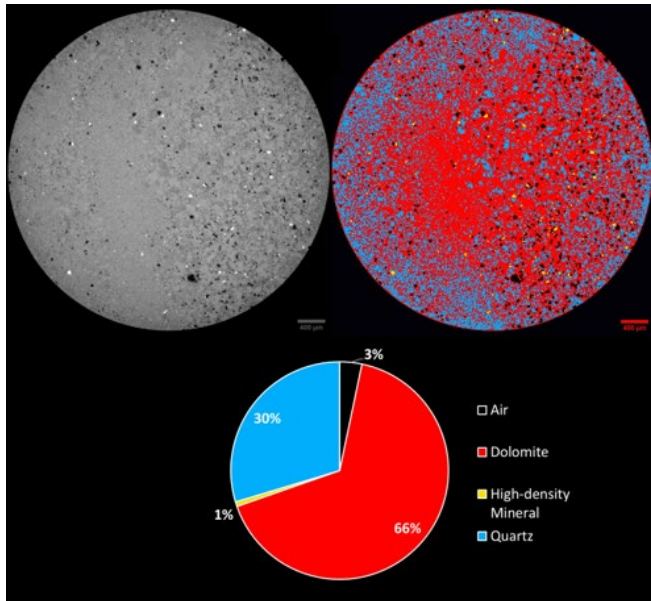


Fig. 8. Lower Arbuckle (Roubidoux) micro-CT image (5,972.12 ft) with a slice of the volume showing the CT image unprocessed on left and segmentation results on right (400 μm scale is shown on the bottom right of both images) and below a pie chart representing the portions of feature classes from the volume.

The Lower Arbuckle (Roubidoux) at 5,972.12 ft (Fig. 8) was sub sampled in a dolomudstone facies that was within some visible porosity zones. The Ilastik segmentation results, ignoring the outer 350 μm due to beam-hardening effects, show that the sample is primarily made up of dolomite (66%), lighter minerals (likely a combination of quartz, feldspar, and clay minerals) (30%), and high-density minerals (1%) with a porosity of 3%, slightly lower than the log derived porosity. Both the CT image and threshold results show a fabric where a zone of lighter elements has a higher spatial density likely along bedding, porosity also increases within these zones and decreases in the more homogenous dolomite-dominated zones.

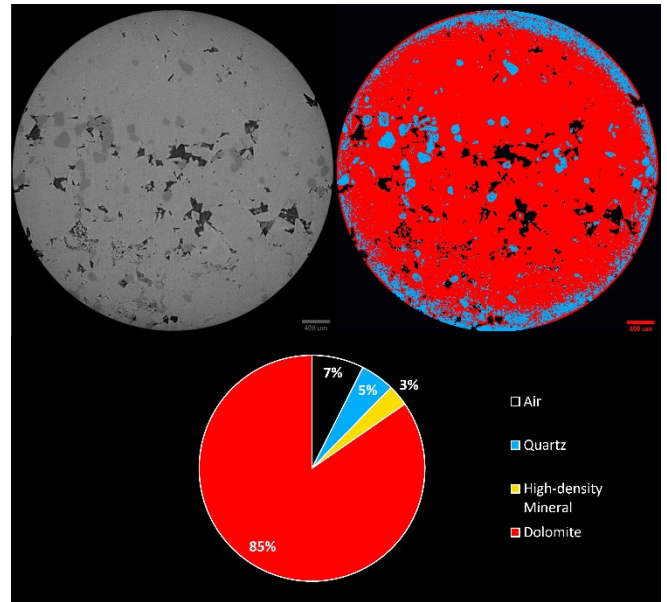


Fig. 9. Bonnetterre-Reagan sand micro-CT image (6,213.5 ft) with a slice of the volume showing the CT image unprocessed on left and segmentation results on right (400 μm scale is shown on the bottom right of both images) and below is a pie chart representing the portions of feature classes from the volume.

Bonnetterre-Reagan Sandstone boundary at 6,213.50 ft (Fig. 9) was sampled just above the glauconitic sandstone that divides the Bonnetterre and Reagan Sandstones. The sample is made up of dolomitic sand and represents a zone of increased porosity (9%) and permeability (about 0.1 mD). The Ilastik segmentation results, ignoring the outer 350 μm of the image due to beam-hardening effects, show the sample is primarily made up of dolomite (85%), quartz (5%), and high-density minerals (3%) with a porosity of 7%. The porosity in this sample is mostly located within the dolomitic sections of the rock with some propagating around the quartz grains. High-density minerals are generally about 10 μm or less through the volume apart from a 1 mm section of high-density mineral fill within the pore space towards the base of the CT volume.

The Reagan Sandstone at 6,222.60 ft (Fig. 10) was sampled from a section of medium-grained sandstone and has a porosity of 9% and a permeability of about 0.1 mD. The Ilastik segmentation results, ignoring the outer 400 μm due to beam-hardening effects, show the sample is primarily made up of dolomite (39.2%), feldspar (33.4%), quartz (17%), mineralized fracture-fill (5.4%), and high-density minerals (0.1%) with a porosity of 4.9%. Porosity in this sample is mostly within the dolomitic cement and surrounding the quartz grains, with minor grains amounts within intragranular fractures within feldspar grains.

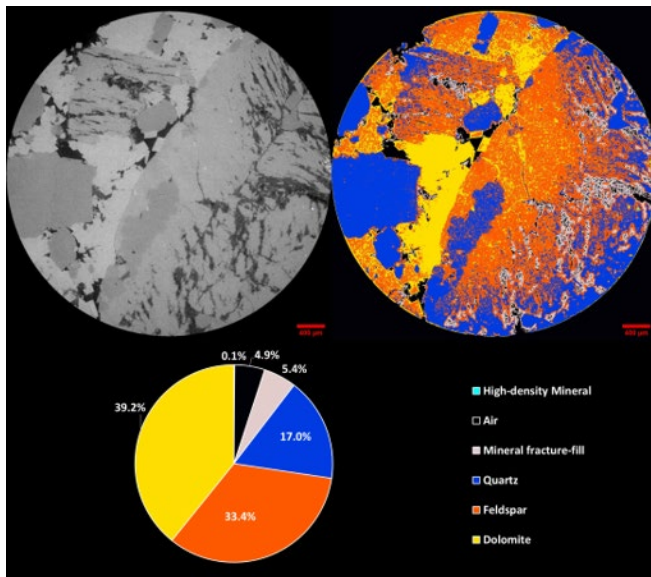


Fig. 10. Reagan Sandstone (6,222.60 ft) with a slice of the volume showing the CT image unprocessed on left and segmentation results on right (400 μm scale is shown on the bottom right of both images) and below is a pie chart representing the portions of feature classes from the volume.

4 Conclusions

Ilastik segmentation allows us to find mineralogy and porosity in a non-destructive manner. Heterogeneous samples create a challenge in dealing with beam-hardening effects at the sample edge. Our solution to this is to train the segmentation around the interior of the core where beam-hardening effects are minimized and create an ROI to ignore the areas where they are most prominent. This method is also limited to the number of samples investigated in this study. Ideally, we would have subsampled more to better represent each formation, however due to time constraints and longer scan times we weren't able to do so. In addition, the segmentation process can be tedious and sometimes takes weeks to come to a good solution. If a solution is found with minimum error, it can be used to train similar lithofacies.

Data from NETL coupled with core laboratory experiments and petrophysical logs allowed for the 625 feet of core from the Patterson #5-25 well to be assessed for reservoir quality at both the mm- and core-scale. We find reservoir potential in the Morrow Sand, Viola Formation, Upper Arbuckle, Lower Arbuckle, and Reagan Sand/Granite wash; and seals in the Atoka Stage, Meramecian Stage, and Osage Stage, as well as a baffle in the upper Bonnetterre Formation. Core characterization analysis is summarized by the formation/group below:

Atoka Stage (4,615 to 4,751 ft) is a good seal with low porosity and permeability within the black shale and mudstone intervals and some thinner silty zones with moderate to high porosity and permeability.

Morrow Sand (4,751 to 4,880 ft) has the best reservoir quality within the Patterson #5-25 well with an average porosity of about 25% and permeability of 20 mD. The Morrow Sand is primarily made up of quartz sand with some minor amounts of clays and feldspars, and thinly bedded

intervals of silt or mudrock. Micro-CT segmentation at 4,771.3 ft reiterates the findings at the core-scale. Porosity is about 20% and the sample is made up primarily of quartz. Porosity in the Morrow sample is found between sand grains with a minor seen within intragranular quartz and feldspar grains.

Meramecian Stage (4,880 to 4,957 ft) has seal potential with most of the mudstone intervals having low porosity and permeability and lack vertical fractures. However, there are vuggy intervals (4,869 to 4990 ft and 4,940 to 4,955 ft) within conglomerate and vuggy mudrock zones that have high porosity (12 to 15 %) and permeability (0.1 to 0.5 mD).

Osage Stage (5,380 to 5,439 ft) has seal potential. The upper 12 feet of the Osage core has the highest porosity and permeability and is made up of mudstone to packstone with intervals of chert. The tight section is made up of mudrock that has lower porosity and permeability. Coring missed the highest porosity interval observed in well logs, which suggests that the interval has good reservoir quality with approximately 10% porosity [2].

Viola Formation (5,640 to 5,719 ft) has reservoir potential, it is made up of dolopackstone with some zones of brecciation and chert. Zones of high porosity and permeability are present in vuggy areas and sections of pinpoint pores with in the packstone.

Upper Arbuckle (5,780 to 5,826 ft) has reservoir potential with an average porosity of about 9% and permeability between 0.01 and 10 mD. The Upper Arbuckle is composed primarily of dolomudstone and dolograinstone. The highest porosity and permeability is found within the dolograinstones. The dolograinstones typically have more open vuggy and pinpoint porosity zones compared to the dolomudstones, which is chert-fill when present. Micro-CT segmentation of a dolograinstone interval at 5,812.4 ft showed the matrix is primarily made up of dolomite with very minor amounts of high-density minerals and quartz/feldspar grains, which were not captured in the segmentation. The sample was within the dolomite and had a porosity of 4.6% and vertical fracture sets.

Lower Arbuckle (5,959 to 6,200 ft) has good reservoir potential, in the Roubidoux Formation and lower Bonnetterre Formation; and a baffle in the upper Bonnetterre. The Roubidoux Formation high porosity and permeability zones are generally found in vuggy zones in doloboundstone and dolograinstone facies and sandy dolostone facies. Micro-CT segmentation of the Roubidoux Formation (5,972.12 ft) focused on a section of dolomudstone above a vuggy zone. The sample showed porosity mostly within heterogeneous zones with both dolomite and quartz/feldspar grains and had generally lower porosity than some other sections of the Roubidoux. The Bonnetterre Formation high porosity zones are similarly found within vuggy zones on the doloboundstone facies and in sandy dolostone. Micro-CT segmentation of the sandy dolomitic facies at the Bonnetterre-Reagan Sand boundary (6,213.5 ft) showed an increase in the proportion of dolomite to sand grains (in this case, quartz) compared to the sample in the Roubidoux Formation. However, porosity is higher (8.9%) and is made up of larger diameter pore space, propagating around the sand grains and within dolomite matrix. The baffle is also made up of dolomudstone and doloboundstone, however the section contains calcite-filled mineralized fractures.

Reagan Sand and Granite wash (6,214 to 6,273 ft) has reservoir potential, with porosity and permeability ranges between 9 to 15% and 0.01 and 10 mD. The Reagan Sand and Granite wash contain medium to fine-grained sandstones, siltstone, and conglomerates. The Reagan Sand is more dolomitic than the Granite wash which is more feldsparic. Micro-CT segmentation and analysis in The Reagan Sand focused on a sample from 6,222.60 ft that was made up of a medium grained dolomitic sandstone. The majority of the porosity in this sample is propagated around sand grains, with minor amounts from intragranular fracturing and within the dolomitic matrix. A couple qualitative observation can be made from the micro-CT segmentation. First, the porosity and likely permeability in the dolomitic sections is primarily from visible secondary porosity features (vugs, pin-point porosity, fractures) evident in the differences between core-scale measurements to the micro-CT result which are of mm-scale matrix. Second, porosity that is found in dolomitic rocks propagate more frequently in heterogenous sections of the sample compared to in the homogenous dolomite.

This observation could be made more robust with addition investigation in future studies. Such as, quantifying the pore space focusing on mineral contacts within the pore space important for wettability in CO₂ injection [11] and would show if heterogeneity is a significant factor in pore development. Exploring pore morphology (pore size and connectivity) is important for a deeper understanding of pressures needed for injection and in the cases of vuggy zones whether matrix pore space is connected for gas injection. the high-resolution digital rocks could be used to determined permeability and primary flow paths through the pore scape using computational fluid dynamics simulations, which could elucidate the role matrix plays in the dolomitic formations. Lastly, Taking the high-resolution pore-scale data from this experiment and understanding how to upscale and relate it to historic well data will be important moving forward.

Acknowledgement: The authors would like to acknowledge the NETL technical staff Karl Jarvis, Brian Tennent, and Scott Workman for providing the CT images in this report.

All data in this project is available on EDX (<https://edx.netl.doe.gov/group/core-characterization>).

This Research was executed through the NETL Research and Innovation Center's Carbon Storage field work proposal. Research performed by Leidos Research Support Team staff was conducted under the RSS contract 89243318CFE000003.

Disclaimer: This work was funded by the Department of Energy, National Energy Technology Laboratory, an agency of the United States Government, through a support contract with Leidos Research Support Team (LRST). Neither the United States Government nor any agency thereof, nor any of their employees, nor LRST, nor any of their employees, makes any warranty, expressed or implied, or assumes any legal liability or responsibility for the accuracy, completeness, or usefulness of any information, apparatus, product, or process disclosed, or represents that its use would not infringe privately owned rights. Reference herein to any specific commercial product, process, or service by trade name, trademark, manufacturer, or otherwise, does not necessarily constitute or imply its endorsement,

recommendation, or favoring by the United States Government or any agency thereof. The views and opinions of authors expressed herein do not necessarily state or reflect those of the United States Government or any agency thereof.

References

1. IPCC, Sustainable Development, and Efforts to Eradicate Poverty. <https://www.ipcc.ch/sr15/>, (2019)
2. J. Walker, K. Smith, Integrated Mid-Continent Stacked Carbon Storage Hub Phase II, Final Summary Report, DOE Agreement/Project #DE-FE0031623, Battelle Project # 100122657. (2020)
3. Y.E. Holubnyak, M. Dubois, Integrated CCS for Kansas (ICKan) Final Technical Report. No. DOE-ICKan-29474. Kansas Geological Survey; University of Kansas Center for Research (2018)
4. Kansas Geological Survey, Patterson Field " <https://chasm.kgs.ku.edu/ords/oil.ogf4.IDProdQuery?FieldNumber=1000149180>" (2022)
5. T. Paronish, N. Mitchell, R. Schmidt, J. Moore, S. Brown, D. Crandall, Computed Tomography Scanning and Geophysical Measurements of the Integrated Mid-Continent Stacked Carbon Storage Hub Patterson #5-25 Well, NETL-TRS-X-2021, NETL Technical Report Series (to be published)
6. Geotek Ltd. Multi-Sensor Core Logger Manual, Version 05-10, <http://www.geotek.co.uk/sites/default/files/MSCLOverview.pdf>, (2010)
7. J. Moore, S. Brown, D. Crandall, S. Workman, P. Dinterman, Computed Tomography of the Tuscarora Sandstone from the Preston 119 Well; NETL-TRS-9-2018; NETL Technical Report Series, 92, (2018)
8. S. Siddiqui, A. Khamees, Dual-Energy CT-Scanning Applications in Rock Characterization (SPE 90520). Society of Petroleum Engineers (2004)
9. C.A. Schneider, W.S. Rasband, K.W. Eliceiri, NIH Image to ImageJ: 25 years of image analysis. Nature Methods, 9, 671–675 (2012)
10. S. Berg, D. Kutra, T. Kroeger, C.N. Straehle, B.X. Kausler, C. Haubold, M. Schiegg, J. Ales, T. Beier, M. Rudy, and K. Eren, Ilastik: Interactive machine learning for (bio) image analysis. Nature Methods, 16, 1-7 (2019)
11. L. E. Dalton, D. Tapriyal, D. Crandall, A. Goodman, F. Shi, F. Haeri, Contact Angle Measurements Using Sessile Drop and Micro-CT Data from Six Sandstones. Transport in Porous Media, 133 (1), 71-83 (2020)

An approach for image-based quantification of fines migration in geologic columns and core samples

Collin R. Sutton^{1,*} and Christopher Zahasky¹

¹University of Wisconsin – Madison, Department of Geoscience, Madison, WI, USA

Abstract. Understanding chemical and colloidal transport processes in conventional and unconventional formations is fundamental to engineering and management of subsurface energy production, carbon capture and sequestration, and hydrogen storage. Migration of variably sized colloids (fines) has been identified as a primary concern for the long-term efficiency of injection and extraction operations in many industry applications. Characterizing the migration of colloids in porous media has been widely studied; however, few studies have quantified sub-core colloidal transport behavior and related this to bulk sample observations. In this study the transport of clay fines through sand packs are analyzed using micro-positron emission tomography (PET) imaging. PET imaging allows for accurate 4-D quantification of clay fines transport at sub-centimeter scale. PET imaging was completed by imaging an aqueous pulse of suspended radiolabeled kaolinite under single-phase flow conditions. This approach allows for the quantification of changes in transport, attachment, and detachment properties at the sub-centimeter scale. Mathematical models were then developed to compare experimental data to the predicted colloidal behavior of the system using a form of the Derjaguin, Landau, Verwey, and Overbeek (DLVO) model to parameterize and interpret solutions of the advection-dispersion-reaction equation. This study provides a novel approach to the quantification of fines migration and colloidal transport behavior in geologic porous media allowing for future work to be done on more complex and heterogeneous cores under multiphase flow conditions.

1 Introduction

Colloids in the environmental and energy resources sciences are typically described as being nanometer to micrometer sized insoluble particles of bacteria, viruses, engineered materials, or geologic particulates such as clay [1]. The migration of clay colloidal particles (fines) is of particular interest due to the extensive occurrence of clay minerals throughout all sedimentary basins and during weathering reactions of many common igneous and metamorphic rocks [2]. Kaolinite, illite, smectites, and chlorites are the common clay minerals in sedimentary basins [3]. Understanding the transport and sorption properties of fines are of importance to a variety of geoscience fields such as environmental remediation, water resources management, subsurface energy extraction, geologic storage of carbon dioxide and hydrogen. For example, unconventional wells typically experience a very sharp initial decline in production followed by a slower long-term decline which is usually attributed to formation damage as a result of the migration of fines [4]. The structure, mineralogy, and chemical exchange capacity of clays have been discussed in detail elsewhere [5]. Kaolinite has been identified as a main contributor to formation damage and has been used widely in coreflooding experiments [6,7,8]

Changes in flow and physiochemical conditions are classically considered to be the two primary mechanisms responsible for the attachment or mobilization of fines [1]. Physical attachment mechanisms have commonly been described using colloid filtration theory (CFT) that relates the

retention of colloids to the collector and the pore water velocity and can be incorporated into the advection-dispersion equation with first-order kinetics [9, 10]. Changes in physiochemical conditions such as fluid pH and ionic strength are well known to influence the migration behavior of fines and can be characterized by the Derjaguin, Landau, Verwey, and Overbeek (DLVO) model [11, 12]. DLVO theory describes the electrochemical forces acting on a colloid and a collector grain as a result of the chemical conditions of the fluid through the summation of the attractive forces (van der Waals forces) and the repulsive forces (electrical double layer and Born Repulsion). DLVO theory has since had extra processes and forces added and is known as extended-DLVO or non-DLVO forces. These extensions of original DLVO theory are not considered in this study. Electrostatic forces dictate the net repulsive or attractive charges between colloids and collector grains (i.e., porous matrix). Most colloids and collector grains will exhibit negative charges under natural chemical conditions [13, 14]. These net negative charges generate unfavorable colloid attachment conditions due to the net repulsion. However, colloids may be immobilized in the secondary minimum that is controlled by van der Waals forces based on the size of the particles and the separation distance.

The net charge between particles in a system is highly dependent on the pH and ionic strength of the fluid in the system. Ionic strength and pH have been shown to play an important role in the migration potential of fines. High ionic strength of a solution will suppress the electrical double layer of a negatively charged particle due to the high concentration of positively charged cations in solution. This suppression of

* Collin R. Sutton: collin.sutton@wisc.edu

the double layer causes the net charge of the particle to become less negatively charged. Likewise, a lower ionic strength solution will cause the electrical double layer to expand and cause the particle to have a more negative charge. As a result, a lower ionic strength solution is expected to cause more migration of fines in a reservoir [15].

In addition to ionic strength, there is a pH-dependent process by which fines have a larger migration potential. Acidic conditions lead to a lower fines migration potential than basic conditions [16]. The reason for this relationship is that by definition more H⁺ ions are present in acidic solutions and will keep the surface potential of the clay low resulting in more positive zeta potentials. As the pH increases, OH⁻ becomes increasingly dominant and will increase the surface potential or cause more highly negative zeta potentials. This logic is supported by literature that shows that acidic environments lead to stable permeability while transitions to basic environments lead to loss of permeability in the formation [6,17]. The isoelectric point, also called the point of zero charge, typically exists between the extreme acidic and basic ranges for colloids. Kaolinite, and clays in general, have a complex chemical structure and the exact isoelectric point can be difficult to determine if one exists at all. Many studies have been conducted and point to a range of possible isoelectric points ranging from below a pH of 3, a pH of between 4 and 7, and none [18,19,20,21]. Overall, formations with more basic pH and lower ionic strength will lead to increased fines migration while more acidic and higher ionic strengths will lead to more stable fines [14,16].

Classical versions of CFT and DLVO theory alone have been shown in literature to not sufficiently summarize the behavior of fines in natural systems [22]. Therefore, the colloidal system is likely controlled by a combination of hydrodynamic and physiochemical properties which need to be combined to better understand the transport phenomena. The aim of this study is to combine modeling techniques with coreflooding experiments to determine the feasibility of using a CFT and DLVO based method to predict fines migration under different ionic strength conditions at a stable pH. A 1-dimensional analytical model is used to model expected kaolinite fines migration behavior based on the advection-dispersion equation with first order attachment. DLVO modeling is done for a kaolinite-quartz system to determine net force charges for the system based on varying ionic strength conditions. Core flooding under brackish and freshwater conditions is conducted and quantified using a UV-Vis spectrophotometer. A novel micro-positron emission tomography (micro-PET) approach and dataset is presented. Spectrophotometry and micro-PET are used to measure the attachment and mobilization of kaolinite fines in response to a transition from high to low salinity fluid injection in sand pack experiments.

2 Methodology

Coreflooding experiments are carried out by performing pulse-type experiments in homogenous sand packed columns. The first method involves using a conservative fluorescent tracer and then a pulse of kaolinite measured downstream of the column through a UV-Vis spectrophotometer. The second method involves using micro-PET to image a conservative

radiotracer and then radiolabeled kaolinite in four-dimensions.

2.1. Materials

Stock solutions of brackish water with a concentration of 100 millimolar (mM) NaCl and slightly saline freshwater with a concentration of 1 mM were prepared for use in the coreflooding experiments. Deionized water was used for mixing all solutions. The pH of all solutions were buffered using Piperazine-1,4-bis (2-ethanesulfonic acid) sesquisodium salt (PIPES) with a molarity of 100 mM. PIPES was chosen to minimize complexation and competitive sorption with heavy metals and buffering capacity from pH of 6.1-7.4 [23]. PIPES was dissolved in 100 mM NaOH before being mixed with DI water and a final pH of 7.0 was obtained by further titration with NaOH.

Kaolinite clay was chosen as the colloid for the experimental study due to being an abundant, naturally occurring clay mineral and has very little capacity for swelling [2]. A kaolinite solution of 150 mM kaolinite was selected and stock solutions of kaolinite in 100 mM NaCl with 100 mM PIPES buffer and kaolinite in 1 mM NaCl with 100mM PIPES buffer were made and agitated for a period of 24 hours on a rotating stirrer. A 150 mM kaolinite solution was determined based from radiolabeling batch-type experiments and will be explained in the following sections.

A relatively homogenous, pure quartz sand was used for the column experiments. Ottawa sand was purchased from ThermoFisher Scientific and sieved to 355-500 micrometers in size. The sand was fired for a period of 24 hours at 550 degrees Celsius to remove any residual organic matter.

2.2 Radiolabeling of Kaolinite with ⁶⁴Cu

⁶⁴Copper²⁺ (⁶⁴Cu²⁺) was chosen as the positron emitting radioisotope for this study due to the well-established sorption capacity of copper to kaolinite [24, 25, 26] and has a half-life of 12.7 hours. These studies have also shown that copper has a strong sorption capacity as pH of the solution increases and as ionic strength decreases. Copper also has a very fast equilibration time with clays which is ideal for radiolabeling and imaging due to the time dependency of radioactive decay [26]. A PIPES buffer was used in all radiolabeling experiments as a result of this pH dependency. Furthermore, ⁶⁴Copper is well studied and used in the medical physics literature with PET imaging [27, 28].

Batch-type experiments were conducted with ⁶⁴Cu²⁺ to validate the literature results and to verify that copper would not desorb during the PET experiment. ⁶⁴Copper²⁺ was obtained from the University of Wisconsin-Madison Cyclotron group as 10 μ L of ⁶⁴CuCl₂ + 0.5M HCl. Batch-type experiments were conducted [29] to quantify Cu sorption to kaolinite over multiple orders of magnitude ranges of molarity at different ionic strengths from 0.1M NaCl to DI water. A dose of 1-2 mCi/mL has been found to be the ideal range of radioactivity in the micro-PET scanner for geologic media [30]. The amount of sorbed versus aqueous ⁶⁴Cu²⁺ was determined by taking bulk samples of radiolabeled kaolinite and solution and comparing those against supernatant from centrifuged radiolabeled kaolinite. Desorption experiments

were conducted by removing all supernatant and resuspending the radiolabeled kaolinite in non-radiolabeled solution. Radioisotope concentrations in bulk solutions and supernatant were measured using a Perkin Elmer Wizard2 Gamma Counter.

2.3 Column Experiments

Homogenous sand columns are used to test the transport and flow behavior of fluorescein and kaolinite clay. Fluorescein is chosen because it is considered to be a conservative tracer in low organic content porous media, and it is easily measured with a UV-Vis spectrophotometer. Kaolinite with a concentration of 150 mM is used for all column experiments based on results of the radiolabeling batch-type experiments explained in the previous section. A serial dilution of kaolinite solutions analysis was performed to identify the linear range of absorbance that may occur in the molarity ranges around 150 mM. A linear trend of molarity to absorbance is needed to allow for a linear regression to be performed to calculate concentration of kaolinite in effluent. Total concentration of kaolinite (in molarity) can then be determined by integrating the total volume of the absorbance breakthrough curve. The dilution analysis is performed by making a kaolinite solution at 250 mM by mixing 3.2g of kaolinite in 10 mL of DI water. Multiple subsets of the solution are diluted in half multiple times to achieve a range of concentrations from 250 mM to 0.977 mM. These samples are then analyzed on a Shimadzu 1900i UV-Vis spectrophotometer to determine absorbance values over a range of kaolinite molarities.

The column used for the experiment is 1-inch in diameter and made of polyetheretherketone (PEEK). PEEK is used for the column design due to having a high tensile strength and does not interfere with imaging systems such as micro-positron emission tomography or x-ray computed tomography. The column is approximately 11.9 cm long with two cylinder caps made of aluminum with a total length of 3.175 cm each. These caps screw into the PEEK and provide a seal at both ends of the column. A 150 mesh filter is placed in the column and then it is wet packed with sand on a vortex mixer to ensure consistent packing with no air gaps.

The column experiments are performed from an experimental cart system (Figure 1) that was designed to be used with varying geologic materials, at varying confining pressures, over a range of temperatures. This system can be transported to different imaging facilities for imaging while running a column experiment. The system uses a Vindum 3.5K water pump to inject water at a constant flow rate into an inlet port on the column. The inlet and outlet caps are designed with a cross pattern and concentric rings to limit the effects of point-source flow. The water is then pumped at 1 mL/min through the sand core until water leaves the effluent port and then enters a flowthrough quartz cuvette in the UV-Vis spectrophotometer. A differential pressure transducer is connected to the side ports of the inlet and effluent caps to monitor differential pressure throughout the experiments.

Columns are saturated for a minimum of 10 pore volumes with DI water before any injection of solute. A 1 mL pulse is

measured by using a pre-cut 1 mL coil of tubing that is attached to a Harvard syringe pump and the Vindum pump through a 6-port Vici valve. First, a 1 mL pulse of the conservative tracer fluorescein is injected into the column at a rate of 1 mL per minute to determine solute advection and dispersivity in the sand pack and to ensure there are no flaws in the column packing. Next, a 1 mL pulse of 150 mM kaolinite is injected and is measured by the UV-Vis spectrophotometer. A second experiment was repeated for 100 mM NaCl + 100 mM PIPES as the saturating fluid and the fluid in the kaolinite suspension. The saturating fluid was injected until no more kaolinite was recorded by the UV-Vis and then the injection fluid was changed to 1 mM NaCl + 100 mM PIPES at a flow rate of 1.8 mL per minute to determine remobilization behavior of kaolinite as a response to changing ionic strength.

2.4 Transport Model

The advection-dispersion equation (ADE) is used to model kaolinite moving through a sand pack. A modified version of the ADE is used to account for first-order kinetics that describe the attachment and detachment behavior of colloids. The ADE and ADE with reactions can be described as:

$$\frac{\partial C}{\partial t} = D \nabla^2 C - v \nabla C \quad (1)$$

Where C is concentration [mol/L], t is time [s], v is the pore water velocity [m/s], D is the dispersion coefficient [$\frac{m^2}{s}$], $D = D_e + \alpha_L v$, where D_e is the diffusion coefficient and α_L is the longitudinal advection [m]. This equation can then be modified to add a first order reaction term based off the differential rate law, $\frac{\partial C_a}{\partial t} = -k C_a$, where some amount of colloids will attach over the transport distance.

$$\frac{\partial C_a}{\partial t} = D \frac{\partial^2 C_a}{\partial x^2} - v \frac{\partial C_a}{\partial x} - k C_a \quad (2)$$

Where C_a is the solute or colloid concentration and k is the first order attachment or detachment coefficient depending on the sign. This approach is especially useful for column experiments with colloidal transport because van Genuchten and Alves [31] have published 1D analytical solutions that solve these flow equations. This analytical solution is written in python to solve mathematically. It is solved with type 1 flux average boundary conditions [32] specifically, $C(x = 0, t) = C_0$ $0 < t \leq t_0$ and $C(x = 0, t) = 0$ $t \geq t_0$. The ADE with first order reaction can then be further used to describe colloid transport because $k C_a$ can be estimated by using colloid filtration theory (CFT) and is described by Yao et al. [9]. The total of the forces described by CFT can be summed as η and then can be used in an attachment coefficient term from Li et al. [33] to describe the colloidal behavior:

$$k = \frac{3(1-\phi)}{2} \frac{v \alpha \eta}{d_c} \quad (3)$$

Where ϕ is porosity, d_c is the diameter of the collector grain [m], and α is the attachment term. The particle size of a kaolinite grain was assumed to be around 1 μm .

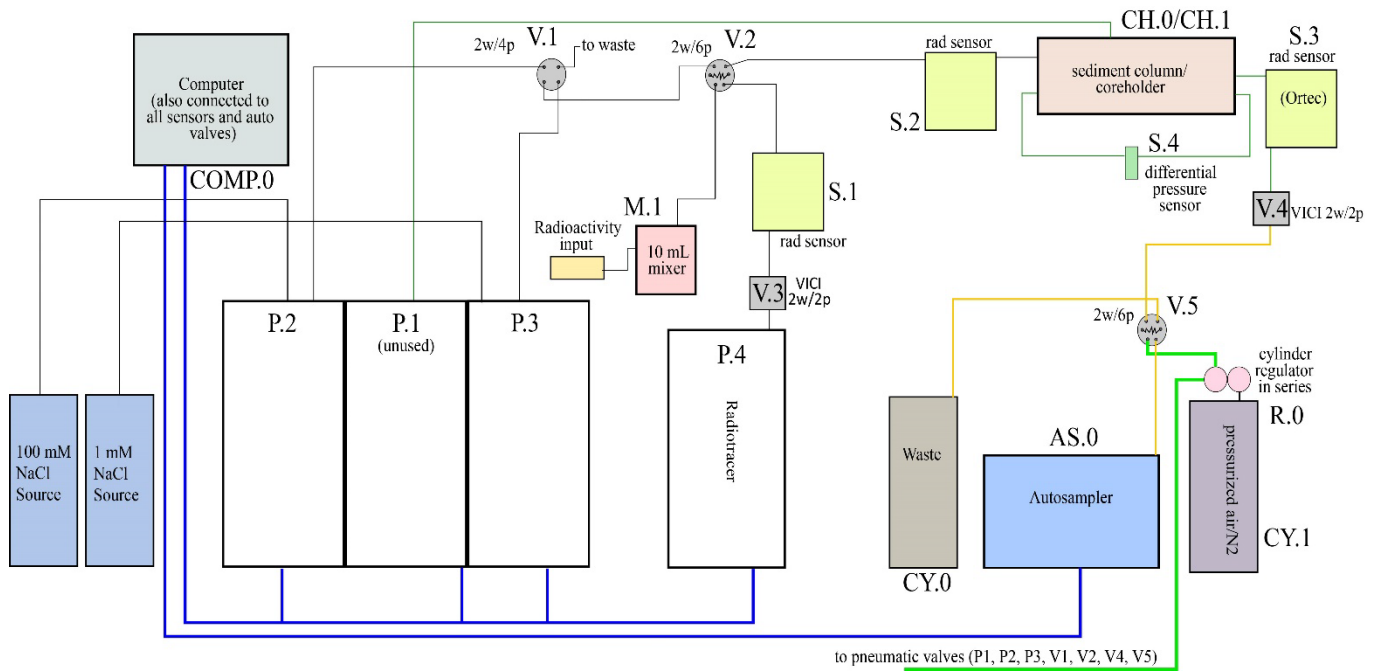


Fig. 1. Schematic diagram of the experimental system for column experiments. Saline solutions were pumped from the source using P.2 and P.3 and were alternated by using V.1. Kaolinite, fluorescein, and radiotracer was loaded and injected by using P.4 and V.2. Radiotracer and radiolabeled kaolinite were monitored in the influent and effluent ends of the column by using S.1, S.2, and S.3. S.4 is the differential pressure sensor and was used to monitor the pressure in the column throughout the experiment. Sample is sampled using a modified Opentrons OT-One sampling system. All gas lines and pneumatic valves are operated using nitrogen gas.

2.5 Derjaguin, Landau, Verwey, and Overbeek model

The DLVO model is used to determine the total repulsive and attractive forces between a colloid and a collector grain [11, 12]. The method used in this study has been sufficiently discussed elsewhere and a detailed description of the methodology and equations can be found [14, 34]. In general, the DLVO model can be characterized as:

$$V_{DLVO} = V_{LDW} + V_{EDL} + V_{BR} \quad (4)$$

Where V_{DLVO} is the total summation of the forces, V_{LDW} is the van der Waals forces, V_{EDL} is the electrical double layer force, and V_{BR} is the Born repulsion force. DLVO forces are controlled by the ionic strength of a solution and the zeta potential of the colloid and the surface grains in the system. Zeta potentials were measured at the University of Wisconsin–Madison Wisconsin Centers for Nanoscale Technology laboratory with a Malvern Zetasizer Nano ZSP. Zeta potentials were measured for kaolinite over a range of pH conditions from 2–10 and over a range of NaCl conditions from 3M to 1mM. Zeta potentials for Ottawa sand were taken from literature [35].

2.6 Micro-Positron Emission Tomography

Micro-Positron Emission Tomography has recently begun to be used as an imaging technique for geologic media [30, 36, 37]. Micro-PET utilizes a 3-D array of photon detectors to simultaneously track photon coincident events across the entire volume of PET scanning field of view. This method allows for a 3-D image reconstruction of a radioisotope distribution through time within a sample. A detailed description of the method and its use with geologic porous

media can be found elsewhere [30]. All micro-PET experiments were conducted at the University of Wisconsin Small Animal Imaging & Radiotherapy Facility using a Siemens Inveion hybrid micro-PET/CT scanner with a 1.2 mm resolution and 13 cm axial field of view. The reconstruction of micro-PET images gives a spatial resolution of 0.077 cm x 0.077 cm x 0.08 cm for each 3D reconstruction within the column.

All experiments are conducted using the same experimental setup as the previous section. The primary differences between the column experiments described above and the micro-PET experiments is that the UV-Vis Spectrophotometer is no longer used in the micro-PET experiments and the kaolinite is radiolabeled with ^{64}Cu to be detected by the micro-PET imaging. ^{18}F radionuclide attached to Fludeoxyglucose (^{18}F]FDG) is used as a conservative tracer and $^{64}\text{Cu}^{2+}$ is used as the radiolabel for kaolinite.

Three trials are conducted as a part of the micro-PET imaging experiment. The sand pack is saturated with a minimum of 10 pore volumes of 100 mM NaCl + 100mM PIPES solution before experiments begin. 100 mM NaCl solution is injected constantly at a rate of 1 mL/min and 1 mM NaCl is injected at 1.8 mL/min. All pulses of tracer and kaolinite are prepared in a solution of 100 mM NaCl and 100mM PIPES to maintain ionic strength and pH. First, a 1 mL pulse of ^{18}F]FDG is injected into the homogenous sand pack to determine the ideal transport behavior of the sand pack. Second, a 1mL pulse of $^{64}\text{Cu}^{2+}$ radiolabeled 150 mM kaolinite is injected into the column and imaged. Lastly, the injecting solution is switched to a 1 mM NaCl + 100 mM PIPES solution to simulate low salinity injection. A modified Opentrons OT-One Robot Pipetting autosampler is used during radiolabeled injection to verify that effluent is radiolabeled clay fines and not free $^{64}\text{Cu}^{2+}$ in solution.

3 $^{64}\text{Cu}^{2+}$ and Kaolinite Radiolabeling

Radiolabeling experiments were conducted according to the method described in the above radiolabeling section to ensure that ^{64}Cu imaged with micro-PET was fully sorbed to the kaolinite and not in solution. Results of radiolabeling indicate that $^{64}\text{Cu}^{2+}$ has a strong affinity to sorb with kaolinite under all ionic strengths tested for this study. A higher concentration of kaolinite in solution was determined to correspond to a higher percentage of $^{64}\text{Cu}^{2+}$ sorbed versus $^{64}\text{Cu}^{2+}$ in aqueous phase. An initial concentration of 150 mM kaolinite in DI water had ~2% of initial $^{64}\text{Cu}^{2+}$ remaining in aqueous phase after centrifugation. Higher ionic strength solutions led to less sorption of $^{64}\text{Cu}^{2+}$ but minimally so. Ionic strengths of 100mM NaCl and 1 mM NaCl had ~10% and ~7% of initial $^{64}\text{Cu}^{2+}$ remaining in aqueous phase after centrifugation respectively. Lastly, a wash was done to determine the effects of introducing radiolabeled kaolinite to a dilute solution without radiolabel present. Kaolinite suspensions were washed with the same solution that they were initially suspended in (e.g., 150mM kaolinite suspended in DI water was washed with DI water and so on). Supernatant of washed samples was determined to contain 1-2% of initial $^{64}\text{Cu}^{2+}$ leftover in aqueous phase after centrifugation. This 1-2% was likely due to imperfect separation of centrifuged kaolinite and original supernatant with some residual amounts of $^{64}\text{Cu}^{2+}$ in the sample tubes.

4 Tracer and kaolinite pulse injection with UV-Vis Spectrophotometry

Columns were packed and ran for different ionic strengths to test the hypothesis that ionic strength plays a key role in the attachment and remobilization of kaolinite and to understand potential hysteresis in the attachment and remobilization processes. A tracer of fluorescein was injected into each column (Figure 2) to determine column integrity (i.e., there are no preferential flow paths or residually trapped air) and could be used to determine longitudinal dispersivity for the transport model. The column experiments at different ionic strengths show results that match the theoretically expected results (Figure 2). Column pressure is monitored with a differential pressure sensor (Figure 1). No pressure discrepancies were observed during any injection experiment. The column with initial lower ionic strength (DI water) has more kaolinite in the effluent than does the column with higher initial ionic strength (100 mM NaCl). Both injections appear to stabilize over time with no additional kaolinite flowing through the system. This implies that all remaining kaolinite in the column is attached to sand or has been trapped in pore throats. Kaolinite is remobilized and again seen in the effluent when the 100 mM NaCl solution is transitioned to 1 mM NaCl injection solution (Figure 3). Therefore, lowering the ionic strength of the system also appears to play a role in the detachment or remobilization of kaolinite.

Kaolinite molarity in the effluent was calculated based on the method developed from the dilution analysis. Normalized curves of kaolinite breakthrough could then be plotted (Figure 2). This allows for quantification of total mass of kaolinite that was transported through the column and total mass that was retained inside the column. The DI water

column had a total kaolinite effluent mass of 0.73 mM kaolinite (0.5% of the initial mass) and the high saline column had a total kaolinite effluent of 0.12 mM kaolinite (0.08%). This also validates that high ionic strength leads to stronger attachment of kaolinite than does lower ionic strength. The total mass of kaolinite initially transported and also remobilized during the high to low saline injection transition experiment was 0.42 mM kaolinite (0.28%). This is an increase of 0.3 mM in effluent from decreasing the ionic strength and increasing flow rate of the injection solution. These results indicate that the initial attachment of kaolinite likely has little effect on the stability of colloid attachment.

5 Transport and Electrochemical Modeling

Analytical modeling using the ADE with first-order reactions and CFT was calculated to determine analytical fit to experimental data. First, a tracer data set was used to help fit the longitudinal dispersivity of the analytical solution. The analytical solution fits the experimental breakthrough curve very well (Figure 4). The experimental tracer arrives slightly later and displays slightly more dispersion than does the analytical solution, but this is expected considering fluorescein will show some dispersion in the tubing of the system.

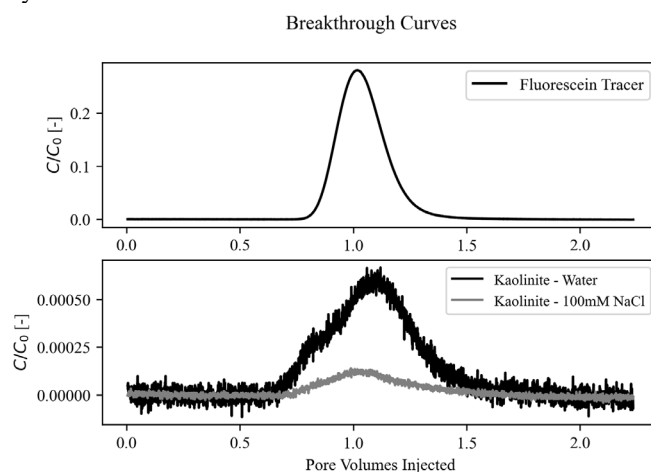


Fig. 2. Top) Normalized breakthrough curve of conservative fluorescein injected into Ottawa sand column that had been saturated with DI water. Bottom) Normalized breakthrough curves of 150mM kaolinite suspended in DI water injected into Ottawa sand column that had been saturated with DI water (black curve with higher peak) and 150mM kaolinite suspended in 100mM NaCl injected into Ottawa sand column that had been saturated with 100mM NaCl (grey curve with lower peak). The pH of all solutions is at a pH of 7. Both plots are plotted as a function of pore volumes injected.

Kaolinite transport can then be modelled using a combination of the ADE with reactions and CFT. Results from the modelled vs experimental kaolinite column experiments can be found in Figure 3. The attachment term, k , can be found in equation 5 and is controlled in part by a fitting parameter, (α) . Values for α used in the modeled results indicate that higher saline solutions create a more favorable environment for kaolinite attachment onto collector grains than does lower saline or DI water solutions. This

agrees with the raw data from the column experiments and from published literature [10].

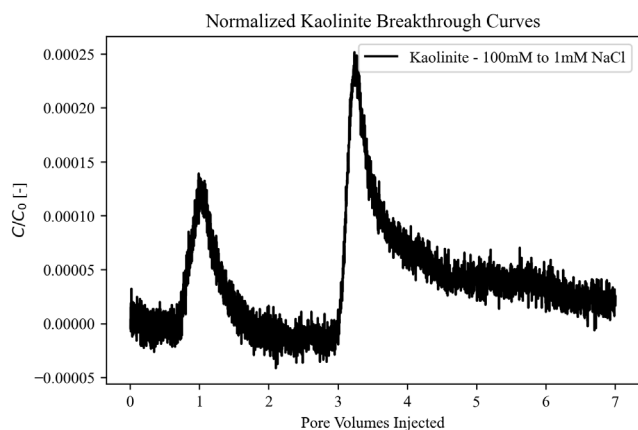


Fig. 3. Normalized breakthrough curve of 150mM kaolinite suspended in 100mM NaCl injected into Ottawa sand column that had been saturated with a 100mM NaCl solution (pH=7). Injection fluid salinity was changed to 1mM NaCl when pore volumes injected was 2.17 (40 minutes).

Modelled results for the kaolinite experiments match very well with the column experiment data. Concentration measurements of kaolinite in effluent resemble experimental data trends closely. Estimates of kaolinite transported through the column were 0.45 mM kaolinite by the analytical solution while the experimental data was 0.73 mM. The saline water analytical model estimated 0.07 mM kaolinite in the effluent while the experimental data was 0.1 mM. Lastly, the curves of the analytical breakthrough are very similar in peak height but tend to peak earlier than the experimental data with less tailing. The experimental kaolinite curves also tend to breakthrough earlier at low ionic strength.

Results of DLVO modeling match published literature and show that a system with kaolinite and quartz sand should be expected to have a deep well of primary attraction at very close separation distances (<1 nm) and higher ionic strengths with a very small or nonexistent energy barrier [9, 24]. The primary attraction decreases with decreasing ionic strength and a larger energy barrier is formed pushing the secondary minimum further from the surface of the collector grain. At further distances, the kaolinite is less likely to be trapped and explains the increase in transport at lower ionic strengths and why the transition from 100mM NaCl to 1mM NaCl remobilizes the previously attached kaolinite

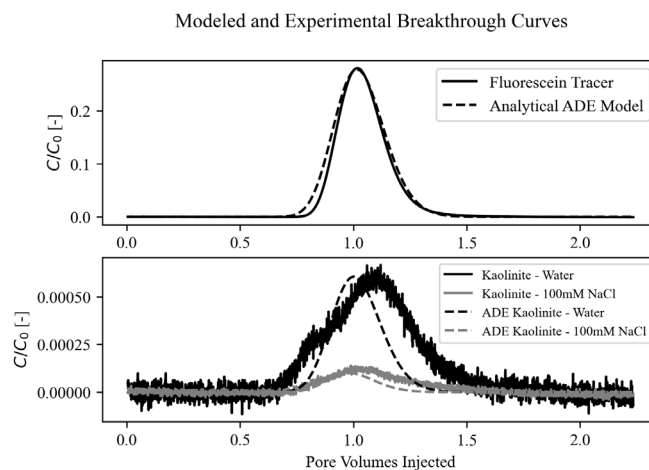


Fig. 4. Top) Normalized experimental tracer from column experiment (solid black) and the analytically modelled tracer (dashed black) from the ADE with reaction solution from Parker and van Genuchten [22]. Bottom) Normalized breakthrough curves of 150mM kaolinite suspended in DI water injected into Ottawa sand column that had been saturated with DI water (black curve with higher peak), analytically derived breakthrough curve (dashed black), 150mM kaolinite suspended in 100mM NaCl injected into Ottawa sand column that had been saturated with 100mM NaCl (grey curve with lower peak), and analytically derived breakthrough curve (dashed grey).

6 Micro-Positron Emission Tomography Imaging

Micro-PET imaging was performed on three sets of experiments: a tracer pulse of [¹⁸F]FDG, a pulse of ⁶⁴Cu²⁺ radiolabeled 150mM kaolinite in a sand pack saturated with 100mM NaCl, and a transition from 100mM NaCl to 1mM NaCl to simulate low saline injection. The results of the tracer pulse are reported in Figure 5 and shows normalized tracer concentration as a function of distance from the column inlet at several different pore volumes injected. Next, a radiolabeled pulse of kaolinite is injected into the sand pack and the results are reported in Figure 6. Lastly, a transition from 100mM NaCl to 1mM NaCl injection fluid is reported in Figure 7.

The saline injection of kaolinite (Figure 6) is exceptionally different than the tracer pulse in Figure 5. The radiolabeled clay penetrates the column to a maximum depth of around 2 cm before it is completely attached and immobilized. Autosampling of effluent and radiation probes at the effluent side of the column also validate this observation that kaolinite was immobilized in the column. Transitioning from 100mM NaCl injection solution to 1mM injection solution should theoretically remobilize the kaolinite and move it through the column. However, we do not see remobilization of kaolinite in response to changes in ionic strength (Figure 7). There may be very slight movement throughout the injection period, but this movement is extremely minor and likely only fractions of a centimeter.

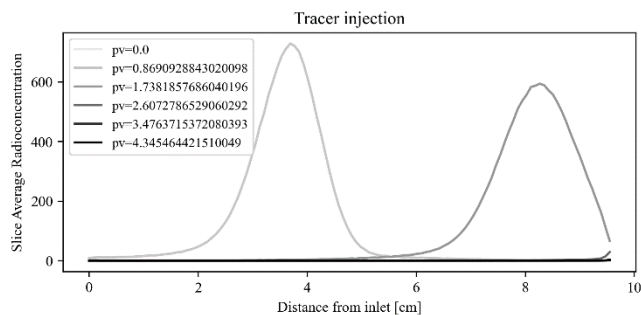


Fig. 5. Normalized [¹⁸F]FDG tracer pulse concentration profiles through a homogenous Ottawa sand pack as a function of column length. Concentration profiles are plotted as a summation of radioconcentration as a function of pore volumes injected.

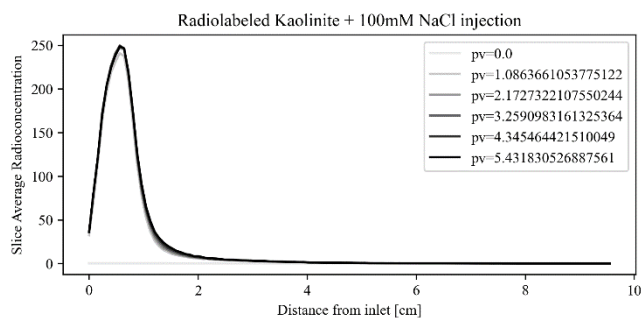


Fig. 6. Normalized ⁶⁴Cu²⁺ radiolabeled kaolinite in 100mM NaCl concentration profiles through a homogenous Ottawa sand pack as a function of column length. This plot shows the injection of kaolinite into the sand pack. Pore volume 0 is seen on the bottom of the plot since no radioisotope has been imaged yet. Breakthrough is plotted as a summation of radioconcentration as a function of pore volumes injected.

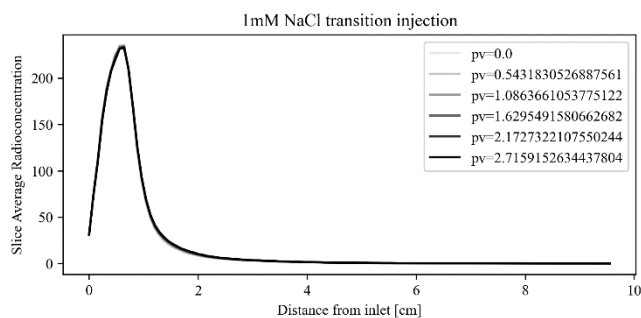


Fig. 7. Transition from ⁶⁴Cu²⁺ radiolabeled kaolinite in 100mM NaCl solution to a 1mM NaCl solution saturating the homogenous Ottawa sand pack column as a function of column length. This plot shows the transition from higher to lower ionic strength, so pore volume 0 is seen on the top of the plot of the plot since radiolabeled kaolinite was in the column when the PET scan began. Concentration profiles are plotted as a summation of radioconcentration at different pore volumes injected.

7 Discussion and Conclusion

Coreflooding experimental data with the UV-Vis spectrophotometer showed kaolinite is transported through the sand packs under all ionic strength conditions. Low ionic strength solutions showed higher tendency for kaolinite transport and less attachment to sand grains. Higher ionic strength solutions displayed higher tendency of kaolinite attachment and less transport through the sand packs. Transitioning from higher to lower ionic strength follows this

trend and results in an increase of kaolinite in the effluent even when kaolinite appears to be immobile under the higher ionic strength condition.

Analytical methods agreed with these observations. Analytical solutions to the 1D ADE with first-order reactions paired with colloid filtration theory give rough approximations of kaolinite transport and accurately can predict the order of magnitude of transport. This method does have limitations, however. The analytical solution does not account for the strong tailing behavior of kaolinite, nor does it account for faster than expected arrival times. There is also no way to account for the second peak that happens as a result of transitioning from 100mM NaCl to 1mM NaCl. DLVO calculations provide valuable context for electrochemical conditions of attachment or repulsion in the system and accurately predict the favorability of colloid transport or retention under NaCl and DI water saturating phase conditions.

Micro-PET experiments showed results that differ drastically from the non-radiolabeled column experiments and the analytical solutions. The [¹⁸F]FDG radiotracer experiment behaved exactly as expected and was similar to fluorescein experiments in terms of timing and transport. The ⁶⁴Cu²⁺ radiolabeled kaolinite displayed transport behavior that was unlike the non-radiolabeled kaolinite in the UV-Vis spectrophotometer. Radiolabeled kaolinite traveled only a few centimeters into the sand pack columns and was completely immobilized. Transitioning from a high ionic strength solution to a low ionic strength solution resulted in essentially no remobilization and transport of kaolinite.

It is likely that the sorption of ⁶⁴Cu²⁺ to kaolinite leads to drastic changes in the surface charge of kaolinite based on the results of the micro-PET imaging experiments. Al-Sarihi et al. [38] present one of the only studies on this topic and identify that CaCl₂ (a divalent cation) leads to no fines migration while NaCl (a monovalent cation) leads to fines migration. This study validates that a monovalent cation alone (NaCl) will lead to migration even at higher ionic strengths while a divalent cation (⁶⁴Cu²⁺) will lead to immobilization. However, the previously mentioned study found that clays with Ca²⁺ sorbed will remobilize when the saturating solution is transitioned to a solution with monovalent cations. This effect was not seen in our study, and it is likely that different types of divalent will behave differently. It is also unlikely that the ⁶⁴Cu²⁺ imaged during the PET scan desorbed and attached to the porous medium rather than the kaolinite due to the lack of desorption seen during batch desorption experiments.

Kaolinite transport, immobilization, and remobilization behavior may heavily rely on the available cations in the system and the flushing solution. This study is a step towards showing that electrochemically driven fines migration is a highly coupled process that is not controlled solely by ionic strength, but also by available cations. Groundwater commonly includes cations such as Ca²⁺, Mg²⁺, Na⁺, and K⁺ which could each impact fines migration and immobilization differently. In the case of low or high salinity injections, fluid chemistry of the injection solution should likely be closely considered in relation to the geochemistry of the natural environment. Further work needs to be done to identify the reversibility of these reactions and the permanence of immobilization.

Acknowledgements

The experimental system used for column and imaging experiments was supported by the National Science Foundation under Grant No. 2002412. Any opinions, findings, and conclusions or recommendations expressed in this material are those of the author(s) and do not necessarily reflect the views of the National Science Foundation. Additional support for this work was provided by the Office of the Vice Chancellor for Research and Graduate Education at the University of Wisconsin-Madison with funding from the Wisconsin Alumni Research Foundation.

Nomenclature

CFT	Colloid Filtration Theory
DLVO	Derjaguin, Landau, Verwey, and Overbeek theory
pH	Potential of Hydrogen
PET	Positron Emission Tomography
mM	milliMolar
PIPES	Piperazine-1,4-bis (2-ethanesulfonic acid) sesquisodium salt
NaOH	Sodium Hydroxide
⁶⁴ Cu ²⁺	⁶⁴ Copper ²⁺
DI	Deionized
μL	Microliter
M	Molar
mCi/mL	Microcurie per Milliliter
g	grams
PEEK	Polyetheretherketone
mL/min	Milliliter per Minute
ADE	Advection Dispersion Equation
C	Concentration
t	Time
v	Pore Water Velocity
D	Dispersion Coefficient
<i>D_e</i>	Diffusion Coefficient
<i>α_L</i>	Longitudinal Advection
<i>C_a</i>	Solute or Colloid Concentration
K	First Order Attachment or Detachment Coefficient
η	Total Forces Described by Colloid Filtration Theory
φ	Porosity
<i>d_c</i>	Diameter of Collector Grain
α	Attachment Term
μm	Micrometer
<i>V_{DLVO}</i>	Total Summation of DLVO Forces
<i>V_{LDW}</i>	van der Waals Forces
<i>V_{EDL}</i>	Electrical Double Layer Forces
<i>V_{BR}</i>	Born Repulsion Forces
cm	Centimeter
¹⁸ F	Fluorine 18
[¹⁸ F]FDG	Fludeoxyglucose Fluorine 18
nm	nanometer
Ca ²⁺	Calcium
Mg ²⁺	Magnesium
K ⁺	Potassium

References

1. C. Shen, B. Li, Y. Huang, Y. Jin, Environ. Sci. Technol. 41 (2007)
2. A. Busch, P. Bertier, Y. Gensterblum, Geomech. Geophys. Geo-energ. Geo-resour. 2 (2016)
3. S.G. Sarkisyan, Sed. Geol. 7, 1 (1972)
4. MIT, The Future of Natural Gas – An Interdisciplinary MIT Study, MIT, (2011)
5. H.H. Murray, Dev. Clay Sci. 2 (2006)
6. S.F. Kia, H. S. Fogler, M.G. Reed, R.N. Vaidya, SPE Prod Eng 2, 04 (1987)
7. F. Civan, Gulf Pro. Pub. (2007)
8. T. Russel, D. Pham, M.T. Neishaboor, A. Badalyan, A. Behr, L. Genolet, P. Kowollik, A. Zeinijahromi, P. Bedrikovetsky, J. Nat. Gas Sci. Eng. 45 (2017)
9. K.M. Yao, M.T. Habibian, C.R. O'Melia, Environ. Sci. Technol. 5 (1971)
10. S. Sasidharan, S. A. Bradford, S. Torkzaban, X. Ye, J. Vanderzalm, X. Du, D. Page, Sci. Total Environ. 603–604 (2017)
11. B.V. Derjaguin, LD. Landau, Acta Phys. Chim. 15 (1943)
12. E.J.W. Verwey, J.Th.G. Overbeek, J. Phys. Chem, 51, 3 (1947)
13. J.A. Redman, S.L. Walker, M. Elimelech, Envi-ron. Sci. Technol. 38 (2004)
14. R. Muneer, M.R. Hashmet, P. Pourafshary, ACS omega. 5, 49 (2020)
15. S. Tangparitkul, A. Saul, C. Leelasuksee, M. Yusuf, A. Kalantariasl, J. Pet. Sci. Eng., 194 (2020)
16. R.N. Vaidya, H.S. Fogler, Col Surf. 50 (1990)
17. K. M. Ahmad, F. Kristaly, Z. Turzo, R. Docs, J Oil Gas Petrochem Sci. 1, 1 (2018)
18. P. Schindler, P. Liechti, J. Westall, J. Colloid Interface Sci. 35, 3 (1987)
19. E. Wieland, W. Stumm, Geochim Cosmochim Aca 59, 9 (1992)
20. A. Ferris, W. Jepson, J. Colloid Interface Sci. 51, 2 (1975)
21. M. Kosmulski, Adv. Colloid Interface Sci. 275 (2020)
22. S.A. Bradford, S. Torkzaban, H. Kim, J. Simunek, Water Resour. Res. 48 (2012)
23. Q. Yu, A. Kandegedara, Y. Xu, D.B. Rorabacher, Anal. Bioch. 253, 1 (1997)
24. P.W. Schindler, P. Liechti, J. C. Westall, J. Ag. Sci. 35 (1987)
25. M. Alkan, B. Kalay, M. Dogan, O. Demirbas, J. Hazard. Mater. 153 (2008)
26. M.Q. Jiang, X.Y. Jin, X.Q. Lu, Z.L. Chen, Desalination 252 (2010)
27. R. Chakravarty, S. Chakraborty, A. Dash, Mol. Pharm. 13 (2016) 10.1021/acs.molpharmaceut.6b00582
28. B. Gutfilen, S. AL Souza, G. Valentini, Drug Des. Dev. Ther. 12 (2018)

29. W. Roy, I.Krapac, S. Chou, R. Griffin, U.S. E.P.A., EPA/530/SW-87/006F (2004)
30. C. Zahasky, T. Kurotori, R. Pini, S.M. Benson, Adv. Water Res. 127 (2019)
31. M. van Genuchten, W.J. Alves, U.S.D.A. Tech. Bul. 1661 (1982)
32. J.C. Parker, M. van Genuchten, W. R. Res. 20, 7 (1984)
33. X. Li, T.D. Scheibe, W.P. Johnson, Env. Sci. Tech. 38 (2004)
34. L. Chequer, P. Bedrikovetsky, T. Carageorgos, A. Badalyan, V. Gitis, W. R. Res. 55, 7 (2019)
35. S.A. Bradford, H. Kim, J Environ Qual. 39, (6) (2010) doi: 10.2134/jeq2010.0156. PMID: 21284301
36. C. Zahasky, S.M. Benson, Adv. Water Res. 115 (2018)
37. T. Kurotori, C. Zahasky, S.A.H. Hejazi, S.M. Shah, S.M. Benson, Chem. Eng. Sci. 196 (2019)
38. A. Al-Sarihi, T. Russell, P. Bedrikovetsky, A. Zeinjahromi, Ener. Fuel. 33 (2019)

An integrated petrophysical analysis based on NMR, organic geochemistry and mineralogy. The Vaca Muerta source rock-unconventional play at different thermal maturities

Diana Masiero^{1*}, Marcos Comerio¹, Esteban Domené¹, Gabriela Vila¹, Bernarda Epele¹, Mariano Cipollone¹, Mariela Silka², Carlos Camacho³, Lourdes Vera López² and Silvina Chiappero²

¹YPF-Tecnología S.A. (Y-TEC-CONICET), Buenos Aires, Argentina

²YPF S.A., Buenos Aires, Argentina

³EQUINOR ASA, Houston, TX, United States of America

Abstract. The Vaca Muerta Formation (Upper Jurassic–Lower Cretaceous) of the Neuquén Basin, Argentina is a world-class source rock and renowned as an unconventional reservoir for both oil and gas. The present study examines rotary sidewall cores representative of the oil and gas windows to analyze correlations between nuclear magnetic resonance (NMR T₂ and T₁-T₂ maps at 2 MHz), Gas Filled Porosity (GFP), Rock-Eval programmed pyrolysis and quantitative X-ray diffraction (XRD) mineralogy. Shale samples are characterized by high present-day total organic carbon contents ranging from 3 to 7.20% (mean: 4.30%) for Well A at the oil window and, 0.72 to 11.77% (mean: 5.86%) for Well B at the gas window. The analyzed set also covers a wide compositional spectrum from carbonate-rich (> 50% of calcite and minor dolomite), mixed carbonate-siliciclastic (30 to 50% of calcite), to siliciclastic-rich (< 30% of calcite) samples. Notably, the clay fraction is dominated by interstratified illite-smectite minerals with less than 10% of expandable layers. Total porosity, calculated from Gas Filled Porosity plus NMR T₂ Cumulative Distribution, is in the range of 10 to 20 porosity units. In this work we also present a new NMR sequence to detect solid-like organic matter with NMR at 2 MHz in an integrated workflow to characterize petrophysical properties of the Vaca Muerta Formation.

1 Introduction

Petrophysical studies are envisioned to characterize both conventional and unconventional reservoirs based on the evaluation of different properties including lithology, wettability, fluid saturation and composition, as well as porosity and permeability [1, 2]. Contrary to conventional reservoirs, a complete petrophysical analysis of unconventional plays, in particular shale rocks characterized by fine-grained components, presence of organic matter, and heterogenous lithologies is still challenging and new case studies are needed to obtain different workflow strategies.

The Vaca Muerta Formation of the Neuquén Basin Argentina, is a marine source rock with excellent characteristics from the perspective of source rock-unconventional plays: (1) high present-day TOC content (1 – 8% with peaks of 12%); (2) original hydrogen index (HIo) estimated to be approximately 680 mg HC/g TOC; (3) moderate depths of 3.150 m; (4) overpressure distribution in the order of 47–61 MPa, (5) lack of expandable clays in mature areas; and (6) different landing zones for the production of oil, wet gas and dry gas [3, 4, 5, 6, 7, 8].

In addition to the organic geochemical patterns of the Vaca Muerta Formation, petrophysical properties are key factors in hydrocarbon production. Several works correlate laboratory measurements and downhole log information to identify main reservoir properties [9, 10, 11]. However, in the Vaca Muerta Formation reservoir properties and fluid types seem to vary significantly both laterally and vertically suggesting that each interval of interest must be addressed and analyzed separately [11]. Nuclear magnetic resonance (NMR) is a widely used technique to characterize the porosity framework and fluid properties of shale plays due to its non-invasive nature and the possibility of performing in-situ measurements. Recently, the application of low field NMR laboratory measurements to detect both fluid (water and hydrocarbons) and solid-like organic matter components in Vaca Muerta samples was demonstrated, making low field NMR a powerful technique to improve the petrophysical characterization of this unit [12].

The present study examines two wells located in areas where according to regional maturity maps the unit ranges in maturity from the oil window to the gas window [6]. The

* Corresponding author: diana.m.masiero@ypftecnologia.com

main objective of this work is to obtain a workflow that allows a full and integrated petrophysical characterization of the Vaca Muerta Formation. This is achieved by combining different techniques and performing a detailed comparison and integration of the obtained results. The experimental techniques explored in this work include low-field NMR T_1 - T_2 maps, organic geochemistry, gas filled porosity, microCT imaging and mineralogical analysis.

2 Data and methods

The present study shows petrophysical, mineralogical and organic geochemistry results integrated with 3D micro-scale reconstructions from rotary sidewall and core samples from two wells: Well A and Well B (Figure 1). The study includes shale samples (13 from Well A, 15 from Well B), but lithologies such as altered tuffs (1 sample, Well A) were also taken into consideration.

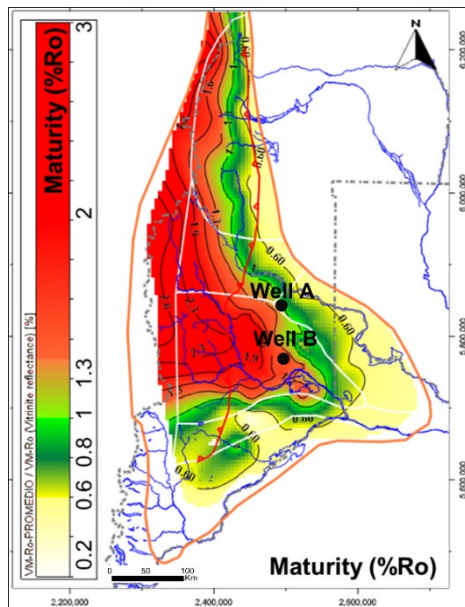


Fig. 1. Vaca Muerta Formation regional maturity map based on Brisson [6], and location of Well A and Well B analyzed in this work.

2.1 Workflow

In Fig. 2 the proposed workflow for characterization of rock samples from the Vaca Muerta formation is presented. This workflow can be applied to any non-conventional rock sample. Special emphasis is made on treating samples “as received” and performing non-destructive measurements to preserve as much sample as possible.

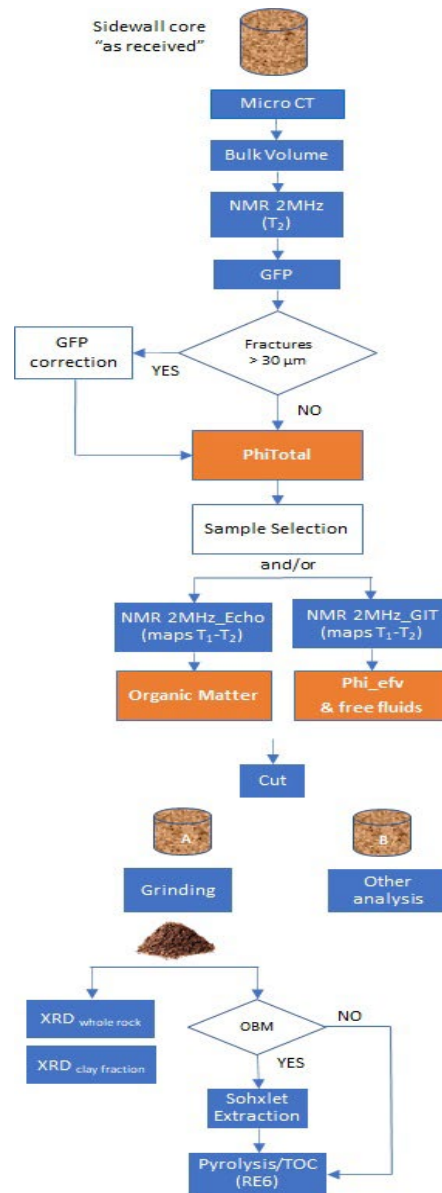


Fig. 2. The integrated workflow used for the analysis of sidewall core samples from Well A and Well B is presented.

2.2 Nuclear Magnetic Resonance (NMR)

NMR measurements were performed at 2.27 MHz with an Oxford Geospec2 analyzer. Samples were measured bulk as received; the average mass of the samples was 40–50 g, approximately. T_2 measurements were carried out with a standard CPMG sequence with echo time 100 μ s. This experiment allows to quantify the fluid-filled pore space; total porosity is obtained by adding this value to the GFP porosity (see below).

T_1 - T_2 maps were acquired with the SR-FID-ECHO-CPMG sequence introduced by Silletta et al. [12], a scheme that allows to probe the decay of both solid-like and liquid components of shale samples in a single measurement. In this setup, T_1 was encoded with a saturation recovery (SR) sequence with delay time from 21 μ s to 390 ms in 50

logarithmic steps. In the T_2 dimension, a CPMG pulse sequence was applied (echo time 200 ms, 500 echoes) sampling one data point at the echo tops. Furthermore, 18 points were sampled during the FID (dwell time 8 ms) before the first 180° pulse of the CPMG; to increase the FID acquisition time a spin echo of $t = 200$ ms was introduced before the CPMG echo train. The numerical inversion was performed applying the algorithm presented in [13] with exponential kernels in both dimensions. The zones in the T_1 - T_2 maps were interpreted as in [12].

2.3 Gas Filled Porosity (GFP)

The empty pore space inside the rock sample is quantified using results from two separate experiments: a Hg pycnometer and GFP. The first, the Hg pycnometer, allows the characterization of the bulk volume. It uses a container filled with Hg whose density is characterized beforehand. Then the sample is fully submerged in the Hg and the change in weight is registered by a scale. The Archimedes method is used to estimate the outer volume of the sample.

The second experiment is known as GFP and is performed using a He Porosimeter from Vinci Technologies. The equipment itself measures grain volume. It has a sample chamber to house the sample and a reference chamber which is loaded with He at 200 psi; both chambers are connected, and the final stabilization pressure is detected. Therefore, the empty space in the sample chamber can be obtained, and by knowing the total volume of the chamber, the grain volume is deduced. It is important to point out that the time it takes the He to occupy the empty pore space will depend directly on the permeability of samples. Thus, lower permeability samples will take longer times than higher permeability ones. A long stabilization time (around 10 minutes) with a strict pressure tolerance (± 0.03 psi) for unconventional rocks is considered. We also repeat the experiment at least three times to make sure that measurements are repeatable.

By combining the bulk volume measurement of the rock with the grain volume, the empty pore space is quantified. This value refers to the part of the porosity that is empty (filled with air) and accessible from the outer surface of the rock.

2.4 X-ray diffraction (XRD)

For mineralogical analysis both bulk rock and clay fraction analysis were done. For bulk rock analysis samples were ground to a fine particle size using a Retsch MM400 mixer mill. X-ray diffraction patterns were collected on random powder specimens using a D8 Advance Bruker X-ray diffractometer (Ni-filtered $\text{CuK}\alpha$, 40 kV, 40mA). A 5–70 deg 2θ range was acquired, with 0.02 deg steps and 0.5 second counting time. Diffraction data were analyzed using DIFFRAC.EVA software for identification of mineralogical

phases. Weight percentages of observed phases were calculated using quantitative Rietveld analysis with DIFFRAC.TOPAS.

Determination of clay minerals was performed on the fraction less than 2 μm . Three oriented aggregates were prepared (air-dried, ethylene glycol solvated and calcinated) and their XRD patterns collected in the range of 3–30 deg 2θ with 0.02 deg steps and 0.5 second counting time. Identification of clay mineral phases was based on diagnostic peaks according to Moore and Reynolds [14] and their quantification using NEWMOD program as described in Moore and Reynolds [14].

2.5 Rock Eval programmed pyrolysis

The characterization of organic matter (OM) was performed using a Rock-Eval 6 [15]. Powdered whole rock samples were placed in an oven and first heated to 300°C under an inert atmosphere and then gradually pyrolyzed up to 650°C . After the pyrolysis was completed, samples are gradually heated up to 850°C in the presence of air. The S1 (free hydrocarbons) was not considered since samples were solvent extracted due to the use of oil-based mud during drilling operations. The S2 (hydrocarbons generated by kerogen cracking) and S3 (releasable oxygen) measures allowed to calculate hydrogen and oxygen indices (HI, OI) and estimate kerogen types (from I to IV), using the modified Van Krevelen diagram [16]. The thermal maturity was based on the determination of T_{max} [17]. This parameter increases with the maturation degree of the organic matter and was used to obtain a thermal maturity estimation of the analyzed samples.

2.6 X-ray micro-Computed Tomography (microCT)

As a nondestructive technique, X-ray microcomputed tomography provides the required insight into opaque objects eliminating the need of sectioning. Specimens were imaged in a Bruker SkyScan 1173 High Energy desktop microCT at 130 kV and 61 μA with a 0.25 mm brass filter. The cubic voxel size was fixed at 35.72 μm and the samples were rotated around 360° at angular increments of 0.80° . The microCT radiograph projections were reconstructed using NRecon version 1.6.9.8 to obtain an axial slice image dataset. The 8-bit (256 grey values) image dataset was imported into DataViewer version 1.5.0 for visualization. The images obtained provide detailed visualization of the internal fabric and recognition of heterogeneities including fractures [18]. In grayscale images black correspond to air, dark grays to low X-ray absorbing minerals like quartz or feldspars and bright grays to higher X-ray absorbing phases such as calcite or, in white, pyrite. Segmentation and analysis of microCT images allow for the quantification of porosity associated with open fractures (> 30 μm thick) as observed for Well A (Figure 4). With image processing percentage of open fractures, in dark gray, was calculated with respect to the total volume. As

pores in the internal structure have sizes lower than the resolution of the images, they are not considered in the segmentation. Thus, GFP was corrected only to include pores in the internal structure of the rock.

3 Results and Discussion

3.1 Well A

Shale samples are characterized by high present-day TOC contents ranging from 3–7.20% (mean: 4.30%), with maximum values registered in siliciclastic-rich (< 30% of calcite) samples (Table 1). The S2 peak which coincides with the remaining potential of hydrocarbon generation ranges from 2.84–12.75 mg_{HC}/g_{rock} (mean: 5.75); whereas the HI shows values between 103–177 mg_{HC}/g_{TOC} (mean: 130). Rock Eval® Tmax values (458–462°C, mean: 460) point to analyzed samples being mature in the late oil window (Fig. 3). As expected, anomalous values of TOC (< 1%) and S2 (< 1 mg/g) were determined in altered tuff levels.

According to whole rock XRD analysis, siliciclastic-rich shales are mainly composed of quartz (22–41%, mean: 31), plagioclase (13–19%, mean: 16), and clay minerals (12–21%, mean: 16) with minor proportions of K-feldspar, pyrite and apatite. On the contrary, carbonate-rich samples show a predominance of calcite (50–60%, mean 53). Mixed carbonate-siliciclastic (30–50% of calcite) shales exhibit variable proportion of quartz (18–25%, mean: 23), plagioclase (9–12%, mean: 11), and clay minerals (9–15%, mean: 11). The composition of the clay fraction does not display vertical differences with illite-smectite (expandable layers < 10%) as the dominant phase.

In some siliciclastic-rich samples, microCT images reveal original depositional features with very thin parallel lamination and organized in lenticular fabrics (Fig. 4). Massive fabrics are observed in carbonate-siliciclastic and carbonate-rich samples. There is no evidence of internal disposition, possibly because the main components are smaller than the resolution achieved. MicroCT was an important tool to resolve the occurrence of fracture porosity, considering they derive from the extraction of samples from the well. In such cases, GFP values were corrected by subtracting the porosity associated with fractures. Due to experimental limitations on the microCT resolution, only fractures greater than 30 µm thick were considered.

The combination of GFP and T₂ measurements yield for shale samples values in the order of 12 – 19 porosity units (pu), with maximum porosities registered in siliciclastic shales (Table 1).

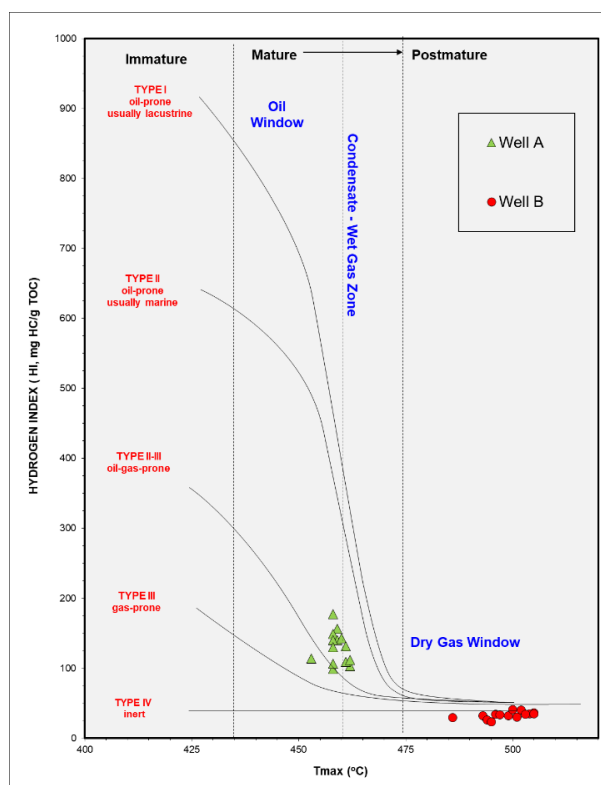


Fig. 3. HI vs. Tmax diagram for the analyzed samples from Well A and Well B (type lines modified from Espitalié et al. [16]).

Table 1. Summary with results for Well A. Minimum, maximum and mean values are presented.

	Siliciclastic shales (n: 5)	Carbonate-siliciclastic shales (n: 3)	Carbonate shales (n: 5)
TOC [%]	3 – 7 (5)	3 – 5 (4)	2 – 4 (3)
Carbonates [%]	15 – 29 (25)	31 – 48 (45)	52 – 61 (57)
Qz + Feld [%]	40 – 62 (49)	31 – 39 (35)	27 – 34 (30)
Clays [%]	12 – 21 (16)	9 – 15 (11)	7 – 9 (8)
GFP_AR [pu]	3 – 6 (4)	4 – 6 (5)	3 – 6 (4)
PhiRMN_AR [pu]	10 – 13 (12)	10 – 13 (11)	8 – 11 (9)
PhiTotal_AR [pu]	14 – 19 (16)	15 – 17 (16)	12 – 16 (14)

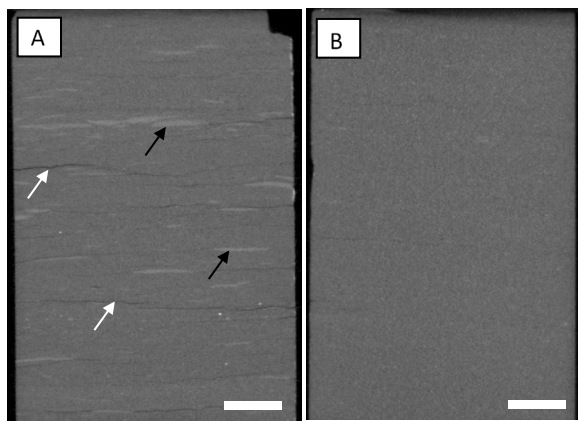


Fig. 4. Examples of microCT images from Well A samples. A) Lenticular fabric observed in organic-rich shales with carbonate lenses disposed parallel to bedding planes (black arrows). Note the presence of empty fractures (white arrows). B) Massive aspect observed in carbonate-rich samples. Scale bar = 5 mm.

Further characterization of the components inside the rock was achieved by NMR measurements. Fluid contribution to porosity was obtained from T_2 NMR measurements (Table 1). T_1 - T_2 maps give further information on the hydrogen rich components present in the rock. A typical map for Well A can be seen in Fig. 5. The following zone identification is adopted from [12]: zone 1 corresponds to hydroxyl groups present in the inorganic components of shales (clay or other minerals); zone 2 is associated with solid organic matter, kerogen, bitumen and light hydrocarbons inside the kerogen network; zone 3 is attributed to clays; zone 4 is corresponds to moveable hydrocarbons.

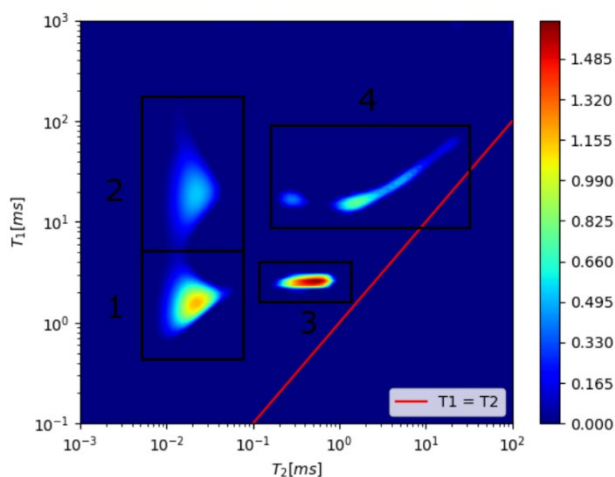


Fig. 5. NMR T_1 - T_2 map for a representative sample of Well A. Four zones are clearly marked by black rectangles.

Quantification of NMR signal per zone is performed for each of the 13 samples from Well A. NMR results are integrated with XRD and Rock-Eval measurements. Zone 3 is correlated with clay content from XRD (Fig. 6); zone 2 is correlated with TOC values from Rock Eval pyrolysis (Fig. 7). Both

integrations show a very good correlation. This indicates that the three experimental techniques are comparable. Also, since both XRD and Rock-Eval only consider less than 2–3 grams of mass, while NMR is performed on whole rock (approximately 40 grams for Well A samples), the good correlation points to representativity of subsample extraction and homogeneity of the sample.

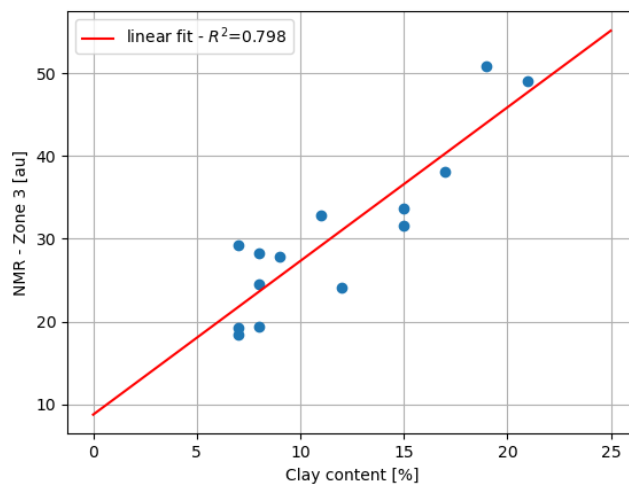


Fig. 6. NMR signal from zone 3 is plotted against clay content in the rock from XRD. A linear fit is performed (red line). R^2 stands for the coefficient of determination of the least-squares.

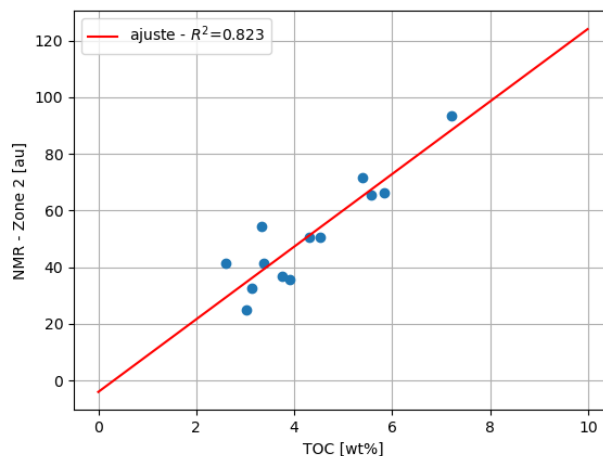


Fig. 7. NMR signal from zone 2 is plotted against TOC value from Rock-Eval pyrolysis. A linear fit is performed (red line). R^2 stands for the coefficient of determination of the least-squares.

3.2 Well B

Shale samples from Well B also show high present day TOC contents (0.72–11.77%, mean: 5.86), with S2 peak ranging from 0.21–4.14 mgHC/grock (mean: 1.93) and HI of 23–40 mgHC/gTOC (mean: 32). Rock Eval® Tmax values (486–506°C, mean: 499) are higher than those presented for Well A, indicating that in the position of Well B the unit reached the wet gas window (Fig. 3).

Based on the adopted compositional scheme, most analyzed samples are siliciclastic-rich (< 30% of calcite) with the highest TOC contents (Table 2). They are composed of quartz (15–37%, mean: 26), plagioclase (9–34%, mean: 20), and clay minerals (18–43%, mean: 28) with minor proportions of K-feldspar, pyrite and apatite. Two samples of the analyzed set correspond to the mixed carbonate-siliciclastic (30–50% of calcite), whereas only one represents the carbonate-rich (> 50% of calcite) shales. However, the latter shows important micro-fractures filled with calcite which impacted in the calculated whole rock composition. Calcite mm-thick micro-fractures were observed under microCT acquisitions as well as interbedded laminae showing compositional and grain size changes (Fig. 8).

According to GFP and T_2 measurements shale samples show porosity values of 10 – 17 pu (Table 2).

Table 2. Summary with results for Well B. Minimum, maximum and mean values are presented.

	Siliciclastic shales (n: 12)	Carbonate-siliciclastic shales (n: 2)	Carbonate shales (n: 1)
TOC [%]	1 – 12 (6)	5 – 6	6
Carbonates [%]	12 – 29 (19)	43 – 45	60
Qz + Feld [%]	36 – 53 (46)	41 – 43	27
Clays [%]	18 – 43 (28)	8 – 11	10
GFP_AR [pu]	2 – 10 (7)	7 – 8	6
PhiRMN_AR [pu]	6 – 10 (7)	5	4,5
PhiTotal_AR [pu]	11 – 17 (14)	12 – 13	10,5

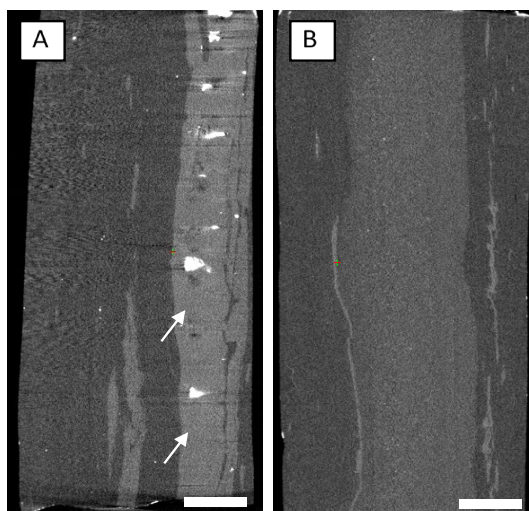


Fig. 8. Examples of microCT images from Well B samples. A) Organic-rich, siliciclastic shale with calcite microfractures (white arrows). B) Siliciclastic shale with internal heterogeneities as result of compositional and grain-size changes. Scale bar = 5 mm.

A similar NMR workflow was performed on samples from Well B, where T_2 measurements account for the porosity associated with fluids in the rock, while NMR T_1 - T_2 maps allow for component typification. In Fig. 9 a representative T_1 - T_2 map for a sample in Well B is shown. Four different zones are marked with black rectangles.

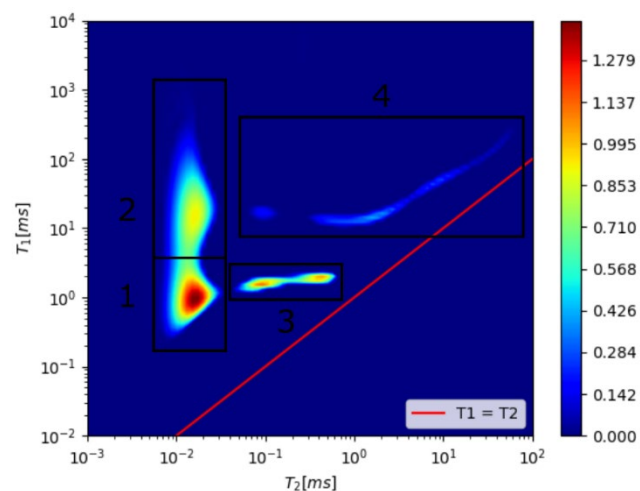


Fig. 9. NMR T_1 - T_2 map for a representative sample of Well B. Four zones are clearly marked by black rectangles.

The NMR signal corresponding to each zone is calculated and the results are compared to XRD and Rock-Eval pyrolysis. Zone 3 is compared to clay content (Fig. 10) while zone 2 is compared to TOC (Fig. 11). As in the case of Well A, NMR signal from zone 3 strongly correlates to clay content obtained from XRD analysis. In the case of zone 2 and TOC values, the correlation is not as strong, and the data points show a larger dispersion compared with Well A. We consider that different variables might have controlled the observed uncertainty: (1) Wells represent different maturity window, oil window for Well A and gas window for Well B; (2) the analyzed set for both Wells does not strictly represent the same organic-rich intervals of the Vaca Muerta Formation; and (3) the internal heterogeneities documented through microCT images. Another possible reason for this discrepancy in correlation could come from the difference in measured mass in Rock-Eval (less than 2–3 grams) and NMR (whole rock, more than 40 grams). Accordingly, further work is necessary to find the cause of the dispersion in values of NMR zone 2 for Well B samples.

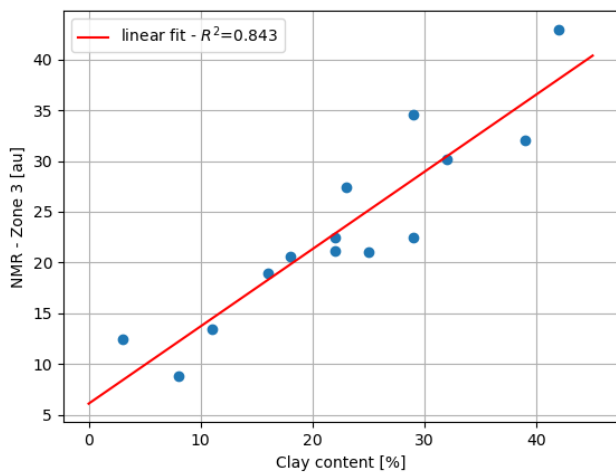


Fig. 10. NMR signal from zone 3 is plotted against clay content in the rock from XRD. A linear fit is performed (red line). R^2 stands for the coefficient of determination of the least-squares.

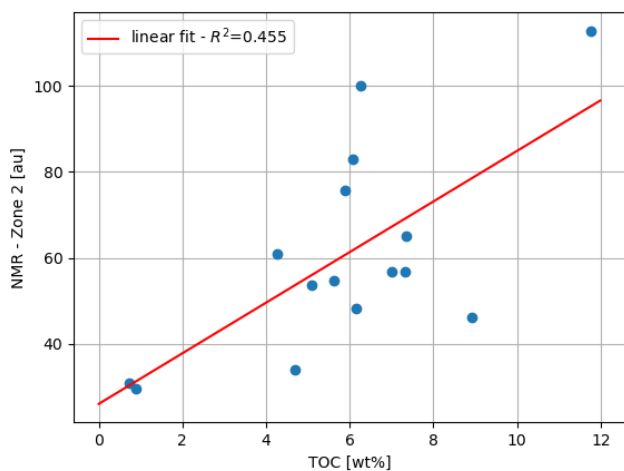


Fig. 11. NMR signal from zone 2 is plotted against TOC value from Rock-Eval pyrolysis. A linear fit is performed (red line). R^2 stands for the coefficient of determination of the least-squares.

4 Conclusions

The present study analyzed samples of the Vaca Muerta Fm based on RMN T_1 - T_2 maps at 2 MHz combined with GFP, XRD, Rock-Eval pyrolysis and microCT data with the intent of defining a multi-scale and multidisciplinary petrophysical workflow that can be used for the evaluation of sidewall and core samples at different thermal maturities.

The unit is an heterogenous system independent of the scale of work. GFP and T_2 measurements have shown total porosity values ranging from 10 pu to 19 pu, with maximum porosities recorded in siliciclastic shales (< 30% of calcite). Rock-Eval pyrolysis confirm that a part of the analyzed siliciclastic shales has the largest organic carbon contents.

MicroCT images reveal different types of heterogeneities including open fractures as those recorded in Well A. In such cases, indirect measurements of parameters

(e.g., porosity by GFP) do not account for the origin of pores and, for example, do not determine whether the sample is fractured or not. Imaging techniques, such as microCT, together with Digital Rock Analysis (DRA), allow the study of heterogeneities in the rock, as those described in this work, and are of great importance to discriminate open or closed fractures and achieve more reliable porosity measurements.

The presence of heterogeneities as well as other variables, such as the difference in measured mass, might impact in the correlation between NMR and direct rock analysis (e.g., TOC% via pyrolysis Rock Eval). In the future, new measurement strategies can be refined to reliably discern the causes of data dispersion.

This study is published with the permission of YPF, EQUINOR and Y-TEC. We are especially grateful to C. Smal, M. Sánchez, G. Bobrovsky and J. P. Alvarez (Y-TEC) and V. Consoli, D. Cecon, M. Foster, C. Bernhardt, M. Fasola, I. Brisson and G. Sagasti (YPF) for allowing us to publish the present data.

Special thanks for the technical staff at Y-TEC (J. Juárez, D. Robledo, G. Otegui, J. Acosta, K. Irvicelli, I. Loyza, R. Panno) for the preparation and acquisition of core samples and data analyzed in this study.

References

1. R.L. Kleinberg, W.E. Kenyon, P.P. Mitra, J. Magn. Reson Ser A, **108**, 206-214 (1994)
2. G.R. Coates, L. Xiao, M. Prammer. Nmr Logging, 251, (1999)
3. M. Uliana, L. Legarreta, Journal of Petroleum Geology, **16**, 397-420, (1993)
4. G. Sagasti, M. Foster, D. Hryb, A. Ortiz, V. Lazzari, *Unconventional Resources Technology Conference*, 797-816, (2014)
5. R.F. Dominguez, M. Di Benedetto, *Unconventional Resources Technology Conference*, 5114-5128, (2019)
6. I.E. Brisson, M.E. Fasola, H.J. Villar, *Integrated geology of unconventional: The case of the Vaca Muerta play, Argentina*, AAPG Memoir **121**, 297-328, (2020)
7. J.B. Spacapan, M. Comerio, I. Brisson, E. Rocha, M. Cipollone, J.C. Hidalgo, Basin Research, **33**, 3183-3211 (2021)
8. J.B. Spacapan, M. Comerio, R. Ruiz, E. Rocha, Journal of Petroleum Geology **45**, 219-248, (2022)
9. A. Askenazi, P. Biscayart, M. Cáneva, S. Montenegro, S., M. Moreno, M, Society of Petroleum Engineers (SPE), (2013)
10. S. Cuervo, E. Lombardo, D. Vallejo, L. Crousse, C. Hernandez, L. Mosse, Unconventional Resources Technology Conference (URTeC), 778-796, (2016)
11. A.C. Ortiz, L. Crousse, C. Bernhardt, D. Vallejo, L. Mosse, *Integrated geology of unconventional: The case of the Vaca Muerta play, Argentina*, AAPG Memoir **121**, 329-350, (2020)
12. E.V. Silletta, G.S. Vila, E.A. Domené, M.I. Velasco, Fuel, **312**, 122863, (2022)

13. P. Teal, C. Eccles C., *Inverse Probl.*, **31**, 045010, (2015)
14. D.M. Moore, R.C. Reynolds, *X-ray diffraction and the identification and analysis of clay minerals*, (1989)
15. E. Lafargue, F. Marquis, D. Pillot, *Revue de l'institut français du pétrole*, **53**, 421-437, (1998)
16. J. Espitalié,, G. Deroo, F. Marquis, *Revue de l'institut Français du Pétrole*, **41**, 73-89, (1986)
17. K.E. Peters, *AAPG Bulletin*, **70**, 318–329, (1986)
18. M. Comerio, D.E. Fernández, N. Rendtorff, M. Cipollone, P.E. Zalba, P.J. Pazos, *AAPG Bulletin*, **104**, 1679-1705, (2020)

SOME USEFUL GUIDELINES FOR WHOLE CORE CT-SCANNING FOR PETROPHYSICAL APPLICATIONS

Shameem Siddiqui^{1,2*}

¹Halliburton Consulting, 3000 N. Sam Houston Pkwy, E, Houston, TX 770, USA

²ResVisions LLC, 16902 Cook Landing Drive, Richmond, TX 77407

Abstract. From the time CT-scanning was introduced in the oil and gas industry, its use could be divided into SCAL and routine type applications. The first involves flowing fluids through the cores, whereas the second involves scanning, mainly the whole cores, in their native (preserved or unpreserved) state. For whole core CT-scanning, there has been a constant shift from qualitative to quantitative analysis. The size of whole cores is ideal for scanning them with a ‘converted’ medical CT-scanner but obtaining meaningful data requires more than just artifact-free images. In this paper, useful guidelines are offered for extracting meaningful quantitative data from whole core CT-scanning. Today’s fast, multi-slice medical CT-scanners generally provide sufficient image resolution for most of the whole core related applications. However, they usually require some modifications to the equipment and the calibration procedures. Special solid phantoms matching the size and density should be used for calibrating the scanner at different X-ray energies. A set of calibration ‘standards’ is necessary for converting the CT numbers into density and Z_{eff} (Effective Atomic numbers), which should be scanned under the similar ‘environment’ as the whole cores. Using pilot scans is highly recommended for every core tube to reduce uncertainties. For dual energy scanning, it is important to take scans at the exact same locations, selecting the right energy pair and corresponding calibration tables. For image processing, important guidelines include aligning the first and last slices for selecting the largest region-of-interest, quality controlling each slice and assigning depths to each slice before converting from CT numbers to bulk density and Z_{eff} . Additional information is provided for scanning with industrial CT-scanners which have both advantages and disadvantages. Guidelines such as the ones mentioned above allow the data from whole core CT imaging useful for a number of applications. Such data were successfully used for bulk density and porosity determination, heterogeneity quantification, lithology determination, dual-energy based mineralogy detection, density-based micro-imaging, core-log correlations and depth matching, fracture characterization, formation damage evaluation, and many others. Several examples are included in this paper. Adherence to strict guidelines help extracting artifact-free, meaningful data on whole cores that can improve our understanding of rocks. This paper demonstrates at least 10 different applications of CT-scanners along with the proper guidelines that can be useful for engineers and geoscientists.

1 Introduction

CT-scanning has been used for core characterization and flow visualization in reservoir rocks for over 35 years. In the flow visualization category, CT-scanning has been successfully used for porosity and pore volume compressibility determination, two- and three-phase flow visualization and quantification, and for evaluating core treatments such as acidizing, foam injection, EOR fluid injection, etc. CT-based core plug screening has been one of the most popular early uses of the technology. Although the other core characterization applications came a little later, CT-based characterization includes evaluating core quality, identifying and quantifying bulk lithology, measuring density and porosity, integrating CT-derived density and porosity with log-derived data, depth matching, quantifying heterogeneity, detection of fractures, visualization and evaluation of mud or treatment fluid invasion, etc. While most of these petrophysical applications apply equally to whole cores and plugs, the focus will be on whole core CT-scanning only.

Cores collected from reservoirs during the exploration and development phases can provide very important petrophysical, paleontological, sedimentological, petrographic, and diagenetic information and therefore, utmost care should be taken to avoid damaging the cores. Some of the best practices in core handling involves onsite sectioning of the cores, while inside their aluminum or fiberglass sleeves, into 3 ft (about 1 m) long sections, marking the depths and identifying tops (typically with two parallel lines, red and black), putting caps on both ends and then putting

these sleeves in reservoir compatible brine inside a PVC core box in order to preserve wettability (Fig. 1). The core box, without brine, also serves to protect the core integrity during transportation. After carefully transporting the core boxes to the core handling facility, CT-scanning should be one of the first operations executed on core samples because core integrity is compromised once the core is extracted from its sleeve (Fig. 2) for core description, slabbing and plugging. This way the three-dimensional, mostly density-related data remains available for any future qualitative and quantitative use, even after the core becomes subjected to extensive slabbing and plugging.



Fig. 1. Photograph of PVC core boxes at the loading dock of a CT Lab.

* Corresponding author: siddiqui.shameem@gmail.com

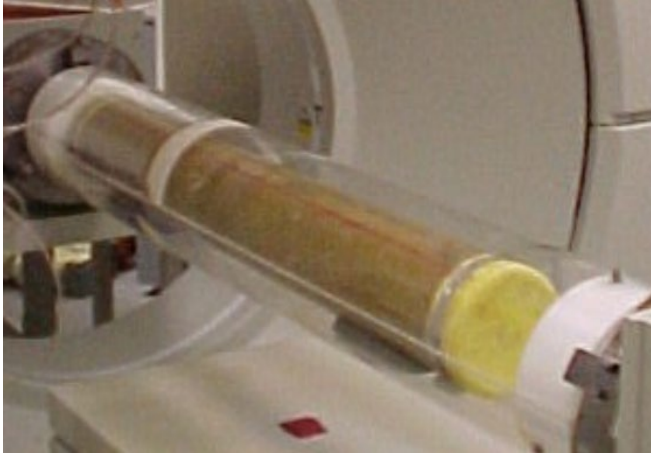


Fig. 2. Fiberglass core sleeve with rubber caps at the two ends placed concentrically in the Plexiglas housing of a converted medical CT-scanner before scanning.

Both medical and industrial CT-scanners can be used for whole core CT-scanning, with each one having its own advantages and disadvantages. A comparison between the two types of scanners for various petrophysical applications is presented in Ref. [1]. The industrial CT-scanners, which include micro and nano CT-scanners, offer a wide range of X-ray voltages and intensities, and provide excellent spatial resolution, sometimes to the pore level. They are more preferred for evaluating small plugs and cuttings rather than whole cores, mainly because the scanning speed is very slow and the samples have to be rotated in a vertical position during scanning, which may be detrimental to the sample integrity, especially for unconsolidated or naturally fractured cores.

Medical CT-scanners, with their large weight capacity, reasonable spatial resolution (typically 0.3 to 0.5 mm pixel length) and fast speed (especially with multi-slice technology), are ideal for scanning whole cores for various petrophysical applications. Although a properly calibrated Medical CT-scanner is capable of generating high quality images for most reservoir rocks, the data are not always sufficient for quantitative analysis that may be required for advanced petrophysical applications. In the next section, a discussion is made on the necessary modifications that would make a medical CT-scanner useful for scanning various types of reservoir rocks and for getting meaningful quantitative data for integrated reservoir studies.

2 CT-Scanner Modifications Needed for Petrophysical Applications

The selection of the medical scanner for petrophysical applications is of primary importance. Some of the points that should be considered during the selection process include maximum voltage, whether or not it is dual-scan capable, number of slices (for multi-slice CT-scanners), capability to do pilot scans and their lengths, etc. Medical CT-scanners are designed for human subjects and exposure of soft tissues, where maximum X-ray voltage, scanning speed are all very important considerations. Due to safety and intellectual property issues, many manufacturers are generally not willing

to share advanced calibration and data transfer information with the non-medical clients and it is therefore, essential to obtain necessary permissions before purchasing a new scanner from a particular vendor. Sometimes it is more convenient to go through a third-party vendor with good connections with the CT-scanner manufacturers and good familiarity of petrophysical CT-scan requirements.

In general, modifications are needed in three major areas in order to convert a medical CT-scanner into one that is capable of being used for petrophysical applications. The first one is the modification of the patient bed into a sturdier metallic table. The strong cantilever arm used to support the patient bed is not designed to align, a 3 ft long core box, and since core alignment is crucial for petrophysical measurements, it is better to replace the soft patient bed with a steel table fitted with a pair of vises to ensure the proper centering of the core box or core tube. Fig. 2 shows how a vise mounted on the modified patient table (right) and another vise mounted on an added rear table are used to align a Plexiglas tube, which in turn, holds and centers the fiberglass core sleeve with the help of foamed plastic rings.

The second required modification is that of the internal calibration tables. Having the access to the calibration tables and permissions to modify them in order to scan the rocks is very important. Normally the manufacturers calibrate the scanner with a “water phantom” containing a radiopaque salt (typically sodium iodide) in water, which is sufficient for scanning human subjects. Reservoir rocks with typical grain density of 2.65 (quartz) to 2.86 (dolomite) g/cm³ require calibration with solid phantoms of similar grain density, such as fused quartz, Macor, etc; it ensures artifact-free images at the different anticipated energy levels (X-ray voltage/intensity combinations). An experienced user or a designated service technician should be able to make these calibration tables so that they can be used by the operator readily for different materials (e.g., carbonates or clastic rocks), different sizes of scanned objects (e.g., 6” diameter core box, 4.5” diameter core sleeve, 1.5” diameter core plugs, etc.), as well as for different energy levels. Every time the X-ray tube is replaced, new calibration tables must be created again.

The third modification relates to transferring data from the CT-scanner. The image processing software that are usually packaged with the CT-scanners are only good for general viewing and quality control (QC), as far as petrophysical applications are concerned. So, transferring data to workstations loaded with specialized image processing software is very important. In the past, different manufacturers used different data formats and some of them would deliberately make it difficult to track the data (due to patient data security concerns) or to transfer the data as straight files.

Today the process has mostly been streamlined and most manufacturers conform to the DICOM format, which is also readable by most of the image processing programs designed for petrophysical analysis of CT data. Many CT-scanners allow direct retrieval of data on USB drives rather than going through the network, which simplifies matters further.

3 Use of Calibration Standards

For whole core CT-scanning, usually the actual cores remain out of sight unless it is decided to scan bare cores, extruded from their aluminum or fiberglass sleeves. They are either devoid of any liquid or have some initial liquid saturation. Therefore, a set of calibration ‘standards’ is necessary to extract meaningful data such as density, porosity, etc. from the CT images. The only quantitative data that a CT-scan slice provides is the CT number (CTN or Hounsfield Units, HU) for each voxel (volume element, 3D pixel). CT number is a function of both Z_{eff} (Photoelectric Effect, predominant at low energies such as 80 kV) and electron density (Compton Scattering, predominant at high energies such as 140 kV). The medical CT-scanners are generally calibrated to read a value of -1000 for air and 0 for water. Wellington and Vinegar [2] suggested using 140 kV as the threshold for these two effects.

Most medical CT-scanners are limited at 150 kV as the highest voltage in order to prevent severe damage to human soft tissues and therefore, it is a common practice in petrophysical CT-scanning with a medical CT-scanner to use either 140 or 150 kV (for single energy scanning), which allows good X-ray penetration for larger whole cores such as the 4” diameter ones in their sleeves and core boxes.

In order to convert CT numbers into bulk density for the scanned cores, Wellington and Vinegar [2] proposed to use a calibration curve similar to the one in Fig. 3, using clean sandstone samples, used as ‘standards’ and with known measured bulk densities, from different quarries or reservoirs. This works relatively well for extruded dry cores. However, for preserved cores inside fiberglass/aluminum sleeves and/or core boxes, it is strongly recommended to scan the standards in the same ‘environment’ as the actual cores to avoid making adjustments.

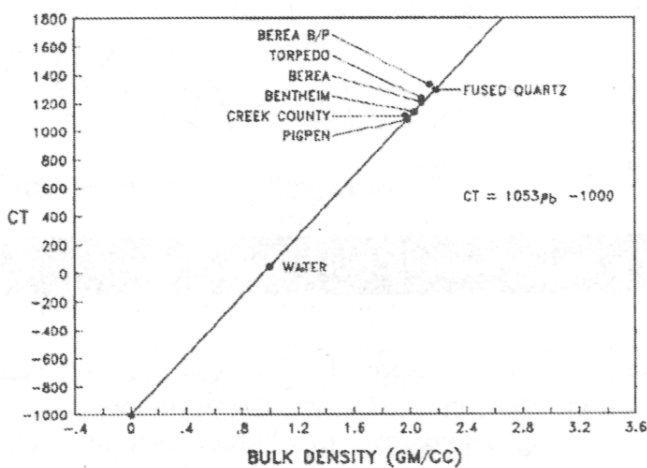


Fig. 3. Calibration curve of bulk density vs. CT numbers for sandstones. After Wellington and Vinegar [2].

For developed reservoirs, it is always possible to obtain bulk densities of a few cleaned (using Soxhlet extraction) representative core plugs and use them as ‘standards’ in addition to the solid ‘standards’ such as fused quartz, Macor, etc. prior to a whole core CT-scan job. Fig. 4 shows some of the ‘standards’ that are scanned inside the blank core sleeves prior to a whole core CT-scanning project. Scanning of these

‘standards’ does not take too much additional time and it should be done regularly, as these data are extremely important for conversion of CT data into bulk density.

For this case, with only one representative cleaned sandstone ‘standard’, the CT-derived bulk density, $(\rho_b)_{CT}$ (also called pseudo bulk density, PBD), is calculated using a straight-line relationship between CTN and ρ_b , for air and the representative cleaned sandstone plug, respectively. Both should be within a circular region of interest (ROI) inside the rock matrix for the core contained in the sleeve and core box, as shown in Eq. 1. Here A is the slope of the ρ_b vs. CTN curve and B is the intercept.

$$(\rho_b)_{CT} = A * CTN + B \quad (1)$$



Fig. 4. Calibration ‘standards’ - quartz, Macor, Berea and a representative cleaned sandstone (top). Blank PVC core box and fiberglass core sleeve (bottom).

It is strongly recommended to scan multiple calibration standards each time - both solid standards and porous rock standards, although the latter group works best for converting data for reservoir rocks. In the calibration curve of ρ_b vs. CTN (inverse of the graph shown in Fig. 3), it is recommended to use 0.001225 g/cm³ as the density of air rather than 0, as it represents air density at room temperature and at 1 atm, at sea level. Also, there is no need to draw data for water as it may skew the data in one direction or the other. It is not recommended to mix data for carbonate and sandstone reservoir rocks in the same calibration curve. If multiple calibration standards (say, representing different facies of a clastic reservoir) are to be scanned, only data for those standards should be plotted along with the air data.

The solid ‘standards’ mainly help observing the drift in the X-ray tube but they are usually not so good for converting CTN into $(\rho_b)_{CT}$, as they do not have any porosity. In the early days of CT-scanner use for routine and SCAL (special core analysis) evaluation of reservoir rocks, it was common to wrap small rods (about ½ inch in diameter) of different materials or tubes filled with different liquids as ‘standards’ around the core holder or core sleeves. Better results can be obtained by scanning solid plugs of about 1½ inch diameter placed tightly next to one another, as shown in Fig. 5, mainly because one can use a larger ROI and also, the standards can be easily placed in the same environment that the actual sample is in.

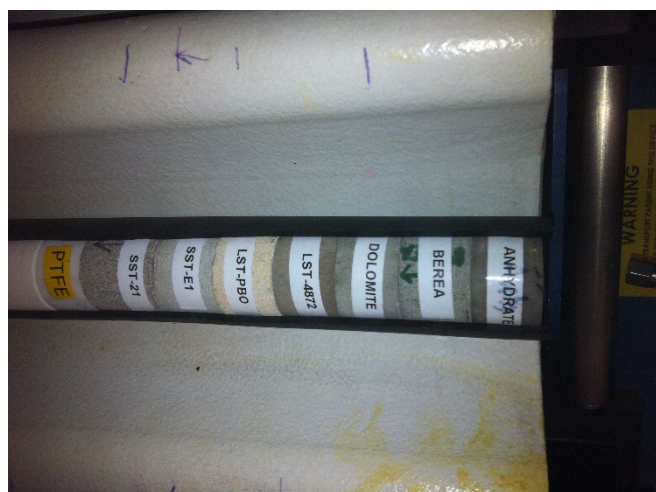


Fig. 5. 1½ inch diameter calibration ‘standards’ placed next to one another inside a rubber sleeve for bare whole cores and plugs.

4 Matching CT Density Data with Logs

One of the challenges of whole core CT-scanning is matching CT based density, $(\rho_b)_{CT}$ data with bulk density log (RHOB) data. Three points should be considered for that – the first one is selection of proper calibration standards to convert the data, which is described in the previous section; the second one is fluid effect, which will be discussed below; and the third is the depth shifting issue, which will also be discussed later.

When logging is done in the wellbore, it is generally filled with mud and the adjacent formation is fully saturated with native fluids, with some degrees of invasion by the filtrate. Since the radius of investigation of density log is only about 6 inches, it mostly measures bulk density of the invaded zone, filled with a combination of fluids. When a core is sectioned at the wellsite, the difference between reservoir pressure and atmospheric pressure (except with specific pressure coring) causes a good part of the reservoir fluid contained in the pores to be expelled and replaced by air, which is harder to remove even when the sectioned core is placed with or without sleeve, capped or uncapped, inside the brine-filled core box. Leaks during the transportation and storage prior to CT-scanning may also introduce more air into the cores being scanned. So, chances are high for the scanned core to have its pore space filled with air rather than liquids. Because the conversion of CTN into ρ_b (Eq. 1) involves dry calibration standards, the CT-derived bulk density, $(\rho_b)_{CT}$ is essentially a bulk density with air-filled pores. A correction must be applied to the $(\rho_b)_{CT}$ data in order to match the log-derived bulk density, $(\rho_b)_{log}$, which, applies to liquid-filled bulk density and this is shown in Eq. 2.

$$(\rho_b)_{log} = (\rho_b)_{CT} + \phi_{CT} * (\rho_{water} - \rho_{air}) \quad (2)$$

Here, ρ_{water} and ρ_{air} are the densities of water and air (in g/cm^3), respectively, and ϕ_{CT} is the porosity of the CT slice. The CT-derived porosity, ϕ_{CT} , can be calculated from the bulk density and matrix density, ρ_{matrix} , through the relation shown in Eq. 3.

$$\phi_{CT} = (\rho_{matrix} - (\rho_b)_{log}) / (\rho_{matrix} - \rho_{water}) \quad (3)$$

This so-called liquid correction involves an iterative process because at the initial stages of calculation, the $(\rho_b)_{log}$ is not known and has to be estimated with an initial value for porosity. For matrix density the values shown in Table 1 are generally used.

Table 1. Matrix Density of Primary Minerals

	Primary Mineral Name	Matrix Density, g/cm^3
1	Calcite	2.71
2	Dolomite	2.86
3	Anhydrite	2.95
4	Quartz	2.65
5	Clay/Shale	2.65

For the liquid correction process, it is also recommended to use tube average or facies average porosity data rather than individual slice porosity data, otherwise the calculations become very tedious, especially if large number of CT slices are involved (i.e., for thick reservoirs). The steps for this iterative process, using EXCEL, are given below:

1. Create a table with the following columns - the depth of the CT-slice, $(\rho_b)_{log}$ from Eq. 2, ϕ_{CT} from Eq. 3. The calculation of $(\rho_b)_{log}$ should also include A, B and the respective CTN values used in Eq. 1.
2. Create the following additional columns – average depth of the core tube, average $(\rho_b)_{log}$ for core tube and average ϕ_{CT} for core tube.
3. Create an additional column for average porosity containing the same value for a core tube or for certain facies. Create a last column in which the numerical data are pasted from the previous column. Note that the porosity value for liquid correction in Eq. 2 points to the very last column only.
4. For the first pass, fill up the entire last column with one initial value, say 0.15, for the entire CT-scanned interval. Because of the way the equations are set up, the second column will have an initial value of $(\rho_b)_{log}$, which will then be used to calculate a ϕ_{CT} for each of the slices. The second-to-last column will then get updated with a new value for each core tube (or facies, covered by several core tubes). Manually copying the entire column data and pasting the numerical value into the last column will start the second pass, and so on.
5. At the end, the data in both the second-to-last and the last columns will be the same and at that time the second column will contain the liquid-corrected $(\rho_b)_{log}$ data and the third column, the corresponding ϕ_{CT} data. The depths in the first column, with the CT-derived density and porosity data can then be used for comparing against logs.

If some additional slice quality control is also done to ignore the CT artifacts and missing/bad data, this workflow can produce excellent CT versus log correlations. It should be noted that typical vertical resolution of a logging tool is about 6 inches whereas multislice CT-scanners are capable of taking several slices per inch, making a continuous map of

CT numbers within each slice. Unless there are operational limitations for taking single scans, it is recommended to scan the whole cores at fixed intervals such as 0.5-inch, 1-inch, 2-inch, etc. This reduces the number of slices and thus, the image processing time; and the resolution is sufficient for slice-by-slice calculations for core to log comparison.

The last piece of work that needs to be done is the depth correction. It is quite common to have some mismatch between driller's depths (that all cores use) and logging depth. This causes a problem for core-log integration, core sample selection for SCAL and routine core analyses, well treatment design, etc. In typical core operations, the Core Gamma tool is commonly used to align core depths with log depths. It works on matching the spikes seen in shale streaks in clastic rocks in both logs and cores. It generally works better if the cores are already extruded from the sleeves. For carbonate cores, which mainly contain calcite and dolomite, gamma ray variations are not very noticeable but the large density difference between calcite and dolomite makes CT a better tool for depth matching for carbonates compared to Core Gamma [2, 3]. Overall, the depth accuracy improves a lot if the depth of the top of the core in each tube is accurately known through pilot scans (also called scout scans). For scanners without the pilot scan feature, tilting the core box to move the core sleeve inside the core box to one side, prior to the CT-scans, and scanning from approximately the same position for all core boxes may result in reduction of location errors.

For dual energy CT-scanning, one of the important factors to consider is the positioning of the samples at the exact same location. Some of the most recent CT-scanners can take a high-energy scan and a low-energy scan in one single pass and for those scanners positioning is not an issue. However, in the case of older CT-scanners requiring an elaborate process for changing voltage settings for dual energy CT-scanning, the scanning has to start from the same starting point and to be repeated at each slice location. Minor shifts can make the dual-energy CT-scanning analysis very difficult. It should be remembered that in order to ensure artifact-free data, appropriate calibration tables should be used for each energy and sometimes, it is more than just pushing the 140 kV or 80 kV button on the control screen.

5 CT Image Artifacts

Just like its medical counterpart, petrophysical CT-scanning also has to deal with several CT image artifacts during data processing. The most common ones are streaks (aliasing), ring, and beam hardening [4, 5]. Streaks appear as dark lines that radiate away from sharp corners. For the cylindrical cores this is usually not a problem as the cross section is circular. However, if the core inside the sleeve or core box is fractured naturally or during the coring process, it is possible to get sharp edges, and streaks can be observed. For the extruded, dry cores, if they are already slabbed before scanning, streaks may also be encountered from the sharp edges. Also, if core plugs are scanned in sagittal position, which presents a rectangular cross-section to the scanner, X-shaped streaks may be observed [Fig. 6]. There is hardly any post-processing correction for the streaks and during data analysis slices containing streaks should not be considered.

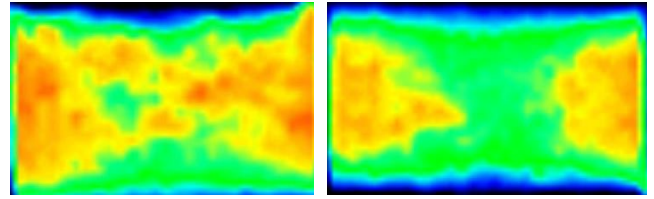


Fig. 6. Examples of X-shaped streaks in core plugs (sagittal case).

The ring artifacts, which appear as a series of off-centered concentric rings in some CT slices, are rare for medical CT-scanners, but are more common for industrial CT-scanners. It is caused by the imperfect detector elements at a specific position in the detector array. The large number of detectors used by the medical scanners as well as good centering of core samples within the CT gantry makes them rare.

The last and the most common artifact seen during whole core CT-scanning is the beam hardening artifact. The filtering of a polychromatic X-ray beam by the scanned object causes beam-hardening (cupping) artifacts. Because of beam-hardening, a perfectly homogeneous object appears to have a dense periphery. If one draws a profile on the CT slice, going from one end of the object to the other end through the center, the profile looks like a cup.

It is preferable to eliminate all the artifacts before the image is acquired through improved remedial actions and improved calibrations. In general, the medical CT-scanner calibration process with relatively large circular phantoms (having a slightly larger size than the largest object scanned) appropriate for the density range of the objects to be scanned helps minimize or eliminate this artifact.

Beam hardening is more common in bare core images rather than images of cores within core boxes and core sleeves because the polychromatic X-ray beams get pre-hardened before penetrating the rock materials. Insufficient penetration due to lower energy for large objects can also have the appearance of beam hardening on the images. In Fig. 6, the calibration was right for the vuggy carbonate core, pictured on the left, which shows no beam hardening. However, the image on the right shows strong beam hardening due to the calibration phantom not being appropriate for the material (anhydrite) in the core slice.

Beam hardening directly affects whole core CT-scanning results and forces one to use smaller ROI, away from the edges, thus reducing the sample population for the voxels. Some image processing software include the beam hardening correction which may be used if there are no other alternatives. Since beam hardening may not be present in all the slices, the quantitative data from the beam hardening-corrected images may have some consistency issues when compared against non-corrected images.

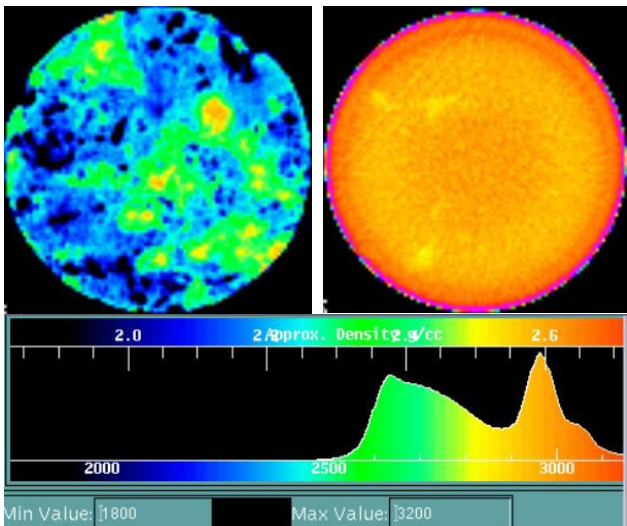


Fig. 7. Example of slices without (left) and with beam hardening (right). Histogram with overall range for all the slices scanned in the batch is shown at the bottom.

6 Image Processing

There are several image processing software packages, both commercial and non-commercial, for processing the CT-scan images. They are also compatible with multiple image data formats that are commonly used by the CT-scanners. Most of this software is designed for medical imaging of human subjects and may therefore not be able to cater to the need of petrophysical CT-scanning. It is not within the scope of this paper to review various software available and describe their advantages. However, some of the essential or useful features for petrophysical CT-scanning software are listed below:

1. Ability to import and read multiple image data formats generated by various manufacturers of CT-scanners. It should also be able to select multiple images at will from a group of image files.
2. Ability to digitally align the slices as it is almost impossible to have perfect alignment of slices for a core tube before scanning.
3. Ability to do ROI statistics with multiple ROI options such as circular, elliptical, polygonal, square, etc. The statistical data should include mean, minimum, maximum, standard deviation, and histograms. It should also allow drawing profiles on any slice and extract the CTN on the profile.
4. Ability to use an array calculator with functions such as add, subtract, multiply, divide, absolute, log, exponential etc. and also to apply various filters. This feature allows reporting of whole core data in terms of density or porosity units; and SCAL data in terms of saturations; rather than CTN.
5. Ability to use multiple color schemes such as grayscale, heat, rainbow, etc.; and some continuous and discrete color schemes; and also, the ability to create new color scales, if needed.
6. Ability to create orthogonal slabs (similar to slabbed cores), both horizontal and vertical.
7. Ability to do segmentation and thresholding.

8. Ability to generate 3D volumes (volume rendering such as iso-surface plots) from CT-slices with ability to pan, rotate, move etc.

Some of the desired advanced features specific to routine and also SCAL type petrophysical CT-scanning should include the following:

9. Beam hardening correction.
10. Dual-energy CT calculation (Bulk density and Z_{eff}) using analysis similar to reference [6].
11. Individual fluid phase calculations using advanced image subtraction with radiopaque solution (dopant) mixed in oil, water and gas phases.

7 List of Some of the Applications of Whole Core CT-scanning

CT-scanning has been used for evaluating reservoir rocks for over 35 years and many good reviews of various routine and SCAL type of applications are available in the literature [4, 7, 8 and 9]. While more and more applications are coming up, CT is currently being used for at least the following applications for the whole cores:

1. Bulk density determination: details are discussed in this paper.
2. Porosity determination from bulk density: details are discussed in this paper.
3. Quick preview of the core tubes for sample selection: Fig 8 from Ref. [9] shows density variations in CT slices taken at 2-inch intervals for 20 core tubes covering about 60 ft of a reservoir. This provides a quick preview of the condition of the preserved cores and helps in determining what samples are intact and can be used for plugging.
4. Depth matching: It is discussed in Refs. [2, 3] and Fig. 9 is taken from Ref. [10]. The images on the left are the slab images (horizontal and vertical) for five core tubes. The log data (RHOB) are shown with the red lines, the CT-derived density data (PBD) are shown with black lines, for the tube average data and with green dots, for the slices.
5. Formation damage due to mud: Fig. 10 is taken from Ref. [11] and it shows a CT slice of a 4 in diameter whole core from a sandstone reservoir. The barite-laden mud is shown to penetrate deep inside the core. The yellow outer ring is the aluminum sleeve, the bright red inner ring is the barite mud at the periphery and the dark blue material is the sandstone core. The black channels filled with mud are the fractures, possibly induced during coring. Ref. [12] has more examples of mud invasion.
6. Heterogeneity quantification and SCAL sample selection: Fig. 11, which is taken from Ref. [13], shows two types of heterogeneity that can be defined by analyzing CT-scan slices. The nine slice images at the left (inter-slice heterogeneity case) show the presence of a distinct anhydrite nodule in the last three slices. The nine slice images at right (intraslice heterogeneity case) show large CTN variations within each slice, with relatively small channels

available for flow. Both of these plugs were determined unsuitable for SCAL tests.

7. Lithology variation: Fig. 12, which is taken from Ref. [10], is a composite image showing 19 CT-Scan slices on the left, taken 2-inch apart from each other, and representing a 3 ft section of preserved sponge core from a sandstone reservoir. The bright color in the middle is due to lithology change from sand to shale.
8. Dual-energy based mineral characterization: Fig. 13, which is taken from Ref. [6,], shows the application of dual-energy CT-scanning for mineral characterization in a carbonate reservoir. By scanning these cores at the same slice locations at 80 kV and 140 kV, respectively, it was possible to see the streak containing dolomites. Dual energy CT is also discussed in Ref. 14.
9. CT density-based FMI type logs: Fig. 14, taken from Refs. [15, 10] shows how CT-slice image data can be used to generate density-based FMI-type images. The example image, shown in the rightmost panel, was created by combining continuous CT-scan data for a 34 ft section of core through a process of collecting the surface slice data and unrolling them. The cores were depth-shifted prior to placing against the FMI logs.
10. Fracture Characterization: Fig. 15, which is taken from Ref. [11] shows a 360-degree core photograph next to a CT-generated unrolled image of a fractured core that was also plugged. The CT image displays the fracture with dark blue lines and is able to show additional fractures not visible on the surface.

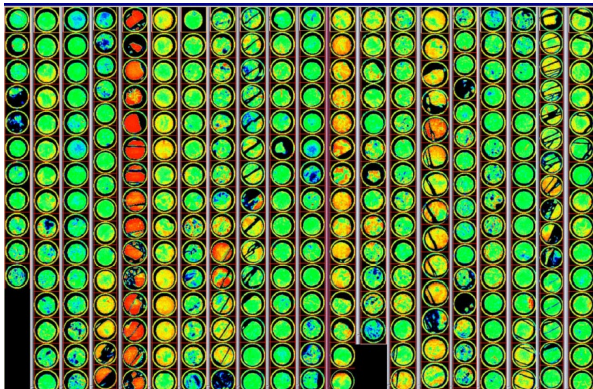


Fig. 8. Example of quick preview of the condition of the preserved cores.

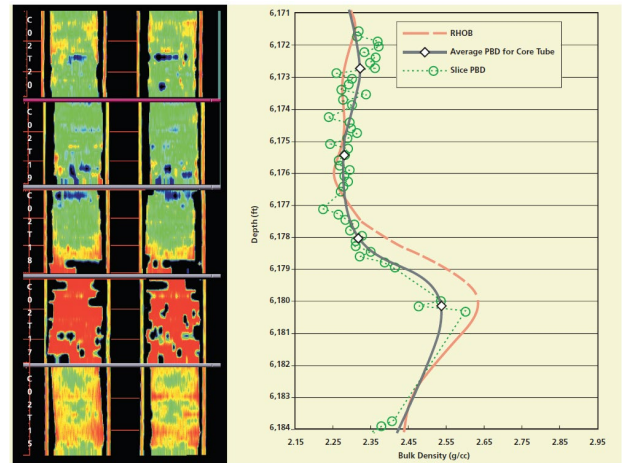


Fig. 9. Example showing how CT generated density data are used for depth shifting in a 15-ft section of a carbonate core.

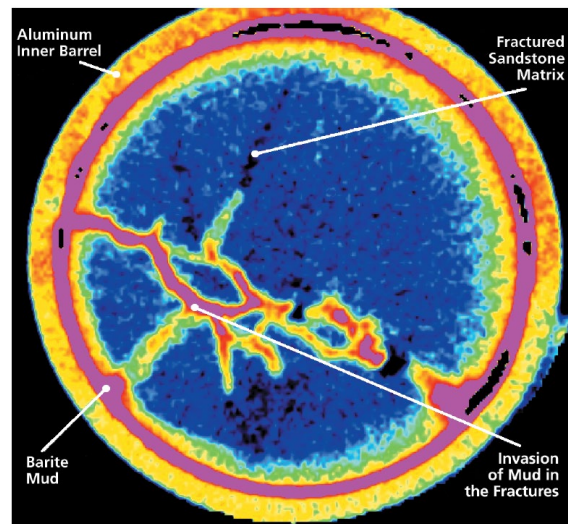


Fig. 10. Example of mud invasion in a core during the coring process.

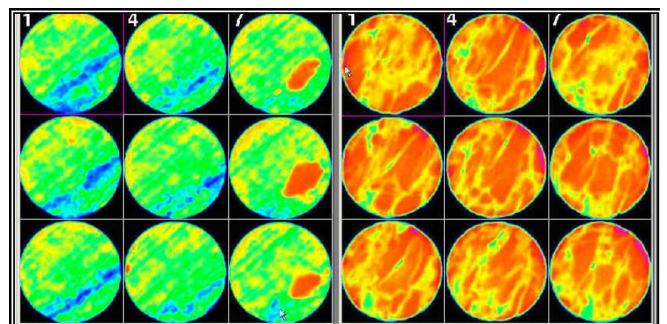


Fig. 11. CT-Scan slices for two core plugs showing case of inter-slice heterogeneity (left images), and intra-slice heterogeneity (right images).

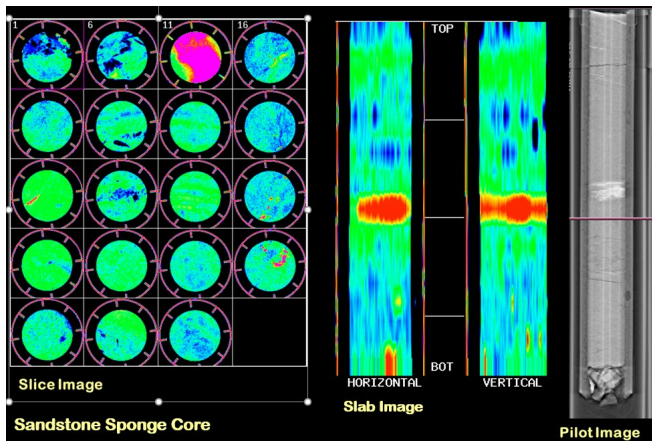


Fig. 12. Example of lithology variation within a core tube.

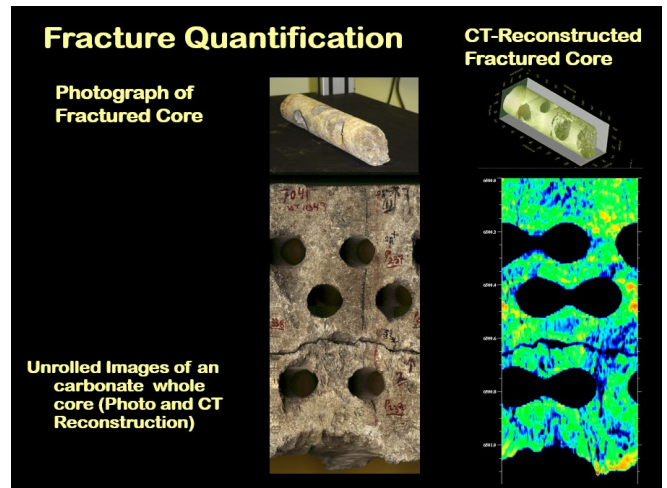


Fig. 15. Example of fracture characterization in whole cores.

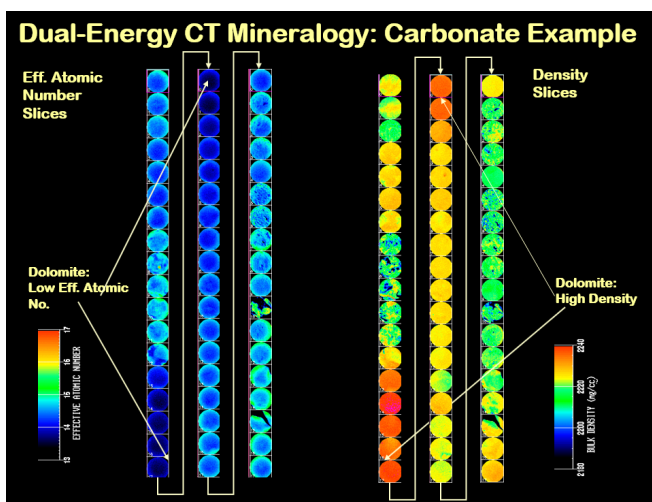


Fig. 13. Example of dual-energy based mineralogy determination using CT-Scan slices for three core tubes taken from a carbonate reservoir containing both calcite and dolomite.

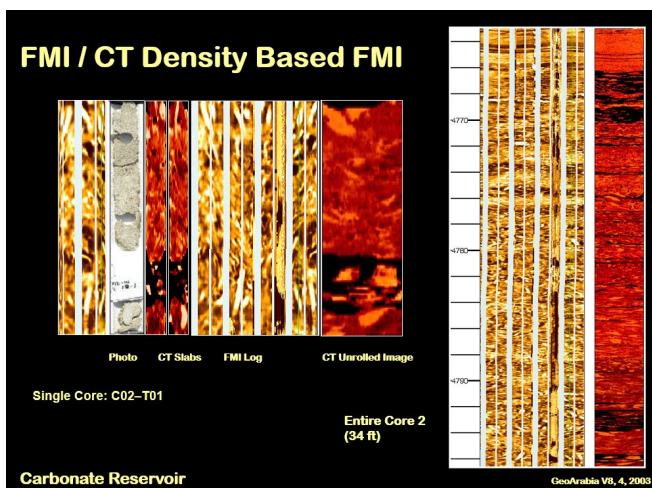


Fig. 14. Example of CT-generated density-based FMI (formation micro imager log) type images (rightmost panel).

8 Conclusions

In this paper an attempt has been made to present some of the interesting applications of computerized tomography (CT) for evaluating whole cores. Starting with what changes are needed to convert a purely medical CT-scanner into one that is capable of generating artifact-free images of reservoir rock samples, this paper covers discussions on calibration standards and how they can be used to generate bulk density and porosity data. Step-by-step instructions on how to use an iterative approach to correct for liquid effects in order to match the CT-derived bulk density and porosity data with the logs are also provided.

This paper also covers common CT artifacts that may be encountered while using a medical CT for whole core CT-scanning. Necessary features for the petrophysical use of a CT image analysis software are also discussed. Finally, a list of ten specific applications applicable to whole core CT-scanning, with examples and references, is presented with the hope that more and more new applications of this very useful non-destructive imaging technology will be developed by the future petroleum engineers and geoscientists in order to broaden our understanding of the reservoir rocks.

9 Acknowledgments

The author expresses his deep appreciation for his mentors Abraham Grader, Paul Hicks and Phillip Halleck for their help and support. The author also thanks his former colleagues at the Saudi Aramco R&D Center in Dhahran, KSA, who made it possible to explore new ideas. The author appreciates the support of Bob Kehl of Kehlco, Inc. for his *VoxelCalc* petrophysical image processing software, which was used for generating some of the images.

Nomenclature

Z_{eff}	Effective Atomic Number
CTN	CT Number
RHOB	Log-derived bulk density, g/cm ³
$(\rho_b)_{\text{log}}$	Log-derived bulk density, g/cm ³
A, B	Slope and intercept of ρ_b vs. CTN graph
$(\rho_b)_{\text{CT}}$	CT-derived bulk density, g/cm ³
$(\phi)_{\text{CT}}$	CT-derived porosity, fraction
ρ_{matrix}	Matrix (grain) density, g/cm ³
ρ_{air}	Air density, g/cm ³

References

1. M.R.H. Sarker and S. Siddiqui. "Advances in Micro-CT Based Evaluation of Reservoir Rocks." Paper presented at the SPE Saudi Arabia Section Technical Symposium, Al-Khobar, Saudi Arabia, May 2009. doi: <https://doi.org/10.2118/126039-MS>
2. S.L. Wellington and H.J. Vinegar. "X-Ray Computerized Tomography." JPT, August 1987, p. 885.
3. S. Siddiqui. "Method for depth-matching using computerized tomography." US Patent number: 6876721, 2003.
4. S. Akin, and A. R. Kovscek. "Computed tomography in petroleum engineering research." In Applications of X-ray computed tomography in the geosciences, F. Mees; R. Swennen; M. Van Geet; P. Jacobs (Eds.), Jan. 2003. doi: <https://doi.org/10.1144/GSL.SP.2003.215.01.01>.
5. R.P. Kehl and S Siddiqui. "Two Less-Used Applications of Petrophysical CT-Scanning." in Advances in Computed Tomography for Geomaterials: GeoX 2010, pp.180-188. doi:<https://doi.org/10.1002/9781118557723.ch22>.
6. S. Siddiqui, S. and A.A. Khamees. "Dual-Energy CT-Scanning Applications in Rock Characterization." Paper presented at the SPE Annual Technical Conference and Exhibition, Houston, Texas, September 2004. doi: <https://doi.org/10.2118/90520-MS>.
7. E.M. Withjack, C. Devier, and G. Michael. "The Role of X-Ray Computed Tomography in Core Analysis." Paper presented at the SPE Western Regional/AAPG Pacific Section Joint Meeting, Long Beach, California, May 2003. doi: <https://doi.org/10.2118/83467-MS>.
8. E.M. Withjack. "Computed Tomography for Rock-Property Determination and Fluid-Flow Visualization." SPE Formation Evaluation, December, 1988, p. 696.
9. A. Kantzas, "Investigation of Physical Properties of Porous Rocks and Fluid Flow Phenomena in Porous Media Using Computer Assisted Tomography." In Situ, Vol. 14, No. 1, 1990, p. 77.
10. S. Siddiqui, "Understanding Reservoir Rocks through Computerized Tomography (CT) Imaging." SPE Distinguished Lecturer Presentation, Society of Petroleum Engineers, 2013-14.
11. S. Siddiqui, "Application of Computerized Tomography in Core Analysis at Saudi Aramco." Saudi Aramco Journal of Technology, Winter 2001, pp. 2-14.
12. H.J. Vinegar and S.L. Wellington. "Method of Determining Drilling Fluid Invasion." US Patent No. 4540882A, 1983.
13. S. Siddiqui, T.M. Okasha, J.J. Funk, and A.M. Al-Harbi. "Improvements in the selection criteria for the representative special core analysis samples." SPEREE 9, 06 (2006), pp. 647-653.
14. J.G.C. Coenen, and J.G. Maas. "Material Classification by Dual-Energy Computerized X-ray Tomography." Proceedings of the International Symposium on Computerized Tomography for Industrial Applications, Berlin, Germany, 1994, pp. 120-127.
15. G.W.G. Hughes, S. Siddiqui, and R.K. Sadler. "Shu'aiba rudist taphonomy using computerised tomography and image logs, Shaybah field, Saudi Arabia." GeoArabia 8, 4, pp. 585-596.

Investigation Pore Geometry Wettability Preference in Oolitic Oil Reservoir: Pore Scale Imaging and Modelling Study

Hussien Al-Ajaj¹, Ralph Flori¹, Saleh Alsayegh^{1,2}, Haidar AlMubarak³, and Waleed Al-Bazzaz⁴ *

¹University of Missouri Science & Technology, Rolla, Missouri, USA

²Kuwait Oil Company, Ahmadi, Kuwait

³Saudi Electronic University, Riyadh, Saudi Arabia

⁴Kuwait Institute for Scientific Research, Petroleum Research Center, Ahmadi, Kuwait

Abstract. This study evaluates the wettability preference of Oolitic fresh core plug from a native Kuwaiti reservoir. This Oolitic calcite formation hosts hundreds of spherical grains (ooids) with thousands of pore-shapes. Thousands of tortuous pore/ grain-wall boundaries and their subsequent shapes are captured, of which boundaries geometry, size, and distribution are processed in an Oolite matrix images format. Level of information is reported at different magnifications X40 (mm), X400 (μm), and X4000 (nm), where statistical wettability contact angle distinct morphological feature is closely examined. The objective of this study is to investigate the size and shape driven static contact angle measured by 2D technology digitally captured images of available fresh cores utilizing SEM-BSE segmentations, of which high-quality images are generated. In abstract, the method utilizes counting complete contact angles manifested at pore area and pore/ grain -wall boundary system, which is scale-characterized at: pore-body, pore-throat, and nano-pores available in these Oolitic core plugs. However, in specific, pore-wall boundary contact angle wettability performance and recovery efficiency contributions is also captured, measured, processed and modeled. To model natural pore-wall boundary system static contact angle wettability is to understand the new physics that will advance reservoir characterization and production improvement.

Introduction

Oolite is a type of a chemical carbonate sedimentary rock, mainly limestone (Calcite) and to lesser degree dolomite, in a form of ooids that are cemented together. Ooids are spherical grains that forms when a particle of sand or other nucleus is coated with layers of calcite or other minerals. Ooids often form in shallow marine water.

Kuwaiti Oolite is considered as an Oolitic calcite in thick limestone oil reservoir, which exhibits significant amounts of hydrocarbons. These hydrocarbons are difficult/ slow in oil production [1]. There are many factors to delay EOR productions; however, according to this study, incomplete concept of quantitative wettability is considered the significant factor that controls reservoir fluids location, reservoir fluid flow, and reservoir fluid distribution inside this Oolitic calcite pore system. Wettability or its alteration process will affect core and hydrocarbon production studies, including porosity, permeability, Mean Hydraulic Radius (MHR or Pore Throat), Pore Size Distribution (PSD), capillary pressure (P_c), relative permeability (K_{rw} and K_{ro}), waterflood behavior, electrical properties, and any designed recipe of chemical, thermal, or mechanical tertiary recovery [2]. Therefore, this Oolite reservoir study highlights new measured and Unit-Circle-Trigonometry quantified contact angles (Fig. 6). Using the unit circle, wettability contact angles are measured in accurate, precise and repeatable big-data format to all captured pore/ grain wall including those which are greater than 180° and less than

360° (Fig.6). Digital contact angles are, then, morphologically distributed along thousands pore-wall boundaries (Fig-2-7) and (Tables 3-5) as big data format. This big data is, then, suitable to characterize and model wettability attributes of this fresh Oolitic core representations.

Previous methods have investigated the wettability measurement. Some methods are quantitative, such as contact angles, imbibition and forced displacement (Amott), and USBM wettability method. Others are qualitative methods, such as imbibition rates, microscope examination, flotation, glass slide method, centrifugal relative permeability curves, permeability/ saturation relationships, capillary pressure curves, displacement capillary pressure, reservoir logs, nuclear magnetic resonance (NMR), and dye adsorption [3].

Anderson (1986) described contact-angle measurement have been used the tilting plate method, sessile drops or bubbles, vertical rod method, tensiometric method, cylinder, method, and capillary rise method to measure the wettability in petroleum industry [4]. Okasha, et. al., (2007) was measuring the wettability by using contact angle method and the results showed the material recovered from the Unayzah reservoir rock with characteristics of the water-wet for both oil-brine/rock system and oil-brine/quartz system [5]. AlOtaibi, Azmy and Nasr-El-Din (2010) studied the Amott and wetting contact angle wettability. The outcome of the study gave a better result for recovery of oil [6]. Yuan and Lee (2016), investigated droplets on solid surfaces allow wetting methods

* Corresponding author: wazzaz@hotmail.com

to be examined down to the nanometer scale, providing new insight into contact angle phenomena and wetting behavior [7]. Alhakeem, et. al. (2017 and 2017*), measured the Wettability using contact angle, the results was successfully captured using morphological analyses of the thin section (TS) imaging. Better geological and petrophysical background is involved with obtaining big data from 2D images where accurate decisions made to describe Wettability features [8] and [9].

The prepared Oolitic Kuwaiti reservoir rock sample is in the form of a rock fragment and it is imaged and then characterized for pore area, and pore/ grain wall-wettability contact angle. The contact angles are in 2D format utilizing SEM-BSE imaging techniques. The generated images are quantified using pre-defined K-Means logics. K-Means clustering is a method of vector quantization that aims to distribute several thousand contact angle observations into $K = 10$ clusters in which each observation belongs to the wettability contact angle cluster with the nearest mean. K-Means Clustering algorithm is a useful tool for statistical wettability contact angle preference measurement. The contact angles data generated are used to estimate the wettability classification. Each image captured at X40, 400X, and 4000X magnifications will be investigated for matrix pore-body, pore/ grain boundary and nano-pore system to ensure all possible wettability size classifications as well as distribution from captured representations of the matrix features [10].

The study aims to investigate Kuwaiti Oolitic reservoir's wettability preference by using imaging methods for capturing rock physics. The approach used for this study is counting then clustering contact angles in the measured pore/ grain wall using high resolution 2D imaging technology formats [11]. The processed big data is modeled using K-Means Clustering algorithm to essential unsupervised machine compassionate algorithm. K-Means clustering algorithm computes the centroids of 10 defined boundary contact angle clusters, cluster 1 is the smallest in area and cluster 10 is the largest in area available from the captured image. K-Means clustering algorithm iterates all 10 clusters until optimal centroid is found. In comparison, conventional administered big data to machine knowledge algorithms, K-Means endeavors to evaluate data without first being trained with labeled data. Once the algorithm has been run, and the groups are defined, any new data can be easily assigned to the most relevant group. Useful applications of K-Means are wettability preference profiling and contact angle boundary segmentations.

Problem Statement

The authors feel that this study will narrow the gap in contact angle wettability characterization from static conditions standpoint and, hence, the reservoir crude oil recovery history profile. Capturing and measuring detail static physical pore-wall contact angles through big data contact angles characterization is a key understanding of subsurface crude oil recovery programs from planning to forecasting production. Also

the forecasted duration for each recovery stage when total rock Wettability distribution is manifested. In this study, valuable information from the literature is integrated and utilized in developing unique static characterization pre-logic to understand the nature degree wetness of the Oolitic calcite pore-wall size wettability distribution and its attributes on recovery efficiency [12].

Results & Discussions

In this study, two dimensional images 2D are used to characterize the morphology of Oolitic calcite grains and pores, using two-step technique process, image capturing and image mathematical processing. In the first step, the image is captured using backscattered electron detector (BSE), digital electron microscopy imaging, and the second step, the statistical pore/ grain-wall geometry features are counted, pore area are measured, and pore/ grain-wall shape contact angles are also measured. These big data obtained from the captured image is the 2D digital approach for processing technology. All of sample grain/ pore features captured in the image are reported in millimeter, micrometer, and nanometer length units. In the second step, the pore area and pore contact angles of such features are scanned using image analysis software that has the ability to accurately measure several morphological parameters of pore and grain spaces (Tables 4-6).

A robust technique of visual estimate is used, which has the advantage of speeding the image analysis process. The visual analysis software tool counts different pores and grains and also measures their shapes boundaries and sizes that are crucial for contact angle wettability calculations. Several pore morphological models have been considered for optimum accuracy comparisons, including: pore/ grain-wall relationships (Area/ Perimeter), pore contact angle (θ), and pore count. Wettability preference is estimated based on refracted angle of the pore/grain-wall boundaries measured from two-dimensional images [12].

Wettability Attributes in Oolitic Reservoir

The wettability in this Oolitic reservoir study has six tasks experimental designs and attributes. The designed factors are: general mineral description, sample preparation, surrounding environment, macroscopic/ microscopic measurement scale, surface roughness, Surface Contamination and Organic Matter (Fig 1). This study will start with general mineral description task. According to Oolite physical, chemical, Crystallography, Optic, Crystal Habitat, and other Optic System properties and description suggests the contribution of Calcite in regards to wettability preference is principle and tends towards weakly-oil-wet (WOW) or contact angle θ° is between 90° - 120° .

The second and third tasks are sample preparation and surrounding environment. Only one rock sample is selected for this study from an end plug rock core fragment. The rock is

fresh Oolitic sample without removing its fluids. The sample is gently/ slowly cut to fit the Scattered Electron Microscope (SEM) chamber. No coating is required to maintain the pollution of sample at zero level. From previous studies, Al-Bazzaz et. al (2018) and (Almudhhi et.al 2019 & 2021), purity of the sample must be honored (As much as possible) to examine the mineral in its natural arrangement. High voltage 30 KeV is used to produce high quality images. The sample is subject to 24-hours vacuum treatment and images are then captured at slow scan.

The fourth task is Macroscopic/ Microscopic Measurement Scale. Reservoir Rock sample imaging and testing for Oolitic Calcite reservoir is highly successful. Oolite sample is represented with one sample throughout the vertical thickness and three SEM magnifications are studied at X40 (mm), X400 (μm), and X4000 (nm) (Fig. 2). The images are captured using backscattered electron detector (BSE) digital electron microscopy. As a result, this (SEM-BSE) imaging tool is excellent to characterize the morphology of the areas of grains and pores (Fig. 3). Also, the boundary angles captured (Fig. 4) is scanned using image analysis software to measure several morphological parameters twice for each selected image – once for pore area morphology and once for boundary angle morphology. Big angle data is produced, counted, and statistically numerated.

The fifth task is the Mineral Surface Roughness. This digital imaging method has successfully captured the roughness inside the Oolite pore space. Rough surfaces can complicate contact angle wettability measurements. Averaged electron bombardments have successfully reflected hundreds of Oolitic calcite grain-wall surfaces that surrounds the pore. An example of captured 2D boundary of one Oolitic pore at a 4000X (Nanometer) is included in Figure 5. The green-color tortuous surfaces correspond to the boundary pore/ grain-wall, which are measured independently, and then, an overall mean average contact angle captured and measured is reported. Then an overall technical average is calculated and modeled for all pores captured in the 2-D image.

The final task is surface contamination by the Organic Matter (OM). This task, unfortunately, is not completed up to date of this manuscript. As a result, the analysis of OM on Oolite pore/ grain-wall will not be included in this research.

Wettability Classification

Oolite show all wettability contact angles from electron measured refractions (Almudhhi et.al 2021) spanning from 0°-360°. These pore/ grain-wall refracted angles are successfully located and distributed in the images. A new classification is based on the big data generated (Fig. 6-7) and (Table 1). Eighteen classes show the degree of wetness preference that each pore area or pore/ grain boundary can possess.

One interesting find is zero angles (Fig. 7) are now possible to be measured in the imaging laboratory. They are the majority pores available in any matrix in general, as well as in

this Oolite sample in particular. Also, the zero angle size of pores is considered nano-pores, and understanding this pore wettability will help unlock future unconventional tight oil. The nano region in Oolitic matrices is considered as an absolute water wet region (AHWW). AHWW region will be reported in 0° degrees or 360° degrees, and shows as “water-film” shape of the water rather than a droplet-like shape. Also their natural orientation is horizontally measured just like Unit-Circle-Trigonometry.

Another interesting find is measuring the true vertical mixed wettability (TVMW), which are the 90° and the 270° respectively. These angles are mirrored of each other [10-12]. They are the same but available upside of each other as nature rock orientation dictates. They will also represent the true mixed wettability preference in this Oolitic calcite.

While 180° is the absolute horizontal oil wet (AHOW). AHOW, it is the strongest oil wet preference region available in this Oolite. AHOW is described as “paint-like” or “stain-like” shape on the calcite grain-wall. Removing this “paint-like” or “stain-like” oil molecules will suggest 100% recovery of oil. These pores and subsequent boundaries should be the ultimate goal for any EOR/ IOR program. AHOW requires extreme thermal, chemical, or mechanical EOR/ IOR recipe techniques to dispatch this paint-like droplets of oil from the calcite-grain-mineral-wall and make it mobile in the production stream. All reservoirs have this phenomenon, but at different percent-quantities and distributions. Due to existing and reporting of these contact angles, the authors will recommend more research work towards these difficult oil regions.

This Oolitic Calcite rock sample has captured all 18 wettability classified regions of contact angles from reported images at mm 40X, μm 400X, and nm 4000X (Fig. 2-5) (Table 1). This method is classified by reflected angles between 0° - 360° [9-12]. Eighteen (18) classes are identified with distinct colors. Next smallest nano-pore angles with tan orange color 0°-36° is the strong water wet region SWW. But angles with blood red color 144° - 180° are identified with strong oil wet SOW.

Wettability Using Clustering Algorithm

From the Oolite rock sample, three levels of magnifications are determined 40X, 400X, and 4000X. The 40X magnification (Fig. 2-4) & (Table 3) is an extensively significant capture of the rock sample illustrated in the millimeter scale. This scale is useful to study the largest pores, pore bodies. In the 40X image, 3,283 pores are manifested for processing and the yielded wetting contact angle is 52.4°. This overall average medium-water-wet (MWW) preference is suitable for a long successful secondary water injection program. The 400X is the micrometer scale of pore-spaces Fig. 2-4) & (Table 4). This magnification scale, 400X image, represents pore throat region of the matrix. Image captures has yielded 2,223 pores for processing the wetting contact angle preference, and the wetting preference is 55.99°. This result suggests the overall

wettability contact angle is medium-water-wet (MWW). Also good region for secondary water injection program. The final pore system is the 4000X (Fig. 2-4) & (Table 5), this region shows the nanometer-scale. The 4000X image captures and produces 1,340 pores for processing. the overall average wetting contact angle is 33.2° (Al-Bazzaz et al. Pore Counting Method, 2007) [1].

In the K-Mean clustering model, the maximum number of pores are 3,283 pore at 40X measurement. All counted pores, and the SEM-BSE process tested the pore-wall contact angles. Hence, the region angles are determined, and the group regions (clusters) wettability preference overall average is technically computed. The technical average assists us in understanding the contact angle in each tenth clusters shown in the (Figures 8-11) & (Table 2). Furthermore, the more pores in any cluster, the better the wettability contact angle estimation. From the result, we observed that clusters 1, 2, 7, 9 and 10 have more pores than the other clusters. Therefore, in this study, we are neglecting the other cluster of 3, 4, 5, 6, and 8 for limited data. Only the model will focus on the following clusters: 1, 2, 4, 7, and 10.

The model has the following results: cluster 1 captures 3,886 boundary surfaces of 0° (AHWW) contact angles spanned over 99.5% confidence of pores/ grain-wall boundaries. Cluster 2 captures 123 surfaces of 120° - 150° within cluster dominance spanned over 95.1% confidence. Cluster 2 will be considered as Medium-Oil-Wet system (MOW) within the cluster preference. This region requires thermal and chemical EOR/ IOR treatments. Cluster 4 is modeled at and 90° spanned over 87.7% confidence. Cluster 4 is the True-Vertical Mixed Wettability (TVMW), Light thermal, Low Salinity (LoSal), or surfactant treatment (or mix-and-match recipe) will enhance the recovery in this region. Cluster 8 is modeled at Medium-Water-Wet (MWW) at 30° - 60° spanned over 84.5% confidence. This cluster will estimate secondary water injection treatments. The final cluster, cluster 10 is 150° - 180° spanned over 62.8% confidence. This region is considered as Strong-Oil-Wet (SOW), which means aggressive thermal, chemical, and mechanical treat might work for this portion of Oolite rock.

The Kuwaiti overall pore/ grain-wall wettability preference is 84.3% towards generally water wet spread between (AHSW & SWW) and (MWW). However, the remaining overall pore/ grain-wall boundaries tends towards 15.7% general oil wet spread between mixed wet (TVMW & MOW) and Strong-Oil-Wet (SOW). This Oolitic reservoir will be an excellent candidate for water displacement developments.

Conclusions

From measured data and computed logics, the majority portions of natural pore voids/ grain walls and discrete nanopores in size, and mineral grain-walls are Absolute-Strongly-Water-Wet (ASWW); however, some pore/ grain walls show mixed and strongly oil wetting. The main factors in the un-

derstanding the Oolite wettability are matrix pore-size distribution and pore-numbers, and morphology where pore/ grain-wall boundary is directly measured, hence, suggests the wettability likely affinity preference. This study shows natural pores connectivity contact angles measurements are important in crude oil recovery as well as water productions performance through the life time crude recovery stages of Kuwaiti Oolite reservoir. Reported measured contact angle can assist in planning for oil potential recovery such as water injection. Also, big data measured contact angle also show some new interesting feature characterizations.

Acknowledgments

The Authors would like to express their thanks and gratitude to the University of Missouri Science & Technology for academic support, Kuwait oil Company, Saudi Electronic University, and Kuwait Institute for Scientific Research for guidance in SEM measurements. The authors would like to give a special recognition to Dr. Dawood Bahzad, Kuwait Institute for Scientific Research, KISR, to award our group the opportunity to conduct this work and the utilization of KISR's property equipment to conduct all measurements (2022). I would like to give special thanks to our KISR team members who helped us carry out image capturing (2022).

References

1. W. H. Al-Bazzaz, Y. Al-Mehanna, & A. Gupta. Permeability Modeling Using Neural Network Approach for Complex Maaddud-Burgan Carbonate Reservoir. SPE Middle East Oil and Gas Show and Conference. (2007). doi:10.2118/105337-ms
2. W. Anderson. Wettability Literature Survey- Part 2: *Wettability Measurement*. *JPT*, **38(11)**, 1246–1262. (1986). doi:10.2118/13933-pa
3. Yuan, Y., & Lee, T. R. (2013). Contact Angle and Wetting Properties. *Springer Series in Surface Sciences*, 3–34. doi:10.1007/978-3-642-34243-1_1
4. W. G. Anderson. Wettability Literature Survey- Part 1: Rock/Oil/Brine Interactions and the Effects of Core Handling on Wettability. *JPT*, **38(10)**, 1125–1144. (1986). doi:10.2118/13932-pa
5. T. M. Okasha, J. J. Funk, & H. N. Rashidi. Fifty Years of Wettability Measurements in the Arab-D Carbonate Reservoir. *SPE Middle East Oil and Gas Show and Conference*. (2007). doi:10.2118/105114-ms
6. M. B. Alotaibi, R. Azmy, & H. A. Nasr-El-Din. Wettability Challenges in Carbonate Reservoirs. *SPE Improved Oil Recovery Symposium*. (2010). doi:10.2118/129972-ms
7. Y. Yuan, & T. R. Lee. Contact Angle and Wetting Properties. *Springer Series in Surface Sciences*, **3–34**. (2013). doi:10.1007/978-3-642-34243-1_1
8. A. Alhakeem, H. Almubarak, K. Liu, W. Al-Bazzaz. 3D seismic attribute analysis for structure and stra-

- tigraphy identification in Maui field, Taranaki Basin, New Zealand. *New Zealand Petroleum Conference*. (2017).
9. A. Alhakeem, K. Liu, W. Al-Bazzaz. Up-Scaled Petrophysical Analyses Using Micro-Level Field-Of-View Petrographic Images for the Kapuni Group, Taranaki Basin, New Zealand. *AAPG 2017 Annual Convention and Exhibition*, Houston, Texas, United States, (2017).
 10. W. Al-Bazzaz, S. AlMuddhhi, & M. AlOstath. Investigation Wettability Contact Angle Measurement in Kuwaiti Heavy Oil Reservoir and Modeling Using 2D Imaging Technologies. *SPE International Heavy Oil Conference and Exhibition*. (2018). doi:10.2118/193706-ms
 11. W. Albazzaz, S. Almudhhi & M. Alostath. Investigating wettability contact angle measurement in Kuwaiti heavy oil reservoir and modeling using 2D imaging technologies. *PETROL SCI TECHNOL*. VOL. 37, NO. 6, 694–700. (2019). doi:10.1080/10916466.2018.1564767
 12. S. Almudhhi, M. Alostath, W. Al-Bazzaz, H. Sharifigaliuk, & A. Qubian. “An unconventional approach in investigating wettability contact angle measurement in shale resources.” *PETROL SCI TECHNOL*, Vol. 40, Issue 8, Pages 893-936. (2021). <https://doi.org/10.1080/10916466.2021.2008969>



Figure 1 Hydrophilic (Water Wet) and Hydrophobic (Oil Wet) Wettability Attributes in Oolitic Reservoir Minerals

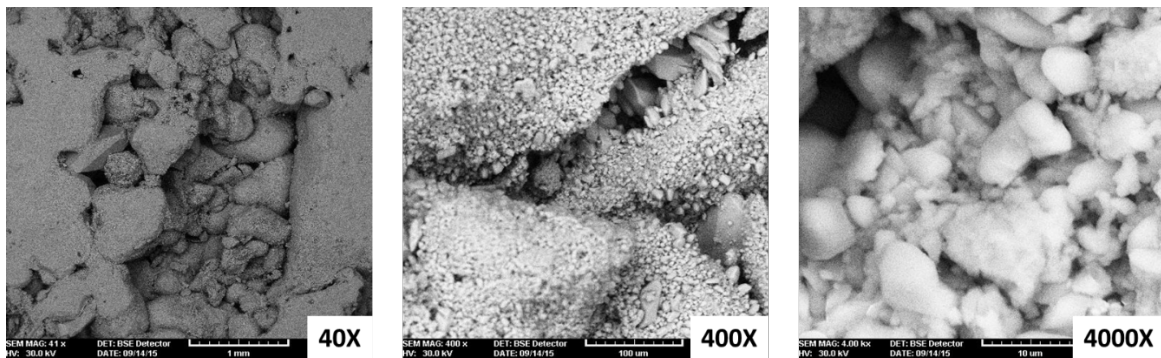


Figure 2 Oolite Rock SEM-BSE image capturing at different magnifications, X40 (mm), X400 (μm), X4000 (nm)

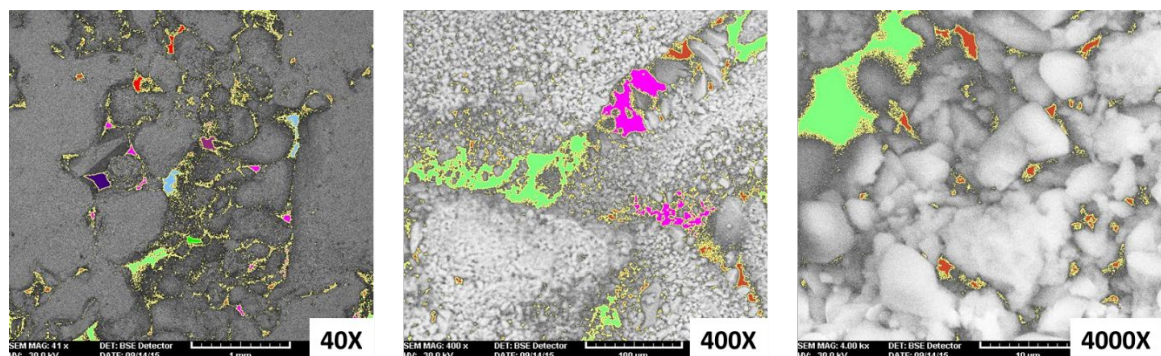


Figure 3 Captured 10 Pore Area Clusters in all Magnifications X40, X400, and X4000 in the Oolite Core Sample.

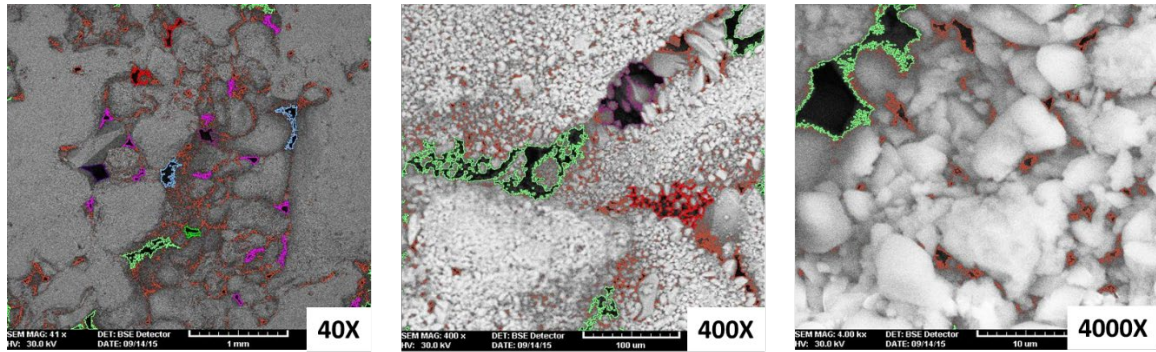


Figure 4 Measured Thousands of Pore/ Grain Wall Surface Boundaries in the Three Scales, X40, X400, X4000 in 2D Image Technology of the Oolitic Calcite.

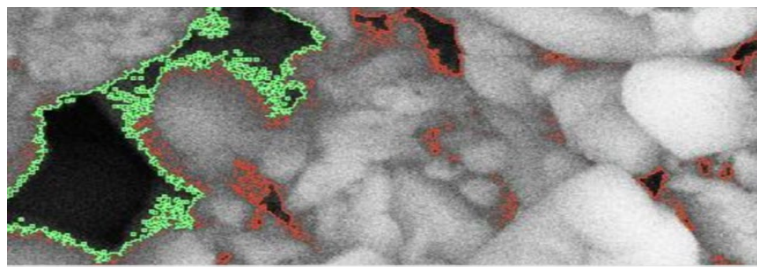


Figure 5 Example of Captured 2D Boundary of one Oolitic pore at a 4000X (Nanometer). The Boundaries between the Grain and the Pore Are Measured and Then Mean Average Contact Angle for Each Pore is Reported. Hundreds of Tiny Surfaces Are Captured Inside One Pore System as Seen in This Nano-scale Image. All These Surfaces Are Accurately Quantified Per Al-Bazzaz et.al (2018-2019) Contact Angle Wettability Statistical Classifications.

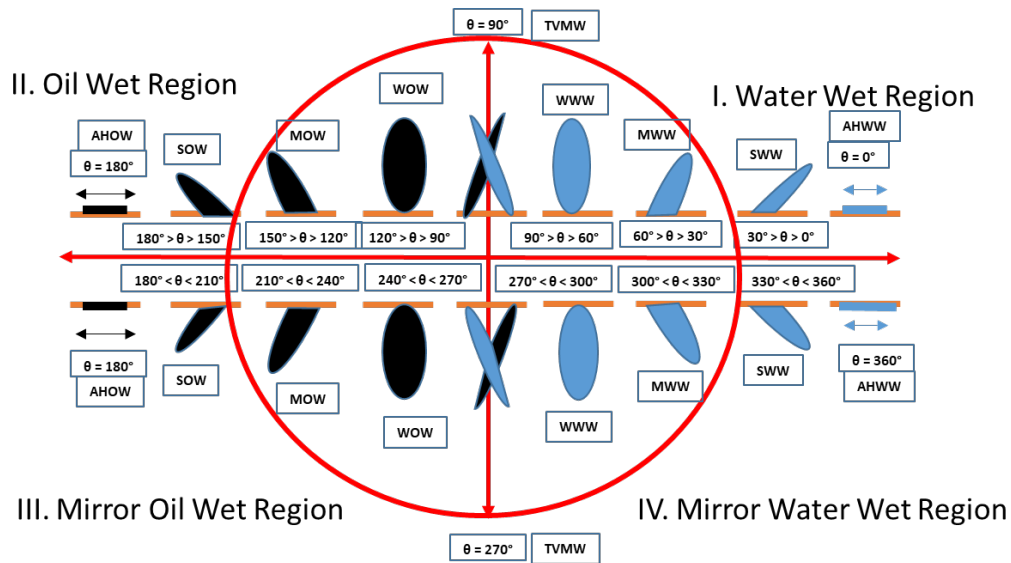


Figure 6 Al-Bazzaz Wettability contact angle(Θ°) Classification Chart. All Angles Follow the Central Angle Theorem in a Unit-Circle-Trigonometry (Red Circle). Blue Droplets Angles Define Water Wet Angles and Black Droplets Angles Define Oil Wet Angles. The Orange Surface Resembles the Grain Wall/ pore Boundary.

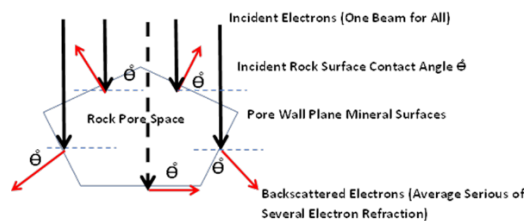


Figure 7 The Incepted Wetting Contact Angle Measurement through Backscattered Electron Refracted Angles from All Minerals Pore-Walls Surrounding the Pore-Space.

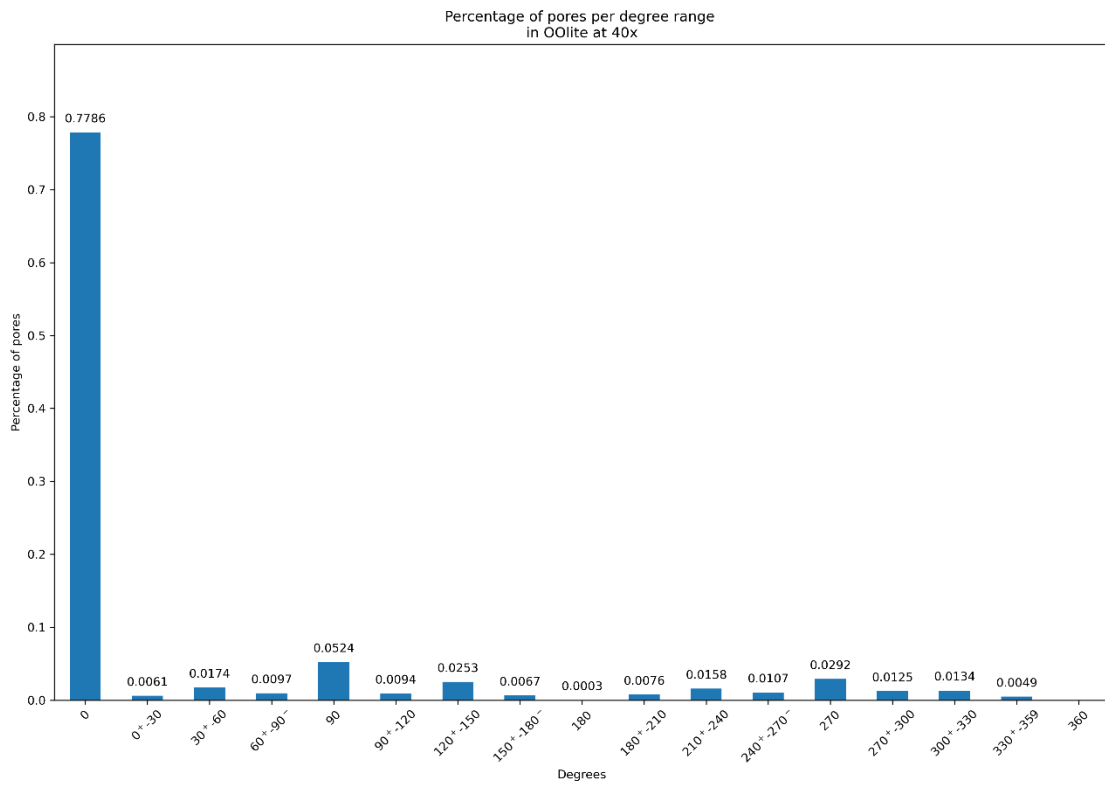
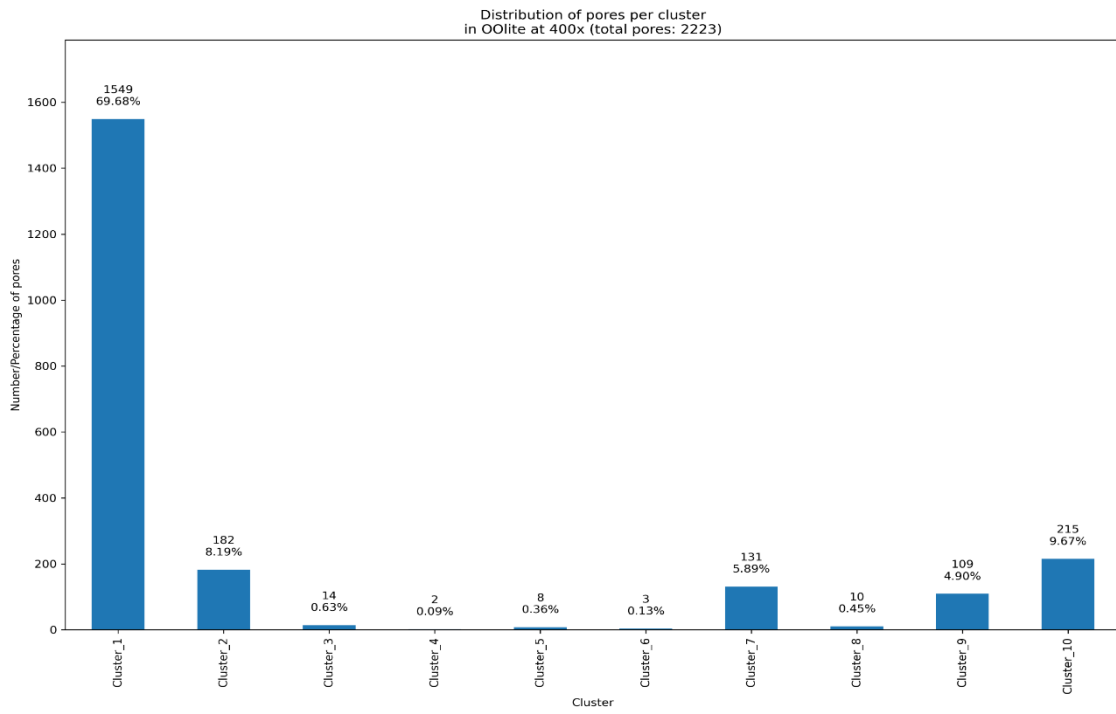


Figure 8 K-Mean Clustering Algorithm Using Python Distributions Using Counting Numbers of Pores Per 10-Clusters, and Per 18-Class 0° - 360° Contact Angle Classifications in the Oolitic Reservoir Sample at 40X (mm).

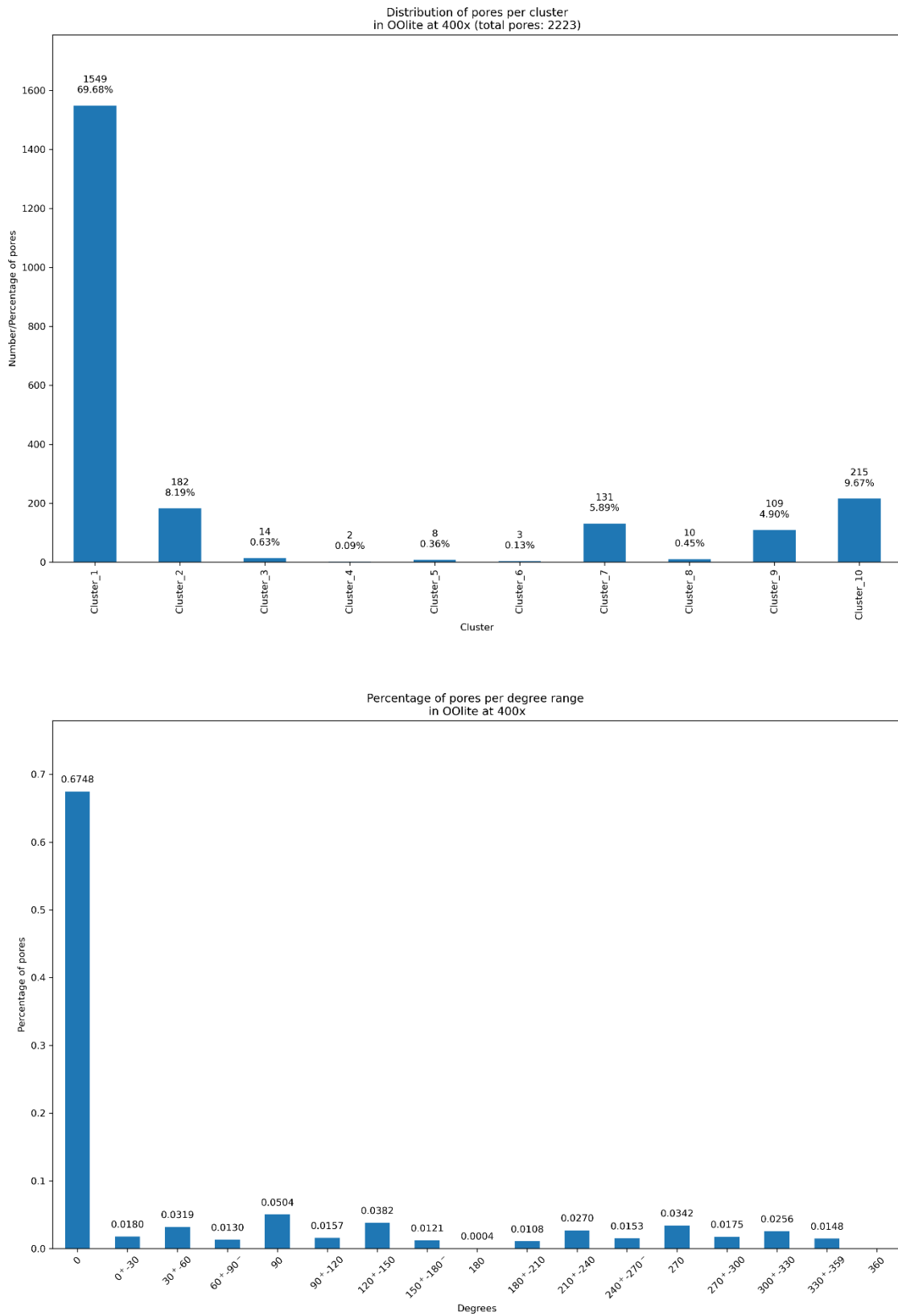


Figure 9 K-Mean Clustering Algorithm Using Python Distributions Using Counting Numbers of Pores Per 10-Clusters, and Per 18-Class 0° - 360° Contact Angle Classifications in the Oolitic Reservoir Sample at 400X (µm).

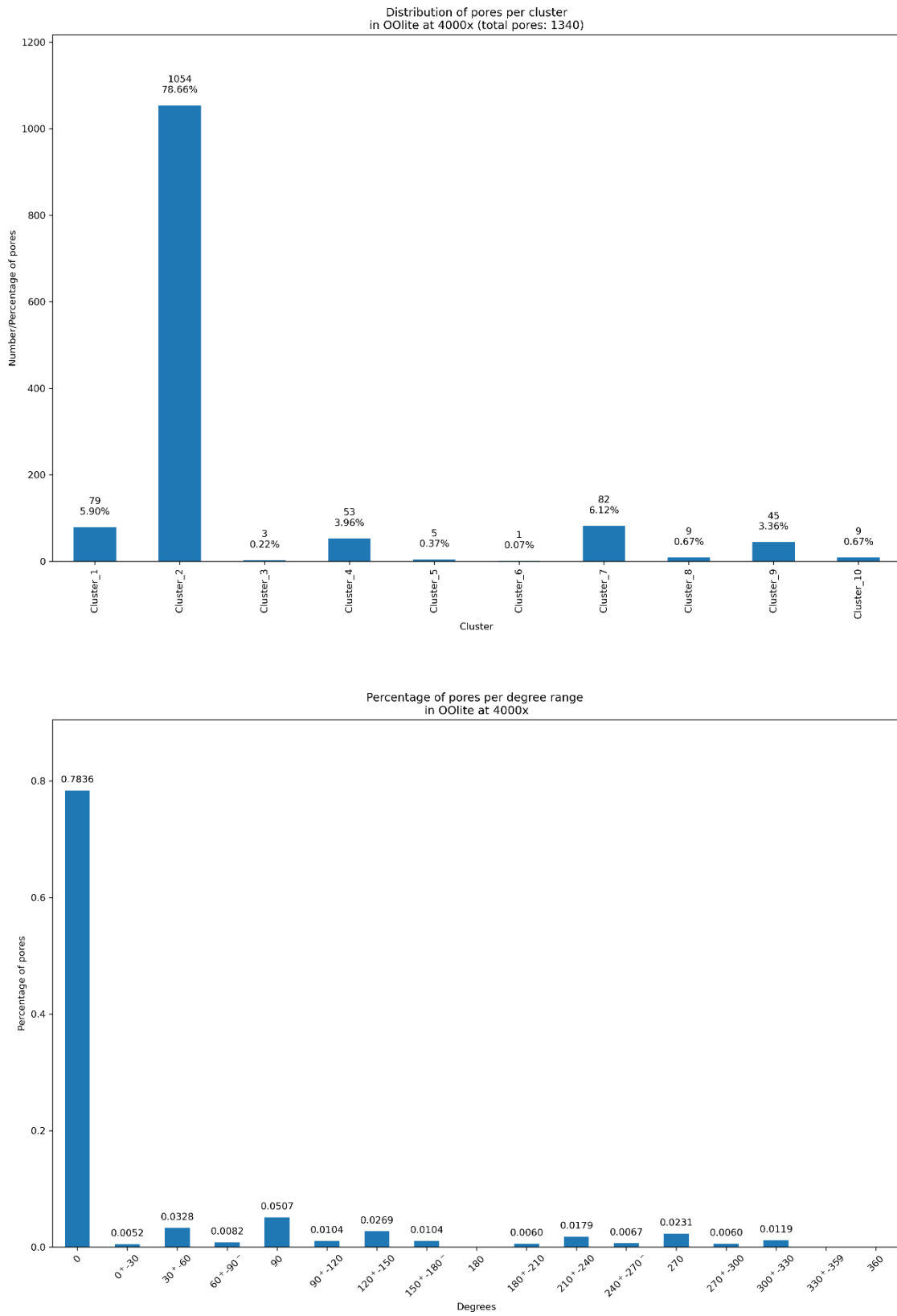


Figure 10 K-Mean Clustering Algorithm Using Python Distributions Using Counting Numbers of Pores Per 10-Clusters, and Per 18-Class 0° - 360° Contact Angle Classifications in the Oolitic Reservoir Sample at 4000X (nm).

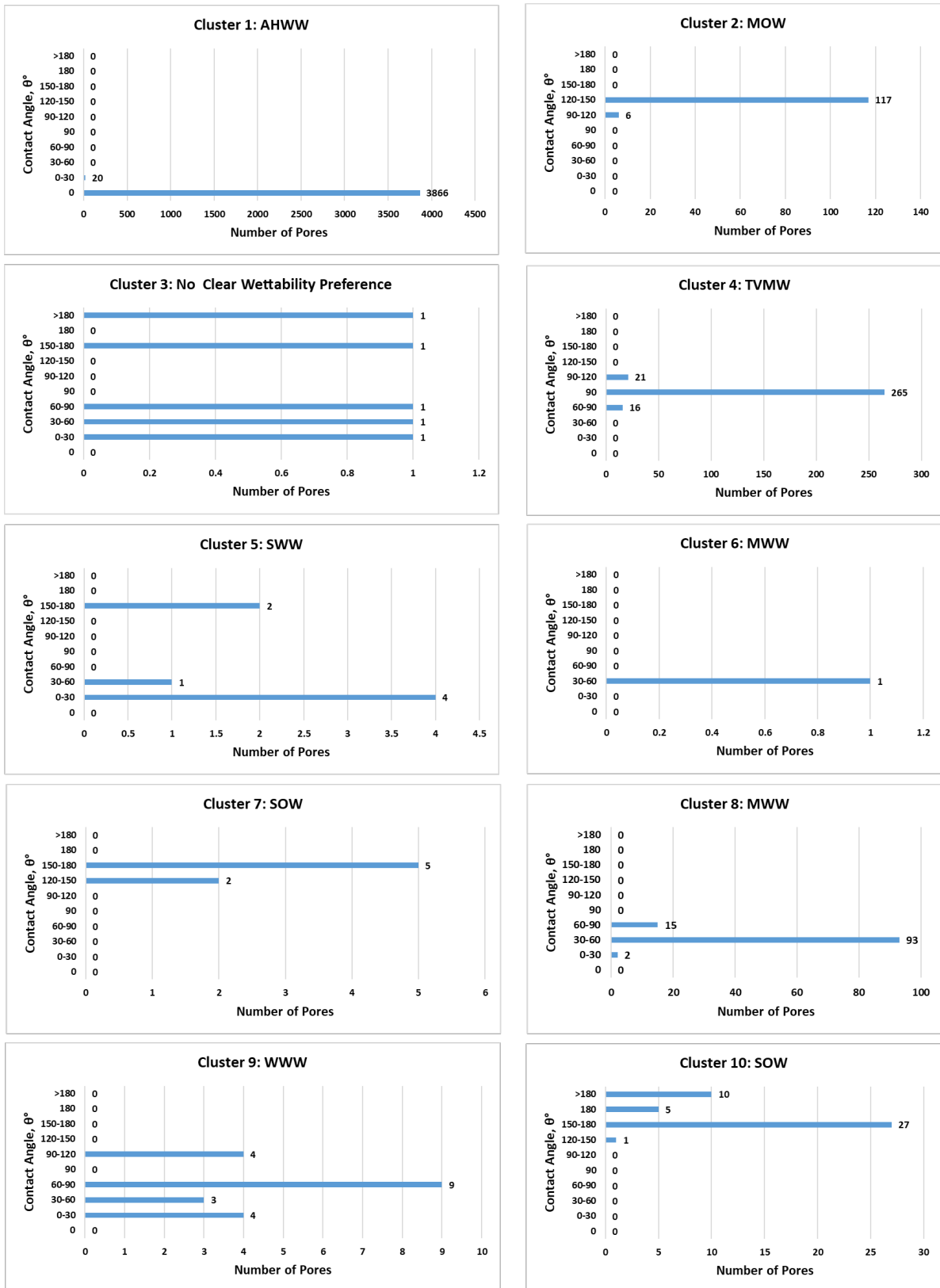


Figure 11 K-Mean Contact Angle and Wettability Preference at Each Cluster

Table 1 The Complete 2D Digital Angle Measurements Classification Inside the Oolite Reservoir Sample

Pore/ Grain Boundary Cluster Class #	Cluster Mean Wettability Contact Angle (θ°)	Unit Circle Wettability Quadrant Region	Wetting Preference According to Al-Bazzaz et. al. (2018-2019)	Symbol	Description
1	$\theta^\circ = 0^\circ$	I. Water Wet Region	Absolute Horizontal Water Wet	AHWW	Only Water Film on the Grain Wall
2	$0^\circ < \theta^\circ < 30^\circ$	I. Water Wet Region	Strongly Water Wet	SWW	Grain Wall Forces Attract Water Droplets and Resist Oil Droplets
3	$30^\circ < \theta^\circ < 60^\circ$	I. Water Wet Region	Medium Water Wet	MWW	Grain Wall Forces Attract More Water Droplets than Resist Oil Droplets
4	$60^\circ < \theta^\circ < 90^\circ$	I. Water Wet Region	Weak Water Wet	WWW	Grain Wall Forces Attract Water Droplets Slightly More than Resisting Oil Droplets
5	$\theta^\circ = 90^\circ$	I. (Water Wet) & II. (Oil Wet)	True Vertical Mixed Wet	TVMW	Grain Wall Forces will Not Distinguish Between Water Droplets and Oil Droplets
6	$90^\circ < \theta^\circ < 120^\circ$	II. Oil Wet Region	Weak Oil Wet	WOW	Grain Wall Forces Attract Oil Droplets Slightly More than Resisting Water Droplets
7	$120^\circ < \theta^\circ < 150^\circ$	II. Oil Wet Region	Medium Oil Wet	MOW	Grain Wall Forces Attract More Oil Droplets than Resisting Water Droplets
8	$150^\circ < \theta^\circ < 180^\circ$	II. Oil Wet Region	Strong Oil Wet	SOW	Grain Wall Forces Attract Oil Droplets and Resist Water Droplets
9	$\theta^\circ = 180^\circ$	II. Oil Wet Region	Absolute Horizontal Oil Wet	AHOW	Only Oil Film on the Grain Wall
10	$\theta^\circ = 180^\circ$	III. Mirror Oil Wet Region	Absolute Horizontal Oil Wet	AHOW	Only Oil Film on the Grain Wall
11	$180^\circ < \theta^\circ < 210^\circ$	III. Mirror Oil Wet Region	Strong Oil Wet	SOW	Grain Wall Forces Attract Oil Droplets and Resist Water Droplets
12	$210^\circ < \theta^\circ < 240^\circ$	III. Mirror Oil Wet Region	Medium Oil Wet	MOW	Grain Wall Forces Attract More Oil Droplets than Resisting Water Droplets
13	$240^\circ < \theta^\circ < 270^\circ$	III. Mirror Oil Wet Region	Weak Oil Wet	WOW	Grain Wall Forces Attract Oil Droplets Slightly More than Resisting Water Droplets
14	$\theta^\circ = 270^\circ$	III. (Mirror Oil Wet) & IV. (Mirror Water Wet)	True Vertical Mixed Wet	TVMW	Grain Wall Forces will Not Distinguish Between Water Droplets and Oil Droplets
15	$270^\circ < \theta^\circ < 300^\circ$	IV. Mirror Water Wet Region	Weak Water Wet	WWW	Grain Wall Forces Attract Water Droplets Slightly More than Resisting Oil Droplets
16	$300^\circ < \theta^\circ < 330^\circ$	IV. Mirror Water Wet Region	Medium Water Wet	MWW	Grain Wall Forces Attract More Water Droplets than Resist Oil Droplets
17	$330^\circ < \theta^\circ < 360^\circ$	IV. Mirror Water Wet Region	Strong Water Wet	SWW	Grain Wall Forces Attract Water Droplets and Resist Oil Droplets
18	$\theta^\circ = 360^\circ$	IV. Mirror Water Wet Region	Absolute Horizontal Water Wet	AHWW	Only Water Film on the Grain Wall

Table 2 Wettability Preference Based on Number of Static Contact Angle Distribution Measured in the Oolitic Reservoir Sample on K-Mean Clustering Algorithm

Contact Angle, θ°	Cluster 1	Cluster 2	Cluster 3	Cluster 4	Cluster 5	Cluster 6	Cluster 7	Cluster 8	Cluster 9	Cluster 10
0	3866	0	0	0	0	0	0	0	0	0
0-30	20	0	1	0	4	0	0	2	4	0
30-60	0	0	1	0	1	1	0	93	3	0
60-90	0	0	1	16	0	0	0	15	9	0
90	0	0	0	265	0	0	0	0	0	0
90-120	0	6	0	21	0	0	0	0	4	0
120-150	0	117	0	0	0	0	2	0	0	1
150-180	0	0	1	0	2	0	5	0	0	27
180	0	0	0	0	0	0	0	0	0	5
>180	0	0	1	0	0	0	0	0	0	10
Σ Contact Angles	3886	123	5	302	7	1	7	110	20	43
Wettability Preference within Cluster Dominance %	99.5	95.1	20.0	87.7	57.1	100.0	84.5	84.5	45.0	62.8
Wettability Preference	AHWW	MOW	No Clear preference	TVMW	SWW	MOW	SOW	MWW	WWW	SOW

Table 3 Captured and Measured Morphological Pore Area Contact Angles for Oolitic Sample at 40X (mm).

Total Pore Objects #	Area (μm ²)	Perimeter (μm)	Length (μm)	Width (μm)	Roundness	Elongation	Lgn.Prin.Long (μm)	Lgn.Prin.Short (μm)	Equiv. diameter (μm)	Angle [°]
15,257										
Mean	89.041	16.178	11.145	7.673	1.079	1.169	4.211	1.578	8.953	52.459
Deviation	245.104	41.452	11.407	6.553	0.467	4.846	6.771	3.505	5.763	95.505
Minimum	27.013	0	5.197	5.197	1	0	0	0	5.865	0
Maximum	16936.924	1542.98	289.48	246.632	16.133	42.968	158.206	100.158	146.849	360

Table 4 Captured and Measured Morphological Pore Area Contact Angles for Oolitic Sample at 400X (μm).

Total Pore Objects #	Area (μm ²)	Perimeter (μm)	Length (μm)	Width (μm)	Roundness	Elongation	Lgn.Prin.Long (μm)	Lgn.Prin.Short (μm)	Equiv. diameter (μm)	Angle [°]
2,229										
Mean	7.775	4.293	1.979	1.316	1.115	1.348	1.055	0.781	0.324	55.992
Deviation	128.105	34.782	5.899	3.023	0.919	0.526	4.328	3.04	1.338	98.731
Minimum	0.549	0	0.741	0.741	1	1	0	0	0	0
Maximum	5136.392	1212.896	198.513	85.325	22.893	7	41.447	103.499	36.083	359.225

Table 5 Captured and Measured Morphological Pore Area Contact Angles for Oolitic Sample at 4000X (nm).

Total Pore Objects #	Area (μm ²)	Perimeter (μm)	Length (μm)	Width (μm)	Roundness	Elongation	Lgn.Prin.Long (μm)	Lgn.Prin.Short (μm)	Equiv. diameter (μm)	Angle [°]
1,346										
Mean	0.085	0.305	0.165	0.116	1.074	0.733	0.057	0.022	0.132	33.212
Deviation	1.961	3.049	0.587	0.287	0.507	3.907	0.308	0.123	0.3	75.674
Minimum	0.005	0	0.074	0.074	1	0	0	0	0.084	0
Maximum	71.605	105.865	19.061	9.032	12.455	41.447	10.097	3.741	9.548	342.848

Rapid, High Resolution Probe Screening Techniques for Core Analysis and their Potential Usefulness for Hydrocarbon or Energy Transition Applications

*Emmanuel Okwoli and David K. Potter**

Department of Physics, University of Alberta, Edmonton, Alberta, T6G 2E1, Canada

Abstract. Core analysis techniques have traditionally been used mainly for hydrocarbon reservoir applications. However, the same techniques are equally applicable to reservoir issues associated with energy transition, such as geothermal, carbon geosequestration and hydrogen storage. Traditionally much core analysis has been performed successfully using core plugs. However this approach has certain drawbacks: (1) the selected plugs may not necessarily be representative of the full range of lithologies, (2) key features (e.g., naturally cemented or fractured zones) may be missed, (3) high resolution detail at the lamina scale may be missed, (4) depth shifting to well logs may not be sufficiently accurate, and (5) this strategy may be more sensitive to missing core. In this paper we highlight the usefulness of probe core analysis techniques on slabbed core and powdered samples. For many reservoirs relevant to energy transition it is crucial to have a high resolution continuous record of petrophysical properties so that key features are not missed (e.g., seals and fractures that may be important for CO₂ or H₂ storage applications). Probe measurements are less-destructive, without the need to cut core plugs, and provide: (1) high resolution data at the lamina scale, so that key features and small scale heterogeneities can be identified, (2) improved depth matching to well log data, and (3) rapid, cost effective data. In this paper we will describe examples highlighting a number of different probe techniques. Whilst some are well known, such as probe permeability, others such as probe acoustics, probe luminance (from linear X-ray measurements) and probe magnetics are less familiar to core analysts, but are very well suited for analyzing cores from reservoirs associated with hydrocarbons and energy transition. For example, certain geothermal projects will involve studying igneous as well as sedimentary rock cores, and differences in the magnetic susceptibility signals using the small, portable magnetic probe can quickly differentiate the higher signals of the igneous samples from the much lower values of the sedimentary rocks. The acoustic probe can be used to: (1) rapidly identify anisotropy (by orienting the acoustic transmitter-receiver bracket in different directions), (2) identify open microfractures via longer transit times, and (3) produce high resolution porosity profiles (after correlation of transit times with some representative plug or well log porosity data). Probe luminance and associated linear X-ray images, which are related to density, can indicate the full extent of natural cemented zones that may not be seen from mere visual observations of the slabbed core surface.

1 Introduction

The most common laboratory petrophysical analysis technique has been to cut and analyze cylindrical core plugs [1-3]. Core plugs are useful for characterizing 3D properties, and for simulating reservoir conditions through pressure and temperature experiments, and have yielded important information for formation evaluation and reservoir characterization (e.g., [4,5]) However, there remain some limitations of traditional core plug analyses and their sampling strategies:

(i) Cutting routine core plugs every 1 foot along the whole core sample is expensive and time-consuming and more destructive to core than probe measurements on slabbed core.

(ii) Depth shifting to well logs may not be sufficiently accurate even when cutting plugs every 1 foot.

(iii) This sampling strategy is sensitive to missing core.

(iv) The selected plugs might not represent the full range of lithologies or features. For instance, vital geologic features such as thin, naturally cemented zones that could act as permeability seals (i.e., barriers to fluid flow) may be missed.

Therefore, in this present study, we analyzed some datasets comprising novel probe measurements undertaken mainly on slabbed cores (though in one case powdered samples). Slabbed core creates a flat surface that allows probe measurements to conveniently be taken

* Corresponding author: dkpotter@ualberta.ca

at high resolution along the core. These probe high resolution and less-destructive screening techniques have advantages over the conventional 1 core plug per foot sampling strategy as follows:

(i) They allow high resolution measurements (at the small lamina scale) to be undertaken, so that key features and small scale heterogeneities can be identified. For example, identifying naturally cemented zones comprised of barite or quartz overgrowths. The high resolution profiles also allow better depth matching to well log data.

(ii) They are rapid screening methods, thus saving time by allowing quick petrophysical appraisals of the core samples to be made long before the routine or special core analysis plug data becomes available.

(iii) They are less-destructive, which is particularly useful for unconsolidated samples such as oil sands.

(iv) They do not require any special preparation of the sample. Some other core laboratory techniques require significant sample preparation. For example, laboratory nuclear magnetic resonance (NMR) generally requires the sample to be saturated with an appropriate fluid.

This paper will first describe a variety of probe techniques, some of which may be less familiar to core analysts. The advantages of probe permeability profiling (rapid, high resolution measurements) on slabbed core have been recognized for some time [6]. More recent studies have related probe permeability measurements to fluid flow and hardness in selected formations in western Canada [7], and modelling the effect of anisotropy on probe permeability [8]. Whilst there has been a recent study applying a new linear X-ray technique to measure the attenuation coefficients of various materials such as plastic, plexiglas, silicone rubber and paraffin wax [9], linear X-ray and quantitative point X-ray (probe luminance) measurements on rocks have received little attention since the work of Duncan et al [10]. Likewise there is little mention of probe acoustics techniques in the literature. We have, however, conducted recent studies using a probe magnetic device for characterizing some turbidite, shale and oil sands samples [11, 12]. In this paper we will present some examples of the usefulness of each of the above mentioned probe techniques, which can be applicable not only for hydrocarbon reservoir analyses but also for reservoirs associated with energy transition.

2 Experimental Probe Methods

2.1 Linear X-ray Images and Quantitative Point X-ray (Probe Luminance)

A schematic of the linear X-ray experimental setup is shown in **Figure 1** (after [10]). X-rays from the source pass through the rock sample and create an inverted image on an electronic image intensifier. The visible image is picked up by a charge coupled device (CCD) camera and digitized. The image can be viewed in real time and approximately 6-7 inches (roughly 15-18 cm) of rock core can be observed at any one time within the

camera frame. The frames can be combined to produce composite images (about 3 ft or 1 m in length in the present study). Overlaps of roughly 1 inch between neighbouring frames are utilized to achieve optimum matching in the composite image.

Typically, 3 ft lengths of cylindrical whole core with a diameter of 4 inches (just over 10 cm) are analyzed. Slabbed core can also be analyzed or, alternatively, a slice from the whole core of constant thickness (about 0.4 inches or 1 cm) can be used. Such slices are often impregnated with resin and referred to as resinated slabs. In parts of the core where there may be no rock, for example when a small core plug has been cut and removed from the larger core sample, the X-ray image appears very bright (white). This is the result of saturation or burn out within the image intensifier, due to the higher intensity of X-rays where there is no rock to block them.

The digital X-ray images are composed of pixels of varying gray scale (arbitrarily set between 0 and 255). The gray scale, known as the luminance, can be read in real time at any point across the image. By taking regularly spaced point readings (about every 0.032 ft or 1 cm in the current study) a quantitative high resolution profile of gray scale variation can be produced along the core sample, which in the present study will be referred to as “probe” luminance data. The luminance values represent the penetrability of the rock core to X-rays and are inversely related to the density of the rock [10]. Higher luminance values (lighter images) represent lower density, whilst lower luminance values (darker images) represent higher density.

The point probe luminance values (averaged over an area of about 0.5 cm diameter) can be taken in just a few seconds and are dependent on the thickness of the rock sample. To ensure all results in the present study were obtained from a similar thickness of slabbed core the luminance measurements were taken along the central axial line of the slabbed core, which had a constant thickness of 2 inches (just over 5 cm). This ensured that true variations in density could be identified without needing to correct for changes in core thickness. Also, in the absence of any independent bulk density data (which could otherwise be used to correlate with the luminance values) an aluminium block calibration standard of known density can be placed at the top and bottom of each 3 ft section and its luminance value measured in order to help produce density data for the rock core from the rock’s luminance results.

2.2 Probe Magnetic Susceptibility

Magnetic susceptibility is usually expressed in terms of magnetic susceptibility per unit volume k as:

$$k = J/H \quad (1)$$

or in terms of magnetic susceptibility per unit mass χ as:

$$\chi = M/H = k/\rho \quad (2)$$

where J is the magnetization per unit volume, M is the magnetization per unit mass, H is the applied external magnetic field, and ρ is the density of the material. A Bartington MS2E probe sensor can be used to perform high resolution measurements of magnetic susceptibility along the flat surface of slabbed core, or on individual smaller samples, or powdered rock samples. We have used this type of sensor for some other recent reservoir analyses on consolidated, unconsolidated, conventional and unconventional samples [11, 12]. However, all our previous studies were related to sedimentary reservoirs. We will show an example here of the use of this sensor in a potential geothermal setting where one encounters not only sedimentary samples, but also igneous core samples. The sensor tip at the end of a ceramic tube (label 1 in **Figure 2 (A)** and label 4 in **Figure 2 (B)**) senses a rectangular surface area of 3.8 mm x 10.5 mm on the sample. This allows high resolution measurements to be made at the lamina scale. The sensor is calibrated to measure true volume magnetic susceptibility (k) when against a flat surface of a sample greater than 10 mm in thickness. Most of the magnetic susceptibility signal is acquired within a penetration depth of up to about 5 mm into the sample. The ceramic tube is mounted on a metal enclosure that houses the electronic circuitry. When the sensor is connected to the MS2 meter (**Figure 2 (C)**) via a cable and the power is supplied, a low intensity alternating field (about 80 Am⁻¹ and about 2 kHz in frequency) is generated. This applied field penetrates a few mm into the sample when the tip of the sensor is gently placed on the flat surface of the slabbed core or individual sample. For samples with a weak magnetic susceptibility signal, such as the majority of sedimentary rocks, a background reading (in 12 seconds) followed by the sample measurement (in 12 seconds) can be made on the sensitive setting. For strong magnetic susceptibility samples, such as igneous and metamorphic rocks, each measurement can be made in just 1 second on the less sensitive setting. Another small sensor connected to a furnace (**Figure 2 (D)**) can make magnetic susceptibility measurements at different temperatures so that, for example, the effects of borehole temperatures can be simulated.

2.3 Pressure Decay Probe Permeametry

The experimental setup for the probe permeability measurements is shown in the photo of **Figure 3** and the schematic of **Figure 4 (a)**. In the example we show in the results **section 3.2** a Core Laboratories PDPK-400 unsteady state pressure decay probe permeameter was used to take point readings at exactly the same points along the slabbed core where the probe luminance values were taken. The tank shown in **Figures 3** and **4a** is first filled with nitrogen gas to a pre-defined pressure, and the valve closed. The probe tip is then sealed onto the core sample (in this case the surface of the slabbed core). A small probe tip of internal diameter 0.524 cm was used in the present study, which was comparable to the area of the point luminance measurements. The valve is then opened and the decay of pressure with time is recorded.

After some time, a smooth pressure gradient is established in the sample. The slope of the pressure decay curve is equal to the instantaneous flow rate function. This type of probe permeameter generally gives readings faster than the older steady state permeameters, which require one to wait for an equilibrium position to be reached at which the pressure and flow rate are constant. The permeameter delivers the permeability value of highly permeable rocks in a few seconds, whilst the value of low permeability rocks may take several minutes since the nitrogen gas will take longer to penetrate into the sample.

2.4 Probe Acoustics

The Core Laboratories PDPK-400 permeameter also enables the probe tip to be replaced with a small acoustics bracket (a simplified schematic is shown in **Figure 4 (b)**) to allow rapid, high resolution acoustic measurements of p - and s -wave transit times to be made on core samples. The bracket consists of two pyramidal point transducers (essentially two upside down pyramids separated by a distance of just under 10 cm), one being the transmitter (producing an acoustic pulse at a frequency of 1 MHz) and the other the receiver. The acoustic pulse penetrates just a few millimetres into the surface of the core, and measures the transit time (which can be converted to a velocity) over the interval between the transducers on the slabbed core. One advantage of these measurements is that the bracket can be rotated to make measurements in different orientations in order to gain information on the acoustic anisotropies of the different rock lithologies. In the present study we have measurements taken in two orthogonal directions, horizontally and vertically along the slabbed core surface. For the horizontal or vertical measurements, the mid-point of the acoustic bracket was placed over the points at which the luminance and probe permeability measurements were taken. Another advantage of the acoustic measurements is that by calibrating with a few core porosity measurements one can estimate porosity values from the probe acoustic results, and thus provide a high resolution “probe porosity” profile along each slabbed core section.

3 Results and discussion

3.1 An example of the usefulness of linear X-ray and probe luminance measurements

Figure 5 shows an example of the additional information that can be acquired from linear X-ray and luminance measurements. The slabbed core visible light image in **Figure 5 (a)** shows the presence of a very thin naturally cemented fracture vein containing barite (BaSO₄). Almost all the barite filled fracture veins observed in this well (in the North Sea) appeared very thin and of limited extent on the flat surface of the slabbed core in visible light. However, linear X-ray images such as that in **Figure 5 (b)** showed that most of these barite filled fracture zones were much more

extensive in 3D. Many of them exhibited a dendritic pattern with a thicker “trunk” region and thinner “branches” at right angles to the “trunk.” It is important to know the true extent of these barite filled fracture veins either in cases where you may want a good seal (e.g., for CO₂ or H₂ storage applications), or in cases where you don’t want a low permeability sealing interval. Relying only on visible light images of the core may not necessarily identify the full 3D extent of these natural cemented features.

Figure 6 shows that the luminance values from the linear X-ray images of **Figure 5 (b)** correlate reasonably well with the borehole bulk density log values. The smoothed luminance values in this case are 7 point running vertical averages over 1.5 ft intervals. This interval size was taken to compare directly with the vertical interval over which the wireline bulk density log averaged each reading.

3.2 An example of a comparison between probe luminance, probe permeability and probe acoustics

Figure 7 shows the raw probe measurement profiles (probe luminance, probe permeability and probe acoustic transit times for the *p*-waves) with depth for a 36 ft slabbed core interval from a well in the North Sea. **Figure 7** also shows the different lithological units within this interval of interest. These comprise the main good reservoir unit (white sections), which is a quartz sandstone shoreface facies intercalated with clay, a calcite dogger (yellow sections) comprising calcite and clays, and a micaceous sandstone (green section). Note that the depths are merely the depths from the top of the interval studied (as the real depths are confidential). The best reservoir (white sections) is part of the Etive formation in the North Sea. The micaceous sandstone (green section) is still reservoir, but of lower quality, and is part of the Rannoch formation in the North Sea. The calcite doggers (yellow sections) are essentially natural cemented zones with very low porosity and permeability.

Figure 7 shows quite similar overall profiles with depth for the probe luminance and probe permeability. Both are low in the calcite dogger sections, generally higher in the good reservoir Etive formation, and generally lower again in the lower quality Rannoch formation. Higher values of probe luminance and probe permeability in the Etive tend to be pure quartz sandstone with little clay, whereas lower values in the Etive are generally associated with intercalated clay laminae. The probe acoustic transit times follow a generally similar overall pattern as the other probe results, being lower in the calcite doggers and Rannoch micaceous sandstone and higher in the Etive reservoir. Two sets of probe acoustic results are shown: one set where the acoustic bracket made measurements horizontally down the slabbed core, and another set where the acoustic bracket made measurements vertically down the slabbed core. There is a significant difference between the horizontal and vertical probe acoustic measurements in the Rannoch micaceous

sandstone. This is due to anisotropy caused by the small mica flakes that aligned along the bedding plane (the ancient horizontal) when the rock formed, causing the transit time to be lower in the horizontal (higher velocity) and longer in the vertical direction (lower velocity). Detecting this anisotropy from these rapid measurements is very useful, particularly since the standard sonic log for this well only measured the transit time over vertical intervals (as is the case for many wells), and gave a profile close to that of the vertical probe acoustics. Thus the standard sonic log data would not have identified the anisotropy.

In the Etive reservoir sections there are some zones where the horizontal and vertical probe acoustic results are very similar. These represent zones that are close to being isotropic and correspond to clean quartz sandstone zones (i.e., where there is little or no clay). There are other parts of the Etive reservoir where the horizontal and vertical probe acoustic results are very different. These represent anisotropic zones where the quartz sandstone is intercalated with thin clay laminae.

To compare the different petrophysical probe parameter results, we first crossplotted the raw data points and observed correlations, though the coefficients of determination (R^2) were relatively low. This could be due to small differences in depth matching of the crossplotted parameters. The raw data points for different parameters need to be very accurately matched to exactly the same depth (which can be quite challenging) for good correlations to be observed. We then crossplotted smoothed data over different vertical running averages (1 ft, 1.5 ft, and 2 ft). The smoothed data averages the results over a particular interval and so any small inaccuracies in depth matching will have minimal effect since most of each interval will match for both parameters concerned. Another reason for smoothing the data was because the acoustic probe measures the transit time over an interval of just under 10 cm (and is thus an average over this interval rather than being a point measurement), whereas the probe permeability and probe luminance are essentially point measurements over a small area (as detailed in the experimental methods **section 2**). Therefore, it was logical to compare all of the probe results by using a running average (i.e., smoothing). The vertical acoustic measurements, in particular, were often taken across different thin laminae and fractured sections, so it was important to average the other point probe measurements across the same intervals. The smoothing significantly improved the coefficient of determination (R^2) values, with the highest R^2 values obtained when averaging over a 2 ft vertical interval. The correlation between probe luminance and probe permeability gave an R^2 value of 0.48 when comparing the raw data points and a much improved R^2 value of 0.76 when the smoothed 2 ft vertically averaged data was crossplotted. For the vertical probe acoustics versus probe permeability, an R^2 value of 0.41 was obtained for the raw data, and an R^2 value of 0.85 for the data averaged vertically over 2 ft intervals. For the horizontal probe acoustics versus probe permeability the R^2 value was only 0.37 for the data averaged vertically over 2 ft intervals (and lower for the

raw data crossplot). This was mainly due to lower correspondence in the top calcite dogger interval (the reason is not clear at present). However, there was good correspondence throughout the rest of the 36 ft interval. Moreover the horizontal acoustics correlated with permeability better than the vertical acoustics in the micaceous sandstone interval. We believe this was a result of the anisotropy. Both the horizontal acoustics and probe permeability essentially measured in the horizontal plane of the mica grains, whereas the vertical acoustics measured perpendicular to that plane. For the vertical probe acoustics and probe luminance measurements, an initial R^2 value of 0.51 was obtained for the raw data, and a value of 0.70 for the data averaged vertically over 2 ft intervals. More extensive comparative analyses of this large dataset, involving multiple linear regression and artificial neural networks, is being prepared for publication elsewhere.

Figure 8 shows another example from this dataset of the usefulness probe permeability measurements. It shows the same probe permeability profile as in **Figure 7**, but also shows the core plug permeability values for comparison. One observation is that the core plug values tend to be higher on average than the probe values at corresponding depths. We believe this is because the core plugs were cleaned by hot soxhlet cleaning, and some of the permeability controlling clays are likely to have been washed out of the samples prior to the permeability measurements. This would have led to higher permeability values than for the uncleaned slabbed core with the original clay content. We have previously quantified the removal of clay in other core plug samples using magnetic susceptibility measurements before and after cleaning [13].

Figure 8 also shows that the probe permeability values exhibit much more detail, due to the higher measurement resolution (at the lamina scale), and a much larger range of values compared to the core plugs. This level of detail can be crucial for identifying thin naturally cemented zones, or thin open fractures, or thin laminae (which could be low permeability seals or high permeability conduits), not only in hydrocarbon reservoirs but also in potential reservoirs for CO_2 or H_2 storage. Sampling of core plugs tends to avoid some of features. This may also partly explain the smaller range of plug permeability values compared to the probe permeability values in **Figure 8**.

3.3 Probe magnetic susceptibility measurements on samples from a pilot exploration well from a potential geothermal project in Northern Alberta

In Northern Alberta, the thickness of the Phanerozoic sedimentary succession is quite variable (between about 500 and 2400 m). Previous studies [14, 15] indicated that temperatures above about 80°C for geothermal purposes will only be found below the base of sedimentary rocks in the Precambrian crystalline basement. Thus it is crucial to be able to identify the depths of the boundary between the sedimentary succession and the crystalline basement rocks. We proposed that magnetic

susceptibility could easily identify the boundary between the sedimentary succession and the crystalline granitic basement rocks better than most other techniques. **Table 1** shows our probe volume magnetic susceptibility measurements for some test powdered samples from a deep pilot well to assess the viability of a geothermal project. The powdered samples were held in small plastic containers (about 1 cubic inch in volume), which were open at one end, allowing the probe magnetic susceptibility device to be gently placed on the top surface of each powdered sample to take the measurements. Sample H22 is still part of the sedimentary succession (but may possibly be slightly metamorphosed) and has a low volume magnetic susceptibility. Samples H25 and H28 are within the crystalline granitic basement and have significantly higher volume magnetic susceptibility values. It thus appears that magnetic susceptibility is a good means of identifying the depth at which the crystalline basement starts. The compositions of the samples, from electron microprobe data and whole rock geochemistry, are given in **Table 2**. However, it is not these major components listed in **Table 2** that are primarily responsible for the large differences in magnetic susceptibility between the sediment sample and the two basement samples. It turns out that the small fraction of ferrimagnetic iron oxides in the samples is the key factor. Whilst the sediment sample contains an extremely small amount of stable single domain ferrimagnetic particles (which we identified from magnetic hysteresis measurements similar to those described in [16]) that don't increase the overall magnetic susceptibility of the sample significantly, the two crystalline basement samples contain small amounts of superparamagnetic ferrimagnetic particles (also identified from magnetic hysteresis measurements) that do contribute significantly to the higher magnetic susceptibility of these samples.

3.4 Summary of the probe techniques and examples of hydrocarbon and energy transition applications

Table 3 summarizes the different probe techniques described in this paper, and lists some of the potential significant/relevant applications to hydrocarbon and energy transition studies. The probe luminance and probe permeability measurements are essentially point readings over small (very similar diameter) areal extents, as detailed in **sections 2.1 and 2.3**, and can give data at the lamina (a few millimetres) scale. The probe magnetic susceptibility measurements are also essentially a point reading, but over a slightly larger rectangular areal extent and also at the lamina (a few millimetres scale) as detailed in **section 2.2**. The probe acoustics tool gives a transit time over an interval of just under 10 cm as detailed in **section 2.4**, and will give the transit time of individual thin laminae if the transducer bracket is placed parallel to the laminae, and may give an average value of a number of laminae if the transducer bracket is placed perpendicular to laminae that are thinner than the distance between the transmitter and receiver transducers.

4 Conclusions

The following overall conclusions can be drawn:

1. Probe measurements have the potential to provide rapid, high resolution, less destructive measurements compared to core plugs, and provide additional complementary tools for analyzing reservoir samples for hydrocarbons or energy transition (e.g., CO₂ and H₂ storage, and geothermal applications).
2. Linear X-ray measurements allow one to see the full 3D extent of features such as naturally cemented zones (e.g., barite filled fracture veins). Probe luminance values can be used to provide a high resolution profile of density variation, and can be correlated with other probe petrophysical techniques (such as probe permeability and probe acoustics).
3. Probe permeability can rapidly characterize variations at high resolution (at the lamina scale) on slabbed core. In contrast, routine core plug sampling strategies generally only cut plugs every 1 foot, and thus could miss certain key features (e.g., thin naturally cemented zones). Core plug cutting and analysis is also time consuming, and more destructive to the core. Also certain core cleaning processes such as hot soxhlet cleaning can potentially remove some permeability controlling clays, as quantified in our previous study [13]. This will subsequently produce overestimated permeability values, and is the likely reason for the high core plug permeability values compared to the probe permeability values in the example we give in the present paper in **Figure 8**.
4. Probe acoustic measurements taken in different orientations can quickly identify and quantify anisotropy (of acoustic transit time) in different lithologies. This can be particularly useful if one only has access to standard sonic log data, which averages transit times over vertical intervals, and so wouldn't identify anisotropy.
5. Probe magnetic susceptibility measurements can rapidly distinguish sedimentary from crystalline granitic basement samples for geothermal applications. This is in addition to other applications of probe magnetic susceptibility (e.g., for turbidites, shales, and oil sands) that we have described previously [11, 12].

D. K. P. thanks the Natural Sciences and Engineering Research Council of Canada (NSERC) for a Discovery Grant. We thank Core Laboratories for their help with the probe permeability and probe acoustic measurements, and Corex (formerly Robertson Research) for their help with the linear X-ray and luminance measurements. Olga Vizika and Subhash Ayirala are thanked for their constructive review comments, which helped improve the manuscript.

5 References

1. A. Donaldson and G. M. Clydesdale. Accurate reservoir evaluation – quality core samples – a good starting point. *In: Advances in Core Evaluation – Accuracy and Precision in Reserves Estimation (Ed. P.F. Worthington)*, p. 35–53. Gordon & Breach Science, New York (1990)
2. B. Levallois. Core petrophysical measurements on unconsolidated sands in deep water reservoirs. *Proceedings of the 2000 International Symposium of the Society of Core Analysts, Abu Dhabi, UAE, 18-20 October*, Paper SCA2000-34 (2000)
3. C. E. Ubani, B. Y. Adeboye and B. A. Orij. Advances in coring and core analysis for reservoir formation evaluation. *Petroleum & Coal*, **54**, 1-15 (2012)
4. T. A. Zorski, J. S. Ossowski, N. Rodo and T. Kawiak. Evaluation of mineral composition and petrophysical parameters by the integration of core analysis data and wireline well log data: The Carpathian Fore deep case study. *Clay Minerals*, **46** (1), 25–45 (2011)
5. H. M. Sbiga and D. K. Potter. Prediction of resistivity index by use of neural networks with different combinations of wireline logs and minimal core data. *SPE Reservoir Eval. Eng.* **20** (1), 240–250 (2017) <https://doi.org/10.2118/181751-PA>.
6. D. J. Goggin. Probe permeametry: is it worth the effort? *Marine and Petroleum Geology*, **10**, Issue 4, 299-308 (1993)
7. C. P. Vocke, C. R. Clarkson, S. Aquino, A. Vahedian, D. C. Lawton, K. Osadetz and A. Ghanizadeh. Application of profile (probe) permeability and mechanical (rebound) hardness tests for characterization of fluid transport and geomechanical properties of selected formations in western Canada. *GeoConvention 2016: Optimizing Resources, Calgary*, (2016)
8. K. Al-Azani, H. Al-Yousef and M. Mahmoud. Effect of permeability anisotropy on probe permeameter measurements. *SPE Middle East Oil and Gas Show and Conference, Manama, Bahrain*, Paper SPE-194769-MS (2019)
9. A. Mousa, K. Kusminarto and G. B. Suparta. A new simple method to measure the X-ray linear attenuation coefficients of materials using micro-digital radiography machine. *International Journal of Applied Engineering Research*, **12**, number 21, 10589-10594 (2017)
10. A. R. Duncan, G. Dean and D. A. L. Collins. Quantitative density measurements from X-ray radiometry. *In: Harvey, P. K. and Lovell, M. A. (eds) Core-Log Integration*, Geological Society, London, Special Publications, **136**, 17-24 (1998)
11. T. H. To, D. K. Potter, A. Abiola, and V. T. Ebufegha. Probe magnetics as a rapid, non-destructive screening tool for consolidated and unconsolidated core in conventional and unconventional reservoirs. *Proceedings of the 2018 International Symposium of the Society of Core*

Analysts, 27-30 August 2018, Trondheim, Norway.
Paper SCA 2018-057 (2018)

12. T. H. To and D. K. Potter. Comparison of high resolution probe magnetics, X-ray fluorescence and permeability on core with borehole spectral gamma ray and spontaneous potential in an oil sand well. *Proceedings of the 34th International Symposium of the Society of Core Analysts*, Paper SCA2021-035, (2021)
13. D. K. Potter, A. Ali, S. Imhmed and N. Schleifer. Quantifying the effects of core cleaning, core flooding and fines migration using sensitive magnetic techniques : implications for permeability determination and formation damage. *Petrophysics*, 52 (no. 6), 444-451 (2011)
14. F. W. Jones, H. L. Lam and J. A. Majorowicz. Temperature distributions at the Paleozoic and Precambrian surfaces and their implications for geothermal energy recovery in Alberta. *Canadian Journal of Earth Sciences*, **22**, 1774-1780 (1985)
15. J. Majorowicz, M. Unsworth, T. Chacko, A. Gray, L. Heaman, D. K. Potter, D. Schmitt and T. Babadagli. Geothermal energy as a source of heat for oil sands processing in Northern Alberta, Canada. In : F. J. Hein, D. Leckie, S. Larter and J. Suter, eds., *Heavy-oil and oil sand petroleum systems in Alberta and beyond*. AAPG Studies in Geology, **64**, 1-22 (2012)
16. O. P. Ivakhnenko and D. K. Potter. The use of magnetic hysteresis and remanence measurements for rapidly and non-destructively characterizing reservoir rocks and fluids. *Petrophysics*, **49**, (issue 1), 47-56 (2008)

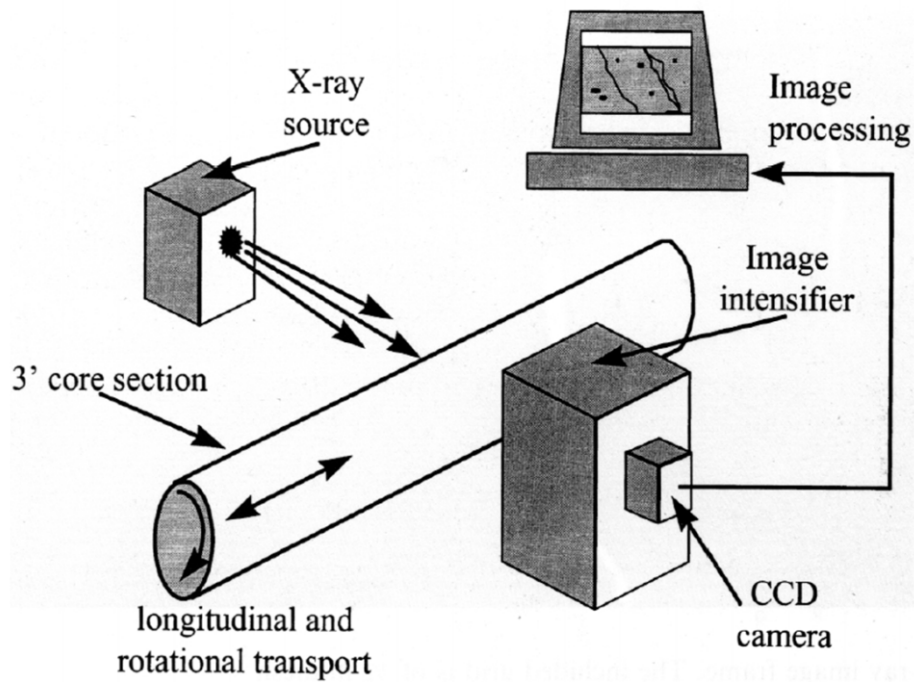


Fig. 1. Schematic of the equipment for linear X-ray and probe luminance measurements (after [10]).

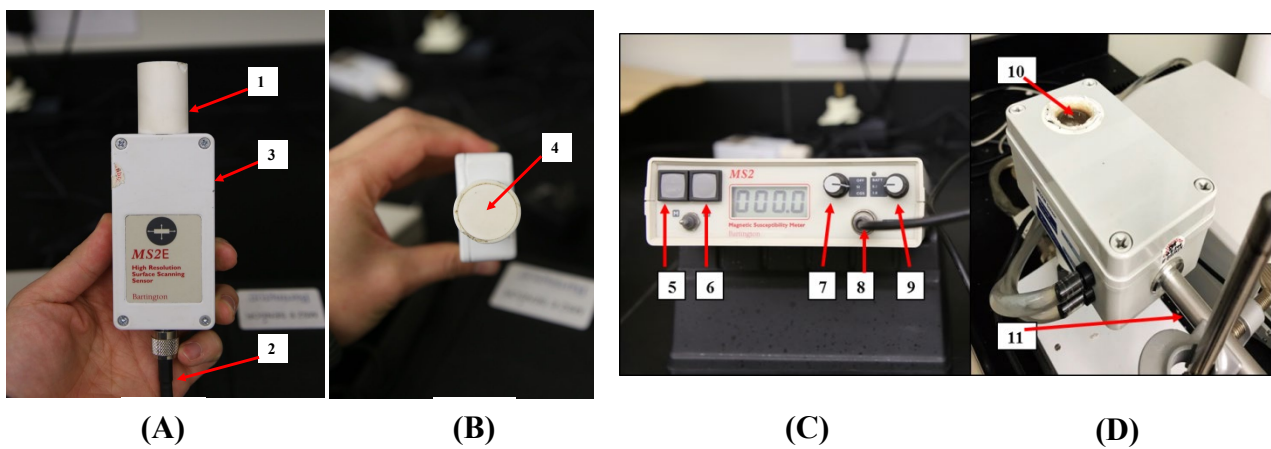


Fig. 2. MS2E probe for magnetic susceptibility measurements on slabbed core. (A) side view showing: 1 the probe tip with a ceramic guard and a sensor located at the end of the tube, 2 the cable connected to the MS2 meter, 3 a metal enclosure housing the electronic circuitry. (B) top view 4 shows the cross section of the probe sensor tip that is gently applied to the surface of the slabbed cores. (C) View of the magnetic susceptibility meter showing: 5 the measuring button, 6 the zeroing button, 7 is the magnetic unit (SI or CGS) system selector knob, 8 the cable connecting the MS2 meter to the sensor, 9 the sensitivity scale selector knob. The digital readout between 6 and 7 records the magnetic susceptibility value. (D) is the MS2W sensor for temperature dependent measurements (e.g., to simulate borehole temperatures) where 10 is the sample chamber and 11 is the input for the cable 8 shown in (C) to connect with the meter.

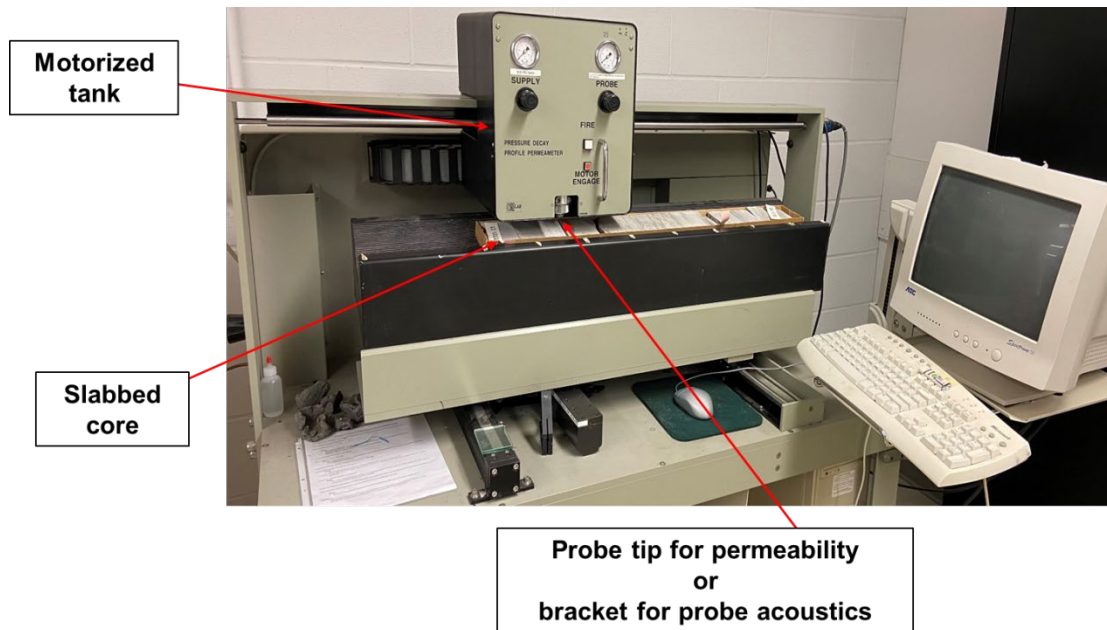


Fig. 3. Core laboratories PDPK-400 for probe permeametry and probe acoustics.

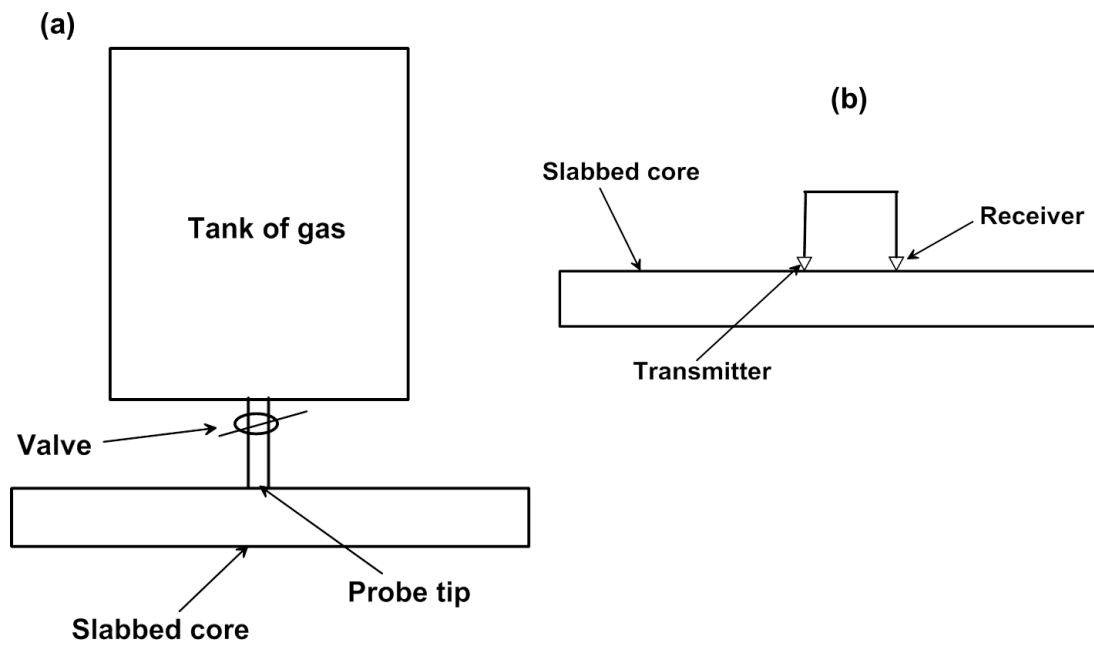


Fig. 4. Schematics of (a) the probe permeameter, and (b) the acoustic transducers.

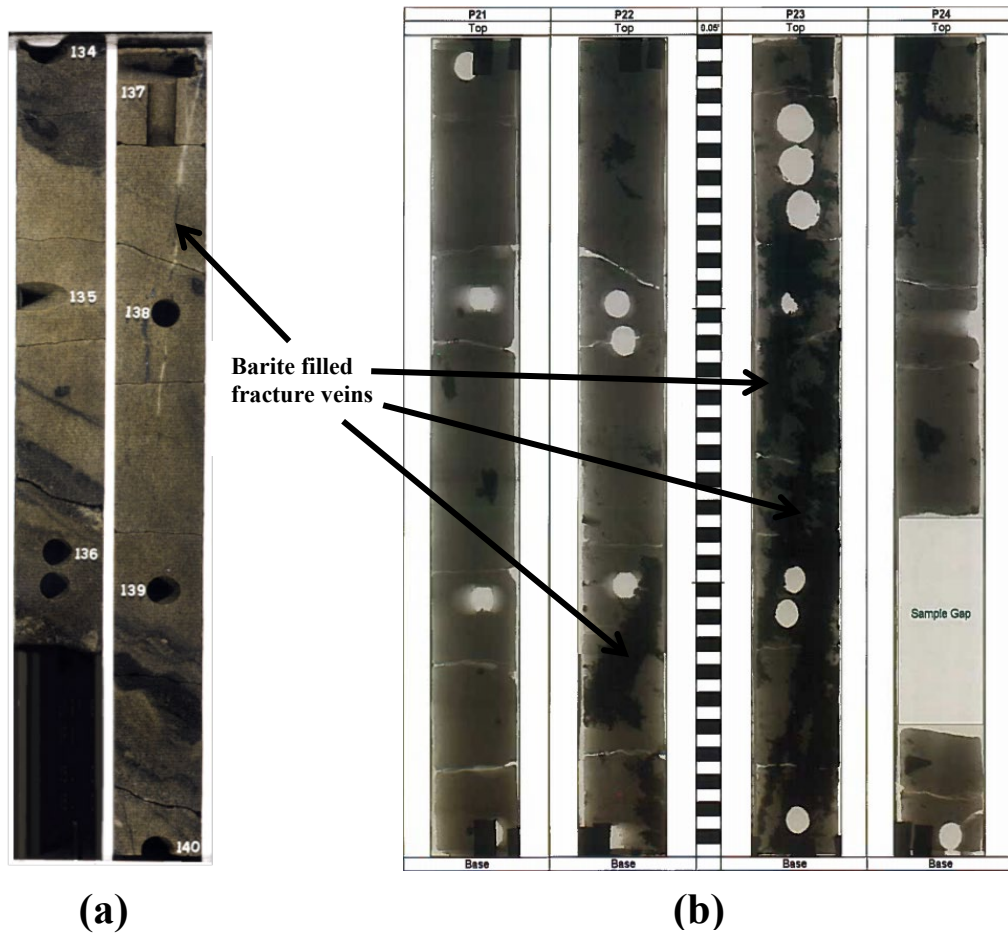


Fig. 5. (a) Visible light image of part of the slabbed core from a well in the North Sea, showing a thin barite filled fracture vein. The width of the core is 4 inches. **(b)** Linear X-ray images of core from the same well as in **(a)** showing that the barite filled fracture veins (black regions) are more extensive in linear X-ray than they appear in visible light. The lighter grey regions are quartz sandstone.

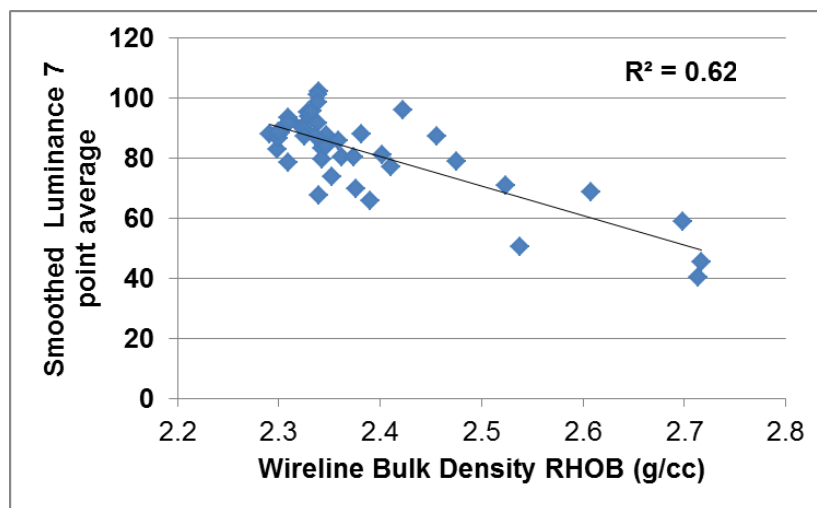


Fig. 6. Crossplot of wireline bulk density versus smoothed luminance 7 point average (averaged over 1.5 feet vertically) for the interval shown in **Figure 5 (b)**.

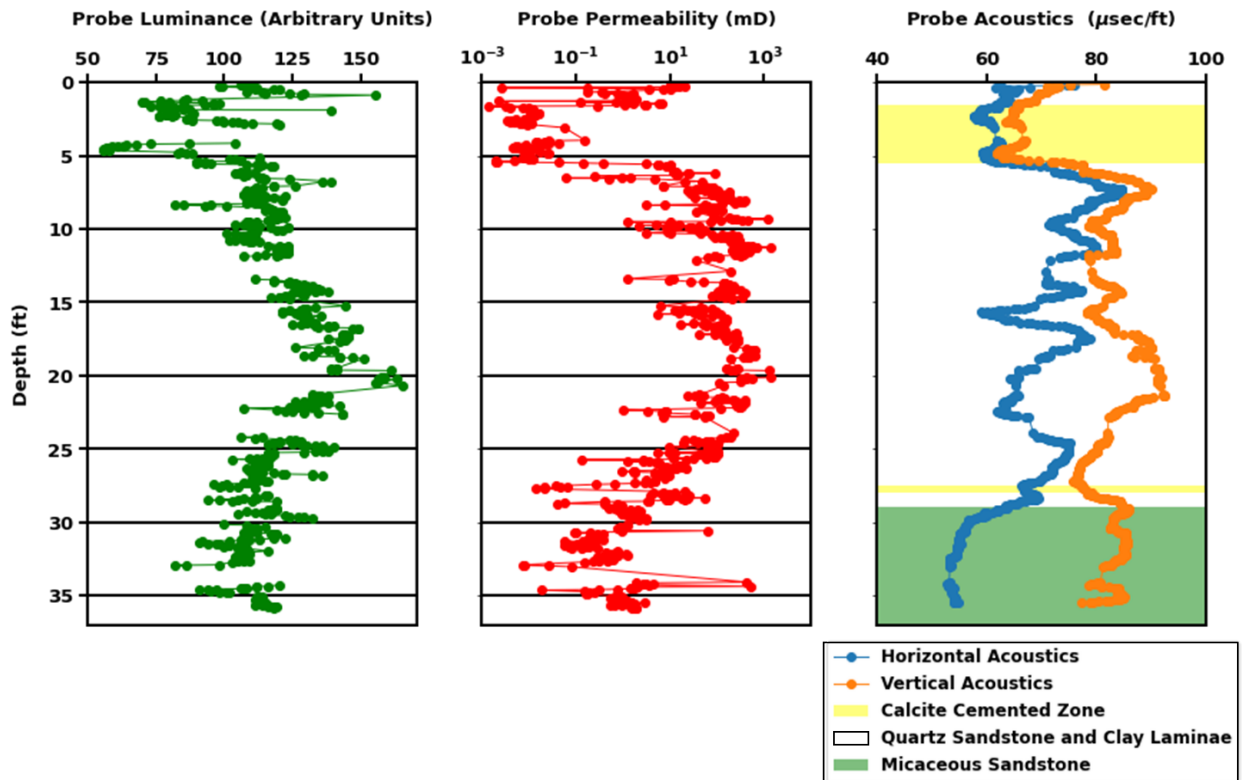


Fig. 7. Lithology and the variation with depth of (left) probe luminance (middle) probe permeability and (right) probe acoustic p -wave transit time measurements, for a well in the North Sea. The measurement uncertainties in each case are smaller than the plotted symbols. Typical uncertainties are as follows: for probe luminance ± 1 ; for probe permeability it depends somewhat on the magnitude being typically around ± 0.01 mD for permeabilities of 1 mD and around ± 10 mD for permeabilities of 1000 mD; for probe acoustics $\pm 1 \mu\text{sec/ft}$.

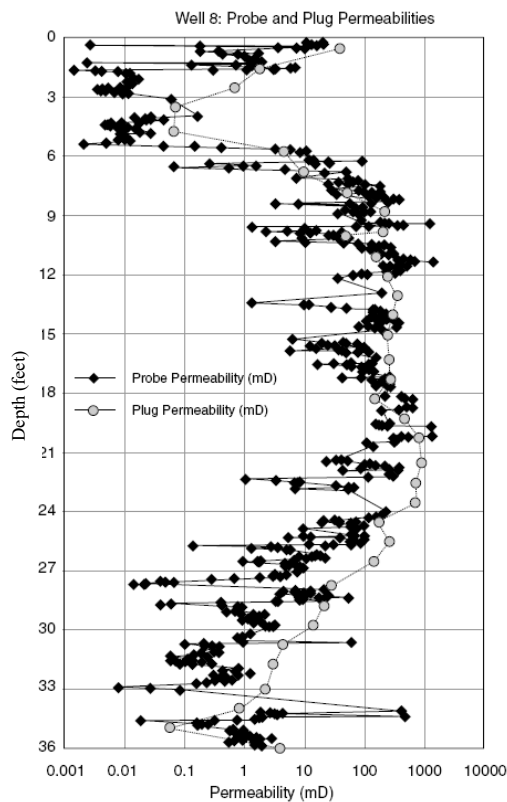


Fig. 8. Plot of the probe permeability values from Figure 7, and also showing the core plug permeability values for comparison.

Table 1. Low field probe volume magnetic susceptibility measurements on three powdered rock samples from a Well in Northern Alberta that is part of a pilot geothermal project study. The low field measurements were taken with a Bartington MS2E sensor. The sediment sample is clearly distinguished from the two crystalline basement samples on the basis of the magnetic susceptibility.

Sample name	Sample depth (m)	Low field probe volume magnetic susceptibility at room temperature (10^{-5} SI)
H22 (sediment)	1657	19
H25 (crystalline basement)	2350	506
H28 (crystalline basement)	2364	239

Table 2. Major components of the three powdered rock samples from **Table 1** from electron microprobe data and whole rock geochemistry.

Sample	Quartz (%)	K-feldspar (%)	Plagioclase (%)	Orthopyroxene (%)	Other (%)
H22 (sediment)	52	4	32	0	12 (mainly biotite)
H25 (crystalline basement)	25	13	53	6	3
H28 (crystalline basement)	28	13	50	6	3

Table 3. Summary of the probe techniques and some examples of their significance/relevance to hydrocarbon and energy transition applications.

Probe Technique	Applications to Hydrocarbon and/or Energy Transition
Probe Luminance	High resolution density, and identifying the 3D extent of naturally cemented intervals (important for reservoir seals for hydrocarbons, and for CO ₂ and H ₂ storage).
Probe Permeability	High resolution fluid flow, for identifying thin naturally cemented zones, open fractures, and laminae (which could be low permeability seals or high permeability conduits), for hydrocarbons, and for CO ₂ or H ₂ storage. Probe permeability measurements on uncleaned slabbed core do not suffer from clay removal caused by some cleaning processes on core plugs [13]). Permeability anisotropy can be estimated if the probe measurements are taken on slabs cut in different orientations.
Probe Acoustics	High resolution <i>p</i> - and <i>s</i> -wave transit times, and porosity profiles. Measurements can be made in different orientations in order to identify and quantify acoustic anisotropy (e.g., in 2D on the flat face of slabbed core). All these applications are relevant to hydrocarbon and energy transition reservoirs.
Probe Magnetic Susceptibility	Particularly useful for geothermal studies where identification of crystalline basement igneous and/or metamorphic rocks is important (where the magnetic susceptibility signals are high, and where many of the main heat producing minerals reside, compared to the much lower magnetic susceptibility signals of the sedimentary cover rocks). Applications for high resolution lithology discrimination, quantifying mineral content, and permeability prediction in turbidites, shales and oil sands have also been demonstrated [11, 12].

Applications of Temperature Dependent Paramagnetic Properties for Quantifying Mineral Content and Extending the Use of Paramagnetic Dopants for Laboratory or Borehole Analysis of NMR Data

Cody W. Good and David K. Potter*

Department of Physics, University of Alberta, Edmonton, Alberta, T6G 2E1, Canada

Abstract. Firstly, we extend previous work [1, 2] on the theoretical modelling of the temperature dependence of the magnetic susceptibility of paramagnetic minerals, and how this can be used to quantify paramagnetic mineral content from temperature dependent magnetic susceptibility measurements on core samples in the laboratory, or from borehole magnetic susceptibility data. We will further show the effects of porosity and fluid type within the pores on the results. Mass magnetic susceptibility is less dependent on porosity than volume magnetic susceptibility, and is potentially more useful for mineral quantification in the laboratory where the mass of core samples can easily be measured. Borehole sensors, however, measure volume magnetic susceptibility, since the mass of the formation rock is not measured (though it can be estimated from bulk density log data). Furthermore, we will show how low temperature measurements increase the paramagnetic signal, which is particularly useful for quantifying extremely small amounts of paramagnetic minerals in core samples in the laboratory. Secondly, recent work by Mitchell et al [3] showed how the addition of a paramagnetic dopant (in aqueous form) to the brine phase of a carbonate reservoir sample could be used to improve the separation of the brine from the oil NMR T₂ relaxation time peaks in the laboratory at room temperature. The effect was shown to be dependent upon the concentration of the dopant. Our present study shows how modelling the temperature dependent paramagnetic susceptibility of the dopant can potentially be used to predict how such a paramagnetic dopant would behave with depth in a borehole for in-situ applications. Since the paramagnetic susceptibility of the dopant decreases with increasing temperature, we show how the paramagnetic susceptibility signal could potentially be used as a proxy for “effective paramagnetic molar concentration” values of the dopant at different temperatures. This could potentially broaden the applicability of Mitchell et al’s [3] technique to a borehole setting. Also, since the dopant’s paramagnetic susceptibility signal increases with decreasing temperature (thus increasing its “effective paramagnetic molar concentration”), then laboratory NMR T₂ time measurements taken at temperatures slightly lower than room temperature could further improve the separation of the brine and oil peaks compared to Mitchell et al’s [3] room temperature measurements.

1 Introduction

One motivation for this study was to extend the theoretical modelling of the temperature dependence of magnetic susceptibility of samples that contain a paramagnetic mineral. This would produce theoretical curves of magnetic susceptibility with temperature that could subsequently be used to provide a means of quantifying the paramagnetic mineral content by comparing with laboratory heating or cooling magnetic susceptibility measurements, or by comparing with borehole magnetic susceptibility data. The magnetic susceptibility of paramagnetic minerals such as illite is temperature dependent (as described in the theory and methods **section 2** below), whereas the magnetic susceptibility of diamagnetic minerals such as quartz is independent of temperature. Some preliminary

modelling was previously undertaken [1, 2] but was restricted to mass magnetic susceptibility. Now we also show modelling for volume magnetic susceptibility, since this is measured by borehole magnetic susceptibility tools measure as the sensor does not take account of the mass of the formation rock (although the volume magnetic susceptibility values could potentially be converted to mass magnetic susceptibility using the bulk density log data). In the present study we also model the effects of low temperature, as well as porosity and pore fluid type on both the volume magnetic susceptibility and the mass magnetic susceptibility.

Increasing temperature causes the magnetic susceptibility of paramagnetic minerals to decrease. Thus temperature dependent magnetic susceptibility measurements in the laboratory can be used to provide a sensitive means of identifying the presence of

* Corresponding author: dkpotter@ualberta.ca

paramagnetic minerals. Theoretical curves of temperature dependent magnetic susceptibility for single minerals or mineral mixtures can be used to quantify the paramagnetic mineral content in relatively simple systems, even in rocks with a very low paramagnetic mineral content and a high diamagnetic mineral content. The mineral mixture curves can also simultaneously quantify the diamagnetic mineral content in relatively simple systems. A further beneficial consequence of the temperature dependence of paramagnetic minerals is that cooling a rock core sample increases the paramagnetic susceptibility signal, so that extremely small amounts of a paramagnetic mineral or minerals in a rock can be identified at low temperature even if they are not apparent from traditional room temperature measurements.

It is particularly important to take account of the temperature dependence of paramagnetic minerals in order to obtain reliable paramagnetic mineral content estimates from borehole magnetic susceptibility data, since temperature and thus magnetic susceptibility varies with depth. This potentially allows a means of estimating in-situ paramagnetic mineral content.

A second motivation for this study was influenced by a recent paper [3] which demonstrated how the addition of a paramagnetic dopant (manganese chloride, $MnCl_2$, in aqueous form) to the brine phase of a carbonate reservoir sample could be used to improve the separation between the brine and the oil NMR T2 peaks in the laboratory at room temperature. The effect was dependent upon the concentration of the dopant. Since the paramagnetic susceptibility of the manganese chloride dopant should decrease with increasing temperature, we will show how theoretical modelling of the temperature dependent paramagnetic susceptibility signal could be used as a proxy to produce curves of “effective paramagnetic molar concentration” of the dopant at different temperatures. This could potentially broaden the applicability of the technique described in [3] to an in-situ borehole setting where temperature varies with depth, as well as providing the theoretical background for the technique to be applied at different temperatures in the laboratory. The relationship between molar concentration and NMR T2 relaxation times of the paramagnetic dopant from [3] was then used to produce curves of NMR T2 times with temperature using our model “effective paramagnetic molar concentration” values. We will also show how the NMR T2 curves behave with depth by converting the temperature scale to depth using an appropriate geothermal gradient.

2 Theory and Methods

2.1 Modelling the dependence of magnetic susceptibility on temperature, porosity and pore fluid type

Magnetic susceptibility is usually expressed in terms of magnetic susceptibility per unit volume k as:

$$k = J/H \quad (1)$$

or in terms of magnetic susceptibility per unit mass χ as:

$$\chi = M/H = k/\rho \quad (2)$$

where J is the magnetization per unit volume, M is the magnetization per unit mass, H is the applied external magnetic field, and ρ is the density of the material.

The temperature dependence of magnetic susceptibility per unit volume or per unit mass for a paramagnetic mineral is given by the Curie equation:

$$k = C_v/T \text{ or } \chi = C_m/T \quad (3)$$

where C_v and C_m are the mineral specific Curie constants for volume magnetic susceptibility or mass magnetic susceptibility respectively, and T is the temperature in Kelvin. Knowing the volume magnetic susceptibility (VMS) or the mass magnetic susceptibility (MMS) at room temperature then **Equation (3)** allows us to construct curves of VMS or MMS with temperature. This can be done for a single paramagnetic mineral, or for a combination of paramagnetic minerals if one knows the proportions of the minerals, or for a mixture of paramagnetic and diamagnetic minerals (since the magnetic susceptibility of diamagnetic minerals is temperature independent). In the present study we will first model the temperature dependence of magnetic susceptibility for simple two component mixtures comprising of a paramagnetic mineral (illite clay) and a diamagnetic mineral (quartz). We chose this combination since these minerals are often the two key components in sandstones and shales. For volume magnetic susceptibility the total measured signal of this mineral mixture is given by [4]:

$$k_T = \{(F_I) (k_I)\} + \{(1-F_I) (k_Q)\} \quad (4)$$

where k_T is the total volume magnetic susceptibility of the mixture, F_I is the illite fraction per unit volume, $(1-F_I)$ is the quartz fraction per unit volume, and k_I and k_Q are the volume magnetic susceptibilities of illite (41×10^5 SI [5]) and quartz (-1.64×10^5 SI [6, 7]) respectively. In our models we vary the fractions of illite and quartz, and the value of k_I will be temperature dependent, but the value of k_Q will be temperature independent. Likewise there is a similar expression for mass magnetic susceptibility as follows [8]:

$$\chi_T = \{(F_I) (\chi_I)\} + \{(1-F_I) (\chi_Q)\} \quad (5)$$

where χ_T is the total mass magnetic susceptibility of the mixture, F_I is the illite fraction per unit volume, $(1-F_I)$ is the quartz fraction per unit volume, and χ_I and χ_Q are the mass magnetic susceptibilities of illite ($15 \times 10^8 \text{ m}^3 \text{ kg}^{-1}$ [5]) and quartz ($-0.62 \times 10^8 \text{ m}^3 \text{ kg}^{-1}$ [6, 7]), respectively. Again we can vary the fractions of illite and quartz, and the value of χ_I will be temperature dependent, but the value of χ_Q will be temperature independent.

We also modelled the effect of porosity simply by decreasing the total magnetic susceptibility in **Equations**

(4) and (5) by the chosen porosity fraction, and added an extra term for the fluid in the pore space. In our model examples to model different porosities we chose North Sea Forties field formation water to fully saturate (i.e., 100% saturation) the pore space. The mass magnetic susceptibility and volume magnetic susceptibility of the Forties field formation water is given in **Table 1** [6, 9].

Table 1. Magnetic susceptibility data for different Forties field (North Sea) reservoir fluids [6, 9].

Fluids	Mass magnetic susceptibility ($10^{-8} \text{ m}^3 \text{ kg}^{-1}$)	Volume magnetic susceptibility (10^{-6} SI)
Formation water	-0.8729	-9.121
Crude oil	-1.0206	-8.134
Crude oil desalted	-1.0072	-8.163
Gasoline stabilized	-1.0744	-7.018
Kerosine	-0.9764	-7.991
Light gas oil	-0.9987	-8.277
Vacuum gas oil	-0.9788	-8.437
Heavy gas oil	-0.9861	-8.535

We also modelled the effects of other fluid types (all from the Forties field) in the pore space. Again we decreased the total magnetic susceptibility in **Equations (4) and (5)** by the chosen porosity fraction, and added an extra term for the fluid in the pore space. The magnetic susceptibility values for the different fluids modelled are given in **Table 1** and are based on previously published data [6, 9]. The mass magnetic susceptibility values of these fluids are the volume magnetic susceptibility divided by the density (**Equation (2)**). The density values are given in **Table 2** [6].

Table 2. Density data for different Forties field (North Sea) reservoir fluids [6].

Fluids	Density (kg m^{-3})
Formation water	1044.9
Crude oil	797.0
Crude oil desalted	810.4
Gasoline stabilized	653.2
Kerosine	818.4
Light gas oil	828.7
Vacuum gas oil	862.0
Heavy gas oil	865.5

2.2 Modelling the temperature dependent magnetic susceptibility of a paramagnetic dopant MnCl_2

In the study of reference [3] different molar concentrations of MnCl_2 were added to the brine phase in a carbonate sample to act as a paramagnetic dopant in order to separate out the NMR T2 relaxation time brine and oil peaks. Their study, however, was restricted to

laboratory NMR measurements at room temperature. Since the dopant is paramagnetic then temperature dependent magnetic susceptibility modelling of concentrations of MnCl_2 similar to those described in **section 2.1** potentially allows the technique from [3] to be used more extensively as follows:

1. In a borehole setting where temperature changes with depth.
2. In laboratory heating and cooling experiments.

Therefore we firstly modelled the temperature dependent magnetic susceptibility of similar molar concentrations of MnCl_2 to those of [3] using **Equation (3)**. We then used the modelled magnetic susceptibility curves as a proxy to produce curves of “effective paramagnetic molar concentration” with temperature by normalising the magnetic susceptibility values to the value at room temperature (20°C) for the 1 M curve. Thus the “effective paramagnetic molar concentration” at 20°C for the 1 M curve was taken to be 1M, and all values at higher temperatures than 20°C on this curve will have a lower “effective paramagnetic molar concentration” and conversely all values at lower temperatures than 20°C on this curve will have a higher “effective paramagnetic molar concentration.” Curves with lower initial molar concentrations at room temperature will act in a similar way, but have lower overall values.

We then converted the “effective paramagnetic molar concentration” scale to an NMR T2 relaxation time using data from reference [3]. **Figure 1** shows the NMR T2 peaks for the brine phase with the added MnCl_2 dopant, compared to the peaks for the oil phase, for a carbonate saturated sample [3]. We have highlighted the MnCl_2 doped brine peaks with red arrows. The four different peaks result from four different molar concentrations of MnCl_2 as indicated. The peaks with the longer T2 times (without the red arrows) are all due to the oil phase. For the four MnCl_2 doped brine peaks we plotted the MnCl_2 molar concentrations against NMR T2 time (**Figure 2**) and obtained a power law relationship as follows:

$$y = 0.0746 x^{-1.513} \quad (6)$$

where y corresponds to molar concentration and x corresponds to NMR T2 relaxation time. Solving for x as follows:

$$x = \frac{0.0746^{\frac{1}{1.513}}}{y^{\frac{1}{1.513}}} \quad (7)$$

allows one to calculate NMR T2 relaxation times from our values of “effective paramagnetic molar concentration” which were derived from the temperature dependent magnetic susceptibility data. This allowed us to then produce curves of NMR T2 time against temperature, which can also be converted into NMR T2 time with depth for borehole applications by using an appropriate geothermal gradient or from direct temperature log measurements.

3 Results and discussion

3.1 Modelling the temperature dependence of paramagnetic susceptibility: an example with a two component mineral mixture

We first present the temperature dependence of two component mineral mixtures comprising quartz (a diamagnetic mineral) and illite (a paramagnetic mineral). We chose this example as it is a simple approximation to some sandstones and shales, depending upon the relative contents of each mineral. The illite has a temperature dependent magnetic susceptibility given by the Curie equation (**Equation (3)**), whereas the magnetic susceptibility of the quartz is temperature independent. **Figure 3** shows the variation of volume magnetic susceptibility (VMS) with low temperature for various illite contents (ranging between 1-10%), and so it is mainly applicable for clean to muddy sandstones. The curves show how the magnetic susceptibility increases with decreasing temperature, and thus the potential of cooling experiments in the laboratory for identifying small concentrations of illite that may not be apparent from traditional room temperature measurements.

Figure 4 shows the variation of VMS with higher temperatures for the same illite contents as **Figure 3**. Both **Figures 3** and **4** can be used to quantify the illite and quartz contents (by comparing the theoretical curves from these figures with experimental temperature dependent VMS measurements), if these two minerals are known to be the two main minerals in the rock sample (e.g., from thin section analysis, or X-ray diffraction etc.). **Figure 4**, and similar types of theoretical curves for other paramagnetic minerals and mixtures, is potentially useful for correctly quantifying mineral content from borehole magnetic susceptibility measurements where temperature generally increases with depth. A borehole temperature profile is often measured, or can be generated at each depth if one knows the local geothermal gradient.

We previously undertook similar modelling for mass magnetic susceptibility (MMS) for an identical two component system [1, 2]. However, VMS is more relevant for borehole measurements as we mentioned earlier. We have also modelled the VMS and MMS curves with temperature for higher concentrations illite, but have not shown those due to space limitations in the present paper.

3.2 Modelling the effects of porosity and pore fluid type on temperature dependent magnetic susceptibility: examples for shale and muddy sand

Figure 5 shows the effect of different porosities (ranging from 0-40% porosity) on the volume magnetic susceptibility over a temperature range of 20°C to just under 450°C for model shale and muddy sandstone samples. The shale samples have an illite to quartz ratio of 4:1, whilst for the muddy sandstone samples the ratio is 1:10. The higher porosity values for the simulated "shale" samples we recognize are unrealistic (as shale

samples normally have lower porosities), but we included them merely for modelling purposes to compare with similar porosities for the muddy sandstone. All the model samples are assumed to be 100% saturated with Forties field formation water, whose volume magnetic susceptibility is given in **Table 1**. **Figure 5** clearly shows that as the porosity increases the volume magnetic susceptibility decreases.

Figure 6 shows the effects of different Forties field fluids (7 hydrocarbons and 1 formation water, whose magnetic susceptibility values are given in **Table 1**) on the volume magnetic susceptibility over the same temperature range as for **Figure 5** for a simulated sample with an illite to quartz ratio of 4:1 and a porosity of 40%. We used a high porosity value in order to enhance the effects of the different fluids. However, **Figure 6** shows that the different fluids have almost the same effect on the results, with only slight differences between them. Lower values of porosity exhibited even smaller differences between the fluids.

Figures 7 and **8** show similar plots for the effects of porosity and pore fluid porosity on identical model samples to **Figures 5** and **6**, but this time for mass magnetic susceptibility. **Figure 7** shows that the effect of porosity on the mass magnetic susceptibility appears to be slightly less within each sample type (shale or muddy sandstone) compared to the volume magnetic susceptibility. This might be expected and can be explained simply because volume magnetic susceptibility will decrease with increasing porosity for the samples considered, whilst for mass magnetic susceptibility the masses (and densities) of the samples are also decreasing with increasing porosity, which has the effect of causing less of a variation in the mass magnetic susceptibility values for a particular sample type (since the parameters k and ρ are both decreasing in **Equation (2)** and so the ratio is less affected).

Figure 8 shows the effects of the different Forties field fluids on the mass magnetic susceptibility over the same temperature range as the equivalent plot for volume magnetic susceptibility (**Figure 6**). In this case there is slightly more separation between the different fluid curves compared to **Figure 6** for the volume magnetic susceptibility case. This is largely due to the different densities of the fluids (**Table 2**), which affect the mass magnetic susceptibility (**Equation (2)**).

3.3 Modelling the temperature dependent behaviour of a paramagnetic dopant: extending its use for borehole applications and laboratory heating or cooling experiments

Figure 9 shows the modelled temperature dependence of magnetic susceptibility for different molar concentrations of manganese chloride (MnCl_2) in aqueous solutions, using the methodology described in **section 2.2**. We used the same molar concentrations that were used in Mitchell et al's [3] study, where MnCl_2 was used as a paramagnetic dopant added to the brine phase. The magnetic susceptibility of a 1 molar (1M) solution of MnCl_2 was taken to be $14350 \times 10^{-6} \text{ cm}^3 \text{ mol}^{-1}$ at a

room temperature of 20°C [10]. The variations in the magnetic susceptibility with temperature can potentially be used as a proxy for an “effective paramagnetic molar concentration” of the MnCl₂ with temperature. **Figure 10** shows a plot of this “effective paramagnetic molar concentration” with temperature, which is derived by normalising the molar magnetic susceptibility values in **Figure 9** to the value at room temperature (20°C) for the 1 M curve. This means that in **Figure 10** the “effective paramagnetic concentration” at 20°C for the 1 M curve is 1M (as detailed in **section 2.2**).

Since Mitchell et al [3] reported values of the NMR T2 relaxation time for the four different molar concentrations of MnCl₂ (see **Figure 1**) we identified a power law relationship between molar concentration of MnCl₂ and NMR T2 relaxation time of the doped brine (see **Figure 2**), as detailed in **section 2.2**. This subsequently allowed us to associate each of our “effective paramagnetic molar concentrations” from **Figure 10** with corresponding NMR T2 values, using **Equations (6) and (7)** as described in **section 2.2**. This then enabled us to produce plots of NMR T2 versus temperature (**Figure 11**) for the four initial molar concentrations of MnCl₂ at room temperature (i.e., 0.005 M, 0.04 M, 0.3 M and 1 M at 20°C). The results show that as the temperature increases the NMR T2 time increases for each molar concentration. This data can be used to quantify how the NMR T2 time for the MnCl₂ doped brine should vary with depth in a borehole setting where temperature is generally increasing with increasing depth.

In order to provide an example of a relevant depth plot we used an appropriate geothermal gradient from the Middle East, since this was where Mitchell et al’s [3] carbonate samples came from that were saturated with brine containing the different MnCl₂ concentrations. We used a geothermal gradient of 35°C/km [11] to convert temperature to depth and produced plots of NMR T2 time with depth (**Figure 12**) for the four initial molar concentrations of MnCl₂ at room temperature (i.e., 0.005 M, 0.04 M, 0.3 M and 1 M at 20°C). **Figure 12** illustrates that as the depth increases the NMR T2 time for the MnCl₂ doped brine increases.

Figures 11 and 12 demonstrate the potential of the technique proposed by Mitchell et al [3] to now also be applied to a borehole setting. One implication of **Figures 11 and 12** is that as temperature and depth increase, then the separation of the NMR T2 peaks between the MnCl₂ doped brine and the oil will become less. Another interesting implication of **Figure 11** is that cooling the MnCl₂ dopant below room temperature will decrease the NMR T2 time, and thus increase the separation between the NMR T2 peaks of the MnCl₂ doped brine and the oil. Thus, in a laboratory setting, cooling the sample saturated with the MnCl₂ doped brine and oil (even by just a few degrees below room temperature) will potentially provide an even better separation of the NMR T2 peaks, providing a further improvement over the results obtained by Mitchell et al [3], which were taken at room temperature.

4 Conclusions

The following overall conclusions can be drawn:

1. Model template curves were constructed of the temperature dependence of volume magnetic susceptibility for different mixtures of a paramagnetic and a diamagnetic mineral. The curves allow the paramagnetic and diamagnetic mineral contents to be quantified by directly comparing them with experimental laboratory or borehole volume magnetic susceptibility measurements. The “high” temperature template curves (**Figure 4**) are potentially useful both for laboratory heating experiments, and borehole magnetic susceptibility measurements where temperature usually increases with increasing depth. The “low” temperature template curves (**Figure 3**) are especially useful for laboratory cooling experiments where the increased paramagnetic signal allows small concentrations of paramagnetic minerals to be identified that may otherwise be missed from traditional room temperature measurements. (We previously [1] showed some comparisons between our initial template curves for mass magnetic susceptibility and experimental laboratory measurements for some shoreface and turbidite samples for the high temperature case).
2. The effect of porosity on the temperature dependent magnetic susceptibility curves for different paramagnetic + diamagnetic mixtures showed that increased porosity caused the magnetic susceptibility to decrease in the modelled samples, since the amount of the paramagnetic mineral (which has a positive magnetic susceptibility) is decreased. Porosity appears to have less of an effect on the mass magnetic susceptibility compared to the volume magnetic susceptibility, mainly because the mass and density also decrease with increasing porosity. The mass magnetic susceptibility is the volume magnetic susceptibility divided by the density (k/ρ), and so if both k and ρ are decreasing the ratio (the mass magnetic susceptibility) may be less affected compared to k (the volume magnetic susceptibility) alone.
3. Different pore fluids were shown to have little effect on the volume magnetic susceptibility, and some slight (though minor) effect on the mass magnetic susceptibility. The reason for the latter is mainly due to the different densities of the fluids, which affect the mass magnetic susceptibility.
4. Modelling the temperature dependence of a paramagnetic dopant (MnCl₂ in the aqueous phase) allows one to construct plots of “effective paramagnetic molar concentration” with temperature. Using previous data from Mitchell et al [3] that related the MnCl₂ doped brine concentration to NMR T2 relaxation time, we could construct plots of NMR T2 time versus temperature for the MnCl₂ dopant from our “effective paramagnetic

molar concentration” versus temperature curves. Using an appropriate geothermal gradient, we could also produce typical plots of NMR T2 time with depth for the MnCl₂ doped brine phase. The modelled results potentially increase the application of Mitchell et al’s [3] technique (which used the dopant in the brine in order to separate out the brine NMR T2 peak from the oil NMR T2 peak, but only at room temperature in the laboratory) to an in-situ borehole setting where the temperature varies with depth. One consequence of the modelling for borehole applications is that as temperature and depth increase the separation of the NMR T2 times between the MnCl₂ doped brine and the oil signal will become less.

5. A further implication of the MnCl₂ dopant modelling is that cooling the sample with the MnCl₂ dopant (even by just a few degrees below room temperature) will decrease the NMR T2 time of the doped brine, which would potentially provide an even greater separation between the MnCl₂ doped brine and oil NMR T2 times, thus further improving the results obtained by Mitchell et al [3] that were undertaken at room temperature.

D. K. P. thanks the Natural Sciences and Engineering Research Council of Canada (NSERC) for a Discovery Grant. Eric Withjack and Holger Ott are thanked for their constructive review comments, which helped improve the manuscript.

5 List of abbreviations

MMS	Mass Magnetic Susceptibility
NMR	Nuclear Magnetic Resonance
T2	NMR T2 transverse relaxation time
VMS	Volume Magnetic Susceptibility

6 References

1. A. Ali and D. K. Potter. Model templates for quantifying permeability controlling paramagnetic clay minerals at in situ reservoir temperatures. *Proceedings of the 2011 International Symposium of the Society of Core Analysts, 18-21 September 2011*, Austin, Texas, USA. Paper SCA2011-047 (2011)
2. A. Ali and D. K. Potter. Temperature dependence of the magnetic properties of reservoir rocks and minerals and implications for in situ borehole predictions of petrophysical parameters. *Geophysics*, **77** (no.3), 211-221 (2012)
3. P. Mitchell, L. Gromala and M. Siddiqui. The use of paramagnetic dopants in optimizing the accuracy of critical and residual oil saturation determination. *Proceedings of the 2017 International Symposium of the Society of Core Analysts, 27 August – 1 September 2017*, Vienna, Austria. Paper SCA2017-063 (2017)
4. T. H. To and D. K. Potter. Comparison of high resolution probe magnetics, X-ray fluorescence and permeability on core with borehole spectral gamma ray and spontaneous potential in an oil sand well. *Proceedings of the 2021 International Symposium of the Society of Core Analysts*, (Online 13-16 September 2021), Paper SCA2021-035 (2021)
5. C. P. Hunt, B. M. Moskowitz and S. K. Banerjee. Magnetic properties of rocks and minerals. In: *Rock Physics and Phase Relations: A Handbook of Physical Constants*, T. J. Ahrens (Ed.). American Geophysical Union Reference Shelf 3, 189-204 (1995)
6. O. P. Ivakhnenko. Magnetic analysis of petroleum reservoir fluids, matrix mineral assemblages and fluid-rock interactions. PhD thesis, Heriot-Watt University, Institute of Petroleum Engineering, Edinburgh, UK, pp. 210 (2006)
7. D. K. Potter, T. M. AlGhamdi, and O. P. Ivakhnenko. Sensitive carbonate reservoir rock characterization from magnetic hysteresis curves and correlation with petrophysical properties. *Petrophysics*, **52** (issue 1), 50-57 (2011)
8. D. K. Potter. Magnetic susceptibility as a rapid, non-destructive technique for improved petrophysical parameter prediction. *Petrophysics*, **48** issue 3), 191-201 (2007)
9. O. P. Ivakhnenko and D. K. Potter. Magnetic susceptibility of petroleum reservoir fluids. *Physics and Chemistry of the Earth*, **29**, 899-907 (2004)
10. J. R. Rumble, ed. *CRC Handbook of Chemistry and Physics*, 102nd Edition (Internet Version 2021), CRCPress/Taylor and Francis, Boca Raton, FL (2021)
https://hbcpc.chemnetbase.com/faces/documents/04_08/04_08_0001.xhtml
11. Swart, P.K., Cantrell, D.L., Arienzo, M.M. and Murray, S.T. Evidence for high temperature and ¹⁸O-enriched fluids in the Arab-D of the Ghawar Field, Saudi Arabia. *Sedimentology*, **63**, 1739-1752 (2016)

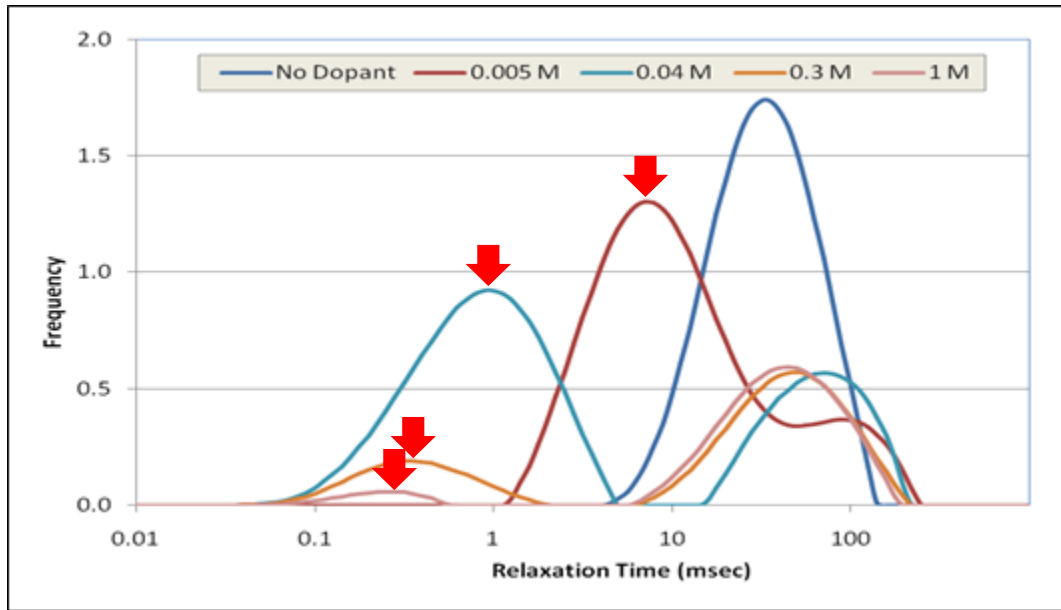


Fig. 1. Separation of brine and oil NMR T₂ relaxation time peaks in a carbonate sample for different molar concentrations of paramagnetic MnCl₂ dopant added to the brine phase. The vertical “Frequency” axis is in arbitrary units. The red arrows indicate the peaks for the brine + MnCl₂ dopant and are the shorter relaxation times. The peaks for the oil phase are the ones with the longer relaxation times, without the red arrows. (Modified from Mitchell et al [3]).

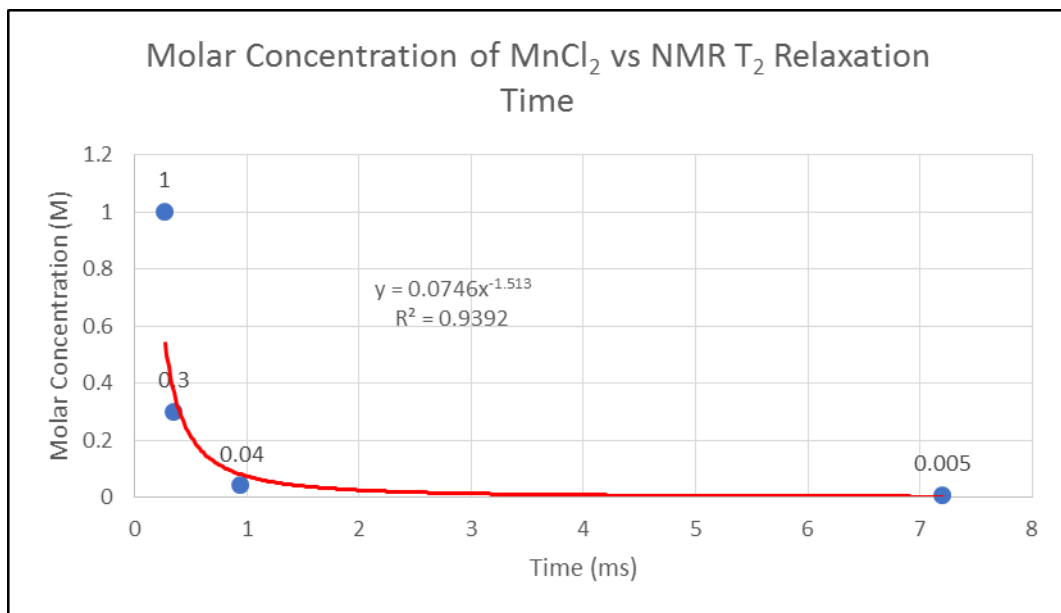


Fig. 2. Plot of the molar concentration of paramagnetic MnCl₂ dopant versus NMR T₂ relaxation time of the doped brine derived from **Figure 1**. The red regression line shows a power law fit to the data with a coefficient of determination of $R^2 = 0.94$. The regression equation shown (see also **section 2.2** of the text) was used in conjunction with the “effective paramagnetic molar concentration” of **Figure 10** to produce the NMR T₂ relaxation times for the doped brine shown in **Figures 11** and **12**.

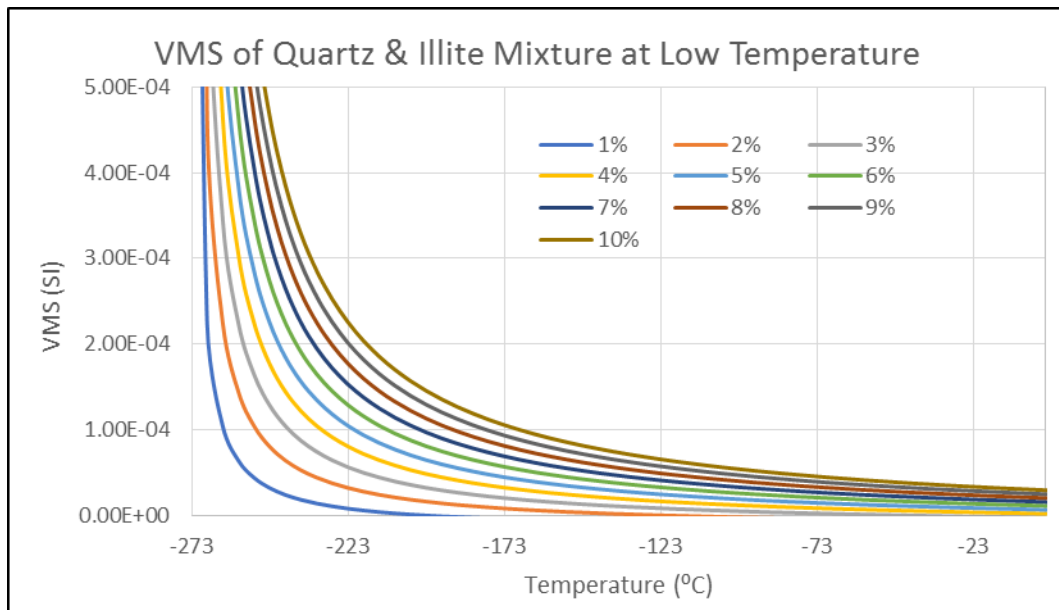


Fig. 3. Model template curves showing the dependence of volume magnetic susceptibility (VMS) on temperature for low temperature conditions for varying mixtures of illite ranging from 1-10% (shown in the legend) + quartz ranging, respectively, from 99-90% (so the total percentage of the two minerals is 100% for each curve). Illite is paramagnetic and so its VMS is temperature dependent in accordance with the Curie equation (**Equation (3)** in **section 2.1**), whereas quartz is diamagnetic and its VMS is temperature independent. Note that these curves do not include porosity (i.e., porosity = 0%), but **Figures 5** and **7** show VMS and MMS (mass magnetic susceptibility) results for different porosities. The curves in **Figure 3** are potentially useful for identifying and quantifying small amounts of illite (and similar curves can be produced for other paramagnetic minerals) by comparing with laboratory low temperature dependent VMS measurements. The increased VMS signal at low temperatures could be particularly useful for identifying minute amounts of illite that may not be evident from traditional room temperature measurements.

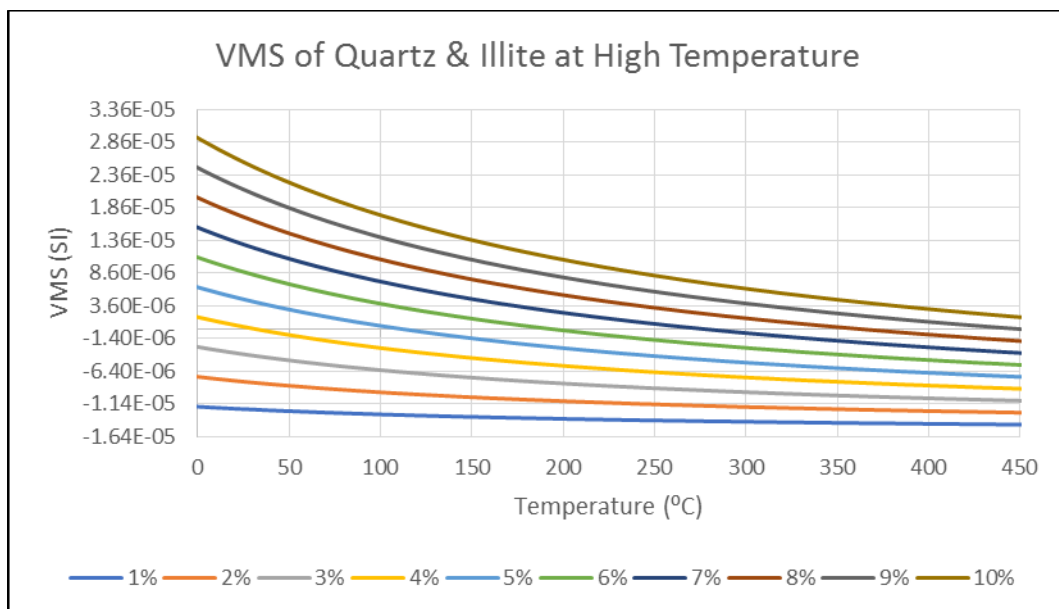


Fig. 4. Model template curves showing the dependence of volume magnetic susceptibility (VMS) on temperature for high temperature conditions for varying mixtures of illite ranging from 1-10% (shown in the legend) + quartz ranging, respectively, from 99-90%. These curves are potentially useful for quantifying the mineral contents in samples with similar mineral components by comparing with laboratory temperature dependent VMS measurements, or with borehole VMS data. These curves do not include porosity (i.e., porosity = 0%), but **Figures 5** and **7** show VMS and MMS (mass magnetic susceptibility) results for different porosities.

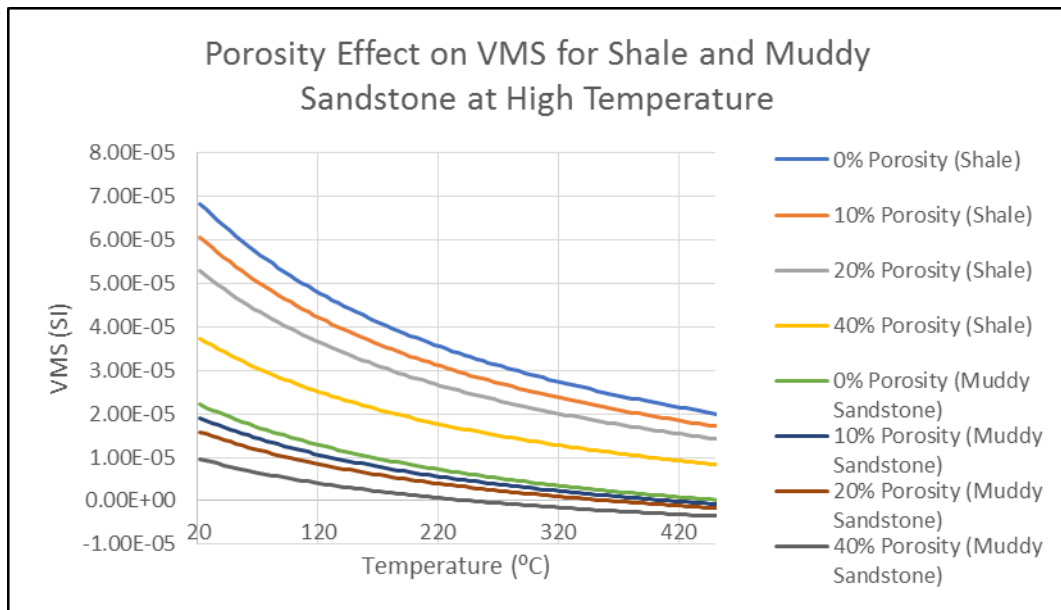


Fig. 5. Model curves of volume magnetic susceptibility (VMS) versus temperature (high temperature range) for varying porosity values in simulated shale and muddy sandstone samples 100% saturated with Forties Field formation water (see **Table 1**). An illite to quartz ratio of 4:1 was used for the simulated shale samples, whilst an illite to quartz ratio of 1:10 was used for the simulated muddy sandstone samples.

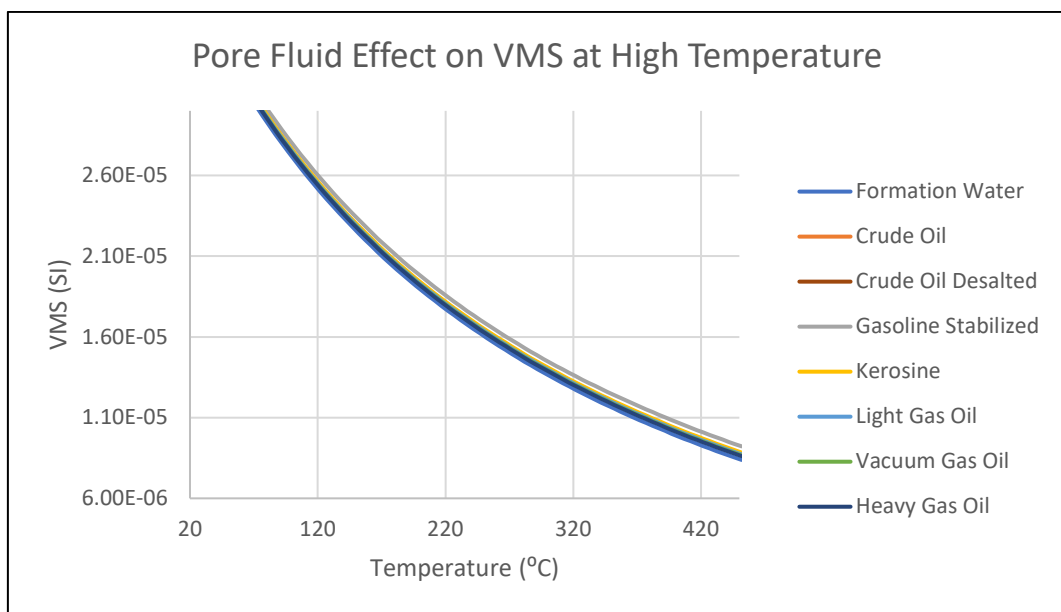


Fig. 6. Model curves of volume magnetic susceptibility (VMS) versus temperature (high temperature range) for a simulated shale composition (illite to quartz ratio of 4:1) 100% saturated with different Forties Field reservoir fluids in the pore space (see **Table 1**). The porosity was taken to be 40% in this example. We recognize this is unrealistic for a shale, but we used a high porosity value in order to enhance the effects of the different fluids. Lower values of porosity exhibited even smaller differences between the fluids.

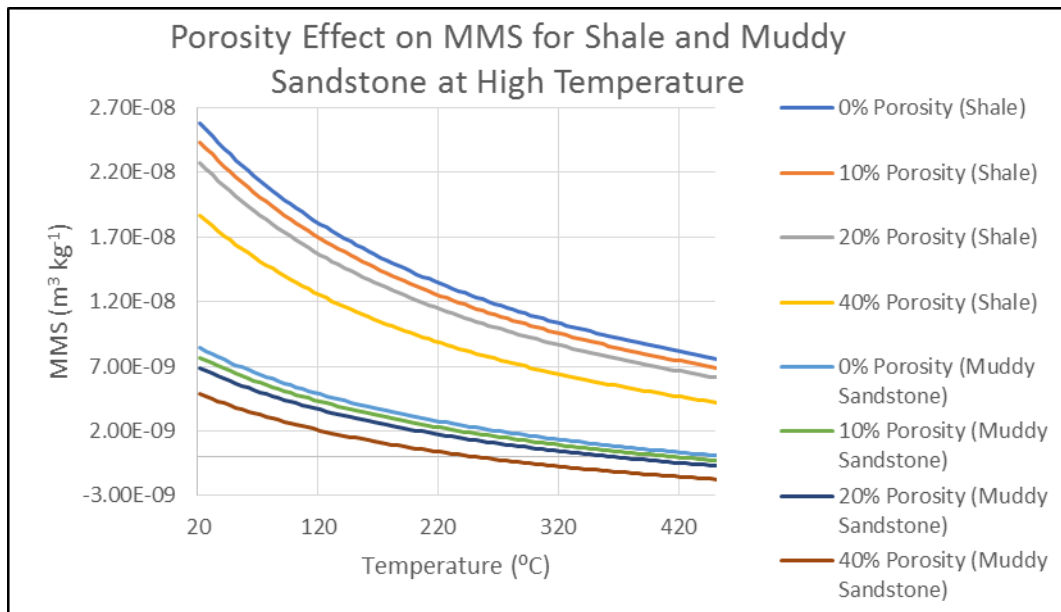


Fig. 7. Model curves of mass magnetic susceptibility (MMS) versus temperature (high temperature range) for varying porosity values in simulated shale and muddy sandstone samples 100% saturated with Forties Field formation water (see **Table 1**). An illite to quartz ratio of 4:1 was used for the simulated shale samples, whilst an illite to quartz ratio of 1:10 was used for the simulated muddy sandstone samples.

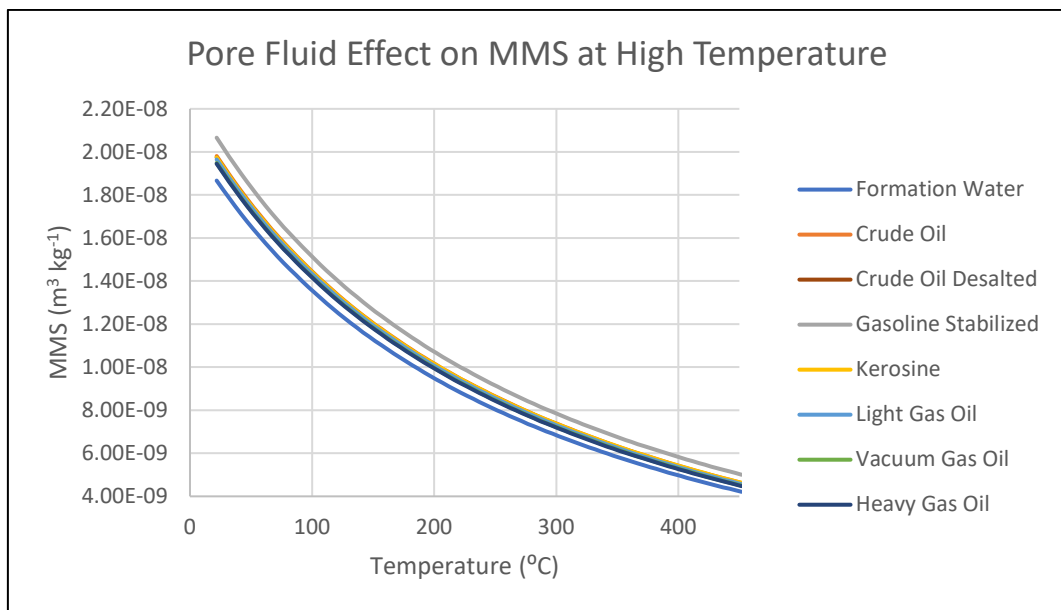


Fig. 8. Model curves of volume magnetic susceptibility (VMS) versus temperature (high temperature range) for a simulated shale composition (illite to quartz ratio of 4:1) 100% saturated with different Forties Field reservoir fluids in the pore space (see **Table 1**). The porosity was taken to be 40% in this example. Again we recognize this is unrealistic for a shale, but we used a high porosity value in order to enhance the effects of the different fluids. The slightly greater separation of the curves compared to the VMS results of **Figure 6** are mainly due to differences in density (see **Table 2**) since mass magnetic susceptibility is the volume magnetic susceptibility divided by the density.

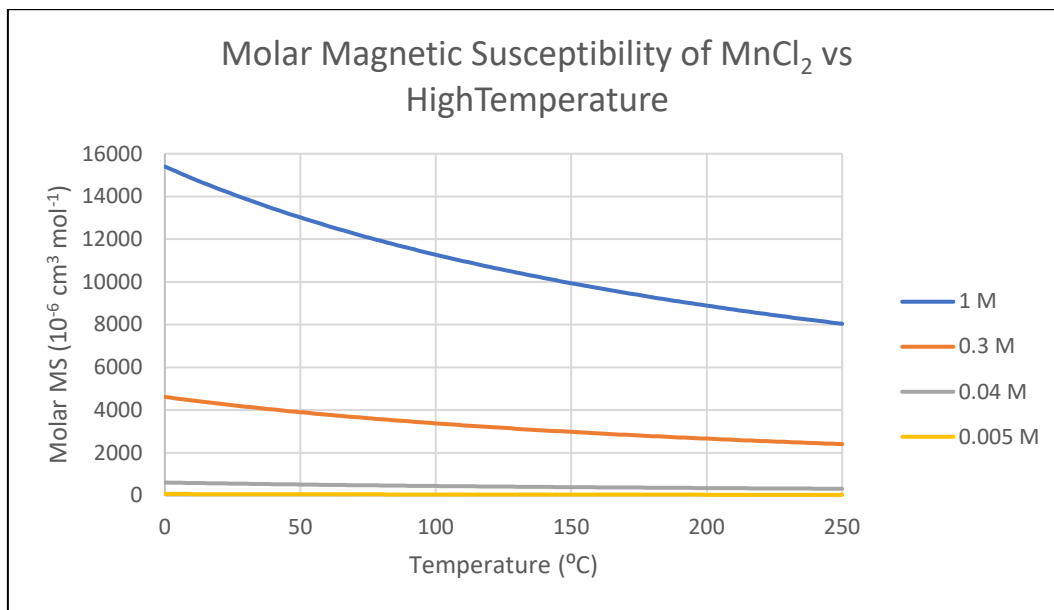


Fig. 9. Model curves of molar magnetic susceptibility calculated for the different initial molar concentrations of the paramagnetic dopant MnCl_2 used by [3] (1 M, 0.3 M, 0.04 M and 0.005 M at room temperature of 20°C) versus temperature for the high temperature range. For the modelling we used a molar magnetic susceptibility value of $14350 \times 10^{-6} \text{ cm}^3 \text{ mol}^{-1}$ at a room temperature of 20°C [10] for a 1 molar (1M) solution of MnCl_2 .

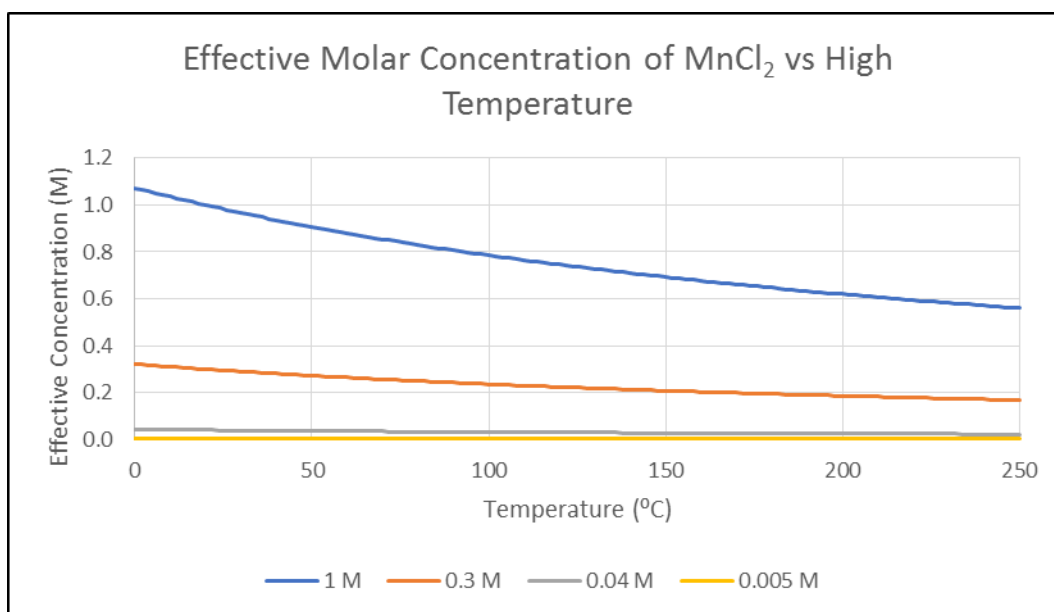


Fig. 10. Model curves of the effective paramagnetic molar concentrations of MnCl_2 versus temperature for the high temperature range. The effective paramagnetic molar concentration values were derived by normalising the molar magnetic susceptibility values in **Figure 9** to the value at room temperature (20°C) for the 1 M curve (i.e., the effective paramagnetic molar concentration at 20°C for the 1 M curve is 1M).

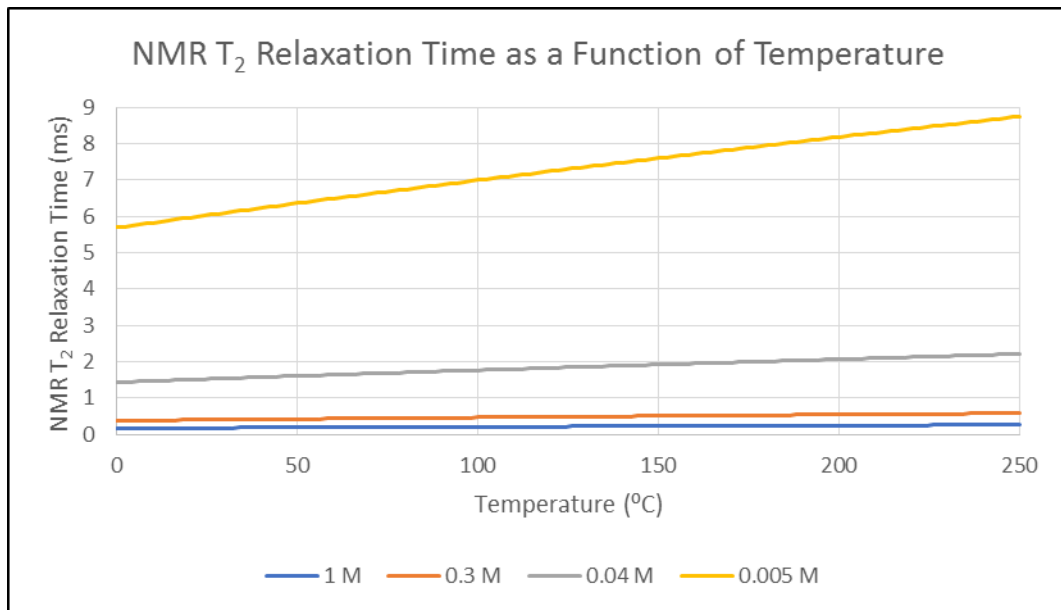


Fig. 11. Model NMR T₂ relaxation times of the doped brine for the different initial molar concentrations of the paramagnetic dopant MnCl₂ (1 M, 0.3 M, 0.04 M and 0.005 M at a room temperature of 20°C) versus temperature for the high temperature range. The NMR T₂ times were derived from the relationship between the molar concentrations and NMR T₂ times for the doped brine shown in **Figure 2** (the relationship is also shown in **Equations (6)** and **(7)**) using the effective paramagnetic molar concentrations from **Figure 9**.

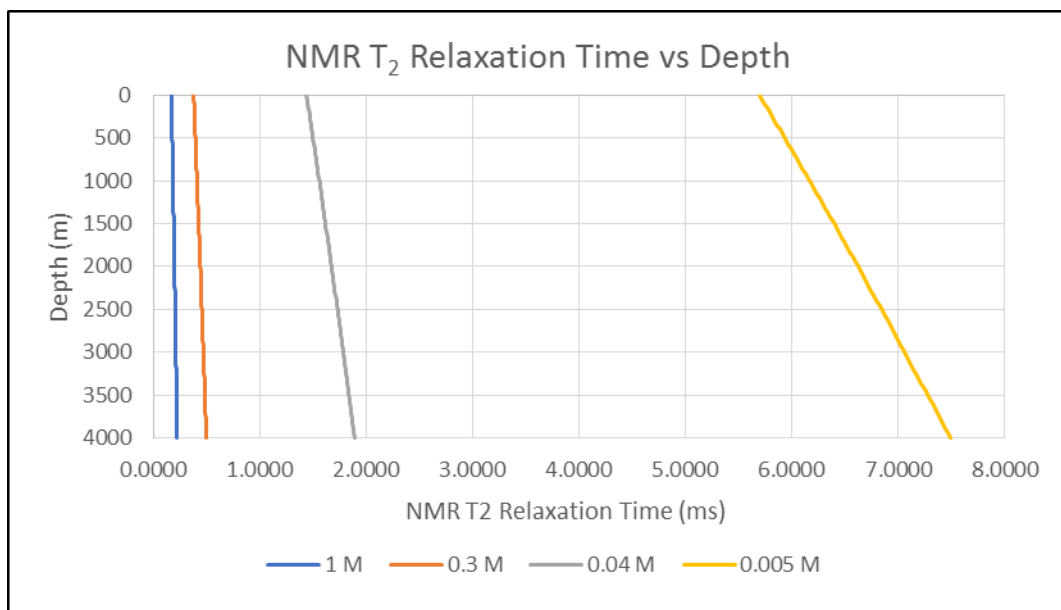


Fig. 12. Model NMR T₂ relaxation times of the doped brine for the different initial molar concentrations of the paramagnetic dopant MnCl₂ (1 M, 0.3 M, 0.04 M and 0.005 M at a room temperature of 20°C) versus depth. The depth scale was derived from the temperature scale of **Figure 11** using a geothermal gradient of 35°C/km [11], which is relevant to the Middle East (specifically Saudi Arabia) where the carbonate samples in Mitchell et al's [3] study originated.

Modification of the SDR equation for permeability prediction

Andreas Weller^{1,*}, and Zeyu Zhang¹

¹Technische Universität Clausthal, Institut für Geophysik, 38678 Clausthal-Zellerfeld, Germany

Abstract. We evaluate the potential of permeability prediction of the original and modified versions of the Schlumberger-Doll Research (SDR) equation that is applied to data of nuclear magnetic resonance (NMR) relaxometry. Different definitions of characteristic relaxation time are considered. In a further modification, pore radius replaces the characteristic relaxation time in the original SDR equation. Only a good estimate of the surface relaxivity enables a reliable transformation from the relaxation time distribution (RTD) into the pore radius distribution (PRD). A recently published approach considers the specific surface area per unit pore volume (S_{por}) and the weighted harmonic mean ($T_{2\text{hm}}$) of the RTD for the determination of an individual value of surface relaxivity for each sample. The evaluation is performed for three sample sets originating from different sandstone formations. The good predictive quality of the original SDR equation is confirmed. However, the prefactors have to be adjusted by calibrating with core data. We demonstrate that the use of average pore radii instead of average relaxation times enables a better permeability prediction. The weighted harmonic mean of the PRD, which proves to be a reliable proxy for the effective hydraulic radius, provides a high quality permeability prediction.

1 Introduction

Permeability prediction for reservoir rocks is still a challenge in geophysical exploration. Porosity and pore radius are the most relevant parameters used in models of permeability prediction. A variety of petrophysical experiments or logging tools provide reliable porosity values. The effective hydraulic radius r_{eff} controls the fluid flow through porous rocks with a certain pore radius distribution (PRD).

Nuclear magnetic resonance (NMR) relaxometry provides an estimate of porosity and a relaxation time distribution (RTD). The maximum or mean values of the RTD are regarded as proxies for the effective hydraulic radius. The original Schlumberger-Doll Research (SDR) equation relates the weighted geometric mean of the transverse relaxation time and porosity to permeability. In the common form of SDR equation, the relaxation time is raised to the 2nd power and porosity to the 4th power.

Using NMR data of samples originating from three sandstone formations, we investigate the relationships between different characteristic relaxation times and r_{eff} . In a further step, we evaluate the predictive quality of the original and modified SDR equations.

The transformation of characteristic relaxation times into characteristic pore radii requires the knowledge of the surface relaxivity [1]. Using the procedure of [2], we determine an individual value of surface relaxivity for each sample. We investigate whether the different characteristic pore radii can be used as suitable proxies for r_{eff} . In a further modification of the SDR equation, we replace the characteristic relaxation time by a characteristic pore radius. We demonstrate that this substantial modification enables an improvement of permeability prediction.

2 Theory

Numerous theoretical approaches for permeability estimation of porous rocks have been presented. They link parameters of pore space geometry to permeability. A simple model, which considers the fluid flow through capillary bundles with uniform pore radius, relates permeability to the pore radius r and the resistivity formation factor F (e.g., [3, 4]):

$$k = r^2 / (8F). \quad (1)$$

Using the first Archie equation [5], which describes the relationship between F and porosity ϕ :

$$F = \frac{1}{\phi^m}, \quad (2)$$

where m is the cementation exponent, we get a permeability prediction model that considers the two parameters pore radius r and porosity ϕ :

$$k = \frac{1}{8} \phi^m r^2. \quad (3)$$

The porosity exponent m proves to be variable. For straight and parallel capillaries, an exponent $m = 1$ should be selected, whereas $m = 2$ is a good choice for consolidated sandstones. Larger exponents m are found especially for vuggy reservoir rocks (e.g., [6, 7]). Considering the physical dimensions of k (in m^2) and r (in m), the exponent of r seems to be fixed at two. A more general form of equation 3 reads

$$k = a \phi^b r^2, \quad (4)$$

with two adjustable parameters: the prefactor a and the porosity exponent b . Equation 4 suggests that the quality of permeability prediction depends on reliable values of porosity

* Corresponding author: andreas.weller@tu-clausthal.de

and pore radius. There are several procedures applicable in the laboratory or in well logging that provide good estimates of porosity. Considering the wide variation of pore radii in porous rocks, the determination of the relevant characteristic pore radius is challenging.

The application of equation 4 requires a good proxy for the pore radius r . Regarding equation 1, the effective hydraulic radius

$$r_{eff} = \sqrt{8Fk} \quad (5)$$

can be determined for rock samples with known values of F and k . In this study, we use the effective hydraulic radius concept [8] to evaluate the predictive quality of proxies of the pore radius in equation 4.

The NMR method records the decay of magnetization after an excitation impulse has changed the magnetic orientation of the hydrogen nuclei. The measured transverse decay curve is transformed in a discrete distribution of relaxation times $b_i(T_{2i})$, where the index i is the sequential number of the predefined relaxation time T_2 , and b_i is the resulting normalized amplitude. The normalization considers that the sum of all individual b_i equals one [2].

The Schlumberger-Doll Research (SDR) equation for permeability prediction from NMR relaxometry reads (e.g., [9]):

$$k^* = a_1 \phi^4 \bar{T}_2^{-2}, \quad (6)$$

where k^* is the predicted permeability and \bar{T}_2 a characteristic relaxation time that is determined from the transverse relaxation time distribution. The empirical coefficient a_1 is adjusted for lithology by calibrating with core data. Equation 6 corresponds to the general form of equation 4 with the porosity exponent $b = 4$. The characteristic relaxation time \bar{T}_2 is used as a proxy for the pore radius. Different characteristic values are determined from the relaxation time distribution $b_i(T_{2i})$. The original form of the SDR equation applies the weighted geometric mean as a characteristic relaxation time:

$$T_{2lm} = \exp(\sum_{i=1}^n b_i \ln T_{2i}). \quad (7)$$

Since the geometric mean uses a weighting of the logarithms of T_2 , several authors use the name log-mean (e.g., [9]). We adopt this term and use the standard subscript lm for this weighted mean value. Other characteristic values are the weighted harmonic mean T_{2hm} that is calculated by

$$T_{2hm} = \frac{1}{\sum_{i=1}^n \frac{b_i}{T_{2i}}}, \quad (8)$$

or the weighted arithmetic mean

$$T_{2am} = \sum_{i=1}^n b_i T_{2i}. \quad (9)$$

T_{2peak} is another characteristic relaxation time \bar{T}_2 that corresponds to the maximum of the relaxation time distribution.

We evaluate the relationships between different characteristic relaxation times \bar{T}_2 and r_{eff} for selected sample sets in order to identify the most suitable characteristic relaxation time. The prefactors a_1 in equation 6 are adjusted for the individual sample sets.

It has been shown in a variety of studies (e.g., [9, 10]) that a linear relationship between a characteristic pore radius \bar{r} and characteristic relaxation time \bar{T}_2 can be assumed:

$$\bar{r} = 2\rho\bar{T}_2, \quad (10)$$

where ρ is the transverse surface relaxivity. We use the approach of [2] to determine an individual value of surface relaxivity for each sample:

$$\rho = \left[S_{por} \times \left(\frac{2T_{2min}}{\lambda_2} \right)^{(D_t - D_f)} \times T_{2hm} \right]^{\left(\frac{-1}{1 + D_t - D_f} \right)}, \quad (11)$$

where D_f is the fractal dimension and $D_t = 2$ the topological dimension of the pore surface area. The specific surface area per unit pore volume S_{por} is determined from the nitrogen adsorption method with the resolution $\lambda_2 = 0.4$ nm.

Using equation 10 with different characteristic relaxation times and the individual values of surface relaxivity of each sample, we get the weighted characteristic pore radii r_{lm} , r_{hm} , and r_{am} . T_{2peak} is converted into r_{dom} in the same way. We investigate whether the resulting characteristic pore radii are suitable proxies for r_{eff} .

3 Samples and methods

The evaluation of the original and modified versions of the SDR equation is based on data from three different sandstone formations:

1) The first set of samples originates from the Shahejie Formation in the Dongpu Depression, Wenliu Oilfield, being located in the Northeast of Henan Province, China, between latitudes N 35° and N 36° and longitudes E 114°30' and E 115°30'. The geological age of this formation is Eocene Epoch, Paleogene Period (approx. 35-56 Ma old). The samples have been collected in six boreholes in the depth interval between 3332 m and 3738 m. This set of 24 samples was used in studies related to permeability prediction, which were reported in [2] and [11].

2) The second set of samples was collected from the outcrops of Araba Formation in Wadi Saal, east central Sinai, Egypt, between latitude N 29° and N 30° and longitude E 34° and E 35°. This formation is of Carboniferous age or older (Lower Paleozoic). Considering the weak clay content, most of the investigated samples can be classified as clean sandstones. Petrographically, the 14 sandstone samples of the studied Araba Formation can be classified into three facies associations: (i) quartz arenite, (ii) sublithic quartz arenite, and (iii) calcareous quartz arenite. These facies are characterized by the presence of some pyrite and iron oxides as cement [12].

3) The third set, which consists of 20 samples, originates from the Cretaceous Nubia Formation, which reaches an approximate thickness of 40 m. Samples were taken in Wadi Ras El-Esh in the Red Sea area of Eastern Desert, Egypt, at longitude N 27° 27' 58" and latitude E 33° 30' 51". These sandstone beds are yellowish, highly dissected, cross-bedded, and rarely fossiliferous. The sandstone samples were differentiated into five microfacies associations: quartz arenite, lithic quartz arenite, calcareous quartz arenite, quartz

wacke, and gypsum quartz arenite. This formation includes both clean and clay-cemented sandstones.

The sample sets of the Araba and Nubia Formations have been integrated in a previous study on permeability prediction that is published in [13].

Cylindrical plugs with a diameter of about 25 mm and a length of about 30 mm have been prepared from all samples. This plug size is suitable for the required petrophysical experiments. Gas permeability k is determined in a steady state flow experiment following the guidelines of [14]. The resistivity formation factor F was measured in an electrical experiment with the plugs saturated with a high salinity brine (~ 15 S/m). The specific surface area per unit mass was determined by nitrogen adsorption method.

The NMR experiments were performed on the MARAN 7 instrument that is operating at a Larmor frequency of 7 MHz. The samples were saturated with a low salinity brine (~ 0.5 g/l NaCl) before the measurements. The signal decay curve, which was measured in the transverse mode, was transformed into a relaxation time distribution (RTD) using a least-squares algorithm that minimizes the deviation between measured and calculated curves. The weighted mean values T_{lm} , T_{hm} , and T_{am} of the RTD consider the interval between $T_{2min} = \tau_{echo} = 0.6$ ms and $T_{2max} = 3$ s.

4 Results

The relationships between characteristic relaxation times and r_{eff} are compared for the three sandstone formations in double logarithmic plots as shown in Figures 1 and 2 for T_{lm} and T_{hm} , respectively. A power law fitting was performed for each sample set. The resulting equations and the coefficient of determination (R^2) are displayed in the legend.

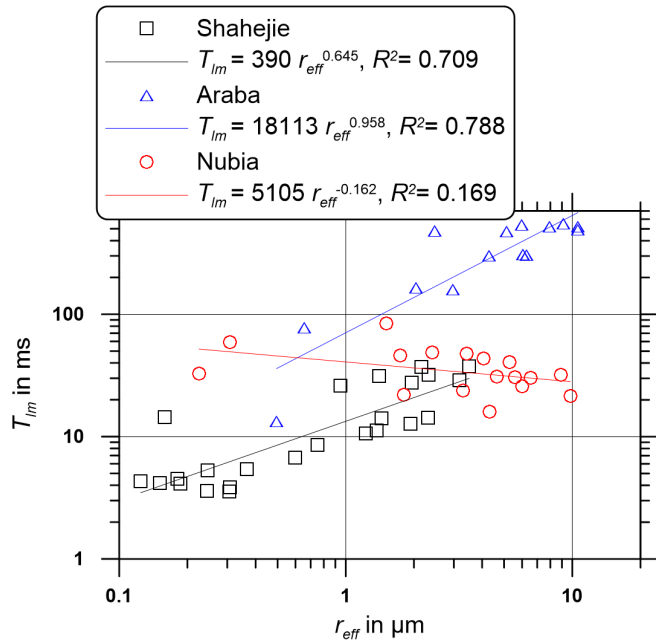


Fig. 1. Relationships between r_{eff} and T_{lm} for three sandstone formations.

The relationships between the logarithm of r_{eff} and the logarithm of the characteristic pore radii r_{lm} and r_{hm} are shown in Figure 3 and 4, respectively. The fitting equation assumes

a linear relationship between the characteristic pore radius and r_{eff} .

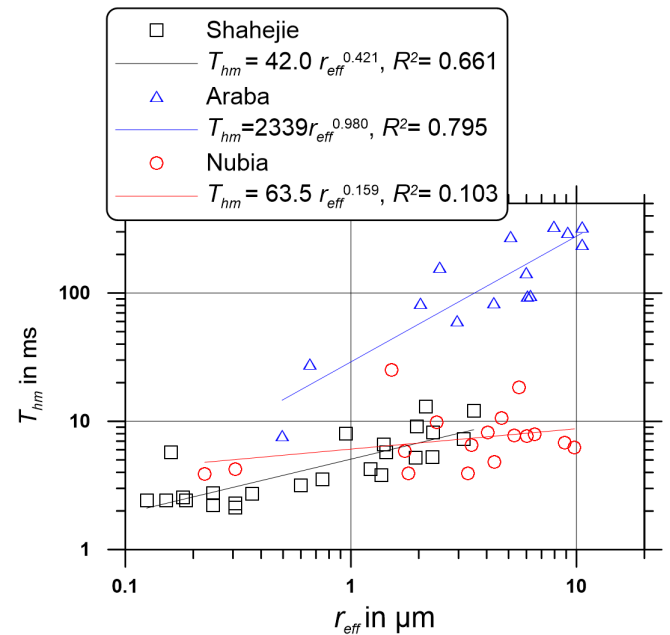


Fig. 2. Relationships between r_{eff} with T_{hm} for three sandstone formations.

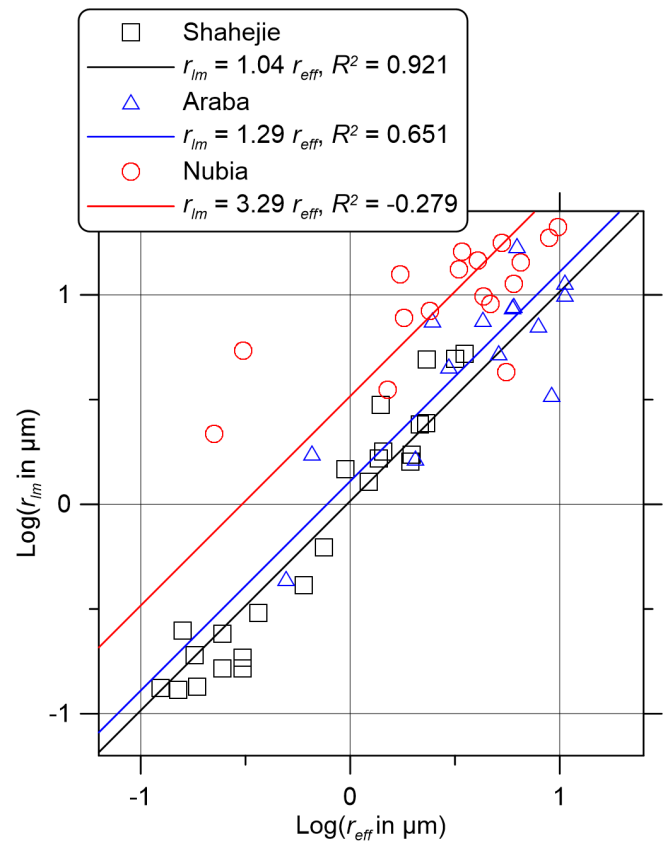


Fig. 3. Relationship between r_{eff} and characteristic pore radii r_{lm} for three sandstone formations.

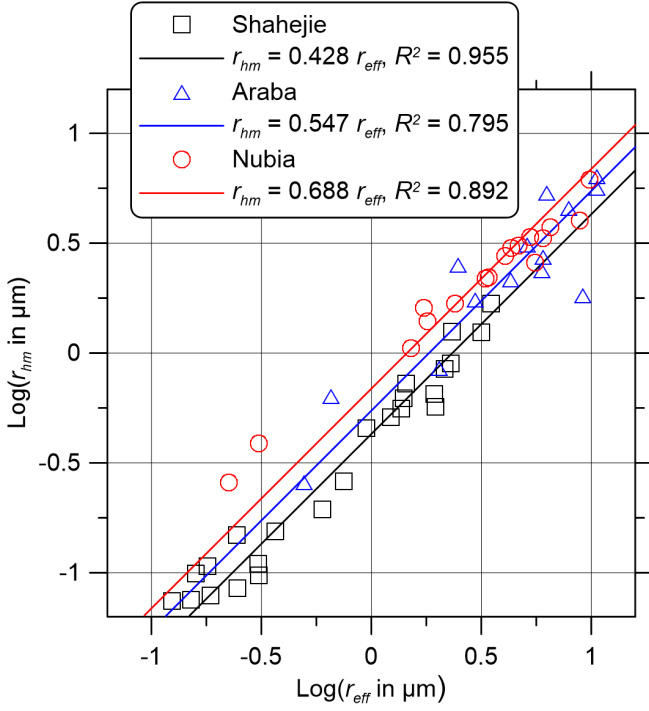


Fig. 4. Relationship between r_{eff} and characteristic pore radii r_{hm} for three sandstone formations.

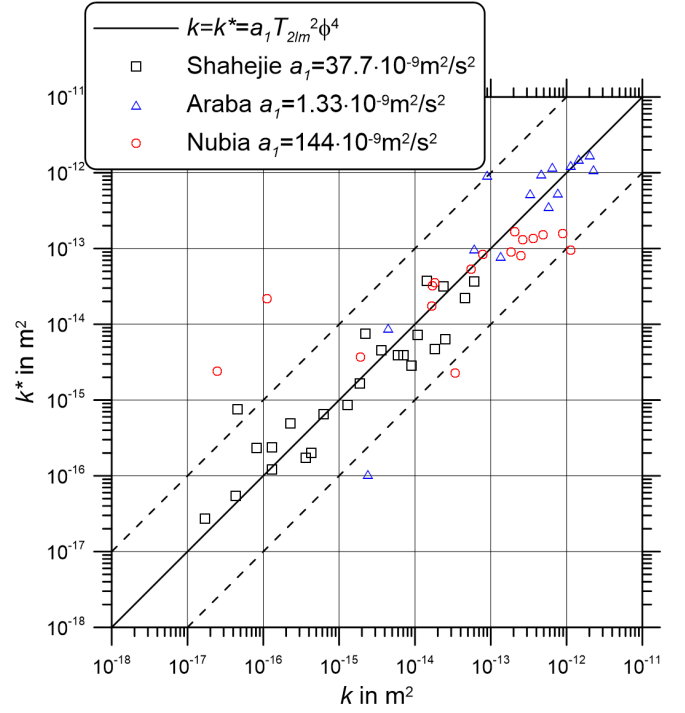


Fig. 6. Comparison of measured permeability k with $k^* = a_1 T_{2lm}^2 \phi^4$ (original SDR equation 6) for three sandstone formations. Individual prefactors a_1 have been determined for the three sandstone formations. The two dashed lines on either side of the diagonal indicate a deviation of one order of magnitude from the measured permeability value.

In order to evaluate the predictive quality of the original or modified SDR equations, we determine the average absolute deviation (in log space) between predicted permeability k^* and the measured permeability k (e.g., [15]):

$$d = \frac{1}{n} \sum_{j=1}^n |\log_{10}(k_j) - \log_{10}(k_j^*)|. \quad (12)$$

A value of $d = 1$ denotes an average absolute deviation of one order of magnitude (or a factor 10). One order of magnitude above or below the measured value is rated as an acceptable estimation if samples of different formations are regarded [16]. In the case of samples originating from the same formation, we aim at a better predictive quality with values considerably smaller than $d = 0.5$.

Figure 5 compares the measured permeability k with the permeability k^* predicted by the original SDR equation 6 with $\bar{T}_2 = T_{2lm}$. A prefactor $a_1 = 24.4 \cdot 10^{-9} \text{ m}^2/\text{s}^2$ has been determined considering all samples of the three formations in the adjustment procedure. We get a moderate agreement between measured and predicted permeability with $d = 0.822$.

The use of a separate adjustment procedure for each sandstone formation yields a better agreement $d = 0.410$ between measured and predicted permeability as demonstrated in Figure 6. The legend indicates the individual prefactors for the three sandstone formations that vary over two orders of magnitude.

Figure 7 displays the comparison between measured permeability k and the permeability k^* predicted by the SDR equation 6 using T_{2hm} instead of T_{2lm} . A uniform prefactor $a_1 = 214.6 \cdot 10^{-9} \text{ m}^2/\text{s}^2$ has been determined using all samples

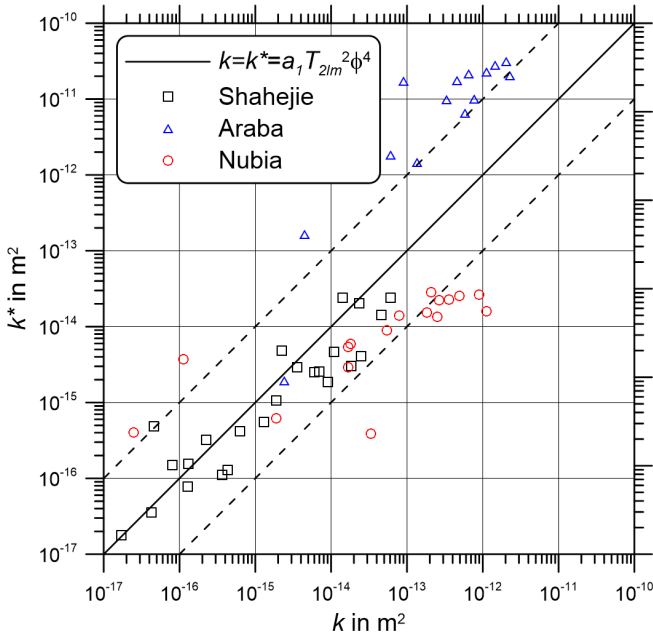


Fig. 5. Comparison of measured permeability k with $k^* = a_1 T_{2lm}^2 \phi^4$ (original SDR equation 6) for three sandstone formations. A uniform prefactor $a_1 = 24.4 \cdot 10^{-9} \text{ m}^2/\text{s}^2$ has been determined considering the samples of the three formations. The two dashed lines on either side of the diagonal indicate a deviation of one order of magnitude from the measured permeability value.

of this study. The deviation between measured and predicted permeability is $d = 0.936$.

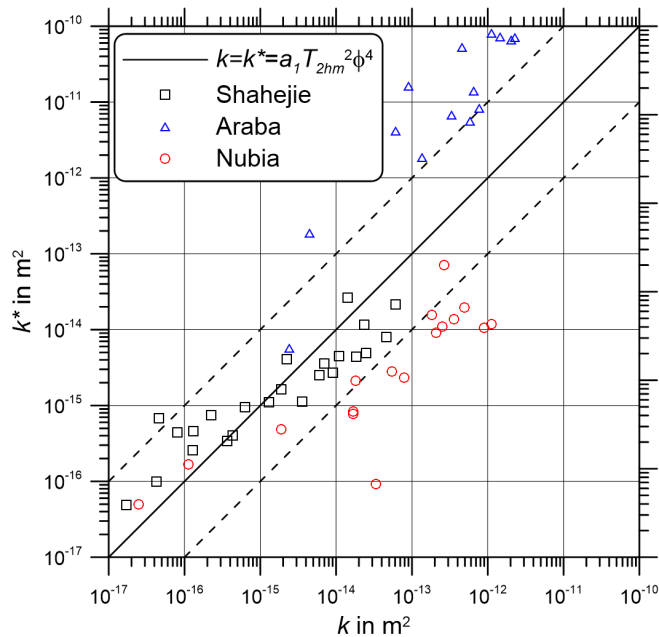


Fig. 7. Comparison of measured permeability k with $k^*=a_1 T_{2hm}^2 \phi^4$ (equation 6) for three sandstone formations. A uniform prefactor $a_1 = 214.6 \cdot 10^{-9} \text{ m}^2/\text{s}^2$ has been determined considering the samples of the three formations. The two dashed lines on either side of the diagonal indicate a deviation of one order of magnitude from the measured permeability value.

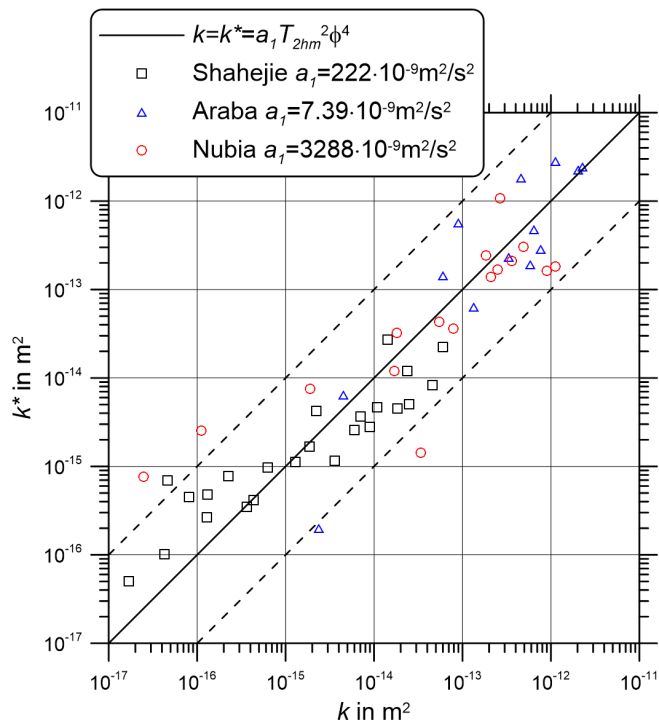


Fig. 8. Comparison of measured permeability k with $k^*=a_1 T_{2hm}^2 \phi^4$ (equation 6) for three sandstone formations. Individual prefactors a_1 have been determined for the three sandstone formations. The two dashed lines on either side of the diagonal indicate a deviation of one order of magnitude from the measured permeability value.

Figure 8 displays the comparison of measured permeability k and the permeability k^* predicted by the SDR equation using T_{2hm} instead of T_{2lm} with individual prefactors ($d = 0.435$).

The original SDR equation 6 considers a porosity exponent $b = 4$. Previous investigations have confirmed the suitability of this exponent. However, it is questionable whether the same exponent b should be used if characteristic pore radii replace the characteristic relaxation times. We investigate the predictive quality of equation 4 with different characteristic pore radii as proxies for r . The exponent b varies from 0 to 10. Figure 9 displays the average logarithmic deviation d as a function of the exponent b . The curves r_{am} , r_{lm} and r_{hm} indicate a minimum in the investigated range of the exponent b . We get the lowest average logarithmic deviation with $d = 0.211$ for the weighted harmonic mean r_{hm} and a porosity exponent $b = 2$.

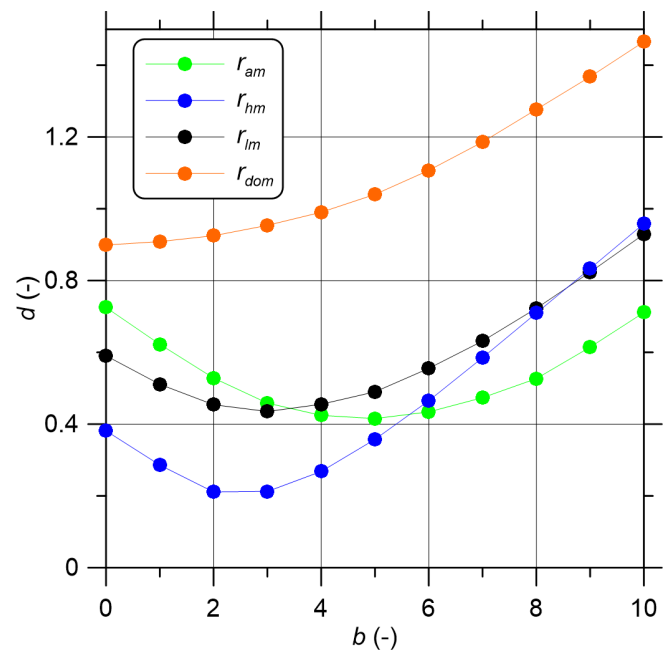


Fig. 9. Average logarithmic deviation d as function of the porosity exponent b in equation 4 using different characteristic pore radii \bar{r} of the three sets of sandstone samples

Figure 10 shows the very good agreement between measured and predicted permeability for the model using the weighted harmonic mean of pore radius in equation 4.

The resulting prefactors a_1 of equation 6 (with $b = 4$) and the prefactors a of equation 4 (with $b = 2$) and the corresponding deviations d are compiled in Table 1.

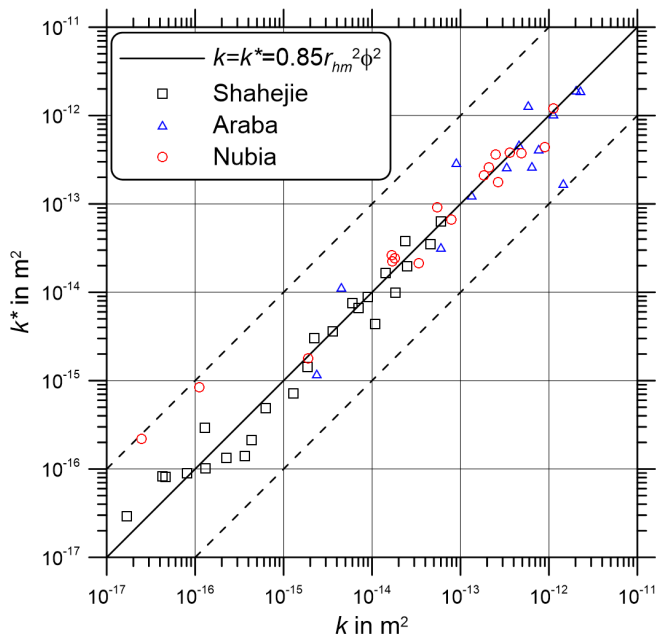


Fig. 10. Comparison of measured permeability k with $k^* = a r_{hm}^2 \phi^2$ (equation 4) for three sandstone formations. A uniform prefactor $a = 0.85$ has been determined considering the samples of the three formations. The two dashed lines on either side of the diagonal indicate a deviation of one order of magnitude from the measured permeability value.

Table 1. The prefactors a_i of equation 6 (in 10^{-9} m²/s²) and the prefactors a of equation 4 (dimensionless) with the resulting average deviations d (equation 12)

	Shahejie		Araba		Nubia		All samples	
Equation 6 ($b = 4$)	a_i	d	a_i	d	a_i	d	a_i	d
T_{2am}	3.11	0.443	0.54	0.323	17.3	0.769	3.38	0.745
T_{2hm}	221.56	0.411	7.39	0.373	3289	0.520	214.63	0.936
T_{2lm}	37.75	0.314	1.33	0.336	144.42	0.608	24.37	0.822
T_{2peak}	23.47	0.517	0.54	0.437	497.82	1.258	23.13	1.102
Equation 4 ($b = 2$)	$a (-)$	d	$a (-)$	d	$a (-)$	d	$a (-)$	d
r_{am}	0.01	0.222	0.08	0.445	0.003	0.675	0.01	0.528
r_{hm}	0.92	0.173	1.03	0.253	0.65	0.217	0.85	0.211
r_{lm}	0.16	0.280	0.18	0.401	0.03	0.488	0.10	0.454
r_{dom}	0.10	0.760	0.08	0.525	0.10	1.490	0.09	0.925

5 Discussion

Various models of permeability prediction require porosity and average pore radius as input parameters. The porosity can be derived either from NMR relaxation or by petrophysical laboratory experiments (e.g., triple weighing). The original SDR equation considers the log-mean relaxation time T_{2lm} as a proxy for the pore radius. A linear relationship between r_{eff} and the log-mean relaxation time is expected. We recognize from the graphs in Figure 1 that only the samples of the Araba Formation indicate a nearly linear relationship with a power

law exponent 0.956. The slope in the double logarithmic plot is considerably smaller for the samples of the Shahejie Formation. The situation becomes even worse for the Nubia Formation with a negative slope and a coefficient of determination $R^2 = 0.169$.

The weighted harmonic mean T_{2hm} can be used as an alternative proxy for the pore radius. A look at Figure 2 indicates only slight changes. A nearly linear relationship between r_{eff} and T_{2hm} is found for the Araba Formation. The samples of the Nubia formation indicate a weak positive slope. The weighted arithmetic mean T_{2am} indicates similar relationships with weak correlations. The maxima T_{2peak} show a more or less linear relationship with r_{eff} for all three formations with $R^2 > 0.73$ for the Shahejie and Araba Formations but a low value for the Nubia Formation ($R^2 = 0.25$).

The transformation of characteristic relaxation time into a characteristic pore radius uses equation 10 with an individual value of surface relaxivity for each sample. The algorithm of ρ -determination requires an additional expense to get the specific surface area per unit pore volume S_{por} . Considering a wide variation in S_{por} for the samples of a single formation, we get a similar variation in ρ . The graphs in Figure 3 confirm linear relationships between r_{eff} and the characteristic pore radii r_{lm} for the samples of Shahejie and Araba Formations. The situation improves if r_{lm} is replaced by r_{hm} . The resulting graphs in Figure 4 present linear relationships with coefficients of determination $R^2 > 0.79$ for all sandstone formations. The factors of the linear relationship vary in a narrow range between 0.428 and 0.688. Therefore, the characteristic pore radius r_{hm} proves to be a reliable proxy for r_{eff} with a linear relationship $r_{hm} = c r_{eff}$. The factor $c = 0.528$ has been determined considering all samples of the three formations. The harmonic mean attributes more weight to the smaller pores or to the pore throats that control the fluid flow. This might be a possible explanation why r_{hm} proves to be a better proxy of r_{eff} in comparison with r_{lm} .

The permeability prediction based on the original SDR equation 6 with $\bar{T}_2 = T_{2lm}$ provides only limited predictive quality if a constant prefactor a_i is used for all sandstone formations. As shown in Figure 5, the permeability prediction works well for the samples of the Shahejie Formation, whereas the SDR equation overestimates k for most samples of the Araba Formation and underestimates k for some samples of the Nubia Formation. An improvement can be achieved if separate prefactors a_i are determined for each formation (see Figure 6). The variation in the prefactors is related to the average values of surface relaxivity. We get the lowest prefactor with $a_i = 1.33 \cdot 10^{-9}$ m²/s² for the Araba Formation, which is characterized by a low average surface relaxivity ($\rho = 9.7$ μ m/s), and the highest prefactor with $a_i = 144 \cdot 10^{-9}$ m²/s² for the Nubia Formation with a higher average surface relaxivity ($\rho = 140$ μ m/s). The wide variation in the prefactor a_i underlines the significance of ρ in permeability prediction with the original SDR equation.

We included other characteristic relaxation times in our study. As summarized in Table 1, the use of T_{peak} causes the largest values of the average deviation d and consequently the lowest predictive quality for all considered sandstone formations. The weighted harmonic mean T_{hm} proves to be advantageous for the Nubia Formation, whereas the weighted

arithmetic mean T_{am} results in the lowest d for the Araba Formation.

The direct use of a characteristic pore radius in equation 4 improves considerably the permeability prediction for all sandstone formations. The weighted harmonic mean of pore radii r_{hm} , which proves to be the best proxy for the r_{eff} , enables a high quality permeability prediction with average deviations $d \leq 0.25$ for all considered formations. The porosity exponent $b = 2$ is in good agreement with the theoretical model of equation 4 with $m = 2$. The prefactors a that have been adjusted for the single formations vary only in a narrow range between 0.65 and 1.03. The application of a mean value of the prefactor a provides a reliable predictive quality without any adjustment procedure. However, the better predictive quality can only be achieved if reliable values of surface relaxivity are available for the individual samples. The results of this study confirm the suitability of the approach of ρ -determination as proposed in [2].

6 Conclusions

Three sets of sandstone samples from China and Egypt with a variation of permeability over four orders of magnitude have been selected for the evaluation of the original and modified SDR equations. Our study confirms the applicability of the SDR equation for permeability prediction with the porosity raised to the 4th power. The use of T_{2lm} in the SDR equation has proved to be an appropriate choice. The prefactor in the SDR equation largely depends on the surface relaxivity. Therefore, a calibration procedure has to be applied to adjust the prefactor for a certain lithology.

We modified the SDR equation by replacing the characteristic relaxation time by a characteristic pore radius. The modified equations enable an improved predictive quality. The best results are achieved with weighted harmonic mean r_{hm} that proves to be a reliable proxy for the effective hydraulic radius r_{eff} . However, the transformation of relaxation time into pore radius requires the knowledge of the specific surface area for each sample to determine an individual value of surface relaxivity.

We confirm the potential of the SDR equation in NMR applications. A careful calibration of the equation with suitable values for the prefactor and exponents will contribute to an improved permeability prediction.

Acknowledgements

The authors would like to thank M. Kassab (Egyptian Petroleum Research Institute) for providing the sandstone samples of the Araba and Nubia Formations and contributing to the petrophysical measurements.

References

1. K. R. Brownstein, C. E. Tarr, Importance of classical diffusion in NMR studies of water in biological cells: *Physical Review A*, **19**, 2446–2453, doi: 10.1103/PhysRevA.19.2446 (1979).
2. Z. Zhang, A. Weller, Estimating the nuclear magnetic resonance surface relaxivity of Eocene sandstones: A comparison of different approaches: *Geophysics*, **86**, 2, JM11-JM22, doi: 10.1190/GEO2020-0501.1 (2021a).
3. H. Pape, L. Riepe, J. R. Schopper, A pigeon-hole model for relating permeability to specific surface: *The Log Analyst*, **23**, 5–13 (1982).
4. Z. Zhang, A. Weller, A comparative study of permeability prediction for Eocene sandstones —Part 1: Application of modified Swanson models to mercury injection capillary pressure and nuclear magnetic resonance data: *Geophysics*, **86**, 6, M233-M243, doi: 10.1190/GEO2021-0194.1 (2021b).
5. G. E. Archie, The electrical resistivity log as an aid in determining some reservoir characteristics: *Transactions of American Institute of Mineralogists Metallurgists and Petroleum Engineers*, **146**, 54-62 (1942).
6. J. H. Schön, *Physical properties of rocks: A workbook* (Elsevier, 2011).
7. G. Towle, An analysis of the formation resistivity factor-porosity relationship of some assumed pore geometries: Paper C presented at third annual meeting of SPWLA, Houston (1962).
8. A. Weller, L. Slater, Permeability estimation from induced polarization: an evaluation of geophysical length scales using an effective hydraulic radius concept: *Near Surface Geophysics*, **17**, 581–594, doi: 10.1002/nsg.12071 (2019).
9. R. L. Kleinberg, Utility of NMR T2 distributions, connection with capillary pressure, clay effect, and determination of the surface relaxivity parameter, ρ_2 : *Magnetic Resonance Imaging*, **14**, no. 7–8, 761–7, doi: 10.1016/S0730-725X(96)00161-0 (1996).
10. D. O. SeEVERS, A nuclear magnetic method for determining the permeability of sandstones, in *SPWLA 7th Annual Logging Symposium*, edited, p. 14, Soc. of Petrophys. and Well Log Anal (1966).
11. Z. Zhang, A. Weller, Fractal dimension of pore space geometry of an Eocene sandstone formation: *Geophysics*, **79**, no. 6, D377-387. doi: 10.1190/GEO2014-0143.1 (2014).
12. M. Kassab, A. Weller, H. Abuseda, Integrated petrographical and petrophysical studies of sandstones from the Araba Formation for reservoir characterization: *Arabian Journal of Geosciences*, **15**:944, doi: 0.1007/s12517-022-10221-3 (2022).
13. A. Weller, M.A. Kassab, W. Debschütz, C.D. Sattler, Permeability prediction of four Egyptian sandstone formations, *Arabian Journal of Geosciences*, **7**, 5171-5183, doi: 10.1007/s12517-013-1188-7 (2014).
14. API (American Petroleum Institute), *Recommended Practices for Core Analysis, API Recommended Practice 40, chapter 6 – permeability determination, second edition*, (1998).
15. A. Weller, L. Slater, A. Binley, S. Nordsiek, S. Xu, Permeability prediction based on induced polarization: Insights from measurements on sandstone and unconsolidated samples spanning a wide permeability range: *Geophysics*, **80**, 2, D161-D173, doi:10.1190/GEO2014-0368.1 (2015).

16. J. Robinson, L. Slater, A. Weller, K. Keating, T. Robinson, C. Rose, and B. Parker, On permeability prediction from complex conductivity measurements using polarization magnitude and relaxation time: *Water Resources Research*, **54**, 3436-3452, doi: 10.1002/2017WR022034 (2018).

Towards Multiscale Digital Rocks: Application of a Sub-Resolution Production Model to a multiscale Sandstone

Rafael Salazar-Tio^{1,*}, Andrew Fager¹, Guangyuan Sun¹, Bernd Crouse¹, Rui Xu¹, Brett Wendt², and Adam Lewis²

¹Dassault Systèmes, USA

²ConocoPhillips Alaska, USA

Abstract. Many digital rock methodologies use a direct simulation approach, where only resolved pores are accounted for. This approach limits the types of rocks that can be analyzed, excluding some types of carbonates, unconventional, and complex sandstones from the digital rock analysis. This is due to the challenge for single scale imaging to capture the full range of relevant pore sizes present in multiscale rocks. In this paper, a physical model is presented, within the context of an established direct simulation approach, to predict the production of hydrocarbons including the contribution of sub-resolution pores. The direct simulation component of the model employs a multiphase lattice Boltzmann method to simulate multiphase fluid flow displacement in resolved pores. In the production model, the amount of hydrocarbons present in the sub-resolution pores is identified and a physical description of the production behavior is provided. This allows a relative permeability curve to be predicted for rocks where mobile hydrocarbons are present in pores smaller than the image resolution. This simplified model for the oil movement in the unresolved pore space is based on a physical interpretation of different regions marked by simulation resolution limits in a USBM wettability test curve. The proposed methodology is applied to high-resolution microCT images of a sandstone that contains pores at multiple scales, some resolved and some not resolved. To allow for benchmarking, experimental routine and special core analysis data was also obtained. Good agreement to experimental results is observed, specifically in absolute and relative permeability. The presented multiscale model has the potential to extend the classes of reservoir rocks eligible for digital rock analysis and paves the way for further advancements in the modelling of multiscale rocks, particularly unconventional and carbonates.

1 Introduction

Reservoir characterization is a critical step in oil field exploration and production. Well logging analysis and petrophysical interpretation is usually supported by laboratory property measurements of physical core samples from the wells, such as porosity, saturations, capillary pressure (P_c), wettability, absolute permeability (K_0) and relative permeability (k_r). Laboratory core analysis can be a time consuming and costly process, and considering that most wells are not core sampled, the value extracted from the available core needs to be maximized, trying to make economically efficient use of these limited core samples [1]. Additionally, core analysis planning needs to consider also that conducting laboratory core analysis experiments sometimes leads to destructive impact on the rock samples. Relative permeability, in particular, is a difficult and time-consuming measurement that, depending on rock type, can take several weeks to a year to complete. With all these considerations, and with the advance of pore scale imaging techniques and computer power in the past decades, digital rock approaches have become more and more a promising technology to complement laboratory measurements [2-4].

Although digital rock technology is promising, there are still challenges when dealing with real applications involving less than ideal rocks, like heterogeneous lithologies or high clay content sandstones for instance. It is computationally costly to simulate a high-resolution large domain model that

can resolve pore sizes over multiple orders of magnitude. On one hand, one would like to use a small field of view microCT imaging in order to capture pore-throat connections with a sufficient number of voxels. On the other hand, a large enough field of view is required in order to obtain a statistically representative elementary volume (REV) [5]. For instance in a clay-rich sandstone sample, we could find two different scale of pores sizes: inter granular pores with pore throat diameter around $\sim 10\mu\text{m}$ scale and clay internal pores around $\sim 10\text{nm}$ scale. In order to achieve an REV model, microCT images need to be taken at a voxel resolution consistent with inter granular pores. At this scale clay internal pores fall below the voxel resolution and will be missed. In this case it is impossible to cover all pore scales in one digital rock analysis. There are several studies on the effect of unresolved pores and how to predict petrophysical properties, such as porosity, capillary pressure, absolute and relative permeabilities [6-10, 26-30] but none, to our knowledge, on how to predict relative permeability curves by using multiphase fluid flow from direct numerical simulation in high clay content sandstones, such as the case just described, leading to a model with significant amount of unresolved porosity.

This work investigate this case, a high clay content sandstone, by using an extension of current numerical digital rock workflows [11] to simulate fluid flow in rocks where a connected pore-space is resolved and unresolved pores do not provide a significant contribution to single phase flow,

* Corresponding author: Rafael.SalazarTio@3DS.com

however for multiphase flow can provide critical connectivity paths for the wetting phase and impact the overall behavior of k_r and P_c curves. The two samples used for this work are clay-rich reservoir sandstones; having nearly 50% porosity not resolved at typical microCT resolutions. In the remainder of this paper, we present the methodology and results of this application: A multi-mineral image segmentation is used to identify pores, grains and clay. A capillary pressure based physical model is presented to emulate oil movement in unresolved pore volumes. Porosity, k_0 and k_r are calculated in the total pore space and are compared well with SCAL laboratory measures available for these samples.

2 Method

The workflow contains three parts: pre-simulation work, simulation, and post-simulation work, which we describe in this section.

2.1. Pre-sim work

The main goal of the pre-sim workflow is to ensure that the microCT images for the selected mini-plug are suitable for digital rock analysis with a good resolution in a representative region. In the mini-plug sample preparation step, we consider sample location, sample size and microCT image resolution. Once the microCT image is done, it follows the image processing to obtain a 3D segmented image. The pore space is analyzed for connectivity and sufficient statistics. Finally, an estimation of total porosity is done.

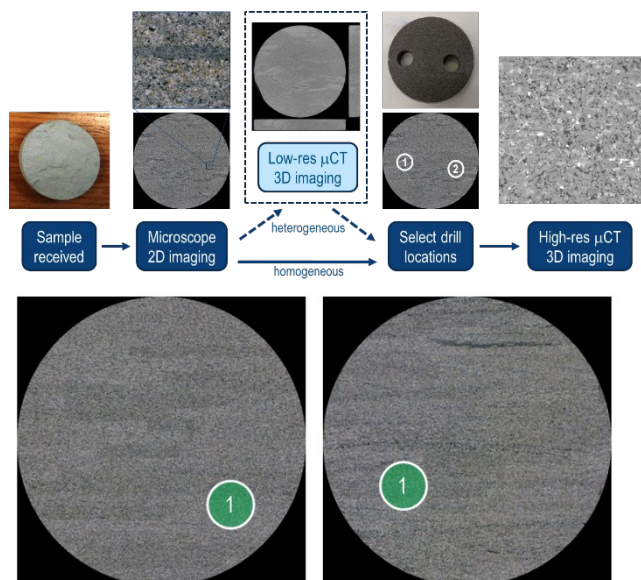


Fig. 1. Schematics of the pre-sim workflow (top). In the bottom, microscopy image of Rock A (left) and Rock B (right) with selected mini-plug locations.

2.1.1 Sample preparation

A schematic of the workflow for sample selection is shown in Figure 1. First, a large panoramic microscopy image is obtained of a polished surface of the available core sample, typically a few inches square at $4 \mu\text{m}/\text{voxel}$ resolution. If heterogeneities are observed on the sample, an optional 3D

microCT image can be taken of the core material at low resolution, typically $20 \mu\text{m}/\text{voxel}$. These images are used in two ways: to select a suitable location for the mini-plug, and to get a rough estimation of grain size. A rule of thumb of 8-10 grains along the diameter of the mini-plug is used for the sample size [5], and the corresponding voxel-size is estimated by dividing the diameter by the number of voxels on the micro-CT camera. For the two samples in this paper, a 2.5 mm mini-plug diameter was estimated, which implies $1.0 \mu\text{m}/\text{voxel}$ resolution given the 2500 voxels in the microCT camera. We also show in Figure 1 the two-sample mini-plug locations used in this paper, Rock A, and Rock B.

2.1.2 Image processing

MicroCT images from mini-plugs typically require some image processing before they can be used successfully for segmentation. In the workflow, we first remove artefacts like beam hardening, rings, and intensity biases along the z-axis. The image noise level is reduced to our standard operational range by using a total variation filter, and grey-scale intensity is set to some default reference values. The main objective is to capture an accurate grey-scale interphase between pore-solid, in order to obtain the sub-resolution accuracy of the surface elements that are a defining feature of the LBM flow simulator utilized here.

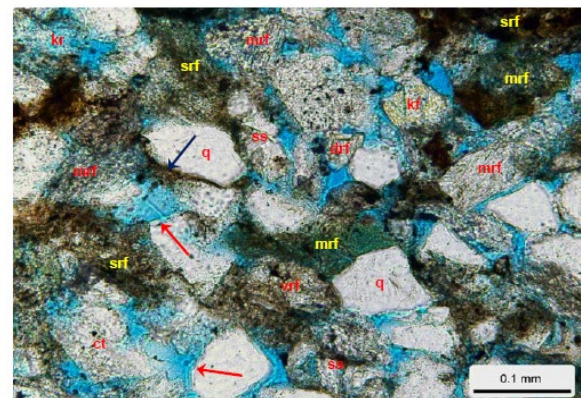


Fig. 2. Different mineral grains in Rock A, showing high clay content and metamorphic rock fragments. Quartz (q), metamorphic (mrf), shale (srf), chert (ct), dolostone (drf), siltstone (ss), volcanic (vrf), K-feldspar (kf), intergranular pores (blue).

In many cases, when complex mineralogy is present on the rock sample (see example in Figure 2), a multi-phase segmentation into different minerals is required. This is particularly important in cases with high clay content, with some partially dissolved grains of feldspars, or in cases with other unresolved porous structures, like in some carbonates. Some of these additional phases can contribute to the total porosity with pores of sizes smaller than the microCT resolution; therefore, an estimation of these fractions is necessary. A multi-mineral segmentation can also be used to model local wettability differences, in mix-wet multi-phase flow simulation scenarios.

An example of a multi-mineral segmentation is shown in Figure 3. This segmentation uses differences in grey values and intensity gradients to identify voxels along the solid-pore boundary and produce the resolved pore structure to be used

in the flow simulation. An additional segmentation for just the solid phase was done, mainly to estimate the porosity contribution from the clay regions, by using the differences in texture to separate minerals [25]. The mineral segmentation is then merged back to the solid-pore segmentation as shown in Figure 3 for Rock A, where we can identify the following volumetric fractions: 10.8% resolvable porosity (black), 12.2% microporous clay-type (yellow), grains 65% (light blue), heavy grains 9% (orange), bright grains 3% (dark blue).

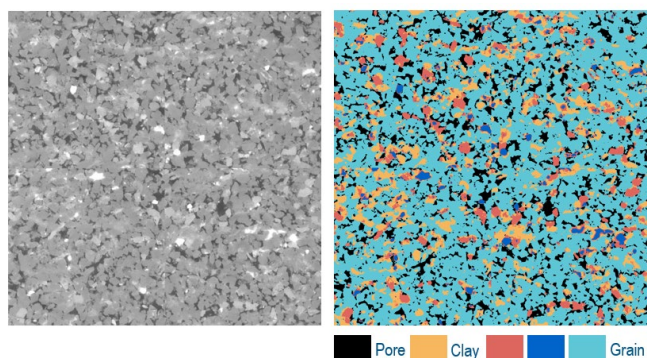


Fig. 3. Sample microCT image for Rock A and corresponding multi-mineral segmented image.

2.1.3 Pore Size Analysis

A pore space analysis (PSA) of the segmented resolvable pore phase is done as part of the pre-sim workflow in order to determine the voxel resolution and REV size for the final simulation model. Starting from calculating a coverable map for maximal inscribed sphere, a pore-size distribution can be computed as the distribution of pore volumes for each sphere radius. In this spherical approximation, the diameter of pores with a large aspect ratio can be underestimated. We also compute another similar volume distribution, but constrained by connectivity to an inlet surface for the model, and for decreasing values of the sphere radius. This connected accessible volume is used to estimate mercury intrusion capillary pressure (MICP) laboratory measurements by using the Young-Laplace relationship between capillary tube radius and capillary pressure, and to compute the critical radius for which the connectivity between inlet and outlet is established. A minimum of 3 voxels is used to ensure accuracy in our multiphase flow simulation results, which corresponds to 3 μm for the microCT resolution used in this study. Finally, we estimate the convergence of the coefficient of variation (COV) of porosity and estimated permeability for different model sizes. COV is defined as the ratio of the standard deviation to the mean value. From the COV convergence analysis we determine what model size is statistically REV.

2.1.4 Estimation of total porosity

Given the physical limit imposed by the voxel-size in the microCT image, the fraction of the total porosity corresponding to pores smaller than the voxel-size cannot be directly measured from the image. However, using some considerations, an estimation of this unresolved porosity can be done. The first consideration follows the method described

in [12] to estimate the non-clay unresolved porosity by fitting a Thomeer model for capillary pressure versus saturation as calculated using the PSA-MICP method described in the previous section. Using the resolvable porosity, voxel-size, critical radius and Thomeer G parameter, the non-clay unresolved porosity is estimated [12]. The second consideration involves including porosity contributions of some segmented phases from the image that could potentially have sub-resolution pores, like the clay phase shown in Figure 3 in yellow. Based on some clay mineral porosity studies [13, 14], we consider here an average of 50% contribution of the volume fraction corresponding to this segmented clay phase to complement the porosity estimation.

2.2 Simulation setup

The fluid flow numerical simulation approach used in this study is the Lattice Boltzmann method (LBM), which has been extensively used in digital rock applications, as a direct simulation approach for resolvable pore-scale events and capturing physical properties, such as residual oil on wettability dependence scenarios, capillary number effects and viscous fingering phenomena [11, 15-18]. The LBM is based on the kinetic equation, and represents a statistical description of the molecular behavior of fluid particles. The LBM can be used to simulate the dynamic behavior of fluid flow without directly solving the continuum fluid mechanics equations. Moreover, the LBM based fluid solvers are considered competitive alternatives to traditional Navier-Stokes PDE-based numerical methods [19, 20], particularly in applications involving complex geometries, like porous media flow in digital rock. The decoupling of streaming and collision steps also makes the LBM faster and more efficient in terms of computational efforts, at least compared to classical FE/FD-solvers.

The LBM solver used for this work is based on an extension of the multiphase Shan-Chen model (SC-LBM) [21]. Some of the recent extensions improve numerical stability and accuracy under the operating conditions required for digital rock workflows, such as low-resolution models and it includes the ability to deal with high viscosity ratios of the immiscible fluid phases [22-24]. In this multiphase LBM model, the fluid phase separation is the result of interaction forces between fluid components, while wettability is determined by interaction forces between fluid and pore walls [22]. Regarding the model geometry used in this LBM solver, in addition to the 3D volume elements corresponding to the voxels from the microCT scanned images, pore/solid surface elements, called surfels, are also used, which allow high fidelity representation of the pore/solid geometry interface with an effective sub voxel resolution accuracy [25, 26]. No slip boundary condition is applied between fluid and surfels.

2.2.1 Absolute permeability setup

Single-phase fluid flow can be simulated with the LBM solver in the resolved pore space. As per definition in Darcy's law, permeability is the linear proportionality ratio between flow rate and pressure gradient, which in this study is realized by a driving force applied in the flow direction, another option is to use pressure boundary conditions. The setup for

this simulation is used to simulate absolute permeability individually in each direction: x, y, z. A periodic boundary condition is applied in the flow direction, while no-flow boundary conditions are used in the directions transversal to the flow. The permeability is calculated using Darcy's Law when flow rate have converged.

2.2.2 Relative permeability setup

A similar setup as in single phase absolute permeability is used here, regarding the driving force applied in the flow direction, and no-flow boundary conditions in the directions transverse to flow, but using a multiphase LBM solver within a steady-state relative permeability displacement setup. In this setup, the water fractional flow starts from zero and keeps increasing until a predefined water saturation is reached. After both water and oil flow become stable, effective permeabilities are calculated and fractional flow increases again until the next water saturation.

Additional details for this method can be found in [11]. In multiphase fluid flow simulation, another parameter that needs to be defined is surface wettability by assigning a contact angle value to each surfel element. In our setup we consider a distribution of contact angles specified throughout the surface based on local contact by oil, as illustrated in Figure 4, where some pores/solid surface regions are considered more water wet and others more oil/neutral wet.

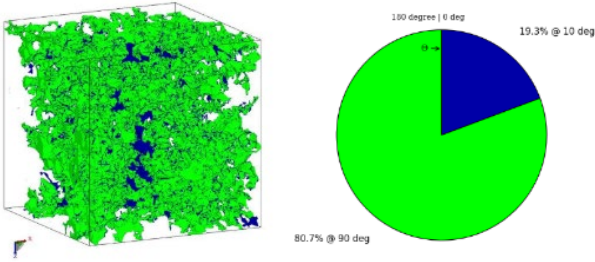


Fig. 4. Wettability setting for Steady-State K_r simulation.

The steady-state relative permeability displacement is conducted at constant capillary number N_c . The definition of capillary number used in this work is:

$$N_c = \frac{U_w * \mu_w + U_o * \mu_o}{IFT} \quad (1)$$

Where $U_{w,o}$ are the superficial velocities of water and oil, and $\mu_{w,o}$ are the dynamic viscosities of water and oil, while IFT is the interfacial tension between water and oil. In this work we use $N_c = 5 \times 10^{-7}$.

2.3 Post-sim and multi-scale model

2.3.1 Absolute permeability post-processing

Absolute permeability is calculated based on Darcy's law

$$K_{eff} = \frac{\nu U}{g} \quad (2)$$

Where, ν is the kinematic viscosity, U is the volumetric superficial velocity from simulation, and g is the body force applied in the flow direction. The resulting absolute permeability value reflects only the flow contribution from the resolved pore space, while the contribution from the unresolved pore space is considered negligible in comparison. For the high clay content (above 10%) sandstones we are considering in this study, up to half of the pore space can be unresolved in the microCT images. However, as pointed out earlier, pores within clay can be several orders of magnitude smaller than inter granular resolved pores. Since permeability is proportional to pore-throat radius square, the flow contribution from clay pores is negligible when compared to the contribution from the resolvable pores, therefore the need for a multiscale procedure for absolute permeability in this case is less important [9].

2.3.2 Multi-scale post-processing for relative permeability

The resolved pore space relative permeability values for water and oil are calculated by Darcy's law at each converged saturation [11]. In this multiphase flow scenario, the fractional flow contribution from clay pores is also negligible when compared to the contribution from the resolvable pores, therefore we also consider here negligible the contributions of unresolved clay pores to the total flow, and use as a good approximation to the total flow the simulated flow only in the resolved pores, and the corresponding calculated relative permeability values K_r . However, the representation of $K_r(Sw_{sim})$ curves only considering saturations in the resolved pore space Sw_{sim} is incomplete and unsuitable for comparison with experimental results. The correct unknown curves are $K_r(Sw_{total})$ that consider saturations in the total pore space Sw_{total} instead. In this section, we explain how we can use a simplified model for the oil movement in the unresolved pore space and how we can rescale Sw_{sim} to Sw_{total} at each permeability calculation. This simplified model is based on a physical interpretation (capillary, wettability) of different regions marked by simulation resolution limits in a USBM wettability test curve.

One of the challenges in computing relative permeability curves in high clay content sandstones is that the unresolved pore space percentage can be larger than the initial water saturation percentage in experimental measurements. This indicates that there is oil in the unresolved pore space too. Such an amount of oil can be calculated from a USBM wettability test result. Figure 5 shows a schematic plot of a wettability test, illustrating the relationship between capillary pressure and water saturation. Let us consider the Young-Laplace equation to interpret the simulation resolution limits in this curve

$$\Delta P = \frac{IFT * 2 \cos \theta}{R} \quad (3)$$

Assuming a contact angle $\theta = 0$ near the end of USBM test and a minimum value for the pore radius R given by the microCT resolution, we can estimate a maximum limit for the capillary pressure ΔP that can be simulated in the resolved pore space of $IFT \times 2 / resolution$, where IFT is the

interfacial surface tension between oil and water. Finer resolution values could resolve smaller pores and simulate a larger range of pressures, but at a higher computational cost.

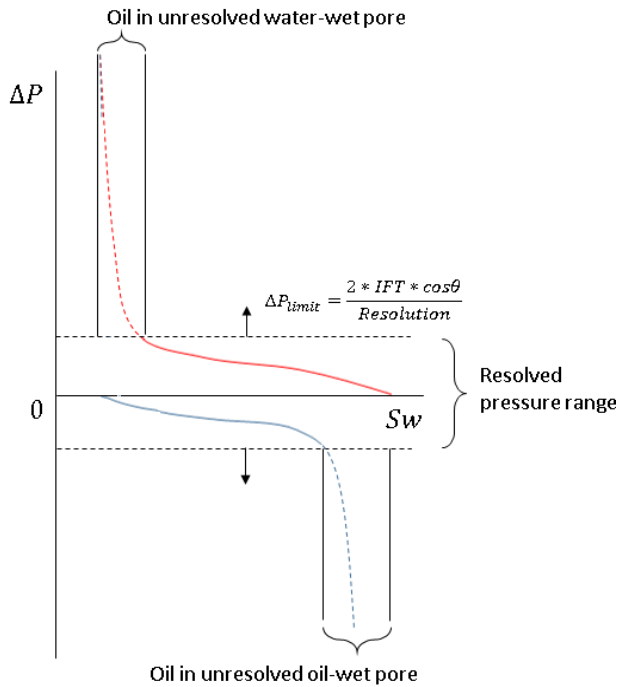


Fig. 5. Schematic plot illustrating the relationship between resolution, capillary pressure and amount of oil in unresolved water-wet and oil wet pore space.

The direct numerical simulation for relative permeability K_r can only be performed within the resolved pressure range shown in Figure 5. The red dash line in Figure 5 shows the amount of oil in the unresolved water-wet pore, which will be spontaneously imbibed before the beginning of the K_r simulation. The blue dash line shows the amount of oil in the unresolved oil-wet pore, which will not be displaced by water in the K_r simulation. For the rest of unresolved oil, we can assume a mix wet condition and model the oil displacement linearly during the K_r simulation. Figure 6 shows a schematic plot of how and when each part of the unresolved oil changes during the K_r simulation in the proposed model.

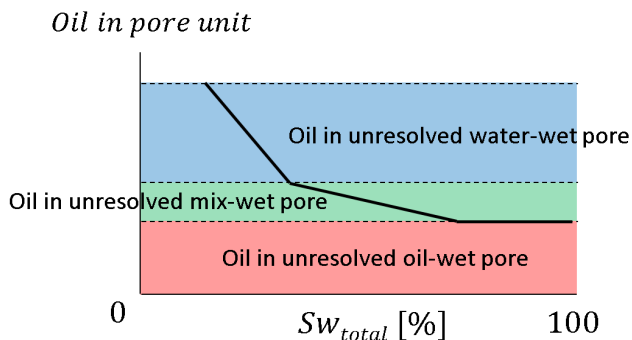


Fig. 6. Schematic plot of the amount of unresolved oil changes with saturation in the total pore space.

Since the proposed simplified model for the oil movement in the unresolved pore space is the main

contribution in this paper, it is worthy to present next a summary of the steps to implement the model:

1. Provide an estimate of the total porosity and decompose it in resolvable and unresolvable porosities. Provide an estimate of the initial water saturation with respect to the total porosity.
2. Compute the amount of water/oil in the unresolvable pore space using the previous quantities.
3. Compute resolvable pressure simulation range using Equation (3); use it in the USBM wettability test curve to identify the regions marked in Figure 5, and estimate the allocation of oil in the unresolved pore space in 3 categories:
 - a. water-wet: un-accessible pore volume above the max simulation pressure ΔP
 - b. oil-wet: un-accessible pore volume below the min simulation pressure $-\Delta P$
 - c. mix-wet: remaining pore volume to complete the total amount of oil in the unresolved pore space
4. Use a simple oil production model in the unresolved pore space (Figure 6):
 - a. Oil in unresolved water-wet pore (blue): displaced before the simulation starts.
 - b. Oil in unresolved oil-wet pore (red): never displaced by water.
 - c. Oil in unresolved mix-wet pore (green): displaced from beginning to end of simulation using a linear rate.

The physical interpretation behind this model is based on simple relations between capillary displacements for different wettability and pore-size cases.

3 Results

We present in this section the results of the application of the methodology detailed in the previous sections to two reservoir rock samples: Rock A, and Rock B, both being tight sandstones with more than 10% clay content, some organic content, and other non-quartz minerals. As indicated in section 2.1.1 the microCT voxel-size used for both samples is $1 \mu\text{m}/\text{voxel}$, and the REV estimated from the COV analysis described in section 2.1.3, about 800 voxels with a COV value around 25%. We select 1000^3 voxels model size for porosity analysis and K_0 simulations, which are not too computationally expensive, but we just use 800^3 voxels for K_r simulations that are computationally more demanding.

3.1 Porosity

We apply the method described in section 2.1.4 to the segmented models of Rock A and Rock B. It is worth to notice that these rock samples have about half porosity unresolved below $1 \mu\text{m}$, being from a digital rock perspective very challenging to characterize, however the resolved porosity is connected and the critical radius is properly resolved for flow simulations. The different values of porosity contributions are presented in Table 1.

Table 1. Porosity Calculation of Rock A, B

	Rock A	Rock B
Experimental	20.7%	19.6
Resolved	10.8%	10.2%
Resolved connected	10.2%	9.5%
Correct resolved connected	13.78%	12.37%
Clay image fraction	12.2%	13.9%
Clay porosity (assuming 50%)	6.1%	6.95%
Total porosity (calculated)	19.88%	19.32%

Experimental values of porosity are available for these two samples, and are compared with the image based total porosity estimation in Figure 7. The differences between experimental values and image estimations are within 5%, which is quite remarkable for samples with such significant unresolved porosity. Given the availability of the experimental porosities, for the sake of accuracy in the following simulations, we will be using the experimental values of total porosity; however, image porosity estimation can be used if experimental values were not available.

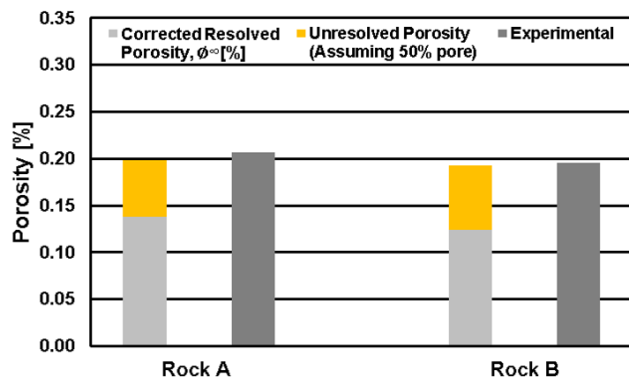


Fig. 7. Porosity Calculation of Rock A, and Rock B

3.2 Absolute Permeability

The results of the single-phase flow simulation setup described in section 2.2.1 in the resolved pore space are shown in Figure 8 where the flow velocity magnitude is represented in a color log scale. Flow in large connected channels contributes the most to the average flow speed and total permeability. Usually once the main flow paths in the pore space backbone are properly captured by the resolved porosity, the unresolved pore space contribution to flow seems to not be relevant anymore.

In Figure 9 we present the resolved pore space absolute permeability simulation results of Rock A and Rock B in x, y, z directions compared with the experimental values. The average simulated absolute permeability for Rock A is 21.2 mD versus the experimental value 19.7 mD. The average simulated absolute permeability for Rock B is 16.0 mD versus the experimental value 14.5 mD.

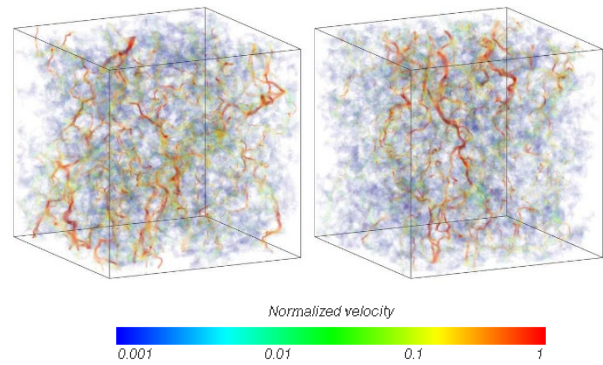


Fig. 8. Resolved pore space 1000^3 absolute permeability simulation in z-direction result of rock A (left) and rock B (right)

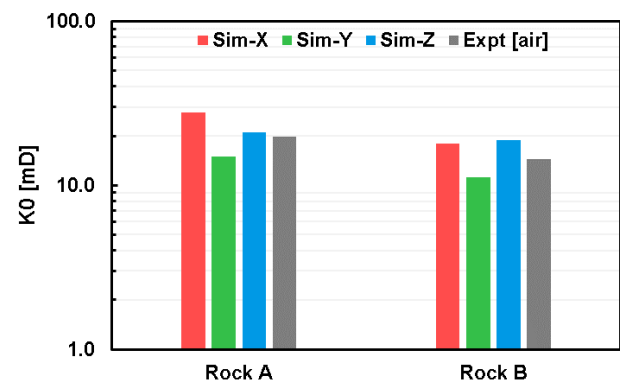


Fig. 9. Absolute permeability K_0 in x, y, z direction vs. experimental data

3.3 Relative Permeability

Following the methodology described in section 2.2.2, we setup the system wettability based on previous experience, knowledge of reservoir properties and USBM wettability lab measurements, as weakly water-wet to neutral-wet condition, by assigning a combination of 10 and 90 degrees contact angles as shown in Figure 4. The initial water saturation in the simulation for the resolved pore space must be considered together with the unresolved initial water saturation, to be consistent with the experimental expected initial water saturation. In the simulation for the resolved pore space, we use an initial water saturation close to zero by assuming all water is in the unresolved pore space. This setup is consistent with the experimental initial water saturation for Rock A, which is 32.3%, considering that from the microCT images we can only resolve 52.2% of the total pore space, being 47.8% unresolved pore space missing in simulation. We use the same wettability and initial water setup for Rocks A and B.

In Figure 10 we illustrate the resolved pore space K_r simulation results for Rock A with two snapshots of oil and water distribution at early and late stages of displacement. At the bottom of Figure 10, we show the oil blobs color coded by blob size in log scale. Dark red represents the largest blob. Blue represents the smallest blob. At initial stages oil is well connected. At late stages when water saturation increases, oil blobs are more disconnected as more oil blobs are snapped off. The corresponding steady-state relative permeability

curve calculated from simulation in the resolved pore space $K_r(Sw_{sim})$ is shown in Figure 12 using green lines.

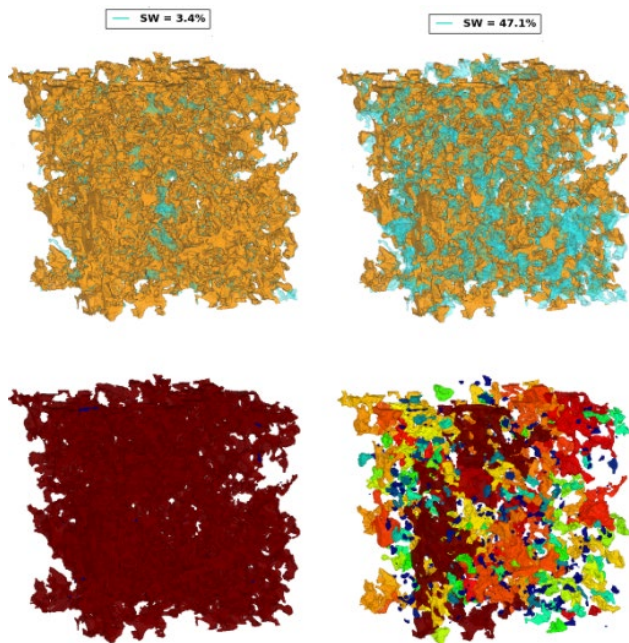


Fig. 10. Resolved pore space 800^3 voxels model for Rock A and steady-state relative permeability simulation results. Water (green)-oil (yellow) iso-surface visualisation (top). Oil blob iso-surface visualisation by blob size (dark red is largest blobs, blue is smallest blobs) (bottom).

We introduced an unresolved pore space oil production model in section 2.3.2 to describe how oil moves in the unresolved pore in order to calculate the correct $K_r(Sw_{total})$ curves for the total pore space by using USBM lab test results. In this study, the microCT resolution is $1.0 \mu\text{m}/\text{voxel}$, IFT is $26 \text{ mN}/\text{m}$, so using Equation (3), the pressure limit is 7.54 psi . In Figure 11 we show the USBM test results for Rock A together with the estimated resolved pore space simulation pressure limits.

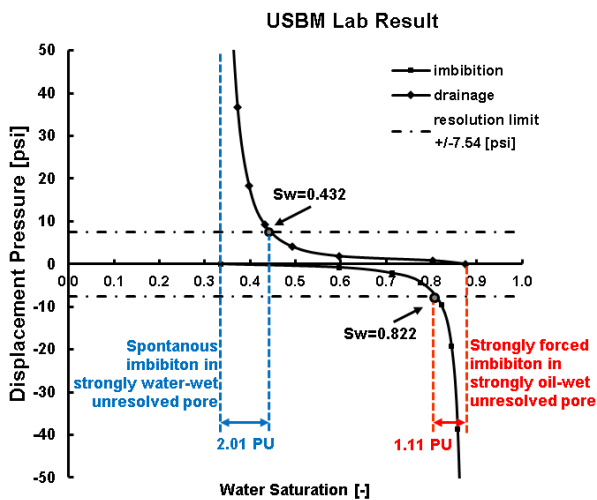


Fig. 11. USBM wettability test results for Rock A

The total porosity is 20.7% for Rock A, which corresponds to 20.7 Pore Unit (PU). Figure 11 shows that

there is 2.01 PU of oil in unresolved water-wet pores and 1.11 PU of oil in unresolved oil-wet pores. Table 2 shows how the percentage of oil in neutral-wet unresolved pores is calculated, assuming $Sw_i = 0$ in the resolvable pore space simulation.

Table 2. Pore Unit calculation of initial oil in the unresolved pore space for Rock A: water-wet, neutral-wet and oil-wet.

	Percentage	Pore Unit
Total porosity (Lab)	20.7 %	20.7 PU
Resolved pore (Simulation pore space)	10.2 %	10.2 PU
Unresolved pore	10.5 %	10.5 PU
Connate water saturation in total pore space	32.2 %	6.67 PU
Assumed initial water in unresolved pore		6.67 PU
Derived initial oil in unresolved pore		3.83 PU
From USBM Result:		
Oil in water-wet unresolved pore		2.01 PU
Oil in oil-wet unresolved pore		1.11 PU
Oil in neutral-wet unresolved pore		0.71 PU

Following the linear production oil model illustrated in Figure 6, and using the input values from Table 2, we compute the red curves in Figure 12, that shows $K_r(Sw_{total})$ curves in total pore space after rescaling water saturation from resolved pore to total pore in sample Rock A, the black dots are lab test results. Overall, the simulation results and the experimental values match well in most of the K_r curves, which is remarkable considering that the resolved pore space in the simulation is only half of the total pore space. The mismatch of the first K_r point could be because the simulation computes the oil permeability at a lower oil saturation and a lower capillary pressure compared with lab, when oil has already been fully drained from the unresolved water-wet pore space. The direct numerical simulation reaches S_{OR} at the end of the solid line. An additional step is used to model the oil displacement through the unresolved pore space. The mismatch on the S_{OR} point could be due to such an effect. Another baseline for comparison can be obtained by compressing the green curve in the range 50%-100%, which corresponds to considering the half-unresolved porosity filled with unmovable water; this will overestimate the saturation crossing point.

Figure 13 shows $K_r(Sw_{sim})$ curves for Rock B simulated in the resolved pore space and $K_r(Sw_{total})$ in the total pore space by applying the same sub-resolution oil production model as per Rock A. Due to lack of lab results, a possible S_{OR} point from extended run was not done here for comparison. The simulated prediction for K_r is promising since Rock A and Rock B are similar rock types. Both have similar average grain size, belong to the same formation, have

similar mineralogy components, and clay content, the use of a similar oil production model is therefore justified.

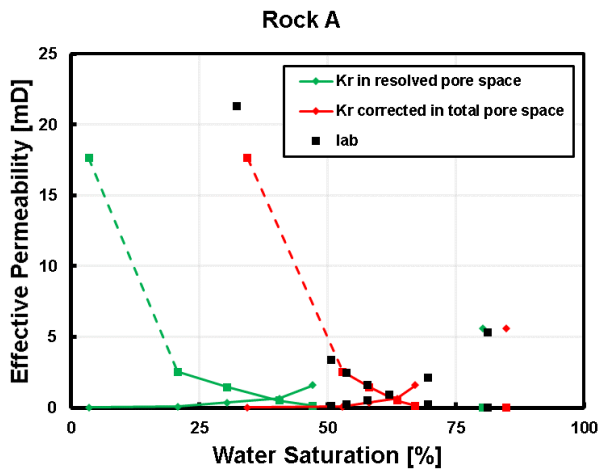


Fig. 12. $K_r(SW_{sim})$ curves in the resolved pore space from direct simulation, $K_r(SW_{total})$ curves in the total pore space using a production oil model, lab K_r results for Rock A.

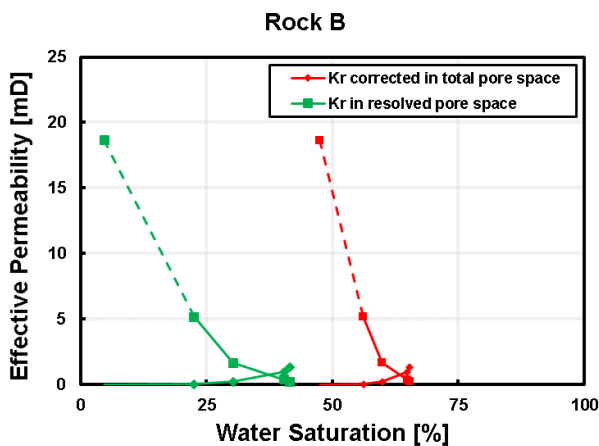


Fig. 13. $K_r(SW_{sim})$ curves in the resolved pore space from direct simulation, $K_r(SW_{total})$ curves in the total pore space using a production oil model, for Rock B.

4 Conclusions

A novel physics based sub-resolution oil production model is presented, which together with a digital rock workflow for multiphase fluid flow is applied to two clay rich sandstone reservoir rocks containing pores at two different scales. This simplified model is based on a physical interpretation (capillary, wettability) of different regions marked by simulation resolution limits in a USBM wettability test curve. For these high clay content sandstones, with half of the pore space below the microCT image resolution, the current workflow predicts porosities within 5%, absolute permeability within 10% and relative permeability K_r curves consistent with existing lab results. The current workflow demonstrate that is possible to use simplified models to extend the scope of application of digital rock technology to some challenging rock types, like high clay content sandstones, without having to explicitly simulate fluids

movement in the unresolved pore regions using other multiscale multiphase flow methods such as [26-30]. In cases where the main percolating path is capture, but still a significant pore space fraction is unresolved, the method proposed in this paper could be computationally less expensive than full multiscale multiphase fluid flow methods [26-30].

References

1. J.J. Buckles, R. D. Hazlett, S. Chen, K. G. Eggert, D. W. Grunau, W. E. Soll, *Los Alamos Science*, **22**, 112-121, 1994.
2. S. Bakke, P. E. Øren, SPE 35479, *SPE Journal*, **2**, 136-149, 1997.
3. H. Andrä, N. Combaret, J. Dvorkin, E. Glatt, J. Han, M. Kabel, Y. Keehm, et al., *Computers & Geosciences*, **50**, 25-32, 2013.
4. H. Andrä, N. Combaret, J. Dvorkin, E. Glatt, J. Han, M. Kabel, Y. Keehm, et al., *Computers & Geosciences*, **50**, 33-43, 2013.
5. J. Bear, *Dover Publications Inc.*, 1988.
6. H. Long, C. Nardi, N. Idowu, A. Carnerup, M. A. Knackstedt, T. Varslot. SCA 2013-013, *Int. Symp. Soc. Core Analysts*, 2013.
7. S. Zhang, A. Byrnes, J. Howard, URTEC 2019-416, *Unconventional Resources Technology Conference*, Denver, Colorado, USA, 2019.
8. S. N. Apourvari, C. H. Arns, *Advances in Water Resources*, **95**, 161-175, 2016.
9. M. S. Jouini, S. Vega, A. A. Ratrouf, *Geophysical Prospecting*, **63**, 405-421, 2014.
10. H. Zhang, P. Yuan, J. Wu, A. Mezzatesta, G. Jin, R. Satti, N. Koliha, J. Bautista, B. Crouse, and D. Freed, SPE 183883, *Middle East Oil and Gas Show & Conf.*, 2017
11. G. R. Jerauld, J. Fredrich, N. Lane, Q. Sheng, B. Crouse, D. M. Freed, A. Fager, and R. Xu, SPE 188688, *2017 SPE Abu Dhabi Int. Pet. Exhib. & Conf.*, Abu Dhabi, U.A.E., Nov. 13-16, 2017.
12. N. Saxena, A. Hows, R. Hofmann, J. Freeman, M. Appel, *Transp Porous Med* **129**, 403-412, May, 2019
13. P.H. Nadeau, A. Hurst, *Journal of Sedimentary Research*, **61**, 921-925, 1991.
14. A. Alansari, A. M. A. Salim, H. T. Janjuhah, A. H. B. A. Rahman, N. M. Fello, *Journal of Natural Gas Geoscience*, **4**, 139-150, 2019
15. B. Crouse, D. M. Freed, N. Koliha, G. Balasubramanian, R. Satti, D. Bale, and S. Zuklic, SCA 2016-058, *Int. Symp. Soc. Core Analysts*, Snow Mass, CO, USA. Aug. 2016.
16. R. Xu, B. Crouse, D. M. Freed, A. Fager, G. R. Jerauld, N. Lane, Q. Sheng, SCA 2018-066, *Int. Symp. Soc. Core Analysts*, Trondheim, Norway, Aug. 2018.
17. G. Sun, B. Crouse, D. M. Freed, R. Xu, J. Bautista, R. Zhang, H. Otomo, Y. Li, H. Chen, H. Fan, M. Dressler, *Fuentes, el reventón energético*. **16**, no. 2, 2018.
18. A. Fager, B. Crouse, G. Sun, R. Xu, D. M. Freed, SPE 195734, *2019 SPE Offshore Europe Conf. & Exhib.*, Aberdeen, UK, Sep. 2019

19. S. Chen, H. Chen, D. Martinez, and W. Mattheus, *Phys. Rev. Lett.*, **67**, no. 27, 3776-3779, Dec. 1991.
20. H. Chen, S. Chen, W. Mattheus, *Phys. Rev. A*, **45**, no. 8, R5339-R5342, Apr. 1992.
21. S. Chen and G. Doolen, *Annu. Rev. Fluid Mech.*, **30**, no. 1, 329-264, 1998.
22. H. Otomo, H. Fan, R. Hazlett, Y. Li, I. Staroselsky, R. Zhang, R., and H. Chen, H., *Comptes Rendus Mécanique*, **343**, 559 (2015).
23. H. Otomo, H. Fan, Y. Li, M. Dressler, I. Staroselsky, R. Zhang, and H. Chen, *Jour. Comp. Sci.*, 17, 334 (2016).
24. H. Otomo, B. Crouse, M. Dressler, D.M. Freed, I. Staroselsky, R. Zhang, H. Chen, *Computer Fluids*, 172, 674 (2018)
25. I. Aranda-Carreras, V. Kaynig, C. Rueden, K.W. Eliceiri, J. Schindelin, A. Cardona, and H. Sebastian Seung, *Bioinformatics*, 33, 2424 (2017)
26. S. K. Masalmeh, X. Jing, S. Roth, C. Wang, H. Dong, M. Blunt, Society of Petroleum engineers SPE-177572-MS (2015)
27. L. C. Ruspini, G. Lindkvist, S. Bakke, L. Alberts, A. M. Carnerup, and P. E. Øren, Society of Petroleum Engineers SPE-180268-MS (2016)
28. O. Dinariev, N. Evseev, D. Klemin, SCA 2019-002, *Int. Symp. Soc. Core Analysts*, 2019.
29. M. Suhrer, X. Nie, J. Toelke, Proceedings of international petroleum technology conference, IPTC 20035 (2020)
30. A. Fager, H. Otomo, R. Salazar-Tio, G. Balasubramanian, B. Crouse, R. Zhang, H. Chen, J. Schembre-McCabe, *Int. Symp. Soc. Core Analysts*, 2021

Chemostratigraphic analysis as a powerful tool for the lateral continuity of structurally complex reservoirs. A case study.

Liborius-Parada Andreina^{1}, Medina-Macedo Marlen^{1*}, Tonner Dave¹, Hughes Simon² and McCulley Meri²*

^{1,2} Diversified Well Logging LLC, 9780 Pozos Ln. Conroe Texas 77303, United States.

¹ Pemex Exploración y Producción - Subdirección de Proyectos de Explotación Estratégicos, Avenida Adolfo Ruíz Cortines, Edificio Pirámide, No. 1202, Piso 4, ala B, Fracc. Oropeza Villahermosa, Tabasco, C.P. 86030, México.

Abstract.

The Upper Jurassic Kimmeridgian is one of the most important targets and one of the most significant oil discoveries in the Pilar-Reforma-Akal geological province in Mexico. It is laterally heterogeneous and interpreted to be deposited in a marine inner ramp of dark gray oolitic, pelletal, and bioclastic limestone, mostly dolomitized, with anhydrite and shale beds and much dark brown and gray shale. The southern region of the Pilar-Reforma-Akal geological province displays a diverse scale of geological structures that affects the understanding of the lateral extension. The structural complexity can be associated with body salt intrusions, shale diapirism, and listric faults. Preliminary results have shown that the complex modeling workflow obtained by seismic data affected the velocity models, increasing the uncertainty and misinterpreting the depositional environment, formation tops, and lateral continuity. This work aims to establish the reservoir continuity of well G to understand the compositional variation of the Jurassic Kimmeridgian target to investigate relationships between the production intervals and their association with offset wells. This study utilizes a portable, energy-dispersive X-ray fluorescence (ED-XRF) spectrometer for 1156 cutting samples within 4 vertical wells targeting the Jurassic Kimmeridgian in the "X" field. The cuttings were collected every 3-5 meters, revealing broad trends, in conjunction with an extensive QA/QC process that generated a quantitative stratigraphic control during drilling. The principal elements used in this study to indicate detrital sedimentation are zirconium (Zr), titanium (Ti), silicon (Si), cobalt (Co), lead (Pb), niobium (Nb), aluminum (Al), potassium (K), thorium (Th), and phosphorus (P). The amount of quartz, both biogenic and detrital, is inferred using a Si/Al ratio. Biogenic quartz is inferred when detrital influx cannot account for the amount of quartz observed. Strontium (Sr), calcium (Ca), magnesium (Mg), and manganese (Mn) are elements associated with carbonate proxies, and nickel (Ni), copper (Cu), zinc (Zn), uranium (U), molybdenum (Mo), vanadium (V), and sulfur (S) are indicators of basin restriction and associated with paleo-redox/anoxic environments. With the dense database obtained from the offset wells (Well A, B, and I) 3 chemostratigraphic packages and 9 chemofacies were determined for the field of study; the Upper Cretaceous and Middle Cretaceous were characterized by high concentrations of carbonate and detrital proxies, mainly associated with shaley intervals, biogenic quartz, and an increase in the anoxic proxies with a reasonably high pseudo-TOC model, typical of an epicontinental sea. At the same time, the Lower Cretaceous indicated a marked variation of detrital, anoxic proxies with a lower pseudo-TOC. The Upper Middle-Lower Tithonian Jurassic was characterized by oscillations in carbonate, detrital, and anoxic proxies with a variable pseudo-TOC model ranging from "good" to "excellent". On the other hand, the Upper Jurassic Kimmeridgian target indicated the highest Mg concentrations and (the) anoxic conditions not seen in any previously studied Upper Jurassic studied. The chemostratigraphic analysis and the stratigraphic control reduced uncertainty and optimized decision-making during the drilling of well G, acting as a powerful tool to understand the lateral continuity of a structurally complex reservoir.

1. Introduction

Chemostratigraphy is a technique that can be applied to outcrops, cores, or cuttings samples with an equivalent degree of certainty. It generates a visual and quantitative representation, in real-time, processing the element concentration after the analyses are performed on the rig-site while drilling, generating a chemostratigraphic profile and element ratios of the major, trace, and anoxic elements. These profiles can be used to develop stratigraphic frameworks and correlate units through sedimentary basins as complex as those studied in the present field. Compared with petrography, X-ray diffraction, and TOC data, chemostratigraphy through a large number of measured elements provides an important correlation parameter since it allows the recognition of detrital, carbonate, and paleo-redox/paleoenvironmental indicators using inorganic geochemical proxies also referred to as "chemozones" [1].

The use of chemostratigraphy, among other disciplines such as biostratigraphy and petrography, optimizes the integrated geological-operational model, increasing the efficiency of field development and improving the stratigraphic positioning and formation top picks, which have been pre-determined using downhole petrophysical logs.

Based on the association of elements established by Craigie in 2018 [2], the associations used for these interpretations were classified into three main types:

1. Elements associated with detrital proxies and clay content: zirconium (Zr), titanium (Ti), silicon (Si), cobalt (Co), lead (Pb), niobium (Nb), aluminum (Al), potassium (K), thorium (Th), phosphorus (P)

* Corresponding author: andreinaliborius@dwl-usa.com

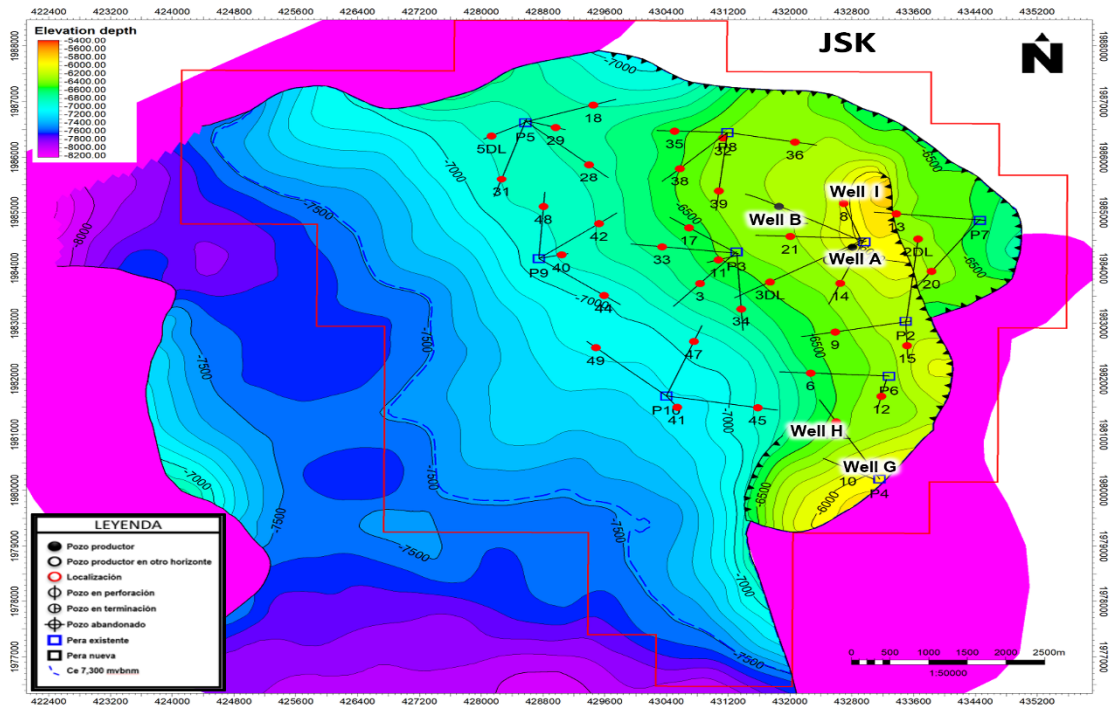


Fig. 1. Structural map of the field of study. From D.R. Petroleos Mexicanos, 2021

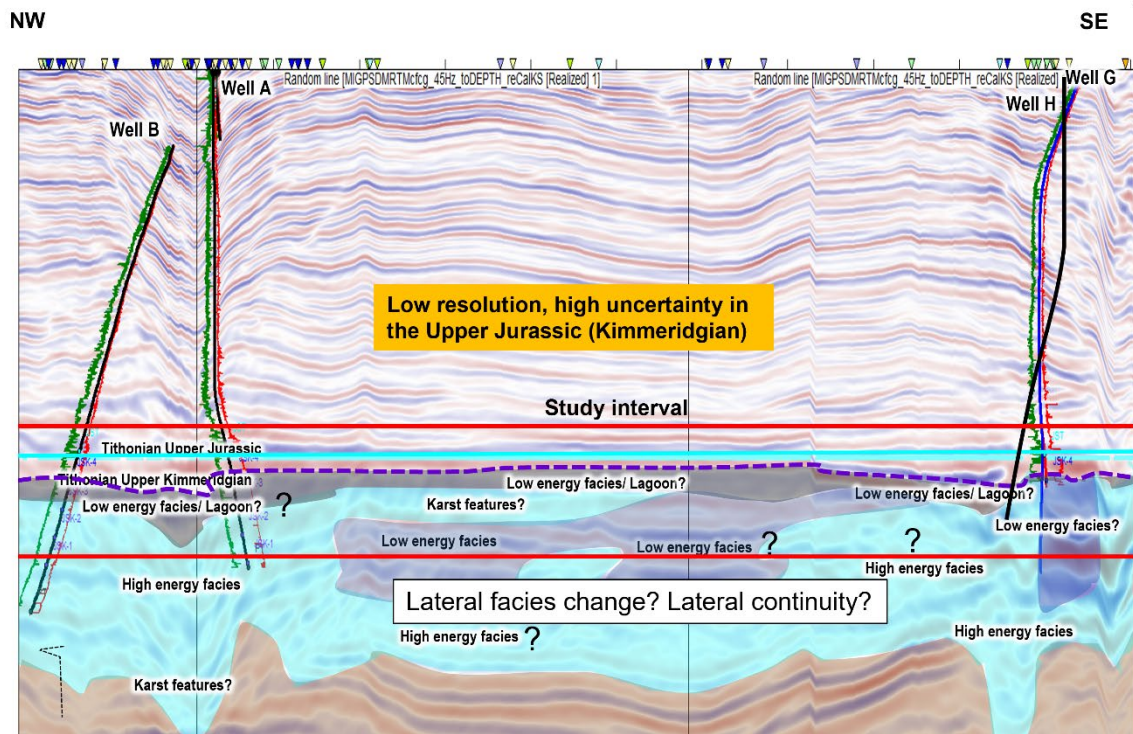


Fig. 2. Seismic profile of the study area where the structural complexity is reflected due to the karstic and saline depositional environment. From D.R. Petroleos Mexicanos, 2021.

2. Elements associated with carbonate proxies: strontium (Sr), calcium (Ca), magnesium (Mg), manganese (Mn)
3. Elements associated with paleo-redox / anoxic proxies: nickel (Ni), copper (Cu), zinc (Zn), uranium (U), molybdenum (Mo), vanadium (V), and sulfur (S)

The field of study is characterized by an asymmetric anticline with preferential direction NW-SE with a 3-way closure against saline and reverse faults (Figure 1), where there is a high degree of uncertainty due to the structural complexity and low seismic resolution generated by the salt bodies present in the geological structure (Figure 2). The reservoir's sedimentary model and the environment of deposition correspond to an internal ramp consisting of dolomitized carbonate rocks presenting the development of oolitic banks (Figure 3). The complex stratigraphic settings, together with a high degree of diagenetic alteration, generated significant dolomitic intervals that modify the lateral continuity developing new facies towards the SW. The application of chemostratigraphy, when integrated with other datasets, aided in identifying ideal acreage positions and defining well target zones with the highest reservoir quality.

2. Methodology

The methodology performed for chemostratigraphic analyses was based on the collection and integration of cuttings samples from offset wells for a subsequent preliminary interpretation of their chemo-facies. ~10 gr of the sample is washed, rinsed with water in a sieve, and dried at ~40 Celsius. ~5g of sample is ground into a powder in a mechanical mill, and XRF analyses is performed on the powder.

Samples are placed in the upper sieve (mesh # 8), with the mesh #120 sieve under it. In some instances where exceptionally heavy sludge (more than 13ppg) is used, it may be necessary to use an ultrasonic cleaner to loosen and remove stubborn contamination and Barite from the sample. The main reason for the rigorous sample cleaning process before XRF analysis is to remove contamination from samples, that may have been introduced by the

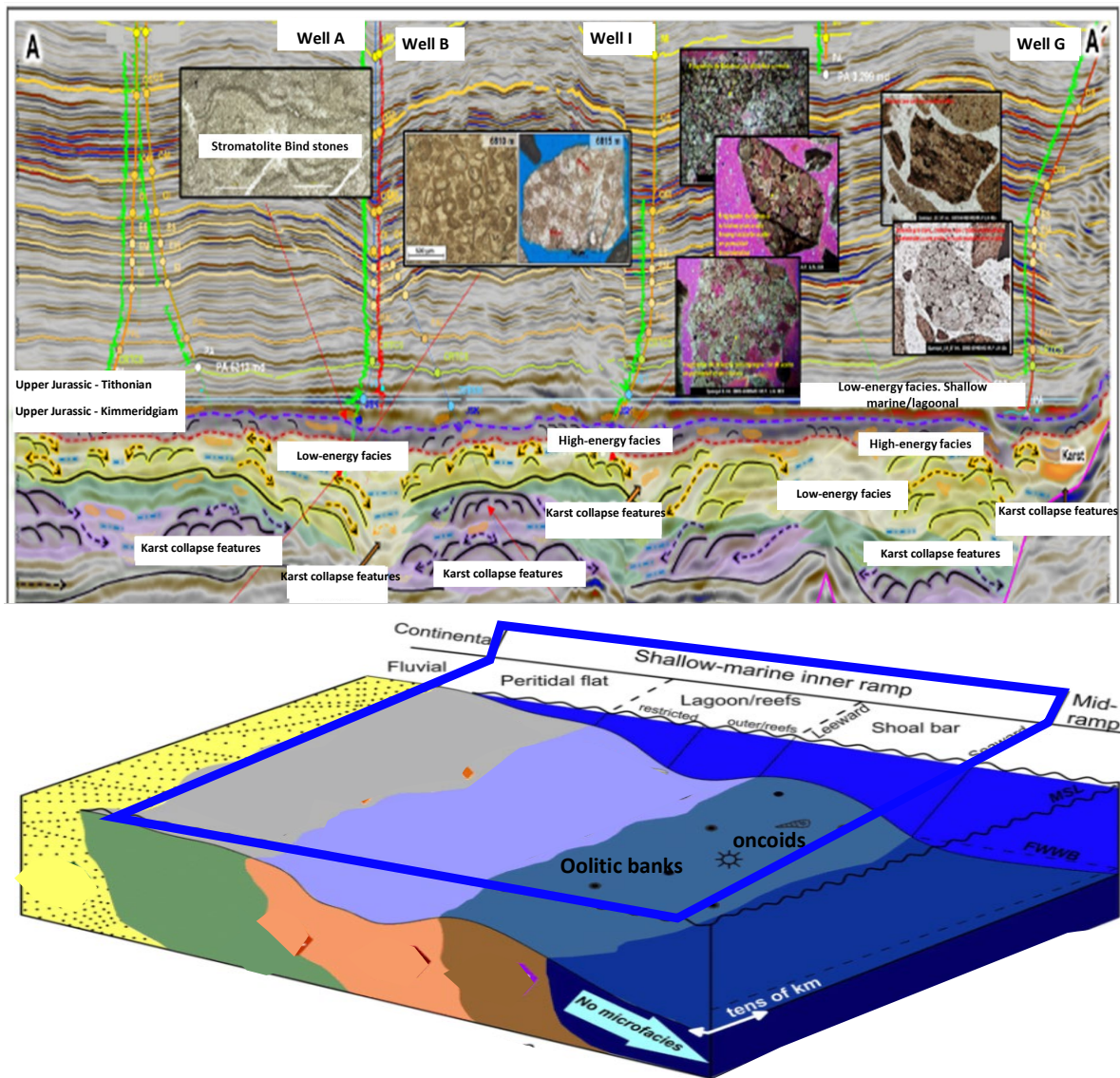


Fig. 3. Sedimentary model and lateral facies distribution. From D.R. Petroleos Mexicanos, 2021

sludge system, well structure, platform systems, or other

sources. Contaminants will significantly affect the quality and reliability of the data we provide to the customer, and effective and thorough cleaning is essential to provide quality data.

Complete drying of the sample is essential for accurate analysis and reliable and continuous operation of the XRF machine. If moisture or liquid is present in any amount of sample material, it will instantly convert to steam when the vacuum is applied to the sample chamber, causing internal contamination in the sample chamber. This will have a substantial adverse effect on the data and, over time, will cause contamination to accumulate on the tube and X-ray detector surface, further degrading the data's quality and the machine's longevity. For this reason, the preferred method of drying is by heat.

Lastly, samples are pulverized to start the analysis process. It is necessary to grind the XRF samples into a fine powder to homogenize (mix thoroughly) the sample to ensure that the machine analyzes the full range of forming material in the sample.

X-ray Fluorescence (XRF) analyses is carried out in a portable, energy-dispersive X-ray fluorescence (ED-XRF) spectrometer in conjunction with an extensive QA/QC process which ensures legitimate sample representation, not impacted by any contamination processes, thus providing a quantitative stratigraphic control during drilling.

Stratigraphic chemo and biostratigraphic controls are generated to determine the formation tops and the associated chemofacies. Once the samples have been processed, they are analyzed and integrated, incorporating other data sources with information from different wireline tools, among other disciplines (petrography, petrophysics, 3D seismic interpretation). Each step is explained in detail below.

A. QA/QC process (Quality assurance/quality control every five samples).

One of the most important and determining characteristics is correct geological evaluation and stratigraphic control. This is achieved through the evaluation of major and trace elements relationships.

To obtain accurate values and validate the variations and interpretations, these element analyses must undergo strict quality control. Each element is calibrated based on standards from the United States Geological Survey (USGS). This ensures that the sample measurements have not been affected by contamination by sludge, barium, or other agents that can modify the elemental concentrations.

B. Generation of a chemo-stratigraphic database of the well in sequence:

With the large database obtained from the offset wells (Well A, B, and I) 3 chemostratigraphic packages and 9 chemofacies were determined for the field of study, making it possible to reduce the uncertainty in the determination of the geological column in real-time during the drilling of the study well (Well G).

This methodology applies to all project wells and fields with geological complexity. This technique is of vital importance when the biostratigraphy information is scarce or non-existent, seismic resolution is poor, and the area to be studied is complex. Chemostratigraphic correlations indicate position in the geological column and serve as a reference to indicate fault zones and denote the changes in the paleoenvironment.

C. Elemental Gamma Ray (EGR).

Gamma radiation emitted by elements such as K, Th, and U and their decay products (also called ground-based radiation) exists at trace levels in all subsoil formations. It represents the primary external source of irradiation. Based on this principle, we can offer field records with mineralogy, lithology, and elementary gamma rays based on gamma radiation emitted by uranium, thorium, and potassium (U + Th + K), guaranteeing the quality of the sampling.

This data is beneficial (since it allows an elementary GR record in API units), especially when the LWD tools fail, avoiding the need to rerun tools leading to Non-productive Time (NPT). The higher the sampling density in the well, the greater the utility of the tool as it approaches the depth resolution of a GR Logging While Drilling (LWD) log.

D. Oxides and major elements.

Oxides of major elements are those that predominate in rock chemistry analyses. Among the elements measured in these analyses are Si, Ti, Al, Fe, Mn, Mg, Ca, Na, K, and P, and their concentrations are expressed in the percentage (% wt.) of the oxide. Through a proprietary stoichiometric model developed by Diversified Well Logging, mineralogical modeling was generated from X-ray fluorescence, which contains the most important minerals when performing real-time mineralogical correlations and at the regional level. The elements obtained from the mineralogical model are the following: Quartz, Clay (Illite, Chlorite, Kaolinite), Calcite, Dolomite, Apatite, and Halite.

E. Trace elements or oligo-elements

Trace element analysis can provide critical information for improving geological and oil system models by providing substitutes for paleo-depositional and redox environments. In geochemistry, a trace element is one whose concentration is less than 1000 ppm or 0.1% of the composition of a rock. This suite of elements mainly helps proxies.

F. Paleoredox Indicators.

Understanding the depositional configuration of organically rich sediments in the geological record is crucial to reconstructing the paleoclimate of sedimentary basins and the occurrence of oil source rocks [3,4,5,6]. When organic geochemical analyses are unavailable, the elemental paleoredox proxies (U, Mo, V, P₂O₅, Cu, Ni, Zn) are typically helpful in evaluating the chemical conditions of old water bodies, degree of oxygenation, salinity, and stratification of the water column in fine-grained sediments. Previous studies had strongly supported that Ni is a clear indicator of the organic sinking

flux, explained by the occurrence of diatoms, which dominate productivity in these systems [7,8,9]; Ni tends to be more soluble under oxidizing conditions and less soluble under reducing conditions. This particularity confers Ni as an excellent element to associate with organic matter concentration. By a linear correlation generated with the Total Organic Content of the pilot well, a proprietary pseudo-TOC model developed by Diversified Well Logging was generated for this study.

G. Plots-Binary Geochemical Correlations.

Through different elementary relationships, the correlation of binary plots provided an important degree of correlation ranging from 85-98% accuracy in defining

Micropaleontological and petrographic analyses were compared with the chemostratigraphic data, and the ratios of Ni/Al₂O₃, SiO₂/Al₂O₃, Th/K₂O, MgO/Fe₂O₃, CaO/Sr, and Al₂O₃/Zr and net intensities were found to be the most informative and discriminant. Binary plots correlated each geological period with its specific chemostratigraphic association, decreasing the geological column's uncertainty when drilling.

I. Cretaceous

Chemostratigraphic Package 1 (Units 1.1, 1.2, 1.3, and 1.4) mainly comprises the Upper, Middle, and Lower Cretaceous (Figure 4). The Upper Cretaceous (unit 1.1, 1.2) was characterized by a marked increase of the

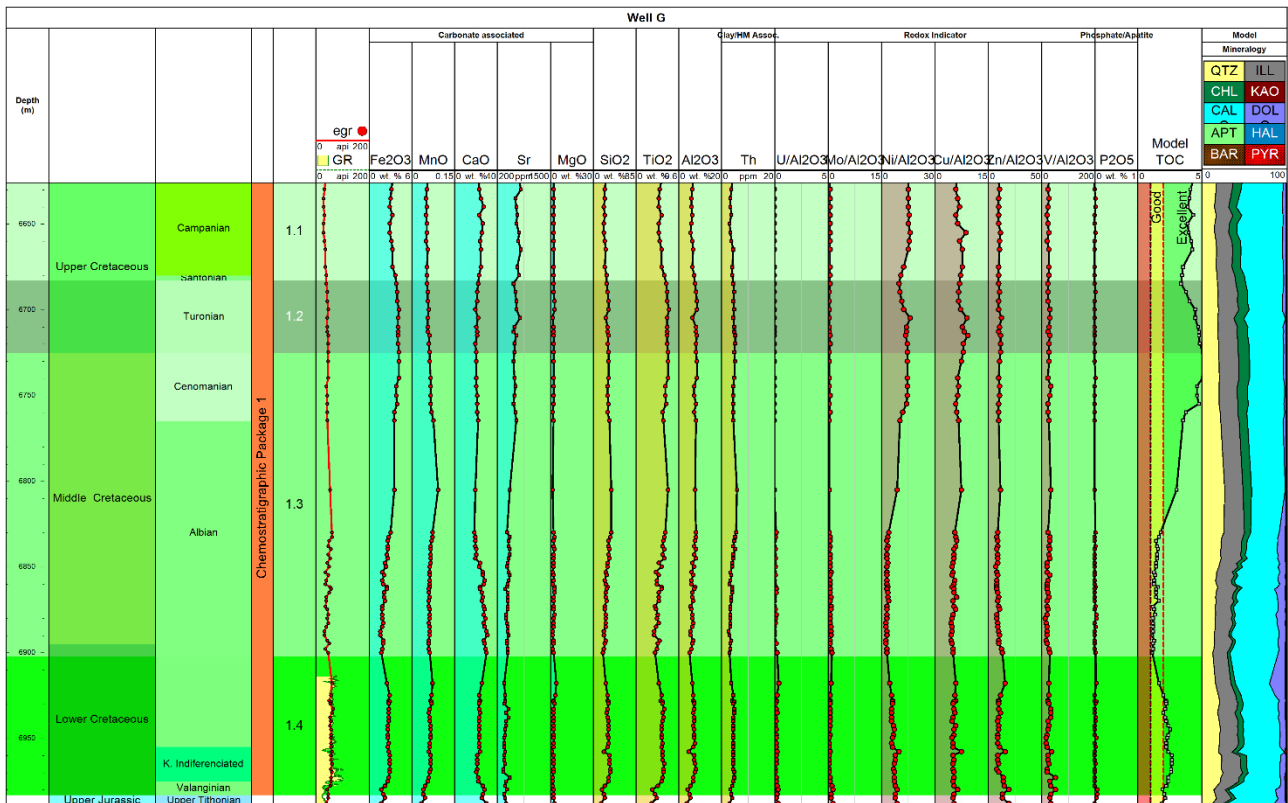


Fig.4. Chemostratigraphic profile of majors, trace elements, and paleoredox proxies from the Upper, Middle and Lower Cretaceous

the chemo-stratigraphic units used to correlate the offset wells with the I and G wells.

H. Potential types of clay generated from the binary plot of Potassium and Thorium.

Based on the high concentrations of potassium and thorium in the clays and through the stoichiometric calibration of K₂O, a preliminary clay model can be generated from this binary plot. This plot has been very helpful in estimating expansive clays that may affect well conditions or in the geological characterization of anoxic intervals with a high rate of organic matter.

3. Chemostratigraphic interpretations and their association with the geological periods

carbonate proxies with 25 wt.% Ca, and low concentrations of Mg and Mn at 2.7 and 0.06 wt.% and 780 ppm Sr on average, respectively. Detrital proxies

displayed a noticeable increase with 29 wt.% Si, 9 wt.% Al, 0.45 wt.% Ti, 2.3 wt.% K, 2.9 wt.% Fe on average.

The mineralogical model generated from the elemental data denotes a high presence of calcite with low concentrations of magnesium, possibly generated from secondary diagenetic processes, and moderate concentrations of quartz, illite, and chlorite associated with shaley intervals. Given the carbonate nature of this sequence, uranium concentrations are typically low. Anoxic proxies remain high throughout the whole interval (179 ppm V, 27 ppm Ni, 39 ppm Cu, and 66 ppm Zn) with a reasonably high pseudo-TOC model. In the Middle Cretaceous (unit 1.3), especially at 6765m-6835m, similar

concentrations for carbonate and detrital proxies remained constant throughout the interval (Carbonate proxies displayed 30 wt.% Ca, 1.97 wt.% Mg, 0.06 wt.% Mn and 450 ppm Sr, and detrital proxies, indicated 25 wt.% Si, 8 wt.% Al, 0.35 wt.% Ti, 2.01 wt.% K, 2 wt.% Fe on average). The anoxic proxies and the pseudo-TOC model remained moderate-high (with 170 ppm V, 29 ppm Ni, 30 ppm Cu, and 63 ppm Zn, on average). As calcium levels reduced at 22 wt.%, uranium concentrations moderately increased at 0.77 ppm. After 6835m, the detrital proxies progressively declined (at 34 wt.% Si, 9 wt.% Al, 0.40

wt.% Ti, 2.5 wt.% K, 3.1 wt.% Fe on average). In contrast, the carbonate proxies notably increased (32 wt.% Ca, 4.65 wt.% Mg, 0.07wt.% Mn, and 525 ppm Sr, on average), going for an elemental and lithological transition from homogeneous (marly) claystone to increasingly CaCO₃-rich marls and limestones. Anoxic proxies decrease simultaneously (with 156 ppm V, 26 ppm Ni, 25 ppm Cu, and 50 ppm Zn, on average), and the pseudo-TOC model declines significantly.

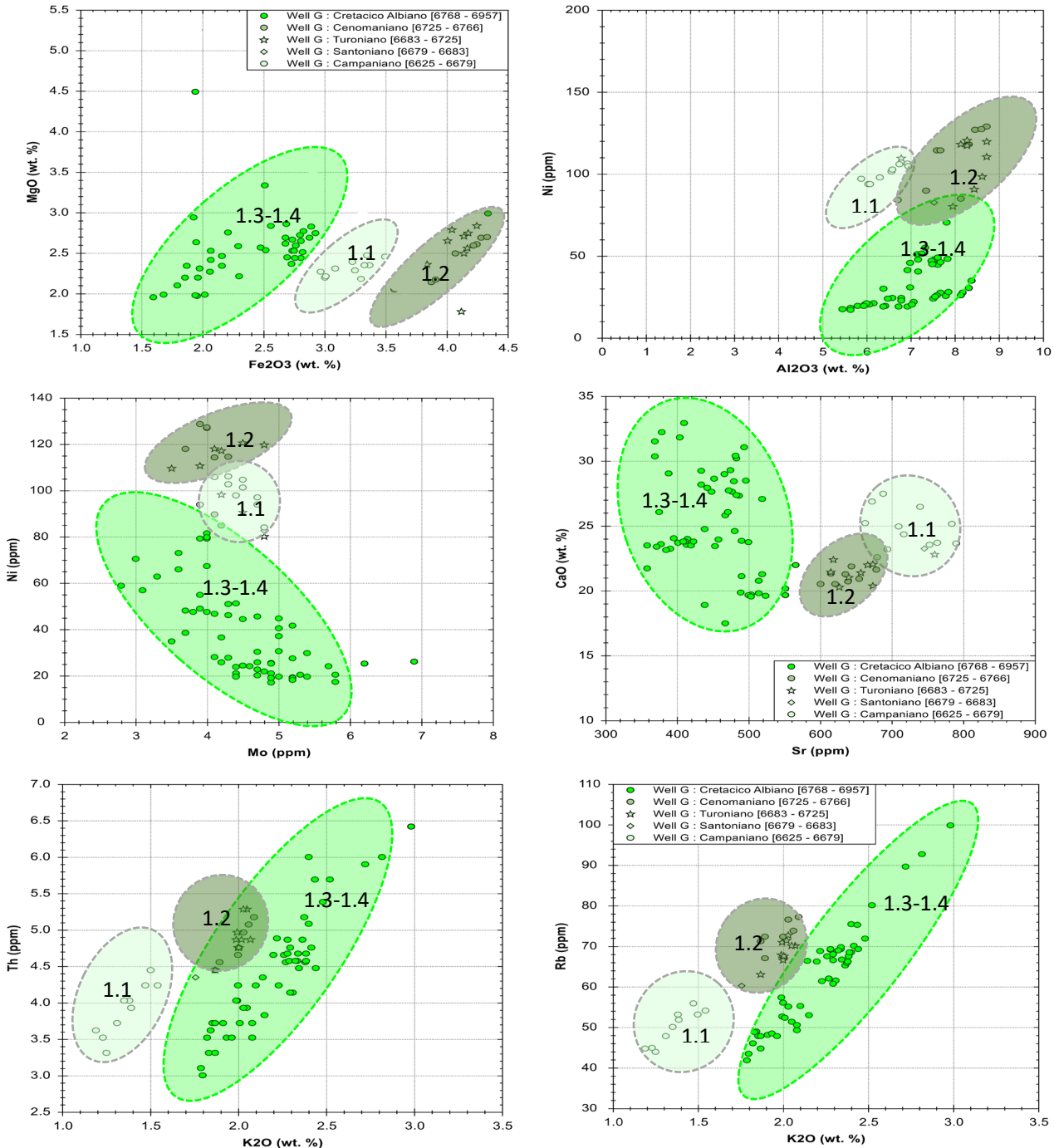


Fig. 5. Discrimination of chemostratigraphic units 1.1 and 1.2. Binary plots and association of chemo-facies in the Cretaceous (Albian, Cenomanian, Turonian, Santonian, and Campanian). A dashed bright green circle is associated with the Albian; a dashed olive-grey circle to the Cenomanian-Santonian, and a light green dashed circle to the Campanian

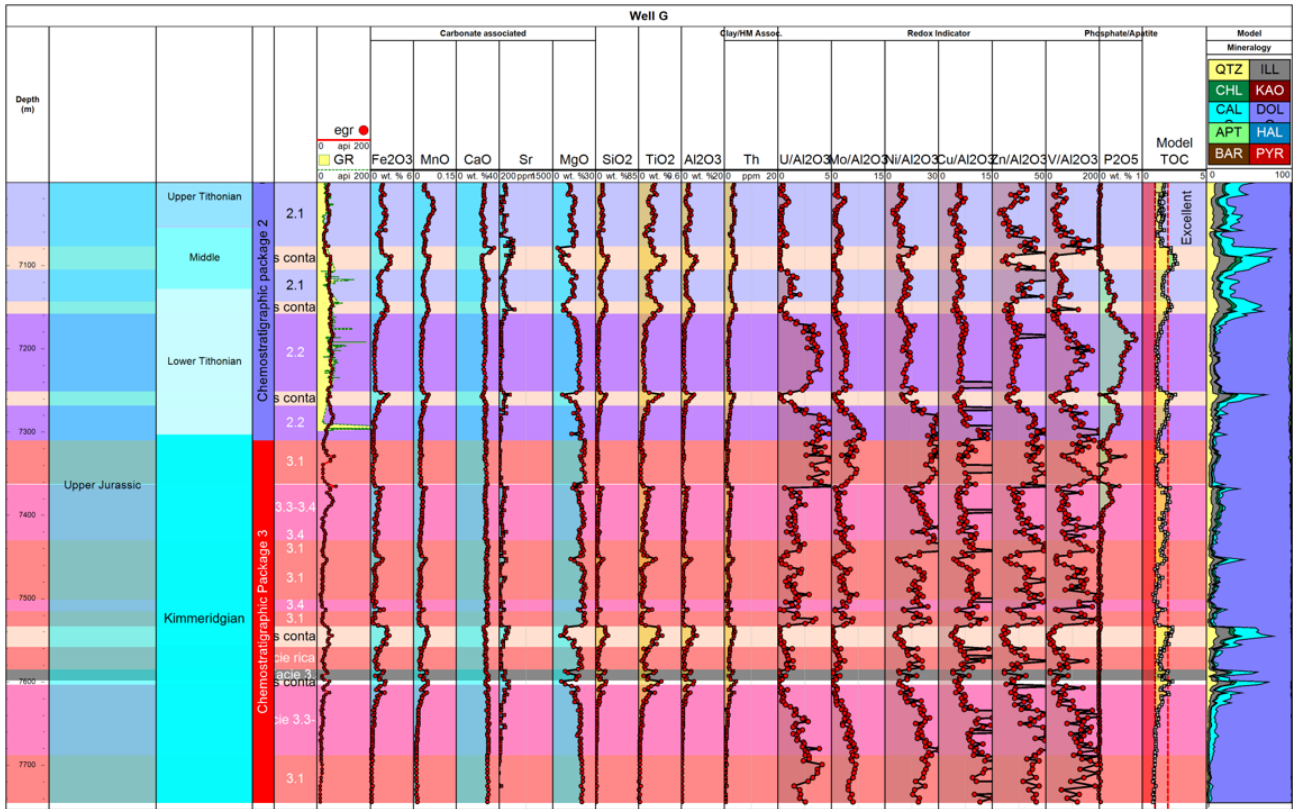


Fig. 6. Chemostratigraphic profile of majors, trace elements, and paleoredox proxies from the Upper Jurassic

Biostratigraphic data was absent in the Lower Cretaceous, at depths 6925m-6977m. However, the high sample density obtained from previous wells developed a chemostratigraphic correlation by the use of binary plots in Figure 5 (MgO/Fe₂O₃; Ni/Al; Ni/Mo; CaO/Sr; Th/K₂O and Rb/K₂O) that allowed to correlate the biologically barren interval with the 1.1 unit. The present correlation displays one of the most important correlations when we no longer can rely on biostratigraphic data.

Furthermore, in the Lower Cretaceous, at depths 6902m-6926m, a marked increase in the carbonate and paleoredox proxies (carbonate proxies at 34 wt.% Ca, 4.7 wt.% Mg, 0.09wt.% Mn, and 630 ppm Sr and paleoredox proxies at 280 ppm V, 47 ppm Ni, 40 ppm Cu, and 103 ppm Zn and 2.53 ppm U on average) displayed a new chemostratigraphic unit markedly differs from the previous units.

This horizon was named the chemostratigraphic unit 1.4. From the sequence-stratigraphic point of view, unit 1.4 could be associated with a maximum flooding surface often seen in the Albian in equivalent formations worldwide, where high paleoredox proxies displayed exceptionally high U, V, Cu, Mo, Zn, and Ni enrichments, representing environments associated with low oxygen concentrations.

II. Jurassic

It is known worldwide that in the Upper Jurassic, the Tithonian dolomite-rich beds were predominantly confined to the mound facies; The initial massive matrix dolomitization can be related to pressure dissolution during a very shallow burial, at temperatures of at least 50°C, where burial compaction provided sufficient fluids for dolomitization [10]. For well G, the Upper Jurassic Tithonian at a depth interval of 6990m-7303m was characterized by a noted reduction of detrital proxies (6 wt.% Si, 1.4 wt.% Al, 0.09 wt.% Ti, 0.53 wt.% K, 0.72 wt.% Fe on average) and a marked increase of the carbonate proxies (32 wt.% Ca, 19 wt.% Mg, 0.03 wt.% Mn, and 263ppm Sr on average), where magnesium concentrations remained constant throughout the whole interval. Despite the importance of magnesium in the early Upper Jurassic, calcium concentrations can be found as high as 20-23 wt. %.

From base to top, anoxic proxies represented a significant increase in V, Ni, Cu, Mo, and Zn (at 260 ppm; 240 ppm; 5 ppm, and 50 ppm, respectively) with a marked increase in phosphorus of 0.87 wt.% at the end of the Lower Tithonian, which according to some authors [11], represents an increase in phosphorus accumulation rate from microfauna, coincided with the worldwide Nannofossil Calcification Event, related to a bloom of strongly calcified calcareous nannoplankton taxa. The mineralogical model displayed a noticeable presence of dolomite with fewer calcite, illite, chlorite, and quartz

percentages. The pseudo-TOC model remained steady and is categorized as "good." This interval is associated with the chemostratigraphic package 2, units 2.1 and 2.2.

While analyzing samples in real-time at the rig-site, we came across intervals that, according to the previously mentioned binary plots association, denoted the presence of unit 1.1, along with highly contaminated barium

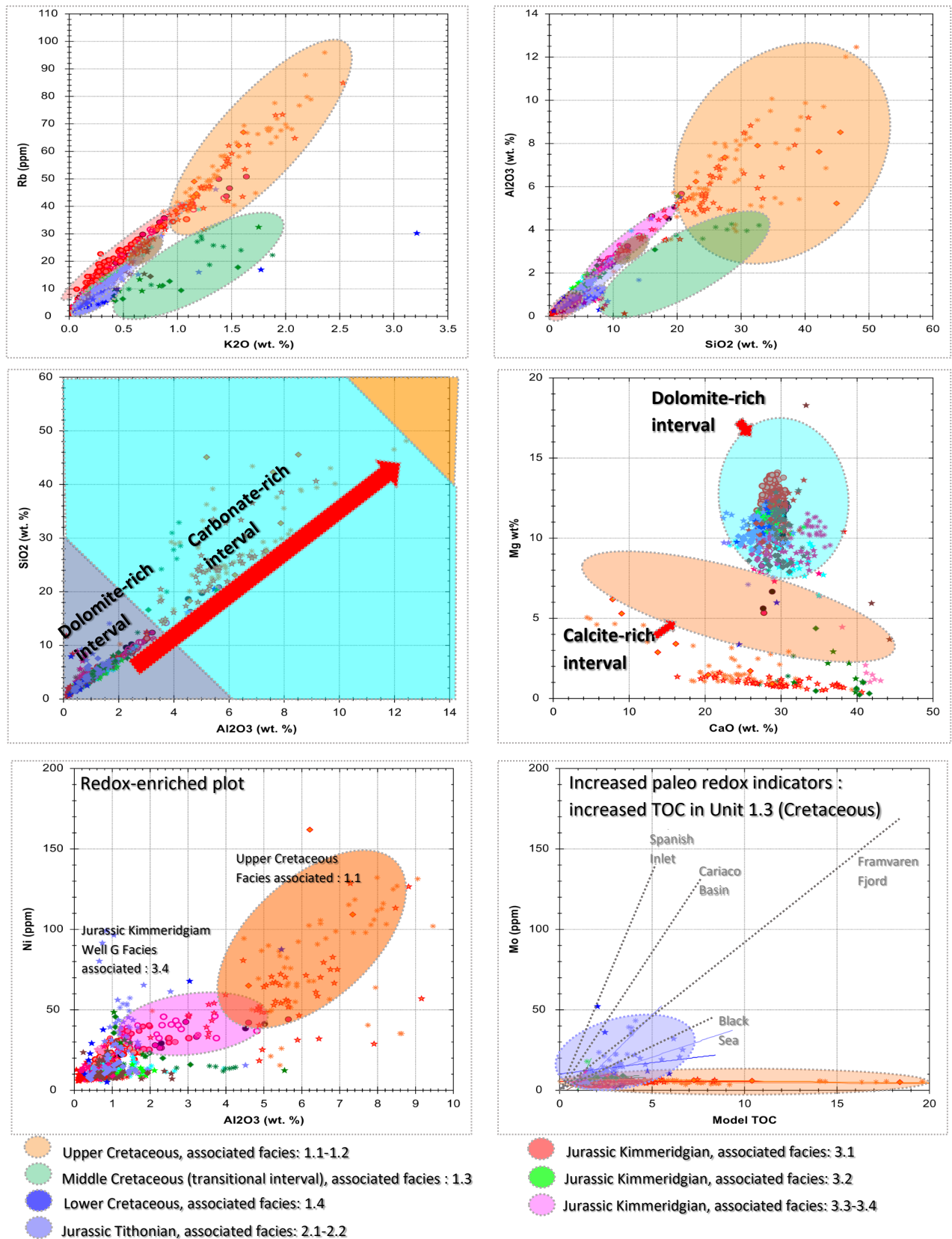


Fig. 7. Discrimination of chemostratigraphic units in the Cretaceous and the Jurassic period. Binary plots (Ni (ppm) vs. Al₂O₃ (wt.%); Rb vs. K₂O and Mo (ppm) vs. the pseudo-TOC model) and association of chemo-facies to the geological period. The light-orange circle is associated with Upper Cretaceous (Unit 1.1-1.2), Dark-green with Middle Cretaceous (Unit 1.3); Blue with Lower Cretaceous (Unit 1.4); Light-purple with Jurassic Tithonian (Unit 2.1-2.2); Light-red with Jurassic Kimmeridgian (Unit 3.1); Light-green with Jurassic Kimmeridgian (Unit 3.1, 3.2 and 3.3) and light-pink with Jurassic Kimmeridgian (Unit 3.4).

intervals where it was expected to see the Upper Jurassic samples. Based on the data obtained from chemostratigraphy and the reported biostratigraphy, it was interesting to notice that each time the well resumed operations, cuttings from above were contaminating the first interval samples, not displaying an accurate representation of the data.

This example can highlight the importance of real-time chemostratigraphy to differentiate contaminated intervals from variations in the depositional environment properly. In addition, chemostratigraphic sampling can provide important operational information to improve hole cleaning and wellbore stability. Furthermore, the Upper Jurassic Kimmeridgian (Figure 6) indicated the highest magnesium-rich interval, not previously seen in any of the wells previously studied in the field.

As mentioned before, specific proxies and binary relationships such as Ni (ppm) vs. Al₂O₃ (wt.%); SiO₂ (wt.%) Vs. Al₂O₃ (wt.%); Th vs. K₂O; Rb vs. K₂O and Mo (ppm) vs. the pseudo-TOC model allowed the understanding of the paleoenvironmental conditions for the Lower and Upper Cretaceous and Upper Jurassic (Figure 7).

When compared with the Upper Jurassic, a noticeable enrichment in the paleoredox proxies' concentrations was observed for the Upper Cretaceous; The anoxic proxies reduced, becoming more oxidizing (decreased concentrations in the paleoredox proxies at 128 ppm V, 34 ppm Ni, 11 ppm Cu, and 45 ppm Zn and 1.50 ppm U on average) generating a new chemostratigraphic package 3 (units 3.1, 3.3 and 3.4). However, the G well behaved slightly differently from the previous wells in the field since it displayed a lateral variation of chemo-facies with higher Mg, Al, Fe, and Zr concentrations as well as an increase of the paleoredox proxies such as U, Mo, V, P₂O₅, Cu, Ni, and Zn.

From the chemostratigraphic point of view, it could be predicted that the G well might display a much more favorable environment of deposition prone to developing good preservation of organic matter. Furthermore, it is also believed that the structural complexity could also affect the oil window, generating a better prospectivity than the previously analyzed nearby wells.

Figure 8 shows a structural section that displays the integration of geological data generated by the chemostratigraphy and biostratigraphy interpretation. Undoubtedly, the synergy of the two disciplines determined a better stratigraphic correlation for the structurally complex field of study.

Uncertainty was reduced when the formation tops were quantitatively picked, developing an accurate geological column in real-time, which showed an increase in thickness towards the southeast for the Upper Tithonian

and Kimmeridgian interval, perhaps associated with the karstic and subsalt structural control that potentially affected the thickness and even the diagenesis of the latest deposits.

Conclusions

Chemostratigraphic analyses, in conjunction with the ages provided by biostratigraphy, generated stratigraphic control while drilling, reducing the uncertainty and optimized decision-making during the wellbore completion process.

Chemostratigraphic interpretations are augmented through a comprehensive understanding of the mineralogical relationships between the elements and the regional geology.

The methodology generated by the QA/QC control and the elaboration of a mineralogical model from the elemental data recognizes subtle changes in the depositional environment that a standard set of records or even a visual inspection cannot detect.

A noticeable enrichment of paleoredox proxies was observed for the Upper Cretaceous in G well, where the paleoredox proxies associated with elements such as U, Mo, V, P₂O₅, Cu, Ni, and Zn displayed an increase in the redox conditions and a lateral variation of chemo-facies more favorable environment of deposition, prone to developing good preservation of organic matter for well G.

Furthermore, according to seismic data, the structural complexity found in the study area (salt intrusions, shale diapirism, and listric faults) could also affect the oil window, generating a better prospectivity than the nearby wells analyzed. It is important to understand when mineralogical composition and/or organic matter content is lacking while drilling. Chemostratigraphy would reduce the level of uncertainty as a helpful tool for understanding the lateral continuity of a geologically complex area.

Another advantage of using real-time chemostratigraphic interpretations could be attributed to the fauna's absence during the development of the geological column. Certain intervals in the geological column denoted scattered / absent fauna for some of the drilled Upper Jurassic intervals with no age dating for the specific intervals. Chemostratigraphic relationships and binaries plots correlated areas where biostratigraphy was absent, generating a chemostratigraphic association between units that determined lateral chemo-facies changes. An increase in diagenetical processes toward SE and especially for the G-well could be caused by the mechanical and chemical compaction in the sediments' primary textural and mineralogical composition at the deposition time and after

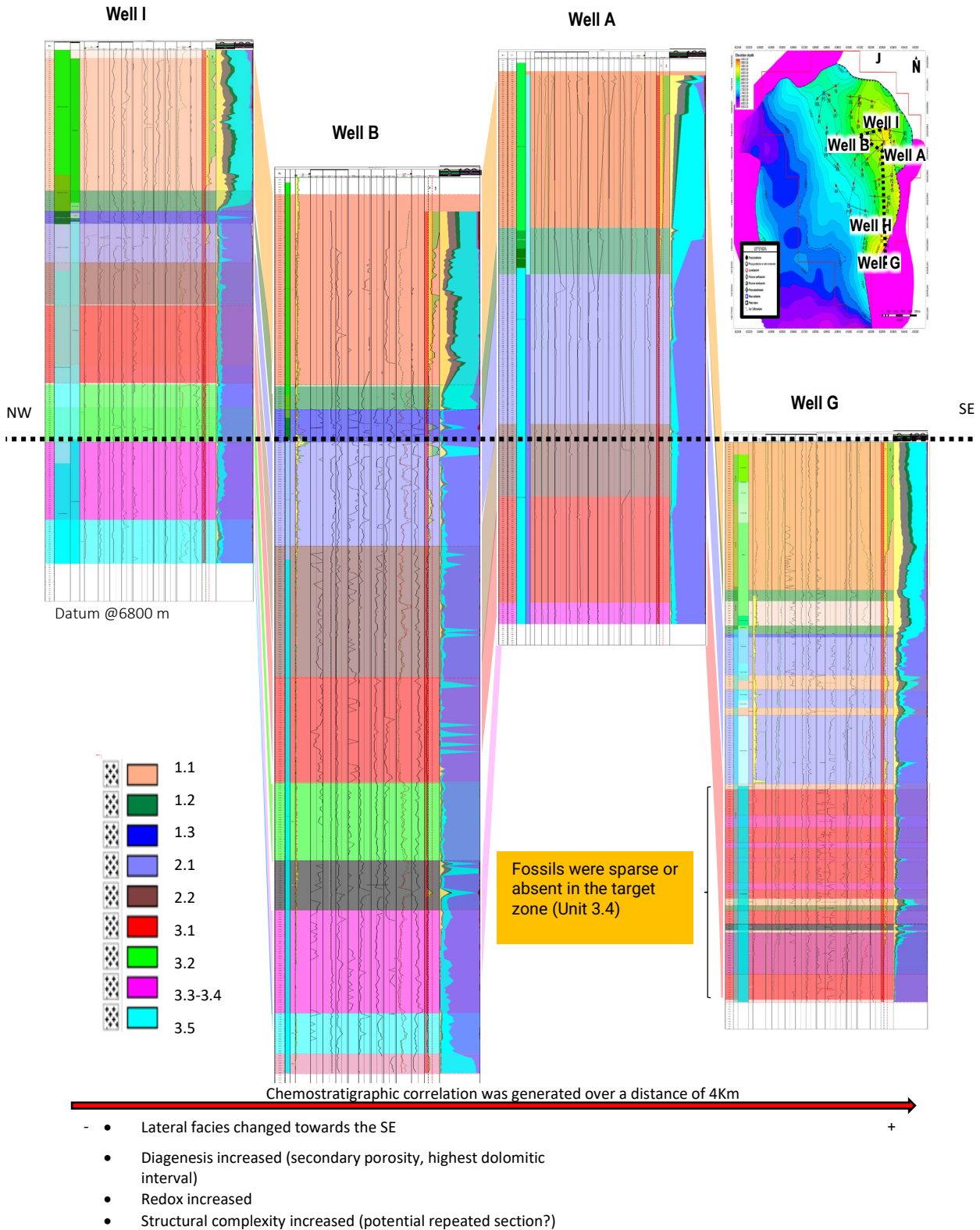


Fig. 8. Final chemostratigraphy correlations (per chemostratigraphy unit) for the Cretaceous and Upper Jurassic formations (structural cross-section).

burial diagenesis. Real-time petrographic and lithological analyses have validated these results with higher concentrations of Mg, Al, Fe, and Zr. The increase of the paleoredox proxies (U, Mo, V, P₂O₅, Cu, Ni, Zn) and the pseudo-TOC model predict a

In conjunction with micropaleontological and petrographic analyses, real-time chemostratigraphy contributed to successful well completion. It generated a high-level regional stratigraphic correlation, allowing an understanding of the lateral variation and deposition environment using the chemofacies as vertical correlation parameters.

Through the information provided by these analyses in developing a comprehensive stratigraphic framework, it is possible to improve well construction decision-making through greater geological certainty. This has practical applications for geo-stopping, geo-steering, picking casing points, picking coring points, and other real-time decisions.

Acknowledgments

Special thanks to the PETRICORE geoteam: Isaac Montes Silva, Miguel Martinez, Alejandro Pumarino, and Dr. Jose Berlanga Garcia. Thank you for the biostratigraphic data to culminate this project.

References

1. Ratcliffe, K., Martin, J., Pearce, T., Hughes, A., Lawton, D., & Wray, D. 2006. Regional chemostratigraphically defined correlation framework for the Late Triassic TAG-I formation in blocks 402 and 405a, Algeria. *Petroleum Geoscience*, 12(1), 3-12.
2. Craigie, N. 2018. *Principles of Elemental chemostratigraphy: A Practical User Guide*. New York, NY: Springer International Publishing, 189p.
3. Demaison, G. J., & Moore, G. T. 1980. Anoxic environments and oil source bed genesis. *AAPG Bulletin*, 64(8), 1179-1209
4. Calvert, S. E., Bustin, R. M., & Pedersen, T. F. 1992. Lack of evidence for enhanced preservation of sedimentary organic matter in the oxygen minimum of the Gulf of California. *Geology*, 20(8), 757-760.
5. Arthur, M. A., & Sageman, B. B. 1994. Marine black shales: depositional mechanisms and environments of ancient deposits. *Annual Review of Earth and Planetary Sciences*, 22(1), 499-551.
6. Sageman, B. B., Murphy, A. E., Werne, J. P., Ver Straeten, C. A., Hollander, D. J., & Lyons, T. W. 2003. A tale of shales: the relative roles of production, decomposition, and dilution in the accumulation of organic-rich strata, Middle-Upper Devonian, Appalachian basin. *Chemical Geology*, 195(1-4), 229-273.
7. Böning, P., Shaw, T., Pahnke, K., & Brumsack, H. J. 2015. Nickel is an indicator of fresh organic matter in upwelling sediments. *Geochimica et Cosmochimica Acta*, 162, 99-108.
8. Lewan, M. D., & Maynard, J. B. 1982. Factors controlling enrichment of vanadium and nickel in the bitumen of organic sedimentary rocks. *Geochimica et Cosmochimica Acta*, 46(12), 2547-2560.
9. Filby, R. H. 1994. Origin and nature of trace element species in crude oils, bitumens, and kerogens: implications for correlation and other geochemical studies. *Geological Society, London, Special Publications*, 78(1), 203-219.
10. Reinhold, C. 1998. Multiple episodes of dolomitization and dolomite recrystallization during shallow burial in Upper Jurassic shelf carbonates: eastern Swabian Alb, southern Germany. *Sedimentary Geology*, 121(1-2), 71-95.
11. Grabowski, J., Haas, J., Stoykova, K., Wierzbowski, H., & Brański, P. (2017). Environmental changes around the Jurassic/Cretaceous transition: New nannofossil, chemostratigraphic, and stable isotope data from the Lókút section (Transdanubian Range, Hungary). *Sedimentary Geology*, 360, 54-72.

Carbon Capture and Storage (CCS), Evaluation of Carbon Dioxide Storage Efficiency at the Western Siberia Field.

*Pavel Golub*¹, *Andrei Cheban*², and *Evgenii Romanov*³

¹Coretest Service, Deputy Chief Centre, 2a Lenina st., Russia

²Coretest Service, Head of the Laboratory, 2a Lenina st., Russia

³Coretest Service, General Director, 2a Lenina st., Russia

Abstract. Measures need to be taken to reduce the amount of carbon dioxide (CO₂) in the atmosphere due to climate change around the world. Storing CO₂ allows for more efficient carbon management practices. To date, the improvement of technologies for partial replacement of the buffer volume of gas in underground gas storages (UGS) with CO₂ and its disposal in a porous medium is an urgent task. Also, partial replacement of buffer gas by CO₂ will allow decreasing capital costs for UGS by means of the buffer gas volume decrease. The geological properties of UGS facilities determine the reliability of CO₂ capture and storage. The laboratory research stage is a fundamental component of the introduction of technologies. In the article, experiments were carried out on the injection of liquid CO₂ into a porous medium, and the processes occurring in the reservoir during the injection and storage of CO₂ were studied. The effect of liquid CO₂ on the mineral composition and reservoir properties of core samples was evaluated. The complex of filtration studies consisted of experiments on single-core samples of the target reservoir bed. The assessment of the impact of liquid CO₂ injection and holding at 7 days was carried out on core samples with residual water saturation in reservoir conditions. The article presents an analysis of the effect of liquid CO₂ on the mineral and reservoir properties of the core. On the basis of the research carried out, technical solutions were obtained for the efficient use of UGS facilities for CO₂ storage in Western Siberia.

A joint workflow towards a reliable quantification and understanding of NMR surface relaxivity

Matthias Halisch^{1,}, Raphael Dlugosch², Zeyu Zhang³, and Andreas Weller³*

¹Leibniz Institute for Applied Geophysics, Dept. 5 Petrophysics & Borehole Geophysics, D-30655 Hannover, Germany

²Federal Institute for Geosciences and Natural Resources (BGR), D-30655 Hannover, Germany

³Clausthal University of Technology (TUC), Institute of Geophysics, D-38678 Clausthal-Zellerfeld, Germany

Abstract. Nuclear Magnetic Resonance is a common tool for the oil and gas industry, as well as for academia and science in order to characterize porous rocks under different perspectives. It is utilized to characterize the pore fillings, i.e. if the pores contain oil, gas or other hydrocarbons, water / brine, or any mixture of the mentioned fluids. Besides, porosity and the related pore size distribution are of utmost importance to quantify the storage volume and transport properties of porous rock and according formations. Nevertheless, in order to transform transversal relaxation time spectra into a pore size distribution, a “tuning parameter” needs to be defined: the so-called surface relaxivity value, which is more or less the ratio of the surface area related to the pore volume. Very often, this parameter is estimated from nitrogen adsorption measurements, which can provide direct information about the specific surface area related to mass or to pore volume of the investigated specimen. Unfortunately, this approach tends to fail for many different rock types, especially, if the “mineralogical and textural complexity” (i.e., clay type and content, as well as occurrence of Fe- / Fe-oxide/-hydroxide minerals) increases in comparison to classic reservoir rocks (i.e., Berea or Bentheimer type rocks). Accordingly, this parameter is part of an ongoing discussion within the core analysis community for a long time by now. Here we would like to present a joint workflow (a combination of petrophysical and mineralogical methods, including 2-D and 3-D imaging) that is able to deliver very reliable and individual surface relaxivity values for core samples. Within this case study, we have tested about a dozen different sandstones, all together covering a large range of mineralogical and petrophysical complexity and data. The Workflow and the according results will be presented and discussed in detail in comparison to “conventional” approaches.

Comparison of Geophysics- and Core-based Wettability Assessment Methods: An Experimental Study using Artificial Grain Packs

Zulkuf Azizoglu and Zoya Heidari

The University of Texas at Austin, 78712 200E Dean Keeton St, Austin, TX, USA

Abstract. Conventional methods for wettability assessment are time-consuming and subject to non-uniqueness. We recently developed wettability models based on 2-dimensional Nuclear Magnetic Resonance (2D-NMR) and/or electrical resistivity measurements to address the aforementioned limitations. However, these methods require core-scale verification, which has been challenging due to the uncertainties in wettability distribution inside the core samples as well as lack of a reliable ground truth for wettability of a given sample. The objectives of this paper include (a) creating cylindrical synthetic rock models with controlled and wide range of wettability, (b) measuring 2D-NMR and resistivity responses in the synthetic samples, and (c) evaluating the performance of the new geophysics-based wettability models. We aggregate glass beads of different wettability levels to create cylindrical artificial grain packs with controlled wide range of wettability. Then, we alter water saturation and perform the aforementioned geophysics-based measurements. Results demonstrated that water saturation and wettability can be simultaneously estimated by integration of 2D NMR and electrical-resistivity measurements with average relative errors of less than 15% and 20%, respectively. We observed up to 50% relative difference in USBM indices and the fraction of water/hydrocarbon-wet beads. The outcomes of this work shed light on the reliability of different wettability quantification models/workflows.

Multi-Scale 3D Carbonate Digital Rock Reconstruction: Traditional or Machine Learning Approaches?

Yiteng Li^{1,}, Xupeng He¹, Marwa AlSinan², Hyung Kwak² and Hussein Hoteit¹*

¹King Abdullah University of Science and Technology, Thuwal, Saudi Arabia

²Saudi Aramco, Dhahran, Saudi Arabia

Abstract. This work aims to reconstruct multi-scale carbonate rocks using a model hybrid with Wasserstein generative adversarial network with gradient penalty (WGAN-GP) and variational auto-encoder (VAE). In particular, the WGAN-GP is trained to reconstruct macro-porosities, while the VAE reproduces microscopic porosity invisible in the μ -CT imaging process. The fine-scale structures are extracted from 2D SEM images by imposing a probability distribution on the latent space so that extracted features match input images. An automated workflow is proposed including dataset preparation, model training, and result screening. To obtain sufficient training datasets, we extract numerous subsamples from the original rock image with data augmentation techniques. To evaluate synthetic carbonate rocks, we compare both morphological and hydraulic properties of generated rocks with those of training samples. Morphological properties including two-point auto-correlation, Minkowski functionals and pore size distribution, are examined. In addition, we will calculate the single-phase effective permeability, relative permeability and capillary pressure to verify the connectivity and conductivity of synthetic rocks. It is observed that the combination of WGAN-GP with VAE shows great potential in reconstruction of multi-scale heterogeneous carbonate rocks. In contrast to other GANs using Jensen-Shannon divergence, the WGAN-GP honors a stable training even without any heuristics. Instead of frequently visual check of the training process, the loss curve of the discriminator provides an explicit indicator of the quality of the trained model.

NMR T2 Response versus Roughness: A Numerical and Analytical Study

Yiteng Li^{1,*}, *Xupeng He*¹, *Marwa AlSinan*², *Hyung Kwak*² and *Hussein Hoteit*¹

¹King Abdullah University of Science and Technology, Thuwal, Saudi Arabia

²Saudi Aramco, Dhahran, Saudi Arabia

Abstract. This work aims to develop an upscaling model using NMR T2 responses in smooth pore systems to evaluate T2 responses in rough pore systems. An upscaling factor is introduced as a function of a few dimensionless parameters (e.g. relative roughness, roughness density and shape factor) to characterize the surface-roughness effect. The proposed workflow has three main steps, including design and generation of synthetic 3D structures, simulation of NMR T2 responses, and modeling of roughness impact. Latin hypercube sampling is used to design rough pore structures with different relative roughness, roughness density and shape factor. Then random walk simulations are implemented and a robust T2 inversion algorithm is used to calculate NMR T2 responses in rough pore systems. We also evaluate the effective radii of smooth pores so that the corresponding T2 responses match up with NMR T2 responses in rough pore systems. Eventually, we establish a “value-to-value” model using machine learning to map the nonlinear relationship between the roughness parameters as input and the upscaling factor as output. The accuracy of the proposed model is validated by comparing NMR T2 responses with those directly simulated in rough pore systems. Numerical results show that the proposed model can estimate NMR T2 responses in rough pore systems using NMR T2 responses in smooth pore systems, with remarkable speedup around three orders of magnitude. We note that the generated surface roughness is supposed to have the characteristics of both diversity and representativeness. Missing either of them could damage the quality and reliability of the trained model. Previous work incorporating the roughness effect into surface relaxivity more likely violate the assumption of fast diffusion limit. Instead, the proposed model mitigates this limitation by introducing an upscaling factor, which incorporates multiple dimensionless parameters.

Nuclear magnetic resonance laboratory study of a tight sandstone for robust permeability prediction

Jun Gao^{1*}, *Hyung Kwak*¹, *Abdullah Alkhaldi*¹, and *Gabor Hursan*¹

¹Saudi Aramco, 31311 Dhahran, Saudi Arabia

Abstract. Laboratory nuclear magnetic resonance (NMR) rock core experiment to obtain calibration parameters is essential for accurate formation property assessment from the NMR logs. These parameters may include T2cutoff to distinguish bulk volume irreducible (BVI) and bulk volume movable (BVM) and coefficients (C, m, and n) in the Timur-Coates equation. Unconventional tight sandstones may be desaturated by sufficiently high pressures through trial and error. This study reports a new experimental and data analysis procedure to develop the T2cutoff models from two tight gas wells and to determine parameters of Timur-Coates permeability equation with both effective and total porosity. A modified exponential model is applied to fit the T2cutoff data as a function of desaturation pressure to obtain the asymptotic T2cutoff at irreducible saturation for all samples. T2cutoff values (~15ms) are derived for two groups from their different average experimental results (16.2 and 32.1ms) at different desaturation pressures. The parameters of Timur-Coates permeability equation are obtained by an optimization procedure which minimizes difference to the 1 to 1 line in a measured vs. predicted permeability plot. The proposed laboratory calibration procedure overcomes certain instrument and sample selection limitations and determines the calibration parameters following a standardized optimization procedure instead of the qualitative criteria for different interpretation scenarios. Furthermore, the developed T2cutoff model and optimized Timur-Coates permeability equation parameters have been successfully applied to 4 tight gas wells which verified to be agreed well with production and laboratory data.

NMR Spin-spin Relaxation in Unconventional Source Rocks

Z. Harry Xie¹*

¹Core Laboratories, 6316 Windfern Road, Houston, Texas 77040, USA

Abstract. NMR spin-spin relaxation, often known as T2 relaxation or transverse relaxation, has been successfully used in well logging and core analysis. The T2 is commonly measured using the Carr-Purcell Meiboom-Gill (CPMG) sequence. Such an experimental method is based on a key factor that the actual NMR signal decay rate (intrinsic T2) is significantly longer than the decay rate of the free induction decay (T2*). In other words, the CPMG echo train technique is mostly applicable to less restricted liquid cases. When dealing with unconventional tight rocks, where the spin-spin relaxation has much faster rates of sub-milliseconds range, the traditional CPMG method of measuring T2 faces challenges. In this work, the general conditions of using the CPMG pulse sequence is reviewed. Examples of T2 distributions with various inter-echo spacing times (TE) from unconventional shale samples demonstrate the non-exponential nature of the spin-spin relaxation in source rocks. Simply shortening TE is not a solution. The early-time NMR signals from rigid solids in source rocks provide further evidence of the non-exponential characteristics of the spin-spin relaxation process. The experimental observations of this work will lead to more accurate interpretations of NMR data of both well logging and core analysis for unconventional reservoirs.

SEM image-constrained process-based modeling for relative permeability estimation of carbonate-rich mudrock

Christopher J. Landry^{1,*}, Masa Prodanovic¹

¹University of Texas at Austin

Abstract. Here we present a digital rock physics approach to estimating the hydrocarbon-water relative permeability of carbonate-rich mudrocks. Bench-scale ‘plug’ steady-state relative permeability measurement of mudrocks (i.e. lithologies with sub-microdarcy permeability) typically requires weeks to months to reach convergence which limits the number of measurements available, while providing limited information of the fluid distribution (i.e. a ‘black box’ type issue). We investigate the relative permeability of oil-water flow in a carbonate-rich lithology from the Eagle Ford formation in southeast Texas using a digital rock physics approach. We utilize high-resolution large-area SEM image mosaics to collect bulk measurements of porosity, primary porosity, and porous solid bitumen (PSB) volume fraction, as well as pore size and shape distributions of the primary porosity (grain-scale) and porous solid bitumen (PSB-scale). These measurements are used to constrain process-based primary porosity (grain-scale) and PSB-scale three-dimensional models pore space. The distribution of PSB in the primary pore space, as well as the absolute and relative permeability of the pore space models were measured using pore-scale lattice Boltzmann methods (LBM). The primary porosity measured from SEM images is estimated by the grain-scale models to be well connected. For the primary porosity, and PSB volume fractions measured from SEM images the grain-scale models estimate the primary porosity to be obstructed by the PSB, therefore pore connectivity (at SEM resolution: ~5-10 nm pores, 1-3 nm pixel side-length) would require a connected path through the pores in the PSB. The porosity of the PSB falls below the percolation threshold of the PSB pore models. The pores of the SEM images are not estimated to be connected by the process-based models; however, it can be speculated that there is a connected molecular-scale pore network that exists below the resolution of the SEM images. Considering our ‘large-area’ images are approximately the size of the cross-section of a human hair, we explore the hydrocarbon-water permeability of the imaged lithology without PSB. The models predict a permeability jail for water saturations between 0.42 and 0.85, 0.46 and 0.76, 0.55 and 0.67 for primary porosity of 11.7, 14.5, 17.7%, respectively.

Multi-Phase Flow in Fractured Rocks: From Pore-Scale Processes to Field-Scale Responses

Xupeng He^{1,*}, *Marwa AlSinan*², *Hyung Kwak*² and *Hussein Hoteit*¹

¹King Abdullah University of Science and Technology, Thuwal, Saudi Arabia

²Saudi Aramco, Dhahran, Saudi Arabia

Abstract. This work introduces a workflow to quantify how pore-scale processes impact the field-scale responses through multi-scale uncertainty quantification and sensitivity analysis. There are three components within our workflow: 1) performing high-resolution Navier-Stokes (NS) simulation at pore-scale to obtain hydraulic aperture of discrete single fractures, 2) performing two-phase flow simulations at pore-scale to construct relative permeability curves, and 3) embedding pore-scale parameters into core-scale for predicting field-scale objective, such as recovery factor. At pore-scale, we start with three parameters that characterize the fractures: roughness, tortuosity, and mechanical aperture. We then construct hydraulic aperture, relative permeability, and fracture's volume surrogates using polynomial chaos expansion (PCE). At core-scale, we perform Monte Carlo simulation and deploy Kernel Density Estimator (KDE) to re-construct hydraulic aperture, relative permeability, and fracture's volume distributions. We also use Gaussian copula to accommodate the correlation among them. The objective function is recovery factor at field-scale. The final results are time-varying probability density function (PDF) of recovery factor and its sensitivity analysis. Using Sobol indices, we can obtain multi-scale sensitivity analysis to quantitatively demonstrate the effect of pore-scale parameters to the recovery factor at field-scale. From this study, fracture roughness significantly influences the hydraulic aperture estimation and further impacts the core-scale hydraulic properties estimation, and finally significant effect on recovery factor calculation. Therefore, in the future, pore-wall roughness should be included into the NFR characterization workflow.

Direct measurement of in-situ hydrogen-water-quartz system relative permeability for Underground Hydrogen Storage in A Depleted Gas Reservoir

Scott Higgs¹, Ying Da Wang¹, Jonathan Ennis-King², Samuel J. Jackson², Ryan T. Armstrong¹, Peyman Mostaghimi¹

¹School of Minerals & Energy Resources Engineering, University of New South Wales, Kensington, NSW 2052, Australia

²CSIRO Energy, Clayton South, Victoria, Australia

Abstract. Underground Hydrogen Storage (UHS) is considered a long-term storage solution which allows excess energy developed from renewable energy sources, such as solar PV and wind turbines, to be stored in the subsurface and retrieved when energy demand increases. Research into UHS has been increasing in recent years. Petrophysical properties of hydrogen interacting with fluid and solid in subsurface porous media, such as wettability, interfacial tension and relative permeability have emerged to provide a practical basis for simulation models. Our work elucidates for the first-time, direct measurement of in-situ wettability during co-injection core floods with hydrogen and water. Analysis of micro-CT images coupled with MICP and simulation data has enabled a thorough and accurate investigation of saturation in the bentheimer core. Relative permeability curves have been validated with laboratory experiment, direct simulation on micro-CT images and simulation using MRST, a multiphysics simulation platform which has been used to implement multiphase flow in porous media. The bentheimer core sample used is representative of many target formations for UHS particularly depleted gas reservoirs and aquifers. We have developed site-specific models using our direct petrophysical measurements to analyse the practical application of UHS at the field scale with simulation models in MRST. Our results have allowed us to reliably predict the amount of hydrogen that can be stored and retrieved in the cyclical storage process and to quantify expected rates of injectivity and deliverability during operation. They also demonstrate the significance of depleted gas reservoirs for the energy transition and their use for storage of hydrogen at a large scale.

Characterization of surface conductivity of clays

*Viacheslav Emelianov*¹, *Zeyu Zhang*², *Konstantin Titov*¹, *Matthias Halisch*^{3,*}, and *Andreas Weller*²

¹Institute of Earth Sciences, Department of Geophysics, St. Petersburg, Russia

²Technische Universität Clausthal, Institut für Geophysik, Clausthal-Zellerfeld, Germany

³Leibniz-Institut für Angewandte Geophysik (LIAG), Sektion 5 –Gesteinsphysik & Bohrlochgeophysik, Hannover, Germany

Abstract. Clay minerals are extensively used in a wide range of applications. They are a key component in the production of ceramics, concrete, drilling fluids, molding sands, paints, and paper. Furthermore, clay formations can be used as radioactive waste repository. However, the hydrodynamic regime within such kind of storage should be considered due to possible interactions with groundwater. Electrical resistivity tomography can be used as one of the monitoring methods. A conclusive interpretation of field data requires reliable knowledge on the electrical properties of clays that are gained in laboratory experiments. The main purpose of this study is the investigation of the electrical properties of clay samples with a special focus on the contribution of surface conductivity. The influence of water content on complex conductivity values for four clay powder samples was investigated by the spectral induced polarization method. Experiments were conducted with kaolinite, illite, bentonite clays, and a breccia containing saponite (~ 90%). We also employed density, cation exchange capacity and specific surface area measurements to characterize the samples. The measured complex conductivity spectra indicate a decrease of the real part of electrical conductivity with rising water content for the illite, bentonite and saponite breccia samples. The electrical conductivity of kaolinite does not show any significant changes with water content. Kaolinite indicates an iso-conductivity situation with similar conductivities of the solid and liquid phases, whereas the total conductivity of the other three samples is dominated by the contribution of surface conductivity. The imaginary part of electrical conductivity increases with water content. Moreover, we observed an increasing porosity and decreasing surface conductivity with increasing water content. Finally, the ratio between imaginary conductivity and surface conductivity increased with increasing water content (i.e. with a decrease of clay content).

Manganese-Ion Based Tailored Waterflooding Processes for Carbonates

Amani Alghamdi^{1*}, Saleh Salah¹, Mohammed Otaibi¹, Subhash Ayirala¹, Ali Yousef¹

¹Saudi Aramco

Abstract. In this experimental study, we explored the wettability alteration capability of divalent foreign metal constituents, such as manganese ions, in the injection water for enhanced oil recovery (EOR) in carbonates. The wettability alteration capability of manganese ions is first evaluated by measuring zeta-potentials at calcite/brine and crude oil/brine interfaces. These measurements were then extended to carbonate rocks and reservoir cores by performing contact angle and spontaneous imbibition tests at reservoir conditions.

The zeta potential results indicated that the addition of 100-1,000 ppm of manganese ions to the high salinity injection water (57,670 ppm TDS) can favorably alter the wettability towards water-wet conditions in carbonates. These wetting transitions were confirmed by the resulting increased values of same polarity negative surface charges measured at both oil/brine and calcite/brine interfaces. Such interesting trend of enhanced negative zeta potentials observed with manganese ions at the calcite/brine interface can be attributed to the selective incorporation of foreign metal ion into the calcite crystal structure to modify its surface chemistry. The contact angle data demonstrated good agreement with zeta potential results. Manganese ions were able to drastically decrease the contact angles from 156° to 88° to confirm the favorable wettability alteration from oil-wet to intermediate/water-wet conditions. The results from spontaneous imbibition experiments showed about 10% increase in oil recoveries due to enhanced imbibition of manganese containing injection water into the carbonate cores at the reservoir temperature. These consistent trends obtained from micro-macro-core scale experiments thereby revealed the promising potential of manganese ion based tailored water flooding processes for enhanced oil recovery in carbonates.

This work for the first time highlighted the beneficial effects of including manganese ions in the waterflooding injection water to enhance the wetting transition in carbonates. The presented novel findings have also identified manganese ions as cheap and sustainable wettability modifiers for advanced waterflooding applications in carbonate reservoirs.

Development and testing of a new 10000 PSI NMR overburden probe

*Michael Dick*¹, *Dragan Veselinovic*¹, *Taylor Kenney*¹ and *Derrick Green*¹

¹Green Imaging Technologies, Fredericton, NB, Canada

Abstract. It is well known the measurements at overburden pressures can greatly affect any petrophysical properties, most notably porosity and permeability. NMR measurements are also affected by overburden pressures. Existing NMR compatible pressure vessels are limited in pressure, have signals from the vessel itself that makes interpreting the NMR results difficult or lack sufficient pressure safety measures. Previously, we presented work which employed an Oxford Instruments P5 overburden cell (SCA2016, Dick et al., SCA2018, Dick et al., SCA2019, Dick et al.). This cell's design was optimized from a signal to noise standpoint as its NMR components were embedded into the vessel itself. However, it was limited in its operating pressure (<5000 PSI) and had significant background signals from the cell itself.

In this work, we expand on the original design of the P5 overburden cell to remove background signals and increase the working pressure to 10k psi. Modification to internal components to NMR invisible materials and changing the secondary containment system to metal are the main modifications. The investigation included exploring various grades of metals for their use within an NMR instrument. Specifically, the magnetic susceptibility and the production of magnetic field eddy current due to the magnetic field switching used in an NMR were explored. Further, the pressure seals within the probe have all been upgraded allowing a maximum confining pressure of 10000 PSI to be achieved. Finally, the NMR frequency of the probe has been changed from 2MHz to 12 MHz improving the SNR performance by approximately 10X.

A semi-analytical model for capillary entry pressure of pores in carbonates with varying wettability states

Yanbin Gong^{1,*}, Bradley William McCaskill¹, Mohammad Sedghi¹, Mohammad Piri¹

¹Center of Innovation for Flow through Porous Media, Department of Petroleum Engineering, University of Wyoming, Laramie, Wyoming 82071, United States

Abstract. Pore-network modeling has served as a practical simulation tool for predicting multiphase flow functions (e.g., relative permeability and capillary pressure curves) of porous media, owing to its superior computational efficiency. However, in traditional pore-network models, the rock pore space is largely simplified, and the fluid flow and solute transport are solved in a network of pore elements with idealized geometries. Such simplification can lead to inaccurate predictions when the original pore space features highly diverse and complex geometries as those observed in carbonates. To address this issue, we propose to couple the pore-network modeling approach with a semi-analytical model that can faithfully and efficiently predict capillary entry pressure and the corresponding fluid configuration of piston-like displacements using real, two-dimensional (2D) images of the pore space. To this end, an algorithm for identifying and extracting 2D pore cross sections from the corresponding 3D images of the pore space is developed and incorporated within an existing pore-network extraction platform. Enhanced pore networks, which contain images of real pore and throat cross sections, are constructed from high-resolution micro-computed tomography (micro-CT) images of carbonate rock samples. Next, we apply the semi-analytical model to the pore and throat elements of the enhanced pore networks to estimate their capillary entry pressures under different wettability conditions. The results are then compared against predictions obtained from a traditional pore-network model on a pore-by-pore basis. We show that characterizing the multiphase flow properties of the carbonate pores with a sole reliance on the inscribed radius and the shape factor, which is a common practice adopted in traditional pore-network models, is insufficient. We further explore other geometric properties (e.g., convexity, solidity, and aspect ratio) of the pore space and analyze their effects on the final estimation of the capillary entry pressures.

In-situ Characterization of Carbonate/Oil/SmartWater Interfacial Layers Using Advanced EM Techniques

Dongkyu Cha^{1,*}, *Mohammed B. AlOtaibi*¹, *Subhash Ayirala*¹, *Ahmed Gmira*¹ and *Ali A. Yousef*¹

¹Saudi Aramco, EXPEC ARC, Dhahran 31311, Saudi Arabia

Abstract. The visualization and characterization of interactions between SmartWater, oil and carbonate rock play a major role to understand the causative mechanisms behind wettability alteration and enhanced oil recovery. However, conventional imaging methods fail to provide such important analysis due to limited resolution and visualization capabilities.

To address this gap, cryogenic electron microscope (EM) and liquid cell holder have been utilized in this study. The results from each of these techniques are discussed and compared. The liquid cell transmission electron microscope (TEM) holder with an encapsulation function feature successfully enabled the direct observation and analysis of liquid sample close to its native conditions. Energy dispersive spectroscopy (EDS) analyses have been simultaneously utilized to provide the chemical mapping of rock-fluid interfaces. These results provide, for the first time, nano-scale images of oil droplets, calcite nanoparticles and dissolved salt ions in their native environment. The compositional distribution of multiple elements and elemental mapping of the structures in solution are also presented.

The presented novel nanoscale characterization brings a new insight about the rock-oil-brine interactions and this understanding can become critical to optimize the salinity and SmartWater compositions used for enhanced oil recovery in carbonate reservoirs.

Study on Adsorption Behavior of a New Type Gemini Surfactant onto Quartz Surface by Molecular Dynamics Method

Weifeng Lyu^{1,*}

¹State Key Laboratory of Enhanced Oil Recovery, Research Institute of Petroleum Exploration & Development, CNPC, Beijing, China

Abstract. Compared with traditional single-chain surfactants, Gemini surfactants have lower critical micelle concentration (CMC) and higher surface activity. The adsorption mechanism of the branched quaternary ammonium salt Gemini surfactant (Gemini C3) at the water-surfactant-quartz interfaces is studied by Molecular Dynamics (MD) method. Simulation snapshots of the Gemini C3 adsorption configuration show the molecules in the first layer are adsorbed with all the head groups facing the neutral quartz surface, and those in the second layer move into the water layer forming micelles by self-assembly. The relative concentration profile is higher in the first layer. Mean square displacement (MSD) curve of surfactant molecules gradually increases in the range from 150 to 500 ps, and become significantly larger than that of the water molecules after 250 ps. for the moving of surfactant molecules and the separation of two layers. More water molecules around the head group of the surfactant molecules are observed after the response to imply the formation of aggregated structure with increasing interaction between them. This work revealed the microscopic adsorption mechanism of the Gemini C3 surfactant onto the quartz surface, and provided theoretical guidance for controlling the wetting properties and surface modification of the rock, highlighting the potential for EOR.

Novel Evaluation of Oil Recovery in Rock-Like Mixed-Wet Microfluidic Systems

Abdullah AlOmier¹, Antonia Sugar¹, Dongkyu Cha², Subhash Ayirala², Mohammed AlOtaibi², Ali Yousef², and Hussein Hoteit^{1,}*

¹ Ali I. Al-Naimi Petroleum Engineering Research Center, King Abdullah University of Science and Technology, Thuwal 23955, Saudi Arabia

² PE&D, Saudi Aramco, Dhahran 34464, Saudi Arabia

Abstract. Oil-brine-rock wettability is an important petrophysical feature that affects fluid distribution and multiphase flow in hydrocarbon reservoirs. The industry is highly interested in assessing the recovery mechanisms in mixed-wet systems like carbonate and shale reservoirs. Microfluidics is a technology that can directly visualize and assess flow dynamics at the pore scale. However, when it comes to simulating mixed-wet environments, this approach has several drawbacks. For the first time, we use microfluidic devices to study the impact of wettability on oil recovery in formations with single and mixed wettabilities. The microfluidic system is designed to mimic the true pore network of an oil-bearing reservoir rock, as determined by thin-section photographs of a core. The microdevices were made of silicon for its compatibility with oil. The microfluidic substrates with regulated wettability, including water- and mixed-wet systems, were built using a unique approach that mimicked pore-network formations with varied pore-throats. We performed several sets of comparative experiments to investigate the wettability effect on oil recovery at the pore scale. Fluid flow was conducted in silicon-based microfluidic devices holding the same pore-network structure but differed in the wetting state. One microdevice did not undergo any surface modification processes and had a hydrophilic surface, mimicking a water-wet system. A second microdevice underwent selective wettability alteration and had hydrophilic and hydrophobic surface regions, mimicking a mixed-wet system. The flow experiments conducted shared identical conditions: water injection in oil-saturated microdevices. Results showed a reduction in the oil recovery and thus a higher remaining oil saturation in the mixed-wet compared to the water-wet microdevice with distinct phase distributions. The results highlight the importance of using accurately designed microdevices to mimic mixed-wet formations when evaluating oil recovery, as single-wetting state microdevices may under-, or over-estimate the recovery process.